The Proceedings

Fourth International Conference on

Numerical Ship Hydrodynamics

24–27 September 1985
National Academy of Sciences
Washington, D.C.

The
Proceedings

Fourth
International
Conference on

NUMERICAL SHIP HYDRODYNAMICS

Edited by
Justin H. McCarthy

Sponsored by

David W. Taylor
Naval Ship Research and Development Center

Naval Studies Board of the
National Research Council

Office of Naval Research

24-27 September 1985
National Academy of Sciences
Washington, D.C., U.S.A.

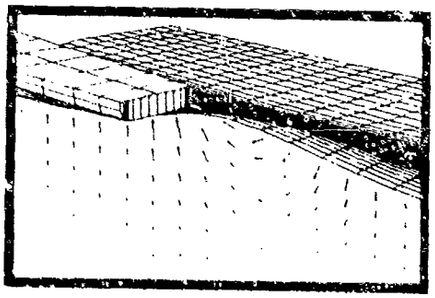

David W. Taylor Naval Ship R&D Center
Bethesda, MD 20084

NOTICE: The project that is the subject of this report was approved by the Governing Board of the National Research Council, whose members are drawn from the Councils of the National Academy of Sciences, the National Academy of Engineering, and the Institute of Medicine. The members of the committee responsible for the report were chosen for their special competences and with regard for appropriate balance.

This report has been reviewed by a group other than the authors according to procedures approved by a Report Review Committee consisting of members of the National Academy of Sciences, the National Academy of Engineering, and the Institute of Medicine.

The National Research Council was established by the National Academy of Sciences in 1916 to associate the broad community of science and technology with the Academy's purposes of furthering knowledge and of advising the federal government. The Council operates in accordance with general policies determined by the Academy under the authority of its congressional charter of 1863, which establishes the Academy as a private, nonprofit, self-governing membership corporation. The Council has become the principal operating agency of both the National Academy of Sciences and the National Academy of Engineering in the conduct of their services to the government, the public, and the scientific and engineering communities. It is administered jointly by both academies and the Institute of Medicine. The National Academy of Engineering and the Institute of Medicine were established in 1964 and 1970, respectively, under the charter of the National Academy of Sciences.

This work related to Department of Navy Contract N00014-85-G-0130 issued by the Office of Naval Research under contract authority NR 201-124. However, the content does not necessarily reflect the position or the policy of the Department of the Navy or the government, and no official endorsement should be inferred.

Copies available from:

Naval Studies Board
National Academy of Sciences
2101 Constitution Avenue
Washington, D.C. 20418

PREFACE

The Fourth International Conference on Numerical Ship Hydrodynamics was held in Washington, D.C., U.S.A., on 24-27 September 1985 at the National Academy of Sciences. The Conference was sponsored jointly by the David W. Taylor Naval Ship Research and Development Center, The Naval Studies Board of the National Research Council, and the Office of Naval Research.

As in the three previous Conferences on Numerical Ship Hydrodynamics, the majority of the papers, presented in the first five sessions, dealt with seakeeping or wave resistance problems. The remaining two sessions dealt with maneuvering of submerged bodies, body geometry and viscous flows on hulls and propeller blades. The papers were of high quality and the opportunities for discussion, during and outside of the formal sessions, were numerous. It was particularly gratifying to see an increase in the number of papers which carefully investigated numerical accuracy, convergence and grid independence of solutions.

The success of the Conference was due to the collective efforts of many individuals. Special thanks go to Mrs. Joan McCoy of DTNSRDC, who served as Secretary to the Conference, for her dedicated assistance with most aspects of the Conference, and to her coworker Mrs. Ruth McClair. In addition we wish to thank Ms. Elizabeth Lucks and Ms. Mary Gordon of the Naval Studies Board for their invaluable and expert help in making all arrangements for the meeting site and hotel reservations for Conference participants.

ORGANIZATION AND PAPERS COMMITTEE

Henry J. Haussling
Thomas T. Huang
Lee M. Hunt
George K. Lea
Choung M. Lee
Hans J. Lugt
Justin H. McCarthy, Chairman
Francis L. Noblesse
Joanna W. Schot

CONTENTS

Keywords: Free surface Green's function; Algorithms; Water waves; Time domain analysis; Ship motion; Hydrodynamic coefficients; Harmonic heave motion; Computational fluid dynamics; Floating bodies; Finite element analysis; Surface waves; Radiation; Diffraction; Nonlinear free-surface conditions; Three-dimensional/potential flow; Ships; boundary layer; Viscous effects; Unsteady hydrodynamic characteristics; Ship hulls/wake; Propeller blades; Vortex generation; Symposia. (EDC)

WELCOMING ADDRESS

Alan Powell

Technical Director, David Taylor Naval Ship R&D Center

On behalf of the David Taylor Naval Ship R&D Center it is a great pleasure for me to join with the Naval Studies Board of the National Research Council and the Office of Naval Research in welcoming all of you to Washington and to the Fourth International Conference on Numerical Ship Hydrodynamics.

Thirty-five papers will be presented over the next three and one half days. More than 150 participants are attending the Conference representing fifteen countries: Australia, Canada, China, Denmark, Finland, France, Germany, Italy, Japan, the Netherlands, Norway, the Soviet Union, Spain, the United Kingdom and the United States. It is truly an international Conference!

This is the fourth Conference in ten years, the first two having been held in the United States in 1975 and 1977 and the third in France in 1981. Each has left its special mark in promoting wider communication among experts in ship hydrodynamics and numerical mathematics. Each has been comprised of a diverse collection of high-quality papers. As in the past Conferences, the majority of papers in the present Conference deal with free-surface flow problems associated with ship wavemaking and ship motions in waves. While these topics, together with cavitation, are unique to ship hydrodynamics, other important topics represented in both the present and past conferences include boundary-layer and vortex flows and specification of geometry.

These are exciting times for us. There are those among us who started off with mechanical desk top calculators. The solutions we will hear about in this Conference would have been beyond belief. Those with their career ahead of them accept these things without question. They accept satellites and their computer control just as we accepted trains and their mechanical signals. A whole new discipline has arisen. We might give some thought to the future as far ahead as the mechanical calculator is behind us when we simply mechanized our hand calculations. Will the complex research program of today become transformed into user-friendly versions for the run-of-the-mill engineer? Probably so. Will the really tough hydrodynamics problems be solved? Probably so.

But more than numerical finesse will be needed. The demand for more knowledge about the physics of fluids will become insistent. One obvious area will be the physics of cavitation and the bubbles of breaking waves and wakes. This emphasizes that a sophisticated numerical solution and their hypnotizing contours do not convey an understanding of the mechanism involved. Only the skilled interpreter will see the message. Therefore will not the need for the type of understanding that comes from analytical methods become even greater? And for physical experiments to match numerical ones? And for numerical experiments to test new hypotheses, which express the essence of a complex phenomenon, or to provide new insights which are fundamentally impossible to do in the real world, such as involve ship flow?

For the full benefits to be gleaned for the benefits of mankind, the various communities need to have a symbiotic, synergistic relationship: the computational scientist, analytical mathematician and physicist and the physical experimenters.

The ship hydrodynamic community, which you so ably represent, is a leader in this respect, and therefore I particularly wish you continued success and a prosperous and technically rich future as well as a rewarding conference.

Finally I would like to express our gratitude to the National Academy of Sciences for hosting the Conference in this lovely auditorium and to the Naval Studies Board of the National Research Council, and the Office of Naval research for joining once again with the Center in sponsoring this Conference. I hope that your stay in Washington will be rewarding both technically and socially. Ladies and gentlemen, welcome!

Session I

LINEAR SEAKEEPING AT FORWARD SPEED

Session Chairman
J.V. Wehausen
University of California
Berkeley, CA, U.S.A.

THE EVALUATION OF FREE-SURFACE GREEN FUNCTIONS

By J. N. Newman
Dept. of Ocean Engineering
Massachusetts Institute of Technology
Cambridge, MA 02139

Summary

Computational methods are described for evaluating the source potential, and its derivatives, in the presence of a linearized free surface. The emphasis is on the use of series expansions, rational-fraction approximations, and multi-dimensional polynomial approximations, as opposed to conventional numerical integration. Appropriate nondimensional source and field-point coordinates are used to reduce the number of independent variables, and different algorithms are used in complementary domains where they are most efficient. With sufficient effort devoted to the development of these algorithms, boundary-integral methods can be applied to linear free-surface problems with little additional computational cost compared to the analagous problems without a free surface.

Specific examples which are treated include the two-dimensional oscillatory source in infinite depth, the three-dimensional oscillatory source in infinite and finite depth, and the three-dimensional transient source in infinite depth. A description is given of a special transient Green function applicable to the axisymmetric exterior domain in a matching approach, and to preliminary work on the steady-state three-dimensional Green function with forward speed.

1. Introduction

The Green function, or source potential, is fundamental to most analytical descriptions of floating or submerged bodies in an ideal fluid. Appropriate formulae for this function are well known [1] in various cases involving a linearized free surface, and a fluid domain which is otherwise unbounded except (optionally) by a fixed horizontal bottom at a finite depth h beneath the free surface.

The use of the free-surface Green function is associated primarily with boundary-integral methods, including the special case of thin-ship theory, and also with the construction of solutions based on multipole expansions of singularities located in the interior of the body. Other techniques such as hybrid finite-element methods, matched boundary-integral solutions, and slender-body theories based on matched asymptotics, utilize the same Green functions (or closely-related potentials such as "wavemaker" solutions) to describe the flow in an exterior domain away from the body. The hybrid or matched boundary-integral techniques can be extended to the analysis of nonlinear numerical solutions, provided the effects of nonlinearity are confined to a finite domain; in this case a linear free-surface Green function may be used to close the solution in the complementary exterior region [2].

The complexity of free-surface Green functions has impeded their use, and has encouraged the development of alternative procedures. Examples of the latter are finite-element methods, and boundary-integral methods based on the elementary "Rankine" Green function, where the fluid domain is regarded as finite or where a numerical radiation condition is employed. The principal drawback of these approaches is that a relatively large computational domain must be accepted in exchange for the simplicity of avoiding the free-surface Green function.

The mathematical complexity of free-surface Green functions should not be regarded as a reason for avoiding their use, but as a challenge in the context of numerical analysis. Given an appropriate library of subroutines, the numerical ship hydrodynamicist should be just as willing to use a free-surface Green function as its simpler Rankine counterpart. In practice, this ideal state requires extensive work, but the effort is justified by the fundamental role of Green functions and by the frequency of their evaluation in practical computations.

The development of appropriate subroutines for the free-surface Green functions is a diverse task. If attention is restricted to the conventional point-source beneath a free surface, we must distinguish between two and three dimensions, finite and infinite depth, and various time-dependences including (1) oscillatory motion, (2) steady translation, (3) combined oscillatory motion with steady translation, and (4) transient motion with the

source strength described by a step-function or delta-function. From this list alone there are 16 cases to be studied.

Nor will the list above satisfy every need. For example, in numerical techniques where the free-surface Green function is employed on a matching boundary, maximum efficiency is achieved by choosing a special Green function which satisfies an appropriate boundary condition on that boundary. (The "wavemaker" solution for an oscillatory vertical wall, or a vertical axisymmetric cylinder, is a closely related expression.) Generally this will imply a more complicated analytic expression for the Green function, but a restricted computational domain in which its values are required.

The classical representation of a free-surface Green function is in the form of a Fourier integral over the appropriate wavenumber space. An obvious computational technique is to evaluate these integrals directly by numerical quadrature. More efficient algorithms can be developed by combining approaches such as

1. Eigenfunction expansions
2. Power-series expansions
3. Asymptotic expansions
4. Continued fractions
5. Multidimensional polynomial approximations

This list is arranged, generally speaking, in increasing order of analytical effort and decreasing order of computational effort. Given this conflicting state, some compromise may be appropriate unless an "ultimate" subroutine is desired. Examples in each category will be described below.

Useful analogies may be drawn with the development of subroutines for the evaluation of special functions of a single variable, such as the Bessel functions. There an extensive literature exists, and a variety of computational methods may be employed. The use of Chebyshev expansions, economized polynomials, and rational-fraction approximations are particularly effective.

In developing subroutines one must consider in advance the desired degree of accuracy, and the generality. To illustrate the latter point one must decide in advance if a conventional Bessel-function subroutine is to be used only for one type of function and order, or for several related functions to be computed simultaneously. Similarly, in the context of the Green function, one must weigh the simplicity and efficiency of a subroutine which only returns values of the function itself against the greater utility and overall efficiency if several derivatives are also evaluated.

It is especially difficult to estimate the necessary degree of accuracy, since this is not easily related to the ultimate accuracy of the overall solution. In the boundary-integral formulation, for example, a large system of simultaneous equations must be solved by algebra after using the Green function and its derivatives to evaluate the coefficient matrix and right-hand-side. Several decimals may be lost in the solution if the system is large, especially in the vicinity of the irregular frequencies.

In using a conventional computing system with single-precision floating-point arithmetic performed to six or seven decimals, it may be appropriate to seek an absolute accuracy of 6D in computations of the Green function. It is obviously desirable to employ algorithms which are sufficiently well conditioned to achieve this level of accuracy without special precautions which increase the computing time, such as the use of double-precision arithmetic. (An example will be described in Section 4 where, in the absence of more extensive analysis, double precision is required.) This concern is less important if a subroutine is written specifically for a system with a more accurate single-precision arithmetic, such as the CDC or Cray machines.

This paper describes several computational approaches for the evaluation of free-surface Green functions. Complete algorithms will be described for four of the sixteen point sources enumerated above, and for one matching boundary. Collectively these represent only a partial solution to the overall problem, but this subset illustrates the range of approaches which ultimately may make a broad variety of free-surface Green functions as transparent to the user as the Rankine source potential.

Section 2 describes algorithms for the relatively simple Green function associated with oscillatory motion in two dimensions and infinite depth. This function is applicable to the strip theory of ship motions, and with minor modifications also to the case of steady translation with constant velocity. Moreover, this Green function is related directly to the complex exponential integral, and thus is useful more generally as a constituent of three-dimensional Green functions. (This connection is illustrated in Section 6.)

In Section 3 we review a comprehensive "ultimate" approach for the three-dimensional oscillatory case, both in infinite and finite depth; this work is described more completely in [3]. In Section 4 a more pragmatic approach is described for the three-dimensional transient point source in infinite depth, and in Section 5 a transient axisymmetric solution is developed for effective use on a circular matching boundary.

In Section 6 preliminary studies are described of the steady translating source in three dimensions, i.e. the "wave-resistance" Green function. The principal result is a pair of Chebyshev-polynomial expansions suitable for the evaluation of the double integral

component when the source and field point have the same transverse coordinate. The latter expansions serve to illustrate the effectiveness of multi-dimensional polynomial approximations in evaluating free-surface Green functions. In the concluding Section 7 a numerical comparison is shown between the steady-state moving source and its transient counterpart set in motion for a finite period of time.

2. Two-Dimensional Oscillatory Source

The Green function for oscillatory motion in two dimensions, with infinite depth, is given by

$$G=[\log(r/r_1)-2\int_0^\infty (k-1)^{-1}e^{-kY}\cos(kX)dk]\cos(\omega t) - 2\pi e^{-Y}\cos X \sin(\omega t) \quad (1)$$

Here (r,r_1) denote the radial distances from the source or its image to the field point, ω is the radian frequency of the motion, t is time, and the wavenumber $K= \omega^2/g$ is used to nondimensionalize the coordinates X,Y of the field point relative to the image source above the free surface. The integral in (1) is defined in the Cauchy principal-value sense. This expression is equivalent to equation 13.31 of Wehausen and Laitone [1], with the source strength set equal to 2π. Note that the nondimensional vertical coordinate Y is defined to be positive, or zero, and the horizontal coordinate X may be assumed non-negative without loss of generality.

We consider only the computation of the integral in (1), which may be replaced by the real part of the complex function

$$F(X,Y) = \int_0^\infty e^{-kY+ikX}(k-1)^{-1}dK \quad (2)$$

One feature of this form is that the derivatives of (2) with respect to X and Y can be evaluated from the same function:

$$F_X = -iF - i(Y-iX)^{-1} \quad (3)$$

$$F_Y = -F - (Y-iX)^{-1} \quad (4)$$

Anticipating the need for (3), both the real and imaginary parts of (2) will be considered in the following analysis.

The integral (2) can be reduced to a standard form involving the complex exponential integral. For this purpose it is convenient to replace the principal-value integral first by a contour passing above the pole, and then change the variable of integration in accordance with the relation $t=(k-1)(Y-iX)$. In this manner it follows that

$$F = e^{-Y+iX}\int_{-Y+iX}^\infty e^{-t}t^{-1}dt + \pi i e^{-Y+iX} = e^z E_1(z) + \pi i e^z \quad (5)$$

where the exponential integral is defined by

$$E_1(z) = \int_z^\infty e^{-t}t^{-1}dt \quad (|\arg z|<\pi) \quad (6)$$

and the complex variable $z=-Y+iX$ has been introduced. The exponential integral is defined with a branch-cut along the negative real axis, and the point z lies in the second quadrant of the complex plane. In the limit where the horizontal coordinate X tends to zero, z must approach the negative real axis from above. The product $e^z E_1(z)$ is a slowly-varying function, with typical magnitude of order one.

The application of the complex exponential integral to the two-dimensional Green function is limited to the second quadrant of the plane $z=x+iy$, since the vertical coordinates of the source and field point must be negative or zero. However the same integral is of interest more generally, and in its application to the steady translating three-dimensional source potential, in Section 6, the complex exponential integral will also be required for values of the argument z in the first quadrant. For this reason we consider here the more general case where z is in either of the first two quadrants. (Quadrants 3 and 4 may be accommodated simply by considering the conjugate of all complex quantities.)

The simplest algorithm for evaluating (5) is based on the ascending power series for E_1, as described in Section 2.1. However this approach is limited to small or moderate values of the modulus of z, and it must be complemented by other algorithms when z is large. Section 2.2 describes a method of evaluation based on the continued-fraction expansion of E_1; this is computationally efficient when the modulus of z is moderate or large, except in a narrow domain where y is small and x takes on moderate negative values, i.e. adjacent to the negative real axis. A third expansion is derived in Section 2.3 to cover the latter domain. The objective in each case is to utilize a finite-series approximation to (6) with a moderate number of terms, which is not subject to serious loss of accuracy due to round-off or cancellation errors. Another desirable feature is to retain an arbitrary degree of accuracy in the computations, adjusting the number of terms in the finite series to suit the desired precision.

The sections which follow are abbreviated from an unpublished report [4] which also contains a Table of the first term in (5), and a FORTRAN subroutine for its evaluation. (In that reference z is restricted to the third quadrant, and a different truncation of the continued fraction is employed.)

2.1 Ascending Series

A series expansion for the Green function follows immediately from the corresponding series for the exponential integral ([5], equation 5.1.11):

$$F(X,Y) = e^{z}\left[-\gamma-\ln(z) - \sum_{n=1}^{\infty} \frac{(-z)^n}{n\ n!} + \pi i\right] \qquad (7)$$

Here γ=.57721566... is Euler's constant. This series is absolutely convergent in the cut z-plane, and computationally efficient when the modulus of z is small.

Programming of (7) is straightforward. The number of floating-point operations for the series can be reduced to one (complex) multiplication and one addition per term, if the coefficients are precomputed and stored in an array, and if nested multiplication is used to evaluate the truncated series. In order to avoid underflow the precomputed coefficients should be multiplied by the corresponding power of the maximum modulus of z (or a number of similar magnitude), and z divided by the same number.

The required number of terms for an absolute accuracy of 6D is shown in Table 1 for the rectangular domain $-10<x<10$, $0<y<8$. For larger values of y, and small values of x, the ascending series suffers from a loss of accuracy due to cancellation. For example, there is a loss of one significant decimal at y=4, x=0. For this reason, as well as the obvious increasing number of terms required, the ascending series should not be used for values of y larger than 4 or 5.

x:	-10	-8	-6	-4	-2	0	2	4	6	8	10
y											
8	32	30	29	28	27	28	30	34	38	42	46
7	31	28	26	25	25	25	27	31	36	40	44
6	29	27	25	23	22	23	25	29	34	38	43
5	28	25	23	21	20	20	22	26	32	36	41
4	27	24	21	19	17	17	20	24	30	35	40
3	26	23	20	17	15	14	17	22	29	34	39
2	26	22	19	16	13	11	15	21	28	33	39
1	25	22	18	15	11	8	13	20	27	33	38
0	25	22	18	15	10		12	20	27	32	38

Table 1 -- Number of terms required in the ascending series (7) for 6D accuracy.

2.2 Continued-Fraction Expansion

The product $e^{z}E_1(z)$ can be expressed in terms of the continued fraction ([5], equation 5.1.22)

$$e^{z}E_1(z) = \frac{1}{z+}\ \frac{1}{1+}\ \frac{1}{z+}\ \frac{2}{1+}\ \frac{2}{z+}\ \frac{3}{1+}\ \frac{3}{z+}\ \cdots \qquad (8)$$

If this sequence is truncated after the term z in the fraction with numerator N, the result is equivalent to the following iteration:

$$F_{N+1} = z \qquad (9)$$

$$F_n = z + nF_{n+1} \ / \ (n + F_{n+1}) \qquad (10)$$

$$e^{z}E_1(z) = 1/F_1 \qquad (11)$$

Each iteration requires two additions, one multiplication, and one division with complex arithmetic.

This algorithm is well conditioned, with no observed loss of significance in the domain where it can be used with a moderate number of iterations. However one should be aware of a set of N poles on the negative real axis in the truncated form of (8), and hence in (9-11). For N<15 these poles are distributed within the blank area of Table 2. Thus the entries shown in Table 2 are safe to use, but difficulties would be encountered close to the negative real axis if an excessive number N were to be employed. (For example, N=4 is sufficient for 6D accuracy at (-16,0), and any larger value of N up to and including N=10 is conservative, but a slight loss of accuracy occurs thereafter, and when N=16 the first quotient in (10) is zero.)

Table 2 shows the starting value N required in (9) for 6D accuracy. This may be compared with the corresponding entries in Table 1 to determine an optimum partition between the domains where the continued fraction and ascending series are used. Since the continued fraction requires two complex additions, one multiplication and one division per term, it is desirable to locate the partition where the number of terms in the continued fraction is about half that of the ascending series.

The asymptotic expansion in inverse powers of z ([5], equation 5.1.51) is a more familiar alternative to the continued fraction (8). The asymptotic expansion is only useful for very large values of the modulus of z, and it offers no apparent advantages relative to (8). Other alternatives logically equivalent to continued fractions are the Pade approximants given by Luke ([6], Table 64.5), and the approximation by a sum of residues given by Hershey [7]. Both of the latter results require the storage of sets of coefficients for each choice of N, and thus are less convenient for programming. (The scheme based on Pade approximation offers a small advantage in computing time, since N-1 floating-point divisions are replaced by multiplications.)

x:	-20	-18	-16	-14	-12	-10	-8	-6	-4	-2	0	2	4	6	8	10	12	14	16
y																			
15	2	2	2	2	2	2	2	2	2	2	2	2	2	2	2	2	2	2	2
14	2	2	2	2	2	2	2	3	3	3	3	2	2	2	2	2	2	2	2
13	2	2	2	2	2	2	3	3	3	3	3	3	3	2	2	2	2	2	2
12	2	2	2	2	2	3	3	3	3	3	3	3	3	2	2	2	2	2	2
11	2	2	2	2	2	3	3	3	3	3	3	3	3	3	2	2	2	2	2
10	2	2	2	3	3	3	3	3	3	3	3	3	3	3	3	2	2	2	2
9	2	2	2	3	3	3	3	4	4	4	4	3	3	3	3	2	2	2	2
8	2	2	2	3	3	3	4	4	4	4	4	4	3	3	3	2	2	2	2
7	2	2	3	3	3	4	4	5	5	5	4	4	3	3	3	3	2	2	2
6	2	2	3	3	4	4	5	6	6	6	5	4	4	3	3	3	2	2	2
5	2	2	3	3	4	5	7	7	8	7	6	5	4	3	3	3	2	2	2
4	2	2	3	3	5	7	9	11	11	10	8	6	4	4	3	3	2	2	2
3	2	3	3	4	7	11	15	18	18	14	10	6	4	4	3	3	2	2	2
2	2	2	3	4	12	22	31	35	36	28	15	7	5	4	3	3	2	2	2
1	2	3	3	11	39	78				94	30	9	5	4	3	3	3	2	2
0	2	3	3									9	5	4	3	3	3	2	2

Table 2 -- Number N required for 6D accuracy in the continued-fraction recursion (9-11). Blank entries indicate no convergence at N=99, or poles encountered on the real axis before convergence.

2.3 Expansion for Small y/x

Anticipating the need for a third expansion in the region near the negative real axis, when $|z|$ is not small, the integrand of (2) can be expanded in powers of iky and, for $x<0$, integrated term-by-term [4]. Alternatively, without restriction to $x<0$, the product $e^z E_1(z)$ may be expanded in a Taylor series about $y=0$. Proceeding in the latter manner we first observe that

$$\frac{d^n}{dz^n}\left(e^z E_1(z)\right) = e^z E_1(z) + \sum_{m=1}^{n} \frac{(m-1)!}{(-z)^m} \qquad (12)$$

It follows that for $x>0$

$$e^z E_1(z) = \sum_{n=0}^{\infty} \frac{(iy)^n}{n!} \left[e^x E_1(x) + \sum_{m=1}^{n} \frac{(m-1)!}{(-x)^m} \right] \qquad (13)$$

For negative values of x, in quadrant 2, $E_1(x)$ is replaced by $E_1(-x+i0) = -Ei(|x|) - i\pi$, where Ei denotes the principal-value exponential integral ([5], equation 5.1.2). Combining these results, (5) may be evaluated directly from the expansion

$$F(X,Y) = \sum_{n=0}^{\infty} \frac{(iX)^n}{n!} \left[\sum_{m=1}^{n} \frac{(m-1)!}{Y^m} - e^{-Y} Ei(Y) \right] \qquad (14)$$

The double-series (13-14) are convergent for $y<|x|$. If the coefficients $1/n$ are predetermined and stored, each term in the sum over n requires two additions and five multiplications, in real arithmetic, or about the same number of floating-point operations as in the ascending series.

For a given accuracy, the number of terms required in (13-14) depends primarily on the ratio y/x. The entries in Table 3 are practically independent of x, throughout the domain of interest.

Standard approximations or subroutines may be used to evaluate the real exponential integrals $E_1(x)$ and $Ei(-x)$, but it is more efficient to derive special approximations for the particular ranges where (13) or (14) is to be used. Special rational-fractions are given in [4] with minimax accuracy for the range $-16<x<-8$.

y/|x|:	0.1	0.2	0.3	0.4	0.5
	5	7	10	13	17

Table 3 -- Maximum value of index n required for 6D accuracy in (13-14).

2.4 Conclusions

The three algorithms described above can be used to evaluate the function $e^z E_1(z)$ and its derivatives, with six decimals absolute accuracy. The tables presented permit a determination of the optimum domain for each algorithm, and of the number of terms required. Partitions between the three algorithms can be selected as follows:

Quadrant 1

$2x+y < 4$: ascending series (7)
$2x+y > 4$: continued fraction (8-9)

Quadrant 2

-8<x<0 and y<4:	ascending series
y>4 or 3y>2x+32:	continued fraction
-10<x<-8 and y<4:	double series (14)
-16<x<-10 and 3y<2x+32:	double series (14)

For application specifically to the 2D oscillatory Green function, where both terms in (5) must be evaluated, a maximum of 1.2 milliseconds is required on the VAX 11/750. Only the ascending series requires more than 0.7 milliseconds. Since the double-series (14) is substantially faster than the ascending series, in the domain where both may be used, some gain in average computing time would follow by using the double series for the domain where $y/|x|<0.5$ and $-8<x<4$.

The approach followed here should be compared with that described below in Section 3.1 for the analogous three-dimensional Green function. In both cases analytical expansions are used in appropriate sub-domains, and there are close relationships between the respective formulae. Unlike the three-dimensional case, we compromise here stopping short of the development of economized polynomial approximations which replace or supplement the analytic expansions where relatively large numbers of terms are required. In the two-dimensional case polynomial approximations could be derived with some additional effort, with a probable improvement in the maximum computational time on the order of 20-40%, but with the need to store large arrays of polynomial coefficients. Another advantage of leaving the results in their present form is that the accuracy can be controlled by modifying the number of terms retained in each expansion and the partitions between their respective domains.

3. Three-Dimensional Oscillatory Source

The three-dimensional Green function of oscillatory strength is especially important in the analysis of offshore structures, and a variety of panel and finite-element programs have been developed for use in this field. Here we present in abbreviated form a summary of the algorithms which are described in [3].

3.1 Infinite-depth case

In three dimensions the analogue of the integral in (2) is ([1], equation 13.17)

$$F(X,Y) = \int_0^\infty \frac{k+1}{k-1}\, e^{-kY}\, J_0(kX)\, dk \qquad (15)$$

Here J_0 denotes the Bessel function of the first kind, order zero, and X is the nondimensional horizontal distance between the source and field points. (In addition, the total three-dimensional Green function includes the Rankine source and an imaginary term equal to half of the residue from the singularity in (15).) The essential task is to evaluate F(X,Y) for all possible values of the two arguments, or throughout the quadrant where X and Y are nonnegative.

For this particular case an alternative integral representation exists in the form

$$F(X,Y) = (X^2+Y^2)^{-\frac{1}{2}} - \pi e^{-Y}[H_0(X)+Y_0(X)] - 2\int_0^Y e^{t-Y}(X^2+t^2)^{-\frac{1}{2}}\, dt \qquad (16)$$

where H_0 denotes the Struve function ([5], Chapter 12). Direct numerical integration of (16) is relatively easy, unless the coordinate X is small, but this procedure is less efficient than the algorithms described below.

For sufficiently small values of X the Bessel function in (15) can be expanded in even powers of kX and integrated term-by-term. The result is a double infinite series ([3], eq. 4) with positive powers of X and negative powers of Y. This expansion was first derived by Hess and Wilcox [8] and subsequently by Noblesse [9]. The domain of convergence is X<Y. For 6D accuracy this series can be truncated with $n \le 9$, provided $X/Y<0.5$. The analogy with (14) should be noted.

An alternative series expansion ([3], eq. 5) is derived [10] by expanding the last exponential in (16) in powers of t, and integrating term-by-term. This series involves positive powers or both coordinates (X,Y) and is uniformly convergent throughout the full domain of interest. A comparison may be noted with the ascending series (7) for the two-dimensional Green function. If this series is truncated, and economized in both variables, 6D accuracy can be achieved in the domain $0<X<3.7$, $0<Y<2$ with a total of 33 terms in the resulting polynomial.

When the ratio X/Y is large, an asymptotic expansion can be derived by expanding the inverse square-root in (16) in even powers of t/X and integrating term-by-term. The resulting series ([3], eq. 6) involves positive powers of Y and negative even powers of X. Truncation with four terms gives 6D accuracy in the domain $X>3.7$ provided $X/Y>4$. The same accuracy can be achieved throughout the domain $2<X/Y<4$ if the series is transformed to a continued fraction.

Finally, when both X and Y are large, the integral in (15) may be integrated repeatedly by parts to yield an asymptotic expansion where the integrated terms are spherical harmonics ([3], eq. 8). Truncating this asymptotic expansion with five terms gives 6D accuracy throughout the domain $X>8$, $Y>20$.

At this stage relatively simple expansions have been developed for all but a central domain of the X,Y quadrant. The remaining task is to seek numerical approximations more directly, for intermediate values of the co-

ordinates. The last asymptotic expansion is used as a guide to suggest a form ([3], eq. 9) where the residual factor R(X,Y) is slowly-varying, throughout this domain, and can be approximated by two-dimensional polynomials. The numerical procedure used for this purpose can be described briefly as follows. The function R(X,Y) is evaluated with double-precision accuracy in the manner outlined in [11]. Double Chebyshev polynomial expansions are then generated for this function, and truncated to the desired accuracy by neglecting all coefficients smaller than the prescribed tolerance. Conversion of the Chebyshev expansions to finite double series in ordinary powers of X and Y facilitates the subsequent routine use of the algorithm. It has been found that subdividing the central domain at Y=4 and again at Y=8 enables R(X,Y) to be approximated in each of the three subdomains with a maximum of 37 nonzero polynomial coefficients.

Collectively, the algorithms described above serve to evaluate the infinite-depth Green function for all relevant values of X and Y. The derivatives of the source potential can be obtained by analytic differentiation of the same algorithms.

3.2 The finite-depth case

The oscillatory source potential in a fluid of finite depth h is expressed either by an integral analogous to (15), or by an eigenfunction expansion which has certain features in common with (16). These two alternative expressions ([3], eqs. 10a,b) are given by Wehausen and Laitone ([1], eqs. 13.18-19).

The eigenfunction expansion is summed directly, over the spectrum of real and imaginary wavenumbers defined by the roots of the transcendental equation $k\tanh(kh)=K$, where K is the infinite-depth wavenumber. These roots can be found efficiently from a second-order Newton-Raphson algorithm, which requires only one iteration for 6D accuracy. Each term involves the modified Bessel function K_0 as a factor, with its argument the product of the imaginary root and the horizontal radial coordinate R. Thus the convergence is exponential, for moderate or large values or R/h. A maximum of 12 terms gives 6D accuracy in the domain $R/h>1/2$. Since the argument of the modified Bessel function is greater than $\pi/4$ in this domain, a single rational-fraction approximation can be used to evaluate this function.

For small values of R/h the eigenfunction expansion is not efficient, and the integral representation analogous to (15) must be used as a starting point. A total of four nondimensional parameters are involved in this integral, by comparison to only two in the infinite-depth case. However the product formula for hyperbolic cosines can be employed to express the original integral as the sum of two terms involving the auxiliary function

$$L(X,V,H) = (X^2 + V^2)^{-\frac{1}{2}} + \int_0^\infty \frac{(k+1)\cosh(KV)}{k\sinh kH - \cosh kH} e^{-kH} J_0(kX)\,dk \qquad (17)$$

Here X has the same meaning as in Section 3.1, H is the nondimensional depth Kh, and V is a nondimensional vertical parameter in the range between 0 and 2H. Anticipating the approximation of the integral in terms of multi-dimensional polynomials, the replacement of one function of four parameters by two evaluations of a function with only three parameters represents a major simplification.

The rate of convergence of the last integral can be accelerated by adding and subtracting an appropriate function which is asymptotically equivalent to the integrand for large k. A judicious choice for this function leads to the result

$$L(X,V,H) = (X^2+V^2)^{-\frac{1}{2}} + F(X,2H-V) + F(X,2H+V) + \int_0^\infty \left(\frac{1}{k\sinh kH - \cosh kH} - \frac{2e^{-kH}}{k-1} \right) (k+1)\cosh(kV)e^{-kH}J_0(kX)\,dk \qquad (18)$$

As k tends to infinity the integrand in (18) is of order $\exp(-2kH)$ or smaller. The two additional functions F in this decomposition are the integrals of the two portions of the function subtracted from the integrand which correspond to the expansion of the hyperbolic cosine $\cosh(kV)$ in a pair of exponential functions, and hence are identical to the infinite-depth source potential (15) with indicated values of the vertical coordinate.

The regular behavior of the integral which remains in (18) implies that it can be expanded as a polynomial in even powers of the coordinates X and V, multiplied by polynomials in H. The derivation of these approximations is described in [3]. With partitions at H=2 and H=4, approximately 300 coefficients are needed in each subdomain to achieve 6D accuracy. In the usual application where many evaluations are required with different values of X,V, for the same H, the polynomials in H can be evaluated and stored as a total of 33 nonzero coefficients for the remaining two-parameter polynomials in X and V.

The procedure just described uses the infinite-depth Green function to aid in the computation for finite depth. The respective integrands with respect to the dummy variable k are asymptotically identical for large values of k, corresponding physically to the fact that the finite depth is not significant for very short wavelengths. In the mathematical context, the difference between the

finite- and infinite-depth integrals is more rapidly convergent, hence more regular, and therefore is more amenable to approximation by polynomials. The same procedure can be used to accelerate the convergence when the finite-depth integral representation is evaluated directly by numerical quadratures; this approach has been used by Boreson and Faltinsen [12] in the more complicated case of the oscillatory source potential moving with constant forward velocity.

4. The Three-Dimensional Transient Source

The potential of a submerged point source with arbitrary time dependence, in a fluid of infinite depth, is given by Wehausen and Laitone ([1], eq. 13.49). We shall analyse the case where the source strength is a unit step function, jumping from zero to one at time t=0. The source with delta-function time dependence can be obtained by differentiation, and arbitrary time-dependent motions can be obtained by convolution.

In its dimensional form, the step-function source potential can be expressed in the equivalent forms

$$G = \frac{1}{r} - \frac{1}{r_1} + 2\int_0^\infty [1-\cos(g^{\frac{1}{2}}k^{\frac{1}{2}}t)]J_0(kx_1)e^{-ky_1}dk$$
$$= \frac{1}{r} + \frac{1}{r_1}$$
$$-2\int_0^\infty \cos(g^{\frac{1}{2}}k^{\frac{1}{2}}t)J_0(kx_1)e^{-ky_1}dk \qquad (19)$$

Here (r,r_1) denote the distances from the source or its image above the free surface to the field point, (x_1,y_1) denote the horizontal and vertical components of r_1, and y_1 is defined to be positive. If the last form of (19) is nondimensionalized with respect to r_1, and $\theta = \cos^{-1}(y_1,r_1)$, it follows that

$$G = \frac{1}{r} + \frac{1}{r_1}$$
$$-\frac{2}{r_1}\int_0^\infty \cos(k^{\frac{1}{2}}\tau)J_0(k\sin\theta)e^{-k\cos\theta}dk \qquad (20)$$

where the nondimensional time $\tau = t(g/r_1)^{\frac{1}{2}}$.

In the special case $y_1 = 0$ the integral in (20) may be expressed in a particularly simple form involving products of Bessel functions of fractional order ([1], eq. 22.18 et seq.). Effective algorithms for evaluating these Bessel functions are given by Luke ([6], Tables 35 and 39).

In order to derive more general expansions it is convenient to regard the integral in (20) as the real part of the complex function

$$F = -2\int_0^\infty e^{ik^{\frac{1}{2}}\tau}J_0(k\sin\theta)e^{-k\cos\theta}dk \qquad (21a)$$
$$= -4\int_0^\infty e^{i\omega\tau}J_0(\omega^2\sin\theta)e^{-\omega^2\cos\theta}\omega d\omega \qquad (21b)$$

If the complex exponential in (21a) is expanded in a Taylor series, the integral of each term may be evaluated ([13], section 13.21, eq. 3). In this manner the following expansion is obtained in spherical harmonics:

$$F = -2\sum_{n=0}^{\infty}\frac{(i\tau)^n}{n!}\Gamma(\tfrac{1}{2}n+1)P_{\frac{1}{2}n}(\cos\theta) \qquad (22)$$

where Γ is the gamma function and $P_{n/2}$ is the Legendre function of the first kind. The real part of (22) involves only the Legendre polynomials, and has been derived by Terazawa [14].

The expansion (22) is effective for small or moderate values of the time parameter τ. Only the real part is of physical relevance, and since forward recursion is stable for the Legendre polynomials it is remarkably simple to evaluate this component of (22). However the number of terms required for a given accuracy increases in proportion to τ, and for large values of τ there is a loss of significant figures due to cancellation error; since the number of decimals lost is approximately equal to $0.1\tau^2$, double precision must be used for values of τ greater than 3 or 4, and extended precision is required beyond $\tau = 10$.

An asymptotic analysis of (21b) reveals two distinct contributions. The first is from the lower limit of integration, where repeated integration by parts yields an asympotic expansion in inverse powers of time:

$$F \sim -4\sum_{n=1}^{}(i/\tau)^n\left[\frac{\partial^{n-1}}{\partial\omega^{n-1}}J_0(\omega^2\sin\theta)e^{-\omega^2\cos\theta}\omega\right]_{\omega=0}$$
$$= 4\sum_{n=0}^{}\frac{(2n+1)!}{n!}\tau^{-2n-2}P_n(\cos\theta) \qquad (23)$$

In an exponentially thin layer near the free surface an additional wave-like component exists, analogous to the more familiar Cauchy-Poisson problem. This component is associated with the contribution to (21b) near $\omega = \frac{1}{2}i\tau e^{-i\theta}$, where the product of the exponential and Bessel functions is temporarily stationary. Systematic asymptotic expansion of the Bessel function, for large values of its argument, and then of the resulting integral, yields a sequence of terms with negative powers of τ^2. From this analysis the following result is obtained, after adding the slowly-varying component (23):

$$F \simeq 4 \sum_{n=0} \frac{(2n+1)!}{n!} \tau^{-2n-2} P_n(\cos\theta)$$

$$-2\left(\frac{2}{\sin\theta}\right)^{\frac{1}{2}} \exp[-\tfrac{1}{4}\tau^2 e^{-i\theta} - \tfrac{1}{2}i(\theta - \tfrac{\pi}{2})] \cdot$$

$$\{1 - \tfrac{1}{2}iw^{-1} + (3iv - \frac{9}{8})w^{-2}$$

$$+(-30iv^2 + \frac{45}{2}v + \frac{75}{16}i)w^{-3}$$

$$+(420iv^3 - \frac{945}{2}v^2 - \frac{1575}{8}iv + \frac{3675}{128})w^{-4}$$

$$+ O(w^{-5})\} \qquad (24)$$

where $v = \sin\theta e^{-i\theta}$

and $w = \tau^2 \sin\theta e^{-2i\theta}$

An equivalent expression to (24) is derived by Beck and Liapis [15] using an asymptotic analysis based on the Dawson integral.

The three expansions (22-24) can be used collectively to evaluate (19) and its derivatives, for all possible values of the coordinates and time. To achieve six decimals accuracy for the Green function and its first derivatives, the real part of (22) is summed in double precision, for values of τ^2 less than $75 + 10 \cos\theta$, with the total number of terms equal to $[18+0.74\tau^2]$. For larger values of time the asymptotic expansion (24) is used, and the slowly-varying component (23) is used alone when $\cos\theta > 0.95$. Typical computing times are a few milliseconds on the VAX 11/750.

Further computational efficiency could be achieved by deriving polynomial approximations in two nondimensional variables, analogous to those developed in Section 6 for the steady translating Green function. The asymptotic form (24) provides a convenient starting point for such an extension; if the factor in braces is expressed in double economized polynomials, the validity of (24) may be extended to smaller values of time. This would obviate the summation of (22) in double precision, and substantially reduce the maximum computing time.

5. The Transient Axisymmetric "Wavemaker"

In the development of a matching analysis, such as the hybrid finite-element method, or the boundary-integral technique used in [2] to study nonlinear forced motions of an axisymmetric body, a linear solution is constructed in an exterior domain of the fluid, and connected to the complementary interior solution on a cylindrical matching boundary. The free-surface point source can be used to construct the exterior solution, from an appropriate distribution on the matching boundary. However the solution is improved in efficiency and accuracy if a more complicated Green function is employed which satisfies a delta-function Neumann boundary condition on the matching boundary. (This situation is analogous to the conventional utilization of Green's theorem, where the "dipole" term with density equal to the unknown potential can be removed by the use of a source potential which satisfies a homogenous Newmann condition on the boundary. In matching interior and exterior solutions the use of such a Green function serves only to eliminate one integral inversion for the unknown potential on the matching boundary.)

From the physical standpoint, the desired Green function can be interpreted as the solution of a cylindrical "wavemaker" problem where the prescribed normal velocity is a delta-function at an arbitrary position on the wavemaker boundary; the more general solution with continuous normal velocity follows by an appropriate distribution of this singular solution. For harmonic time-dependence Havelock's [16] solution for an axisymmetric wavemaker is generally used in hybrid finite-element solutions (cf. Mei [17]).

For time-domain analyses it is necessary to find a solution of Laplace's equation in the domain exterior to a vertical circular cylinder, subject to the same conditions as (19) but with an additional homogeneous Neumann condition imposed on the cylinder. Alternatively, if the source point is on the cylinder, the radial derivative on this boundary is given by a delta function.

In hybrid matching applications the exterior solution is required only on the matching boundary, hence the source and field points are both restricted to this domain. This implies a reduction in the number of independent variables which must be accomodated in the numerical analysis of the Green function.

Here we consider the special case where the fluid motion is axisymmetric, and the desired Green function has the same property. The radial components of the source and field points are ultimately restricted to be equal to the cylinder radius, and this radius is used to nondimensionalize the radial and vertical coordinates (r,z). If the radial velocity on the cylinder is a delta function in time, and also in space, the Green function must satisfy the boundary condition

$$\frac{\partial G}{\partial r} = \delta(z-\zeta)\delta(t) \qquad (25)$$

on $r=1$.

Following a familiar procedure for point sources ([1], section 13) a solution is derived in the form of an elementary "Rankine" singularity, a negative image above the free surface, and a regular function which ensures that the sum satisfies the free-surface condition.

Considering the Rankine singularity first, we seek a harmonic function for all values of z, regular throughout the domain r>1 and satisfying the boundary condition (25). Excluding the time-dependent factor, the solution can be obtained by separation of variables and Fourier integration, in the form

$$G_R(r,z;\zeta) = \frac{-1}{\pi}\int_0^\infty \cos k(z-\zeta)\,\frac{K_0(kr)}{kK_1(k)}\,dk \qquad (26)$$

Here the subscript R is used to denote the Rankine singularity, and K_n is the modified Bessel function of the second kind.

It is convenient to recast (26) in an alternative form. Following the notation of [5], Section 9.6, the Hankel function of imaginary argument may be substituted in place of K_n, with the result

$$G_R = \mathrm{Re}\,\frac{i}{\pi}\int_0^{i\infty}\frac{H_0^{(1)}(ur)}{uH_1^{(1)}(u)}\,e^{-u|z-\zeta|}du$$

$$= \frac{1}{\pi}\int_0^\infty \frac{J_0(ur)Y_1(u)-J_1(u)Y_0(ur)}{u[J_1^2(u)+Y_1^2(u)]}\,e^{-u|z-\zeta|}du \qquad (27)$$

The last expression follows by deforming the contour of integration, and ignoring the contribution from a circular quadrant at infinity which is exponentially small if r>1.

For the solution of the free-surface boundary condition, the obvious extension from the corresponding point-source solution analogous to (19) takes the form

$$G = \delta(t)[G_R(r,z;\zeta) - G_R(r,z;-\zeta)]$$

$$+\frac{2}{\pi}\int_0^\infty \frac{J_0(ur)Y_1(u)-J_1(u)Y_0(ur)}{u^{\frac{1}{2}}[J_1^2(u)+Y_1^2(u)]}$$

$$e^{u(z+\zeta)}\sin(u^{\frac{1}{2}}t)du \qquad (28)$$

where the time t has been nondimensionalized in terms of the cylinder radius and g.

The limiting value of (28) on the cylinder can be interpreted in a direct manner. Taking advantage of the Wronskian for the Bessel functions, the final expression for the Green function is given by

$$G(1,z;\zeta;t) = \delta(t)[G_R(|z-\zeta|) - G_R(|z+\zeta|)]$$

$$+ G_F(|z+\zeta|,t) \qquad (29)$$

where

$$G_R(z) = -\frac{2}{\pi^2}\int_0^\infty \frac{dk}{k^2(J_1^2+Y_1^2)}\,e^{-kz} \qquad (30)$$

and

$$G_F(z,t) = -\frac{4}{\pi^2}\int_0^\infty \frac{dk}{k^{3/2}(J_1^2+Y_1^2)}\,e^{-kz}\sin(k^{\frac{1}{2}}t) \qquad (31)$$

In a collocation method where the Green function is integrated over vertical segments, the integrals of (30) and (31) with respect to z may be performed analytically.

For nonzero values of z, the integrals (30) and (31) may be evaluated numerically. In a time-stepping procedure it is effective to calculate (31) simultaneously for several values of t. In evaluating the integrands, for values of k larger than (say) 3, polynomial or rational-fraction approximations [18] for the modulus of the Hankel function should be used in preference to computing the two Bessel functions separately. The apparent singularity at k=0 is cancelled by the singular behavior of Y .

The Rankine integral (30) is a function of only one variable, and can be approximated by conventional techniques. With the coefficients listed in Table 4, the following polynomial approximations are accurate to between 6 and 7 significant figures, for all values of z:

0<z<2:

$$G_R \approx \sum_{n=0}^{7} a_n z^n + \sum_{n=0}^{3} b_n z^n \log z \qquad (32)$$

2<z<∞:

$$G_R \approx z^{-3}\log z + \sum_{n=0}^{8} c_n z^{-n-1} \qquad (33)$$

n	a_n	b_n	c_n
0	-1.451670E-01	3.183099E-01	-4.999995E-01
1	-2.500060E-01	-5.968310E-02	-4.023183E-04
2	6.337102E-02	6.527839E-03	-2.524457E-01
3	3.097314E-02	-8.198656E-04	-3.756222E+00
4	-6.579578E-03		2.193911E+01
5	-4.254071E-03		-5.918514E+01
6	1.387933E-03		9.681989E+01
7	1.008506E-04		-8.950611E+01
8			3.572895E+01

Table 4 -- Coefficients for the polynomial approximations (32-33).

6. The wave-resistance Green function

The Green function for three-dimensional motion with constant horizontal velocity U has been widely studied in connection with the theory of wave resistance. Restricting our attention to the case of infinite depth, the basic expression for the source potential is given by Wehausen and Laitone [1], equation 13.36, as the sum of a double integral and a single integral, together with the usual Rankine singularity ($1/r$) and its image ($1/r_1$) above the free surface. If the coordinates are normalized by the wavenumber g/U^2, and (X,Y,Z) are the Cartesian components of r_1 with Z defined to be positive downwards, the Green function may be expressed in the form

$$G = \frac{1}{r} - \frac{1}{r_1} - \frac{2}{\pi}\int_{-\pi/2}^{\pi/2} \sec^2\phi \ \mathrm{Re}\{e^u E_1(u)\}\, d\phi + 4\int_{-\pi/2}^{-\alpha} \sec^2\phi \ \mathrm{Im}\{e^u\}\, d\phi \qquad (34)$$

where

$$u(\phi) = \sec^2\phi(-Z + iX\cos\phi + i|Y|\sin\phi) \qquad (35)$$

and $\alpha = \tan^{-1}(X/|Y|)$ is the polar angle in the horizontal plane.

Note that in the first integral of (34) the complex exponential integral E_1 is used to replace the more conventional "double integral". The latter designation will be retained, despite the simpler appearance of this term in (34), to distinguish it from the "single" integral in the last term.

Extensive studies of this Green function have been made by Noblesse (cf.[19] and [20]) and Euvrard [21]. The last two references emphasize an alternative form for the source potential with some computational advantages:

$$G = \frac{1}{r} - \frac{1}{r_1} - \frac{2}{\pi}\int_{-\pi/2}^{\pi/2} \cos\phi \ \mathrm{Im}\{e^v E_1(v)\}\, d\phi - 4\,H(-X)\int_{-\pi/2}^{\pi/2} \sec^2\phi \ \mathrm{Im}\{e^u\}\, d\phi \qquad (36)$$

where

$$v(\phi) = -Z\cos^2\phi + Y\cos\phi\sin\phi + i|X|\cos\phi \qquad (37)$$

and $H(x)$ denotes the Heaviside unit step function.

Traditionally it has been thought that the greatest computational effort must be devoted to the double integral in (34) or (36), but if efficient subroutines are available for the product $e^z E_1(z)$, then such a conclusion is naive. In a more careful analysis one must note that the single integral, or last term is not only wave-like, but also singular in a complicated manner along the track downstream of the source, when Z=0. By comparison the double integral in (36) is regular, except for a weak logarithmic singularity at the origin. Nevertheless, accurate evaluation of this integral by means of numerical quadratures requires a substantial number of ordinates to accomodate the singularity at the lower limit of integration.

We shall consider here the special case Y=0, where the source and field points are in the same longitudinal vertical plane. In this case a comparison of (34) and (36) indicates that the respective double integrals are identical in value, and either form may be used as a starting point in the analysis. Numerical integration can be applied to either form, but a substantial computational burden is involved to achieve even modest precision.

To provide a more effective technique for evaluation of the double integral, we shall derive approximations in terms of two-dimensional expansions involving Chebyshev polynomials. Polar coordinates (R,θ) are used in the vertical plane, with $X=R\sin(\theta)$ and $Z=R\cos(\theta)$. Note that the polar angle θ is restricted to the interval $(0,\pi/2)$, and while the double integral is an even function of X, the discontinuity when X=0 precludes effective polynomial approximations involving only even powers of θ.

In the "near-field" domain, $0<R<2$, the approximation is sought in the form of polynomials in R and θ, after subtracting a three-term asymptotic approximation of the logarithmic singularity at R=0. In the complementary domain, R>2, the asymptotic form of the double integral is used to suggest an appropriate form for the approximation in negative powers of the radius.

6.1 Near-field approximation

In the domain $0<R<2$, the principal task is to account for the singular behavior at the origin. Proceeding with the double integral as it is expressed by (36), this behavior is associated with the logarithmic singularity of the exponential integral (cf. equation 7). This leads us to consider the component

$$\frac{2}{\pi}\int_{-\pi/2}^{\pi/2} \cos\phi \ \mathrm{Im}\{e^v \log(v)\}\, d\phi$$

$$\sim \frac{2}{\pi}\int_{-\pi/2}^{\pi/2} \cos\phi \ \mathrm{Im}\{(1+v+\tfrac{1}{2}v^2+\ldots)\log(v)\}\, d\phi$$

$$= 2I_1 + 2XI_2 - (2Z + X^2)I_3 - 2XZI_4 + Z^2I_5 + \ldots \qquad (38)$$

where

$$I_n = \frac{2}{\pi} \begin{pmatrix} \mathrm{Re} \\ \mathrm{Im} \end{pmatrix} \int_0^{\pi/2} \cos^n\theta \, \log(-Z\cos\theta + iX)\, d\theta$$

$$\text{for } n = \begin{pmatrix} \text{even} \\ \text{odd} \end{pmatrix} \tag{39}$$

Note that a factor $\cos(\theta)$ has been deleted from the argument of the logarithmic function in (39), to simplify the analysis. This is justified since the contribution from this factor to (39) is independent of X and Z and hence regular in terms of (38). (One convenient feature of this type of numerical analysis is that contributions which are regular can be ignored temporarily!)

To evaluate the integrals (39) in a systematic manner, we first integrate the derivative of the integrand, multiplied by $\tan(\theta)$, to obtain the recurrence relation

$$nI_n = (n-1)I_{n-2} + \Lambda_n \qquad (n=2,3,4,\ldots) \tag{40}$$

where

$$\Lambda_{2n} = \frac{2}{\pi} Z^2 \int_0^{\pi/2} \frac{\sin^2\theta \, \cos^{2n}\theta}{Z^2\cos^2\theta + X^2} \, d\theta \tag{41}$$

and

$$\Lambda_{2n+1} = (X/Z)\Lambda_{2n} \tag{42}$$

Algebraic reduction of the integrand in (41) yields the recurrence relation

$$\Lambda_{2n} = -(X/Z)^2 \Lambda_{2n-2} + \frac{1\cdot3\cdot\ldots\cdot(2n-3)}{2\cdot4\cdot\ldots\cdot(2n)} \tag{43}$$

Appropriate starting values for these recurrence relations are given by the corresponding elementary integrals, and it follows that

$$I_0 = \log\left(\frac{R+X}{2}\right) \tag{44}$$

$$I_1 = 1 + \left(\frac{R-X}{R+X}\right)\frac{1}{4} \tag{45}$$

$$\Lambda_2 = \frac{1}{2}\left(\frac{R-X}{R+X}\right) \tag{46}$$

The coefficients in (38) can be evaluated to an arbitrary order of approximation, using (39-46). Here we include the second-order terms displayed in (38), regard this as an approximation for the singularity of the double integral at the origin, and expand the remaining "regular" function in a double Chebyshev series:

$$-\frac{2}{\pi}\int_{-\pi/2}^{\pi/2} \cos\phi \ \mathrm{Im}\{e^{v}E_1(v)\}\, d\phi$$

$$= 2I_1 + 2XI_2 - (2Z+X^2)I_3 - 2XZI_4 + Z^2I_5$$

$$+ \sum_{m=0}^{M}{}' \sum_{n=0}^{N}{}' C_{mn}\, T_m(1-\tfrac{1}{2}R)\, T_n(-1+\frac{4}{\pi}\theta)$$

$$(0 < R < 2, \quad 0 < \theta < \tfrac{\pi}{2}) \tag{47}$$

Here $T_n(x)$ is the usual notation for the Chebyshev polynomial ([5], ch. 22), and we follow the convention [22] where the primed summation denotes that the terms m=0 or n=0 are halved (thus the term m=n=0 is multiplied by one-fourth).

The coefficients shown in Table 5 may be used in (47) to evaluate the double integral with approximately 4 decimals absolute accuracy. These coefficients have been evaluated by means of the orthogonality relations for the Chebyshev polynomials, evaluation of the integral in (47) by Romberg quadrature, and subtraction of the singular terms on the right side of this equation. As in the more conventional representation of a function of one variable, the convergence and accuracy of this scheme can be confirmed by the rate at which the coefficients in Table 5 tend to zero.

6.2 Far-field approximation

To complement the results derived above, we now consider the approximation of the double integral for the domain R>2. For sufficiently large values of the radial coordinate R, the asymptotic approximation of $e^{u}E_1(u)$ suggests that the double integral in (34) can be expanded in negative powers of R. (For the details of the corresponding asymptotic expansion see [19].) Thus we seek a systematic approximation in the form

$$-\frac{2}{\pi}\int_{-\pi/2}^{\pi/2} \cos\phi \ \mathrm{Im}\{e^{v}E_1(v)\}\, d\phi$$

$$\simeq \sum_{m=1} f_m(\theta) R^{-m}$$

$$\simeq \sum_{m=0}^{M}{}' \sum_{n=0}^{N}{}' C_{mn}\, T_m(-1+\frac{4}{R})\, T_n(-1+\frac{4}{\pi}\theta)$$

$$(2 \le R < \infty, \quad 0 \le \theta \le \tfrac{\pi}{2}) \tag{48}$$

After proceeding in an analogous manner to that described at the end of Section 6.1, the coefficients shown in Table 6 are evaluated. It should be emphasized that the asymptotic expansion of the double integral has been used here only to deduce an appropriate form for the polynomial approximation, and that the latter has a much wider range of validity than the formal asymptotic expansion.

m	n=0	1	2	3	4	5	6	7
0	-0.26491	0.53367	-0.69926	-0.22860	0.06774	0.01049	-0.00219	-0.00018
1	-0.08190	-0.52550	0.51353	0.16520	-0.04838	-0.00725	0.00154	0.00012
2	0.22182	0.28929	-0.17935	-0.05469	0.01601	0.00204	-0.00048	
3	-0.00796	-0.02631	0.01490	0.00275	-0.00132			
4	0.00044	-0.00360	0.00069	0.00079	-0.00017			
5	0.00006	-0.00055	-0.00007	0.00019				
6		-0.00011						

Table 5 -- Chebyshev coefficients for 0<R<2. (Blank entries are less than 5E-05 in magnitude.)

m	n=0	1	2	3	4	5
0	1.89175	-0.26534	0.02978	-0.00433	0.00011	
1	0.91714	-0.16691	0.02386	-0.00410	0.00040	-0.00006
2	-0.03689	-0.02545	0.00897	-0.00229	0.00050	-0.00009
3	-0.00848	0.00984	-0.00151	0.00009	0.00005	
4	0.00053	0.00014	-0.00106	0.00042	-0.00012	
5	0.00080	-0.00086	0.00054	-0.00012		
6	-0.00020	0.00017	-0.00002	-0.00005		
7	-0.00008	0.00008	-0.00008	0.00005		
8	0.00006	-0.00006				

Table 6 -- Chebyshev coefficients for R>2. (Blank entries are less than 5E-05 in magnitude.)

6.3 Discussion

The coefficients listed in Tables 5 and 6 in conjunction with equations (47-48) permit the evaluation of the double integral in a simple and effective manner, for all values of the source and field points in the plane Y=0. To emphasize the efficiency of this approach, we note that a direct numerical integration of the double integral in (36) using Romberg quadratures and a convergence requirement of 1E-4 absolute accuracy, with the algorithms described in Section 2 used to evaluate the integrand, requires about 150 milliseconds per evaluation on the VAX 11/750. By comparison, the approximations (47-48) require about 3 milliseconds per evaluation, corresponding to a reduction in computation time between one and two orders of magnitude.

The approximations (47-48) in terms of Chebyshev polynomials may be converted to ordinary polynomials in R and θ, by multiplying each set of coefficients by the appropriate transformation vectors for Chebyshev polynomials in each variable. In addition to its more elementary form, the ordinary polynomial can be evaluated slightly faster since one less floating-point addition is required for each term. On the other hand, the Chebyshev form offers advantages that the improved accuracy (and convergence) associated with extra terms can be immediately estimated from the magnitude of the respective coefficients. Finally it should be noted that cancellation errors are more likely to occur in the ordinary polynomial form, unless the variables R and θ are replaced by shifted coordinates with the origin at the center of the domain of application.

Greater accuracy may be achieved by retaining more coefficients in the Chebyshev expansions, but two complications should be anticipated in this context: first, it is necessary to strike a balance between the number of terms retained in the expansion (38) of the singular component and the accuracy of the Chebyshev expansion for the "regular" remainder, in order to retain a reasonable degree of convergence in the latter expansion. [Indeed, it is likely that the convergence shown in Table 5 could be improved somewhat by using an extended version of (38)]. Secondly, when evaluating the coefficients of the Chebyshev expansion, it generally is necessary to retain substantially greater precision in the numerical evaluations of the function being approximated than is ultimately required by the approximation in terms of a truncated expansion; thus one must be prepared to evaluate the original integrals for the Green function to a relatively high degree of accuracy if the present approximations are to be refined.

7. Transient vs. Steady Fields

As in the classical analysis of ship waves by Lord Kelvin, the steady-state Green function analysed in Section 6 may be evaluated by distributing the transient source potential of Section 4 along the ship's track. Thus

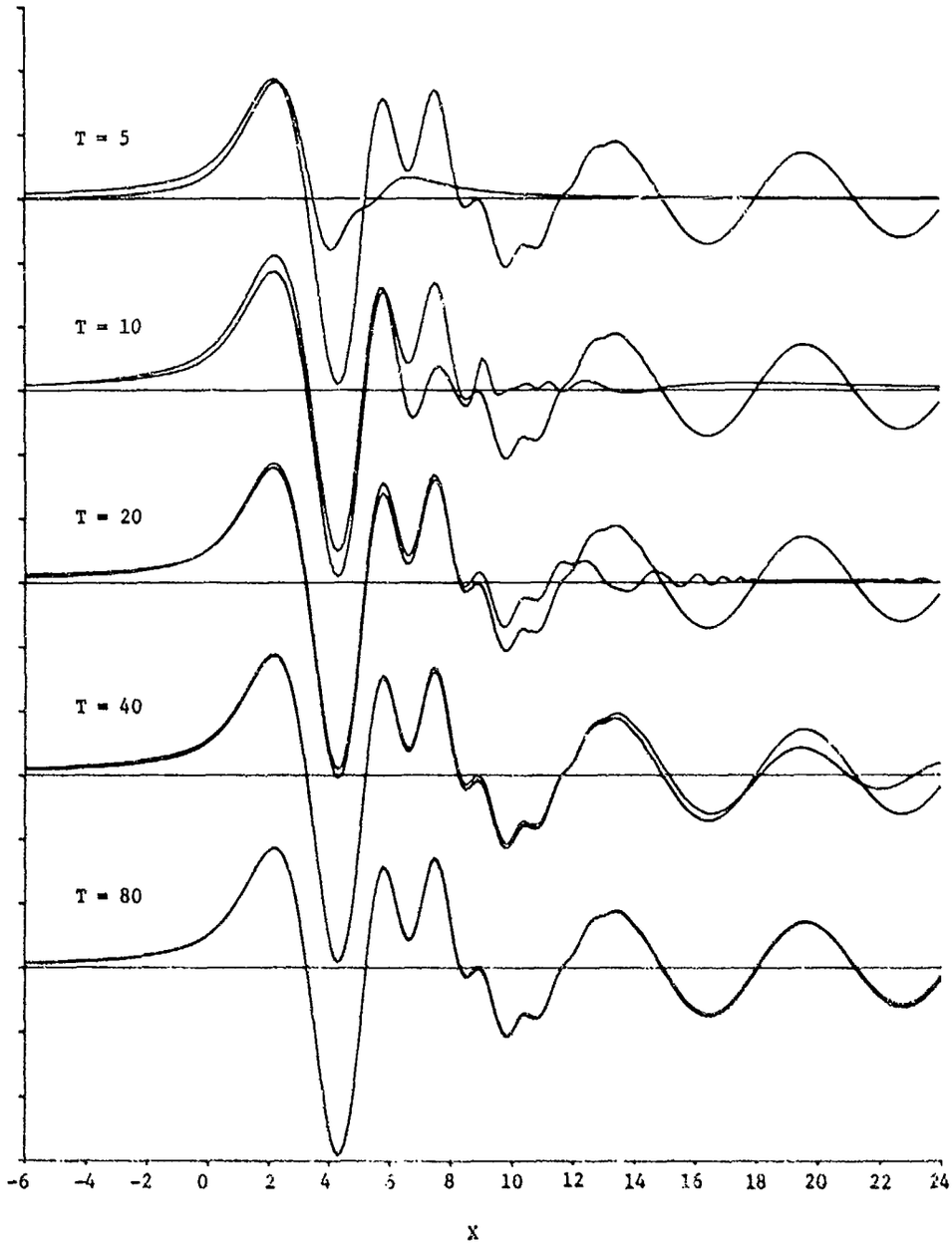

Figure 1 — Comparisons of steady and transient ship-wave fields. The curve which is repeated in each figure is the steady-state potential along a longitudinal track, based upon direct evaluation of (34) with transverse coordinates Y=1 and Z=0.1. The second curve shown in each figure is the result of integrating the transient source potential (19) along the X-axis between T and the origin, in accordance with (49). The coordinates are nondimensionalised with respect to the forward velocity and gravity.

$$G_S = \lim_{T\to\infty} \int_{-T}^{0} G_t(X+\tau,Y,Z,-\tau)d\tau \qquad (49)$$

where the subscript S denotes the steady-state translating Green function (34), and the subscript t denotes the time-derivative (in accordance with a delta-function time-dependent strength) of the transient Green function (19)

The algorithms described in Section 4 can be used to evaluate the integrand of (49), and the integral may be evaluated numerically for finite values of T. It is of interest to compare this approach with the more direct evaluation of the steady Green function described in Section 6.

A numerical comparison is shown in Figure 1, for various values of the parameter Γ in (49). It is obvious that the steady-state limit is approached when T is increased, and X is fixed. Graphical accuracy is achieved if $T = 4|X|$. For large values of X the dominant error is a sinusoidal function of T with phase T/4, which can be effectively filtered by averaging successive computations of (49) with T increased over an interval of 8π. Similar oscillations are evident from the analysis of transient wave resistance by Wehausen [23].

One appealing aspect of (49) is that this integral is regular, for all finite values of T, along the track of the source on the free surface. Thus (49) may be a preferable alternative to (34) or (36), in the vicinity of the singular track. (In effect, by restricting T to be finite in (49), the very short diverging waves responsible for the singularity in the last "single" integrals of (34) or (36) when Y=Z=0 are filtered out.) The desirability of such a filter depends on the application. In the context of continuous surface distributions of sources and dipoles on a surface-piercing body this approach may be more appropriate than pragmatic approximations such as the use of a single discrete singularity at the submerged mid-point of each panel adjacent to the free surface.

8. Summary and Conclusions

A wide variety of numerical methods can be used to evaluate free-surface Green functions. With sufficient effort devoted to their refinement and implementation, these methods will greatly facilitate the implementation of such Green functions in numerical solutions of engineering problems involving the interaction of water waves with ships or offshore structures.

Various types of Green functions have been considered here, including two- and three-dimensional sources with oscillatory time dependence, the transient three-dimensional source potential, and the steady-state three-dimensional "wave-resistance" source. Only the oscillatory three-dimensional source is analyzed for finite depths of fluid, but the approach followed there may be applicable more generally, using suitable superpositions of the infinite-depth potential to improve the convergence and computational simplicity of the finite-depth case.

In the context of offshore structures, the most important Green functions involve oscillatory time dependence without a mean horizontal translation. For these applications the results of Section 3 are directly applicable, and the relatively refined analysis of this Section has been motivated by the practical importance of such computations.

Future research may be devoted increasingly to time-domain analyses, including the possibilities for matching a linear outer solution to a nonlinear inner domain. For this purpose the transient Green function studied in Section 4 is required. Further efforts should be devoted to the refinements indicated at the end of Section 4, and the corresponding extension to the finite-depth case.

For the analysis of ships in steady motion, including the computation of wave resistance, the Green function studied in Section 6 is of universal importance. The polynomial approximations derived here for the "double-integral" component may be extended to the most general case where the transverse coordinate is nonzero, and this should greatly facilitate the evaluation of what has been regarded traditionally as the most difficult part of the steady-state source potential. Further analysis is required to provide an accurate and efficient scheme for evaluating the remaining single integral in the vicinity of the ship's track on the free surface, and for filtering the short diverging waves which cause the singularity on this track in a manner commensurate with the overall computations. One possible technique to provide this filtering is described in Section 7.

Acknowledgements

This work was supported by the Office of Naval Research and the National Science Foundation.

References

1. J. V. Wehausen and E. V. Laitone, "Surface Waves", Handbuch der Physik 9, pp. 446-778. Springer-Verlag, Berlin (1960).

2. Lin, W.-M., Newman, J. N., and Yue, D. K. "Nonlinear Forced Motions of Floating Bodies", 15th Symp. Naval Hydrodynamics, Hamburg (1984).

3. Newman, J. N. "Algorithms for the Free-Surface Green Function", J. Eng'g. Maths. 19, pp. 57-67 (1985).

4. Newman, J. N. "Note on the Computation of the Two-Dimensional Green Function", Unpublished manuscript, (1984).

5. M. Abramowitz, M., and I. A. Stegun, Handbook of Mathematical Functions with Formulas, Graphs, and Mathematical Tables, Government Printing Office, Washington, and Dover, New York (1964).

6. Y. L. Luke, The Special functions and Their Approximations II, Academic Press (1969).

7. A. V. Hershey, Approximations of Functions by Sets of Poles, Tech. Rpt. TR-2564, US Naval Weapons Laboratory (1971).

8. J. L. Hess and D. C. Wilcox, Progress in the Solution of the Problem of a Three-Dimensional Body Oscillating in the Presence of a Free Surface -- Final Technical Report, McDonnell Douglas Company Rep. DAC 67647 (1969).

9. F. Noblesse, "The Green Function in the Theory of Radiation and Diffraction of Regular Water Waves by a Body", J. Eng. Maths. 16, pp. 137-69 (1982).

10. J. N. Newman, "An Expansion of the Oscillatory Source Potential. Appl. Ocean Res. 6, pp. 116-7 (1984).

11. J. N. Newman, "Double-Precision Evaluation of the Oscillatory Source Potential. J. Ship Res. 28, pp. 151-4 (1984).

12. R. Borresen and O. M. Faltinsen, "Ship Motions in Shallow Water by Unified Theory", 15th Symp. Naval Hydrodynamics, Hamburg (1984).

13. G. N. Watson, Theory of Bessel Functions, Cambridge University Press, 2nd ed. (1944).

14. K. Terazawa, "On Deep-Sea Water Waves Caused by a Local Disturbance on or Beneath the Surface", Proc. Roy. Soc. A 92, pp. 57-81 (1916).

15. R. F. Beck and S. Liapis, "Transient Motions of Floating Bodies at Zero Forward Speed", Unpublished manuscript, submitted to J. Fluid Mech. (1985).

16. T. H. Havelock, "Forced Surface-Waves on Water", Phil. Mag.(7) 8, 569-76 (1929).

17. C. C. Mei, Applied Dynamics of Ocean Surface Waves, Wiley (1983).

18. J. N. Newman, "Approximations for the Bessel and Struve functions", Math. Comp. 43, 551-6 (1984).

19. F. Noblesse, "The Near-Field Disturbance in the Centerplane Havelock Source Potential", Proc. 1st Intl. Conf. on Num. Ship Hydro., (1975), 481-501.

20. F. Noblesse, Alternative Expressions for the Green Function of the Theory of Ship Wave Resistance, MIT Sea Grant Rep. 79-23 (1979).

21. D. Euvrard, Les Mille et Une Faceties de la Function de Green du Probleme de la Resistance de Vagues, Ecole Nationale Superieure de Techniques Avancees, Rep. 144 (1983).

22. L. Fox and I. B. Parker, Chebyshev Polynomials in Numerical Analysis, Oxford University Press (1970).

23. J. Wehausen, "Effect of the Initial Acceleration Upon the Wave Resistance of Ship Models", Journal of Ship Research, Jan. (1964), pp. 38-50.

Discussion
of the Paper
by J. N. Newman

"THE EVALUATION OF FREE-SURFACE GREEN FUNCTIONS"

DISCUSSION
"A Method for the Rapid Evaluation of Free-Surface Green Functions"
by F. Noblesse

I wholeheartedly support Professor Newman's comments with regard to the utility of efficient and accurate methods for evaluating the most usual Green functions for free-surface flows, and I wish to congratulate him on his efforts toward the development of such a library of subroutines. I hope these subroutines will be published in the open literature so that they can be used by anyone in the ship hydrodynamics community.

I have also tried to work in the same direction for several years. In particular, I would like to mention here a Fortran subroutine, developed by John Telste and myself at DTNSRDC, for calculating the Green function, and its gradient, for the case of water wave radiation and diffraction at zero forward speed [1]. The subroutine is mostly based on the use of the four complementary series expansions obtained in [2]. More precisely, the domain of definition of the Green function is divided into five subdomains in which we use an asymptotic expansion, a uniformly-convergent ascending series, two complementary Taylor series about the horizontal and vertical coordinate axes, and a numerical approximation in a central domain where none of these four series expansions is useful. This method permits the Green function and its gradient to be evaluated with an absolute error no larger than 10^{-6} quite efficiently. Specifically, the computing time for any one subroutine call has been found to vary between about 20 and 60 microseconds on a CDC CYBER 176 computer.

However, it should be noted that this method for evaluating the diffraction-radiation Green function (or other free-surface Green functions), which is based on the use of various series expansions or polynomial approximations valid in complementary domains as was already noted, is ill-suited to vectorization. This shortcoming is circumvented in the alternative method outlined in [3] for the Green function of steady flow about a ship in forward motion in calm water. This alternative method is explained here for the case of diffraction-radiation in infinite depth and at zero forward speed.

Equation 10 in [1] expresses the diffraction-radiation Green function in the form

$$4\pi G = -(1/r+1/r')-2fN_0-2\pi f[E_0(h)+iJ_0(h)]\exp(v).$$

The gradient of the Green function is expressed in equations 10a,b in [1] in a similar form. The singular terms $(1/r + 1/r')$ correspond to the limiting case when the frequency parameter $f = \omega^2 L/g$ takes the value zero and the free surface acts like a rigid wall. The terms $[E_0(h)+iJ_0(h)]\exp(v)$, where J_0 is the usual Bessel function and E_0 is the Weber function that is closely related to the Struve function H_0 defined in [4], represent circular surface waves propagating away from the pulsating singularity. The wave functions E_0, J_0 and the closely related functions E_1, J_1 involved in the expression for VG are everywhere continuous, as is shown in figure 3 in [1], and in fact are infinitely differentiable. Furthermore, the functions J_0, J_1, E_0, E_1 can readily be evaluated numerically [5]. Our task therefore consists in evaluating the nonoscillatory near-field term N_0 and the similar term N_1 involved in the expression for VG. The functions N_0 and N_1 are depicted in figures 2a,b in [1]. An essential feature of the near-field terms N_0 and N_1 are that they are nonoscillatory, unlike the oscillatory terms

$$R_0(h,v)=N_0(h,v)+\pi E_0(h)\exp(v) \text{ and}$$
$$R_1(h,v)=N_1(h,v)+\pi E_1(h)\exp(v)$$

which are evaluated in the Fortran subroutine given in [1].

The functions N_0 and N_1 are singular at the origin $d = (h^2+v^2)^{1/2} = 0$, as may be seen from figures 2a,b in [1]. More precisely, equations 9a,b and equations 21 and 26 in [1] yield the following first few terms in the ascending series of the functions N_0 and N_1 about the origin $d = 0$:

$$N_0 \simeq -(1+v)\ln(d-v)+\ln(2)-\gamma$$
$$N_1 \simeq h(1+d)/d(d-v)-2-(h/2)(1+v)\ln(d-v),$$

where terms $O(d^2\ln d)$ and $O'd)$ have been neglected. For large values of d, equations 9a,b and equations 19a,b and 20a,b in [1] yield the following first terms in the asymptotic expansions of the functions N_0 and N_1 about the point at infinity $d = \infty$:

$$N_0 \simeq -1/d+2h\exp(v)/(1+h^2),$$
$$N_1 \simeq -h/d^3+2h\exp(v)/(1+h^3).$$

The method explained in [3] relies on the use of a simple composite analytical approximation based on the foregoing analytical approximations about the points $d = 0$ and $d = \infty$. More precisely, the simple analytical approximations N_0^a and N_1^a defined by

$$(1+d^2)N_0^a=-\{\ln(d-v)\}/(1-v)+\{\ln(2)-\gamma\}$$
$$-d\{1-2dh[\exp(v)]/(1+h^2)\}$$

$$(1+d^4)N_1^a= h(1+d)/d(d-v)-2-h[\ln(d-v)]/2(1-v)$$
$$-hd\{1-2d^3h[\exp(v)]/(1+h^3)\}$$

yield the previously-given approximations as $d\to 0$ and $d\to\infty$. More refined analytical

approximations N_0^a and N_1^a can obviously be defined. The main purpose for defining the analytical approximations N_0^a and N_1^a is that the functions N_0 and N_1 may now be expressed in the form

$$N_0 = N_0^a + N_0^r \text{ and } N_1 = N_1^a + N_1^r,$$

where the remainders N_0^r and N_1^r are everywhere continuous and, in particular vanish both as $d \to 0$ and as $d \to \infty$. Specifically, the functions N_0^r and N_1^r are $O(d)$ as $d \to 0$, whereas we have $N_0^r = O(1/d^2)$ and $N_1^r = O(1/d^3)$ as $d \to \infty$. The functions N_0^r and N_1^r may be expressed in the form

$$N_0^r = 3A_0 d/\delta_0[2+d^3/\delta_0^3]+R_0/(1+d),$$
$$N_1^r = 4A_1 d/\delta_1[3+d^4/\delta_1^4]+R_1/(1+d^2),$$

where the first terms on the right sides of these two expressions are made to provide rough approximations to the functions N_0^r and N_1^r by properly selecting the functions $A_0(h/d), A_1(h/d), \delta_0(h/d), \delta_1(h/d)$. In this manner, the remainders $R_0(h,v)$ and $R_1(h,v)$ are fairly small for all values of h and v. The change of variables $\rho = (d-1)/(d+1)$ and $\alpha = (d+2v)/d$ maps the infinite domain $0 \leq h \leq \infty$, $0 \geq v \geq -\infty$ into the square $-1 \leq \rho \leq 1$, $-1 \leq \alpha \leq 1$. The remainders R_0 and R_1 can now be approximated by means of a single approximation within the square $-1 \leq \rho \leq 1$, $-1 \leq \alpha \leq 1$, for instance by using the classical Chebyshev approximation

$$R = \sum_{m,n} C_{mn}\, T_m(\rho) T_n(\alpha),$$

which Professor Newman has used in his paper. The practical usefulness of the method explained in the foregoing evidently depends on the number of terms in the Chebyshev series that are required for approximating the remainders R_0 and R_1, which clearly depends on how smooth the functions $R_0(\rho,\alpha)$ and $R_1(\rho,\alpha)$ are. The smoothness of the functions R_0 and R_1 can be adjusted by properly selecting the analytical approximations N_0^a and N_1^a, that is by retaining just the appropriate number of terms in the expansions of the functions N_0 and N_1 about the points $d = 0$ and $d = \infty$. In particular, it clearly is less crucial to incorporate the far-field behavior of the functions N_0 and N_1 into the analytical approximations N_0^a and N_1^a than to incorporate their near-field behavior since the functions N_0 and N_1 are singular as $d \to 0$ but vanish as $d \to \infty$ (see figures 2a,b in [1]).

The method outlined in [3] for the steady-ship-wave Green function and explained in more detail above for the diffraction-radiation Green function may be applied to other free-surface Green functions. Briefly, the method consists in the following steps: (i) seek integral representations in which the Green function is expressed as the sum of a nonoscillatory near-field disturbance and a wave disturbance; it should be noted in this respect that various integral representations can be used but that they are not all equally useful, as is discussed in [6,2]: (ii) the first few terms in the ascending series about the singular point at the origin and in the far-field asymptotic expansion must then be obtained for the nonoscillatory near-field disturbance, as in [7,8,2]: (iii) these few terms in the series expansions for small and large values of the arguments can then be used for building a single composite analytical approximation to the nonoscillatory near-field term in the Green function, in the manner explained in the foregoing: (iv) the remainder terms must finally be approximated, for instance by using truncated Chebyshev series, after mapping the infinite flow domain onto a finite domain.

The wave disturbance in the expression for the Green function must be treated separately from the nonoscillatory near-field term. The wave disturbance for the diffraction-radiation Green function is particularly simple, as was already noted. The wave term in the steady-ship-wave Green function is considerably more complex, although in the special case considered by Professor Newman in his study relatively-simple series representations have been obtained [9]. In the general case, however, it seems preferable to treat the wave term in the steady-ship-wave Green function in the indirect manner explained in [10].

1. J.G. Telste and F. Noblesse, "Numerical Evaluation of the Green Function of Water Wave Radiation and Diffraction," Journal of Ship Research, to appear.
2. F. Noblesse, "The Green Function in the Theory of Radiation and Diffraction of Regular Water Waves by a Body," Journal of Engineering Mathematics, Vol. 16 (1982) pp. 137-169.
3. F. Noblesse, "Numerical Study of a Slender Ship Theory of Wave Resistance," Journal of Ship Research, Vol. 29 (1985) pp. 81-93.
4. M. Abramowitz and I. A. Stegun, "Handbook of Mathematical Functions," Dover Publications, New York (1965).
5. J. N. Newman, "Approximations for the Bessel and Struve Functions," Mathematics of Computation, Vol. 43 (1984) pp. 551-556.
6. F. Noblesse, "Alternative Integral Representations for the Green Function of the Theory of Ship Wave Resistance," Journal of Engineering Mathematics, Vol. 15 (1981) pp. 241-265.
7. F. Noblesse, "On the Fundamental Function in the Theory of Steady Motion of Ships," Journal of Ship Research, Vol. 22 (1978) pp. 212-215.
8. F. Noblesse, "The Near-Field Disturbance in the Centerplane Havelock Source Potential," Proc. First International Conference on Numerical Ship Hydrodynamics, (1975) pp. 481-501.
9. F. Noblesse, "The Steady Wave Potential of a Unit Source, at the Centerplane," Journal of Ship Research, Vol. 22 (1978) pp. 80-88.
10. A. Barnell and F. Noblesse, "Numerical Evaluation of the Near- and Far-Field Wave Pattern and Wave Resistance of Arbitrary Ship Forms," Proc. Fourth International Conference on Numerical Ship Hydrodynamics, (1985).

Author's Reply

Dr. Noblesse emphasizes the importance of distinguishing between non-radiating near-field terms and radiating wavelike terms in the various free-surface Green functions. For the oscillatory stationary source (Section 2-3) this is clearly the case when computations are performed for field points relatively far from the source; the decomposition in (16) is an example of this strategy. For the same Green function in the near field, however, it is preferable in my view to evaluate both components together. (Indeed, when X is small the decomposition in Equation (16) is clearly undesirable due to the equal and opposite logarithmic singularities of the two components.) For the wave-resistance Green function, on the other hand, the very different forms and numerical problems associated with the wavelike (single) and near-field (double) integrals suggests that they should be treated with relative ease, using the polynomial coefficients in Tables 5 and 6 for points on the centerplane. (Generalizations of this approach to field points off the centerplane have been completed, and will be submitted for publication in the Journal of ship Research. Typically, the evaluation of the double integral for arbitrary field points with an accuracy of 5 or 6 decimals requires about 200 floating point multiplications and additions).

DISCUSSION
by by G. McKee

Have you considered using rational function approximations instead of polynomials. They are also quick to evaluate and can approximate singularities.

Author's Reply

In reply to the question by Dr. McKee regarding rational-fraction approximations, I have found these to be very useful for functions of a single variable, although somewhat laborious to compute with minimax accuracy. An example is noted at the end of Section 2.3, for the exponential integral Ei(-x), with the results tabulated in Reference 4. Reference 18 includes several approximations of this type which are particularly efficient for computations of the Bessel and Struve functions in the evaluation of the infinite-depth oscillatory source potential. The extension of such methods to functions of several variables is a challenging task, which I have not studied.

DISCUSSION
by B. Yim

The numerical evaluation of the Green function is one of the most important and useful efforts in numerical ship hydrodynamics. In this sense, the author should be commended for his excellent work in this area. One thing I would like to mention is the singular behavior of the Green function near the free surface. For example, a point source or a point doublet located on the free surface in a uniform flow has infinite wave resistance. Therefore it may be tempting to locate it slightly beneath the free surface to have a finite value. However, because of the singular behavior of these singularities near the free surface, one can obtain any resultant value of physical quantities desired by adjusting the submergence and the strength of singularities. This could give false satisfaction

Author's Reply

Dr. Yim's discussion emphasizes the singularity of the wave-resistance Green function when the source and field points are in the free surface. The fundamentally correct approach to this difficulty is to use a continuous distribution of singularities over the hull surface in proximity to the free surface. A more common numerical approach is to submerge the point source and dipole beneath the free surface, e.g. at the centroid of each panel. The proposal in the final paragraph of Section 7 is put forth as an alternative approach with somewhat greater rationality. Two possibilities may exist to adopt the continuous distribtuion: (1) to extract the analytical form of the singularity and integrate this over the relevant panels; and (2) to integrate the Green function analytically over the panel, prior to the evaluation of the integral representation (in effect, interchanging the orders of integration). The first possibility is more attractive, and follows the simpler analogy of dealing with the fundamental Rankine singularity on a panel in the manner of Hess and Smith. In zero-speed radiation/diffraction problems we have adopted the same procedure to accommodate the logarithmic singularity in the oscillatory Green function (Breit, et al, 1985). However, further analysis is required to determine the analytic form of the singularity in the single integral of (36), before this procedure can be implemented for the wave-resistance problem.

Additional Reference:

Breit, S.R., Newman, J.N. and Sclavounos, P.D., "A new generation of panel programs for radiation/ diffraction problems", Proc. 4th Intl. Conf. on Behaviour of Offshore Structures (BOSS 85), Delft, The Netherlands, July 1-5, 1985, pp. 531-544.

DISCUSSION
by K. Eggers

Entering the adventure of evaluating such analytical experiments, one may find relief if agreement is found with alternative formulations not obviously equivalent. On the other hand, if there is such result from a terse (though ingenious) analysis, we may feel encouraged to work out a more detailed derivation if such agreement of numerical results has been observed.

It is from this aspect that I would like to amplify on Prof. Newman's synoptical representation and to call attention to two genuine single-integral representations of the Green-function wave part for the case of an oscillatory source in steady advance, which should contain not only the steady-state case but even the pure oscillation case as a limit. Th[illegible] have independently been derived by Bessho [illegible] Japan (1964, 1977) and by Simmgen in Germany (1968). I hope that it was inadvertently that so far they did not find the attention deserved.

Simmgen derived his 3-D solution from a 2-D analysis for dipoles of constant moment distributed over straight horizontal lines of different orientation against the x-axis, making use of the fact that the 3-D Rankine source may be representated as an integral average of such potentials by the relation

$$1/r = \mathrm{Im}(i/\pi) \int_{-\pi/2}^{\pi/2} (x \cos\theta + y \sin\theta + iz)^{-1} d\theta$$

From classical arguments we know that in order that the Laplace and free surface equations should be satisfied for <u>any</u> point, the integrand function should already satisfy these conditions for such simple integral. However, due to splitting off $1/r$ and $1/r_1$ an inhomogeneous free surface condition has to be satisfied. This is taken care of by the occurance of a variable lower limit of integration, corresponding to

$$\alpha + i\beta = \ln(x+r) - \ln\zeta + i \arctan y/t$$

in Bessho's notation for the steady advance case, I would like to emphasize that for satisfying the Laplace equation it is not sufficient that $(\Delta\ \alpha+i\beta) = 0$ everywhere save the wake line of the source. If, in addition, the scalar product of the gradient of $\alpha + i\beta$ with that of the integrand function evaluated there would vanish, this will be sufficient.

According to my findings (1976), the result of Simmgen differs from that of Bessho by a contour integral of finite extent with constant limits of integration contributing only to the representation of the near field.

I advocate that this issue should be attacked by younger members of our community endowed with the necessary capacity of brainpower. As far as I can see, the conventional far field integrals can easily be extracted. The near field then is represented by contour integrals of finite extent, independent from path selected; if we expand the integrand (an entire function) in a Taylor series, we may intergrate termwise and obtain a near field expansion in the vicinity of the source which I feel will be in accord with the pioneering findings of F. Noblesse.

Bessho, M., On the fundamental function in the theory of wave making resistance of ships. Mem. Defense Academy, IV No 4, 1964 Yokosuka, Japan.

Bessho, M., On the fundamental singularity in the theory of ship motion in a seaway. Mem. Defense Academy, XVIII, No 3, 1977 Yokosuka, Japan

Simmgen, M., Beitrag fur linearisierten Theorie des periodisch instationar angestromten Unterwasser frag flugels, ZAMM <u>48</u>, 1968, pp 99-119

Eggers, K., Eine einfache Darstellung des dreidimensionalen Geshwindigheit felder van Singularitoten fur periodische Schiffbeuegungen in Vordasfahrt, Schiffstechnik <u>23</u>, 1976, PP 169-173

<u>Author's Reply</u>

Professor Eggers has corrected my oversight in regard to the remarkable studies by Bessho and Simmgen, which have been further advanced by Professors Eggers and also by Ursell (IMA J1. of Appl. Math., 32, 1984). In addition to his derivation of expressions for the forward-speed Green functions in terms of single integrals alone, Bessho (1964, equation 4.2) also presents an effective Neumann series expansion for the single integral.

A FAST ALGORITHM FOR COMPUTATION OF 3-D SHIP MOTIONS AT MODERATE FORWARD SPEED

R.H.M. Huijsmans* and A.J. Hermans**

The Netherlands

Abstract

In this paper the problem of a ship advancing in waves will be addressed. The mathematical formulation of the problem will be given. The solution of the problem will be presented for low to moderate forward speeds. In this case the Green's function of an oscillating translating source can be approximated using the Green's function of an oscillating source at zero forward speed. Results are presented for the comparison of the exact Green's function at low forward speed and the zero speed Green's function. For the validation of the presented algorithm a comparison was made between the presented procedure and the results from computations made by Ecole Nationale Supérieur de Mécanique of Nantes using a method developed by A. Grekas et al. For the computations a series 60 (block .70) ship was used. From this comparison it can be concluded that the correlation between these two programs is quite satisfactory.

1. Introduction

In the last decades many theories have been developed to compute ship motions. Major attention is directed towards thin and slender ships sailing at forward speed in waves. An important development is the slender body approximation by Newman [15] and Newman and Tuck [16] for both zero and non-zero forward speed. Faltinsen [7] improved the formulation of Ogilvie and Tuck [19] and obtained results in better agreement with experiments. The unified ship theory introduced by Newman [17] again gave better results in several cases and is extended by several authors.

Meanwhile some very powerful programs have been developed to treat the zero speed case for the ship motion, without any geometrical simplifications.

One of the first diffraction programs, making use of source distributions over the actual hull was reported by Van Oortmerssen [21]. Since then several similar programs have been developed. Some care is needed to evaluate the pulsating wave source. Newman [18] reported a very efficient algorithm for the computation of the wave source at zero speed. The results are very satisfactory. The availability of the diffraction program makes it possible to calculate the second order low frequency wave drift force, which causes low frequency motions at the natural period of moored systems. Pinkster [20] shows excellent agreement of the calculated wave drift forces with experiments. An unsolved problem is still the computation of the motion of moored ships especially if the mooring is unstable. Wichers et al. [24] also reported that the damping at the natural periods of the mooring system has to be considered carefully. Careful experiments showed that a large part of the damping at these natural periods could be contributed to the velocity dependent wave drift forces.

In other words a version of the diffraction program must be developed where the forward speed effect is taken into account. This can be done in principle by changing the wave source function into the pulsating translating wave source function and by taking into account certain line integrals. This approach has been attempted by Bougis [1], Chang [4] and Inglis and Price [12]. Until now this approach is not generally applicable. The computations are time consuming and not very accurate in the general case. An approximative way of incorporating forward speed into the 3-D ship motion problem has e.g. been presented by Inglis [11] and Huijsmans et al. [10]. For the offshore application we have in mind, we have to deal with low to moderate speeds and it is expected that the term linear with speed leads to the correct "damping" if the speed has been taken into account in the computation of the second order drift force.

* Scientific Officer, Maritime Research Institute Netherlands (MARIN), Wageningen.
** Professor, Delft University of Technology and MARIN.

The total potential function will be split in a steady and a non-steady part in a well known way:

$$\Phi(\underline{x},t) = -Ux + \Phi(\underline{x};U) + \bar{\Phi}(\underline{x},t;U) \qquad (1.1)$$

The steady problem gives rise to a highly non-uniform problem in the case U tends to zero as has been shown by among others Hermans [9], Brandsma and Hermans [2] and Eggers [5] especially in the case of non-thin and non-slender ships. On the other hand this part does not contribute to the pulsating force directly. It plays a role in the free surface condition. This effect is taken into account in the "parabolic" approach of Nestegard and Sclavounos [13] and Nestegard [14] in the case of slender ships. We do not take this effect into account and neglect the contribution of $\Phi(\underline{x};U)$ totally. The time dependent oscillatory potential $\Phi(x,t;U)$ will be written as a source distribution along the hull and the waterline and it will be expanded with respect to small values of U.

Several aspects have to be regarded. First it will be shown that the pulsating wave source function can be split into a part which can be expanded regularly in a power series with respect to the small velocity while the remainder does not allow a regular perturbation series. It cannot be neglected on beforehand. The source strength is also expanded as a power series in the velocity parameter of which the first two terms can be computed with the zero speed pulsating source distribution. We shall indicate that to compute higher order terms one should take care of a line integral and of the non-uniform part of the asymptotic expansion of the pulsating translating wave source. We restrict ourselves to the deep water case. The theory will be explained for the unit motion potential where the motion of the ship is oscillatory in the x-direction and applied to a more general case.

2. Mathematical formulation

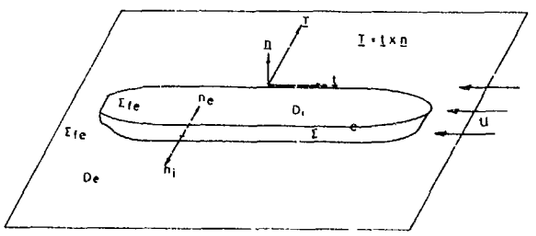

Figure 1. System of axes

The problem for the time harmonic potential $\bar{\Phi}(\underline{x},t;U)$ can be written as:

$$\Delta\bar{\Phi} = 0 \qquad \text{in the fluid domain} \qquad (2.1)$$

$$\bar{\Phi}_{tt} - 2U\,\bar{\Phi}_{tx} + U^2\bar{\Phi}_{xx} + g\,\bar{\Phi}_z = 0 \text{ at } z=0 \qquad (2.2)$$

$$(\nabla\bar{\Phi}\cdot\underline{n}) = V(\underline{x})e^{-i\omega t} \qquad \text{at } \underline{x}\in S \qquad (2.3)$$

an appropriate radiation condition.

Where $V(\underline{x}) = n_x$ if the ship exhibits a unit oscillation in the x-direction. In the case of wave diffraction and motions in other modes $V(\underline{x})$ is defined accordingly.

We assume $\bar{\Phi}(\underline{x},t;U)$ to be oscillatory.

$$\bar{\Phi}(\underline{x},t;U) = \phi(\underline{x};U)\,e^{-i\omega t} \qquad (2.4)$$

The free surface condition (2.2) results in:

$$-\omega^2\phi + 2i\omega U\phi_x + U^2\phi_{xx} + g\,\phi_z = 0 \text{ at } z=0$$

and the condition on the hull:

$$(\nabla\phi\cdot\underline{n}) = V(\underline{x})$$

Brard [3] applies Green's theorem to a problem in D_i inside S and to the problem in D_e outside S where S is the ship's hull. In this way it can be shown that the problem can be described by means of a source and vortex distribution.

We assume that a Green's function $G(\underline{x},\underline{\xi})$ is known, satisfying the Laplace equation, a suitable radiation condition and the adjoint free surface condition.

$$-\omega^2 G - 2i\omega UG_\xi + U^2G_{\xi\xi} + gG_z = 0 \text{ at } z=0 \qquad (2.5)$$

This Green's function has the form:

$$G(\underline{x},\underline{\zeta};U) = -\frac{1}{r} + \frac{1}{r_1} - \psi(\underline{x},\underline{\xi};U) \qquad (2.6)$$

where $r = |\underline{x}-\underline{\xi}|$ and $r_1 = |\underline{x}-\underline{\xi}'|$, where ξ' is the image of ξ with respect to the free surface. The function $\psi(\underline{x},\underline{\xi})$ shall be specified later on. We define ϕ_e as the potential in $\underline{x}\in D_e$ and ϕ_i as the potential in $\underline{x}\in D_i$ and apply Green's theorem in D_e on S and in D_i respectively. We obtain for $\phi_e(\underline{x};U) = \phi_e(\underline{x})$:

$$\iint_S \left[\phi_e(\underline{\xi})\frac{\partial}{\partial n_e}G(\underline{x},\underline{\xi}) - G(\underline{x},\underline{\xi})\frac{\partial}{\partial n_e}\phi_e(\underline{\xi})\right]dS_\xi +$$

$$- 2i\frac{\omega U}{g}\int_c \phi_e(\underline{\xi})\,G(\underline{x},\underline{\xi})\,d\eta + \frac{U^2}{g}\int_c \cdot$$

$$\cdot\left[\phi_e(\underline{\xi})\frac{\partial}{\partial\xi}G(\underline{x},\underline{\xi}) - G(\underline{x},\underline{\xi})\frac{\partial}{\partial\xi}\phi_e(\underline{\xi})\right]d\eta =$$

$$= \begin{cases} 4\pi\,\phi_e\,, & \underline{x}\in D_e \\ 2\pi\,\phi_e\,, & \underline{x}\in S \\ 0\,, & \underline{x}\in D_i \end{cases} \qquad (2.7)$$

and for $\phi_i(\underline{x};U) = \phi_i(\underline{x})$:

$$\iint_S \left[\phi_i(\xi)\frac{\partial}{\partial n_e}G(\underline{x},\underline{\xi}) - G(\underline{x},\underline{\xi})\frac{\partial}{\partial n_e}\phi_i(\xi)\right]d S_\xi +$$

$$+ 2i\frac{\omega U}{g}\int_c \phi_i(\xi)\,G(\underline{x},\underline{\xi})d\eta - \frac{U^2}{g}\int_c \cdot$$

$$\cdot\left[\phi_i(\xi)\frac{\partial}{\partial\xi}G(\underline{x},\underline{\xi}) - G(\underline{x},\underline{\xi})\frac{\partial}{\partial\xi}\phi_i(\xi)\right]d\eta =$$

$$= \begin{cases} 0 & , \underline{x}\in D_e \\ 2\pi\,\phi_i & , \underline{x}\in S \\ 4\pi\,\phi_i & , \underline{x}\in D_i \end{cases} \qquad (2.8)$$

where c is the waterline.

We consider $\underline{x}\in D_e$ and add (2.7) and (2.8) while we write $\phi_i - \phi_e = \hat{\phi}$, we then obtain:

$$4\pi\,\phi_e = \iint_S \hat{\phi}(\xi)\frac{\partial}{\partial n}G(\underline{x},\underline{\xi})\,d\,S_\xi +$$

$$- \iint_S G(\underline{x},\underline{\xi})\frac{\partial}{\partial n}\hat{\phi}(\xi)\,d\,S_\xi +$$

$$+ 2\,i\frac{\omega U}{g}\int_c \hat{\phi}(\xi)\,G(\underline{x},\underline{\xi})\,d\eta +$$

$$- \frac{U^2}{g}\int_c \hat{\phi}(\xi)\frac{\partial}{\partial\xi}G(\underline{x},\underline{\xi})\,d\eta +$$

$$+ \frac{U^2}{g}\int_c G(\underline{x},\underline{\xi})\frac{\partial}{\partial\xi}\hat{\phi}(\xi)\,d\eta \qquad (2.9)$$

The potential ϕ_e may be considered as a source and dipole distribution along the hull and the waterline:

$$\sigma(\xi') = \frac{\partial}{\partial n}\hat{\phi}(\xi') \text{ and } \gamma(\xi') = -\hat{\phi}(\xi')$$

together with the notations:

$$\alpha_t = \cos(0x,\underline{t}),\ \alpha_T = \cos(0x,\underline{T}),\ \alpha_n = \cos(0x,\underline{n})$$

where $\underline{n}$ is the normal and $\underline{t}$ the tangent to the waterline and $\underline{T} = \underline{t}\times\underline{n}$ the binormal. We obtain:

$$-\iint_S \gamma(\xi)\frac{\partial G}{\partial n}(\underline{x},\underline{\xi})d\,S_\xi - \iint_S \sigma(\xi)\,G(\underline{x},\underline{\xi})\,d\,S_\xi +$$

$$- 2i\frac{\sigma U}{g}\int_c \gamma(\xi)\,G(\underline{x},\underline{\xi})\,d\eta +$$

$$+ \frac{U^2}{g}\int_c \left[\gamma(\xi)\frac{\partial}{\partial\xi}G(\underline{x},\underline{\xi}) - \left\{\alpha_t\gamma_t(\xi) + \alpha_T\gamma_T(\xi)\right\}\right.$$

$$\left.G(\underline{x},\underline{\xi})d\eta\right] + \frac{U^2}{g}\int_c \alpha_n\,\sigma(\xi)\,G(\underline{x},\underline{\xi})\,d\eta =$$

$$= \begin{cases} 4\pi\,\phi_e & , x\in D_e \\ 4\pi\,\phi_i & , x\in D_i \end{cases} \qquad (2.10)$$

It is clear that with the choice $\gamma(\underline{\xi}) = 0$ the integral along the waterline gives no contribution to the solution up to order U. Hence, for our purpose a source distribution is the appropriate choice. The source strength $\sigma(\underline{\xi})$ is a solution of the integral equation:

$$-2\pi\,\sigma(\underline{x}) + \iint_S \sigma(\underline{\xi})\frac{\partial}{\partial n_x}G(\underline{x},\underline{\xi})\,d\,S_\xi +$$

$$+ \frac{U^2}{g}\int_c \alpha_n\sigma(\underline{\xi})\,G(\underline{x},\underline{\xi})d\eta = 4\pi\,V(\underline{x}) \text{ for } \underline{x}\in S \qquad (2.11)$$

while ϕ_e is given by (2.10) with $\gamma(\underline{\xi}) = 0$. If we wish to calculate ϕ_e up to order U the last integral in (2.10) and the second integral in (2.11) can be neglected. We then obtain:

$$\phi(\underline{x};U) = \frac{1}{4\pi}\iint_S \sigma(\underline{\xi};U)\,G(\underline{x},\underline{\xi};U)dS_\xi,\ \underline{x}\in D_e \qquad (2.12)$$

and:

$$-\tfrac{1}{2}\sigma(\underline{x};U) + \frac{1}{4\pi}\iint_S \sigma(\underline{\xi};U)\frac{\partial}{\partial n_x}G(\underline{x},\underline{\xi};U)dS_\xi =$$

$$= V(\underline{x}),\ \underline{x}\in S \qquad (2.13)$$

We consider the case where $\tau = \frac{U\omega}{g} << 1$ in Section 4 it will be shown that σ and ϕ can be expanded with respect to τ as follows:

$$\sigma(\underline{x};U) = \sigma_0(\underline{x}) + \tau\sigma_1(\underline{x}) + \tilde{\sigma}(\underline{x};U)$$

$$\phi(\underline{x};U) = \phi_0(\underline{x}) + \tau\phi_1(\underline{x}) + \tilde{\phi}(\underline{x};U) \qquad (2.14)$$

where $\tilde{\sigma}$ and $\tilde{\phi}$ are $O(\tau^2)$ as $\tau\to 0$ while $G(\underline{x},\underline{\xi};U)$ has to be treated less trivial as shall be shown in the next section.

3. The Green's function

In this section we present an asymptotic expansion of the Green's function $G(\underline{x},\underline{\xi};U)$ for $\tau = \frac{U\omega}{g} << 1$ and $\nu = \frac{g\cdot L}{U^2} >> 1$.

This can be obtained by means of constant frequency ω and constant length scale L for $U\to 0$. For convenience sake we chose L=1 hence, $\nu = \frac{g}{U^2} >> 1$.

The Green's function follows from the source function presented in Wehausen et al. [23]. With the notation (2.6) we obtain for $\tau < \frac{1}{4}$:

$$G(\underline{x},\underline{\xi};U) = -\frac{1}{r} + \frac{1}{r_1} - \psi(\underline{x},\underline{\xi};U)$$

$$= \tilde{G}(\underline{x},\underline{\xi}) - \psi(\underline{x},\underline{\xi};U) \qquad (3.1)$$

with:

$$\psi(\underline{x},\underline{\xi};U) = \frac{2g}{\pi}\int_0^{\pi/2} d\theta \int_{L_1} dk\,F(\theta,k) +$$

$$+ \frac{2g}{\pi}\int_{\pi/2}^{\pi} d\theta \int_{L_2} dk\,F(\theta,k)$$

when:

$$F(\theta,k) =$$

$$= \frac{k\,\exp\left[k\left[z+\zeta+i(x-\xi)\cos\theta\right]\right]\cos\left[k(y-\eta)\sin\theta\right]}{gk - (\omega+kU\cos\theta)^2} \qquad (3.2)$$

The contours L_1 and L_2 are given as follows:

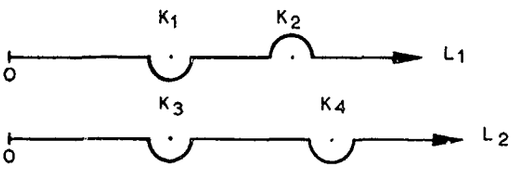

Figure 2. Contours L_1 and L_2

These contours are chosen such that the radiation conditions are satisfied. The waves are outgoing. The values k_i are the poles of $F(\theta,k)$.

$$\sqrt{gk_1},\ \sqrt{gk_3} = \frac{1-\sqrt{1-4\tau\cos\theta}}{2\tau\cos\theta}\,\omega$$

$$\sqrt{gk_2},\ -\sqrt{gk_4} = \frac{1+\sqrt{1-4\tau\cos\theta}}{2\tau\cos\theta}\,\omega$$

For small values of τ these poles behave as follows:

$$\sqrt{gk_1},\ \sqrt{gk_3} \sim \omega + O(\tau) \text{ as } \tau\to 0 \qquad (3.3)$$

$$\sqrt{gk_2},\ -\sqrt{gk_4} \sim \frac{\omega}{\tau\cos\theta} + O(1) \text{ as } \tau\to 0 \qquad (3.4)$$

The behaviour in (3.3) gives rise to a regular perturbation series with respect to τ. In contrast, (3.4) originates a highly oscillating contribution which gives rise to a non-uniform expansion. However, the position of the last two poles moves to infinity. Therefore it can be treated separately. If $\tau\to 0$ the contours L_1 and L_2 become the same.

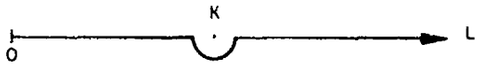

Figure 3. The contours L_1 and L_2 if $\tau\to 0$

We may take L on L* if appropriate. We write:

$$F(\theta,k) = E(\theta,k)\,\frac{1}{gk-(\omega+kU\cos\theta)^2}$$

$$\sim E(\theta,k)\left\{\frac{1}{gk-\omega^2}+\frac{2kU\omega\cos\theta}{(gk-\omega^2)^2}\right\}+O(\tau^2),\ \text{as } \tau\to 0$$

where:

$$E(\theta,k) =$$

$$k\exp\{k[z+\zeta+i(x-\xi)\cos\theta]\}\cos\{k(y-\eta)\sin\theta\}$$

and with $\psi(\underline{x},\underline{\xi};U) = \psi_0(\underline{x},\underline{\xi}) + \tau\psi_1(\underline{x},\underline{\xi}) + \ldots$.

$$\psi_0(\underline{x},\underline{\xi}) = \frac{2g}{\pi}\int_0^{\pi} d\theta \int_L \frac{dkE(\theta,k)}{gk-\omega^2} =$$

$$= 2g\int_L \frac{ke^{k(z+\zeta)}}{gk-\omega^2}J_0(kR)dk \qquad (3.5)$$

$$\psi_1(\underline{x},\underline{\xi}) = \frac{4g^2}{\pi}\int_0^{\pi} d\theta \int_{L^*} \frac{dkE(\theta,k)}{(gk-\omega^2)^2}k\cos\theta =$$

$$= 4ig^2\cos\theta'\int_{L^*}\frac{k^2e^{k(z+\zeta)}}{(gk-\omega^2)^2}J_1(kR)dk \qquad (3.6)$$

where: $R^2 = (x-\xi)^2+(y-\eta)^2$ and $\theta' = \operatorname{arctg}\left(\frac{y-\eta}{x-\xi}\right)$

Expression (3.5) in (3.1) gives the pulsating source function, which can be calculated with the algorithm Fingreen, see Newman [18]. Expression (3.6) is a correction for small values of τ. It will be clear that one should operate carefully. The second order singularity needs special care. With the help of Sonine integrals and some analytic manipulations it can be computed with the help of Fingreen just as well. In this way a series expansion of the Green's function has been obtained. However, the poles at infinity cause trouble. The poles k_2 and k_4 can be combined for large values of $\nu = \frac{g}{U^2}$. We write:

$$\psi(\underline{x},\underline{\xi};U) = \psi_0(\underline{x},\underline{\xi}) + \tau\psi_1(\underline{x},\underline{\xi}) + \ldots$$

$$+ \tilde{\psi}_0(\underline{x},\underline{\xi}) + \nu^{-1}\tilde{\psi}_1(\underline{x},\underline{\xi}) + \ldots \qquad (3.7)$$

and find:

$$\tilde{\psi}_0(\underline{x},\underline{\xi}) = -4\nu\int_0^{\pi/2}\exp\{\nu(z+\zeta)\sec^2\theta\}\ *$$

$$* \sin\{\nu(x-\xi)\sec\theta\}\ \cdot$$

$$\cdot \cos\{\nu(y-\eta)\sin\theta\sec^2\theta\}\sec^2\theta\, d\theta \qquad (3.8)$$

Expression (3.8) in (3.1) gives the translating source function in still water (see equation 13.36 of Wehausen and Laitone [23]). This term is highly oscillating and the amplitude becomes infinite at first sight. In making a perturbation expansion of (2.13) it generates a Kelvin pattern related to the oscillating source strength. Because of this oscillating behaviour it gives contribution to (2.14) of $O(\tau^2)$ as $\tau\to 0$ and can be disregarded in our analysis. In the appendix this is explained for thin ships. For other ship forms the situation is more complex and the problem is related to the low Froude number theories, see Brandsma and Hermans and Eggers.

4. Expansion of the source strength

In this section an approximate solution of (2.13) will be derived. Inserting (2.14) and (3.7) in (2.13) one obtains:

$$-\tfrac{1}{2}(\sigma_0 + \tau\sigma_1 + \tilde{\sigma}) + \frac{1}{4\pi}\iint_S (\sigma_0 + \tau\sigma_1 + \tilde{\sigma}) *$$

$$* \frac{\partial}{\partial n_x}(G_0 - \tau\psi_1 - \tilde{\psi}_0 - \nu^{-1}\tilde{\psi}_1 + \ldots)dS_\xi = V(\underline{x}) \quad (4.1)$$

where $G_0 = \tilde{G} - \psi_0$

In the appendix it is shown, for thin ships, that in the case that σ_i are regular functions the functions $\tilde{\psi}_i$ do not lead to a contribution to the source strength. Hence, we obtain for the unknown functions σ_i:

$$-\tfrac{1}{2}\sigma_0(\underline{x}) + \frac{1}{4\pi}\iint_S \sigma_0(\underline{\xi})\frac{\partial}{\partial n_x}G_0(\underline{x},\underline{\xi})dS_\xi = V(\underline{x}) \quad (4.2)$$

and:

$$-\tfrac{1}{2}\sigma_1(\underline{x}) + \frac{1}{4\pi}\iint_S \sigma_1(\underline{\xi})\frac{\partial}{\partial n_x}G_0(\underline{x},\underline{\xi})dS_\xi =$$

$$= \frac{1}{4\pi}\iint_S \sigma_0(\underline{\xi})\frac{\partial}{\partial n_x}\psi_1(\underline{x},\underline{\xi})dS_\xi \quad (4.3)$$

where $G_0(\underline{x},\underline{\xi})$ is the zero speed pulsating wave source.

This perturbation approach leads to a fast algorithm to take into account speed effects once a fast method is available for the zero speed diffraction problem. At MARIN the diffraction program has been extended with the Finngreen subroutines of Newman. The diffraction program has been adjusted to compute the right-hand side of (4.3) just as well.

The potential functions (2.14) now become:

$$\phi_0(\underline{x}) = \frac{1}{4\pi}\iint_S \sigma_0(\underline{\xi})\, G_0(\underline{x},\underline{\xi})dS_\xi$$

$$\phi_1(\underline{x}) = -\frac{1}{4\pi}\iint_S \sigma_0(\underline{\xi})\, \psi_1(\underline{x},\underline{\xi})dS_\xi + \quad (4.4)$$

$$+ \frac{1}{4\pi}\iint_S \sigma_1(\underline{\xi})\, G_0(\underline{x},\underline{\xi})dS_\xi$$

It can be shown (appendix) that the integral

$$\iint_S \sigma_0(\underline{\xi})\, \tilde{\psi}_0(\underline{x},\underline{\xi})dS_\xi$$

contributes to the term proportional to $\frac{1}{\nu} = \frac{U^2}{g}$. Hence, for small values of U the source strength is hardly influenced by the Kelvin part, whereas the potential function is influenced in the U^3 term. These U^3 terms will be neglected together with U^2, the contribution of the integral along the waterline. For the offshore application we have in mind the linear correction terms suffice.

Once the potentials $\phi_0(\underline{x})$ and $\phi_1(\underline{x})$ are known, the pressure from the linearized Bernoulli equation can be derived:

$$p(\underline{x},t) = -\rho\frac{\partial}{\partial t}\bar{\phi}(\underline{x},t) - \rho U\frac{\partial}{\partial x}\bar{\phi}(\underline{x},t) \quad (4.5)$$

also defining:

$$p(\underline{x},t) = p_0(\underline{x},t) + \tau\, p_1(\underline{x},t) \qquad \text{gives:}$$

$$p_0(\underline{x},t) = -\rho\frac{\partial}{\partial t}\bar{\phi}_0(\underline{x},t) \qquad \text{and}$$

$$p_1(\underline{x},t) = -\rho\frac{\partial}{\partial t}\bar{\phi}_1(\underline{x},t) - \rho U\frac{\partial}{\partial x}\bar{\phi}_0(\underline{x},t) \quad (4.6)$$

Integration of the pressure over the mean wetted surface results in the hydrodynamic reaction force:

$$F_k = -\int_S p \cdot n_k\, ds$$

Substitution of the pressure expansion (4.6) delivers:

$$F_k^{(0)} = -\int_S p_0 \cdot n_k\, ds$$

$$F_k^{(1)} = -\int_S p_1 \cdot n_k\, ds$$

with:

$$F_k = F_k^{(0)} + \tau\, F_k^{(1)}$$

For the unit motion in the j-mode one is now able to write the added mass and damping coefficients:

$$-\omega^2 a_{kj}^{(0)} = \text{real } F_{kj}^{(0)}$$

$$-i\omega\, b_{kj}^{(0)} = \text{imag } F_{kj}^{(0)},$$

with similar definitions for $a_{kj}^{(1)}$ and $b_{kj}^{(1)}$.

F_{kj} is the reaction force in the k-mode due to a unit oscillatory motion in the j-th mode.

5. Computations

In order to evaluate the practicability of the proposed Green's function (3.5) and (3.6), calculations have been made on the one hand using an adapted version of the Fingreen algorithm and on the other hand using standard IMSL subroutines. We are able to transform the expression of ψ_1 in (3.6) into an expression which only contains derivatives of ψ_0. The term ψ_0 in (3.5) and also ψ_1 in (3.6) can then be evaluated using Fingreen. The function ψ_1 has also been computed using standard IMSL subroutines. However, care must be taken for large values of R, the horizontal distance, in the calculation of expression (3.6). A transformation in the complex plane gives an equivalent expression for ψ_1, which yields:

$$\psi_1(\underline{x}) = -\frac{\pi}{2}\frac{d}{dk}\left[k^2 e^{k(z+c)} Y_1(kR)\right]_{k=k_0} +$$

$$-\frac{2}{\pi}\int_0^\infty \frac{k^2 K_1(kR)}{(k^2+k_0^2)}\left[2kk_0\cos k(z+\zeta) + \right.$$

$$\left. + (k_0^2 - k^2)\sin k(z+\zeta)\right]dk +$$

$$+ 2\pi i \cdot (\text{residue of (3.6) in } k=k_0) \qquad (5.1)$$

Table 1 displays for a few values of R in $z+\zeta$ the results of Fingreen and the results of IMSL subroutines for the expression (3.6) and (5.1). The accuracy of the Fingreen results amount to approximately 5 significant figures. The computer time needed for the evaluation (3.6) and (5.1) using IMSL subroutines was approximately 100 to 500 times larger than the time needed using an adapted version of the Fingreen subroutine.

Table 1. Results of computations for ψ_1

$z+\zeta = -1.0$, $k_0 = 0.2$

R	0.01	0.1	0.5	2.0	10.0	100.0
FINGREEN	.7142E-2	.7100E-1	.31171	.50836	-.46203	.14721
IMSL (3.6)	.7142E-2	.7100E-1	.31163	.50807	-.46165	-
(5.1)	-	-	.31171	.50836	-.46203	.14721

$z+\zeta = -10.0$, $k_0 = 0.2$

R	0.01	0.1	0.5	2.0	10.0	100.0
FINGREEN	.814E-4	.814E-3	-.4076E-2	-.1676E-1	-.9231E-1	-.2357E-2
IMSL (3.6)	.813E-4	.813E-3	-.4071E-2	-.1674E-1	-.9216E-1	-.2240E-2
(5.1)	-	-	-	-.1676E-1	-.9231E-1	-.2357E-2

$z+\zeta = -30.0$, $k_0 = 0.2$

R	0.01	0.1	0.5	2.0	10.0	100.0
FINGREEN	.118E-6	.118E-5	-.575E-5	-.122E-4	-.1097E-2	-.1249E-2
IMSL (3.6)	.121E-6	.121E-5	-.600E-5	-.132E-4	-.1089E-2	-.1217E-2
(5.1)	-	-	-	-.122E-4	-.1097E-2	-.1249E-2

The dashes in Table 1 indicate that expression (3.6) or (5.1) does not result in accurate figures.

The computer time needed for the calculation of the forward speed influence was negligible compared with the zero speed computations. The total computer time increases by approximately 5%. Once these forward speed influence coefficients have been computed, the calculation for other forward speeds only depends on some little extra addition/multiplications.

At the moment very little data is available on the hydrodynamic reaction coefficients of ship type vessels at low Froude numbers. In order to validate the presented algorithm, computations have been made with a series 60 ship (block .70) as was used by Vugts [22].

Also computations have been performed by the Ecole Nationale Supérieur de Mêcanique of Nantes [6] for the same ship and frequency range with a program as developed by Grekas et al. [8]. In the E.N.S.M. program also use is made of a low forward speed approximation, however their approach is different then the algorithm presented in this study.

The influence of forward speed effects is most clearly expressed by the hydrodynamic reaction coefficients A_{53}, A_{35}, B_{53} and B_{35}, the added mass and damping coefficients of heave into pitch and pitch into heave. In Figures 4 and 5 the results are presented for these coupling coefficients for $F_n = 0.0$ and 0.05. The zero speed hydrodynamic coefficients of the two programs which are not presented here in detail, correspond up to 3 significant figures.

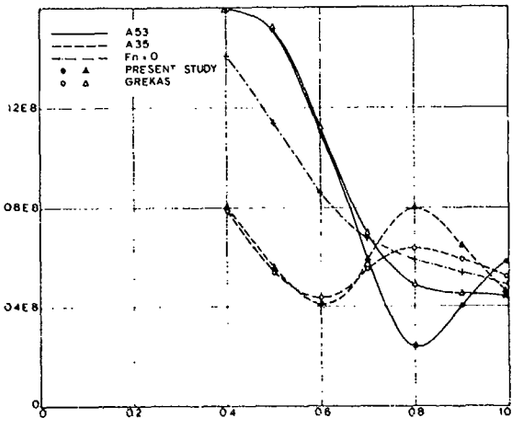

Figure 4. Added mass coupling coefficients A_{35}, A_{53} (Ns^2) for $F_n = 0.0$ and 0.05

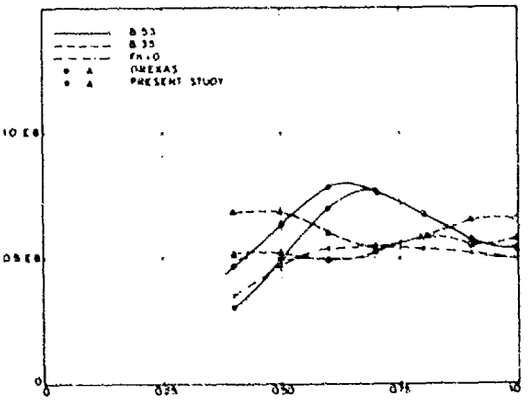

Figure 5. Damping coupling coefficients B_{35}, B_{53} (Ns) for $F_n = 0.0$ and 0.05

From the presented coefficients one may conclude that the correlation of the two programs is quite reasonable. In the low frequency range the added mass terms A_{35} and A_{53} correspond very good and in the higher frequency range the damping terms B_{53} and B_{35} show a reasonable fit.

In spite of the reasonable correlation of the two algorithms one still, however, feels the need of the correlation with model test experiments.

Appendix

In this appendix we study the influence of $\tilde{\psi}_0$ on the source strength and the potential. First it will be shown that the integral

$$\iint_S \sigma_0(\underline{\xi}) \frac{\partial \tilde{\psi}_0}{\partial n_x}(\underline{x},\underline{\xi})\, dS_\xi \qquad (A.1)$$

is asymptotically small. We rewrite the function ψ_0 as:

$$\tilde{\psi}_0(\underline{x},\underline{\xi}) = \mathrm{Im}\, \chi(\underline{x},\underline{\xi}) =$$

$$= -\mathrm{Im}\, 2\nu \int_{-\pi/2}^{\pi/2} \exp[\nu \sec^2\theta(z+\zeta+i\tilde{\omega})] \sec^2\theta d\theta \qquad (A.2)$$

with $\tilde{\omega} = (x-\xi)\cos\theta - (y-\eta)\sin\theta$ and $\nu = \frac{g}{U^2}$

For thin ships the approximation $\frac{\partial}{\partial n_x} \approx \frac{\partial}{\partial y}$ holds and the source distribution (A.1) can be written as a distribution along the projection S of S on the(x,z) plane. We then obtain:

$$\frac{\partial \chi}{\partial y} = 2\nu^2 i \int_{-\pi/2}^{\pi/2} \sec^4\theta \sin\theta \cdot$$

$$\cdot \exp[\nu \sec^2\theta(z+\zeta+i\tilde{\omega})] d\theta \qquad (A.3)$$

where $\tilde{\omega} = (x-\xi)\cos\theta$.

We therefore consider the integral

$$I(x,z) = 2\nu^2 i \int_{-\pi/2}^{\pi/2} \{\iint_{\tilde{S}} \sigma_0(\xi,\zeta) \exp[\nu \sec^2\theta(z+\zeta)] \cdot$$

$$\cdot \exp[i\nu \sec\theta(x-\xi)] d\xi d\zeta\} \sec^4\theta \sin\theta d\theta \qquad (A.4)$$

in the limit $\nu = \frac{g}{U^2} \to \infty$.

First, we consider the integral along $\tilde{S}$. Integration by parts results in the major contribution because no stationary points are situated on $\tilde{S}$ or its boundary. We obtain:

$$\iint_{\tilde{S}} \sigma_0(\xi,\zeta) \exp[\nu(\zeta \sec^2\theta - i\,\xi \sec\theta)] d\xi\, d\zeta =$$

$$= \frac{-1}{i\nu^2 \sec^3\theta} [\sigma_0(\xi^+,0) \exp(-i\xi^+ \nu \sec\theta) +$$

$$- \sigma_0(\xi^-,0) \exp(-i\xi^- \nu \sec\theta)] + O(\frac{1}{\nu^3}) \qquad (A.5)$$

where $(\xi^\pm,0)$ are the endpoints of the ship at the waterline. The integral I(x,z) in (A.4) consists of two parts $I^\pm(x,z)$ with:

$$I^\pm(x,z) = \mp 2 \int_{-\pi/2}^{\pi/2} \sec\theta \sin\theta\, \sigma_0(\xi^\pm,0) \cdot$$

$$\cdot \exp[\nu\{z \sec^2\theta + i(x-\xi^\pm)\sec\theta\}] d\theta$$

$$\text{as } \nu \to \infty \qquad (A.6)$$

The main contribution is generated by the endpoints. This is well known for low Froude number expansions. Further asymptotic expansion leads to:

$$I^\pm(x,z) = \mp \frac{2\,\sigma_0(\xi^\pm,0)}{\nu} \frac{\cos^2\theta}{2z + i(x-\xi^\pm)\cos\theta} \cdot$$

$$\cdot \exp[\nu\{z \sec^2\theta + i(x-\xi^\pm) \sec\theta\}] \Big|_{-\pi/2}^{\pi/2} + O(\frac{1}{\nu^2})$$

$$= O(\frac{i}{\nu^2}) \qquad (A.7)$$

If we proceed with partial integration each next term gives zero, even if z=0. The next term with $\tilde{\psi}_1(\underline{x},\underline{\xi})$ in (4.1) gives no contribution to $\sigma_1(\underline{\xi})$ just as well.

To study the influence of $\tilde{\psi}_0(\underline{x},\underline{\xi})$ on the potential we study the integral:

$$J(\underline{x}) = \iint_{\tilde{S}} \sigma_0(\underline{\xi}) \chi(\underline{x},\underline{\xi})\, dS_\xi = -2\nu \int_{-\pi/2}^{\pi/2} \{\iint_{\tilde{S}} \sigma_0(\xi,\zeta) \cdot$$

$$\cdot \exp[\nu \sec^2\theta(z+\zeta+i\tilde{\omega})] d\xi\, d\zeta\} \sec^2\theta\, d\theta \qquad (A.8)$$

with $\tilde{\omega} = (x-\xi)\cos\theta - y\sin\theta$.

The integral along $\tilde{S}$ can be evaluated by means of partial integration. Making use of (A.5) we obtain:

$$J^\pm(\underline{x}) = \pm \frac{2}{i\nu} \sigma_0(\xi^\pm,0) \cdot$$

$$\cdot \int_{-\pi/2}^{\pi/2} \exp[\nu(z \sec^2\theta + i(x-\xi^\pm) \sec\theta +$$

$$- i\, y \sec^2\theta \sin\theta)] \cdot \frac{d\theta}{\sec^3\theta} \qquad (A.9)$$

For arbitrary values of $\underline{x}$ a further asymptotic expansion of $J^\pm(\underline{x})$ is possible by means of the method of stationary phase. A Kelvin pattern is generated at the bow and stern. The main term behaves like:

$$J^\pm(\underline{x}) = O(\frac{1}{\nu^{3/2}}) = O(U^3)$$

which means that a contribution at higher order than the linear term has been obtained in the wave height. For the calculation of the pressure at the ship a similar analysis shows that higher order terms are obtained as well. Hence, we may neglect these terms if one is interested in linear correction terms.

References

1. Bougis, J.: "Etude de la diffraction radation dans le cas d'un flotteur indeformable animé par une houle sinusoidale de faible amplitude", Ph.D. Thesis Université de Nantes, 1980.
2. Brandsma, F.J. and Hermans, A.J.: "A quasi-linear free surface condition in slow ship theory", Schiffstechnik, April, 1985.
3. Brard, R.: "The representation of a given ship form by singularity distribution when the boundary condition on the free surface is linearized", Journal of Ship Research, Vol. 16, pp. 79-92, 1972.
4. Chang, M.S.: "Computation of three-dimensional ship motions with forward speed", 2nd International Conf. on Numerical Ship Hydrodynamics, Berkely, 1977.
5. Eggers, K.: "Non-Kelvin dispersive waves around non-slender ships", Schiffstechnik, Bd. 8, 1981.
6. E.N.S.M. Report: "Calculs de diffraction-radiation avec vitesse d'avance", Report 8513, E.N.S.M., Nantes, 1985.
7. Faltinsen, O.M.: "A rational ship theory of ship motions", Part II, Report 113, University of Michigan, 1977.
8. Grekas, A. and Delhommeau, G.: "Diffraction-radiation en presence d'un courant", Proceedings of the Association Technique Maritime et Aeronautique (ATMA), Paris, 1983.
9. Hermans, A.J.: "The wave pattern of a ship sailing at low speed, Report 84A, University of Delaware, 1980.
10. Huijsmans, R.H.M. and Dallinga, R.P.: "Non-linear ship motions in shallow water", Int. Workshop on Ship and Platform Motions, Berkeley, 1983.
11. Inglis, R.B.: "A 3-d analysis of the motion of a rigid ship in waves", Ph.D. Thesis, University College of London, 1980.
12. Inglis, R.B. and Price, W.G.: "A three-dimensional ship motion theory comparison between theoretical predictions and experimental data of the hydrodynamic coefficients at forward speed", Trans. Ray. Inst. Nav. Ach. W2, 1981.
13. Nestegard, A. and Sclavounos, P.D.: "A numerical solution of two-dimensional deep water wave-body problems", J. of Ship. Res., 28, 1984.
14. Nestegard, A.: "End effects in the forward speed radiation problem for ships", Ph.D. Thesis, M.I.T, 1984.
15. Newman, J.N.: "A slender body theory for ship oscillations in waves", J. Fl. Mech., 18, 1964.
16. Newman, J.N. and Tuck, E.O.: "Current progress in the slender-ship theory of ship motions", 5th Symp. on Naval Hydrodynamics, Washington D.C., 1964.
17. Newman, J.N.: "The theory of ship motions", Adv. Appl. Mech. 18, 1978.
18. Newman, J.N.: "Three dimensional wave interactions with ships and platforms", Int. Workshop on Ship and Platform Motions, Berkeley, 1983.
19. Ogilvie, T.F. and Tuck, E.O.: "A rational strip theory of ship motions", Part I. Report 013, University of Michigan, 1969.
20. Pinkster, J.A.: "Low frequency second order wave exciting forces on floating structures", Ph.D. Thesis, Report 650, MARIN (N.S.M.B.), 1980.
21. Oortmerssen, G. van: "The motions of a moored ship in waves", Ph.D. Thesis, Report 510, MARIN (N.S.M.B.), 1976.
22. Vugts, J.H.: "The hydrodynamic forces and ship motions in waves", Ph.D. Thesis, Delft, 1970.
23. Wehausen, J.V. and Laitone, E.V.: "Surface waves", Handbook of Physics, Vol. 9, 1960.
24. Wichers, J.E.W. and Huijsmans, R.H.M.: "On the low frequency hydrodynamic damping forces acting on offshore moored vessels", OTC Paper No. 4813, Houston, 1984.

DISCUSSION
of the paper
by R.H.M. Huijsmans and A.J. Hermans

"A FAST ALGORITHM FOR COMPUTATION OF 3-D SHIP MOTIONS OF MODERATE FORWARD SPEED"

DISCUSSION
by J.H.M. Bsar

The authors have presented a very original and efficient approach to the forward speed ship motion problem. In the introduction the authors make mention of the large CPU-requirements of programs based on the distribution of translating, pulsating sources. The CPU-requirements of such programs, however, tend to decrease drastically at the subcritical Strouhal numbers considered by the authors. The required CPU is in such cases comparable to that of zero Froude number program based on pulsating source distributions. The proposed algorithm formally relies on expansions with respect to the Strouhal number. Specifically, quadratic and higher order terms are neglected. However, it seems not trivial that on this basis the waterline contour integral may be neglected, as is done by the present authors. As a matter of fact, the omission of this term appears to be in contradiction with results obtained in the low Froude number theory of wave resistance. Moreover, a simple but effective approximation to the line integral may easily be obtained at little extra costs, as pointed out by Inglis in Ref. 11.

Author's Reply

We thank the discusser for this comment on our paper. We are aware of the fact that nowadays there exist efficient programs for the calculation of the Green's function for a translating, oscillating source at subcritical Strouhal numbers. However, the computer time needed for those calculations is still linearly dependent on the number of forward speeds used. This is not the case in our approach, where only for the first forward speed calculation some computational overhead is needed with respect to the zero speed calculations.

For other forward speed values there is no additional computer time needed. The remark of the discusser with respect to the deletion of the waterline integral in our representation for the potential and the source strength can be answered by using the same arguments as used in the appendix of our paper.

The waterline integral will then give terms in the order of the Strouhal number to power four or higher for the source strength and the potential. Therefore this waterline contribution can be disregarded from our analysis.

DISCUSSION
by R. Yeung

The authors are to be congratulated on a very interesting paper which proposes a forward-speed modification of the zero-speed hydrodynamic coefficient in a low-speed sense. Embedded in this approximation is also the fundamental restriction that the oscillation frequency must be low. Thus, it is perhaps not so surprising that one would expect a disagreement of the "genuine 3-D" results with those obtained by the authors' approximation (Fig. 4) in the higher frequencies. It seems puzzling, however, that the opposite trend is observed for the case of damping (Fig. 5). Another peculiar feature of the results shown on these figures is that the relatively small Froude-No. (Fn=0.05) calculations show no tendency of approaching the zero-Froude No. calculations in the low frequency limit. Since the leading-order correction proposed by the authors is proportional to $\tau=U\omega/g$, it appears to suggest that such a forward-speed purturbation may nor converge uniformly to the zero-speed limit. It will be helpful if a more extensive set of results, including the diagonal values of the added-mass and damping matrix, are available for comparison. Can the authors comment on some of the apparent anomalies raised here? Incidentally, the exact definition of the abscissa in Figs. 4-5 are missing in the preprint.

Author's Reply

The results shown in our paper for a Series 60 ship concern the heave-pitch coupling hydrodynamic coefficients, since for these coefficients the forward speed effect is most pronounced. The diagonal values of added mass and damping were not presented in our paper for $Fn = 0$ and $Fn = 0.05$ because they agreed up to 2 significant figures for the translational modes. It may be misleading to suppose from Figs. 4 and 5 that for the low frequencies there is no tendency of approaching the zero speed limit, since the lowest calculated frequency amounts to 0.4 rad/s. If the value of τ approaches zero all the correction terms in our analysis approach zero in a uniform way. It is still not very clear to us why the differences between our computations and those from ENSM [6] take a different form for the presented added mass and damping coefficient; it seems that more different calculations have to be performed to gain more insight in that matter.

DISCUSSION
by H. Wang

I wish to commend the authors for simplifying the calculation of the Green's functionfor an oscillating, translating source by taking a series expansion approach. I have the following three questions:

1. The contour L* appearing in Eq. (3.6) does not appear to be defined.
2. Does the troublesome behavior of Ψ_0 as $\tau \to 0$ impose a lower limit on the values of τ for which your approach is applicable?
3. In view of your statement that the computer time needed to calculate the forward speed influence is small compared to the zero speed computations, have you considered a more compelex approach for the forward speed effect?

Author's Reply

The discusser raises the question regarding the integration L* as displayed in formula (3.5). This integration contour L* is chosen in the complex plane away from L by some arbitrary small parameter ϵ. In short $L^* \Delta L + i\epsilon$. In this way it is possible to use partial integration on formula (3.6). The remark concerning the behaviour of $\hat{\Psi}_0$ with respect to τ is treated in detail in the appendix of the paper. The troublesome behaviour of Ψ itself is not of interest to us, only its influence potential $\phi(\underline{x},t)$ and on the source strength $\sigma(\underline{x},t)$. It appears from the appendix that the influence is of order (τ^3) or higher. For our purposes we are only interested in the linear correction term of the Green's function expansion. It is possible though to extend the analysis up to order (τ^2).

SEAKEEPING COMPUTATIONS USING TIME-DOMAIN ANALYSIS

S. Liapis and R.F. Beck
The University of Michigan
Ann Arbor, Michigan

Abstract

The problem of a ship traveling at constant forward speed and forced to oscillate around its mean position is formulated using linear time-domain analysis. The hydrodynamic forces acting on the body are expressed in terms of convolution integrals of the arbitrary motion with impulse response functions. The determination of the impulse response functions involves solving a set of integral equations for the velocity potential due to an impulsive velocity (a step change in displacement). The integral equations are solved numerically for bodies of arbitrary shape using a panel method. One of the integral equations must be solved by time stepping, but the kernel matrix is the same at each time step and is closely related to the kernel matrix used to solve the time independent integral equations. The added mass and damping in the frequency domain is found by Fourier transforming the time-domain solution.

Numerical results are obtained for the added mass and damping coefficients in heave and pitch of a Series 60, C_B = .70 hull. Comparisons are shown between the results of the time-domain calculations, the more conventional frequency-domain calculations, and experiments. In general, the comparisons are good.

I. Introduction

During the last twenty years there has been growing interest in numerical methods for calculating ship motions and predicting wave loads. The well known strip theory was the first numerical method which was used as a practical design tool. Despite its utility, strip theory gives poor results at low frequencies and at large ship speeds. The advent of large, high-speed computers led to the development of three-dimensional theories that removed some of the deficiencies of strip theory. Most of these theories use a singularity distribution and reduce the problem to solving a Fredholm integral equation of the second kind on the body surface. Several authors (Chang (1977), Inglis and Price (1982), Guevel and Bougis (1982)) have presented such models to compute ship motions with forward speed and found good agreement with experimental results. In all these models the problem is formulated in the frequency domain leading to equations that have meaning only if the body motions are strictly sinusoidal in time. In more general situations, such as a ship performing a maneuver with varying speed, the frequency-domain approach is meaningless. An alternative to the frequency-domain approach is to formulate the problem directly in the time domain. The solutions in the frequency domain and time domain can be related through the use of Fourier transforms. For any particular problem involving only zero forward speed, one formulation or the other may be more convenient. However, for problems involving forward speed it appears that the time-domain approach requires much less computational effort and can be easily extended to more general cases.

Cummins (1962) and Ogilvie (1964) first discussed the use of time-domain analysis to solve unsteady ship motion problems. The zero forward speed problem is examined in detail by Wehausen (1967, 1971). The method of analysis is based on the work of Finkelstein (1957), which is expanded on in both Stoker (1957) or Wehausen and Laitone (1960).

Few results using time-domain analysis are available and they are all for zero forward speed. Direct solutions in two-dimensions are presented by Adachi and Ohmatsu (1980), Ikebuchi (1981) and Yeung (1982). Two-dimensional time-domain analysis was also used by Daoud (1975) and Yeung and Kim (1984) as part of the development for slender-body theories of ships with constant forward speed. Ursell (1964) and Maskell and Ursell (1970) developed solutions in the time domain for a floating semi-circle using the Fourier transform of the frequency-domain solution. The same technique was used by Kotik and Lurye (1968) for a floating hemisphere. Lin (1966) developed a mathematical formulation of the time-domain problem with forward speed. His formulation leads to equations that are very complicated and are not amenable to numerical computation.

Recently, Newman (1985) has used time-domain analysis to determine the impulse response function for a right circular cylinder.

Because of the axial symmetry he was able to use "ring sources" and reduce the problem to solving a one-dimensional integral equation at at each time step.

Beck and Liapis (1985) use time-domain analysis to solve the radiation problem for arbitrary bodies at zero forward speed. The solution is obtained by solving a pair of integral equations using panel methods. One of the integral equations must be solved by time stepping, but the kernel matrix is identical at each time step and need only be inverted once. Comparisons with other published results showed excellent agreement. Excellent agreement with experiment was also found for the time history of the vertical displacement of a floating sphere released from an initial displacement.

The work presented in this paper is the next step in the continuing development of the time-domain analysis method. The computed results presented in Beck and Liapis (1985) for simple geometrical shapes at zero forward speed have been extended to a Series 60, $C_B = .70$ ship at both zero and constant forward speed.

The computed results presented here are not complete because, as discussed in section IV, simplified expressions for the forward-speed body boundary condition and Bernoulli's equation are used. The simplified expressions are obtained by replacing the steady forward motion potential with the free-stream potential. The use of simplified expressions greatly eases the computational burden but does not affect the part of the calculations dealing with time-domain analysis. Demonstration of the viability of time-domain analysis at forward speed can be made just as well with the simplified expressions as with the complete expressions. For the Series 60 hull used in the present calculations, Inglis and Price (1982) found that this simplification has little effect on the added mass and damping coefficients in the frequency domain.

In the paper consideration is only given to the radiation problem of a ship moving at a constant forward speed and forced to oscillate about a mean position. The extension to non-constant forward speed and curved trajectories is in principle straight forward. Work on the exciting force problem has just started at The University of Michigan.

II. Mathematical Formulation

The axis system shown in Figure 1 is used to formulate the linearized problem in the time domain. The axis system is fixed to the mean position of the ship and travels in the positive x-direction with constant velocity U_o. The z-axis points upward and positive x is toward the bow. The x-y plane is coincident with the calm water level and the origin is at midship. The ship is undergoing small unsteady motions around its mean position in otherwise calm water.

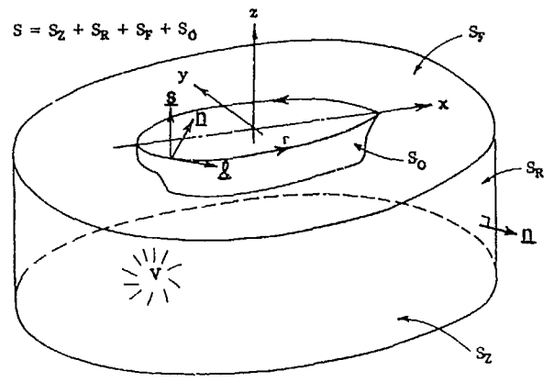

Figure 1. Coordinate System and Control Volume

It is assumed that the fluid is incompressible and inviscid and that the flow is irrotational. To set up a linearized problem it is assumed that the fluid disturbances due to the steady forward motion and the unsteady oscillations are small and can be separated. In this case the total velocity potential can be written as

$$\Phi_T = -U_o x + \Phi_o(x,y,z) + \phi(x,y,z,t) \qquad (1)$$

where the term $\left(-U_o x + \Phi_o(x,y,z)\right)$ is the potential due to the steady translation of the vessel and the potential $\phi(x,y,z,t)$ contains all the unsteady effects. In the fluid domain, each of the potentials must satisfy the Laplace equation subject to boundary conditions on the free surface, the body, at infinity and appropriate initial conditions.

The free surface condition is linearized on the assumption of small elevation. Furthermore the interaction at the free surface between the steady perturbation velocities and the unsteady potential are neglected so that the boundary condition on the radiation potential reduces to

$$\left(\frac{\partial}{\partial t} - U_o\frac{\partial}{\partial x}\right)^2\phi + g\frac{\partial}{\partial z}\phi = 0 \quad \text{on } z = 0 \qquad (2)$$

where g = acceleration on gravity. The kinematic boundary condition on the hull can be linearized to give

$$\frac{\partial \phi}{\partial n} = \sum_{k=1}^{6} (n_k\dot{\zeta}_k + m_k\zeta_k) \quad \text{on } S_o \qquad (3)$$

where

S_o = mean underwater hull surface
n_k = components of generalized unit normal out of fluid domain
$(n_1, n_2, n_3) = \underline{n}$
$(n_4, n_5, n_6) = \underline{r} \times \underline{n}$
$\underline{r} = (x, y, z)$

ζ_k = amplitude of unsteady motion in six degrees of freedom

$(\zeta_1, \zeta_2, \zeta_3)$ = linear translation along the x,y,z axes respectively

$(\zeta_4, \zeta_5, \zeta_6)$ = rotational motions about the x,y,z axes respectively

m_k = gradients of the steady velocities in the normal direction

$(m_1, m_2, m_3) = -(\underline{n}\cdot\nabla)\underline{W}$

$(m_4, m_5, m_6) = -(\underline{n}\cdot\nabla)(\underline{r}\times\underline{W})$

$\underline{W}$ = velocity vector due to steady translation

$= \nabla(-U_o x + \Phi_o)$

and the overdot represents differentiation with respect to time.

Since an initial value problem is being solved the gradient of the radiation potential must vanish at infinity. In addition the initial conditions of

$$\Phi = 0 \quad \text{for} \quad t < 0$$

$$\frac{\partial\Phi}{\partial t} = 0 \quad \text{for} \quad t < 0 \tag{4}$$

must be imposed.

An integral equation for the potential on the body surface can be derived using Green's theorem and a Green function for an impulsive source below a free surface. The appropriate Green function is

$$G(P,Q,t-\tau) = \left(\frac{1}{r} - \frac{1}{r'}\right)\delta(t-\tau) + H(t-\tau)$$

$$\times\, 2\int_0^\infty dk\, \sqrt{kg}\, \sin\left(\sqrt{kg}(t-\tau)\right)\, e^{k(z+\zeta)}\, J_o(kR)$$

$$= \left(\frac{1}{r} - \frac{1}{r'}\right)\delta(t-\tau) + H(t-\tau)\tilde{G}(P,Q,t-\tau) \tag{5}$$

where

$P = (x, y, z)$

$Q = (\xi, \eta, \zeta)$

$r^2 = (x-\xi)^2 + (y-\eta)^2 + (z-\zeta)^2$

$r'^2 = (x-\xi)^2 + (y-\eta)^2 + (z+\zeta)^2$

$R^2 = (x-\xi+U_o(t-\tau))^2 + (y-\eta)^2$

$\delta(t-\tau)$ = delta function

$H(t-\tau)$ = unit step function

$= 0 \quad t < 0$

$= 1 \quad t > 0$

The Green function represents the potential at the field point P and at time t due to an impulsive source at the point Q suddenly created and annihilated at time τ. This source acts like an underwater disturbance which generates a Cauchy-Poisson type wave system as represented by the $\tilde{G}(P,Q,t-\tau)$ term. The integrated form of (5) is given by Wehausen and Laitone (1960) as the potential for a source of arbitrary strength moving below a free surface. It is easily shown that the Green function satisfies the following problem:

$$\nabla^2 G = -4\pi\,\delta(P-Q)\,\delta(t-\tau)$$

$$\left(\frac{\partial}{\partial t} - U\frac{\partial}{\partial x}\right)^2 G + g\frac{\partial}{\partial z}G = 0 \quad \text{on } z = 0$$

$$G,\ \frac{\partial G}{\partial t} = 0 \quad \text{for} \quad t < 0 \tag{6}$$

Applying Green's theorem to the fluid volume shown in Figure 1 and enclosed by $S_z \cup S_r \cup S_f \cup S_o$ yields

$$\iiint_V [\Phi\nabla^2 G - G\nabla^2\Phi]\, dV = \iint_S \left(\Phi\frac{\partial G}{\partial n} - G\frac{\partial\Phi}{\partial n}\right)dS \tag{7}$$

Integrating both sides of (7) with respect to τ from 0^- to t^+ and using the properties of $G(P,Q,t-\tau)$ and the fact that Φ satisfies the Laplace equation everywhere in the fluid domain gives:

$$\Phi(P,t) = -\frac{1}{4\pi}\int_0^t d\tau \iint_S dS \left\{\Phi(Q,\tau)\frac{\partial G(P,Q,t-\tau)}{\partial n_Q}\right.$$

$$\left. - G(P,Q,t-\tau)\frac{\partial\Phi(Q,\tau)}{\partial n_Q}\right\} \tag{8}$$

The contribution to the right hand side from the surfaces at infinity vanish because both G and Φ vanish at infinity.

The contribution to (8) from the surface integral over the free surface can be reduced to a line integral about the waterline of the vessel. From equation (2) it is found that the free surface boundary condition gives

$$\frac{\partial}{\partial n} \equiv \frac{\partial}{\partial\zeta} = -\frac{1}{g}\left(\frac{\partial}{\partial\tau} - U_o\frac{\partial}{\partial\xi}\right)^2 \quad \text{on } z = 0$$

Hence the contribution to (8) from the free surface may be written:

$$\Phi_F = \frac{1}{4\pi g}\int_0^t d\tau \iint_{S_F} dS \left[\Phi(Q,\tau) \times \left(\frac{\partial}{\partial\tau} - U_o\frac{\partial}{\partial\xi}\right)^2 G(P,Q,t-\tau) - G(P,Q,t-\tau)\left(\frac{\partial}{\partial\tau} - U_o\frac{\partial}{\partial\xi}\right)^2\Phi(Q,\tau)\right] \tag{9}$$

Φ_F may be separated into two parts which can be reduced independently as follows:

$$\Phi_F = \Phi_{F1} + \Phi_{F2} \tag{10}$$

$$\begin{aligned}\Phi_{F1} &= \frac{1}{4\pi g}\int_0^t d\tau \iint_{S_F} dS \left[\Phi(Q,\tau)\, G_{\tau\tau}(P,Q,t-\tau) - G(P,Q,t-\tau)\,\Phi_{\tau\tau}(Q,\tau)\right] \\ &= \frac{1}{4\pi g}\iint_{S_F} dS \int_0^t d\tau \frac{\partial}{\partial\tau}\left[\Phi(Q,\tau)\, G_\tau(P,Q,t-\tau) - G(P,Q,t-\tau)\,\Phi_\tau(Q,\tau)\right] \\ &= \frac{1}{4\pi g}\iint_{S_F} dS \left[\Phi(Q,\tau)\, G_\tau(P,Q,t-\tau) - G(P,Q,t-\tau)\,\Phi_\tau(Q,\tau)\right]_0^t\end{aligned} \tag{11}$$

where the subscript denotes differentiation with respect to the given variable. Because of the initial conditions on Φ and G the last expression equals zero. The Φ_{F2} term is

$$\Phi_{F2} = \frac{1}{4\pi g}\int_0^t d\tau \iint_{S_F} dS \left[U_o^2\,(\Phi G_{\xi\xi} - G\Phi_{\xi\xi}) - 2U_o\,(\Phi G_{\xi\tau} - G\Phi_{\xi\tau})\right]$$

Integrating one half of the last term by parts with respect to τ gives:

$$\begin{aligned}\Phi_{F2} &= \frac{1}{4\pi g}\int_0^t d\tau \iint_{S_F} dS \left[U_o^2\,(\Phi G_{\xi\xi} - G\Phi_{\xi\xi}) - U_o\,(\Phi_\xi G_\tau - G_\xi\Phi_\tau + \Phi G_{\xi\tau} - G\Phi_{\xi\tau}\right] \\ &= \frac{1}{4\pi g}\int_0^t d\tau \iint_{S_F} dS \frac{\partial}{\partial\xi}\left[U_o^2\,(\Phi G_\xi - \Phi_\xi G) - U_o\,(\Phi G_\tau - \Phi_\tau G)\right]\end{aligned} \tag{12}$$

Applying Stokes' theorem to the last form of (12) yields

$$\Phi_{F2} = -\frac{1}{4\pi g}\int_0^t d\tau \oint_\Gamma d\eta \left[U_o^2\,(\Phi G_\xi - \Phi_\xi G) - U_o\,(\Phi G_\tau - \Phi_\tau G)\right] \tag{13}$$

where Γ = intersection of the mean hull surface and the plane $z = 0$. The positive sense of the line integral is in the counter-clockwise direction.

The final result for Φ at a point in the fluid is

$$\begin{aligned}\Phi(P,t) = &-\frac{1}{4\pi}\int_0^t d\tau \iint_{S_o} dS \left[\Phi\frac{\partial G}{\partial n} - G\frac{\partial\Phi}{\partial n}\right] \\ &+ \frac{1}{4\pi g}\int_0^t d\tau \oint_\Gamma d\eta \left(U_o^2\left(G\frac{\partial\Phi}{\partial\xi} - \Phi\frac{\partial G}{\partial\xi}\right) - U_o\left(\frac{\partial\Phi}{\partial\tau}G - \Phi\frac{\partial G}{\partial\tau}\right)\right)\end{aligned} \tag{14}$$

Although equation (14) is derived for constant foward speed along a straignt trajectory, it may easily be generalized for arbitrary speed and trajectory (see Liapis (1985)).

In the usual manner of potential theory equation (14) can be reduced to a pure source distribution by considering the interior flow and subtracting it from equation (14). The final result is:

$$\begin{aligned}\Phi(P,t) = &-\frac{1}{4\pi}\int_0^t d\tau \iint_{S_o} dS\; G(P,Q,t-\tau)\,\sigma(Q,\tau) \\ &-\frac{U_o^2}{4\pi g}\int_0^t d\tau \oint_\Gamma d\eta\; \sigma(Q,\tau)\, n_1\, G(P,Q,t-\tau)\end{aligned} \tag{15}$$

For the case of steady state oscillation of frequency ω at constant forward speed, equation (15) can be reduced by setting $\sigma(Q,\tau) = \sigma(Q)\, e^{i\omega\tau}$. Making the substitutions and interchanging the orders of integration it can be found:

$$\begin{aligned}\Phi(P) = &-\frac{1}{4\pi}\iint_{S_o} dS\; \sigma(Q) \int_0^t d\tau\; e^{i\omega\tau}\, G(P,Q,t-\tau) \\ &-\frac{U_o^2}{4\pi g}\oint_\Gamma d\eta\; \sigma(Q)\, n_1 \int_0^t d\tau\; e^{i\omega\tau}\, G(P,Q,t-\tau)\end{aligned} \tag{16}$$

As $t \to \infty$ Wehausen and Laitone (1960) show that the time integration of the Green function reduces to the usual Green function for a source translating with constant forward speed and sinusoidal strength. In this case equation (16) is identical to the form of the potential used by Chang (1977).

An integral equation for the source strength may be found by differentiating (15) with respect to the normal on the body and setting it equal to the body boundary condition. Thus, we may write:

$$\frac{\partial \Phi}{\partial n_p} = -\frac{\sigma(P,t)}{2} - \frac{1}{4\pi}\int_0^t d\tau \iint_S dS\ \sigma \frac{\partial G}{\partial n_p} - \frac{U_o^2}{4\pi g}\int_0^t d\tau \oint_\Gamma d\eta\ \sigma\ n_1 \frac{\partial G}{\partial n_p} \qquad (17)$$

Since the body boundary condition is represented by the sum of six individual components, it is useful to divide the potential into six individual problems each of which satisfies:

$$\frac{\partial \Phi_k}{\partial n} = n_k \dot{\zeta}_k + m_k \zeta_k \qquad (18)$$

The coefficients m_k as defined in (3) contain the influence of the steady velocity field on the body boundary condition.

Similar to the method proposed by Cummins (1962) or Ogilvie (1964) we can consider a ficticious case where at $t = 0$ the ship jumps instantaneously from 0 to 1 in the k^{th} mode. This jump is impulsive, so that the velocity is $\dot{\zeta}_k = \delta(t)$. For this special case of motion the body boundary condition is:

$$\frac{\partial \phi_k}{\partial n} = n_k \delta(t) + m_k H(t) \qquad (19)$$

The body boundary condition (19) suggests that the potential ϕ_k can be decomposed into an impulsive and a memory part such that:

$$\phi_k(P,t) = \psi_{1k}(P)\delta(t) + \chi_k(P,t) \qquad (20)$$

If we set

$$\frac{\partial \psi_{1k}}{\partial n} = n_k \quad \text{on } S_o \qquad (21)$$

$$\frac{\partial \chi_k}{\partial n} = m_k \quad \text{on } S_o$$

then the body boundary condition (19) is satisfied for all time.

The integral equations which must be solved to determine ψ_{1k} and χ_k are found by applying integral equation (14) on the body surface and substituting equations (20) and (21). Gathering terms proportional to $\delta(t)$ gives an integral equation for ψ_{1k} and the remaining terms yield an equation for χ_k . The details of the derivation may be found in Liapis (1985); the final results are:

$$\psi_{1k}(P) + \frac{1}{2\pi}\iint_{S_o} dS\ \psi_{1k}\frac{\partial}{\partial n_Q}\left(\frac{1}{r} - \frac{1}{r'}\right) = \frac{1}{2\pi}\iint_{S_o} dS\ \left(\frac{1}{r} - \frac{1}{r'}\right) n_k \qquad (22)$$

$$\chi_k(P,t) + \frac{1}{2\pi}\iint_{S_o} dS\ \chi_k \frac{\partial}{\partial n_Q}\left(\frac{1}{r} - \frac{1}{r'}\right) + \frac{1}{2\pi}\int_0^t d\tau \iint_{S_o} dS\ \chi_k \frac{\partial \tilde{G}(P,Q,t-\tau)}{\partial n_Q} + \frac{U_o^2}{2\pi g}\int_0^t d\tau \oint_\Gamma d\eta\ \left(\chi_k \frac{\partial \tilde{G}}{\partial \xi} - \tilde{G}\frac{\partial \chi_k}{\partial \xi}\right) - \frac{U_o}{\pi g}\int_0^t d\tau \oint_\Gamma d\eta\ \chi_k \frac{\partial \tilde{G}}{\partial \tau}$$

$$= \frac{1}{2\pi}\iint_{S_o} dS\ m_k\left(\frac{1}{r} - \frac{1}{r'}\right) + \frac{1}{2\pi}\int_0^t d\tau \iint_{S_o} dS\ m_k\, \tilde{G}(P,Q,t-\tau) + \frac{1}{2\pi}\iint_{S_o} dS\ n_k\, \tilde{G}(P,Q,t) - \frac{1}{2\pi}\iint_{S_o} dS\ \psi_{1k}\frac{\partial \tilde{G}(P,Q,t)}{\partial n_Q} \qquad (23)$$

The ψ_{1k} problem describes the fluid motion during the impulsive stage and may be interpreted as an infinite fluid problem satisfying

$$\psi_{1k} = 0 \quad \text{on} \quad z = 0$$

$$\frac{\partial \psi_{1k}}{\partial n} = n_k \quad \text{on} \quad S_o$$

$$\nabla \psi_{1k} \to 0 \quad \text{at} \quad \infty$$

The χ_k potential represents the motion of the fluid subsequent to the initial impulse and can be considered as composed of two components. The first results because of a change in body orientation due to the impulse in velocity. After the impulse in velocity the body will have a unit displacement in the k^{th} mode, which, in the presence of the steady velocity flow field, results in a change of fluid velocity on the body surface. In order for the body boundary condition to remain satisfied this change must be cancelled out. Therefore, $\partial\chi_k/\partial n$ must have the value m_k on the body surface for all $t > 0$.

The second component is the result of the

impulsive velocity (the ψ_{1k} problem) inducing a disturbance into the flow field which in subsequent times will propogate as a wave motion away from the body. Consequently, χ_k will satisfy the complete free surface condition for $t > 0$. At $t = 0$ χ_k will meet the following initial conditions

$$\chi_k = 0 \qquad \text{on } z = 0$$

$$\frac{\partial \chi_k}{\partial t} = -g \frac{\partial \psi_{1k}}{\partial z} \qquad \text{on } z = 0$$

To aid in computational efficiency it is convenient to explicitly identify the two components of χ_k as

$$\chi_k(P,t) = \psi_{2k}(P)\, H(t) + \bar{\chi}_k(P,t) \tag{24}$$

In equation (24) the $\psi_{2k}(P)$ function represents the value of χ_k during the impulsive phase of the motion. It satisfies the following boundary conditions:

$$\frac{\partial \psi_{2k}}{\partial n} = m_k \quad \text{on } S_o$$

$$\psi_{2k} = 0 \quad \text{on } z = 0 \tag{25}$$

$$\nabla \psi_{2k} \to 0 \quad \text{at } \infty$$

In order for χ_k to meet the proper boundary conditions it is not difficult to show that $\bar{\chi}_k(P,t)$ satisfies the following conditions:

$$\bar{\chi}_k = 0 \qquad \text{at } t = 0$$

$$\frac{\partial \bar{\chi}}{\partial t} = -g \frac{\partial \psi_{1k}}{\partial z} \qquad \text{on } z = 0 \text{ at } t = 0$$

$$\frac{\partial \bar{\chi}_k}{\partial n} = 0 \qquad \text{on } S_o \text{ for } t > 0$$

$$\left(\left(\frac{\partial}{\partial t} - U_o \frac{\partial}{\partial x}\right)^2 + g \frac{\partial}{\partial z}\right)(\bar{\chi}_k + \psi_{2k}) = 0 \quad \text{on } z = 0 \text{ for } t > 0 \tag{26}$$

From the boundary conditions on the free surface and the integral equation for $\bar{\chi}_k$ it can be shown that

$$\frac{\partial^2 \bar{\chi}_k}{\partial t^2} = -g \frac{\partial \psi_{2k}}{\partial z} \qquad \text{on } z = 0 \quad t = 0 \tag{27}$$

The integral equation for $\psi_{2k}(P)$ is found by taking the limit of the integral equation for χ_k (equation (23)) at $t = 0$. This gives

$$\psi_{2k}(P) + \frac{1}{2\pi} \iint_{S_o} dS\, \psi_{2k}(Q) \frac{\partial}{\partial n_Q}\left(\frac{1}{r} - \frac{1}{r'}\right) = \frac{1}{2\pi} \iint_{S_o} dS\, m_k \left(\frac{1}{r} - \frac{1}{r'}\right) \tag{28}$$

Subtracting (28) from (23) gives the following integral equation for $\bar{\chi}_k(P,t)$:

$$\begin{aligned}
&\bar{\chi}_k(P,t) + \frac{1}{2\pi} \iint_{S_o} dS\, \bar{\chi}_k \frac{\partial}{\partial n_Q}\left(\frac{1}{r} - \frac{1}{r'}\right) \\
&+ \frac{1}{2\pi} \int_0^t d\tau \iint_{S_o} dS\, \bar{\chi}_k \frac{\partial \tilde{G}(P,Q,t-\tau)}{\partial n_Q} \\
&+ \frac{U_o^2}{2\pi g} \int_0^t d\tau \oint_\Gamma d\eta \left(\bar{\chi}_k \frac{\partial \tilde{G}}{\partial \xi} - \tilde{G} \frac{\partial \bar{\chi}_k}{\partial \xi}\right) \\
&- \frac{U_o}{\pi g} \int_0^t d\tau \oint_\Gamma d\eta\, \bar{\chi}_k \frac{\partial \tilde{G}(P,Q,t-\tau)}{\partial \tau} \\
&= \frac{1}{2\pi} \int_0^t d\tau \iint_{S_o} dS\, m_k\, \tilde{G}(P,Q,t-\tau) \\
&+ \frac{1}{2\pi} \iint_{S_o} dS\, n_k\, \tilde{G}(P,Q,t) \\
&- \frac{1}{2\pi} \iint_{S_o} dS\, \psi_{1k} \frac{\partial \tilde{G}(P,Q,t)}{\partial n_Q} \\
&- \frac{1}{2\pi} \int_0^t d\tau \iint_{S_o} dS\, \psi_{2k} \frac{\partial \tilde{G}(P,Q,t-\tau)}{\partial n_Q}
\end{aligned} \tag{29}$$

The potential for an arbitrary forced motion in the k^{th} direction is found as the convolution of $\phi_k(P,t)$ with the velocity of the motion. Using equations (19) and (24), the expression for the velocity potential due to arbitrary motion becomes:

$$\begin{aligned}
\Phi_k(P,t) &= \int_0^t d\tau\, \phi_k(P,\tau) \dot{\zeta}_k(t-\tau) \\
&= \psi_{1k}(P) \dot{\zeta}_k(t) + \psi_{2k}(P) \zeta_k(t) \\
&+ \int_0^t d\tau\, \bar{\chi}_k(P,\tau) \dot{\zeta}_k(t-\tau)
\end{aligned} \tag{30}$$

where the integral equation which must be solved to find $\psi_{1k}(P)$, $\psi_{2k}(P)$ and $\bar{\chi}_k(P,t)$ are given by (22), (28) and (29) respectively. It is easily shown (see Cummins (1962) or Liapis (1985)) that $\Phi_k(P,t)$ satisfies the body boundary condition, the free surface condition, and the conditions at infinity for all t .

The form of the general potential (30) can be directly compared to the formulation developed by Ogilvie (1964, equation (11)). Ogilvie has four potentials Ψ_{1k}, χ_{1k}, Ψ_{2k}, and χ_{2k}. His Ψ_{1k} and Ψ_{2k} are identical to the presently defined Ψ_{1k} and Ψ_{2k}. Ogilvie's memory potentials, χ_{1k} and χ_{2k}, have been combined into the present $\bar{\chi}_k$. In fact, it can be shown that

$$\bar{\chi}_k = \chi_{1k} + \int_0^t d\tau\ \chi_{2k} \quad . \tag{31}$$

After determining the hydrodynamic forces acting on the body, Ogilvie uses an integration by parts to combine the effects of χ_{1k} and χ_{2k} into a single memory function K_{jk}. In the present work, χ_{1k} and χ_{2k} have just been combined at an earlier stage of the development. Integral equation (29) for $\bar{\chi}_k$ can be obtained by combining the integral equations which would have to be solved to determine Ogilvie's χ_{1k} and χ_{2k}. The advantage of the present formulation is that it saves computational effort, since only one integral equation needs to be solved.

The unsteady pressure in the fluid is given by the linearized Bernoulli equation:

$$p = -\rho \frac{\partial \Phi_k}{\partial t} - \rho \underline{W} \cdot \nabla \Phi_k \tag{32}$$

The forces acting on the body are found by integrating the pressure over the instantaneous underwater hull surface. However, it is much more convenient to be able to integrate the pressure over the mean position of the hull. To do this, the pressure is expanded in a Taylor series about the undisturbed hull position and integrated. Furthermore, because of the waves on the free surface and the motion of the hull, an additional contribution is obtained from a line integral around the waterline of the undisturbed hull. The details of this derivation may be found in Ogilvie (1964). The resulting expressions for the forces involve the usual pressure integral terms over the undisturbed hull surface given in equation (33) and extra terms involving products of the steady perturbation velocities and gradient of the unsteady potential. These extra terms are generally assumed small and neglected. Apparently, there are no numerical results to verify this assumption. Since the extra terms increase the complexity of the expressions for the hydrodynamic forces acting on the body, and because they will all equal zero under the simplifying assumption made for the numerical calculations presented in this paper, the extra term will be left off in the subsequent derivation. The reduced expression for the linearized forces acting on the body is

$$F_{jk}(t) = -\rho \iint_{S_o} dS\ p\ n_j$$

$$= -\rho \iint_{S_o} dS\ \frac{\partial \Phi_k}{\partial t} n_j - \rho \iint_{S_o} dS\ (\underline{W} \cdot \nabla \Phi_k)\ n_j \tag{33}$$

The second term of (33) involves derivatives of the Φ_k potential, a quantity which is difficult to evaluate. This gradient of the potential may be eliminated using the following theorem developed by Tuck and presented in Ogilvie and Tuck (1969) (or see Ogilvie (1977)):

$$\iint_{S_o} dS\ [m_j \Phi_k + n_j (\underline{W} \cdot \nabla \Phi_k)] = -\oint_\Gamma d\ell\ n_j\ \Phi_k\ (\underline{\ell} \times \underline{n}) \cdot \underline{W} \tag{34}$$

where $\underline{\ell}$ = unit vector tangential to the waterline curve Γ. For wall-sided vessels $(\underline{\ell} \times \underline{n}) = \underline{k}$, the unit vector in the z-direction. Applying (34) to the second term in (33), the expression for the unsteady forces acting on the hull is:

$$F_{jk}(t) = -\rho \iint_{S_o} dS\ \frac{\partial \Phi_k}{\partial t} n_j + \rho \iint_{S_o} dS\ \Phi_k\ m_j$$

$$+ \rho \oint_\Gamma d\ell\ n_j\ \Phi_k\ (\underline{\ell} \times \underline{n}) \cdot \underline{W} \tag{35}$$

Equation (35) can be reduced further by using the form of Φ_k given in (30). The final expression for the unsteady force acting on the body in the j^{th} direction due to arbitrary motion in the k^{th} direction is

$$F_{jk}(t) = -\mu_{jk} \ddot{\zeta}_k(t) - b_{jk} \dot{\zeta}_k(t) - c_{jk} \zeta_k(t)$$

$$- \int_0^t d\tau\ K_{jk}(t - \tau)\ \dot{\zeta}_k(\tau) \tag{36}$$

where

$$\mu_{jk} = \rho \iint_{S_o} dS\ \Psi_{1k}\ n_j$$

$$b_{jk} = \rho \left[\iint_{S_o} dS\ \Psi_{2k}\ n_j - \iint_{S_o} dS\ \psi_{1k}\ m_j \right.$$

$$\left. - \oint_\Gamma d\ell\ \psi_{1k}\ n_j\ (\underline{\ell} \times \underline{n}) \cdot \underline{W} \right]$$

$$c_{jk} = \rho \left[-\iint_{S_o} dS\ \psi_{2k}\ m_j \right.$$

$$\left. - \oint_\Gamma d\ell\ \psi_{2k}\ n_j\ (\underline{\ell} \times \underline{n}) \cdot \underline{W} \right]$$

$$K_{jk}(t) = \rho\Big[+ \iint_{S_o} dS \frac{\partial \bar{X}_k(Q,t)}{\partial t} n_j - \iint_{S_o} dS\, \bar{X}_k(Q,t)\, m_j - \oint_{\Gamma} d\ell\, n_j\, \bar{X}_k(Q,t)\, (\underline{\ell}\times\underline{n})\cdot\underline{W} \Big]$$

Equation (36) is in a form useful for the calculation of ship motions because all of the coefficients are independent of the past history of the unsteady motion. The coefficient μ_{jk} is a constant depending only on ship geometry, b_{jk} and c_{jk} are constants which depend on ship geometry and forward speed. In the equations of motion for the vessel the c_{jk} term adds to the hydrostatic restoring force coefficient. The μ_{jk} and b_{jk} are part of the added mass and damping terms respectively. All the memory of the fluid response is contained in the function $K_{jk}(t)$, which is dependent on ship geometry, speed, and time.

The coefficients μ_{jk}, b_{jk}, c_{jk} and K_{jk} can be directly related to the more usual frequency-domain coefficients. Consider a motion amplitude of the form

$$\zeta_k(t) = 0 \qquad t < 0$$
$$= e^{i\omega t} \qquad t > 0 \tag{37}$$

Substituting the motion (37) into the force equation (36) and taking the limit as ti.. goes to infinity yields

$$F_{jk}(t) = \Big[\omega^2\mu_{jk} - i\omega b_{jk} - c_{jk} - \int_0^{\infty} d\tau\, i\omega e^{-i\omega\tau} K_{jk}(\tau)\Big] e^{i\omega t} \tag{38}$$

In the frequency domain, the hydrodynamic force on the body for sinusoidal motion is given by

$$F_{jk} = \big[\omega^2 A_{jk}(\omega) - i\omega B_{jk}(\omega) - C_{jk}\big] e^{i\omega t} \tag{39}$$

where

$A_{jk}(\omega)$ = added mass coefficient in frequency domain

$B_{jk}(\omega)$ = damping coefficient in frequency domain

C_{jk} = restoring force coefficient

Equating the real and imaginary parts of (38) and (39) gives the following expressions for A_{jk}, B_{jk}, and C_{jk} in terms of the time-domain coefficients:

$$A_{jk}(\omega) = \mu_{jk} - \frac{1}{\omega}\int_0^{\infty} d\tau\, K_{jk}(\tau)\sin\omega\tau$$

$$B_{jk}(\omega) = b_{jk} + \int_0^{\infty} d\tau\, K_{jk}(\tau)\cos\omega\tau$$

$$C_{jk} = c_{jk} \tag{40}$$

As can be seen from equation (40), μ_{jk} and b_{jk} are the frequency independent parts of the added mass and damping respectively. All frequency dependence of the added mass and damping are contained in the memory function K_{jk}. The coefficient C_{jk} is a frequency independent modification to the hydrostatic restoring force coefficient.

The same type of decomposition, which has just been developed for the potential method, can also be used for the source distribution technique. The development exactly parallels the potential method. Therefore, only the final expressions will be given here. Similar to (20) and (24) the source strength and potential are decomposed into

$$\sigma_k(P,t) = \alpha_k(P)\delta(t) + \beta_k(P)H(t) + \gamma_k(P,t) \tag{41}$$

and

$$\psi_{1k}(P) = -\frac{1}{4\pi}\iint_{S_o} dS\, \alpha_k(Q)\Big(\frac{1}{r} - \frac{1}{r'}\Big)$$

$$\psi_{2k}(P) = -\frac{1}{4\pi}\iint_{S_o} dS\, \beta_k(Q)\Big(\frac{1}{r} - \frac{1}{r'}\Big)$$

$$\bar{X}_k(P,t) = -\frac{1}{4\pi}\int_0^t d\tau \iint_{S_o} dS\, \gamma_k(Q,\tau)\, G(P,Q,t-\tau) - \frac{U_o^2}{4\pi g}\int_0^t d\tau \oint_{\Gamma} d\eta\, n_1\, \gamma_k(q,\tau)\, \tilde{G}(P,Q,t-\tau) - \frac{1}{4\pi}\iint_{S_o} dS\, \gamma_k(Q)\, \tilde{G}(P,Q,t) - \frac{1}{4\pi}\int_0^t d\tau \iint_{S_o} dS\, \beta_k(Q)\, \tilde{G}(P,Q,t-\tau) \tag{42}$$

where

$\alpha_k(P)$ = part of source strength due to impulsive velocity in k^{th} direction

$\beta_k(P)$ = part of source strength due to displacement in k^{th} direction

$\gamma_k(P,t)$ = time dependent part of source strength due to motion in the k^{th} direction

ψ_{1k}, ψ_{2k}, $\bar{X}_k$ = same meaning as in (20) and (24)

The integral equations for α_k, β_k and γ_k are found by gathering terms after substituting (41) into (17) and using (19). The final results are:

$$-\frac{\alpha_k(P)}{2} - \frac{1}{4\pi}\iint_{S_o} dS_Q\, \alpha_k(Q)\, \frac{\partial}{\partial n_p}\left(\frac{1}{r} - \frac{1}{r'}\right) = n_k \tag{43}$$

$$-\frac{\beta_k(P)}{2} - \frac{1}{4\pi}\iint_{S_o} dS_Q\, \beta_k(Q)\, \frac{\partial}{\partial n_p}\left(\frac{1}{r} - \frac{1}{r'}\right) = m_k \tag{44}$$

$$\begin{aligned} -\frac{\gamma_k(P,t)}{2} &- \frac{1}{4\pi}\iint_{S_o} dS_Q\, \gamma_k(Q,t)\, \frac{\partial}{\partial n_p}\left(\frac{1}{r} - \frac{1}{r'}\right) \\ &- \frac{1}{4\pi}\int_0^t d\tau \iint_{S_o} dS_Q\, \gamma_k(Q,\tau)\, \frac{\partial}{\partial n_p}\tilde{G}(P,Q,t-\tau) \\ &- \frac{U_o^2}{4\pi g}\int_0^t d\tau \oint_\Gamma d\eta\, n_1 \gamma_k(Q,\tau)\, \frac{\partial}{\partial n_p}\tilde{G}(P,Q,t-\tau) \\ &= \frac{1}{4\pi}\iint_{S_o} dS_Q\, \alpha_k(Q)\, \frac{\partial}{\partial n_p}\tilde{G}(P,Q,t) \\ &+ \frac{1}{4\pi}\int_0^t d\tau \iint_{S_o} dS_Q\, \beta_k(Q)\, \frac{\partial}{\partial n_p}\tilde{G}(P,Q,t-\tau) \end{aligned} \tag{45}$$

The source strength at any time for a prescribed motion is found by a convolution of σ_k and the motion velocity as follows

$$\begin{aligned} \sum_k(P,t) &= \int_0^t d\tau\, \sigma_k(P,\tau)\, \dot{\zeta}(t-\tau) \\ &= \alpha_k(P)\dot{\zeta}(t) + \beta_k(P)\zeta(t) \\ &+ \int_0^t d\tau\, \gamma_k(Q,\tau)\dot{\zeta}(t-\tau) \end{aligned} \tag{46}$$

The hydrodynamic forces acting on the body, the added mass, the damping and the hydrostatic restoring forces are found by substituting equations (42) into (36) and (40).

III. Numerical Methods

The integral equations for the potential method (eq. (22), (28) and (29)) or the source method (eq. (43), (44) and (45)) are solved numerically using a panel method. The body surface is approximated by an ensemble of plane quadrilateral elements of constant potential (or source) strength. This discretization reduces the continuous singularity distribution to a finite number of unknown potential (or source) strengths. The integral equations are satisfied at collocation points located at the null points of each panel. This gives a system of algebraic equations which are solved for the unknown potential (or source) strengths.

In the presentation which follows only the numerical solution to the potential method will be discussed. The techniques used in the source method are very similar and therefore will be omitted.

The integral equations (22) and (28) for ψ_{1k} and ψ_{2k} contain no memory terms. To solve them the method of Hess and Smith (1964) is followed. Assuming constant values for ψ_{1k} and ψ_{2k} over each quadrilateral, equations (27) and (28) may be discretized as:

$$\sum_{m=1}^{M} A_{im}\,(\psi_{qk})_m = (B_q)_i \qquad \begin{matrix} i = 1,2,\ldots,M \\ q = 1,2 \end{matrix} \tag{47}$$

where

M = number of quadrilateral elements

$(\psi_{qk})_m$ = strengths of ψ_{1k}, ψ_{2k} over the m^{th} element

$$A_{im} = 1 \qquad i = m$$

$$= \frac{1}{2\pi}\iint_{S_m} dS\, \underline{n}_m \cdot \nabla\left(\frac{1}{r} - \frac{1}{r'}\right) \qquad i \neq m$$

S_m = surface area of m^{th} quadrilateral

$\underline{n}_m$ = unit normal vector to m^{th} quadrilateral

$r^2 = (x_i - \xi)^2 + (y_i - \eta)^2 + (z_i - \zeta)^2$

$r'^2 = (x_i - \xi)^2 + (y_i - \eta)^2 + (z_i + \zeta)^2$

x_i, y_i, z_i = coordinates of the i^{th} collocation point

$$(B_1)_i = \frac{1}{2\pi}\sum_{m=1}^{M}\iint_{S_m} dS\, \left(\frac{1}{r} - \frac{1}{r'}\right)(n_k)_m$$

$$(B_2)_i = \frac{1}{2\pi}\sum_{m=1}^{M}\iint_{S_m} dS\, \left(\frac{1}{r} - \frac{1}{r'}\right)(m_k)_m$$

$(n_k)_m$ $(m_k)_m$ are defined in eq. (3)

The evaluation of the coefficients A_{im} and $(B_q)_i$ involves integrals of the infinite fluid potential ($1/r$) and its derivatives over each panel. They are evaluated by using the numerical techniques developed by Hess and Smith (1964). For small values of r the integrals are done exactly. For intermediate values of r a multipole expansion is used. For large values of r a simple monopole expansion is used.

To solve equation (29) for $\bar{X}_k(P,t)$ a time stepping method must be used. A trapezoidal rule is used to evaluate the convolution integrals with the result that:

$$\bar{X}_k(P,t) + \frac{1}{2\pi}\iint_{S_o} dS\ \bar{X}_k(Q,t)\ \frac{\partial}{\partial n_Q}\left(\frac{1}{r} - \frac{i}{r'}\right)$$

$$+ \frac{\Delta t}{2\pi}\sum_{n=1}^{N}{}'\iint_{S_o} dS\ \bar{X}_k(Q,t_n)\ \frac{\partial \tilde{G}(P,Q,t-t_n)}{\partial n_Q}$$

$$+ \sum_{n=1}^{N}{}'\ \Delta t\ \Big[\ \frac{U_o^2}{2\pi g}\oint_\Gamma d\eta\ \Big(\bar{X}_k(Q,t_n)\ \frac{\partial \tilde{G}(P,Q,t-t_n)}{\partial \xi} - \tilde{G}(P,Q,t-t_n)\ \frac{\partial \bar{X}_k(Q,t_n)}{\partial \xi}\Big)$$

$$+ \frac{U_o}{\pi g}\oint_\Gamma d\eta\ \bar{X}k(Q,t_n)\ \frac{\partial \tilde{G}(P,Q,t-t_n)}{\partial t}\ \Big]$$

$$= \frac{1}{2\pi}\iint_{S_o} dS\ \Big(n_k\tilde{G}(P,Q,t) - \psi_{1k}\ \frac{\partial \tilde{G}(P,Q,t)}{\partial n_Q}\Big)$$

$$+ \frac{\Delta t}{2\pi}\sum_{n=1}^{N}{}'\iint_{S_o}\Big(m_k\ \tilde{G}(P,Q,t-t_n) - \psi_{2k}\ \frac{\partial \tilde{G}(P,Q,t-t_n)}{\partial n_Q}\Big) \qquad (48)$$

where Δt = constant time step size and the prime on the summation symbol denotes that 1/2 weights are to be used for the end points of the trapezoidal integration rule.

The time stepping is started at $t_o = 0$ where $\bar{X}_k$ equals zero. At each subsequent time step only $\bar{X}_k(P,t_N)$ is unknown; all other values of $\bar{X}_k(P,t)$ (i.e. $\bar{X}_k(P,t_{N-1})$, $\bar{X}_k(P,t_{N-2})$, ..., $\bar{X}_k(P,t_o)$) are known. Gathering terms, equation (48) may be rewritten to yield an equation for the unknown $\bar{X}_k(P,t_N)$ at the latest (t_N) time step:

$$\bar{X}_k(P,t_N) + \frac{1}{2\pi}\iint_{S_o} dS\ \bar{X}_k(Q,t_N)\ \frac{\partial}{\partial n_Q}\left(\frac{1}{r} - \frac{1}{r'}\right)$$

$$+ \frac{\Delta t}{4\pi}\iint_{S_o} dS\ \bar{X}_k(Q,t_N)\ \frac{\partial \tilde{G}(P,Q,0)}{\partial n_Q}$$

$$+ \frac{\Delta t}{2}\Big[\ \frac{U_o^2}{2\pi g}\Big(\oint_\Gamma d\eta\ \Big(\bar{X}_k(Q,t_N)\ \frac{\partial \tilde{G}(P,Q,0)}{\partial \xi} - \tilde{G}(P,Q,0)\ \frac{\partial \bar{X}_k(Q,t_N)}{\partial \xi}\Big)$$

$$+ \frac{U_o}{\pi g}\oint_\Gamma d\eta\ \bar{X}k(Q,t_N)\ \frac{\partial \tilde{G}(P,Q,0)}{\partial t}\ \Big]$$

$$= \frac{1}{2\pi}\iint_{S_o} dS\ \Big(n_k\tilde{G}(P,Q,t_N) - \psi_{1k}\ \frac{\partial \tilde{G}(P,Q,t_N)}{\partial n_Q}\Big)$$

$$+ \frac{\Delta t}{2\pi}\sum_{n=1}^{N}{}'\iint_{S_o}\Big(m_k\ \tilde{G}(P,Q,t_N-t_n) - \psi_{2k}\ \frac{\partial \tilde{G}(P,Q,t_N-t_n)}{\partial n_Q}\Big) \qquad (49)$$

$$- \frac{\Delta t}{2\pi}\sum_{n=1}^{N-1}\iint_{S_o} dS\ \bar{X}_k(Q,t_n)\ \frac{\partial \tilde{G}(P,Q,t_N-t_n)}{\partial n_Q}$$

$$- \Delta t\ \sum_{n=1}^{N-1}\Big[\ \frac{U_o^2}{2\pi g}\Big(\oint_\Gamma d\eta\ \bar{X}_k(Q,t_n)\ \frac{\partial \tilde{G}(P,Q,t_N-t_n)}{\partial \xi} - \tilde{G}(P,Q,t_N-t_n)\ \frac{\partial \bar{X}(Q,t_n)}{\partial \xi}\Big)$$

$$+ \frac{U_o}{\pi g}\oint_\Gamma d\eta\ \bar{X}_k(Q,t_n)\ \frac{\partial \tilde{G}(P,Q,t_N-t_n)}{\partial t}\ \Big]$$

Because $\partial \bar{X}_k/\partial \xi$ is difficult to evaluate numerically, the term involving it is simplified based on a method used by Guevel and Bougis (1982). The term may be resolved into its components in the local ξ-n-s coordinate system as shown in figure 1 and then reduced as follows:

$$\oint_\Gamma d\eta \, \frac{\partial \bar{X}}{\partial \xi} \tilde{G} = \oint_\Gamma d\eta \, (\underline{n}\cdot\underline{i}) \, \frac{\partial \bar{X}}{\partial n} \tilde{G}$$

$$+ \oint_\Gamma d\eta \, (\underline{s}\cdot\underline{i}) \, \frac{\partial \bar{X}}{\partial s} \tilde{G} + \oint_\Gamma d\eta \, (\underline{\ell}\cdot\underline{i}) \, \frac{\partial \bar{X}}{\partial \ell} \tilde{G} \qquad (50)$$

The first term is zero because $\partial \bar{X}/\partial n = 0$ on the body surface. For a wall sided ship $(\underline{s}\cdot\underline{i}) = 0$ and the second term equals zero. For the computed results in this paper, this term has been neglected for all vessels based on the assumption that most bodies of interest are wall sided over most of their length. The third term can be integrated by parts to eliminate $\partial \bar{X}/\partial \ell$. Assuming the variations along the waterline of the direction cosines of $\underline{\ell}$ are small, the final approximation for the waterline integral is:

$$\oint_\Gamma d\eta \, G(P,Q,t-t_n) \, \frac{\partial \bar{X}_k(Q,t_n)}{\partial \xi}$$

$$= - \oint_\Gamma d\eta \, \bar{X}_k(Q,t_n) \, \frac{\partial \tilde{G}(P,Q,t-t_n)}{\partial \ell} \, (\underline{\ell}\cdot\underline{i}) \qquad (51)$$

At each time step equation (49) is solved using the same panel discretization used to solve for ψ_{1k}, ψ_{2k}. The line integral is evaluated by subdividing Γ into a series of straight line segments. The strength of $\bar{X}_k$ on a line segment is assumed equal to the strength of the panel below it. The system of equations which must be solved at each time step has the form:

$$\sum_{m=1}^{M} A_{im} \, (\bar{X}_k(t_N))_m = B_i \qquad i = 1,2,\ldots,M \qquad (52)$$

where

N = number of quadrilateral elements

N = number of time steps

$(\bar{X}_k(t_N))_m$ = value of $\bar{X}_k(P,t)$ on the m^{th} panel at the t_N time step

$$A_{im} = 1 + \left\{ \frac{\Delta t U_o}{\pi} \int_{\Gamma_m} d\eta \, \frac{\partial}{\partial x} \frac{1}{r'} \right\} \qquad i = m$$

$$= \frac{1}{2\pi} \iint_{S_m} dS \, \underline{n}_m \cdot \nabla \left(\frac{1}{r} - \frac{1}{r'} \right)$$

$$+ \left\{ \frac{\Delta t U_o}{\pi} \int_{\Gamma_m} d\eta \, \frac{\partial}{\partial x} \frac{1}{r'} \right\} \qquad i \neq m$$

$$B_i = \frac{1}{2\pi} \sum_{m=1}^{M} \Bigg\{ (n_k)_m \iint_{S_m} dS \, \tilde{G}(P,Q,t_N)$$

$$- (\psi_{1k})_m \iint_{S_m} dS \, \frac{\partial \tilde{G}(P,Q,t_N)}{\partial n_Q} \Bigg)$$

$$+ \frac{\Delta t}{2\pi} \sum_{n=1}^{N}{}' \Bigg[(m_k)_m \iint_{S_m} dS \, \tilde{G}(P,Q,t_N-t_n)$$

$$- (\psi_{2k})_m \iint_{S_m} dS \, \frac{\partial \tilde{G}(P,Q,t_N-t_n)}{\partial n_Q}$$

$$- \iint_{S_m} dS \, (\bar{X}_k(t_n))_m \, \frac{\partial \tilde{G}(P,Q,t_N-t_n)}{\partial n_Q} \Bigg] \Bigg\}$$

$$- \sum_{m^*} \Delta t \sum_{n=1}^{N-1} \left\{ \frac{U_o^2}{2\pi g} \, (\bar{X}_k(t_n))_{m^*} \int_{\Gamma_{m^*}} d\eta \right.$$

$$\times \left(\frac{\partial \tilde{G}(P,Q,t_N-t_n)}{\partial \xi} + (\underline{\ell}\cdot\underline{i}) \, \frac{\partial \tilde{G}(P,Q,t_N-t_n)}{\partial \ell} \right)$$

$$\left. + \frac{U_o}{\pi g} (\bar{X}_k(t_n))_{m^*} \int_{\Gamma_{m^*}} d\eta \, \frac{\partial \tilde{G}(P,Q,t_N-t_n)}{\partial t} \right]$$

Note that for A_{im} the line integral terms in large brackets are only used for panels on the free surface. Furthermore, m^* denotes that only the panels on the free surface are used in the summation for the line integral terms.

In the derivation of the above, use is made of the fact that

$$\tilde{G}(P,Q,0) = 0$$

$$\frac{\partial \tilde{G}(P,Q,0)}{\partial n} = 0$$

$$\frac{\partial \tilde{G}(P,Q,0)}{\partial t} = 2g \, \frac{\partial}{\partial z} \frac{1}{r'} \qquad (53)$$

A very important property of the coefficient matrix A_{im} in equation (52) is that it is independent of time. As a result it needs to be inverted only once at the beginning of the time stepping. For a sufficiently large number of panels this property results in a significant computational advantage over the frequency domain formulation.

The right-hand side term B_i involves the integrals of the Green function and its deri-

vatives over each quadrilateral. They are evaluated by using coordinate mapping and Gauss quadrature. The arbitrary quadrilateral is first mapped into a square. A product Gauss rule is then used to evaluate the integral. Over most of the panels for the Series 60 ship discussed in the next section a 2×2 Gauss rule was sufficiently accurate. For certain panels a 4×4 Gauss rule was required. The line integrals are evaluated by a one-dimensional trapezoidal rule along the water line.

The evaluation of $G(P,Q,t)$ with an efficient and accurate method is one of the most important elements in this problem. Depending on the values of P, Q, and t three methods are used to evaluate $G(P,Q,t)$: a power series expansion, an asymptotic expansion and a Filon integration scheme. The details may be found in Beck and Liapis (1985 Appendix B).

IV. Numerical Results

The results presented in this section are for a Series 60 model forced to oscillate in heave and pitch. The Series 60 model is a parent form ($L/B = 7.0$, $B/T = 2.5$, $LCB/L = .5\%$ forward) for the $C_B = .70$ series. This model has been tested by Gerritsma (1966) and Gerritsma and Beukelman (1964). In addition, Chang (1977), Inglis (1980) and Inglis and Price (1982) have presented numerical results using frequency-domain calculations.

As previously mentioned, for the numerical results presented in this paper two simplifications have been made. The first is that m_j has been approximated by

$$m_j = (0,\ 0,\ 0,\ 0,\ +U_o n_3,\ -U_o n_2) \tag{54}$$

The approximation (54) is equivalent to neglecting the effects of the steady perturbation velocities on the body boundary condition. This approximation was made because of the difficulty of determining ϕ_o. The use of the complete value for m_j, as given in equation (3) would not alter the time-domain computer program; it would mearly require different input values.

The second simplifying assumption is that in the computation for the hydrodynamic pressure the steady velocity vector, $\underline{W}$, can be approximated by the free stream-vector:

$$\underline{W} \approx (-U_o,\ 0,\ 0) \tag{55}$$

This assumption is consistant with neglecting the steady perturbation potential in the body boundary condition. The elimination of the steady perturbation velocities in equations (54) and (55) greatly eases the computational burden but it does not affect the time-domain analysis procedure.

The quadralateral elements into which the body surface was subdivided for most of the calculations presented in this section are shown in figure 2. There are 108 panels on the half-body. The panels are smaller near the ends because they are critical for the pitch calculations. It has been found that the results can vary up to 5% depending on the panel distribution for a fixed number of panels.

One of the major problems with time-domain analysis is the oscillatory tail which occurs in the memory functions, $K_k(P,t)$, at large time as they approach zero. Figure 3 is a plot of the memory function in heave at zero forward speed versus time. The three curves correspond to the potential method of calculation (equations (22), (28) and (29)) for 76 and 108 panels respectively and the source method (equations (42), (43) and (44)) for 75 panels. The time step size, Δt, is shown in the nondimensional form defined as:

$$\Delta t^* = \Delta t \sqrt{g/L} \tag{56}$$

For the smaller number of panels the oscillatory tail is clearly visible.

The oscillatory error at large time is apparently the result of the integral equation method of solution and not numerical inaccuracies. Adachi and Ohmatsu (1979, 1980) examined the two-dimensional problem and found that the oscillatory error in the time-domain is the equivalence of the irregular frequencies in the frequency domain. Since irregular frequencies also exist in three-dimensions, it is assumed that the oscillatory errors seen in figure 3 are also the equivalence of irregular frequencies.

Adachi and Ohmatsu show that using the source method the oscillatory error cannot be eliminated regardless of time step size or number of panels. However, using orthogonality arguments they show analytically that the

Figure 2. Panel Distribution

potential method can have a solution which is free of oscillatory error. Because of numerical errors the computed results might not be free of these oscillations, but at least the potential method should converge to the proper solution given a sufficient number of panels and small enough time step size.

Figure 3 shows that for small times all three methods give approximately the same results. At large time the potential method does have less oscillatory error than the source method. Furthermore, when the number of panels is increased to 108 and the time step size decreased to $\Delta t^* = .06264$ the oscillatory error almost disappears. There are still slight oscillations and flat spots in the $M = 108$ curve but they are small. Presumably a further increase in the number of panels and a decreased step size would eliminate them further.

Figure 4 is reproduced from Beck and Liapis (1985) and is presented to demonstrate that the oscillatory error can be eliminated given a sufficient number of panels and a small enough time step size. The figure shows the memory function for a sphere in heave. It should be noted that the memory function in Beck and Liapis is defined in terms of the acceleration of the motion. Thus, $K(t)$ used in this paper is the time derivative of $\bar{K}(t)$. The solid curve is the analytic result of Barakat (1962) obtained by Fourier transforming his frequency-domain result. As shown in the figure the oscillatory error has almost disappeared. The agreement between the present numerical computations and the analytic result is excellent.

Figures 5-9 show the nondimensional added mass and damping coefficients (A_{jk} and B_{jk}) for the Series 60 ship as a function of nondimensional frequency. Five different sets of data are presented. The solid lines are the results computed by time-domain analysis using the potential method presented in this paper. For the calculations 108 panels on the half-body were used and the time step size was $\Delta t^* = 0.6264$. The small-dash curves are the experimental results of Gerritsma (1966) for zero forward speed and Gerritsma and Beukelman (1964) for a Froude number of .2. The large-dash curves are strip theory results. The strip theory results were computed using the coefficients of Salvesen, Tuck and Faltensen (1970) and a source distribution technique to solve the two-dimensional problem. The results computed by three-dimensional methods in the frequency domain using source panel techniques are shown as crosses and asterisks. The crosses are the results of Inglis (1980) for zero forward speed and Inglis and Price (1982) for a Froude number of .2. The results are for their IP2 method which corresponds to the method presented in this paper. The asterisks were presented by Chang (1977). Chang's results are plotted in dimensional form and no model length or density are given in the paper. To nondimensionalize Chang's results a model length of 10 ft (3.048 m) was used. Note that not all of the coefficients were plotted by Chang.

Figure 5 shows the added mass and damping in heave for zero forward speed. As can be seen all the results agree reasonably well. For the added mass the present calculations fall between those of Chang and Inglis. The singularity in Inglis' results around $\omega^* = 5.0$ is the irregular frequency in the frequency domain calculation. The time domain calculations also exhibit erratic behavior in this region. Presumably if more panels were taken in the numerical model the curves would be smoother as was found in Beck and Liapis (1985) for a sphere.

Figure 6 presents the cross-coupling coefficient between heave and pitch. At zero forward speed $A_{35} = A_{53}$ and $B_{35} = B_{53}$; thus only A_{35} and B_{35} are plotted. The differences in the computed values of A_{35} , B_{35} and A_{53} , B_{53} are less than 3% in all cases. The cross-coupling coefficients are the most sensitive measures of the numerical accuracy of the program because they involve taking the differences between the two ends of the model, which have been exaggerated due to a multiplication by the lever arm. The reason Inglis' results are so much larger than the others is not known. Note that both the present results and the experimental results cross zero and become negative.

The pitch added mass and damping is presented in figure 7. As with heave the time-domain curves are not smooth at high frequencies due to a presumed lack of the number of panels and too big a time step size. Similar to A_{35} , Inglis' results for A_{55} are too large around the peak values.

The added mass and damping coefficients for the ship moving at a constant forward speed of Froude number equal to .2 are shown in figures 8 and 9. The computational time for these results is almost the same as for the zero forward speed case. The additional calculations which must be made to include the line integral terms has very little effect on the total computer time. Arbitrarily deleting the line integral term from the calculations alters the results a maximum of 20%. Most of the alteration to the memory function curve due to the effect of the line integrals occurs around the peak of the curve and at large time.

The forward speed results all suffer from oscillations in the memory function at large time. This is the same problem as discussed in reference to figure 3. The same paneling was used for both $F_n = 0$ and $F_n = .2$. While the paneling was sufficient for the zero speed case, it apparently needs further refinement in the forward speed case. In addition the time step size and maximum time for the calculations has to be adjusted in order to improve the predictions. As can be seen in figures 8 and 9 the oscillations in the tail of the memory functions has lead to oscillations in the added

mass and damping coefficients.

The heave added mass and damping is shown in figure 8. For the added mass all the results agree reasonably well; the damping shows a much larger spread between the various predictions. The hook at high frequency in the time-domain analysis curve is false and is the result of the oscillatory tail.

The pitch added inertia, pitch damping, and heave-pitch cross-coupling curves all show strong influences of the oscillatory tail and need further investigation. When compared to the other theoretical calculations and to the experiments the time-domain predictions will have the correct magnitude, but the curves are not smooth. As an example, figure 8 shows the added mass and damping in pitch. The time-domain curves are not shown in the low frequency range because the results in that region depend on the arbitrary method of closure of the memory function at large time. A closure technique was necessary because the computer run was inadvertantly stopped before the memory function return to zero. Lack of time and computer funds prevents a re-run. As can be seen the results are in the proper range. The oscillations and low frequency results can be improved by better numerical techniques at large time.

V. Conclusions

The use of time-domain analysis has been shown to be a viable alternative to the frequency-domain approach for solving the radiation problem. Either method can be used to find the added mass and damping. However, the time-domain solution can be extended to problems of variable forward speed and curved trajectories.

As compared to a frequency-domain formulation, time-domain technique can be extended from zero to constant forward speed with only minor modifications. The computer time for the forward speed case is only slightly larger than the zero speed case.

The major disadvantages of time-domain analysis are all related to the behavior of the memory functions at large time. Related to the irregular frequencies in the frequency domain, an oscillatory error appears in the tail of the time-domain memory function as it approaches zero at large time. By solving for the velocity potential directly, the oscillatory error can presumably be made as small as necessary by using time steps and quadrilateral elements which are sufficiently small. Unfortunately, this greatly increases the computer time. For the calculations presented in this paper using constant time step size and simple trapezoidal time integration, 50% of the computer time is used to obtain the tail of the memory function. To make time-domain analysis useful for routine calculations a method must be found to give good definition to the tail of the memory function without tremendous expenditure of computer time. Variable time step size and/or asymptotic analysis will be investigated in the near future.

Acknowledgement

This work was supported by the Fluid Mechanics Program of the Office of Naval Research, Contract Number N00014-85-K-0118.

References

1. Adachi, H. and Ohmatsu, S. (1979). On the influence of irregular frequencies in the integral equation solutions of the time-dependent free surface problems. Journal of Engineering Mathematics, Vol. 16, No. 2, pp. 97-119.

2. Adachi, H. and Ohmatsu, S. (1980). On the time dependent potential and its application to wave problems. Proceedings 13th Symposium on Naval Hydrodynamics, ONR, Washington D.C., pp. 281-302.

3. Barakat, R. (1962). Vertical motion of a floating sphere in a sine-wave sea. Journal of Fluid Mechanics, Vol. 13, pp. 540-556. Also corrections in an unpublished report entitled "Forced periodic heaving of a semi-immersed sphere."

4. Beck, R.F. and Liapis, S. (1985). Transient motions of floating bodies at zero forward speed. Submitted for publication to the Journal of Fluid Mechanics.

5. Chang, M.-S. (1977). Computation of three-dimensional ship-motions with forward speed. Proceedings Second International Conference on Numerical Ship Hydrodynamics, University of California, Berkeley, pp. 124-135.

6. Cummins, W.E. (1962). The impulse response function and ship motions. Schiffstechnik, Vol. 9, pp. 101-109.

7. Daoud, N. (1975). Potential flow near to a fine ship's bow. Report No. 177, Department of Naval Architecture and Marine Engineering, The University of Michigan.

8. Finkelstein, A.B. (1957). The initial value problem for transient water waves. Communications on Pure and Applied Mathematics, Vol. 10, pp. 511-522.

9. Gerritsma, J. and Beukelman, W. (1964). The distribution of the hydrodynamic forces on a heaving and pitching shipmodel in still water. Report No. 22, Shipbuilding Laboratory, Technological University of Delft, Delft, Netherlands.

10. Gerritsma, J. Distribution of hydrodynamic forces along the length of a ship model in waves. Report No. 144, Shipbuilding Laboratory, Technological University of Delft, Delft, Netherlands.

11. Guevel, P. and Bougis, J. (1982). Ship-motions with forward speed in infinite depth. International Shipbuilding Progress, Vol. 29, No. 332, pp. 105-117.

12. Hess, J.L., and Smith, A.M.O. (1964). Calculation of nonlifting potential flow about arbitrary three-dimensional bodies. Journal of Ship Research, Vol. 8, No. 2, pp. 22-44.

13. Ikebuchi, T. (1981). Hydrodynamic forces on a body moving arbitrary in time on a free surface. Journal Kansai Society of Naval Architects, Japan, No. 181, pp. 45-53.

14. Inglis, R.B. (1980). A three-dimensional analysis of the motion of a rigid ship in waves. Ph.D. thesis, Department of Mechanical Engineering, University College, London.

15. Inglis, R.B. and Price, W.G. (1982). A three-dimensional ship motion theory -- comparison between theoretical prediction and experimental data of the hydrodynamic coefficients with forward speed. Transactions Royal Institution of Naval Architects, Vol. 124, pp. 141-157.

16. Kotik, J., and Lurye, J. (1968). Heave oscillation of a floating cylinder or sphere. Schiffstichnik, Vol. 15, pp. 37-38.

17. Liapis, S. (1985). Time-domain analysis of ship motions. Ph.D. thesis, Department of Naval Architecture and Marine Engineering, The University of Michigan, in preparation.

18. Lin, W.C. (1966). An initial-value problem for the motion of a ship moving with constant mean velocity in an arbitrary seaway. Report No. NA-66-9 of College of Engineering, University of California, Berkeley.

19. Maskell, S.J., and Ursell, F. (1970). The transient motion of a floating body. Journal of Fluid Mechanics, Vol. 44, part 2, pp. 303-313.

20. Newman, J.N., (1985). Transient axisymmetric motion of a floating cylinder. submitted for publication in the Journal of Fluid Mechanics.

21. Ogilvie, T.F. (1964). Recent progress toward the understanding and prediction of ship motions. Proceedings 5th Symposium on Naval Hydrodynamics, ONR, Washington, D.C., pp. 3-128.

22. Ogilvie, T.F. and Tuck, E.O. (1969). A rational strip theory of ship motion: Part 1. Report No. 13, Department of Naval Architecture and Marine Engineering, The University of Michigan, Ann Arbor.

23. Ogilvie, T.F. (1977). Singular perturbation problems in ship hydrodynamics. Advances in Applied Mechanics, Vol. 17, pp. 91-188.

24. Salvesen, N., Tuck, E.O., and Faltinsen, O. (1970). Ship motions and sea loads. Transactions Society of Naval Architects and Marine Engineers, Vol. 78, pp. 250-287.

25. Stoker, J.J. (1957). Water waves. Interscience Publishers, Inc., New York.

26. Ursell, F. (1964). The decay of the free motion of a floating body. Journal of Fluid Mechanics, Vol. 19, pp. 305-314.

27. Yeung, R.W. (1982). The transient heaving motion of floating cylinders. Journal of Engineering Mathematics, Vol. 16, pp. 97-119.

28. Yeung, R.W., and Kim, S.H. (1984). A new development in the theory of oscillating and translating slender ships. Proceedings 15th Symposium on Naval Hydrodynamics, ONR, Washington, D.C., pp. 195-218.

29. Wehausen, J.V. and Laitone, E.V. (1960). Surface waves. Handbuch der Physik, Springer-Verlag, Berlin, pp. 446-778.

30. Wehausen, J.V. (1967). Initial-value problem for the motion in an undulating sea of a body with fixed equilibrium position. Journal of Engineering Mathematics, Vol. 1, pp. 1-19.

31. Wehausen, J.V. (1971). The motion of floating bodies. Annual Review of Fluid Mechanics, Vol. 3, pp. 237-268.

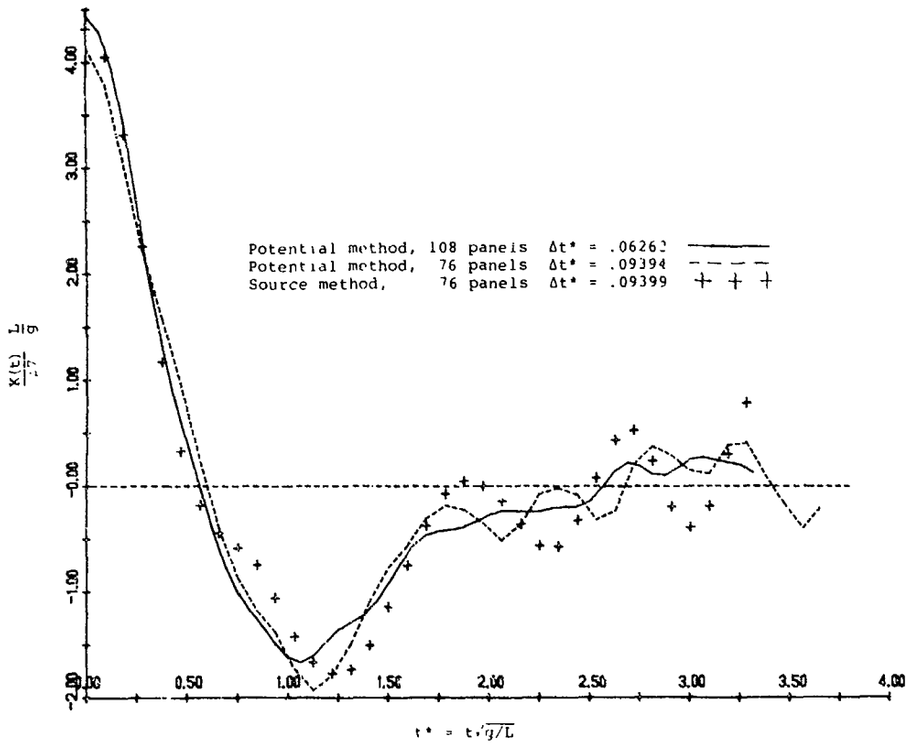

Figure 3. Memory Function for Heave Force on a Series 60 (C_b = .70) model at Fn = 0

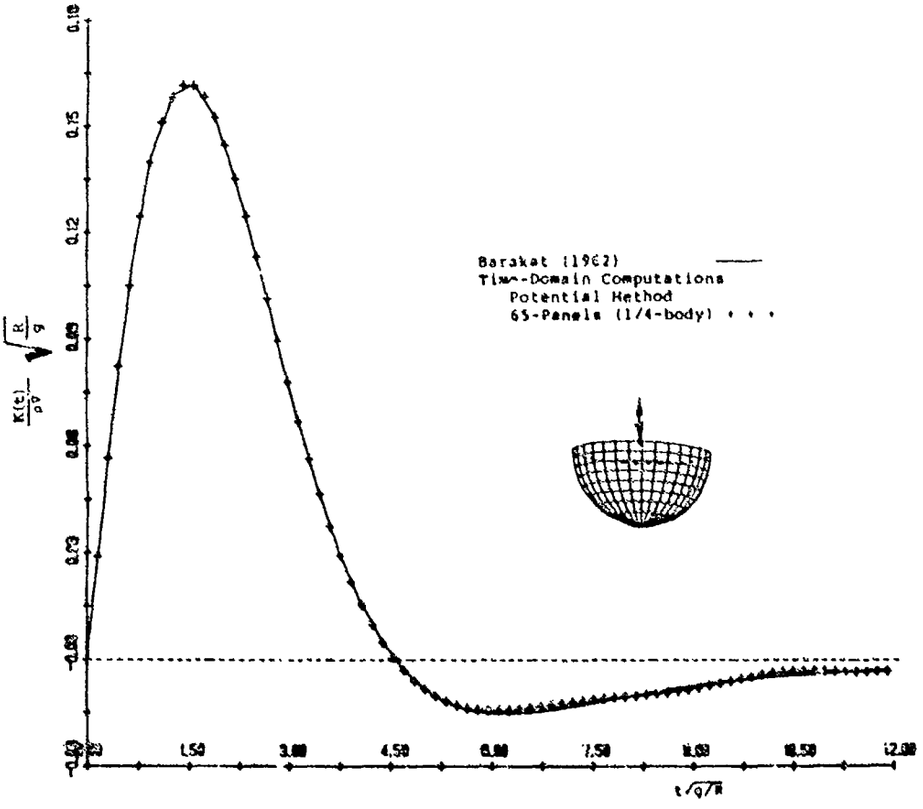

Figure 4. Memory Function for Heave Force on a Hemisphere

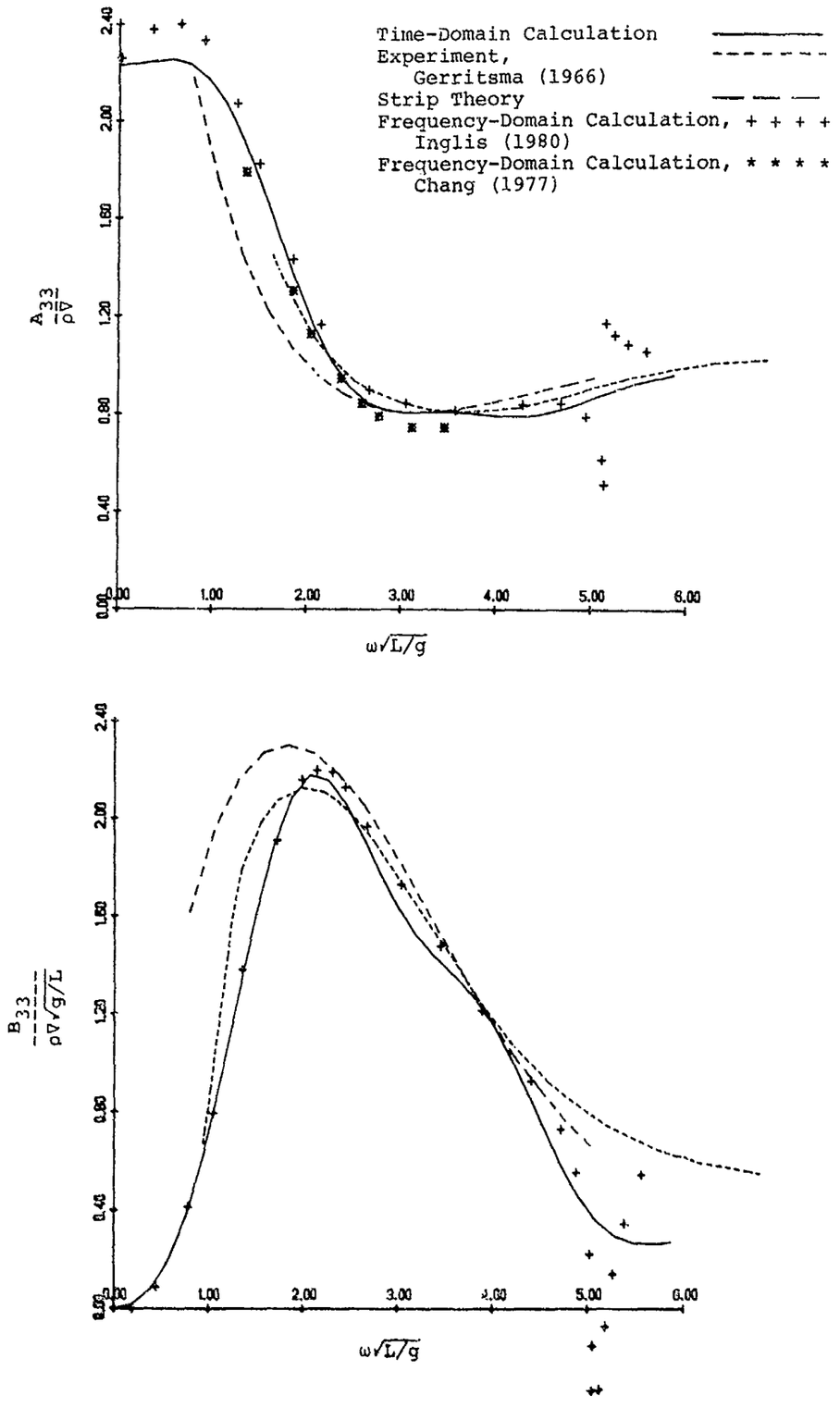

Figure 5. Heave Added Mass and Damping Coefficients for a Series 60 (C_B = .70) Model at Fn = 0

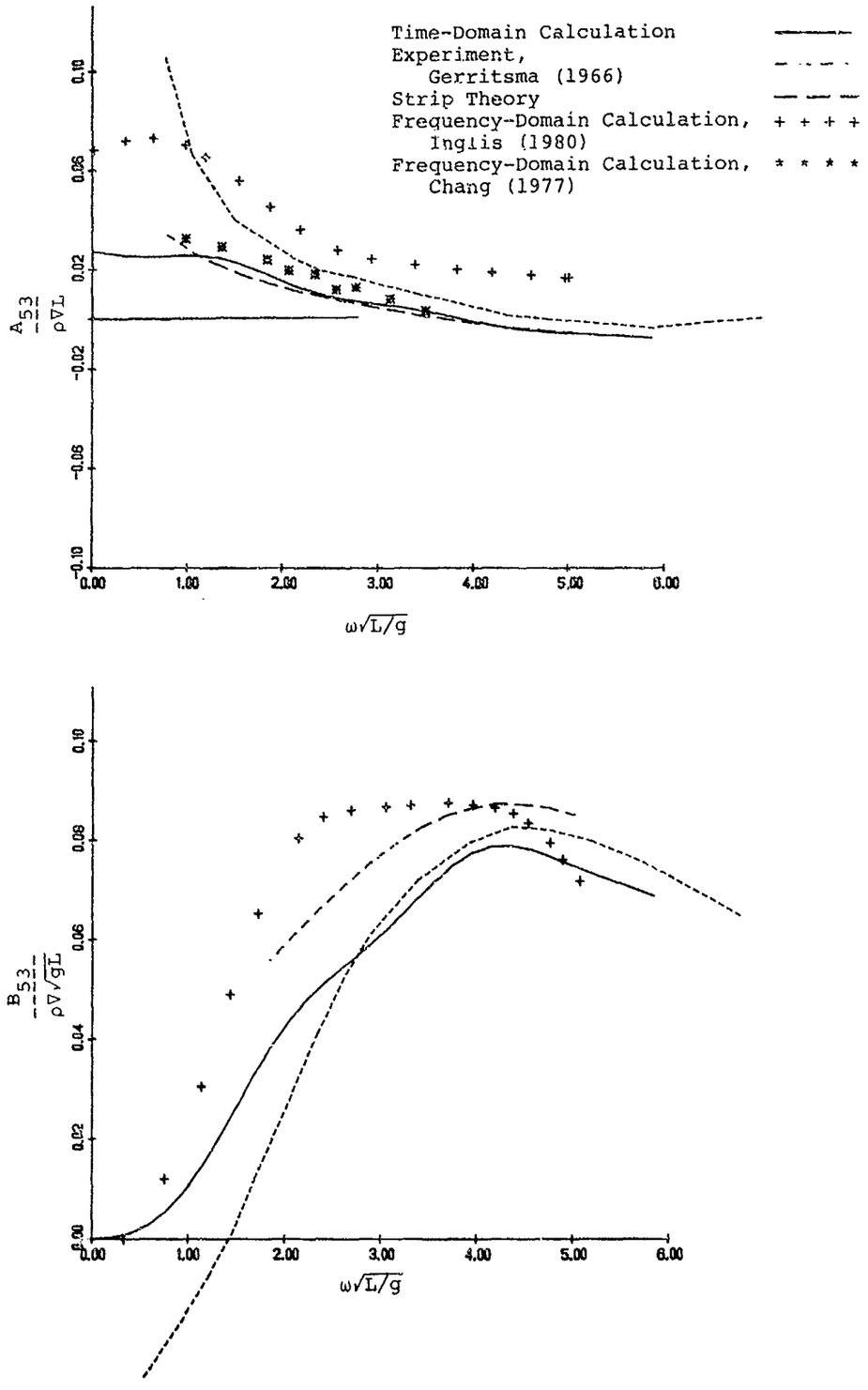

Figure 6. Heave-Pitch Cross Coupling Coefficients for a Series 60 (C_B = .70) Model at Fn = 0

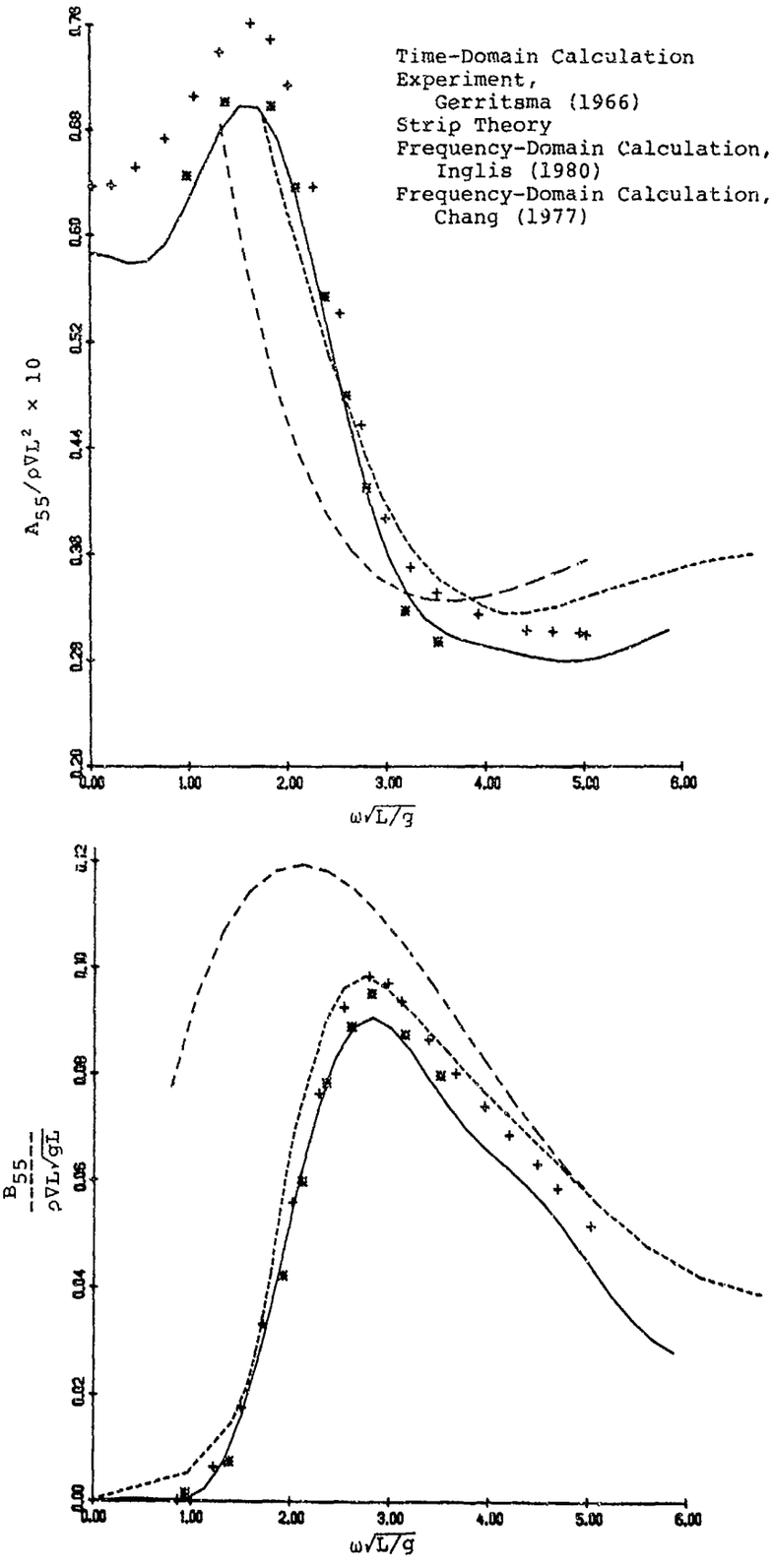

Figure 7. Pitch Added Mass and Damping Coefficients for a Series 60 (C_B = .70 Model at Fn = 0

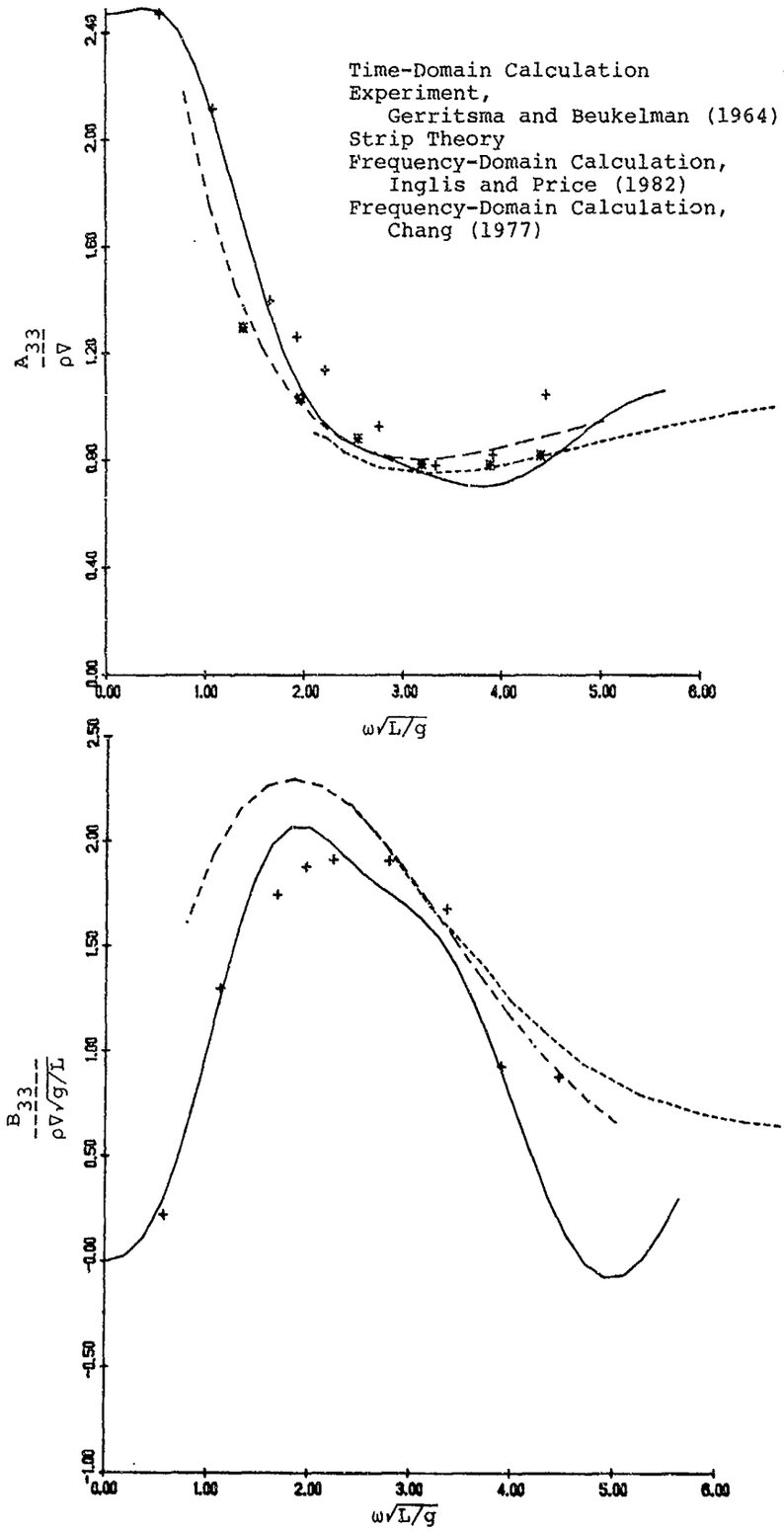

Figure 8. Heave Added Mass and Damping Coefficients for a Series 60 (C_B = .70) Model at Fn = .2

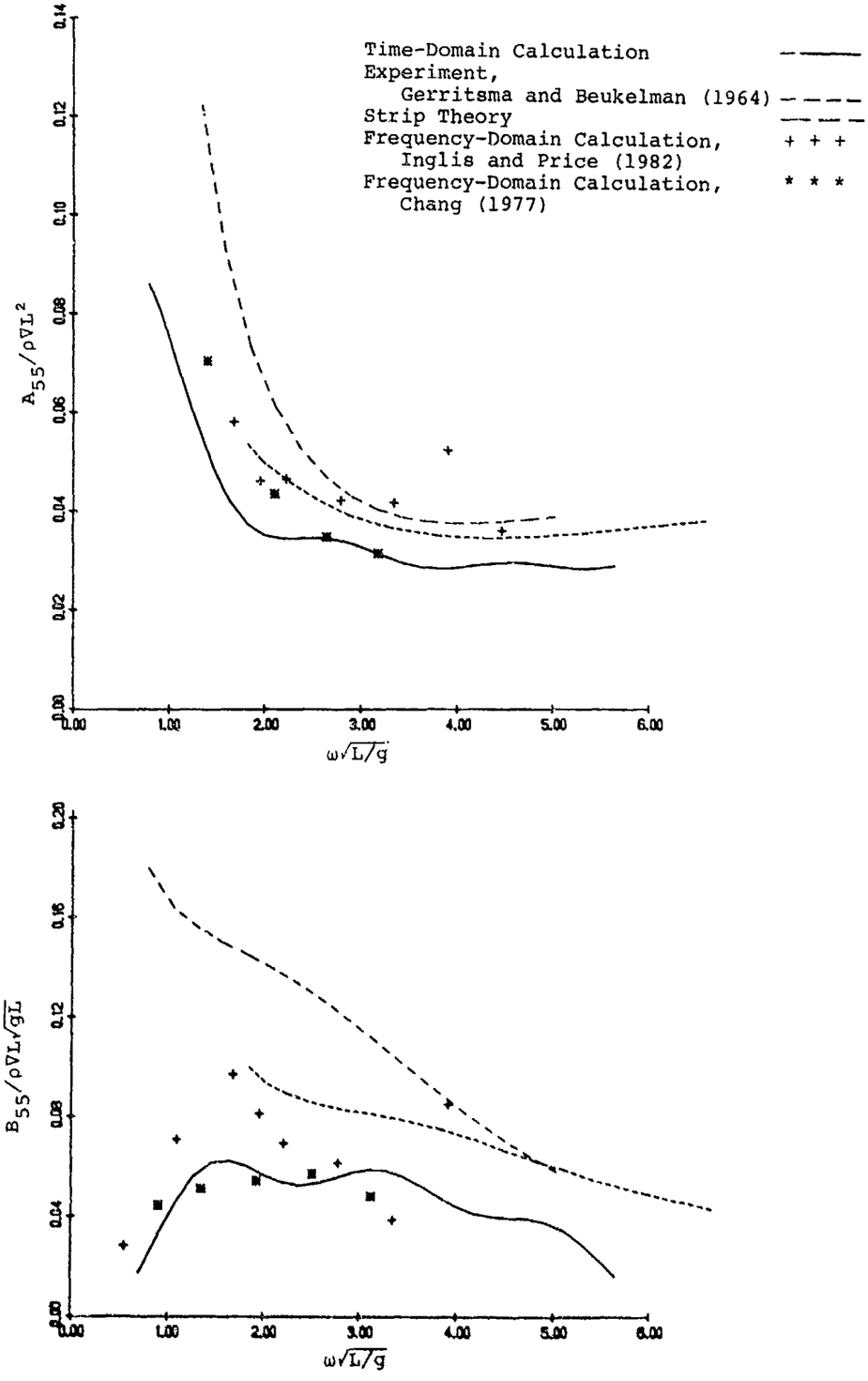

Figure 9. Pitch Added Mass and Damping Coefficients for a Series 60 (C_B = .70) Model at Fn = .2

DISCUSSION
of the paper
by S. Liapis and R.F. Beck

"SEAKEEPING COMPUTATION USING TIME-DOMAIN ANALYSIS"

DISCUSSION
by H. Wang

I extend my congratulations to the authors for successfuly completing the calculations for a three-dimensional time-domain analysis for an oscillating ship advancing with nonzero forward speed. It should serve as a useful alternate calculation procedure to the more usual frequency-domain approaches.

At several places in your paper, you mention that your approach, for the forward speed case, requires much less computation effort than the frequency-domain approach. I believe that the principal reason for this, which is never explicitly mentioned in your paper, is due to the fact that even for the forward speed case, you are able to retain a relatively simple expression for the Green function, given in Eq. (5). It contains only a single integral with a regular integrand. By contrast, the Green function for this case in the frequency domain approach contains double integrals, whose integrands contain poles.

Author's Reply

We would like to thank H.T. Wang for his comments. Certainly the time domain approach has several advantages over the more conventional frequency domain. First, one is not constrained to solving sinusoidal problems. The method can be used to solve seakeeping problems, wave resistance problems, maneuvering problems or any combination. Secondly, there should be a computational advantage. The time-domain Green function is computationally far simpler than the Green function for a pulsating and translating source It should be noted here that the Green function may be evaluated for both cases of zero and non-zero forward speed in the same way. Furthermore, the kernel matrix in equation (52) is identical for all times, and need only be inverted once. For a large number of panels this is a significant advantage over the frequency domain. The main problem of this method is, as discussed in the paper, related to the oscillatory behavior of the memory functions at large time. This oscillatory error, which is due to the irregular frequencies. may be reduced to any desirable tolerance by increasing the number of panels and time steps. Unfortunately, this greatly increases the computer time and we are presently investigating more efficient alternatives.

LINEAR HYDRODYNAMIC COEFFICIENTS OF SHIPS WITH FORWARD-SPEED DURING HARMONIC SWAY, YAW AND ROLL OSCILLATIONS

Keiichi Yamasaki
Nippon Kokan K. K.
Tsu, Japan
and
Masataka Fujino
University of Tokyo
Tokyo, Japan

Abstract

This paper describes a numerical method for calculating the lateral hydrodynamic forces and moments acting on a ship with a hull of arbitrary shape during such lateral motions as sway, yaw and roll. For the purpose of investigating the validity of the present method, the linear hydrodynamic coefficients of several kinds of ship-like bodies such as a flat plate, Series 60 model, and a container ship-model are calculated and compared with the experimental results of forced oscillating tests as well as the numerical values obtained by the Strip Method. It was seen that the present method has excellent prediction value regarding both the effects of forward speed and the frequency of motion of the various hydrodynamic coefficients when compared to the Strip Method.

1. Introduction

The so-called Strip Method has been generally used to predict the lateral hydrodynamic forces and moments acting on a ship. There remain, however, several problems to be resolved regarding the prediction accuracy of the Strip Method. For example, the effects of a ship's forward speed on the lateral hydrodynamic coefficients cannot be adequately predicted by this method. In the Strip Theory synthesis, the fluid motions around a ship are described in an approximate manner by the two-dimensional fluid motion in transverse planes normal to the longitudinal axis of the ship. Consequently, the three-dimensional effects on the hydrodynamic forces cannot be successfully identified by the Strip Method. Therefore, it is necessary to establish a calculation method by which the three-dimensional effects, in particular, the effect of a ship's forward speed on the hydrodynamic coefficients can be determined in a valid manner.

According to the slender body assumption as indicated by Chapman [1] [2], the fluid motion around a three-dimensional body may be approximately determined by unsteady two-dimensional flow in space-fixed planes normal to the longitudinal axis of the body. That is to say, the fluid motion in an arbitrary space-fixed plane normal to the ship's longitudinal axis is determined by repeatedly calculating the fluid motion at various instances after the ship's bow begins to penetrate this plane.

By determining the fluid motion in the transverse planes, which are placed at equal intervals along the ship's longitudinal axis, the three-dimensional fluid motion around a ship can be obtained; then, the hydrodynamic forces and moments acting on a ship can be evaluated by integrating the hydrodynamic pressure over the entire wet surface of the hull.

In the following, the two-dimensional fluid motion in the above-stated transverse planes is obtained using the numerical method. At the time of calculation, the two-dimensional infinite region is replaced by a finite region by introducing an artificial open boundary at a distance of sufficient distance from the ship. At the boundary, it is necessary for the waves generated by a ship's motion to pass outwardly through the boundary in a manner that a boundary does not exist. For this purpose, Orlanski[3] and Chan[4] imposed Sommerfeld's radiation condition on the open boundary and treated it by means of the finite difference scheme. In this paper as well, Sommerfeld's radiation condition is imposed on the open boundary and treated in a manner similar to the above. The radiation condition, however, is replaced by a more relaxed condition, that is to say, a numerical error is positively allowed to exist in the equation describing Sommerfeld's radiation condition. By making use of a relaxed condition instead of an exact radiation condition, it becomes possible to have the free surface waves, which are generated by ship's motion and then propagated toward the outer region, pass smoothly through the open boundary.

In addition to the radiation condition, the linearized free surface condition and body surface condition are demanded as boundary conditions to be satisfied. The two-dimensional Laplace's equation, which is the

governing equation in the fluid, is solved by means of the Boundary Element Method (B.E.M.).

By utilizing the present method, the hydrodynamic forces and moments acting on a ship are calculated for an arbitrary motion if the ship's motions are known. In the following, however, the linear hydrodynamic coefficients of sway, yaw and roll motions are exclusively calculated and compared with the experimental data. Comparisons are made for three cases consisting of a flat plate, Series 60 model, and a container ship. In particular, the effects of the ship's forward speed on the hydrodynamic coefficients are disccussed by presenting the numerical and experimental results. Furthermore, the hydrodynamic coefficients of the Series 60 model obtained by the Strip Method are compared with the numerical results obtained by the present method.

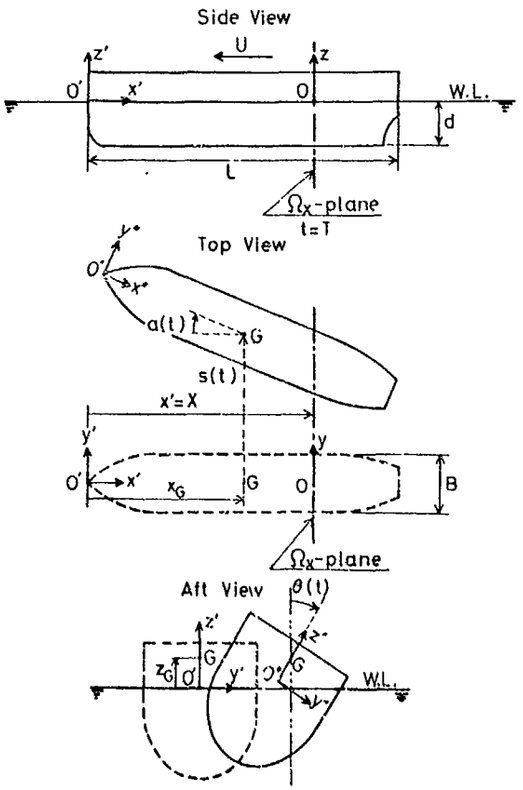

Fig. 1 Coordinate systems used in formulation

2. Formulation

In order to calculate the hydrodynamic lateral forces acting on the ship advancing on a free surface, the following conditions are assumed to exist:

(i) The fluid is incompressible, irrotational and inviscid.
(ii) The ship's lateral motions are infinitesimal.
(iii) The ship's hull can be regarded as a slender body.

The coordinate systems used for the formulation are shown in Fig. 1. O"-x"y"z" is a body-fixed coordinate system with its origin at the intersection of the ship's bow and waterline. Another system O'-x'y'z' advances in a straight manner in the mean course of the ship at a forward speed of U. The velocity potential Φ describing the fluid motion around a ship is as follows:

$$\Phi(x',y',z',t) = Ux' + \varphi(x',y',z',t) \qquad (1)$$

The velocity potential φ of the right-hand side denotes the fluid motion as a result of unsteady ship motion. The three-dimensional Laplace's equation, the kinematic and dynamic conditions of the free-surface, which the velocity potential φ satisfies, are as follows:

$$(L)\quad \frac{\partial^2\varphi}{\partial x'^2}+\frac{\partial^2\varphi}{\partial y'^2}+\frac{\partial^2\varphi}{\partial z'^2}=0 \qquad \text{in fluid,} \qquad (2)$$

$$(K)\quad \frac{\partial\zeta}{\partial t}+\left(U+\frac{\partial\varphi}{\partial x'}\right)\frac{\partial\zeta}{\partial x'}+\frac{\partial\varphi}{\partial y'}\frac{\partial\zeta}{\partial y'}=\frac{\partial\varphi}{\partial z'} \qquad \text{on } z'=\zeta, \qquad (3)$$

$$(D)\quad \frac{\partial\varphi}{\partial t}+U\frac{\partial\varphi}{\partial x'}+\frac{1}{2}\left\{\left(\frac{\partial\varphi}{\partial x'}\right)^2+\left(\frac{\partial\varphi}{\partial y'}\right)^2+\left(\frac{\partial\varphi}{\partial z'}\right)^2\right\}+g\zeta=0$$

$$\text{on } z'=\zeta, \qquad (4)$$

where ζ is the elevation of the free surface and g the acceleration of gravity.

In consideration of the above-stated assumptions (ii) and (iii), eqs. (2), (3) and (4) may be reduced to the following;

$$(L)\quad \frac{\partial^2\varphi}{\partial y'^2}+\frac{\partial^2\varphi}{\partial z'^2}=0 \qquad \text{in fluid,} \qquad (5)$$

$$(K)\quad \left(\frac{\partial}{\partial t}+U\frac{\partial}{\partial x'}\right)\zeta=\frac{\partial\varphi}{\partial z'} \qquad \text{on } z'=0, \qquad (6)$$

$$(D)\quad \left(\frac{\partial}{\partial t}+U\frac{\partial}{\partial x'}\right)\varphi+g\zeta=0 \qquad \text{on } z'=0, \qquad (7)$$

Based on the assumption that lateral displacement s(t), yaw angle a(t), and roll angle $\theta(t)$ are sufficiently small, the coordinate systems, O'-x'y'z' and O"-x"y"z", have the following relation:

$$x'' = x' - y'a(t), \qquad (8)$$

$$y'' = y' - s(t) - (x_0 - x')a(t) - (z' - z_0)\theta(t), \qquad (9)$$

$$z'' = z' + y'\theta(t) , \qquad (10)$$

where x_G is the horizontal distance from the ship's bow to the center of gravity, and z_G the height of the center of gravity from the surface of the water.

Let the hull shape be represented by

$$H(x'', y'', z'') = 0 , \qquad (11)$$

then the body surface condition is described by

$$\dot{x}'' \frac{\partial H}{\partial x''} + \dot{y}'' \frac{\partial H}{\partial y''} + \dot{z}'' \frac{\partial H}{\partial z''} = 0$$

$$\text{on } H(x'', y'', z'') = 0 , \qquad (12)$$

Considering that the ship's motion is small, the body surface condition can be satisfied on mean ship hull surface $H(x', y', z')=0$ rather than on the exact ship hull surface. By substituting eqs. (1), (8), (9) and (10) into eq. (12), the body surface condition at the mean hull surface may be expressed as follows:

$$U\frac{\partial H}{\partial x'} + \frac{\partial \varphi}{\partial y'}\frac{\partial H}{\partial y'} + \frac{\partial \varphi}{\partial z'}\frac{\partial H}{\partial z'} = \left\{\dot{s}(t) - U a(t) + (x_G - x')\dot{a}(t) + (z' - z_G)\dot{\theta}(t)\right\}\frac{\partial H}{\partial y'} - y'\dot{\theta}(t)\frac{\partial H}{\partial z'}$$

$$\text{on } H(x', y', z') = 0. \qquad (13)$$

Using the coordinate system O-yz defined in a space-fixed transverse plane Ω_x which is situated at $x'=X$ at the instance $t=T$ (see Fig. 1), eqs. (5), (6), (7) and (13) may be newly expressed as indicated by Chapman [2] as follows:

$$\frac{\partial^2 \varphi}{\partial y^2} + \frac{\partial^2 \varphi}{\partial z^2} = 0 \qquad \text{in fluid}, \qquad (14)$$

$$\frac{\partial \zeta}{\partial t} = \frac{\partial \varphi}{\partial z} \qquad \text{on } z = 0 , \qquad (15)$$

$$\frac{\partial \varphi}{\partial t} + g\zeta = 0 \qquad \text{on } z = 0 , \qquad (16)$$

$$\frac{\partial \varphi}{\partial y}\frac{\partial H}{\partial y} + \frac{\partial \varphi}{\partial z}\frac{\partial H}{\partial z} = -\frac{\partial H}{\partial t} + \left[\dot{s}(t) - U a(t) + \left\{x_G - X + U(T-t)\right\}\dot{a}(t) + (z - z_G)\dot{\theta}(t)\right]\frac{\partial H}{\partial y} - y\dot{\theta}(t)\frac{\partial H}{\partial z}$$

$$\text{on } H(y, z, t) = 0 , \quad \text{at } T - \frac{X}{U} \le t \le T. \qquad (17)$$

In the Ω_x plane, the hull surface H is a function of time t as described by the first term on the right-hand side of eq. (17). The remaining terms on the right-hand side of eq. (17) denote contributions of such lateral motions as sway, yaw, and roll.

The velocity potential φ may be divided into two parts:

$$\varphi(y,z,t) = \varphi_F(y,z,t) + \varphi_L(y,z,t) \qquad \text{in } \Omega_x , \qquad (18)$$

where φ_F and φ_L correspond to longitudinal and lateral motion of a ship, respectively. By decomposition of φ into φ_F and φ_L, the body surface condition (17) may be divided into the following equations:

$$\frac{\partial \varphi_F}{\partial y}\frac{\partial H}{\partial y} + \frac{\partial \varphi_F}{\partial z}\frac{\partial H}{\partial z} = -\frac{\partial H}{\partial t} , \qquad (19)$$

$$\frac{\partial \varphi_L}{\partial y}\frac{\partial H}{\partial y} + \frac{\partial \varphi_L}{\partial z}\frac{\partial H}{\partial z} = \left[\dot{s}(t) - U a(t) + \left\{x_G - X + U(T-t)\right\}\dot{a}(t) + (z - z_G)\dot{\theta}(t)\right]\frac{\partial H}{\partial y} - y\dot{\theta}(t)\frac{\partial H}{\partial z}. \qquad (20)$$

Moreover, φ_F and φ_L must satisfy the radiation condition at the open boundary. The radiation condition may be commonly expressed as follows:

$$\frac{\partial \varphi}{\partial t} + C\frac{\partial \varphi}{\partial \ell} = 0 , \qquad (21)$$

where $\partial/\partial \ell$ is the differentiation in the normal outward direction at the open boundary, and C is the phase speed of the waves.

Namely, φ_F is determined by solving the eqs. (14), (15), (16), (19), and (21), and φ_L by solving the eqs. (14), (15), (16), (20), and (21), respectively. On the assumption that lateral motions of a ship are sufficiently small, the free surface conditions eqs. (15) and (16), which are satisfied by φ_L, may be satisfied along the streamlines on $z=0$ generated by uniform longitudinal motion.

On the other hand, the free surface condition for φ_F is substituted by the rigid wall condition.

$$\frac{\partial \varphi_F}{\partial z} = 0 \qquad \text{on } z = 0 . \qquad (22)$$

This substitution does not seriously affect the predicted hydrodynamic lateral forces because φ_F has no significant effect on the hydrodynamic lateral forces.

3. Hydrodynamic Lateral Forces and Moments

The hydrodynamic lateral force $f(T, X)$ and roll moment $m(T, X)$ acting on a ship's section, which is situated in the space-fixed plane Ω_x at $x'=X$ at the instance $t=T$, are expressed by

$$f(T,X) = -2\rho \int_K^F \frac{\partial \varphi_L}{\partial t} n_y \, ds , \qquad (23)$$

$$m(T,X) = -2\rho \int_K^F \frac{\partial \varphi_L}{\partial t}\left\{n_y(z - z_G) - n_z y\right\} ds , \qquad (24)$$

where ρ is fluid density, $n=(n_y, n_z)$ is a normal inward unit vector of the ship's hull.

Contour integration is performed along the surface of the hull from the keel to the intersection of the hull and waterline.

Consequently, the hydrodynamic lateral force Y(T), yaw moment N(T), and roll moment M(T) acting on the entire ship at the instance t=T are obtained by integrating eqs. (23) and (24) over the ship length.

$$Y(T)=\int_0^L f(T,X)dX \tag{25}$$

$$N(T)=\int_0^L (x_0-X)f(T,X)dX \tag{26}$$

$$M(T)=\int_0^L m(T,X)dX \tag{27}$$

4. Determination of Hydrodynamic Coefficients

With the body-fixed coordinate system shown at the top of Fig. 2, the linear equations of sway and yaw motions are described by

$$m\dot{v}=Y_{\dot{v}}\dot{v}+Y_v v+Y_{\dot{r}}\dot{r}+(Y_r-mU)r\,, \tag{28}$$

$$I_{zz}\dot{r}=N_{\dot{v}}\dot{v}+N_v v+N_{\dot{r}}\dot{r}+N_r r\,. \tag{29}$$

m is the mass of a ship, and I_{zz} the mass moment of inertia. Using the space-fixed coordinate system, on the other hand, the linear equations of sway, yaw and roll motions are described as follows (see the bottom of Fig. 2):

$$A_{22}\ddot{\eta}_2+B_{22}\dot{\eta}_2+A_{24}\ddot{\eta}_4+B_{24}\dot{\eta}_4+A_{26}\ddot{\eta}_6+B_{26}\dot{\eta}_6=F_2 \tag{30}$$

$$A_{44}\ddot{\eta}_4+B_{44}\dot{\eta}_4+C_{44}\eta_4+A_{42}\ddot{\eta}_2+B_{42}\dot{\eta}_2+A_{46}\ddot{\eta}_6+B_{46}\dot{\eta}_6=F_4 \tag{31}$$

$$A_{66}\ddot{\eta}_6+B_{66}\dot{\eta}_6+A_{62}\ddot{\eta}_2+B_{62}\dot{\eta}_2+A_{64}\ddot{\eta}_4+B_{64}\dot{\eta}_4=F_6 \tag{32}$$

η_2, η_4 and η_6 denote sway, roll and yaw, respectively, and Aij, Bij, Cij the hydrodynamic coefficients. F_2, F_4 and F_6 represent the external forces acting on a ship, if any.

In order to determine the hydrodynamic coefficients of eqs. (28) - (32) as functions of frequency ω by experiments, the following harmonic motions are imposed on the model of a ship:

(I) pure sway:

$$s(t)=\sin\omega t\ ,\quad a(t)=\theta(t)=0\,, \tag{33}$$

(II) pure yaw:

$$a(t)=\sin\omega t\ ,\quad \dot{s}(t)-Ua(t)=0\ ,\quad \theta(t)=0\,, \tag{34}$$

(III) combined motion:

$$a(t)=\sin\omega t\ ,\quad s(t)=\theta(t)=0\,, \tag{35}$$

(IV) pure roll:

$$\theta(t)=\sin\omega t\ ,\quad s(t)=a(t)=0\,.$$

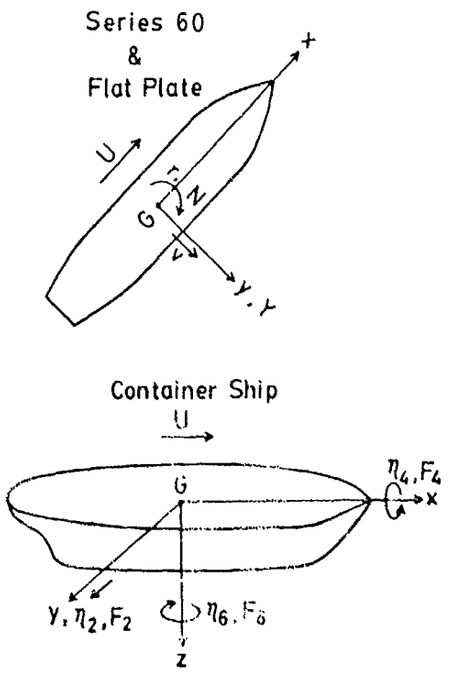

Fig. 2 Coordinate systems used in evaluations of hydrodynamic coefficients

Table 1 Nondimensionalization of hydrodynamic coefficients

Flate plate & Series 60	Container ship
$Y'_{\dot{v}}=Y_{\dot{v}}/(\frac{1}{2}\rho L^2 d)$	$\hat{A}_{26}=A_{26}/(\rho\Delta L)$
$Y'_v=Y_v/(\frac{1}{2}\rho L dU)$	$\hat{A}_{62}=A_{62}/(\rho\Delta L)$
$Y'_{\dot{r}}=Y_{\dot{r}}/(\frac{1}{2}\rho L^3 d)$	$\hat{A}_{66}=A_{66}/(\rho\Delta LB)$
$Y'_r=Y_r/(\frac{1}{2}\rho L^2 dU)$	$\hat{A}_{64}=A_{64}/(\rho\Delta LB)$
$N'_{\dot{v}}=N_{\dot{v}}/(\frac{1}{2}\rho L^4 d)$	$\hat{B}_{26}=B_{26}\sqrt{B/2g}/(\rho\Delta L)$
$N'_r=N_r/(\frac{1}{2}\rho L^3 dU)$	$\hat{B}_{62}=B_{62}\sqrt{B/2g}/(\rho\Delta L)$
$N'_{\dot{v}}=N_{\dot{v}}/(\frac{1}{2}\rho L^3 d)$	$\hat{B}_{46}=B_{46}\sqrt{B/2g}/(\rho\Delta LB)$
$N'_v=N_v/(\frac{1}{2}\rho L^2 dU)$	$\hat{B}_{64}=B_{64}\sqrt{B/2g}/(\rho\Delta LB)$
ρ : fluid density ,	B : ship's beam ,
Δ : volume of displacement ,	d : ship's draft ,
L : ship's length ,	U : forward speed .

In the harmonic oscillation tests, the hydrodynamic forces at the instance T, when the acceleration of the model (or angular acceleration) becomes zero are comprised of hydrodynamic forces dependent only on velocity (or angular velocity). In a similar manner, the hydrodynamic forces at the instance of zero velocity (or zero angular velocity) consist of hydrodynamic forces resulting from only acceleration (or angular acceleration). Therefore, the linear hydrodynamic coefficients of eqs. (28) - (32), which are related to the acceleration and velocity of a ship, are easily determined by selecting the time T of integrals (25) - (27) as the instance when the velocity and acceleration of the model become zero, respectively. The linear hydrodynamic coefficients, which are obtained in this manner, are "nondimensionalized" in the manner shown in Table 1.

5. Numerical Method

In the following, the numerical method for determining the two-dimensional fluid motion in the space-fixed transverse plane Ω_x is described.

5-1. Radiation Condition at the Open Boundary

When calculating the two-dimensional flow in the transverse plane Ω_x, as mentioned in the above, infinite fluid region is replaced by a finite region, which is bordered by an open boundary. Sommerfeld's radiation condition is then imposed on this open boundary. Orlanski[3] and Chan[4] have utilized the finite difference technique in order to deal with Sommerfeld's radiation condition in a numerical manner. Initially, following the technique used by Orlanski and Chan, the authors applied their technique

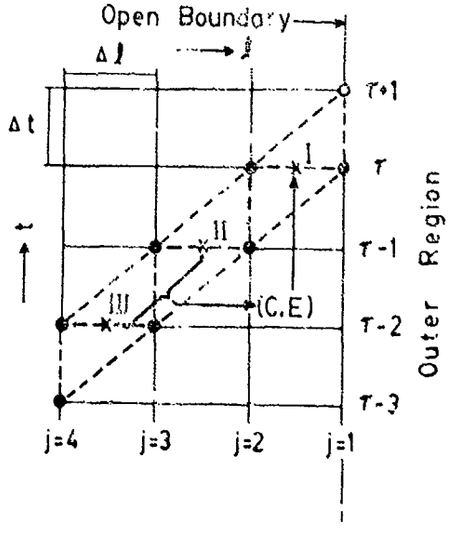

Fig. 3 Finite difference scheme of the open boundary

to the open boundary. However, undesirable contamination of the free surface wave occurred resulting from the presence of the open boundary. In this paper, therefore, the exact radiation condition (21) was replaced by the more relaxed condition expressed as;

$$\frac{\partial \varphi}{\partial t} + C\frac{\partial \varphi}{\partial \ell} = E \tag{37}$$

The non-zero value of E on the right-hand side permits a numerical error for the left-hand side term of the exact radiation condition (21). Fig. 3 shows the finite difference scheme of satisfying eq. (37) in $t-\ell$ plane, where t and ℓ denote the time and the spatial direction normal to open boundary, respectively, in the vicinity of the open boundary. Let $\varphi(\tau, j)$ denote the velocity potential at $t=\tau$ and $\ell=j$, then eq. (37) applied to the point I marked in Fig. 3 is expressed as follows:

$$\varphi(\tau+1,1) = \varphi(\tau-1,2) + (1-2\alpha)\{\varphi(\tau,1) - \varphi(\tau,2)\} + 2\varepsilon, \tag{38}$$

where $\alpha = C\Delta t/\Delta \ell$, and $\varepsilon = E\Delta t$.

In a similar manner, eq. (37) applied to the points II and III is expressed as

$$\frac{1}{2}\{\varphi(\tau,2) - \varphi(\tau-1,2) + \varphi(\tau-1,3) - \varphi(\tau-2,3)\} + \alpha^*\{\varphi(\tau-1,2) - \varphi(\tau-1,3)\} = \varepsilon^*, \tag{39}$$

and

$$\frac{1}{2}\{\varphi(\tau-1,3) - \varphi(\tau-2,3) + \varphi(\tau-2,4) - \varphi(\tau-3,4)\} + \alpha^*\{\varphi(\tau-2,3) - \varphi(\tau-2,4)\} = \varepsilon^*. \tag{40}$$

α^* and ε^* in the above equations correspond to α and ε of eq. (38), respectively.

Since the values of φ in eqs. (39), and (40) are known in advance, α^*, and ε^* can be determined. In order to avoid producing a significant numerical error, which might be caused when the difference of potential values at two adjacent points is significantly small, the following additional restrictions are imposed. Namely, if

$$\left.\begin{array}{l} |\varphi(\tau-1,2) - \varphi(\tau-1,3)| \\ \text{or} \\ |\varphi(\tau-2,3) - \varphi(\tau-2,4)| \end{array}\right\} < |\varphi_{max} - \varphi_{min}| \times 10^{-6}$$

and then

$$\varphi(\tau-1,2) - \varphi(\tau-1,3) = 0$$
or
$$\varphi(\tau-2,3) - \varphi(\tau-2,4) = 0$$

φ_{max} and φ_{min} are the extreme values of φ on the boundaries.

In order to suppress the spurious wave propagation at the open boundary, a reasonable range of eq. (38) is determined by the following equations, which is dependent on α^* value,

$$\alpha = 0 \quad , \quad \text{if} \quad \alpha^* < 0 \quad , \tag{41}$$

$$\alpha = \alpha^* \, , \quad \text{if} \quad 0 \le \alpha^* \le 1 \quad , \tag{42}$$

$$\alpha = 1 \quad , \quad \text{if} \quad 1 < \alpha^* \quad . \tag{43}$$

The value of ε , on the other hand, is determined in the following way; in the case of eq. (42), ε is equal to ε^* , and in the case of eq. (41) (or (43)), ε is replaced by the mean value of ε^* obtained by substituting $\alpha^*=0$ (or $\alpha^*=1$) into eq. (39) and eq. (40). Furthermore, it is important to select Δt and $\Delta \ell$ so that it is possible for the value of α^* may exist between zero and one.

5-2. Free Surface Condition

As previously mentioned, the free surface condition, which φ_F must satisfy, is eq. (22). On the other hand, φ_L must satisfy the more rigorous free surface conditions (15) and (16). The finite difference expression of both equations is as follows:

$$\zeta\left(y+\frac{\Delta y}{2}, t+\frac{\Delta t}{2}\right)=\zeta\left(y-\frac{\Delta y}{2}, t-\frac{\Delta t}{2}\right)+\Delta t \frac{\partial \varphi_L}{\partial z}(y,0,t), \tag{44}$$

$$\varphi_L(y+\Delta y,0,t+\Delta t)=\varphi_L(y,0,t)-g\Delta t\,\zeta\left(y+\frac{\Delta y}{2}, t+\frac{\Delta t}{2}\right), \tag{45}$$

where

$$\Delta y = \Delta t \frac{\partial \varphi_F}{\partial y}(y,0,t). \tag{46}$$

The singularity which occures at the intersection of the ship's hull and free surface was avoided by imposing an additional constraint expressed as

$$\frac{\partial^2 \zeta_1}{\partial y \partial z} = 0 \qquad \text{at} \quad H(y,0,t)=0 \, . \tag{47}$$

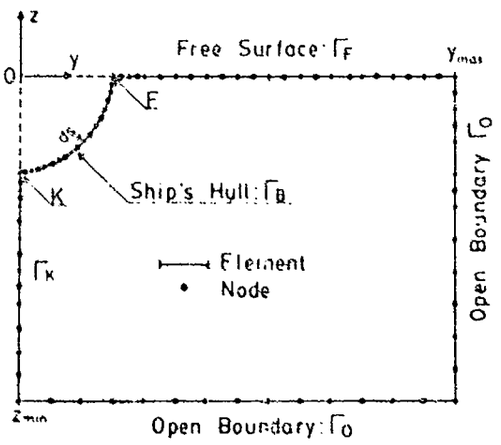

Fig. 4 Boundary elements and nodes

5-3. Numerical Procedure

The fluid motion in the space-fixed Ω_x plane is determined by repeatedly calculating the fluid motion at various instances after the ship's bow penetrates the transverse plane. In order to resolve the two-dimensional boundary value problem, the Boundary Element Method (B.E.M.) was employed. Fig. 4 shows a typical example of the fluid domain and boundaries used in the following numerical computations. The procedure of solving the velocity potential φ_L shall be briefly described hereinafter.

1) at t=0 ; Assume that before the ship's bow penetrates the Ω_x plane, the fluid is at rest, and φ_L is equal to zero on the free surface Γ_F and the open boundary Γ_O as well. At the boundary under the keel, the velocity potential φ_L is constantly zero because of the antisymmetry of the flow caused by the lateral motion.
2) at t=t ; At the time the bow penetrates the Ω_x plane and thereafter, Laplace's equation is solved by B.E.M. in order to satisfy the body surface condition on Γ_B . Then, the values of φ_L on Γ_B and $\partial\varphi_L/\partial_z$ on Γ_F are calculated.
3) at t=t ; Obtain the values of φ_L at the internal points adjacent to the open boundary, which is imperative in the treatment of Sommerfeld's radiation condition. Thereafter, obtain the value of φ_L on Γ_O at the following step of $t=t+\Delta t$.
4) Determine the values of φ_L on Γ_F at time step $t=t+\Delta t$ by using the free surface condition.
5) In order to determine φ_L value at $t=t+\Delta t$, the free surface in the vicinity of the hull and hull surface are again subjected to division because the hull shape at $t=t+\Delta t$ varies from that at t=t.
6) Determine the values of φ_L at the new nodal points on Γ_F by the linear interpolation of φ_L values obtained at the step 4).
7) Return to the step 2).

By repeating the above-mentioned procedure, the values of φ_L in the space-fixed Ω_x plane can be determined. Then the hydrodynamic forces and moments acting on the hull section situated in the plane Ω_x can be easily obtained by eqs. (23) and (24). In order to calculate the hydrodynamic forces and moments acting on the entire ship, the hull was divided into 40 sections, and the fluid motions in 41 transverse planes were obtained in the following numerical calculation procedure; the time step Δt, the size of fluid region, and total number of elements used for calculation are presented in Table 2. Prior to performing numerical calculation, the sectional shapes of the ship's hull, which are not given in the body plan, are estimated

Table 2 Time step, size of fluid region, and total number of elements on the boundaries

Body shape	time step	size of fluid region		total number of elements on boundary
	$\Delta t=(L/U)/N$	y_{max}	z_{min}	
Flat plate	N = 200	4*d	-4*d	132
Series 60 and Container	N = 400	8*d	-6*d	≤ 190

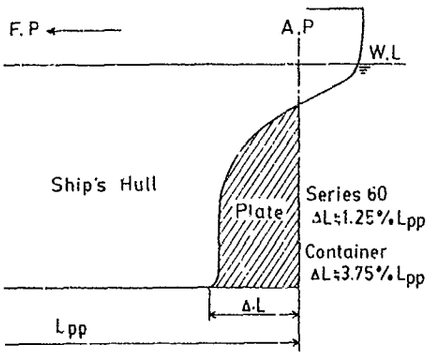

Fig. 5 Treatment of blank space behind the stern frame in numerical calculations

employing the spline interpolation method. Furthermore, in order to carry out the numerical calculation in an efficient manner, the propeller aperture behind the stern frame was filled with a hypothetical piece of dead wood as illustrated in Fig. 5.

6. Numerical Results and Comparisons with Experimental Data

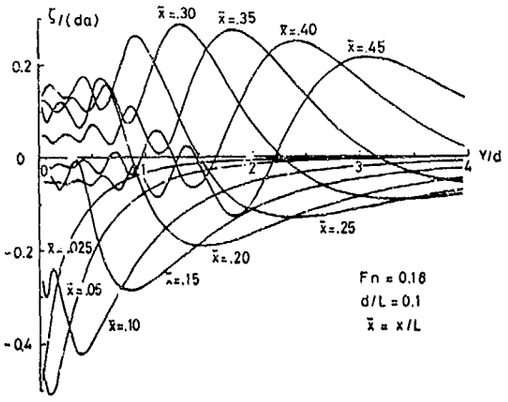

Fig. 6 Free-surface profiles in various transverse planes (flat plate, d/L=0.1, Y_{max}=4d, F_n=0.18)

6-1. Free Surface Waves Generated by a Yawed Flat Plate

For the purpose of assuring that the waves generated by the ship's motions completely pass through the open boundary without being subjected to undesirable contamination, the free surface profiles were calculated for the yawed surface-piercing flat plate having a draft-length ratio (=d/L) of 0.1 and a forward speed equal to F_n=0.18 . Fig. 6 illustrates the calculated free surface elevations in the transverse planes situated at various $\bar{x}$ (=x/L) positions. As shown in this figure, the waves generated by a yawed flat plate completely pass through the open boundary, which is situated at a distance equal to 4d from the plate. The free surface profiles shown in Fig. 6 are in good agreement with the calculation results of Chapman (see Fig. 8 of reference 1)).

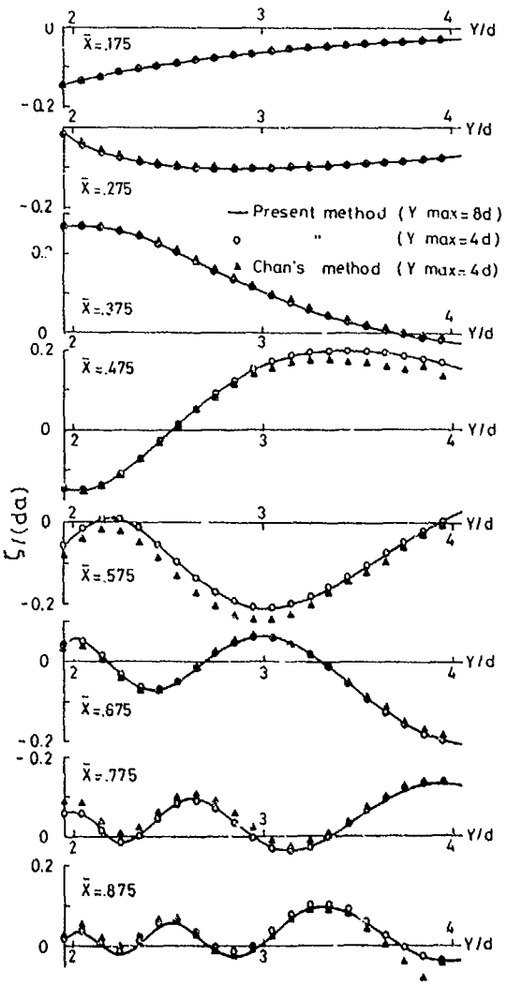

Fig. 7 Comparison of free-surface profiles calculated by the present method and Chan's method (flat plate, d/L=0.1, F_n=0.18)

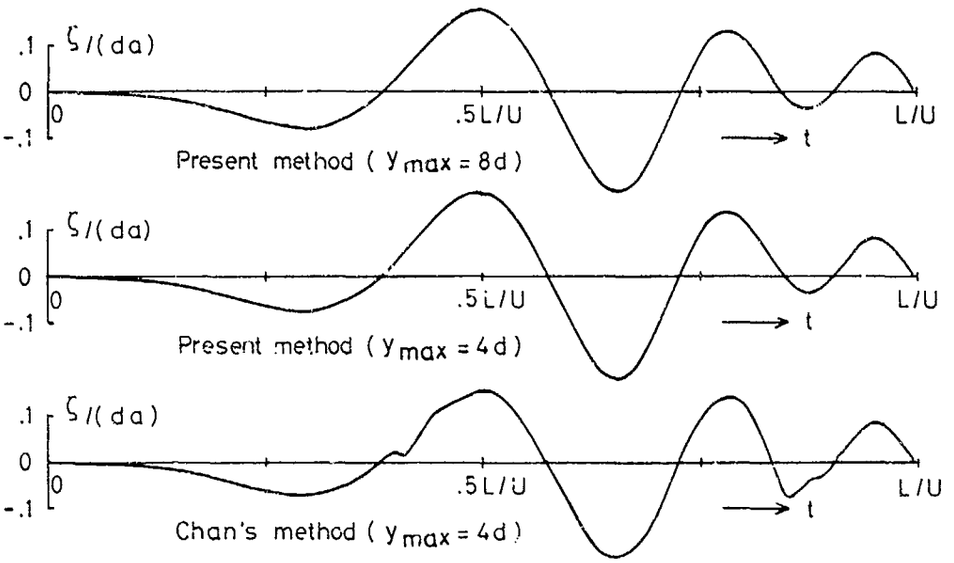

Fig. 8 Free-surface elevations observed at the location y=4d (flat plate, d/L=0.1, F_n=0.18)

In Fig. 7, the results of numerical calculation presented in Fig. 6 are compared with a different numerical result under similar circumstances, which was obtained by making use of a wider fluid region, that is to say, y_{max}=6d as well as the results obtained by Chan's method. Fig. 8 shows the time history of the free surface elevation at the position y=4d. The results obtained by the present method have high correlation among themselves regardless of the difference of the width of the fluid region used at the time of numerical calculation. As far as the wave profile calculated by the authors is concerned, on the contrary, undesirable defects were observed in the wave profile obtained by the method used by Chan.

6-2. Linear Hydrodynamic Derivatives of a Flat Plate

The calculated hydrodynamic derivatives of a flat plate are shown in Figs. 9 and 10, together with the experimental results obtained by Koshiwag[5]. The draft-length ratio of the plate is 0.1, and the Froude numbers during the experiments are 0.2 and 0.4 . The non-dimensional frequency used for the abscissa is defined by $\omega' = \omega\sqrt{L/g}$. As presented in Figs. 9 and 10, both results are in good agreement. In particular, it is interesting to note that the numerical solution is capable of predicting in an effective manner the forward speed effects on the hydrodynamic derivatives.

6-3. Series 60 Model

In Figs. 11 to 18, the calculated hydrodynamic derivatives of the Series 60 model with C_b=0.7 are presented, together with the experimental results obtained by van Leeuwen[6]. Each figure includes three types of numerical results obtained by the present method, which are designated as S. 60, R. C., and F. P., S. 60 denotes the prediction results for the exact Series 60 hull shape. R. C. and F. P., however, indicate the numerical prediction performed by substituting a rectangular cylinder and a flat plate, respectively, for the exact Series 60 hull shape.

In several hydrodynamic derivatives, as seen in Fig. 11 to 18, there exists remarkable difference between the predicted values obtained by the Strip Method and experimental results. In particular, the agreement of the coupling coefficients is poor. On the other hand, the numerical results obtained by the present method under the flat plate approximation explain well the qualitative tendency of the frequency dependence of the hydrodynamic derivatives. However, the frequency at which the hydrodynamic derivatives achieve their peak values cannot be predicted by the flat plate approximation method. Rectangular cylinder approximation significantly improves the agreement of the peak frequencies between numerical prediction and experimental results, but the quantitative agreement of the hydrodynamic derivatives is poor when compared to the results obtained by flat plate approximation. To the contrary, the numerical results obtained for the exact Series 60 hull form shows significantly positive agreement with the experimental results. In particular, the improvement of the prediction accuracy of the derivatives N'_ϕ, N'_v, N'_r and Y'_ϕ are excellent compared with the numerical results obtained using the Strip Method.

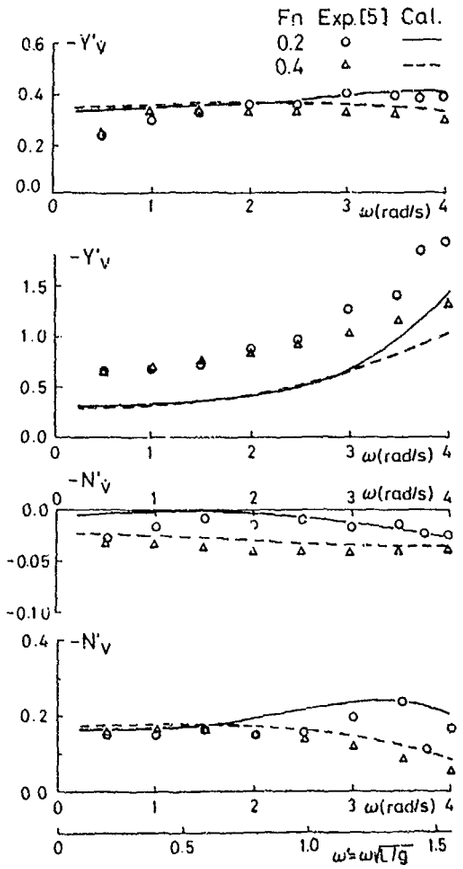

Fig. 9 Linear hydrodynamic derivatives of a flat plate with d/L=0.1 obtained by pure sway

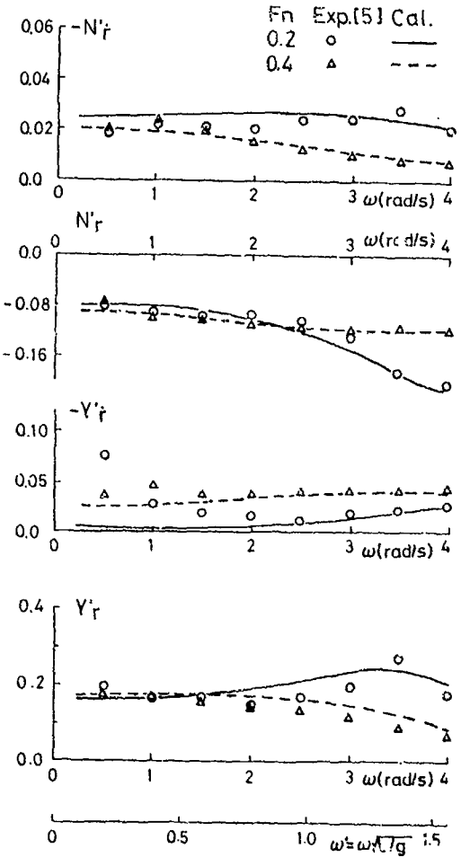

Fig. 10 Linear hydrodynamic derivatives of a flat plate with d/L=0.1 obtained by pure yaw

6-4. Container Ship

The predicted hydrodynamic coupling coefficients of sway-yaw and roll-yaw of a model of container ship are illustrated in Figs. 19 to 26, together with the experimental results[7], as well as the numerical predictions of the New Strip Method. The non-dimensional frequency used for the abscissa of these figures is defined by $\hat{\omega}=\omega\sqrt{B/2g}$.

Except for $\hat{A}_{26}$ in a low frequency range, the hydrodynamic coupling coefficients of sway-yaw obtained by the present method are in good agreement with the experimental results. Furthermore, the forward speed effects on the hydrodynamic coefficients can be positively predicted by the present method. In general, however, differences between the predicted hydrodynamic coefficients of roll-yaw coupling and the experimental results appear to be significant in comparison to the differences observed among other hydrodynamic coefficients. Nevercheless, the present method is capable of excellently predicting the forward speed dependence of the roll-yaw coupling coefficients, with the exception of $\hat{B}_{46}$.

On the contrary, the New Strip Method does not succeed in predicting the numerical values of most hydrodynamic coupling coefficients at a sufficient level of accuracy.

According to the numerical calculation performed by Troesch[8], it is found that the forward speed effect on the coupling coefficients of sway-yaw is predicted well. However, the forward speed effect on the roll-yaw coupling coefficients does not appear to have been positively predicted by the calculation method used by Troesch (see reference 8)).

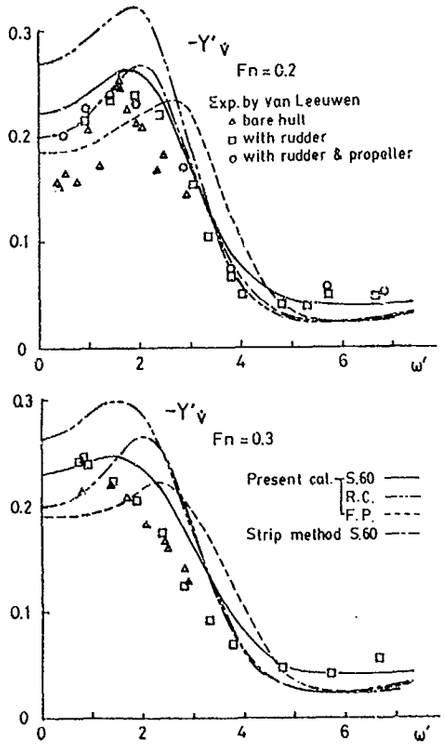

Fig. 11 $Y'_{\dot{v}}$ versus ω' for Series 60 model

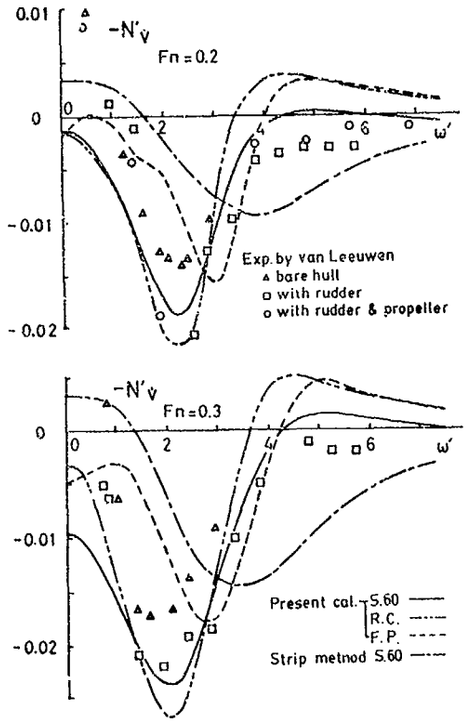

Fig. 13 $N'_{\dot{v}}$ versus ω' for Series 60 model

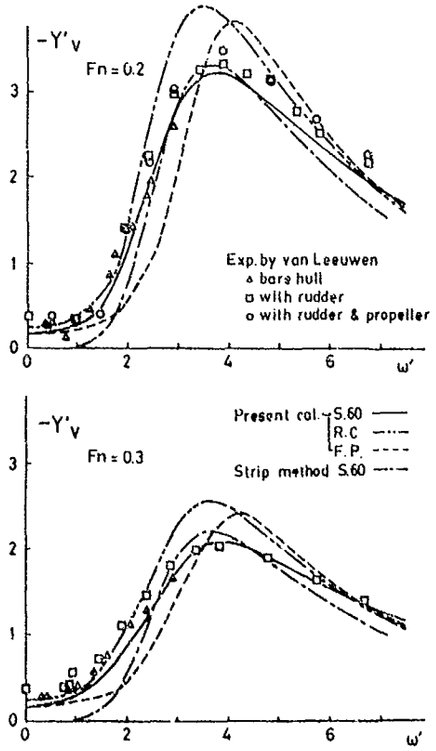

Fig. 12 Y'_v versus ω' for Series 60 model

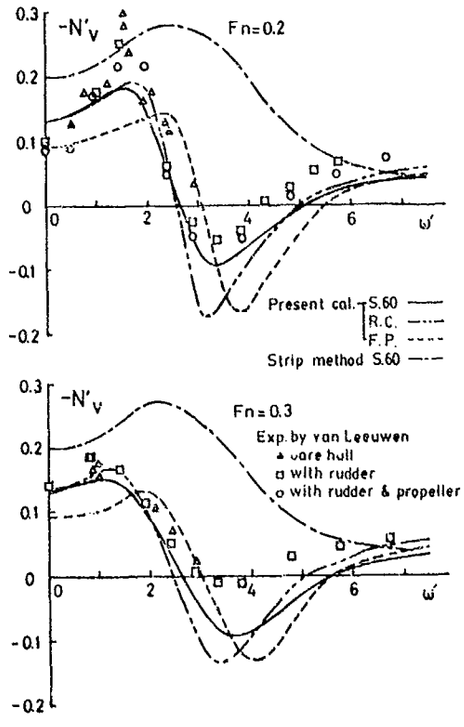

Fig. 14 N'_v versus ω' for Series 60 model

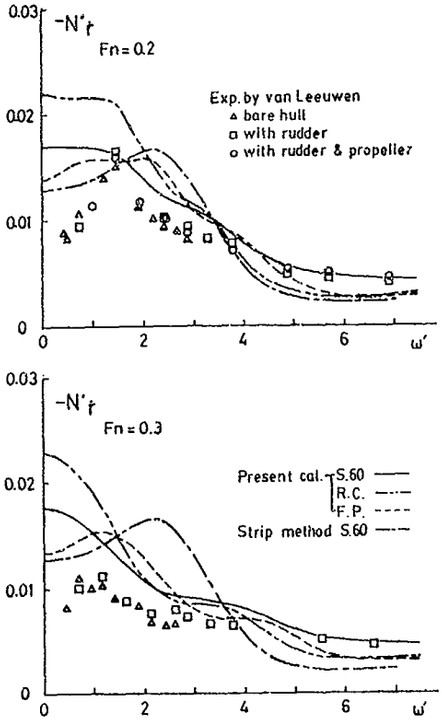

Fig. 15 $N'_{\dot{r}}$ versus ω' for Series 60 model

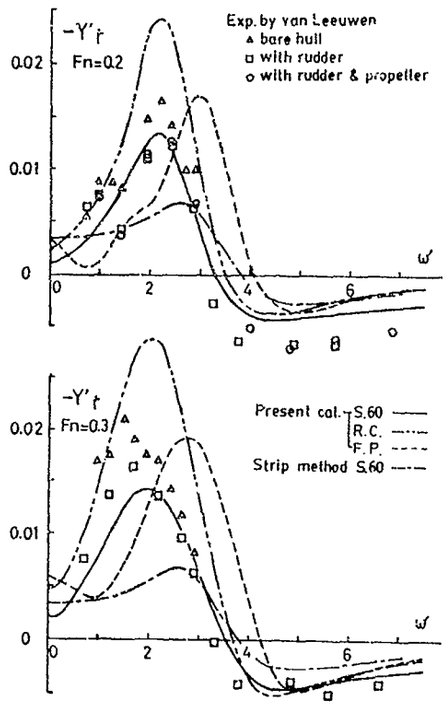

Fig. 17 $Y'_{\dot{r}}$ versus ω' for Series 60 model

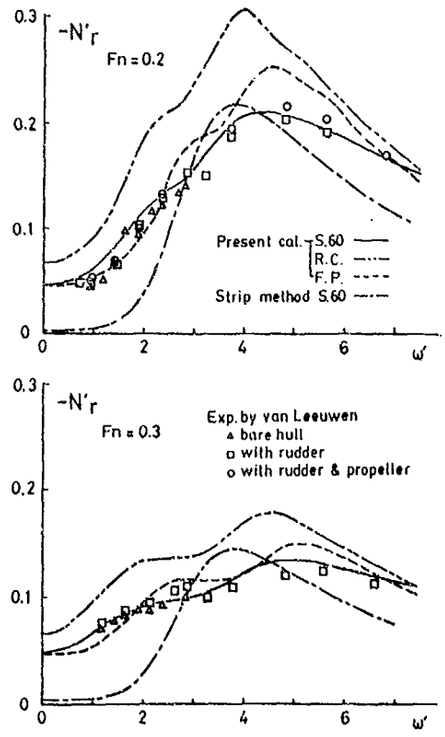

Fig. 16 N'_{r} versus ω' for Series 60 model

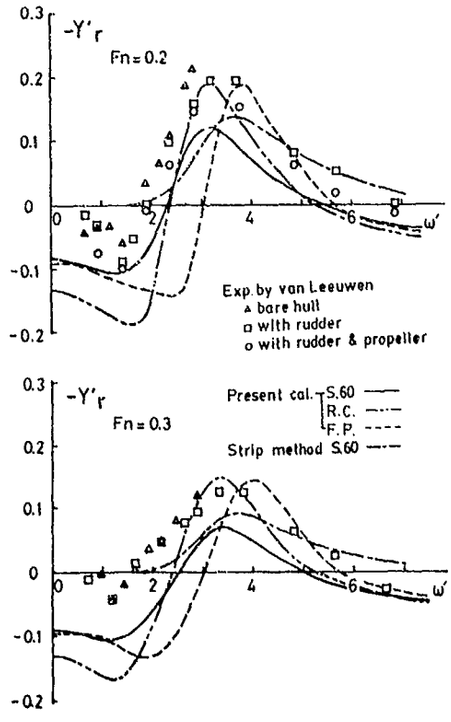

Fig. 18 Y'_{r} versus ω' for Series 60 model

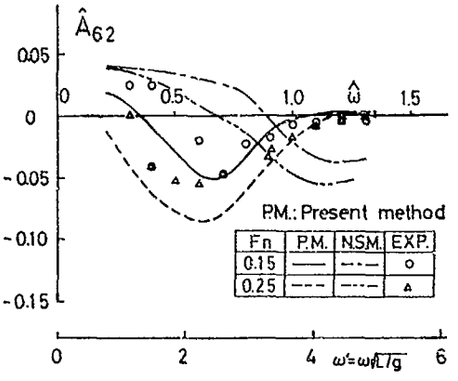

Fig. 19 $\hat{A}_{62}$ versus $\hat{\omega}$ for a container ship-model

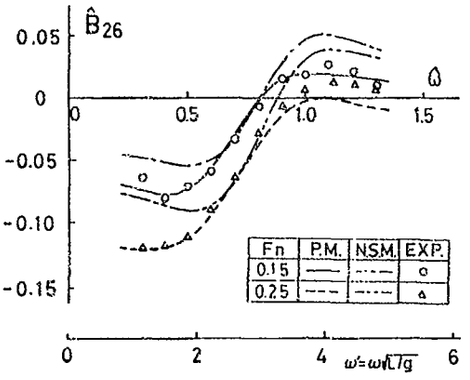

Fig. 22 $\hat{B}_{26}$ versus $\hat{\omega}$ for a container ship-model

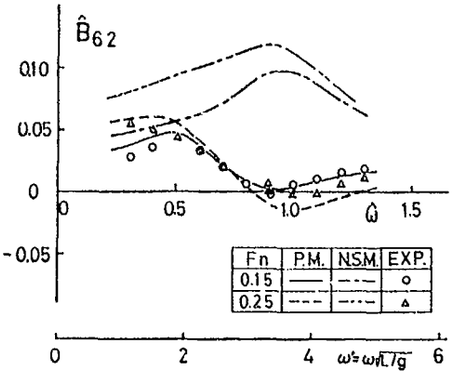

Fig. 20 $\hat{B}_{62}$ versus $\hat{\omega}$ for a container ship-model

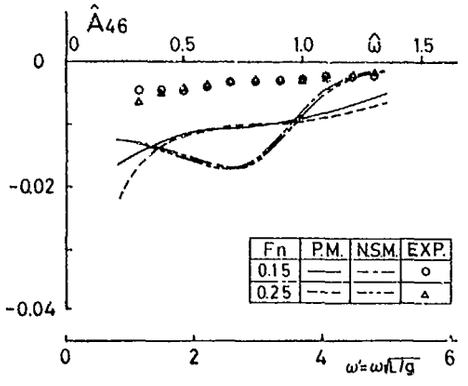

Fig. 23 $\hat{A}_{46}$ versus $\hat{\omega}$ for a container ship-model

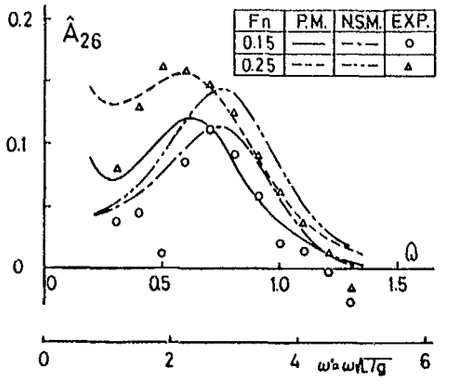

Fig. 21 $\hat{A}_{26}$ versus $\hat{\omega}$ for a container ship-model

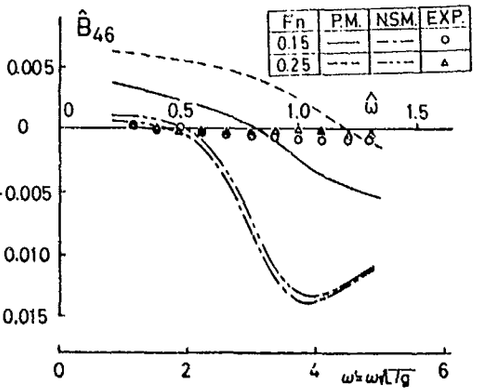

Fig. 24 $\hat{B}_{46}$ versus $\hat{\omega}$ for a container ship-model

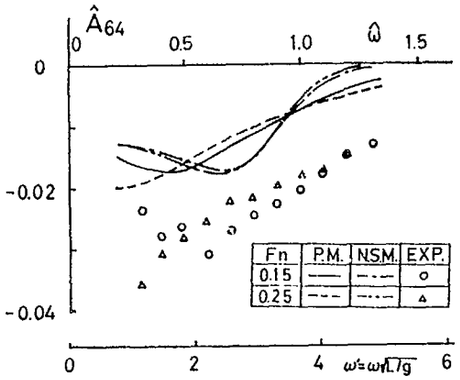

Fig. 25 $\hat{A}_{64}$ versus $\hat{\omega}$ for a container ship-model

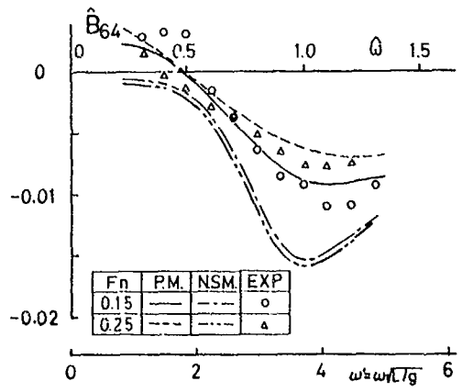

Fig. 26 $\hat{B}_{64}$ versus $\hat{\omega}$ for a container ship-model

7. Conclusions

As a result of comparing the numerical hydrodynamic coefficients predicted by the present method with the experimental results, it is found that the present method effectively predicts both the effects of the ship's forward speed and frequency of motion on the hydrodynamic coefficients of a ship-like three-dimensional body. In particular, the prediction accuracy of the hydrodynamic coupling coefficients between sway, yaw, and roll motion is significantly improved using the present method, particularly when compared to the so-called Strip Method. Needless to say, however, it is emphasized that attempts to improve the predicted value of hydrodynamic coefficients must be continuously made since the present method is not sufficiently accurate regarding the predicted value of a small number of hydrodynamic coefficients.

Although the numerical calculations described in this paper are restricted to the radiation problem of lateral ship motions, needless to say, the present methodology may be applicable to the radiation problem of such vertical ship motions as heave and pitch, and to the diffraction problem of waves.

8. Acknowledgements

The authors wish to express their gratitude to the staff members of the Seakeeping and Manoeuvring Laboratory, Department of Naval Architecture, University of Tokyo, for the helpful assistance they kindly extended to the authors.

References

1) Chapman, R. B. : Free Surface Effects for Yawed Surface-Piercing Plates, Journal of Ship Research, Vol. 20, No. 30 (1976).
2) Chapman, R. B. : Numerical Solution for Hydrodynamic Forces on a Surface-Piercing Plate Oscillating in Yaw and Sway, Proceedings of 1st International Conference on Numerical Ship Hydrodynamics (1975).
3) Orlanski, I. : A Simple Boundary Condition for Unbounded Hyperbolic Flows, Journal of Computational Physics, Vol. 21 (1976).
4) Chan, R. K. C. and Chan, F. W. K. : Numerical Solution of Transient and Steady Free-Surface Flow about a Ship of a General Hull Shape, Proceedings of 13th Symposium on Naval Hydrodynamics (1980).
5) Kashiwagi, T. : On Stability Derivatives of a Ship Advancing at a High Speed, Journal of the Kansai Society of Naval Architects, Japan, No. 189 (1983).
6) van Leeuwen, G. : The Lateral Damping and Added Mass of a Horizontally-Oscillating Ship-Model, International Ship building Progress, Vol. 12, No. 126 (1956).
7) SR 131 Panel : Measurement of the Hydrodynamic Coefficients of the Equations for Lateral Motions of a Ship, Report of The Shipbuilding Research Association of Japan, No. 213 (1976).
8) Troesch, A. W. : Sway, Roll, and Yaw Motion Coefficients Based on a Forward-Speed Slender-Body Theory-Part 2, Journal of Ship Research, Vol. 25, No. 1 (1981).

DISCUSSION
of the paper
by K. Yamazaki

"LINEAR HYDRODYNAMIC COEFFICIENTS OF SHIPS WITH FORWARD SPEED DURING HARMONIC SWAY, YAW AND ROLL OSCILLATIONS"

DISCUSSION
by R. Yeung and s. Kim

The authors are to be congratulated on an extensive set of computations and comparison with experiments. The formulation used here is what we called the "Forward-speed Transient Formulation" in the paper of Yeung and Kim (1984), in which a short review of a number of modern ways of computing hydrodynamic coefficients was given. The transient approach appears to offer some additional potential compared with the traditional "strip theory" and the more recent "unified theory" that utilized time-harmonic two-dimensional solutions. In a paper presented in the last meeting of this conference (Yeung & Kim, 1981), we have provided similar comparison of numerical and experimental results for the heave and pitch motions of three-dimensional hull. The authors are apparently aware of our work since their fixed-and-moving frames space-time relations were initially exploited by us for conceptual clarity. Our work also explained how, in the presence of a body of finite lateral dimension, the solution obtained in a single transverse plane of the fixed frame of reference could be used to obtain the hydrodynamic coefficients for time-harmonic motions. Such a procedure ceases to be useful if the free-surface condition is non-linear as the authors' initial formulation. Indeed, the nonlinear conditions were simply irrelevant in such a theory. These points have apparently been taken for granted by the authors in this work.

Our work in 1981 led us to think about the exact role played by the presence of transverse waves in such a formulation. Our 1984 paper explained how such missing transverse-wave effects terms can be recovered. We wonder if the authors can comment on the importance of transverse-wave effects on their lateral-motion hydrodynamic calculations.

The method used by the authors to solve the unsteady two-dimensional problem utilized an open boundary condition that can only accomodate a single phase velocity. Such a condition breaks down when waves of various frequencies exist and is propagating through this boundary simultaneously. Since the only test indicated in the paper was that due to a flat plate in steady motion, we are curious how it actually performed in situations where waves are generated by lateral oscillations as well by the change in the body dimension. Can some numerical results be included to assess the effectiveness of the proposed boundary condition in such a situation?

Finally, can the authors justify why the open boundary condition (21) is compatible with the forward-speed steady potential ϕ_P, which satisfies the rigid free-surface condition? We feel that they are inconsistent.

Yeung R.W. & Kim, S.H. (1981):
"Radiation Forces on Ships with Forward Speed" Proc, 3rd Int. Conf. Numer. Ship Hydrodyn. p 499-515, Bassin d' Essais des Crenes, Paris France.

Yeung, R.W. & Kim, S.H. (1984)" "A New Development in the Theory of Oscillating and Translating Slender Ships", Proc. 15th Symp. Naval Hydrodyn. pp195-212, Hamburg, W. Germany.

Author's Reply

The authors are grateful to Prof. Yeung and Dr. Kim for their discussions. Both the calculation method presented in our paper and the method indicated by the discussers are the modifications of the method indicated initially by Chapman. Therefore, it is natural that there are some similar points in the conception of both methodologies. In our method, the hydrodynamic forces are predicted by calculating the time-histories of the fluid motions in the various space-fixed transverse planes, which are independent respectively. This method makes it easy to impose the nonlinear condition to the free surface in the two-dimensional transverse planes. Our final aim is to predict the hydrodynamic forces and moments acting on ships during the arbitrary motions, not the time-harmonic motions.

The effects of the transverse waves on the lateral hydrodynamic forces occur in the low frequency region of ship motions at the low forward-speed. However, the lateral forces in such a frequency region are largely influenced by viscosity rather than by the transverse waves, and then it may not be thought that we can get better results than those obtained in our paper, even if the transverse waves are taken into account. As the result of comparisons between the predicted hydrodynamic coefficients and experimental results, shown in our paper, it appears that the calculation method presented in our paper may provide considerably improved predictions of hydrodynamic coefficients, although the effects of transverse waves cannot be completely neglected.

In the space-fixed transverse plane, the waves generated by the oblique towing of a flat plate can be regarded as the waves which are generated by imposing the lateral velocity with a step-like shape on the flat plate. The

generated waves, therefore, have the components of all frequencies as shown in Fig. 6. Consequently, the open boundary condition (21) can make the waves pass through the open boundary in the situation as mentioned by the discussers.

The open boundary condition (21) indicates that the time-differenciation of some physical quantity, which expresses the velocity potential in our paper, relative to the frame of reference advancing together with the quantity is null at the instance when the quantity passes through the open boundary. We consider, therefore, that equation (21) holds good regardless of other conditions satisfied by the quantity.

Session II

NONLINEAR MOTIONS/SLAMMING

Session Chairman
J.C. Dern
Bassin D' Essais Des Carenes
Paris, France

FREE SURFACE POTENTIAL OF A PULSATING SINGULARITY IN HARMONIC HEAVE MOTION

A. CLEMENT, P. FERRANT
Laboratoire d'Hydrodynamique Navale
ENSM - 1, Rue de la Noé - 44300 NANTES
FRANCE

Abstract

Several expressions of the Green function relative to a pulsating source of strength $q(t) = q_0 \cos \omega t$, heaving harmonically at the same frequency under the free-surface of a perfect fluid are given. The free-surface condition is linearized and, as we assume steady state conditions, the kinematic quantities are periodical in time. The velocity potential is then given as a Fourier series, each term of this expansion being a function of its proper wavenumber $n^2\omega^2/g$ and of the amplitude parameter a/b. The free-surface is shown to be a superposition of regular waves at frequency $n\omega$ instead of a simple monochromatic wave as in the case of the stationary pulsating source. The numerical results presented hereafter show that the amplitude of the harmonic components of the wave field are not monotonous functions of the frequency.

1. Introduction

The modelization of the ship motions in a seaway by the potential flow theory leads, at the first step, to a fully nonlinear mathematical problem. Even in the simple case of a surface piercing body at zero forward speed in a regular wave train, nonlinearities arise from the three following circumstances:

- the free-surface condition includes quadratic terms of the fluid velocity;
- in the mechanical equations of motion, several terms may be nonlinear as, for example, the hydrostatic restoring forces and the mooring forces;
- the fluid domain is bounded by moving surfaces: the free-surface and the submerged body surface.

The perturbation expansion techniques based on single or multiple small parameters [OGILVIE (1963), LEE (1968), POTASH (1971), PAPANIKOLAOU & NOWACKI (1980),...] permit to reduce this complex problem into several linear problems. Considering only the first-order terms, we are led to the classical radiation-diffraction problem which has received, in the last years, many solutions by various numerical approaches.

This linear problem is generally solved in the frequency domain and the resulting numerical predictions of forces and motions are sufficiently accurate to satisfy the common engineering needs. Unfortunately, the situations when the basic assumptions of the linear theory become no longer valid are of critical interest in ships and offshore structures design. In particular, the analysis of their safety and survivability requires a good knowledge of their response in very steep waves or near their resonance frequency which are cases where nonlinear behaviours may appear and must be carefully investigated.

At the present time, the simulation methods based on time marching procedures seem to be the most powerful to modelize such phenomena [FALTINSEN (1977), GREENHOW and al.-(1982), VINJE and al.(1983), LIN and al.-(1984), ...]. Their major advantage is to take simultaneously into account the different nonlinearities of the problem. Nevertheless, the lack of a suitable radiation condition in the time domain restricts their use to the study of transient problems over short periods of time. Furthermore, the large amount of computing time necessary to treate simple 2D geometries indicates that one cannot reasonably hope to modelize realistic 3D cases in that way for the moment, and even in a near future.

The resolution of the complete nonlinear problem in the frequency domain is not more conceivable at the moment. But we believe that such an approach could be helpful to refine our knowledge of the nonlinear phenomena involved in the seakeeping problem. In order to simplify that task, it is essential to study uncoupled problems presenting only a single type of nonlinearity. It will help us to clearly separate the effect of the wave steepness, the body motions amplitudes, the nonlinearity of the restoring forces,..., on the global result. With that point of view we began to study the case of fully submerged bodies performing forced harmonic motions of large amplitude. The frequency parameter and the depth of immersion are chosen such that the free-surface condition may still be linearized. For this particular kind of wave radiation problems, the nonlinearities arise only from the body boundary condition. When the amplitude of the forced motion becomes at least as large as a typical body dimension, the usual

linearization based on an expansion of the potential into Taylor series around the mean body position is not longer valid. In such a situation, we can imagine to solve the problem by means of integral equations written on the actual time-depending boundary instead of its mean position. This implies the use of moving singularities of pulsative strength. The new Green functions relative to these singularities are formulated by somewhat complex expressions which must be transformed in order to make them more suitable for numerical computations. The study of the heaving pulsating source potential is presented in this paper

2. Mathematical formulation.

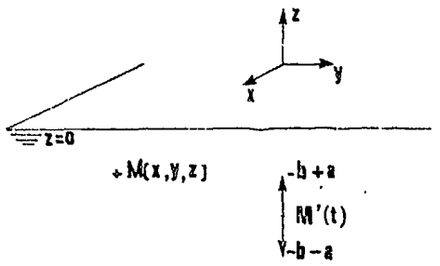

The fluid is of infinite depth and lateral extent; it is assumed to be inviscid, homogeneous and incompressible. Surface tension and free-surface nonlinearities are neglected. The flow is irrotational and is represented by a velocity potential Φ, which is a function of the space coordinates and of the time t.

A source of pulsative strength $q=q_o\cos\omega t$ located under the free-surface is subject to a forced heaving motion at the same frequency ω. Its position is given by:

$$M'(0.,0.,-b + a\cos\omega t)\ , \qquad (2.1)$$

with the condition $a < b$

The velocity potential is the solution of the following mathematical problem, for M located in the lower half-space D_- :

$$\Delta\Phi(M,t) = \delta(M,M')\cos\omega t \qquad (2.2.a)$$

$$\left.\frac{\partial^2\Phi}{\partial t^2} + 2\sigma\frac{\partial\Phi}{\partial t} + g\frac{\partial\Phi}{\partial z}\right|_{z=0} = 0 \qquad (2.2.b)$$

$$\vec{\nabla}\Phi \longrightarrow 0\ ,\ z \longrightarrow -\infty \qquad (2.2.c)$$

The radiation condition is intrinsically satisfied by the solutions of this problem, owing to the additional vanishing term $2\sigma\,\partial\Phi/\partial t$ in the linearized free-surface condition. A particular solution of (2.2.a) is given by:

$$\Phi_o = -\frac{\cos\omega t}{4\pi|MM'|} \qquad (2.3)$$

In order to simplify further calculations, we shall rather take:

$$\Phi_o = -\frac{\cos\omega t}{4\pi}\left[\frac{1}{|MM'|} - \frac{1}{|MM'_1|}\right] \qquad (2.4)$$

M'_1 being the image point of M' with respect to the mean free-surface plane z = 0; the general solution of (2.2) is then written as follows:

$$\Phi(M,M',t) = -\frac{q_o\cos\omega t}{4\pi}\left[\frac{1}{|MM'|(t)} - \frac{1}{|MM'_1|(t)}\right] + \phi(M,M',t) \qquad (2.5)$$

The use of (2.5) in (2.2) yields the following problem for ϕ:

$$\begin{cases} \Delta\phi = 0 \quad \text{for } M \in D_- \\ \left.\dfrac{\partial^2\phi}{\partial t^2} + 2\sigma\dfrac{\partial\phi}{\partial t} + g\dfrac{\partial\phi}{\partial z}\right|_{z=0} = -\dfrac{gq_o\cos\omega t}{4\pi}\dfrac{\partial}{\partial z}\left[\dfrac{1}{|MM'(t)|} - \dfrac{1}{|MM'(t)|}\right] \\ \vec{\nabla}\phi \longrightarrow 0 \quad \text{as } z \longrightarrow -\infty \end{cases} \qquad (2.6)$$

This type of problem is commonly solved by using a double Fourier transform over the horizontal coordinates x and y.

With the help of the following identities:

$$\frac{1}{|MM'|} = \frac{1}{\pi}\,Re\int_{-\pi/2}^{+\pi/2} d\Theta \int_{-\infty}^{+\infty} e^{k[-(z-z')+i\Omega]}dk$$
$$\frac{1}{|MM'|} = \frac{1}{\pi}\,Re\int_{-\pi/2}^{+\pi/2} d\Theta \int_{-\infty}^{+\infty} e^{k[(z+z')+i\Omega]}dk \qquad (2.7)$$

valid for z=0, with $\Omega = (x-x')\cos\Theta + (y-y')\sin\Theta$, the free-surface boundary condition is then transformed into an ordinary differential equation for the Fourier transform $\tilde{\phi}$ of ϕ:

$$\left[\frac{\partial^2}{\partial t^2} + 2\sigma\frac{\partial}{\partial t} + gk\right]\tilde{\phi}\,(\Theta,k,t) = -\frac{q\,q(t)}{2\pi}\,e^{k[z'(t)-i(x'\cos\Theta+y'\sin\Theta)]} \qquad (2.8)$$

$\tilde{\phi}$ being defined by:

$$\phi(M,M',t) = \frac{1}{\pi}\,Re\int_{-\pi/2}^{+\pi/2} d\Theta \int_0^{+\infty} \tilde{\phi}(\Theta,k,t)\,e^{k[z+i(x\cos\Theta+y\sin\Theta)]}\,kdk \qquad (2.9)$$

3. Classical results

For a stationary source, z'(t) is constant ($z'_o = -b$) and the right-hand side of (2.8) is a simple-harmonic function of time, since we have $q(t) = q_o\cos\omega t$. Considering only the steady-state solutions, (2.8) is solved immediately, and gives:

$$\tilde{\phi}(\Theta,k,t) = -\frac{q_o}{4\pi}\,e^{k[z'_o - i(x'\cos\Theta + y'\sin\Theta)]} \cdot \left[\frac{e^{i\omega t}}{k-k_1+\frac{2i\sigma}{g}} + \frac{e^{-i\omega t}}{k-k_1-\frac{2i\sigma}{g}}\right] \qquad (3.1)$$

where $k_1 = \omega^2/g$ (3.2)

The function $\phi(M,M',t)$ may now be obtained by taking the inverse double Fourier transform of ϕ according to (2.9), and at last $\Phi(M,M',t)$ is obtained through (2.4). As it is well known, Φ is a simple-harmonic function of the time, and may be written as:

$$\Phi(M,M',t) = \mathrm{Re}[G(M,M')\, e^{-i\omega t}] \qquad (3.3)$$

where $G(M,M')$ is the Green function of the problem. This function has been widely studied, and the most known expressions of it are given below. [(3.5 to (3.8)]

In the following, we shall take b as the reference length, and account for the fact that G is axisymmetric about the vertical axis passing through M'. The new variables are then:

$$K_1 = \frac{\omega^2 b}{g} = bk_1$$

$$Z = \frac{z}{b} \qquad (3.4)$$

$$R = [(x-x')^2 + (y-y')^2] / b$$

$$M'(R',Z') \longrightarrow M'(0.,-1.)$$

The denominations are given according to F. Noblesse (1980).

Wehausen-Laitone

$$G(M,M') = -\frac{1}{4\pi}\left[\frac{1}{|MM'|} + PV\int_0^{+\infty} \frac{K+K_1}{K-K_1} e^{K(Z-1)} J_0(KR)\, dK\right] + 2i\pi K_1 e^{K_1(Z-1)} J_0(K_1R) \qquad (3.5)$$

Haskind

$$G(M,M') = -\frac{1}{4\pi}\left[\frac{1}{|MM'|} + \frac{1}{|MM'_1|} + 2K_1 e^{K_1(Z-1)}\int_\infty^{K_1(Z-1)} \frac{e^t\, dt}{(t^2+K_1^2R^2)^{1/2}} - 2\pi K_1 e^{K_1(Z-1)}\left[Y_0(K_1R) - i\, J_0(K_1R)\right]\right] \qquad (3.6)$$

Haskind (modified)

$$G(M,M') = -\frac{1}{4\pi}\left[\frac{1}{|MM'|} + \frac{1}{|MM'_1|} - 2K_1 e^{K_1(Z-1)}\int_0^{K_1(1-Z)} \frac{e^t\, dt}{(t^2+K_1^2R^2)^{1/2}} - \pi K_1 e^{K_1(Z-1)}\left[H_0(K_1R) + Y_0(K_1R) - 2i\, J_0(K_1R)\right]\right] \qquad (3.7)$$

Near-field

$$G(M,M') = -\frac{1}{4\pi}\left[\frac{1}{|MM'|} + \frac{1}{|MM'_1|} + \frac{4K_1}{\pi}\int_0^{\pi/2} \mathrm{Re}\left[e^{K_1(Z-1+iR\cos\Theta)} E_1[K_1(Z-1+iR\cos\Theta)]\right] d\Theta - 2\pi K_1 e^{K_1(Z-1)}\left[H_0(K_1R) - i\, J_0(K_1R)\right]\right] \qquad (3.8)$$

These results are well-known: the details and demonstrations may be found in the referenced papers.

4. Heaving source.

In the general case of a periodically moving singularity of pulsative strength, the same basic method can be used to derive the Green function. Let us apply it to the case of the heaving source.

The first difference from the stationary source problem lies in equation (2.8), which gives now:

$$\left(\frac{\partial^2}{\partial t^2} + 2g\frac{\partial}{\partial t} + gk\right)\tilde{\phi}(\Theta,k,t) = -\frac{gq_0\cos\omega t}{2\pi}\, k(-1 + A\cos\omega t)\, e \qquad (4.1)$$

where

$$M'(x',y',z'=-b+a\cos\omega t) \longrightarrow M'(0,Z'=-1+A\cos\omega t),$$

with cylindrical coordinates, and b being taken as the reference length.

The right-hand side of (4.1) is not longer a simple-harmonic function of the time, but it is still periodical, and may therefore be written as a Fourier series.

From the identity:

$$e^{x\cos\alpha} = I_0(x) + 2\sum_{n=1}^{\infty} I_n(x)\cos n\alpha \quad , \qquad (4.2)$$

one may derive :

$$\cos\omega t\; e^{kA\cos\omega t} = I_1(Ak) + \sum_{n=1}^{\infty}\left[I_{n-1}(Ak) + I_{n+1}(Ak)\right]\cos n\omega t \qquad (4.3)$$

The equation (4.1) is solved separately for each term of the Fourier expansion of its right-hand side, and once again, we shall retain only the steady-state solutions. The double Fourier transform of ϕ is therefore:

$$\tilde{\phi}(\Theta,k,t) = -\frac{q_0}{2\pi}\, e^{-k}\left\{\frac{I_1(Ak)}{k} + \sum_{n=1}^{\infty}\frac{I_{n-1}(Ak) + I_{n+1}(Ak)}{2}\right.$$

$$\left[\frac{e^{in\omega t}}{k-K_n+i(0)} + \frac{e^{-in\omega t}}{k-K_n-i(0)}\right]\Bigg\} \qquad (4.4)$$

where $K_n = n^2 K_1$

ϕ being written as the inverse Fourier transform of $\bar{\phi}$ (2.9), the complete potential Φ is then given by:

$$\Phi(M,M',t) = \frac{q(t)}{4\pi}\left[\frac{1}{MM'(t)} - \frac{1}{MM'_1(t)}\right]$$

$$- \frac{q_o}{4\pi} Re\, \frac{2}{\pi}\int_0^{\pi/2} d\Theta \int_0^{\infty} e^{k(Z-1+iR\cos\Theta)}\left\{\frac{I_1(Ak)}{k}\right. \qquad (4.5)$$

$$\left. + \sum_{n=1}^{\infty} I'_n(Ak)\left[\frac{e^{in\omega t}}{k-K_n+i(0)} + \frac{e^{-in\omega t}}{k-K_n-i(0)}\right]\right\} dk$$

where the interval of integration over Θ has been reduced, since the kernel is an even function of Θ, and (0) is a vanishing positive quantity. The prime of I_n denotes the first derivative of this function. This expression of the velocity potential includes higher-order harmonic terms. Furthermore, the expansion of the kernel of the integral and of the first terms of (4.5) contains stationary components. The total velocity field has consequently a non-zero mean value corresponding to a steady flow. This component will be clearly identified after a re-arrangement of (4.5).

-The calculation of the first part of Φ is straightforward.

-The second part, $\phi(M,M',t)$, may be written as:

$$\phi(M,M',t) = \frac{q_o}{2\pi}\left[H_o(M,M') + \right. \qquad (4.6)$$

$$\left. \sum_{n=1}^{\infty} \left(H_n^1(M,M')\, e^{in\omega t} + H_n^2(M,M')\, e^{-in\omega t} \right)\right]$$

by introducing:

$$H_n^1 = -\frac{2}{\pi}\int_0^{\pi/2} d\Theta \int_0^{\infty} I'_n(Ak)\frac{e^{k(Z-1+iR\cos\Theta)}}{k-K_n+i(0)}\, k\, dk \qquad (4.7)$$

$$H_n^2 = \frac{2}{\pi}\int_0^{\pi/2} d\Theta \int_0^{\infty} I'_n(Ak)\frac{e^{k(Z-1+iR\cos\Theta)}}{k-K_n-i(0)}\, k\, dk$$

With the help of the integral formulation of the modified Bessel functions I_n:

$$I_n(Ak) = \frac{1}{\pi}\int_0^{\infty} \cos n\sigma\, e^{Ak\cos\sigma}\, d\sigma \qquad (4.8)$$

we obtain the alternative form of H_n^1 and H_n^2 :

$$H_n^1 = -\frac{2}{\pi^2}\int_0^{\pi} \cos\sigma\, \cos n\sigma\, d\sigma \int_0^{\pi/2} d\Theta \int_0^{\infty} \frac{e^{k(Z-1+A\cos\sigma+iR\cos\Theta)}}{k-K_n+i(0)}\, kdk$$

$$H_n^2 = -\frac{2}{\pi^2}\int_0^{\pi} \cos\sigma\, \cos n\sigma\, d\sigma \int_0^{\pi/2} d\Theta \int_0^{\infty} \frac{e^{k(Z-1+A\cos\sigma+iR\cos\Theta)}}{k-K_n-i(0)}\, kdk \qquad (4.9)$$

The inner integrals will be written as:

$$\int_0^{\infty} \frac{e^{\zeta}\, kdk}{k-K_n \pm i(0)} = \int_0^{\infty} e^{\zeta} dk + K_n \int_0^{\infty} \frac{e^{\zeta}\, dk}{k-K_n \pm i(0)} \qquad (4.10)$$

We have then to account for the influence of the poles $k' = K_n - i(0)$ and $k'' = K_n + i(0)$.

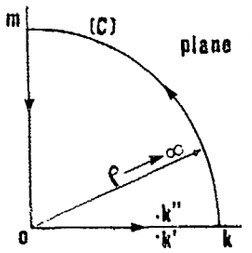

By considering the closed contour (C) in the complex plane $K = k+im = \rho e^{iX}$, for the second integrals in (4.10), we may express H_n^1 and H_n^2 in the form:

$$H_n^1 = -\frac{2}{\pi^2}\int_0^{\pi} \cos n\sigma\, \cos\sigma\, d\sigma \int_0^{\pi/2} d\Theta \left[\frac{-1}{Z-1+A\cos\sigma+iR\cos\Theta}\right.$$

$$\left. + K_n \int_0^{\infty} \frac{e^{im(Z-1+A\cos\sigma+iR\cos\Theta)}}{m+iK_n}\, dm\right] \qquad (4.11)$$

$$H_n^2 = H_n^1 - \frac{4iK_n}{\pi}\int_0^{\pi} \cos n\sigma\, \cos\sigma\, d\sigma \int_0^{\infty} \frac{e^{K_n(Z-1+A\cos\sigma+iR\cos\Theta)}}{m+iK_n}\, dm$$

The last integral term of H_n^2 may be expressed in terms of standard functions, and introducing the new notation:

$$g_n = \overline{H_n^1} + H_n^2 \qquad (4.12)$$

so that:

$$\Phi = \left[g_o + Re \sum_{n=1}^{\infty}\left[g_n\, e^{-in\omega t}\right]\right]\frac{q_o}{2\pi} \qquad (4.13)$$

We have then :

$$g_n(A,R,Z) = -\frac{2}{\pi^2} Re \int_0^{\pi} \cos\sigma \cos n\sigma \int_0^{\pi/2} d\theta \left\{ K_n \int_0^{\infty} \frac{e^{i\zeta m}}{m + iK_n} dm - \frac{1}{\zeta} \right\} d\sigma + 2\pi K_n I_n'(AK_n) \left[H_0(K_nR) - i J_0(K_nR) \right] e^{K_n(Z-1)} \quad (4.14)$$

with $\zeta = Z-1 + A\cos\sigma + iR\cos\theta$

Alternative expressions more suited to numerical computation remain to be developed. Before doing so, let us first identify the terms:

$$-\frac{2}{\pi^2} Re \int_0^{\pi} \cos\sigma \cos n\sigma \, d\sigma \int_0^{\pi/2} \frac{d\theta}{Z-1+A\cos\sigma+iR\cos\sigma} \quad (4.15)$$

For this purpose, we shall use the identity:

$$\frac{1}{MM_1'(t)} = \frac{2}{\pi} Re \int_0^{\pi} d\theta \int_0^{\infty} e^{k(Z-1+A\cos\omega t+iR\cos\theta)} dk = -\frac{2}{\pi} Re \int_0^{\pi/2} \frac{d\theta}{Z-1+A\cos\omega t+iR\cos\theta} \quad (4.16)$$

$$= \frac{-\,sgn(Z-1+A\cos\omega t)}{[(Z-1+A\cos\sigma)^2 + R^2]^{1/2}}$$

It is now obvious that (4.15) represents the coefficient of the n-th order term in the Fourier expansion of $\cos\omega t / MM_1'(t)$ (with a change of sign since $Z < 0$ and $A < 1$), the mean value of which is:

$$\frac{2}{\pi} Re \int_0^{\pi/2} d\theta \int_0^{\infty} I_1(Ak)\, e^{k(Z-1+iR\cos\theta)} dk \quad (4.17)$$

The complete velocity potential may now be expressed as follows:

$$\Phi(A,R,Z,t) = -\frac{q_o \cos\omega t}{4\pi} \left[\frac{1}{MM'(t)} + \frac{1}{MM_1'(t)} \right] - \frac{q_o}{2\pi} \sum_{n=1}^{\infty} Re \left[g_n'(A,R,Z)\, e^{-in\omega t} \right] \quad (4.18)$$

with :

$$g_n' = -\frac{2K_n}{\pi^2} Re \int_0^{\pi} \cos\sigma \cos n\sigma \, d\sigma \int_0^{\pi/2} d\theta \int_0^{\infty} \frac{e^{i\zeta m}}{m + iK_n} dm + 2\pi K_n I_n'(AK_n) [H_0(K_nR) - iJ_0(K_nR)]\, e^{K_n(Z-1)} \quad (4.19)$$

Note: With these new expressions, the steady flow component clearly appears to be the mean value of the velocity potential of two pulsative sources heaving symetrically with respect to the plane Z = 0, without any free-surface effect (i.e. "double-model" steady component). This result is not surprising, since for permanent flows, the free-surface boundary condition is reduced to:

$$\left.\frac{\partial\Phi}{\partial Z}\right|_{Z=0} = 0 \quad (4.20)$$

Double integral formulations.

A look at (4.18) and (4.19) yields the following remark:

The inner double-integral of (4.19) is obviously of the same kind as the basic expression of the Green function of the stationary pulsating source. $Z - Z'$ simply becomes $Z - 1 + A\cos\sigma$, while each harmonic n has its own wavenumber K_n. The expression given in (4.19) is consequently subject to the same transformations that lead to the classical single-integral formulations (3.5)-(3.8). We give thereafter the double-integral expressions we have obtained in that way.

"Haskind-type" formula

$$g_n' = -\frac{2K_n}{\pi} \int_0^{\pi} e^{K_n(Z-1+A\cos\sigma)} \cos\sigma \cos n\sigma \, d\sigma \int_{\infty}^{K_n(Z-1+A\cos\sigma)} \frac{e^t\, dt}{(t^2+K_n^2R^2)^{1/2}} + 2\pi K_n e^{K_n(Z-1)} I_n'(AK_n) \left[Y_0(K_nR) - i J_0(K_nR) \right] \quad (4.21)$$

"Modified Haskind-type" formula

$$g_n' = \frac{2K_n}{\pi} \int_0^{\pi} e^{K_n(Z-1+A\cos\sigma)} \cos\sigma \cos n\sigma \, d\sigma \int_{\infty}^{K_n(Z-1+A\cos\sigma)} \frac{e^t\, dt}{(t^2+K_n^2R^2)^{1/2}} + \pi K_n e^{K_n(Z-1)} I_n'(AK_n) \left[H_0(K_nR) + Y_0(K_nR) - 2i J_0(K_nR) \right] \quad (4.22)$$

"Near-field type" formula

$$g_n' = -\frac{4K_n}{\pi^2} \int_0^{\pi} \cos\sigma \cos n\sigma \, d\sigma \int_0^{\pi/2} Re \left[e^{K_n\zeta} E_1(K_n\zeta) \right] d\theta + 2\pi K_n e^{K_n(Z-1)} I_n'(AK_n) \left[H_0(K_nR) - i J_0(K_nR) \right] \quad (4.23)$$

with $\zeta = Z-1 + A\cos\sigma + iR\cos\theta$

Free-surface elevation.

The free-surface boundary condition being linearized, the wave height is simply given by:

$$\eta(t) = -\frac{1}{g}\frac{\partial\Phi}{\partial t}\bigg|_{Z=0} = \sum_{n=1}^{\infty} \eta_n(t) \qquad (4.24)$$

where the terms $\eta_n(t)$ are the harmonic components of the wave field, which may be obtained through (4.24) from the Fourier expansion of the velocity potential. For instance, the Near-field type formula (4.23) gives, after some manipulations:

$$\eta_n(t) = \frac{n\omega q_o}{g}\left[K_n\, I_n'(AK_n)\, e^{-K_n} \right.$$

$$\left. *\left[J_o(K_nR)\cos n\omega t + H_o(K_nR)\sin n\omega t\right] \right. \qquad (4.25)$$

$$\left. -\frac{|R_e|}{\pi^2}\int_c^{\pi}\cos\sigma\,\cos n\sigma\left[\int_o^{\pi/2}\left[K_n e^{K_n\zeta} E_1(K_n\zeta) - \frac{1}{\zeta}\right]d\theta\,\sin n\omega t\right]d\sigma\right.$$

The classical asymptotic expansions of J_o, H_o, and $e^z E_1(z)$ provide the following asymptotic form of (4.26):

$$\eta_n(R,t) = \frac{n\omega q_o}{g}\left[\frac{2K_n}{\pi R}\right]^{1/2} I_n'(AK_n)\, e^{-K_n} \qquad (4.27)$$

$$* \cos(K_nR - n\omega t - \pi/4) + o\left(\frac{1}{R}\right)$$

The far-field is consequently a superposition of regular waves of celerity $C_n = g/n\omega$. Owing to the linearization of the free-surface, the energy transmitted in the far-field is the sum of the energies transmitted by each ray of the wave spectrum.

5. Numerical results.

The free-surface patterns given in figures 2 and 3 have been computed from the modified-Haskind type formula (4.22) in most cases, and from the Near-Field type formula (4.23) when the radial distance R was approaching zero. In both cases, the double integral was performed by using two successive eight-points Newton-Cotes adaptative integration schemes. The inner integral being evaluated with at least 12 exact decimal digits, the final result is believed to be sufficiently accurate to satisfy our present goal. The special functions J_o, I_n, Y_o, H_o, are evaluated by standard numerical schemes giving a typical accuracy of 10^{-5}.

The wave pattern in the vicinity of the singularity (fig. 2 and 3) clearly exhibits the higher order components generated in the near field propagating outwards. For the sake of legibility, the vertical scales are magnified. In both cases (K_1=0.5 and K_1=1.0 at t=T/2), we give as a reference a view of the free-surface above the "equivalent" stationary source radiating the same amount of energy at infinity.

Figure 4 shows the evolution of the far-field wave amplitude coefficients for values of the fundamental wavenumber in the range [0., 5.]. As in the preceeding and in the following calculations, the total energy transmitted at infinity is set to a constant (=1.) as the frequency is varied. These coefficients are obtained by multiplying the asymptotic expression of the wave height of each harmonic (4.26) by $R^{1/2}$ in order to cancel the radial distance dependancy.

Figure 5 shows the rate of energy transmitted by the first four rays as a function of the fundamental wavenumber: the normalization rule is the same as in the preceeding calculations.

Finally, we give on figure 6 the evolution of these energy rates for the first four harmonics when the amplitude ratio a/b is varied from 0. to 0.96, and the frequency parameter K_1 from 0. to 5. This representation by distinct surfaces gives us a global illustration of the phenomenon. It demonstrates that, for a given amplitude ratio, the variation of the rate of energy transmitted by each ray is not a monotonous function of the fondamental wavenumber. For amplitudes ratios up to 0.7, the maxima of the curves occur for values of the frequency parameter around 0.5.

Although this unexpected behaviour has been highlighted in the case of a single heaving pulsating source, one may believe that a rather similar phenomenon would appear in the case of a submerged body performing large amplitude heaving motions. This remains to be confirmed by the resolution of such a problem by an integral equation method involving moving pulsating singularities. This constitutes the final goal of our present work. Anyhow, we hope that these preliminary results will offer a valuable guideline in the choice of the parameters when studying the nonlinearities associated with the body boundary condition, either in the time or in the frequency domain.

***

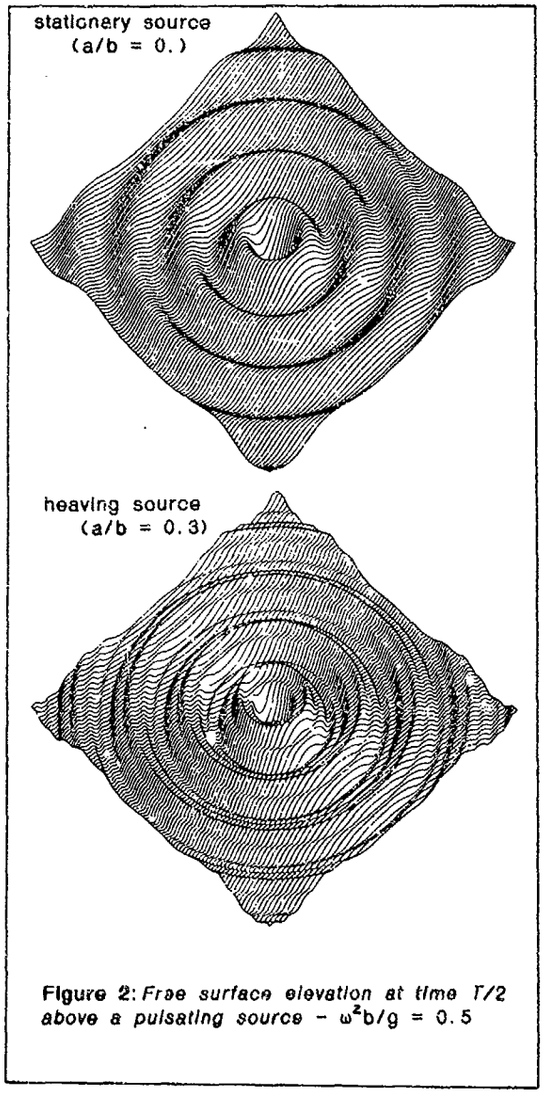

Figure 2: *Free surface elevation at time T/2 above a pulsating source* - $\omega^2 b/g = 0.5$

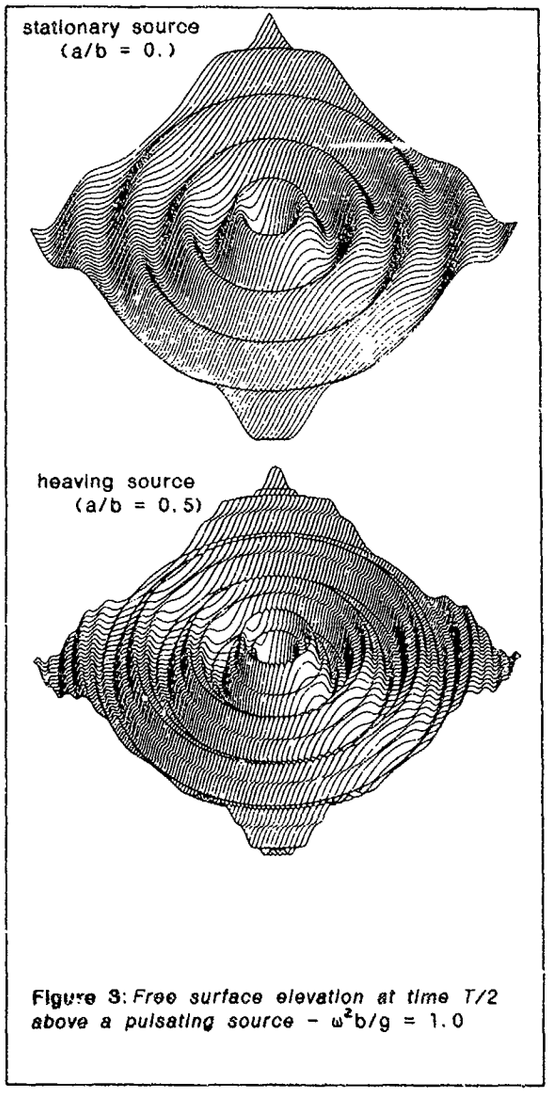

Figure 3: *Free surface elevation at time T/2 above a pulsating source* - $\omega^2 b/g = 1.0$

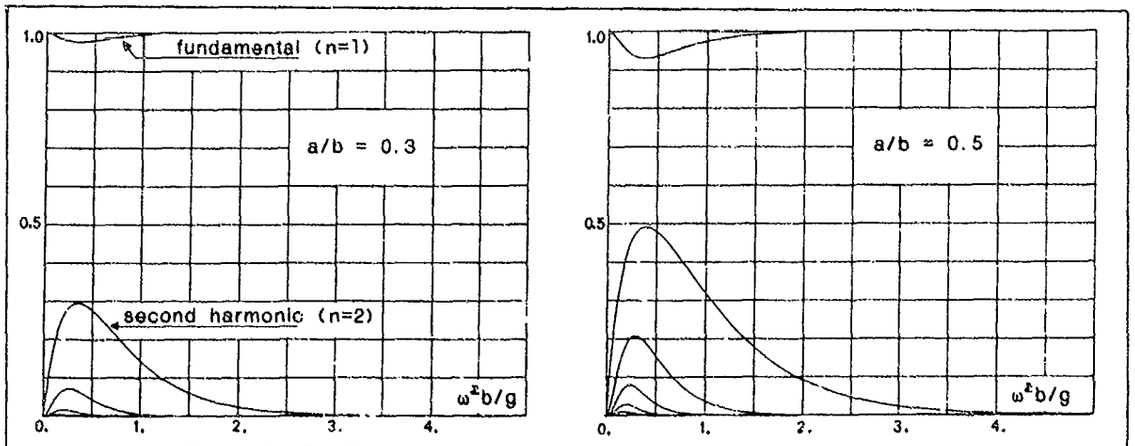

Figure 4: *Far field wave amplitude coefficients of the first rays*

N.B : The total radiated energy is set to a constant as the frequency is varied (see Figure 5)

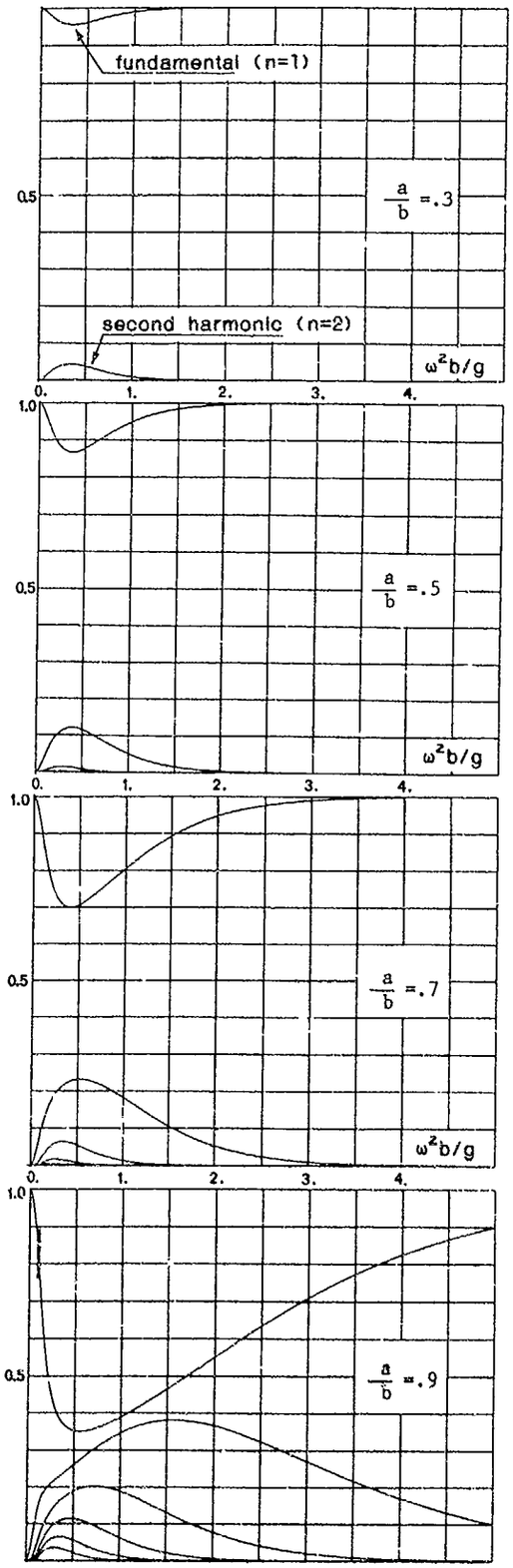

Figure 5: *rate of energy radiated by the first rays versus fundamental wave number*

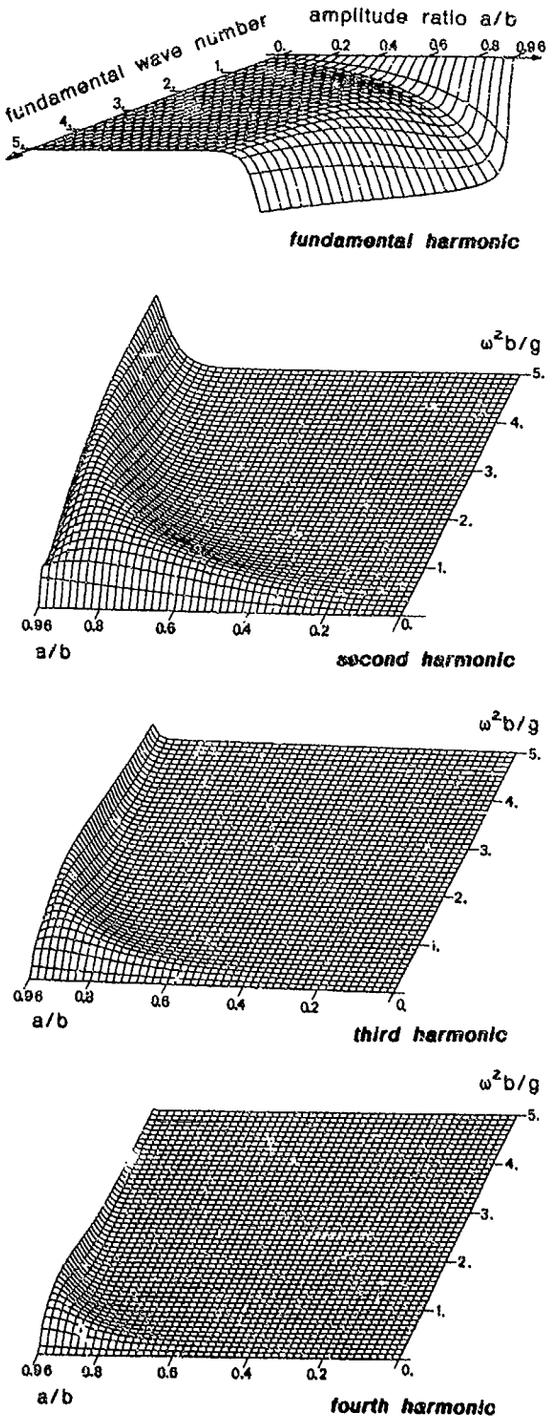

Figure 6: *rate of energy radiated by each of the first four rays as a function of a/b and* $\omega^2 b/g$.

N.B : See figure 5 for precise values on the vertical scale

6. References

T.F. OGILVIE : *"First and Second-Order Forces on a Cylinder Submerged Under a Free Surface"*. Journ. Fluid Mech., 16 (1963), pp 451-472.

C.M. LEE : *"The Second-Order Theory of Heaving Cylinders in a Free Surface"*. Journ. Ship Res., 12 (1968). pp 313-327.

R.L. POTASH : *"Second-Order Theory of Oscillating Cylinders"*. Journ. Ship Res., 15 n°4, (1971), pp 295-324.

A. PAPANIKOLAOU , H. NOWACKI : *"Second-Order Theory of Oscillating Cylinders in a Regular Steep Wave"*. 13th Symp. Nav. Hydr., TOKYO, (1980).

O.M. FALTINSEN : *"Numerical Solutions of Transient Nonlinear Free-Surface Motion Outside or Inside Moving Bodies"*. 2nd Int. Conf. Num. Ship Hydr., BERKELEY, (1977).

M. GREENHOW, T. VINJE, P. BREVIG, J. TAYLOR : *"A Theoretical and Experimental Study of the Capsize of Salter's Duck in Extreme Waves"*. Journ. Fluid Mech., 118, (1982), pp 221-239.

T. VINJE, X. MAOGANG, P. BREVIG : *" A Numerical Approach to Nonlinear Ship Motion"*. 14th Symp. Nav. Hydr., WASHINGTON, (1983).

W.M. LIN, J.N. NEWMAN, D.K. YUE : *"Nonlinear Forced Motions of Floating Bodies"*. 15th Symp. Nav. Hydr., HAMBURG, (1984).

J.V. WEHAUSEN, E. LAITONE : *"Surface Waves"*. Handbuch der Physik. Springer Verlag (1960).

J.N NEWMAN : *"Double-Precision Evaluation of the Oscillatory Source Potential"*. Journ. Ship Res. 28 n°3, pp 151-154 (1984).

M. ABRAMOWITZ, I. STEGUN : *"Handbook of Mathematical Functions"*. Dover Publications.

F. NOBLESSE : *"On The Theory of Flow of Regular Water Waves about a Body"*. M.I.T. Rep. n°80-2 (1980).

G.E. HEARN : *"Alternative Methods of Evaluating Green's Function in Three-Dimensional Ship-Wave Problems"*. Journ. Ship Res. 21 n°2, pp 89-93 (1977).

P. GUEVEL, J.C. DAUBISSE, G. DELHOMMEAU : *"Oscillations des Corps Flottants Soumis aux Actions de la Houle"*. Bulletin del'A.T.M.A. n°78, A.T.M.A., Paris (1978)

A. CLEMENT : *"Optimisation du Calcul de la Fonction de Green de la Tenue à la Mer en Profondeur Infinie"*. E.N.S.T.A. Rep. n°165 (1982)

***

CALCULATION OF FLUID MOTION RESULTING FROM LARGE-AMPLITUDE FORCED HEAVE MOTION OF A TWO-DIMENSIONAL CYLINDER IN A FREE SURFACE

John G. Telste

David W. Taylor Naval Ship Research and Development Center
Bethesda, Maryland 20084

Abstract

Progress in developing a tool to compute large-amplitude ship motions is reported. In particular, a method to calculate transient two-dimensional potential flow about a body moving in a free surface is described. The flow problem is formulated as an initial-boundary value problem in which the velocity potential along the free surface and the positions of the moving boundaries are sought as solutions of a coupled system of differential equations. An implicit finite-difference method is used to advance the solution of the coupled system of equations in time. The auxiliary problem of computing the velocity potential inside the fluid region is solved by a method which is based on boundary-fitted coordinates and is directly extensible to three-dimensional flows. Results from calculating the potential flow about a body in forced heave motion are presented. The hydrodynamic force on the body has been obtained and compared with the hydrodynamic force predicted from second-order perturbation theory.

I. INTRODUCTION

In recent years attention of naval architects and ocean engineers has focused on how vessels and offshore structures react to large-amplitude ocean waves. The attention has been motivated by the capsizing of vessels in large breaking waves and structural failure due to the slamming forces associated with such waves. It is therefore of interest to have a method available to determine the forces on a floating body and how the body will react in these extreme conditions. Since little is known of how a ship reacts even to non-breaking waves, it would even be extremely valuable to have a method available for predicting ship motions in the presence of large-amplitude non-breaking waves. The method would be of practical value in a systematic study of how ship design changes would add stability in rough seas.

Researchers have spent much effort in devising methods for computing large-amplitude ship motions. Their work is usually based on the assumptions that the fluid is incompressible and the fluid motion is irrotational. The assumptions lead to the existence of a velocity potential, which simplifies the problem formulation. But, since the equations describing the free surface are nonlinear and cannot be linearized for large-amplitude waves, great difficulties arise in the computation of solutions to free-surface potential flow problems. When a body is present in the free surface, additional difficulties related to the intersection of the free surface and the body occur. For instance, the potential flow in the region is known to be singular. Lin et. al. [1] have recently described some aspects of the singularity. Dagan and Tulin [2] and Fernandez [3] discuss nonlinearities in fluid flow about blunt bodies. Because of the formidable difficulties, most of the work on nonlinear free-surface flows has been for two-dimensional flows.

Many authors have formulated the 2-D problem as an initial-boundary value problem whose solution is obtained from an integral equation for functions defined along the boundaries of the fluid. Longuet-Higgins and Cokelet [4] used such a method combined with a time-stepping procedure to calculate free-surface heights with no body present. Faltinsen [5] and Vinje and Brevig [6-8] have used the integral-equation approach in their studies of fluid motion in the presence of bodies. They make the restrictive assumption that the fluid domain is periodic and use complex-variable techniques that cannot be extended to three-dimensional problems. Greenhow et. al. [9] have applied the method of Vinje and Brevig to the capsizing of a body in the free surface. Baker et. al. [10] have developed a generalized vortex integral-equation technique that has been used for a body under the free surface. It is not clear whether the generalized vortex method is suitable for numerical computations when a body intersects the free surface or whether it will be computationally efficient when it is extended to three dimensions. Thus, even for

computing nonlinear two-dimensional free-surface potential flows, full generality has not been attained.

This paper describes progress made in developing a tool to compute large-amplitude ship motions. The method discussed is based on an initial-boundary value formulation, and it is a method that is directly extensible to three dimensions. The velocity potential along the free surface and the positions of the moving boundaries are sought as solutions of a coupled system of differential equations. An implicit finite-difference method is used to march the solution of the coupled system of equations forward in time. The auxiliary problem of computing the velocity potential inside the fluid region is solved by a finite-difference method based on boundary-fitted coordinates. Haussling [11] has presented a review of such techniques used for fluid flow problems.

Results from calculating the potential flow about a cylinder in forced heave motion are presented. The hydrodynamic force on the body has been obtained and compared with the hydrodynamic force predicted from second-order perturbation theory.

II. MATHEMATICAL FORMULATION

The physical flow problem is to compute transient two-dimensional flow about a body moving in a free surface. It is formulated mathematically as a potential flow problem in which the velocity potential along the free surface and the position of the moving free surface are sought as the solution of a nonlinear initial-boundary value problem.

In particular, the physical problem is to determine the fluid motion caused by the prescribed movement of a body partially submerged in a fluid and the resulting hydrodynamic force on the body. The prescribed motions are forced harmonic heave motions never so large that the body becomes completely submerged in or rises out of the fluid. The body considered in this paper is a closed U-shaped cylinder. Gravity is the only body force acting on the fluid which is inviscid, incompressible, and initially at rest. The fluid motion is irrotational and thus a velocity potential ϕ' is assumed to exist. Surface tension is neglected.

All variables are nondimensionalized. Lengths are scaled by a length L characterizing the size of the body. Time is scaled by $1/\sigma$ where σ is the frequency of the body motion in radians/second. Velocities are scaled by σL; the velocity potential ϕ', by σL^2; pressure, by $\rho\sigma^2L^2$; and force, by $\rho\sigma^2L^3$. Here ρ is the fluid density. Thus, for example:

$$x' = L\,x, \qquad y' = L\,y, \qquad t' = t/\sigma,$$

$$\phi' = \phi L^2, \qquad p' = \rho\sigma^2L^2p, \qquad F' = \rho\sigma^2L^3F,$$

where (x,y) are variables representing the coordinate system, t is time, p is pressure, and F is force. The primed variables represent dimensional quantities; the nonprimed variables, nondimensional quantities.

The fluid region is described in terms of a fixed (x,y)-coordinate system chosen so that the y-axis points vertically upward and the undisturbed free surface is at y = 0 (Fig. 1).

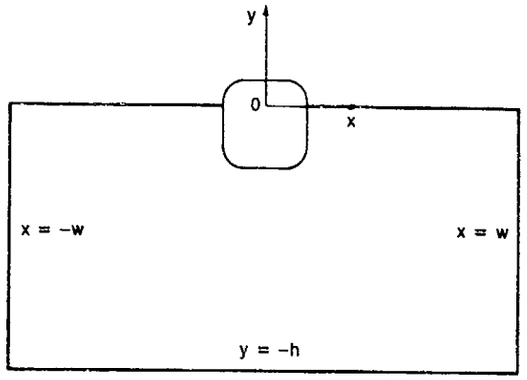

Figure 1 – U-Shaped Body in the Free Surface at Time t = 0.0

A fluid region of infinite depth and infinite lateral extent is modeled by a rectangular tank so deep that the effect of the bottom boundary is insignificant and so wide that no waves reflect from the side boundaries during the time for which the fluid motion is modeled. The rectangular tank is bounded by the lines y = -h, x = w, and x = -w. The contour of the body moving in the free surface is given as a function of time t and a parameter, a, by the equations

$$x = B_x(a,t) = A\,(\cos(a) - 0.1\cos(3\,a)) \qquad (1a)$$

$$y = B_y(a,t) = A\,(\sin(a) + 0.1\sin(3\,a)) - h_0\cos(t) \qquad (1b)$$

where A is a measure of the size of the body, a is the angle measured counterclockwise from the direction of the positive x-axis (Fig. 2), and h_0 is the amplitude of the heave motion. The position of the free surface is given in terms of a parameter e and the time t by $x = x_F(e,t)$ and $y = y_F(e,t)$. The functions $x_F(e,t)$ and $y_F(e,t)$ are to be calculated.

Since the flows considered in this paper are symmetric about the y-axis, only the half of the fluid region where $x \geq 0$ is considered (Fig. 3). The region is bounded by five curves. Across the boundaries AE (x = 0), CD (x = w), and ED (y = -h) there is no flow.

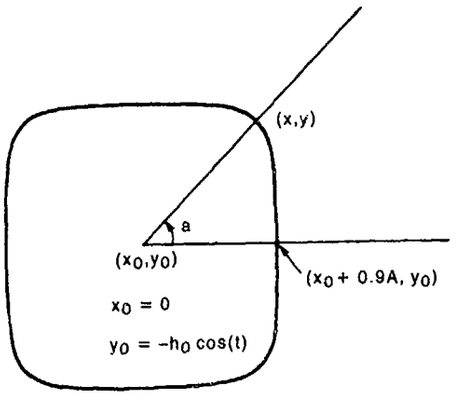

$$x = x_0 + A[\cos(a) - 0.1\cos(3a)]$$

$$y = y_0 + A[\sin(a) + 0.1\sin(3a)]$$

Figure 2 - Geometric Description of the Moving Body Contour

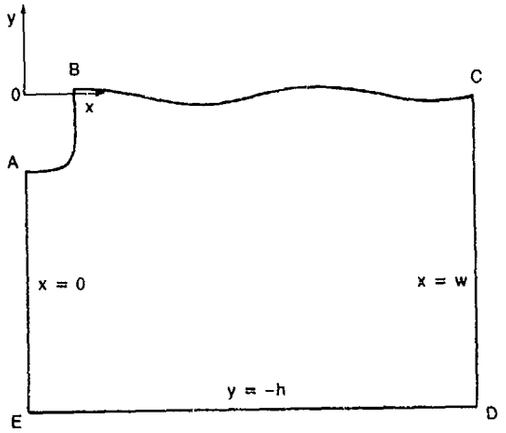

Figure 3 - Fluid Region for Flow Symmetric About the y-Axis

The curved line AB, given by Equations (1a,b), is the contour of the moving body. BC is the free surface, whose location must be computed.

The velocity potential satisfies the Laplace equation

$$\Delta\phi = 0 \qquad (2)$$

in the fluid region and is subject to certain boundary conditions. (Fluid velocity in the x-direction is given by $u = \phi_x$; fluid velocity in the y-direction, by $v = \phi_y$.) At a solid boundary, the normal velocity of the fluid must equal the normal velocity of the solid boundary since fluid cannot penetrate the boundary and no cavities are assumed to form in the fluid. In particular, at stationary boundaries the normal velocity must vanish. At the right vertical boundary of the flow domain, about 16 half-beams away from the body, this condition is given by

$$\phi_x = 0 \text{ at } x = w \qquad (3)$$

Similarly, at the bottom boundary, about six half-beams below the free surface, vanishing normal velocity is specified by the equation

$$\phi_y = 0 \text{ at } y = -h \qquad (4)$$

At the boundary AE directly beneath the body, where a symmetry condition is specified as a wall condition, the velocity potential must satisfy the equation

$$\phi_x = 0 \text{ at } x = 0 \qquad (5)$$

Along the body contour, the normal velocity is known from the prescribed motion of the body. In fact, the normal velocity of the body at $(B_x(a,t),B_y(a,t))$ is

$$v_n(a,t) = n_x\,\partial B_x/\partial t + n_y\,\partial B_y/\partial t$$

where $\vec{n}(a,t) = (n_x,n_y)$ is the unit normal directed into the fluid given by

$$(n_x,n_y) = (\partial B_y/\partial a, -\partial B_x/\partial a) / [(\partial B_x/\partial a)^2 + (\partial B_y/\partial a)^2]^{1/2}$$

The required boundary condition for ϕ at $(B_x(a,t),B_y(a,t))$ on the body contour is thus

$$\frac{\partial\phi}{\partial n} = \phi_x n_x + \phi_y n_y = \frac{\partial B_x}{\partial t} n_x + \frac{\partial B_y}{\partial t} n_y \qquad (6)$$

The free-surface coordinates $x_F(e,t)$ and $y_F(e,t)$ have been parameterized in terms of e. The parameterization e is chosen such that for fixed e the functions $x_F(e,t)$ and $y_F(e,t)$ describe the path of a fluid particle. In other words, e is a Lagrangian variable. The velocity potential on the free surface is also parameterized in terms of the Lagrangian variable e by $\phi = \phi_F(e,t)$. An equation to be satisfied by $\phi_F(e,t)$ can be obtained from Bernoulli's equation, which can be expressed as

$$p + \frac{\partial\phi}{\partial t} + (\phi_x^2 + \phi_y^2)/2 + (g/\sigma^2 L)\,y = 0 \qquad (7)$$

where p is pressure, g is the acceleration of gravity, σ is the frequency of the forced harmonic heaving, and L is the characteristic length. Bernoulli's equation is valid on the free surface and throughout the fluid region. At the free surface, the pressure is assumed to be zero and a particular case of Bernoulli's equation, the dynamic free-surface boundary condition, results:

$$\frac{d\phi_F}{dt}(e,t) = \frac{D\phi}{Dt}(x_F(e,t),y_F(e,t),t)$$

$$= (\phi_x^2 + \phi_y^2)/2 - (g/\sigma^2 L)\, y_F(e,t) \quad (8)$$

Here $D/Dt = \phi_x \partial/\partial x + \phi_y \partial/\partial y + \partial/\partial t$ is the derivative following the motion of a fluid particle. The kinematic free-surface boundary condition, which states that no fluid particle on the free surface can leave the free surface, is expressed by the two equations

$$\frac{dx_F}{dt}(e,t) = \frac{Dx}{Dt}(x_F(e,t),y_F(e,t),t)$$

$$= \phi_x(x_F(e,t),y_F(e,t),t) \quad (9)$$

$$\frac{dy_F}{dt}(e,t) = \frac{Dy}{Dt}(x_F(e,t),y_F(e,t),t)$$

$$= \phi_y(x_F(e,t),y_F(e,t),t) \quad (10)$$

At $t = 0$, the velocity potential on the free surface is given by

$$\phi_F(e,t=0) = 0 \quad (11)$$

and the free surface is such that

$$y_F(e,t=0) = 0 \quad (12)$$

The parameter e and the function $x_F(e,t)$ can be arranged so that

$$x_F(e,t=0) = e \quad (13)$$

It is convenient to parameterize the fluid at the body contour by a Lagrangian variable e so that $x = x_B(e,t)$ and $y = y_B(e,t)$ along this boundary. This is possible since fluid particles along the solid boundary can never leave that boundary, except possibly to become free-surface particles at the intersection of the body and the free surface. Thus

$$\frac{dx_B}{dt}(e,t) = \frac{Dx}{Dt}(x_B(e,t),y_B(e,t),t)$$

$$= \phi_x(x_B(e,t),y_B(e,t),t) \quad (14)$$

$$\frac{dy_B}{dt}(e,t) = \frac{Dy}{Dt}(x_B(e,t),y_B(e,t),t)$$

$$= \phi_y(x_B(e,t),y_B(e,t),t) \quad (15)$$

subject to the initial conditions

$$x_B(e,0) = B_x(a(e),0) \quad (16)$$

$$y_B(e,0) = B_y(a(e),0) \quad (17)$$

where a(e) is a prescribed function.

In summary, we seek the solution of an initial-boundary value problem for $x = x_F(e,t)$, $y = y_F(e,t)$, $\phi = \phi_F(e,t)$ on the free surface and $x = x_B(e,t)$ $y = y_B(e,t)$ on the body contour, in which e is a Lagrangian variable that parameterizes the free surface and the body contour. These five functions obey the evolution Equations (8), (9), (10), (14), and (15) subject to the initial conditions (11), (12), (13), (16), and (17). The velocity potential in these equations must satisfy Equation (2) subject to the Neumann boundary conditions (3), (4), (5), and (6) and a Dirichlet boundary condition along the free surface governed by Equation (8).

The force on the body is calculated by integrating the pressure over the wetted surface of the body. Because the flow problem is symmetric about $x = 0$, the x-component of the force on the body vanishes:

$$F_x = 0 \quad (18)$$

The y-component of the force, positive upward, is given by

$$F_y = -2 \int p(a,t)\, n_y(a,t)\, (ds/da)\, da \quad (19)$$

where (n_x,n_y) is the unit normal at the body contour directed into the fluid and s, increasing in the counterclockwise direction along the body, represents arclength. Because of symmetry, the pressure is integrated over the half the wetted length of the body given by $x = B_x(a,t)$ and $y = B_y(a,t)$ where $-\pi/2 < a < a_R(t)$. (The function $a_R(t)$ depends on the position of the intersection of the free surface and the body contour.)

III. NUMERICAL SCHEME

The functions $x_F(e,t)$, $y_F(e,t)$, $\phi_F(e,t)$ along the free surface and $x_B(e,t)$, $y_B(e,t)$ along the body contour obey five coupled first order differential equations in time with specified initial conditions. In addition, the velocity potential must satisfy specified boundary conditions at all times. To solve these equations a finite-difference method is used.

Boundary Functions

Each of the five boundary functions is discretized with respect to time and space using a fixed time step Δt. The discretized forms of the functions are denoted by

$$x_{Fj}^{(n)} = x_F(e_j, n\Delta t) \quad (20a)$$

$$y_{Fj}^{(n)} = y_F(e_j, n\Delta t) \tag{20b}$$

$$\phi_{Fj}^{(n)} = \phi_F(e_j, n\Delta t) \tag{20c}$$

for $j = 1, \ldots, N$, and

$$x_{Bk}^{(n)} = x_B(e_k, n\Delta t) \tag{20d}$$

$$y_{Bk}^{(n)} = y_B(e_k, n\Delta t) \tag{20e}$$

for $k = 1, \ldots, M$. (The subscript j will be used for a free surface variable and the subscript k for a variable along the body contour.) Thus, the boundary functions are discretized into boundary grid points that are now assumed to move as if they were associated with fluid particles. The evolution Equations (8), (9), (10) for $\phi_F(e,t)$, $x_F(e,t)$, $y_F(e,t)$ and the evolution Equations (14), (15) for $x_B(e,t)$, $y_B(e,t)$ are applicable to these particles and are replaced by finite difference equations based on the Euler-modified method. The finite-difference equations are given by

$$x_{Fj}^{(n+1)} = x_{Fj}^{(n)} + \Delta t \{\phi_{xj}^{(n)} + \phi_{xj}^{(n+1)}\}/2 \tag{21a}$$

$$y_{Fj}^{(n+1)} = y_{Fj}^{(n)} + \Delta t \{\phi_{yj}^{(n)} + \phi_{yj}^{(n+1)}\}/2 \tag{21b}$$

$$\phi_{Fj}^{(n+1)} = \phi_{Fj}^{(n)} + \Delta t \{(\phi_{xj}^{(n)\,2} + \phi_{yj}^{(n)\,2} + \phi_{xj}^{(n+1)\,2} + \phi_{yj}^{(n+1)\,2})/2 - (g/L\sigma^2)(y_{Fj}^{(n)} + y_{Fj}^{(n+1)})\}/2 \tag{21c}$$

$$x_{Bk}^{(n+1)} = x_{Bk}^{(n)} + \Delta t \{\phi_{xk}^{(n)} + \phi_{xk}^{(n+1)}\}/2 \tag{21d}$$

$$y_{Bk}^{(n+1)} = y_{Bk}^{(n)} + \Delta t \{\phi_{yk}^{(n)} + \phi_{yk}^{(n+1)}\}/2 \tag{21e}$$

where

$$\phi_{x\ell}^{(m)} = \phi_x(x_{G\ell}^{(m)}, y_{G\ell}^{(m)}, m\Delta t)$$

$$\phi_{y\ell}^{(m)} = \phi_y(x_{G\ell}^{(m)}, y_{G\ell}^{(m)}, m\Delta t)$$

for $\ell = j$ or k, $m = n$ or $n+1$, and $G = B$ or F. The initial conditions become

$$x_{Fj}^{(0)} = e_j \tag{22a}$$

$$y_{Fj}^{(0)} = 0 \tag{22b}$$

$$\phi_{Fj}^{(0)} = 0 \tag{22c}$$

$$x_{Bk}^{(0)} = x_B(a(e_k), 0) \tag{22d}$$

$$y_{Bk}^{(0)} = y_B(a(e_k), 0) \tag{22e}$$

In Equations (21a-e) and Equations (22a-e), the subscript j runs over all possible free-surface grid points, and the subscript k runs over all possible body grid points. The intersection of the free surface and the body is treated as a body point obeying Equations (21d,e) subject to an initial condition given by Equations (22d,e).

The numerical scheme is implicit. An initial estimate for the five functions at the (n+1)-st time step is obtained by linearly extrapolating from two previous time steps. (For the first time step, the initial estimate is the initial condition.) The functions are corrected iteratively by using Equations (21a-e). The iterative procedure is stopped when the x- and y-values have satisfied an absolute error criterion of the form

$$|f^{(n+1,\ell)} - f^{(n+1,\ell+1)}| < \epsilon_1 \tag{23}$$

and the ϕ-values along the free surface have satisfied the relative error criterion given by

$$|1 - \phi^{(n+1,\ell)}/\phi^{(n+1,\ell+1)}| < \epsilon_2 \quad \text{whenever } |\phi^{(n+1,\ell+1)}| > \epsilon_3 \tag{24}$$

The superscripts $(n+1,\ell)$ and $(n+1,\ell+1)$ in Equations (23) and (24) refer to the ℓ-th and $(\ell+1)$-st corrected solutions of the system of differential equations at time step n+1. Generally, the stopping criteria for the iterative procedure in the Euler-modified method at each time step are that the maximum absolute change in the x- and y-values on the free surface and the body is $\epsilon_1 = 0.001$ and the maximum relative change in the ϕ-values on the free surface is $\epsilon_2 = 0.001$ for ϕ-values greater in absolute value than $\epsilon_3 = 0.000001$.

Each of the five discrete evolution equations has ϕ_x or ϕ_y on the right side. In particular, to compute the right sides of Equations (21a-e), ϕ_x and ϕ_y along the moving boundaries of the fluid region must be computed from the solution of the Laplace equation for ϕ. The solution method for this equation is described in the next section.

To prevent numerical instabilities on the computed free surface from arising, a linear filtering scheme due to Shapiro [12] is used. The filtering scheme has been used successfully by Ohring and Telste [13], Haussling and Coleman [14], and several other researchers. It has been applied at fixed intervals of time, and has been especially helpful near the intersection of the free surface with the body contour.

Unless some method is used to maintain a reasonable grid spacing along the free surface and the body contour, grid points will congregate in some areas and become sparse in other areas. A method is used to keep a uniform distribution of points along the body contour and a prescribed distribution of grid points along the free surface. The prescribed free-surface distribution is such that the free-surface length between the body and the j-th free-surface grid point is a constant fraction of the total free-surface length between the body and the outer boundary. The scheme allows one to follow the movement of boundary grid points within a time step as if they were fluid particles and to shift the grid points to other fluid particles at the end of each time step. To shift the grid points, cubic spline interpolation is used to fit the arclength as a function of grid point number along the free surface and the body contour. The positions of the grid points along the free surface and the hull are shifted and the values of all pertinent functions interpolated, using the cubic splines, to their new values. The redistribution of grid points, of course, affects the initial guess for the Euler-modified method at time step n+1. However, if the shifting is done every time step and the time step is sufficiently small, the redistribution scheme has been found to proceed smoothly.

Because of numerical errors, grid points cannot be expected to remain exactly on the body as the solution of the initial-boundary value problem is advanced in time. Numerical errors arise from the redistribution scheme and from replacing the differential equations by finite difference equations. To correct for for such errors, grid points that move off the body are shifted back to the body. This is accomplished by computing the counterclockwise angle about the center of the body from the direction of the positive x-axis (Fig. 2). Every body grid point at a location slightly off the body surface at a certain value of that angle is relocated to the point on the body having the same value of that angle.

At the intersection of the free surface and the body contour difficulties arise. At this point both the free-surface boundary conditions and the boundary conditions associated with the solid boundary apply at a particular instant of time. However, the fluid particle at the intersection may move to a position on the free surface or may move to a position on the body below the surface. In other words, the intersection point may not move with the fluid. Since the free-surface and hull boundary conditions all involve time derivatives following the fluid motion, they cannot, in general, be directly applied over a time interval to predict quantities at the intersection point. Special methods for handling this point must be developed. However, for heaving motions of an almost wall-sided body, the intersection will be essentially a fluid particle. Therefore for the current study, the body Equations (14) and (15) are applied directly at this point. Inaccuracies in this approach will become apparent in the form of a deviation from zero of the pressure at the intersection point. In fact, such pressure deviations might be used in a method to more accurately follow the intersection point as would be necessary for more complicated body shapes. One such scheme has been tested but has proved to be numerically unstable.

The pressure at all the grid points along the body including the intersection is calculated from a finite-difference version of Bernoulli's equation:

$$p_k^{(n+1/2)} = (\phi_{xk}^{(n)\,2} + \phi_{yk}^{(n)\,2} + \phi_{xk}^{(n+1)\,2} + \phi_{yk}^{(n+1)\,2})/4 - (g/\sigma^2 L)(y_k^{(n+1)} + y_k^{(n)})/2 \qquad (25)$$

The pressure is the pressure at the k-th fluid particle on the body at time $t = (n+1/2)\Delta t$. The force on the body at this time is calculated by numerically integrating the pressure along the body contour. Trapezoidal quadrature is used.

Laplace Solver

To solve the Laplace equation for ϕ, a finite difference method based on boundary-fitted coordinates, due to Thompson et. al. [15], is chosen. The finite-difference method involves mapping the time-dependent fluid region onto a fixed computational region. The coordinates ξ and η in the computational region are such that they obey the Laplace equation with x and y as dependent variables:

$$\xi_{xx} + \xi_{yy} = 0 \qquad (26a)$$

$$\eta_{xx} + \eta_{yy} = 0 \qquad (26b)$$

The boundary conditions for ξ and η along a given boundary are Dirichlet if a particular mesh distribution along the boundary is prescribed. The boundary condition of one coordinate is Dirichlet and that of the other coordinate is Neumann if mesh orthogonality near a particular boundary is desired.

Since all computations are to be done in the fixed (ξ,η)-computational region, it is convenient to interchange the independent and dependent variables. When this is done, the Equations (26a,b) for ξ and η become

$$\alpha x_{\xi\xi} - 2\beta\ x_{\xi\eta} + \gamma x_{\eta\eta} = 0 \qquad (27a)$$

$$\alpha y_{\xi\xi} - 2\beta\ y_{\xi\eta} + \gamma y_{\eta\eta} = 0 \qquad (27b)$$

where

$$\alpha = x_\eta^2 + y_\eta^2 \qquad (27c)$$

$$\beta = x_\xi\ x_\eta + y_\xi\ y_\eta \qquad (27d)$$

$$\gamma = x_\xi^2 + y_\xi^2 \qquad (27e)$$

To obtain a mesh that wraps around the body and conforms to the other boundaries, the physical fluid region is divided into several subregions (Fig. 4).

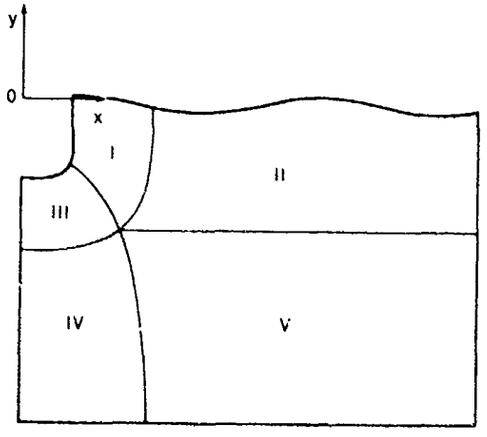

Figure 4 - Subregions into which the Fluid Region is Divided

Each subregion is mapped onto a rectangle of computational space. In each rectangle of computational space, the inverted Laplace equation is solved subject to Dirichlet boundary conditions, transformed Neumann boundary conditions, or matching boundary conditions where rectangles overlap.

The Laplace equation for the velocity potential ϕ transforms exactly as Equations (26a,b). The transformed Laplace equation is given by

$$\alpha\phi_{\xi\xi} - 2\beta\phi_{\xi\eta} + \gamma\phi_{\eta\eta} = 0 \qquad (27f)$$

where α, β, γ are defined by Equations (27c-e).

Wherever possible, central differencing is used to discretize Equations (27a-f). At the boundaries of the fluid region where a Neumann boundary condition is specified, second-order one-sided finite differences replace some of the derivatives in Equations (27a-f). (See Coleman and Haussling [16] for more details.) The resulting system of quasi-linear equations for x, y, and ϕ at the grid points is solved by successive overrelaxation.

Lin et. al. [1] cite the works of various researchers who show that a logarithmic singularity exists in the velocity potential of free-surface potential flow near the intersection of the free surface with a vertical wavemaker in horizontal motion. But, since the body contour for the problem considered is nearly vertical at the intersection with the free surface and since the horizontal velocity component of the body is zero, the logarithmic singularity in the velocity potential may be relatively weak. Thus special numerical treatment of the singularity may not be critical. In fact, nothing special has been included in the numerical method to accommodate such a singularity if it should arise.

IV. RESULTS

Several forced harmonic heave motions of the U-shaped body in the free surface have been considered. The shape of the body has been fixed by setting the parameter A in Equations (1a,b) to 0.7407 in all cases. With A set to this value, the half-beam of the body and the draft of the body are both 0.6667. Amplitudes considered were $h_0/b = 0.05$, 0.3 and 0.4, in which h_0 is the amplitude of the motion and b is the half-beam of the body. Most researchers consider values of the frequency parameter $b\sigma^2/g$ that lie between 0.0 and 2.0. In this study the frequency parameter is restricted to lie in the interval from 1.5 to 2.0 since this interval contains the frequencies for which nonlinear effects are greater.

Linear theory for the problem of an oscillating body in a fluid of infinite depth and lateral extent predicts that the wavelength far from the body will approach

$$\lambda/L = 2\pi\ g/L\sigma^2 = 2\pi\ (b/L)\ g/b\sigma^2$$

asymptotically in time [17]. The dimensions of the rectangular tank are taken to be about one such wavelength deep and four wavelengths in half-length. Thus, if the frequency parameter $b\sigma^2/g$ is no smaller than 1, the depth h should be about 4 and the length should be about 16. This region is long enough that no waves will reach the side boundary during the first few periods of forced motion. Since the region is more than half a wavelength deep, the effects of finite depth can be ignored.

The fluid region has been divided into five time-dependent subregions. Each subregion has been mapped onto a fixed rectangle of

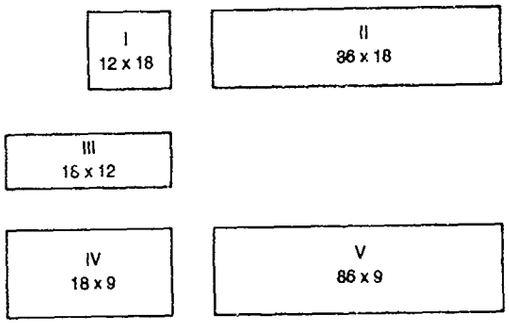

Figure 5 - Mesh Size in Each Subregion of the Computational Region

computational space (Figs. 4, 5). The size of the mesh in each of these subregions has been depicted in Figure 5. A total of 2916 grid points, counting twice those points where two subregions overlap, has been used for the grids that cover the computational and fluid regions. There are 34 equally spaced grid points on the half-body contour. At the far right vertical boundary, at the bottom horizontal boundary, and at the vertical boundary below the body, grid points position themselves in a way that makes the mesh near these boundaries orthogonal. At the far right boundary there are 25 grid points; at the bottom boundary, 102 grid points; on the vertical boundary directly beneath the body, where a symmetry condition is specified as a wall condition, 18 points. The initial distribution of grid points on the free surface is arranged so that the mesh near the intersection of the free surface and the body is approximately uniform in both the x- and y-directions (Fig. 6), and the mesh near the intersection of the free surface and the far right boundary is also approximately uniform in both directions.

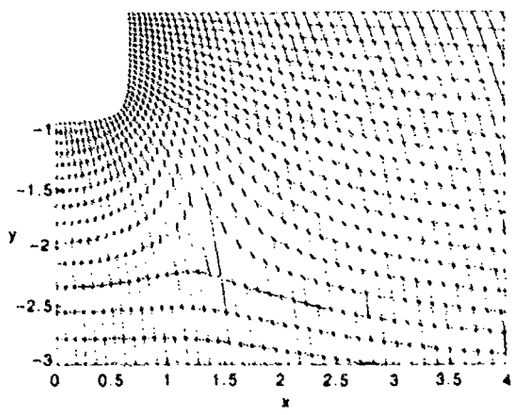

Figure 6 - Initial Mesh Near the Body

There are 90 grid points along the free surface.

The iteration for the solution to the Laplace equations for the changing mesh and for the velocity potential is done simultaneously. It is found that the mesh does not change greatly from time step to time step and hence a test for the convergence of ϕ suffices. This convergence test is that the square root of the sum of the squares of the residuals at the 34 body points should be less than 0.001. A spot check of the solution iterates indicated that the relative change in ϕ near the body was about 0.1 percent when the criterion was satisfied.

For the solution of the Laplace equations, an overrelaxation factor of 1.4 was chosen for grid points inside the computational region. For grid points on the body, where a Neumann boundary condition is specified, such a large relaxation factor caused instabilities in the solution process for ϕ. The instabilities first appeared in areas where the body curvature was large. No completely satisfactory explanation of the problem was found, but numerical experimentation led to the use of underrelaxation factors between 0.75 and 1.0 on the body. Such underrelaxation factors on the body eliminated the instabilities.

Figures 7-10 depict some results of computing the free-surface position during the first two periods of forced motion with the amplitude such that $h_0/b = 0.4$ and the frequency such that $b\sigma^2/g = 2$. A time step of $\Delta t = 0.02$ resolved one period of motion into about 314 time steps. Figures 7 and 8 show the free surface and the body with a fixed coordinate system. Figure 7, corresponding to times between 5.4 and 8.8, shows a rising body and a sinking free surface near the body; Figure 8, for times between 9.0 and 11.4, shows a descending body and a rising free surface. Figures 9 and 10 show similar results, but the coordinate system in these figures is fixed to the heaving body. The time-dependent details of the free surface near the body are clearer in this frame of reference. Figure 9 shows a rising body between the times 6.2 and 9.0; Figure 10, a descending body between the times 9.2 and 12.2. It is interesting to note that the slope of the free surface near the body is largest at about the time the body has attained its maximum height. Results for computing the vertical force on the heaving U-shaped body are depicted in Figure 11. From the figure it is seen that the force has become periodic in less than one period of forced motion. Also shown on the figure is a curve of the force vs. time predicted from the second-order theory of Papanikolaou and Nowacki [18]. The other curve is a linear magnification of the results from calculating the force when the amplitude of motion is eight times smaller ($h_0/b = 0.05$) but the frequency of the motion is the same. Qualitative agreement among the curves appears to be good. The deviation between the computed nonlinear force and either the linear or the second-order force represents aspects of force which could not be predicted from linear or second-order theory.

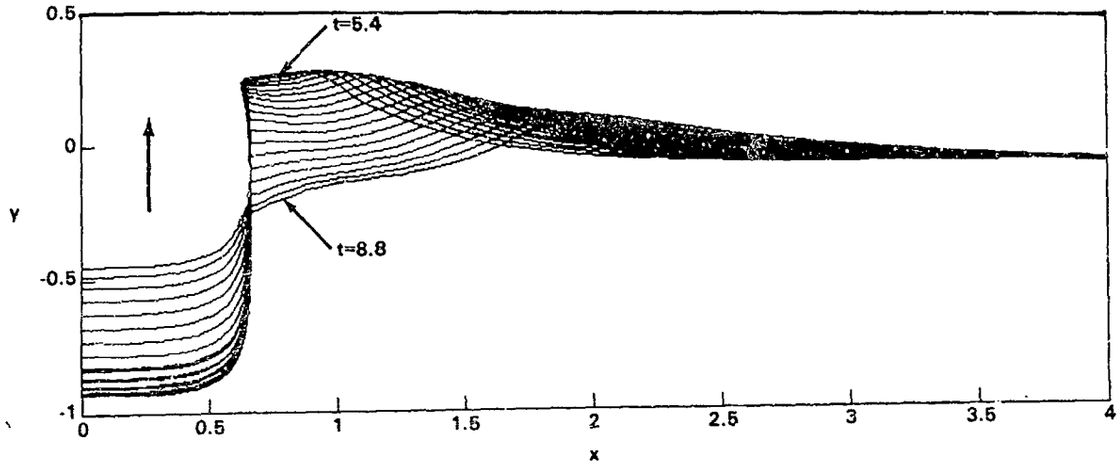

Figure 7 - Free-Surface Elevations Near Body for t = 5.4, 5.6, . . . , 8.8

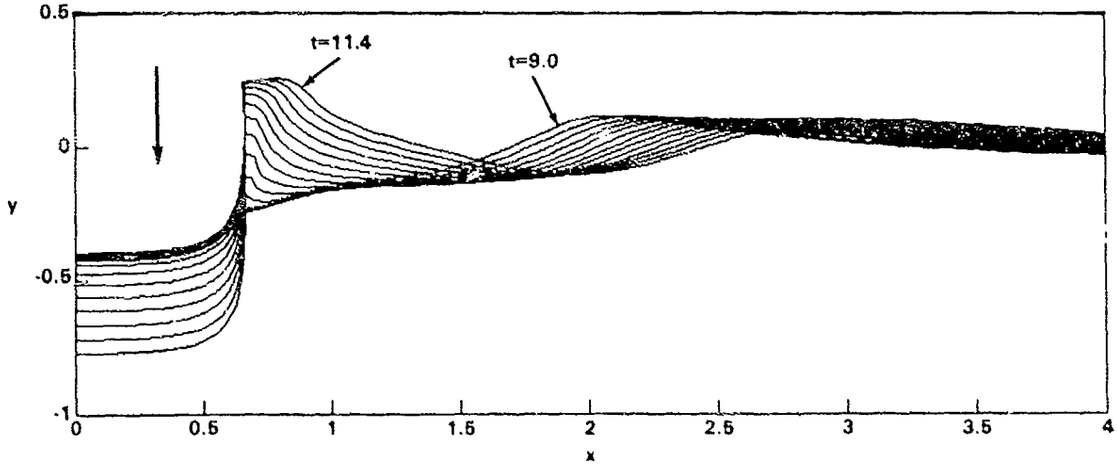

Figure 8 - Free-Surface Elevations Near Body for t = 9.0, 9.2, . . . , 11.4

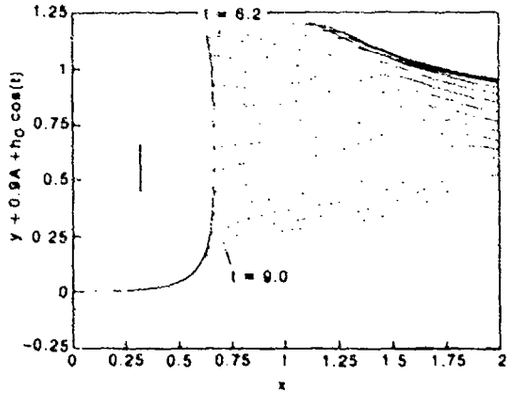

Figure 9 - Free-Surface Positions in a Frame of Reference Fixed to the Body for t = 6.2, 6.4, . . . , 9.0

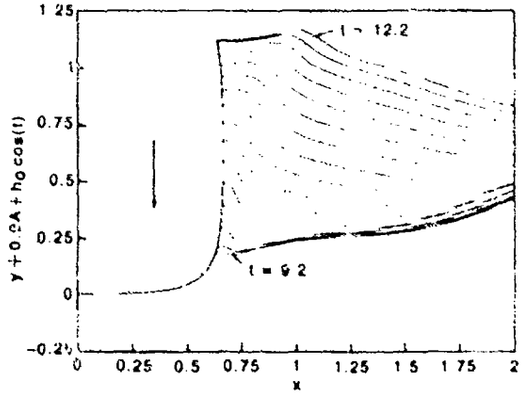

Figure 10 - Free-Surface Positions in a Frame of Reference Fixed to the Body for t = 9.2, 9.4, . . . , 12.2

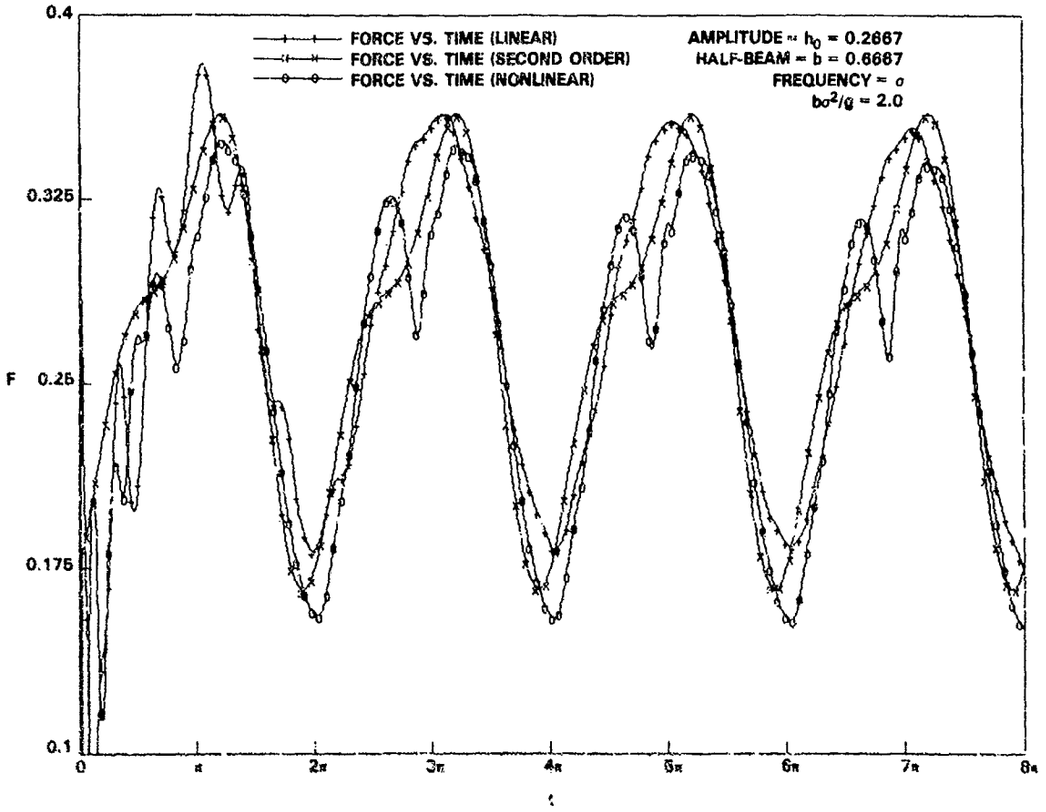

Figure 11 - Comparison of Computed Nonlinear Force with Linear Force and with Second-Order Force as Functions of Time t

Another comparison of the computed force with the force predicted by second-order theory is obtained from a Fourier analysis of the curve of force vs. time for the last period of forced motion. According to second-order theory, the total dimensional force on the body when its center (x_0,y_0) oscillates vertically according to the formula $y_0 = h_0\sin(\sigma t)$ is given by

$$F = 2\rho g A\ (.9\pi/4)$$

$$+ 2\rho g b^2 \epsilon F_1 \sin(\sigma t + \delta_1)$$

$$+ 2\rho g b^2 \epsilon^2 F_{20}$$

$$+ 2\rho g b^2 \epsilon^2 F_{21} \sin(2\sigma t + \delta_2) \quad (28)$$

where $\epsilon = h_0/b$ is the perturbation parameter. The first term represents the hydrostatic force on the body at its neutral water position. The second term represents the first-order force on the body, and the last two terms represent second-order modifications to the first-order force on the body. A Fourier analysis of the computed nonlinear force vs. time curve will produce coefficients of the Fourier expansion in the orthogonal functions $\{1,\sin(nt),\cos(nt)\}$. The coefficients are obtained from the usual integrals by numerical integration. In the case of the computed nonlinear force, the center of the body (x_0,y_0) oscillates vertically according to the formula $y_0 = h_0\cos(\sigma t)$ instead of $y_0 = h_0\sin(\sigma t)$. After considering this difference, the nonlinear results can be used to arrive at the five parameters describing the force in Equation (28). The procedure, of course, assumes that the contribution to the force from third-order effects is insignificant. Table 1 shows how the computed results compare with those of Lee [17], and Papanikolaou and Nowacki [18]. The computed results seem to be good except for the second-order amplitude F_{21}. The discrepancy in the second-order force amplitude is probably due to insufficient accuracy in the computed nonlinear force. Since first-order contributions to the force are dominant, the relative accuracy of the remaining force when the first-order predictions are subtracted is small. The error is compounded since values calculated from the remainder are divided by the square of the perturbation parameter, a small number, to get

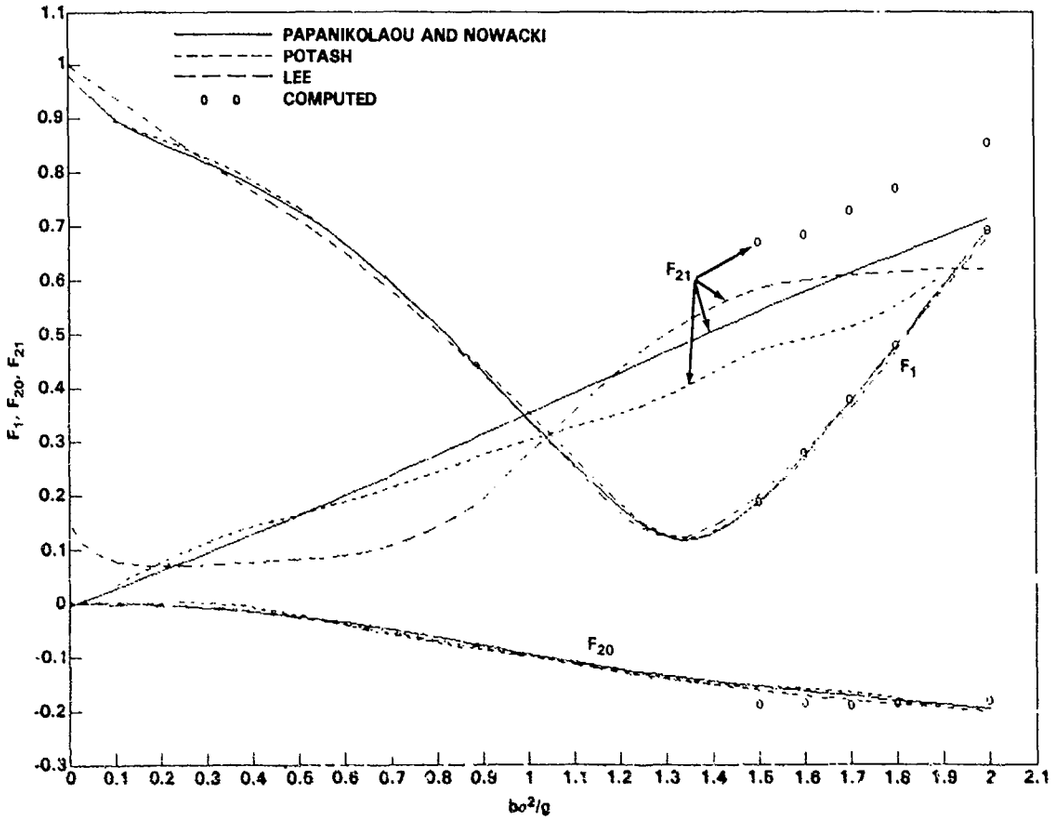

Figure 12 - First- and Second-Order Forces Versus Frequency Number for U-Shaped Cylinder

F_{20} and F_{21}. The computed second-order phase angle is, however, excellent.

TABLE 1. FIRST- AND SECOND-ORDER FORCE COEFFICIENTS

	Lee	Papanikolaou and Nowacki	Computed Nonlinear Results
F_1	0.69	0.68	0.67
ϕ_1	350°	357°	357°
F_{20}	-0.2	-0.19	-0.23
F_{21}	0.62	0.68	0.82
ϕ_2	5°	107°	108°

A rough estimate of the accuracy of the force computations can be obtained from two sets of computations in which only the time step is different. One such numerical test was conducted for this problem with the frequency parameter $\omega^2 b/g = 1.7$ and the amplitude of the motion such that $h_0/b = 0.3$. The two time steps used were $\Delta t = 0.02$ and $\Delta t = 0.01$. After about $t = 2$, the average difference in the computed force was less than one percent. Thus the error seems to be quite small.

Various frequencies of forced motion have been considered for the amplitude corresponding to $h_0/b = 0.3$. Predictions of the coefficients for second-order theory were made and compared with those of Papanikolaou and Nowacki [18], Potash [19], and Lee [17]. The results are presented in Figures 12 and 13. The computed first-order coefficients agree well with the previously computed results. The computed second-order phase angle agrees well with the results of Papanikolaou and Nowacki. The magnitude of the sinkage (the third term in Equation (28)) agrees well with the previously computed results, but the magnitude of the oscillatory part of the second-order force does not agree so well. This is a reflection of the relative error in the nonlinear force when the first-order force, accounting for most of the force, has been subtracted. It is doubtful that there is more than about one digit of accuracy in the computed second-order results. To obtain these results, the fluid motion resulting from about two periods of forced harmonic oscillation was computed, and the force for the last period of the motion was decomposed into its Fourier components.

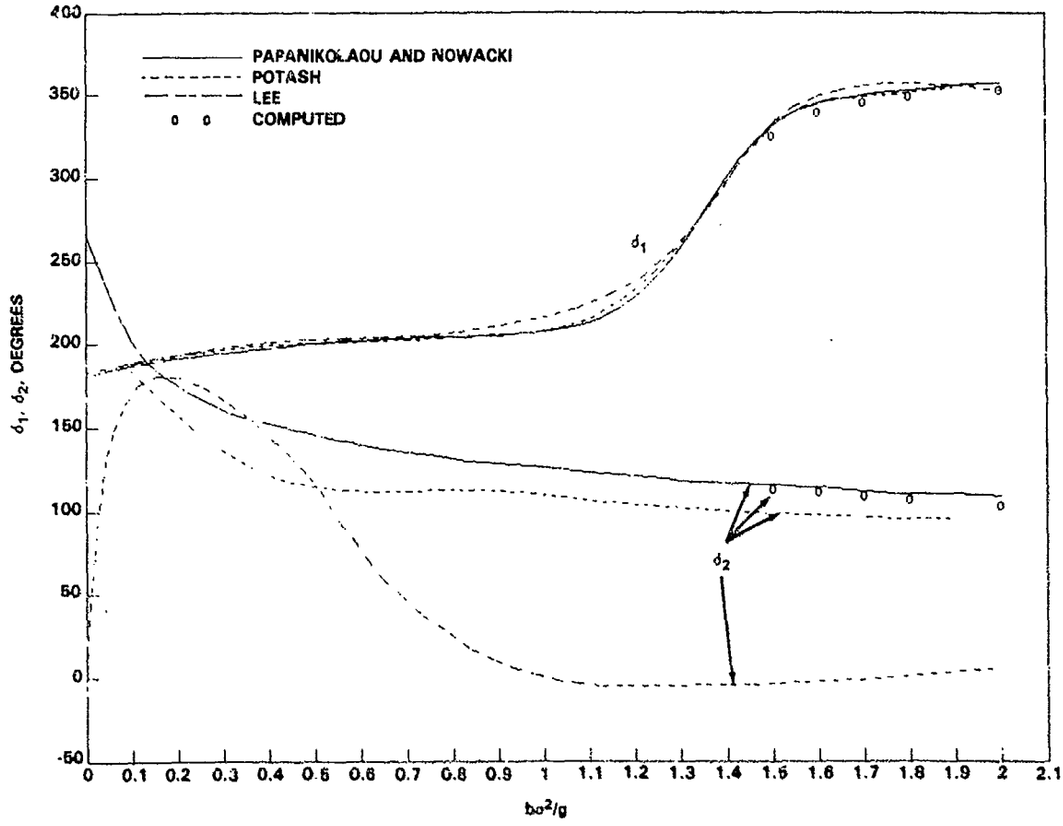

Figure 13 - Phase Angle of Forces of First- and Second-Order Versus Frequency Number for U-Shaped Cylinder

V. CONCLUSION

A computer program to compute the fluid motion resulting from forced harmonic heaving of a U-shaped body in a free surface has been produced. The program computes forces in reasonable agreement with the results of previous researchers who used second-order perturbation theory. The forces have been computed for cases of significant nonlinear fluid motion.

The computer program will be modified to handle a variety of body shapes and motions. Unlike the complex-variable techniques of Faltinsen [5] and Vinje and Brevig [6-8], the method chosen to solve the problem is extensible to the problem of 3D nonlinear ship motions. The fluid domain has not been assumed periodic, as was assumed by Vinje and Brevig [6-8]. The location of the intersection of the free surface and the body has not been found from extrapolation, as was used by Vinje and Brevig [7].

Additional research needs to be performed before this method can be applied to the general problem of ship motions in two or three dimensions. Satisfactory results have been obtained for a heaving U-shaped cylinder, but heaving wedge-shaped bodies or blunt bodies in horizontal motion in the free surface are known to have more singular fluid flow behavior. Before such behavior can be treated properly, a more sophisticated treatment of the flow near the hull/water surface intersection will be required. Such a treatment should include both the dynamic free-surface equation and the kinematic condition associated with the solid boundary of the cylinder.

VI. ACKNOWLEDGMENTS

This work was supported by the Numerical Ship Hydrodynamics Program at the David W. Taylor Naval Ship Research and Development Center. This Program is jointly sponsored by the Office of Naval Research under contract N0001484AF00001, NR-334-001 and by DTNSRDC under its Independent Research Program.

REFERENCES

[1] Lin, W.-M., J. N. Newman and D. K. Yee, "Nonlinear Forced Motions of Floating Bodies," Proceedings of the Fifteenth Symposium on Naval Hydrodynamics, Hamburg, Sept. 1984.

[2] Dagan, G. and M. P. Tulin, "Two-Dimensional Free-Surface Gravity Flow Past Blunt Bodies," Journal of Fluid Mechanics, Vol. 51, pp. 529-543 (1972).

[3] Fernandez, G., "Nonlinearity of the Three-Dimensional Flow Past a Flat Blunt Ship," Journal of Fluid Mechanics, Vol. 108, pp. 345-361 (1981).

[4] Longuet-Higgins, M. S. and E. D. Cokelet, "The Deformation of Steep Surface Waves on Water, I: A Numerical Method of Computation," Proceedings of the Royal Society of London, Series A, Vol. 350, pp. 1-26 (1976).

[5] Faltinsen, O. M., "Numerical Solutions of Transient Nonlinear Free-Surface Motion Outside or Inside Moving Bodies," Proceedings of the Second International Conference on Numerical Ship Hydrodynamics, Berkeley, Sept. 1977.

[6] Vinje, T. and P. Brevig, "Breaking Waves on Finite Water Depths: A Numerical Study," Ship Research Institute of Norway Report R-111.81, March 1981.

[7] Vinje, T. and P. Brevig, "Nonlinear, Two-Dimensional Ship Motions," Ship Research Institute of Norway Report R-112.81, March 1981.

[8] Vinje, T. and P. Brevig, "Nonlinear Ship Motion," Proceedings of the Third International Conference on Numerical Ship Hydrodynamics, Paris, June 1981.

[9] Greenhow, M., T. Vinje, P. Brevig and J. Taylor, "A Theoretical and Experimental Study of the Capsize of Salter's Duck in Extreme Waves," Journal of Fluid Mechanics, Vol. 118, pp. 259-275, 1982.

[10] Baker, G. R., D. I. Meiron and S. A. Orszag, "Applications of a Generalized Vortex method to Nonlinear Free Surface Flows," Proceedings of the Third International Conference on Numerical Ship Hydrodynamics, Paris, 1981.

[11] Haussling, H. J., "Solution of Nonlinear Water Wave Problems Using Boundary-Fitted Coordinate Systems," Numerical Grid Generation, edited by Joe F. Thompson, North-Holland, 1982.

[12] Shapiro, R., "Linear Filtering," Mathematics of Computation, Vol. 29, pp. 1094-1097, 1975.

[13] Ohring, S. and J. Telste, "Numerical Solutions of Transient Three-Dimensional Ship-Wave Problems," Proceedings of the Second International Conference on Numerical Ship Hydrodynamics, Berkeley, 1977.

[14] Haussling, H. J. and R. M. Coleman, "Finite-Difference Computations Using Boundary-Fitted Coordinates for Free-Surface Potential Flows Generated by Submerged Bodies," Proceedings of the Second International Conference on Numerical Ship Hydrodynamics, Berkeley, 1977.

[15] Thompson, J. F., F. C. Thames and C. W. Mastin, "Automatic Numerical Generation of Body-Fitted Curvilinear Coordinate System for Field Containing Any Number of Arbitrary Two-Dimensional Bodies," Journal of Computational Physics, Vol. 15, pp. 299-319, 1974.

[16] Coleman, R. M. and H. J. Haussling, "Nonlinear Waves Behind an Accelerated Transom Stern," Proceedings of the Third International Conference on Numerical Ship Hydrodynamics, Paris, 1981.

[17] Lee, C. M., "The Second-Order Theory of Heaving Cylinders in a Free Surface," Journal of Ship Research, Vol. 12, pp. 313-327, 1968.

[18] Papanikolaou, A. and H. Nowacki, "Second-Order Theory of Oscillating Cylinders in a Regular Steep Wave," Proceedings of the Thirteenth Symposium on Naval Hydrodynamics, Tokyo, 1980.

[19] Potash, R., "Second-Order Theory of Oscillating Cylinders," Journal of Ship Research, Vol. 15, pp. 295-324, 1971.

NUMERICAL SIMULATION OF NONLINEAR FREE SURFACE FLOWS GENERATED BY WEDGE ENTRY AND WAVEMAKER MOTIONS

*Martin Greenhow and **Woei-Min Lin

*Manchester, U.K.
** O.R.I., U.S.A.

Abstract

This paper makes some progress towards the study of the extreme motions of a ship in heavy weather which may result in two types of highly-transient and dangerous behaviour - capsize in beam seas and slamming. Both are essentially two-dimensional potential flow problems requiring treatment of fully nonlinear free surface and body conditions. The method, which is based upon Cauchy's integral theorem was originally proposed by Longuet-Higgins and Cokelet (1976 and 1978) to study nonlinear, time-dependent waves, especially when breaking and further developed by Vinje and Brevig (1981b) to include fixed or moving bodies. For surface piercing bodies the intersection of the free surface with the body surface causes special problems. The treatment of these intersection points used by Lin, Newman and Yue (1984) appears to be robust for the majority of flows but needs modification for some high speed slamming problems in order to include jet separation near the intersection points. Results are presented for transient motion of a wedge displaced from equilibrium and then released in calm water, and for the classical problem of wedge entry into calm water, for which the effect of gravity is important in some respects.

The study of capsize of ship-like bodies will be attempted in a "numerical wave tank" with incident waves moving towards the body being generated by a wavemaker at one end of the tank. As a first step, wave motions in the tank caused by a wavemaker performing simple-harmonic, constant forward velocity and modulated motions are compared with experiments. Excellent results have been obtained, and the study of the capsizing of floating bodies will be undertaken in the light of this experience.

1. Introduction

Over the last decade there has been considerable progress made towards understanding the nonlinear free surface effects which arise when ocean waves become steep. If the waves are assumed to be steady then analytical work (see eg Longuet-Higgins and Fox (1977) and (1978)) shows that as limiting steepness is approached many properties of the wave (eg phase speed, momentum flux, kinetic and potential energies) are no longer monotonic with steepness. Such results have relevance to the phenomena of intermittent whitecapping, which dissipates energy and promotes air-sea exchanges and pollution dispersion. Of more relevance to ocean engineers is the study of the growth of instabilities of waves of less than limiting steepness (see Longuet-Higgins (1978a) and (1978b)). These instabilities cause modulation of the wavetrain, where one crest will grow at the expense of its neighbours. When the crest is close to limiting steepness a local and very fast growing instability arises which leads directly to breaking.

Breaking itself is, of course, highly transient requiring treatment of the time-dependent free surface. Unlike the steady state case, there is no frame of reference which freezes the free surface, although local models of the overturning crest when viewed from a freely falling frame of reference have been proposed (see eg Longuet-Higgins (1980) and Greenhow (1983)). The ejected jet from the wave crest may travel at 2-3 times the phase speed of the wave and is known to give large pressures upon impact with a solid surface (see Cumberbatch (1960)).

On the numerical side there has been considerable progress in calculating a variety of 2-dimensional time-dependent free surface flows using either the point vortex method (see eg Baker, Meiron and Orszag (1982), Roberts (1982)) or the present approach based upon Cauchy's integral theorem (see Longuet-Higgins and Cokelet (1976), New (1983), Dold and Peregrine (1984) and Vinje and Brevig (1981a)). Vinje and Brevig's approach which solves a Fredholm integral equation of the second kind with variables in the physical (rather than transformed) plane, is particularly suited to ocean engineering applications since bodies may be introduced either below the free surface (see Brevig, Greenhow and Vinje (1982)),

Martin Greenhow, Department of Mathematics, University of Manchester, Manchester M13 9PL, UK.
Woei-Min Lin, O.R.I., Rockville, MD. USA.

or on the free surface (see Greenhow, Vinje, Brevig and Taylor (1982)). For this latter case a special problem arises at the intersection points of body and free surfaces, where both the velocity potential ϕ and stream function ψ are specified by the requirement that both free surface and body boundary conditions must be specified here. If, as in Lin, Newman and Yue (1984) and the present paper, we do specify both ϕ and ψ here then flows which are regular (eg a standing wave with a vertical wall through a node or antinode) are correctly treated while for flows with a singularity at the intersection point the numerical scheme approximates the local behaviour in such a way that the global solution, and hence body forces and motions, remain realistic. To understand these remarks we recap on previous work on the implusive start-up to velocity U of a wavemaker at one end of a long tank of finite depth h. By expanding the free surface displacement η and velocity potential in powers of time t, Peregrine (1972) shows that:

$$\eta = \frac{-2Ut}{\pi} \ln[\tanh(\frac{\pi x}{4h})] + O(t^2) \qquad (1)$$

for small t. We see that equation 1 predicts that close to the wavemaker (small x) the free surface elevation becomes logarithmically infinite. (For a similar singularity in steady state linear theory see particularly Kravtchenko (1954)). Experiments of Greenhow and Lin (1983) confirm expression 1 for a variety of depths and velocities U, except close to the wavemaker where a jet is ejected almost perpendicularly to the wavemaker. The numerical results described in Lin, Newman and Yue (1984) also confirm equation 1 except that the free surface displacement near the wavemaker is, of necessity, finite (see figure 5.5). Thus although locally the fluid motion is crudely resolved at the intersection point, the validity of the results away from the intersection is not significantly affected. For other types of wavemaker motion this treatment of the intersection point also appears to give realistic fluid motions (see section 5).

Similar comments apply to the transient motion of a wedge, displaced from equilibrium and then released in calm water (see section 3). In experiments with high speed entry of a wedge into calm water, a narrow jet moves quickly up the wedge side and as the wedge motion is retarded this jet leaves the wedge surface, particles in the jet tip moving almost freely under gravity. In the numerical scheme however the intersection point particle is kept on the wedge surface: this results in negative (though rather small) pressures on the wetted surface of the wedge which is clearly unphysical. A modification of the numerical scheme is described in section 4 to cope with this, but again, apart from the local behaviour of the intersection point the fluid and body motions remain realistic.

The traditional approach to capsize study is based on the static stability of the ship in calm water (see Newman (1980) pp.290-295 and the references therein). This clearly lacks justification and applicability when the ship is in big waves and where hydrodynamic forces are comparable to hydrostatic forces (see Greenhow (1985) for the forces on a half-immersed cylinder in large waves.) Recently the "Ships in Rough Seas (S.I.S)" project in Norway and the "SAFESHIP" project in the U.K. have tried to extend our understanding of ship capsize. On the theoretical side "S.I.S." resulted in the present approach, while the results of "SAFESHIP" included a study of the stability of model equations thought to describe the build-up of rolling of the ship (see Odabasi (1982)). These two approaches appear to be complimentary: for roll motion increasing over many wave cycles the present approach is not very suitable, while sudden capsizing events (against which the helmsman can take little or no action, see Dahle and Kjaerland (1980)) may be realistically calculated. As a first step in this direction section 5 presents free surface elevations generated in a "numerical wave tank" with the wavemaker performing various motions, and the results are compared with experiments. The close agreement obtained encourages further work where ship-like cross sections will be introduced into the numerical wave tank and their motions calculated.

2. Outline of the Mathematical/Numerical Formulation

Apart from the treatment of the intersection points of free and body surfaces, the method used is that of Vinje and Brevig (1981b) while for the wavemaker problem reference can be made to Lin, Newman and Yue (1984). We therefore confine ourselves to an outline of the method only. Under the usual assumptions of two-dimensional flow of an incompressible, homogeneous and irrotational fluid we have a complex velocity potential:

$$\beta(z, t) = \phi(x, y, t) + i\psi(x, y, t) \qquad (2)$$

where $z = x + iy$, ϕ is the velocity potential and ψ is the stream function. Since ϕ and ψ satisfy the Cauchy-Riemann equation β is analytic and hence Cauchy's theorem holds:

$$\oint_C \frac{\beta(z)}{z - z_0} dz = 0 \qquad (3)$$

for z_0 outside any closed contour C within the fluid. Here we take C to be the free surface, wetted body surface, the bottom and two vertical boundaries. For the wedge entry problem these vertical boundaries are distant and although periodicity is assumed here, this is irrelevant since no significant disturbance reaches these boundaries during the time of simulation. For the wavemaker and capsize

simulations, the wavemaker forms one vertical boundary, while for downwave a fixed vertical boundary is imposed. Use of equation 3, which reduces a two-dimensional problem to a one-dimensional problem, is extremely advantageous since the resolution of sharply curved free surfaces, such as occur in wave breaking or slamming, may be obtained on mainframe computers.

On the contour C we know either ϕ on the free surface (designated as C_ϕ) or ψ on the fixed or moving solid boundaries (designated as C_ψ). On the free surface ϕ is specified initially while on the body:

$$\psi(x,y,t) = U_c(y-y_c) - v_c(x-x_c) - \tfrac{1}{2}\dot{\theta}R^2 \qquad (4)$$

where (x_c, y_c) and (u_c, v_c) are the position and velocity of the centre of gravity of the body, $\dot{\theta}$ is the angular velocity and R is the radius vector from (x_c, y_c) to the point considered (x, y). A similar expression gives ψ on the wavemaker while on fixed boundaries $\psi = 0$.

Taking either real or imaginary parts of equation 3 with z_0 on C, we obtain the following Fredholm equations of the second kind:

$$\alpha\psi(x_0, y_0, t) + \mathrm{Re} \int \frac{\phi + i\psi}{z - z_0} dz = 0 \qquad (5)$$

for z_0 on C_ϕ and

$$\alpha\phi(x_0, y_0, t) + \mathrm{Re}\left(i \int \frac{\phi + i\psi}{z - z_0}\right) = 0 \qquad (6)$$

for z_0 on C_ψ. Here α is the angle between two tangents of C at z_0 (mathematically equal to π for any smooth part of C, but generally different from π numerically, especially in regions of sharp curvature.)

The principal valued contour integrals in equations 5 and 6 are not known explicitly since they include unknowns (either ϕ or ψ) at other points around the boundary. Discretising the contour into points z_k along C and assuming a linear variation of the potential along C between points gives a matrix equation for the unknowns. Explicitly we assume:

$$\beta(z) = \sum_{j=1}^{N} \Lambda_j(z)\, \beta_j \qquad (7)$$

with the linear influence function given by:

$$\Lambda_j(z) = \frac{z - z_{j+1}}{z_j - z_{j+1}} \quad \text{for } z \text{ on } C \text{ between } z_j \text{ and } z_{j+1}$$

$$= \frac{z - z_{j-1}}{z_j - z_{j-1}} \quad \text{for } z \text{ on } C \text{ between } z_{j-1} \text{ and } z_j$$

$$= 0 \quad \text{otherwise} \qquad (8)$$

Then equation 3 becomes

$$\oint_C \frac{\beta(z)}{z - z_k} dz = \sum_{j=1}^{N} \Gamma_{kj}\, \beta_j = 0 \text{ for } k = 1 \text{ to } N \qquad (9)$$

where the integrated influence function Γ_{kj} is given by simple logarithmic expressions (see Vinje and Brevig (1981b)).

Taking the real or imaginary parts of equation 9 according to equations 5 and 6 gives the required matrix equation. The contribution from the intersection points, where both ϕ and ψ are known occurs only on the right hand side of this equation.

The above procedure solves the system for the initial time. To step forward in time we apply a mixed Eulerian/Lagrangian scheme, following particles on the free surface but not on the body surface (except at the intersection points.) From Bernoulli's equation we have

$$\frac{D\phi}{Dt} = \tfrac{1}{2}ww^* - gy \qquad (10)$$

giving the new velocity potential at the new free surface position given from the velocity w^* of the particle:

$$\frac{Dz}{Dt} = w^* = u + iv = \left(\frac{\partial\beta}{\partial z}\right)^* \qquad (11)$$

Equations 10 and 11 are stepped forward in time using Runge-Kutta or Hammings's methods.

To solve for the pressures on the body points, and hence integrate to give the body forces and accelerations, requires $\partial\phi/\partial t$ on the body since

$$\frac{-p}{\rho} = \frac{\partial\phi}{\partial t} + \tfrac{1}{2}ww^* + gy \qquad (12)$$

On the free surface

$$\frac{\partial\phi}{\partial t} = -\tfrac{1}{2}ww^* - gy \qquad (13)$$

whilst on the body

$$\frac{\partial\psi}{\partial t} = u_c v - v_c u + [(u_c-u)(x-x_c) + (v_c-v)(y-y_c)].\dot{\theta} + (y-y_c)a_{x_c} - (x-x_c)a_{y_c} - \tfrac{1}{2}R^2\ddot{\theta} \qquad (14)$$

see Vinje and Brevig (1981b). Here (a_{x_c}, a_{y_c}) and $\ddot{\theta}$ are the transitional and rotational accelerations of the centre of gravity. These are unknown but may be factored out of the equations forming four separate problems:

$$\frac{\partial\psi}{\partial t} = \frac{\partial\psi_1}{\partial t} + a_{x_c}\frac{\partial\psi_2}{\partial t} + a_{y_c}\frac{\partial\psi_3}{\partial t} + \ddot{\theta}\frac{\partial\psi_4}{\partial t} \qquad (15)$$

Now Cauchy's theorem, equation 3, holds for each of the four composite problems with ϕ_1 on the free surface given by equation 13 while $\phi_2 = \phi_3 = \phi_4 = 0$ on the free surface. The full nonlinear problem is given by the superposition of these four unphysical problems, giving $\partial\psi/\partial t$ on the body. This gives a 3X3 system of equations for (a_{x_c}, a_{y_c}) and $\ddot{\theta}$, so that the body accelerations and hence motion can be obtained.

The numerical scheme appears to be remarkably stable and no explicit smoothing was used in any of the calculations. For the slamming simulations removal or introduction of points on the free surface was avoided since this generally leads to breakdown within a few time steps. Typically there was 84 points on the free surface, 60 on the body and 180 in total. This degree of accuracy required about 8 seconds per time step on a CYBER 205 used as a scalar machine, 0.[illegible] seconds per time step on a VAX 11/780.

3. Transient Motion and Entry of a Wedge in Initially Calm Water

The problem of slamming of ships in large waves is quite complex but if the wavelength is long it may be approximately correct to consider the hull entering calm water with a velocity equal to the relative velocity of the moving hull and moving free surface in the real situation. Even with this assumption the numerical simulation of bodies entering the water with small deadrise angle is difficult because of the very large velocities encountered in the splash zone. Some preliminary studies of cylinder entry (relevant to the slamming of oil rig cross members) have also encountered this difficulty, and the present study therefore concentrates on accurate simulation of the entry of a wedge of large deadrise angle which is relevant to the slamming of the bow section of some ships, but not to mid-ship slamming.

We first look at the transient motion of a wedge of half-angle $\alpha = 15°$ displaced from equilibrium and then released in calm water. For a circular cylinder, the same problem has been calculated using linearised hydrodynamic theory by Maskell and Ursell (1970) assuming that the displacement from equilibrium of the cylinder is small. With this restriction the results of Vinje and Brevig (1981b) show good agreement at least for the first cycle of oscillation after which the assumption of periodicity of the fluid domain makes comparison invalid. For large displacements from equilibrium nonlinear effects came into play: Yim (1971) and Chapman (1979) attempt to include some of these effects for a wedge by applying the body condition on the exact body position, but still retaining a linearised free surface condition. The present solution is fully nonlinear in both conditions. Figure 3.1 shows the transient motion of the fluid and wedge when the wedge, with vertex just submerged, is released into calm water. The wedge oscillates vertically about tis equilibrium position (vertex at $y = -4.6$). The free surface particle motion is also shown including that of the intersection point which moves in an almost elliptical orbit during the first cycle. Whereas the calculations here could be continued without much trouble, figure 3.2 shows that for heavier wedges (equilibrium position of vertex at $y = -9.2$), the wave travelling away from the wedge breaks. Due to poor resolution at the wave crest we cannot follow the overturning but even with better resolution the calculation would have to be discontinued within a few time steps due to re-entry of the jet ejected from the crest. Also shown is a curious numerical effect caused by poor resolution of the free surface near the intersection point, which causes the fluid to move too far up the wedge side. This effect disappears with better resolution as shown.

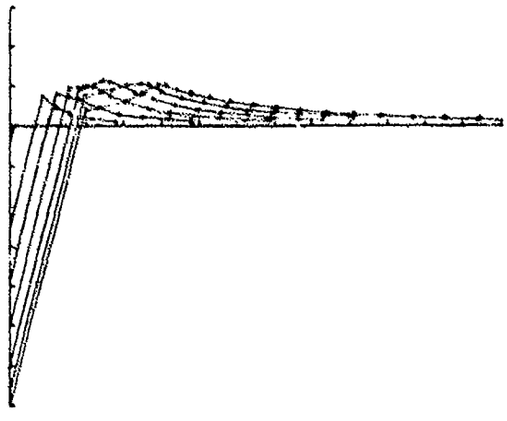

Figure 3.1a. Transient motion of a wedge moving down. Free surface particles are marked x.

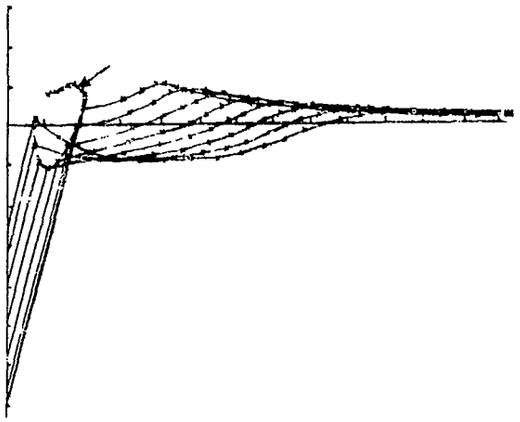

Figure 3.1b. Transient motion of a wedge moving up again. Locus of intersection point marked with the arrow.

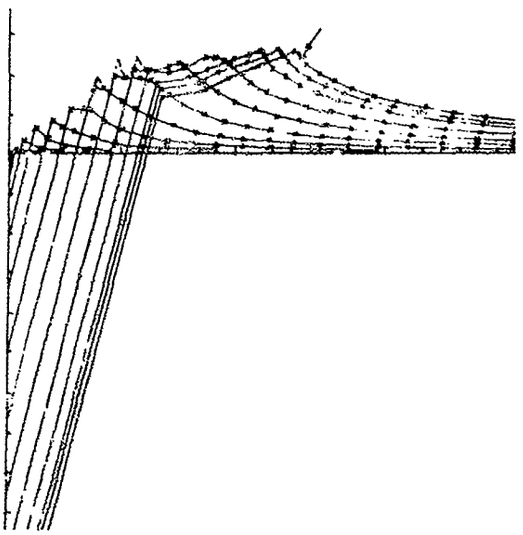

Figure 3.2. Transient motion of a wedge producing a breaking wave (arrowed). Dotted lines are from a simulation with poor resolution.

For high speed entry, or slamming, of a wedge a considerable amount of experimental work is available (see eg Chuang (1967)) while nearly all theoretical work neglects gravity, thereby allowing simpler free surface conditions. This is justified for high entry speeds since locally the fluid acceleration is much higher than gravity. Thus Wagner (1932) approximates wedges by flat plates moving with the initial entry speed in an infinite fluid. This problem has an analytic solution (by conformal mapping) and gives the pressure distribution along the wedge. Von Karman (1929), on the other hand, gives the force on the body during impact and submergence in terms of the rate of change of fluid momentum which is related to the added mass of the body in infinite fluid. More recently Doctors (1981) seeks to simulate a slamming event by a superposition of the solutions of the Cauchy-Poison problem, but this requires non-zero pressures to be applied to the free surface.

If the body velocity or acceleration is constant and gravity is ignored, then some analytical progress is possible since the flow is self-similar (see Gurevich (1965) for a discussion). For the constant velocity case Garabedian (1953) shows that the arc length between any two free surface particles, measured along the free surface, remains constant throughout the motion. Mackie (1969) gives bounds on the contact angle β between the free surface and the wedge: thus $0 < \beta \leqslant \pi/4$ and also $\beta < \pi/2 - \alpha$ which is stronger if the wedge half-angle $\alpha > \pi/4$. Johnstone and Mackie (1973) give the exact relationship between α and β and show that in some cases ($\alpha > 79°$) the free surface cannot remain convex to the fluid unless the pressure on the wetted wedge surface becomes negative. Although the present numerical scheme cannot give definitive answers concerning the relationship between α and β with gravity included, the second effect of negative pressure on the wedge has been observed for $\alpha = 15°$, see figure 3.3. This is clearly unphysical and the experiments of Greenhow and Lin (1983) show that a jet emerges from the wedge, see figure 3.4. The negtive pressure arises because the intersection point is kept on the wedge. In the early stages of entry this is correct, but when the jet rising up the wedge side becomes thin, the pressure gradient within the fluid must become very small. The intersection point particle then moves freely under gravity, but the present scheme continually moves this point back onto the wedge surface. Section 4 seeks to remedy this situation.

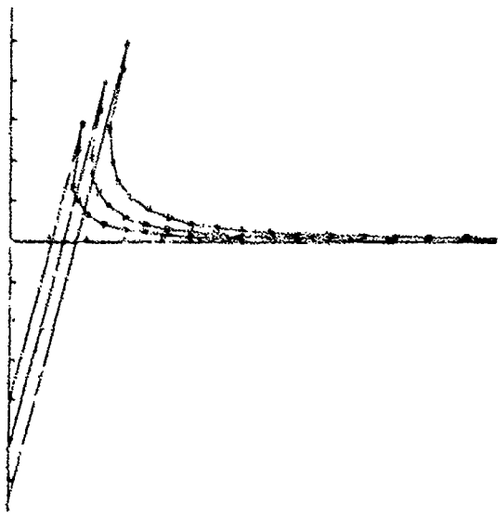

Figure 3.3a. High Speed Entry of a Wedge.

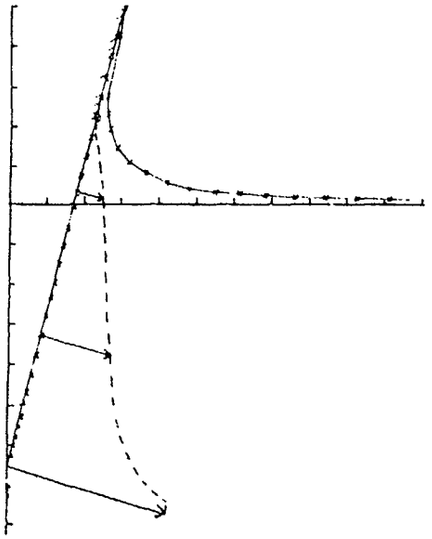

Figure 3.3b. High Speed Entry of a Wedge showing pressure distribution along the wetted surface (dotted). The region of small negative pressure is shaded.

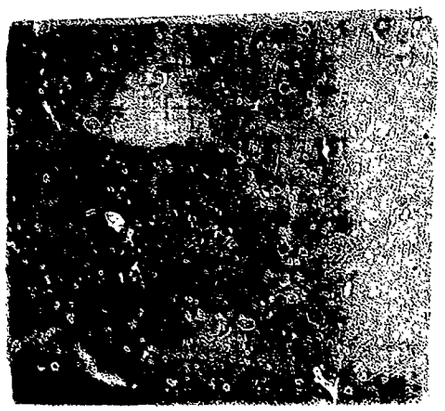

Figure 3.4. Water Entry of a Wedge (from Greenhow and Lin (1983)).

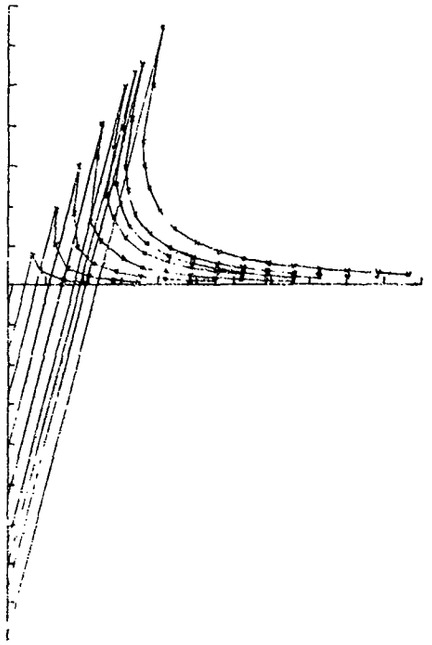

Figure 3.5a. High Constant Speed of Entry of a Wedge.

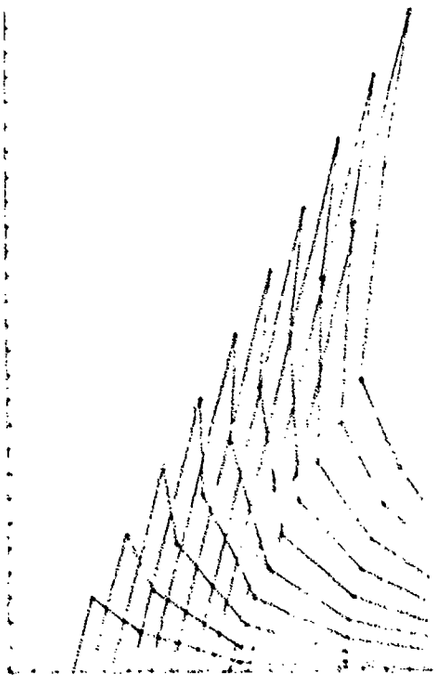

Figure 3.5b. High Constant Speed of Entry of a Wedge - close up near intersection point.

Figure 3.5 shows high constant velocity wedge entry for which gravity should be negligible and for which the constancy of arc length between any two fluid particles should hold. This is approximately true although particles near the intersection point spread out while

those away from it move closer together. The splash height predicted by the conformal mapping technique of Dobrovol'skaya (1969) appears to be too great. This could be a gravity effect, but the comparison is somewhat doubtful: in this numerical scheme the position of the intersection point is strongly dependent on the spacing between the free surface particles (although the position of the rest of the free surface is not), whilst Hughes (1972) casts doubt on Dobrovol'skaya's results.

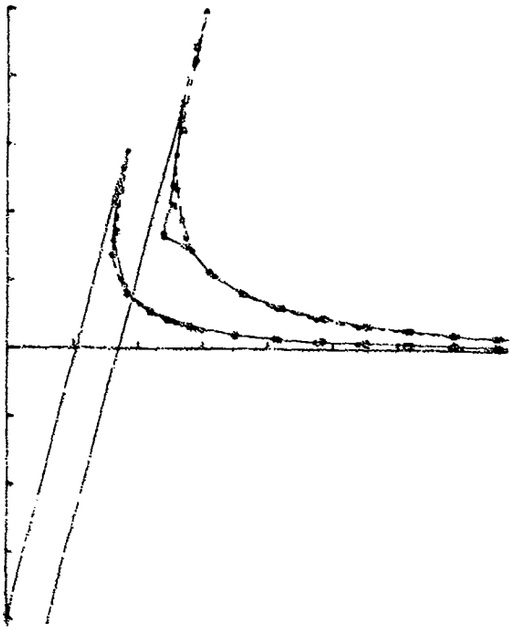

Figure 3.6. Test of self-similarity for different constant velocities of entry of a wedge. (x v=1; 0 v=2; • v = 3.)

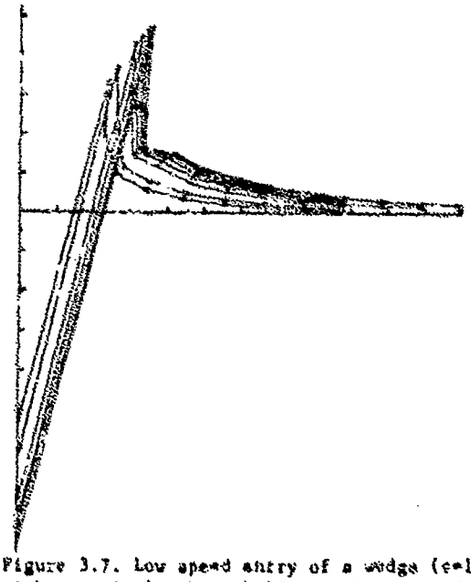

Figure 3.7. Low speed entry of a wedge (v=1) with numerical scheme holding jet onto wedge surface.

For moderate constant velocity of entry figure 3.6 shows that the assumption of self-similarity of the flow (based upon neglecting gravity) is correct in the early stages of entry only. Here we have superposed free surface profiles for wedge velocities of v = 1, 2 and 3 when the wedge has reached two different positions. For the early stages of immersion self-similarity holds quite well, with some discrepancy near the intersection point possibly due to the numerical scheme. When the wedge is well immersed self-similarity only holds for the higher speeds of entry: for moderate speed the jet which had risen up the wedge side starts to fall back into the fluid. This effect is not thought to be numerical (figure 3.7 shows its development) and it occurs later for higher wedge entry velocities. However, although it is clear that gravity plays an important role here, the flow is not entirely physical since the numerical scheme holds the jet onto the wedge resulting in negative pressure on the upper part of the wetted wedge surface. Once again this jet should be allowed to fall off the wedge surface, particles within the jet moving almost freely under gravity: the next section seeks to modify the numerical scheme to allow this to happen.

4. Modification of the Numerical Scheme to allow the jet to leave the wedge surface.

In section 3 we showed that the assumption that the jet of fluid, initially ejected up the wedge surface at large speed, remaining on the wedge is unphysical and results in negative pressures on the wetted wedge surface. Clearly in the very thin jets produced the intersection point particle must behave very much as a projectile (since the pressure gradient in the jet is very small) and thus must move away from the wedge surface in a parabola. In this section we present some preliminary results where this is allowed to happen. The program checks the pressure on the wetted wedge surface at each time step. If this becomes negative the intersection point is regarded as an ordinary free surface point, and a new intersection point is introduced where the pressure on the wetted wedge surface is zero. The velocity potential at this point is also needed and is linearly interpolated between neighbouring points. Thus we have new initial conditions for the program to restart.

The results of such a procedure are only partially successful, since the jet being long and thin, is rather poorly resolved. Consequently the position of the jet tip is unreliable and may in fact move inside the wedge envelope above the free surface. However this is not thought to affect the rest of the fluid significantly, which may be calculated reliably. Figures 4.1a and 4.3 show high and low constant speeds of wedge entry where the intersection point moves down the wetted wedge surface as the jet "peels off" from the wedge. Figure 4.1b shows the pressures on the wetted wedge surface which now remain positive everywhere.

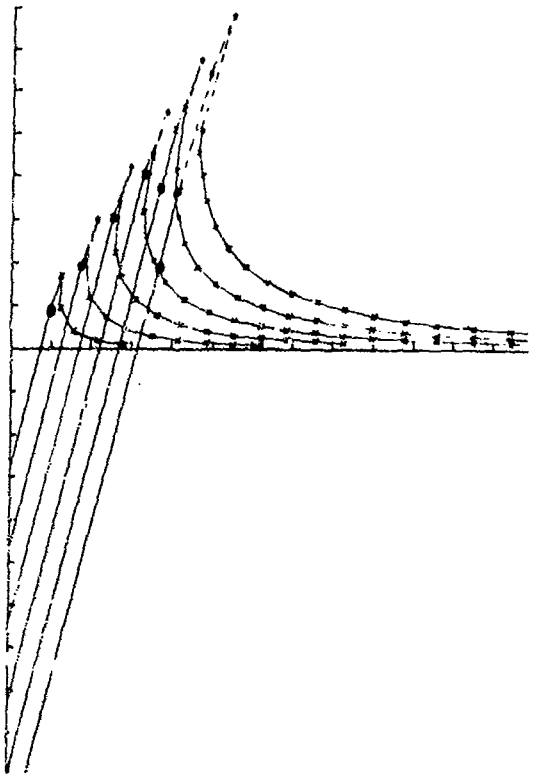

Figure 4.1a. High constant speed entry of a wedge. • indicates intersection point of wedge and free surface. The dotted lines joining points o indicate the jet assuming particles in the jet are in free flight.

To avoid the problems associated with trying to resolve the jet numerically one can assume the intersection point does indeed move off the wedge as a projectile, the velocity of projection being given by previous time steps, or by the assumption of self-similarity in the early stages of entry (which agrees closely with the numerically calculated velocity). This gives the realistic looking dotted lines on figures 4.1 and 4.2. We notice that although the jet overturns, it does not do so as much as in the experiment shown in figure 3.4. This may be due to the theory neglecting viscosity and surface tension.

Further work on this phenomenon, particularly with wedges of different angles, is needed but it is hope that the present study will provide a basis for numerical simulations of the slamming cylinders, both into calm water and in waves.

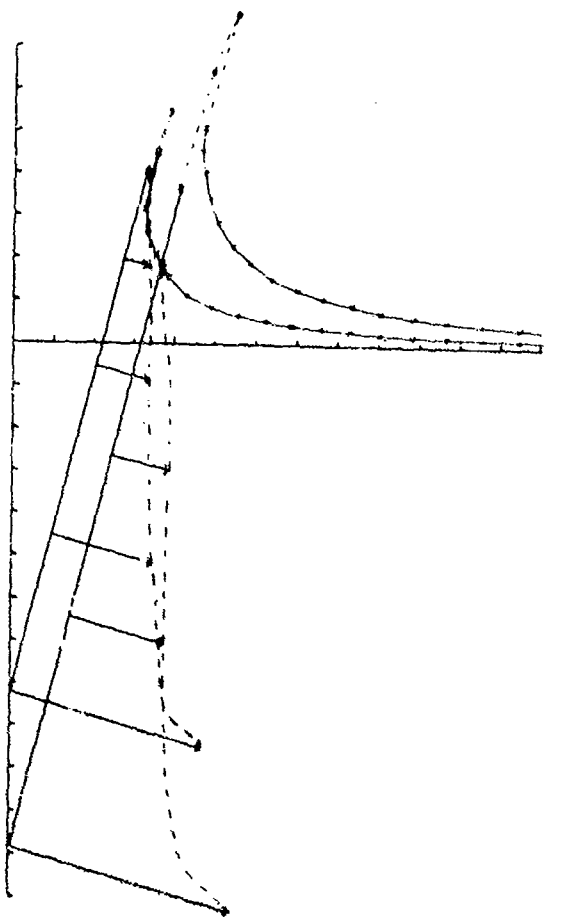

Figure 4.1b. Pressure profiles on the wetted part of the wedge surface.

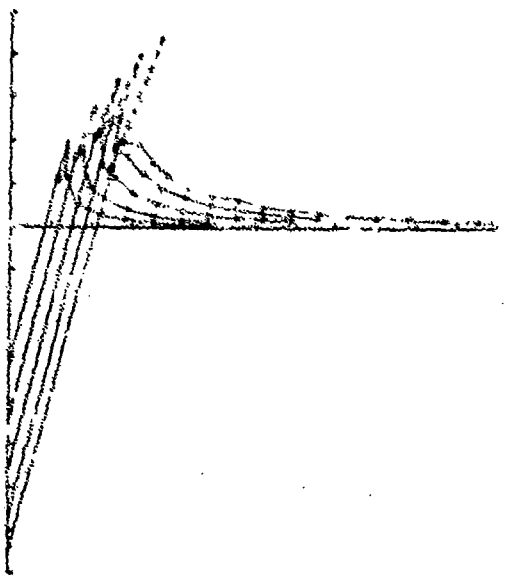

Figure 4.2. Low speed entry of a wedge. Symbols as in figure 4.1a.

5. Nonlinear Waves Generated by a Wavemaker.

As mentioned in the introduction, we now make the first step towards numerical simulation of ship capsize in beam seas. Previous theoretical and experimental work on the survival of a Salter's Duck in extreme waves by Greenhow et al (1982) shows that the present scheme is suitable for the simulation of capsizing behaviour in beam seas. In that study, however, experimental data for the locations of the intersection points of the body and free surface are required, and also the choice of initial conditions is not mathematically justified, but merely suggested by the wave profile in the experiments. The intersection point problem has already been discussed and this section seeks to overcome the problems associated with the choice of initial conditions by setting up a realistic two-dimensional "numerical wave tank" in which to place floating or fixed bodies. Waves are generated by a wavemaker at one end of the tank undergoing different types of motion - simple harmonic, constant forward velocity, and modulated motions. The numerical results are summarised and some of them are compared with experiments. This provides an essential prerequisite for the detailed study of ship capsize.

In the work of Lin (1984), Lin, Newman and Yue (1984), the present numerical scheme is used successfully to simulate the waves generated by simple-harmonic motion of the wavemaker. The numerical results are confirmed by linear wave theory when the wavemaker oscillations are small, and comparisons between the numerical calculations and the experimental measurements are given. The numerical simulation for this case can be continued in time without apparent limitation. More drastic waves can be generated when the stroke of the wavemaker is large. As shown in figure 5.1, a breaking wave is generated by the wavemaker performing cosine motion with full stroke A = 0.30 (nondimensionalised by the depth of the tank h) and frequency $\omega = 1.5539$. The free surface profiles are plotted at times t = 3.4, 3.5 ... 4.4.

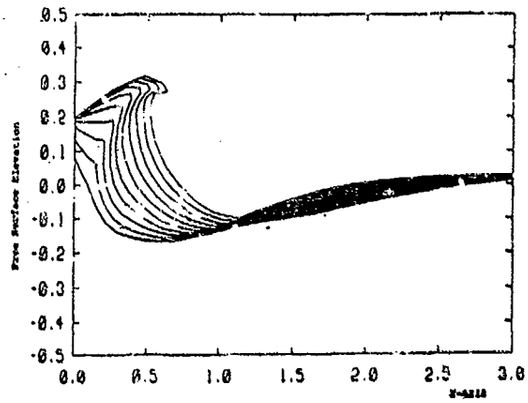

Figure 5.1. Numerical Simulation of a breaking wave. Wavemaker has cosin motion with $\omega = 1.5539$, A = 0.30, t = 3.4, 3.5, ... 4.4. (from Lin, Newman and Yue (1984).)

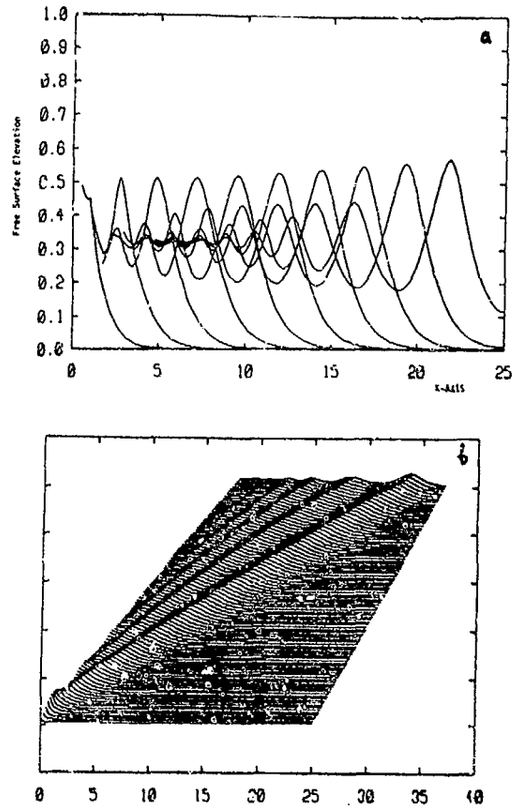

Figure 5.2. Free surface profile of an undular bore. Wavemaker has constant forward velocity U = 0.30, t = 0.2, 0.4, ...20.0.

Further study of the wavemaker problem has been conducted when the wavemaker moves with constant velocity from a state of rest. Figure 5.2a shows the development of undular bore with wavemaker velocity U = 0.40 (nondimensionalised by $\sqrt{gh}$). The leading wave is travelling steadily with an approximate velocity of 1.0 which is the maximum group velocity of the surface wave in shallow water. The evolution of the free surface profiles is plotted at every other time step (t = 0.2, 0.4, ..). For clerity each curve is shifted slightly up and to the right.

For the wavemaker with a higher velocity the leading wave may break. Figure 5.3 shows free surface profiles t = 0.5, 1.0 ... 5.0 with wavemaker velocity U = 0.90 in which case the large wave steepness causes breaking. The numerical scheme breaks down a few steps after the last curve plotted because the free surface intersects itself.

As shown in figure 5.4, it has been found that the mean water level of the undular bore above the original free surface is proportional to the nondimensional forward velocity of the wavemaker. The transition from a nonbreaking undular bore to a breaking wave occurs when U is about 0.35, and the corresponding mean water level is about 30% higher than the original

water depth. This transition is similar to that which occurs when a uniform flow meets an area of still water in a long horizontal channel. The theoretical study by Peregrine (1966) and the experimental measurements by Favre (1935) and Binnie and Orkney (1955), indicate that undular bores form when the ratio of the change in water level to the initial depth of water is less than 0.28. If this ratio is greater than 0.28 but less than 0.75 there are still undulations but the first one at least is breaking. For greater differences in depth there is no undulation.

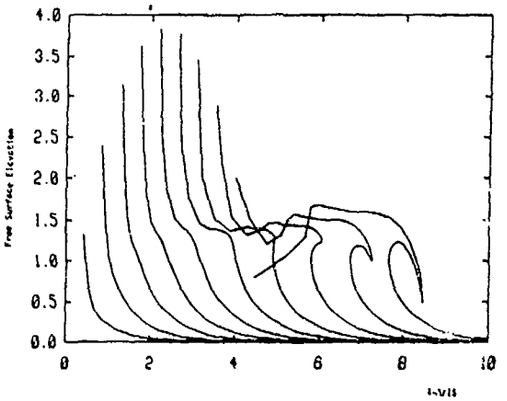

Figure 5.3. Numerical calculation of a breaking wave. Wavemaker has constant forward velocity with U = 0.90, t = 0.5, 1.0, ..., 5.0.

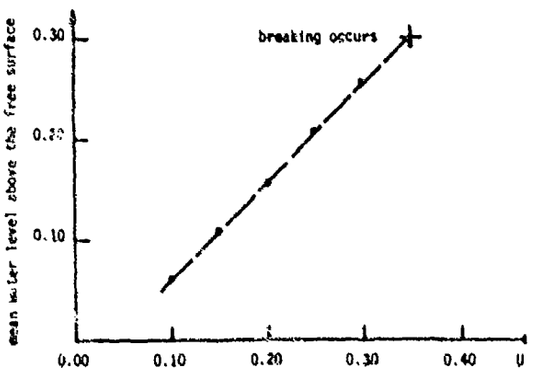

Figure 5.4. Relationship between the mean water level above the free surface and the nondimensional wavemaker forward velocity U.

In the present context, not only is the transition from undular bore to breaking wave similar to the above, but the transition from breaking to another type of free surface motion also takes place. Note that the mean water level in figure 5.3 is about 0.75. For U equal to or greater than 1, there can be no wave in front of the wavemaker because the wavemaker velocity exceeds the wave group velocity. As shown in figure 5.5, fluid near the wavemaker piles up and forms a singular jet at the wavemaker face. For small time the shape of this jet is logarithmic (see equation 1 for the analytic result of Peregrine (1972) or Lin (1984)) and the comparison of analytical and numerical results shown in figure 5.5 is good.

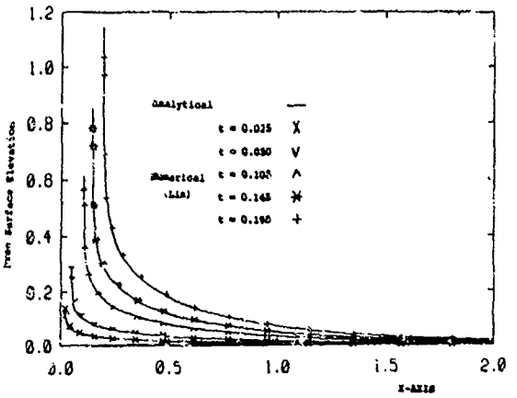

Figure 5.5. Comparison between analytical and numerical results for the free surface elevation. Wavemaker has impulsive motion with U = 1. The analytical solution (equation 1) is from Peregrine (1972) or Lin (1984). (From Lin, Newman and Yue (1984)).

In order to generate a specific wave, especially a breaking wave, at a desired location in the tank, it is necessary to let the wavemaker perform modulated motion. Comparison between the numerical calculations and experimental measurements of the wave profiles, and the fluid particle velocity beneath the wave crest is underway as a joint project between the Department of Ocean Engineering and the Parsons Laboratory, Department of Civil Engineering at M.I.T. Figure 5.6 shows a sample of the wavemaker motion from which a plunging breaker can be generated in the middle of the tank. Figure 5.7 shows a comparison between numerical calculation and experimental measurement of the time history of the wave elevation at a point (wave probe) 1.9m away from the mean wavemaker position. Three types of wave - nonbreaking, spilling breaker and plunging breaker - have been studied. The initial comparisons are promising but final comparisons are still not available.

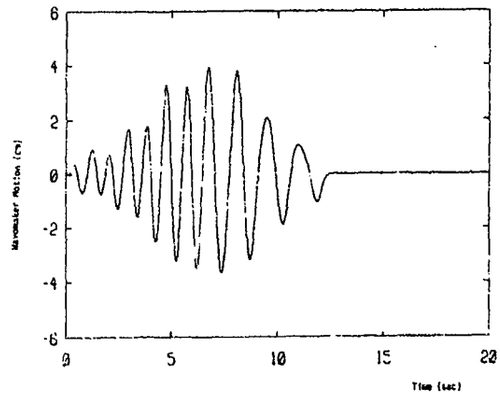

Figure 5.6. Modulated wavemaker motion history in the experiment. Water depth = 60 cm.

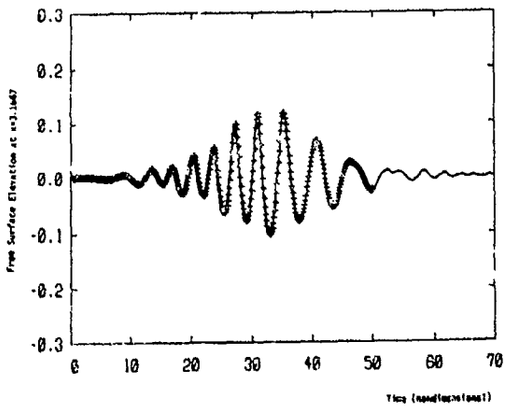

Figure 5.7. Free surface elevation as a time history at a wave probe 1.9m (nondimensional x = 3.1667) away from the mean wavemaker position — experimental measurements + + + numerical calculation.

6. Conclusion

This paper extends and exploits the numerical scheme of Vinje and Brevig (1981) for nonlinear free surface effects with bodies present. Using the treatment of the intersection point of free and body surfaces suggested by Lin, Newman and Yue (1984), the transient motion of a wedge in initially calm water is simulated. However, for slamming of a wedge into calm water this treatment, which seeks to satisfy both free and body boundary conditions, does not allow the fast jet of water moving up the wedge to leave its surface: this results in negative pressure on the upper part of the wetted wedge surface. Physically we need to relax the body boundary condition at the intersection point when this happens. A modified scheme is introduced which allows the jet to "peel off" the wedge surface, although the numerical resolution of the jet itself is poor. Further work on this phenomenon, which occurs in cylinder slamming (see Greenhow and Lin (1983)) and may well occur in some capsize situations, is needed.

In order to study capsize a "numerical wave tank" has been set up and tested for various wavemaker motions. With constant wavemaker velocity, the behaviour of the free surface is dependent on the wavemakers speed: at low speed an undular bore is formed: at moderate speed a breaking wave is produced: at high speed (exceeding the group velocity of the waves) the water simply piles up in front of the wavemaker. These transitions are qualitatively similar to those which occur in experiments where a flow of water meets an area of calm water.

With small amplitude simple harmonic motion the free surface agrees well with linear theory, whilst for impulsive motion the agreement with equation 1 is good. For modulated motion a breaking wave may be produced in the tank which agrees well with experiments. It is hoped to introduce ship-like bodies into such waves and to study their capsizing in detail.

Acknowledgement

W-M.L. would like to thank Professor J.N. Newman for his continuous support and encouragement during the course of this work. Experimental work about the wavemaker was done by E.S. Chen at the Parson Laboratory, Department of Civil Engineering, M.I.T.

References

1. Baker, G.R., Merion, D.I. and Orszag, S.A. "Generalised vortex methods for free-surface flow problems". J. Fluid Mech. Vol.123, pp.477-501 (1982).

2. Binnie, A.M. and Orkney, J.C. 1955."Experiments on the Flow of Water from a Reservoir through an Open Channel. II. The formation of Hydraulic Jump." Proc. Roy. Soc. A, 230, pp.237-46.

3. Brevig, P., Greenhow, M. and Vinge, T. "Extreme wave forces on submerged wave energy devices". Applied Ocean Res. Vol.4, No.4, pp.219-225 (1982).

4. Chapman, R.B., "Large amplitude motion of two-dimensional floating bodies", J. Ship Res. Vol. 23, No.1, March

5. Chuang, S-L., "Experiments on Slamming of Wedge-Shaped Bodies", J. Ship Res., Sept. pp.190-198 (1967).

6. Cumberbatch, E. "The Impact of a Water Wedge on a Wall", J. Fluid Mech., Vol.7, pp.353-374 (1960).

7. Dahle, E. and Kjaerland D., "The Capsizing of M/S Helland-Hansen. The Investigation and Recommendations for Preventing Similar Accidents", Norwegian Maritime Res. No.3 (1980).

8. Dobrovol'skaya,Z.N. "On some problems of similarity flow of fluid with a free surface". J. Fluid Mech Vol.39, part 4 pp.805-829 (1969).

9. Doctors, L.J., "Solution of Two-dimensional Slamming by means of finite pressure elements". 3rd Int. Symp. Num Ship Hydro., June, Paris (1981).

10. Dold, J.W. and Peregrine, D.H. "Steep Unsteady Water Waves : An Efficient Computational Scheme" School of Mathematics, Univ of Bristol rep. no. AM-84-04 (1984).

11. Favre, H. 1935. "Ondes de Translation." Paris: Dunod.

12. Garabedian, P.R. "Oblique Water Entry of a Wedge" Communs. on Pure and Appl. Math. Vol. VI, pp.157-165 (1953).

13. Greenhow, M., Vinje, T., Brevig, P., and Taylor, J. 1982. "A Theoretical and Experimental Study of the Capsize of Salter's Duck in Extreme Waves". J. Fluid Mech., 116, pp.259-275.

14. Greenhow, M. and Lin, W.M. 1983. "Nonlinear Free Surface Effects: Experiments and Theory". MIT, Dept. of Ocean Engineering, Rept. No.83-19.

15. Greenhow, M. "Free surface flows related to breaking waves". J. Fluid Mech. Vol.134, pp.259-275 (1983).

16. Greenhow, M. "Survival of Surface Piercing Wave Energy Devices". Proc. IUTAM Conf. Wave Energy, Lisbon, Portugal (1985).

17. Gurevich, M.I. "Theory of Jets in Ideal Fluids". Academic Press pp.435-446 (1965).

18. Hughes, D.F. "Simulation of the wedge entry problem by numerical confirmal mapping". J. Fluid Mech. Vol.56, part 1, pp.173-192 (1972).

18. Johnstone, E.A. and Mackie, A.G. "The Use of Lagrangian Coordinates in Water Entry and Related Problems". Proc. Camb. Phil. Soc., Vol.74, pp.529-538. (1973).

20. Kravtchenko, J. "Remarques sur le calcul des amplitudes de la houle lineaire engendree par un batteur". Proc. 5th Conf. Coastal Eng. pp.50-61 (1954).

21. Lin, W-M. 1984. "Nonlinear Motion of the Free Surface Near a Moving Body". Ph.D. Thesis, M.I.T., Dept. of Ocean Engineering.

22. Lin, W-M., Newman, J.N. and Yue, D.K. 1984. "Nonlinear Forced Motions of Floating Bodies". Proc. 15th Symposium on Naval Hydrodynamics, Hamburg, Germany.

23. Longuet-Higgins, M.S. and Turner, J.S. "An entraining plume model of a spilling breaker". J. Fluid Mech. Vol.63, part 1, pp.1-20 (1974).

24. Longuet-Higgins, M.S. and Cokelet, E.D. 1976. "The Deformation of Steep Surface Waves on Water, I: A Numerical Method of Computation". Proc. Roc. Soc. Lond., Series A, 350, pp.1-26.

25. Longuet-Higgins, M.S. and Fox, M.J.H. "Theory of the almost highest wave: the inner solution". J. Fluid Mech. Vol.80, part 4, pp.721-741 (1977).

26. Longuet-Higgins, M.S. "The instabilities of gravity waves of finite amplitude in deep water. I. Superharmonics". Proc. Roc. Soc. Lond A Vol.360 pp.471-488 (1978a).

27. Longuet-Higgins, M.S. "The instabilities of gravity waves of finite amplitude in deep water II. Superharmonics. Proc. Roy. Soc. Lond A vol.360 pp.489-505 (1973b).

28. Longuet-Higgins, M.S. and Cokelet, E.D. "The deformation of steep surface waves on water. II Growth of normal mode instabilities". Proc. Roy. Soc. Lond A Vol.364 pp.1-28 (1978).

29. Longuet-Higgins, M.S. and Fox, M.J.H. "Theory of the almost highest wave. Part 2 Matching and Asymptotic Extension". J. Fluid Mech. Vol.85, part 4, pp.769-786 (1978).

30. Longuet-Higgins, M.S. "On the forming of sharp corners at a free surface" Proc. Roy. Soc. Lond A, Vol.371 pp.453-478 (1980).

31. Mackie, A.G. "The Water Entry Problem" Q.J. Mech. Appl. Mech., Vol.XXII, part 1, pp.1-17 (1969).

32. Maskell, S.J. and Ursell, F. "The transient motion of a floating body". J. Fluid Mech. Vol.44, part 2, pp.303-313 (1970).

33. New, A. "On the Breaking of Water Waves". Ph.D. Thesis, University of Bristol 1983.

34. Newman, J.N. "Marine Hydrodynamics" MIT Press, 1st Edition 3rd printing (1980).

35. Oqabasi, A.Y. "Pope's frequency domain Stability Criteria and Stability of Large Amplitude Rolling Motion". Schiffstechnik Bd.29, N.3. (1982).

36. Peregrine, D.H. 1966. "Calculation of the Development of an Undular bore". J. Fluid Mech., Vol.25, part 2, pp.321-330.

37. Peregrine, D.H. 1972. "Flow Due to Vertical Plate Moving in a Channel". Unpublished Notes.

38. Roberts, A. "A Numerical Method for the Investigation of the Nonlinear Behaviour of Unsteady Incerfacial Waves". Chapter 3, Ph.D. Thesis, University of Cambridge.

39. Vinje, T. and Brevig, P. 1981a. "Breaking Waves on Finite Water Depth, a Numerical

Study". SIS Report No.R111.81 Norwegian Hydrodynamic Laboratory, Trondheim.

40. Vinje, T. and Brevig, P. 1981b. "Nonlinear, Two-Dimensional Ship Motion", SIS Report No. 112.81 Norwegian Hydrodynamic Laboratory, Trondheim.

41. Vinje, T. and Brevig, P. 1981. "Nonlinear Ship Motion". Proceedings of 3rd International Conference on Numerical Ship Hydrodynamics, Paris, France.

42. Von Karman, T.H. "The Impact of Seaplane Floats During Landing". N.A.C.A. TN321.

43. Wagner, H. "Uber Stofs-und Gleitvorgange an der Oberflache von Flissigkeiten" Z.A.M.M. Band 12 Heft 4 August, pp.193-215 (1932).

44. Yim, B. "Investigation of Gravity and Ventilation Effects in Water Entry of Thin Foils". Proc. IUTAM Symp. on Nonsteady Flows at High Speed, Leningrad (1971).

NUMERICAL SOLUTION FOR TWO-DIMENSIONAL WEDGE SLAMMING WITH A NONLINEAR FREE-SURFACE CONDITION

B. Yim
David W. Taylor Naval Ship Research and Development Center
Bethesda, MD 20084

Abstract

Using the Cauchy method with a semi-Lagrangian representation of flow, straight-sided and flared wedges are considered with a nonlinear free-surface boundary condition. Singularities at the spray tip and the spray root are identified, and special treatments of the singularities are investigated. Free surface elevations and pressure distributions on the wedges are obtained for half wedge angles of less than 30 degrees for both straight-sided and flared wedges. The numerical solutions are found to be prone to instabilities and/or inaccuracies.

Introduction

It is well known that bow slamming and deck wetting can be serious problems. Design of bow shapes which minimize these unwanted aspects of ship motions in a seaway indeed is an important task for naval architects. This task specifically requires prediction of the pressure distribution on the bow and of the wave height when a ship bow enters the water surface.

The problem was first investigated by Wagner[1]. Many attempts to improve upon Wagner's original approximate solution have been made since. Early studies were mostly concerned with the simplest possible body shapes, namely two-dimensional symmetric wedges; furthermore, gravity effects were ignored. Both analytical approximations[2,3,4] and numerical studies[5,6,7] of this self-similar flow may be found in the literature.

The problem becomes considerably more complex when gravity effects are included. Simplifications based on linearization of the free-surface boundary condition, with the body boundary condition also linearized[8,9] or treated exactly[10], were therefore introduced.

A numerical method for calculating free-surface flows, with the exact nonlinear free-surface boundary condition, was recently proposed by Longuet-Higgins and Cokelet[11] and subsequently used by several investigators[12-15]. In particular, calculation of the complex potential by using Cauchy's formula has been demonstrated to be practical[14,15]. Nevertheless, the method presents difficulties when a solid body intersects the free surface.

This numerical technique is used here to study the slamming problem, with free-surface nonlinearities and gravity effects included. Two two-dimensional body shapes, namely an infinite straight wedge and a flared wedge, are considered. The usual assumptions of incompressible and inviscid fluid and irrotational flow are made. Infinite fluid velocities may then occur at a corner point or at the body and free-surface juncture point.

Singularities at a corner point or at the juncture point may not pose serious problems in practice so long as they only influence the flow locally. However, in the present time-stepping numerical method, the singularity at the juncture point influences the solution at all subsequent time steps, and thus can have disastrous cumulative effects.

Two main methods for calculating the complex potential may be used. One method is based on an application of the Cauchy theorem, the other makes use of source or/and dipole distributions. The Cauchy method is used in the present study.

Problem Formulation

A symmetrical two-dimensional body is supposed to enter, with constant speed and at right angle, the free surface of a liquid initially at rest. The x and y axes are taken along the initial free surface and along the body centerline, respectively, as is shown in Figure 1. The fluid is assumed incompressible and inviscid. The flow can then be represented by means of the velocity potential ϕ, which satisfies the Laplace equation at all times:

$$\nabla^2\phi = 0 \tag{1}$$

Fluid particles on the free surface satisfy the following kinematic and dynamic boundary conditions[11].

$$Dx/Dt = \phi_x \tag{2}$$

$$Dy/Dt = \phi_y \tag{3}$$

$$D\phi/Dt = -g\eta + (\nabla\phi)^2/2 \tag{4}$$

where g is the acceleration of gravity and η the elevation of the free surface. On the body surface, the following boundary condition holds:

$$(\nabla\phi - \bar{V}) \cdot \bar{n} = 0 \tag{5}$$

where $\bar{V}$ is the velocity of the body and $\bar{n}$ is the unit outward normal vector to the body surface. The initial conditions

$$\phi = 0 = \phi_t \tag{6}$$

hold everywhere in the fluid at time $t = 0$.

Only the case of a pointed body entering the free surface impulsively is examined here. Therefore, neither the distortion of the free surface prior to the entrance of the body nor compressibility effects need be considered, as would be necessary for the more-complex case of a flat-bottomed body.

It is convenient to reformulate the problem of a body moving downward into a liquid at rest as an equivalent problem in which the liquid moves upward past the stationary body. Let $F = \Phi + i\Psi$ represent the complex potential for this equivalent flow. The stream function Ψ may be taken equal to zero on the surface of the body. Furthermore, we then have $\Psi \sim -Vx$ as $y \to -\infty$, where V is the upward velocity of the liquid past the body. The complex potential F may be expressed as the sum of the complex potential $Vy - iVx$ corresponding to the uniform stream in the upward direction and of the complex potential $\Phi + i\Psi$ corresponding to the disturbance flow, as follows:

$$F = \Phi + i\Psi = \phi + i\psi + V(y-ix) \tag{7}$$

The condition $\Psi = 0$ on the body surface then yields

$$\psi = Vx \tag{8}$$

This body boundary condition is equivalent to condition (5). The disturbance complex potential $\beta = \phi + i\psi$ is identical to the complex potential of the flow due to a body penetrating the free surface of a liquid at rest. The potential $\phi + i\psi$ satisfies the free-surface boundary conditions (2), (3), (4), the body boundary condition (8) and the initial conditions (6).

The slamming problem is only significant for small values of the time after the initial impact. The far-field boundary is therefore not important for this problem. In the present study, the body is assumed to enter at the center of the free surface of water contained in a rectangular tank.

Nondimensional Parameters

The depth and width of the water tank are taken equal to L and 2L, respectively. Coordinates are rendered nondimensional with respect to L. The nondimensional depth and width of the tank thus are equal to 1 and 2, respectively.

Time is rendered nondimensional with respect to the time $T = L/V$ required for the wedge to travel from the free surface to the bottom of the tank, where V is the speed of the wedge. The nondimensional penetration depth of the wedge tip below the equilibrium free surface therefore is equal to the nondimensional time after initial contact.

The depth L of the tank may be chosen arbitrarily. In this study, the value of L is adjusted to the speed V of the wedge so as to satisfy the relation $gL/V^2 = 1$. The reference time and the reference length L are then related to one another by the relation $L = gT^2$.

Method of Complex Analytic Function

This disturbance potential $\beta = \phi + i\psi$ is a complex analytic function. Therefore, it satisfies the Cauchy integral formula

$$2\pi i\beta(z_0) = \oint_c [\beta(z)/(z-z_0)]dz \tag{9}$$

where the point z_0 is inside the closed contour c. If the real part or the imaginary part of β is specified on the boundary contour c, the Cauchy integral (9) yields a Fredholm integral equation of the second kind by taking its real part or its imaginary part, respectively[13]. The boundary contour c is divided into straight segments within which the complex potential is assumed to vary linearly. A set of linear simultaneous equations for determining the unknown values of the potential or the stream function at the selected knots on the boundary contour can then be defined and solved numerically.

The complex velocity $w(z_0)$ corresponding to the influence function defined by the equation

$$2\pi i w(z_0) = \oint_c [\beta iz)/(z-z_0)^2]dz \tag{10}$$

is singular at the nodal points of the discretized contour. However, this property has no practical effect. Indeed, the values of the complex potential at the nodal points are always finite. Finite values of the complex velocity at the nodal points along the boundary contour are then provided by numerical differentiation of the complex potential along the contour.

The potentials and the positions of the nodal points on the free surface at each time step are determined by using a combination of the Runge Kutta method and the Hammings method for solving the simultaneous ordinary differential equations (2), (3), (4)[13]. Finally, the pressure distribution is obtained from the Bernoulli equation

$$\frac{p}{\rho} = -\frac{d\phi}{dt} + (\nabla\phi)^2/2 - \eta \tag{11}$$

The mathematical nature of the slamming problem considered in the present study is very similar to the wavemaker problem studied by Lin et al[14] by using the method of Vinje and Brevig[13]. Therefore, the numerical techniques used in these previous studies for calculating the complex potential, the complex velocity, and the pressure distribution have been adopted here.

Singularity at a Junction Point

The presence of a singularity at a juncture point between a solid body and a free surface may be illustrated by considering the initial flow due to vertical motion, with speed v, of a flat plate along the segment $|x| < 1$ of an unbounded free surface. At the initial instant $t = 0$, the boundary conditions $u = 0$ for $|x| > 1$ and $v = -V$ for $|x| < 1$ hold on the free surface $y = 0$. Equivalently, the complex potential $\beta = \phi + i\psi$ satisfies the conditions $\phi = 0$ for $|x| > 1$ and $\psi = Vx$ for $|x| < 1$. Far away from the plate, we have $u - iv = 0 = \phi + i\psi$.

This boundary-value problem may be solved if the nature of the solution is specified at the points $z = x + iy = \mp 1$. Thus, if the complex potential is assumed to be finite at $z = \mp 1$, we have the well-known solution

$$\beta = iVz - iV(z^2 - 1)^{1/2}$$

as may be verified. The complex velocity then is given by

$$d\beta/dz = u - iv = iV - iVz/(z^2 - 1)^{1/2}$$

The velocity thus has a square root singularity at the points $z = \mp 1$.

Determination of the pressure, given by the Bernoulli equation

$$p/\rho = -\phi_t - (\nabla\phi)^2/2 - \eta$$

requires the time derivative β_t of the potential ϕ.

On the free surface, the pressure p vanishes and, furthermore, we have $\eta = 0$ and $u = 0$ at the time $t = 0$; this then yields

$$\phi_t = -(\psi_x)^2/2$$

on the free surface $|x| > 1$ at the initial time. Time differentiation of the flat-plate boundary condition $\psi = Vx$ while following a fixed point (x,0) of the flat plate yields

$$\partial\psi/\partial t = 0 = \partial\psi/\partial t - V\partial\psi/\partial y$$

We then have

$$\psi_t = V\phi_x$$

on the flat plate $|x| < 1$ at the initial time. The real part ϕ_t and the imaginary part ψ_t of the time derivative of the complex potential β_t are then specified on the segments $|x| > 1$ and $|x| < 1$ of the real axis, respectively. The solution of the classical problem, given by

$$\pi\beta_t(z_o) = iV(z_o^2 - 1)^{1/2} \int_{-1}^{1} \frac{\phi_x dx}{(x-z_o)(1-x^2)^{1/2}}$$

shows that β_t is singular at the points $z = \pm 1$.

A finite velocity at the points $z = \pm 1$ may be obtained by displacing the singularities at $z = \pm 1$ slightly outside the fluid domain for instance at $z = \pm a$ with $a > 1$, as follows:

$$u - iv = iV - iVz(z^2-1)^{1/2}/(z^2-a^2)$$

The singularities at $z = a$ may be placed close to the spray root, as in the zero-gravity problem[16], by taking the value of a slightly larger than 1.

Thus singularities may be considered to be outside of the fluid domain. This approach is familiar in methods using source or doublet distributions on the boundary. For example, in wing theory the nose singularity may be located slightly inside the actual nose boundary of the wing. In the present case, the singularity at the wedge vertex is considered to be inside the stagnation point.

In the wedge slamming problem singularities may be associated with the spray tip, spray root, and wedge vertex. The most important singularities are the spray tip and root singularities. Nevertheless, when the problem is solved numerically with discretized intervals, all the velocity values are finite even at or near the spray tip. However, if the intervals near the singularity are too small the stability of the solution is affected. This is unlike other hydrodynamic problems, where for a completely smooth and analytical solution, without singularities on the boundary, usually the smaller the size of interval the better the accuracy of the solution. When the half wedge angle is large, the interval which must be taken at $t = 0$ to allow a stable solution is too large to give an accurate solution. This is especially true when the mass conservation is checked. That is, the area under the wave above the $t = 0$ flat free surface should be equal to the area surrounded by the instantaneous position of the wedge surface at time $t > 0$, the wedge surface at time $t = 0$, the $t = 0$ free surface, and the y axis.

Because the spray tip velocity in the present problem is infinite, the finite numerical values of velocity at the spray tip are in a sense arbitrary because the velocity changes very rapidly with distance from the spray tip. The boundary values selected at the spray tip have a very large effect on the solution. Although the free surface condition is satisfied near the spray tip the potential should be obtained as the solution except at $t = 0$ where $\phi = 0$. At $t = 0$ the solution of the free surface is obtained from the Bernoulli equation which contains a velocity squared term. Thus Vinje and Brevig[13] obtained the location of the juncture point by interpolation from the neighbor points and solved for the complex potential. Lin, et al[15], directly computed the values of both the location and the potential of the spray tip and claimed to have obtained a robust stable solution which matches the analytical solution for a simple wave maker problem. At each time step they obtained the velocity at the spray tip by spline curve interpolation from the potentials obtained on the wedge, and the boundary condition on the wedge. Using this value in the spray-tip free-surface condition, the next time step location of the spray tip and the value of the potential at the new spray tip were found. Thus all the physical values at the spray tip were obtained without solving the boundary value problem. These values supplied the quantities required in solving the boundary value problem for the complex potential, Equation (9). The treatment of the juncture conditions needs more careful attention.

Because of irregular boundary conditions, for different kinds of singularities used at the juncture points, different solutions are obtained even though the boundary values are identical. The methods that were investigated are as follows: Method (1), at each time step the location and the potential of the spray tip are obtained from the free surface boundary conditions, equations (2), (3), and (4); Method (2), at each time step the location of the spray tip is interpolated from the neighboring free surface points and the potential is computed by the Cauchy method; Method (3), at each time step the location of the spray tip is obtained from the free surface conditions, equations (2) and (3), and the potential is obtained from the Cauchy solution.

In Figure 2 free surface elevations obtained by the three different methods of treating the singularity are compared. Large differences in the shapes of the free surface near the spray tip occur between the predictions of the different methods. Simple experiments[16,17] indicate that the results of method (1) are much more reasonable than the other two methods. This means that the present problem has the juncture point as a singular point and that the singular point requires full free surface conditions in addition to the wedge boundary condition. If it were not a singular point, the free surface shapes obtained by the three methods should be identical.

In Figure 3 complex potentials obtained by two different methods of treating the singular point are compared: One method takes the potential $\phi = 0$ from the free surface condition and the stream function $\psi = Vx$ from the wedge boundary condition at the juncture point; the complex potentials are obtained by the Cauchy method using the known boundary values including those of the juncture point. The other method assumes that only the stream function is given at the juncture point and solves the complex potentials incuding that of juncture point. The two solutions are very different. If the juncture point were a regular point, the two solutions should be identical.

In addition, in the wedge slamming problem for a large wedge angle, a serious difficulty seems to be associated with the singularity at the spray root. When the free surface interval near the wedge is small, this singularity causes the solution to break down. If the interval is large, a stable solution can be obtained but mass conservation is violated. The mass conservation can be enforced by iteration, adjusting the velocity at the spray tip, because the velocity is singular at the spray tip. Then the wave height at the wedge is a function of the interval. If the interval is too large the free surface height is quite small.

Numerical Results and Discussion

The numerical computations are divided into two major parts: Part (1), solution of the Cauchy problem for complex potentials and complex velocities at each time step; Part (2), solution of simultaneous ordinary differential equations for the locations and potentials of the free surface at the next time step using solutions from the Part (1) computations. Therefore, the singular behavior of even one point affects the whole solution.

The wave heights caused by straight-sided symmetric wedges with half wedge angles of $\alpha = 15°$ and $30°$ are shown in Figures 4-6. These were computed by the Vinje-Brevig-Lin method. When the wedge angle becomes large the free surface interval has to be large to ensure stability, but this leads to inaccurate results because mass conservation is not preserved. When the free surface interval is too small, no matter how small the time step, the solution breaks down with a few time steps. The intervals are shown as dots in Figures 4-6 and in succeeding figures. The corresponding pressure distributions are given in Figures 7 and 8. Negative pressures near the spray tip are noticeable. This may require the consideration of flow separation. When larger intervals are used and the mass conservation condition is enforced smaller free surface elevations are predicted at the wedge, as shown in Figure 9. This shape of free surface does not compare favorably with the experimental results.

For the sake of simplicity we also consider flared wedges with a shape given by:

$$x = a_1(y-d) + a_2(y-d)^2$$

where d is the location of wedge vertex. Since the boundary condition on the body is

$$\psi = Vx$$

The solution can be obtained without any additional difficulty.

The results for flared wedges are shown in Figures 10-13. The narrow initial shape of the flared wedge does not help very much in providing stable solutions. If the flare becomes large, the basic stability trouble still exists for the flared wedge. Figure 11 shows positive pressure over the wedge so that flow separation on the surface will not occur.

As long as wedge angles are reasonably small the present results seem to be reasonable because the mass conservation rule is less violated and the free surface shape is close to the experimental result[16,17]. However, a basic understanding of the singularities at the spray tip and the spray root, especially as associated with numerical stability, is required.

Because the Cauchy solution can be obtained with any closed boundary, where the appropriate boundary values are known even when the boundary is submerged, the spray may be cut away at the thin spray sheet. Then, the spray sheet has one boundary as a free surface and the other as the solid surface of the wedge. When a colocation point is at the free surface side of the thin spray sheet, by connecting this point and an arbitrary point on the wedge, a closed contour can be obtained. The resulting solution does not include the spray tip behavior, but since the spray tip has undesirable features, such a solution may be useful. Figure 14 is such a solution. This is obtained by eliminating the spray tip from the next colocation point at an early time step. The elliptic shape of the free surface resembles the experimental results of wedge entry.[17]

Although the Cauchy method with a semi-Lagrangian representation of the flow is an attractive method for solving the slamming problem with a nonlinear free surface boundary condition, the spray tip and spray root singularities are great hindrances. At $t = 0$, the juncture point of the wedge and the free surface contains these two singularities. Since the stream function on the wedge is known at any time and the potential at $t = 0$ is zero at the juncture point, the value of the complex potential can be obtained at any time from the boundary conditions without using the Cauchy formula. However, the regular Cauchy solution at $t = 0^+$ does not satisfy $\phi = 0$ at the juncture point. That is, the juncture point is not a regular point. In such a problem with a singular point normal numerical procedures do not necessarily give a solution. The singular point needs to be handled separately. Because the velocity at the singular point is infinite, the location of the spray tip should be at infinity. Therefore, interpolation of the velocity at the singular point from velocities at neighboring points, or an approximate value calculated from a neighboring point, is investigated. Because the distance from the singularity cannot be too small in order to maintain a stable solution, and because such a stable solution cannot automatically satisfy the condition of mass conservation, even if we could pick a solution which is close to an experimental value, the basic problem does not seem to be solved numerically in general. Nevertheless, when the wedge angle is sufficiently small the solution is relatively stable and reasonable. This seems to indicate that the spray root singularity is worse than the spray tip singularity.

Acknowledgements

This work was supported by the Numerical Ship Hydrodynamics Program at the David W. Taylor Naval Ship Research and Development Center. This Program is jointly sponsored by the Office of Naval Research and by DTNSRDC.

References

1. Wagner, H. 1932, "Über Stoss Gleitvorgänge an der Oberfläche von Flüssigkeiten," Z. Angew. Math. Mech. 12, 193.

2. Shiffman, M. and D.C. Spencer, 1951, "The Force of Impact on a Cone Striking a Water Surface Comm. Pure Appl. Math 4, 379.

3. Bisplinghoff, R.L. and C.S. Doherty, 1952, "Some Studies of the Impact of Vee Wedges on a Water Surface," J. Franklin Inst. 253, 547.

4. Fabula A.G., 1957, "Ellipse-Fitting Approximation of Impact of Rigid Bodies on Water," Proc 5th Mid-Western Conf. on Fluid Mech. P.299.

5. Garabedian, P.R., 1953, "Oblique Water Entry of a Wedge," Comm. Pure Appl. Math. 6, 157.

6. Borg, S.F., 1957, "Some Contributions to the Wedge: Water Entry Problem," J. Eng. Mech, Div. A.S.C.E., 93 paper no. 1214.

7. Dobrovolskaya, Z.N., 1969, "On Some Problem of Incompressible Fluid with Free Surface," J. Fluid Mech. 36, pp 805-829.

8. Yim, B., 1973, "Investigation of Gravity and Ventilation Effects in Water Entry of Thin Foils," Proc. of the IUTAM Symposium held in Lenningrad, pp. 471-489.

9. Mackie, A.G., 1963, "Initial Value Problem in Water Wave Theory," Australian Math. Soc. J. 3, 340-350.

10. Chapman, R.B., 1979, "Large-Amplitude Transient Motion of Two-Dimensional Floating Bodies," J. of Ship Research 23, No. 1, 20-31.

11. Longuet-Higgins, M.S. and E.D. Cokelet, 1976, "The Deformation of Steep Surface Wave on Water, I.: A Numerical Method of Computation," Proc. R. Soc. London, Series A, 350, pp 1-26.

12. Faltinsen, O.M., 1977, "Numerical Solution of Transient Nonlinear Free-Surface Motion Outside or Inside Moving Bodies," Proc. Second Int. Conf. on Numerical Ship Hydrodynamics, U.C. Berkeley.

13. Vinje, T. and P. Brevig, 1980, "Nonlinear Ship Motion," Proc. of the 3rd Int. Conf. on Numerical Ship Hydrodynamics, Paris.

14. Greenhow, M., T. Vinje, and J. Taylor, 1982, "A Theoretical and Experimental Study of the Capsize of Salter's Dock in Extreme Waves," J. Fluid Mech. 118, pp 221-239.

15. Lin, W-M., J.N. Newman, and D.K. Yue, 1984, "Nonlinear Forced Motion of Floating Bodies." Proc 15th Symp on Naval Hydrodynamics, Hamburg, Germany.

16. Hughes, O.F., 1972, "Solution of the Wedge Entry Problem by Numerical Conformal Mappings," J. Fluid Mech., Vol.. 56, Part 1, pp 173-192.

17. Greenhow, M., and W-M. Lin, 1983, "Nonlinear Free Surface Effects: Experiment and Theory," Report No. 83-19, Dept. of Ocean Engineering, MIT.

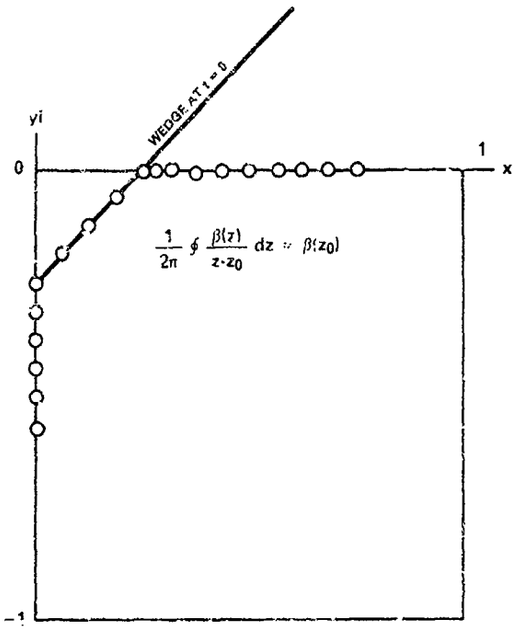

Figure 1 - Boundary Value Problem of Wedge Entry

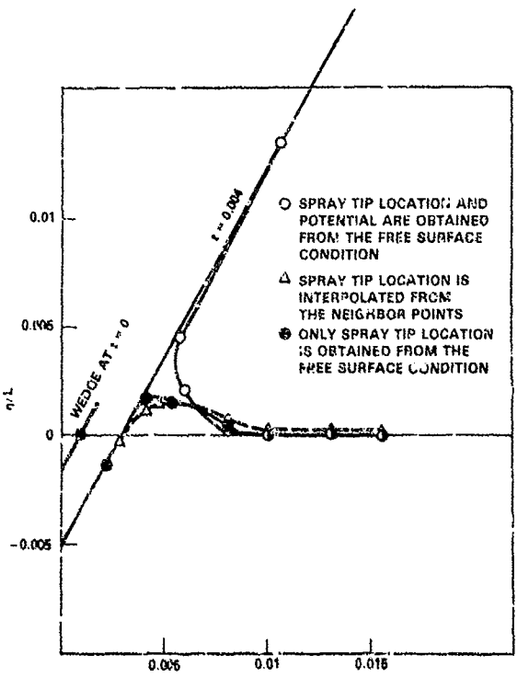

Figure 2 — Comparisons of Free Surface Elevation of 30° Wedge Entry by Three Different Methods at Juncture Points at V = 1

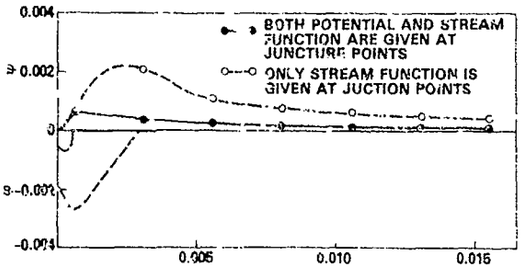

Figure 3 — Comparisons of ϕ and ψ of 30° Wedge Entry by Two Different Methods at Juncture Points at t = + 0, and V = 1

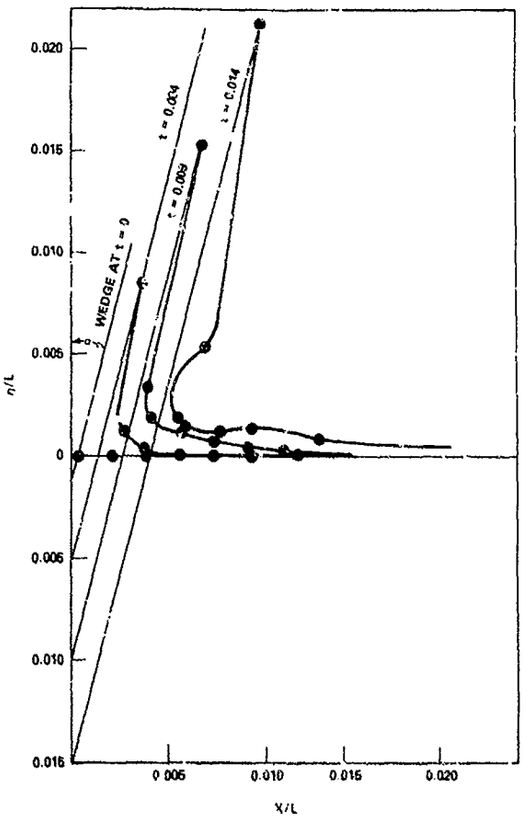

Figure 4 — Free Surface Elevations η at Successive Tim. Intervals Caused by a Wedge with α = 15° and V= 1

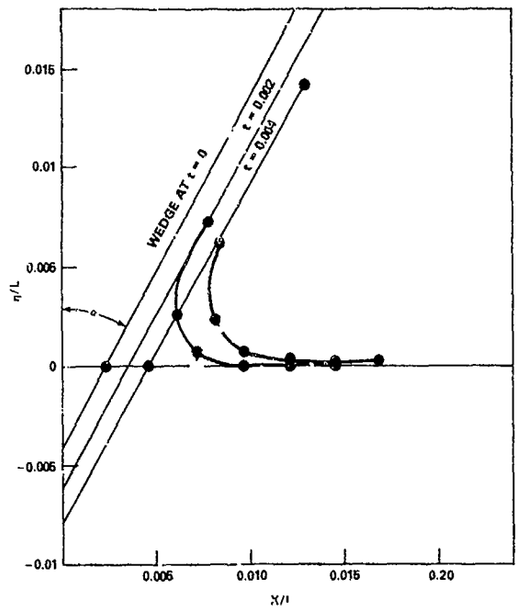

Figure 5 — Free Surface Elevation η Caused by a Wedge with $\alpha = 30°$ and V = 1

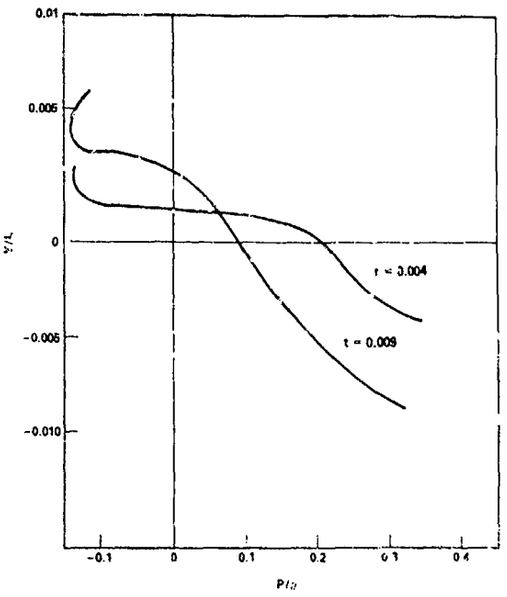

Figure 7 — Pressure Distribution on a Wedge with α = 15° and V = 1

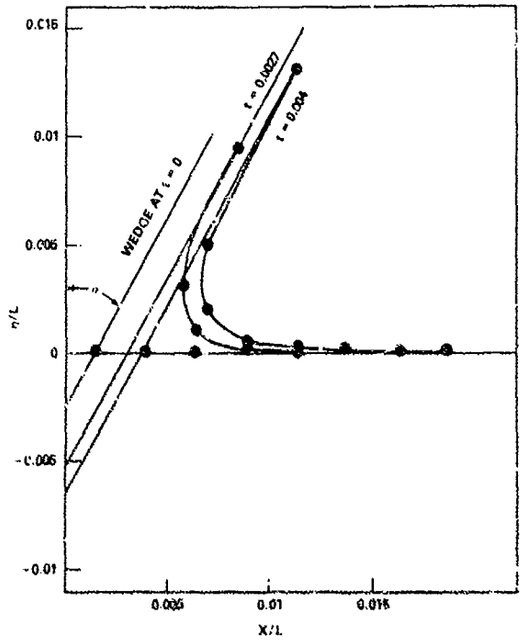

Figure 6 — Free Surface Elevation η Caused by a Wedge with $\alpha = 30°$ and V = 0.5

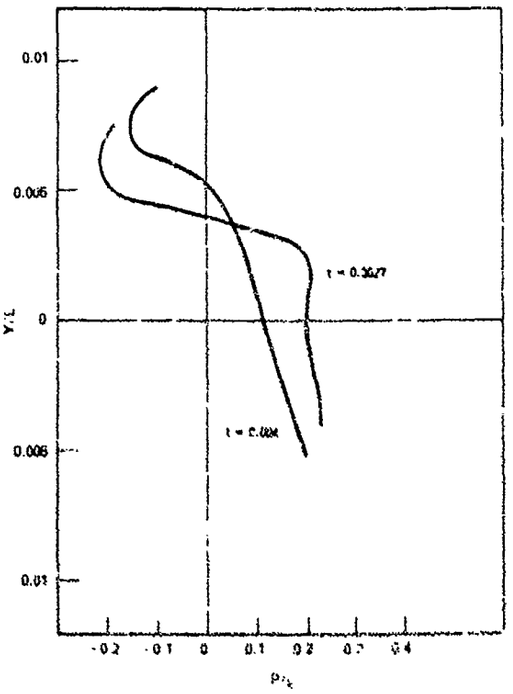

Figure 8 — Pressure Distribution on a Wedge with α = 30° and V = 0.5

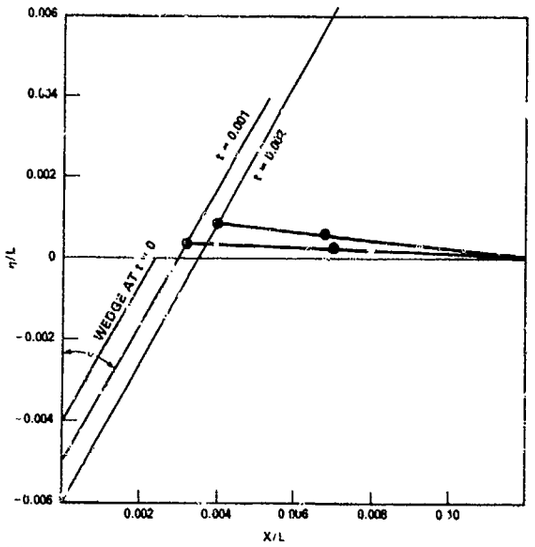

Figure 9 — Free Surface Elevation η Caused by a Wedge with $\alpha = 30°$ and V = 1. Calculated by Enforced Mass Conservation

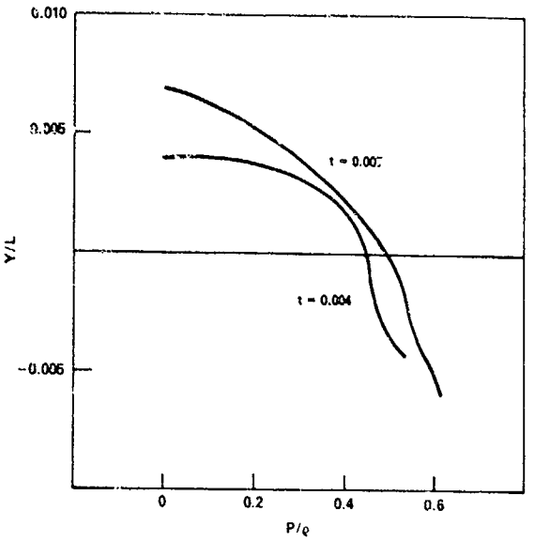

Figure 11 — Pressure Distribution on a Flared Wedge, $x = 0.2618\ (y-d) + 20\ (y-d)^2$, with V = 1

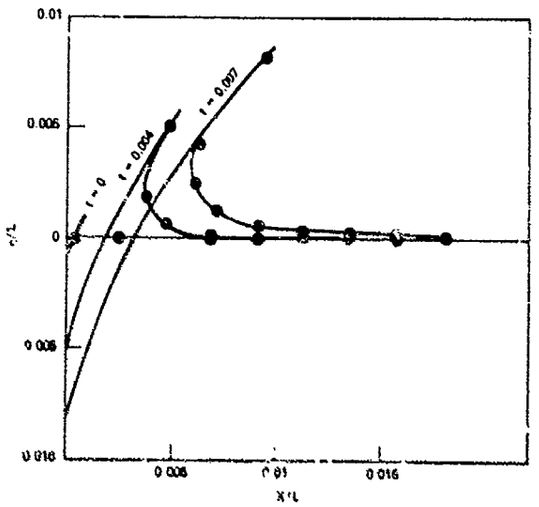

Figure 10 — Free Surface Elevation η Caused by a Flared Wedge, $x = 0.2618\ (y-d) + 20\ (y-d)^2$ with V = 1

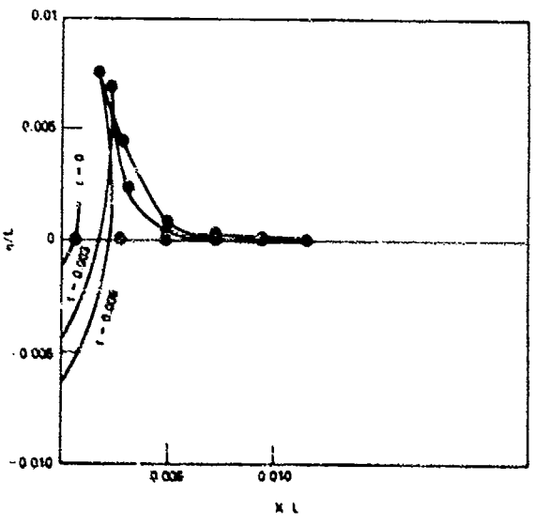

Figure 12 — Free Surface Elevation η Caused by a Convex Wedge, $x = 0.5236\ (y-d) - 30\ (y-d)^2$ with V = 1

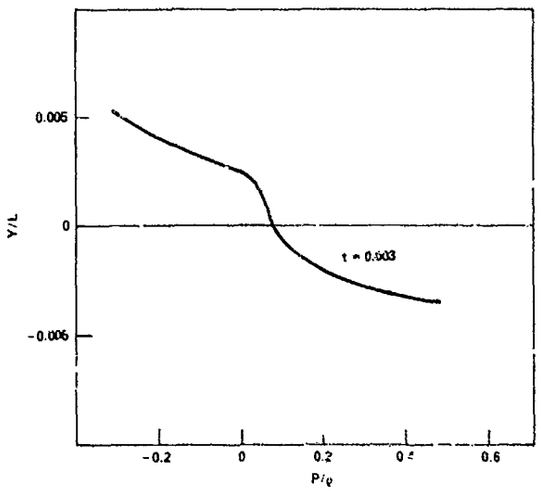

Figure 13 — Pressure Distribution on a Convex Wedge, $x = 0.5236\,(y-d) - 30\,(y-d)^2$ with V = 1

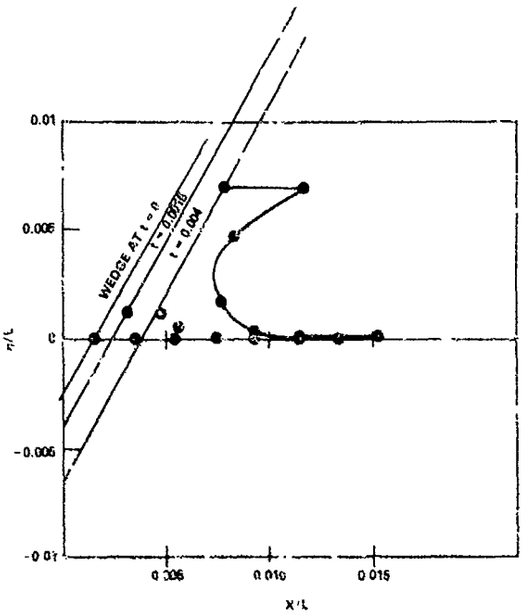

Figure 14 — Free Surface Elevation η Caused by a Wedge with $\alpha = 30°$, V = 1. Calculated with Elimination of Spray tip

DISCUSSION
of the paper
by B. Yim

NUMERICAL SOLUTION FOR TWO-DIMENSIONAL WEDGE SLAMMING WITH A NONLINEAR FREE-SURFACE CONDITION

DISCUSSION
by S.M. Calisal

The author discusses one of the main problems associated with the Cauchy method, that is the condition at the point common to the free surface and the body. As figure 3 of the paper shows a different solution seems to exist corresponding to the method used at the juncture points. This figure suggests that the problem is not really well defined as Fritz John wrote in his paper on "waves in the presence of an inclined barrier". Additional conditions can be imposed on the problem. These conditions are related to the conservation of energy. Following the observation by the author that the method does not conserve mass, I would like to ask the author if the energy of the system is monitored or the energy of the system is considered as a control for the numeric problem. As suggested by John the energy conservation seems to be the key for the proper selection of the "singularity" or the solution.

DISCUSSION
by S. Mori

When the water is dribbling up along the wedge surface, the non-slip condition seems important. And the development of the boundary layer may affect the structure of flow at the top. What do you think about this?

Author's Reply

I thank both discussers for their interest in the present problem. Both are concerned with the flow behavior near the spray tip. I agree with Professor Mori that the consideration of viscosity would change the flow structure near the spray tip. Since the similar problem with viscosity is considered in the paper presented next to mine I hope that we can compare the difference there.

I also agree with Professor Calisal that we might need another condition for the better solution. It would be useful to think about inclusion of both mass and energy conservation conditions in the least mean square sense although we recognize a singularity at the juncture point in the analytical solution and know the kind of singularity is a key to the unique solution, the precise interpretation of this feature in the numerical solution is not easy.

SLAMMING SIMULATIONS: AN APPLICATION OF COMPUTATIONAL FLUID DYNAMICS

P. Gallagher and R.C. McGregor

Department of Naval Architecture and Ocean Engineering
University of Glasgow
Glasgow, Scotland

Abstract

This paper describes a number of finite difference time marching solution techniques and their application to specific problems associated with the slamming of ship sections. Primarily, a hydrodynamic water entry simulation is developed using program SLAM. This code is based on the SOLA/VOF method but includes the use of source distributions in defining the dynamics of rigid bodies within the flow domain. A further feature is the capability of representing the motions of curved boundaries within the constraints of a rectangular finite difference mesh. The results of a number of flow modelling exercises are presented. The paper also describes work carried out to model the effect of a trapped air layer beneath the ship section. One and two dimensional finite difference formulations of the equations of mass and momentum conservation are solved in association with two and three dimensional representations of the fluid/free surface motions. Post-impact behaviour for a flat plate is examined using a specialised model of the trapped air bubble. The data obtained from these tests is used to define future work to simulate the full, three-dimensional ship slamming problem.

1. Introduction

Whilst making a passage in heavy weather, severe motions may cause hydrodynamic impact loadings on certain forward areas of ship hulls. This well recognised phenomenon of slamming may give rise to two distinct forms of loading, namely

a. bow flare loading, and
b. bottom impacts.

The first of these two cases may be examined with regard to the local time rate of change of added virtual mass. The second case may be idealised by the classical water entry problem, though it is thought that air entrapment, surface roughness, marine growth and 'pre-wetting' serve to complicate considerably the modelling process.

Research into slamming on marine vehicles has concentrated in the two distinct areas of seakeeping and local hydrodynamics. For seakeeping, the main aims have been to predict slamming frequency and overall response whereas consideration of the hydrodynamic problem at the point of contact seeks to quantify the local slam loading distribution.

This paper deals with the work carried out in the Department of Naval Architecture and Ocean Engineering at the University of Glasgow, into the use of computational fluid dynamics to model the latter of these two problems.

The hydrodynamics of slamming has often been studied in the past by using the concept of the 'idealised' water entry problem. In particular, during the 1930s, Von-Karman (1) and Wagner (2) sought to quantify the major features of the impact of wedges. Based on this early work, Szebekely (3), Fabula (4) and Bisplinghoff and Doherty (5) all made contributions to improvements in the computation of slam loading. Nevertheless, the loads predicted using such techniques were considerably higher than those measured at sea.

It was not until Chuang (6,7) reported the findings of a series of drop tests using flat plates and wedges that the discrepancy was explained by his finding that considerable quantities of air could be trapped beneath a bluff body as it approached an initally flat free surface. This lead to a cushioning of the impact and reduced the impact pressures considerably.

A number of attempts to compute the formation of this air layer were subsequently made by various authors. Verhagen (8), Lewison and Maclean (9) and, later, Koehler and Kettleboroughs (10) used one-dimensional finite difference models of the conservation equations for the air layer coupled to models of varying degrees of sophistication to describe the fluid free surface motions. The techniques employed all seemed to be capable of providing good numerical models of air entrapment, through no

Drs P Gallagher & R C McGregor, Dept of Naval Architecture and Ocean Engineering, University of Glasgow, Acre Road, GLASGOW, G20 0TL, Scotland. (Gallagher now at W S Atkins, Surrey, England)

rigorous parametric surveys of the effect of impact velocity, mass loading, section deadrise/curvature or surface shape imperfections, were carried out. Furthermore, none of the techniques claimed to be capable of following the impact through the complete impact time history.

The aim of the present study was to provide a complete water entry/air entrapment simulation technique for ship shaped sections or bodies of arbitrary shape. The section was not necessarily to be moving in a direction normal to the free surface, nor was the free surface required to be initially flat or quiescent. It was also specified that the model should not be confined to a two-dimensional representation or inviscid flow formulations.

Section II of this paper deals with the design of a finite difference time marching model of the impact of an arbitrarily shaped body into a viscous or inviscid fluid. Section III briefly describes the early work involved in setting up a separate model of the air entrapment problem in order to study the numerical simulation of this phenomenon in isolation. Section IV proposes a technique to be used to model the hydrodynamics of the slamming problem in full.

II. Hydrodynamic Model

The Computational Domain

Figure 1 illustrates the general computational domain to be examined. The fluid is bounded by a free surface, solid walls (eg the bottom boundary) and radiation boundaries. Upstream influx conditions may also be set. These may be either steady or harmonic in nature, the latter being an analogue of a flap type wave maker.

The fluid domain is also considered to contain free boundaries representing the contours of bodies in steady or accelerated motion. The physical constraints of mass and momentum conservation within this arbitrarily shaped domain may be represented by solutions to the continuity coupled Navier Stokes equations.

Equations of Fluid Motion

The equations stated in this section are for two-dimensional flow of a viscous incompressible fluid. Their derivation may be found in many standard text books on fluid mechanics (11,12). Cartesian (x,y) co-ordinates are used throughout along with the standard convention of representing the x and y components of the velocity vector by u and v, respectively, and pressure by the letter p.

Mass conservation may be represented by the well known continuity equation for an incompressible fluid:-

$$\nabla.\bar{u} = \frac{\partial u}{\partial x} + \frac{\partial v}{\partial y} = 0 \qquad (1)$$

The equations for momentum conservation in a viscous flow may be stated for each co-ordinate direction as:-

$$\frac{\partial u}{\partial t} + u\frac{\partial u}{\partial x} + v\frac{\partial u}{\partial y} = -\frac{\partial p'}{\partial x} + \nu\nabla^2 u \qquad (2)$$

$$\frac{\partial v}{\partial t} + v\frac{\partial v}{\partial y} + u\frac{\partial v}{\partial x} = g - \frac{\partial p'}{\partial y} + \nu\nabla^2 v \qquad (3)$$

where p' = pressure/density

g = acceleration due to gravity

ν = kinematic viscosity.

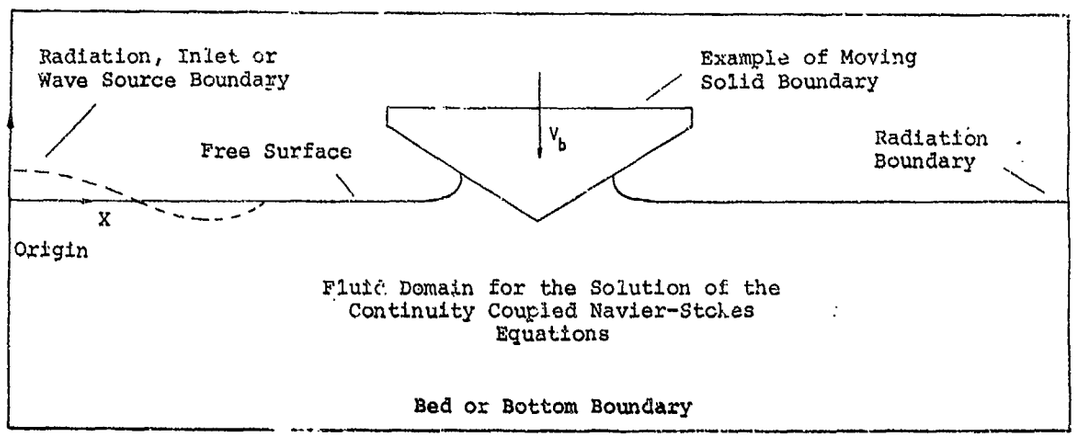

Fig 1

Primitive variables (u,v,p) were used throughout the work. It also proved convenient to formulate the following Poisson equation in pressure:-

$$-\nabla^2 p' = \left(\frac{\partial u}{\partial x}\right)^2 + 2\frac{\partial u}{\partial y}\frac{\partial v}{\partial x} + \left(\frac{\partial v}{\partial y}\right)^2 + \frac{\partial}{\partial t}\nabla.\bar{u} - \nu\nabla^2(\nabla.\bar{u}) \qquad (4)$$

This equation was the basis of many early numerical solutions to free surface problems involving the Navier Stokes equations (13), eg Marker and Cell method.

Boundary Conditions on Fluid Velocity

When considering flow near a solid wall, conditions on normal and tangential velocity components are required. In the former case, the zero normal fluid-flux condition:-

$$\bar{u}.\bar{n} = 0 \qquad (5)$$

was applied.

Two situations exist for the tangential velocity component. For viscous flows, the zero-slip condition:-

$$\bar{u}.\bar{s} = 0 \qquad (6)$$

was used when it was considered that viscous shear effects were negligible. A free-slip condition was applied via the equation:-

$$\frac{\partial^2(\bar{u}.\bar{s})}{\partial n^2} \qquad (7)$$

Downstream or radiation boundaries were generally modelled using the Sommerfeld radiation condition (14) given by:-

$$\frac{\partial \phi}{\partial t} + c\frac{\partial \phi}{\partial x} = 0 \qquad (8)$$

where ϕ may be any variable. Other methods, such as matching techniques or the application of high levels of viscous damping were also studied. However, equation (8) and its numerical analogues proved the most successful.

The free surface boundary was defined to be the outer contour of the fluid as opposed to some mean level at which conditions upon velocity and pressure were to be applied. The application of the continuity conditions was tied directly to the numerical modelling process and, hence, will be discussed later. However, in the case of viscous flow it was possible to define the zero tangential stress condition along the free surface contour as:-

$$\nu(n_x n_y \frac{\partial u}{\partial x} - \tfrac{1}{2}(n_y n_y - n_x n_x)(\frac{\partial u}{\partial y} + \frac{\partial v}{\partial x}) - n_y n_y \frac{\partial v}{\partial y}) = 0 \qquad (9)$$

where $n_x = \frac{\partial \eta}{\partial x}\left[1 + \left(\frac{\partial \eta}{\partial x}\right)^2\right]^{-\frac{1}{2}}$

and $n_y = \left[1 + \left(\frac{\partial \eta}{\partial x}\right)^2\right]^{-\frac{1}{2}}$

This was a difficult equation to satisfy numerically and so some degree of approximation was required. In this respect, the work of Hirt, Nichols and Shannon (15,16) was followed. The details are beyond the scope of this paper but may be found in Reference (24).

Boundary Conditions on Fluid Pressure

For inviscid flow the Neumann condition:-

$$\frac{\partial p'}{\partial n} = 0 \qquad (10)$$

was used at stationary solid boundaries. For viscous flow, the condition:-

$$\frac{\partial p'}{\partial n} = -\frac{1}{R_e}\frac{\partial w}{\partial s} \qquad (11)$$

where R_e = Reynolds number
and w = vorticity
was applied.

Owing to the application of the Sommerfeld radiation condition to the velocity field at the edges of the computational domain, a zero normal pressure gradient condition was thought most appropriate in these areas.

The pressure was generally set to zero along the contour of the free surface for inviscid flows. For computations in which viscosity was considered to be important, the zero normal stress condition was invoked using:-

$$p' - 2\nu\left(\frac{\partial(\bar{u}.\bar{n})}{\partial n}\right) = 0 \qquad (12)$$

in a manner complementary to equation (9) (the zero tangential stress condition).

Accelerating boundaries were given a normal pressure gradient proportional to their rate of change of velocity, thus:-

$$\frac{\partial p'}{\partial n} = -\left(\frac{\partial}{\partial t}(\bar{u}_b.n) + \frac{\partial}{\partial t}(\bar{r}_b \times \bar{w}_b)\right) \qquad (13)$$

where $\bar{u}_b$ = body velocity vector

w_b = rotational velocity vector

and $r_b = ((x - x_g),(y - y_g)(z - z_g))$

where (x,y,z) is the position on the body surface

and (x_g,y_g,z_g) is the position of the body centre of gravity.

The solution algorithm chosen for the continuity equation allowed for a different interpolation of the way in which the accelerating boundary affected the dynamic pressure field. This was the result of a special interpretation of the SOLA code which is described later.

The Finite Difference Method

A number of excellent texts exist on the use of the finite difference method in solving the partial differential equations representing fluid motions (17,18). However, it became evident during this work that most standard finite difference algorithms were unsuitable. These problems generally arose as a result of the presence of the free surface and other moving boundaries. Experimentation with the techniques showed that simple rectangular finite difference meshes produced the fastest numerical solutions to the descretised equations of motion. It was with this in mind that a way was sought in which to represent moving boundaries within a fluid domain which had been discretised using a rectangular mesh.

As a direct result of adopting this philosophy toward the discretisation of the fluid domain, an extremely simple computational mesh could be defined. The mesh was allowed to extend above the initial free surface level forming a computational domain which contained full finite difference cells, partially full cells and empty cells. The continuity equation was solved over full cell's only. The partially full free surface cells were subject to a volume fluxing technique derived from the Volume of Fluid Method (19) which itself satisfied continuity conditions locally. A more detailed description of the technique is given later in this section. A similar method was chosen to represent the contours of moving bodies within the domain and this also is detailed later.

A staggered nodal arrangement, fig. 2-2) was chosen such that:-

a. the horizontal component of velocity was computed at the midpoint of cell sides.

b. the vertical component of fluid velocity was computed at the midpoint of the top and bottom of cell boundaries.

c. the pressure was computed at cell centres.

This arrangement may be recognised as the Los Alamos 'T3' grid. The continuity equation was, thus, descretised using the central difference formula:-

$$\nabla.\bar{u} \approx \frac{(u_{ij+1} - u_{ij})}{\Delta x} + \frac{(v_{i+1j} - v_{ij})}{\Delta y} \qquad (14)$$

with truncation error given by:-

$$\frac{(\Delta x)^2}{12}\frac{\partial^3 u}{\partial x^3} + \frac{(\Delta y)^2}{12}\frac{\partial^3 v}{\partial y^3} \qquad (15)$$

As with the continuity equation, simple time and spacial difference operators were used to descretise the momentum conservation equations. A forward time step:-

$$\frac{\partial u}{\partial t} = \frac{u_{ij}^{n+1} - u_{ij}^{n}}{\Delta t} - \frac{\Delta t}{2}\frac{\partial^2 u}{\partial t^2} + \ldots . 0(\Delta t)^2, \qquad (16)$$

was most commonly applied, though central and higher order forward marching schemes were also examined.

The convection terms were discretised using central difference schemes. None of the instabilities normally associated with this choice of finite difference operator were experienced. There were two possible explanations for this. Firstly, the nature of the dynamic simulation routine required rigorous conservation of mass at each time step. Secondly, a variational algorithm in energy, inspired by the work of Sasaki (20) was applied. In the development of this by Gallagher (21), laws of energy conservation are strictly adhered to, making it difficult for numerical instabilities to grow.

Thus, for the mesh given in fig. 2 the convection terms in equation (2) become:-

$$u\frac{\partial u}{\partial x} = u_{ij}\left(\frac{u_{ij+1} - u_{ij-1}}{2\Delta x}\right) - \frac{u_{ij}(\Delta x)^2}{6}\frac{\partial^3 u}{\partial x^3} \qquad (17)$$

$$+ \ldots\ldots 0(\Delta x)^4$$

$$v\frac{\partial u}{\partial x} = \hat{v}_{ij}\frac{(u_{i+1j} - u_{i-1j})}{2\Delta y} - \frac{\hat{v}_{ij}\Delta y^2}{6}\frac{\partial^3 u}{\partial y^3} \qquad (18)$$

$$+ \ldots\ldots 0(\Delta y)^4$$

where $\hat{v}_{ij}$ is a mean value of v taken from surrounding nodes.

Pressure gradients in equations (2) and (3) were computed using simple central difference formulae, ie:-

$$\left(\frac{\partial p}{\partial x}\right)_{ij} = \frac{(p_{ij+\frac{1}{2}} - p_{ij-\frac{1}{2}})}{\Delta x} - \frac{\Delta x^2}{12}\frac{\partial^3 p}{\partial x^3} \qquad (19)$$

$$+ \ldots\ldots 0(\Delta x)^4$$

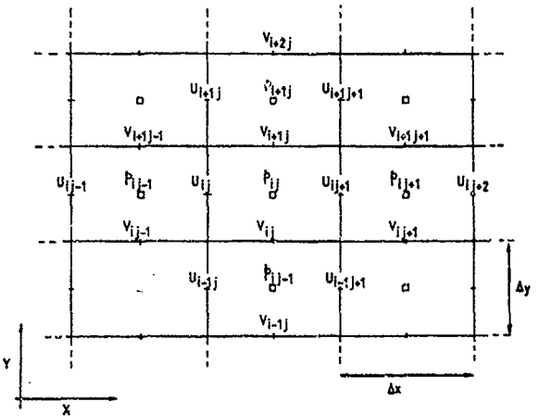

N.B. (i,j) ≡ (x,y)

Fig. 2 'T3' Computational Mesh and Primary Variables (p,U,V)

The diffusion terms were computed using second order central difference formulae:-

$$\nabla^2 u = \frac{(u_{ij+1} + u_{ij-1} - 2u_{ij})}{(\Delta x)^2} + \frac{(u_{i+1j} + u_{i-1j} - 2u_{ij})}{(\Delta y)^2} \qquad (20)$$

$$+ \frac{(\Delta x)^3}{12}\frac{\partial^4 u}{\partial x^4} + \frac{(\Delta y)^3}{12}\frac{\partial^4 u}{\partial y^4} + \ldots. \; O(\Delta x^5, \Delta y^5)$$

The combination of the above simple approximations led to straightforward explicit time marching schemes in velocity. Many more complex solution methods were examined, the QUICK schemes of Leonard (22) being one such example. However, it was found that the accurate solution of continuity at each step of the procedure meant that little difference was evident when higher order difference operators were employed.

The Continuity Solver

The inclusion of the last two terms:-

$$\frac{\partial}{\partial t}(\nabla \cdot \bar{u}) + \nu \nabla^2 (\nabla \cdot \bar{u}) \qquad (21)$$

on the right hand side of equation (4), had previously been used as a correction factor in the time marching of the discretised Navier Stokes equations (13). Consideration of the initial conditions for the water entry problem showed that such a formulation would be inappropriate.

Early in the work, simple iterative continuity solver was applied at each stage in order to overcome the above problem. Later, the SOLA algorithm was found to offer the same facility but with the added advantage of providing the dynamic pressure field. This algorithm has been well documented (23) and will not be redefined here. However, the technique was modified in order to deal with the moving boundaries and a review of these changes is given below.

The contour of each boundary was represented by simple volume source distributions. The continuity equation was, thus, re-written for any computational cell containing some part of the body contour as:-

$$\frac{u_{ij+1} - u_{ij}}{\Delta x} + \frac{v_{i+1j} - v_{ij}}{\Delta y} \qquad (22)$$

$$- \frac{\Sigma Q_m}{\Delta x \Delta y} = D_{ij}$$

where Q_m are the m sources contained within the finite difference cell

and D_{ij} is the cell divergence.

This representation of cell divergence was used to solve for the dynamic pressures and continuity condition via the SOLA code. This algorithm computed the divergence in each finite difference cell and equated it to a change in pressure given by:-

$$\delta p^k_{ij} = - D^k_{ij} / (\frac{\partial D}{\partial p'}), \qquad (23)$$

where $\frac{\partial D}{\partial p'} = \frac{1}{2\Delta t(1/(\Delta x)^2 + 1/(\Delta y)^2)}$.

The velocities at cell sides were then updated using:-

$$u^{k+1}_{ij} = u^k_{ij} - \frac{\Delta t}{\Delta x}\delta p'^k_{ij},$$

$$u^{k+1}_{ij+1} = u^k_{ij+1} + \frac{\Delta t}{\Delta x}\delta p'^k_{ij}, \qquad (24)$$

$$v^{k+1}_{ij} = v^k_{ij} - \frac{\Delta t}{\Delta y}\delta p'^k_{ij},$$

and

$$v^{k+1}_{i+1j} = v^k_{i+1j} + \frac{\Delta t}{\Delta y}\delta p'^k_{ij}.$$

It can be shown that this technique is equivalent to a relaxation solution to the pressure equation given by:-

$$- \nabla^2 p'_{ij} = \frac{\partial}{\partial t} D_{ij}. \qquad (25)$$

By analogy with the pressure wave equation:-

$$\nabla^2 p = \frac{1}{c^2}\frac{\partial^2 p}{\partial t^2} \qquad (26)$$

the change in source strength may be directly related to the pressure field, given that the time step is calculated using the formula:-

$$\Delta t^2 = \frac{1}{2c^2(1/(\Delta x)^2 + 1/(\Delta y)^2)} \qquad (27)$$

The wave phase speed was taken as that given by the shallow water formula:-

$$c = \sqrt{g.d} \qquad (28)$$

where $g = 9.81 ms^{-2}$

and h = depth of the fluid.

The complete computational cycle is shown in fig. 3. It is a simple explicit time marching method which will be familiar to users of the SOLA scheme. A Poisson pressure solver is included for the 'steady' pressure field given by:-

$$-\nabla^2 p' = \left(\frac{\partial u}{\partial x}\right)^2 + 2\frac{\partial u}{\partial y}\frac{\partial v}{\partial x} + \left(\frac{\partial v}{\partial y}\right)^2 \qquad (29)$$

A discretised form of this equation was solved using successive over-relaxation. It will also be noted that stages are included which cover the moving of the body and free-surface and the associated book-keeping routines.

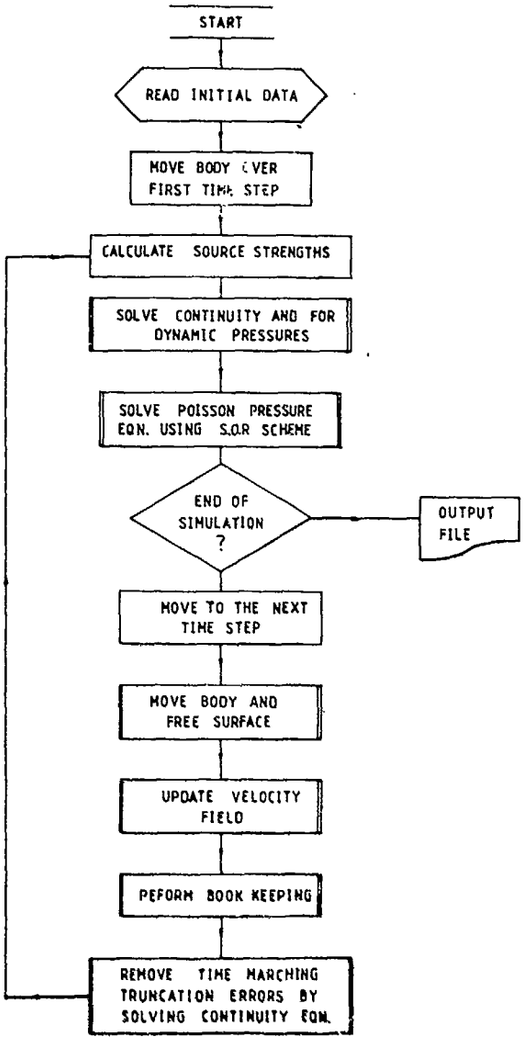

Fig. 3 Complete Computational Cycle

Book-keeping

The major task of the book-keeping routines was to keep track of the shape of the computational domain. It has already been noted that a volume fluxing algorithm was employed to track the free surface shape and an analogous method was used to follow the position of the body. As with the VOF method (19), a fluid fractional volume was defined for each cell as:-

$F_{ij} = 1.0$ - 'full' computational cell

$0 < F_{ij} < 1.0$ - 'surface' computational cell

$F = 0.0$ - 'empty' computational cell

Similar body fractional volumes (FB) were defined to represent the interface between fluid and the (solid) moving boundary.

The computation of the fluid fractional volume at each time step followed a similar method to that employed in the Volume of Fluid method. A transport equation in F:-

$$\frac{\partial F}{\partial t} + u\frac{\partial F}{\partial x} + v\frac{\partial F}{\partial y} = 0 \qquad (30)$$

was discretised in order to supply an explicit time marching formula for the fluid fractional volume. For the control volumes shown in fig. 2, the equation was re-written in conservation form as:-

$$\frac{\partial F}{\partial t} + \frac{\partial Fu}{\partial x} + \frac{\partial Fv}{\partial y} - F\nabla.\bar{u} = 0 \qquad (31)$$

For full cells $\nabla.\bar{u}$ was equal to zero such that the change in F could be equated to volume

fluxes in and out of the cell and was identically zero. For free surface cells, this was not the case. It was found that, centrally differenced schemes for the terms in equation (31) resulted in a simple exchange of fluid between cells. In these cases, equation (31) reduced to equation (30) without the use of the correction term $F\nabla.\bar{u}$. Upwinded schemes required that the correction term be included in order that the transport equation be identically satisfied.

It should be noted that the form of equation (30) is similar to the free-surface kinematic condition given by:-

$$\frac{\partial \eta}{\partial t} = v - u\frac{\partial \eta}{\partial x} \tag{32}$$

For near horizontal free surfaces, it is clear that:-

$$\frac{\partial F}{\partial x} \alpha \frac{\partial \eta}{\partial x}$$

The analogy also shows that a careful evaluation of $\partial F/\partial y$ is required in order to retain accuracy. The VOF technique uses a one-sided or donor-acceptor differencing scheme to overcome this problem. In this work, it was found unnecessary to follow such a method. A book-keeping check was employed to examine the orientation of the free surface relative to the cell. The resulting computation dealt with the discontinuous nature of the function F normal to the free surface in simple and convenient manner (24).

The updating of the body fractional volume was a much simpler task. Owing to the use of discrete sources to represent the motion of the body, the change in body fractional volume at each time step was simply given by:-

$$\Delta FB = \Delta t(\Sigma Q_m)/\Delta x\Delta y \tag{33}$$

where ΣQ_m represents the sum of source strengths within the computational cell.

When the body fractional volume reached a value of 1.0 (to within some fixed computational tolerance) within any finite difference cell, that particular cell was excluded from any further computation. Any cell with FB equal to one was fully within the fluid.

A particularly interesting situation arose when both:-

$$0 < F_{ij} < 1 \quad \text{and} \quad 0 < FB_{ij} < 1$$

For the water entry problem, this condition defined the position of the spray root.

The Variational Energy Balance

A technique (21) which proved useful in bounding the total energy of the system and, hence, supressing numerical instabilities, was derived from the work of Sasaki (20).

The variational statement for fluid kinetic energy:-

$$J = \Sigma(\alpha(u - \hat{u})^2 + \alpha(v - \hat{v})^2)\Delta x\Delta y + \lambda(\Sigma\tfrac{1}{2}\rho(u^2 + v^2)\Delta x\Delta y - KI) = 0 \tag{34}$$

may be made,

where u,v are the final discrete solution,

$\hat{u},\hat{v}$ are the approximate discrete solution,

α is an unknown weighting function,

and λ is the Lagrange multiplier

KI is given originally as the initial kinetic energy of the fluid but may be adjusted to account for free surface potential energy and work done on the system.

Differentiation of equation (34) allows the formulation of a correction factor or fractional adjustment rate x to be made:-

$$x^2 = \frac{KI}{\Sigma\tfrac{1}{2}\rho(\hat{u}^2 + \hat{v}^2)\Delta x\Delta y} \tag{35}$$

Furthermore, this may be used to compute the final discrete solution (u,v) from the values of (us,v), thus:-

$$u = \frac{2\alpha\,\hat{u}}{2\alpha + \rho\lambda} = x\,\hat{u} \tag{37}$$

$$v = \frac{2\alpha\,\hat{v}}{2\alpha + \rho\lambda} = x\,\hat{v} \tag{36}$$

It was not necessary to apply the corrections at every time step to avoid numerical instability though the simplicity of the method generally allowed this to be done without dramatically increasing the computational time.

Experimentation With Numerical Models

Two simple flow models were defined in order to study viscous free surface flows and the SOLA/Source method. From an earlier model (25) a great deal was learned concerning the use of the free surface height convection/volume fluxing routines with this particular code.

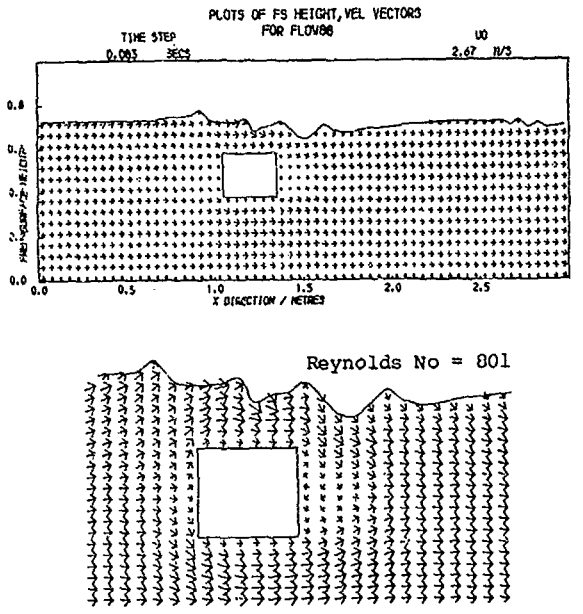

Fig. 4 Viscous Flow Past a Rectangular Box

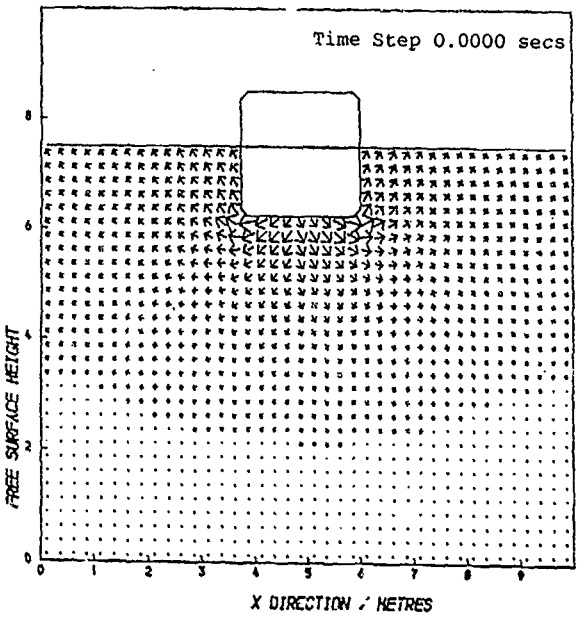

Fig. 6 Heaving Barge in Inviscid Shallow Water

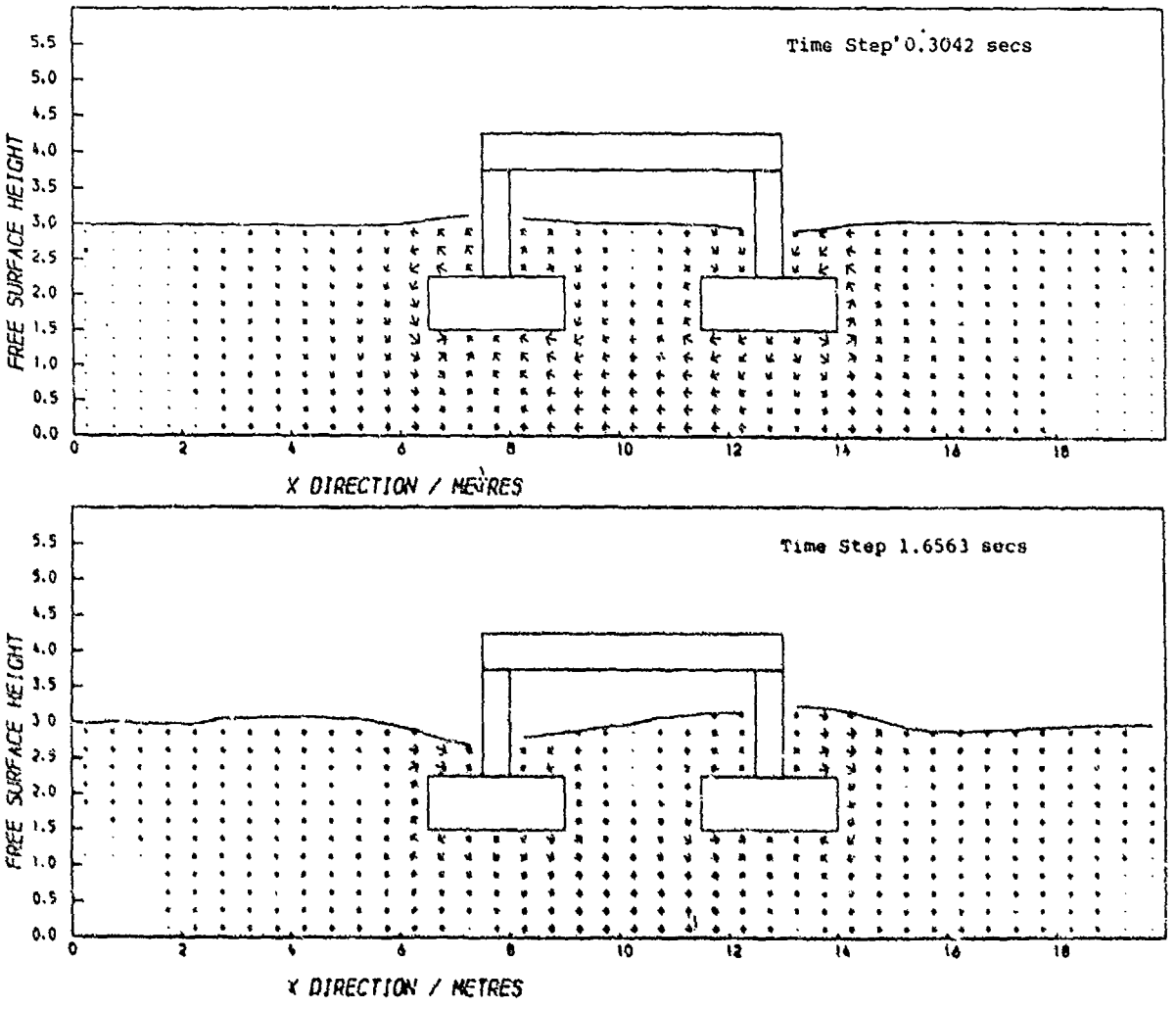

Fig. 5 Flow Past Idealised Semi-Submersible

Figure 4 shows the typical problem of viscous flow past a rectangular prism beneath a free surface at a Reynolds number of 800. Two bound vortices may clearly be seen behind the box.

The mesh size for this computation was $\Delta x = 0.05m$ and $\Delta y = 0.025m$. A 60 x 40 mesh was used which severely taxed the computational resources available. Regretably, it was conceded that this situation was unlikely to change during the course of the research and that most modelling would be confined to inviscid flows.

The SOLA/source method was applied to a number of simple problems. One such example is illustrated in fig. 5. An idealised section through a semi-submersible is defined by a collection of rectangular prisms. Discrete source points were distributed about the contour of the body to which an harmonic roll/heave motion could be applied. The strength of each source was calculated from the resultant local normal velocity vector. The time step was chosen based on equations (27) and (28) (Reference (26)).

A Similar type of problem was examined using the code designed to simulate the water entry problem. Figure 6 shows the initial time step for the solution of the inviscid flow about a heaving barge in shallow water. A series of computations of the added mass coefficient for this barge geometry for various beam to draught and draught to depth ratios were made. Figure 7 shows a comparison of these results with those given by Newman and Flagg (27). The comparison shows that an acceptable level of accuracy was achieved with a tolerance on $\nabla.\vec{u}$ of 10^{-3}.

Finally, an example of the capabilities of program SLAM is presented. This algorithm contained all the features mentioned thus far. The example of the water entry of a circular cylinder is chosen in order to illustrate the use of the SOLA/source algorithm in computing the flow about a curved boundary on a rectangular finite difference grid. Some 360 discrete sources were placed around the contour of the cylinder. A fairly coarse mesh of 0.1 x 0.1m was chosen on a 3.0m deep by 6.0m wide computational domain. The cylinder was of 1m radius.

Figure 8 shows a number of flow visualisations of the water entry of the cylinder. Only alternate velocity vectors are plotted for clarity.

Figure 9 shows a plot of the slam coefficient history versus the non-dimensional immersion given by:-

$$\frac{V_b^2}{D} \qquad (38)$$

where V_b is the impact velocity of the body

t is the elapsed time

and D is the cylinder diameter (2.0m)

A comparison with the time histories deduced experimentally by Campbell et al (28) and the formulae given by Kaplan and Silbert (29), with and without a spray root correction, show good agreement.

Further computations were carried out using ship shaped sections, details of which may be found in Reference (24). It was difficult to find data for slam load time histories from other sources in order to form a basis for comparison. However, in most cases a separate load time history was computed using a rate of change of added virtual mass approach. A Lewis form three parameter mapping technique was used to generate the added mass values at various draughts.

The total slam load could then be computed using the well-known formula:-

$$F_S = \frac{dM_a}{dz} V_b^2 \qquad (39)$$

where F_s is the slam force

M_a is the added virtual mass at draught z

The present method tended to predict higher loadings, perhaps as a result of the presence of the spray root.

III Studies on Air Entrapment

Introduction

An investigation was carried out in order that the solution procedure for the equations of mass and momentum conservation in the air layer strapped beneath a bluff body during impact could be studied in isolation. It was hoped that some insight could be gained as to how to treat the air layer in the post-impact phase of a slam. In particular, some knowledge concerning the thickness of the layer and the magnitude and distribution of pressure was required.

Once satisfied that a consistent numerical model had been developed, a parametric study was undertaken to produce pressure and load time histories for bodies of varying geometry. A further study was carried out into the effect of three-dimensional flow modelling upon the load time histories for the air entrapment problem.

Potential Flow Model of Free Surface Behaviour

Figure 10 shows the fluid domain for the air entrapment problem along with the initial

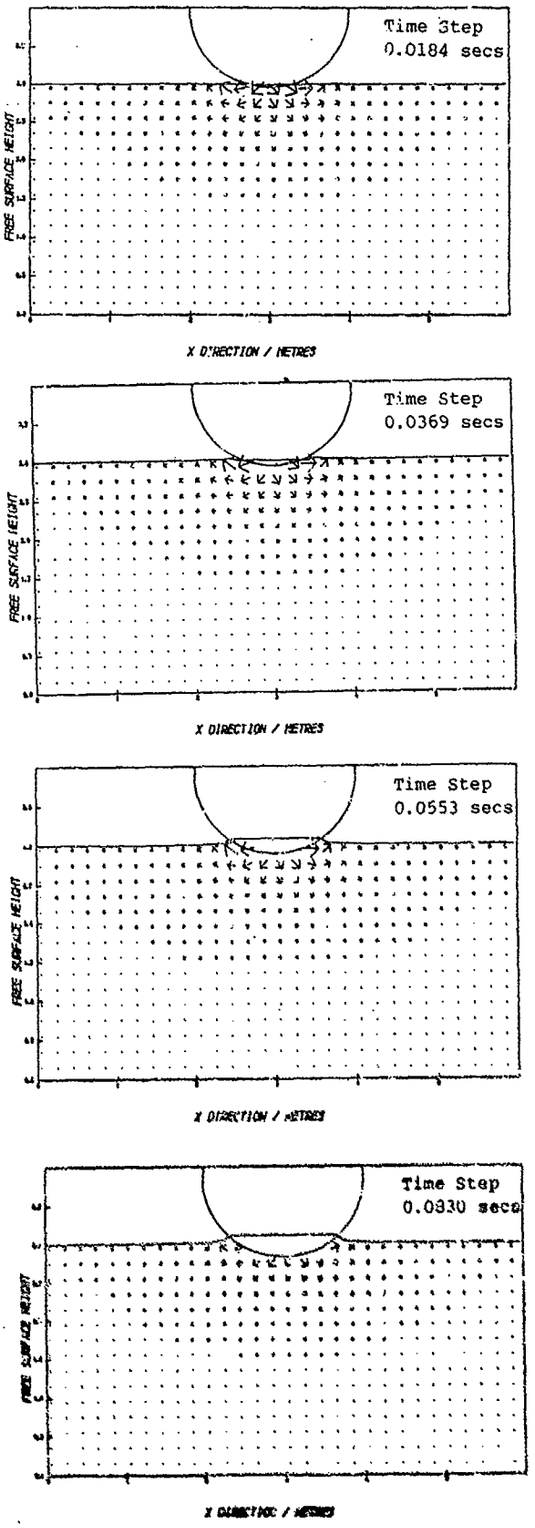

Fig. 8 Flow visualisation of Water Entry of cylinder

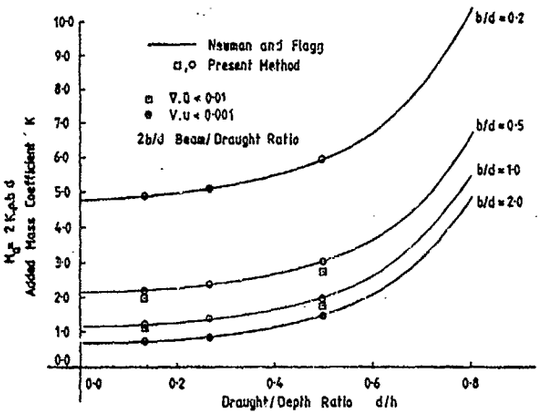

Fig. 7 Added Mass Coefficient for Heaving barges

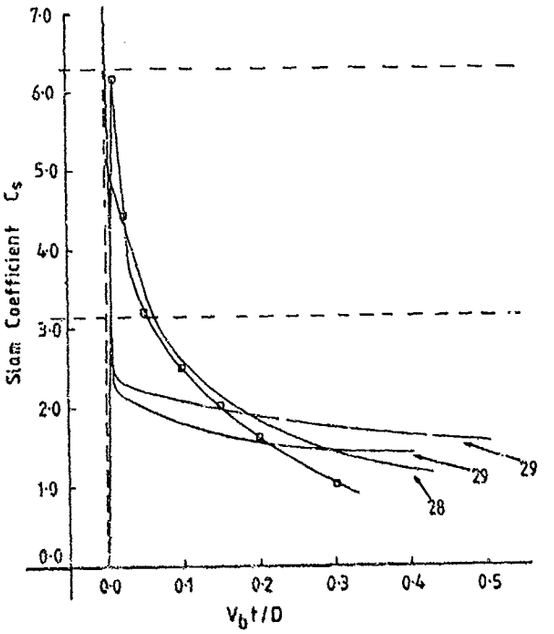

Fig. 9 Comparison of Slam Coefficient Time History

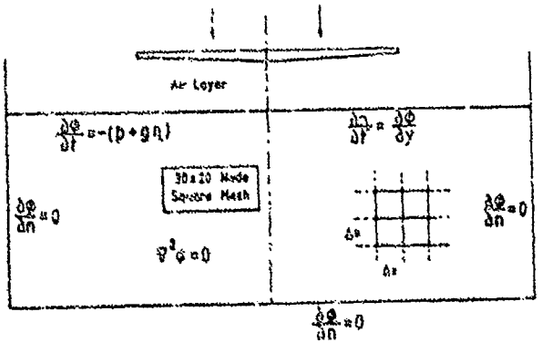

Fig. 10 Fluid Domain for Air Entrapment Problem

conditions for the variables in the air layer. Laplace's equation:-

$$\nabla^2\phi = 0 \qquad (40)$$

was to be solved over the fluid domain, with free slip zero normal flux conditions on the two side and bottom boundaries and the potential at the mean free surface level found from Bernoulli's relationship:-

$$\frac{\partial\phi}{\partial t} + g\eta + \frac{p_a}{\rho_a} \qquad (41)$$

where η is the free surface height

p_a is the pressure in air layer

and ρ is the density of water.

The free surface height is found via the linearised free surface kinematic condition:-

$$\frac{\partial\phi}{\partial t} = v = \frac{\partial\phi}{\partial y} \qquad (42)$$

Equations (40) to (42) were introduced into the time marching simulation via the following time marching procedure. The potential on the free surface at each time step was computed as:-

$$\phi^{n+1}_{ix,j} = \phi^{n}_{ixj} - \Delta t(g\eta^{n} + \frac{p_a}{\rho}^{n})_j \qquad (43)$$

A recursive relationship for the potential within the fluid domain was formulated using successive over relaxation, thus:-

$$\phi^{K+1}_{ij} = (1-w)\phi^{K}_{ij} - \frac{w}{2(1+\beta^2)}(\phi^{K}_{ij+1} + \phi^{K+1}_{ij-1} + \beta^2(\phi^{K}_{i+1j} + \phi^{K+1}_{i-1j})) \qquad (44)$$

applied to $1 < i < ix-1$

$1 < j < jx$

where ij represents the node numbering system in the x and y directions, respectively.

w is the SOR relaxation factor

and β is the mesh ratio $\Delta x/\Delta y$.

A regular 30 x 20 mesh was used to discretise the fluid domain and it was found that the discrete residual of the Laplace equation could be reduced to a value of the order 10^{-8} within one thousand iterations.

The free surface height was computed using the explicit formula:-

$$\eta^{n+1}_{jx} = \eta^{n}_{j} + \Delta t(\phi^{n}_{ix,j} - \phi^{n}_{ix-1,j})/\Delta y \qquad (45)$$

One Dimensional Equations for Air Layer

A one dimensional model of the air layer as shown in fig. 11 was chosen in order to remove the problems associated with mesh contraction along the y axis.

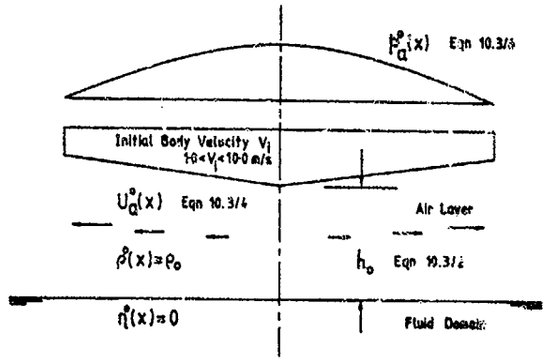

Fig. 11 Initial Conditions for Air Entrapment Problem

This approach is well documented (8,9,10) and was thus considered suitable for the test program to be carried out. Mass conservation may be expressed as:-

$$\frac{\partial(\rho_a h)}{\partial t} + \frac{\partial}{\partial x}(\rho_a u_a h) = 0 \qquad (46)$$

where ρ_a is the density of air layer

h is the air gap thickness

and u_a is the air velocity.

One dimensional conservation of momentum was given by:-

$$\frac{\partial u_a}{\partial t} + u_a\frac{\partial u_a}{\partial x} = -\frac{1}{\rho_a}\cdot\frac{\partial p_a}{\partial x} \qquad (47)$$

where p_a is the pressure in the air layer.

At any given instant the rate of change of the thickness of the air layer was expressed as:-

$$\frac{\partial h}{\partial t} = v_b - \frac{\partial\eta}{\partial t} \qquad (48)$$

Equations (46) to (48) provided the means to solve for the four unknowns u_a, p_a, h and η if a convenient relationship between pressure and density could be found. In practice, the adiabatic formulation:-

$$\frac{p_1}{p_2} = \left(\frac{\rho_1}{\rho_2}\right)^{\gamma} \qquad (49)$$

where $\gamma = 1.4$, the ratio of specific heats, was applied successfully.

Many numerical schemes were experimented with, the full details of which may be found in Reference (24). The most robust methods used a simple explicit time marching formulation and central differencing for the convection terms.

The air layer was split up into a one dimensional finite difference mesh. The mesh was staggered, with U_a nodes at cell sides and h, p_a and ρ_a at cell centres. The pressure nodes coincided in the vertical plane with the free surface potential nodes.

The computational cycle proceeded as follows. The rate of change of air gap thickness (h) was computed first using a discrete form of equation (48):-

$$\left(\frac{\Delta h}{\Delta t}\right)_j = V_b - (\eta_j^n - \eta_j^{n-1})/\Delta t \qquad (50)$$

The velocity field (u_a) was then updated using a backward time step central difference formulation, ie:-

$$u_{aj}^n = u_{aj}^{n-1} - \frac{\Delta t}{2\Delta x} u_{aj}^{n-1} (u_{aj+1}^{n-1} - u_{aj-1}^{n-1}) - \frac{\Delta t}{\Delta x \bar{\rho}_{aj}^{n-1}} (p_{aj+\frac{1}{2}}^{n-1} - p_{aj-\frac{1}{2}}^{n-1}) \qquad (51)$$

where $\bar{\rho}_{aj}$ is the mean density at velocity node j, ie:-

$$\rho_{aj} = \tfrac{1}{2}(\rho_{aj+\frac{1}{2}} + \rho_{aj-\frac{1}{2}})$$

Having updated the velocity field, the discrete density values were updated using the following backward time step, central difference expression:-

$$\rho_{aj}^n = \rho_{aj}^{n-1}\left[1 - \frac{\Delta t}{h_j^{n-1}}\left(\left(\frac{\Delta h}{\Delta t}\right)_j^{n-1} + \frac{\bar{u}_{aj}^{n-1}}{2\Delta x}(h_{j+1}^{n-1} - h_{j-1}^{n-1})\right)\right] - \frac{\bar{u}_{aj}^{n-1}\Delta t}{2\Delta x}\left(\rho_{aj+1}^{n-1} - \rho_{aj-1}^{n-1}\right) - \frac{\rho_{aj}^{n-1}\Delta t}{\Delta x}\left(u_{aj+\frac{1}{2}}^{n-1} - u_{aj-\frac{1}{2}}^{n-1}\right) \qquad (52)$$

where $\bar{u}_{aj}$ is a mean velocity at pressure node j.

The pressure field was then calculated directly using the identity:-

$$\frac{p_{aj}^n}{\rho_{aj}^n} = \frac{p_o}{\rho_o} = C_a^2 \qquad (53)$$

where $C_a = 330 ms^{-1}$.

These pressure values were then used:-

a. to compute the total load on the body

b. in equation (43) to calculate the free surface potential for the next time step.

Figure 12 shows a full flow chart for the computational procedure. A time step of 1.25×10^{-4} was used initially, the full simulation requiring some 100 steps in total.

Numerical experiments were also carried out with a model which included energy transport within the air layer. Few conclusions could be made, however, owing to the lack of information concerning dissipation mechanisms within the flow.

Further studies were carried out with a two-dimensional air layer model coupled to a three-dimensional fluid domain. Figure 13 shows the nodal arrangement for this model. The equations of motion for the air layer were identical to those already given except for the extra terms used to accommodate the variable V_a. The numerical procedure was similar to that previously described. The results of using this model are discussed in a later section.

Results From Simulations Using the One Dimensional Air Entrapment Model

Having run the simulation for a number of different deadrise angles, initial impact velocities and mass loadings, it was realised that there were four possible impact scenarios to be considered prior to including air entrapment in the hydrodynamic slamming model.

These were:-

a. full air entrapment with pressure peak before contact,

b. full air entrapment, pressure peak after contact,

c. air cushioning only, pressure peak before contact,

d. air cushioning only, pressure peak after contact.

Figure 14 shows a plot of the dowsing of beta air as a function of the deadrise angle and the 'momentum per unit area'. It can be seen that plates with deadrise angles (β) up to 0.25° always trapped air. Above this value of

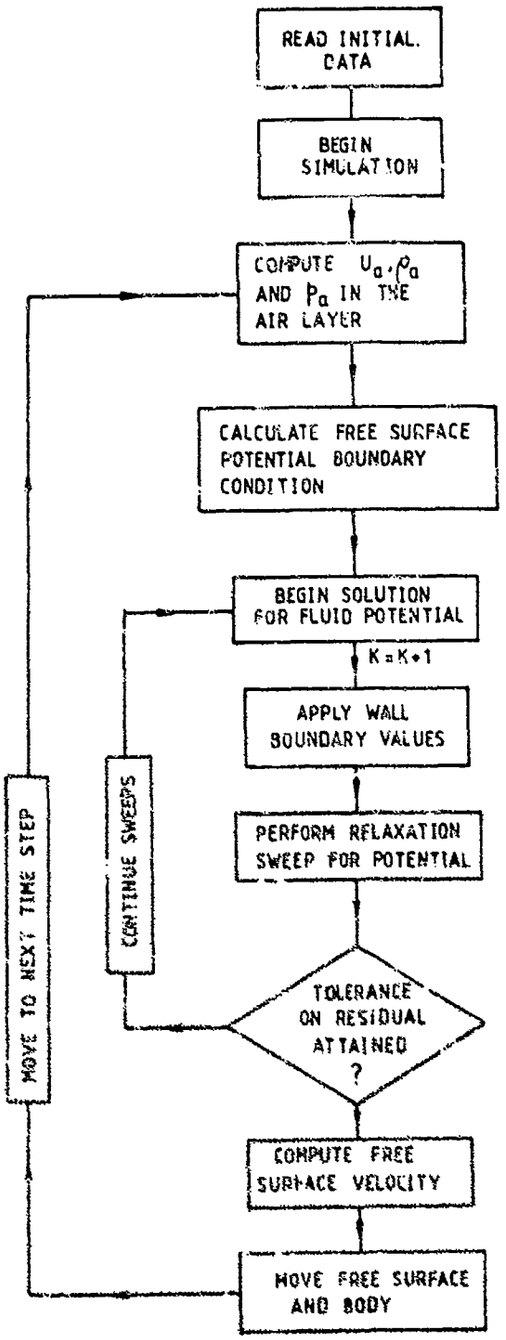

Fig. 12 Flow Chart for Air Entrapment Simulation

the type of impact scenarios depended upon the mass of the body and its initial velocity. Plates with low mass loadings managed to trap air and experience a pressure peak with deadrise angles of up to 2.5°. Pressure peaks could also be experienced for intermediate plate loadings for deadrise angles up to 5°.

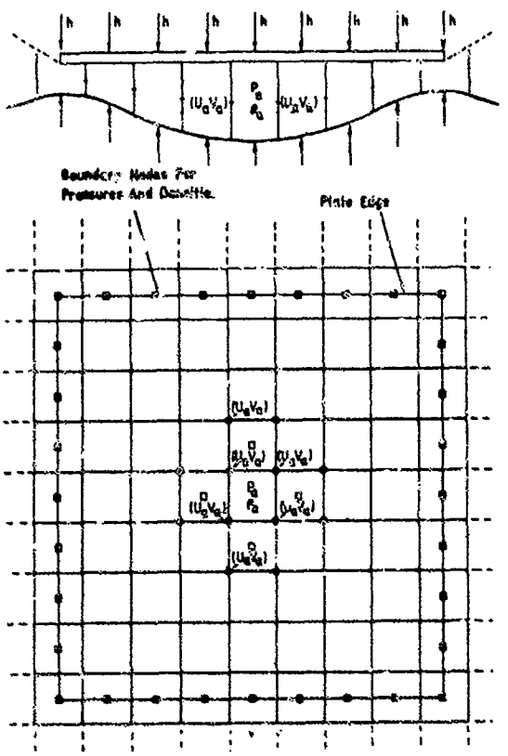

Fig. 13 Arrangement of Nodes and Principal Variables for Three-Dimensional Air Entrapment Simulation

No pressure peaks were experienced for 'heavy' mass loadings though it should be noted that, below deadrise angles of 5.0°, the free surface managed to gain a downward component of velocity at the centreline. This reduced the effective impact velocity and would need to be taken into consideration in design of a unified water entry code.

It became clear that full consideration of all such possible scenarios would be difficult to include in a single code dealing with slamming impact.

Figure 15 shows a typical time history/ pressure distribution from impact scenario d. The horizontal and vertical scales are distorted for clarity, hence the deadrise angle appears greater than its actual value of 1.0°.

Where possible, ie impact categories a. and c., slam load coefficients and peak pressure coefficients were computed as:-

$$K_L = F_{max}/\rho V_i^2 b^2 \qquad (54)$$

$$K_p = p_{max}/\rho V_i^2 \qquad (55)$$

where V_i is the initial impact velocity

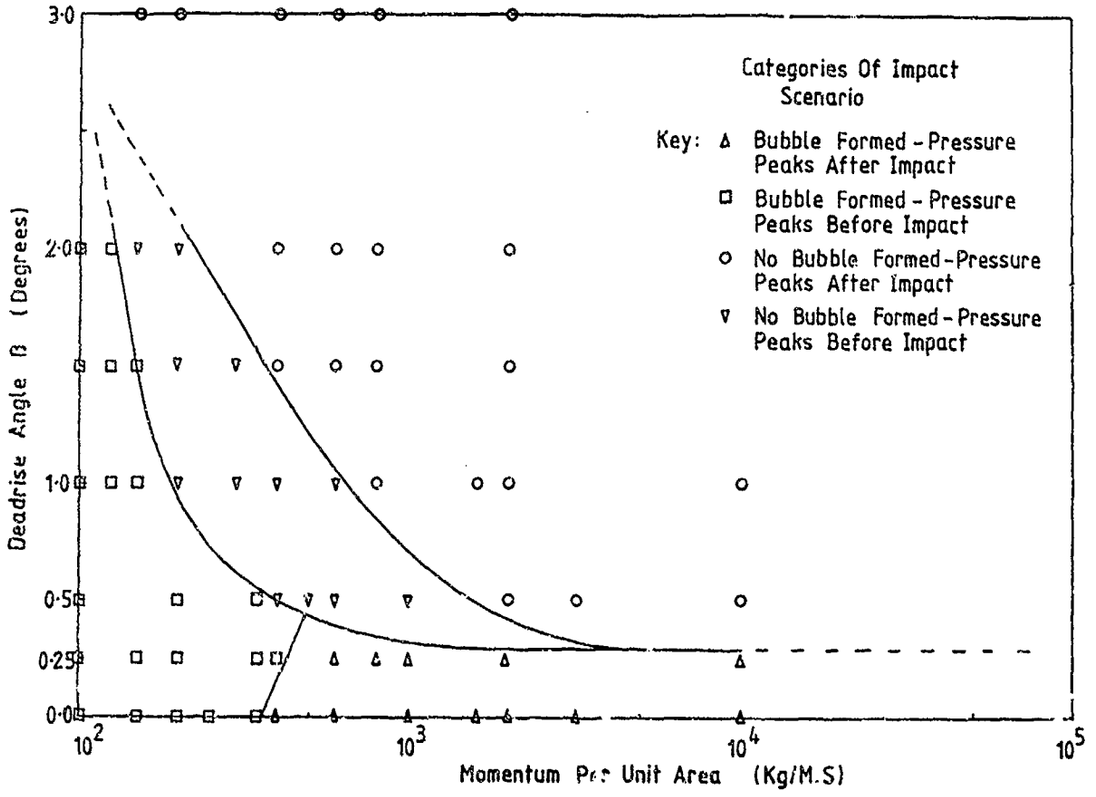

Fig. 14 Domains of Behaviour

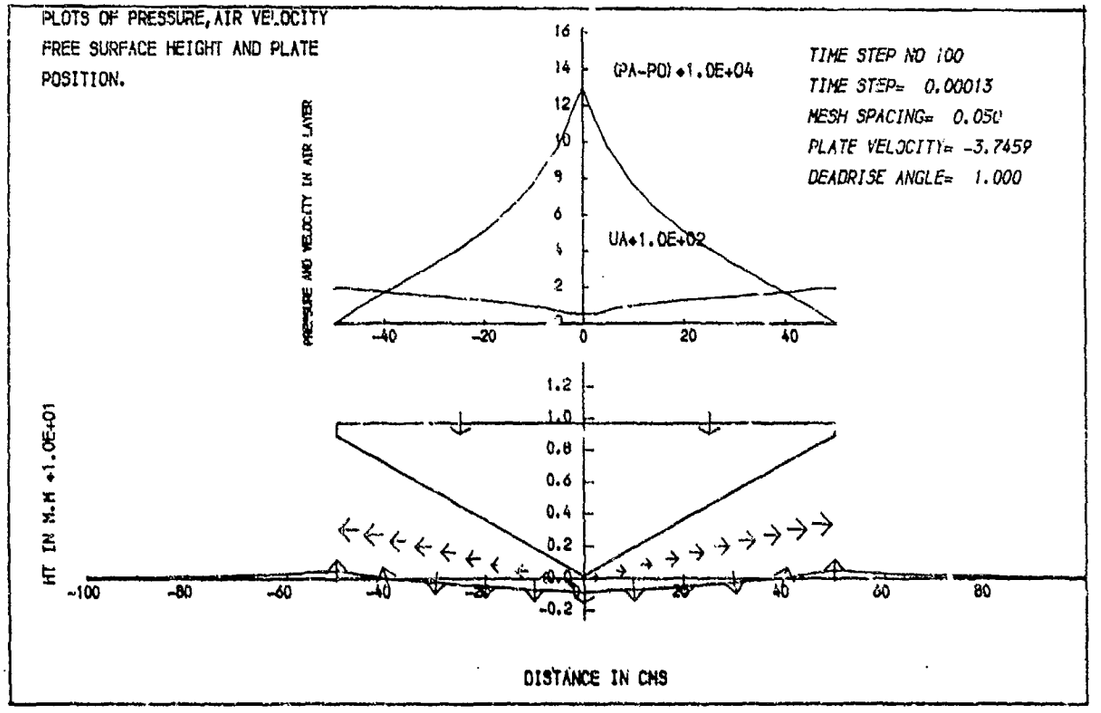

Fig. 15 Typical Time History Pressure Distribution for Case d.

ρ is the density of the water

and b is the beam of the section.

Figure 16 shows a plot of peak load versus the square of the impact velocity, confirming equations (54) and (55) as the basis of the slam coefficients for these light impacts.

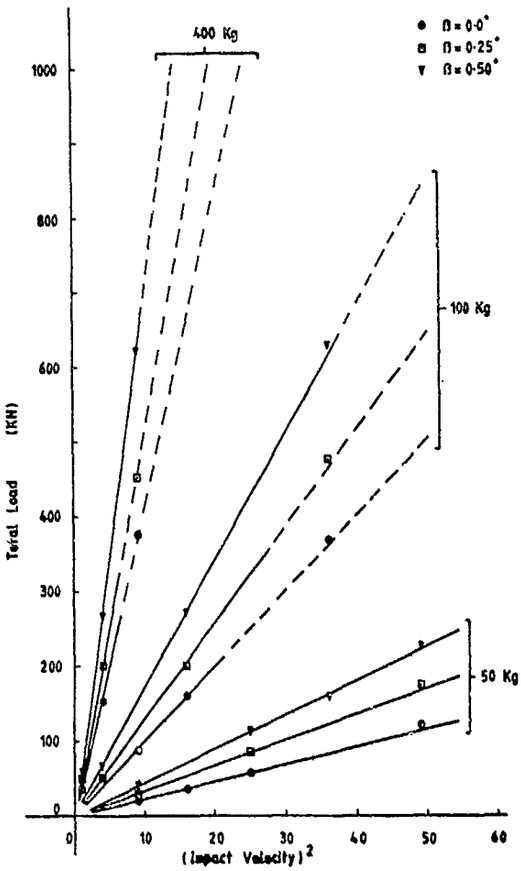

Fig. 16 Plots of Total Load Versus Impact Velocity Squared

The most likely candidates for air entrapment impact scenarios at sea were considered to be cased b. and d., both of which represent 'heavy' impacts, with pressure peaks occurring after impact. It was thought most profitable to orientate the future work toward these two types of impact.

A further study was carried out upon the effect of section curvature. Figure 17 shows free surface shape and pressure distribution in the air layer for the impact of a circular section of radius 10.0m. The computational domain for the air layer was restricted to the region where the modulus of the tangent to the section made an angle of less than 30^{0} with the horizontal. Beyond this the air layer was assumed to behave as a divergent jet.

The most conspicuous problem associated with this type of impact was the way in which the free surface seemed to, in the limit, match the contour of the cylinder. Studies were carried out with varying mesh size in both the fluid domain and the air layer. However, it was impossible to come to any conclusion as to which category, b. or d., this type of impact fitted. Certainly, for this type of idealised model it seemed possible that simultaneous contact could occur over a substantial portion of the width of the section. In such an event, could it also be possible for the relative normal velocity between the body and free surface to be zero? If this were so then the peak loading on the cylinder would be a function of the initial air cushioning phase and not the water entry phase.

In practice, these idealised conditions would never exist. Surface roughness and imperfections caused by marine growths, etc would have a significant role to play in the evolution of the load time history. However, the phenomena described above would need to be reconciled before any unified hydrodynamic/air entrapment model could be designed.

Results From Two-Dimensional Air Layer Model

Running the two-dimensional air layer model coupled to the discretised three-dimensional fluid domain proved highly problematical owing to the large amount of computing time required. A 30 x 30 x 20 node mesh was used for the potential flow solution to the fluid domain. A typical 100 time step simulation required 40,000 seconds CPU on the University of Glasgow ICL 2988 mainframe computer. This restricted the size of any parametric surveys.

Eight tests were run in total. The first four used a 'light' mass loading of 50kg on a 1.0m x 1.0m square plate. Initial impact velocities of 2, 3, 4 and $6ms^{-1}$ were used. Another four tests were run with a high mass loading of 1000kg and an initial impact velocity of $4ms^{-1}$. Various plate aspect ratios were used during these computations in order to ascertain the effect of two-dimensionality upon the quantity of air entrapped.

Figure 18 shows a plot of the free surface distortion at the instant of contact between the 50kg square plate and the fluid. The computer generated graphics have distorted the relative dimensions. However, the depth in the middle is 1.4mm and the height at the edges is some 0.5mm. Figure 19 shows the corresponding pressure distribution over the base of the plate.

Figure 20 shows the effect of the use of a two-dimensional model upon the load time history for the 50kg plate. The peak loading is quite clearly reduced by some 30%.

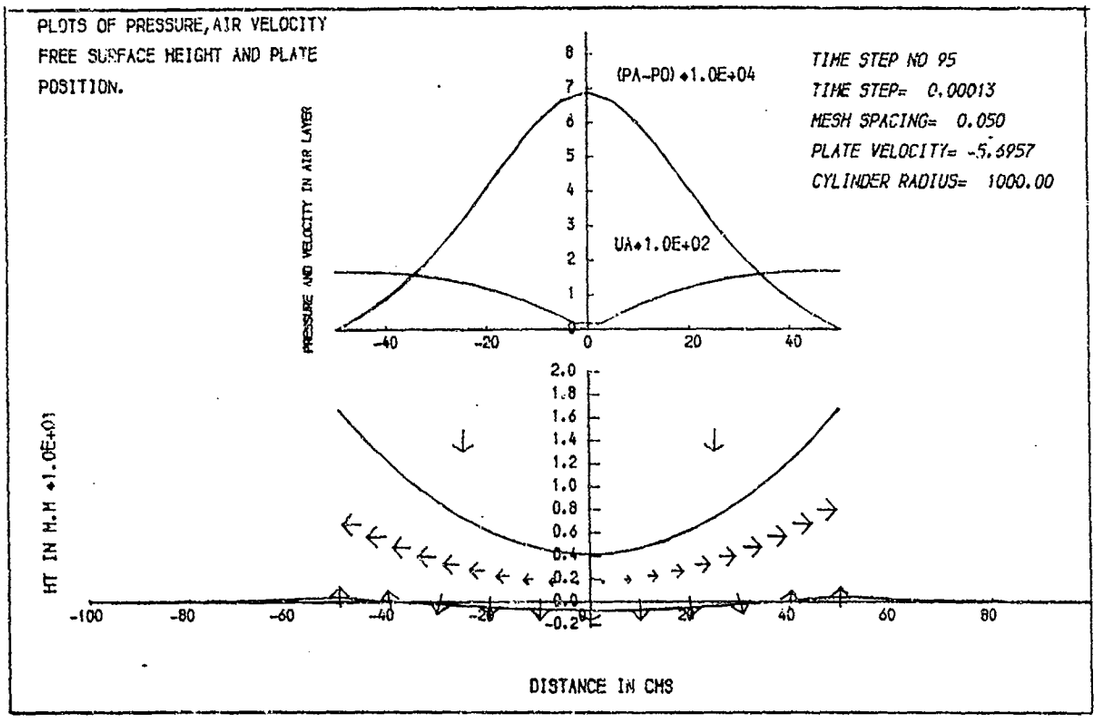

Fig. 17 Free Surface Pressure Distribution in the Air Layer for the Impact of a Circular Cylinder

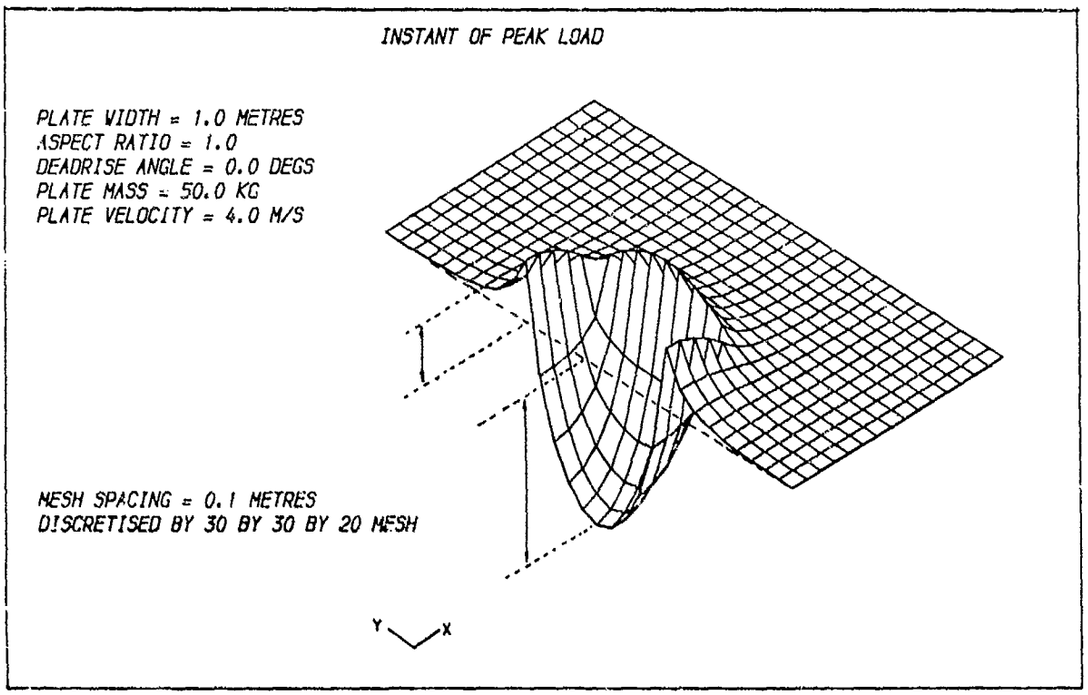

Fig. 18 Free Surface Distortion at Incident of Contact

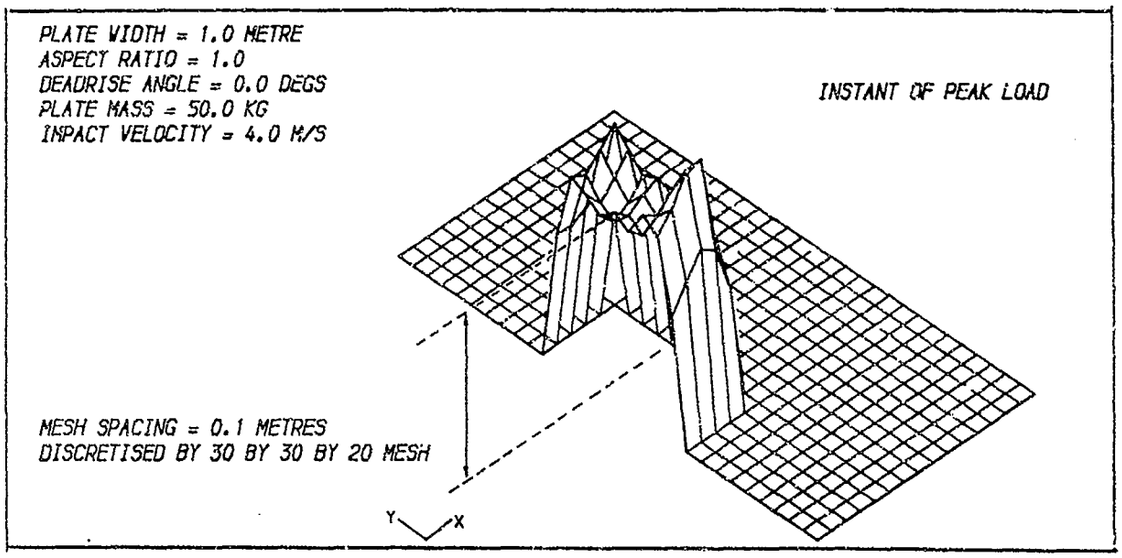

Fig. 19 Pressure Distribution over the Base of the Plate

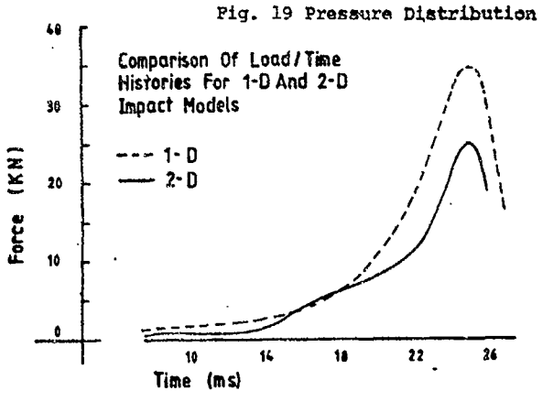

Fig. 20

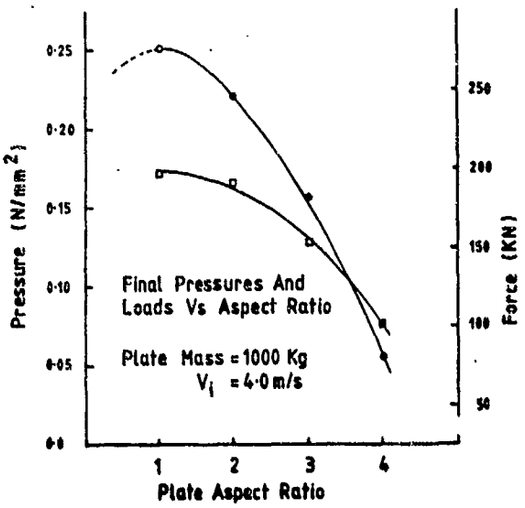

Fig. 21

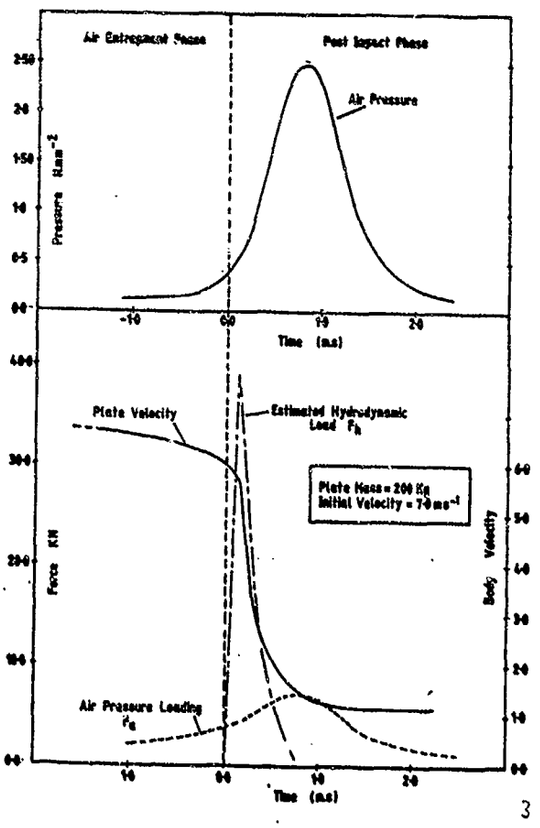

Fig. 22 Typical Impact Load Time History

Finally, fig 21 shows the effect of aspect ratio on peak pressures and loads for the 1000kg plate. As expected, the peak load is experienced on a square plate. The slam load is progressively reduced as the aspect ratio is increased (for constant plate area).

It was concluded that, ultimately, any unified hydrodynamic slam code would need to include the effects of three-dimensionality.

Post Contact Behaviour of Flat Plates

In order to further study the load time history for impact scenario b. and as a preliminary study prior to designing the full impact simulation model, a simplified post processor for the flat plate impact simulation was written.

The trapped air bubble was considered to move with the plate such that a simple gas-spring analogy could be used to compute the pressures within it. A number of further assumptions were made:-

a. The bubble could be represented by a half elipse with major axis b and minor axis h, the air gap thickness along the centreline.

b. During compression, the ratio b/h remained constant.

c. The total added mass for the plate was given by:-

$$M_a = \rho\pi(B - b)^2 \qquad (56)$$

where b = half beam of plate.

d. The resulting hydrodynamic load was generated by the rate of change of added mass:-

$$\frac{dM_a}{dt} = -2\rho\pi(B - b)\frac{db}{dt} \qquad (57)$$

e. The total load on the body consisted of the hydrodynamic load:-

$$F_h = \frac{dM_a}{dt} V_b \qquad (58)$$

and the load generated by compression of the air bubble:-

$$F_a = 2p_a b \qquad (59)$$

The pressure in the air layer was computed using the rate of decrease of bubble volume. Consideration of the particular choice of an eliptical air bubble and constant b/h ratio allowed the change in density and, hence, pressure to be computed using:-

$$\rho_a^{n+1} = \rho_a^n\left(1 - 2\Delta t\left(\frac{dh}{dt}\right)^n / h^n\right) \qquad (60)$$

The resulting simulation was fully interactive. The acceleration of the body being computed using:-

$$\frac{dV_b}{dt} = (F_h + F_a)/(M_b + M_a(t)) \qquad (61)$$

Figure 22 shows a typical impact load time history using the above algorithm. The initial conditions were derived from the last few time steps of the equivalent air entrapment simulation. It had been noted, during the previous work that the total kinetic energy gained by the fluid behaved asymptotically with increasing mass loading on the body. Using the velocity of the body as a representative value, an equivalent added mass was computed which was found to be nearly constant at some 12% of the added mass of the flat plate when fully submerged. This value was used as the initial added mass and an effective value of wetted surface/bubble width, b, could be deduced.

Figure 22 was derived from the results for the post impact behaviour of a 200kg plate with an initial impact velocity of $7.0ms^{-1}$. Although the absolute magnitudes differ, the load time history is very similar in form to those measured by Lewison and Maclean (9).

It was felt that this type of model provided a great deal of useful information concerning pressure (load time histories), peak values, rates of change of bubble size, etc. It was at this point that it was felt that enough data had been gathered to design an air entrapment/ hydrodynamic impact model using the techniques described so far.

IV. Full Hydrodynamic/Air Entrapment Model

The previous sections have described the results of a number of fluid flow modelling exercises which were undertaken in order to understand, and hopefully solve, the problems associated with computing the slam loading on a ship section. It was noted that, from the experiments with the air entrapment routine, there were two candidates for the role of the air layer within the calculation.

Firstly, flat or near flat sections falling toward the free suface would set the fluid in motions, eventually forming an entrapped air bubble at the point of impact (case b.). Secondly, the air layer may serve to set the free surface in motion prior to first contact and yet form no air bubble (case d.). Each of these two cases were to be dealt with separately.

Case d. was clearly the easiest to deal with first. As no air bubble was formed, the last time step from the air entrapment simulations could be used as a set of initial conditions for program SLAM. If confirmation that no air bubble would form for the impact of a curved section, this case could also be dealt with in this way.

It was proposed that case b. would be modelled using similar assumptions to that used in the post impact processor described in the last section. In particular, a simple gas-spring model would be used to compute the (initially uniform) pressure within the trapped air bubble. A secondary row of sources would cover the outer contour of the air bubble. The velocity of the sources would be a function of the body velocity and buble dynamics.

It would be these sources that would be used in equation (22) and the modified SOLA/source algorithm. The pressure in the air layer would be used as a Drichelet boundary condition on the Poisson pressure solver. The thickness of the bubble layer (< 5mm) dictated that the above quasi-empirical approach was more appropriate owing to the mesh dimensions used in the computation.

Unfortunately, time and funds ran out before this work could be completed. This was unfortunate since it is clear that very little work would be required (especially for case d.).

V. Conclusions and Future Work

This paper presents the results of work carried out at the University of Glasgow, Department of Naval Architecture and Ocean Engineering, into the hydrodynamics of slamming.

A novel method of representing the flow about a curved boundary using a rectangular finite difference mesh was developed. The technique was used to model the water entry of a circular cylinder and has been successfully applied to ship sections.

Investigations were also carried out into the effects of air entrapment on slam load histories. Two particularly relevant slam scenarios were identified as being th most likely full scale mechanisms of air cushioning. Studies into the effect of section curvature showed that the modelling of the impact of a circular cylinder on a still free surface may best be explained by taking account of the air layer.

A two dimensional air layer model coupled to a three-dimensional fluid domain illustrated how the level of peak loading could be reduced in comparison to a one dimensional air layer model.

It is clear that there is a promising future for the work described herein. An immediate priority is to carry out the studies suggested in the fourth section.

Further work should also include the development of a three dimensional version of the hydrodynamic model described in the second section. The addition of a 'Multigrid' solver may be required to reduce computing time sufficiently. Further, the study of wave slam and the effect of wave goemetry on the three-dimensional ship slamming problem should also be undertaken. Reference (26) could provide a basis for this task.

Acknowledgement

The authors wish to acknowledge the financial support given by the Science and Engineering Research Council Marine Technology Directorate and by the States of Jersey which enabled this work to be carried out. They also wish to thank Mrs Patricia Peters for typing this paper.

References

1 VON KARMAN, T, 'The Impact of Seaplane Floats During Landing', NACA TN321, Oct 29.

2 WAGNER, H, 'Uber Stoss-Und Gleitvorgenge Und der Oberflache von Flussigkeiten', ZAMM, band 12, heft 4, 1932.

3 SZEBEHELY, V G, 'Hydrodynamic Impact Applied Mechanics Review', Vol 12, 1959.

4 FABULA, A G, 'Ellipse Fitting Approximation of Two Dimensional Normal Symmetric Impact of Rigid Bodies in Water', 5th Midwestern Conf on Fluid Mechanics, Ann Arbor, Michigan, 1957.

5 BISPLINGHOFF, R L, and DOHERTY, C S, 'Some Studies of the Impact of Vee Wedges on a Water Surface', Journal of the Franklin Institute, Vol 253, 1952.

6 CHUANG, S L, 'Experiments on Flat Bottomed Slamming', Jour of Ship Research, Mar 66.

7 CHUANG, S L, 'Experiments on Slamming of Wedge Shaped Bodies', Jour of Ship Research, Sep 67.

8 VERHAGEN, J H, 'The Impact of a Flat Plate Upon a Water Surface', Journal of Ship Research, Dec 67.

9 LEWISON, G, and MALCOLM, W M, 'On the Cushioning of Water Impact by Entrapped Air', Jour of Ship Research, Vol 12, No 2, Jun 68.

10 KOEHLER, and KETTLEBOROUGH, 'Hydrodynamic Impact of a Falling Body on a Viscous Incompressible Fluid', Journal of Ship Research, Vol 23, No 3, 1977.

11 LAMB, H, 'Hydrodynamics', (6th Ed), Dover Publications, New York.

12 SCHLICKLING, H, 'Boundary Layer Theorys', McGraw-Hill, New York, 1968

13 WELCH, HARLOW, SHANNON, and DALY, 'The MAC Method', LASL Report No LA3425, 1966.

14 ORLANSKI, I, 'A Simple Boundary Condition for Unbounded Hyperbolic Flows', Journal of Computational Physics, No 21, 1976.

15 HIRT, C W, and SHANNON, J P, 'Free Surface Stress Conditions for Incompressible Flow Calculations', Journal of Computational Physics, No 2, 1968.

16 NICHOLS, B D, and HIRT, C W, 'Improved Free Surface Boundary Conditions for Numerical Incompressible Flow Calculations', Jour of Computational Physics, No 8, 1971.

17 ROACHE, P J, 'Computational Fluid Dynamics', Hermosa Publishers, Albuquerque, New Mexico.

18 RICHTMYER, R D, 'Difference Methods for Initial Value Problems', Interscience Publishers Inc, 1957.

19 NICHOLS, B D, and HIRT, C W, 'Volume of Fluid Method (VOF) for Dynamic Free Boundaries', Jour of Computational Physics, No 39, 1981.

20 SASAKI, Y K, 'Variational Design of Finite Difference Schemes for Initial Value Problems with an Integral Invariant', Jour of Computational Physics, No 21, 1976.

21 GALLAGHER, P, 'A Finite Difference Time Marching Solution of the Slamming Problem (Water Entry Problem)', Proc 3rd Intl Conf on Numerical Methods in Laminar and Turbulent Flows, Pineridge Press, 1983

22 LEONARD, B P, 'A Stable and Accurate Convective Modelling Procedure Based on Quadratic Upstream Interpolation', Computer Methods in Applied Mechanics and Engineering, Vol 9, Jun 79.

23 HIRT, C W, NICHOLS, D P, and ROMERO, N C, 'SOLA. A Numerical Solution Algorithm for Transient Fluid Flows', Los Alamos Scientific Laboratory Report LA5852, 1975.

24 GALLAGHER, P, 'Slam Simulations: An Application of Computational Fluid Dynamics', PhD Thesis, University of Glasgow, Dept of Naval Architecture and Ocean Engineering, Apr 85.

25 GALLAGHER, P, 'FLOW88. A Program to Resolve Inviscid and Laminar Flow Around Rectangular Bodies and Source Distributions Beneathe a Free Surface', University of Glasgow, Dept of Naval Architecture and Ocean Engineering, Report No NAOE-84-51, 1984.

26 GALLAGHER, P, 'NWAV90. A Program to Simulate Free Surfacxe Waves and Wave Loading on Fixed and Free Floating Structures', University of Glasgow, Dept of Naval Architecture and Ocean Engineering, Report No NAOE-84-50, 1984.

27 FLAGG, C N, and NEWMAN, J N, 'Sway Added Mass Coefficients for Rectangular Profiles in Shallow Water', Jour of Ship Research, Vol 15, 1971.

28 CAMPBELL, I M C. and WEYNBERG, P, 'Measurement of Parameters Affecting Slamming. Final Report', Wolfson Marine Craft Unit, Report No 440, 1980.

29 KAPLAN, P, and SILBERT, M N, 'Impact Forces on Horizontal Members in the Splash Zone', Offshore Technology Conf, Paper OTC 2498, 1976.

DISCUSSION
of the paper
by P. Gallagher and R.C. McGregor

"SLAMMING SIMULATIONS: AN APPLICATION OF COMPUTATIONAL FLUID DYNAMICS"

DISCUSSION
by B. Yim

This is a very interesting paper to me because the authors treated the slamming problem with viscosity while I treated the same problem without viscosity. It seems that the authors did not come across any instability in computation even when they were dealing with slamming of a circular cylinder. Yet Figure 8 shows the wave height near the cylinder without spray as in the case of Chapman's linear theory. As in the experiments by Greenhow and Lin the wave near the slamming body is quite high and breaks. Would your computations how this large breaking wave if your computation proceeded for a longer time? What were the behaviors of the spray tip and the spray root in space and time? I would like to know whether they were singular forms.

References:

Chapman R.B. 1979 "Large-Amplitude Transient Motion of Two-Dimensional Floating Bodies," J. of Ship Research 23, No.1, 20-31

Greenhow, M., and W.M. Lin, 1983, "Nonlinear Free Surface Effects: Experiments and Theory," Report No. 83-19 83-19 Dept. of Ocean Engineering, MIT.

Author's Reply

The authors thank Dr. Yim for his remarks and hope that the following reply will satisfy his questions.

Firstly we must point out that, although the numerical algorithms were developed with viscous flows in mind, owing to limitations on computational power, the impact examples presented were for an invisid fluid, as stated in the paper. For the same reasons, a fairly coarse mesh was often used and it was a result of this that no spray jet structures are visible in Figure 8. When computations were allowed to proceed for a longer time on a coarse mesh, there was evidence that it would be possible to produce a spray jet. However, these jets were of the order 1 to 2 mesh cells in width, and such computations were not considered to be accurate enough for presentation in the paper.

The position of spray tip was not implicitly investigated, though a time history of the wetted beam was produced and may be deduced from figures given in the first author's PhD thesis (reference 24 in the paper).

Finally we consider that this technique would benefit from a much finer mesh structure than that used thus far. The problems associated with the stretching of surface elements encountered in the alternative methods of Dr. Yim and Drs. Greenhow and Lin presented at this conference do not occur in the technique applied in this paper.

INITIAL ASYMPTOTICS IN CONTACT HYDRODYNAMICS PROBLEMS

A.A.Korobkin, V.V.Pukhnachov
Lavrentyev Institute of Hydrodynamics
Siberian Division of the USSR Academy of Sciences
Novosibirsk 630090 USSR

Abstract

This paper investigates an initial stage of an unsteady motion of a liquid due to the blunt body penetration into it. Initially the liquid is at rest, and the body touches its free boundary at a single point. It is appropriate to use the method of matched asymptotic expansions which allows to reduce this complicated problem to consideration of its simpliest elements, some effects, such as nonlinearity, compressibility of liquid, elasticity of a submerging structure and so on being taken into account only within the domains where they are most significant. This approach to solving the problem is applicable for investigation of a wide class of problems about the interaction between a solid body and a free surface.

Introduction

In the early thirties, the water entry problem has been subject of intensive research and development in connection with the problems of landing of flying boats. During the ensuing years, the problems of interaction between a solid body and a liquid at the presence of a free surface attract widespread attention. One has to deal with these problems in strength calculations of ships in ship building (slamming problems), in the study of liquid drop impact with a surface (the problems of erosion) and so on.

They are related to the problems of flows with variable topology. In a numerical investigation of such problems, it is necessary to distinguish the moments of time when the flow topology changes, and to investigate analytically a qualitative picture of the phenomenon with obtaining the solution asymptotics. It is appropriate to use the method of matched asymptotic expansions which allows to reduce a complicated problem to consideration of its simplest elements, some effects such as nonlinearity, compressibility and so on being taken into account only within the domains where they are most significant.

I. The entry of a blunt body into an ideal incompressible fluid

1. Initial asymptotics of the solution of a three-dimensional problem

An initial stage of unsteady motion due to entry of a solid blunt body into a liquid is considered. Initially ($t'=0$) the fluid occupies a semi-space $z'<0$ and is at rest; a solid body touches its free surface at one point $x'=0$, $y'=0$ (here and further dimensional variables are marked by a prime). The liquid is assumed to be ideal and incompressible, the gravity force and surface tension are ignored.

The solid body position in Eulerian coordinates is assumed known and is represented by

$$z' = f(x',y') - Vt', \qquad (1.1)$$

where f is the smooth function of its arguments; $f(0,0)=0$ and $f(x',y')>0$ when $x \neq 0$, $y \neq 0$. Relation (1.1) describes the body motion along z' with a constant velocity V. The main curvatures of the surface $z'=f(x',y')$ at the point $(0,0)$ are designated by k_1, k_2, and it is assumed that $k_1>0$, $k_2 \geqslant 0$, $k_1 \geqslant k_2$.

The curvature radius k_1^{-1} is taken as the length scale, and $(k_1V)^{-1}$ is taken as the time scale. Then let us come over to dimensionless variables which are designated by the above-mentioned terms without a prime. In this case Eq. (1.1) is re-written in the form $z=F(x,y)-t$, where $F(x,y) = k_1 f(k_1^{-1}x, k_1^{-1}y)$. According to the above-mentioned assumptions on the behaviour of function $f(x',y')$, it is appropriate to locate axes x, y so that the expansion in series of function $F(x,y)$ if $x \to 0$, $y \to 0$ is represented by

$$F(x,y) = x^2/2 + (k_2/k_1)y^2/2 + O((x^2+y^2)^{3/2}). \qquad (1.2)$$

In Lagrange coordinates ξ, η, ζ the domain Ω occupied by a liquid is pre-determined and represents a semi-space $\zeta < 0$. A plane $\zeta = 0$ being a boundary of this domain consists of a free surface of the liquid, Σ_1, the con-

tact area between the liquid and the solid body, Σ_2, and the contact line between them. In the Lagrange variables, the dimensionless coordinates x, y, z of a liquid particle holding a position ξ, η, ζ at t=0 are the unknown functions. However, it is more convenient to deal with the displacements X, Y, Z of the liquid particles, which are determined by the relation $\vec{X} = \vec{x} - \vec{\xi}$, where X=(X,Y,Z), x=(x,y,z) and $\vec{\xi} = (\xi, \eta, \zeta)$.

Since the external mass forces are absent, and the motion starts from a rest state, according to the Lagrange theorem, the liquid motion is potential and may be described by the equations [1]:

$$\det J = 1, \quad (J^{*-1}\nabla_\xi) \cdot X_t = 0 \qquad (\zeta < 0),$$

to which the boundary conditions

$$p|_{\Sigma_1} = 0, \quad (X_t, Y_t, Z_t + 1)\cdot\vec{n}|_{\Sigma_2} = 0$$

and the initial ones (1.3)

$$X = 0, \quad X_t = 0 \qquad (t = 0)$$

are to be added. Here $J = \partial(\vec{x})/\partial(\vec{\xi})$ is the Jacobian matrix, J^* is the matrix conjugated with J, p is the pressure, $\vec{n}$ the external normal to the wetted part of the solid body, $\nabla_\xi = (\partial/\partial\xi, \partial/\partial\eta, \partial/\partial\zeta)$.

Let in cylindrical coordinates r, θ, ζ the contact line Γ be described by $r = r(\theta, t)$, $\zeta = 0$, where $r(\theta, t)$ is the smooth function which is to be determined along with the solution of (1.3). Denote the value $(r(\pi/2, t) + r(-\pi/2, t))/2$ through a(t). It is natural to suppose that $a(0) = 0$ and the function a(t) monotonically increases with t. Since for $t \to 0$ the contact area Σ_2 converges to one point, in order to obtain information on the liquid motion at the initial stage of entry, it is convenient to introduce internal variables which are "stretched" as needed:

$$\lambda = \xi/a(t), \quad \mu = \eta/a(t), \quad \nu = \zeta/a(t).$$

An asymptotical expansion of the unknown functions for $t \to 0$ takes the form

$$\vec{X}(\xi, \eta, \zeta, t) = \varepsilon_0(\tau)\vec{X}^{(0)}(\lambda, \mu, \nu) + \varepsilon_1(\tau)\vec{X}^{(1)}(\lambda, \mu, \nu) + \ldots$$

$$r(\theta, t) = \delta_0(\tau)\, r^{(0)}(\theta) + \delta_1(t) r^{(1)}(\theta) + \ldots, \qquad (1.4)$$

where $\tau = a(t)$, and $\varepsilon_i(\tau)$, $\delta_i(t)$, $i = 0, 1, \ldots$ are asymptotical [2]. The unknown functions $\varepsilon_i(\tau)$, $\delta_i(t)$ are determined in compliance with the least degeneracy principle. After integration over t_1 the condition when there is no flow across Σ_2 takes the form:

$$Z = F(\xi + X, \eta + Y) - t.$$

Substituting expansions (1.4) into this expression and using equality (1.2), we obtain that only at $\varepsilon_0(\tau) = \tau^2$, $\delta_0(t) = \sqrt{t}$, a main term of the flow asymptotics depends on the body shape and the law of its motion. In so doing a zero approximation of the condition of the flow absence may be written as follows:

$$Z^{(0)} = \frac{1}{2}\left(\lambda^2 + \frac{k_2}{k_1}\mu^2\right) - a_0^{-2} \quad \text{in } \sigma_2 .$$

Here $a_0 = r^{(0)}(\pi/2)$, σ_1 is the free boundary of the liquid, σ_2 is the contact region in the space of internal variables λ, μ, ν.

Pressure p is connected with functions X, Y, Z by the momentum equation $J^{*-1}\ddot{X} + \nabla_\xi p = 0$ [1]. Substituting (1.4) into this equation and retaining the older-order terms for $t \to 0$, we obtain the constant pressure condition on a free surface in a zero approximation in the form:

$$X^{(0)} = 0, \quad Y^{(0)} = 0 \qquad \text{in } \sigma_1 .$$

The zero approximation of equation of motion (1.3) shows that there exists a function $\Phi(\lambda, \mu, \nu)$ harmonic in a lower semi-space such that $\vec{X}^{(0)} = \nabla_\lambda \Phi$. The boundary-value problem for potential Φ is:

$$\begin{aligned}
&\Delta\Phi = 0 && \text{in } \nu < 0\\
&\Phi_\nu = (\lambda^2 + k_2 k_1^{-1}\mu^2)/2 - a_0^{-2} && \text{in } \sigma_2\\
&\Phi = 0 && \text{in } \sigma_1 \qquad (1.5)\\
&\Phi \to 0 && \text{in } |\vec{\lambda}| \to \infty
\end{aligned}$$

Let us find the solution of (1.5) in $C^2(\Omega) \cap C(\overline{\Omega})$, and a main asymptotics term of the contact line Γ in the set of ellipses with excentricity e and large semi-axis $a_0(\tau)$; in the space (λ, μ, ν) this set is described by the equations

$$(1 - e^2)^{-1}\lambda^2 + \mu^2 = 1, \quad \nu = 0.$$

In case of extending the function Φ to an upper semi-space in an odd manner, the condition on the free boundary is fulfilled automatically, and for derivative $\Psi(\lambda, \mu, \nu) = \partial\Phi/\partial\nu$ the Dirichlet problem beyond an elliptic disk σ_2 is obtained.

Let us determine ellipsoidal coordinates ρ, χ, ω by solving the equation

$$\frac{\lambda^2}{\varkappa^2 - \rho^2} + \frac{\mu^2}{\varkappa^2} + \frac{\nu^2}{\varkappa^2 - 1} = 1$$

with respect to $\varkappa$, if $0 < \omega < \rho < \chi < 1 < \rho$. The relation between ellipsoidal and Cartesian coordinates takes the form:

$$e^2(1 - e^2)\lambda^2 = (\rho^2 - e^2)(\chi^2 - e^2)(e^2 - \omega^2)$$

$$e^2\mu^2 = \rho^2\chi^2\omega^2$$

$$(1 - e^2)\nu^2 = (\rho^2 - 1)(1 - \chi^2)(1 - \omega^2)$$

It should be noted that the contact region σ_2 corresponds to the value $\rho = 1$, and the free surface corresponds to $\chi = 1$. It is required to determine the function $\Psi_0(\rho, \chi, \omega)$ which is harmonic when $\rho > 1$ and which takes a

given value $\Psi_0(1,\chi,\omega)$ when $\varrho = 1$ (here $\Psi_0(\varrho,\chi,\omega) = \Psi(\lambda,\mu,\nu)$). The function $\Psi(\lambda,\mu,\nu)$ was developed in [3]

$$\Psi(\lambda,\mu,\nu) = \frac{1-\varepsilon^2}{2}\left\{\alpha_1\left(1-\frac{m}{\alpha_2}\right)\left(\frac{\lambda^2}{\alpha_1-e^2}+\frac{\mu^2}{\alpha_1}+\frac{\nu^2}{\alpha_1-1}-\right.\right.$$

$$\left.\left.-1\right)\frac{\sigma_1(\varrho)}{\sigma_1(1)}+m\left(\frac{\lambda^2}{\alpha_2-e^2}+\frac{\mu^2}{\alpha_2}+\frac{\nu^2}{\alpha_2-1}-1\right)\frac{\sigma_2(\varrho)}{\sigma_2(1)}\right\}.$$

The finiteness condition of a kinetic energy of the liquid motion results in the equality $a_0^{-2} = (2-\varepsilon^2-e^2)/6$; for a small axis of the interface $b_0 = r^{(0)}(0)$ we have $b_0^2 = 6h/(1+h)$, where $h = (1-e^2)/(1-\varepsilon^2)$. Here $\varepsilon^2 = 1-k_2\cdot k_1^{-1}$, $\alpha_{1,2} = (1+e^2 \pm\sqrt{e^4-e^2+1})/3$.

$$\sigma_{1+j}(\varrho) = \int_{\varrho}^{\infty}\frac{d\varrho}{(\varrho^2-\alpha_j)^2\sqrt{(\varrho^2-1)(\varrho^2-e^2)}} \qquad (j=1,2),$$

$$m = \frac{\alpha_2}{e^2}\cdot\frac{\alpha_2-e^2}{\alpha_1-\alpha_2}\cdot\frac{e^2\alpha_1-e^2}{1-\varepsilon^2}.$$

It should be noted that the representation of the function determined throughout the space is possible with the help of ellipsoidal coordinates ϱ, χ, ω only in case when it is even with respect to λ, μ, ν. Therefore, in order to uniquely reestablish the displacement potential Φ (the function is odd with respect to ν), it is necessary to consider Ψ, Φ only for $\nu < 0$ rather than throughout the space. The function $\Phi(\lambda,\mu,\nu)$ is defined as the problem solution: $\Phi_\nu = \Psi$ when $\nu < 0$; $\Phi \to 0$ when $\nu \to -\infty$, in so doing the condition on the free surface ($\Phi = 0$ in σ_1) in general case is not fulfilled. The study of the function Φ shows that this function satisfies the condition on the free surface if and only if $m(e,\varepsilon) = 0$ or

$$\varepsilon^2 = \frac{3e^2}{1+e^2+\sqrt{e^4-e^2+1}}.$$

This formula defines the interface excentricity e as a function of excentricity ε of the body head. In an axisymmetrical case ($k_1 = k_2$) we have $b_0 = \sqrt{3}$, and in a plane case ($k_2 \to 0$) it is not difficult to define that $h \to 2$ and $b_0 \to 2$. The obtained results are in agreement with the solutions of axisymmetrical and plane problems [3]. Here $e > e(\varepsilon)$ for any ε.

It should be noted that since $S_n(\varrho) < S_n(1)$ for $\varrho > 1$ and $\alpha_1 > e^2$, we have

$$\Psi_0(\varrho,1,\omega) < \Psi_0(1,1,\omega).$$

It means that at sufficiently small values of t, the liquid particles don't penetrate into the "forbidden" zone bounded by the surface $z = (x^2 + k_2k_1^{-1}y^2)/2 - t$.

The constructed asymptotics satisfies the initial equations and boundary conditions with an accuracy of $O(\sqrt{t})$ throughout if $t \to 0$, except for a narrow zone in the vicinity of the interface. To verify the flow structure there, it is necessary to construct an internal expansion. Such construction was made in a plane case (the function $f(x',y')$ in (1.1) is independent of y').

2. Internal expansions. Let us consider a small vicinity of the contact point $\xi = a(t)$, $\zeta = 0$ (the second contact point vicinity $\xi = -a(t)$, $\zeta = 0$ is studied in a similar way). Let us determine internal variables α, β from the formulae [3]: $\xi = a(t) + t^k\alpha$, $\zeta = t^k\beta$. The internal expansion of the functions $X(\xi,\zeta,t)$, $Z(\xi,\zeta,t)$, $p(\xi,\zeta,t)$ is sought as follows:

$$X(\xi,\zeta,t) = t^m Q(\alpha,\beta) + t^{m_1}Q^{(1)}(\alpha,\beta)+\ldots,$$

$$Z(\xi,\zeta,t) = t + t^m P(\alpha,\beta) + t^{m_1}P^{(1)}(\alpha,\beta)+\ldots,$$

$$p(\xi,\zeta,t) = t^{s_1}\Pi(\alpha,\beta)+t^{s_1}\Pi^{(1)}(\alpha,\beta)+\ldots, \qquad (1.6)$$

where k, m, m_i are the positive numbers, and $k > 1/2$, $s_i > s_{i-1}$, $m_{i+1} > m_i > m > 1$ for $i \geq 1$.

It is worthy to note that, as a rule, the method of matched asymptotic expansions [2] is used in the problems comprising a small parameter. In the given problem its role is played by time t.

Let us substitute (1.6) into the equalities (1.3) and retain main terms there at $t \to 0$. The condition of a nontriviality of the solution of the problem obtained with respect to the functions P and Q leads to the requirement $k = m$. In so doing P and Q satisfy the relations:

$$P_{\alpha\alpha}-Q_{\alpha\beta}+P_\beta P_{\alpha\alpha}-P_\alpha P_{\alpha\beta}+Q_\beta Q_{\alpha\alpha}-Q_\alpha Q_{\alpha\beta} = 0$$

$$P_\beta + Q_\alpha + P_\beta Q_\alpha - P_\alpha Q_\beta = 0 \quad \text{for } \beta < 0 \qquad (1.7)$$

$$P_\alpha^2 + Q_\alpha^2 + 2Q_\alpha = 0 \text{ for } \alpha > 0,\ \beta = 0 \qquad (1.8)$$

$$P = 0 \quad \text{for } \alpha < 0,\ \beta = 0 \qquad (1.9)$$

According to the principle of asymptotic expansion matching [2], it follows from the formula for solving the plane problem [3] that

$$t^{m+k/2-3/4}(\alpha+i\beta)^{-1/2}(P+iQ) \to -2 \text{ for } t \to 0$$

($\alpha^{1/2} > 0$ for $\alpha > 0$). Hence $m = k/2 + 3/4$, and then $m = k = 3/2$. From the momentum equation it follows that $s_0 = -1$. Thus, the vicinity of the contact point, where the internal expansion is valid, is of the order of $t^{3/2}$ if $t \to 0$. Now the above mentioned condition gives an outer limit of the internal expansion:

$$(\alpha+i\beta)^{-1/2}(P+iQ) \to -2 \text{ for } |\alpha+i\beta| \to \infty \qquad (1.10)$$

A one-side inequality

$$\zeta + Z - (\xi+X)^2/2 + t \leq 0,$$

which means that particles as they move cannot enter into the "forbidden" region limited by a moving impermeable contour, in internal variables is reduced to:

$$P + \rho < 0 \quad \text{for } \beta \leq 0 \qquad (1.11)$$

Since the region where the internal expansion is constructed disappears in the limit if $t \to 0$, the initial conditions don't lead to additional limitations for the functions P and Q.

Relations (1.7)–(1.11) form a nonlinear boundary-value problem with the limitation on (α, β) plane. In the study of this problem the main difficulty consists in that the quasi-linear system (1.7) is of a combined type: for any solution P,Q of this system there exist two families of complex characteristics and one real family β = const. In order to find characteristic features of the above mentioned problem, an approximate model based on linearization of (1.7) was investigated in [3], a nonlinear condition on the free boundary (1.8) was invariable.

Now let us analyze the problem (1.7)–(1.11) in a full formulation. The conditions $\lambda = P_\alpha$ and $\mu = Q_\alpha$ are taken as the godograph plane coordinates, and the coordinates of a physical plane $\alpha = A(\lambda, \mu)$, $\beta = B(\lambda, \mu)$ are assumed to be the required functions. Then (1.7) can be re-written as follows (the second equation is to be previously differentiated with respect to α):

$$\begin{aligned} &\lambda_\alpha - \mu_\beta + P_\beta \lambda_\alpha - \lambda \lambda_\beta + Q_\beta \mu_\alpha - \mu \mu_\beta = 0, \\ &\lambda_\beta + \mu_\alpha + \mu \lambda_\beta + \mu_\alpha P_\beta - \lambda_\alpha Q_\beta - \lambda \mu_\beta = 0. \end{aligned} \qquad (1.12)$$

It is not difficult to obtain the following formulae

$$\lambda_\alpha = B_\mu / \tilde{\Delta}, \quad \mu_\alpha = -B_\lambda / \tilde{\Delta}, \quad \lambda_\beta = -A_\mu / \tilde{\Delta}, \quad \mu_\beta = A_\lambda / \tilde{\Delta},$$

$\tilde{\Delta} = A_\lambda B_\mu - A_\mu B_\lambda$, using them, (1.12) can be re-written as:

$$B_\mu - A_\lambda + P_\beta B_\mu + \lambda A_\mu - Q_\beta B_\lambda - \mu A_\lambda = 0,$$

$$A_\mu + B_\lambda + \mu A_\mu + P_\beta B_\lambda + Q_\beta B_\mu + \lambda \cdot A_\lambda = 0.$$

This system is of elliptic type.

From (1.7) let us express P_β through Q_β and substitute it into the above system:

$$\begin{aligned} &-(1+\mu)^2 A_\lambda + \lambda (1+\mu) A_\mu - Q_\beta (1+\mu) B_\lambda + (\lambda Q_\beta + 1) B_\mu = 0 \\ &\lambda (1+\mu) A_\lambda + (1+\mu)^2 A_\mu + (\lambda Q_\beta + 1) B_\lambda + Q_\beta (1+\mu) B_\mu = 0. \end{aligned} \qquad (1.13)$$

The equation for Q_β follows from the relation

$$Q_{\beta\alpha} = \mu_\beta = A_\lambda / \tilde{\Delta}.$$

Writing out the α derivative, we obtain

$$B_\mu Q_{\beta\lambda} - B_\lambda Q_{\beta\mu} = A_\lambda. \qquad (1.14)$$

With taking into account (1.14), the equation (1.13) is transformed as follows. The first equation of the system is differentiated with respect to μ and is added up with the second equation differentiated with respect to λ. Then the first equation is differentiated with respect to λ and the second equation is extracted from the first one previously differentiated with respect to μ. The following system is obtained:

$$A_\mu + (1+\mu) \Delta A + Q_{\beta\lambda} B_\lambda + Q_{\beta\mu} B_\mu + Q_\beta \Delta B = 0,$$

$$A_\mu + (1+\mu) \Delta A + Q_{\beta\lambda} B + Q_{\beta\mu} B_\mu + (Q_\beta + \lambda^{-1}) \Delta B = 0,$$

which leads to the equation $\Delta B = 0$. The equations for $A(\lambda, \mu)$ are obtained by omitting the function Q_β in the system (1.13).

Finally on the godograph plane there is the boundary value problem such as:

$$\begin{aligned} &(\lambda^2 + (1+\mu)^2)(A_\lambda B_\mu - A_\mu B_\lambda) = B_\lambda^2 + B_\mu^2, \\ &\Delta B = 0 \text{ in } S, \\ &B = 0 \text{ on } \quad S, \\ &(A + iB)(\lambda + i\mu) \to 1 \quad \text{if } \lambda^2 + \mu^2 \to 0, \end{aligned} \qquad (1.15)$$

where $\Delta = \partial^2/\partial\lambda^2 + \partial^2/\partial\mu^2$ is the Laplace operator, $S = \{ \lambda, \mu \mid \lambda^2 + \mu^2 + 2\mu < 0, \lambda \leq 0 \}$ is the domain of definition of functions $A(\lambda, \mu)$, $B(\lambda, \mu)$. It should be noted that function $\omega = A + iB$ is not analytical in the exact statement of the problem (in contrast to its approximate formulation [3]). The problem (1.5) should be considered as a complex of two problems: first the function $B(\lambda, \mu)$ is determined, then the linear partial differential equation with variable coefficients for $A(\lambda, \mu)$ is solved. Let us consider $B(\lambda, \mu)$ to be an imaginary part of some function analitical in half-circle S, that satisfies the required conditions. Such function was constructed in [2], it is determined uniquely and leads to

$$B = -\mathrm{Im}(1 + 2i/\chi)^2/4, \quad \chi = \lambda + i\mu.$$

Transformation $z = (1 + 2i/\chi)^2$, $z = u + iv$ conformally maps the domain S on the upper half-plane $v > 0$. On plane z the solid wall corresponds to the positive part of real axis, and the free surface – to its negative part. In new variables u,v function B will have the form $B_0(u,v) = -v/4$, and equation for A will be.

$$\begin{aligned} &-\frac{\partial A_0}{\partial u} = \frac{1}{4} + \frac{\sqrt{\varrho} \cos \varphi/2}{1 + \varrho - 2\sqrt{\varrho} \cos \varphi/2} \quad (v > 0, \\ &u^{-1} A_0(u,v) \to -1/4 \quad (|z| \to \infty), \end{aligned} \qquad (1.16)$$

where $\varrho^2 = u^2 + v^2$, $\cos\varphi = u/\varrho$, $B_0(u,v) = B(\lambda(u,v), \mu(u,v))$, $A_0(u,v) = A(\lambda(u,v), \mu(u,v))$. It should be noted that if the second term in the right-hand part of (1.16) is ignored, the function $\omega = A + iB$ is analytical. Agreement between the coordinates of the godograph plane χ and plane z is described by the relations:

$$\begin{aligned} &\lambda = -2\sqrt{\varrho} d \sin \varphi/2, \quad \mu = -2d(\sqrt{\varrho} \cos \varphi/2 + 1), \\ &d = (1 + 2\sqrt{\varrho} \cos \varphi/2 + \varrho)^{-1}. \end{aligned} \qquad (1.17)$$

The problem (1.7)–(1.11) may be solved numerically by the formulae (1.16), (1.17); however,

some characteristics of the flow in the vicinity of the contact point can be calculated directly.

On the free surface ($\varphi = \pi$) the equation (1.16) gives $A_0(u,0) = -u/4$ when $u < 0$. On a solid wall ($\varphi = 0$) we have:

$$A_0(u,0) = \frac{2}{\sqrt{u}-1} - 4\ln|\sqrt{u}-1| - 2\sqrt{u} - \frac{u}{4} \quad (u > 0) \tag{1.18}$$

Formula (1.18) shows that $A_0(u,0)$ when $u>0$ has two branches, one being determined when $0<u<1$ and the other being determined when $u>1$. The joining condition prescribes the choice of the second branch. It should be noted that $A_0 \to +\infty$ when $u \to 1+0$, and consequently there exists such $u_0 > 1$ that $A_0(u_0,0) = 0$ and $A_0(u,0) < 0$ when $u > u_0$ (formula (1.18) gives $u_0 \simeq 2.93$). The main pressure asymptotics term on the wetted part of the contour is determined from the formula

$$\Pi(\alpha,0) = \frac{2\sqrt{u}}{(\sqrt{u}+1)^2} \quad \text{when} \quad u > u_0,$$

the jump of the function $\Pi(\alpha,0)$ at the contact point ($\alpha = 0$) is equal to $\simeq 0{,}48$. Thus, pressure in vicinity of the contact point behaves as t^{-1} when $t \to 0$ and has the jump at the contact point (pressure on the wetted part of the contour is of the order of $t^{-1/2}$).

3. Entering of the blunt body at an attack angle. Let us consider an initial stage of water landing of a circular cylinder. It is assumed that the cylinder generatrix is parallel to an undisturbed liquid surface (a plane problem) during the whole time of motion. The angle between the body velocity direction and the vertical is denoted by α. The condition of the flow absence across the solid surface shows that the zero approximation of the problem solution depends only on a vertical velocity vector component. Therefore, to determine the effect of the horizontal velocity vector component to the flow pattern and the load distribution character on the contact area, it is appropriate to consider the following (first) approximation. The problem for this approximation cannot be solved in an explicit manner, however, it enables representation of the solution in the form of the sum of two terms. One of them is the first approximation in the problem of a vertical symmetric entrance of a parabolic contour into a liquid, and the second is the correction for a basic flow which has been conditioned by the horizontal contour velocity component.

Let in dimensionalless variables the velocity vector of the body has the form $(-\mathrm{tg}\alpha, -1)$, then the condition on the solid surface in the first approximation is written as:

$$z^{(1)} = \lambda x^{(0)} + \frac{a_*}{2} + \frac{\lambda}{4}\mathrm{tg}\alpha \quad (\nu = 0, |\lambda| < 1).$$

If $x^{(1)}$, $z^{(1)}$ is represented as

$$x^{(1)} = \phi(\lambda,\nu) + \overline{x}^{(1)}(\lambda,\nu), z^{(1)} = \varphi(\lambda,\nu) + \overline{z}^{(1)}(\lambda,\nu)$$

where $\overline{x}^{(1)}$, $\overline{z}^{(1)}$ is the first approximation of solving the problem of a vertical contour entrance, the problem for "correction" functions ϕ , φ takes the form:

$$\phi_\lambda + \varphi_\nu = 0 \,,\ \phi_\nu - \varphi_\lambda = 0 \qquad (\nu < 0),$$
$$\varphi = \frac{\lambda}{4}\mathrm{tg}\alpha \qquad (\nu = 0,\ |\lambda| < 1),$$
$$\phi = 0 \qquad (\nu = 0,\ |\lambda| > 1),$$
$$\phi, \varphi \to 0 \qquad (\lambda^2 + \mu^2 \to \infty).$$

Solution of this problem is written down with the help of the Keldysh-Sedov formula [4]

$$\varphi + i\phi = \frac{1}{4}\mathrm{tg}\alpha\,(z - \sqrt{z^2-1}), \tag{1.19}$$

where $z = \lambda + i\nu$, and the radical branch is chosen so that

$$\sqrt{z^2-1} = -\sqrt{\lambda^2-1} \quad \text{when } \nu = 0, \lambda < -1,$$
$$\sqrt{z^2-1} = \sqrt{\lambda^2-1} \quad \text{when } \nu = 0, \lambda > 1,$$
$$\sqrt{z^2-1} = -i\sqrt{1-\lambda^2} \quad \text{when } \nu = 0,\ |\lambda| < 1.$$

Formula (1.19) allows the following conclusions to be made:

a) the flow pattern ceases to be symmetric, and the correction for the horizontal displacement vector component is given by the formula

$$\phi(\lambda,0) = \frac{1}{4}\mathrm{tg}\alpha\sqrt{1-\lambda^2} \quad \text{when } |\lambda| < 1;$$

b) if $\alpha > 0$, in front of the body ($\lambda < -1$) the free surface is lowered by the value

$$\varphi(\lambda,0) = \frac{1}{4}\mathrm{tg}\alpha\,(\lambda + \sqrt{\lambda^2-1}),$$

and behind the body ($\lambda > 1$) it rises

$$\varphi(\lambda,0) = \frac{1}{4}\mathrm{tg}\alpha\,(\lambda - \sqrt{\lambda^2-1})$$

with respect to the free surface position calculated in the problem of a vertical entrance;

c) the "correction" pressure $p_n(\lambda,0)$ is calculated by the formula

$$p_n(\lambda,0) = -\frac{1}{4}\mathrm{tg}\alpha\,\left(\frac{\lambda}{\sqrt{1-\lambda^2}} + \mathrm{arctg}\,\lambda\right) \quad \text{when } |\lambda| < 1,$$

which shows that $p_n \to -\infty$ when $\lambda \to 1-0$ and $p_n \to +\infty$ when $\lambda \to -1+0$;

d) the "correction" pressure doesn't make a contribution due to resistance, but it creates momentum L with respect to the contact area center, which can be found by the formula

$$L = a^2(t)\int_{-1}^{1} \lambda\, p_n(\lambda,0)\,d\lambda\,(1+O(\sqrt{t}))$$

or

$$L'(t') = 2\pi\rho V^3 R^{-1} t'^2 \operatorname{tg}\alpha\,(1+O(\sqrt{t})),$$

where R is the cylinder radius, V is the vertical velocity component of the body, ρ is the liquid density (remind that the dimensional variables are marked by primes). It is worthy to note that $F(t) = O(1)$, and $L(t) = O(t)$ when $t \to 0$, where F(t) is the resistance force acting to the submerging body as viewed from the liquid.

II. Submergence of elastic shells into an ideal incompressible liquid

The elasticity of a submergine structure has a significant effect upon the value and character of distribution of hydrodynamical loads over the contact area. The first attempts to account for the effects of elastic deformations upon the entering process characteristics were made in [4, 5], where the authors were based on simple physical considerations within the framework of the Wagner theory [6]. In 1935 Povitsky A.S. suggested a "quasi-stationary" method based on the consideration that for accounting for elastic deformations, the Wagner equations are used for an rigid body having the same form as a deformable elastic body has. This method gives wittingly incorrect results if the velocity and acceleration of an elastic deformation of the body achieve the same order of magnitude as the velocity and acceleration of the centre of gravity of the body. The theory applicable for describing the interaction between the shell and the liquid in this case has been proposed by E.I.Grigolyuk and A.G.Gorshkov [7].

The aim of this Section is to estimate the effect of elastic properties of a submerging structure on the loading distribution over the contact region when $t \to 0$. A general approach is used for constructing the initial data necessary for numerical investigation of the flow and the elastic body behavior when they interact during the entry process.

1. A mathematical formulation of the problem.

A submergence of a circular cylindrical shell into an ideal incompressible liquid is considered. If the shell generatrix is parallel to the undisturbed liquid surface, at a sufficient distance from the body ends the problem may be considered to be a plane one, the gravity forces and surface tension being ignored. The case of a circular shell is general in that any smooth cylindrical surface in a small vicinity of some generatrix, along which the surface curvature differs from zero, can be approximated by a circular cylinder.

When $t' = 0$, the liquid occupies a semiplace $y' < 0$ and is at rest, and the shell touches its free surface at the point $x' = 0$ and has a velocity V directed vertically downwards. It is required to determine the liquid motion, shell deformation and pressure distribution over the contact area.

Let us assume that the shell radius R and the ratio R/V are the length scale and time scale, respectively, and come over to the dimensionless variables which are not marked by a prime. In the Lagrange variables ξ, η, the functions are the liquid particle displacements $X(\xi, \eta, t)$, $Y(\xi, \eta, t)$ determined by the equalities $X = x(\xi, \eta, t) - \xi$, $Y = y(\xi, \eta, t) - \eta$ and the elastic displacement $w(\theta, t)$, $v(\theta, t)$ of elements of the shell along the surfaces $\theta = \text{const}$, $r = 1$, respectively. Here r, θ are the polar coordinates associated with the shell center.

The liquid motion is described by the equations

$$X_{\eta t} - Y_{\xi t} + X_\xi X_{\eta t} - X_\eta X_{\xi t} + Y_\xi Y_{\eta t} - Y_\eta Y_{\xi t} = 0, \quad (2.1)$$

$$X_\xi + Y_\eta + X_\xi Y_\eta - X_\eta Y_\xi = 0 \quad (\eta < 0), \quad (2.2)$$

the first being the vortex absence condition and the second being the continuity equation (remind that the liquid motion originates from the rest state, and the outer mass forces are absent).

The equations describing a thin cylindrical shell deformation are in the form [8]

$$\varepsilon\left(\frac{\partial^4 w}{\partial\theta^4} + \frac{\partial^2 w}{\partial\theta^2}\right) + w + \frac{\partial v}{\partial\theta} = \alpha p(\theta, t) - \mu_1 \frac{\partial^2 w}{\partial t^2},$$

$$\frac{\partial^2 v}{\partial\theta^2} + \frac{\partial w}{\partial\theta} = \mu_1 \frac{\partial^2 v}{\partial t^2} \quad (2.3)$$

Here $\mu_1 = (1-\nu^2)\rho_1 V^2/E$, $\varepsilon = h^2/(12R^2)$, $\alpha = \mu_1 \rho R/\rho_1 h$, where ρ_1 is the shell material density, ν is the Poisson's ratio, E is the elastic modulus, h is the shell thickness, ρ is the liquid density and $p(\theta, t)$ the external loading.

The equations of motion (2.1)-(2.3) which are to be considered in combination, are added by the boundary conditions

$$(\vec{X}_t - \vec{u})\cdot\vec{n} = 0 \quad (\eta = 0, |\xi| < a(t)), \quad (2.4)$$

$$X_{tt} + X_\xi X_{tt} + Y_\xi Y_{tt} = 0 \quad (\eta = 0, |\xi| > a(t)) \quad (2.5)$$

and the initial ones

$$\vec{X} = \vec{X}_t = 0, \quad \vec{w} = \vec{w}_t = 0 \quad (t = 0) \quad (2.6)$$

Here $\vec{n}(\theta, t)$ is the normal to the deformated surface of the body, $\vec{u}(\theta, t) = (v_* \cos\theta + w_* \sin\theta, v_* \sin\theta - w_* \cos\theta)$ is the shell element velocity, $\vec{X} = (X, Y)$, $\vec{w} = (w, v)$. The relations $\eta = 0$, $\xi = \pm a(t)$ describe the position of the contact points between the free surface of the liquid and the submerged body surface in Lagrange coordinates, and the relations $r = 1$, $\theta = \pm\theta_*(t)$ describe this value in the system of polar coordinates associated with the shell. Then on (x,y) plane the right contact point coordinates x_*, y_* can be expressed in two ways (the second point is considered analogously):

a) $x_* = a(t) + X(a(t), 0, t)$, $y_* = Y(a(t), 0, t)$,

b) $x_* = \sin\theta_*(t) + w(\theta_*(t), t)\sin\theta_*(t) +$

$+ v(\theta_*(t), t)\cos\theta_*(t)$,

$$y_k = 1 - t - \cos\theta_0(t) - w(\theta_0(t), t)\cos\theta_0(t) +$$

$$+ v(\theta_0(t), t)\sin\theta_0(t). \qquad (2.7)$$

From here the two equations for determining the functions $\theta_0(t)$, $a(t)$ follow. It is natural to suppose that $a(t) \to 0$, $\theta_0(t) \to 0$, when $t \to 0$. The external loading $p(\theta, t)$ is found from the momentum equation $X_{tt} + X_\xi X_{tt} + Y_\xi Y_{tt} + p_\xi = 0$, which is to be added by the relation between Lagrange ξ, η and polar r, θ coordinates $\xi + X(\xi, \eta, t) = r\sin\theta$, $Y(\xi, \eta, t) = 1 - t - r\cos\theta$.

2. Asymptotical solution. The problem formulated above is analyzed for small t. Since when $t \to 0$, the contact spot is converged into a point, to obtain information on the initial entrance stage, it is necessary to make tension of space variables: $\xi = a(t)\lambda$, $\eta = a(t)\mu$. An asymptotical expansion of the required functions when $t \to 0$ is searched as follows [11]:

$$\begin{aligned}
&\vec{X}(\xi, \eta, t) = a^2(t)\sum_{k=0}^{\infty} a^k(t)\vec{X}^{(k)}(\lambda, \mu),\\
&w(\theta, t) = \theta_0^3(t)\sum_{k=0}^{\infty} \theta_0^k(t)w^{(k)}(\chi),\\
&v(\theta, t) = \theta_0^6(t)\sum_{k=0}^{\infty} \theta_0^k(t)v^{(k)}(\chi),\\
&p(\theta, t) = \theta_0^{-1}(t)\sum_{k=0}^{\infty} \theta_0^k(t)p^{(k)}(\chi),\\
&a(t) = t^{1/2}\sum_{k=0}^{\infty} t^{k/2} a_k,\\
&\theta_0(t) = t^{1/2}\sum_{k=0}^{\infty} t^{k/2} b_k,
\end{aligned} \qquad (2.8)$$

where $\chi = \theta / \theta_0(t)$, $\vec{X}^{(k)} = (X^{(k)}, Y^{(k)})$.

Substituting the expansions (2.8) into the initial relations and retaining the older-order terms if $t \to 0$, we obtain the boundary-value problem for the zero approximation of the required functions:

$$\begin{aligned}
&X_\lambda^{(0)} + Y_\mu^{(0)} = 0,\ X_\mu^{(0)} - Y_\lambda^{(0)} = 0 \quad (\mu < 0)\\
&Y^{(0)} = \tfrac{1}{2}\lambda^2 - a_0^{-2} \quad (\mu = 0, |\lambda| < 1)\\
&X^{(0)} = 0 \quad (\mu = 0, |\lambda| > 1)\\
&|\vec{X}^{(0)}| \to 0 \quad (\lambda^2 + \mu^2 \to \infty)
\end{aligned} \qquad (2.9)$$

$$p_\chi^{(0)}(\chi) = \frac{a_0^4}{4}\left(\lambda X_\lambda^{(0)} - \lambda^2 X_{\lambda\lambda}^{(0)}\right)\Big|_{\lambda=\chi} \quad (|\chi| < 1) \qquad (2.10)$$

$$\varepsilon\frac{\partial^4 w^{(0)}}{\partial\chi^4} = -\mu_1\frac{a_0^4}{4}\left(\chi^2\frac{\partial^2 w^{(0)}}{\partial\chi^2} - 3\chi\frac{\partial w^{(0)}}{\partial\chi} + 3w^{(0)}\right) + \alpha p^{(0)}(\chi)$$

$$|w^{(0)}| \to 0 \quad (\chi^2 \to \infty) \qquad (2.11)$$

$$\chi^2\frac{\partial^2 v^{(0)}}{\partial\chi^2} - 9\chi\frac{\partial v^{(0)}}{\partial\chi} + 24v^{(0)} = \frac{4}{\mu_1 a_0^2}\frac{\partial w^{(0)}}{\partial\chi}$$

$$|v^{(0)}| \to 0 \quad (\chi^2 \to \infty) \qquad (2.12)$$

The zero approximation of (2.7) gives $b_0 = \varepsilon_0$, $Y^{(0)}(1+0, 0) = 1/2 - a_0^{-2}$. The boundary-value problem for the main term of an initial asymptotics is divided into three problems:

a) the boundary-value problem (2.9) describes the liquid motion without taking into account the entering body deformation;

b) using the known pressure distribution over the contact region (2.10), $w^{(0)}$ is found from (2.11);

c) the tangential component of the shell element displacement vector $v^{(0)}$ is found from (2.12).

The solution of the problem (2.9) was constructed in [3]

$$Y^{(0)} + iX^{(0)} = \frac{1}{4}(z - \sqrt{z^2 - 1})^2, \quad a_0 = 2, \quad z = \lambda + i\mu.$$

Integrating the equation (2.10), the initial asymptotics of the external loading is obtained, which acts to the body as viewed from the liquid:

$$p^{(0)}(\chi) = 2(1 - \chi^2)^{-1/2} \quad (|\chi| < 1),$$

$$p^{(0)}(\chi) = 0 \quad (|\chi| > 1).$$

Let us consider a supplementary problem of beam deflection under a transversal loading $q(\xi, t) = a_1^{-1}(t)p^{(0)}(\xi/a_1(t))$, where $a_1(t) = 2\sqrt{t}$. The beam motion is described in dimensionless variables by the equation [8]

$$\frac{EJ_\beta}{mR^2V^2}\frac{\partial^4 W}{\partial\xi^4} + \frac{\partial^2 W}{\partial t^2} = \frac{\rho R}{m}q(\xi, t), \qquad (2.13)$$

It is necessary to add the initial conditions ($W = W_t = 0$ when $t = 0$) and the condition at infinity ($W \to 0$ when $|\xi| \to \infty$) to (2.13). Here $W(\xi, t)$ is the beam deflection, E is the elastic modulus of the material, J_β is the cross-sectional momentum, m is the length beam mass; in an undisturbed state the beam axis coincides with $O\xi$ axis. It might be well to point out that for the above-mentioned function $q(\xi, t)$ equation (2.13) admits the solution in the form $W(\xi, t) = a_1^3(t)W_1(\xi/a_1(t))$, thereby if $J_\beta = h^3/12(1 - \nu^2)$, $m = \rho_1 h$, the equation for W_1 coincides with (2.11). Thus, instead of the solution of (2.11), it is appropriate to find a self-similar solution of (2.13). It is more expedient to deal with the latter equation, since its solution is written down in quadratures with the help of Fourier and Laplace transforms. In so doing the solution of (2.11) is of the form

$$w^{(0)}(\chi) = \frac{1}{4}\frac{\rho R}{\rho_1 h}A^2\int_0^\infty \cos(\ell u\chi)\left[\int_0^1 J_0[2u\sqrt{\omega}] \times \sin[u^2A^{-2}(1-\omega)]\,d\omega\right]\frac{du}{u^2},$$

where $A = (\mu_1/\varepsilon)^{1/4}$. Specifically, at the point of an initial contact we have

$$w^{(0)}(0) = \frac{1}{3\sqrt{\pi}}\frac{\rho R}{\rho_1 h}A\int_0^\infty \frac{e^{-A^2\chi^2}}{\chi^4 + 1}\,d\chi,$$

$$w^{(\omega)}_{\chi\chi}(0) = -\frac{\rho}{\sqrt{\pi}}\frac{\rho R}{\rho_1 h}A^3\int_0^\infty \frac{e^{-A^2z^2}}{z^4+1}\,z^2\,dz.$$

The shell deformation character is defined by a unique parameter $A_b = VRh^{-1}(\rho(1-\nu^2)/E)^{1/2}$ then $A = \sqrt[4]{12A_b^2}$). It should be noted that the parameter A_b depends on the entering velocity V, as well as on the shell material properties. Consequently, this parameter can be considered as the characteristic of a dynamical rigidity of the submerging structure. The following relations are valid:

$$w^{(0)}(0) = O(\sqrt{A_b}),\ w^{(0)}_{\chi\chi}(0) = O(A^{3/2}) \quad (A_b \to 0).$$

In a plane case the stress asymptotics σ' when $t \to 0$ at the frontal point ($\xi = 0$) is defined by the formula [12]

$$\frac{\sigma'}{Eh} = 2\sqrt{t}\,w^{(0)}_{\chi\chi}(0) + O(t).$$

If the stress at the frontal point dependent on t and entry velocity V is denoted by $\sigma'(t,V)$, for the shells with a high dynamical rigidity ($A_b \to 0$) the following relation is valid:

$$\frac{\sigma'(t,V)}{\sigma'(t,V_0)} = \left(\frac{V}{V_0}\right)^{3/2}(1+O(\sqrt{t}))\,(1+O(A_b))$$

when $A_b \to 0$, $t \to 0$.

In conclusion let us consider the asymptotics of function $w^{(\omega)}(\chi)$ when $A_b \to 0$. Let $z = A\chi$, $w_0^{(\omega)}(A\chi) = w^{(\omega)}(\chi)$, then

$$w_0^{(0)}(z) = \frac{\sqrt{\pi}}{6}\frac{\rho R}{\rho_1 h}A\left\{\sin(z^2+\frac{\pi}{4}) - z^2\cos(z^2+\frac{\pi}{4}) + \right.$$

$$+ \frac{3}{2}\sqrt{\pi}\,z\,[\,S(z^2) - C(z^2)\,] + \sqrt{\pi}\,z^3\,[\,1 - C(z^2) -$$

$$\left. -S(z^2)\,]\right\}\cdot[\,1+O(A_b^{1/3})\,],$$

where S(x), C(x) are the Frenel integrals:

$$S(x) = \frac{1}{\sqrt{2\pi}}\int_0^x \frac{\sin q}{\sqrt{q}}\,dq,\quad C(x) = \frac{1}{\sqrt{2\pi}}\int_0^x \frac{\cos q}{\sqrt{q}}\,dq,$$

when $|z| \to \infty$ we obtain

$$w_0^{(0)}(z) = -\frac{\sqrt{\pi}}{8}\frac{\rho R}{\rho_1 h}A\,\frac{\sin(z^2+\pi/4)}{z^4}\,(1+O(z^{-2}))$$

Thus, the rigid shell deflection (parameter A_b is small) is described by the oscillating function vanishing at infinity.

3. The first approximation. To take into account the effect of elastic properties of a submerging deformable body on the flow pattern and the hydrodynamical loading distribution character over the contact region, it is necessary to consider the problem for the first approximation. It cannot be solved in an explicit form even for an undeformable body, however, it allows the solution to be presented in the form of the sum of two terms (Section I.3), one of them being the first approximation in the problem of water landing of a solid cylinder, and the other being the correction for the basic flow caused by elastic properties of the entering body.

If $X^{(1)}$, $Y^{(1)}$ are represented as $X^{(1)} = \phi(\lambda,\mu) + \overline{X}^{(1)}(\lambda,\mu)$, $Y^{(1)} = \varphi(\lambda,\mu) + \overline{Y}^{(1)}(\lambda,\mu)$, where $\overline{X}^{(1)}$, $\overline{Y}^{(1)}$ is the first approximation of the solution of the problem on a vertical entering of an undeformable solid cylinder, the problem for "correction" functions ϕ, φ takes the form

$$\phi_\lambda + \varphi_\mu = 0,\ \phi_\mu - \varphi_\lambda = 0 \qquad (\mu < 0)$$

$$\varphi = -w^{(\omega)}(\lambda) \qquad (\mu = 0, |\lambda| < 1)$$

$$\phi = 0 \qquad (\mu = 0, |\lambda| > 1)$$

$$\phi \to 0,\ \varphi \to 0 \qquad (\mu^2+\lambda^2 \to \infty).$$

The solution of this problem is written out according to the Keldysh-Sedov formulae [9]. The "correction" (for the first approximation) pressure $\widetilde{p}^{(1)}$ over the contact region is defined by the equality

$$\widetilde{p}^{(1)}_\lambda(\lambda,0) = -4(\lambda^2\phi_{\lambda\lambda} - 3\lambda\phi_\lambda + 3\phi),$$

where

$$\phi(\lambda,0) = -\frac{1}{\pi\sqrt{1-\lambda^2}}\int_{-1}^{1}\frac{w^{(\omega)}(\tau)\sqrt{1-\tau^2}}{\tau-\lambda}\,d\tau$$

when $|\lambda| < 1$.

For a rigid ($A_b \ll 1$) shell we have $w^{(0)}(\chi) = w_0^{(0)}(A\chi) = w^{(\omega)}(0)\,[\,1+O(A_b^{1/3})\,]$ when $|\chi| < 1$. Hence $\phi(\lambda,0) = \lambda(1-\lambda^2)^{-1/2}w^{(0)}(0)\cdot[\,1 + O(A_b^{1/3})\,]$ when $|\lambda| < 1$. The expression for $\widetilde{p}^{(1)}(\lambda,0)$ takes the form:

$$\widetilde{p}^{(1)}(\lambda,0) = \sqrt{2\pi}\frac{\rho R}{\rho_1 h}AG(\lambda)\,[\,1+O(A_b^{1/3})\,],$$

where $G(\lambda) = -(\lambda^4 + 4\lambda^2 - 8/3)(1-\lambda^2)^{-3/2}$.

Thus, taking into account the elastic properties of the submerging body leads to a more uniform (in the first approximation) pressure distribution over the contact range (the vicinity of the contact points is not considered). As would be expected, the less parameter A_b, the less an absolute value of $\widetilde{p}^{(1)}$, more exactly, $\widetilde{p}^{(1)} = O(\sqrt{A_b})$ when $A_b \to 0$.

4. Some remarks. As follows from Sections I.1, I.2, the description of the initial stage of shell submergence into a weakly compressible liquid is divided into several problems. First, without taking into account the body deformation, the liquid motion due to the shell entry is defined, and then regarding for the known pressure distribution over the contact region the deformation value is found. If the functions $w(\theta,t)$, $v(\theta,t)$ are seeked in the form of expansions (a plane case)

$$w(\theta,t) = N^3w^{(0)}(\chi,\tau) + N^4w^{(1)}(\chi,\tau) + \dots,$$

$$v(\theta,t) = M^6 V^{(0)}(\chi,\tau) + M^7 V^{(1)}(\chi,\tau) + \dots ,$$

when $M \to 0$, where $\chi = M^{-1}\theta$, $\tau = M^{-2}t$, the functions $W^{(0)}$, $V^{(0)}$ are defined as the solution of the following problems:

$$\varepsilon \frac{\partial^4 W^{(0)}}{\partial \chi^4} + \mu_1 \frac{\partial^2 W^{(0)}}{\partial \tau^2} = \alpha q(\chi,\tau),$$

$$\frac{\partial W^{(0)}}{\partial \chi} = \mu_1 \frac{\partial^2 V^{(0)}}{\partial \tau^2} .$$

Here $q = Mp$, p is the external loading. Before the shock wave has gone into the free surface, the function $q(\chi,\tau)$ is determined by the explicit expression (3.12), and the displacement vector asymptotics $\vec{w} = (w,v)$ when $M \to 0$ can be numerically calculated at this stage.

The problem for $W^{(0)}$ well coincides with that about the beam deformation determination at a given external loading. Consequently, at an initial stage of entering ($t \ll 1$) deformation of an arbitrary slope shell (soft shells are not considered) is asymptotically similar to the beam deformation under an appropriate loading.

In the axisymmetrical case the expansion of functions $w(\theta,t)$, $p(\theta,t)$, $a(t)$, $\theta_0(t)$ when $t \to 0$ is seeked in the form (2.8), and the expansion of functions $\vec{X} = (X,Y,Z)$, $v(\theta,t)$ is seeked in the form

$$\vec{X}(\xi,\eta,\varsigma,t) = a^2(t)\sum_{k=0}^{\infty} a^k(t)\vec{X}^{(k)}(\lambda,\mu,\nu),$$

$$v(\theta,t) = \theta_0^4(t)\sum_{k=0}^{\infty} \theta_0^k(t) v^{(k)}(\chi),$$

where $\varsigma = a(t)\nu$, functions $\vec{X}^{(k)}(\lambda,\mu,\nu)$ are invariant with respect to rotation in plane λ,μ. Substituting the representations of the required functions into the equations describing the liquid motion and the entering spherical shell deformation [8] as well as the boundary conditions and retaining the older-order terms when $t \to 0$, we obtain that in a zero approximation the initial problem is divided into the sequence of three problems (as in a plane case). At first the liquid motion asymptotics is calculated without taking into account elastic deformations of the shell. In so doing the zero approximation of the external loading $p^{(0)}(\chi)$ acting to the body as viewed from the liquid is given by the formula:

$$p^{(0)}(\chi) = \begin{cases} (3/\pi)(1-\chi^2)^{-1/2}, & |\chi| < 1 \\ 0, & |\chi| > 1. \end{cases}$$

The function $w^{(0)}(\chi)$ is the solution of the problem

$$\varepsilon \nabla^2 \nabla^2 w^{(0)} + \mu_1(\chi^2 w^{(0)}_{\chi\chi} - 3\chi w^{(0)}_{\chi} + 3w^{(0)}) = \alpha p^{(0)}(\chi)$$
$$w^{(0)} \to 0 \qquad (|\chi| \to \infty) \qquad (2.14)$$

Note that the equation

$$D\nabla^2\nabla^2 W + mW_{tt} = q(\xi,t), \qquad (2.15)$$

describing the plate deformation under the action of the external loading $q(\xi,t) = a_1^{-1}(t)p^{(0)}(\xi/a_1(t))$ admits the solution of the form $W = a_1^3(t)W_1(\xi/a_1(t))$, the equation for W_1 coinciding with (2.14) when $D = \varepsilon/\alpha$, $m = \mu_1/\alpha$. Here $a_1(t) = \sqrt{3t}$, $\nabla^2 = \xi^{-1}\partial(\xi\partial/\partial\xi)/\partial\xi$, $D = Eh^3/12(1-\nu^2)$ is the cylindrical rigidity of the plate. A self-similar solution of (2.15) is written out in quadratures through the use of Hankel and Laplace transformations

$$w^{(0)}(\chi) = \frac{1}{\pi\sqrt{3}} \frac{\varrho R}{\varrho_1 h} A^2 \int_0^{\infty} J_0(\sqrt{3}\chi u) \int_0^1 \sin(u\sqrt{3\omega}) \cdot \sin(u^2 A^{-2}(1-\omega))\, d\omega \frac{du}{u^2} ,$$

where parameter A has the same value as in a plane case. For the shells with a greater rigidity ($A_b \ll 1$), the following relations are valid:

$$w^{(0)}(0) = O(A_b), \quad w^{(0)}_{\chi\chi}(0) = O(A_b).$$

In an axisymmetrical case, as in a plane one, the pressure asymptotics when $t \to 0$ is independent of elastic properties of the submerging shell whose deformation character is defined by a unique parameter A_b.

When constructing the models describing an initial stage of the elastic body entrance (the submergence depth is small), the majority of authors usually proceed from the assumption concerning the effect of elastic properties of the body on pressure distribution over the contact region [7]. Naturally this is valid within large time intervals, however, when $t \to 0$, the inertia forces of the rigid shell are higher than those of the liquid, therefore maximum loadings acting to the body at small penetration depths can be calculated without taking into account elastic properties of a submerging structure.

III. Entering of a blunt body into a weakly compressible liquid

As is seen from the experiments, maximum values of the pressure acting to a submerging body are achieved at an initial stage of the process [13]. Investigation of this stage, under the assumption that the liquid is incompressible, leads to an infinite pressure (in the case of a blunt body) at the moment of touching, small as the entering velocity may be. This is due to the fact that the model of an incompressible liquid doesn't enable the description of the important submergence stage. For a blunt body there exists a moment t_* such that when $0 < t < t_*$ the contact line interface between a free liquid boundary and the surface of a solid body moves with a velocity exceeding a sound velocity in the liquid. In this case the perturbation front is attached to the interface, and the disturbed liquid is bounded by a solid surface of the body from one side

and the shock front from the other side. Before t_* the free surface remains undisturbed. To describe correctly this stage of the process independent of a Mach number, it is necessary to use the model of compressible liquid. This model enables determination of the maximum pressure acting to the body as viewed from the liquid, as well as of the moment and place of its application. It is worthy to note that when $t \gg t_*$, i.e. when the shock wave is far from the interface, the solution of the problem of the blunt body entrance into an incompressible liquid well describes the medium motion. In this section only a plane problem will be considered.

1. Formulation of the problem. A plane unsteady isentropic motion of an ideal compressible liquid occupying a semi-plane $y' < 0$ at the moment $t' = 0$ and initially resting is considered (dimensional variables are marked by a prime). Line $y' = 0$ at an initial moment is a free surface. The velocity range is assumed such that the Reynolds number $Re \gg 1$ what allows the liquid to be considered as an ideal one, and the Mach number $M \ll 1$. The surface tension and external mass forces are ignored.

Let R and V be positive constants. At fixed t' the equation

$$y' = \frac{1}{2R} x'^2 - Vt' \qquad (3.1)$$

determines the parabola on x', y' plane which is identified with a solid indeformable contour. When $t' = 0$, this contour touches the free boundary at point $x' = 0$. Relation (3.1) prescribes the contour motion along y' axis with a constant velocity V. It is required to find the arising liquid motion assuming that some part of its boundary which is not the part of a solid contour is free.

Let us take curvature radius R of parabola (3.1) when $x' = 0$ as the length scale, the resting liquid density ρ_0 as the density scale, $\rho_0 V^2$ for the pressure scale, R/V for the time scale, and come over to dimensionless variables (they are designated by the same letter without primes).

Since the motion originates from the rest state and the external mass forces are absent, isentropic flow of an ideal liquid is vortexless. Consequently, there is the velocity potential $\varphi_1(x,y,t)$ which is the solution of the equation [15]

$$c^2(p)\Delta\varphi_1 = \varphi_{1tt} + 2\nabla\varphi_1 \cdot \nabla\varphi_{1t} + \nabla\varphi_1 \cdot \nabla\left(\frac{1}{2}|\nabla\varphi_1|^2\right) \qquad (3.2)$$

over the range Ω_t occupied by the disturbed liquid. Here $c(p)$ is the local velocity of sound. It is necessary to add to (3.2) the boundary (pressure p is constant on a free surface, and the condition when there is no flow across a solid wall is fulfilled) and initial ($\varphi_1 = \varphi_{1t} = 0$ when $t = 0$) conditions, the Cauchy-Lagrange integral

$$\varphi_{1t} + \frac{1}{2}|\nabla\varphi_1|^2 + \int \frac{dp}{\rho(p)} = 0 \qquad \text{in } \Omega_t$$

and the EOS which is in the Tait form $\rho = (1 + nM^2 p)^{1/n}$. Here $M = V/c_0$ is the Mach number, c_0 is the velocity of sound in the resting liquid, n the constant characterizing the medium properties (for water $n = 7.15$).

When the body enters the liquid, the shock wave is generated, at the front of which the equations of a strong discontinuity are to be valid (the liquid is at rest before the front):

$$W^2 = p\rho/(\rho - 1),\ \nabla\varphi_1 \cdot \vec{n}_W = W(\rho - 1)/\rho\ ,$$

$$\nabla\varphi_1 \cdot \vec{s}_W = 0.$$

Here $\vec{n}_W$ is the vector of an external normal, and $\vec{s}_W$ is the vector of a tangential to the shock front, W is the dimensionless velocity of the shock wave in $\vec{n}_W$ direction. If the shock front position is described in the form $g(x,y,t) = 0$ ($g < 0$ before the front), we have $W = g_t/|\nabla g|$.

The assumption that the flow is isentropic is of major importance. Entropy is conserved in the medium particle for continuous flows. If the shock wave passes through the liquid, the entropy behind the shock front may be already unconstant. Nevertheless, in the case of low-intensity shock waves the entropy conservation may be considered approximately, since the entropy jump is the value of the third order of smallness, as compared with the pressure jump value.

When $t > t_*$, the boundary of Ω_t region contains some parts of the free surface. Therefore, to investigate the process after the shock wave separation from the contact line, it is convenient to re-write the problem in Lagrange variables ξ, η. Then the dimensionless coordinates $x(\xi, \eta, t)$, $y(\xi, \eta, t)$ of the liquid particle taking position ξ, η at the moment $t = 0$ will be the required functions. On ξ, η plane the region occupied by the liquid is the semi-plane $\eta < 0$. In new variables the entry problem takes the form

$$c^2(p)D\cdot\vec{x}_t = \varphi_{tt} - \vec{x}_t \cdot \vec{x}_{tt},\quad \vec{x}_t = D\varphi$$

$$(\xi^2 + \eta^2 < r^2(\theta,t),\ -\pi \leqslant \theta \leqslant 0)$$

$$nM^2 p = (1 - M^2(n-1)\left[\varphi_t - \frac{1}{2}|\vec{x}_t|^2\right])^{\frac{n}{n-1}} - 1$$

$$\varphi_t = \frac{1}{2}|\vec{x}_t|^2 \quad (\eta = 0,\ a(t) < |\xi| < r(0,t))$$

$$(\vec{x}_t - \vec{v})\cdot\vec{n} = 0 \quad (\eta = 0,\ |\xi| < a(t))$$

$$W^2 = p\rho/(\rho - 1),\ \vec{x}_t \cdot \vec{n}_W = W(\rho - 1)/\rho\ ,\ \vec{x}_t \cdot \vec{s}_W = 0,$$

$$W = r_t(1 + (r_\theta/r)^2)^{-1/2} \quad (\xi^2 + \eta^2 = r^2(\theta,t),$$

$$-\pi \leqslant \theta \leqslant 0)$$

$$\vec{x}_t \equiv 0 \qquad (\xi^2 + \eta^2 > r^2(\theta,t))$$

$$\varphi = \varphi_t = 0, \quad \vec{x} = \vec{\xi} \quad (t = 0)$$
$$c(p) = M^{-1}(1 + M^2 np)^{\frac{n-1}{2n}}, \quad \rho = (1 + M^2 np)^{1/n} \tag{3.3}$$

Here $J = \partial(\vec{x})/\partial(\vec{\xi})$ is the Jacobian matrix, $\varphi(\vec{\xi}, t) = \varphi_1(\vec{x}(\vec{\xi}, t), t)$, $\vec{x} = (x, y)$, $\vec{\xi} = (\xi, \eta)$, $\nabla = J^{*-1}\nabla_\xi$, J^* is the matrix conjugated to J, $\vec{n}$ is the normal to the wetted part of the body, $\vec{v}$ is the submerging contour velocity vector (in our case $\vec{n} = (x(\xi, 0, t), -1)$, $\vec{v} = (0, -1)$). In the case of a vertical submergence of a symmetric contour, the contact point location is described by the relations $\eta = 0$, $\xi = \pm a(t)$, and the shock front location is described by the relations $\eta = r(\theta, t)\sin\theta$, $\xi = r(\theta, t)\cos\theta$, $\theta = \operatorname{arctg}(\xi/\eta) - \pi/2$. Functions $a(t), r(\theta, t)$ have to be determined along with the solution of (3.3). Let there exist such $T > t_*$ that when $0 < t < T$, the function $y(\xi, 0, t)$ is continuous with respect to ξ (prior to the moment T there is no spraying jet). From here the equation for $a(t)$ is obtained: $y(a(t) + 0, 0, t) = y(a(t) - 0, 0, t)$, where the right-hand side is the known function determined from the condition on the solid surface.

2. An asymptotical solution of the entry problem (3.3) when $M \to 0$ is found in the form of expansions:

$$\vec{x}(\vec{\xi}, t) = \vec{x}^{(0)}(\vec{\xi}, t) + M^2\vec{x}^{(1)}(\vec{\xi}, t) + \dots,$$
$$\varphi(\vec{\xi}, t) = \varphi^{(0)}(\vec{\xi}, t) + M^2\varphi^{(1)}(\vec{\xi}, t) + \dots,$$
$$p(\vec{\xi}, t) = p^{(0)}(\vec{\xi}, t) + M^2 p^{(1)}(\vec{\xi}, t) + \dots,$$
$$r(\theta, t) = M^{-1}r^{(0)}(\theta, t) + Mr^{(1)}(\theta, t) + \dots$$
$$a(t) = a^{(0)}(t) + M^2 a^{(1)}(t) + \dots \tag{3.4}$$

Let us write out the problem for the main term of asymptotics ($J_0 = \partial(\vec{x}^{(0)})/\partial(\vec{\xi})$)

$$(J_0^{*-1}\nabla_\xi)\cdot\vec{x}_t^{(0)} = 0, \quad \vec{x}_t^{(0)} = J^{*-1}\nabla_\xi\varphi^{(0)} \quad (\eta < 0)$$
$$\varphi_t^{(0)} = \frac{1}{2}|\vec{x}_t^{(0)}|^2 \quad (\eta = 0, |\xi| > a^{(0)}(t))$$
$$(\vec{x}_t^{(0)} - \vec{v})\cdot\vec{n} = 0 \quad (\eta = 0, |\xi| < a^{(0)}(t))$$
$$\varphi^{(0)} = \varphi_t^{(0)} = 0, \ \vec{x}^{(0)} = \vec{\xi} \quad (t = 0)$$
$$|\vec{x}_t^{(0)}| \to 0 \quad (\xi^2 + \eta^2 \to \infty) \tag{3.5}$$
$$r_t^{(0)} = (1 + (r_\theta^{(0)}/r^{(0)})^2)^{1/2} \quad (-\pi \le \theta \le 0).$$

The problem (3.5) describing the contour entering into an incompressible liquid was investigated in [3] for an initial stage ($t \ll 1$). The asymptotics of the required functions if $t \to 0$ are given by

$$\varphi^{(0)}(\xi, \eta, t) = \operatorname{Im}(\sqrt{\zeta^2 - (a^{(0)}(t))^2} - \zeta)\cdot$$
$$\cdot(1 + O(\sqrt{t})), \quad \zeta = \xi + i\eta,$$
$$p^{(0)}(\xi, 0, t) = 2([a^{(0)}(t)]^2 - \xi^2)^{-1/2}(1 + O(\sqrt{t}))$$
$$\text{when } |\xi| < a^{(0)}(t), \ a^{(0)}(t) = 2\sqrt{t}(1 + O(\sqrt{t})) \tag{3.6}$$

The zero approximation (3.6) satisfies the relations (3.5) accurate to $O(\sqrt{t})$ throughout, except for narrow zones in the vicinity of the contact points, their size being of the order of $t^{3/2}$ when $t \to 0$. Within these zones, the flow pattern is verified in Section I.2.

As indicated above, the main term of the pressure asymptotics $p^{(0)}$ when $M \to 0$ has a singularity at point $t = 0$, i.e. expansions (3.4) become invalid in a small vicinity of this point. To verify the flow structure within this vicinity, it is necessary to construct an internal expansion.

3. Internal expansion. Let us define internal variables α, β, τ from the formulae $\xi = M\alpha$, $\eta = M\beta$, $t = M^2\tau$ and find an internal expansion of the required functions:

$$\vec{x}(\xi, \eta, t) = M\vec{x}_0(\alpha, \beta, \tau) + \dots,$$
$$\varphi(\xi, \eta, t) = M\varphi_0(\alpha, \beta, \tau) + \dots,$$
$$p(\xi, \eta, t) = M^{-1}p_0(\alpha, \beta, \tau) + \dots, \tag{3.7}$$
$$r(\theta, t) = Mr_0(\theta, \tau) + \dots,$$
$$a(t) = Ma_0(\tau) + \dots.$$

Tension of variables and the kind of expansion of the unknown functions are determined from the matching condition of the internal (3.7) and external (3.4) expansions and the nondegeneracy condition of boundary-value problems for each term of the internal asymptotics [2].

Substituting expansions (3.7) into (3.3) and retaining the main terms if $M \to 0$, we obtain the boundary-value problem for potential $\varphi_0(\alpha, \beta, \tau)$:

$$\varphi_{0\tau\tau} = \Delta\varphi_0 \quad (\alpha^2 + \beta^2 < r_0^2(\theta, \tau))$$
$$\varphi_{0\beta} = -1 \quad (\beta = 0, \ |\alpha| < a_0(\tau))$$
$$\varphi_{0\tau} = 0 \quad (\beta = 0, a_0(\tau) < |\alpha| < r_0(0, \tau))$$
$$\varphi_0 = 0 \quad (\alpha^2 + \beta^2 = r_0^2(\theta, \tau))$$
$$\varphi_0 - \varphi_{0\tau} = 0 \quad (\tau = 0). \tag{3.8}$$

Besides, we have

$$\vec{x}_{0\tau\tau} = 0, \ \vec{x}_{1\tau} = \nabla\varphi_0, \ p_0 = -\varphi_{0\tau} \ (\alpha^2 + \beta^2 < r_0^2(\theta, \tau))$$
$$\vec{x}_0 = \vec{\xi}, \ \vec{x}_1 = 0 \quad (\tau = 0).$$

In the zero approximation the condition of the shock wave emergence into the free surface takes the form $(2\tau_*)^{-1/2} = 1$ (the contact point velocity is equal to the velocity of sound in a resting liquid); hence $\tau_* = M^{-2}t_* = (1/2)(1 + o(1))$. The function $r_0(\theta, \tau)$ is re-

presented as the solution of the problem

$$r_{0\tau} = (1 + (r_{0\theta}/r_0)^2)^{1/2} \quad (-\pi \le \theta \le 0,\ \tau > 0)$$
$$r_0(0,\tau) = \sqrt{2\tau} \quad (0 < \tau < 1/2), \qquad (3.9)$$
$$r_0 = 1/2 + \tau \quad (\tau > 1/2)$$
$$r(\theta,0) = 0 \quad (\tau = 0)$$

Let φ_0 be the known function, then $y_1(\alpha,0,\tau) = \int_0^\tau \varphi_{0\beta}(\alpha,0,\tau_1)d\tau_1$. Since $\varphi_{0\beta}(\alpha,0,\tau) = 0$ when $\tau < \alpha - 1/2$, $\alpha > 1$, the requirement of continuity $y_1(\alpha,0,\tau)$ at the contact point leads to the equation for $a_0(\tau)$

$$\int_{a_0(\tau)-\sqrt{2}}^{\tau} \varphi_{0\beta}\left(a_0(\tau),0,\tau_1\right)d\tau_1 = a_0^2(\tau)/2 - \tau \quad (\tau > 1/2) \qquad (3.10)$$

The joint solution of (3.8) and (3.10) gives the main term of the internal asymptotics of potential φ_0 when $M \to 0$ (the matching of internal and external asymptotics takes place).

4. A hypersonic stage. When $0 < \tau < 1/2$, the contact region expands with a hypersonic velocity, and a shock wave is attached to the contact line. At this stage the function $a_0(\tau)$ is pre-determined: $a_0(\tau) = \sqrt{2\tau}$.

The disturbance wave motion is described by the boundary-value problem (3.9), however, in the zero approximation the shock front is the envelope of the curve family $\beta^2 + (\alpha - \lambda)^2 = (\tau - \lambda^2/2)^2$, $\beta \le 0$, $|\lambda| < \sqrt{2\tau}$, $\tau < 1/2$, which is described parametrically in the form (λ parameter)

$$\alpha = \lambda(\tau + 1 - \lambda^2/2), \quad \beta = -(\tau - \lambda^2/2)\sqrt{1-\lambda^2},$$
$$|\lambda| < \sqrt{2\tau}, \quad \tau < 1/2.$$

The tangential to the shock front at the contact point ($\alpha = \sqrt{2\tau}$, $\beta = 0$) is described by the equation

$$\beta = \sqrt{\frac{2\tau}{1-2\tau}}\,(\alpha - \sqrt{2\tau}), \qquad (3.11)$$

from here it follows that the tangential slope to α axis increases from zero when $\tau = 0$ to $\pi/2$ when $\tau = 1/2$.

It can be shown that (3.8) is equivalent to the following problem ($0 < \tau < 1/2$)

$$\varphi_{0\tau\tau} = \Delta\varphi_0 \ (\beta < 0), \quad \varphi_{0\beta} = -1 \ (\beta = 0, |\alpha| < \sqrt{2\tau}),$$
$$\varphi_0 = 0 \ (\beta = 0, |\alpha| > \sqrt{2\tau}), \quad \varphi_0 = \varphi_{0\tau} = 0 \ (\tau = 0),$$
$$|\nabla\varphi_0| \to 0 \quad (\alpha^2 + \beta^2 \to \infty).$$

Without writing out the solution of this problem, let us find the pressure distribution over the contact region $p_0(\alpha, 0, \tau)$. The boundary values $\varphi_0(\alpha, 0, \tau)$, $\varphi_{0\beta}(\alpha, 0, \tau)$ are connected by the equality

$$\varphi_0(\alpha,0,\tau) = \frac{1}{\pi}\int_{\sigma(\alpha,\tau)} \frac{\varphi_{0\bar\beta}(\bar\alpha,0,\bar\tau)\,d\bar\alpha\,d\bar\tau}{\sqrt{(\tau-\bar\tau)^2 - (\alpha-\bar\alpha)^2}},$$

where $\sigma(\alpha,\tau)$ is the isosceles rectangular triangle on $(\bar\alpha,\bar\tau)$ plane with the top at (α,τ) point and the base on $\bar\alpha$ axis. Let us denote the region bounded by the curve $|\bar\alpha| = \sqrt{2\bar\tau}$ by D and note that when $|\alpha| < \sqrt{2\tau}$, $0 < \tau < 1/2$ in the region $D \cap \sigma(\alpha,\tau)$ we have $\varphi_{0\bar\beta}(\bar\alpha,0,\bar\tau) = -1$, and in the region $\sigma(\alpha,\tau)\setminus D$ we have $\varphi_{0\bar\beta}(\bar\alpha,0,\bar\tau) \equiv 0$. Since $p_0 = -\varphi_{0\tau}$, we have

$$p_0(\alpha,0,\tau) = \frac{1}{\pi}\frac{\partial}{\partial\tau}\int_{D\cap\sigma(\alpha,\tau)} \frac{d\bar\alpha\,d\bar\tau}{\sqrt{(\tau-\bar\tau)^2 - (\alpha-\bar\alpha)^2}}$$
$$(|\alpha| < \sqrt{2\tau},\ 0 < \tau < 1/2).$$

After calculations we obtain:

$$p_0(\alpha,0,\tau) = \frac{\sqrt{2}}{\pi\sqrt{\varkappa}}\,K\left[\frac{1}{\sqrt{2}}\sqrt{1 - \frac{1/2-\tau}{\varkappa}}\right]$$
$$\varkappa(\alpha,\tau) = \sqrt{(\tau+1/2)^2 - \alpha^2} \qquad (3.12)$$
$$(|\alpha| < \sqrt{2\tau},\ 0 < \tau < 1/2),$$

where $K(k)$ is the full elliptic first-order integral. The specific cases of this formula are:

a) let $\tau = 0$, $\alpha = 0$, then $p_0(0,0,0) = 1$, i.e. at the moment of touching, the pressure is equal to the water hammer pressure ($p' = \rho_0 c_0 V$);

b) when $\tau = 1/2$ (the moment of shock wave separation from the contact line) $p_0(\alpha,0,1/2) = (\sqrt{2}/\pi)K(1/\sqrt{2})(1-\alpha^2)^{-1/4}$;

c) when $\alpha = \sqrt{2\tau}$ (at the contact point) $p_0(\sqrt{2\tau},0,\tau) = (1-2\tau)^{-1/2}$.

Thus, with increasing τ the pressure distribution over the contact region becomes more and more nonuniform, and the expansions (3.7) considered up to $\tau = 1/2$ become invalid in a small vicinity of the point $\tau = \tau_*$, $\alpha = \sqrt{2\tau_*}$, $\beta = 0$.

It should be noted that in the study of a hypersonic stage, it is possible to proceed from the formulation of the problem in Eulerian variables. In this case the solution asymptotics has the same form as in Lagrange variables, since $\vec{x} = \vec{\xi}(1 + O(M))$.

5. The flow pattern improvement when $t \to t_* - 0$ in the vicinity of the contact points may be realized in the Eulerian coordinates. Let us define internal variables λ, μ, ν and new unknown functions from the formulae

$$t = t_* + \varepsilon_t(M)\nu, \quad x = \sqrt{2t} + \varepsilon_x(M)\lambda, \quad y = \varepsilon_y(M)\mu,$$
$$\varphi_1(x,y,t) = \varepsilon_\varphi(M)\Psi(\lambda,\mu,\nu,M),$$
$$p(x,y,t) = \varepsilon_p(M)Q(\lambda,\mu,\nu,M), \qquad (3.13)$$
$$g_1(y,t) = \sqrt{2t} + \varepsilon_x(M)F(\mu,\nu,M),$$
$$t_* = \frac{1}{2}M^2 + \varepsilon_t(M)\,t_1(M)$$

(the equation $x = g_1(y,t)$ describes the shock

front location). It is assumed when $M \to 0$ that (i) functions Ψ, Q, F and their derivatives have finite values; (ii) $t_1(M) \to t_1(0)$ where $t_1(0) \neq 0$; (iii) $\varepsilon_t/M^2 \to 0$, $\varepsilon_x/M \to 0$, $\varepsilon_y/M \to 0$, $(M\varepsilon_\varphi)^{-1} \to 0$, $M\varepsilon_\varphi/\varepsilon_x \to 0$, $M\varepsilon_\varphi/\varepsilon_y \to 0$. Designate $\Psi(\lambda,\mu,\nu,0) = \Psi_0(\lambda,\mu,\nu)$, $Q(\lambda,\mu,\nu,0) = Q_0(\lambda,\mu,\nu)$, $F(\mu,\nu,0) = F_0(\mu,\nu)$, $t_1(0) = t_{01}$, $\nu + t_{01} = s$. Functions $\varepsilon_t, \varepsilon_x, \varepsilon_y, \varepsilon_\varphi, \varepsilon_\rho$ are defined from the matching condition of the external (3.7) and internal (3.13) asymptotical expansions, as well as from the least degeneracy condition of the boundary-value problem for the zero approximation Ψ_0, Q_0, F_0.

The external asymptotics (with respect to the vicinity of the contact point) of pressure distribution is given by the formula (3.12), from here it follows that

$$p(x,y,t) = \frac{1}{M}\frac{2}{\pi\sqrt{\xi}} K\left[\frac{1}{\sqrt{2}}\sqrt{1 - \frac{M^2/2 - t}{M^2\xi}}\right] + O(1),$$

where $\xi = M^{-2}[(t + M^2/2)^2 - M^2x^2]^{1/2}$. The pressure asymptotics matching is nontrivial when $\varepsilon_x(M) = M^{-3}\varepsilon_t^2(M)$, $\varepsilon_\rho(M) = \varepsilon_t^{-1/2}(M)$, and the matching condition is as follows:

$$Q_0(\lambda,\mu,\nu) \to \bar{s}^{1/2}\bar{Q}(\lambda/s^2) \quad (\nu \to -\infty,$$

$$\mu \to -\infty, \ \lambda \to -\infty),$$

where $\bar{Q}(v) = (\sqrt{2}/\pi)(2v+1)^{-1/4}K[2^{-1/2}(1 + [2v+1]^{-1/2})]$. The shock front location asymptotics matching leads to the conditions

$$\varepsilon_y \cdot \varepsilon_t^{1/2} = M\varepsilon_x, \quad F_0(\mu,\nu) \to \sqrt{-2s}\ \mu$$

$$(\nu \to -\infty, \ \mu \to -\infty)$$

(in an acoustic approximation the asymptotics in the vicinity of the contact point is described by the formula (3.11)). After substituting the representation (3.13) into the equation of motion (3.2), we come over to the limit when $M \to 0$ (with accounting for the above-mentioned assumptions). The least degeneracy condition of the limiting relation gives $\delta_1(M) = M^{3/3}$, and the equation for $\Psi_0(\lambda,\mu,\nu)$ takes the form

$$\Psi_{0\mu\mu} + ((n+1)\Psi_{0\lambda} + 2s)\Psi_{0\lambda\lambda} + 2\Psi_{0\lambda\nu} = 0$$

The conditions at the shock front in the zero approximation give

$$\frac{n+1}{4}\Psi_{0\lambda} = F_{0\nu} - \frac{1}{2}F_{0\mu}^2 - s, \qquad \Psi_0 =$$

$$(\lambda = F_0(\mu,\nu), \ \mu < 0)$$

As follows throm the Cauchy-Lagrange integral, in the flow region $Q_0 = \Psi_{0\lambda}$. Let us introduce new functions $u(\lambda,\mu,s) = \frac{n+1}{2}\Psi_0(\lambda,\mu,s-t_{01}) - \mu^2 + s\lambda$, $f(\mu,s) = F_0(\mu,s-t_{01})$; the boundary-value problem for these functions is in the form:

$$u_{\lambda s} + u_\lambda u_{\lambda\lambda} + \frac{1}{2}u_{\mu\mu} = 0 \quad (\mu < 0, \lambda < f(\mu,s), s < t_{**})$$

$$u_\mu = -\frac{n+1}{2} \qquad (\mu = 0, \lambda < 0) \tag{3.14}$$

$$u = s f(\mu,s) - \mu^2, \quad u_\lambda = 2f_s - f_\mu^2 - s$$

$$(\mu < 0, \ \lambda = f(\mu,s)).$$

To the above-formulated problem it is necessary to add the matching cinditions

$$s^{1/2}(u_\lambda - s - \bar{s}^{1/2}\bar{Q}(\lambda/s^2)) \to 0$$

$$(s \to -\infty, \ \lambda \to -\infty, \ \mu \to -\infty).$$

Thus, in a small vicinity of the contact point ($t \to t_* - 0$) the motion is of significantly nonlinear character. The equation describing the liquid flow in this zone coincides with that of the theory of short waves [14].

6. Pressure at the contact point when $0 \leq t \leq t_*$ can be found independent of the solution of the boundary-value problem (3.14). For a hypersonic stage in the problem of a liquid drop impact upon a solid plane, the method of determining the unknown functions at the contact point was developed by Lesser [10]. Its modification may be applied to the problem of blunt body entry.

At fixed t the equation $x = x_0(y,t)$ defines the shock wave position on the plane of Eulerian coordinates x, y. The angle between the normal to the shock front at some point D and the axis Ox will be designated by α, then $\cos\alpha = (1 + x_{0y}^2)^{-1/2}$, where the right-hand side of the equality is calculated at point D. The shock conditions are as follows [15]:

$$u\sin\alpha - v\cos\alpha = 0,$$

$$u\cos\alpha + v\sin\alpha = W(\rho - 1)/\rho, \tag{3.15}$$

$$p = W^2(\rho - 1)/\rho.$$

Here u and v are respectively the horizontal and vertical velocity vector components of a liquid particle behind the shock front, W is the velocity of shock wave in the normal direction to its front at point D, ρ is the density, p the pressure behind the shock wave (it should be reminded that the liquid is at rest before the shock wave front). If the function $x_0(y,t)$ is known, the value of W is determined from:

$$W = x_{0t}(1 + x_{0y}^2)^{-1/2} \tag{3.16}$$

Since before t_* the shock wave is attached to the contact point, the function $x_0(0,t)$ when $0 \leq t \leq t_*$ is pre-determined (in our case $x_0(0,t) = \sqrt{2t}$), and the value v at the contact point is equal to the contour submergence velocity (in our case $v = -1$). The values of the contact point are associated by the relations ($v_k(t) = x_{0t}(0,t)$)

$$W = v_k\cos\alpha, \ W/\rho = \sin\alpha/v \quad (0 \leq t \leq t_*),$$

The first of them follows from (3.16), and the second follows from (3.15). Hence,

$v_k^{-2}(t)p^2 - (1 - 1/\varrho)\,p + v^2 = 0 \quad (0 \leq t \leq t_*)$;
for the case under consideration we have

$$2tp^2 - (1 - 1/\varrho)\,p + 1 = 0 \qquad (3.17)$$

Equation (3.17) at sufficiently small t has two positive roots, p_1 , p_2 , from which the less one should be chosen, otherwise $p \to \infty$ when $t \to 0$. With increasing t the difference $p_2 - p_1$ tends to zero and $p_2 = p_1 = p_*$ at some t_*. For $t > t_*$ equation (3.17) has no positive roots. If the right-hand side of (3.17) is designated by $F(p,t)$, the confluence condition of p_1 and p_2 roots has the form $\partial F/\partial p = 0$. Consequently, to determine t_*, p_* we should obtain the system of equations

$$2t_* p_*^2 - (1 - \varrho^{-1}(p_*))\,p_* + 1 = 0,$$

$$4t_* p_* - \varrho^{-2}(p_*)\,c^{-2}(p_*)p_* - 1 + \varrho^{-1}(p_*) = 0.$$

Hence,

$$p_*(1 - [1 + nM^2 p_*]^{-1/n}) - 2 = M^2 p_*^2 (1 + nM^2 p_*)^{-\frac{n+1}{n}} \qquad (3.18)$$

It is natural to suppose that $M^2 p_* \to 0$ when $M \to 0$, then (3.18) gives

$$p_* = \left(\frac{4}{n+1}\right)^{1/3} M^{-4/3}\,[1 + O(M^{1/3})] \quad (M \to 0).$$

Asymptotics $t_*(M)$ takes the form:

$$t_* = \frac{1}{2}M^2 - \frac{3}{2}\left(\frac{n+1}{4}\right)^{2/3} M^{8/3} + O(M^3) \qquad (3.19)$$

This confirms that the internal expansion of the unknown functions and the tension of independent variables was chosed in a correct way. The constant t_{*1} entering the formulation of the boundary-value problem (3.15) is to be considered known. From (3.19) it follows that

$$t_{*1} = -\frac{3}{2}\left(\frac{n+1}{4}\right)^{2/3}.$$

References

1 Nalimov, V.I. & Pukhnachov, V.V. Unsteady motion of an ideal liquid with a free boundary. Novosibirsk, 1975, 174 pp.

2 Cole, F.D. Perturbation Methods in Applied Mathematics. Blaisdell Publ. Company, London, 1968.

3 Pukhnachov, V.V., Korobkin, A.A. Initial Asymptotics in Problem of Blunt Body Entrance into Liquid. - In: Third International Conference on Numerical Ship Hydrodynamics (Paris, 16-20 June, 1981). Paris, 1981.

4 Povitsky, A.S. Impact at landing of flying boat. - Trudy ZAGI, 1935, 199, pp.1-17.

5 Weining, F. Berücksichtigung der Elastizitat beim Aufschlag eines gekielten Flugzeugschwimmers auf das Wasser (Ebenes Problem).- Luftfahrtforschung, 1936, Band 13, S. 155--159.

6 Wagner, H. Über Stoss- und Gleitvorgänge an der Oberfläche von Flüssigkeiten.- ZAMM, 1932, Band 12, Heft 4, S. 193-215.

7 Grigoljuk, E.I., Gorshkov, A.G. Interaction between elastic structures and a liquid. - Leningrad, "Sudostroyenie", 1976, 200 pp.

8 Vlasov, V.V. A general shell theory and its applications in engineering.- Moscow,"Gostehizdat", 1956, 416 pp.

9 Lavrentyev, M.A., Shabat, B.V. Methods for functions theory of complex variable. Moscow, "Nauka", 1973, 736 pp.

10 Lesser, M.V. Analytic Solutions of Liquid--Drop Impact Problems. - Proc. R. Soc. London, Ser. A, 1981, vol. 377, pp. 289-308.

11 Korobkin, A.A. Elastic shell entry into an ideal liquid. - In: Dinamika sploshnoi sredy, Novosibirsk, 1983, N63, pp. 84-93.

12 Kubenko, V.D. Elastic shell entry into a compressible liquid. - Kiev, "Naukova dumka", 1981, 160 pp.

13 Adler, W.F. Mechanics of shock effect of liquid. - In:Erosion, "Academic Press", New York, 1979.

14 Christianovich, S.A. Shock wave at a significant distance from the explosion. PMM, 1956, vol.XX,N 5, pp. 599-606.

15 Ovsjannikov, L.V. Course of Lectures on Gasdynamics Foundations. Moscow, "Nauka", 1981, 368 pp.

Session III

SEAKEEPING
AT ZERO FORWARD SPEED

Session Chairman
A.J. Hermans
Technical University
Delft, The Netherlands

A NUMERICAL SOLUTION FOR THE DIFFRACTION OF SECOND ORDER GROUP-INDUCED WAVES BY A FLOATING BODY

Sun Be-Qi and Gu Mao-Xiang

China Ship Scientific Research Center
Wuxi China

Abstract

This paper presents a 3-D numerical BIE method for calculating the forces and moments acting on a floating body due to diffraction of second-order group-induced waves of low frequency. The total second order wave potential $\phi^{(2)}$ is decomposed into three parts: $\phi_w^{(2)}$, the potential of the second order incident wave; $\phi_R^{(2)}$, the potential of the second order radiated wave and $\phi_d^{(2)}$, the potential of the second order diffracted wave. $\phi_w^{(2)}$ and $\phi_R^{(2)}$ can be calculated by known methods, but $\phi_d^{(2)}$ has been difficult to evaluate either analytically or by numerical methods. The method presented here avoided the direct calculation of $\phi_d^{(2)}$, but evaluated $\iint_\Sigma \phi_d^{(2)} n_j ds$ (j=1, 2, ... 6) using Haskind relationship and developing Molin's idea [11] into a numerical method wich integrates over the free-surface and over the body surface with all its nonlinear terms taken into account of. Numerical results of second order diffraction loads for a semisubmersible drill ship are presented. An approximate concept to relate the second-order load in bichromatic waves to wave damping effect is proposed and a specially designed experiment is conducted to validate the concept. Qualitative agreement between numerical and experimental results are achieved.

1. Introduccion

Large excursions of moored structures at low frequency with accompanying high mooringloads have known to be important in offshore engineering. The forces that excite large low frequency hotizontal motion are known to be of second-order in magnitude as compared to first order wave exciting forces of normal wave frequency. Faltinsen, O.M. and Loken [1], Papanikolaou, A [2], Rahman [3], Eatock Taylor and S.M. Hung [4], Kyozuka, Y. [5], Miao G. P. and Liu Y.Z. [6] have worked out on 2-D theories giving numerical methods for evaluating the diffraction wave potentials and loads on cylinders. Triantafyllou [7], C.C. Mei [8] put forth consistent theories using perturbation method of multiple scales for solving second order forces that give rise to zero order motions. Pinkster [9] Standing [10] Molin [11] have worked out on 3-D theories and numerical methods for computing second-order excitation forces. However, a numerical method treating generally the low frequency diffraction load on a floating body of arbitrary shape has not been developed fully.

At the same time, a governing factor for evaluating the amplitude of excursion and mooring load on floating structuries has been the fluid damping coefficient of such a system. Wichers et al [12], Tagaki [13], Cao [14], Qi investigated experimentally into the damping coefficient of low frequency motions of moored structures and found that damping coefficient of these motions associated with first order motions of the structure in waves are usually higher than the calm-water damping coefficient of the same low frequency oscillations executed by the moored system in calm water. The difference is called wave damping. Cao and Qi [14], found that under certain frequencies damping of slow motions in waves are lighter than chose in calm water, and may give rise to negative wave damping coefficient. The present report relates the in-phase component of second-order diffract load with the second-order incident wave horizontal velocity and found that the force coefficient so obtained is in general agreement with the wave damping coefficient obtained experimentally. A tentative explanation of this effect is given in section 4.

The second order force consists of six parts

$$\vec{F}^{(2)} = -\frac{1}{2}\rho g \int_{WL} \zeta_r^{(1)2} \vec{n}^{(0)} dl + \frac{1}{2}\rho \iint_\Sigma |\nabla\phi^{(1)}|^2 \vec{n}^{(0)} ds + \rho \iint_\Sigma \nabla\phi_t^{(1)} X^{(1)} \vec{n}^{(0)} ds + R^{(1)} \vec{F}^{(1)} + \rho \iint_\Sigma \phi_t^{(2)} \vec{n}^{(0)} ds - \rho g (\eta_3^{(2)} S_{WL} - \eta_5^{(2)} S_{1*} + \eta_4^{(2)} S_{2L}) \vec{e}_3 \quad (1)$$

$$\vec{M}^{(2)} = -\frac{1}{2}\rho g \int_{WL} \zeta_r^{(1)2} (\vec{r}^{(0)} \times \vec{n}^{(0)})\, dl +$$

$$\frac{1}{2}\rho \iint_{\Sigma} \left| \nabla \phi^{(1)} \right|^2 (\vec{r}^{(0)} \times \vec{n}^{(0)})\, dS + \rho \iint_{\Sigma} \nabla \phi^{(1)}$$

$$X^{(1)} (\vec{r}^{(0)} \times \vec{n}^{(0)})\, dS + R^{(1)} \vec{M}^{(1)} + \rho \iint_{\Sigma} \phi_t^{(2)} (\vec{r}^{(0)}$$

$$\times \vec{n}^{(0)})\, dS - \rho g \forall \left(\eta_4^{(2)} x_{38} + \eta_3^{(2)} S_{20}/\forall - \eta_5^{(2)} \right.$$

$$\left. S_{12}/\forall + \eta_4^{(2)} S_{22}/\forall \right) \vec{e}_1 - \rho g \forall \left(\eta_5^{(2)} x_{38} - \eta_3^{(2)} \right.$$

$$\left. S_{10}/\forall + \eta_5^{(2)} S_{11}/\forall - \eta_4^{(2)} S_{12}/\forall \right) \vec{e}_2 \qquad (2)$$

The first term is the integral of the first order wave pressure over the area between the mean waterline on the structure and the surface elevation. The second term is the integral of the quardratic term in velocity over the mean submerged area of the structure. The third term arises from the second order part of the integral over the mean submerged area of the first order wave pressure when that pressure in evaluted at the position of the displaced body. The fourth term arises from the rotation due to roll, pitch and yaw of the total first order fluid force on the structure including the hydrostatic restoring force. The fifth term comes from second order potential. The sixth term is second order hydrostatic restoring force.

When the first order potentials and motions have been solved, the first four terms can be calculated without difficulty. To calculate the fifth term and sixth term, we must evaluate the second-order potential $\phi^{(2)}$ and second order motion response $\eta^{(2)}$.

We decompose the second order potential $\phi^{(2)}$ into three parts, namely:

$$\phi^{(2)} = \phi_M^{(2)} + \phi_D^{(2)} + \phi_R^{(2)}$$

where $\phi_M^{(2)}$ and $\phi_R^{(2)}$ are potential of second order incident waves and radiated waves respectively. They can be calculated wtih relative ease. For $\phi_D^{(2)}$ we have defined a relation between $\iint_{\Sigma} \phi_t^{(2)} n_j ds (j=1,2,\ldots,6)$ and nonlinear terms in the free surface condition and also in the kinematic boundary condition on the mean submerged surface Σ of the structure. Using this relation, the second-order wave exciting force have been obtained which will be discribed in detail in the follwing.

2. Theoretical Formulation

We make as usual the assumption of a perfect and irrotational flow, which allows us to describe the motion by a velocity potential $\Phi(x, y, z, t)$, where (x, y, z) belongs to the undisturbed fluid domain D. We shall use a right-handed frame of coordinate $\{o - xyz\}$ with oz vertically upward and oxy plane corresponding to the undisturbed free-surface, as shown in figure 1. The body coordinates is consistent with the coordinates $\{o - xyz\}$ at t=0.

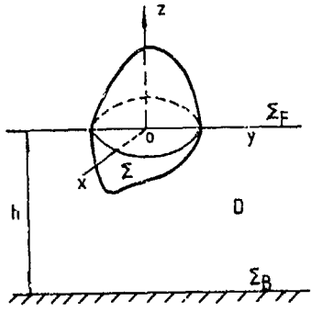

Fig 1

Let ε be a perturbation parameter, identified with the wave steepness $k\zeta$, where k is the wave number, and ζ the wave-amplitude, Φ may be written as:

$$\Phi(x,y,z,t) = \varepsilon \Phi^{(1)}(x,y,z,t) + \varepsilon^2 \Phi^{(2)}(x,y,z,t) + \cdots\cdots$$

and the fluid force acting on the body as

$$F = F^{(0)} + \varepsilon F^{(1)} + \varepsilon^2 F^{(2)} + \cdots$$

From (1) and (2), it is found that the second-order force $F^{(2)}$ contains the term:

$$\iint_{\Sigma} \Phi_t^{(2)} n_j \, ds \,, \quad j = 1, 2, \cdots, 6 \qquad (3)$$

where $n_1 = n_x$, $n_2 = n_y$, $n_3 = n_z$, $n_4 = yn_3 - zn_2$, $n_5 = zn_1 - xn_3$, $n_6 = xn_2 - yn_1$.

In the case of difference frequency which is of main interest to us, expression (3) becomes

$$i(\omega_\mu - \omega_\nu) \iint_{\Sigma} \phi_{\mu\nu}^{(2)} n_j \, ds \, e^{i(\omega_\mu - \omega_\nu)t} \qquad (4)$$

For the sake of convenience, we shall hereafter omit subscripts $\mu\nu$ of $\phi_{\mu\nu}^{(2)}$. The second order potential $\phi^{(2)}$ should satisfy the following set of conditions:

$$(A) \begin{cases} \nabla^2 \phi^{(2)}(x,y,z) = 0 & (x,y,z) \in D \\ -(\omega_\mu - \omega_\nu)^2 \phi^{(2)} + g \phi_z^{(2)} + 2i\omega_\nu \nabla \phi^{(\mu)} \nabla \phi^{(\nu)} + \\ \frac{i}{g} \omega_\mu \omega_\nu^2 \phi^{(\mu)} \phi_z^{(\nu)} - i\omega_\mu \phi^{(\mu)} \phi_{zz}^{(\nu)} = 0 & (x,y,0) \in \Sigma_F \\ \nabla \phi^{(3)} \cdot \vec{n}^{\omega} = \vec{v}^{\omega} \cdot \vec{n}^{\omega} + (\vec{v}^{\omega} - \nabla \phi^{(\mu)}) \vec{n}^{\omega} + \\ (\vec{\Omega}^{\omega} \times \vec{\Sigma}^{\omega} - (\vec{\Sigma}^{\omega} \cdot \nabla) \nabla \phi^{(\nu)}) \vec{n}^{\omega} & (x,y,z) \in \Sigma \\ \phi_z^{(2)} = 0 & (x,y,-z) \in \Sigma_B \end{cases}$$

Radiation condition

where D is the fluid domain, Σ_F is the undisturbed free surface minus the waterplane occupied by the body. Σ is the mean wetted surface of the body and Σ_B is the sea bottom.

Now, as mentioned above:

$$\phi^{(2)} = \phi_w^{(2)} + \phi_b^{(2)} + \phi_d^{(2)} \tag{5}$$

where the $\phi_w^{(2)}$ satisfies conditions

$$\text{(B)}\quad \begin{cases} \nabla^2 \phi_w^{(2)}(x,y,z) = 0 & (x,y,z) \in D \\ -(\omega_\mu - \omega_\nu)^2 \phi_w^{(2)} + g \phi_{wz}^{(2)} + 2i\omega_\nu \nabla\phi_w^{(1)} \nabla\phi_w^{(1)} + \\ \frac{i}{g}\omega_\mu \omega_\nu^2 \phi_w^{(1)} \phi_{wz}^{(1)} - i\omega_\mu \phi_w^{(1)} \phi_{wzz}^{(1)} = 0 & (x,y,0) \in \Sigma_F \\ \phi_{wz}^{(2)} = 0 & (x,y,-\ell) \in \Sigma_B \end{cases}$$

, $\phi_b^{(2)}$ satisfies the conditions

$$\text{(C)}\quad \begin{cases} \nabla^2 \phi_b^{(2)} = 0 & (x,y,z) \in D \\ -(\omega_\mu - \omega_\nu)^2 \phi_b^{(2)} + g \phi_{bz}^{(2)} = 0 & (x,y,0) \in \Sigma_F \\ \phi_{bz}^{(2)} = 0 & (x,y,-\ell) \in \Sigma_B \\ \nabla^2 \phi_b^{(2)} \cdot \vec{n}^{(\mu)} = \vec{v}^{(2)} \cdot \vec{n}^{(\mu)} & (x,y,z) \in \Sigma \\ \sqrt{R}\left(\frac{\partial \phi_b^{(2)}}{\partial R} + i\nu \phi_b^{(2)}\right) \to 0 & R \to \infty \end{cases}$$

and $\phi_d^{(2)}$ satisfies conditions

$$\text{(D)}\quad \begin{cases} \nabla^2 \phi_d^{(2)} = 0 & (x,y,z) \in D \\ -(\omega_\mu - \omega_\nu)^2 \phi_d^{(2)} + g \phi_{dz}^{(2)} = -2i\omega_\mu \nabla\phi^{(1)} \nabla\phi^{(1)} \\ -\frac{i}{g}\omega_\mu \omega_\nu^2 \phi^{(1)} \phi_z^{(1)} + i\omega_\mu \phi^{(1)} \phi_{zz}^{(1)} + 2i\omega_\mu \nabla\phi_w^{(1)} \nabla\phi_w^{(1)} \\ + \frac{i}{g}\omega_\mu \omega_\nu^2 \phi_w^{(1)} \phi_{wz}^{(1)} - i\omega_\mu \phi_w^{(1)} \phi_{wzz}^{(1)} \\ \qquad (x,y,0) \in \Sigma_F \\ \phi_{dz}^{(2)} = 0 & (x,y,-\ell) \in \Sigma_B \\ \nabla\phi_d^{(2)} \cdot \vec{n}^{(\mu)} = (\vec{v}^{(2)} - \nabla\phi^{(1)}) \cdot \vec{n}^{(\mu)} + (\vec{\Omega}^{(2)} \times \vec{x}^{(\mu)} - \\ (\vec{x}^{(\mu)} \cdot \nabla)\nabla\phi^{(1)}) \vec{n}^{(\mu)} - \nabla\phi_w^{(1)} \cdot \vec{n}^{(\mu)} \\ \qquad (x,y,z) \in \Sigma \\ \text{Radiation condition} \end{cases}$$

$\phi_w^{(2)}$ is the second order incident wave potential, $\phi_b^{(2)}$ is the second order radiation potential and $\phi_d^{(2)}$ is the second order diffraction potential. It can be seen that the free waves and waves locked to the first-order wave system are included in the $\phi_d^{(2)}$.

Expression (4) may be rewritten as

$$\iint_S \phi^{(\mu)} n_j \, ds = \iint_\Sigma \phi_w^{(\mu)} n_j \, ds + \iint_\Sigma \phi_b^{(\mu)} n_j \, ds + \iint_\Sigma \phi_d^{(\mu)} n_j \, ds \tag{6}$$

where the factor $i(\omega_\mu - \omega_\nu)$ is omitted.

For finite water-depth the expression for $\phi_w^{(2)}$ has been given by Bowers as:

$$\phi_w^{(2)} = \sum_N b_N \cosh 2k_N(z+\ell) \sin 2(-\omega_N t + k_N x\cos\theta + k_N y \sin\theta + \varepsilon_N) + \sum_{N'} \sum_{N<N'} \left(c_{NN'} \cosh k_N^+(z+\ell) \sin(-\omega_N^+ t + k_N^+ x\cos\theta + k_N^+ y\sin\theta + \varepsilon_N^+) + d_{NN'} \cosh k_N^-(z+\ell) \sin(-\omega_N^- t + k_N^- x\cos\theta + k_N^- y\sin\theta + \varepsilon_N^-) \right) \tag{7}$$

Here the subscripts for wave number and frequency are defined as

$$F_N^+ = F_{N'} + F_N \quad , \quad F_N^- = F_{N'} - F_N \tag{8}$$

, and

$$b_N = \frac{3 a_N^2 g^2 k_N^2}{4\omega_N \cosh^2 k_N \ell (2\omega_N^2 \cosh 2k_N\ell - g k_N \sinh 2k_N \ell)} \tag{9}$$

$$c_{NN'} = \frac{1}{2} g a_N a_{N'} \frac{e_N^+ + 2k_N k_{N'} \omega_N^+ (1 - \tanh k_N \ell \tanh k_{N'} \ell)}{(\omega_N^+)^2 \cosh k_N^+ \ell - g k_N^+ \sinh k_N^+ \ell} \underline{(\omega_N \omega_{N'})^{-1}} \tag{10}$$

$$d_{NN'} = \frac{1}{2} g a_N a_{N'} \frac{e_N^- + 2k_N k_{N'} \omega_N^- (1 + \tanh k_N \ell \tanh k_{N'} \ell)}{(\omega_N^-)^2 \cosh k_N^- \ell - g k_N^- \sinh k_N^- \ell} \underline{(\omega_N \omega_{N'})^{-1}} \tag{11}$$

where a_N is the amplitude of first-order incident wave, i.e.

$$\zeta^{(1)} = \sum_N a_N \cos(-\omega_N t + k_N x\cos\theta + k_N y \sin\theta + \varepsilon_N) \tag{12}$$

and

$$e_N^+ = \frac{k_{N'}^2}{\omega_{N'} \cosh^2 k_{N'} \ell} + \frac{k_N^2}{\omega_N \cosh^2 k_N \ell} \tag{13}$$

$$e_N^- = \frac{k_{N'}^2}{\omega_{N'} \cosh^2 k_{N'} \ell} - \frac{k_N^2}{\omega_N \cosh^2 k_N \ell} \tag{14}$$

The set of conditions (C) referring to second order radiation potential $\phi_b^{(2)}$ is in the same form as that for the first order radiation potentials. Its solution can be obtained by the same method as that used for solving first order radiation potentials.

Now we turn to discuss the integral $\iint_S \phi_d^{(2)} n_j ds$. First we shall investigate the asymptotic behaviour of $\phi_d^{(2)}$.

Asymptotic behaviour of $\phi_d^{(2)}$

Using oz as the veritcal axis, we generate a circular cylinder Σ_C of radius R enclosing the structure. The circular cylinder Σ_C divides the fluid domain D into two parts, as shown in figure 2. D_1 is the inner domain enclosed by Σ_C, Σ_{Fi}, Σ_{Bi} and Σ, where Σ_{Fi} - Σ_{Bi} are free-surface and sea bottom enclosed by Σ_C. D_0 is the outer domain bounded by Σ_C, Σ_{F0}, Σ_{B0} and infinity, where Σ_{F0} and Σ_{B0} are free-surface

and sea bottom outside of circular cylinder Σ_c. Then, the set of conditions (D) may be transformed into two sets of conditions:

For domain D_1,

$$
(E)\quad\begin{cases}
\nabla^2\phi_{di}^{(2)}=0 & (x,y,z)\in D_I\\
-(\omega_\mu-\omega_\nu)^2\phi_{di}^{(2)}+g\phi_{diz}^{(2)}=-i2\omega_\nu\nabla\phi^{(1)}\nabla\phi^{(1)}\\
-\frac{i}{g}\omega_\mu\omega_\nu^2\phi^{(1)}\phi_z^{(1)}+i\omega_\mu\phi^{(1)}\phi_{zz}^{(1)}+2\omega_\nu i\nabla\phi_w^{(1)}\\
\nabla\phi_w^{(2)}+\frac{i}{g}\omega_\mu\omega_\nu^2\phi_w^{(1)}\phi_{wz}^{(1)}-i\omega_\mu\phi_w^{(1)}\phi_{wzz}^{(1)}\\
\qquad (x,y,0)\in\Sigma_{Fi}\\
\phi_{diz}=0 & (x,y,-h)\in\Sigma_{Bi}\\
\nabla\phi_{di}^{(2)}\cdot\vec{n}^{(2)}=\left(\vec{v}^{(1)}-\nabla\phi^{(1)}\right)\cdot\vec{n}^{(1)}+\left(\vec{\Omega}^{(1)}\times\vec{x}^{(1)}\right.\\
\left.-\left(\vec{x}^{(1)}\cdot\nabla\right)\nabla\phi^{(1)}\right)\cdot\vec{n}^{(2)}-\nabla\phi_w^{(2)}\cdot\vec{n}^{(2)} & (x,y,z)\in\Sigma\\
\nabla\phi_{di}^{(2)}\cdot\vec{n}^{(2)}=\nabla\phi_{do}^{(2)}\cdot\vec{n}^{(2)} & (x,y,z)\in\Sigma_c\\
\phi_{di}^{(2)}=\phi_{do}^{(2)} & (x,y,z)\in\Sigma_c
\end{cases}
$$

For domain D_0,

$$
(F)\quad\begin{cases}
\nabla^2\phi_{do}^{(2)}=0 & (x,y,z)\in D_0\\
-(\omega_\mu-\omega_\nu)^2\phi_{do}^{(2)}+g\phi_{doz}^{(2)}=-i2\omega_\nu\nabla\phi^{(1)}\nabla\phi^{(1)}\\
-\frac{i}{g}\omega_\mu\omega_\nu^2\phi^{(1)}\phi_z^{(1)}+i\omega_\mu\phi^{(1)}\phi_{zz}^{(1)}+2\omega_\nu i\nabla\phi_w^{(1)}\\
\nabla\phi_w^{(1)}+\frac{i}{g}\omega_\mu\omega_\nu^2\phi_w^{(1)}\phi_{wz}^{(1)}-i\omega_\mu\phi_w^{(1)}\phi_{wzz}^{(1)}\\
\qquad (x,y,0)\in\Sigma_{Fo}\\
\phi_{doz}^{(2)}=0 & (x,y,-h)\in\Sigma_{Bo}\\
\nabla\phi_{do}^{(2)}\cdot\vec{n}^{(2)}=\nabla\phi_{di}^{(2)}\cdot\vec{n}^{(2)} & (x,y,z)\in\Sigma_c\\
\phi_{do}^{(2)}=\phi_{di}^{(2)} & (x,y,z)\in\Sigma_c\\
\text{Radiation condition}
\end{cases}
$$

where

$$
\phi_d^{(2)}=\begin{cases}\phi_{di}^{(2)} & (x,y,z)\in D_I\\ \phi_{do}^{(2)} & (x,y,z)\in D_o\end{cases}
$$

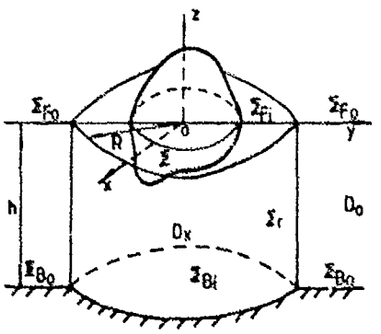

Fig 2

In order to investigate the behaviour of $\phi_d^{(2)}$ at infinity, we need only to investigate that of $\phi_{do}^{(2)}$. When the radius R of the circular cylinder Σ_c is large enough, we have form for first order radiation potentials:

$$
\phi_i^{(1)}\approx 0.797\frac{2\pi(\nu^2-k^2)chkh}{(k^2-\nu^2)h+\nu}\frac{1}{\sqrt{kR}}\sum_{j=1}^{N}\sigma_j\Delta S_j\,ch\,k(\zeta_j+h) \tag{16}
$$

$$
\phi_{iz}^{(1)}\approx 0.798\frac{2\pi(\nu^2-k^2)chkh}{(k^2-\nu^2)h+\nu}\sqrt{\frac{k}{R}}\sum_{j=1}^{N}\sigma_j\Delta S_j\,ch\,k(\zeta_j+h) \tag{17}
$$

$$
\phi_{iy}^{(1)}\approx 0.798\frac{2\pi(\nu^2-k^2)chkh}{(k^2-\nu^2)h+\nu}\sqrt{\frac{k}{R}}\sum_{j=1}^{N}\sigma_j\Delta S_j\,ch\,k(\zeta_j+h) \tag{18}
$$

$$
\phi_{iz}^{(1)}\approx 0.798\frac{2\pi(\nu^2-k^2)chkh}{(k^2-\nu^2)h+\nu}\sqrt{\frac{k}{R}}\sum_{j=1}^{N}\sigma_j\Delta S_j\,ch\,k(\zeta_j+h) \tag{19}
$$

$$
\phi_{izz}^{(1)}\approx 0.798\frac{2\pi(\nu^2-k^2)chkh}{(k^2-\nu^2)h+\nu}k^{3/2}\frac{1}{\sqrt{k}}\sum_{j=1}^{N}\sigma_j\Delta S_j\,ch\,k(\zeta_j+h) \tag{20}
$$

where $\nu=\omega^2/g$

k th $kR=\nu$

$R=\sqrt{x^2+y^2}$

σ_j is the source strength on the jth panel of the structure surface.

Δs_j is the area of jth panel on body surface

From formulae (16)-(20), it may be noted that a radius R_ε can always be found for any arbitrary small positive number ε, for which

$$
\left|-2(\omega_\mu-\omega_\nu)\nabla\phi^{(1)}\nabla\phi^{(1)}-\frac{i}{g}\omega_\mu\omega_\nu^2\phi^{(1)}\phi_z^{(1)}+i\omega_\mu\phi^{(1)}\phi_{zz}^{(1)}+2\omega_\nu i\nabla\phi_w^{(1)}\nabla\phi_w^{(1)}+\frac{i}{g}\omega_\mu\omega_\nu^2\phi_w^{(1)}\phi_{wz}^{(1)}-i\omega_\mu\phi_w^{(1)}\phi_{wzz}^{(1)}\right|<\varepsilon
$$

If ε is small enough, then conditions (F) can be approximated by the following set of conditions:

$$
(G)\quad\begin{cases}
\nabla^2\phi_{do}^{(2)}=0 & (x,y,z)\in D_0\\
-(\omega_\mu-\omega_\nu)^2\phi_{do}^{(2)}+g\phi_{doz}^{(2)}=0 & (x,y,0)\in\Sigma_{Fo}\\
\phi_{doz}^{(2)}=0 & (x,y,-h)\in\Sigma_{Bo}\\
\nabla\phi_{do}^{(2)}\cdot\vec{n}^{(2)}=\nabla\phi_{di}^{(2)}\cdot\vec{n}^{(2)} & (x,y,z)\in\Sigma_c\\
\phi_{do}^{(2)}=\phi_{di}^{(2)} & (x,y,z)\in\Sigma_c\\
\sqrt{R}\left(\frac{\partial\phi_{do}^{(2)}}{\partial R}+i\nu\phi_{do}^{(2)}\right)\to 0 & R\to\infty
\end{cases}
$$

The solution of $\phi_{do}^{(2)}$ can be expressed as follows

$$\phi_{do}^{(2)} = \frac{2\pi(\nu^2-k^2)}{(k^2-\nu^2)k+\nu} ch\,k(z+h) \sum_{j=1}^{N_c} \sigma_j^{(c)} \iint_{S_j^{(c)}} ch\,k(\zeta+h)\left[Y_0(kR) - i J_0(kR)\right] d\xi\, d\eta\, d\zeta + 4\sum_{m=1}^{\infty} \frac{\mu_m^2+\nu^2}{(\mu_m^2+\nu^2)h-\nu} \cos\mu_m(z+h) \sum_{j=1}^{N_c} \sigma_j^{(c)} \iint_{S_j^{(c)}} \cos\mu_m(\zeta+h) K_0(\mu_m R) d\xi\, d\eta\, d\zeta \tag{21}$$

where $R = \sqrt{(x-\xi)^2+(y-\eta)^2}$

$\mu_m \tan \mu_m h + \nu = 0$

$\sigma_j^{(c)}$ and $s_j^{(c)}$ are the source strength and area of the jth panel located on the circular cylinder of radius R_c respectively.

J_0 is zero order Bessel function of first kind.

Y_0 is zero order Bessel function of second kind.

K_0 is zero order modified Bessel function of second kind.

Similar formulae can be obtained for $\phi_{doz}^{(2)}$, $\phi_{dd}^{(2)}$, $\phi_{dox}^{(2)}$, $\phi_{doy}^{(2)}$ and $\phi_{dozz}^{(2)}$ using the same method 17 as in the derivation of formulae (16)-(20). Thus, we have

$$\phi_{do}^{(2)} \approx 0.798 \frac{2\pi(\nu^2-k^2)}{(k^2-\nu^2)k+\nu} ch\,kh \frac{1}{\sqrt{kR}} \sum_{j=1}^{N_c} \sigma_j^{(c)} \Delta S_j^{(c)} ch\,k(\zeta_j+h) \tag{22}$$

Expression (22) is an asymptotic expansion of $\phi_{do}^{(2)}$ at infinity, which holds approximately as $R \gg R_c$.

Formula of calculating $\iint_\Sigma \phi_d^{(2)} n_j ds$

Following Molin's idea [11] and using the asymptotic expansion (22), a relation similar to Haskind relation is obtained. Based on this relation the integral $\iint_\Sigma \phi_d^{(2)} n_j ds$ may be calculated.

Let

$$\Psi_j = Re\left\{\psi_j e^{i(\omega_\mu-\omega_\nu)t}\right\} \tag{23}$$

where $\omega_\mu - \omega_\nu$ corresponds to the difference frequency of potential $\phi_d^{(2)}$ and ψ_j satisfies the following conditions:

$$(H)\quad \begin{cases} \nabla^2\psi_j = 0 & (x,y,z)\in\Omega \\ \dfrac{\partial\psi_j}{\partial n} = n_j & (x,y,z)\in\Sigma \\ g\dfrac{\partial\psi_j}{\partial n} - (\omega_\mu-\omega_\nu)^2\psi_j = 0 & (x,y,0)\in\Sigma_F \\ \dfrac{\partial\psi_j}{\partial n} = 0 & (x,y,-h)\in\Sigma_B \\ \sqrt{R}\left(\dfrac{\partial\psi_j}{\partial R} + i\nu\psi_j\right) \longrightarrow 0 & R\to\infty \end{cases}$$

Using oz as the vertical axis, we generate another circular cylinder Σ_R of radius R enclosing the structure and the circular cylinder of radius R_c. Let $R \gg R_c$. Again the cylinder Σ_R divides the fluid domain D into two parts denoted here by D_i and D_o. Domain D_i is enclosed by Σ_R, Σ_{Fi}, Σ_{Bi} and Σ, while domain D_o is bounded by Σ_R, Σ_{Fo}, Σ_{Bo} and infinity.

In domain D_i, using Green's third identity, we have

$$\iint_\Sigma \phi_d^{(2)} n_j\, ds = \iint_\Sigma \phi_d^{(2)} \frac{\partial\psi_j}{\partial n} ds = \iint_\Sigma \psi_j \frac{\partial\phi_d^{(2)}}{\partial n} ds + \iint_{\Sigma_{Fi}} \left(\psi_j \frac{\partial\phi_d^{(2)}}{\partial n} - \phi_d^{(2)} \frac{\partial\psi_j}{\partial n}\right) ds + \iint_{\Sigma_{Bi}} \left(\psi_j \frac{\partial\phi_d^{(2)}}{\partial n} - \phi_d^{(2)} \frac{\partial\psi_j}{\partial n}\right) ds + \iint_{\Sigma_R} \left(\psi_j \frac{\partial\phi_d^{(2)}}{\partial n} - \phi_d^{(2)} \frac{\partial\psi_j}{\partial n}\right) ds \tag{24}$$

From free-surface conditions of (E) and (H), we may write

$$\iint_{\Sigma_{Fi}} \left(\psi_j \frac{\partial\phi_d^{(2)}}{\partial n} - \phi_d^{(2)} \frac{\partial\psi_j}{\partial n}\right) ds = \frac{1}{g} \iint_{\Sigma_{Fi}} \psi_j f_{free} \tag{25}$$

where

$$f_{free} = -2i\omega_\nu \nabla\phi^{(1)} \nabla\phi^{(1)} - \frac{i}{g}\omega_\mu\omega_\nu^2 \phi^{(1)}\phi_z^{(1)} + i\omega_\mu \phi^{(1)}\phi_{zz}^{(1)} + 2i\omega_\nu \nabla\phi_w^{(1)} \nabla\phi_w^{(1)} + \frac{i}{g}\omega_\mu\omega_\nu^2 \phi_w^{(1)}\phi_{wz}^{(1)} - i\omega_\mu \phi_w^{(1)} \phi_{wzz}^{(1)} \tag{26}$$

On the sea bottom, we have

$$\iint_{\Sigma_{Bi}} \left(\psi_j \frac{\partial\phi_d^{(2)}}{\partial n} - \phi_n^{(2)} \frac{\partial\psi_j}{\partial n}\right) ds = 0 \tag{27}$$

Note that $\phi_d^{(2)} = \phi_{do}^{(2)}$ on Σ_R, we have

$$\iint_{\Sigma_R} \left(\psi_j \frac{\partial\phi_d^{(2)}}{\partial n} - \phi_d^{(2)} \frac{\partial\psi_j}{\partial n}\right) ds \approx \int_{-h}^{0} dz \int_0^{2\pi} (0.798 \frac{2\pi(\nu^2-k^2)ch\,kh}{(k^2-\nu^2)k+\nu} \frac{1}{\sqrt{k}})^2 \left|\sum_{j=1}^{N_b} \sigma_j^{(b)} \Delta S_j^{(b)} ch\,k(\zeta_j^{(b)}+h)\right| \left|\sum_{j=1}^{N_c} \sigma_j^{(c)} \Delta S_j^{(c)} ch\,k(\zeta_j^{(c)}+h)\right| \frac{1}{\sqrt{R}} \frac{1}{R^{3/2}} R\, d\theta$$

$$= \frac{2\pi h}{R} \left\{0.798 \frac{2\pi(\nu^2-k^2)ch\,kR}{(k^2-\nu^2)k+\nu} \frac{1}{\sqrt{R}}\right)^2 \left|\sum_{j=1}^{N_b} \sigma_j^{(b)} \Delta S_j^{(b)} ch\,k(\zeta_j^{(b)}+h)\right| \left|\sum_{j=1}^{N_c} \sigma_j^{(c)} \Delta S_j^{(c)} ch\,k(\zeta_j^{(c)}+h)\right|$$

$$= O\left(\frac{1}{R}\right) \tag{28}$$

where $\sigma_j^{(b)}$, $\Delta s_j^{(b)}$, $\zeta_j^{(b)}$ are sourcestrength, area, control point of the jth panel and N_b, the total number of panels on the structure surface respectively. $\sigma_j^{(c)}$, $\Delta s_j^{(c)}$, $\zeta_j^{(c)}$ are source strength, area, control point of the jth panel and N_c, the total number of panels on the surface of the circular cylinder of radius R_c respectively.

Using relation of (25)-(28), expression (24) may be rewritten as:

$$\iint_\Sigma \phi_d^{(2)} n_j\, ds = \iint_\Sigma \psi_j \frac{\partial\phi_d^{(2)}}{\partial n} ds + \frac{1}{g} \iint_{\Sigma_{Fi}} \psi_j f_{free}\, ds + O\left(\frac{1}{R}\right) \tag{29}$$

as $R \to \infty$, we have

$$\iint_\Sigma \phi_d^{(2)} n_j\, ds = \iint_\Sigma \psi_j \frac{\partial\phi_d^{(2)}}{\partial n} ds + \frac{1}{g} \iint_{\Sigma_F} \psi_j f_{free}\, ds \tag{30}$$

Using relation (30) and substituting in the known body surface condition for $\frac{\partial\phi_d^{(2)}}{\partial n}$ from (E),

we can ultimately evaluate the integral $\iint_\Sigma \phi_d^{(2)} n_j ds$ and hence also $\iint_\Sigma (\phi_o^{(2)} + \phi_d^{(2)}) n_j ds$.

3. Numerical Results

We consider the first-order wave elevation in a regular wave group consisting of N regular waves with frequency ω_i, i=1,2,···, N.

$$\zeta^{(1)} = \sum_{i=1}^{N} \zeta_i^{(1)} \cos(\omega_i t + \varepsilon_i)$$

In the numerical example thirty frequencies are used. See Tab. 1.

TABLE 1

Designation	Value	ω	ω
L	2.036 m	1.414	4.748
B	1.439 m	1.636	4.970
D	1.427 m	1.859	5.192
∀	0.221 m^3	2.081	5.414
H	4.0 m	2.303	5.637
S_{22}	0.715 m^4	2.525	5.859
S_{11}	0.67 m^4	2.748	6.081
I_{44}	0.00759 Tt^2/m	2.970	6.303
I_{55}	0.00828 Tt^2/m	3.192	6.525
I_{66}	0.1 Tt^2/m	3.414	6.748
Z_g	−0.1 m	3.637	6.970
Z_b	−0.235 m	3.859	7.192
S_{10}	0.0 m^3	4.081	7.414
		4.303	7.636
		4.525	7.806

The second-order force associated with such a wave train has the following form

$$F_K^{(2)} = \sum_{i=1}^{N}\sum_{j=1}^{N} \zeta_i^{(1)}\zeta_j^{(1)} (P_{K1ij} + P_{K2ij} + \cdots + P_{K6ij}) \cos((\omega_i-\omega_j)t + \varepsilon_i - \varepsilon_j) + \sum_{i=1}^{N}\sum_{j=1}^{N} \zeta_i^{(1)}\zeta_j^{(1)} (Q_{K1ij} + Q_{K2ij} + \cdots + Q_{K6ij}) \sin((\omega_i-\omega_j)t + \varepsilon_i - \varepsilon_j)$$

$$= \sum_{i=1}^{N}\sum_{j=1}^{N} \zeta_i^{(1)}\zeta_j^{(1)} [\tfrac{1}{2}(P_{K1ij} + P_{K1ji}) + \tfrac{1}{2}(P_{K2ij} + P_{K2ji}) + \cdots + \tfrac{1}{2}(P_{K6ij} + P_{K6ji})] \cos((\omega_i-\omega_j)t + \varepsilon_i - \varepsilon_j) + \sum_{i=1}^{N}\sum_{j=1}^{N} \zeta_i^{(1)}\zeta_j^{(1)} [\tfrac{1}{2}(Q_{K1ij} - Q_{K1ji}) + \tfrac{1}{2}(Q_{K2ij} - Q_{K2ji}) + \cdots + \tfrac{1}{2}(Q_{K6ij} - Q_{K6ji})] \sin((\omega_i-\omega_j)t + \varepsilon_i - \varepsilon_j)$$

$$= \sum_{i=1}^{N}\sum_{j=1}^{N} \zeta_i^{(1)}\zeta_j^{(1)} \bar{P}_{Kij} \cos((\omega_i-\omega_j)t + \varepsilon_i - \varepsilon_j) + \sum_{i=1}^{N}\sum_{j=1}^{N} \zeta_i^{(1)}\zeta_j^{(1)} \bar{Q}_{Kij} \sin((\omega_i-\omega_j)t + \varepsilon_i - \varepsilon_j)$$

and the quardratic transfer function

$$T_{Kij} = \sqrt{\bar{P}_{Kij}^2 + \bar{Q}_{Kij}^2}$$

, the phase

$$\varepsilon_{TKij} = \tan^{-1}(\bar{P}_{Kij} / \bar{Q}_{Kij})$$

where

$$\bar{P}_{Kij} = \tfrac{1}{2}(P_{K1ij} + P_{K1ji}) + \tfrac{1}{2}(P_{K2ij} + P_{K2ji}) + \cdots + \tfrac{1}{2}(P_{K6ij} + P_{K6ji})$$

$$\bar{Q}_{Kij} = \tfrac{1}{2}(Q_{K1ij} - Q_{K1ji}) + \tfrac{1}{2}(Q_{K2ij} - Q_{K2ji}) + \cdots + \tfrac{1}{2}(Q_{K6ij} - Q_{K6ji})$$

and subscript K, ℓ, i,j(ℓ=1,2,···,6) denote respectively second-order force(moment) in the kth direction, due to the lth term of formula (1) or (2) and due to the (i,j)th pair of bi-frequency, the superscript¯ denotes difference frequency. (Appendix 1)

Computation has been carried out for 1/50th model of a six column , two-floater semisubmersible, the principal particulars of which are given in table 1 and Fig.3

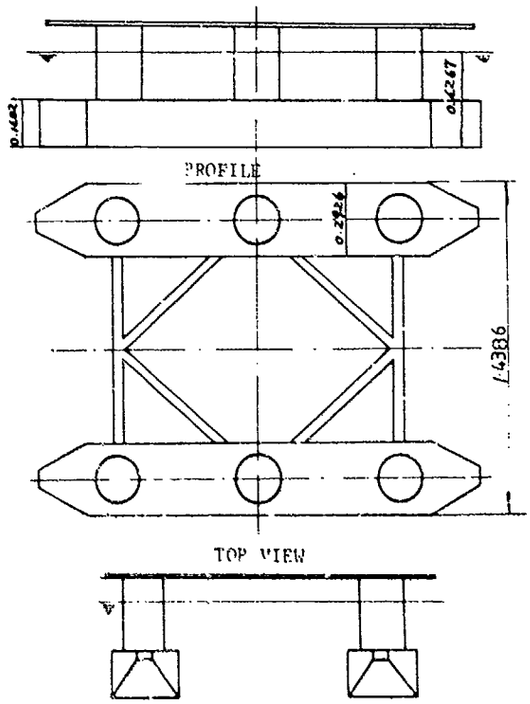

Fig. 3

From(30), it is shown that calculating the second order diffraction force may be reduced to the evaluation of integral.

$$I_1 = \iint_S \psi_j \frac{\partial \phi_d^{(2)}}{\partial n} dS$$

and

$$I_2 = \frac{1}{g} \iint_{S_f} \psi_j f_{free} dS$$

To calculate integral I_1, the wetted surface of the hull is approximated by a total of 244 plane facet elements. The facet schematisation of a quarter of the hull is shown in Fig. 4. Thus

$$I_1 = \iint_S \psi_j \frac{\partial \phi_d^{(2)}}{\partial n} dS = \sum_{K=1}^{244} \iint_{\Delta S_K} \psi_j \frac{\partial \phi_d^{(2)}}{\partial n} dS$$

and the integral is approximated by the summation

$$I_1 = \sum_{k=1}^{244} \iint_{\Delta S_k} \psi_j \frac{\partial \phi_d^{(2)}}{\partial n} dS = \sum_{k=1}^{244} \left(\psi_j \frac{\partial \phi_d^{(2)}}{\partial n}\right)_k \Delta S_k \qquad (31)$$

where $(\cdot)_k$ denotes the value of the function $\psi_j \frac{\partial \phi_d^{(2)}}{\partial n}$ at the center of the kth panel and Δs_k is the area of kth panel.

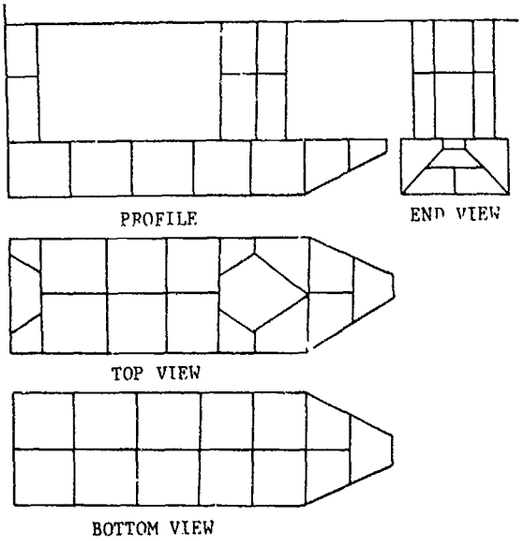

Fig. 4

The second integral $I_2 = \frac{1}{g} \iint_{\Sigma F} \phi_j f_{Fee} ds$

theoretically should be integrated over an infinite area of free surface. This infinite area is divided into two fields by a circle of radius R_a. The near field free surface (i.e. $R \leq R_a$) is approximated by 228 plane facet elements, and I_2 is evaluated by summation as in (31). The far field free surface (i.e. $R > R_a$) is approximated by the following integral

$$I_2 = \frac{1}{g} \iint_{\Sigma_F} \psi_j f_{Fee} dS = \frac{1}{g} \int_0^{2\pi} \int_{R_a}^{\infty} \psi_j f_{free} r dr d\theta$$

$$= \sum_{k=1}^{M} W_k (\psi_j f_{free})_{\xi_k} \qquad (32)$$

where Gauss approximate integral formulae

$$\int_0^{\infty} g(x) dx \approx \sum_{k=1}^{N} \lambda_k^{(n)} e^{\xi_k^{(n)}} g(\xi_k^{(n)})$$

and

$$\int_{-1}^{1} f(x) dx \approx \sum_{k=1}^{N} \lambda_k^{(n)} f(\xi_k^{(n)})$$

are used. w_k are the integrated coefficients and ξ_k are integrated nodes.

Since only the lowfrequency long-scale case is considered, the function $\phi_j f_{Fee}$ does not have the character of high frequency oscillation and hence is amenable to such methods of approximation.

The computation is carried out on an IBM3031 computer. Fig. 5 and Fig. 6 show the calculated results for quardratic transfer function of second-order forces in surge and heave in a following sea. The dotted line takes into account of the first four terms of eq.(1) and (2) only. The chain line includes the above four terms and the incident wave force in addition, i.e. the integral $\iint_\Sigma \phi_w^{(2)} n_j ds$. The solid line further takes into account of the integral $\iint_\Sigma \phi_d^{(2)} n_j ds$, i.e. the force due to diffraction. It is observed that the difference between them is very small for secondary heave force response and that the force due to incident and diffracted second order wave force could for all practical purpose be neglected. However, this is not in the case of surge, the second order diffraction force $\iint_\Sigma \phi_d^{(2)} n_j ds$ seems to be important, especially for the frequency range below 5.60. Nevertheless, the force due to incident wave $\phi_w^{(2)}$, i.e. the term $\iint_\Sigma \phi_w^{(2)} n_j ds$ is still small and could be neglected. One should bear in mind, however, that frequencies on a model scale of less than 5.60 corresponds to a full scale of 0.8 sec^{-1}, which is usually the energy gathering district of a wind wave spectrum.

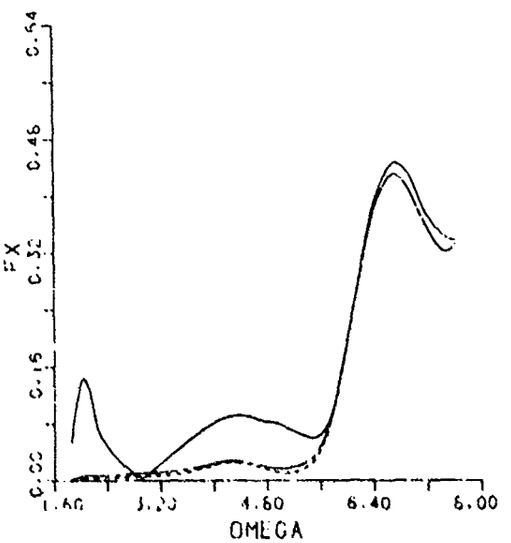

Fig 5

4. Experimental Results

i) A floating body executing free slow surge oacillations (ω_o) in calm water under a soft spring is described by

$$A_o \ddot{X} + B_o \dot{X} + C_o X = 0 \qquad (33)$$

where $A_o = m+a$, m is the body mass, and a is the added mass at ω_o; B_o is the calm water damping coefficient, the potential part of which is due to radiation waves $\phi_R^{(2)}$ of frequency ω_o.

Dividing throughout by A_o, we have

$$\ddot{X} + 2\mu_o\omega_o\dot{X} + \omega_o^2 = 0$$

where $2\mu_o = \frac{B_o}{2\sqrt{A_oC_o}}$, and $\omega_o = \sqrt{\frac{C_o}{A_o}}$

μ_o is determined experimentally by extinction tests by Cao[14] for the semi-submersible concerned and found to be 0.1025.

ii) The same mooring system and body is next placed in a regular wave of frequency ω_i, and the same extinction test performed. Another set of values $\mu(\omega_i, \omega_1)$, $\omega_1(\omega_i)$ is determined. In this case the motion is described by

$$A_o\ddot{X} + B_o\dot{X} + C_oX = \bar{F}^{(2)} + F_{11}^{(2)} + F_{21}^{(2)} \qquad (34)$$

where $F^{(2)}$ is the mean drift force due to regular wave ω_i

$F_{11}^{(2)}$ is the second order force in opposite phase with $\dot{X}$, and hence a damping force

$$F_{11}^{(2)} = -\frac{\partial F_{11}^{(2)}}{\partial \dot{X}}\dot{X}$$

$F_{21}^{(2)}$ is the second order force in opposite phase with $\ddot{X}$, and hence an added mass

$$F_{21}^{(2)} = -\frac{\partial F_{21}^{(2)}}{\partial \ddot{X}}\ddot{X}$$

Let $a_\zeta = \frac{\partial F_{21}^{(2)}}{\partial \ddot{X}}$, $B_\zeta = \frac{\partial F_{11}^{(2)}}{\partial \dot{X}}$ be the added mass and damping coefficient due to waves, then rearranging (2) and dropping out the mean force $\bar{F}^{(2)}$ for it does not contribute to the oscillation motion, we have

$$A_1\ddot{X} + B_1\dot{X} + C_oX = 0 \qquad (35)$$

where $A_1 = A_o + a_\zeta$

$B_1 = B_o + B_\zeta$

Again putting it in normalized form

$$\ddot{X} + 2\mu_1\omega_1\dot{X} + \omega_1^2X = 0 \qquad (36)$$

where $\mu_1 = \frac{B_1}{2\sqrt{A_1C_o}}$

$\omega_1 = \sqrt{\frac{C_o}{A_1}}$

Define $\mu_\zeta = \mu_1 - \mu_o = \frac{B_\zeta}{2\sqrt{A_1C_o}} - \mu_o\frac{a_\zeta}{2A_o}$ (for $\frac{a_\zeta}{A_o} \ll 1$) and plot the experimental results nondimensionally, the points in Fig. 7 are obtained.

In the figures $\mu'_\zeta = \mu_\zeta\left(\frac{0.1L}{2\zeta_a}\right)^2$ (37)

and the abscisea is $\omega\sqrt{\frac{L}{g}}$, L being the length of the semisubmersible and $2\zeta_a$ the wave height.

iii) The same mooring system and body may be placed in a brichromatic wave field of frequency (ω_i, ω_j), $j > i$, propagating in the +x direction, and the same extinction test conducted. In this case when the transient of freq. ω_1 dies out, there will remain a stable forced oscillation of frequency $\omega^- = \omega_j - \omega_i$. The motion may be described by

$$A_o\ddot{X} + B_o\dot{X} + C_oX = \bar{F}^{(2)} + F_{12}^{(2)} + F_{22}^{(2)} + F_2^{(2)}$$

where A_o, B_o, C_o, $\bar{F}^{(2)}$, carry the same meaning as before.

$F_{12}^{(2)} = \frac{\partial F_{12}^{(2)}}{\partial \dot{\xi}}\dot{\xi}$ = hydrodynamic force in phase with $\dot{\xi}$; the hydrodynamic force being due to $\phi_\omega^{(2)}$ and $\phi_D^{(2)}$ of frequency $\bar{\omega}$, and $\dot{\xi}$ being the horizontal orbital velocity induced by $\phi_\omega^{(2)}$.

$F_{22}^{(2)} = \frac{\partial F_{22}^{(2)}}{\partial \ddot{\xi}}\ddot{\xi}$ = hydrodynamic force in phase with $\ddot{\xi}$; the hydrodynamic force being due to $\phi_\omega^{(2)}$ and $\phi_D^{(2)}$ of frequency ω^-, and $\ddot{\xi}$ being the horizontal orbital acceleration induced by $\phi_\omega^{(2)}$.

$F_\varepsilon^{(2)}$ = second order exciting forces of frequency ω^-, which are the sum of the first four terms of (1). These components are related only to the products of first order potential, motions and their derivatives, and hence without direct bearing to the second order potential $\phi_\omega^{(2)}$, $\phi_D^{(2)}$.

However, it is not easy to carry out such an experiment accurately and besides, it is impossible to break up the various components on the RHS experimentally.

Therefore, a special case for our numerical model is taken, i.e. the body is restrained from second order motion — but free to execute first order motions — and the forces $F_{12}^{(2)}$, $F_{22}^{(2)}$, $F_\varepsilon^{(2)}$ obtained from numerical computation.

The basic assumption now is:

$$\frac{\partial F_{12}^{(2)}}{\partial \dot{\xi}} = \frac{\partial F_{11}^{(2)}}{\partial \dot{X}} \quad ; \quad \frac{\partial F_{22}^{(2)}}{\partial \ddot{\xi}} = \frac{\partial F_{21}^{(2)}}{\partial \ddot{X}}$$

i.e. the second order hydrodynamic forces experienced by a body in a bichromatic wave should be approximately the same, be it be streamedpast by an oscillating current or be it be doing the oscillation itself.

With this in mind, the numerically calculated forces due to $\phi_\omega^{(b)}$ and $\phi_D^{(2)}$ in the present example are reduced to the same form as Cao, viz:

$$\mu'_\zeta = \left(\frac{F_{12}^{(2)}}{\dot{\xi}}\right)\left(\frac{0.1L}{2\sqrt{A_oC_o}}\right)^2 \times 1000 \qquad (38)$$

The constant 1000 converts tons into kilograms, while all computations are based on ζ_i, ζ_j of unit amplitude, and $\omega^- = 0.222$ sec^{-1}, a figure convenient for calculation but being near to ω_o and ω_1 of the experiment.

The plot of μ'_ζ between numerical and experimental results agree reasonably well.

5. Concluding Remarks

This paper presents a numerical solution to the practical problem of calculating second order oscillating diffraction loads on a semisubmersible. The diffraction component is trivial with respect to heave force, but is considerable for certain frequencies of first

order waves in surge force. These frequencies, furthermore, are usually the frequencies of high energy density in a moderate wind wave spectrum. Hence second order diffraction load in general should not be neglected.

A preliminary comparison of hydrodynamic coefficient related to second order orbital wave velocity is compared with the "wave damping" coefficient obtained from extinction experiment. Reasonable agreement is obtained, however, further work is required in future.

6. Acknowledgement

This research has been sponsored by the China State Economic Commission under a general contract relating to investigation of behaviours of moored systems on high sea.

7. Notations

n	Unit normal to structure surface
r	Location vector on structure surface
$\chi^{(1)}$	First-order displacement
$F^{(1)}$	Total first-order force
$M^{(1)}$	Total first-order moment
ζ	Amplitude of wave elevation
S_{wl}	Waterplane
wl	Waterline
	Displaced volume
S_{io}	$\int_{swl} x_i ds \quad i=1,2$
S_{ij}	$\int_{swl} x_i x_j ds \quad i,j=1,2$
$\zeta_r^{(1)}$	Relative wave elevation = $\zeta^{(1)} - (\eta_3^{(1)} + \eta_4^{(1)} y)$
η_i	Motion response in the mode i
x_{3B}	Height of the center of buoyancy
H	Water depth
$R^{(1)}$	$\begin{pmatrix} 0 & -\eta_6^{(1)} & \eta_5^{(1)} \\ \eta_6^{(1)} & 0 & -\eta_4^{(1)} \\ -\eta_5^{(1)} & \eta_4^{(1)} & 0 \end{pmatrix}$
P_{k1ij}, Q_{k1ij}	in-phase and out-phase components of $-\frac{1}{2}\rho g \int_{wl} \zeta_r^{(1)2} n_k dl$
P_{k2ij}, Q_{k2ij}	in-phase and out-phase components of $\frac{1}{2}\rho \iint_\Sigma \lvert\nabla\phi^{(1)}\rvert^2 n_k ds$
P_{k3ij}, Q_{k3ij}	In-phase and out-phase components of $\rho \iint_\Sigma \nabla\phi_t^{(1)} \chi^{(1)} n_k ds$
P_{k4ij}, Q_{k4ij}	In-phase and out-phase components of $R^{(1)} F^{(1)}$
P_{k5ij}, Q_{k5ij}	In-phase and out-phase components of $\rho \iint_\Sigma \phi_t^{(2)} n_k ds$
P_{k6ij}, Q_{k6ij}	In-phase and out-phase components of second-order hydrastatic restoring force
T_{kij}	Quadratic transfer function for second-order force
ϵ_r	Phase
Σ	Structure's mean wetted surface
ρ	water density
superscripts $^{(0)}, ^{(1)}, ^{(2)}$	denote zeroth, first and second order quantities

Reference

1. Faltinson, O.M. and Loken A.E., "Slow drift oscillations of a ship in irregular waves", Appl. Ocean Res., Vol.1, No.1, 1979

2. Papanikolaou, A,"Second-order theory of oscillating cylinders in a regular steep wave" 13th Symp. on Naval Hydrodynamics, 1980

3. Rahman, M.,"Wave diffraction by large offshore structures: an exact second-order theory", Appl. Ocean Res., Vol.6, No.2, 1984

4. Eatok Taylor and Hung, S.M., "Comments on 'wave diffraction by large offshore structures: an exact second-order theory' by Rahman, M.", Appl. Ocean Res., Vol.7, No.1, 1985

5. Kyozuka, Y., "Non-linear hydrodynamic forces acting on two-dimensional bodies" I.S.P. Report, diffraction problem, in Japanese, Vol. 184, pp 49-57, 1980

6. Miao G.P. and Liu Y.Z., "A theoretical study on the second-order wave forces for two dimensional bodies"

7. Triantafyllou, M.S., "A consistent hydrodynamic theory for moored and positioned vessels", J.S.R. 26, 9F-105, 1982

8. Mei, C.C. "Slow drift motions by multiple scale analysis" International workshop on ship and platform motions, October 26-28, 1983

9. Pinkster, J.A., "Low frequency second-order wave exciting forces on floating structures" NSMB, Rep. No. 65, 1980

10. Standing, R.G., Dacunha, N.M.C. and Matter, R.B.,"Slowly-varying second-order wave forces: theory and experiment" NMI, R138, Oct. 1981

11. Molin, B. "Second-order diffraction loads upon three-dimensional bodies" Appl. Ocean Res., Vol.1, No.4, 1979

12. Wichers, J.E.W. and Huijsmans, R.M.H., "On the low-frequency hydrodynamic damping forces acting on offshore moored vessels" OCT. 4813, 1984

13. Takaki, M. et al:"Written contributions to the technical report of Ocean Engineering Committee, I.T.T.C. 84, Göteborg, Sweden"

14. Cao, J.E., Fu, Y.F. and Feng, Y., "Hydrodynamic coefficient of a moored semisubmersible in surge at low frequency" CSSRC Report 1984

15. Gu, M.X. and Sun, B.Q., "Wave load on large floating body" CSSRC lecture, 1984

16. Bowers, E.C., "Long period oscillations of moored ship subject to short wave seas" Trans. Roy. Inst. Nav. Archit., London, Vol.118 pp 181-191, 1976

17. Sun, B.Q. and Gu, M.X., "A discussion about second-order potential $\phi^{(2)}$ CSSRC Report, 1984

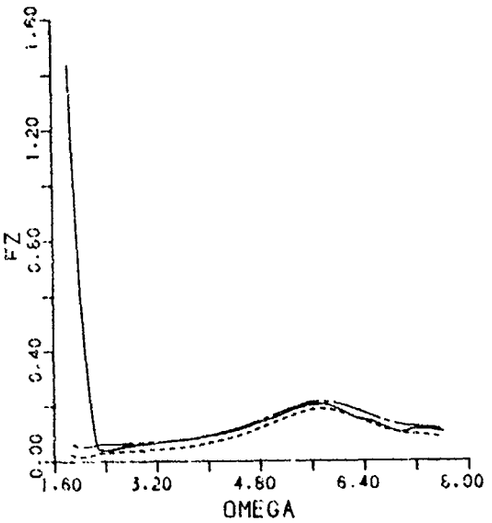

Fig. 6

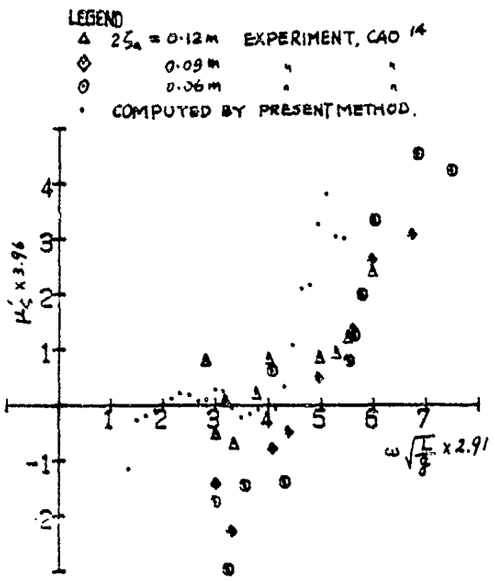

Fig. 7

Appendix

It is known that the first-order reponse q in an irregular wave, for example the first-order force response or the first-order motion reponse, has the following form:

$$q = \sum_{i=1}^{N} \zeta_i \left(Re(q_i) + i\, \mathcal{I}m(q_i) \right) e^{i(\omega_i t + \varepsilon_i)}$$

where ζ_i is the amplitude of the ith component wave, q_i is the first-order response corresponding to the frequency ω_i, $q_i = q_{im} e^{i\varepsilon_{qi}}$, q_{im} is the module corresponding to the frequency ω_i and ε_{qi} is the phase.

Now discuss the multiplication of two first-order response p and q.

$$Re(P)\cdot Re(q) = \sum_{i=1}^{N} \zeta_i P_{im} \cos(\omega_i t + \varepsilon_i + \varepsilon_{pi}) \cdot \sum_{j=1}^{N} \zeta_j q_{jm} \cos(\omega_j t + \varepsilon_j + \varepsilon_{qj}) = \sum_i \sum_j \zeta_i \zeta_j P_{im} q_{jm} \cos(\omega_i t + \varepsilon_i + \varepsilon_{pi}) \cos(\omega_j t + \varepsilon_j + \varepsilon_{qj}) = \sum_i \sum_j \zeta_i \zeta_j P_{im} q_{jm} \cdot \frac{1}{2} \left(\cos((\omega_i+\omega_j)t + \varepsilon_i + \varepsilon_j + \varepsilon_{pi} + \varepsilon_{qj}) + \cos((\omega_i-\omega_j)t + \varepsilon_i - \varepsilon_j + \varepsilon_{pi} - \varepsilon_{qj}) \right) = \frac{1}{2} \sum_i \sum_j \zeta_i \zeta_j P_{im} q_{jm} \left(\cos((\omega_i+\omega_j)t + \varepsilon_i + \varepsilon_j) \cos(\varepsilon_{pi} + \varepsilon_{qj}) - \sin((\omega_i+\omega_j)t + \varepsilon_i + \varepsilon_j) \sin(\varepsilon_{pi} + \varepsilon_{qj}) + \cos((\omega_i-\omega_j)t + \varepsilon_i - \varepsilon_j) \cos(\varepsilon_{pi} - \varepsilon_{qj}) - \sin((\omega_i-\omega_j)t + \varepsilon_i - \varepsilon_j) \sin(\varepsilon_{pi} - \varepsilon_{qj}) \right) = \frac{1}{2} \sum_i \sum_j \zeta_i \zeta_j \left(P_{im} q_{jm} \cos(\varepsilon_{pi} + \varepsilon_{qj}) \cos((\omega_i+\omega_j)t + \varepsilon_i + \varepsilon_j) - (P_{im} q_{jm} \sin(\varepsilon_{pi} + \varepsilon_{qj})) \sin((\omega_i+\omega_j)t + \varepsilon_i + \varepsilon_j) + (P_{im} q_{jm} \cos(\varepsilon_{pi} - \varepsilon_{qj})) \cos((\omega_i-\omega_j)t + \varepsilon_i - \varepsilon_j) - (P_{im} q_{jm} \sin(\varepsilon_{pi} - \varepsilon_{qj})) \sin((\omega_i-\omega_j)t + \varepsilon_i - \varepsilon_j) \right) = \frac{1}{2} \sum_i \sum_j \zeta_i \zeta_j \left(Re(P_i q_j) \cos((\omega_i+\omega_j)t + \varepsilon_i + \varepsilon_j) - \mathcal{I}m(P_i q_j) \sin((\omega_i+\omega_j)t + \varepsilon_i + \varepsilon_j) + Re(P_i \bar{q}_j) \cos((\omega_i-\omega_j)t + \varepsilon_i - \varepsilon_j) - \mathcal{I}m(P_i \bar{q}_j) \sin((\omega_i-\omega_j)t + \varepsilon_i - \varepsilon_j) \right)$$

of which the difference frequency

$$Re(P_i \bar{q}_j) \cos((\omega_i-\omega_j)t + \varepsilon_i - \varepsilon_j) - \mathcal{I}m(P_i q_j) \sin((\omega_i-\omega_j)t + \varepsilon_i - \varepsilon_j)$$

On the other hand, from (7) the second-order incident waves also have the difference parts

$$A \cos((\omega_i-\omega_j)t + \varepsilon_i - \varepsilon_j) \;;\; B \sin((\omega_i-\omega_j)t + \varepsilon_i - \varepsilon_j)$$

Therefore the second-order difference frequency force can be written as

$$F_k^{(2)} = \sum_{i=1}^{N} \sum_{j=1}^{N} \zeta_i^{(1)} \zeta_j^{(1)} \left(P_{k1ij} + P_{k2ij} + \cdots + P_{k6ij} \right) \cos((\omega_i-\omega_j)t + \varepsilon_i - \varepsilon_j) + \sum_{i=1}^{N} \sum_{j=1}^{N} \zeta_i^{(1)} \zeta_j^{(1)} \left(Q_{k1ij} + Q_{k2ij} + \cdots + Q_{k6ij} \right) \sin((\omega_i-\omega_j)t + \varepsilon_i - \varepsilon_j)$$

A LOCALIZED FINITE ELEMENT METHOD APPLIED TO THE 3-D SEAKEEPING PROBLEM

by

Marc Lenoir and Jean-Philippe Richer

Groupe d'Hydrodynamique Navale (*)
Ecole Nationale Supérieure de Techniques Avancées
Chemin de la Hunière, 91120 Palaiseau, France

Institut de Recherches de la Construction Navale
47, rue de Monceau, 75008 Paris, France

Abstract

This paper is concerned with the 3-D linear diffraction-radiation problem in a fluid of finite depth. An extension of the Localized Finite Element Method, derived from the two-dimensional method developed by K.J. Bai, is presented. After a description of the method, we shall give some results about the convergence properties of the numerical problem and a first numerical experience devoted to the study of the ratio between accuracy and computational time. Further possible developments will also be indicated as concluding remarks.

I. Introduction

The importance of the diffraction and radiation effects of natural obstacles or man-made structures on water waves is meaningfull in ocean engineering. The linearized problem has received analytical or asymptotical solutions in particular limiting cases. Numerical techniques have been developed for arbitrary geometries, based on various methods that have already scored successes during the past decades.

Then, although research has been engaged towards new problems with non linear boundary conditions for instance, from the numerical point of view, investigations have still been carried on so as to reduce computational times, storages and costs while increasing accuracy and generality of the programs. Linear diffraction-radiation analysis must be now considered as a very standard calculation and only a first step in the complete analysis of offshore structures, which must be iterated a large number of times, at various frequencies, including finite depth cases.

The finite depth occurs in many applications and it may be taken into account by various means. When the method requires the evaluation of the Green function, the finite depth assumption leads to rather expensive calculations and up till now, no work is known where this calculation would have been optimized as in the case of infinite depth (Newman /1/). The Localized Finite Element Method avoids the evaluation of the Green function. On the counterpart, the number of degrees of freedom is increased. But we finally expect an improvement of the computational costs.

The method has been developed in the frame of a 3-D diffraction-radiation code based on the Jami-Lenoir method of coupling between integral representation and finite elements /2/. Many tasks (discretization...) and calculations are common to both methods. When performing a complete analysis of a given structure in the frequency range, this will avoid duplicated work, if both finite and infinite depth situations must be taken into account.

As a short review will show, a complete three-dimensional development of the method was still lacking although every element was already known.

A short review

The Localized Finite Element Method stems from earlier works by Bai and Yeung during the years 1973-1974. But the first complete presentation is due to K.J. Bai /3/ and C.C. Mei (1974) /4/ who first used finite elements combined with eigenfunctions expansion. They were dealing with the "two-dimensional boundary value problem for time harmonic free surface flow in water of arbitrary bottom topography". C.C. Mei /5/ gave a very interesting review of numerical methods in water wave diffraction and radiation which is

---

(*) the GHN research team is associated with the Centre National de la Recherche Scientifique and l'Université de Paris VI. It is also sponsored by the Direction des Recherches, Etudes et Techniques of the Ministère de la Défense.

devoted to the comparison between integral equation methods and hybrid element methods. In a recent paper (1981), Grilli /6/ compared the numerical properties of the Localized Finite Element Method to those of a pure finite element method with the Sommerfeld radiation condition applied at finite distance from the body. This is an example of the persistant interest of investigating further numerical properties of linear diffraction radiation numerical solutions.

Several authors paid attention to some theoretical results that ensure the validity of the method :
Aranha et al /7/ established the uniqueness of the solution for the long wave problem in shallow water and Lenoir and Tounsi /8/, more generally, studied the convergence of the discrete solution. The results presented below have been derived from their work.

Instead of finite elements, integral equation formulations can be combined with the eigenfunctions expansion. This possibility has been investigated by Yeung /9/ for the 2-D time harmonic water wave problem.
A true 3-D numerical method which is to some extend related to the Localized Finite Element Method, has been developed by Chenot /10/. The method consists in solving a series of Neumann problems, the various Neumann boundary conditions being given by the normal derivative of each term of the series expansion. The various solutions are then combined in such a way to minimize the discrepancy with the outer solution. Unfortunately, numerical shortcomings (eigenfrequencies) appear due to the Neumann boundary condition. Nevertheless a program was derived from this method, that probably was the first 3-D finite element program in this field.

The Localized Finite Element Method has also been extended to other problems as the two-dimensional steady ship-wave problem (Bai /11/), the 3-D ship motions in a channel, (Bai /12/), the two-dimensional wave resistance problem where an original extension was successfully attempted to match a non linear formulation in the inner domain to a linear one in the outer domain, by Lenoir and Cahouet /13/.

II. Formulation of the 3-D problem

We consider here a fluid domain delimited by a free surface and a bottom at finite depth. The domain goes to infinity in the horizontal direction. A rigid body is piercing the free surface. denotes the boundary between the body and the fluid.

The fluid is assumed to be inviscid and incompressible. The bottom is supposed to be flat at least beyond a finite distance from the body.

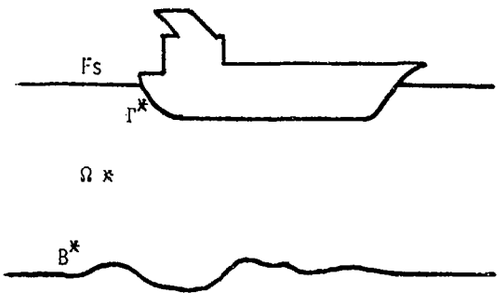

The linear diffraction radiation problem settled in domain Ω^* is a boundary value problem governed by Laplace's equation and is usually formulated as follows :

Φ^* denotes the velocity potential, it satisfies the following set of conditions :

$$\Delta\Phi^* = 0, \text{ in } \Omega^*$$
$$\partial\Phi^*/\partial n = \nu\Phi \text{ on } F_s^*$$
$$\partial\Phi^*/\partial n = 0 \text{ on } B^* \quad (P^*)$$
$$\partial\Phi^*/\partial n = h \text{ on } \Gamma$$
$$\lim_{r\to\infty} \iint_{\sigma(r)} |\partial\Phi^*/\partial n - i\nu_0\Phi^*| d\sigma = 0$$

where $\partial/\partial n$ denotes the normal derivative
ω denotes the pulsation of the incident wave
γ_0 denotes the unique positive root of the equation : $th\gamma_0 H = \gamma/\gamma_0$
H is the depth at infinity
$\sigma(r)$ is a cylindrical surface going from free surface to bottom and surrounding the body.

The last condition is the so called Rellich radiation condition which ensures that the solution has a convenient decreasing asymptotic behaviour /14/.

The uniqueness of the solution of problem (P) has been established by John /15/ under restrictive geometric assumptions : the immersed part of the body must be contained in the vertical cylinder lying on the water line. Maz'ja /16/ gave an other set of geometric assumptions valid for immersed bodies which also ensures uniqueness. Let us also quote a more recent proof due to Ursell which is only devoted to the two-dimensional problems, but is in fact a real improvement /17/.

From now on, we shall assume uniqueness and existence of the solution.

The numerical methods available today for solving this 3-D problem are based, generally speaking, on boundary integral equations or finite element techniques. They have lead to various programs that work successfully now, although a few numerical difficulties may still remain (irregular frequencies...). Most of these methods require the use of a Green function which expression is now well known but not very easy to handle from the numerical point of view (see Martin /18/ and Newman /1/). Especially in the finite depth case, it becomes rather expensive to compute.

The Localized Finite Element Method, valid in the finite depth case, is an interesting alternative to these methods,as it does not make use of any Green function. The development of this method has been shortly discussed in the introduction. As far as the 3-D diffraction radiation problem is concerned, we are not aware of any numerical development.

Let us recall the first main principles of the method as K.J. Bai established them. Even if at first sight our formulation seems different, we nevertheless followed his tracks.

The fluid domain is divided into two subregions. The inner domain will be discretized into finite elements while an analytical representation of the solution will be used in the outer domain.

Let us denote by Ω the inner domain delimited by :

- F_S the free surface
- B the bottom
- Γ the body surface
- Σ a ficticious outer boundary

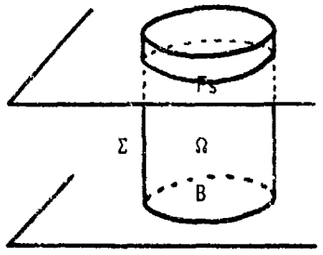

In domain Ω the restriction of the solution Φ of problem (P^*) satisfies :

$$\Delta\Phi_i = 0, \text{ in } \Omega,$$
$$\partial\Phi_i / \partial n = \nu\Phi_i \text{ on } F_S,$$
$$\partial\Phi_i / \partial n = h \text{ on } \Gamma, \quad (P_i)$$
$$\partial\Phi_i / \partial n = 0 \text{ on } B$$

In the outer domain Φ satisfies :

$$\Delta\Phi_e = 0,$$
$$\partial\Phi_e / \partial n = \nu\Phi_e \text{ on } F_S,$$
$$\partial\Phi_e / \partial n = 0 \text{ on } B \quad (P_e)$$

+ radiation condition

Let us now assume that Φ_i and Φ_e satisfy (Pe) and (Pi) together with :

$$\Phi_e|_\Sigma = \Phi_i|_\Sigma, \quad \frac{\partial \Phi_e}{\partial n}\Big|_\Sigma = \frac{\partial \Phi_i}{\partial n}\Big|_\Sigma$$

then they will match analytically along Σ and respectively be equal to Φ/Ω and $\Phi/\Omega^* /\Omega$ to $\Phi/\ \Omega^*/\Omega$.

So let us define the operator :

$$T : H^{1/2}(\Sigma) \to H^{-1/2}(\Sigma)$$
$$f \to -\frac{\partial \Phi_e}{\partial n}$$

where Φ_e satisfies (Pe) and the Dirichlet condition $\Phi_{e/\Sigma} = f$.

By Φ we denote the solution of problem (P) :

$$\Delta\Phi = 0 \text{ in } \Omega,$$
$$\partial\Phi/\partial n = \nu\Phi \text{ on } F_S,$$
$$\partial\Phi/\partial n = h \text{ on } \Gamma, \quad (P)$$
$$\partial\Phi/\partial n = 0 \text{ on } B,$$
$$\partial\Phi/\partial n = -T\Phi \text{ on } \Sigma$$

Through this last matching condition, we in fact impose to Φ a condition which is strictly equivalent to the radiation condition at infinity.

So Φ is equal to Φ^* /Ω and problem (P), though settled in a bounded domain, is strictly equivalent to (P^*). The problem can now be treated by numerical methods.

The main interest of the method lies in the fact that we can express operator T explicitly, by means of the so called eigenfunctions of the outer problem which are easy to evaluate, provided Σ is a cylinder of vertical axis and circular basis. This, of course, may be a drawback when the shape of the body is very different from a cylinder. It will lead to a complicated mesh.

Spectral decomposition of operator T

The eigenfunctions of the following problem provide a spectral decomposition of operator T :

$$\Delta\Phi_k = \tau_k \Phi_k$$

$$\partial\Phi_k(0)/\partial n = \nu\Phi_k(0)$$

$$\partial\Phi_k(-H)/\partial n = 0$$

where $\tau_0 = \gamma_0^2$ $\tau_k = \gamma_k^2$ and $\Phi_k(z)$ is defined over $(-H, 0)$.

This set of eigenfunctions can be easily obtained. We have :

$$k = 0$$

$$\Phi_0(z) = \mathrm{ch}\ \nu_0(z+H)/\alpha_0$$

$$k > 1$$

$$\Phi_k(z) = \cos\ \nu_k (z+H)/\alpha_k$$

$$\mathrm{th}\ \nu_0 H = \nu/\nu_0$$

$$\mathrm{tg}\ \nu_k H = -\nu/\nu_k$$

α_k, $k = 0, \infty$ have been determined so that $\|\Phi_k\|_{L^2(-H, 0)} = 1$

We can show, by means of the compact self adjoint operators theory, that the Φ_k make an orthogonal basis of $H'(\Omega^*/\Omega)$ and a total set in $H^{1/2}(\Sigma)$.
Let f be a function defined over Σ . We have :

$$f(\theta, z) = \sum_{n=-\infty}^{+\infty} C_n(z) e^{in\theta}$$

Every coefficient $Cn(z)$ can be expressed in terms of the eigenfunctions of (Pk) and f can be expressed in the following way :

$$f = \sum_{n=-\infty}^{+\infty} \sum_{k=0}^{+\infty} (f, \Phi_{nk})\ \Phi_{nk}$$

where $\Phi_{nk} = \Phi_{ke}^{in\theta}$ and $(\ ,\ )$ denotes some scalar product in $L^2(0, 2\pi) \times (-H, 0)$

$$(f, g) = \frac{1}{2\pi} \int_0^{2\pi} \int_{-H}^{0} fg\, d\theta dz$$

We have :

$$(\Phi_{nk}, \Phi_{n'k'}) = \delta_{nkn'k'}$$

(Kronecker symbols)

Thus :

$$Tf = \sum_{n=-\infty}^{+\infty} \sum_{k=0}^{+\infty} (f, \Phi_{nk})\, T(\Phi_{nk})$$

We then solve $Pe(\Phi_{nk})$ (i.e. (Pe) with Φ_{nk} as Dirichlet condition on Σ). The solution is of the following type :

$$\Phi_{nk} = \Psi_{nk}(r)\ \Phi_{nk}(\theta, z)$$

Substituting this relation in the Laplace's equation, formulated in cylindrical coordinates, we easily identify the functions $\Psi_{nk}(r)$ as being the Bessel functions /19/ :

$$n = 0 \qquad \Psi_{0k} = H_0^1(\nu_k r)$$

$$n > 1 \qquad \Psi_{nk} = K_n(\nu_k r)$$

The associated functions H_0^2 and Im have been eliminated, because of their asymptotic behaviour which does not satisfy the radiation condition.
Then we have :

$$T(\Phi_{nk}) = -\frac{\partial}{\partial r} \Phi_{nk}^{e}(R, \theta, z)$$

where

$$\frac{\partial}{\partial r} \Phi_{nk}^{e} = \Psi'_{nk}(r)/\Psi_{nk}(R) \times \Phi_{nk}(\theta, z)$$

and R radius of Σ ; consequently :

$$Tf = \sum_{n=-\infty}^{+\infty} \sum_{k=0}^{+\infty} \nu_k \frac{\Psi'_{nk}}{\Psi_{nk}}(R)\ \Phi_k(z) e^{in\theta}$$

We then introduce this formula into problem (P).

III. Convergence with respect to the rank of truncation of the expansion series

For obvious numerical reasons, we must limit the expansion series to a finite rank. But doing this, we must verify that the solution of the truncated problem tends to the solution of the real problem when the number of terms

in the expansion series increases to infinity. It is also interesting to know whether this number of terms may be small for a given accuracy, because of the influence it will have on the computational costs.

we are lead to characterize the difference between Φ , expressed by the whole series and Φ^{NK} ,denoting the truncated series to N Fourier coefficients and K eigenfunctions of (Pk), by an expression using N and K. This will imply the convergence of Φ^{NK} , solution of the truncated problem :

$$\Delta\Phi^{NK} = 0 \text{ in } \Omega$$

$$\partial\Phi^{NK}/\partial n = \nu\,\Phi^{NK} \text{ on } F_c$$

$$\partial\Phi^{NK}/\partial n = h \text{ on } \Gamma \quad (P_{NK})$$

$$\partial\Phi^{NK}/\partial n = 0 \text{ on } B$$

$$\partial\Phi^{NK}/\partial n = -\sum_{n=-\infty}^{+\infty}\sum_{k=0}^{+\infty} \Psi'_{nk}(R)\,(f, \Phi_{nk})\Phi_{nk}$$

The various convergence properties of the Localized Finite Element Method applied to the 2-D sea-keeping problem have already been studied by Lenoir and Tounsi /8/. We shall sum up their arguments for the convergence of the truncated problem relatively to K.
Then, their will be very little work to do to extend the result to the 3-D problem, by means of some properties of the Fourier series expansion.

Lenoir and Tounsi give an estimation of convergence related to the rank of the truncated series, by applying interpolation theory between Sobolev spaces /20/, /21/, in relation to the weak formulation of the eigenvalue problem (Pk) defined on the interval (-H,0). They first studied the convergence of the truncated series expansion of . This problem is similar to the one of the convergence of Fourier series. But here, as the functions involved are not periodic functions with respect to z, difficulties appear at each extremity of the interval. That makes things more complicated and leads to weaker results. This may be noticed in the definition of the Sobolev spaces they used :

$$H_B^s(-H,0) = H^s(-H,0),\ 0 < s < \frac{3}{2}$$

$$H_B^s(-H,0) = \{v \in H^s(-H,0) / \frac{dv}{dy}(0) = v'(0)$$

$$\frac{dv}{dy}(-H) = 0\ \} \qquad \frac{3}{2} < s < \frac{7}{2}$$

$$H_B^s(-H,0) = \{v \in H^s(-H,0) / \frac{d^3v}{dy^3}(0) = \frac{d^2v}{dy^2}(0)$$

$$\frac{dv}{dy}(0) = v(0), \frac{d^3v}{dy^3}(-H) = 0, \frac{dv}{dy}(-H) = 0\ \}$$

$$\frac{7}{2} < s < 4$$

The interpolation theory gives :

$$H_B^s(-H,0) = \left(H_B^4(-H,0), L^2(-H,0)\right)_{1-s/4}$$

$$0 < s < 4,\ s = \frac{3}{2},\ s = \frac{7}{2}$$

The usual topology on interpolated Sobolev spaces and the spectral decomposition of operator T defined above, lead us to :

$$\chi \in H_B^3(-H,0),\ \|\chi - \Pi^k\chi\|_{H^1} < \frac{A}{K^{5/2}}\,\|\chi\|_{H_B^3}$$

where $\Pi^k\chi$ denotes the truncated expansion of χ to rank K.

As far as the 3-D problem is concerned, let us recall a result concerning coefficient Ck of the Fourier series expansion of a function f :

$$f \in {}^{m}, M_m, \quad k \in N,$$

$$|Ck(f)| < \frac{M_n}{|k|^m}$$

The velocity potential that we have expended in Fourier series is C^∞ with respect to Θ . If $\Pi^N\Phi$ denotes the truncated Fourier series associated to Φ , and $\Pi^{NK}\Phi$ the expansion of $\Pi^N\Phi$ over the K first eigenfunctions, we have :

$$\|\Phi - \Pi^{NK}\Phi\| < \|\Phi - \Pi^N\Phi\| + \|\Pi^N\Phi - \Pi^{NK}\Phi\|$$

$$C,\ m,\ A_m$$

$$\|\Phi - \Pi^{NK}\Phi\|_{H1/2} < \frac{A_m}{N^m} + \frac{C}{K^{5/2}}$$

IV. Variational formulation

The extension of Bai's method to the 3-D case has been undertaken complementary to the Jami-Lenoir finite element - integral representation method. This is the reason why problem (P) has been discretized into finite elements. Nevertheless, other methods could be applied.

When applied to the velocity potential ϕ and a trial function ψ , the Green formula gives :

$$\int_\Omega \Delta\Phi\Psi \, dw = \int_{\partial\Omega} \partial\Phi/\partial n \, \Psi \, d\sigma - \int_\Omega \nabla\Phi\nabla\Psi \, dw$$

$$\partial\Omega = F_S \cup \Sigma \cup B \cup \Gamma$$

As :
as :

$$\Delta\Phi = 0$$

$$\int_\Omega \nabla\Phi\nabla\Psi dw = \nu\int_{F_S}\Phi\Psi \, d\sigma + \int_\Gamma h\Psi d\sigma - \int_\Gamma T\Phi\Psi d\Sigma$$

where

$$T\Phi = \sum_{n,k} (\Phi, \Phi_{nk}) \frac{\partial\Phi_{nk}}{\partial_r}$$

Let us call (w_i) i=1, M the shape functions of the discretization with M nodes. We can write $\Phi = \Sigma\Phi_i w_i$, where Φ_i denotes the value of Φ at the node number i.
As trial function ψ , we must choose any shape function wi. We thus obtain equation (2) in a matrix form :

$$\sum \Phi_i \int \nabla w_i \nabla w_j = \nu \sum \Phi_i \int w_i w_j + \int_k w_j - \sum \Phi_i \int T w_i w_j$$

We can develop the coupling term :

$$\sum_{n,k} R \frac{\hat{\Psi_{nk}}}{\Psi_{nk}} (R)(w_i, \Phi_{nk})(\Phi_{nk}, w_j) =$$

$$\sum_k R \frac{\Psi'_{nk}}{\Psi_{nk}} (R)((w_i,\Phi_{ok})(w_j,\Phi_{ok}) +$$

$$\sum_{n=1}^{\infty} (w_i,\Phi_{nk})(\Phi_{nk},w_j) + (\Phi_{nk},w_i)(w_j,\Phi_{nk}))$$

It follows that the matrix is symmetrical though not selfadjoint.
Strictly speaking, the shape functions wi are x,y,z dependent. But it is more convenient to replace them in the integration over Σ , by two-dimensional shape functions Wi(z ϕ) which lead to analytical integration.
When using finite elements of second order, as it will be done below, the two formulations are consistant, and we can consider that the discrepancy due to these different interpolations is negligible, when compared to that due to all other sources of discrepancies. This should be nevertheless justified.

The discretisation we exposed gives a matrix of the following type :

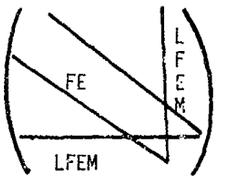

A part of the narrow banded finite element matrix is modified by the boundary terms and filled up as nodes of the boundary are coupled with each other.

Remark :

An other possible discretization is obtained by using Lagrange multipiers as J. Bai did it himself.
This method consists in considering that the coefficients $\beta_{nk}=(\Phi \ \Phi_{nk})$ of the analytical representation are supplementary unknowns. The missing equations are given by the matching condition on Σ :

$$\beta_{nk} - \sum \Phi_i (w_i , \Phi_{nk}) = 0$$

This formulation leads to a bigger matrix but offers the advantage of giving the coefficients of the analytical representation and thus the velocity potential outside of the inner domain without any other calculation.
In this case we can give the following sketch of the matrix :

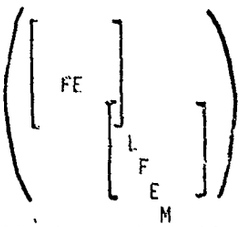

As we said, the matrix is bigger than the finite element matrix itself, but with a lot of zeros and the part due to the finite elements (which is narrow banded) is not modified by the boundary terms.

V. Numerical results

We present a few numerical results that will help to precise the main characteristics of the Localized Finite Element Method by means of appropriate exaamples.

We have studied the diffraction of an incident Airy wave by a circular and an elliptic vertical cylinder reaching the bottom and piercing the free surface . Radiation due to sway motions has also been calculated.

Only a quarter of the fluid domain has been discretized (see scheme 1), by taking into account symmetry and antisymmetry properties of the solution with respect to the planes

x = 0 and y = 0. number of nodes on (s) and the total number of elements : E. The main characteristics of the different meshes we used are presented on table 1 : numbers of elements with respect to r, σ and z (respectively I,J and L), total number of nodes (M), number of nodes on Σ (S), and total number of elements (E) and the radius of Σ (R). The table also indicates the characteristic size of the mesh, denoted by h. This length is the largest dimension of all elements in the mesh.

In the case of diffraction by a circular cylinder, the calculated velocity potential has been compared to an analytical expression, called Mac-Camy formula /22/. The discrepancy has been measured by evaluating :

$$\varepsilon = \sup_{i=1,M} \frac{|\Phi^i_e - \Phi^i_{ex}|}{|\Phi^i_{ex}|}$$

where Φ^i_e denotes the value of the calculated velocity potential at node i, and Φ^i_{ex} the exact value of the potential at the same node. This comparison allowed us to test the validity of our code.

When the exact solution is not known we replaced it by calculated values with a sufficiently fine mesh. This did not spoil the investigation we made of the influence of the various parameters on the solution, for we only needed a reference. Then, the error has been denoted by ε. It is sometimes worth of interest to evaluate the discrepancy only on Σ. Then, the error has been denoted by ε_Σ.

Tests with eigenfunctions

The eigenfunctions (Φ_{nk}) are solutions of problem (P) with an appropriate Neumann condition on Σ. Thus, they can be used as exact solutions to evaluate the accuracy of the discretization.
This accuracy can be measured in two different ways. The evaluation of ε, as defined above, provides local information as well as global information, if the discrepancy is analyzed point to point.
But an other way is to calculate the scalar product of the eigenfunction chosen, as the test function with itself and the others. The vector thus obtained can be compared to the Kronecker symbols.
Such results concerning the first eigenfunction (n=0, k=0), are presented on table 2. Both error evaluations give significant results, but they do not have exactly the same meaning. The scalar product calculation gives a mean evaluation of the discrepancy that can be related to the evaluation of global quantities as efforts. The other error calculation indicates the greater discrepancy among all nodes of discretization. In this particular case, the Kronecker symbols are approximated with an accuracy of 5 and 0.5, while the maximum relative errors are 7.2 and 1.23.

Convergence of the discretization

We know that the error due to the discretization into finite elements of characteristic length h, satisfies :

$$\varepsilon < A\, h^3 \,\mathrm{Log}\,(h)$$

This has been tested here on the diffraction by a circular cylinder for fixed values of K, N and R.

As shown on figure 1, we could verify that the Localized Finite Element Method follows this law. The particular set of shape functions used on Σ does not introduce significant discrepancy.

Convergence with respect to N and K

We have then paid attention to the variation of the accuracy with respect to the number of Fourier series terms N and eigenfunctions K.

We have first solved the diffraction problem with several values of parameter P, P = N + K, with N = K. This has been done for a given fine mesh (m), and in fact for a given position of Σ. The error we have measured is plotted on figure 2.a. Although it is a rather rough test, we can notice that the convergence with respect to P is very fast. As a matter of fact, as soon as P=4, the error is no longer due to a lack of terms in the expansion series but to the roughness of the mesh.
Of course, the velocity potential of the diffraction by a vertical cylinder is a rather smooth function. It is a reason why we needed only a few eigenfunctions. Thus, in order to investigate further the separate influences of N and K, we have solved the radiation problem of the sway motion of an elliptic cylinder. Each parameter N and K took the values 2, 4, 6, 8, 10 while the other one was fixed to 10. A previous convergence study had shown that K=N=10 with the mesh m, gives a quite accurate solution, which could replace the analytical solution in the evaluation of ε. The results are plotted on figure 2-b. We must first point out that it is only casual that the first points are so close. Other examples would give separate points. However, it is very interesting to notice that the speed of convergence is less strong than previously, as the function is more disturbed. We even can say that the solution is more disturbed with respect to σ than to z. This explains why, for a given mesh, the convergence with respect to z is faster than that with respect to σ.

Size of the domain and discretization

For testing the influence of the position of Σ, we solved the diffraction by a circular cylinder, using different meshes : m_2, m_3, m_4, m_5, m_6, corresponding to increasing R, for given values of N and K. The results presented in table 3 show an increasing error. This is unexpected as the radiation condition, taken into account by expansion series on Σ, is better satisfied when Σ is farther. But if we pay more attention to the meshes we used, this is in fact a very significant result. For increasing the radius of Σ, we only added elements on the exterior part of the domain, without changing the discretization with respect to σ, (except for the last mesh). It follows that the characteristic length of the mesh, h, was increased very quickly. By looking at the evaluation of ε, also mentioned in table 3, we can notice that such meshes are of no need as ε_T is unchanged while ε increases quickly.
The last mesh, m_6, has one more slice of elements with respect to σ. We can notice that is not much improved, for h has not been substancially improved; but ε_T decreases significantly.
This is a good example of the relative influence of parameters R, N, K, h, for this type of problem . In this case, the discretization of the incident wave, that provides the Neumann condition on Γ, is essential. This explains that the influence of N is very sensitive to parameter N. This suggests to introduce in the code a few simple tests to determine these values.

Computational times

An investigation of the computational costs is of main interest as they are expected to be small compared to those of methods requiring the Green function evaluation.
We already can predict the time rates with respect to the parameters involved :

- we know that the finite element computation time increases as M , (M denotes the total number of degrees of freedom).

- the linear system is solved by means of a Gauss method with partial pivoting. The time is known to be proportional to M .

- as far as coupling terms are concerned, if S denotes the number of degrees of freedom on Σ, we can establish that the computational time is proportional to $S^2 (N + K)$, for the calculations with respect to K and to N can be made separately.

This last formula can be verified on figure 4-a, where times corresponding to several numbers of terms in the expansion series have been plotted. The values of M (and R) were fixed. We can notice a very good agreement with the formula.

Although some care has been devoted to the computation, the program used cannot be considered as a production computer-program. Thus, time results are only to be considered relatively to others.

An example corresponding to a "realistic" case is presented here. Several meshes of increasing accuracy have been used to solve the diffraction by a vertical circular cylinder. Times corresponding to finite elements calculation, coupling terms calculation and resolution have been evaluated separately. All these results have been plotted on figure 4-b with respect to M and S. We first can notice that the expected behaviours of the computational times are verified. But the main remark is that the computational costs for finite element calculation and for the solution of the linear system increase drastically, while they stay at moderate level for the coupling terms. Two main conclusions can be drawn from this remark :

- as expected, the calculations replacing the Green function evaluation require small time

- on the contrary, it is worth it improving the solution method, by taking into account the fact that a large part of the matrix is narrow banded, so as to make resolution times comparable to those of other methods.

Concluding remarks

The results presented here are only a first investigation of the main characteristics of the Localized Finite Element Method. Nevertheless, they encourage to a more complete investigation of the possibilities of the method.

It would be very meaningfull to compare the case of a very deep bottom to infinite depth case, so as to determine more precisely when this assumption is valid. The method could also be compared to infinite element techniques, that have been developed in fluid-structure analysis /23/.

References

/1/ Newman, J.N. : "Three dimensional wave interactions with ships and platforms", Proceedings of the international workshop on Ship and Platform Motions, Berkeley, 1983

/2/ Jami, A. and Lenoir, M. : "A variational formulation for exterior problems in linear hydrodynamics". Computer methods in Applied Mechanics and Engineering, Vol. 15, p 341-359, 1978.

/3/ Bai, K.J : "A variational Method in Potential Flows with a Free Surface", College of Engineering, University of California, Berkeley, Report N 72-2, 1972

/4/ Mei, C.C. and Chen, H.S. : "Oscillations and wave forces in a man-made harbour in the open sea", Proceedings of the tenth Symposium on Naval Hydrodynamics, Cambridge (1974), pp573-596.

/5/ Mei, C.C. : "Numerical Methods in Water-Wave Diffraction and Radiation", Ann. Rev. Fluid Mech. 1978, 10:393-416

/6/ Grilli, S. : "Etude de l'action de la houle sur les structures flottantes par éléments frontières. Comparaison avec les éléments finis", ATMA, Association Technique Maritime et Aeronautique, 47 rue de Monceau, 75008 Paris, Session 1984.

/7/ Aranha, J.A, Mei, C.C. and Yeu, D.K.P. : "Some properties of a hybrid element method for water waves", International Journal for numerical methods in Engineering, Vol. 14, 1979.

/8/ Lenoir, M. and Tounsi, A. : "The localized Finite Element Method and its applications to the 2-D sea-keeping problem", rapport ENSTA, GHN ERA070664.

/9/ Yeung, R.W. : "A Hybrid Integral - Equation Method for Time-harmonic free surface flow", Proceedings of the first International Conference on Numerical Ship Hydrodynamics, Gaithersburg, 1975.

/10/ Chenot, J.L. : "Méthode numérique de calcul du mouvement d'un corps flottant soumis à l'influence d'une houle périodique en théorie linéaire", Revue de l'Institut Français du Pétrole, Vol. xx, n° 5.75024, 1975

/11/ Bai, K.J. : "A localized finite element method for steady two-dimensional free-surface flow problems". Proceedings of the First International Conference on Numerical Ship Hydrodynamics, 1975.

/12/ Bai, K.J. : "A localized finite element method for steady three-dimensional free surface flow problems", Proceeding of the Second International Conference on Numerical Ship Hydrodynamics, Berkeley, 1977.

/13/ Cahouet, J. : "Etude numérique et expérimentale du problème bidimensionnel de la résistance de vague non linéaire", Thèse ENSTA, Paris 1984

/14/ Rellich, F. : "Uber das asymptotische Verhalten der Losungen von in unendlichen Gebieten'", Jahresbericht der Deutschen Mathem. Vereinigung, LIII. 1. Abt. Heft 1.

/15/ John, F. : "On the motions of floating bodies", I and II, communications on pure and applied mathematics, Vol. 2, 1949, Vol.3 1950.

/16/ Maz'ja : "Contribution au probleme stationnaire des petites oscillations d'un fluide en presence d'un corps immerge". Seminaire Sobolev, Novosibirsk, 1977.

/17/ Simon, M.J. and Ursell, F. : "Uniqueness in linearized two-dimensional water wave problems", Journal of Fluid Mechanics, 1984.

/18/ Martin, D. : "Etude numérique et théorique du problème linéarisé du mouvement sur la houle tridimensionnel", rapport ENSTA no 124, 1982.

/19/ Abramowitz, M. and Stegun, A. : "Hanbook of mathematical functions" Dover publications, Inc., New York.

/20/ Grisvard, P. and Cea, J. : "Calcul numérique de solutions singulières de problèmes aux limites", colloque d'analyse numérique, Giens, 1978.

/21/ Lions, J.L. and Magenes, E. : "Problèmes aux limites non homogènes et applications", Travaux et Recherches Mathématiques, Dunod, 1968.

/22/ Sarpkaya, T. and Isaacson, M. : "Mechanics of wave forces on offshore structures", Van Nostrand Reinhold Company, New-York, 1981.

/23/ Orsero, P. : "Vibrations of submerged structures - Numerical approach by Fluid Finite/Infinite Elements", Int. Conf. on Finite Element Methods, Shangai, August 1982.

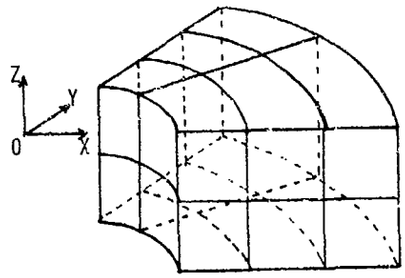

Mesh m_3 : I = 3, J = 2, L = 2
Scheme 1

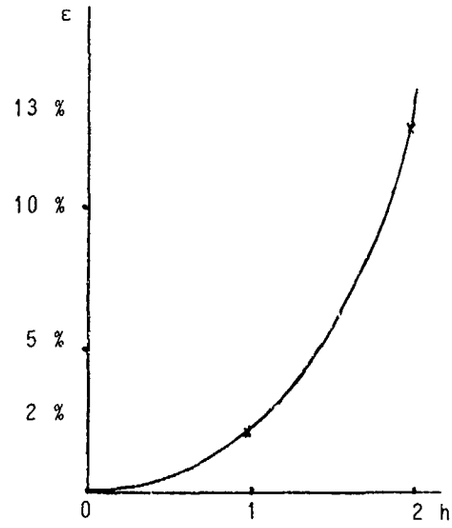

Figure 1 : Finite element convergence (Diffraction of an Airy wave by a vertical cylinder)

Mesh	I	J	L	M	S	R	h
m_1	1	1	1	27	9	2	2
m_{12}	2	2	2	125	25	2	1
m_3	3	2	2	175	25	2.5	1
m_4	4	2	2	225	25	3	1
m_5	5	2	2	275	25	3.5	1
m_6	5	3	2	385	30	3.5	1

Table 1 : Main characteristics of the meshes used

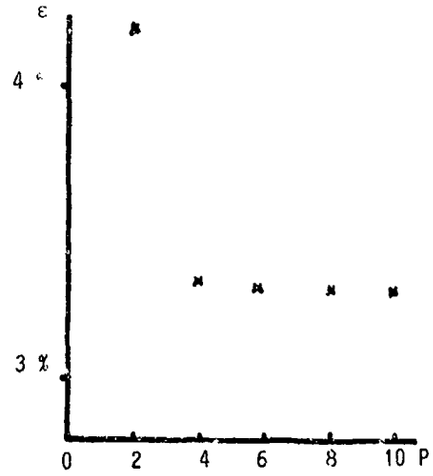

2-a Diffraction of an Airy wave by a vertical cylinder

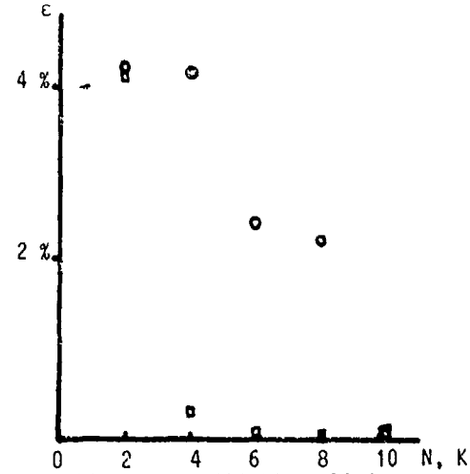

2-b Sway motion of an elliptic cylinder

Figure 2 : Influence of the truncation of the expansion series

Nb of nodes	125	175	225	275	385
Nb of elts	8	12	16	20	30
ε	2.3 %	3.2 %	9.1 %	20.0 %	18.0 %
ε	2.0 %	2.0 %	2.0 %	2.0 %	0.5 %

Diffraction of an Airy wave by a cylinder
Table 2 : Size of the domain and discretization

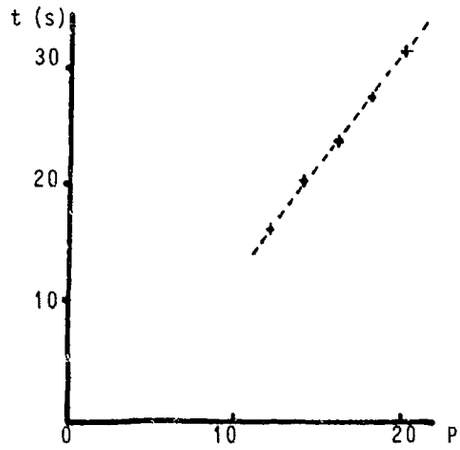

Figure 3-a : Time costs of coupling terms calculation

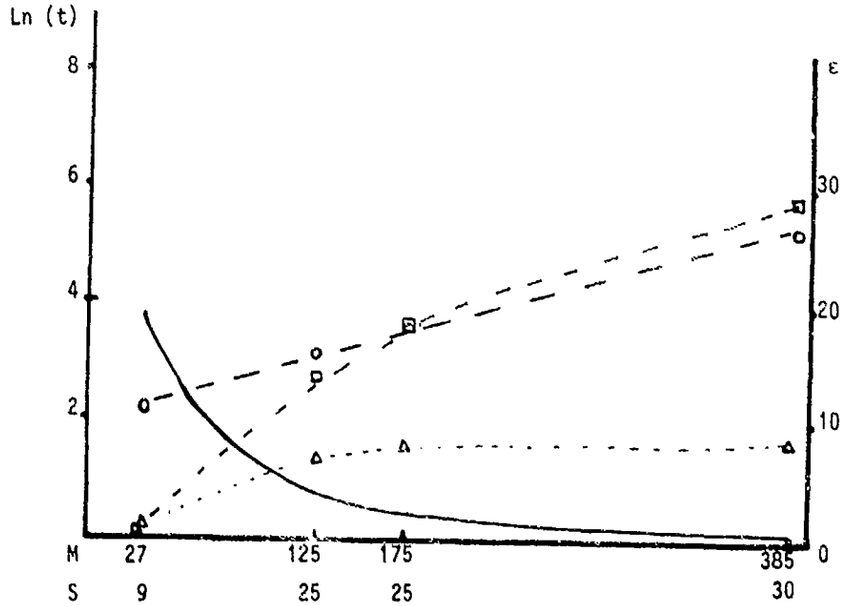

Figure 3-b : Comparative calculation times for several meshes

TOPICS ON BOUNDARY-ELEMENT SOLUTIONS OF WAVE RADIATION-DIFFRACTION PROBLEMS

Paul D. Sclavounos and Chang-Ho Lee

Department of Ocean Engineering
Massachusetts Institute of Technology
Cambridge, Massachusetts 02139

Abstract

Two topics on the numerical solution of boundary-integral equations arising in linear wave-body interactions are discussed. The properties of a spectral technique for the solution of the integral equation are analyzed and compared to the conventional collocation method. It is shown that, using this technique, hydrodynamic forces predicted by the source-distribution method are identical to those obtained from the direct solution for the velocity potential. The second part of the paper investigates the numerical properties of a method which removes the effects of the irregular frequencies for bodies of general shape at a small computational and algorithmic overhead. Its performance is illustrated in the evaluation of the heave and sway hydrodynamic coefficients of a circle and a rectangle.

1. Introduction

The solution of boundary-integral equations for the evaluation of the linear wave loads on marine structures is a common task in today's practice. Its success is due to its algorithmic simplicity, the ease of describing the surface of a three-dimensional body by a collection of facets and the moderate size of the linear systems to be solved. These are illustrated by its widespread use by aerodynamicists [Hess and Smith (1966)].

In the presence of a free surface, the efficiency of the method relies on the fast evaluation of the wave-source potential which is a substantially more complex function to compute than its counterparts in an infinite fluid and an acoustic medium. Existing methods for the computation of its values and derivatives are hard to evaluate, since it is the performance of the integrated radiation-diffraction computer programs that is usually reported. For the three-dimensional computations reported in the present paper, a set of very efficient algorithms developed by Newman (1985a) for water of finite and infinite depth and coded in the subroutine FINGREEN have been utilized.

A distinct feature of wave boundary-integral equations are the " irregular " frequencies. They coincide with the eigenfrequencies of the interior Dirichlet or Neumann problems, and are known to introduce large errors in the predicted hydrodynamic forces, often over a substantial band of frequencies. A comprehensive analysis of the mathematical properties of boundary-integral equations, (with emphasis in acoustics), along with a survey of techniques used for the removal of the irregular frequencies, is given in the recent book of Colton and Kress (1983). The numerical aspects of boundary-integral, as well as finite-element, hybrid-integral and finite-element/boundary-integral methods in free-surface flows are reviewed by Mei (1978), Yeung (1982) and Euvrard (1983).

The first part of the paper analyzes the properties of a technique for solving boundary-integral equations. It is often quoted in the literature as the Galerkin method. In most implementations of the boundary-integral formulation, the body surface is approximated by a collection of N plane quadrilaterals or triangles. The conventional collocation method enforces the validity of the equation at a single point on each panel, usually the centroid. The method proposed here, averages the equation over each panel and avoids the need to select a collocation point. It belongs in the general category of "spectral" techniques which express the solution in terms of N basis functions, and then pre-integrate the product of the equation to be solved with each function of this set. Here, the i-th basis function has the value one on the i-th panel and zero on the rest of them.

The Galerkin technique has a set of interesting symmetry properties. The diagonal elements in the added-mass and damping matrices obtained from the source-distribution and the Green method are identical. The off-diagonal coefficients A_{ij}, B_{ij} obtained from one method are identical to the A_{ji}, B_{ji} coefficients which follow from the other. Moreover, the exciting forces obtained from the solution of the Green integral equation for the diffraction velocity potential, are identical to those obtained from the Haskind

relations with the radiation velocity potential supplied by the source-distribution method, and vice versa. Analogous results do not hold in the collocation method.

Computations of the hydrodynamic coefficients for a semi-submerged spheroid and a truncated vertical circular cylinder have been carried out by Breit, Newman and Sclavounos (1985). No substantial difference from the predictions of the collocation method has been observed. Near the irregular frequencies, the Galerkin method led to a reduction of the error and the frequency bandwidth over which it occurs. In principle, it requires an additional numerical integration for the evaluation of the infuence of panel i on panel j. In Section 2, an algorithm is proposed which reduces substantially this overhead, while maintaining the main features of the Galerkin technique.

For the Green integral equation, the irregular frequencies coincide with the eigenfrequencies of the interior Dirichlet problem. Both in two and three dimensions, they can be suppressed by adding an artificial lid on the interior free surface as suggested by Ohmatsu (1975) in connection with the source-distribution method, and by Kleinman (1982) for the Green integral equation. This approach is effective, but may lead to a substantial increase in the computational effort, especially in three dimensions. Ogilvie and Shin (1977) suggested an alternative route by adding a wave source at the origin of the coordinate system, assumed to lie on the interior free surface, acting as an absorber of the energy associated with the interior Dirichlet eigensolutions. This approach was implemented in two-dimensions and was shown to successfully remove the first irregular frequency, at a small additional computational effort. Ursell (1982) later established that any number of irregular frequencies can be removed if a sufficient number of singularities are added at the origin. No implementation of this method in three dimensions is known to the authors.

Related work in acoustics predates the studies of marine hydrodynamicists by about a decade. Refe rences to early studies can be found in Colton and Kress (1983). Burton and Miller (1971) proposed a methodology which exploits the different location of the irregular frequencies of integral equations of the first and second kind. The linear combination of two such equations for the exterior Neumann problem has a unique solution on the entire real frequency axis, and thus is free of irregular frequencies. The condition for this to occur is that one of the two equations must be multiplied by the imaginary unit times a positive constant. It turns out that the associated interior homogeneous problem is of mixed Dirichlet and Neumann type, the two being 90 degrees out of phase. Non-trivial eigen solutions cannot exist since on the interior boundary the normal velocity is 90 degrees out of phase from the velocity potential, or in phase with the pressure. Thus energy may flow out of the interior domain preventing the persistence of eigensolutions. The direction of the energy flux is controlled by the sign of the constant used in the linear combination of the two equations.

Euvrard, Jami, Lenoir and Martin (1981) were the first to adapt this methodology to wave-body interaction problems. Their formulation combines a layer of finite elements in the fluid domain which encloses the body boundary, with a boundary-integral representation in the exterior domain analogous to that outlined in the preceding paragraph. Computations of the hydrodynamic coefficients of three-dimensional bodies were found free of the effects of irregular frequencies.

In the present paper the method of Burton and Miller (1971) is applied to the solution of the radiation problem. It corresponds to the limit of a finite-element layer of zero thickness in the scheme of Euvrard et al. A circle and a rectangle have been analyzed. Their boundary has been approximated by straight segments and the equation has been satisfied at their mid-point, according to the collocation method. In both the heave and sway added mass and damping coefficients, errors have been suppressed at and in the vicinity of the irregular frequencies.

The associated computational and algorithmic overhead is small, since the effort involved in the computation of the second derivatives of the wave source potential (they appear in the kernel of the equation of the first kind) is not large relative to that required by its value and first derivatives. In deep water this overhead is negligible because of the existence of recurrence relations which relate derivatives of high to those of lower order. Moreover, the size of the linear system is unaffected by the superposition of two equations over the same number of panels.

The method is currently being extended to three-dimensional problems where the irregular-frequency effects are generally less pronounced, and is expected to be effective for bodies of general shape. This is believed to be the case because the addition of the integral equation of the first kind to the Green equation essentially corresponds to an additional singularity distribution on the actual body surface rather than at a selected set of points internal to its boundary.

2. The Galerkin method

We are interested to evaluate the hydrodynamic pressure on the surface of a body interacting with regular free-surface waves. Linearity, and the assumption of irrotational flow, allows the reduction of the problem to the evaluation of a velocity potential $\phi(x)$ which satisfies the Laplace equation in the fluid domain, the linear free-surface condition, a prescribed normal gradient $v(x)$ on the body surface, the vanishing of its gradient at large depths and a radiation condition at infinity.

Two boundary-integral formulations are common, and both can be derived from Green's theorem. According to the source-distribution method, $\phi(x)$ is represented by a distribution of wave sources on the body surface,

$$\phi(x) = \int_S \sigma(\xi) G(x;\xi) d\xi \qquad (2.1)$$

where $G(x;\xi)$ is the wave-source potential at the point x due a unit source located at the point ξ. Enforcing the normal velocity on the body boundary leads to an integral equation for the strength $\sigma(x)$ of the source distribution,

$$-\frac{1}{2}\sigma(x) + \int_S \sigma(\xi) \frac{\partial G(x;\xi)}{\partial n_x} d\xi = \frac{\partial \phi}{\partial n_x} = V(x) \qquad (2.2)$$

The application of a different variant of Green's theorem leads to an integral equation with the velocity potential itself as the unknown,

$$-\frac{1}{2}\phi(x) + \int_S \phi(\xi) \frac{\partial G(\xi;x)}{\partial n_\xi} d\xi = \int_S \frac{\partial \phi}{\partial n_\xi} G(\xi;x) d\xi \qquad (2.3)$$

Equations (2.2) and (2.3) are adjoint Fredholm integral equations of the second kind, since the kernel of (2.2) is obtained from the transposition of the arguments of the kernel of (2.3). The preference of the one versus the other depends on the application for which they are being considered. If, for example, the flow velocities are required then equations (2.1)-(2.2) appear to be at an advantage since the evaluation of the second derivatives of G is not necessary. If, on the other hand, only quantities dependent on the velocity potential are needed, then (2.3) must be preferred due to the reduced storage requirements.

Their numerical solution is usually obtained by approximating the body boundary by a collection of plane quadrilaterals or triangles, assuming that the unknown functions have constant values on each panel. The equations are enforced at a set of collocation points usually taken to be the centroids. The Galerkin technique, proposed here, averages instead the equations over each panel. In discrete form, equations (2.1)-(2.2) become,

$$\phi_i = \frac{1}{A_i} \sum_{j=i}^{N} \sigma_j \int_{S_i} dx \int_{S_j} d\xi\, G(x;\xi) = \frac{1}{A_i} \sum_{j=1}^{N} G_{ij}\sigma_j \qquad (2.4)$$

$$G_{ij} = \int_{S_i} dx \int_{S_j} d\xi\, G(\xi;x) \qquad (2.5)$$

$$-\frac{1}{2}\sigma_i A_i + \sum_{j=1}^{N} D_{ij}^{(S)} \sigma_j = V_i A_i , \quad i = 1,\ldots,N \qquad (2.6)$$

$$D_{ij}^{(S)} = \int_{S_i} dx \int_{S_j} d\xi \frac{\partial G(x;\xi)}{\partial n_x} \qquad (2.7)$$

and equation (2.3),

$$-\frac{1}{2}\phi_i A_i + \sum_{j=1}^{N} D_{ij}^{(G)} \phi_j = \sum_{j=1}^{N} G_{ij} V_j , \quad i = 1,\ldots,N \qquad (2.8)$$

$$D_{ij}^{(G)} = \int_{S_i} dx \int_{S_j} d\xi \frac{\partial G(\xi;x)}{\partial n_\xi} \qquad (2.9)$$

where A_i is the area of the i-th panel. The integration with respect to the x-variable introduced by the Galerkin averaging, allows the matrices $D^{(S)}$, $D^{(G)}$ and G to preserve the symmetry properties of the corresponding operators in the continuous case. In particular, the matrix G is symmetric, thus

$$G_{ij} = G_{ji} \qquad (2.10)$$

and the matrices $D^{(G)}$ and $D^{(S)}$ are the transpose of each other, or

$$D_{ij}^{(G)} = D_{ji}^{(S)} \qquad (2.11)$$

The proof of (2.10) follows from the symmetry of the wave-source potential with respect to its arguments, and of (2.11) by exchanging the role of the dummy variables under the integral signs in (2.7) and transposing the i and j indices. Analogous results do not hold in the

collocation method, where the corresponding matrix elements are obtained by replacing the integration with respect to the x-variable in (2.4)-(2.9) by the selection of a collocation point.

Let $A = \mathrm{diag}(A_i)$, and define,

$$D = -\frac{1}{2} A + D^{(G)} \qquad (2.12)$$

The solution for the velocity potential obtained from equations (2.4)-(2.7) in terms of the matrices A, D and G, is given by

$$\vec{\phi}^{(S)} = A^{-1} G (D^T)^{-1} A \vec{v} \qquad (2.13)$$

and the solution of (2.8) by

$$\vec{\phi}^{(G)} = D^{-1} G \vec{v} \qquad (2.14)$$

For an arbitrary normal-velocity vector $\vec{v}$, a necessary condition for the identity of the two solutions (2.13) and (2.14) is the equality of the matrix $D^{-1}G$ with the matrix $A^{-1} G (D^T)^{-1} A$, or equivalently the symmetry of the matrix

$$W = A D^{-1} G \qquad (2.15)$$

A proof that W is symmetric did not prove possible. Numerical experiments for a model problem in two dimensions in an infinite fluid revealed that the matrix W is "almost symmetric", meaning that elements with symmetric locations relative to the principal diagonal agreed to 2-3 significant digits. This suggests the proximity of the values for the velocity potential obtained from each method.

The hydrodynamic forces can be obtained from the solutions (2.13) and (2.14) by multiplying the velocity potential by the panel area A_i and the vector u_i which represents the "direction" of the force we are interested to evaluate. This operation is equivalent to a pre-multiplication of the velocity-potential vector by the vector $(A\vec{u})^T$. The resulting hydrodynamic force obtained form the source-distribution method is given by

$$H^{(S)} = \vec{u}^T W^T \vec{v} \qquad (2.16)$$

and from the direct solution of the Green integral equation,

$$H^{(G)} = \vec{u}^T W \vec{v} \qquad (2.17)$$

Both $H^{(S)}$ and $H^{(G)}$ are complex scalars. Three properties follow from equations (2.16) and (2.17) :

1) For the diagonal hydrodynamic coefficients $H_{kk} = A_{kk} - i B_{kk}/\omega$, $k = 1, \ldots, 6$, the vectors u_j and v_j are equal to the values on the j-th panel of the unit vector $\vec{n}_k$ which points out of the fluid domain. In this case the hydrodynamic coefficients predicted by the two methods are identical, since

$$\vec{v}^T W \vec{v} = \vec{v}^T W^T \vec{v} \qquad (2.18)$$

2) For the off-diagonal coefficients, it follows from (2.16) and (2.17) that

$$H^{(S)}_{K\ell} = H^{(G)}_{\ell K} \qquad (2.19)$$

3) For the diffraction exciting force, we define

$$v_j = -\left(\frac{\partial \phi_0}{\partial n}\right)_j \qquad (2.20)$$

where ϕ_0 is the incident-wave velocity potential. If X_k is the diffraction exciting force in the k-th direction, it can be deduced from (2.16) and (2.17) that the force predicted by the source-distribution/Green method by directly solving the diffraction problem, is identical to the force obtained from the use of the Haskind relation with the velocity potential supplied by the solution of the Green/source-distribution integral equation.

Computations of the hydrodynamic coefficients of a spheroid and a vertical circular cylinder using both methods have been carried out by Breit, Newman and Sclavounos (1985). A radiation-diffraction computer program has been written for the hydrodynamic analysis of bodies of general shape. Their wetted surface is approximated by a collection of plane quadrilaterals and triangles, as illustrated in Figures 1 and 2 for a quarter of the spheroid and the vertical cylinder respectively.

For inter-panel distances small compared to their characteristic dimensions, the Rankine singularity (including when appropriate its image with respect to the free surface and the sea bottom) is subtracted from the wave-source potential and integrated analytically over the panels. For large distances between the panels the total wave-source potential is integrated by quadrature. The algorithms for the integration of the Rankine singularities on plane quadrilaterals and for the evaluation of the wave-source potential

have been developed by Newman (1985a & b) and coded in the subroutines FINGREEN and RPAN respectively. The four-node Gauss-Legendre quadrature, adapted to a plane quadrilateral of general shape, has been used for the evaluation of influence coefficients in both the collocation and Galerkin methods. Suggestions on the order of the quadrature to be used in a production radiation-diffraction computer program are discussed at the end of the section.

The hydrodynamic-force predictions of the collocation and Galerkin methods did not differ substantially away from the irregular frequencies. Tabulated results of high accuracy are reported in Breit, Newman and Sclavounos. Figures 3 and 4 illustrate the behaviour of the two methods at the first heave irregular frequency of the spheroid and the cylinder respectively. The solid lines represent the predictions of an independent curvilinear-panel program for the spheroid, and a Fourier-transformed time-domain solution for the cylinder. The Galerkin predictions appear to be less sensitive to the irregular-frequency errors, especially for the spheroid coefficients.

The Galerkin technique requires an additional integration for the evaluation of each element in the D_{ij} and G_{ij} matrices, [eq. (2.4), (2.9)] relative to the collocation method. It is reasonable to assume that the accuracy in the integration over the i-th panel needs to be no higher than that over the j-th panel. Concerning the Rankine source and dipole, analytical expressions for the double integral over a pair of plane quadrilaterals are not known to the authors. When the analytical expressions are utilized for the evaluation of the Rankine source and dipole integrals over the j-th panel, a four-node Gauss-Legendre quadrature is suggested for the integration over the i-th panel. Since this result is frequency-independent it may be evaluated once and stored.

The integrals of the remaining slowly-varying but frequency-dependent parts, can be evaluated using a quadrature scheme of the same order for the j-th and i-th panels. In the collocation method, the use of a four-node Gauss quadrature causes an increase by a factor of four in the number of evaluations of the wave-source potential, versus the single-node centroid integration. This factor may be as high as sixteen in the Galerkin method. Optimality requires that errors due to quadrature and the approximation of the geometry by plane panels must be of comparable magnitude. This may be achieved by increasing the number of panels and utilizing a single-node quadrature. This decision depends on the efficiency in the evaluation of the wave-source potential, the solution of the linear system and the computing environment. If the single-node-quadrature route is selected, the collocation and Galerkin methods are comparably expensive over a large number of frequencies.

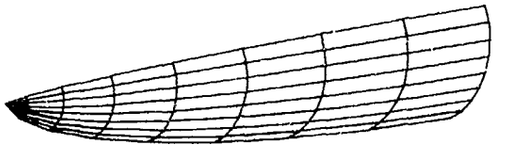

Figure 1 : Discretization of a quarter of the surface of a prolate sphepoid (B/L = 1/8) by 64 panels.

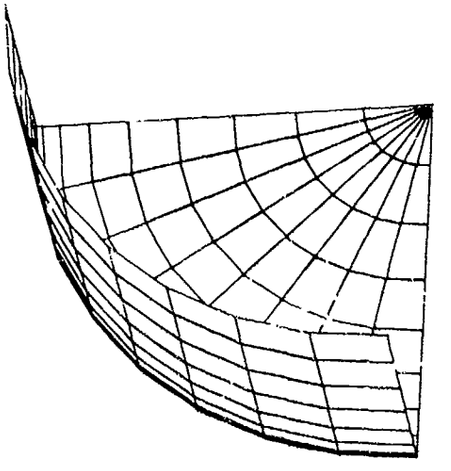

Figure 2 : Discretization of a quarter of the wetted surface of a truncated vertical cylinder (R/T = 2) by 128 panels.

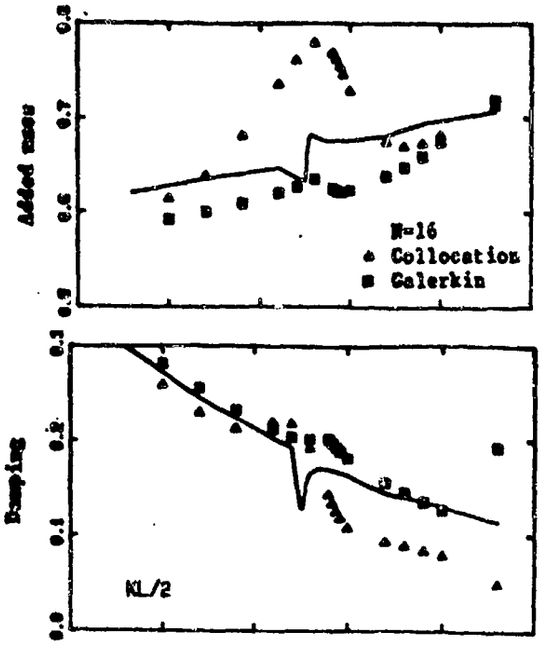

Figure 3 : Heave added-mass and damping coefficients of a prolate spheroid (B/L = 1/8) near the first irregular frequency, made non-dimensional by the displaced volume the water density and the frequency of oscillation. The solid line is obtained from an independent curvilinear-panel program and the tick marks are predictions form the plane-panel program. [From Breit, Newman and Sclavounos (1985)]

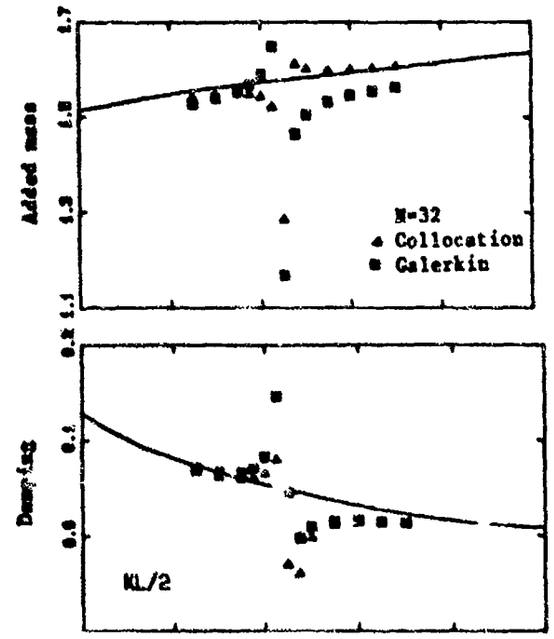

Figure 4 : Heave added-mass and damping coefficients of a truncated vertical cylinder near the first irregular frequency, made non-dimensional by the displaced volume the water density and the frequency of oscillation. The solid line is obtained from the Fourier transform of an independent time-domain program and the tick marks are predictions form the plane-panel program. [From Breit, Newman and Sclavounos (1985)]

3. Irregular frequencies

The Green integral equation (2.3) is known to possess non-vanishing homogeneous solutions at a discrete set of frequencies which correspond to the eigenfrequencies of the interior Dirichlet problem. Their detrimental effect in the numerical predictions of the added-mass and damping coefficients of surface-piercing bodies has been illustrated in Figures 3 and 4.

Although a discrete set in the continuous case, their presence in the discrete problem is manifested by substantial errors, often over a quite wide frequency band around their exact location. This is due to the bad "conditioning" of the integral equation (2.3) not only at, but also in the vicinity of the irregular frequencies. Bad conditioning is known to cause large errors in the solution when a small perturbation is imposed on the equation. In wave-body interactions sources of such perturbations are:

1) The approximation of the body boundary.

2) The approximation of the velocity potential.

3) Errors in the evaluation of the wave-source potential.

4) Quadrature errors in the evaluation of the influence coefficients.

5) The approximate way in which the equation is being satisfied.

6) Roundoff errors in the solution of the linear system.

A measure of the ratio of the output versus the input errors in the solution of integral equations is often supplied by the "condition number". Explicit definitions of it are known for matrix equations. Thus the discrete form of an integral equation may be used to obtain an estimate of it.

Numerical experiments indicate that the errors and frequency bandwidth of the irregular frequencies decrease with increasing numbers of panels. The associated computational cost, however, prevents this to be considered a viable treatment in practice. A short survey of successful methods for the removal of the irregular-frequency effects has been given in the introduction.

The method of Burton and Miller (1971), developed for the solution of an acoustic scattering integral equation, is here adapted to the wave-body interaction problem. The Green equation (2.3) is valid for a point x on the body boundary. If x lies in the fluid

domain, the factor 1/2 which multiplies the first term needs to be replaced by unity. Taking the derivative of both sides in the direction of the unit vector $\hat{n}$ which points out of the fluid domain, and letting the point x approach the body boundary, we obtain

$$-\frac{\partial\phi(x)}{\partial n_x}+\frac{\partial}{\partial n_x}\int_S \phi(\xi)\,\frac{\partial G(\xi;x)}{\partial n_\xi}\,d\xi =$$

$$-\frac{1}{2}\frac{\partial\phi}{\partial n_x}+\int_S \frac{\partial\phi}{\partial n_\xi}\,\frac{\partial G(x;\xi)}{\partial n_x}\,d\xi \qquad (3.1)$$

For a prescribed normal velocity, (3.1) is an integral equation of the first kind for the velocity potential on the body boundary. Its irregular frequencies correspond to the eigenfrequencies of the interior Neumann problem. Burton and Miller (1971) show that the linear combination (2.3) + i α(3.1), or

$$-\frac{1}{2}\phi(x)+\int_S \phi(\xi)\frac{\partial}{\partial n_\xi}\left(1+i\alpha\frac{\partial}{\partial n_x}\right)G(\xi;x)d\xi =$$

$$\frac{i\alpha}{2}\frac{\partial\phi}{\partial n_x}+\int_S \frac{\partial\phi}{\partial n_\xi}\left(1+i\alpha\frac{\partial}{\partial n_x}\right)G(x;\xi)d\xi \qquad (3.2)$$

has no real irregular frequencies for real and positive values of the parameter α. Numerical experimentation suggests that for values of the parameter α ranging from 0.2 to 0.3, the performance of (3.2) is optimal. A discussion of the properties of equations (2.3), (3.1) and (3.2) for acoustic-wave problems, is given by Colton and Kress (1983).

Approximating the body boundary by a collection of panels S_j, and satisfying (3.2) at collocation points located at the panel centroids, we obtain the discrete set of equations

$$-\frac{1}{2}\phi_i+\sum_{j=1}^{N}\phi_j\int_{S_j}\frac{\partial}{\partial n_\xi}\left(1+i\alpha\frac{\partial}{\partial n_{x_i}}\right)G(\xi;x_i)d\xi$$

$$=-\frac{i\alpha}{2}V_i+\sum_{j=1}^{N}V_j\int_{S_j}\left(1+i\alpha\frac{\partial}{\partial n_{x_i}}\right)G(x_i;\xi)d\xi$$

$$i=1,\ldots,N \qquad (3.3)$$

The integral of the double normal derivative of the singular part of the wave-source potential needs careful interpretation. For i=j, it is equal to the normal velocity on the panel due to a distribution of dipoles of constant strength on its surface. This value is known to exist at points not lying on its edges.

The numerical conditioning of equation (3.1) is worse than that of the Green equation (2.3). This is generally known to be true for integral equations of the first kind. Hence, the perturbations 1-6 cause errors in the solution of (3.1) large relative to those in the solution of (2.3).

The effect of equation (3.1) on the solution of (3.2) is controlled by the magnitude of the positive quantity α. If α=0, (3.2) reduces to the Green equation. For finite values of α, (3.2) is expected to be free of irregular frequency effects. This turns out not to be the case in practice for very small values of α which damp excessively the effect of equation (3.1). In this case the error in the hydrodynamic hydrodynamic coefficients near the irregular frequencies of (2.3), although reduced, is still substantial. For large values of α, the effects of equation (3.1) are dominant. The predicted coefficients are now erroneous near its own irregular frequencies. Smaller, but still noticeable, errors are also present for all frequencies due to its poor conditioning. The magnitude of both can be obviously controlled by the selection of a sufficiently small value of α which strikes a balance between the errors coming from the irregular frequencies of the Green equation (2.3) and those coming from the ill-conditioning of equation (3.1).

Computations of the heave and sway coefficients of a circle and a rectangle (B/T=2), indicate that the value of α=0.2 produces satisfactory results over a wide range of frequencies. A value of less than one is not surprising. If the error in the solution of (3.2) resulting from the presence of equations (2.3) is to be comparable to the error due to equation (3.1), the value of α must be comparable to the ratio of their condition numbers which is a quantity with magnitude less than one.

A computer program has been written for the hydrodynamic analysis of sections of general shape in deep water [Sclavounos (1985)]. The computational effort involved in the setup and solution of the discrete equations (3.3), is for all practical purposes comparable to that required when α=0. This is due to the existence of recurrence relations which express higher derivatives of the wave-source potential in terms of derivatives of lower order. The size of the linear system is unaffected by the addition of (3.1) to the Green equation.

Figure 5 presents the heave hydrodynamic coefficients of the circle and the rectangle near the first irregular frequency of equation (2.3). Predictions for α=0, 0.02 and 0.2 are compared to those obtained from the hybrid-integral solution of Nestegard and Sclavounos (1984) which is known to be free of irregular-frequency effects. The corresponding results for sway are presented in Figure 6 with analogous conclusions.

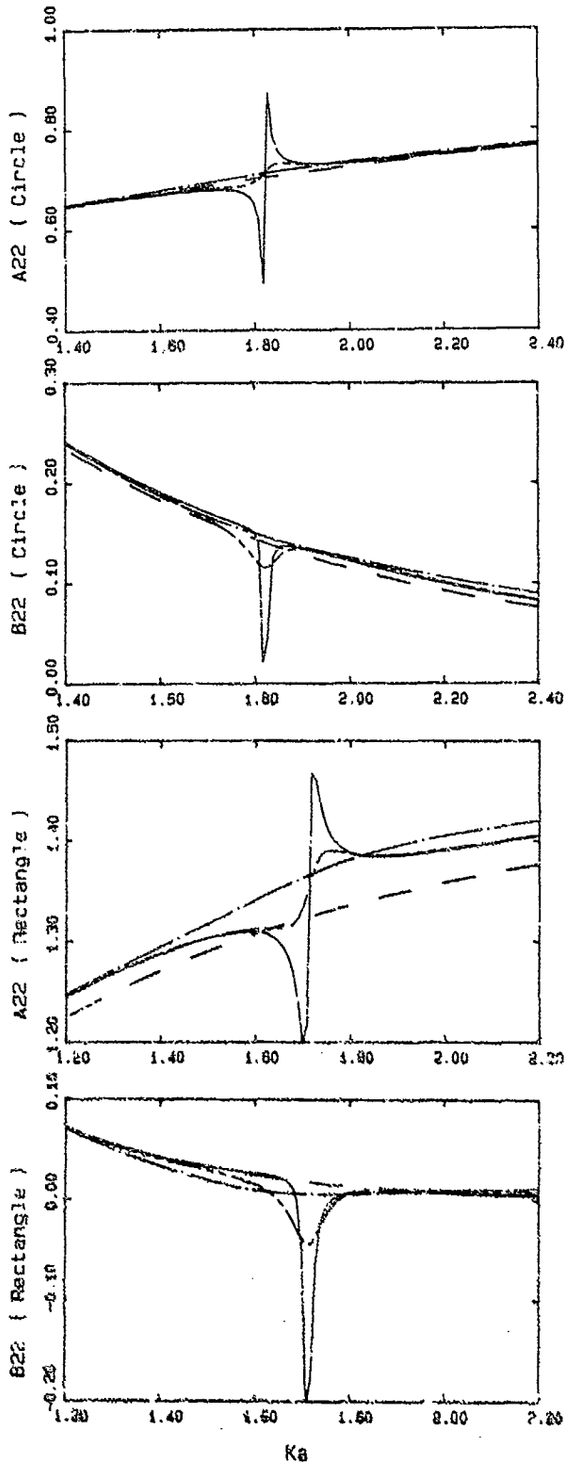

Figure 5

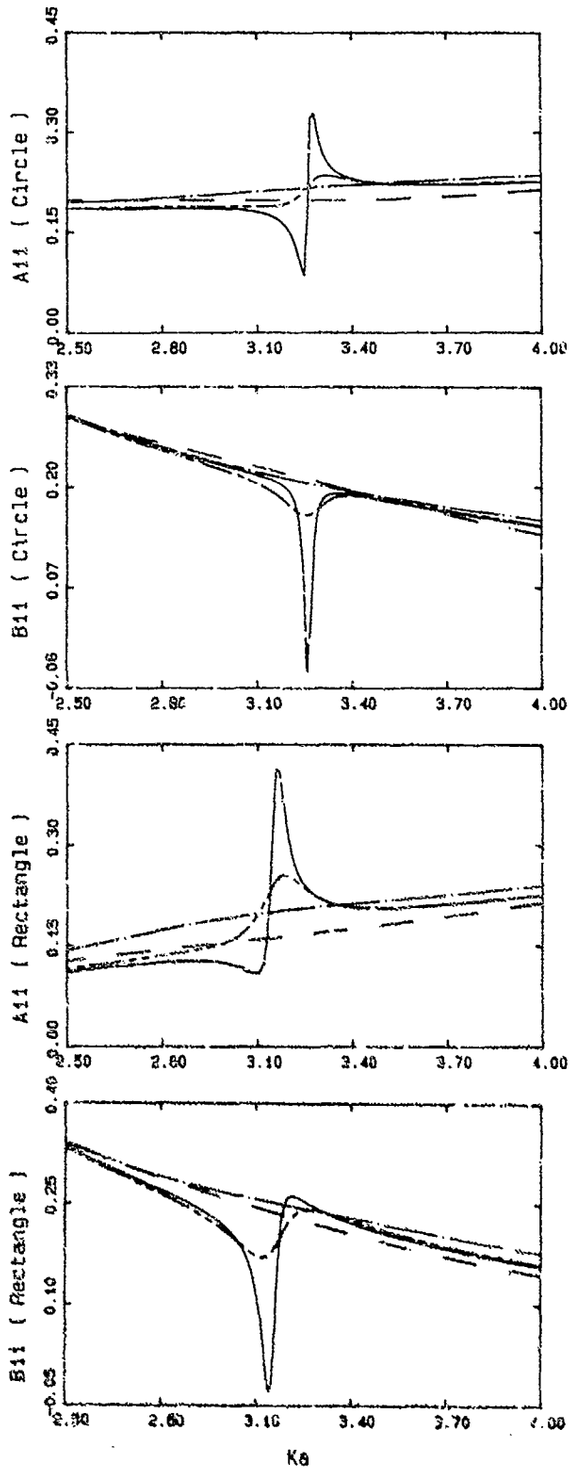

Figure 6

Heave and sway added-mass and damping coefficients near the first irregular frequency of the Green equation (2.3), obtained from the solution of equation (3.3) : (———) $\alpha = 0$; (—·—·—) $\alpha = 0.02$; (—··—··—) $\alpha = 0.2$; (— — —) hybrid-integral solution of Nestegard and Sclavounos (1984).

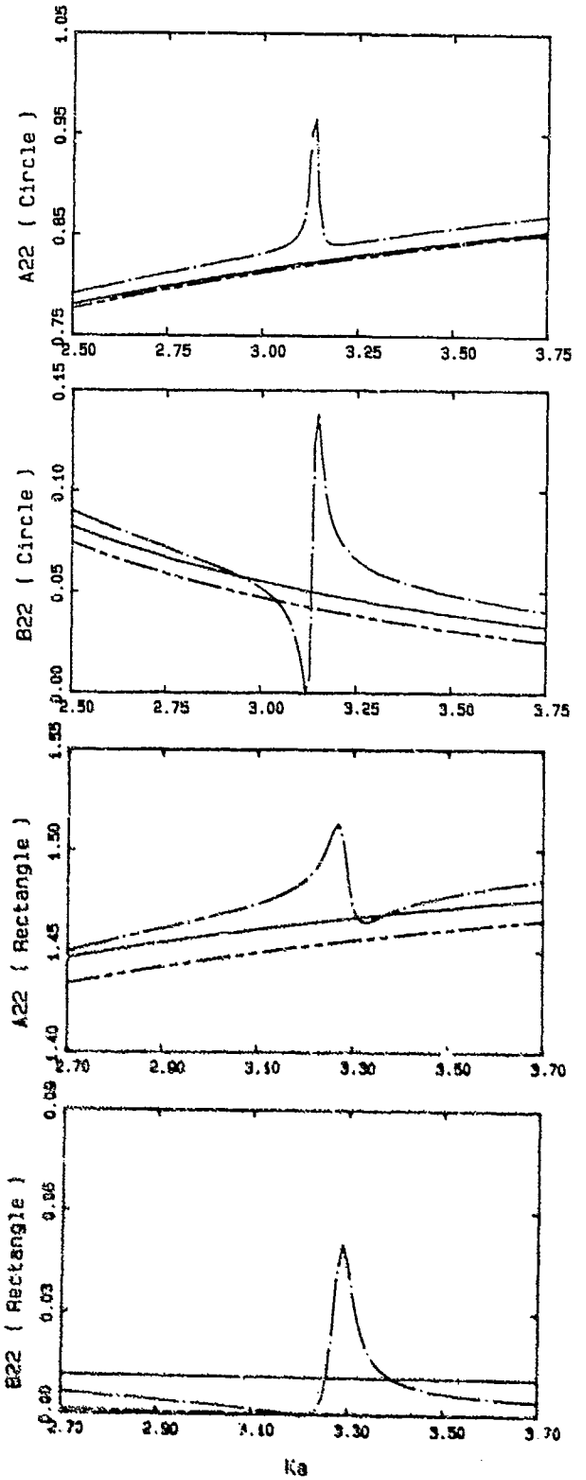

Figure 7

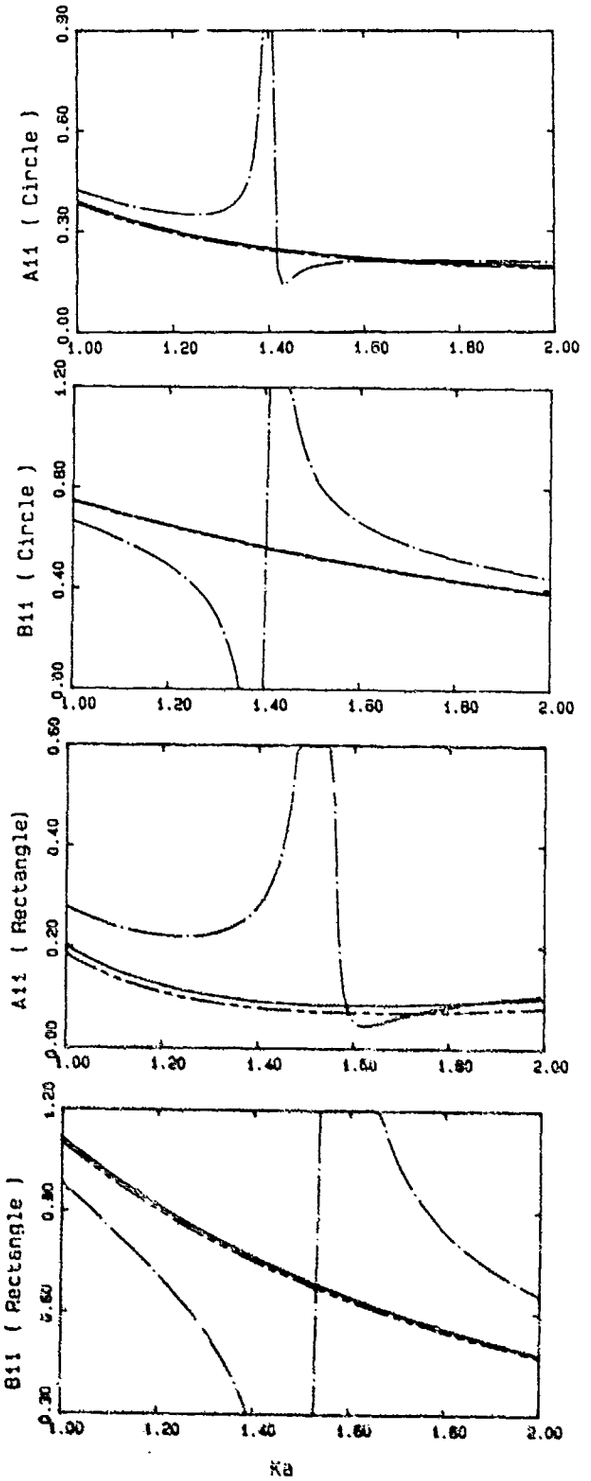

Figure 8

Heave and sway added-mass and damping coefficients near the first irregular frequency of equation (3.1), obtained from the solution of equation (3.3) : (———) $\tau = 0$; (– – – –) $\tau = 0.2$; (—·—·—) equation (3.1).

Figures 7 and 8 illustrate the performance of equation (3.3) near the first irregular frequency of equation (3.1). Results are presented for α = 0, 0.2 and from the solution of equation (3.1) alone. The predictions for α=0 are accurate over that frequency range, and are in good agreement with the results for α =0.2. The larger discrepancies occur in the heave damping coefficients, but these are probably due to its small values. The predictions from equation (3.1) display the excpected error near its first irregular frequency. Evident is also a non-negligible error over a wider frequency range, mainly in the sway coefficients. This is larger than the corresponding error associated with equation (2.3), and is due to the larger condition number of equation (3.1). The effect of (3.1) in the composite equation (3.3) is here reduced by the selection of a value for α equal to 0.2.

In all cases tested, half of the boundary of the sections analysed has been approximated by 10 straight segments. Away from the irregular frequencies, the agreement between the coefficients obtained from equation (3.3) for α =0.2 and the numerical scheme of Nestegard and Sclavounos is very good. Work is currently in progress for the extention of the present method to three dimensions.

Acknowledgements

The present study has been supported by the David W. Taylor Ship Research and Development Center (Contract N00167-84-R-0144), the Office of Naval Research (Special Focus Program on Numerical Ship Hydrodynamics, Contract N0014-822-K-0198) and the National Science Foundation (Grant 8219649-A01-MEA). The work of the first author in this area did benefit by a two-month visit with the Naval Hydrodynamics group at the Ecole Nationale Superieure de Techniques Avancees (ENSTA) in Paris.

Reference

Breit, S. R., Newman, J. N. and Sclavounos, P. D. (1985). "A new Generation of Panel Programs for Radiation-Diffraction Problems". Proc. BOSS'85 Conf., Delft.

Burton, A. J. and Miller, G. F. (1971). "The Application of Integral Equation Methods to the Numerical Solution of Some Exterior Boundary-value Problems". Proc. Royal Soc. London A323, pp. 201-220.

Colton D. and Kress R. (1983). Integral Equation Methods in Scattering Theory. Wiley Interscience.

Euvrard, D., Jami, A., Lenoir, M. and Martin, D. (1981). "Recent Progress Towards an Optimal Coupling of Finite Elements and Singularity Distribution Procedures in Numerical Ship Hydrodynamics". Proc. 3rd Intl. Conf. Num. Ship Hydrodyn., Paris.

Euvrard, D. (1983). "Sur Quelques Methodes de Resolution Des Problemes Lineaires en Domaine non Borne". ENSTA publication.

Hess, J. L. and Smith, A. M. O. (1966). "Calculation of Potential Flows Around Arbitrary Bodies". Prog. Aero. Sciences, Vol. 8.

Kleinman, R. E. (1982). "On the Mathematical Theory of the Motion of Floating Bodies - An Update". DTNSRDC Report 82/074.

Mei, C. C. (1978). "Numerical Methods in Water-Wave Diffraction and Radiation". Ann. Rev. Fluid. Mech., (10), pp. 393-416.

Nestegard, A. and Sclavounos, P. D. (1984). "A numerical Solution of Two-Dimensional Deep Water Wave-Body Problems". J. Ship Res., Vol. 28, No. 1, pp. 48-54.

Newman, J. N. (1985a). "Algorithms for the Free-Surface Green Function". J. Eng'g. Maths. (19), pp. 57-67.

Newman, J. N. (1985b). "Distributions of Sources and Normal Dipoles over a Quadrilateral Panel". To be published.

Ogilvie, T. F. and Shin, S. Y. (1977). "Integral-Equation Solutions for Time-Dependent Free-Surface Problems". J. Soc. Nav. Arch. Japan 143, 43-53.

Ohmatsu, S. (1975). "On the Irregular Frequencies in the Theory of Oscillating Bodies". Papers of Ship Res. Inst., No. 48.

Sclavounos, P. D. (1985). "The User Manual od NIIRID - A General Purpose Program for Wave-Body Interactions". Internal publication.

Ursell, F. (1981). "Irregular Frequencies and The Motion of Floating Bodies". J. Fluid Mech., Vol. 105, pp. 143-156.

Yeung, R. W. (1982). "Numerical Methods in Free-Surface Flows". Ann. Rev. Fluid Mech., (14), pp. 395-442.

FINITE ELEMENT SOLUTION FOR THE TRANSIENT FLOW PAST A FREELY FLOATING BODY

A. Jami and G. Pot
Ecole Nationale Supérieure des Techniques Avancées *
Chemin de la Hunière - 91120 Palaiseau (France)

Abstract

Fully three-dimensionnal solution for the transient free and forced motion of a floating (or immersed) body is given. The linear system of equations is considered for small amplitude motions of the body. The numerical method is widely described and proceeds in four steps : (i) reduction to a bounded domain using an integral representation, (ii) variational formulation in the bounded domain of the continuous problem, (iii) second order finite-differences discretization in time, (iv) second order finite element discretization in space. Many numerical applications ensure the stability and the convergence of this algorithm and the efficiency of the numerical code. Some results of practical interest are also given.

I.Introduction

With the increasing power of computers, the numerical study of real flow situations is every day nearing the goal. For mechanical systems, the first step in this study is the solution of linear approximations. In naval hydrodynamics, periodic and steady solutions are still in progress ; nevertheless, some major contributions, during the last decade, have already been devoted to the solution of unsteady motions. Recently, we gave the solution of the irrotationnal flow past a submerged body undergoing forced motions of small amplitude [1].

Here, we present an extension in the large of the previous paper. The case of a floating body leads to a formulation of the problem in terms of the velocity potential and the free surface elevation ; a time discretization of the linearized free surface condition have been introduced and the way of reducing the problem to a bounded domain by an integral representation formula have been generalized following [2]. Moreover the dynamical equations for the rigid body have been added to the previous set of fluid equations.

Therefore general motions of small amplitude of arbitrarily shaped 3-D bodies initially at rest and subject to any external forces can be considered. Such a general situation is not often analyzed and the bibliography, except some theoretical studies, is not very large ; only 2-D flows have already been considered [3], [4], [5] where moreover, only initial displacements have been given to the body and no sustained forces. Thus in our studies, the validity of the numerical results has to be proved using either general results of applied mathematics when an exact transient solution can be worked out, or elementary physical considerations.

Before giving any further detail on our formulation and its description in this paper, let first introduce the linear set of equations to be solved.

Consider a floating body which hull is denoted by S_t at time t in a fixed frame of reference (O ; x, y, z) where Oy is upward vertical as shown in figure 1 ; at the same time the moving free surface is denoted by Γ_t with equation $y = \eta(x, z ; t)$ and the fluid domain by Ω_t. The body-fluid system is supposed to be at rest at the initial time $t = 0$, its free surface being the plane ($y = 0$).

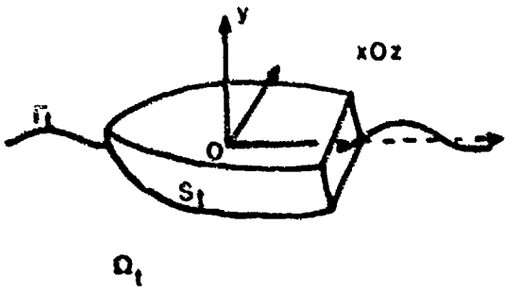

Fig.1 : The Floating Body and the Free Surface at time t.

*The Groupe d'Hydrodynamique Navale (ENSTA) is associated with the CNRS and the Université Pierre et Marie Curie (PARIS VI).

The irrotational motion of an inviscid fluid past the body is described by the velocity potential $\Phi(x, y, z ; t)$ in Ω_t ; using the continuity equation for the incompressible fluid motion, the Bernoulli and kinematic conditions on the free surface and the slip condition on the hull for forced motions, the general system of equations for (Φ, η) forms a well known non-linear problem set in an unknown unbounded domain [6]. No attempt to give a complete solution of this problem is yet possible ; moreover, when the body is freely floating, the position of the hull S_t is also unknown and it is necessary to add to the previous system the fundamental equations of dynamics for the body.

When motions of small amplitude are considered, it is also well known that the system described above can be linearized and reads, in non-dimensional form :

$$\Delta\Phi = 0 \qquad \text{in } \Omega_o \text{ for } t > 0 \qquad (1)$$

$$\left.\begin{aligned} &\frac{\partial\Phi}{\partial y} - \frac{\partial\eta}{\partial t} = 0 \qquad (2)\\ &\eta + \frac{\partial\Phi}{\partial t} = 0 \qquad (3)\end{aligned}\right\} \quad \text{on } \Gamma_o \text{ for } t > 0$$

$$\Phi = 0 \quad \text{on } \Gamma_o \qquad \text{and } \eta = 0 \text{ at } t = 0 \qquad (4)$$

$$\frac{\partial\Phi}{\partial n} - \frac{d\vec{X}}{dt} \cdot \vec{N} = 0 \qquad \text{on } S_o \text{ for } t > 0 \qquad (5)$$

$$\mathbb{M}\frac{d^2\vec{X}}{dt^2} + \mathbb{B}\frac{d\vec{X}}{dt} + \mathbb{C}\vec{X} = -\frac{d}{dt}\int_S \Phi\vec{N}\, ds + \vec{F}_o + (Vo - M)\vec{Y} \qquad (6)$$

$$\vec{X} = \vec{X}_o \text{ and } \frac{d\vec{X}}{dt} = 0 \text{ at } t = 0 \qquad (7)$$

where notations are as follows ;

- $\vec{X} \in \mathbb{R}^6$ is the vector of instantaneous position and rotation of the body with $\vec{X}_o$ the location of S_o at $t = 0$
- Vo and M are respectively the immersed volume and the mass of the body
- $\vec{N} = (\vec{n}, \vec{OM} \wedge \vec{n})$ is the generalized normal pointing inside the body at point M on S_o
- $\mathbb{M}$ and $\mathbb{C}$ are respectively the generalized mass-matrix and the matrix of hydrostatic restoring coefficients
- $\vec{F}_o$ and $\mathbb{B}$ are given data ; $\vec{F}_o$ being the exciting external vector of force and moment and $\mathbb{B}$ a matrix of damping coefficients derived from experimental data to take into account the effect or viscosity.

Problem (1)-(5) with a given $\vec{X}$ is referred to as the "fluid problem" ; general results are given in § II where two kinds of reduction to a bounded domain for the continuous problem is detailed, namely the Dirichlet-(as in ref.[1]) and Fourier-Integral Boundary conditions. Note that this formulation is fondamentally different from Boundary Integral Equations as used in [3] and [4]. The dynamic equations for the rigid body are derived in § III.

A theorem of existence and uniqueness for the problem (1)-(7) has been derived in [7] in the case of a finite depth of the ocean ; the corresponding proof in the infinite depth case, referring to the functionnal analysis of problem (1)-(5) given in [1], can easily be performed. The complete problem is considered in § IV. The convergence results for the numerical schemes, based on the knowledge of a transient exact solution, are given in § V and some numerical applications are presented in § VI.

II - THE FLUID PROBLEM

We shall consider here the system of equations (1)-(5). Note first that equations (2) and (3) can be combined, eliminating the free surface elevation η and thus resulting to a single free surface condition for the velocity potential which reads

$$\frac{\partial^2\Phi}{\partial t^2} + \frac{\partial\Phi}{\partial y} = 0 \text{ on } \Gamma_o \text{ for } t > 0 \qquad (8).$$

Moreover from equations (3) and (4) the initial conditions for Φ become

$$\Phi = 0 \text{ and } \frac{\partial\Phi}{\partial t} = 0 \text{ on } \Gamma_o \text{ at } t = 0 \qquad (9).$$

Let us now suppose

$$v = \frac{d\vec{X}}{dt}\cdot\vec{N} \qquad \text{on } S_o \text{ for } t > 0 \qquad (10)$$

is a given data. We then denote $P_\Phi(v)$ the complete unsteady problem for Φ defined by equations (1), (8), (9) and (5).

For the case of a submerged body, a theorem of existence and uniqueness for problem $P_\Phi(v)$ with regular data v is given in [8].

II.1 Functional analysis

We denote $L^2(\Theta)$ the space of square integrable functions defined over Θ : the latter being a bounded or unbounded set in $\mathbb{R}^3$ or any bounded or unbounded surface in $\mathbb{R}^3$. The subspace $H^1(\Theta)$ of $L^2(\Theta)$ is the space of elements of $L^2(\Theta)$ whose first derivatives are also in $L^2(\Theta)$. $H^1_{loc}(\Theta)$ is the space of functions whose restrictions to any compact subset K of Θ belong to $H^1(K)$. Note also that, for subsequent use in the text, the traces on the boundary $\partial\Theta$ of functions in $H^1(\Theta)$ belong to the subspace of $L^2(\partial\Theta)$ denoted $H^{1/2}(\partial\Theta)$. In the case where elements of $H^1(\Theta)$ have their Laplacian in $L^2(\Theta)$, from Green's identity considered in the sense of distributions, the normal derivatives of those elements on the boundary $\partial\Theta$ belong to the space $H^{-1/2}(\partial\Theta)$, which is thus defined as the dual space of $H^{1/2}(\partial\Theta)$.

Neglecting the lowerscript 0, let us now return to the notations of our problem. Ω is the unbounded domain in $\mathbb{R}^3$ with boundaries S, bounded, and Γ unbounded. Problem $P_\Phi(v)$ is split into two problems, the first of which denoted $Q(\phi,v)$ is similar to $P_\Phi(v)$ but has a given Dirichlet condition ϕ on Γ instead of (8) ; the second problem is a wave-type equation for ϕ such that the solution of $Q(\phi,v)$ is also a solution of $P_\Phi(v)$.

Lemma 1 : *For given* $v \in H^{-1/2}(S)$ *and* $\phi \in H^{1/2}_{loc}(\Gamma) \cap L^2(\Gamma)$, *problem* $Q(\phi,v)$ *has a unique solution with first derivatives in* $L^2(\Omega)$.

The proof of coerciveness of $Q(\phi,v)$ is a consequence of general results of [9] and [10] ; the lemma follows then from LAX-MILGRAMM theorem. Solution of $Q(\phi,v)$ are said of *bounded kinetic energy* in Ω.

We now introduce solutions Φ_0 of $Q(0,v)$ and Φ_1 of $Q(\phi, 0)$; from the general functional notations above, it is an easy matter to define the normal derivatives of Φ_0 and Φ_1 on Γ. We thus define the operators

$$K_0 : v \mapsto K_0 v = \frac{\partial \Phi_0}{\partial y}\Big|_\Gamma \qquad (11)$$

and

$$K_1 : \phi \mapsto K_1 \phi = \frac{\partial \Phi_1}{\partial y}\Big|_\Gamma \quad ; \qquad (12)$$

K_0 is a bounded operator in $L^2(S)$ and K_1 is a self-adjoint positive unbounded operator in $L^2(\Gamma)$ with domain $H^1(\Gamma)$. This allows, for real s, the definition of the power K_1^s [11] with domain $H^s(\Gamma)$, [12].

The unsteady part of our problem is now entirely reduced to finding the proper data ϕ such that $\Phi_0 + \Phi_1$ is a solution of $P_\Phi(v)$. Using (8) we look for the solution ϕ of the wave-type equation

$$\frac{\partial^2 \phi}{\partial t^2} + K_1 \phi = - K_0 v \text{ in } L^2(\Gamma) \text{ for} \qquad (13)$$

$t > 0$, with zero initial data.

Lemma 2 : *The equation* (13) *with right-hand-side* $f \in L^2(\Gamma)$ *and given data* $\phi = f_0$ *and* $\frac{\partial \phi}{\partial t} = f_1$ *in* $L^2(\Gamma)$ *at* $t = 0$ *has a unique solution which reads* (space arguments are ignored)

$$\phi(t) = \int_0^t S_1(t-\tau) f(\tau) d\tau + \frac{dS_1}{dt}(t).f_0 + \qquad (14)$$

$$+ S_1(t).f_1$$

where

$$S_1(t) = K_1^{-1/2} \sin(t K_1^{1/2}) \qquad (15)$$

is a bounded operator in $L^2(\Gamma)$.

This is a well known result of [13] ; it will be also used in the next paragraph.

With some additionnal results which can be found in [8], we can give the

Theorem 1 : *At each time* $t > 0$, *problem* $P_\Phi(v)$ *has a unique solution* $\Phi \in H^1_{loc}(\Omega)$ *of bounded kinetic energy with trace on* Γ, $\phi \in H^1(\Gamma)$. *Moreover the time derivative* $\frac{\partial \phi}{\partial t}$ *belong to* $L^2(\Gamma)$.

As existence of such a solution is a consequence of the construction above, only uniqueness has to be proved ; it is then easy to see that the total energy

$$E(t) = \int_\Omega |\text{grad } \Phi|^2 + \int_\Gamma |\frac{\partial \phi}{\partial t}|^2 , \qquad (16)$$

is a constant for vanishing data v. Thus the only solution of the homogeneous problem $P_\Phi(0)$ is a constant which can only be zero.

II.2 Integral representations

We denote $\mathbb{R}^3$ the lower half space ($y < 0$). For any fixed point M in $\mathbb{R}^3$, we define

$$G_M(P) = - \frac{1}{4\pi}\left[\frac{1}{|M\,P|} - \frac{1}{|M'P|}\right] \qquad (17)$$

as an elementary solution of the Laplace operator in $\mathbb{R}^3$; M' being the symmetric of M with respect to the plane $y = 0$. Note that $G_M(P)$ vanishes on Γ and can thus be considered as a Green function for $Q(\phi,v)$.

The solution Φ of $P_\Phi(v)$ can be, at each time represented in Ω by $\Phi = \psi_0 + \psi_1$ where

$$\psi_0(M;t) = \int_S [\Phi(P;t)\frac{\partial G_M}{\partial n_P}(P) - v(P;t) G_M(P)]\, ds_P, \qquad (18)$$

and

$$\psi_1(M;t) = \int_\Gamma \phi(P;t)\frac{\partial G_M}{\partial n_P}(P)\, d\gamma_P \quad ; \qquad (19)$$

ψ_0 is harmonic in Ω and vanishes on Γ, ψ_1 is harmonic in $\mathbb{R}^3$ and ϕ is therefore its trace on Γ. We then have an integral representation, at each time, for Φ in terms of its traces on S and Γ. Moreover as Γ can be identified to $\mathbb{R}^2$, (19) is a convolution in the horizontal (x,z) variables and can be computed by Fourier transform. But, evidently, as Γ is an unbounded boundary, such an integral representation is of no use for us.

Consider the well-posed problem $Q(\phi)$ set in $\mathbb{R}^3$ (equivalent to $Q(\phi,v)$ but without

obstacle) ; ψ_1 is its unique solution and we define the operator

$$K : \phi \longrightarrow K\phi = \frac{\partial \psi_1}{\partial y}\Big|_\Gamma \quad . \tag{20}$$

As K is of convolution type its Fourier transform is a multiplication operator which can be easily evaluated ; this was not the case for the operator K_1. Namely, the Fourier transform $\tilde{K}$ of K is $|s|$ where s is the polar radius in the Fourier transformed plane.

Then, as ψ_o vanishes on Γ at any time, the trace ϕ of our solution is also a solution of equation

$$\frac{\partial^2 \phi}{\partial t^2} + K\phi = - K \psi_o|_\Gamma \quad , \tag{21}$$

with homogeneous initial data.

From (11) and (15) with K and S replacing K_1 and S_1 respectively, we have

$$\phi(t) = \int_0^t S(t-\tau)[- K \psi_o|_\Gamma (\tau)]\, d\tau \quad ; \tag{22}$$

the evaluation of which, using the definition of ψ_o and the fact that S is a fixed boundary, leads to computing $S(t).K.G_M$ which is easily done by Fourier transform.

Finaly, ψ_1 can be represented as a convolution in the time variable applied to ψ_o and Φ has the integral representation

$$\Phi(M;t) = \psi_o(M;t) + \int_0^t \int_S [\Phi(P;\tau) \frac{\partial F_M}{\partial n_p}(P;t-\tau) - v(P;\tau) F_M(P;t-\tau)] ds_p d\tau \tag{23}$$

where

$$F_M(P;t) = - \frac{1}{2\pi} \int_0^\infty \sqrt{s}\, e^{zs} J_0(rs) \sin(\sqrt{s}t) ds \tag{24}$$

with (r,z) the cylindrical coordinates of $\overrightarrow{M'P}$, ($|M'P|^2 = r^2 + z^2$, $z < 0$). A similar result has been given, a long time ago, although derived by different arguments, by FINKELSTEIN [14]. For computational efficiency, other expressions of F_M have been derived which are given in [8].

Note that, and it is of interest in the sequel, any space derivative of Φ can have an integral representation similar to (23) where only the kernels $G_M(P)$ and $F_M(P;t)$ are replaced by their corresponding derivative with respect to their argument M.

Moreover, all the results given in this chapter can be extended to the case of a surface-piercing body without any restriction.

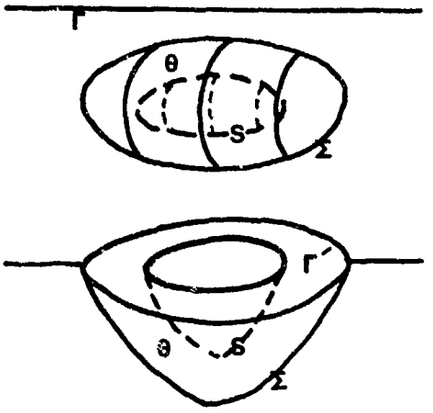

Fig. 2 : The bounded domain Θ

As, thanks to (23), the solution Φ can be expressed anywhere in the fluid domain Ω in terms of its history on the body S, a reduction of $P_\Omega(v)$ to an essentially arbitrary domain can be performed. For the sake of simplicity we shall first details the method in the case of problem $Q(0;v)$ and then proceed to the general unsteady case of $P_\Phi(v)$.

II.3 Problem Q(0;v) set in a bounded domain

Let Σ be a regular arbitrary surface surrounding S as shown in fig. 2 ; we denote Θ the bounded domain with boundaries S, Σ and Γ', if S is not too close to Γ . The solution Φ_o of $Q(0;v)$ has the integral representation

$$\Phi_o(M) = \int_S [\Phi_o(P) \frac{\partial G_M}{\partial n_p} - v(P) G_M(P)] ds_p. \tag{25}$$

Φ_o belongs to $H^1(\Theta)$ and satisfies the following set of equations

$$\begin{cases} \Delta \Phi_o = 0 \quad , & (26) \\ \dfrac{\partial \Phi_o}{\partial n}\Big|_S = v \quad , & (27) \\ \Phi_o|_\Gamma = 0 \quad , & (28) \end{cases}$$

To complete the problem set in Θ we can use (25) for M on Σ as a coupling condition between S and Σ ; this will further be denoted as problem $Q_D(v)$, the subscript D refering to a *DIRICHLET-type coupling condition*.

Let us now introduce the boundary operator ∂_λ on Σ, defined for positive λ by

$$\partial_\lambda u = (\frac{\partial u}{\partial n} + \lambda u)_{|\Sigma}, \tag{29}$$

for any u belonging to $H^1(\Theta)$ with Laplacian in $L^2(\Theta)$. By a preceeding remark, we know that $\partial_\lambda \Phi_o$ has an integral representation similar to (25) with $\partial_\lambda G_M$ instead of G_M. When this is used as a coupling boundary condition on Σ, we shall refer to problem $Q_F^\lambda(v)$, the subscript F meaning a *FOURIER-type coupling condition.*

From our construction, Φ_o is trivially a solution of $Q_D(v)$ and $Q_F^\lambda(v)$, moreover, as S and Σ have no common points, the kernels $G_M(P)$ and $\partial_\lambda G_M(P)$ together with there normal derivatives on S (with respect to the variable P) are regular. But such a reduction to a bounded domain could lead to problems with more than one solution. This is a well-known difficulty for example in the case of the sea-keeping problem when irregular frequencies appear. Therefore we give a short proof of the uniqueness of the solution of Q_D and Q_F^λ.

Theorem 2 : $Q_D(0)$ *and* $Q_F^\lambda(0)$ *have the only trivial sclution.*

Let ψ_o be a non-zero solution of $Q_D(0)$, (resp. $Q_F^\lambda(0)$) ; by the third Green identity applied to ψ_o and G_M in Θ we can define

$$w(M) = \psi_o(M) - \int_S \psi_o(P) \frac{\partial G_M}{\partial n_p}(P)\, dS_p, \qquad (30)$$

with

$$w(M) = \int_\Sigma \left[\psi_o(P) \frac{\partial G_M}{\partial n_p}(P) - \frac{\partial \psi_o}{\partial n_p}(P) G_M(P)\right] d\sigma_p \qquad (31)$$

Thus, from (31), w is harmonic in the whole domain Ξ interior to Σ and vanishes on Γ ; and from (30) $w_{|\Gamma} = 0$ (resp. $\partial_\lambda w = 0$). We conclude that w vanishes in Ξ ; then ψ_o has an analytic continuation in the whole domain Ω defined by the integral in (30), is harmonic in Ω, vanishes on Γ. Therefore ψ_o is a solution of $Q(0,0)$ and must vanish in Ω and *a fortiori* in Θ.

We can then conclude that $Q_D(v)$ and $Q_F^\lambda(v)$ for $\lambda > 0$ are two new versions of $Q(0,v)$ but are set in the bounded domain Θ.

II.4 Variationnal formulation for $Q_D(v)$

As for classical Dirichlet-type problem, we introduce a continuous extension operator

$$E : H^{1/2}(\Sigma) \to H^1_{0,S}(\Theta) = (w \in H^1(\Theta)\ /\ w_{|S} = 0) \qquad (32)$$

and we define

$$H^1_{0,\Sigma}(\Theta) = (w \in H^1(\Theta)/w_{|\Sigma} = 0).$$

We now consider for a given data $v \in L^2(S)$, the function

$$\tilde{\Phi}_o = \Phi_o - E\{\int_S (\Phi_o \frac{\partial G_M}{\partial n} - v\, G_M) ds\} \qquad (33)$$

which belongs to $H^1_{0,\Sigma}(\Theta)$ and coindides with Φ_o on S. Our variational problem then reads

$$R_D(v) \begin{cases} \textit{Given } v \in L^2(S), \textit{ find } \tilde{\Phi}_o \in H^1_{0,\Sigma}(\Theta) \\ \textit{such that, } \forall \psi \in H^1_{0,\Sigma}(\Theta), \\ a(\tilde{\Phi}_o + E\{\int_S \tilde{\Phi}_o \frac{\partial G_M}{\partial n} ds\}, \psi) = \\ \int_S v\, \psi\, ds + a(E\{\int_S v\, G_M\, ds\}, \psi), \end{cases} \qquad (34)$$

where

$$a(\Phi,\psi) = \int_\Theta (\vec{grad}\ \Phi | \vec{grad}\ \psi) dw, \qquad (35)$$

is a coercive bilinear form on $H^1_{0,\Sigma}(\Theta)$. Note that the scalar product in $H^1(\Theta)$ is defined as

$$(\Phi,\psi)_{H^1(\Theta)} = a(\Phi,\psi) + \int_\Theta \Phi\psi\, dw. \qquad (36)$$

From RIESZ representation theorem we then introduce the operator T_D defined by the functional relation, $\forall \Phi,\psi \in H^1_{0,\Sigma}(\Theta)$

$$(T_D\Phi,\psi)_{H^1(\Theta)} = -\int_\Theta \Phi\psi\, dw + a(E\{\int_S \Phi \frac{\partial G_M}{\partial n} ds\}, \psi), \qquad (37)$$

and there exists an element $F \in H^1_{0,\Sigma}(\Theta)$ such that, $\forall \psi \in H^1_{0,\Sigma}(\Theta)$,

$$(F,\psi)_{H^1(\Theta)} = \int_S v\psi\, ds + a(E\{\int_S v\, G_M\, ds\}, \psi). \qquad (38)$$

From these notations, problem $R_D(v)$ can be written

$$(I + T_D)\tilde{\Phi}_o = F \text{ in } H^1_{0,\Sigma}(\Theta) \quad , \qquad (39)$$

where I is the identity operator, and we have

Theorem 3 : $R_D(v)$ *has a unique solution* $\tilde{\Phi}_o$ *which is the restriction to* Θ *of the solution* Φ_o *of* $Q_D(v)$.

The proof of this result, which is detailed in [8] lies on the regularity of the kernel $\frac{\partial G_M}{\partial n}$, the continuity of the extension E and the coerciveness of the bilinear form a on $H^1_{0,\Sigma}(\Theta)$; as a matter of fact, the operator T_D is compact (completely continuous) and (39) is a Fredholm equation of second order. Theorem 3 is then a consequence of the Fredholm alternative and the uniqueness result of theo-

rem 2.

The variational formulation $R_D(v)$ of problem $Q_D(v)$ ensures the convergence of a classical finite element method [15], and from [16] errors estimates are conserved, even for isoparametric high order finite elements in the case of curved boundaries.

II.5 Finite-element discretization of $R_D(v)$

For a general introduction to the finite-element method, we refer to [17]. Let h be a measure of the size of the elements in a regular triangulation τ_h of the domain Θ with N_Θ nodal points (a_j) $j=1,N_\Theta$. V_h denote a subspace of $H^1_{0,\Sigma}(\Theta)$ of finite dimension N_Θ, whose elements are generated by a polynomial basis (w_j) such that $w_j(a_i) = \delta_{ij}$ (the Kronecker symbol).

As τ_h would not, in general, cover the whole domain Θ, the discretized problem will be set in the approximate domain Θ_h with boundaries S_h, Σ_h and Γ'_h. Our notations are then as follows.

$$a_{ij} = \int_{\Theta_h} (\vec{\text{grad}}\, w_j | \vec{\text{grad}}\, w_i)\, dw, \qquad (40)$$

and

$$\delta^J_{ij} = \int_{J_h} w_j . w_i \, ds \quad , \qquad (41)$$

for any boundary J of Θ_h with N_J nodal points.

In our formulation, the domain Θ can be arbitrarily small ; we then choose only *one layer of elements between* S_h *and* Σ_h. Moreover as the extension operator E is also arbitrary, we use only the N_Σ nodal values on Σ_h to define it ; thus, we denote $N'_\Theta = N_\Theta - N_\Sigma$;

$$A^D_{ij} = a_{ij} \text{ for } i = 1,N'_\Theta \text{ and } j = 1,N_\Sigma \qquad (42)$$

for a will fitted numbering of the nodes beginning by those on Σ_h.

Then $R_D(v)$ is reduced to a set of N'_Θ equations, its discretized form being

Find the nodal values $(\tilde{\Phi}_{oj}) = 1,N'_\Theta$ *such that*

$$\begin{cases} \sum_{j=1}^{N'_\Theta} \tilde{\Phi}_{oj}\left(a_{ij} + \Delta^D_{ik}\, D\Gamma_{k\ell}\, \delta^S_{\ell j}\right) = \\ \sum_{j\in I_s} v_j\left(\delta^S_{ij} + \Delta^D_{ik}\, \Gamma_{k\ell}\, \delta^S_{\ell j}\right) \end{cases} \qquad (42)$$

where

I_s is the set of values of j for nodes a_j belonging to S_h, $v_j = v(a_j)$ for $j \in I_s$

$\Sigma_{k\ell} = G_{a_k}(a\ell)$, $D\Gamma_{k\ell} = \frac{\partial}{\partial n_\ell} G_{a_k}(a_\ell)$ with a_k (resp. a_ℓ) a nodal point on Σ_h (resp. S_h) and n_ℓ denote the normal to S_h at point a_ℓ unitary and exterior to Θ_h ; summation over k = 1 to N_Σ and $\ell \in I_s$ are undertood.

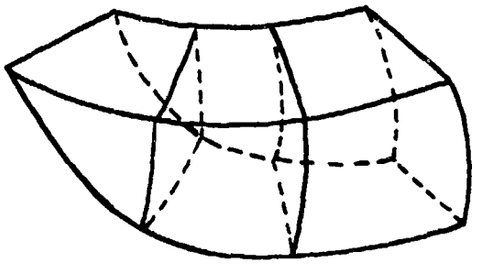

Fig.3 : Prismatic and cubic elements around a half ship-like form.

Note that the coupling terms involve rectangular full and non-symmetric matrices $\Gamma_{k\ell}$ and $D\Gamma_{k\ell}$. Solution of the system (42) is performed via Gauss elimination. Once this solution is obtained the values of Φ_o on Σ_h are determined by using the discretized form of the integral representation ; namely, for k = 1 to N_Σ we have

$$\Phi_{ok} = \sum_{j\in I_s} \left[\tilde{\Phi}_{oj} D\Gamma_{k\ell} - v_j\, \Gamma_{k\ell}\right] \delta^S_{\ell j}. \qquad (43)$$

II.6 Finite-element formulation for Q^λ_F (v)

The variational formulation for $Q^\lambda_F(v)$ is simpler than for the case of $Q_D(v)$ because no extension operator is needed ; it reads

$$R^\lambda_F(v)\begin{cases} \textit{Given } v \in L^2(S),\ \textit{find } \Phi_o \textit{ in } H^1(\Theta) \textit{ such that } \forall \psi \in H^1(\Theta) : \\ a(\Phi_o,\psi) + \lambda\int_\Sigma \Phi_o\, \psi\, d\sigma \\ - \int_\Sigma \psi(M)\int_S \Phi_o \frac{\partial}{\partial n}(\partial_\lambda G_N)\, ds\, d\sigma_N \\ = \int_S v\, \psi\, ds - \int_\Sigma \psi(M)\int_S v(\partial_\lambda G_N)\, ds\, d\sigma_N. \end{cases} \qquad (44)$$

The problem $R^\lambda_F(v)$ can also be expressed in the form of the functional equation

$$(I + T^\lambda_F)\Phi_o = G_\lambda \text{ in } H^1(\Theta), \qquad (45)$$

where, $\forall \Phi, \psi \in H^1(\Theta)$,

$$(T^\lambda_F \Phi,\psi)_{H^1(\Theta)} = -\int_\Omega \Phi\psi - \int_\Sigma \psi \int_S \Phi_o \frac{\partial}{\partial n}(\partial_\lambda G_N)\, ds\, d\sigma + \lambda\int_\Sigma \Phi\psi \qquad (46)$$

and

$$(G_\lambda,\psi)_{H^1(\Theta)} = \int_S v\psi \, ds - \int_\Sigma \psi \int_S v \, \partial_\lambda G_M \, ds \, d\sigma. \quad (47)$$

T_F^λ being again a compact operator in $H^1(\Theta)$, (45) is a second order Fredholm equation ; thus, theorem 3 holds for $R_F^\lambda(v)$ with any positive (or null) constant λ.

The finite-element discretization is also nearly the same and leads, with the same notations to the linear system :

Find the nodal values $(\Phi_{oj})_{j=1,N_\Theta}$ *such that*

$$\sum_{j=1}^{N_\Theta} \Phi_{oj}\{a_{ij} + \lambda\,\delta^\Sigma_{ij} - \delta^\Sigma_{ik}\, D\Gamma^\lambda_{k\ell}\, \delta^S_{\ell j}\} = \sum_{j\in I_S} v_j \{\delta^S_{ij} - \delta^\Sigma_{ik}\, \Gamma^\lambda_{k\ell}\, \delta^S_{\ell j}\} \quad (48)$$

The same remarks as for (42) hold with

$$D\Gamma^\lambda_{k\ell} = \left(\frac{\partial}{\partial n_k} + \lambda\right) \frac{\partial}{\partial n_\ell} G_{a_k}(a_\ell),$$

$$\Gamma^\lambda_{k\ell} = \left(\frac{\partial}{\partial n_k} + \lambda\right) G_{a_k}(a_\ell)$$

where n_k is the unitary outer normal to Σ_h at a_k ; note also that, contrarily to the preceeding formulation, the sum over j in the r.h.s. does contain the nodal points on Σ_h. Consequently it is not necessary here, to evaluate the nodal values on Σ_h after solving (48).

II.7 The coupling method applied to $P_\Phi(v)$.

Again we go on with the same notations. A problem Q(v) is set in the bounded domain Θ which takes advantage of the integral representation (18)-(23). Further we give a time discretization of the convolution integral which tranforms problem Q(v) in a set of problems (Q_n) at each time step t_n. Each one of the problems (Q_n) are then very similar to $Q_D(v)$ or $Q_F^\lambda(v)$; therefore the same theoretical results and the same finite-element discretization apply as above.

We first suppose that our solution Φ is known for all time $\tau < t$; on the other hand we know that $\Phi(t)$, neglicting the space arguments, is in $H^1_{\ell oc}(\Theta)$. For the sake of consiseness we shall only give the formulation in the case of the Dirichlet coupling ; similar results are obtained for the Fourier coupling and will be used in the case of a floating body.

Theorem 4 : *The problem* (Q) *set in* $\Theta \times [0,t]$:

$$(Q) \quad \begin{cases} \Delta\Phi(t) = 0, \ \Phi(t) \in H^1(\Theta) \\ \dfrac{\partial \Phi}{\partial n}(t)\Big|_S = v(t) \in L^2(S) \\ \Phi(t)\Big|_\Sigma \text{ given by (18) and (23)} \end{cases}$$

with homogeneous initial conditions has a unique solution.

By considering ψ_o a solution of the homogeneous problem, the proof follows exactly the lines of that of theorem 2 except that w, as defined by (30) and (31), and by the coupling condition does not vanish on Σ. On the contrary w is harmonic in the whole domain R^3_- and is expressed by the convolution term in (23). Then, ψ_o has an analytic continuation to $\Omega \times [0,t]$ which satisfies the conditions of $P_\Phi(0)$ as only the null function can do ! The same result is obtained for the Fourier-coupling method.

In the case of the floating body, condition (8) on Γ' is added to problem (Q) ; tne same proof holds again but, for the homogeneous inner problem set in $\Xi \times [0,t]$ associated to

$$w(M;t) = \int_0^t \int_S \psi_o(\tau) \frac{\partial F_M}{\partial n}(t-\tau)\, ds\, d\tau$$

we refer to [18].

II.8 Time discretization ; submerged body case

In this case only the time discretization of the convolution integral is involved. We consider *a constant time step* Δt and set $t_n = n\,\Delta t$; upperscript n will refer to functions taken at time t_n. Let us denote by $w^n(M)$ the approximation of this convolution integral, see (23). On each time interval, we assume that Φ and v are linear and F_M is constant ; the latter taking its value at the mid-point time, thus resulting in a second order collocation for evaluating $w^n(M)$ which reads :

$$w^n(M) = \frac{\Delta t}{2} \int_S \left\{ \Phi^n \frac{\partial}{\partial n} F_M^{n-1/2} - v^n F_M^{n-1/2} \right\} ds + \frac{\Delta t}{2} \sum_{m=1}^{n} \int_S R_M^{m,n}\, ds, \quad (49)$$

where

$$R_M^{m,n} = \frac{\partial}{\partial n} F_M^{m-1/2}\{c_m \Phi^{n-m+1} + c'_m \Phi^{n-m}\} - F_M^{m-1/2}\{c_m v^{n-m+1} + c'_m v^{n-m}\}, \quad (50)$$

with

$$\varepsilon_1 = 0 \ ; \ \varepsilon_m = 1, \ 1 < m \leqslant n \qquad (51)$$
$$\varepsilon'_n = 0 \ ; \ \varepsilon'_m = 1, \ 1 \leqslant m < n.$$

The integral representation, used on Σ for the Dirichlet coupling has then the form

$$\phi^n(M) = \int_S [\phi^n \frac{\partial}{\partial n} \tilde{G}_M - v^n \tilde{G}_M + \frac{\Delta t}{2} \sum_{m=1}^{n} R_M^{m,n}] ds \qquad (52)$$

where $\tilde{G}_M = G_M + \frac{\Delta t}{2} F_M^{1/2}$.

The variational formulations for (Q), in this submerged body case are then given by :

- Dirichlet coupling

Given $v^1,\ldots,v^n$ *and* $\tilde{\phi}^1,\ldots,\tilde{\phi}^{n-1}$ *in* $L^2(S)$, *find* $\tilde{\phi}^n \in H^1_{0,\Sigma}(\Theta)$ *such that* $\forall \psi \in H^1_{0,\Sigma}(\Theta)$

$$R_D^n(v) \begin{cases} a(\tilde{\phi}^n + E\{\int_S \tilde{\phi}^n \frac{\partial G_M}{\partial n} ds\}, \psi) = \int_S v^n \psi \, ds \\ + a(E\{\int_S [v^n \tilde{G}_M - \frac{\Delta t}{2} \sum_{m=1} \tilde{R}_M^{m,n}] ds\}, \psi), \end{cases}$$

where $\tilde{R}_M^{m,n}$ is $R_M^{m,n}$ with ϕ replaced by $\tilde{\phi}$.

After solving $R_D^n(v)$, (52) is used to determine the values $\phi_{|\Sigma}$.

- Fourier-Coupling

Given $v^1,\ldots,v^n$ *and* $\phi^1,\ldots,\phi^{n-1}$ *in* $L^2(s)$ *find* $\phi^n \in H^1(\Theta)$ *such that* $\forall \psi \in H^1(\Theta)$

$$R_F^{\lambda,n}(G) \begin{cases} a(\phi^n,\psi) + \lambda \int_\Sigma \phi^n \psi \, d\sigma \\ - \int_\Sigma \psi(M) \int_S \phi^n \frac{\partial}{\partial n}(\partial_\lambda G_M) ds \, d\sigma_M = \\ \int_S v^n \psi \, ds - \int_\Sigma \psi(M) \int_S v^n (\partial_\lambda \tilde{G}_M) ds \, d\sigma_M \\ - \int_\Sigma \psi(M) \int_S \frac{\Delta t}{2} (\sum_{m=1}^{n} \partial_\lambda R_M^{m,n}) ds \, d\sigma_M \end{cases}$$

where $\partial_\lambda R_M^{m,n}$ is $R_M^{m,n}$ with F_M replaced by $\partial_\lambda F_M$.

These two variational forms are evidently very similar to R_D and R_F^λ respectively ; their expression as a second order Fredholm equation is straightforward and the corresponding compact operators $\tilde{T}_D$ and $\tilde{T}_F^\lambda$ differ from T_D and T_F^λ by the single change from G_μ to $\tilde{G}_M$. Existence and uniqueness of the solution at each time step is therefore ensured.

Following the lines of § II.5 to II.7 the finite-element discretization can be performed easily. It is worth noticing that only the r.h.s. changes from one time step to another ; the matrix of the linear system can therefore be factorized once.

II.9 Time discretization ; floating body-case

We are now concerned with the time discretization of the free surface condition. In order to formulate our problem with only first order derivatives in time, we go back to equations (2) and (3) conserving the free surface elevation as an unknown. We first present the numerical algorithm using only these equations as if the problem were set in a bounded domain. Let us denote K' the operator which relates the trace ϕ^n on Γ' at time t_n of the solution to its normal derivative ; equations (2) and (3) take then the form

$$\begin{cases} K'\phi - \frac{\partial \eta}{\partial t} = 0 \\ \frac{\partial \phi}{\partial t} + \eta = 0 \end{cases} \qquad (53)$$

Note that even for vanishing initial conditions as (4), this problem is not homogeneous because K' is not linear but affine unless $v(t) = 0$ as it will be seen later.

We use a second order centered scheme , namely the trapezoïdal rule to discretize the system (53) ; it is written at time $t_{n+\frac{1}{2}}$ using values of ϕ and η at time t_{n+1} and t_n and reads

$$\begin{cases} K'\phi^{n+1} - \frac{2}{\Delta t} \eta^{n+1} = - K'\phi^n - \frac{2}{\Delta t} \eta^n \\ \frac{2}{\Delta t} \phi^{n+1} + \eta^{n+1} = \frac{2}{\Delta t} \phi^n - \eta^n. \end{cases} \qquad (54)$$

Now eliminating η in (54) we are lead to the equation for ϕ

$$(K' + \frac{4}{\Delta t^2})\phi^{n+1} = -(K' + \frac{4}{\Delta t^2})\phi^{n-1} - 2(K' - \frac{4}{\Delta t^2}) \phi^n \qquad (55)$$

which shows that the problem set for ϕ^{n+1} will contain a Fourier boundary condition on Γ' with the positive constant $\frac{4}{\Delta t^2}$; this could not bring any spurious eigen value in our operators.

A discretized form for the total energy E(t) can be expressed at time t_{n+1} by

$$E^{n+1} = \int_{\Gamma'} [K'\phi^{n+1}.\phi^{n+1} + (\eta^{n+1})^2] d\gamma \ ; \qquad (56)$$

Theorem 5 : *If* K' *is self-adjoint, the discretized form* (54) *of the free surface condition is conservative.*

This means that E^n as defined by (56) is

independant of n ; it is easily obtained by linear combinations of equations (54). The self-adjointness of K' being effective only either for a continuous original problem set in a bounded domain with homogeneous boundary conditions or for the original problem with vanishing data v(t) and unbounded Γ'.

We shall only give the definition of the operator K' in both cases of Dirichlet and Fourier coupling boundary condition

- Dirichlet-coupling : $\forall\ \psi \in H^1_{0,\Sigma}(\Theta)$,

$$\begin{aligned}&\int_{\Gamma'}(K'\tilde{\phi}^n).\psi\ d\gamma = a(\tilde{\phi}^n,\psi) + \\ &+ a(E\{\int_S \tilde{\phi}^n \frac{\partial}{\partial n}\tilde{G}_M\ ds\},\psi) - \int_S v^n\ \psi\ ds \\ &- a(E\{\int_S [v^n\tilde{G}_M - \frac{\Delta t}{2}\sum_{m=1}^{n}\tilde{R}_M^{m,n}]\ ds\},\psi)\end{aligned} \tag{57}$$

- Fourier-coupling $\forall\ \psi \in H^1(\Theta)$

$$\begin{aligned}&\int_{\Gamma'}(K'\phi^n).\psi\ d\gamma = a(\phi^n,\psi)+\lambda\int_\Sigma \phi^n\psi d\sigma - \int_S v^n\psi ds \\ &- \int_\Sigma \psi(M)\int_S [\phi^n \frac{\partial}{\partial n}\partial_\lambda\tilde{G}_M - v^n\,\partial_\lambda\tilde{G}_M]ds d\sigma_M \\ &- \int_\Sigma \psi(M)\int_S \frac{\Delta t}{2}[\sum_{m=1}^{n}\partial_\lambda R_M^{m,n}]\ ds\ d\sigma_M\end{aligned} \tag{58}$$

Using (54) and (57), the variational form of $R_D^n(v)$ in the case of a floating body is

Find $(\tilde{\phi}^{n+1},\eta^{n+1}) \in H^1_{0,\Sigma}(\Theta) \times L^2(\Gamma')$ *such that* $\forall(\psi,\mu) \in H^1_{0,\Sigma}(\Theta) \times L^2(\Gamma')$,

$$\begin{cases} * \int_{\Gamma'}(K'\tilde{\phi}^{n+1} - \frac{2}{\Delta t}\eta^{n+1})\psi d\gamma = \\ \int_{\Gamma'}(-K'\tilde{\phi}^n - \frac{2}{\Delta t}\eta^n)\psi d\gamma \\ * \int_{\Gamma'}(\frac{2}{\Delta t}\phi^{n+1} + \eta^{n+1})\mu\ d\gamma = \\ \int_{\Gamma'}(\frac{2}{\Delta t}\phi^n - \eta^n)\mu\ d\gamma \end{cases}$$

where $\phi^n = \tilde{\phi}^n + E\{\int_S [\tilde{\phi}^n \frac{\partial}{\partial n}\tilde{G}_M - v_n\tilde{G}_M]ds\}$

$$- E\{\int_S [\frac{\Delta t}{2}\sum_{m=1}^{n} R_M^{m,n}]\ ds\}.$$

With (54) and (58), the variational form of $R_F^{\lambda,n}(v)$ in the case of a floating body is identical to (59) but with $\tilde{\phi} \in H^1_{0,\Sigma}(\Theta)$ replaced by $\phi \in H^1(\Theta)$.

In these cases, conservation of energy does not occur as, even for vanishing v^p for all $p < n+1$, the integral representation realizes the correct flux of energy through the boundary Σ.

II.10 The numerical evaluation of forces and moments.

The action of the fluid on the body is given, from the linearized Bernoulli equation, by integration of the unsteady pressure

$$p(M;t) = -\frac{\partial\Phi}{\partial t}(M;t) \text{ on } S \tag{60}$$

in non dimensional form ; it discretized form is, at time t_{n-1} :

$$p^{n-1}(M) = -\frac{1}{2\Delta t}(\Phi^{n+1}(M) - \Phi^{n-1}(M)) \text{ on } S \tag{61}$$

We denote $\vec{N} \in \mathbb{R}^6$ the generalized normal to the body which three first components are those of the unitary outer normal $\vec{n}$ and three last components are those of $G\vec{M} \wedge \vec{n}$ at point M on S, where G is the center of mass of the rigid body. The generalized force coefficient is then given by

$$\vec{F}(t) = \int_S p(M;t)\vec{N}(M)\ ds\ ; \tag{62}$$

its discretized form being, at time t_{n-1}

$$\vec{F}^{n-1} = \frac{1}{2\Delta t}\sum_{i,j\in I_s}(\Phi_i^{n+1} - \Phi_i^{n-1})\vec{N}_j\ \delta^s_{ij}. \tag{63}$$

Results for the forced motion of a 3-D submerged body are given in [1].

III - THE DYNAMIC EQUATIONS FOR THE RIGID BODY

We now introduce the set of equations governing the motion of the rigid body , the notations of which are given in § I and G(t) (resp. C (t)) $\in \mathbb{R}^3$ is the instantaneous position of the center of mass (resp. center of immersed volume), M is the total mass of the body and V the measure of the immersed volume

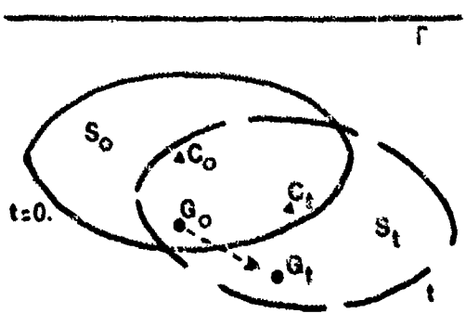

Fig. 4 : Body Geometry.

III-1 Forces acting on the body

Let us recall that all terms are non-dimensionalized with respect to the density of the fluid, the gravity constant and a diameter of the body.

The force resulting from the potential fluid flow is given by (60) and (62) or by the time derivative of $\vec{Q}(t) = \int_S \Phi . \vec{N}\, ds.$ (64)

If $\vec{y}$ is the unit vector upward vertical and y_M the vertical coordinate of a point M on the body, the total weight of the body is $-M\vec{y}$ and the Archimedian thrust is

$$-\int_S y_M . \vec{N}\, ds = V\vec{y} - \mathbb{C}\vec{X} \quad , \qquad (65)$$

where $\mathbb{C}$ is the generalized matrix of hydrostatic restoring coefficients ; note that $\mathbb{C}$ may differ according to a submerged or a floating body [19].

Let us denote

$$\vec{V} = \frac{d\vec{X}}{dt} \quad , \qquad (66)$$

the generalized velocities of the body ; the general equation for the dynamic of the body then takes the form

$$M\frac{d\vec{V}}{dt} + B\vec{V} + \mathbb{C}\vec{X} = -\frac{d}{dt}\vec{Q} + (V-M)\vec{y} + \vec{F}_0 , \qquad (67)$$

where the damping matrix B and the generalized force $\vec{F}_0$ are given data

Equations (66) and (67) form a set of differential equations of first order which describes, when $\vec{Q}$ is given, the motion of the body. In the case where $\vec{F}_0 = 0$, a static equilibrium position of the body is given by $\vec{X}_r$ such that

$$\mathbb{C}\vec{X}_r = (V - M)\vec{y} \qquad (68)$$

Finally, the total energy of the body reads

$$E_d(t) = \vec{V} M \vec{V} + (\vec{X}-\vec{X}_r)\,\mathbb{C}\,(\vec{X}-\vec{X}_r), \qquad (69)$$

which is conserved (i.e. $\frac{dEd}{dt} = 0$) when $\vec{Q}$, B and $\vec{F}_0$ vanish.

III.2 Time discretization of the dynamic equations.

Refering to the previous notations and according to the numerical scheme presented in § II.9, we are led to the system

$$\begin{cases} * \left(\frac{2}{\Delta t}M + B\right)\vec{V}^{n+1} + \mathbb{C}\vec{X}^{n+1} = \left(\frac{2}{\Delta t}M - B\right)\vec{V}^n - \mathbb{C}\vec{X}^n \\ \quad - \frac{2}{\Delta t}(\vec{Q}^{n+1} - \vec{Q}^n) + 2(V-M)\vec{y} + 2\vec{F}_0^{n+\frac{1}{2}} \qquad (70) \\ * \vec{V}^{n+1} + \frac{2}{\Delta t}\vec{X}^{n+1} = \vec{V}^n + \frac{2}{\Delta t}\vec{X}^n \qquad (71) \end{cases}$$

with initial conditions $\vec{X}^\circ = \vec{X}_o$ and $\vec{V}^\circ = 0$. It is easily shown that this numerical scheme is still conservative, the discretized dynamic total energy being defined by

$$E_d^n = \vec{V}^n M \vec{V}^n + (\vec{X}^n - \vec{X}_r)\,\mathbb{C}(\vec{X}^n - \vec{X}_r) \qquad (72)$$

IV - THE FLUID-BODY SYSTEM

Interactions between the fluid and the body act as follow : the motion of the fluid is induced by the velocities of the body in the Neumann boundary condition (5) and the motion of the body is influenced by the fluid motion by the unsteady pressure and resulting added mass $\vec{Q}$ in (67). A global formulation of the problem can thus be described.

A theoretical frame for this complete formulation is given in [5] and [7] in the case of a bottom at finite depth ; as for the fluid-system alone, the case of an infinite depth is very similar modifying some of the functional spaces. In the case where no sustained force $\vec{F}_0(t)$ is acting on the body a result of *local decay of energy* is given ; this will be observed in our numerical results where the fluid energy is only evaluated in the bounded domain Θ and results from the radiation of energy out of this domain.

Some of the possible complete discretization in time and space resulting from our study of § II and III are given in appendix. Let us recall that the matrix of the linear system is a constant and can still be factorized once, the numerical burden being only due to the *memory* effect of the free-surface flow.

V - NUMERICAL CONVERGENCE

Numerical tests have been performed to confirm the convergence of our algorithm with respect to the mesh-size h and the time-step Δt. Two cases have been considered for a sphere of unit radius totally immersed (a) with center one diameter below the free surface or half-immersed (b). The domain Θ is filled with isoparametric prismatic finite-elements of second order as shown of fig. 5. An analytic solution is chosen using a source of unit amplitude from t = 0 and located inside the body ; this solution is simply a time integral of the unsteady Green function which is performed by a Simpson rule

The ℓ^2 error norm ε is the relative mean quadratic error measured on all the nodes of the space discretization at each time. As results for the cases (a) and (b) are quite similar, only case (a) will be treated here.

On fig. 6, convergence with respect to the mesk-size of order h^3 is shown for fixed $\Delta t = .25$ and $t = \Delta t$. On fig. 7, convergence with respect to the time step of order Δt^2 is shown for fixed $h = .8$ and $t = \Delta t$; we notice that for $\Delta t = .5$ the error is mostly due to the space discretization. On fig. 8 the error is plotted versus time for fixed $h = 1.$ and $\Delta t = .25$; this error is maximum at the first time step and decrease asymptotically to the space discretization error limit. We then conclude that, for fixed h, the error at any time cannot be worse than that plotted on fig. 7.

For the fluid-body system several tests have been worked out ; as a matter of fact, Dirichlet and Fourier coupling formulations gave similar results. The first test performed was the vertical free motion of a spherical balloon without free-surface effect for which the complete problem can be solved analytically ; added-mass and acceleration were found in very good agreement with there respective theoretical values. Other tests are presented in the two next paragraphs.

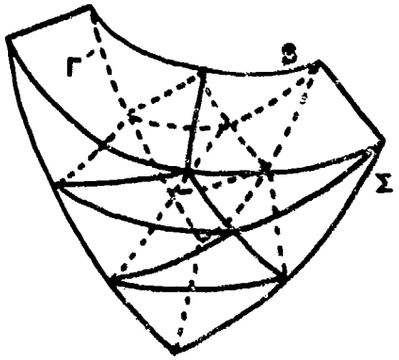

Fig. 5 : Discretization of an eight of a sphere of unit radius : h = 1.4, 7 prismatic elements, 66 nodal values in the domain (Φ) and 15 on the free surface (η).

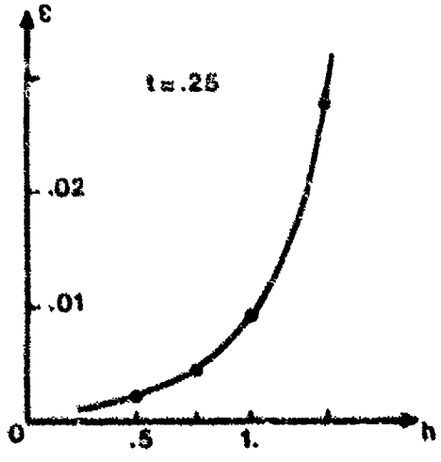

Fig. 6 : Convergence versus mesh-size.

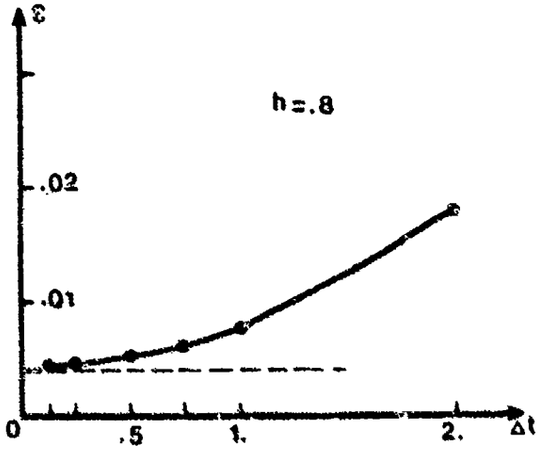

Fig. 7 : Convergence versus time step.

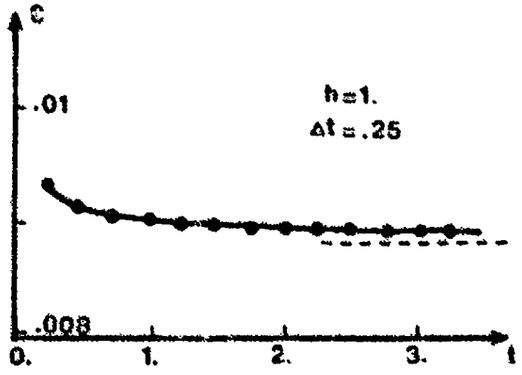

Fig. 8 : Convergence versus time.

VI - NUMERICAL RESULTS. THE SUBMERGED BODY

We study the pitch motion of a sphere of unit radius with an initial pitch angle of desequilibrium for various values of its mass M, vertical coordinate of its center of mass y_G and depth y_C of its center. On fig. 9 and 10, M = .25, y_G = -3., y_C = -2. ; position, velocity and angular acceleration are plotted versus time on fig. 9 while fig. 10 shows the kinetic, potential and total energies of the body. We notice that the period of the damped oscillations are greater than the period of the corresponding dynamic system without fluid interaction ("free oscillator") ; also the decay of total energy is roughly proportional to 1/t.

Some more results are given for various values of the parameter defined above ; the period during the transient towards a steady equilibrium position can then be measured and consequently a corresponding added-mass can be evaluated. On fig. 11 these periods are plotted together with those of the "free oscillator" versus the distance GC and for three values of the body mass. The evaluated actual periods are weakly related to the depth of immersion of the body considered (y_C = - 3. and -2.). On fig. 12 the added-mass is plotted versus GC ; its value, proportional to GC^3 depends neither of the depth of immersion nor of the mass of the body. These are the kind of practical results such a study can give to be used in modelisation procedures which only solve the dynamic equations.

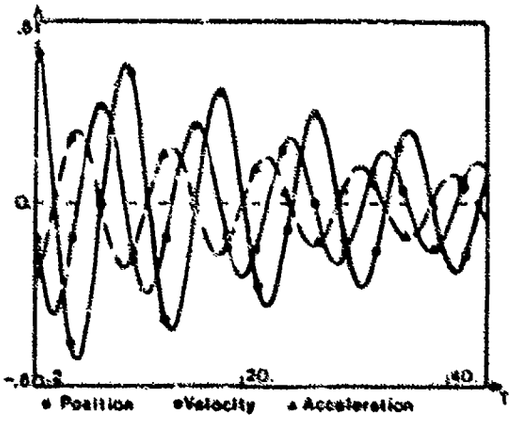

Fig. 9 : Sphere with initial pitch angle of desequilibrium ; displacements.

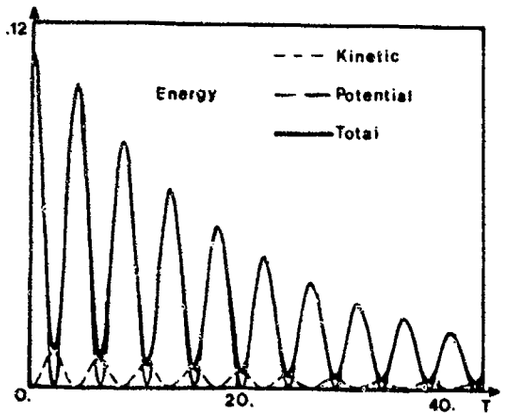

Fig. 10 : Sphere with initial pitch angle of desequilibrium ; energies of the body.

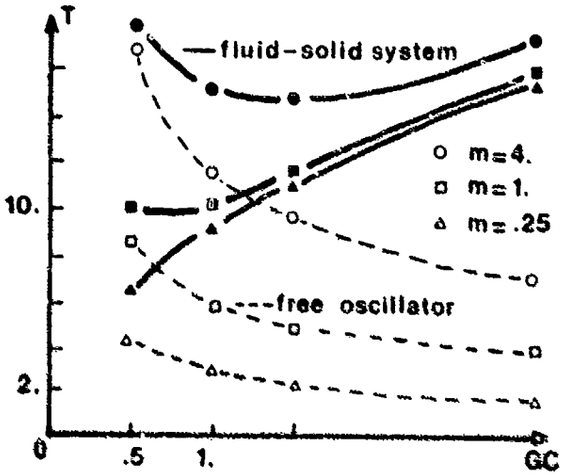

Fig. 11 : Differences between periods of free oscillator and fluid body system versus GC

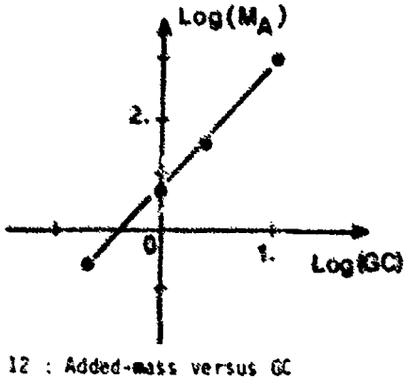

Fig. 12 : Added-mass versus GC

VII - NUMERICAL RESULTS - THE FLOATING BODY

A half-immersed sphere of unit radius of mass 1.5 is initially elevated ; a damped heave motion is then observed. Fig. 13 gives the position, velocity and acceleration, while fig. 14 gives the energies of the body and fig. 15 gives the various forces acting on the body versus time. The rapid decay of all these curves with respect to time compares with the corresponding results in the 2-D case (see [5] for example).

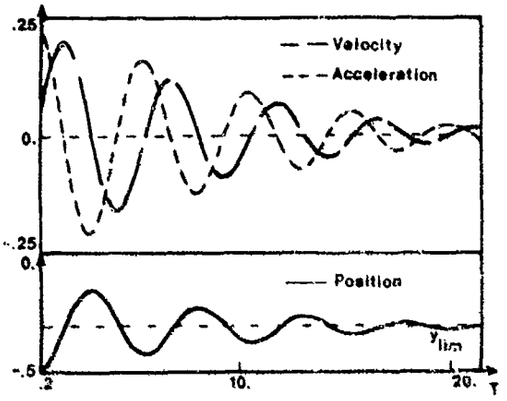

Fig. 13 : Half a sphere heave : motions.

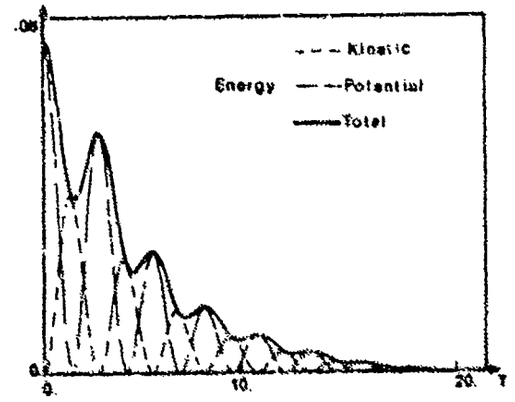

Fig. 14 : Half a sphere heave : energies.

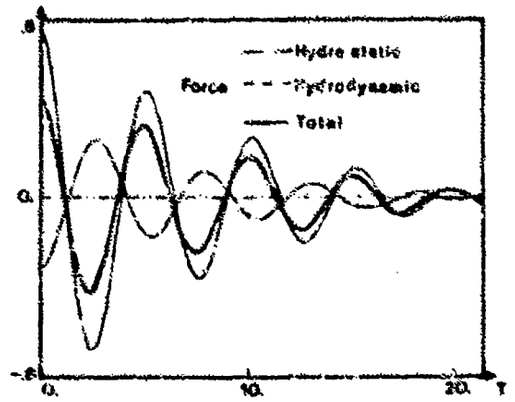

Fig. 15 : Half a sphere heave : forces.

VIII - CONCLUSION

An attempt to solve the complete linear problem for a floating body has been made. It is shown that the numerical algorithm is stable and gives accurate results ; applications for more general bodies can now be performed. We have shown that this type of approach can already give some information on the added - mass and damping coefficient related to the memory effect of the free-surface for any initial position of the body or any sustained external force applied on the body.

Further developments may concern the motions of large amplitude of the body including horizontal motions.

AKNOWLEDGMENTS

This work has been supported by the Direction des Recherches, Etudes et Techniques Ministère de la Défense, under contracts 82/1121 and 84/1061.

REFERENCES

[1] A. JAMI : *"Transient Flow around a Submerged body"*, Intal conf. on Transient and Coupled Problems, 1984, Venise, Italy.

[2] A. JAMI, M. POLYZAKIS : *"A finite element solution of diffraction problems in unbounded domains"*, Computer Methods in Applied Mechanics and Engineering, Vol. 29, p. 1-18 (1981).

[3] S. OHMATSU : *"On the irregular frequencies in the theory of oscillating bodies in a free surface"*, Papers of Ship Research Institute, Tokyo (1975).

[4] R.W. YEUNG : *"The transient heaving motion of floating cylinders"*, J. Engng. Math. (1981).

[5] C. LICHT : *"Evolution of a fluid-floating body system"*, Journal de Mecanique théorique et appliquée, Vol. 1, n° 2, p. 211-235 (1982).

[6] J.V. WEHAUSEN, E.V. LAITONE : *"Surface waves"*, Handbuch der Physik, Vol. IX, Springer Verlag (1960).

[7] J.T. BEALE : *"Eigenfunction Expansion for Objects Floating in an Open Sea"*, Comm. Pure. Appl. Math. Vol. 30, p. 283-313 (1977).

[8] A. JAMI : *"Etude théorique et numérique de phénomènes transitoires en hydrodynamique navale"*, ENSTA-Report 154 (1982).

[9] B. HANOUZET : *"Espaces de Sobolev avec poids ; application au problème de Dirichlet dans un demi espace"*, Rend. della Sem. Math. della Universita di Padova, Vol. 46, p. 227-272, (1971).

[10] J. BARROS NETO : *"In homogeneous boundary value problems in a half space"*, Annali della Sevola Normale Superiore di Pisa, Science Fisiche e Matematiche, p. 331-365 (1965).

[11] N. DUNFORD, J. SCHWARTZ : *"Linear Operators"*, New-York, Interscience Publishers Inc. (1957).

[12] A. FRIEDMAN, M. SHINBROT. *"The initial value problem for the linearized equations of water waves"*, Journal of Math. and Mech., Vol. 17, n° 2, (1967) and Vol. 18, n° 12, (1969).

[13] F. RIESZ, B . NAGY : *"Functional Analysis"*, New-York, Interscience Publishers, Inc. (1955).

[14] A. FINKELSTEIN : *"The initial value problem for transient water waves"*, Comm. on Pure and Appl. Math. Vol. 10, p. 511-522, (1957).

[15] J.P. AUBIN : *"Approximation of elliptic boundary-value problems"*, Pure and Applied Mathematics, Vol. 26, Wiley Interscience pub. (1972).

[16] M. LENOIR : *"Error estimates for the coupling of finite elements and an integral representation, application to the linear sea-keeping problem"*, ENSTA Report 164, (1982).

[17] P. CIARLET : *"The finite element method for elliptic problems"*, Studies in Mathematics and its Applications, Vol. 4, North Holland publishing compagny (1978).

[18] J. BOUJOT : *"Sur l'analyse des caractéristiques vibratoire d'un liquide contenu dans un réservoir"*, Journal de Mécanique, Vol. 11, n° 4, p. 649-671, Paris (1972).

[19] F. JOHN : *"On the motions of floating bodies, I and II"*, Comm. on Pure and Appl. Math., Vol. 2, p. 13-57, (1949), Vol. 3, p. 45-101, (1950).

APPENDIX

Let V_k, X_k and N^k, k=1,6 be the 6 componants of $\vec{V}$, $\vec{X}$ and $\vec{N}$ respectively. According to the time and space discretization described in § II and III we have :

(a) General formulation in the case of a submerged body with a Dirichlet-type of coupling.

"For n>1, find the nodal values $(\tilde{\Phi}_j^n)_{j=1,N'_\Theta}$ and the vectors (V_k^n, X_k^n) k = 1,6 such that" :

$$\begin{cases} * \sum_{j=1}^{N'_\Theta} \tilde{\Phi}_j^n \{a_{ij} + \Delta^D_{ik} D\tilde{\Gamma}_{k\ell}\, \delta^s_{\ell j}\} - \sum_{j\in I_s} V_k^n \{\delta_{ij} + \Delta^D_{ik} \tilde{\Gamma}_{k\ell}\, \delta^s_{\ell j}\} N_j^k = - \sum_{m=1}^{n} \sum_{j=1}^{N'_\Theta} \Delta^D_{ip}\, \tilde{R}_p^{m,n} \\ * \sum_{j\in I_s} \left(\frac{2}{\Delta t}\delta^s_{ij} N_i^k\right) \tilde{\Phi}_j^n + \left(\frac{2}{\Delta t}\mathbb{M}+\mathbb{B}\right)_{k\ell} V_\ell^n + \mathbb{C}_{k\ell} X_\ell^n = \left(\frac{2}{\Delta t}\mathbb{M}-\mathbb{B}\right)_{k\ell} V_\ell^{n-1} - \mathbb{C}_{k\ell} X_\ell^{n-1} \\ \qquad + \sum_{j\in I_s} \left(\frac{2}{\Delta t}\delta^s_{ij} N_i^k\right) \tilde{\Phi}_j^{n-1} + 2(\mathbb{V}-\mathbb{M})\, D_{2k} + 2F_{0_k}^{n-\frac{1}{2}} \\ * - V_k^n + \frac{2}{\Delta t} X_k^n = V_k^{n-1} + \frac{2}{\Delta t} X_k^{n-1} \end{cases} \tag{73}$$

where all the terms are defined as in § II and § III, and :

$$\tilde{R}_p^{m,n} = D\Lambda^m_{p\ell}\delta^s_{\ell j} \left(\varepsilon_m \tilde{\Phi}_j^{n-m+1} + \varepsilon'_m \tilde{\Phi}_j^{n-m}\right) - \Lambda^m_{p\ell}\delta^s_{\ell j} N_j^k \left(\varepsilon_m V_k^{n-m+1} + \varepsilon'_m V_k^{n-m}\right)$$

D_{ij} : Kronecker symbol

Φ_i^n on Σ is then obtained by :

$$* \Phi_i^n = \sum_{j\in I_\Sigma} \left(D\tilde{\Gamma}_{i\ell} \tilde{\Phi}_j^n - \tilde{\Gamma}_{i\ell} N_j^k V_k^n\right) \delta^s_{\ell_j} + \sum_{n=1}^{n} \tilde{R}_i^{m,n} \tag{74}$$

(b) General Formulation in the case of a Floating body with a Fourier type of coupling

"For $n > 1$, Find the nodals values $(\Phi_j^n)_{j=1,N_\Theta}$, $(\eta_j^n)_{j=1,N_{\Gamma'}}$ and the vectors (V_k^n, X_k^n) such that" :

$$
\left\{
\begin{aligned}
&\star \sum_{j=1}^{N_\Theta} \Phi_j^n \Big(a_{ij} + \lambda\,\delta_{ij}^{\Sigma} - \delta_{ik}^{\Sigma}\, D\tilde{\Gamma}_{k\ell}^{\lambda}\,\delta_{\ell j}^{S}\Big) - \sum_{j\in I_{\Gamma'}} \frac{2}{\Delta t}\,\delta_{ij}^{\Gamma'}\,\eta_j^n - \sum_{j\in I_S} V_k^n \{\delta_{ij}^S - \delta_{ik}^{\Sigma}\,\tilde{\Gamma}_{k\ell}^{\lambda}\,\delta_{\ell j}^{S}\} N_j^k = \\
&\quad - \sum_{j=1}^{N_\Theta} \Phi_j^{n-1}\{a_{ij} + \lambda\delta_{ij}^{\Sigma} - \delta_{ik}^{\Sigma}\, D\tilde{\Gamma}_{k\ell}^{\lambda}\delta_{\ell j}^{S}\} - \sum_{j\in I_{\Gamma'}} \frac{2}{\Delta t}\,\delta_{ij}^{\Gamma'}\,\eta_j^{n-1} + \sum_{j\in I_S} V_k^{n-1}\{\delta_{ij}^S - \delta_{ik}^{\Sigma}\,\tilde{\Gamma}_{k\ell}^{\lambda}\,\delta_{\ell j}^{S}\} N_j^k \\
&\quad + \sum_{j=1}^{N_\Theta} \Big\{ \sum_{m=1}^{n} \delta_{ij}^{\Sigma}\, R_j^{m,n\lambda} + \sum_{m=1}^{n-1} \delta_{ij}^{\Sigma}\, R_j^{m,n-1,\lambda} \Big\} \\
&\star \sum_{j\in I_\Gamma'} \Big\{\frac{2}{\Delta t}\,\delta_{ij}^{\Gamma'}\,\Phi_j^n + \delta_{ij}^{\Gamma'}\eta_j^n\Big\} = \sum_{j\in I_\Gamma'} \Big\{\frac{2}{\Delta t}\,\delta_{ij}^{\Gamma'}\Phi_j^{n-1} - \delta_{ij}^{\Gamma'}\eta_j^{n-1}\Big\} \\
&\star \sum_{j\in I_S} \Big(\frac{2}{\Delta t}\,\delta_{ij}^{S} N_i^k\Big)\Phi_j^n + \Big(\frac{2}{\Delta t}\,\mathbb{M} + \mathbb{B}\Big)_{k\ell} V_\ell^n + \mathbb{C}_{k\ell}\, X_\ell^n = \Big(\frac{2}{\Delta t}\,\mathbb{M} - \mathbb{B}\Big)_{k\ell} V_\ell^{n-1} - \mathbb{C}_{k\ell}\, X_\ell^{n-1} \\
&\qquad\qquad + \sum_{j\in I_S} \Big(\frac{2}{\Delta t}\,\delta_{ij}^{S} N_i^k\Big)\Phi_j^{n-1} + 2(V - M)D_{2k} + 2\,F_{o_k}^{n-\frac{1}{2}} \\
&\star - V_k^n + \frac{2}{\Delta t}\,X_k^n = V_k^{n-1} + \frac{2}{\Delta t}\,X_k^{n-1}
\end{aligned}
\right. \qquad (75)
$$

where $\tilde{G}_M$, F_M^n are replaced by $\partial_\lambda \tilde{G}_M$, $\partial_\lambda F_M^n$.

A HIGHER-ORDER PANEL METHOD FOR SURFACE WAVE RADIATION AND DIFFRACTION BY A SPHEROID

By Stephen R. Breit
Department of Ocean Engineering
Massachusetts Institute of Technology
Cambridge, MA 02139
U.S.A.

Abstract

Higher-order panels and a very efficient scheme for evaluating the free-surface source potential are employed in a panel-method computation of linear radiation and diffraction by a floating spheroid. The method is based on a direct application of Green's theorem. Panels which conform exactly to the spheroid's surface are defined in terms of orthogonal curvilinear coordinates. The velocity potential is approximated on each panel by a bidimensional series of Chebyshev polynomials and the unknown coefficients are determined by collocating at a sufficient number of points on the panel. Benchmark values of the hydrodynamic coefficients are established and serve as a basis for comparing the performance of various higher-order panels. For comparable computing time, piecewise-quadratic panels yield a significant improvement in accuracy over piecewise-constant panels. The behavior of the numerical scheme in the vicinity of irregular frequencies is also investigated.

1. Introduction

The panel method was pioneered by Hess and Smith (1964) in the context of infinite-fluid flow. Basing their work on a source-distribution formulation, they used plane quadrilateral panels and determined a constant source density on each panel by collocating at the panel centroid. Numerous others, among them Garrison (1977), the Netherlands Ship Model Basin and Det Norske Veritas of Norway, have since followed the same approach in computing the radiation and diffraction of linear surface waves by stationary floating bodies.

The main difficulty in extending the Hess and Smith approach to free-surface problems is in evaluating the free-surface source potential or "Green function". Recent work by Newman (1985) has lead to the development of a very efficient subroutine for evaluating the Green function in infinite or finite depth. Known as FINGREEN, it evaluates the infinite-depth Green function and its derivatives to six decimal places in about the same time as four calls to a Bessel function routine in the IMSL subroutine library. Roughly four times as much effort is required for the finite-depth Green function.

The objectives of the present investigation are: 1) exploiting the FINGREEN subroutine to provide benchmark hydrodynamic coefficients and exciting forces for a floating body, and 2) determining the possible benefits of using curvilinear panels with higher-order descriptions of the velocity potential on each panel.

The spheroid has been chosen for this study because its surface can be mathematically defined in terms of orthogonal curvilinear or "spheroidal" coordinates. Spheroidal coordinates have been previously employed by Kim (1965) who computed the hydrodynamic coefficients of a family of spheroids using the Hess and Smith approach. Kim presents low-frequency results for a model with 36 panels on one quarter of the submerged surface. Yeung (1973) and Shin (1979) also modeled spheroids, but with plane panels.

Green's theorem is solved directly for the velocity potential in the present work. Within each panel the velocity potential is approximated by a bidimensional series of Chebyshev polynomials. Keeping just the lowest-order term in the series is equivalent to assuming the potential is constant on each panel or "piecewise constant". Higher-order variations are referred to as piecewise linear, quadratic and so on. The unknown coefficients multiplying the terms in the polynomial expansion are determined by collocating at M^2 points on each panel, M^2 being the number of terms in the polynomial representation.

Higher-order panels have been previously analyzed by Hess (1979) for lifting or non-lifting potential flow without a free surface. He shows, for a source-distribution formulation, that a consistent higher-order panel has a polynomial expansion of the source distribution which is one order less than the polynomial representation of the panel geometry. Accordingly, he implements a quadrilateral panel with quadratic shape and a piecewise

linear source distribution. Unfortunately, this scheme is not easily extended to a panel with cubic shape and a piecewise-quadratic source distribution.

The panel geometry is exact in the present work, so the algorithm is simpler than for Hess' higher-order panels. Due to expanding the velocity potential in a series of orthogonal polynomials and locating the collocation points on the interiors of the panels, the algorithm is the same for tenth-order as it is for second-order panels. This has permitted a systematic investigation of the scheme's convergence with respect to the number of panels and the order of the polynomial representation on each panel.

Throughout this work, special care has been taken to accurately evaluate the integrals over the panels. Singular terms are subtracted from the integrands under circumstances to be discussed in Section 3. The regular and singular terms are then integrated by different numerical quadrature schemes, both of which provide results to a prescribed accuracy. This approach is computationally inefficient, but it virtually eliminates the quadrature schemes from consideration as a possible source of error.

2. Boundary Value Problem

We consider a floating body oscillating about its static equilibrium position. The body's motions are defined with respect to a Cartesian coordinate system oriented such that z=0 coincides with the free surface and z is positive upwards. Following the usual approach to linear seakeeping, the fluid is assumed to be inviscid and incompressible, and the fluid motion irrotational. After further assuming small amplitude waves and body motions relative to the wavelength and a characteristic body dimension, the problem is reduced to a linear boundary-value problem for the complex velocity potential $\phi(x,y,z)$. The complex time dependance $e^{i\omega t}$, where ω is the circular frequency and t is time, has already been factored out and will henceforth be understood. The boundary conditions are satisfied at the mean positions of the free surface and body boundary.

The complex potential satisfies

$$\nabla^2\phi = \left(\frac{\partial^2}{\partial x^2} + \frac{\partial^2}{\partial y^2} + \frac{\partial^2}{\partial z^2}\right)\phi = 0 \quad \text{in } V \tag{1}$$

$$\phi_z - K\phi = 0 \quad \text{on } z = 0 \tag{2}$$

$$\nabla\phi \to 0 \quad \text{as } z \to -\infty \tag{3}$$

where V denotes the fluid domain, K is the wavenumber, and g is the gravitational constant. The wavenumber satisfies the dispersion relation $\omega^2 = gK$ for water of infinite depth.

The body boundary condition is more easily stated after making the linear decomposition

$$\phi = A(\phi_0 + \phi_7) + \sum_{j=1}^{6} \phi_j \xi_j \tag{4}$$

where, A is the amplitude of the free-surface elevation due to the incident wave and ξ_j, j=1,..,6 are the complex amplitudes of the rigid-body motions. The modes j=1,2,3 correspond to translation in the x,y,z directions and modes j=4,5,6 to rotation about the same axes respectively. The normalized velocity potentials ϕ_0, ϕ_j; j=1,6 and ϕ_7 govern the incident, radiated and diffracted wave flows respectively.

The incident waves are regular plane-progressive waves and are described by the velocity potential

$$\phi_0 = i\frac{g}{\omega} e^{K(z - ix\cos\beta - iy\sin\beta)} \tag{5}$$

where β is the angle between their direction of propagation and the positive x-axis. The diffraction velocity potential accounts for interaction between the body, fixed at its mean position, and the incident waves. Thus on the body's wetted surface S_B it offsets the incident-wave normal velocity

$$\vec{n}\cdot\nabla\phi_7 = -\vec{n}\cdot\nabla\phi_0 \quad \text{on } S_B \tag{6}$$

where the unit normal vector $\vec{n}$ is taken to point out of the fluid domain. The radiated waves are generated by the forced oscillation of the body in otherwise calm water. The radiation velocity potentials satisfy the inhomogeneous conditions

$$\vec{n}\cdot\nabla\phi_j = i\omega n_j \quad \text{on } S_B; \quad j = 1,2,\ldots 6 \tag{7}$$

where the normal components n_j are defined by

$$\vec{n} = (n_1, n_2, n_3)$$
$$\vec{x}\times\vec{n} = (n_4, n_5, n_6) \tag{8}$$

Finally, to ensure well-posedness the radiation and diffraction potentials must satisfy a radiation condition of outgoing waves at large distances from the body.

3. Free-surface Green Function

The Green function is an elementary solution of the linear boundary-value problem, consisting of a Rankine source and a regular part which satisfies the free-surface boundary condition. Explicit expressions of the Green

function for finite or infinite depth are given by Wehausen and Laitone (1960). For the present purposes it is only necessary to distinguish between the singular and regular components.

We introduce the vector notation $\vec{x}$ for the (x,y,z) coordinates of a field point. The locations of the source point and its image above the free surface are denoted by $\vec{x}' = (x',y',z')$ and $\vec{x}'_I = (x',y',-z')$ respectively. Then the distances between these points and a field point $\vec{x}$ are given by

$$r = |\vec{x} - \vec{x}'|$$

$$r' = |\vec{x} - \vec{x}'_I|$$

With these definitions, the Green function can be written in the form

$$G(\vec{x},\vec{x}';K) = \frac{1}{r} + \frac{1}{r'} + 2K[\log Kr' + \log(1+\cos\theta)] + H(\vec{x},\vec{x}';K) \qquad (9)$$

where H is a wavelike term which is regular everywhere and the angle θ is defined in Figure 1. The Rankine source 1/r is singular whenever the field and source points are close together, but the image source 1/r' and the first logarithmic term log Kr' are also singular when the field and source points are close to each other and to the free surface.

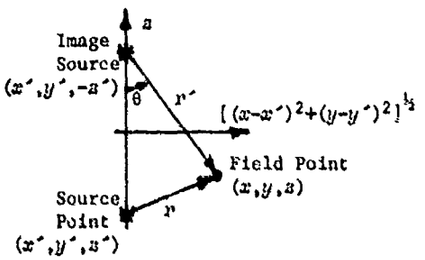

Figure 1: Definitions of r,r' and θ

Since the numerical scheme requires integrating the Green function and its normal derivative over the body surface, it is essential to integrate the singular terms separately in the vicinity of the source point. The FINGREEN subroutine facilitates this by optionally subtracting off some or all of the singular terms. In general, the logarithmic terms should be subtracted whenever the image source is subtracted. The second logarithmic term is not actually singular, but numerical experience has shown that it should be lumped with the 1/r' and log Kr' terms.

4. Boundary-Integral Formulation

Substituting the Green function and one of the canonical potentials ϕ_j, j = 1,2,...,7 into Green's theorem leads to the boundary-integral equation

$$2\pi\phi_j(\vec{x}') + \int_{S_B} d\vec{x}\,\phi_j(\vec{x})\,\frac{\partial}{\partial n_x}\,G(\vec{x},\vec{x}') = \int_{S_B} d\vec{x}\,\frac{\partial}{\partial n}\,\phi_j(\vec{x})G(\vec{x},\vec{x}') \qquad (10)$$

where $\vec{x}'$ coincides with the body surface. Since the normal derivative of ϕ_j is known from the boundary condition (7) or (8), equation (10) is a Fredholm integral equation of the second kind for which a unique solution always exists except at a set of discrete frequencies known as "irregular frequencies". Henceforth, the j subscript shall be omitted and the prescribed normal velocity $\partial\phi_j/\partial n$ denoted by V.

Sloan (1980) summarizes the various numerical methods for solving Fredholm equations of the second kind. The simplest approach for arbitrary geometries and the most widely used in free-surface problems is the collocation method. The velocity potential is approximated in the form

$$\phi(\vec{x}) = \sum_{n=1}^{N} a_n\psi_n(\vec{x}) \qquad (11)$$

where ψ_n are a set of basis functions and a_n are unknown coefficients which are determined by satisfying (10) at N discrete locations or "collocation points". Each basis function is defined on the domain S_n and vanishes elsewhere; S_n may be either identical to S_B or a subdomain of it. The S_n associated with each basis function can be unique, shared by other basis functions, or overlapping the domains of other basis functions. Based on these definitions, (10) can be rewritten in the discrete form

$$\sum_{n=1}^{N}\left[2\pi\psi_n(\vec{x}_m) + \iint_{S_n} d\vec{x}\,\psi_n(\vec{x})\,\frac{\partial}{\partial n_x}\,G(\vec{x},\vec{x}_m)\right]a_n = \iint_{S_B} d\vec{x}\,V(\vec{x})G(\vec{x},\vec{x}_m) \quad ; \quad m=1,2,\ldots,N \qquad (12)$$

where $\vec{x}_m$ are the N collocation points. The only restriction on the location of the collocation points is that there must be one point for each basis function defined within a particular subdomain.

5. Spheroidal Coordinates

We now transform the integrals in (10) to spheroidal coordinates. The transformation between the spheroidal (α,β,γ) and Cartesian (x,y,z) coordinates is given by

$$x = \frac{\cosh\gamma}{\cosh\gamma_o}\cos\alpha$$

$$y = \varepsilon\frac{\sinh\gamma}{\sinh\gamma_o}\sin\alpha\cos\beta$$

$$z = -\varepsilon\frac{\sinh\gamma}{\sinh\gamma_o}\sin\alpha\sin\beta \qquad (13)$$

where γ_o is an arbitrary constant and ε is determined from the relation $\varepsilon = \tanh\gamma_o$. Setting $\gamma = \gamma_o$ defines a spheroidal surface with halflength unity and diameter-to-length ratio ε. Of course other constant γ surfaces may be chosen, but ε will lose its physical significance.

It is convenient to define the scale factors

$$h_\alpha = \left|\frac{\partial\vec{x}}{\partial\alpha}\right|_{\gamma=\gamma_o} = [\sin^2\alpha + \varepsilon^2\cos^2\alpha]^{\frac{1}{2}}$$

$$h_\beta = \left|\frac{\partial\vec{x}}{\partial\beta}\right|_{\gamma=\gamma_o} = \varepsilon|\sin\alpha|$$

$$h_\gamma = \left|\frac{\partial\vec{x}}{\partial\gamma}\right|_{\gamma=\gamma_o} = h_\alpha \qquad (14)$$

Then an incremental element of area on the surface of the $\gamma = \gamma_o$ spheroid is simply $dS = h_\alpha h_\beta d\alpha d\beta$ and the unit normal vector is given by

$$\vec{n} = -\frac{1}{h_\gamma}\left(\frac{\partial\vec{x}}{\partial\gamma}\right)_{\gamma=\gamma_o} \qquad (15)$$

Substituting these definitions in (10), we have

$$2\pi\phi(\alpha',\beta') = -\int_0^{\pi/2}\int_0^{\pi/2} d\alpha d\beta h_\alpha h_\beta \phi(\alpha,\beta)\left\{\frac{1}{h_\gamma}\left(\frac{\partial\vec{x}}{\partial\gamma}\right)_{\gamma=\gamma_o} \cdot \nabla_{\vec{x}} G(\vec{x},\vec{x}')\right\}$$
$$= \int_0^{\pi/2}\int_0^{\pi/2} d\alpha d\beta h_\alpha h_\beta V(\alpha,\beta) G(\vec{x},\vec{x}') \qquad (16)$$

where $\vec{x}$ and $\vec{x}'$ are obtained by the explicit transformations

$$\vec{x} = \vec{x}(\alpha,\beta,\gamma_o)$$

$$\vec{x}' = \vec{x}(\alpha',\beta',\gamma_o)$$

Here it should be recognized that the domain has been reduced to one-quarter of the submerged surface by exploiting the spheroid's symmetry. Thus the function denoted by G is not identically the wave source defined in Section 3, but is constructed from such wave sources by the method of images to satisfy appropriate boundary conditions on the planes of symmetry.

6. Numerical Scheme

To facilitate a numerical solution of (16), the rectangular domain of integration in the $\gamma = \gamma_o$ plane is subdivided into a grid of rectangular panels. The grid is characterized by the numbers N_α, N_β corresponding to the number of equal divisions of the α, β axes respectively. The dimensions of each panel are therefore

$$\Delta\alpha = \pi/(2N_\alpha)$$

$$\Delta\beta = \pi/(2N_\beta)$$

In order to define a basis-function representation of the velocity potential within a panel, it is convenient to map the panel to a square in the (r,s) plane with its centroid at the origin and sides of half-length unity. The coordinate transformation for a panel with indices i,j is given by

$$\alpha = (r + 2i - 1)\frac{\Delta\alpha}{2} \quad ; \quad i=1,2,\ldots,N_\alpha$$
$$\beta = (s + 2j - 1)\frac{\Delta\beta}{2} \quad ; \quad j=1,2,\ldots,N_\beta$$

The potential is approximated within each panel by a truncated bidimensional series of Chebyshev polynomials of the form

$$\phi(r,s) = \sum_{k=1}^{M_\alpha}\sum_{\ell=1}^{M_\beta} a_{ijk\ell}\, T_{k-1}(r)T_{\ell-1}(s) \qquad (17)$$

where $a_{ijk\ell}$ are unknown coefficients, T_k is the Chebyshev polynomial of order k and M_α-1, M_β-1 are the orders of the highest-degree polynomials in the α, β directions respectively.

Since there are $M_\alpha M_\beta$ terms in the series expansion, $M_\alpha M_\beta$ collocation points must be chosen on each panel. The error in approximating an arbitrary function by a series of Chebyshev polynomials up to order M-1 is minimized by locating the collocation points at the zeros of the order M Chebyshev polynomial. We therefore locate the collocation points at the zeros of the order M_α and M_β Chebyshev polynomials. The Cartesian coordinates of a collocation point are denoted by $\vec{x}_{ijk\ell}$, where the i,j subscripts indicate the panel where the point is located and the k,l subscripts indicate its position on that panel.

Using the above definitions, (16) may be rewritten in the discretized form

$$2\pi \sum_{k=1}^{M_\alpha} \sum_{\ell=1}^{M_\beta} a_{i'j'k\ell}\, T_{k-1}(r_{k'}) T_{\ell-1}(s_{\ell'})$$

$$+ \frac{1}{4} \Delta\alpha\Delta\beta \sum_{i=1}^{N_\alpha} \sum_{j=1}^{N_\beta} \sum_{k=1}^{M_\alpha} \sum_{\ell=1}^{M_\beta} a_{ijk\ell} \int\int_{-1}^{1} dr\,ds$$

$$\times \{h_\beta T_{k-1}(r) T_{\ell-1}(s) [\frac{\partial \vec{x}}{\partial \gamma} \cdot \nabla_x G(\vec{x}, \vec{x}_{i'j'k'\ell'})]\}$$

$$= \frac{1}{4} \Delta\alpha\Delta\beta \sum_{i=1}^{N_\alpha} \sum_{j=1}^{N_\beta} \int\int_{-1}^{1} dr\,ds\, h_\beta (h_\alpha V) G(x, x_{i'j'k'\ell'})$$

$$; \quad i'=1,2,\ldots,N_\alpha$$
$$j'=1,2,\ldots,N_\beta$$
$$k'=1,2,\ldots,M_\alpha$$
$$\ell'=1,2,\ldots,M_\beta \qquad (18)$$

Many combinations of N_α, N_β, M_α and M_β are possible with this approach. If $N_\alpha = N_\beta = 1$ then (17) is a global representation and M_α, M_β must be fairly large to obtain an accurate solution. If on the other hand $M_\alpha = M_\beta = 1$, the potential is piecewise-constant on each panel and N_α, N_β must be large. Any choice with M_α or M_β greater than unity will be referred to as a "higher-order" representation.

Equation (18) must be put in the canonical form (12) to facilitate assembling and solving the system by standard matrix methods. This is achieved by mapping the indices i,j, k,l and i',j',k',l' to the single indices n and m respectively. The best mapping from the standpoint of placing the largest coefficients close to the main diagonal has been found to be

$$n = (i-1)N_\beta M_\alpha M_\beta + (j-1)M_\alpha M_\beta + (k-1)M_\beta + \ell$$

An analogous mapping is used between the primed indices and m.

We now turn our attention to evaluating the integrals or "influence coefficients" in the discrete equations (18). As discussed in Section 3, singular terms are subtracted from the integrands and treated separately. All remaining terms are regular and are integrated by an iterative procedure based on bidimensional Gauss quadrature in order to control the error in the influence coefficients. Starting with second-order Gauss quadrature, the order is increased until the absolute difference between successive values is less than a specified tolerance.

The integrals of the singular terms have the forms

$$I_1 = \int_{\alpha_1}^{\alpha_2} \int_{\beta_1}^{\beta_2} d\alpha d\beta h_\beta [h_\gamma V(\alpha,\beta)] (\frac{1}{|\vec{x}-\vec{x}'|}) \qquad (19)$$

$$I_2 = \int_{\alpha_1}^{\alpha_2} \int_{\beta_1}^{\beta_2} d\alpha d\beta h_\beta \psi(\alpha,\beta) [\frac{\partial \vec{x}}{\partial \gamma} \cdot \nabla_x (\frac{1}{|\vec{x}-\vec{x}'|})] \qquad (20)$$

where $\vec{x}'$ is the singular point and (α_1, α_2) and (β_1, β_2) are the ranges of integration in the α and β directions respectively. These integrals are evaluated numerically after making a coordinate transformation. We denote by h'_α, h'_β the values of the scale factors h_α, h_β at (α', β'), and make the transformation

$$h'_\alpha (\alpha - \alpha') = \rho \cos\sigma$$

$$h'_\beta (\beta - \beta') = \rho \sin\sigma$$

where ρ, σ are elliptical coordinates centered on the source point in the (α, β) plane. Substituting into (19) and (20) gives

$$I_1 = \frac{1}{h'_\alpha h'_\beta} \int_0^{2\pi} d\sigma \int_{\rho_1(\sigma)}^{\rho_2(\sigma)} \rho d\rho h_\beta [h_\gamma V(\alpha,\beta)] (\frac{1}{|\vec{x}-\vec{x}'|}) \qquad (21)$$

$$I_2 = \frac{1}{h'_\alpha h'_\beta} \int_0^{2\pi} d\sigma \int_{\rho_1(\sigma)}^{\rho_2(\sigma)} \rho d\rho h_\beta \psi(\alpha,\beta) [\frac{\partial \vec{x}}{\partial \gamma} \cdot \nabla_x (\frac{1}{|\vec{x}-\vec{x}'|})] \qquad (22)$$

where ρ_1, ρ_2 are the lower and upper limits of integration with respect to ρ and are computed for each angle σ. The lower limit is of course zero when the singular point lies within the domain of integration. The integrals (21) and (22) can be evaluated numerically because their integrands have a finite limit as ρ vanishes. The logarithmic terms in (9) are more weakly singular, so the same coordinate transformation is applicable. The contributions of all singular terms are computed to arbitrary accuracy by means of nested Romberg integration algorithms.

7. Numerical Results

The numerical scheme has been tested extensively for the case of a spheroid with diameter-to-length ratio $\varepsilon = 1/8$ in water of infinite depth. The spheroid is floating such that its major axis coincides with the free surface. The primary output quantities are the added mass/moment and damping coefficients in the five nontrivial modes of motion and the corresponding exciting forces/moments (hereafter moments shall be understood) for three wave headings. These quantities are defined in the Appendix.

Parameters such as the quadrature tolerances and the ratio N_α/N_β have been investigated to find their optimum values. Absolute tolerances of 5×10^{-3} and 5×10^{-4} have been used for the Gauss and Romberg schemes respectively because the hydrodynamic coefficients are unchanged to four decimal places when more stringent tolerances are imposed. (Different tolerances are required for the Gauss and Romberg schemes because the convergence tests are applied to different quantities. In the iterative Gauss procedure, the integral over an entire panel must converge, whereas the nested Romberg procedures first check for convergence in the ρ direction and then in the σ direction.) The ratio N_α/N_β has only a slight effect on the results, so all results presented here are for $N_\alpha = N_\beta$ and $M_\alpha = M_\beta$. The subscripts will henceforth be omitted from these parameters.

Results have been obtained for the cases N=1,2,...,9 and M=1 (piecewise-constant panels) over an extended frequency range. As expected, the hydrodynamic coefficients appear to converge to their exact values as N^2 increases with an error which behaves roughly like $1/N^2$, where N^2 is the total number of panels. Richardson extrapolation has been employed to improve the accuracy of the results. For example, if $P(N^2)$ and $P(N^2/4)$ are predictions obtained with the body geometry discretized by N^2 and $N^2/4$ panels respectively, the error in the extrapolated prediction $(4/3)P(N^2) - (1/3)P(N^2/4)$ is expected to be of order $1/N^4$. Further reduction of the error is possible if the estimate $P(N^2/16)$ is available. A more detailed explanation of Richardson extrapolation is given in, for example, Dahlquist and Bjork (1974).

The hydrodynamic coefficients computed by the present scheme have been compared with values given by Kim (1966) and Yeung (1973). The present results generally agree with Kim to two significant digits and with Yeung to within one unit in the second significant digit.

Table 1 lists the hydrodynamic coefficients and exciting forces at six dimensionless wavenumbers; the dimensionless wavenumber KL/2 is based on the length L of the spheroid. The exciting forces have been obtained by solving the integral equation directly as opposed to using the Haskind relation. All values except the exciting-force phases have been extrapolated from the sequence 16,36,81 panels on one quarter of the submerged surface; the phase angles are based on the 81-panel results alone. With the exception of the surge coefficients and the phases, all values are believed to be accurate to within one unit in the third decimal place. The surge coefficients are believed to be accurate to within one unit in the fourth decimal place. These results are regarded as benchmarks for subsequent comparisons.

The same results are also plotted in Figures 3 through 7. In addition to the wavenumbers listed in Table 1, the following values were used to make the plots: 0.16, 0.32, 2.4, 4.0, 4.8, 5.6, 7.2, 8.0, 8.8, 9.6, 10.4. The triangular tick marks in the plot of head-seas heave exciting force and phase have been read from plots in Shin (1979) and provide further confirmation of the present results.

We next investigate the accuracy of the numerical scheme for the various combinations of the parameters N and M listed in Table 2. In all cases the total number of collocation points is no greater than 100. The heave and pitch hydrodynamic coefficients computed with each of these combinations are plotted against the reciprocal of the number of collocation points in Figures 8 and 9. Also shown in Figure 8 are values from the plane-panel program described in Breit, Newman and Sclavounos (1985). Other than their common use of FINGREEN, the plane-panel and spheroidal-panel programs are completely independent. A number of interesting observations can be made about these plots:

1) In most cases the values from related models fall nearly on a straight line. This applies especially to the piecewise-constant plane- and spheroidal-panel results and justifies the assumption made when applying Richardson extrapolation that the error is linearly proportional to $1/(N^2M^2)$.

2) Values which coincide with the left axes of these plots have been obtained by repeated Richardson extrapolation. Although only the piecewise-constant panel results have been extrapolated, the agreement between plane- and spheroidal-panel extrapolated results and the apparent convergence of the higher-order-panel results substantiate the claim made earlier regarding the accuracy of the benchmark values in Table 1.

3) Extrapolation was not as effective for the plane-panel results at the highest wavenumber (KL/2 = 8.0), probably because the coarsest plane-panel model had only four panels. Had the results from the coarsest model been neglected, the extrapolated plane-panel values would have been much closer to the extrapolated spheroidal-panel values.

4) Comparing the slopes of the lines corresponding to different types of panels gives an indication of their relative performance. If a permissible error is specified and the slope associated with one type of panel is twice that of a second type, then twice as many panels of the first type will be required to achieve the same accuracy. This is a significant difference

because the computational effort increases at least quadratically with the number of panels. Considering just the piecewise-constant panels, we see that the slope for plane panels is in fact considerably greater than for spheroidal panels at KL/2 = .08 and 3.2 with a less marked difference at KL/2 = 8.0.

The results from the higher-order spheroidal panels have also been compared in a different manner. The sway, heave and roll coefficients at 8 dimensionless wavenumbers, evenly spaced between KL/2=.08 and 11.2, have been computed for each combination of N and M. Differences between these values and the benchmarks may be regarded as the absolute error due to discretizing the velocity potential. The accuracy of a particular model has been judged by counting the number of these discretization errors which exceed a given value, say .005. The percent of exceedances for each combination of N and M is given in Table 3 which is organized so that combinations with the same number of collocation points are listed in the same row. With three modes of motion, two coefficients for each mode, and eight frequencies, a maximum of 48 exceedances is possible. Therefore the resolution of the values in Table 3 is about 2%. From looking across the rows, we conclude that for a fixed number of collocation points it is better to use piecewise-quadratic than piecewise-constant panels, but piecewise-linear panels provide no improvement over piecewise-constant panels.

Table 1: Benchmark values for the hydrodynamic coefficients and exciting forces/moments of $\varepsilon = 1/8$ spheroid, based on extrapolating from the sequence 16, 36, 81 piecewise-constant panels on one quarter of the submerged surface. The dimensionless quantities listed in this table are defined in the Appendix. The exciting force/moment for each wave heading β is given as a pair of numbers where the first number is the modulus and the second is the phase in degrees. The waveheading β is defined in Section 2. All values are accurate within one unit in the third decimal place except for the surge coefficients and exciting forces which are accurate to within one unit in the fourth decimal place.

Mode	KL/2	Added Mass	Damping	Exciting force/moment					
				$\beta = 0°$		$\beta = 45°$		$\beta = 90°$	
Surge	0.08	0.0298	0.0000	0.0102	90	0.0072	90		
	0.80	0.0360	0.0032	0.0854	90	0.0624	90		
$j=1$	1.60	0.0381	0.0137	0.1185	94	0.0965	94		
	3.20	0.0242	0.0239	0.0710	119	0.1063	112		
	6.40	0.0135	0.0182	0.0313	306	0.0166	223		
	11.20	0.0090	0.0131	0.0137	241	0.0142	73		
Sway	0.08	0.9543	0.0000			0.0137	90	0.0194	90
	0.80	1.0564	0.0153			0.1330	90	0.1940	90
$j=2$	1.60	1.2027	0.1132			0.2428	87	0.3906	87
	3.20	1.2565	0.5618			0.2906	76	0.7145	77
	6.40	0.6847	0.8450			0.0687	257	0.8644	70
	11.20	0.3121	0.6277			0.0440	59	0.7504	83
Heave	0.08	2.4067	0.1799	1.4647	0	1.4654	0	1.4660	0
	0.80	2.1058	1.1113	1.1047	5	1.1510	5	1.1980	5
$j=3$	1.60	1.5029	1.3385	0.7332	15	0.8822	15	1.0490	15
	3.20	0.8406	1.0537	0.1391	59	0.4304	35	0.9368	28
	6.40	0.6240	0.5958	0.0480	263	0.1125	205	0.7203	47
	11.20	0.6245	0.2965	0.0307	204	0.0579	36	0.5030	74
Pitch	0.08	1.4844	0.0002	0.1476	90	0.1044	90		
	0.80	1.7365	0.1303	1.2206	90	0.8865	90		
$j=5$	1.60	1.8208	0.5572	1.7048	94	1.3492	94		
	3.20	1.2481	1.0337	1.2001	115	1.5036	113		
	6.40	0.6852	0.6652	0.3491	294	0.3373	162		
	11.20	0.5853	0.3681	0.1049	205	0.1283	16		
Yaw	0.08	0.8477	0.0000			0.0007	360		
	0.80	0.8992	0.0004			0.0709	360		
$j=6$	1.60	0.9862	0.0118			0.2631	360		
	3.20	1.2183	0.2285			0.7927	354		
	6.40	0.8600	0.7420			0.3805	328		
	11.20	0.4217	0.6756			0.1115	153		

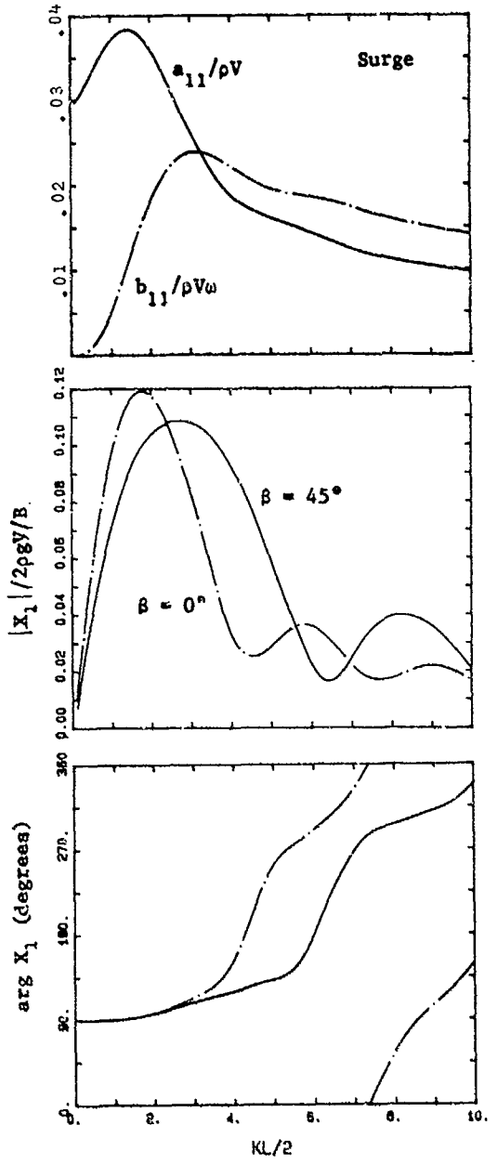

Figure 3: Surge coefficients and exciting force for $\varepsilon = 1/8$ spheroid based on 81 piecewise-constant panels.

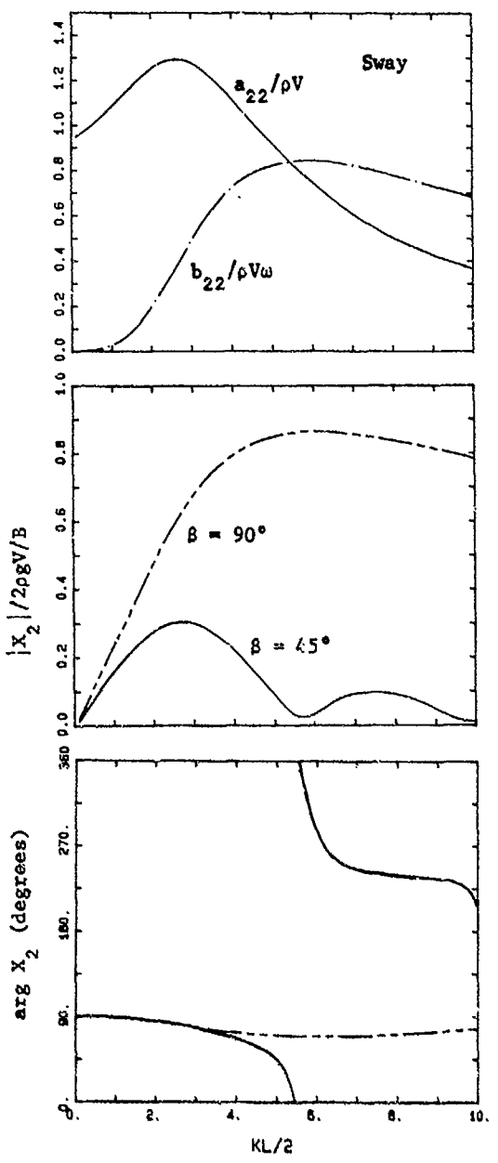

Figure 4: Sway coefficients and exciting force for $\varepsilon = 1/8$ spheroid.

Perhaps the major shortcoming of boundary-integral formulations of free-surface problems is the presence of "irregular frequencies" which correspond to the eigenfrequencies of the interior homogeneous Dirichlet problem. The behavior of the spheroidal-panel model has been investigated in the vicinity of the first irregular frequency.

The heave added-mass and damping coefficients based on 81 piecewise-constant panels are plotted in Figure 10. This figure has been included to show the detailed behavior of a fairly refined model; each tick mark represents an actual computed value. The first irregular frequency appears to be at $KL/2 \approx 15$. Below this wavenumber the curves are smooth, but above it some minor kinks are observable. Of particular note is a bump at $KL/2 \approx 17$ which will be referred to later in the context of twin spheroids.

Results based on 9,16,36 and 81 piecewise constant panels are plotted in Figure 11. The 81-panel results are the same as those in Figure 10 and are represented by a solid line

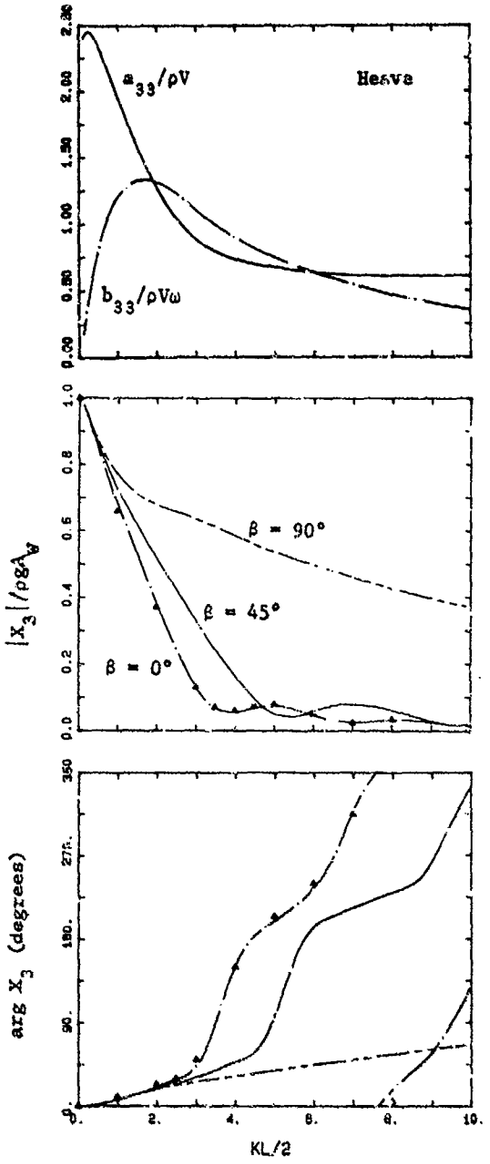

Figure 5: Heave coefficients and exciting force for ε = 1/8 spheroid. Beam seas exciting force modulus and phase from Shin (1979) are shown for comparison (A).

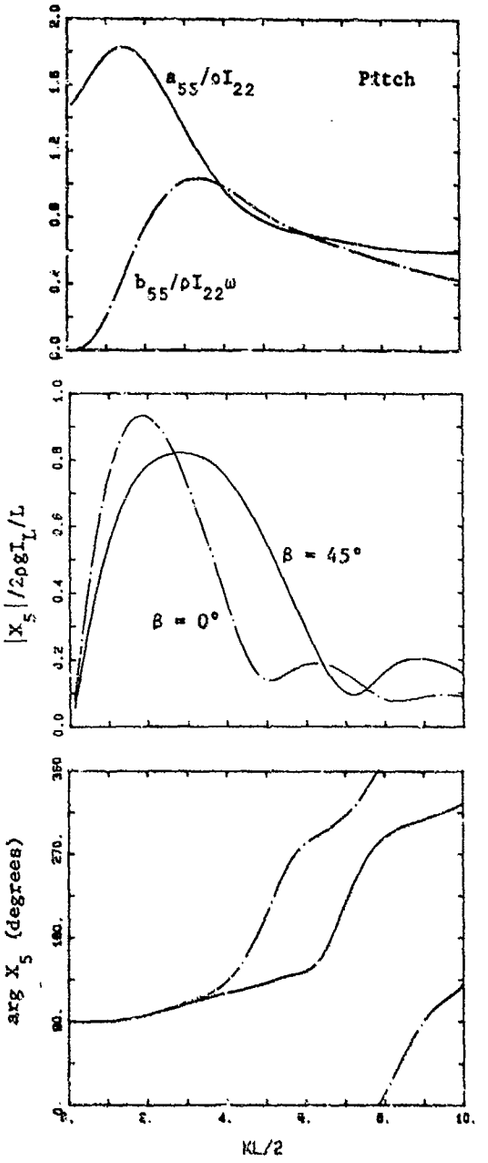

Figure 6: Pitch coefficients and exciting moment for ε = 1/8 spheroid.

even though there is uncertainty as to whether the curves are continuous at the irregular frequency. In the 9- and 16-panel results the apparent location of the irregular frequency is shifted to the right. Rather than a continuous shift to the left as the number of panels increases, however the apparent irregular frequency is actually further to the right for 16 than for 9 panels. The amplitude and bandwidth of the irregular frequency disturbance generally decrease with more panels, but the 16-panel results contradict this trend too.

Figure 12 shows the heave coefficients computed from 81 piecewise-constant panels and 4 and 9 piecewise-quadratic panels. It should be noted that 9 piecewise-quadratic panels require the same number of collocation points as 81 piecewise-constant panels. Although piecewise-quadratic panels performed better than piecewise-constant panels at low to moderate frequencies, the quadratic-panel results are erratic above the first irregular frequency.

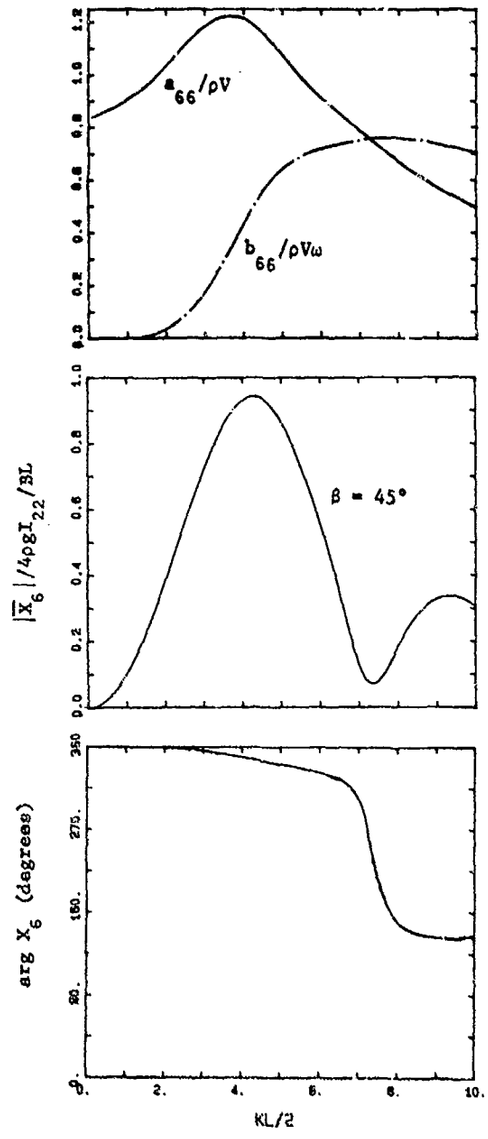

Figure 7: Yaw coefficients and exciting moment for $\epsilon = 1/8$ spheroid.

Figure 13 shows the heave added mass and damping of twin spheroids in the vicinity of the first irregular frequency. The spheroids are arranged in a catamaran configuration with a separation between their centerlines of one quarter their length. For purposes of comparison the 81-panel results for a single spheroid and a far-field approximation for twin spheroids (described in Breit, 1985) are also included. The far-field approximation does not suffer from irregular frequencies, thus in an unusual turn of events it serves here as a standard for judging the supposedly "exact" panel-method results. Indeed the panel-method results appear to converge to the far-field approximation as the number of panels is increased from 81 to 256. In addition to the disturbance in the panel-method results at the first irregular frequency, which coincides with that of a single spheroid, there are also irregularities, particularly in the damping coefficient, at KL/2 = 17,21 and 23. The first of these coincides with the aforementioned bump in the single-spheroid coefficients (Figure 10), but is certainly more prominent.

Table 2: Number of collocation points required for various combinations of the parameters N and M. The parameter N is the number of panels in a transverse or longitudinal strip of panels, thus N^2 is the number of panels on one quarter of the submerged surface. M-1 is the order of the polynomial representation of the velocity potential within each panel. The number of collocation points required is N^2M^2. Results have been obtained for all listed combinations.

N \ M	1	2	3	4	5
1			9	16	25
2		16	36	64	100
3	9	36	81		
4	16	64			
5	25	100			
6	36				
7	49				
8	64				
9	81				
10	100				

Based on recent work by Wu and Price (1985) it is likely that the irregularities observed for single and twin spheroids at KL/2 = 17 correspond to the second irregular frequency in heave. They have computed the hydrodynamic coefficients in all modes of a slender horizontal cylinder with a triangular cross section and show analytically that the first two irregular frequencies in heave occur well below the first one in sway. In so far as this body vaguely resembles a prolate spheroid, the locations of the irregular frequencies of the two bodies should be similar. The spheroid's first irregular frequency in sway occurs slightly above KL/2 = 24, so the second heave irregular frequency must be within the range shown in Figures 10 through 13. In fact, Figure 13 closely resembles some numerical results presented by Wu and Price, both in the relative locations of the first and second irregular frequencies and in the relative magnitudes of their disturbances.

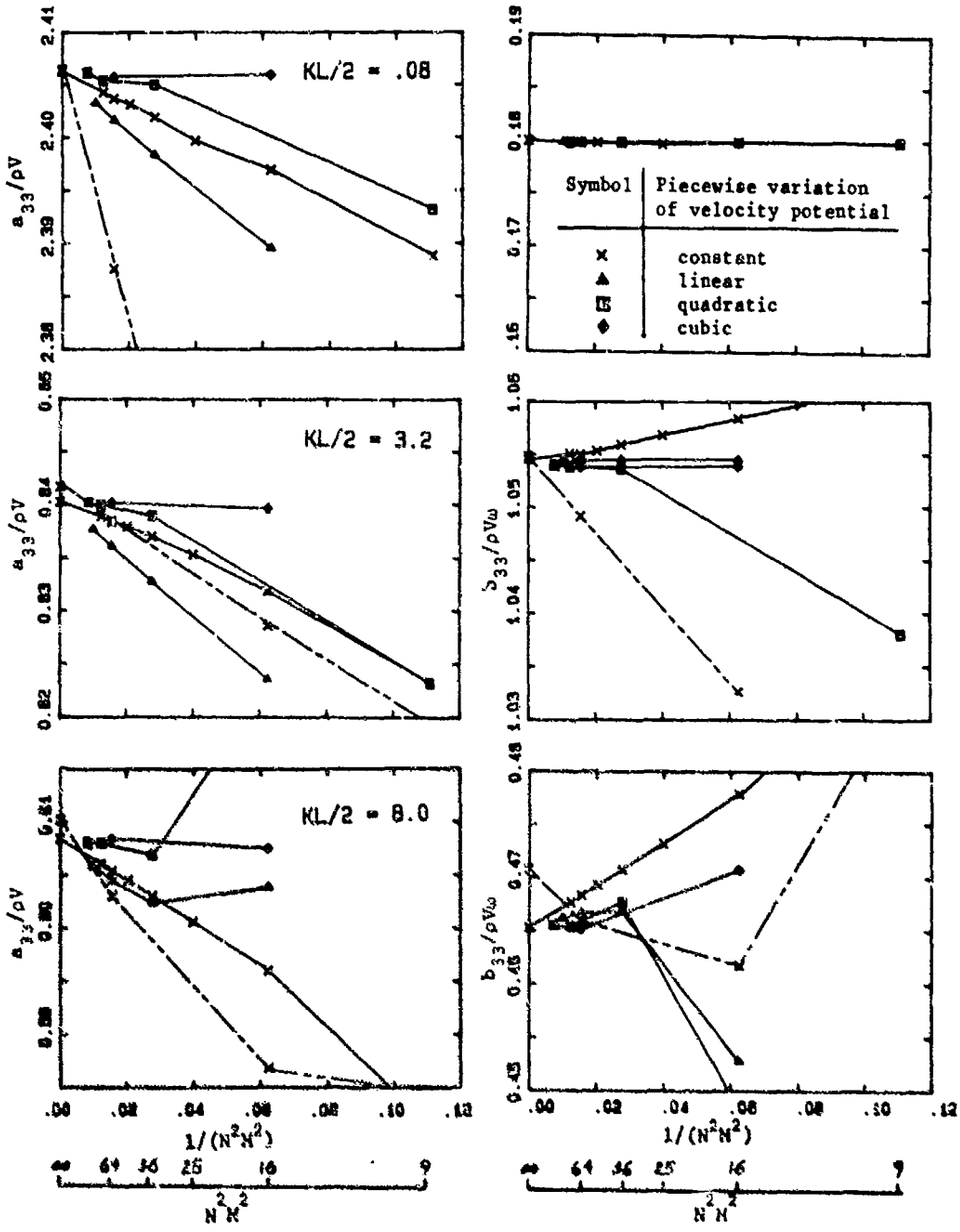

Figure 8: Heave added-mass and damping coefficients of $\epsilon = 1/8$ spheroid versus reciprocal of the number of collocation points, N^2M^2, at three wavenumbers for five types of panels. Actual data points are indicated by tick marks; spheroidal- and plane-panel results are connected by solid and dashed lines respectively.

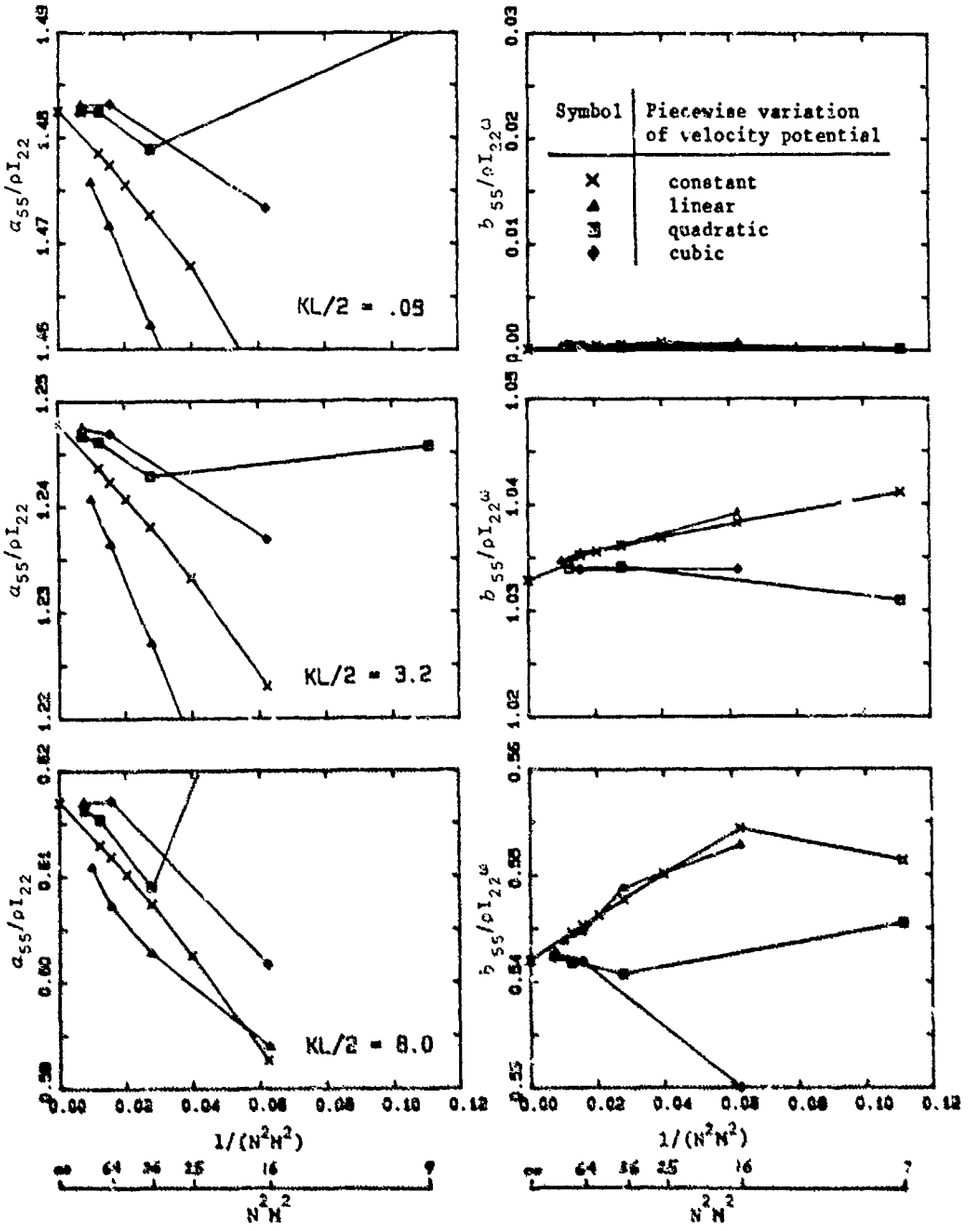

Figure 9: Pitch added-moment and damping coefficients of $\epsilon = 1/8$ spheroid versus reciprocal of the number of collocation points, N^2M^2.

Table 3: Percent exceedance of permissible error for various combinations of the number of panels N^2 and the order M-1 of the polynomial approximation of the velocity potential. For each combination, the sway, heave and pitch added-mass and damping coefficients were computed at eight wavenumbers, equally spaced between KL/2 =.08 and 11.2, for a total of 48 coefficients. The absolute differences between these coefficients and the benchmarks were computed. The number of differences which exceeded the permissible error δ were counted and divided by 48 to obtain the percentage of exceedances. The benchmark values were obtained by Richardson extrapolation of the 16,36 and 81 piecewise-constant-panel results.

δ = .002

N^2 \ M	1	2	3	4	5
9	88		90		
16	90	88		60	
25	88				29
36	79	65	38		
49	75				
64	65	58		4	
81	52		3		
100		44			0

δ = .005

N^2 \ M	1	2	3	4	5
9	80		77		
16	75	75		44	
25	65				13
36	50	50	8		
49	31				
64	23	25		0	
81	2		0		
100		19			0

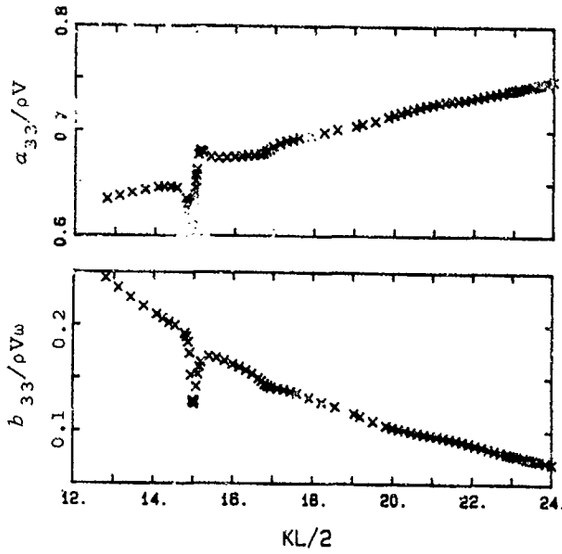

Figure 10: Heave added mass and damping of ε = 1/8 spheroid in vicinity of first irregular frequency. Each mark represents a numerical computation based on 81 piecewise-constant panels.

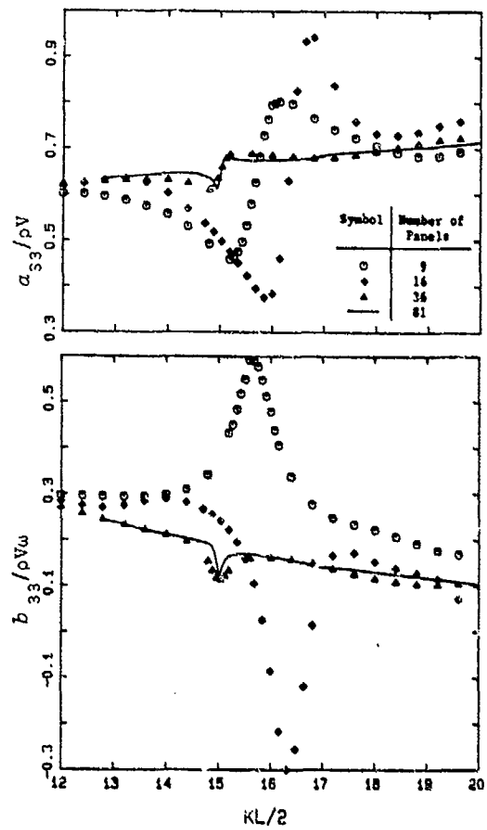

Figure 11: Heave added mass and damping of ε = 1/8 spheroid in vicinity of first irregular frequency; according to four models with different numbers of piecewise-constant panels. 81-panel results are same as Figure 10.

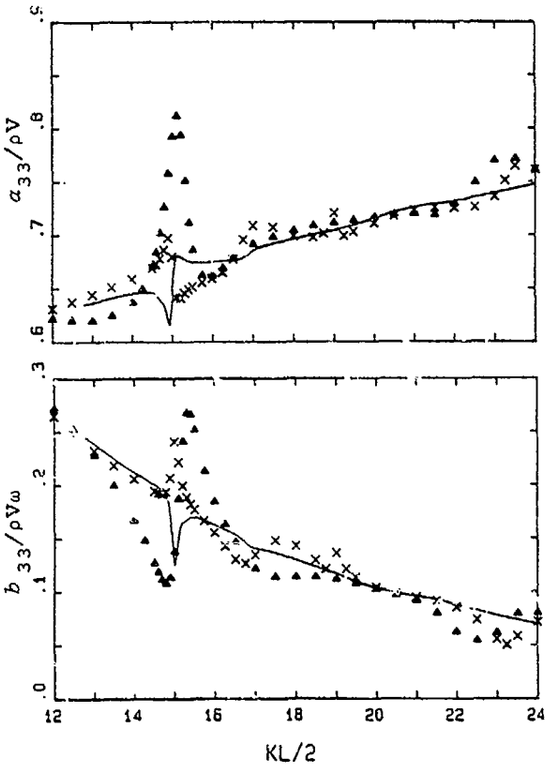

Figure 12: Heave added mass and damping of $\varepsilon = 1/8$ spheroid in vicinity of first irregular frequency; according to 81 piecewise-constant panels (————), 4 piecewise-quadratic panels (Δ), and 9 piecewise-quadratic panels (x).

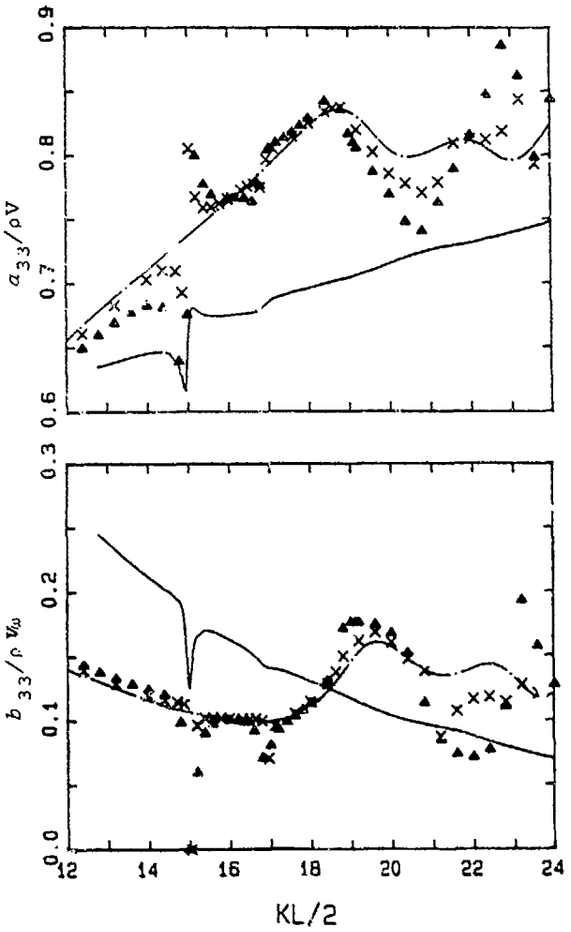

Figure 13: Heave added mass and damping of twin $\varepsilon = 1/8$ spheroids in vicinity of first irregular frequency. Spheroids are arranged in a catamaran configuration with a separation between their centerlines of one quarter their length. Results presented are from far-field approximation (——.——.——), 81 piecewise-constant panels (Δ) and 256 piecewise-constant panels (x). 81-panel results for one spheroid (————) are shown for comparison.

8. Conclusions

A very accurate algorithm for computing the radiation and diffraction of linear surface waves by a floating spheroid has been implemented. The geometry is represented exactly and the accuracy of the influence coefficients is carefully controlled, so errors in the hydrodynamic coefficients and exciting forces are primarily a consequence of approximating the velocity potential and solving by the collocation method.

The algorithm has been used to compute benchmark values of the hydrodynamic coefficients of an $\varepsilon = 1/8$ spheroid. In this connection, Richardson extrapolation proved to be a useful technique for improving accuracy without increasing computational effort. However, caution is advised when extrapolating from very coarse models at higher frequencies.

The comparison of curvilinear and plane panels, both with piecewise-constant approximations of the velocity potential shows the curvilinear panels to be superior, although the difference is more significant at low frequencies. This suggests that even with a piecewise-constant potential, improved accuracy can be gained just by accounting for curvature in the geometry.

The flexibility of the algorithm has permitted a thorough investigation of higher-order approximations of the potential on each panel. The higher-order panels have been compared on the basis of the number of collocation points, not the number of panels. On this basis, piecewise-linear panels are no better than piecewise-constant panels, but quadratic panels yield a large improvement in the rate of convergence. Piecewise-cubic panels provide a further improvement, but the difference is not as great as between quadratic and linear panels. Thus for a fixed number of collocation points, the higher-order panels are more accurate. Moreover, the improved accuracy is achieved without significantly increasing the complexity of the program because the collocation points are located on the interior of each panel and no continuity conditions are imposed between adjacent panels.

The present approach of representing the potential by a series of orthogonal functions could be used in more general applications. Many offshore structures are composed of multiple cylindrical members, so a panel based on circular cylindrical coordinates would be a logical extension. An entire member could be modeled by a single panel with more conventional panels used at its intersections with other members. This would reduce the required geometric input, the storage requirements and, if the present experience is any indication, improve the rate of convergence.

Finally, the investigation of irregular frequencies has shown that both the bandwidth and magnitude of the irregular-frequency disturbance diminishes as the number of panels increases. The effects of the second and higher irregular frequencies in heave are negligible for a sufficiently refined model of a single floating body, but are somehow amplified when several identical bodies are present.

Acknowledgements

I was supported by an Office of Naval Research Graduate Fellowship during the period this work was carried out. Thanks are due to Professor J. N. Newman for providing the FINGREEN subroutine and to Professor P. D. Sclavounos for supplying the plane-panel results shown in Figure 8. I also thank both of them for their guidance throughout my graduate studies.

References

1. Breit, S. R. (1985) "Wave Interaction Between Adjacent Slender Bodies by a Slender-Body Approximation and a Panel Method", Ph.D. thesis, Department of Ocean Engineering, Massachusetts Institute of Technology.

2. Breit, S. R., Newman, J. N. & Sclavounos, P. D. (1985) "A New Generation of Panel Programs for Radiation-Diffraction Problems", Proceedings of the 4th International Conference on the Behavior of Offshore Structures.

3. Dahlquist, G. & Bjorck, A. (1974) Numerical Methods, Englewood Cliffs: Prentice-Hall.

4. Garrison, C. J. (1977) "Hydrodynamics of Large Objects in the Sea", J. Hydronautics 8, No. 5.

5. Hess, J. L. & Smith. A. M. O. (1964) "Calculation of Nonlifting Potential Flow About Arbitrary Three-Dimensional Bodies", J. Ship Research 8, No. 2, pp. 22-44.

6. Hess, J. L. (1979) "A Higher Order Panel Method for Three-Dimensional Potential Flow Problems", Report No. MDC-J8519 or NADC-77166-30.

7. Kim, W. D. (1965) "On the Harmonic Oscillations of a Rigid Body on a Free Surface", J. Fluid Mech. 21, pp. 427-

8. Kim, W. D. (1966) "On a Free-Floating Ship in Waves", J. Ship Research, 10, pp. 182-200.

9. Newman, J. N. (1985) "Algorithms for the Free-Surface Green Function", J. Eng'g. Math., 19, pp. 57-67.

10. Shin, Y. S. (1979) "Three-Dimensional Effects on the Hydrodynamic Coefficients and Wave Exciting Forces Used in Predicting Motions of Ships", Ph.D. Thesis, Dept. of Naval Arch. & Marine Eng'g., U. of Michigan.

11. Sloan, I. H., R. S. Andersson, ed. (1980) The Application and Numerical Solution of Integral Equations, Netherlands: Sijthoff and Noordhoff, pp. 51-74.

12. Wu, X. J. & Price, W. G. (1985) "Irregular Frequencies Associated with Singularity Distribution Techniques", Manuscript.

13. Wehausen, J. V. & Laitone, E. V. (1960) "Surface Waves", Handbuch der Physic (S. Flugge, ed.) 9, pp. 446-778.

14. Yeung, R. W. (1975) "A Singularity-Distribution Method for Free-Surface Flow Problems with an Oscillating Body", Report No. NA 75-6, Col. of Eng'g, U. of Cal., Berkeley.

Appendix

The definitions of the added mass and damping coefficients a_{ij} and b_{ij}, and exciting force/moment X_i are

$$\omega^2 a_{ij} - i\omega b_{ij} = -i\omega\rho \iint_{S_B} n_i \phi_j dS \quad ;$$

$$i,j = 1,2\ldots,6$$

$$X_i = -i\omega\rho \iint_{S_B} n_i(\phi_0+\phi_7)dS \quad ;$$

$$i = 1,2,\ldots,6$$

where n_i is the generalizied normal component given by equation (8). These quantities are nondimensionalized by the geometric properties of a spheroid having a length L and a maximum diameter B and floating such that its longitudinal axis of symmetry coincides with the free surface. The required geometric properties are:

Displaced volume

$$\nabla = \frac{2}{3}\pi\left(\frac{L}{2}\right)\left(\frac{B}{2}\right)^2$$

Inertia of displaced volume about y axis

$$I_{22} = \frac{2}{15}\pi\left(\frac{L}{2}\right)^3\left(\frac{B}{2}\right)^2\left[1+\left(\frac{B}{L}\right)^2\right]$$

Waterplane area

$$A_w = \pi\left(\frac{L}{2}\right)\left(\frac{B}{2}\right)$$

Inertia of waterplane area about y axis

$$I_L = \frac{1}{4}\pi\left(\frac{L}{2}\right)^3\left(\frac{B}{2}\right)$$

The dimensionless coefficients are denoted here and in Section 7 by overbars and are defined as follows:

Translational modes:

$$\omega^2\rho\nabla(\bar{a}_{jj} - i\bar{b}_{jj}) = \omega^2 a_{jj} - i\omega b_{jj} \quad ; j = 1,2,3$$

$$\frac{2\rho g\nabla}{B}\bar{X}_j = X_j \quad ; \qquad j = 1,2$$

$$\rho g A_w \bar{X}_3 = X_3$$

Rotational modes:

$$\omega^2\rho I_{22}(\bar{a}_{jj} - i\bar{b}_{jj}) = \omega^2 a_{jj} - i\omega b_{jj}; \quad j = 5,6$$

$$\rho g I_L \bar{X}_5 = X_5$$

$$\frac{4\rho g I_{22}}{BL}\bar{X}_6 = X_6$$

Session IV

SHIP WAVES AND WAVEMAKING RESISTANCE

Session Chairman
W.B. Morgan
David Taylor Naval Ship
Research and Development Center
Bethesda, MD, U.S.A.

A Method of Computation for Steady Ship-Waves with Non-linear Free Surface Conditions

Hajime Maruo
Yokohama National University, Yokohama

Seikoo Ogiwara
Ishikawajima-Harima Heavy Industries, Yokohama

1. Introduction

The theory of ship waves is a substantially non-linear problem. The method which has been commonly used in order to solve this problem is the perturbation analysis with the assumption of small beam/length ratio of the ship. The Michell thin ship theory is the first approximation of the perturbation and a great number of examples of wave resistance computation has been published so far. Tsutsumi et al.(1) compared the wave resistance determined by the wave pattern analysis of mathematically defined ship model of variable breadth with corresponding computations by Michell's formula, and concluded that Michell's formula could predict the wave resistance within the torelable accuracy in case of beam/length ratio not greater than one fifteenth.

Since practical hull forms exceed this limitation, Michell's formula is not useful for the purpose of prediction of wave resistance. The higher approximation of the thin ship perturbation has been attempted by several researchers(2)(3)(4), but the results are not so promising, because of the highly singular behavior of the Kelvin source which prevents the feasibility of the higher approximation.

Another possibility of the perturbation analysis is the low Froude number approach. This method assumes the series expansion of the solution with respect to the Froude number. The starting point is the flow at zero Froude number which is identical with the flow around a double model in an unbounded fluid. The free surface condition for the disturbance potential is then linearized and the solution is simplified to a great extent. This idea was firstly suggested by Ogilvie(5) for the motion in two-dimensions, and applications to the three-dimensional case have been discussed by Baba et al.(6) and Maruo et al(7). Dawson(8) proposed a purely numerical method to solve the boundary value problem with the free surface condition similar to the above approximation by the aid of the distribution of Rankine sources over the still water plane together with the hull surface. A computer program for this method applicable to arbitrary hull forms was developod by Ogiwara(9) who calculated the wave profile, pressure distribution on the hull surface and the wave resistance and examined the feasibility of this method in the practical field.

Apart from the technique of linearized free surface conditions, the possibility of the direct solution of the boundary value problem in its original non-linear form depends only on numerical methods. A typical method of this kind is the finite difference technique, by which the solution is obtained by the step by step integration of the unsteady Euler or Navier-Stokes equation with respect to time. Several results of computation by the finite difference technique applied to hull forms have been published by Chan et al.(10) and Aoki et al.(11). Serious disadvantages of this method are that an enormous computer time is required before the steady state is finally attained and that a proper treatment of the condition at the open boundary with which the domain of computation is encompassed is hardly possible. On account of these defects, it is quite unlikely for the accuracy of computation by this method to be able to attain the level of practical feasibility.

The method proposed here is a kind of the boundary element method with the Rankine source as the kernel function. The steady non-linear free surface flow around a hull placed in a uniform stream is determined by iteration so as to fulfil the non-linear free surface condition and the hull surface condition, starting from the solution of double model linearization such as Dawson's problem. An advantage of this method is that the computer program for the double model linearization which is now at hand, is fully utilized. Other points of merit is that an analytical expression can be given to the solution at the final stage by means of the source distribution over the boundary and that the condition at infinite depth is fulfiled automatically. It has been found on carrying out the computation, that the stability in computation process is a serious problem, and several techniques to suppress the instability are indispenable. In order to examine problems associated to numerical technique, computations are executed for the two-dimensional motion of a submerged cylinder(12). Then numerical examples of three dimensional calculation are shown with respect to the wave pattern, pressure distribution and wave resistance of mathematically defined hull forms(13).

2. Basic formulation

Take cartesian coordinates with axes of x and y in the undisturbed free surface, and z axis in the vertically upward direction. Consider a ship hull fixed in a uniform flow of velocity U in the direction of x axis and assume an irrotational motion of an inviscid and incompressible fluid around the hull. The flow field is then defined by a velocity potential ϕ which satisfied the Laplace equation in the domain occupied by the fluid.

$$\phi_{xx}+\phi_{yy}+\phi_{zz}=0 \tag{1}$$

where subscripts mean partial derivatives. Designate the free surface elevation by the equation

$$z=\zeta(x,y) \tag{2}$$

and the boundary conditions on the free surface are as follows.

kinematical condition
$$\phi_x\zeta_x+\phi_y\zeta_y-\phi_z=0 \quad (z=\zeta) \tag{3}$$

dynamical condition
$$\frac{1}{2}(\phi_x^2+\phi_y^2+\phi_z^2-U^2)+g\zeta=0 \quad (z=\zeta) \tag{4}$$

where g is the acceleration of gravity. There is a condition at infinity such as $\phi=Ux$ at $x^2+y^2+z^2=\infty$. We have to consider generally the radiation condition that there is no wave motion at infinite upstream, but results of computations have shown that this condition is fulfilled by adoption a suitable computation algorithm. The free surface conditions, (3) and (4), have to be satisfied on the elevated free surface $z=\zeta(x,y)$, but trial computation has shown that the adoption of values at the real free surface at each step of iteration causes an unavoidable tendency of divergence. Therefore we employ an approximation that each value at $z=\zeta$ is expanded in Taylor series around $z=0$ and higher order terms are omitted. Resulting equations are

$$\begin{aligned}&\phi_x\zeta_x+\phi_y\zeta_y-\phi_z-\phi_{zz}\zeta\\&=\phi_x\zeta_x+\phi_y\zeta_y-\phi_z+(\phi_{xx}+\phi_{yy})\zeta=0 \quad (z=0)\end{aligned} \tag{5}$$

$$\begin{aligned}&\frac{1}{2}(\phi_x^2+\phi_y^2+\phi_z^2-U^2)\\&+\{\phi_x\phi_{zx}+\phi_y\phi_{zy}-\phi_z(\phi_{xx}+\phi_{yy})\}\zeta\\&+g\zeta=0 \quad (z=0)\end{aligned} \tag{6}$$

These equations are satisfied on the plane z=0.

The method of solution is based on the decomposition of the velocity potential into the double model flow potential ϕ_0 and the deviation from it such as

$$\phi=\phi_0+\phi_1 \tag{7}$$

The double model potential is regarded as a known function. Substituting (7) in (5) and (6), one obtains after some reduction

$$\begin{aligned}&\phi_{0x}\zeta_x+\phi_{1x}\zeta_{0x}+\phi_{0y}\zeta_y+\phi_{1y}\zeta_{0y}\\&-\phi_{1z}+D_1(x,y)=0 \quad (z=0)\end{aligned} \tag{8}$$

$$\begin{aligned}\zeta=&\frac{1}{2g}(U^2-\phi_{0x}^2-\phi_{0y}^2-2\phi_{0x}\phi_{1x}-2\phi_{0y}\phi_{1y})\\&+D_2(x,y) \quad (z=0)\end{aligned} \tag{9}$$

where

$$\zeta_0=\frac{1}{2g}(U^2-\phi_{0x}^2-\phi_{0y}^2) \tag{10}$$

$$\begin{aligned}D_1(x,y)=&\phi_{1x}(\zeta_x-\zeta_{0x})+\phi_{1y}(\zeta_y-\zeta_{0y})\\&+(\phi_{0xx}+\phi_{0yy}+\phi_{1xx}+\phi_{1yy})\zeta\end{aligned} \tag{11}$$

$$\begin{aligned}D_2(x,y)=&-\frac{1}{2g}(\phi_{1x}^2+\phi_{1y}^2+\phi_{1z}^2)\\&-\frac{1}{g}\{(\phi_{0x}+\phi_{1x})\phi_{1xx}+(\phi_{0y}+\phi_{1y})\phi_{1xy}\\&-\phi_{1z}(\phi_{0xx}+\phi_{0yy}+\phi_{1xx}+\phi_{1yy})\}\zeta\end{aligned} \tag{12}$$

$D_1(x,y)$ and $D_2(x,y)$ indicate the non-linear effect. If we omit the non-linear terms, i.e. $D_1(x,y)=0$, $D_2(x,y)=0$ we have the boundary condition for the double model linearized solution.

$$\begin{aligned}&\frac{1}{2}\{\phi_{0x}(\phi_{0x}^2+\phi_{0y}^2)_x+\phi_{0y}(\phi_{0x}^2+\phi_{0y}^2)_y\}\\&+\{\phi_{0x}(\phi_{0x}\phi_{1x}+\phi_{0y}\phi_{1y})_x\\&+\phi_{0y}(\phi_{0x}\phi_{1x}+\phi_{0y}\phi_{1y})_y\}\\&+\frac{1}{2}\{\phi_{1x}(\phi_{0x}^2+\phi_{0y}^2)_x+\phi_{1y}(\phi_{0x}^2+\phi_{0y}^2)_y\}\\&+g\phi_{1z}=0 \quad (z=0)\end{aligned} \tag{13}$$

If we take the length s along the streamline on the plane z=0 of the double model flow, the above equation can be transformed into

$$\phi_{0s}^2\phi_{1ss}+2\phi_{0s}\phi_{0ss}\phi_{1s}+g\phi_{1z}=-\phi_{0s}^2\phi_{0ss} \quad (z=0) \tag{14}$$

This equation is identical with the double model linearized free surface condition which was employed by Dawson.

The boundary condition on the hull surface is the usual form

$$\frac{\partial\phi}{\partial n}=\frac{\partial\phi_0}{\partial n}+\frac{\partial\phi_1}{\partial n}=0 \tag{15}$$

where n is taken along the outward normal of the hull surface. Since the double model flow satisfies the hull surface condition, i.e. $\partial\phi_0/\partial n=0$, the boundary condition for ϕ_1 becomes

$$\frac{\partial\phi_1}{\partial n}=\phi_{1x}n_x+\phi_{1y}n_y+\phi_{1z}n_z=0 \tag{16}$$

where n_x, n_y, n_z are direction cosines of the normal.

We express the double model potential by a distribution of sources over the double hull surface such as

$$\phi_0(x,y,z)=Ux-\iint_{S_0}\sigma_0\left(\frac{1}{r_0}+\frac{1}{\bar{r}_0}\right)ds \tag{17}$$

where

$$r_0=\sqrt{(x-x')^2+(y-y')^2+(z-z')^2}$$
$$\bar{r}_0=\sqrt{(x-x')^2+(y-y')^2+(z+z')^2}$$

The velocity potential ϕ_1, on the other hand, is expressed by sources distributed on the hull surface S_0 and still water plane outside the hull S_1 as follows.

$$\phi_1(x,y,z)=-\iint_{S_0}\Delta\sigma_0\left(\frac{1}{r_0}+\frac{1}{\bar{r}_0}\right)ds-\iint_{S_1}\sigma_1\frac{1}{r_1}ds \tag{18}$$

where

$$r_1=\sqrt{(x-x')^2+(y-y')^2+z^2}$$

Now the boundary value problem is stated in such a manner that the source distribution densities $\sigma_1, \Delta\sigma_0$ are to be determined so as to make the velocity potentials ϕ_0 and ϕ_1 satisfy the boundary conditions (8),(9) and (16).

3. The numerical method of solution

The method of solution is an iterative procedure that the free surface conditions (8) and (9) are satisfied by assuming the non-linear terms $D_1(x,y)$and $D_2(x,y)$ are given by the solution of preceding step of iteration. In the first place, the double model source distribution σ_0 in (17) is determined in such a way that the hull boundary condition.

$$\frac{\partial\phi_0}{\partial n}=0 \tag{19}$$

is satisfied. Then the first approximation is obtained by determining the source densities $\Delta\sigma_0$ and σ_1 in (18) so as to satisfy the double model linearized free surface condition (14) together with the hull boundary condition (16). Next the functions $D_1(x,y)$, and $D_2(x,y)$ are calculated making use of the first approximation for ϕ_1. The first approximation for the free surface elevation is determined by substitution of ϕ_1 in (9) by the first approximation obtained above. The second approximation for the source densities $\Delta\sigma_0$ and σ_1 in (18) is determined so as to satisfy the hull boundary condition (16) and the free surface condition (8) in which $D_1(x,y)$ is determined by the first approximation. A similar process is repeated in further approximation.

The computation program, which has been developed for the solution of double model linearization, is effectively utilized in this iterative solution. It is found by a sample calculation, that inherent instability results divergence in repeated computation. In oder to eliminate this instability, a relaxation factor $\alpha_1<1.$ is mutiplied to the non-linear terms $D_1(x,y)$and $D_2(x,y)$.

The numerical work is carried out with discretization of the boundary surfaces. We make the hull surface S_0 consist of M_0 panels and take a finite area S_1 on the plane z=0, which is divided into M_1 elements, as the domain of computation. If the density of source is constant in one panel, velocity of the disturbance potential ϕ_1 are given by

$$\begin{aligned}\phi_{1x}&=\sum_{j=1}^{M_0}\Delta\sigma_0(j)CX_0(ij)+\sum_{j=1}^{M_1}\sigma_1(j)CX_1(ij)\\ \phi_{1y}&=\sum_{j=1}^{M_0}\Delta\sigma_0(j)CY_0(ij)+\sum_{j=1}^{M_1}\sigma_1(j)CY_1(ij)\\ \phi_{1z}&=\sum_{j=1}^{M_0}\Delta\sigma_0(j)CZ_0(ij)+\sum_{j=1}^{M_1}\sigma_1(j)CZ_1(ij)\end{aligned} \tag{20}$$

where (CX_0, CY_0, CZ_0) and (CX_1, CY_1, CZ_1) are velocities due to unit sources distributing on each panel and are given by

$$\begin{aligned}CX_0(ij)&=\iint_{S_{0j}}(x_i-x_j)\left(\frac{1}{r_{0ij}^3}+\frac{1}{\bar{r}_{0ij}^3}\right)ds\\ CY_0(ij)&=\iint_{S_{0j}}(y_i-y_j)\left(\frac{1}{r_{0ij}^3}+\frac{1}{\bar{r}_{0ij}^3}\right)ds\\ CZ_0(ij)&=\iint_{S_{0j}}\left(\frac{x_i-x_j}{r_{0ij}^3}+\frac{x_i+x_j}{\bar{r}_{0ij}^3}\right)ds\\ CX_1(ij)&=\iint_{S_{1j}}\frac{x_i-x_j}{r_{1ij}^3}ds\\ CY_1(ij)&=\iint_{S_{1j}}\frac{y_i-y_j}{r_{1ij}^3}ds\\ CZ_1(ij)&=\iint_{S_{1j}}\frac{x_i}{r_{1ij}^3}ds\end{aligned} \tag{21}$$

Integrals are performed in each panel on the hull surface or on the still water plane.

Because of the application of the relaxation factor α_1, the free surface condition takes the form like

$$\phi_{0x}\zeta_x+\phi_{1x}\zeta_{0x}+\phi_{0y}\zeta_y+\phi_{1y}\zeta_{0y}-\phi_{1z}+\alpha_1\cdot D_1(x,y)=0 \tag{22}$$

$$\zeta=\frac{1}{2g}(U^2-\phi_{0x}^2-\phi_{0y}^2-2\phi_{0x}\phi_{1x}-2\phi_{0y}\phi_{1y})+\alpha_1\cdot D_2(x,y) \tag{23}$$

Substituting (11) in (22), one obtains

$$\phi_{1x}A_x+\phi_{1y}A_y+\alpha_1\cdot\zeta(\phi_{1xx}+\phi_{1yy})-\phi_{1z}=B \tag{24}$$

where

$$A_x=\zeta_{0x}+\alpha_1(\zeta_x-\zeta_{0x}) \tag{25}$$

$$A_y=\zeta_{0y}+\alpha_1(\zeta_y-\zeta_{0y}) \tag{26}$$

$$B=-\phi_{0x}\zeta_x-\phi_{0y}\zeta_y-\alpha_1\cdot\zeta(\phi_{0xx}+\phi_{0yy}) \tag{27}$$

The free surface elevation is calculated by (23),(12) as follows.

$$\zeta=\frac{1}{2}\frac{U^2-\phi_{0x}^2-\phi_{0y}^2-2\phi_{0x}\phi_{1x}-2\phi_{0y}\phi_{1y}-\alpha_1(\phi_{1x}^2+\phi_{1y}^2+\phi_{1z}^2)}{g+\alpha_1\{\phi_x\phi_{1xz}+\phi_y\phi_{1zy}-\phi_{1z}(\phi_{xx}+\phi_{yy})\}} \tag{28}$$

The boundary conditions on the free surface and on the hull surface are written in discretized forms like

$$\sum_{j=1}^{M_0}\Delta\sigma_0(j)A_0(ij)+\sum_{j=1}^{M_1}\sigma_1(j)A_1(ij)+2\pi\sigma_1(i)=B(i) \tag{29}$$

$$(i=1,2,\cdots,M_1 \text{ on } S_1)$$

$$\sum_{j=1}^{M_0}\Delta\sigma_0(j)N_0(ij)+\sum_{j=1}^{M_1}\sigma_1(j)N_1(ij)=0 \tag{30}$$

$$(i=1,2,\cdots,M_0 \text{ on } S_0)$$

where

$$A_m(ij)=CX_m(ij)A_x(i)+CY_m(ij)A_y(i)+\alpha_1\zeta(CXX_m+CYY_m) \tag{31}$$

$$B(i)=-\phi_{0x}(i)\zeta_x(i)-\phi_{0y}(i)\zeta_y(i)-\alpha_1\zeta(i)\{\phi_{0xx}(i)+\phi_{0yy}(i)\} \tag{32}$$

$$CXX_m=\{CX_m(x=x_i)-CX_m(x=x_i-dx)\}/dx$$
$$CYY_m=\{CY_m(y=y_i)-CY_m(y=y_i-dy)\}/dy \tag{33}$$

$$N_m(ij)=CX_m(ij)\cdot n_x(i)+CY_m(ij)\cdot n_y(i)+CZ_m(ij)\cdot n_z(i) \tag{34}$$
$$N_0(ii)=2\pi+n_z(i)\iint_{S_{ii}}\frac{dS}{4\pi r^2}$$

Subscript m=0 means the contribution of sources on the hull surface and m=1 means that on the still water plane. The equation (29) and (30) give a system of simultaneous equations which determine the source densities σ_1 and $\Delta\sigma_0$.

4. A simplified method

The method of computation stated in the preceding section requires long computer time because the boundary conditions on the hull surface and those on the free surface should be satisfied simultaneously. This fact is a serious disadvantage in view of the practical application. A simplified method is proposed here under this circumstance. Assume the hull surface source $\Delta\sigma_0^{(k)}$ and free surface elevation $\zeta^{(k)}$ at k-th step to be given. Then the free surface source $\sigma_1^{(k+1)}$ at (k+1)-th step is determined by the equation

$$\sum_{j=1}^{M_1}\sigma_1(j)^{(k+1)}A(ij)+2\pi\sigma_1(i)^{(k+1)}=C(i)^{(k)} \tag{35}$$

$$(i=1,2,\cdots,M_1 \text{ on } S_1)$$

where

$$C(i)^{(k)}=B(i)-\sum_{j=1}^{M_0}\Delta\sigma_0(j)^{(k)}A_0(ij) \tag{36}$$

The source distribution thus obtained induces the normal velocity on the hull surface given by

$$v_n(i)=\sum_{j=1}^{M_1}\{\sigma_1(j)^{(k+1)}-\sigma_1(j)^{(k)}\}N_1(ij) \tag{37}$$

In order to compensate the above velocity, source of density

$$\varepsilon=-\frac{1}{4\pi}v_n(i) \tag{38}$$

are added to the hull surface sources. Then the source distribution on the hull surface is of the density $\Delta\sigma_0(i)+\varepsilon$. The computation begins with the first approximation which is obtained from the double-model-linearized solution with free surface condition (14). The first approximation for ζ is obtained from

$$\zeta(x,y)=\frac{1}{2g}(U^2-\phi_{0x}^2-\phi_{0y}^2-2\phi_{0x}\phi_{1x}-2\phi_{0y}\phi_{1y}) \tag{39}$$

The second approximation for the free surface source density σ_1 is determined by solving the simultaneous equations (35) and the hull surface source density is obtained from (37) and (38). The similar process is repeated in the further approximation untill a stationary value is obtained. It has been found during trial computations, that adjustment of interval between each step is needed during iteration in order to keep stability. Therefore another relaxation factor $\alpha_2<1$, by which ζ in the (k+1)-th step is modified such as

$$\bar{\zeta}(i)^{(k+1)}=\zeta(i)^{(k)}+\alpha_2\{\zeta(i)^{(k+1)}-\zeta(i)^{(k)}\} \tag{40}$$

The flow diagram of the numerical work is shown in Fig.1. The partial derivatives, which are necessary for the determination of coefficient in (35), are calculated by the following fashion.

Consider a function f(x,y) in x-y plane and define a plane given by the equation

$$ax+by+cf=1 \tag{41}$$

on which three point $(x_i, y_i, f_i,\ i=1,2,3)$ are located. Then the partial derivatives of f(x,y) are approximated by

$$f_x=-\frac{a}{c},\quad f_y=-\frac{b}{c} \tag{42}$$

A trial computation for the two-dimensional problem of a submerged elliptic cylinder shows that results obtained by the simplified method are sufficiently accurate when compared with the results by the more complicated method in the preceding section.

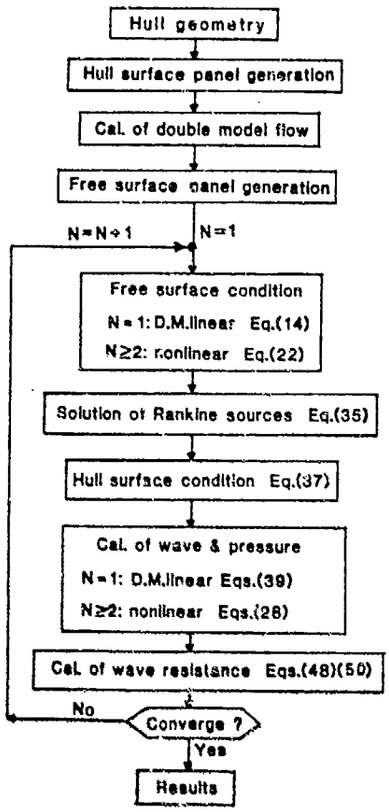

Fig.1 Flow diagram of numerical computation

5. The wave profile of a submerged elliptic cylinder

In oder to examine the validity of the computation method mentioned above, the method of section 3 is applied to the two-dimensional problem of the wave profile which accompany a submerged cylinder of elliptic section. The numerical example is concerning the shape with the ratio between two axes a/b=4.

Fig.2 shows the results of computation at each step of iteration for the case of $Fn=U/\sqrt{2ga}=0.5$, $f/a=1.7$ (f is the depth of immersion of the center) when the relaxation factor α_1, α_2 are not applied. Instability of computation is observed which make the result diverge at the 7th step. After some study, it is found that stable results are obtained by application of the relaxation factor $\alpha_1=0.75$, $\alpha_2=0.25$ as shown in Fig.3. The convergence of the computation is examined by the quantity

$$E(s)=\sum_{i=1}^{M_1}|\eta_i^{(s+1)}-\eta_i^{(s)}|^2 \qquad (43)$$

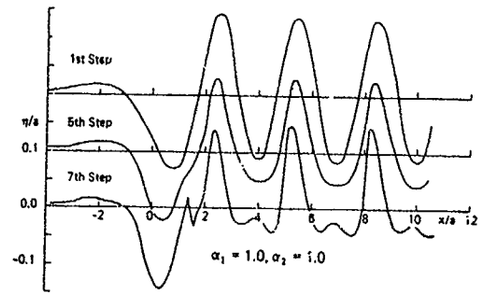

Fig.2 Wave profile at each step of iteration process (f/a=1.7, Fn=0.50, α_1=1.0, α_2=1.0)

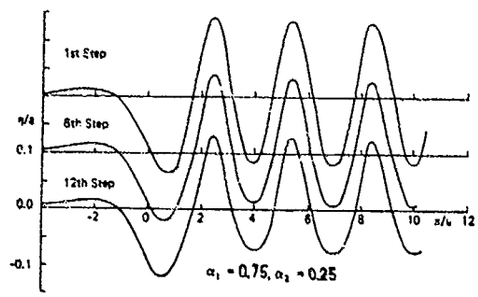

Fig.3 Wave Profile at each step of iteration process (f/a=1.7, Fn=0.50, α_1=0.75, α_2=0.25)

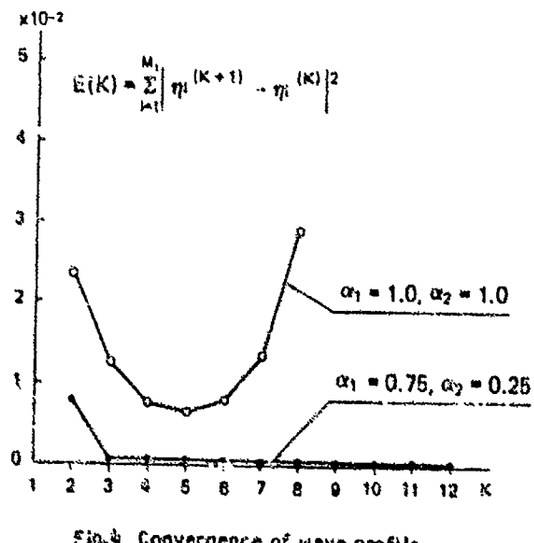

Fig.4 Convergence of wave profile (f/a=1.7, Fn=0.50)

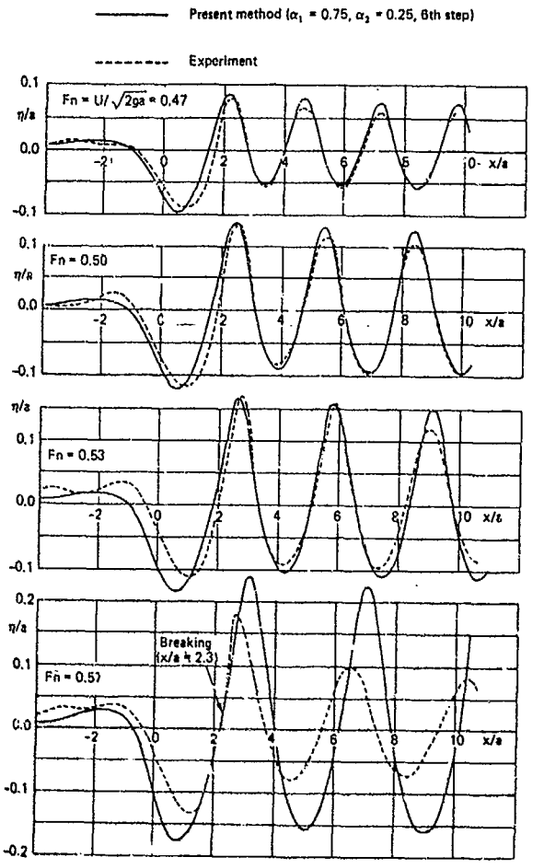

Fig.5 Comparison of wave profiles at various Froude number (f/a=1.7)

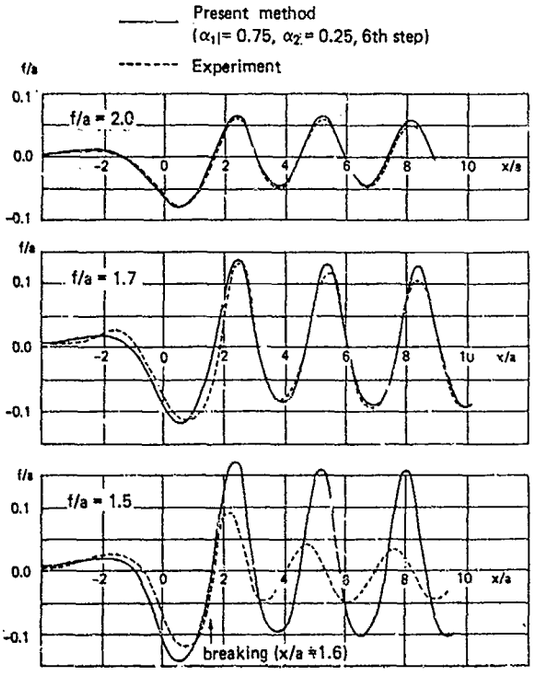

Fig.6 Comparison of wave profiles at various depth of immersion (Fn=0.50)

where $\eta_{(i)}^{(k+1)}$, $\eta_{(i)}^{(k)}$ are free surface elevations at (k+1)-th and k-th steps respectively. It is shown in Fig.4, that the computation with α_1=0.75, α_2=0.25 converges very rapidly.

Experiments are conducted in the circulating water channel to measure the wave profile and results are compared with computation. Fig.5 shows results at various Froude numbers. The wave breaking takes place slightly behind the cylinder at Fn=0.57. Fig.6 shows results with changing depth of immersion at Fn=0.50. The wave breaking takes place in the case of f/a=1.5. The computed wave profile agrees very well with the measurement unless the wave breaking appears. Fig.7 shows measured and computed fluid velocities below the first crest of the wave. Agreement is very good except the case of Fn=0.57 where the wave breaking is observed.

A simplified method is proposed in the previous section. In order to examine its accuracy, computations of the case of Fn=0.5, f/a=1.7 are carried out by both original and simplified methods. Fig.8 shows a good agreement between results of two methods.

6. The ship wave pattern

As shown in the previous section, the simplified method mentioned in section 4 predicts the flow field with sufficient accuracy. Therefore we employ the simplified method in the present computation of the wave pattern of three-dimensional hull forms.

The first example of the hull form is a slender ship of mathematical form defined by the equation

$$y(x,z) = w(x)\left(1-\frac{z^2}{d^2}\right) \tag{44}$$

where

$$w(x) = \begin{cases} \dfrac{B}{2}\left\{1-\left(\dfrac{x}{l}\right)^2\right\}(1-a)+a\left\{1-\left(\dfrac{x}{l}\right)^n\right\} \\ \qquad (-l \leq x \leq 0) \\ \dfrac{B}{2}\left\{1-\left(\dfrac{x}{l}\right)^n\right\} \\ \qquad (0 \leq x \leq l) \end{cases} \tag{45}$$

$l = L/2$, $a = 0.3$, $n = 12$, $L/B = 10$, $B/d = 1.6$

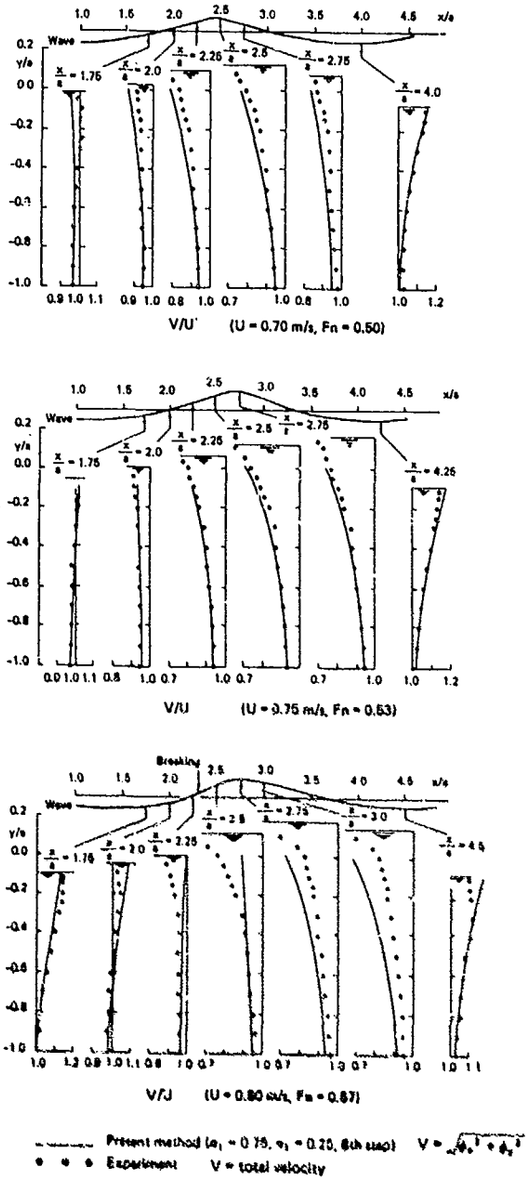

Fig.7 Comparison of velocity distribution beneath free surface (f/a=1.7)

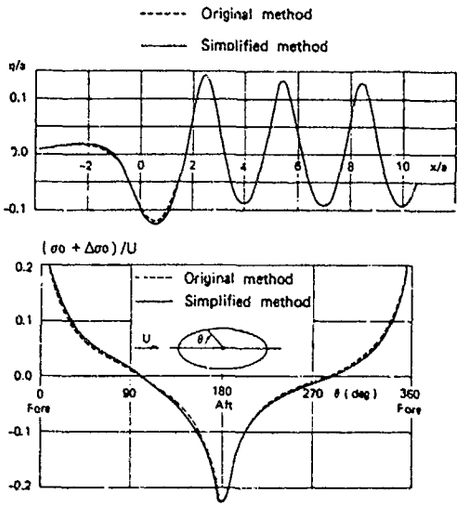

Fig.8 Comparison of wave profile (above) and source distribution on the elilpse(bellow) (Fn=0.50, f/a=1.7, α_1=0.75, α_2=0.25, 6th step)

This is a version of Wigley model, with fuller entrance. The panel division on the hull surface and on the still water plane is shown in Fig.9. The number of panels on the hull surface on one side is 27x10 and that on the still water plane is 44x9.

The effect of the relaxation factors is studied in the first place by computations with variable α_1 and α_2. Fig.10 gives the wave profiles with changing α_1 applied. The effect of variation in α_2 is shown in Fig.11. According to these results, stable iteration may be obtained by the adoption of α_1=0.50 and α_2=0.10, but instability still takes place at $Fn=U/\sqrt{gl}$=0.267 in this case. It is understood that the instability due to non-linearity appears in a limited zone near both ends of the hull, and the application of α_1 is needed only in the above zone. Therefore we apply the relaxation factor in two circular regions of radius $l/2$ with centers at F.P. and A.P. of the hull as shown in Fig.12. Here l is the wave length $l=2\pi U^2/g$. The distribution of α_1 is given by

$$\alpha_1=\begin{cases}\alpha_4+2r(\alpha_3-\alpha_4)/l & (0\leq r\leq l/2)\\ \alpha_4 & (r>l/2)\end{cases} \qquad (46)$$

We employ α_3=1.0, α_4=0.25, α_2=0.1 in further computations. Fig.13 shows the results of computation at each step of iteration process. Change of value is significant at both ends of the hull. The results of computation are compared with measurements in the towing tank. Fig.14 shows the comparison of wave profile alongside the model (Model A), and Fig.15 shows the computed and measured pressure distribution at the level z/d=-0.52. Much better agreement with measured results is obtained by the present method than by the Michell thin ship theory.

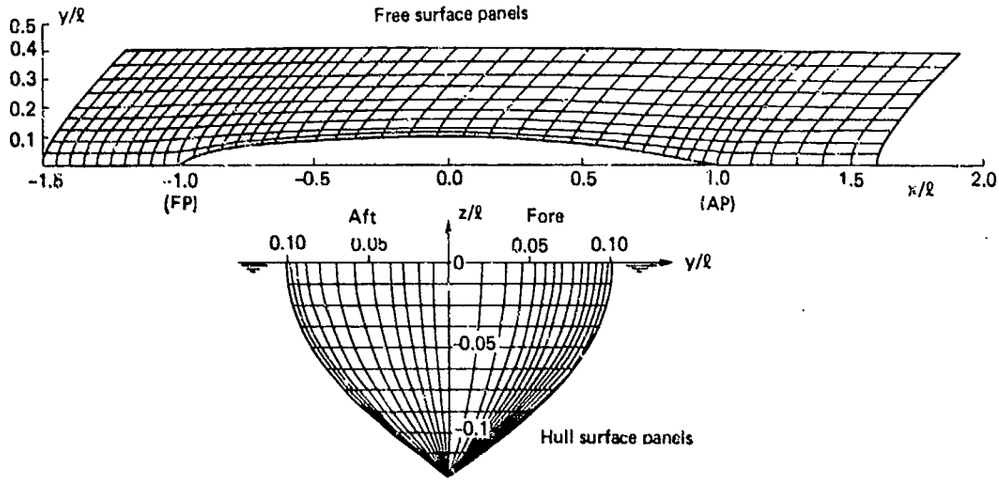

Fig.9 Panel division on the boundary surfaces for Model A

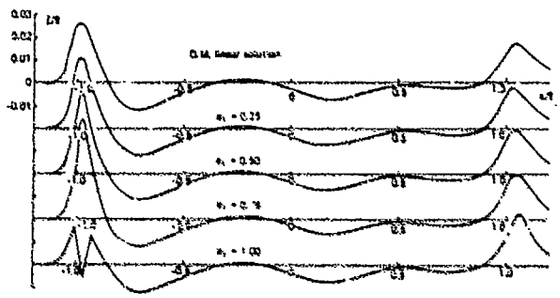

Fig.10 The effect of correction factor A1 on wave profile (Model A, Fn=0.250, σ_1=0.10, 4th step)

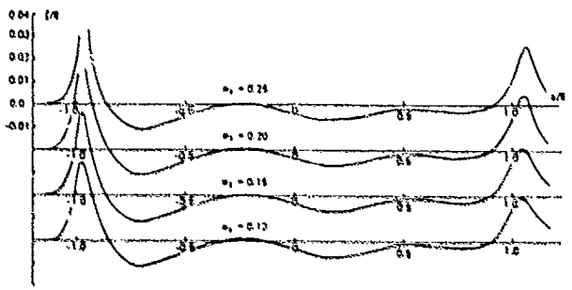

Fig.11 The effect of correction factor A2 on wave Profile (Model A, Fn=0.250, σ_1=0.50, 4th step)

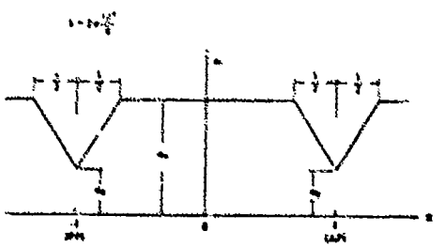

Fig.12 Distribution of correction factor

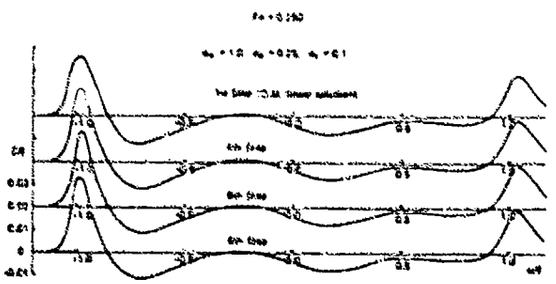

Fig.13 Wave profile at each step of iteration process (Model A)

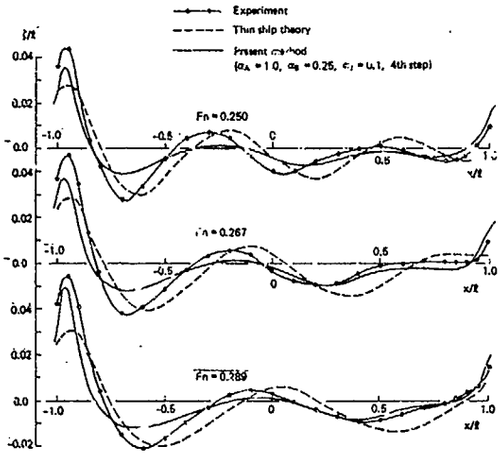

Fig.14 Comparison of wave profiles of Model A

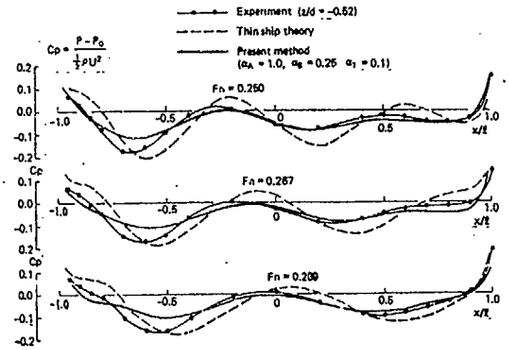

Fig.15 Comparison of pressure distribution for Model A at z/d=-0.52

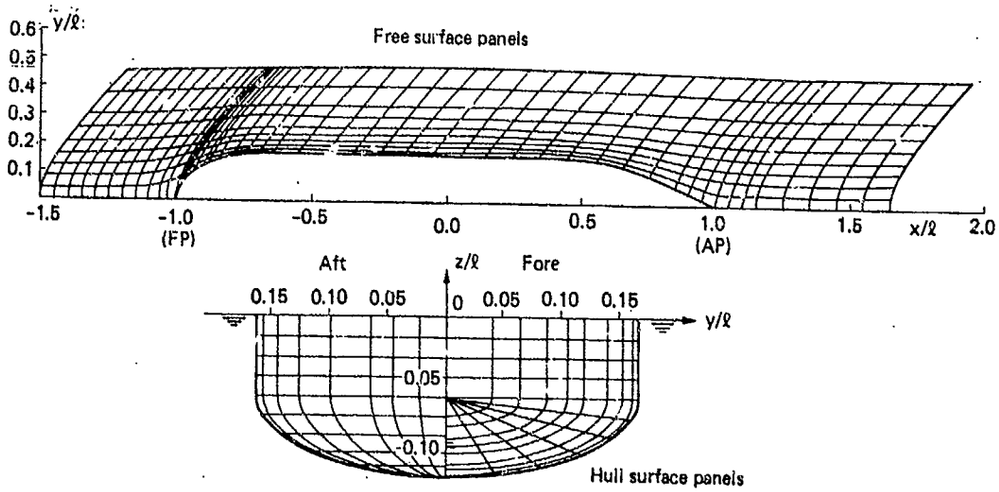

Fig.16 Panel division on the boundary surfaces for Model B

The second example is a much fuller model (Model B) with elliptic bow waterline and elliptic frame lines. The panel division for the numerical work is shown in Fig.16, and the mathematical expression for the hull surface is given in Table 1.

Fig.17 shows the comparison of the computed wave profile with the measurement and Fig.18 shows the pressure distribution at the level z/d=-0.3. Good agreement is observed in the fore-body, but there are some discrepancies in the aft-body. The difference between the computation and the measurement in the aft-body may be attributed to the viscosity effect. Fig.19 gives a schematical illustration of wave patterns of both models.

7. The wave resistance

The fluid pressure is given by Bernoulli's theorem such as

$$p-p_0=\frac{1}{2}\rho\{U^2-\phi_{0x}^2-\phi_{0y}^2-\phi_{0z}^2-2\phi_{0x}\phi_{1x} -2\phi_{0y}\phi_{1y}-2\phi_{0z}\phi_{1z} -\alpha_1(\phi_{1x}^2+\phi_{1y}^2+\phi_{1z}^2)\} \tag{47}$$

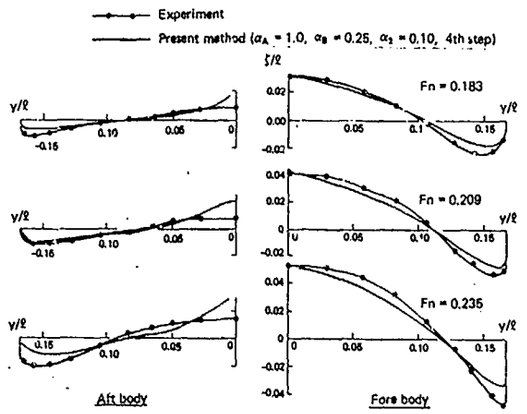

Fig.17 Comparisin of wave profiles for Model B

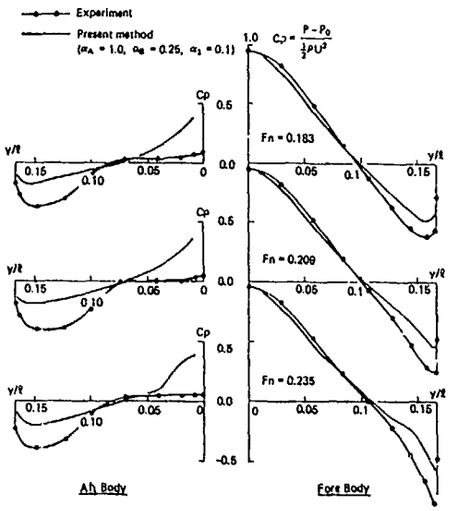

Fig.18 Comparion of pressure distribution for Model B at z/d∞=0.3

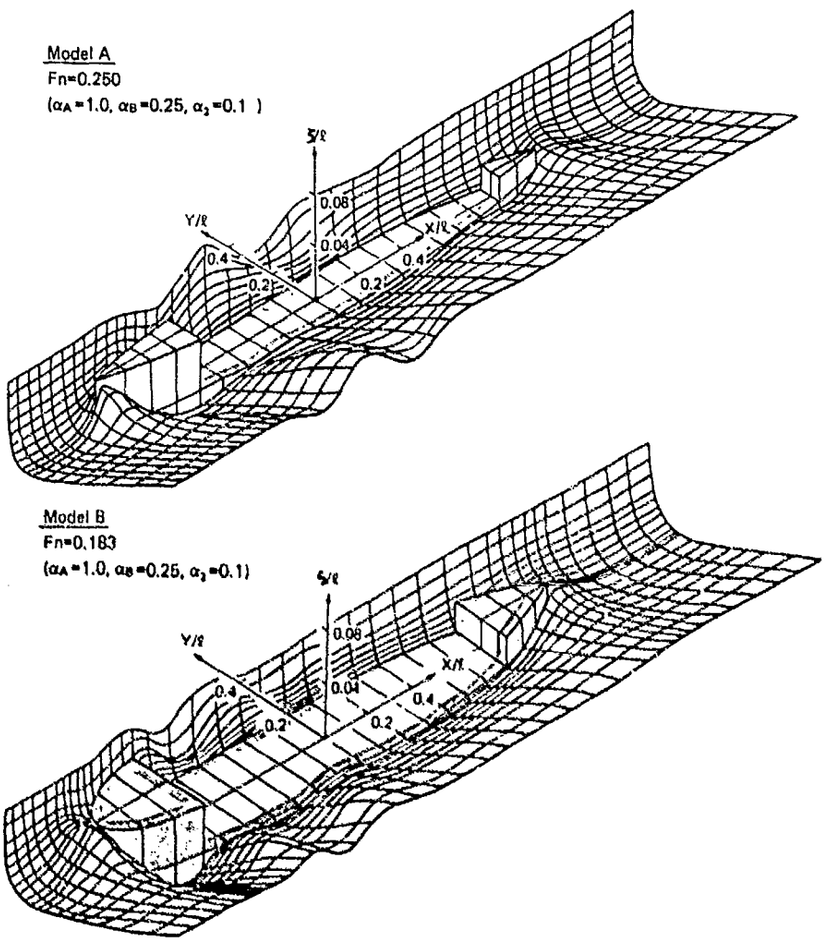

Fig.19 Computed wave patterns around mathematical hulls

Table 1 Mathematical representation of half breadth y for Model R

z \ x	Elliptic form $-\frac{L}{2}\le x\le -\frac{L}{3}$	Parallel part $-\frac{L}{3}\le x\le \frac{L}{6}$	Parabolic form $\frac{L}{6}\le x\le \frac{L}{2}$
$-\frac{d}{2}\le z\le 0$	$\frac{B}{2}\sqrt{1-\frac{(x+L/3)^2}{(L/6)^2}}$	$\frac{B}{2}$	$\frac{B}{2}\left\{1-\frac{(x-L/6)^2}{(L/3)^2}\right\}$
$-d\le z\le -\frac{d}{2}$	$\frac{B}{2}\sqrt{1-\frac{(x+L/3)^2}{(L/6)^2}-\frac{(z+d/2)^2}{(d/2)^2}}$	$\frac{B}{2}\sqrt{1-\frac{(z+d/2)^2}{(d/2)^2}}$	$\frac{B}{2}\left\{1-\frac{(x-L/6)^2}{(L/3)^2}\right\}\sqrt{1-\frac{(z+d/2)^2}{(d/2)^2}}$

L ; ship length B ; ship breadth d ; draft

The wave resistance is defined by the pressure integral over the hull surface. If the pressure is calculated at each point and is assumed uniform in each panel $ds(i)$, the wave resistance is given by

$$R_w=-\sum_{j=1}^{M_1}\{p(i)-p_0\}n_x(i)ds(i) \tag{48}$$

Though the fluid velocities are defined in the space below the still water plane z=0, the pressure integral must be taken over the real wetted hull surface under the elevated free surface. Therefore the pressure acting on the hull surface between real free surface and the still water plane should be taken into account. In the present computation, we assume a linear variation of pressure such as

$$p-p_0=p_w\left(1-\frac{z}{\zeta}\right) \tag{49}$$

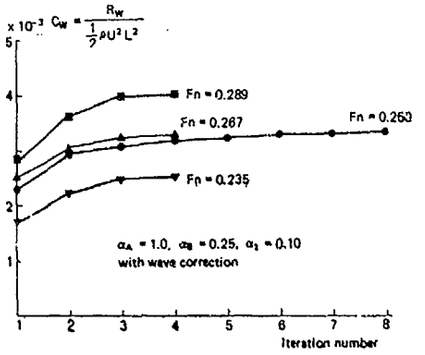

Fig.20 Change of Cw value due to iteration number for Model A

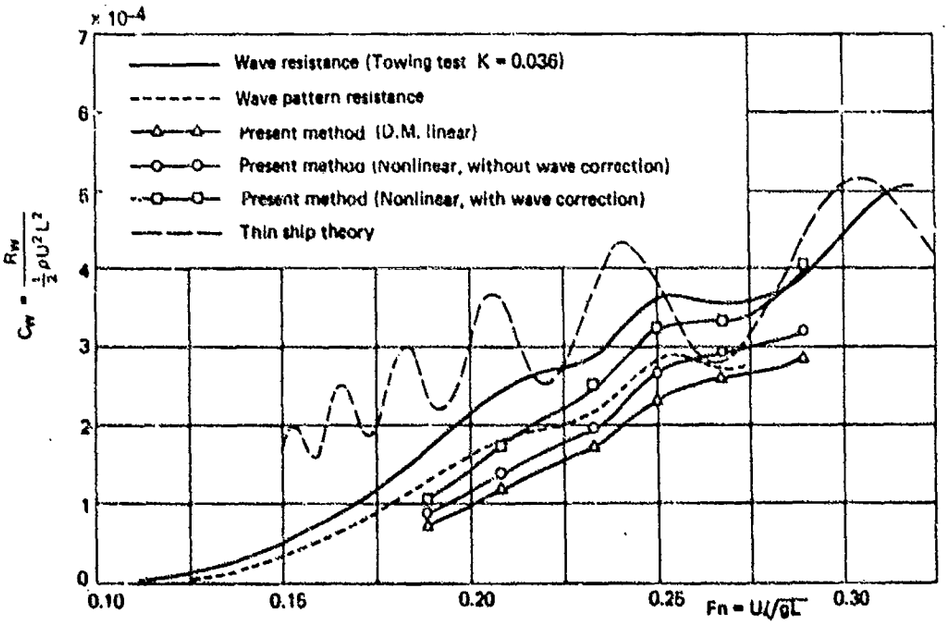

Fig.21 Comparison of wave resistance of Model A

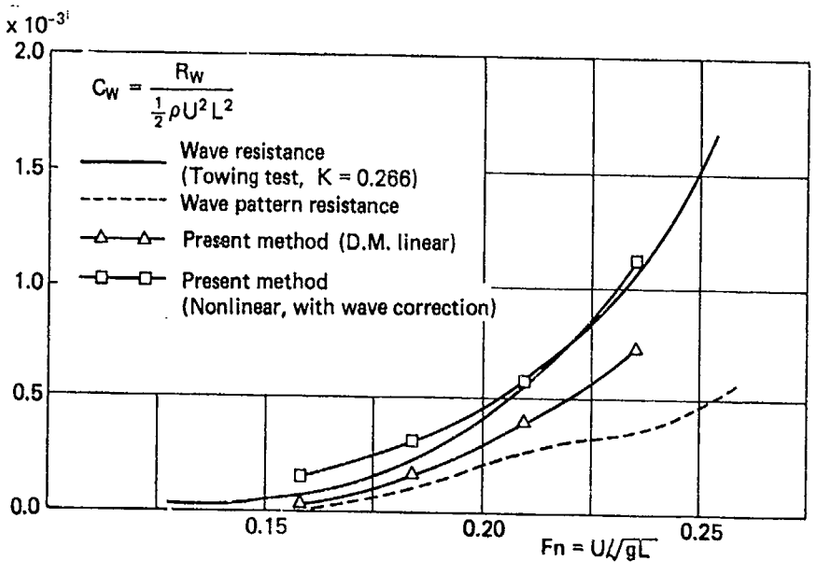

Fig.22 Comparison of wave resistance of Model B

where p_w is the pressure calculated at the still water surface. One can put $p_w=\rho g\zeta(x)$. Then the correction term to be added to equation (48) is

$$\Delta R_w = -\rho g\int_{-l}^{l}\zeta^2(x)\cdot n_x\cdot dx \qquad (50)$$

Fig.20 shows the result of computation of R_w of Model A at each step of iteration. It is observed that the iteration converges at above fourth step. Curves for the wave resistance coefficient as a function of Froude number computed by different methods are compared in Fig.21. In this figure, D.M.Linear means the double model linear solution which is the first approximation of the iteration procedure. The importance of the non-linear effect and that of the wave correction term ΔR_w are clearly observed.

Fig.22 compares the computed and measured wave resistance of Model B. In these figures, the results by the present method have attained a remarkable improvement in agreement with measurement.

8. Concluding remarks

The present work has proposed a method of theoretical computation for the wave pattern and wave resistance by which the non-linearity in the free surface condition is taken into account. The wave profile, pressure distribution on the hull surface and wave resistance of models with simple hull forms are computed and the results are compared with measurement in the towing tank. The conclusion is as follows.

(1) The results of computation by the present method show fairly good agreement with measurements, so that this method has a feasibility as a practical method of computation for arbitrary hull forms.

(2) The adoption of the relaxation factor α_1 and α_2 enables the iteration process to be stable. α_1 has a function of supressing non-linear instability at excessively high wave crest by which the wave breaking is liable to take place.

(3) The computed wave profile, pressure distribution and wave resistance show a plausible agreement with measurement in both fine and full models in general, but some discrepancy is observed in the wave profile and pressure distribution at the stern of full model where the boundary layer separation is likely to take place

(4) The non-linear effect is significant near the bow and stern ends of the hull where the wave crest is much steeper than that predicted by the double-model-linearized approximation.

(5) The wave resistance computed by the present method is considerably higher than that predicted by the double-model-linearized approximation.

Acknowledgements

The numerical work was carried out by using HITAC M-280H computer of the Computer Center of University of Tokyo, through the remote station at Yokohama National University Computer Center. The authors express their thanks to Dr.K.Suzuki and Mr.I.Okada for assistance in the computation.

The experimental work was carried out at the ship model basin of Research Institute of Ishikawajima-Harima Heavy Industries Co.,Ltd. The authors are grateful to Prof.T.Jinnaka, Dr.R.Tasaki, Mr.N.Namimatsu, Mr.T.Yamasaki and Dr.T.Tsutsumi for their useful advice.

References;

1. Tsutsumi,T.,Ogiwara,S., On the principal particulars of ship hull form and wave pattern resistance (II), Journ. Soc.Naval Arch. Japan Vol.137 (1975)
2. Wehausen,J.V., An approach to thin ship theory, Int.Seminar on Theoretical Wave Resistance, Ann Arbor (1963)
3. Maruo,H., A note on the higher order theory of thin ships, Bull. Faculty Eng. Yokohama Nat. Univ. Vol.15 (1966)
4. Eggers,K.W.H., Second oder contribution to ship waves and wave resistance, 6th Symp. Naval Hydro. Washington D.C. (1966)
5. Ogilvie,T.F., Wave resistance, the low speed limit. Rep.No.002, Dept. Naval Arch. Marine Eng. Univ. Michigan (1968)
6. Baba,E., Takekuma,K., A study on free surface flow around bow of slowly moving full forms, Journ. Soc. Naval Arch. Japan, Vol.137 (1975)
7. Maruo,H.,Suzuki,K., Wave resistance of a ship of finite beam predicted by the low speed theory, Journ. Soc. Naval Arch. Japan, Vol.142 (1977)
8. Dawson,C.W., A practical computer method for solving ship wave problem, 2nd Int. Conf. Numerical Ship Hydro., Berkeley (1977)
9. Ogiwara,S., A method to predict free surface flow around ship by means of Rankine sources, Journ. Kansai Soc. Naval Arch. Japan, Vol.190 (1983)
10. Chan,R.K.C.,Chan,F.W.K., Numerical solution of transient and steady free surface flow about a ship of general hull shape, 13th Symp. Naval Hydro., Tokyo (1980)
11. Aoki,k., Miyata,H., Masuko,A.,Kajitani,H., A numerical analysis of nonlinear wave generated by ships of arbitrary waterline, Journ. Soc. Naval Arch. Japan, Vol.154 (1983)
12. Ogiwara,S., A numerical method of non-linear solution for steady waves induced by two-dimensional submerged bodies, Journ. Soc. Naval Arch. Japan, Vol.156 (1984)
13. Ogiwara,S.,Maruo,H., A numerical method of non-linear solution for steady waves around ships, Journ. Soc. Naval Arch. Japan Vol.157 (1985)

DISCUSSION
of the paper
by Maruo and Ogiwara

"A METHOD OF COMPUTATION FOR STEADY SHIP-WAVES WITH NONLINEAR FREE SURFACE CONDITIONS"

DISCUSSION
by B.H. Cheng

(1) How sensitive are the values of the relaxation factors to ship geometry? Do you have to do a study on the relaxation factors for each new ship hull forms?

(2) The results from your paper seem to indicate that one of the effects of nonlinearity is to increase the wave resistance coefficient. However, in the paper authored by Lawrence K. Forbes, presented in this conference, the results seem to indicate that the nonlinear effects tend to decrease the wave resistance coefficient. Can you comment on these seemingly contradictory trends?

Author's Reply

We examined the behavior of relaxation factors relating to the stability of the solution. Fig. A shows the criterion of the stability for Model A. The region that gives a stable solution is reduced as Froude number and α_z increase. According to the computation results for several kinds of ship forms, the values of relaxation factors are sensitive to Froude number rather than to ship geometry.

Linear solution by using Rankine source distribution seems to give lower values of wave resistance than experimental values [14]. In the present method, the effect of nonlinearity appears remarkably in the bow wave as shown in Fig. B. Increase of wave resistance due to nonlinearity is caused by the increase of pressure acting on the hull at the bow wave.

[14] Dawson, C.W., "Calculation with the XYZ Free Surface Program for Five Ship Models", Proc. Workshop on Ship Waves Resistance Computations, DTNSRDC, Bethesda, 1979.

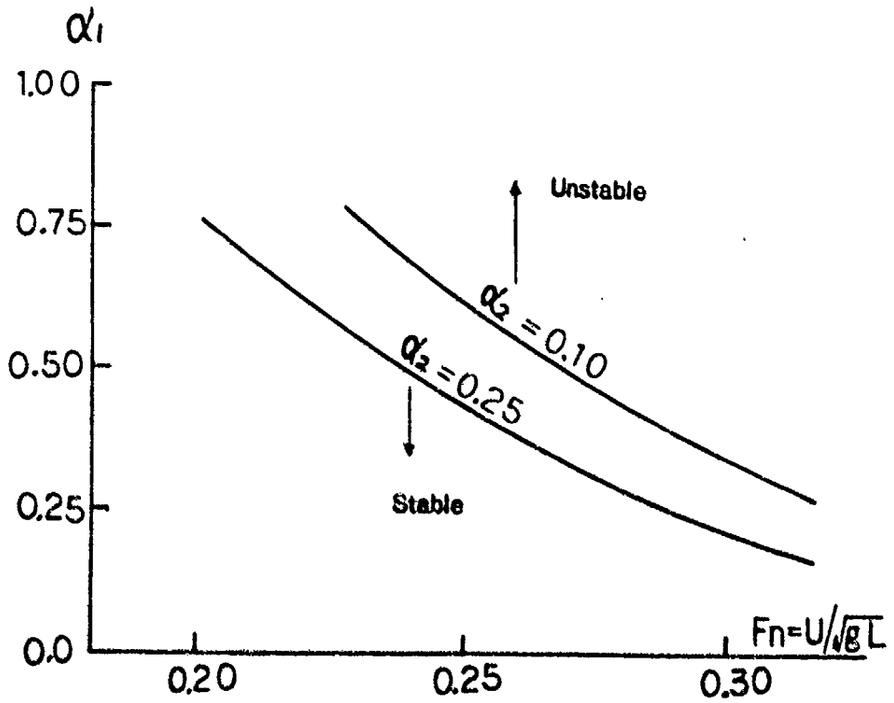

Fig.A Stability study on relaxation factors for Model A

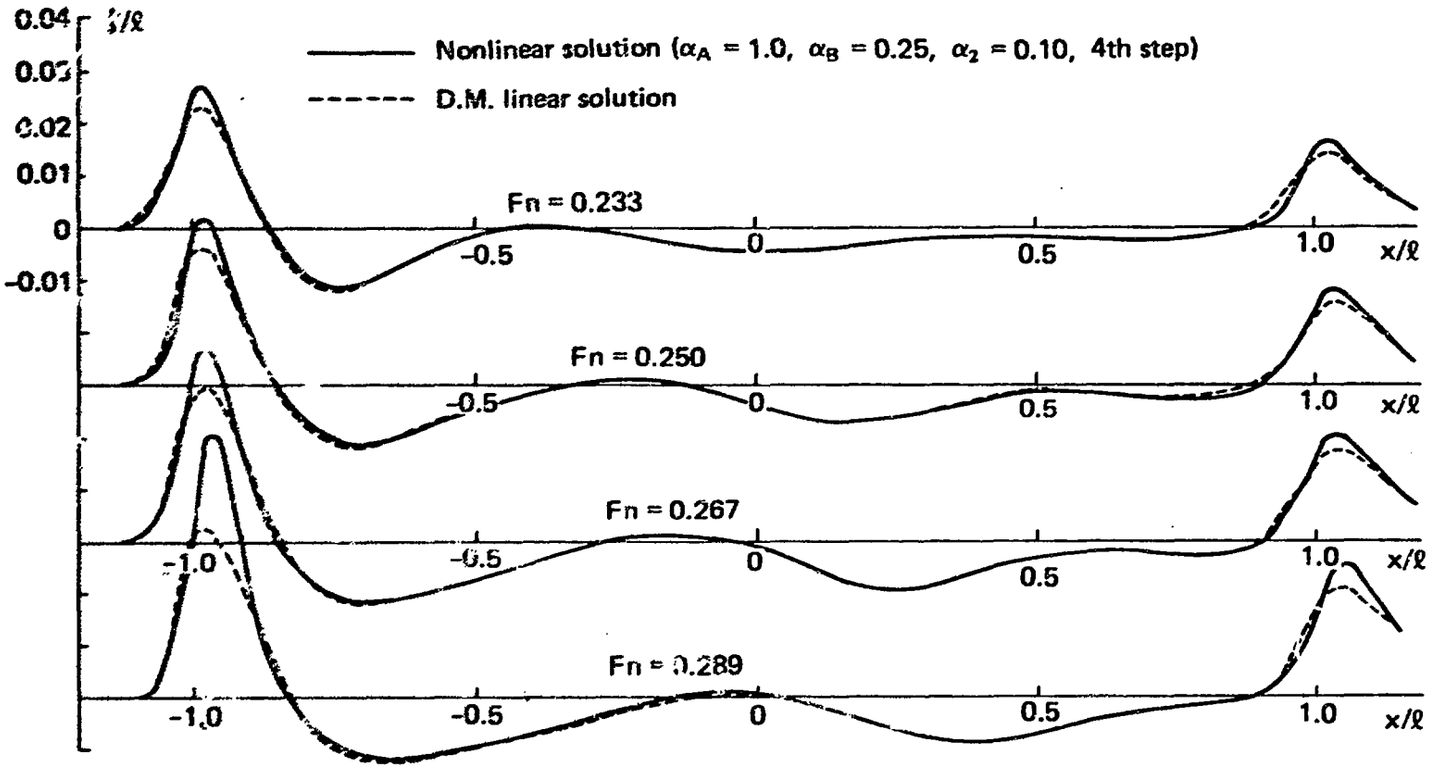

Fig.8 Comparison of wave profile on the hull surface of Model A

DISCUSSION
by S.M. Yen

The first order panel method of assuming constant source strength is known to be inappropriate because the solution is sensitive to the change in distribution of the size and shape of the panels. The problem may be alleviated by using either bilinear or quadratic source distributions. I would like to suggest that the authors use a higher order scheme in the future studies.

Author's Reply

We agree with Professor Yen's opinion. The higher order scheme will certainly improve the accuracy of results. Our aim is to devel-op a practical method of computation which is suitable to works of ship builders and ship designers in the practical field. Therefore we have employed the simplest method so as to minimize the complexity of computation algorithm and computer time. It is known that the method of Hess and Smith for the computation of the potential flow around a body in an unbounded fluid works well, and it employs the first order scheme of source distribution. This fact may become a basis of the feasibility of the present method. However we will examine in the future task the accuracy of our computation method including computations by a higher order scheme. Professor Yen's suggestion is very much appreciated.

DISCUSSION
by K. Mori

The authors simply concluded that the discrepancy seen in Fig. 18 is due to the neglect of viscosity. It may be true partially. But in your computation, you use just five panels behind the A.P. I suspect the effects of the downstream reflection is still existing.

Author's Reply

We have thoroughly examined the effect of truncation in the downstream boundary by the two-dimensional computation of the submerged cylinder, for which the effect of downstream truncation appears more seriously than in the three-dimensional case. The result shows that the finite difference from upstream is able to avoid the truncation effect including the wave reflection at the computation boundary. Therefore the results in the three-dimensional case do not suffer from the wave reflection effect.

DISCUSSION
by H. Wang

I wish to congratulate the authors on obtaining such good agreement with experimental results, particularly in the case of the wave resistance. In your approach it is necessary to take partial derivatives of the potential ϕ in order to obtain the wave resistance. It is well known that the accuracy of the derivatives is usually less that that of the function itself. For example, from my experience, I find that an approach similar to your Equation (48), where the calculated pressure is summed over all the panels, gives values of drag (for a body in infinite fluid) which deviate substantially from the theoretical value of zero. Is your reported value of wave resistance the difference between the value given by Equation (48) and a similar calculation for the infinite fluid case?

Also, have you made comparisons of the accuracy and computer time requirements of your method with those of the commonly used Neumann-Kelvin approach? Since only four iterations are needed to obtain convergence your method appears to be quite efficient. It has, of course, the added advantage that it takes better account of the free surface condition.

Author's Reply

Dr. Wang's discussion seems to have a common implication with the discussion by Professor Yen. We tried to make the computation scheme as simple as possible, because this kind of computation necessitates a long computing time even if a computer of large capacity is used. The present method is generally used in the case of computation of pressure distribution on a body in an unbounded fluid by means of the Hess-Smith method. We have not yet examined the accuracy of Equation (48) by carrying out the computation of infinite fluid case. This will become the future task of our work to examine the accuracy of our method, and we appreciate your suggestion. There have been several attempts of Neumann-Kelvin approach, but it is not applied to the case of full hull forms. As far as we know it is said that the computation of the Kelvin kernel is very difficult to attain a high accuracy level, unless a large computer time is consumed. The Rankine-source kernel employed in our method is much easier to handle in this respect.

NONLINEAR FLOW ABOUT A THREE-DIMENSIONAL TRANSOM STERN

Roderick M. Coleman

David W. Taylor Naval Ship Research and Development Center
Bethesda, Maryland 20084

Abstract

A finite difference method is used to analyze unsteady waves generated by the transom stern of a three-dimensional semi-infinite ship hull moving in the water surface. The flow is assumed to detach from the base of the transom or farther upstream if the hull pressure falls to zero. The wetted area of the hull is computed as part of the solution. A direct mapping is used to transform the irregular physical region into a box computational region. The mapping is chosen to ensure that the grid lines are concentrated in the areas in which accuracy is needed, such as near the point of contact between the free surface and the side walls. The solution is advanced in time by a marching scheme which couples the solution of the Laplace equation and hull boundary condition with the dynamic and kinematic free-surface conditions. All boundary conditions are treated in their fully nonlinear form so that the solution of the Laplace equation is computed using values at the exact hull and free-surface positions. Results are presented for a transom-stern hull and compared with linear and experimental results.

I. Introduction

The hydrodynamic responses of a ship are determined by the details of the flow near the bow and stern. Accordingly, many experimental and theoretical studies have been made of these flow fields, including the free-surface waves produced. Because of the difficulties involved, researchers have often restricted themselves to semi-infinite hulls with only a bow or stern. However, the complexity of the three-dimensional (3-D) formulation has limited most nonlinear studies of even these simpler problems to only two dimensions. Steady nonlinear flows generated by sterns of two-dimensional (2-D) semi-infinite hulls were investigated by Dagan & Tulin [1], Vanden-Broeck & Tuck [2], Vanden-Broeck et al [3], and Vanden-Broeck [4]. Haussling [5] and Coleman & Haussling [6] considered the unsteady nonlinear flows caused by transom sterns of 2-D, semi-infinite hulls.

When 3-D studies have been made, the problem has often been simplified by linearizing the governing equations or by making assumptions on the shape and speed of the hull or both. Casling [7] and Casling & King [8] assumed infinite Froude number in considering a planing hull with a low aspect ratio. The shape of the hull was restricted to ensure that the flow detached only at the transom stern. Van Eseltine & Haussling [9] studied the stern flow generated by a semi-infinite, 3-D transom stern hull moving at a constant speed. The location and shape of the hull were fixed, and the wetted area was determined as part of the linearized solution. In order to treat realistic hull shapes accurately, one nonlinear term had to be included in the boundary conditions. This indicated that consideration of nonlinear effects is crucial to the understanding of the complicated flow which occurs near the stern of a typical Navy combatant ship.

The current work extends the numerical scheme used by Van Eseltine & Haussling to treat the fully nonlinear 3-D problem. A single hull shape is considered for several draft-based Froude numbers. Pressures, wave elevations, and flow fields are presented and compared with linear, nearly-linear, and experimental results. Good agreement with these data is shown. The nonlinear solution is used to study details of the flow field which cannot be obtained from the linearized solution, such as the motion of the fluid about the stern but near the free-surface. This paper demonstrates the usefulness of the nonlinear solution in understanding the complicated free-surface problem for a given hull and range of Froude numbers.

II. Mathematical Formulation

We consider the flow resulting from the abrupt acceleration from rest to final speed U of a semi-infinite ship hull moving in a free water surface. The hull has no bow and forward of a certain station has a constant cross section of beam b and draft h. We assume that the flow is irrotational and that the fluid is incompressible and lacks surface tension. A

right-handed coordinate system moving with the hull has its origin at the intersection of the stern, the hull centerline, and the undisturbed free surface as illustrated in Figure 1.

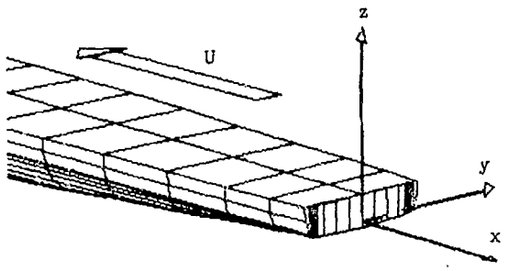

Figure 1: Transom Stern and Coordinate System

The fliud region is infinite in extent with the exception that it is bounded above by the wetted area of the hull, dO_H, and the free surface, dO_F, as shown in Figure 2.

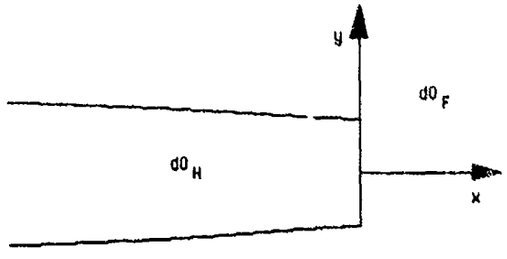

Figure 2: Aerial View of Stern and Coordinate System

We assume that the water surface can be described in parametric form at any time t by specifying z as a single-valued function of x and y: $z = \eta(x,y;t)$. The hull is described by $z = f(x,y)$ and thus $\eta = f$ in dO_H. We also assume the velocities, pressures, and the water surface all to be continuous for $t > 0$.

We further assume that the flow detaches at the base of the transom stern immediately after the abrupt acceleration. The wetted area is uniquely determined by two conditions: (1) the pressure on the part of the water surface that coincides with the hull must be greater than zero (atmospheric), and (2) the free water surface must be below the hull, i.e. $\eta < f$ for all (x,y) in dO_F where f is defined.

The length variables are nondimensionalized with respect to draft h, time with respect to h/U, and ϕ, the velocity potential relative to a reference frame at rest, with respect to hU. The initial/boundary value problem in the moving frame is as follows:

1. in the region occupied by the fluid

$$\phi_{xx} + \phi_{yy} + \phi_{zz} = 0 \qquad \begin{cases} -\infty < x,y < \infty \\ -\infty < z < 0 \end{cases} \tag{1}$$

2. at the hull (x,y in dO_H)

$$\phi_z = \eta_x + \eta_x\phi_x + \eta_y\phi_y \ , \ z = f \tag{2}$$

$$\eta = f(x,y) \tag{3}$$

$$p > 0 \tag{4}$$

3. at the free surface (x,y in dO_F)

$$\eta_t = -\eta_x - \eta_y\phi_y - \eta_x\phi_x + \phi_z \qquad z = \eta \tag{5}$$

$$\phi_t = -\eta_x - \eta/Fr^2 - (\phi_x^2 + \phi_y^2 + \phi_z^2)/2 \tag{6}$$

$$\eta < f(x,y) \quad \text{(where f is defined)} \tag{7}$$

4. in the far field

$$\phi_x = 0 \qquad x = \pm\infty \tag{8}$$

$$\phi_y = 0 \qquad y = \pm\infty \tag{9}$$

$$\phi_z = 0 \qquad z = -\infty \tag{10}$$

5. and initially (t = 0)

$$\phi = 0$$

$$\eta = \begin{cases} f(x,y) & x,y \text{ in } dO_H \\ 0 & \text{elsewhere} \end{cases} \tag{11}$$

where subscripts x, y, z, and t denote partial differentiation with respect to these variables and $Fr = U/\sqrt{gh}$ is Froude number based on draft.

The pressure on the hull can be computed from the Bernoulli equation

$$p = -\phi_t - \phi_x - f/Fr^2 - (\phi_x^2 + \phi_y^2 + \phi_z^2)/2 \qquad (12)$$

Therefore, we consider the pressure to be composed of a hydrostatic pressure p_h and a dynamic pressure p_d, where

$$p_h = -f/Fr^2 \qquad (13)$$

and

$$p_d = -\phi_t - \phi_x - (\phi_x^2 + \phi_y^2 + \phi_z^2)/2 \qquad (14)$$

III. Transformation and Numerical Scheme

Taking advantage of the symmetry about the centerline, we need consider only one-half of the physical region and thus can replace Equation (9) by

$$\phi_y = 0 \quad \text{at } y = -\infty \text{ and } y = 0 \qquad (15)$$

In addition, the physical region can be truncated suitably far upstream and downstream without loss of computational accuracy. Therefore, Equation (8) is approximated by

$$\phi_x = 0 \quad \text{at } x = -L1 \text{ and } x = +L2 \qquad (16)$$

where L1 and L2 are sufficiently large. To optimize the distribution of grid points, an exact mapping is applied in the y- and z-directions before the problem is discretized.

The mapping used is

$$y = a_1/(r+1) + a_2 r + (a_3/2)r^2 + (a_4/3)r^3 + (a_5/4)r^4 + a_6 \qquad (17)$$

and

$$z = (\ln(s))/c + \eta(x,r) \qquad (18)$$

These transformations are applied to map the infinite physical region in (x,y,z)-space onto a box computational region in (x,r,s)-space as seen in Figure 3. The parameters c and a_1 to a_6 are used to control the spacing of the grid lines in physical space. The transformation in the y-direction is the same as that used by Van Eseltine & Haussling [9]. In the nonlinear formulation, however, the transformation in the z-direction must be a function of η since the free-surface boundary condition is satisfied at $z = \eta$. This relationship introduces a time-dependency into the transformation so that the mapping adjusts automatically to changes in the shape of the free surface as the flow solution evolves.

The governing equations must then be transformed to the computational region according to the relations

$$\begin{aligned} (\phi_x)|_{y,z=\text{const}} &= (\phi_x)|_{r,s=\text{const}} - (\phi_s/z_s)(\phi_x)|_{r=\text{const}} \\ \phi_y &= \phi_r/y_r - (\phi_r/y_r)(\phi_s/z_s) \\ \phi_z &= \phi_s/z_s \end{aligned} \qquad (19)$$

where subscripts r and s denote partial differentiation.

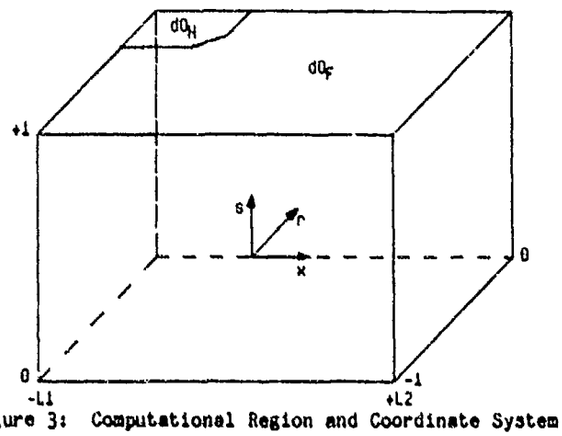

Figure 3: Computational Region and Coordinate System

Under this transformation, the Laplace equation becomes

$$A\phi_{xx} + B\phi_{rr} + C\phi_{ss} + D\phi_{xs} + E\phi_{rs} + F\phi_{s} + G\phi_{r} = 0 \qquad (20)$$

where

$$\begin{aligned} A &= 1 \\ B &= 1/y_r^2 \\ C &= c^2 s^2 (\eta_x^2 + \eta_r^2/y_r^2 + 1) \\ D &= -2cs\eta_x \\ E &= -2cs\eta_r/y_r^2 \\ F &= cs[\, 2c(\eta_x^2 + \eta_r^2/y_r^2) - \eta_{xx} + c \\ &\qquad - \eta_{rr}/y_r^2 + \eta_r y_{rr}/y_r^3 \,] \\ G &= -y_{rr}/y_r^3 \end{aligned} \qquad (21)$$

In the computational region, x derivatives imply that (r,s) rather than (y,z) are being held constant.

The domain of the computational region is replaced by a uniformly spaced 101 x 41 x 21 grid system. The grid spacing is defined by Δx in the x-direction, Δr in the r-direction, and Δs in the s-direction. The parameter c of Equation (18) is chosen to obtain the desired rate of expansion of z grid lines, while the parameters a_1 through a_6 are used to control the spacing of the y grid lines.

The time advancement of the solution of the boundary-value problem has three basic parts: 1) determining the wetted area of the hull, 2) advancing in time the free-surface elevation, η, and the free-surface potential, ϕ_f, and 3) solving the Laplace equation (20), given the boundary conditions of Equations (2), (10), (15), (16), and a known ϕ_f from part 2. A more complete discussion of the solution procedure, as applied to the linearized problem and including numerical instabilities that were encountered, can be found in Van Eseltine & Haussling [9].

A computer program was written for a Cray-1S computer to implement the nonlinear numerical scheme. The calculations were vectorized by using a "red-black" method of sweeping the grid for the iterative procedure. Each time step averaged four or five iterations and required about 0.75 seconds of central processor time. The solutions presented in this paper were computed for approximately 800 time steps, thus taking about 10 minutes of central processor time for each Froude number. By the last time step, the transient effects near the stern were no longer significant, and the flow near the stern could be considered almost at steady-state. The results presented are for these late times and therefore represent steady-state solutions.

IV. Results

The numerical scheme was applied to a semi-infinite hull whose cross-sectional shape varied with x to simulate the stern of a typical Navy combatant ship. Figure 4 shows the body plan of this hull and Table 1 gives the values of the pertinent parameters used in the numerical scheme.

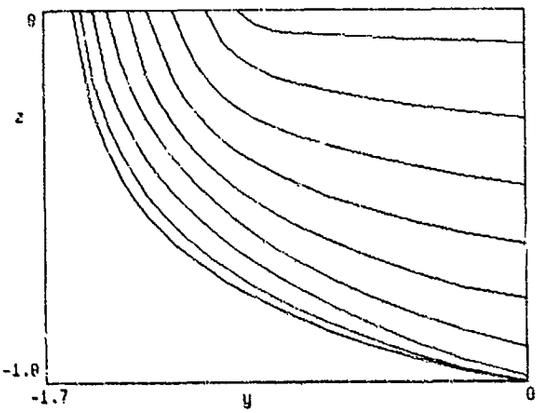

Figure 4: Body Plan of Hull

TABLE 1 - LIST OF PARAMETERS

Parameter	Value
b	3.15
L1	56.0
L2	24.0
dx	0.8
dr	0.025
ds	0.05
dt	0.25
c	0.4
a1	-0.1651
a2	19.8348
a3	-414.4292
a4	-2217.4637
a5	-2710.3631
a6	0.1651

The shape of the hull is the same as that of the model tested by O'Dea [10], except that the cross-sectional shape at the maximum beam

of the model was extended infinitely far upstream for use in the numerical scheme. A perspective view of a portion of the stern wave field produced by the computer program is displayed in Figure 5 for Fr = 1.66, in Figure 6 for Fr = 2.14, and in Figure 7 for Fr = 2.67. Also shown in these figures is the stern of the hull used in the experiment. As Fr increases, the first peak behind the transom moves farther downstream, and its amplitude tends to increase until Fr = 2.14 is reached, after which the amplitude decreases.

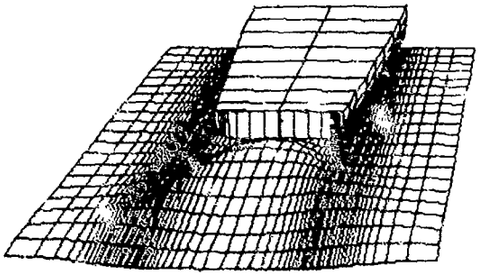

Figure 5: Computed Stern Wave Field for Fr = 1.66

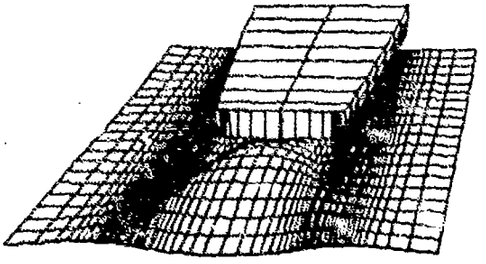

Figure 6: Computed Stern Wave Field for Fr = 2.14

Comparisons of computed and measured dynamic pressure on the hull centerline near the transom for Froude numbers 1.66, 2.14, and 2.67 are shown in Figure 8. Agreement is good with the greatest deviation occurring in the region near the transom. Also, the wave profiles in the report by O'Dea [10] indicate that the bow wave probably has more effect on

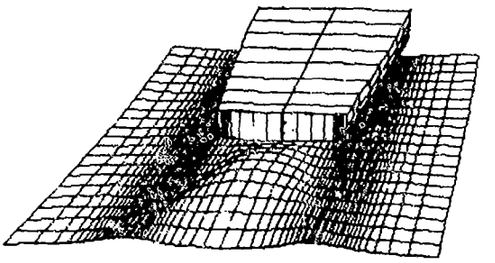

Figure 7: Computed Stern Wave Field for Fr = 2.67

the stern flow at higher Froude numbers due to longer wave lengths. Therefore, some of the disagreement between the computational and experimental results at the higher Froude numbers may be due to the bow wave which is not included in the numerical scheme.

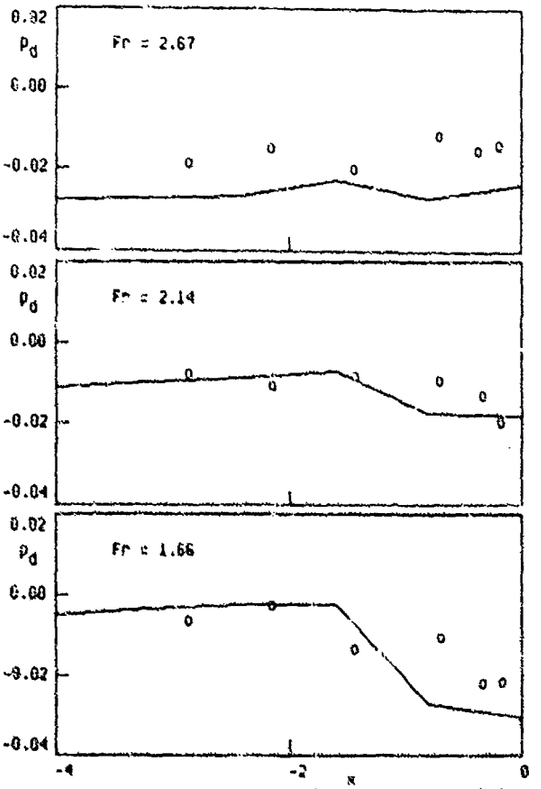

Figure 8: Computed (——) and Measured (o) Dynamic Pressure Near the Transom at Various Froude Numbers

Figures 9 through 13 display velocity vectors in various longitudinal planes for Fr = 1.66. The nonlinear effects are the largest while the bow wave effects are the smallest at this Froude number. It should be remembered that these velocity vectors were computed using the potential relative to a reference frame at rest, so that the magnitudes and directions indicated by these vectors are those induced, in water otherwise at rest, by the movement of the hull from right to left through the frame. It is also well to note that these vectors are two-dimensional and thus do not convey information about fluid motion in the transverse direction. The velocity vectors in the centerplane clearly show that the water beneath the stern is drawn upward to fill the region vacated by the retreating hull. An even larger upward motion is present immediately downstream from the stern. Here the water has just been released from the restriction imposed by the presence of the hull and responds by rising rapidly toward the mean water level. The upward motion of the water is so great that the mean water level is exceeded and an oscillatory wave field is established.

In each of these figures, a cross-section of the hull in the centerplane is shown and the mean water level is indicated. The wetted portion of the hull in the plane of interest is plotted as a solid line, and the free surface is shown as a broken line. As we move out into the fluid and away from the centerplane, the wetted portion of the hull is closer to the mean water level due to the curvature of the hull (Figures 10-13). The free surface may detach ahead of the transom in cross-sectional planes other than the centerplane as a result of interaction between flow dynamics and hull shape (Figures 11-13). In Figure 10, the wetted part of the hull continues to the transom, but the free surface leaves the hull at a slightly higher point than in the centerplane because of the curvature of the bottom of the transom. Figures 11 and 12 display transverse cross-sections in which the wetted part of the hull waterline does not extend to the transom since the detachment point occurs farther upstream. The cross-sectional plane illustrated in Figure 13 does not contain any portion of the hull, and therefore only the free-surface level is indicated.

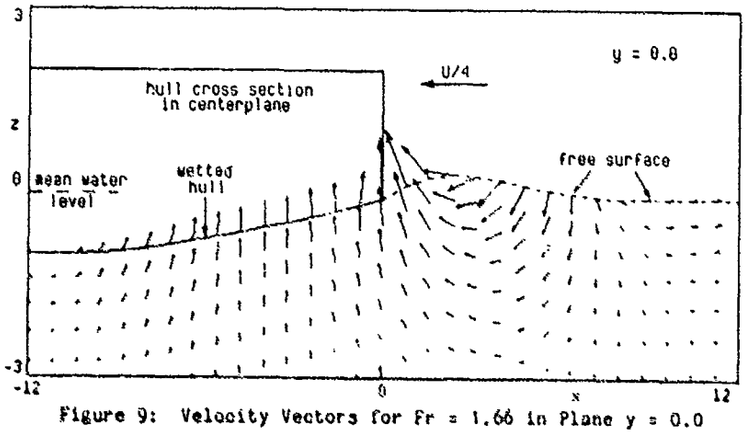

Figure 9: Velocity Vectors for Fr = 1.66 in Plane y = 0.0

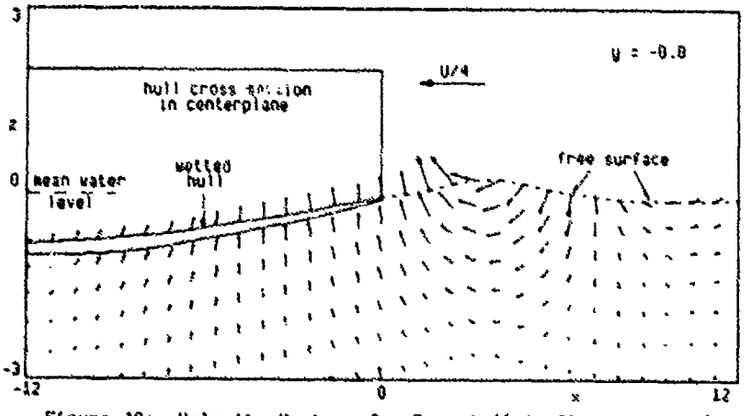

Figure 10: Velocity Vectors for Fr = 1.66 in Plane y = -0.8

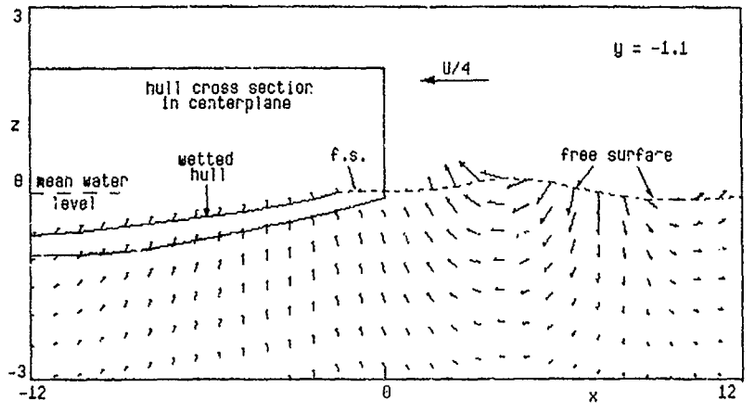

Figure 11: Velocity Vectors for Fr = 1.66 in Plane y = -1.1

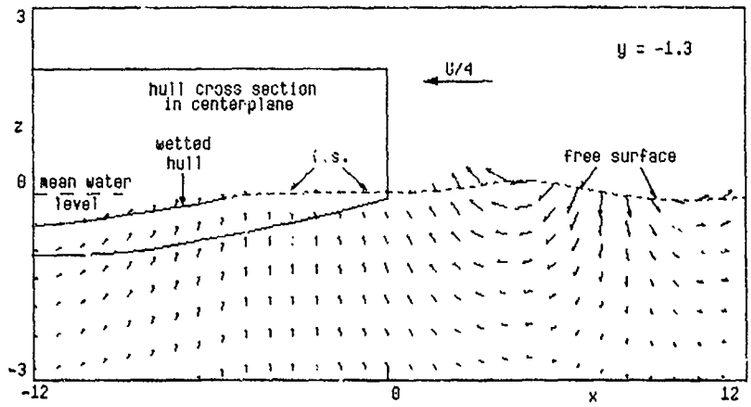

Figure 12: Velocity Vectors for Fr = 1.66 in Plane y = -1.3

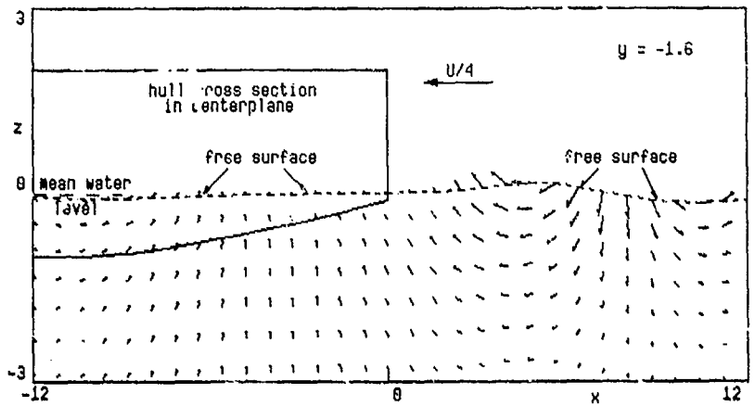

Figure 13: Velocity Vectors for Fr = 1.66 in Plane y = -1.6

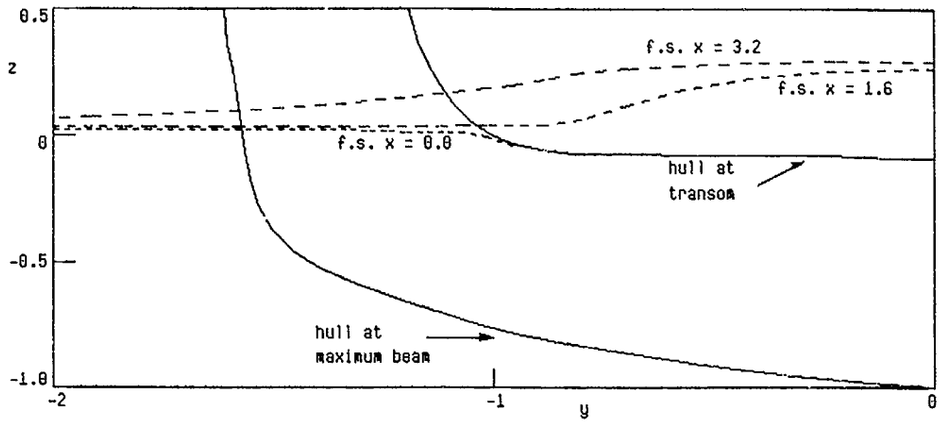

Figure 14: Nonlinear Free Surface for Fr = 1.66

Three beam-wise cross-sectional views of the nonlinear free surface for Fr = 1.66 are plotted in Figure 14. Also shown are cross-sectional views of the hull at the transom and at the point of maximum beam. At x = 0.0, the end of the hull, the free surface is in contact with the hull due to the detachment of the flow at the transom. At x = 1.6, just downstream of the transom, the free surface exhibits a region of high curvature directly behind the stern connecting a region of relatively undisturbed water away from the centerplane with a fairly broad wave elevation behind the stern. This region of high curvature has become less pronounced at x = 3.2 as the free surface reaches its maximum height behind the stern and the free-surface disturbance caused by movement of the hull spreads farther from the centerplane.

Velocity vectors in the transverse planes of Figure 14 are shown in Figures 15, 16, and 17. Figure 15 displays the velocity vectors at x = 0.0, just as the water leaves the hull. Here the water has a strong upward motion toward the centerplane which will produce the wave train behind the transom. In Figure 16, x = 1.6, the velocity vectors downstream of the transom are seen to have a similar pattern with the free surface approaching its maximum height above the mean level. The velocity vectors in Figure 17, x = 3.2, show that the water near the centerplane is now moving downward, indicating that the free surface has reached its peak in this region and is beginning to fall. This view also shows that the water farther from the centerplane has an upward and outward motion as the wave formed behind the transom begins to spread.

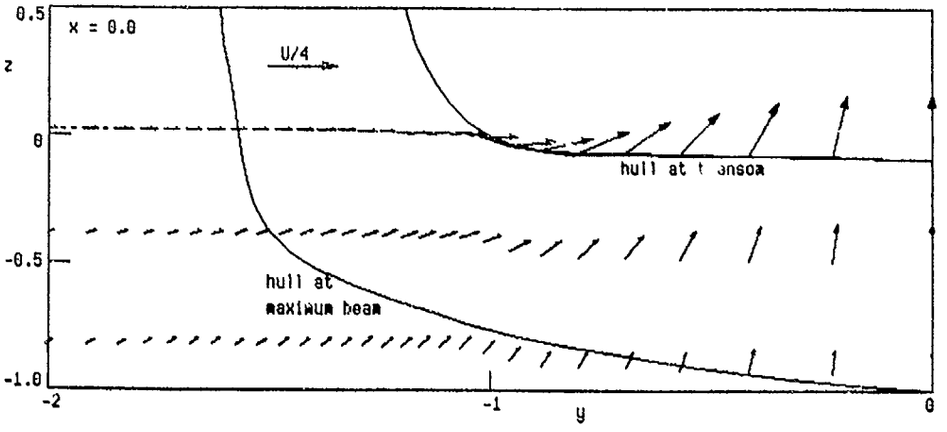

Figure 15: Velocity Vectors for Fr = 1.66 in Plane x = 0.0

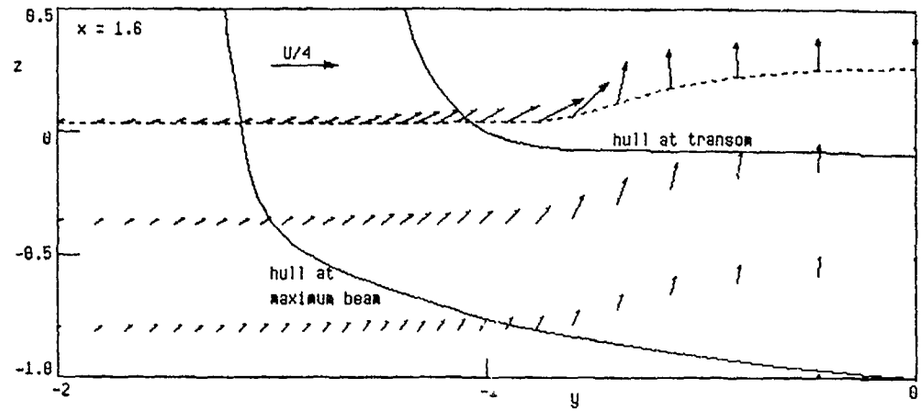

Figure 16: Velocity Vectors for Fr = 1.66 in Plane x = 1.6

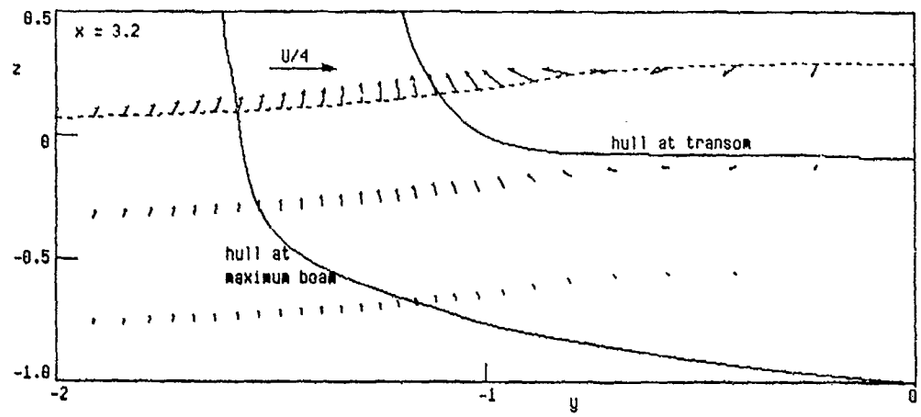

Figure 17: Velocity Vectors for Fr = 1.66 in Plane x = 3.2

Computed and measured wave elevations at various distances behind the stern are compared in Figures 18, 19, and 20. Each of these figures compares linear, nonlinear, XYZ Free Surface (XYZFS), and experimental results at various distances behind the transom for a particular Froude number. The linear results were obtained using the finite-difference program of Van Eseltine & Haussling [9]. That program, which also excludes bow effects, uses a formulation of the free-surface condition which includes a nonlinear term, $\eta_y \phi_y$, needed to handle the steep sidewalls of the hull. This nearly-linear boundary condition is satisfied at the mean water level. The XYZFS results were calculated with the 1984 version of that program [11], which uses a source distribution on both the body and free surface. The method satisfies the linearized free-surface and exact ship hull boundary condition at the hull surface below the undisturbed free surface. The entire hull, including the bow, is taken into account for the XYZFS calculations. The experimental results come from the report by O'Dea [10] who measured steady wave elevations downstream of the hull. All of the computed results appear to be in reasonable agreement with the experimental data. Differences can be attributed to inaccuracies in both the numerical and experimental procedures. The nonlinear results tend to indicate higher wave elevations than the linear results, although the shape of the free surface is virtually identical. In regions of greatest curvature, the nonlinear results are in better agreement with experimental values than are the XYZFS results which tend to "smooth-out" the free surface in these areas.

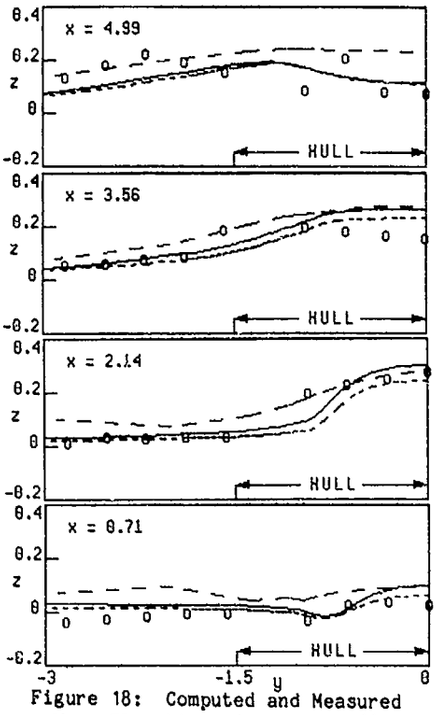

Figure 18: Computed and Measured Wave Elevations for Fr = 1.66
Nonlinear —— ; Linear ----;
Experiment o ; XYZFS – – –

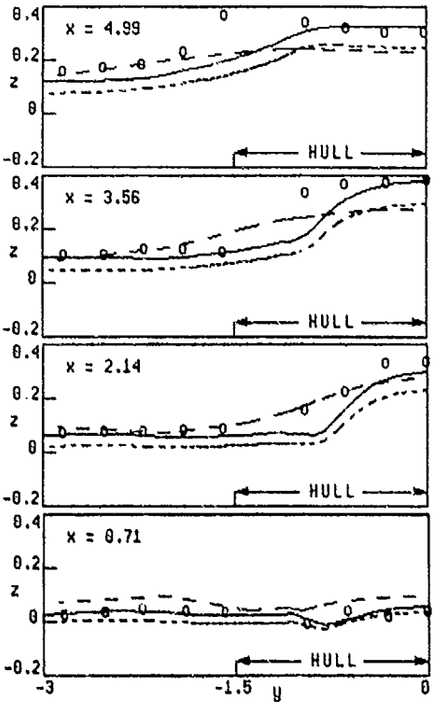

Figure 19: Computed and Measured Wave Elevations for Fr = 2.14
Nonlinear —— ; Linear ----;
Experiment o ; XYZFS – – –

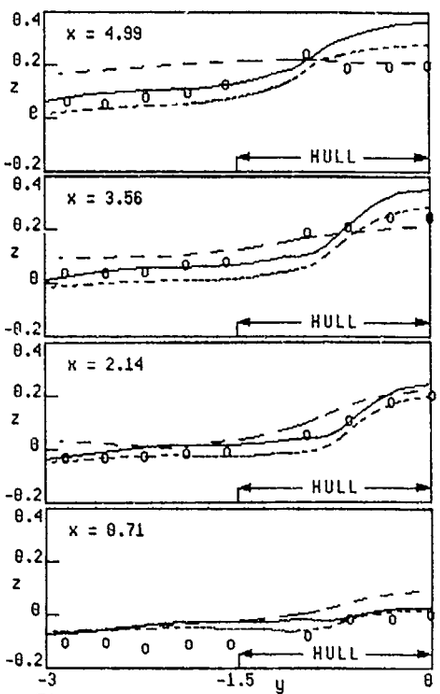

Figure 20: Computed and Measured Wave Elevations for Fr = 2.67
Nonlinear —— ; Linear ----;
Experiment o ; XYZFS – – –

These comparisons indicate that a particular computational method may produce wave heights which are closer to experimental values than those of another method for a given Froude number and distance from the hull. No single method considered here is clearly in better agreement with experiments for the range of Froude numbers and flow regions studied. However, the fully nonlinear scheme can provide the most complete picture of this complex flow-field since the solution is obtained at the exact free-surface and hull boundaries. In particular, the motion of the fluid near the hull and the surface can be studied using the nonlinear approach.

V. Conclusion

A numerical method has been developed and used to analyze the nonlinear waves generated by the stern of a 3-D semi-infinite hull in the water surface. The unsteady flows approached steady-state solutions asymptotically. The flow is assumed to detach from the base of the transom stern or farther upstream if the hull pressure fell to zero. The wetted area is computed as part of the solution.

As the Froude number increases for a realistically shaped hull, the wetted area tends to decrease and the location of the first peak behind the transom tended to move downstream. The amplitude of this peak

reached a maximum at Fr = 2.14. Wave elevations compared well with experimental data, especially in regions of high free-surface curvature. Also, the dynamic pressure was in good agreement with experimental results. This work demonstrates that a numerical scheme based on fully nonlinear free-surface potential flow can yield results useful in understanding the complex flow about transom sterns. Additional work is still needed to develop the capability of handling bow effects so that the entire ship hull can be included in the computational scheme.

VI. Acknowledgements

This work was supported by the Numerical Ship Hydrodynamics Program at the David W. Taylor Naval Ship Research and Development Center. This program is jointly sponsored by DTNSRDC and the Fluid Mechanics Program of the Office of Naval Research, Contract Number N0001484AF00001, NR-334-001. The author would like to thank Mr. Bill Cheng for his assistance in providing the XYZFS results.

VII. References

[1] Dagan, G. and M.P. Tulin, "Two-Dimensional Free-Surface Gravity Flow Past Blunt Bodies," J. Fluid Mech., Vol. 51, p.529 (1972).

[2] Vanden-Broeck, J.M. and E.O. Tuck, "Computation of Near-Bow or Stern Flows, Using Series Expansion in the Froude Number," Proc. of the Second International Conf. on Numerical Ship Hydrodynamics, University of California, Berkeley, CA, p. 371 (1977).

[3] Vanden-Broeck, J.M. et al, "Divergent Low Froude Number Series Expansion of Nonlinear Free-Surface Flow Problems," Proc. Roy. Soc. London, A 361, p. 207 (1978).

[4] Vanden-Broeck, J.M., "Nonlinear Stern Waves," J. Fluid Mech., Vol. 96, p. 603 (1980).

[5] Haussling, H.J., "Two-dimensional Linear and Nonlinear Stern Waves," J. Fluid Mech., Vol. 97, p. 759 (1980).

[6] Coleman, R.M. and H.J. Haussling, "Nonlinear Waves Behind an Accelerated Transom Stern," Proc. of the Third International Conf. on Numerical Ship Hydrodynamics, Paris, France, p. 111 (1981).

[7] Casling, E.M., "Planing of a Low-Aspect-Ratio Flat Ship at Infinite Froude Number," J. of Engineering Math., Vol. 12, No. 1, p. 43 (Jan 1978).

[8] Casling, E.M. and G.W. King, "Calculation of the Wetted Area of a Planing Hull with a Chine," J. of Engineering Math., Vol. 14, No. 3, p. 191 (Jul 1980).

[9] Van Eseltine, R.T. and H.J. Haussling, "Flow About Transom Sterns," Proc. of the Third International Conf. on Numerical Ship Hydrodynamics, Paris, France, p. 121 (1981).

[10] O'Dea, J. et al, "Flow Characteristics of a Transom Stern Ship," DTNSRDC Report 81/057 (Sep 1981).

[11] Dawson, C.W., "A Practical Computer Method for Solving Ship Wave Problems," Proc. of the Second International Conference on Numerical Ship Hydrodynamics, University of California, Berkeley, CA, p. 30 (1977).

DISCUSSION
of the Paper
by R. M. Coleman

NONLINEAR FLOW

DISCUSSION
by K. Eggers

For better understanding of your approach, could you tell me what happens if you invert the direction of the incoming flow input. Would you obtain a bow flow, i.e. the case of the ship traveling stern ahead? Would there be waves ahead of the body then?

Author's Reply

I would like to thank Prof. Eggers for raising an interesting question. If the direction of the flow were reversed, we should obtain a bow flow with a large bow wave but otherwise calm water ahead of the ship. However, this flow would be more complicated than the stern flow considered in this paper due to complications which arise in handling breaking waves and the intersection of the free surface and the hull. For the Froude numbers studied in the current work, the water leaves the hull smoothly with the detachment occurring either at the bottom of the transom or farther upstream. If we attempted to compute the flow generated by the body moving astern, we would be faced with the more difficult problem of determining the position of the contact line where the water surface meets the equivalent of a blunt bow. For Froude numbers of interest, the water surface cannot be assumed to be smooth in this region and might well be discontinuous if spray or breaking is present. In the mathematical formulation of the bow flow problem, we must allow for the presence of singularities along this contact line and it is not yet clear how to treat these singularities accurately. The singular nature of the contact line is a significant feature of the flow about surface-piercing bodies and one which requires a great deal of further study. Some of the papers presented at this conference address this important problem and should provide some insight into its solution.

NUMERICAL SOLUTION OF THE NONLINEAR SHIP WAVE PROBLEM[†]

R. R. Chamberlain[*] and S. M. Yen
Coordinated Science Laboratory, University of Illinois
Urbana, Illinois 61801

Abstract

This work presents the development of a new finite difference computational technique for the solution of the nonlinear ship wave problem. Previous computational complexities concerning implementation of the exact hull boundary condition, the open boundary condition and the nonlinear free surface conditions are resolved. The Laplace equation is solved by a fast direct method, while locally body fitted cooordinates are used to treat the exact hull geometry. The nonlinear free surface conditions are successively approximated by iteration, and the open boundary condition is found to be nonreflective. Results are presented for the thin ship, the Neumann-Kelvin and the full nonlinear problems. The nonlinear wave resistance is observed to behave in accordance with the thin ship results at low Froude numbers.

I. Introduction

The solution of the full nonlinear ship wave problem for arbitrary hull forms is recognized as one of the ultimate challenges of modern numerical ship hydrodynamics research. This paper presents the development of a general, time dependent finite difference approach to the solution of the nonlinear ship wave problem and describes how it differs from previous numerical approaches. Although we shall restrict our immediate attention to the Wigley hull, the method to be developed can be applied to other geometries as well. Since the present approach does contain several key concepts which differ in many important aspects from those previously considered, this paper shall compare and contrast our procedures with those of others.

Our initial study of the nonlinear ship wave problem for the Wigley hull began with a finite difference approach in which body fitted coordinates were used throughout the computational domain so as to properly accommodate the hull geometry. Furthermore, the motion of the free surface was followed by a time dependent mesh system which conformed to the boundary at each time step. This procedure has also been described by Chan [1] and by Chan and Chan [2]. The matrix structure arising from the finite difference representation of the Laplace equation in this nonorthogonal and time dependent mesh system was found to be extremely awkward. The matrix was non-symmetric and was not diagonally dominant, but we still applied successive line overelaxation to the solution of this problem. The convergence of this iterative method, if indeed it does converge under the present conditions, is generally quite slow. However, in all cases using the body fitted mesh system about the Wigley hull, we found that the iterative method did not converge sufficiently to give an accurate prediction of wave resistance.

Another point under study was the treatment of the downstream or open boundary condition. When using a time dependent approach for surface wave problems, it is usually thought that one must provide a means for the waves to cleanly pass through

[†] This work supported by the Office of Naval Research under Contract N00014-80-C-0740

[*] Present Address: Department of Aerospace Engineering, University of Alabama, University, AL 35486

S. M. Yen, Coordinated Science Laboratory, 1101 W. Springfield, Urbana, IL 61801

the boundary of a finite computational region. Methods have been developed [1] based on a scheme proposed by Orlanski [3] to allow the specification of the flow variables at such an open boundary. We have found, however, that specifying the solution at the downstream boundary drastically reduces the efficiency of solving the nonlinear ship wave problem. Furthermore, there is an alternative treatment which gives valid results and which is simpler in the sense that the issue of accurately estimating advection speeds can be avoided.

The purpose of the present study is to explore some recent developments which have been designed to alleviate the previous computational difficulties. We shall begin with a review of the governing equations followed by the development of the numerical solution technique. The basic algorithm is then applied to the linearized, the Neumann-Kelvin and the full nonlinear problems for the case of the Wigley hull.

II. Governing Equations and Boundary Conditions

The Wigley hull is placed symmetrically within a three dimensional domain so that only half of the flow field needs to be considered (Fig. 1). In cartesian coordinates the governing equation is the Laplace equation, which is written in terms of the perturbation potential ϕ as

$$\nabla^2\phi = \phi_{xx} + \phi_{yy} + \phi_{zz} = 0 . \qquad (1)$$

The kinematic condition at the free surface, stating that no fluid may cross the boundary is

$$\eta_t + (U_s + \phi_x)\eta_x + \phi_y\eta_y = \phi_z . \qquad (2)$$

The function $\eta(x,y;t)$ is the free surface height above an arbitrary reference plane which initially coincides with the xy plane. Furthermore, U_s is the instantaneous speed of the ship in the $-x$ direction.

We also have the dynamic condition which requires the pressure to be zero on the free boundary. In a reference frame which moves with the ship, this condition is written on $z = \eta(x,y;t)$ as

$$\phi_t + U_s\phi_x + \frac{1}{2}(\phi_x^2 + \phi_y^2 + \phi_z^2) + \frac{\eta}{Fr^2} = 0. \qquad (3)$$

In the above equations, all lengths are nondimensionalized by the ship length, L, velocity by the maximum forward speed, U_∞, and time by L/U_∞. The Froude number, Fr, is defined $Fr = \frac{U_\infty}{(gL)^{1/2}}$. We note also that the range for U_s is $0 \le U_s \le 1$ since the instantaneous speed of the ship changes during its initial acceleration up to the maximum speed U_∞.

The remaining boundary conditions for $\phi(x,y,z;t)$ may be summarized as follows:

$$\begin{aligned} &\phi_x = 0 , && \text{upstream} \\ &\phi_x = 0 , && \text{downstream} \\ &\phi_y = 0 , && \text{symmetry} \\ &\phi_y = 0 , && \text{lateral} \\ &\phi_z = 0 , && \text{bottom.} \end{aligned} \qquad (4)$$

The exact hull boundary condition, requiring that the resultant fluid velocity relative to the moving ship be tangent to the surface, is stated as

$$\nabla\phi \cdot \hat{n} = \frac{U_s f_x}{\gamma_1} \qquad (5)$$

where $\hat{n}$ is the unit normal vector (positive into the fluid) and $y = f(x,z)$ describes the shape of the hull. The cartesian components of $\hat{n}$ are expressed as $(-f_x/\gamma_1, 1/\gamma_1, -f_z/\gamma_1)$ in which $\gamma_1 = (1 + f_x^2 + f_z^2)^{1/2}$. For the present study, we consider the Wigley hull which is defined by the equation

$$f(x,z) = \frac{b}{2}(1 - 4x^2)(1 - (z/h)^2) \qquad (6)$$

for $-\frac{1}{2} \le x \le \frac{1}{2}$ and $-h \le z \le 0$. The parameters b and h are defined as b = beam = 0.10 and h = draft = 0.0625.

The Neumann-Kelvin problem is recovered from the full nonlinear problem by simply neglecting the nonlinear terms in Eqs. (2) and (3). The linearized free surface conditions thus become

$$\eta_t + U_s\eta_x = \phi_z \qquad (7)$$

and

$$\phi_t + U_s\phi_x + \frac{\eta}{Fr^2} = 0 . \qquad (8)$$

These conditions are now applied on the plane of the undisturbed free surface, i.e., on $z = 0$. The remaining boundary conditions, particularly the exact hull condition, are unaltered in this formulation. The fully linearized problem, however, makes one further simplification and approximates the hull boundary condition as

$$\phi_y = U_s f_x \tag{9}$$

and applies it on the hull centerplane, y=0, as opposed to the exact hull location, $y = f(x,z)$.

III. Development of the Numerical Method

For any time dependent, finite difference approach to the nonlinear ship wave problem, the most time consuming task is the numerical solution of the Laplace equation at each time step. It is thus very important to have an extremely efficient numerical technique. The most efficient algorithms belong to the class of direct methods, as discussed by Ohring [4]. The present algorithm is a very general approach based on the FFT and is described by Swartztrauber and Sweet [5].

Consider the general Poisson equation in cartesian coordinates, for which the seven point difference approximation is

$$\begin{aligned} & C_1[\phi_{i-1,j,k} - 2\,\phi_{i,j,k} + \phi_{i+1,j,k}] \\ & + C_2\,[\phi_{i,j-1,k} - 2\,\phi_{i,j,k} + \phi_{i,j+1,k}] \\ & + a_k\,\phi_{i,j,k-1} - b_k\,\phi_{i,j,k} \\ & + c_k\,\phi_{i,j,k+1} = r_{i,j,k}\,. \end{aligned} \tag{10}$$

The constants C_1 and C_2 are $\frac{1}{\Delta x^2}$ and $\frac{1}{\Delta y^2}$, respectively, while the variable coefficients in the z direction are defined as

$$\begin{aligned} a_k &= \frac{2}{h_{k-1}(h_k + h_{k-1})} \\ b_k &= \frac{2}{h_k\, h_{k-1}} \\ c_k &= \frac{2}{h_k(h_k + h_{k-1})} \end{aligned} \tag{11}$$

where $h_k = z_{k+1} - z_k$. These definitions allow the use of nonuniform grid spacing in the vertical direction so that the shallow draft of the Wigley hull can be accommodated without using an excessive number of grid points.

We now assume that the solution and the right hand side can be written as

$$\phi_{i,j,k} = \sum_{\ell=1}^{L} E_{\ell,L}\, \bar{\phi}^{\ell}_{j,k} \cos(\ell-1)\theta_i \tag{12}$$

and

$$r_{i,j,k} = \sum_{\ell=1}^{L} E_{\ell,L}\, \bar{r}^{\ell}_{j,k} \cos(\ell-1)\theta_i \tag{13}$$

where $\theta_i = \frac{(i-1)\pi}{(L-1)}$ for $i=1,2,\ldots,L$. The normalizing factor $E_{i,j}$ is defined as

$$E_{i,j} = \begin{cases} 1/2 & \text{if } i=1 \text{ or } i=j \\ 1, & \text{otherwise.} \end{cases}$$

In the x direction, the Fourier coefficients of the solution and the right hand side are represented by $\bar{\phi}^{\ell}_{j,k}$ and $\bar{r}^{\ell}_{j,k}$, respectively. It can be seen from Eqs. (12) and (13) that the number of coefficients required to exactly represent the solution and the right hand side in the x direction is just L, the total number of x grid points. Furthermore, the cosine transform is used since it satisfies the boundary conditions $\phi_x = 0$ exactly at both the upstream and downstream boundaries.

We now substitute Eqs. (12) and (13) into Eq. (10), multiply through by $E_{i,L}$ $\cos(m-1)\,\theta_i$ and sum over the range of i. Using the orthogonality relations

$$\sum_{i=1}^{L} E_{i,L} \cos(\ell-1)\theta_i \cos(m-1)\theta_i = \begin{cases} \frac{(L-1)}{2} & \text{if } \ell = m \neq 1 \text{ or } L \\ L-1 & \text{if } \ell = m = 1 \text{ or } L \\ 0 & \text{if } \ell \neq m \end{cases}$$

and

$$\sum_{i=1}^{L} E_{i,L} \sin(\ell-1)\theta_i \cos(m-1)\theta_i = 0\,,$$

we obtain the system

$$C_2[\bar{\phi}^{\ell}_{j-1,k} - 2\bar{\phi}^{\ell}_{j,k} + \bar{\phi}^{\ell}_{j+1,k}] + a_k\bar{\phi}^{\ell}_{j,k-1}$$

$$- b_k\bar{\phi}^{\ell}_{j,k} + c_k\bar{\phi}^{\ell}_{j,k+1} - \lambda_{\ell}\bar{\phi}^{\ell}_{j,k} = \bar{r}^{\ell}_{j,k} \quad (14)$$

in which $\lambda_{\ell} = 4C_1\sin^2\frac{(\ell-1)\pi}{2(L-1)}$ for

$\ell=1,2,\ldots,L$.

By applying the above procedure in the x direction, we have uncoupled the finite difference equations so that there is no longer any x (i) dependence. We now have a sequence of L two dimensional linear systems to be solved. This sequence can be further reduced to LxM tridiagonal systems (one dimensional) by transforming in the y (j) direction, which contains M unknowns per mesh line. A completely analogous transformation then yields

$$a_k\bar{\bar{\phi}}^{\ell,m}_{k} - [b_k + \lambda_{\ell} + \lambda_m]\bar{\bar{\phi}}^{\ell,m}_{k}$$

$$+ c_k\bar{\bar{\phi}}^{\ell,m}_{k+1} = \bar{\bar{r}}^{\ell,m}_{k} \quad (15)$$

in which $\lambda_m = 4C_2\sin^2\frac{(m-1)\pi}{2(M-1)}$ for

$m=1,2,\ldots,M$.

The procedure for the exact solution of the Poisson equation in a three dimensional region is now outlined as follows. The right hand side of Eq. (15) is obtained in two steps as

$$\bar{r}^{\ell}_{j,k} = \sum_{i=1}^{L} E_{i,L}\, r_{i,j,k}\cos(\ell-1)\theta_i \quad (16)$$

for $\ell=1,2,\ldots,L$ and all j,k followed by

$$\bar{\bar{r}}^{\ell,m}_{k} = \sum_{j=1}^{M} E_{j,M}\,\bar{r}^{\ell}_{j,k}\cos(m-1)\theta_j \quad (17)$$

for $m=1,2,\ldots,M$ and all ℓ, k (θ_j is analogous to θ_i). Once $\bar{\bar{r}}^{\ell,m}_{k}$ is known, Eq. (15) is solved for each vertical (z) mesh line to obtain $\bar{\bar{\phi}}^{\ell,m}_{k}$. The exact solution $\phi_{i,j,k}$ is then found in two steps as

$$\bar{\phi}^{\ell}_{j,k} = \sum_{m=1}^{M} E_{m,M}\,\bar{\bar{\phi}}^{\ell,m}_{k}\cos(m-1)\theta_j \quad (18)$$

for $j=1,2,\ldots,M$ and all ℓ,k followed by

$$\phi_{i,j,k} = \sum_{i=1}^{L} E_{i,L}\,\bar{\phi}^{\ell}_{j,k}\cos(\ell-1)\theta_i \quad (19)$$

for $i=1,2,\ldots,L$ and all j,k. The Fourier sums in Eqs. (16)-(19) are efficiently computed using an FFT routine. We note that there are no restrictions on the number of grid points in any direction, and thus the programmer has great flexibility in designing the mesh system.

Implementation of the Boundary Conditions

The boundary conditions in Eqs. (4) are directly implemented through the use of the cosine transform, or, in the case of $\phi_z = 0$, in the tridiagonal solution of Eq. (15). The right hand side of the Laplace equation remains zero even at these boundaries since the zero gradient conditions do not introduce any source terms. The only non-zero terms which appear on the right hand side do so at the hull and the free surface.

For the fully linearized problem, the hull and free surface conditions are implemented in a straightforward manner. The hull condition of Eq. (9) simply modifies the right side of Eq. (10) on the centerplane grid points. The free surface conditions, Eqs. (7) and (8), are advanced in time using the numerical scheme of Chan [1], and the new values of ϕ at the free surface are used as Dirchlet conditions for the Laplace equation. Since these conditions are always applied on the plane z=0, the coefficients a_k, b_k and c_k in Eq. (10) are constant in time.

The mesh system used for the implementation of the exact hull and nonlinear free surface conditions is shown in Fig. 2. This system is locally body fitted so that the hull geometry is exactly accommodated while the interior field is described by a cartesian grid. Furthermore, the top grid plane, orignally representing z=0, is now allowed to move with the free surface so that the z coefficients in Eq. (10) now vary with time. This variation, however, is limited to the first grid plane below the free surface.

The linearized and exact implementations of the hull condition are compared in Fig. 3. In both cases, the fictitious quantity $\phi_{i,0,k}$ is eliminated from the finite difference system using the boundary condition. This implementation differs from that used by Ohring and Telste

[6,7] in that no Taylor series approximations are used to simulate the actual hull. This treatment, however, still requires a modification of the fast Poisson solver since the grid is no longer entirely rectangular. The capacitance matrix technique is used for this purpose, and an excellent discussion of this method is given by Buzbee [9]. The basic idea is that two fast direct solutions plus the solution of a small, dense matrix system will provide the exact solution to the finite difference equations in this locally body fitted mesh system. A simple test problem showing the accuracy of this technique is described in [8].

With the linearized free surface conditions applied on the plane z=0, the modified Poisson solver may be applied directly to the solution of the Neumann-Kelvin problem. However, since the capacitance matrix technique requires that the geometry remain fixed, an additional modification is necessary in order to apply the Dirichlet conditions for ϕ on the moving free surface. We first define the matrix A such that the linear system $A\phi = r$ describes the discretization of the Laplace equation in the region whose boundaries include the exact hull and the moving free surface. Similarly, we define the matrix B to be that for the Neumann-Kelvin problem, since linear systems involving B are efficiently solved by the modified fast Poisson solver. Now consider the splitting $A = B - N$, where N represents only the time dependent part of A due to the motion of the free surface. This leads naturally to the following iteration to solve $A\phi = r$:

$$B\phi_{s+1} = r + N\phi_s \qquad (20)$$

where s denotes the iteration count. The new right hand side of Eq. (20) is again zero everywhere except near the hull and free surfaces. Furthermore, since N involves only the time dependent equations near the free surface, it allows the Dirichlet conditions there to be increasingly better approximated at each iteration.

We now make some comments concerning the optimization of the fast Poisson solver. Since the right hand side of the Laplace equation is entirely zero below the keel of the ship, we see from Eqs. (16) and (17) that the Fourier coefficients are also zero. It is thus not necessary to provide storage for these quantities. In addition, since we are only interested in the solution for ϕ near the free surface and on the hull, we do not need to compute the Fourier amplitudes or store the solution in the region below the keel. This is seen to be possible upon consideration of Eqs. (18) and (19) where it is observed that the solution in the region of interest depends only upon the Fourier amplitudes in the xy planes. Thus, only the Fourier data between the keel and the free surface are required.

Finally, we observe that the downstream condition $\phi_x = 0$ is necessary for the storage and computational efficiency of the present method. The specification of the solution for ϕ at the downstream boundary would introduce non-zeros on the right hand sides of Eqs. (10) and (15). In this case, the solution would have to be computed and stored in the entire region, and this would seriously degrade the efficiency of the present optimized solver.

IV. Results

The present time dependent, finite difference technique is first applied to the linearized, thin ship problem for the purpose of resolving the issue of the open boundary condition $\phi_x = 0$. We consider two domain sizes, 6.6 x 2.0 x 1.0 and 4.95 x 2.0 x 1.0, containing 129 x 33 x 20 and 97 x 33 x 20 grid points, respectively. For these cases, we note that it was only necesarry to compute and store the solution for ϕ on 7 horizontal (xy) planes since this is the number of z grid points used between the free surface and the keel. We compare the surface wave patterns for these domains at t = 7, 8 and 9 in Fig. 4. This figure shows that the steady state solution is independent of the domain length. This is strong numerical evidence for the use of our simple open boundary treatment since any adverse effects on the solution would clearly be evident in this comparison. Furthermore, we have observed that the solutions on the hull surface are identical for both domains. Since less computational work is involved in the short domain, this is the one we have used throughout this study.

In order to validate the present method for the linearized problem, we compare in Fig. 5 the steady state (t = 9) hull wave profile for Fr = 0.266 with that from the classical Michell solution (η nondimensionalized by $U_\infty^2/2g$). The agreement is seen to be quite good. Figure 6 shows a similar comparison with an experiment by Shearer and Cross [10] for Fr = 0.350. The qualitative features for this case have also been reproduced well by the present numerial approach.

The implementation of the nonlinear

boundary conditions at the exact location of the free surface requires several iterations, according to Eq. (20). Our computer code uses the iteration parameter IC, defined so that IC-1 iterations are performed. Figure 7 shows the effect of IC = 2, 4 and 6 on the hull wave profiles at t = 9 for Fr = 0.233. The differences in the profiles are insignificant, and typically two or three iterations are sufficient.

We now conclude this section with a discussion of the wave resistance. This quantity is computed at each time step by integrating the pressure obtained from Bernoulli's equation. The wave resistance coefficient C_w is just the resistance nondimensionalized by $\frac{1}{2}\rho_\infty U_\infty^2 S$, where S is the wetted hull area at rest. Figure 8 shows the comparison of C_w vs. Fr for the thin ship, the Neumann-Kelvin and the full nonlinear problems. Both of the linearized calculations exhibit the characteristic humps and hollows in C_w, while the nonlinear curve is not as exaggerated. It is interesting to note that the nonlinear effect on the wave resistance is most pronounced for moderate Froude numbers, $0.25 < Fr < 0.30$. For low Froude numbers, the nonlinear and thin ship results exhibit the same trend, as would be expected when the slope and amplitude of the waves are small.

V. Summary

The present numerical development has been designed to specifically address several key computational issues which are inherent in the nonlinear ship wave problem. Instead of using slowly convergent iterative methods for the Laplace equation, we employ a fast Poisson solver to obtain the exact solution to the linear system. This choice necessitates the concept of the locally body fitted mesh system for implementation of the exact hull condition since most of the domain must remain cartesian. The irregular computational stars arising from the deformed region on and adjacent to the hull are handled exactly by the capacitance matrix method. Furthermore, in order to optimize the direct solver by not computing or storing the potential at any grid point below the keel, we apply the condition $\phi_x = 0$ at both the upstream and downstream boundaries. This treatment of the open boundary has been shown by numerical experiments to be accurate.

Wave profiles, surface wave patterns and wave resistance coefficients are calculated for the Wigley hull using the present method. The results are seen to reproduce the features of linearized theory and experiments. For low Froude numbers, the nonlinear wave resistance reduces the behavior which is predicted by the thin ship results.

Three computer codes were used to compute the present results. These codes, along with a detailed users manual, will be made available upon request to those interested.

References

1. Chan, R.K.-C, "Finite Difference Simulation of the Planar Motion of a Ship," Proceedings of the Second International Conference on Numerical Ship Hydrodynamics, University of California, Berkeley, CA, September 1977, pp. 39-52.

2. Chan, R.K.-C. and F.W.-K. Chan, "Numerical Solution of Transient and Steady Free Surface Flows About a Ship of General Hull Shape," Tokyo Conference, 1980.

3. Orlanski, I., "A Simple Boundary Condition for Unbounded Hyperbolic Flows," J. Comp. Phys. 21 (1976), p. 251.

4. Ohring, S., "A Fast Fourth Order Laplace Solver for Application to Numerical Three Dimensional Water Wave Problems," First International Conference on Numerical Ship Hydrodynamics, Gaithersburg, MD, October 1975, p. 641.

5. Swartztrauber, P. and R. Sweet, "Efficient FORTRAN Subprograms for the Solution of Elliptic Partial Differential Equations," NCAR TN/IA-109, 1975.

6. Ohring, S. and J. Telste, "Numerial Solution of Transient Three Dimensional Ship Wave Problems," Second International Conference on Numerical Ship Hydrodynamics, University of California, Berkeley, September 1977, p. 86.

7. Ohring, S. and J. Telste, "The Direct Matrix Imbedding Technique for Computing Three Dimensional Potential Flows About Arbitrarily Shaped Bodies," Comp. Meth. in Apl. Mech. and Eng. 21 (1980), p. 315.

8. Chamberlain, R. R. and S. M. Yen, "Numerical Solution of the Nonlinear Ship Wave Problem," Report T-150, Coordinated Science Laboratory, University of Illinois, Urbana, IL, January 1985.

9. Buzbee, B. L., "A Capacitance Matrix Technique," Sparse Matrix Computations, J. Bunch and D. Rose (eds.), Academic Press, New York, 1976.

10. Shearer, J. R. and J. R. Cross, "The Experimental Determination of the Components of Ship Resistance for a Mathematical Model," Trans. RINA 107 (1965), p. 459.

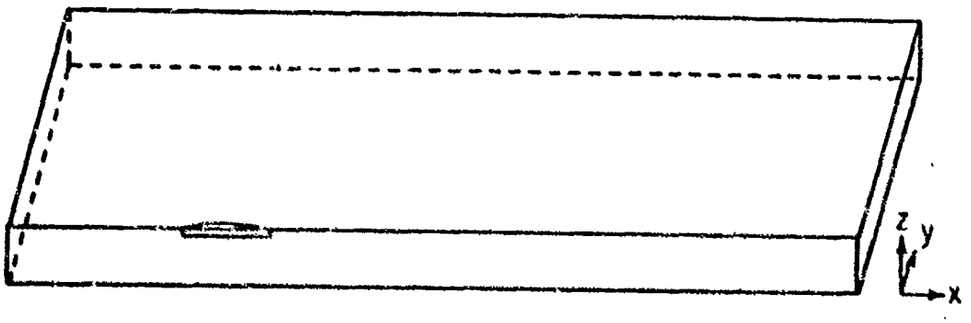

Figure 1. Placement of the ship within the Cartesian coordinate system, denoted by (x,y,z). The coordinate system follows the forward ($-x$ direction) motion of the ship.

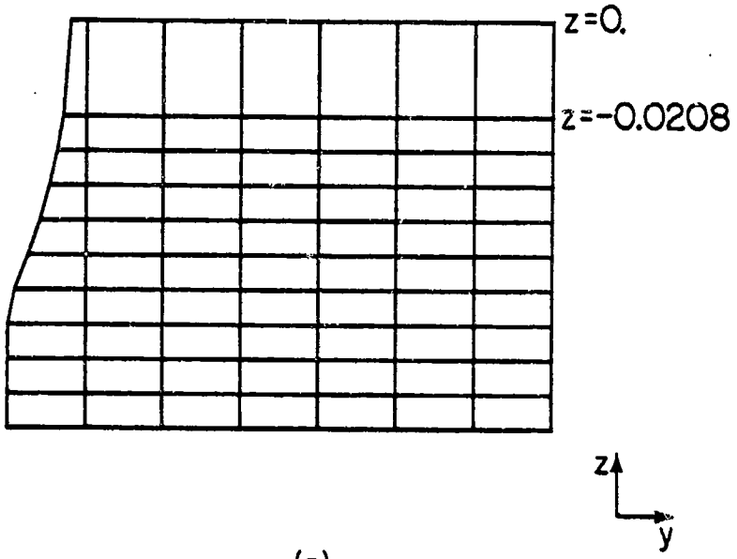

(a)

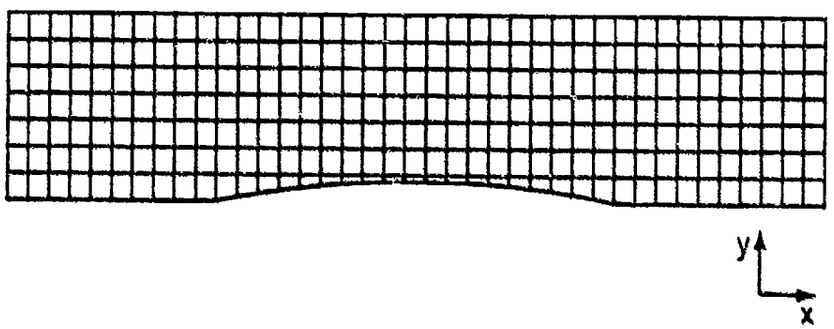

(b)

Figure 2. Two views of the locally body fitted mesh system for the Wigley hull. Note that only the finite difference equations on and near the hull are perturbed due to the coordinate transformation. (a) A side view in the (y,z) plane showing the hull accommodation (b) A top view in the (x,y) plane.

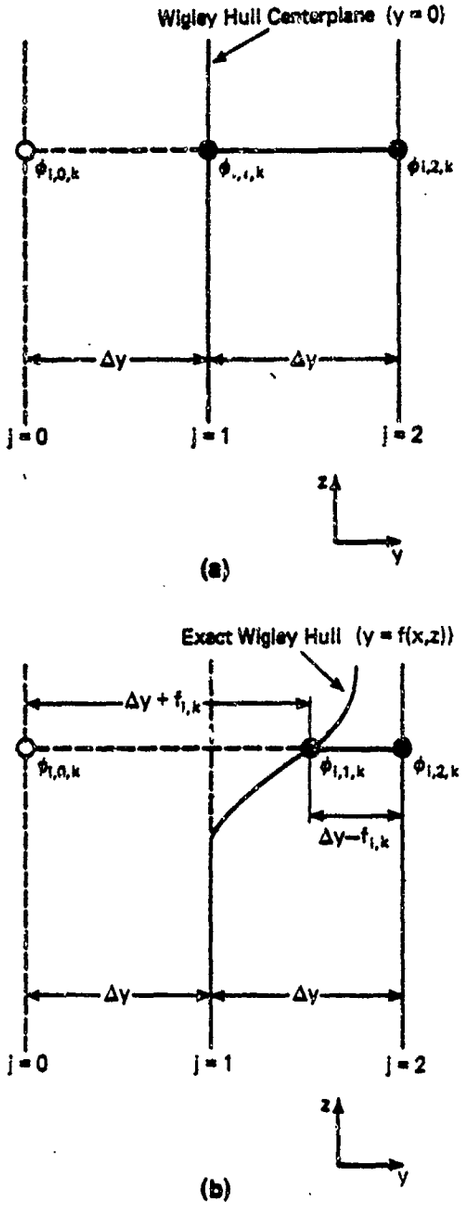

Figure 3. Comparison of the thin ship and exact hull mesh systems and their relationship to the implementation of the Neumann body condition. (a) The unknown $\phi_{i,0,k}$ is located a distance Δy outside of the domain and is easily eliminated from the equations by using the thin ship condition. (b) The unknown $\phi_{i,0,k}$ in the locally body fitted mesh system is no longer located a uniform distance outside of the domain. Special derivative formulas must therefore be used in order to eliminate it from the system of equations.

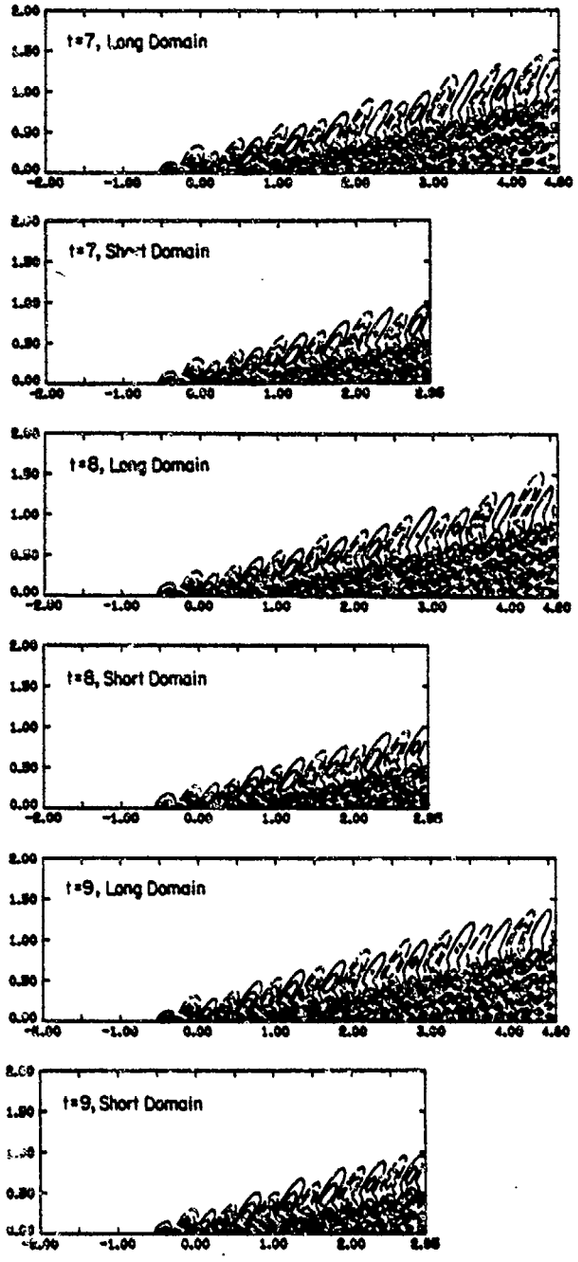

Figure 4. A time sequence of the thin ship wave profiles generated by the translating Wigley hull for both the Long Domain and the Short Domain. t = 7,8 and 9; Fr = 0.266.

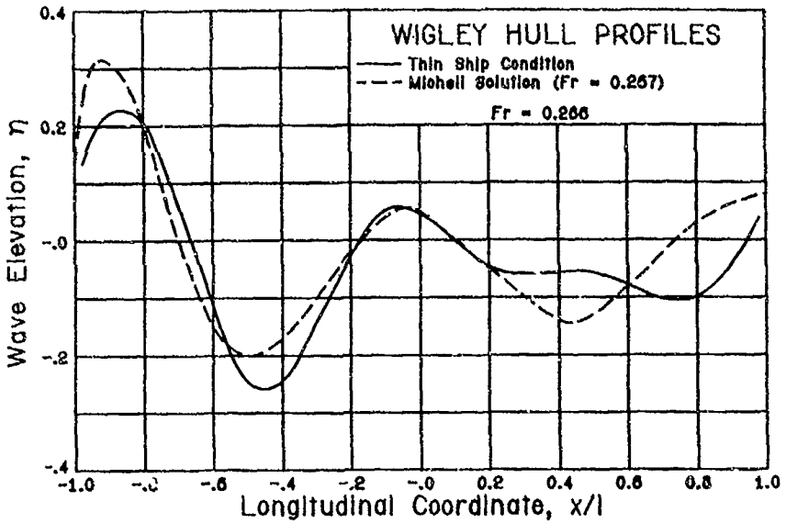

Figure 5. Comparison of the Wigley hull wave profile using the thin ship condition with the Michell solution for Fr = 0.266.

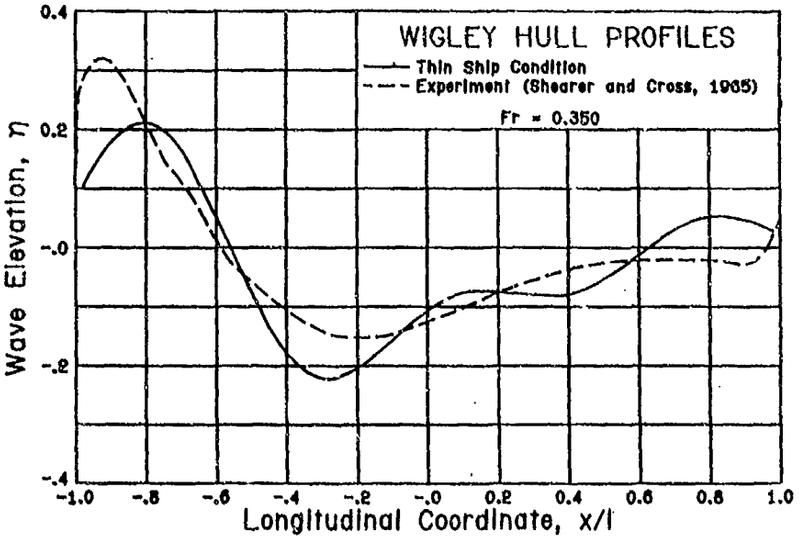

Figure 6. Comparison of the Wigley hull wave profile using the thin ship condition with an experiment for Fr = 0.350.

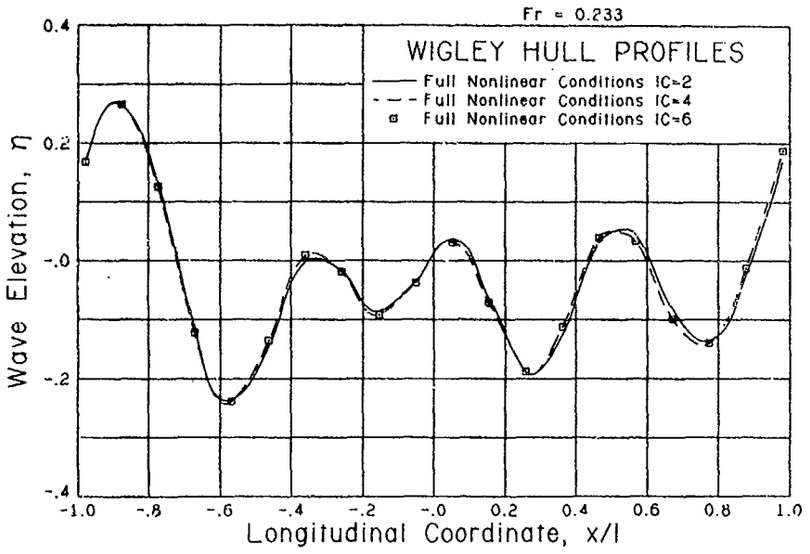

Figure 7. Comparison of the Wigley hull wave profiles for Fr = 0.233 and IC = 2, 4 and 6.

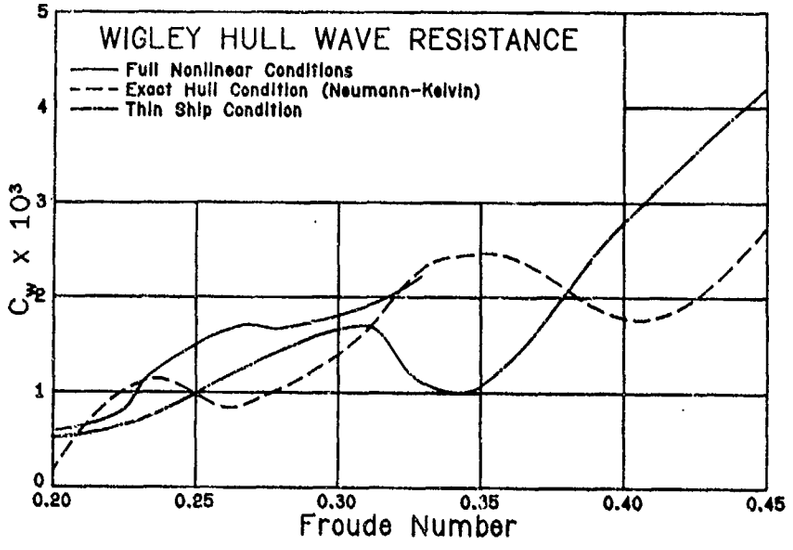

Figure 8. Comparison of the Wigley hull wave resistance vs. Froude number for the full nonlinear conditions, the exact hull condition and the thin ship condition.

DISCUSSION
of the Paper
by R.R. Chamberlain and S.M. Yen

NUMERICAL SOLUTION OF THE NONLINEAR SHIP WAVE PROBLEM

DISCUSSION
by S.M. Yen

I would like to encourage the colleagues in naval hydrodynamics to accept our offer to use our method to solve the full nonlinear ship wave problem for hull surfaces other than the Wigley hull. We will send anyone upon request a copy of our computer program package as well as a user's manual. We will also help the user to run the program. We believe that only through close working contact and by sharing computer programs, the progress in numerical ship hydrodynamics can be expedited.

DISCUSSION
by Henry T. Wang

In your paper you repeatedly refer to the boundary conditon $\phi_x = 0$ at the downstream y-z plane as the "open boundary condition". This would seem to imply that you are allowing the waves to propagate through the downstream plane, whereas, in fact, you are applying a solid wall (or reflecting boundary) condition on this plane.

Author's Reply

This discussion is especially significant since it brings up one of the most important issues which we have attempted to address. We feel that all references to the condition $\phi_x=0$ as an 'open boundary condition' are fully justified in this case, especially after consideration of the compelling numerical evidence presented in Figure 4. The two sets of calculations shown in this figure are identical except for the length of the domain. In particular, the so-called solid wall condition $\phi_x=0$ has been employed at both downstream boundaries, and yet no wave disturbances are seen to be reflected from either of these artificial boundaries. In fact, the short domain and the long domain solutions are essentially identical, both in phase as well as in amplitude. This result could hardly be expected from a reflecting boundary.

In our experience with the nonlinear ship wave problem as well as with problems in computational aerodynamics, we have encountered similar findings many times before. Fortunately the numerical solutions in many cases seem relatively insensitive to the approximations made at the downstream boundary, especially when the disturbances there are small. It must be remembered that ϕ is the perturbation potential, and we are thus allowing the mean flow to pass uniformly out of the domain. The errors involved in applying the condition $\phi_x = 0$ are not significant enough to cause any serious degradation of our solutions.

FINITE DIFFERENCE SIMULATION OF NON-BREAKING 3-D BOW WAVES AND BREAKING 2-D BOW WAVES

by Hideaki Miyata*, Shinichi Nishimura**, Hisashi Kajitani*

* Department of Naval Architecture, University of Tokyo
Hongo, Bunkyo-ku, Tokyo
** Kobe Shipyard, Mitsubishi Heavy Industries Ltd.,
Wadamisaki, Hyogo-ku, Kobe

Abstract

Two versions of the finite difference method called TUMMAC method are explained with a number of computed examples. The TUMMAC-IVvm1 method is developed for the purpose of simulating 3-D nonlinear ship waves. Since the exact inviscid free surface conditions are implemented on the full surface and the free-slip body boundary conditions are fulfilled on the surface of the approximated hull, the simulated wave formation shows fairly good agreement with the measured. The difference of wave geometry due to the variation of bow configuration are exemplified with two series of practical hull forms. The other version called TUMMAC-Vot method is a 2-D version that can simulate the wave breaking motion. The simulation of 2-D bow waves elucidates the process of wave breaking, from wave steepening, overturning, impinging to vortex generation.

I. Introduction

As is well known, the hull forms have experienced innovative improvement. A bow bulb has been proved to be very effective in the past three decades [1] and its application is still continuing to extend, for instance, to fishing boats and small cargo boats. In the last decade another bulb for a stern called stern-end-bulb is developed [2] [3] [4] [5] and the configuration of a bow bulb is refined into a thin long-protrudent one for middle and low speed ships [6] [7].

The success in hull form improvement owed much to the sound understanding of physical phenomenon. The development of a gigantic bulbous bow [8] was promoted not only by the wave making theory but also by the wave pattern analysis using stereo-photographing technique which clearly showed the nonlinear wave making in the near-field. Wave making theories have been incompetent to explain stern wave generation and then the development of a stern-end-bulb was conducted through experiments. An intuitive idea forwarded the horizontal-bow-fin (HBF) and the movable bulb[9]. The refinement of bulb configuration, from bulbous to thin protrudent type for low and middle speed ships, was commenced by the recognition of the presence of wave breaking phenomenon [10] and accelerated by the understanding of the distinctive characteristics of steep nonlinear waves called free surface shock wave (FSSW) that is likely to break [11] [12] [13] [14]. The role of linear wave making theories in the engineering problems has not been so significant as mathematically oriented researchers expected.

The understanding of the complicated physical phenomena of water flow around a ship elucidated the shortcomings of the current wave resistance theories. This is another important role of experimental investigations. The wave contour maps computed by linear theories do not show satisfactory agreement with experimental results. The claimed agreement in the value of wave resistance is supposed to be questionable when the agreement in wave formation is not demonstrated.

Excessively gross approximation of boundary conditions seems to render substantial difficulties in explaining the nonlinear wave motions in the near field which are the source of subsequent complicated motions of wave breaking, vortex generation and so forth. The exact free surface conditions must be satisfied on the exact location of the free surface. The no-slip body boundary conditions must be fulfilled on the body surface taking into account the wave motion. These are requested by the substantial sensitiveness of wave resistance and by the nonlinear characteristics of ship waves. The recognition of the nonlinear aspects of ship waves obtained from experimental studies led the authors to the development of a MAC-type [15] finete difference method that solves the Navier-Stokes (NS) equations by time-marching. It is called TUMMAC method (Tokyo University Modified Marker-And-Cell method).

In this paper two versions of the TUMMAC method are explained with a lot of computed examples. One is the TUMMAC-IVvm1 (variable mesh in one direction) method for 3-D ship waves and the other is the TUMMAC-Vot (overturning) method for breaking 2-D waves. The explanation of the TUMMAC-IVvm1 method and computations of waves of a bulk carrier and a tanker are made and its availability in the design of hull forms is discussed in PART 1. The explanation of the TUMMAC-Vot method and the numerical experiment of breaking 2-D waves are made in PART 2. PART 1 deals with the generation of steep nonlinear bow waves before breaking, and PART 2 deals with further complicated nonlinear motions that starts with wave breaking in the framework of a 2-D flow. The former study seems to have practical availability in hull form improvement. The latter fundamental study seems to be important for the further improvement of the numerical simulation method of ship waves and for the elucidation of the nonlinear wave mechanics.

PART 1
NON-BREAKING 3-D BOW WAVES

II. Free Surface Shock Wave

Experimental studies on the complicated wave motions in the near field of ships clarified the typical characteristics of ship waves [14]. They are as follows.

(a) Steepness of the wave slope.
(b) Formation of lines of discontinuity.
(c) Turbulence on the free surface on and behind the wave fronts.
(d) Systematical change of the wave-crest-line angle.
(e) Fulfillment of the Froude's law of similarity.
(f) Approximate satisfaction of a kind of shock relation across the wave fronts.
(g) Dissipation of wave energy into momentum loss far behind.

From these distinctive characteristics, partly analogous to shock waves in supersonic flow and nonlinear shallow water waves, nonlinear waves in the near field of ships in deep water are called free surface shock wave (FSSW).

How to understand these features of nonlinear ship waves determines the approaches to be taken. The characteristics (a), (d) and (e) imply that it is substantially wave making motion, and (a) and (d) discriminate FSSW from classical ship waves. Discontinuity may be produced by the steep wave configuration which can form a corner on the free surface, and furthermore it is accentuated by the occurrence of wave breaking. The characteristics (c) and (g) are results of the dissipative process of waves which starts with breaking as a natural consequence of the steep wave generation. Steep waves called FSSWs are usually generated in the near field and they are usually so steep as to be liable to break especially when the Froude number based on draft Fd is large. The steep waves themselves show nonlinear features and the dissipative motion cause further complicated fluid behavior.

The generation of FSSW directly contributes to wave resistance. Whether its energy is dissipated into momentum loss or spread by dispersion in the far field, the wave resistance is not influenced in the first-order approximation. The effect of the dissipative flow on wave making seems to be a higher-order mechanics. The first problem to be attacked is the theoretical explanation of the generation of FSSW, since it is the source of other nonlinear free surface motions and of dispersive wave propagation as well. The MAC-type finite difference method seems to be most powerful for this problem, since it excludes any linearizing postulations.

III. TUMMAC-IVvm1 Method

Two primitive versions of the TUMMAC method for 3-D waves were developed. They are the TUMMAC-I method for waves around a wedge-shaped bow [16] [17] [18] [19] and the TUMMAC-II method for waves around a ship of arbitrary waterline [20] [21]. Being based on the techniques developed in these previous versions the TUMMAC-IV method was developed for waves generated by a ship of arbitrary configuration. Since the version with the mesh system of equal spacing (TUMMAC-IVa) is already described in Ref. [22] and the attained accuracy of the improved version with a variable mesh system in vertical direction (TUMMAC-IVvm1) is described in Ref. [23]. The computational procedure is described only briefly here.

A rectangular inflexible mesh system is employed with variable spacing in the vertical direction. The horizontal spacing DX and DY are common to all the cells, while DZ varies with respect to the z-coordinate. Velocities are defined on the six surfaces of a cell and pressure at the center of a cell. Suppose (i, j, k) denote the location of the center of a cell, then the NS-equations are approximated into a finite difference form by forward differencing in time and centered differencing in space except the convective terms.

$$u^{n+1}_{i+\frac{1}{2},j,k}=\xi_{i+\frac{1}{2},j,k}-(\psi_{i+1,j,k}-\psi_{i,j,k})/DX.DT$$

$$v^{n+1}_{i,j+\frac{1}{2},k}=\eta_{i,j+\frac{1}{2},k}-(\psi_{i,j+1,k}-\psi_{i,j,k})/DY.DT \quad (1)$$

$$w^{n+1}_{i,j,k+\frac{1}{2}}=\zeta_{i,j,k+\frac{1}{2}}-(\psi_{i,j,k+1}-\psi_{i,j,k})/DZ_k.DT$$

where

$$\xi_{i+\frac{1}{2},j,k}$$
$$=u_{i+\frac{1}{2},j,k}-DT.UC_{i+\frac{1}{2},j,k}$$
$$+\nu.DT[(u_{i+\frac{3}{2},j,k}+u_{i-\frac{1}{2},j,k}-2u_{i+\frac{1}{2},j,k})/DX^2$$
$$+(u_{i+\frac{1}{2},j+1,k}+u_{i+\frac{1}{2},j-1,k}-2u_{i+\frac{1}{2},j,k})/DY^2$$

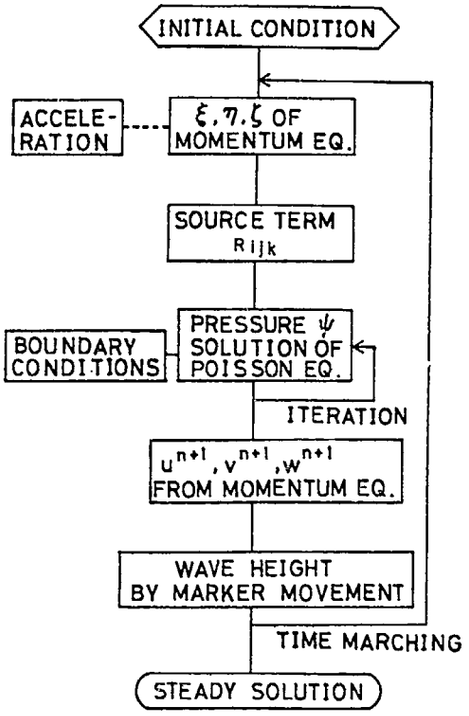

Fig.1 Block diagram of TUMMAC-IVvm1

$$+(u_{i+\frac{1}{2},j,k+1}+u_{i+\frac{1}{2},j,k-1}-2u_{i+\frac{1}{2},j,k})/DZ_k^2]$$

$$\eta_{i,j+\frac{1}{2},k}=v_{i,j+\frac{1}{2},k}-DT.VC_{i,j+\frac{1}{2},k}+\nu.DT[---] \quad (2)$$

$$\zeta_{i,j,k+\frac{1}{2}}=w_{i,j,k+\frac{1}{2}}-DT.WC_{i,j,k+\frac{1}{2}}+\nu.DT[---]+g$$

Here DT is time increment and UC, VC and WC are the convective terms. By use of continuity equation the following Poisson equation for pressure is derived.

$$\psi_{i,j,k}$$
$$=\frac{1}{2}(1/DX^2+1/DY^2+1/(DZ_{k-\frac{1}{2}}.DZ_{k+\frac{1}{2}}))^{-1}$$
$$\times\left(\frac{\psi_{i+1,j,k}+\psi_{i-1,j,k}}{DX^2}+\frac{\psi_{i,j+1,k}+\psi_{i,j-1,k}}{DY^2}\right. \quad (3)$$
$$\left.+\frac{DZ_{k-\frac{1}{2}}.\psi_{i,j,k+1}+DZ_{k+\frac{1}{2}}.\psi_{i,j,k-1}}{DZ_{k-\frac{1}{2}}.DZ_{k+\frac{1}{2}}(DZ_{k-\frac{1}{2}}+DZ_{k+\frac{1}{2}})/2}-R_{i,j,k}\right]$$

where

$$R_{i,j,k}=(\xi_{i+\frac{1}{2},j,k}-\xi_{i-\frac{1}{2},j,k})/(DT.DX)$$
$$+(\eta_{i,j+\frac{1}{2},k}-\eta_{i,j-\frac{1}{2},k})/DT.DY) \quad (4)$$
$$+(\zeta_{i,j,k+\frac{1}{2}}-\zeta_{i,j,k-\frac{1}{2}})/(DT.DZ_k)$$

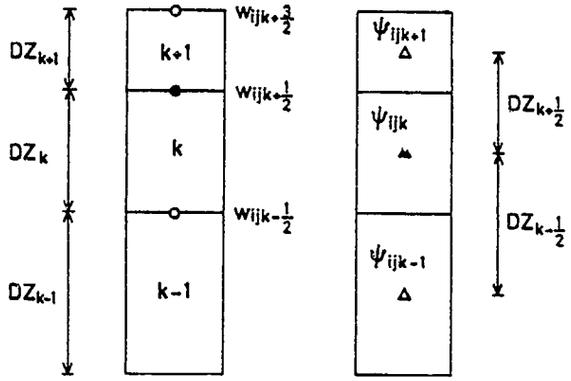

Fig.2 Variable spacing in vertical direction.

$$DZ_{k\pm\frac{1}{2}}=\frac{1}{2}(DZ_k+DZ_{k\pm1}) \quad (5)$$

Eq.(3) is solved by a simultaneous iterative method through the following equation.

$$\psi^{m+1}_{i,j,k}$$
$$=\psi^{m}_{i,j,k}-\omega[D^m_{i,j,k}$$
$$\div\{2\ DT\{1/DX^2+1/DY^2+1/(DZ_{k-\frac{1}{2}}.DZ_{k+\frac{1}{2}})\}\}] \quad (6)$$

where

$$D^m_{i,j,k}=(u^m_{i+\frac{1}{2},j,k}-u^{m+1}_{i-\frac{1}{2},j,k})/DX$$
$$+(v^m_{i,j+\frac{1}{2},k}-v^{m+1}_{i,j-\frac{1}{2},k})/DY \quad (7)$$
$$+(w^m_{i,j,k+\frac{1}{2}}-w^{m+1}_{i,j,k-\frac{1}{2}})/DZ_k$$

Here, superscripts denote the number of iteration and D is divergence of a cell.

At every time step of the time-marching the pressure field is updated by the new velocity field and the new pressure field gives a new velocity field by advancing one time step by Eq.(1). The procedure is illustrated in Fig.1.

For the differencing of the convective term the combination of the centered differencing and the second-order upstream differencing (donor-cell method) is employed following Hirt et al. [24]. With this differencing method the term $\partial(w^2)/\partial z$, for example, becomes

$$W2C=1/(4.DZ_{k+\frac{1}{2}})[w_{i,j,k+\frac{1}{2}}+w_{i,j,k+\frac{3}{2}})^2$$
$$-(w_{i,j,k-\frac{1}{2}}+w_{i,j,k+\frac{1}{2}})^2$$
$$+\alpha|(w_{i,j,k+\frac{3}{2}}-w_{i,j,k+\frac{1}{2}})$$
$$\times[w_{i,j,k+\frac{3}{2}}+w_{i,j,k+\frac{1}{2}}| \quad (8)$$

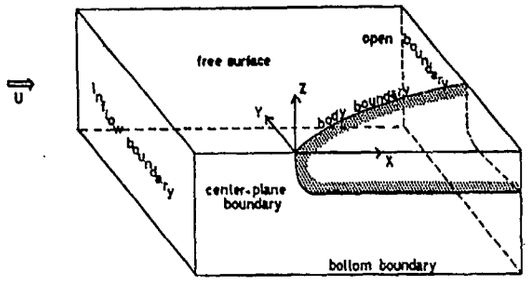

Fig.3 Domain of computation.

$$-(w_{i,j,k-\frac{1}{2}}-w_{i,j,k+\frac{1}{2}})$$
$$\times|w_{i,j,k-\frac{1}{2}}+w_{i,j,k+\frac{1}{2}}|\}]$$

The velocity points are shown in Fig.2, in which a black circle indicates the point at which W2C is estimated. α is a combination factor.

By the use of a variable mesh system the degree of accuracy of the finite differencing is lowered by order one. Eq.(3) does not have second-order accuracy in the vertical direction. The differencing of the convective term also becomes less accurate as explained below.

By Taylor series expansion of Eq.(8) about the location $z_{k+\frac{1}{2}}$ W2C is written as

$$W2C=\frac{(2+\alpha)DZ_k+(2-\alpha)DZ_{k+1}}{2(DZ_k+DZ_{k+1})}\frac{\partial(w^2)}{\partial z}$$
$$+w_{i,j,k+\frac{1}{2}}(DZ_{k+1}-DZ_k$$
$$-\alpha\frac{DZ_k^2+DZ_{k+1}^2}{2(DZ_k+DZ_{k+1})})\frac{\partial^2 w}{\partial z^2} \quad (9)$$
$$-\alpha\frac{DZ_k^2+DZ_{k+1}^2}{2(DZ_k+DZ_{k+1})}(\frac{\partial w}{\partial z})^2+O(DZ^2)$$

When α =1.0, i.e. the case of the donor-cell method,

$$W2C=\frac{3DZ_k+DZ_{k+1}}{2(DZ_k+DZ_{k+1})}\frac{\partial(w^2)}{\partial z}+O(DZ) \quad (10)$$

and when α =0.0, i.e. the case of the centered differencing,

$$W2C=\frac{\partial(w^2)}{\partial z}+w_{i,j,k+\frac{1}{2}}(DZ_{k+1}-DZ_k)\frac{\partial^2 w}{\partial z^2}$$
$$+O(DZ^2) \quad (11)$$

However, the formal reduction of the degree of accuracy can be easily compensated by using a very fine cells near the free surface where high resolution is required.

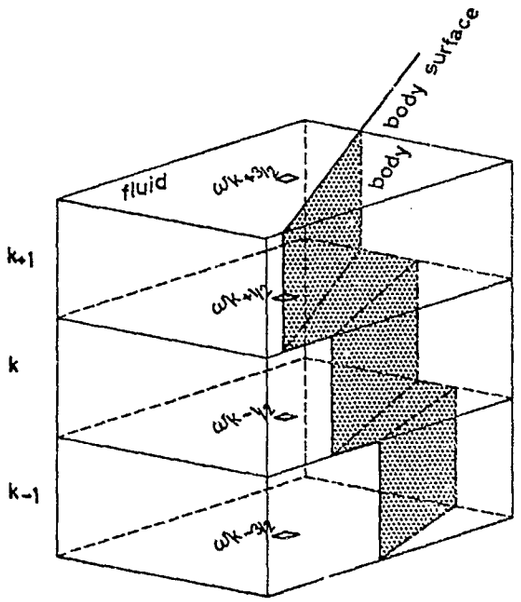

Fig.4 Approximation of hull surface.

The computational domain is shown in Fig.3 for the case of bow wave computation. Proper boundary conditions must be imposed and fulfilled on all the boundaries.

Since a water-line of a ship is approximated by a succession of line segments and a frame-line by steps, the body surface becomes as shown in Fig.4. Free slip body boundary conditions are imposed on the vertical surfaces. In order to let the water flow along the frame-lines smooth, the ratio of the portion of a horizontal plane through which water flow vertically is considered in the fulfillment of the zero-divergence condition of the fluid region of a boundary cell. The exact inviscid free surface conditions are approximately satisfied. Use is made of the "irregular star" and the "marker particle" techniques.

IV. Waves of a Bulk Carrier

Two hull forms of a bulk carrier of 26000 deadweight tonnage is chosen for the computation. The original hull M55F0 has a conventional bow bulb and the improved one M55F1 a long-protrudent thin bulb. The latter was designed by the authors and was applied to a full-scale ship equipped with sails. The length (Lpp), breadth (B) and draft (d) of the models are 3.000m, 0.497m and 0.090m (ballast condition) or 0.209m (full-load condition), respectively. The computations were executed with these dimensions of models.

The forebodies are considered and an example of cell division is as shown in Fig.5.

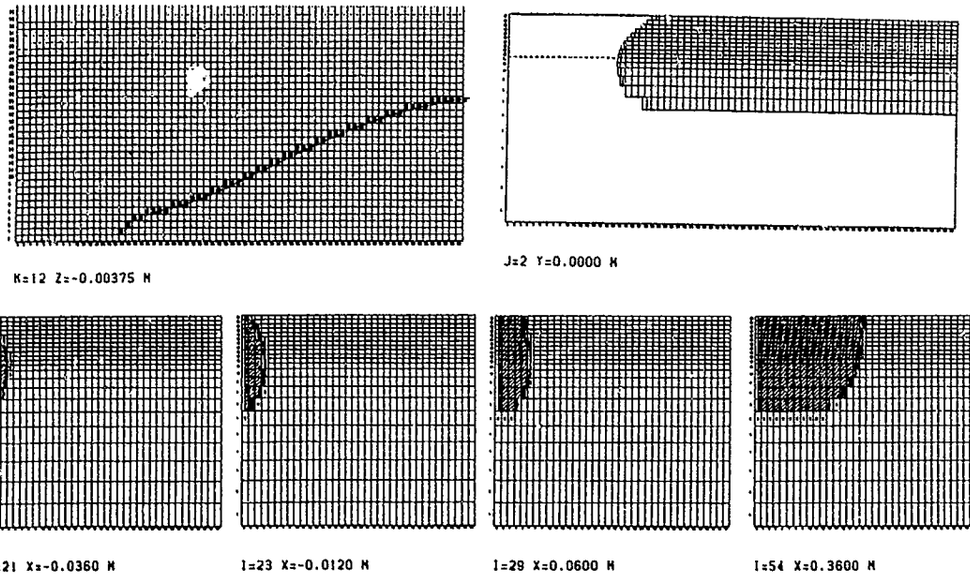

Fig.5 Cell division of M55F0 for ballast condition.

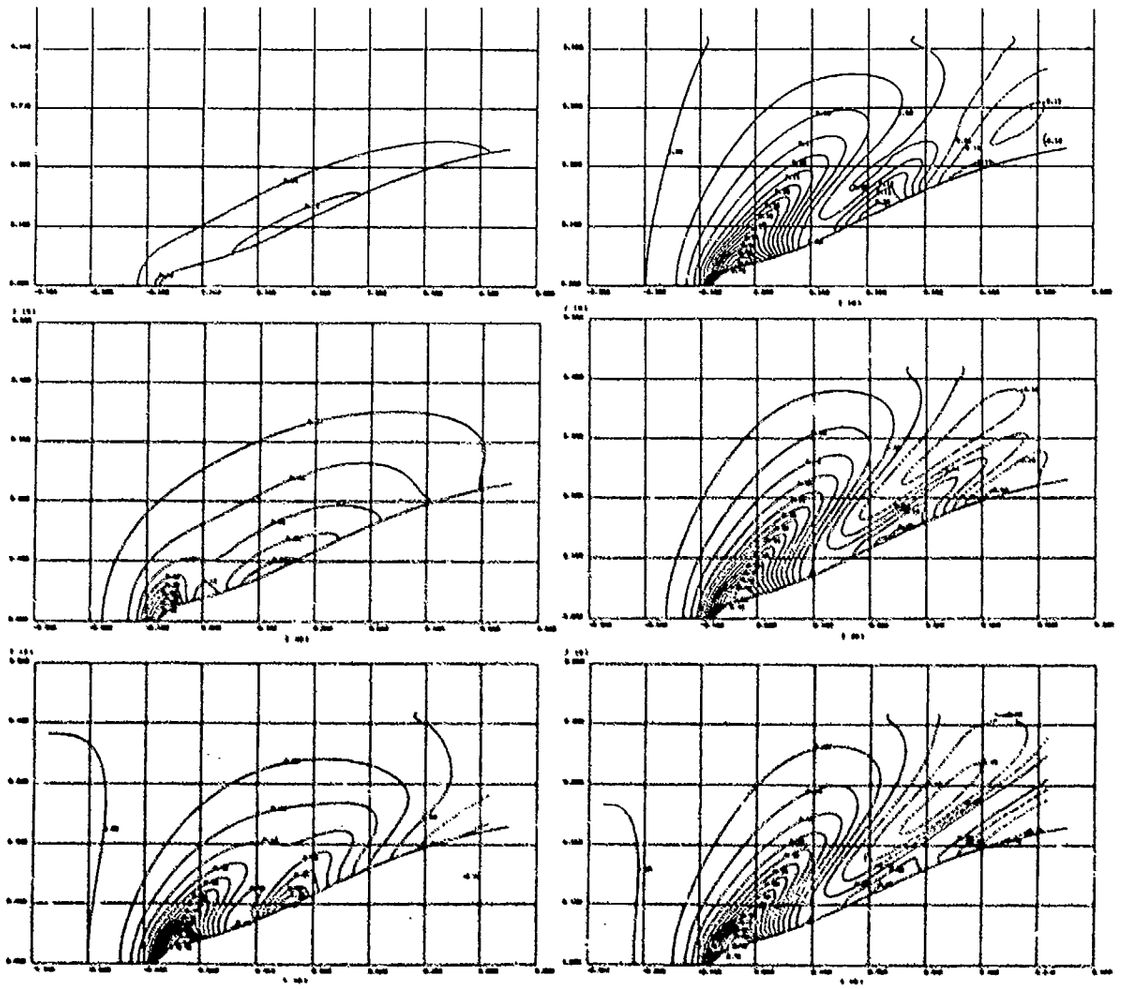

Fig.6 Time sequence of wave contours of M55F0 in ballast condition at Fn=0.18, from 100th to 600th time step with the interval of 100 steps.

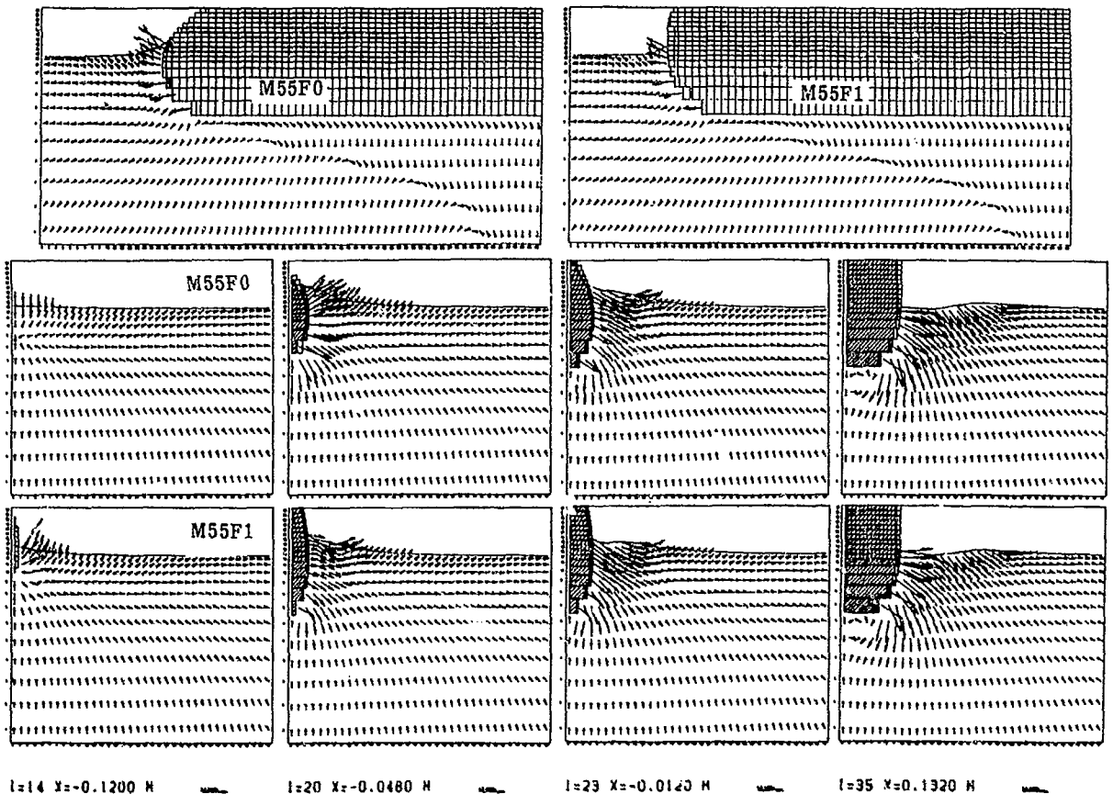

Fig.7 Velocity vector field of M55F0 and F1 in ballast condition at Fn=0.18.

For the case of ballast condition the cell size DX x DY x DZ is 12 x 12 x 7.5 - 40.5mm and the computational domain is -0.276m < x < 0.540m, 0m<y<0.420m and -0.288m<z< 0.075m. Then, the approximate number of cell in which pressure is computed is about 28000. For the case of full-load condition, DX x DY x DZ is 14 x 14 x 10.3 - 55.4mm and the computational domain is -0.420m<x< 0.546m, 0m<y< 0.420m and -0.493m< z< 0.072m. Then the cell number is about 31000.

The time increment is 3.23 and 3.63 millisecond for ballast and full-load condition, respectively. The uniform flow is accelerated for 300 time steps and the computation is continued to the 600th time step when the steady state in reached. The Froude number based on Lpp (Fn) reached at the steady state is 0.18 and 0.20 for ballast condition and 0.18 for full-load condition. The Froude number based on d (Fd) is 1.04 and 1.15 for ballast condition and 0.682 for full-load condition.

The time sequence of wave contours is shown in Fig.6 for the case of M55F0 in ballast condition. The wave height in contours in PART 1 is all made dimensionless with respect to the head of uniform stream H ($=U^2/2g$). The maximum wave height of 0.75H appears just when the acceleration of the inflow is ceased and the foremost wave does not show remarkable variation after the 400th time step, but the development of the second wave crest needs a little more time steps.

The velocity vector fields are compared between the two models in Fig.7 for ballast condition and in Fig.8 for full-load condition. The blunter bow of M55F0 causes greater disturbance velocities, which is related with higher wave height and consequently higher wave resistance. The downward velocities form a vortical motion beneath the hull. This corresponds to three-dimensional separation of forebodies. Despite that free-slip body boundary conditions are imposed, the qualitative agreement is good. In a strict sense it is safe to consider it as a consequence of numerical error. However, these figures indicate that the three-dimensional separation is initiated by boundary layer separation, the role of which is played by numerical error in these cases, and the ratational flow is formed by the velocities outside a boundary layer.

Computed wave contour maps at the steady state are shown in Fig.9, and those measured by a wave recorder are in Fig.10. Perspective views in the same conditions are shown in Figs.11 and 12. The reduction ratio of the two contours is the same, although the coordinate is dimensional in Fig.9 and dimensionless in Fig.10. The overall agreement between computation and experiment is fairly good. With the increase of Froude number the fore-

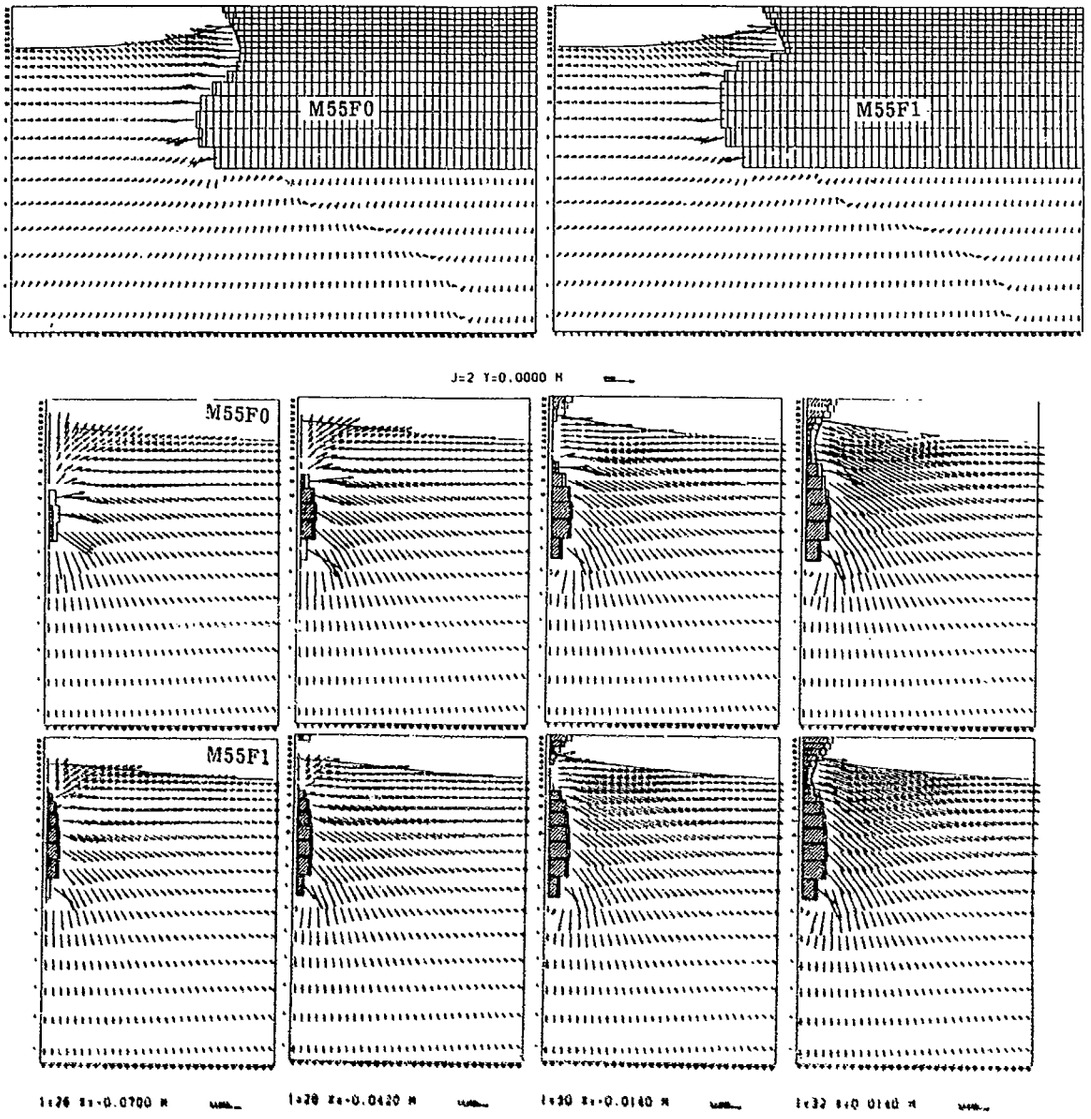

Fig.8 Velocity vector field of M55F0 and F1 in full-load condition at Fn=0.18.

most wave extends and the second wave crest disappears. The angle of wave crest decreases with the increase of Froude number, which is one of the typical characteristics of FSSW. The difference of wave geometry between the two load conditions is obviously noted. Although this is partly attributable to the difference of hull configuration, the most dominant cause is the difference of Froude number based on draft. When it is low and/or the bow configuration is blunt, a wave with circular geometry called normal FSSW is generated as in the cases of full-load condition. The foremost wave of a bow which is not extremely blunt is deformed into an oblique FSSW when Froude number is sufficiently large as in the cases of ballast condition. The simulated angle of wave crest line is smaller than the measured in ballast condition but it is contrary in the full load condition. The agreement of the maximum wave height is fairly good and the difference is usually about 0.05H.

The superiority of M55F1 to M55F0 in ballast condition is obvious. The maximum and minimum wave height are both reduced and the area of large wave height is reduced. On full-load condition slight reduction of waves is also observed but its degree is not so significant. The results of towing test indicate that wave resistance is reduced by 40% at Fn=0.18 in ballast condition. The computed results also demonstrate the effectiveness of a thin long-protruded bulb for such a middle-speed ship. Thus, the simulations by the TUMMAC-IVvm1 method is proved to be effective for the procedure of hull form optimization. The discrimination of a better hull form will be made more reasona-

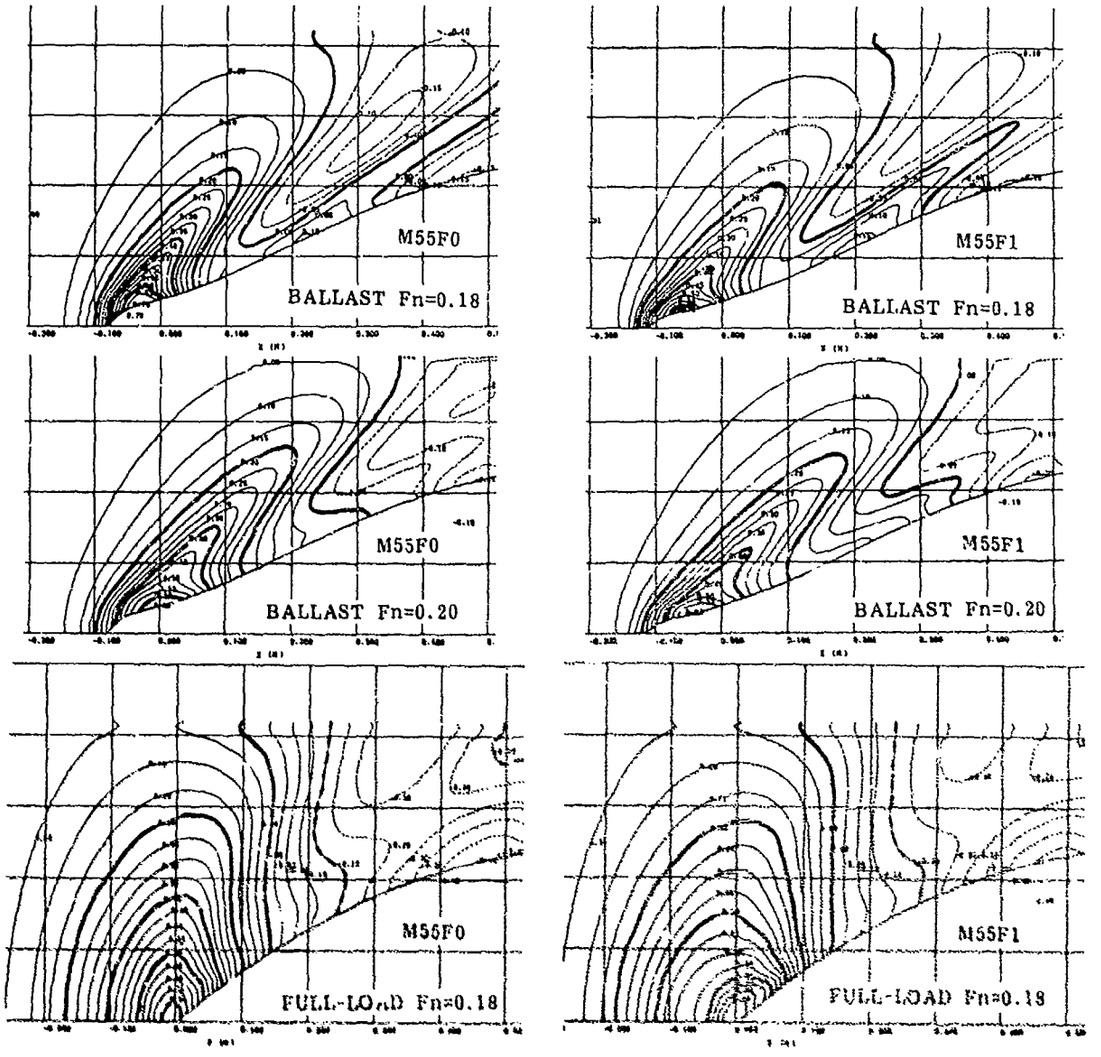

Fig.9 Computed wave contour maps of M55F0 (left) and F1 (right).

bly, when ingenious use is made of the integration of the pressure distribution on the hull surface or that of the wave energy in the computational domain.

V. Waves of a Tanker

For another example a series of tanker model M57 is chosen. The dimension of the model is Lpp x B x d = 3.60m x 0.509m x 0.066m (ballast) or 0.168m (full-load). The series is composed of two without a bulb and two with a bulb as shown in Fig.13. The bulb configuration of M57F3 is that currently applied to low-speed full hull forms of tankers and large bulk carriers. M57F5 has an extremely long thin bulb which is expected to reduce FSSW and its breaking in ballast condition. M55F6 has a round bow without a bulb, which may be preferable when wave resistance can be safely ignored.

The formbodies are considered in the computation, and cell division for ballast condition is shown in Figs.14 to 16. The cell size DX x DY x DZ is 16.5 x 16.5 x 7.37 - 25.05mm for ballast condition and 16.5 x 16.5 x 8.21 - 44.14mm for full-load condition. The lengh and width of the computational domain is 1.122m and 0.495m, respectively, common to the two draft condition and the water depth is 0.211m for ballast condition and 0.393m for full-load condition. Then the approximate number of cell is 29000 and 33000 for the respective case.

The time increment is 3.36 and 4.22 millisecond for ballast and full-load conditions, respectively. The uniform flow is accelerated for 300 time steps and the computation is continued to the 800th time step. Fn is 0.15 for all the cases, and Fd is 0.975 in ballast

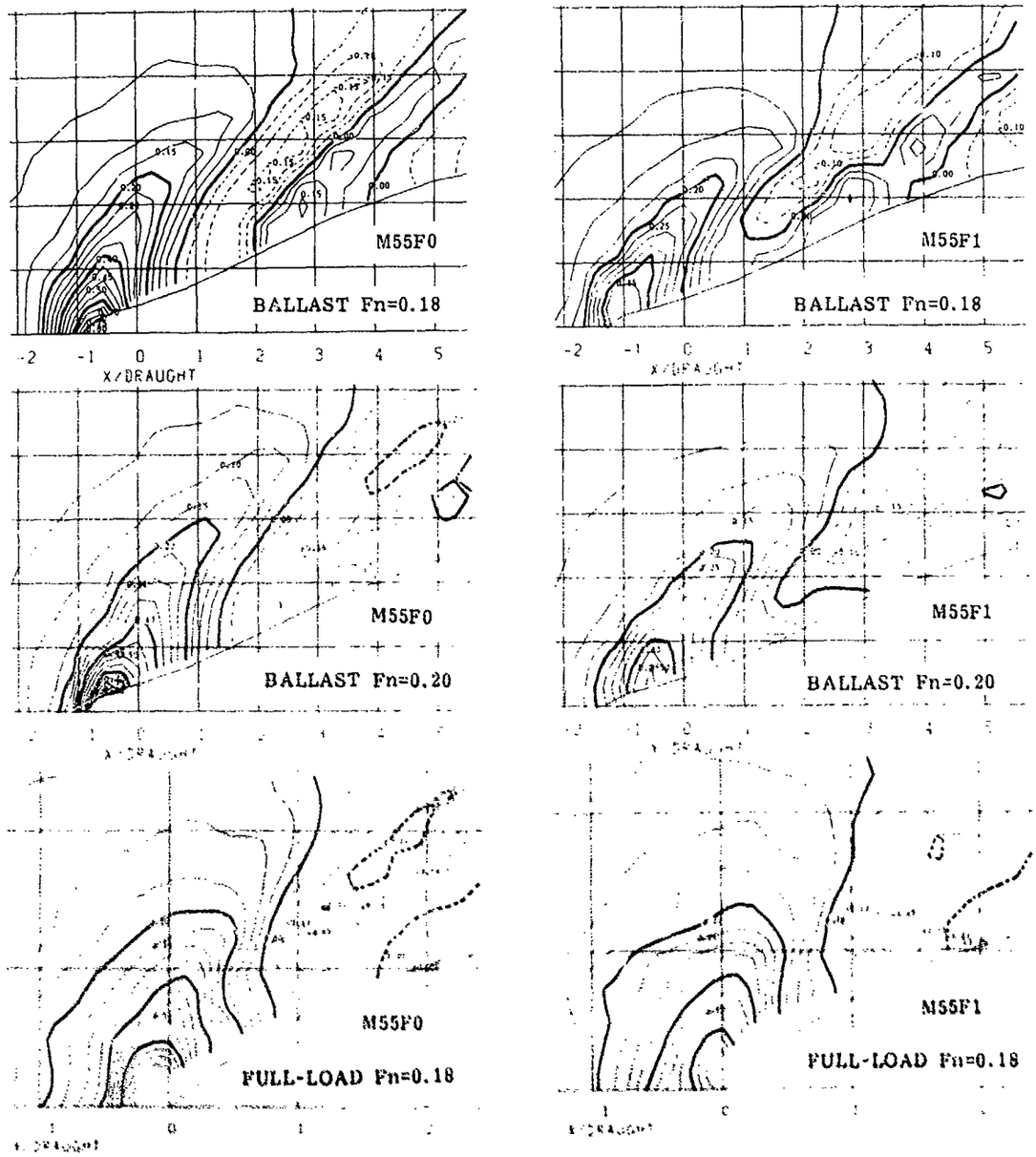

Fig.10 Measured wave contour maps of M55F0 (left) and F1 (right).

condition and 0.616 in full-load condition.

The computed velocity vector fields are shown in Figs.17 and 18. The rotational flow beneath the hull is more clear than in the case of M55 owing to the selected section behind FP.

Wave geometry is compared between the four series models in ballast condition in Figs. 19 and 20. The maximum wave height of M57F0, F3, F5 and F6 is 0.95H, 0.85H, 0.75H and 0.95H, respectively, which implies the favorable effect of a bow bulb. The suppression of the foremost wave crest is most significant by the thin long-protrudent bulb, although the second wave crest is largest among the four. The new-type bow configuration of M57F5 will be useful at Fn=0.15 or greater when the reduction of wave resistance is not compensated by the increase of viscous resistance due to the increase of wetted-surface area. The difference in waves is very small between M57F0 and F6. The round bow configuration seems to have negligible influence on wave generation.

In the [illegible] conditions trim and sinkage are restricted while they are usually free in usual towing tests. If the effect of this restriction

BALLAST Fn=0.18

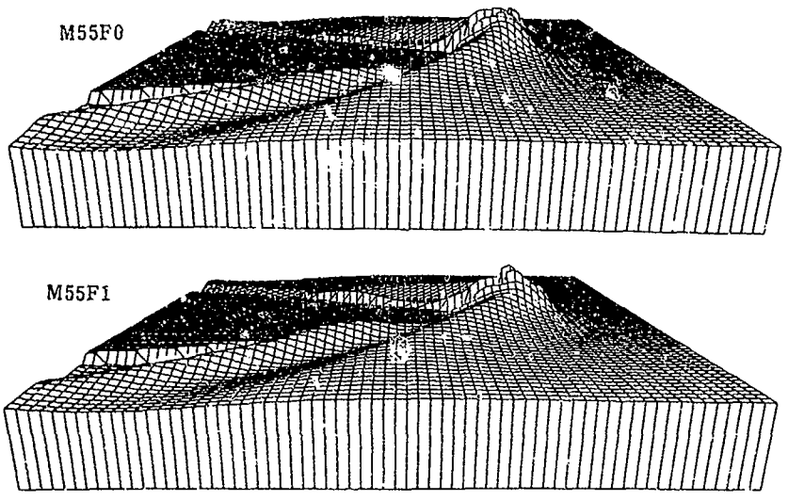

BALLAST Fn=0.20

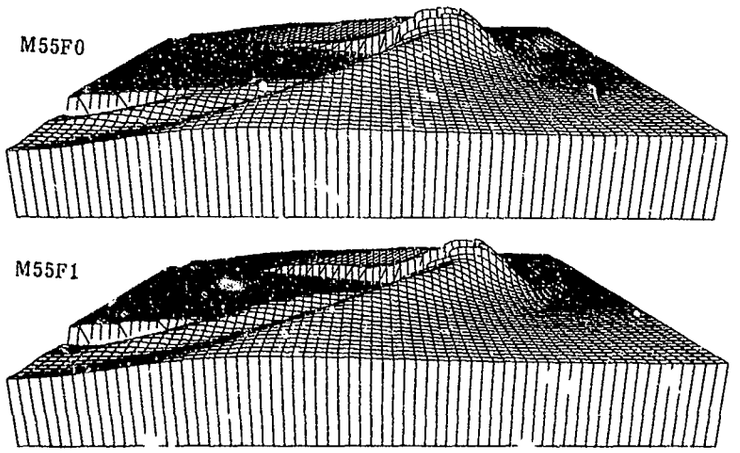

FULL-LOAD Fn=0.18

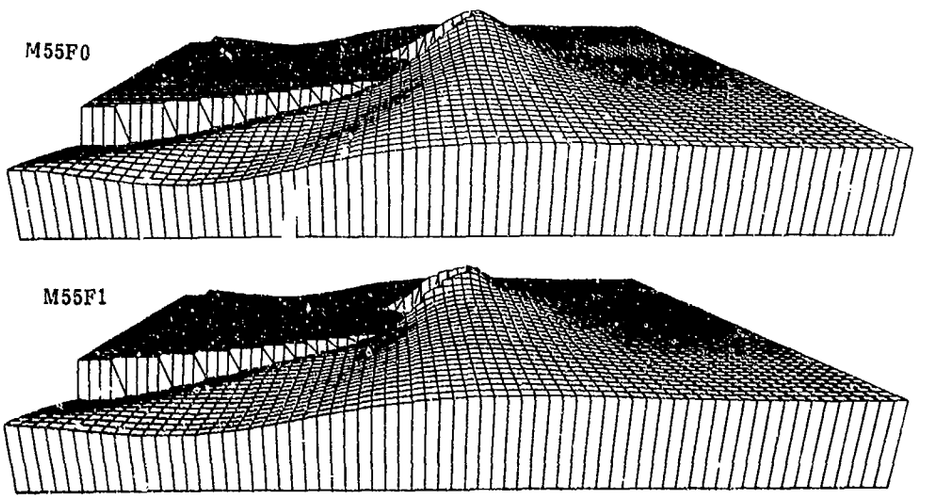

Fig.11 Computed perspective views of M55F0 and F1.

BALLAST Fn=0.18

M55F0

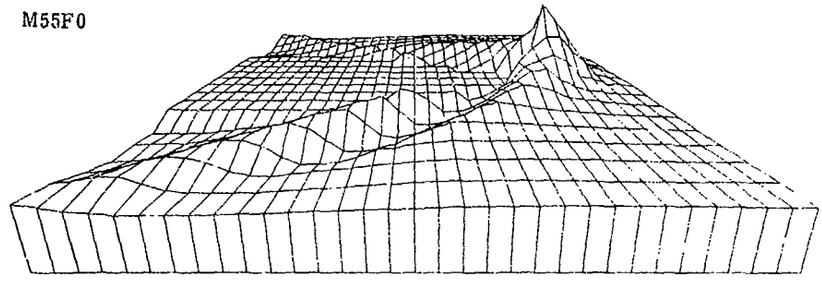

M55F1

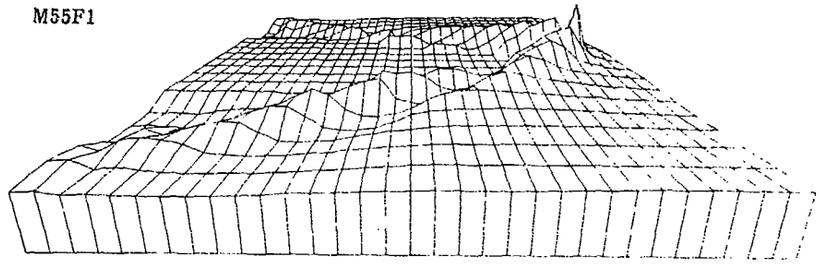

BALLAST Fn=0.20

M55F0

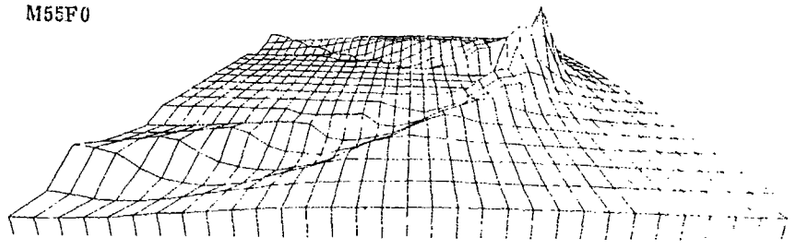

M55F1

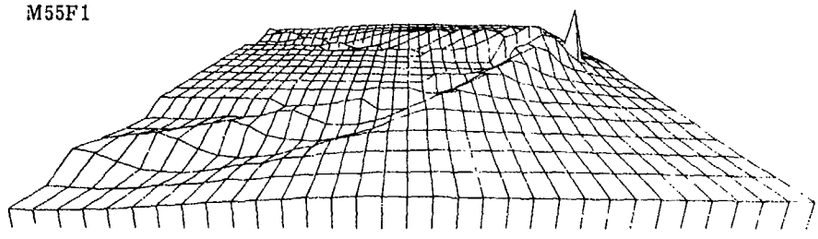

FULL-LOAD Fn=0.18

M55F0

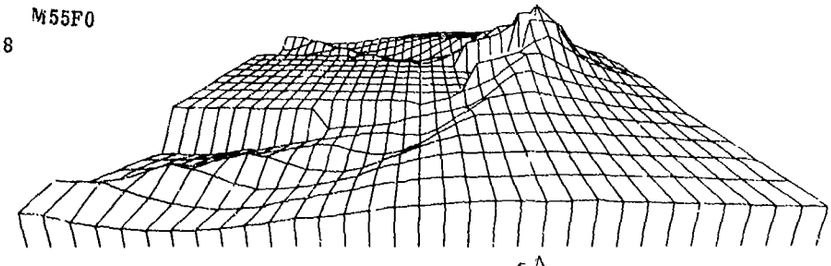

M55F1

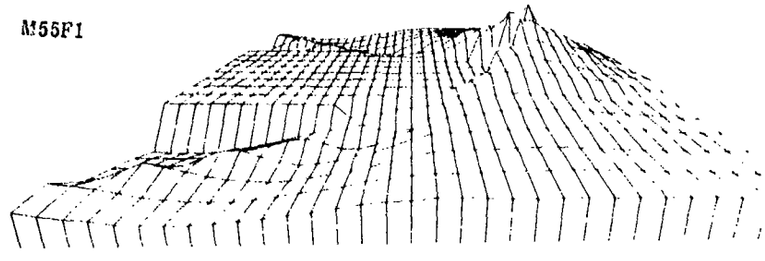

Fig.12 Measured perspective views of M55F0 and F1.

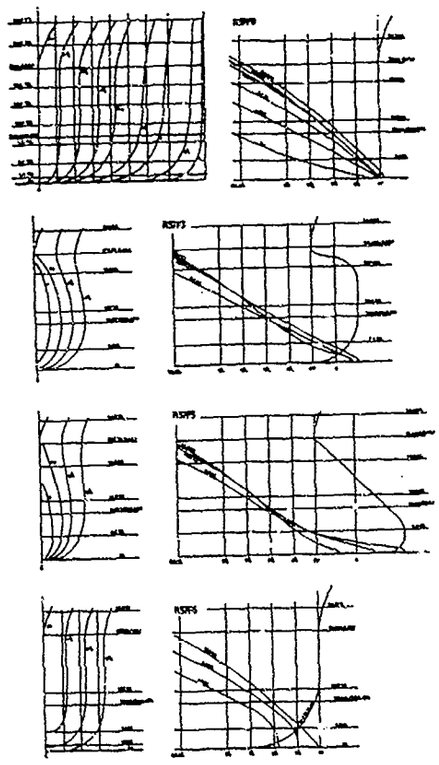

Fig.13 Lines of M57 series models.

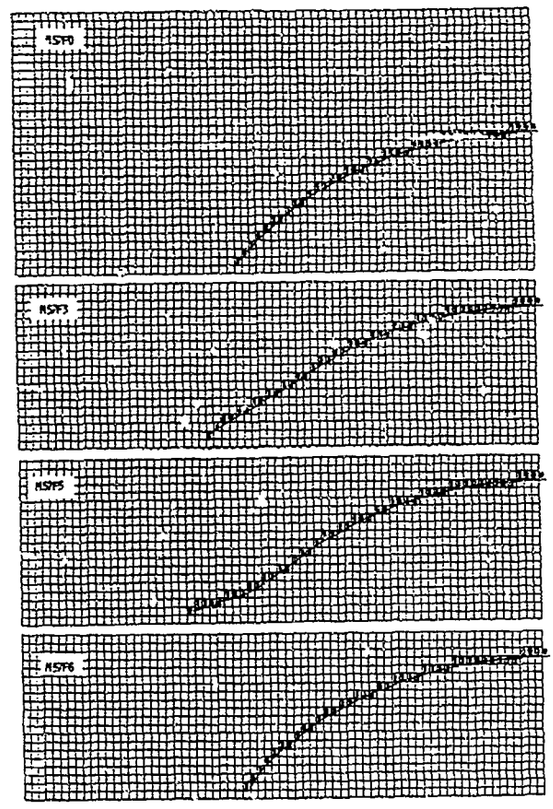

Fig.15 Cell division on a horizontal plane for ballast condition.

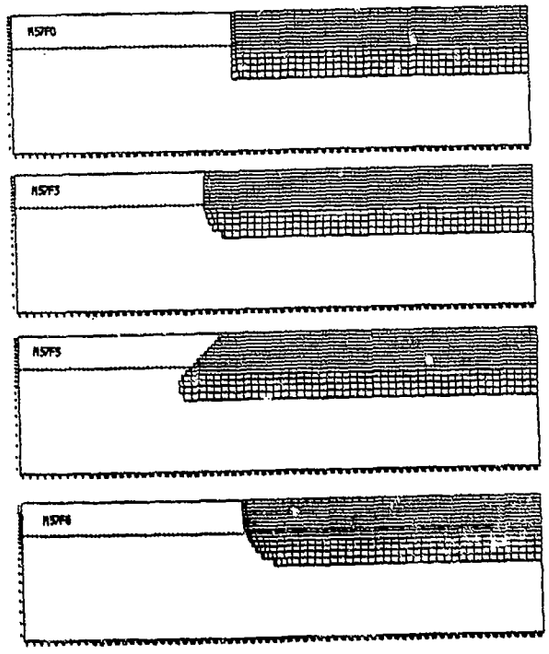

Fig.14 Cell division on hull surfaces for ballast condition.

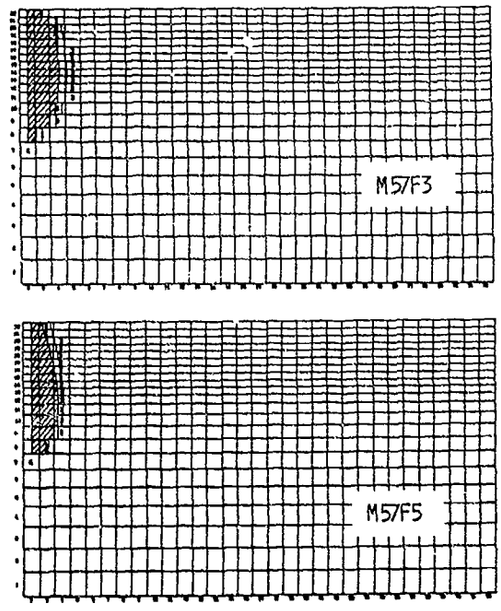

Fig.16 Cell division on a vertical plane at FP for ballast condition.

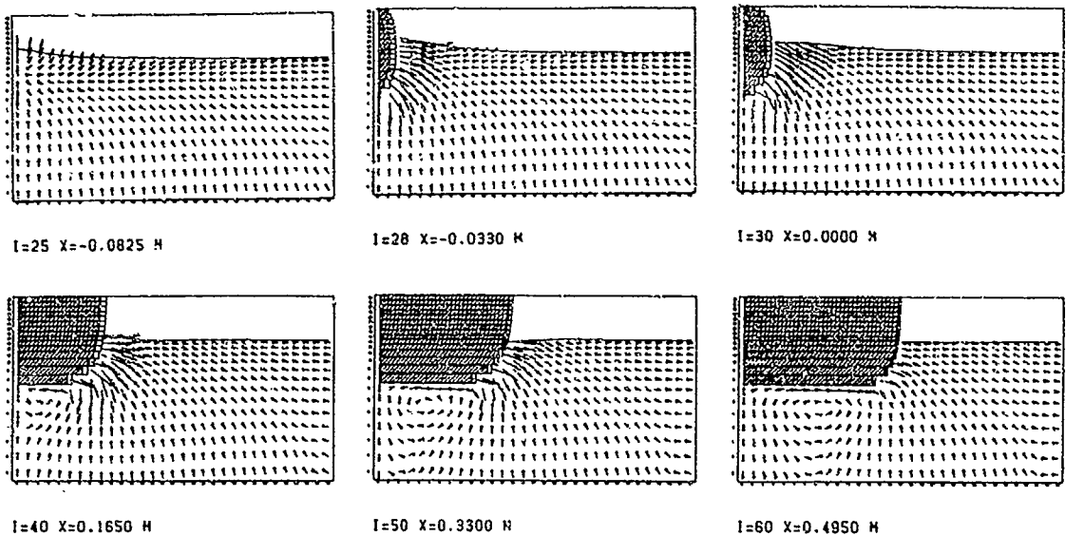

Fig.17 Velocity vector field at vertical sections of M57F3 in ballast condition.

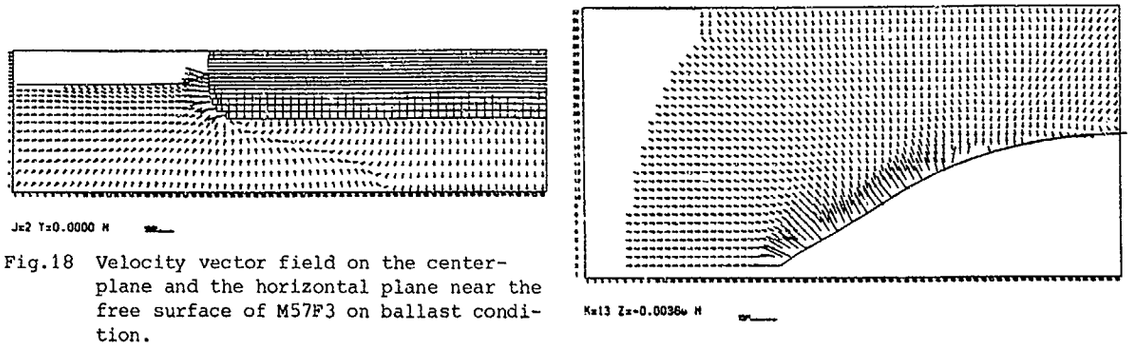

Fig.18 Velocity vector field on the center-plane and the horizontal plane near the free surface of M57F3 on ballast condition.

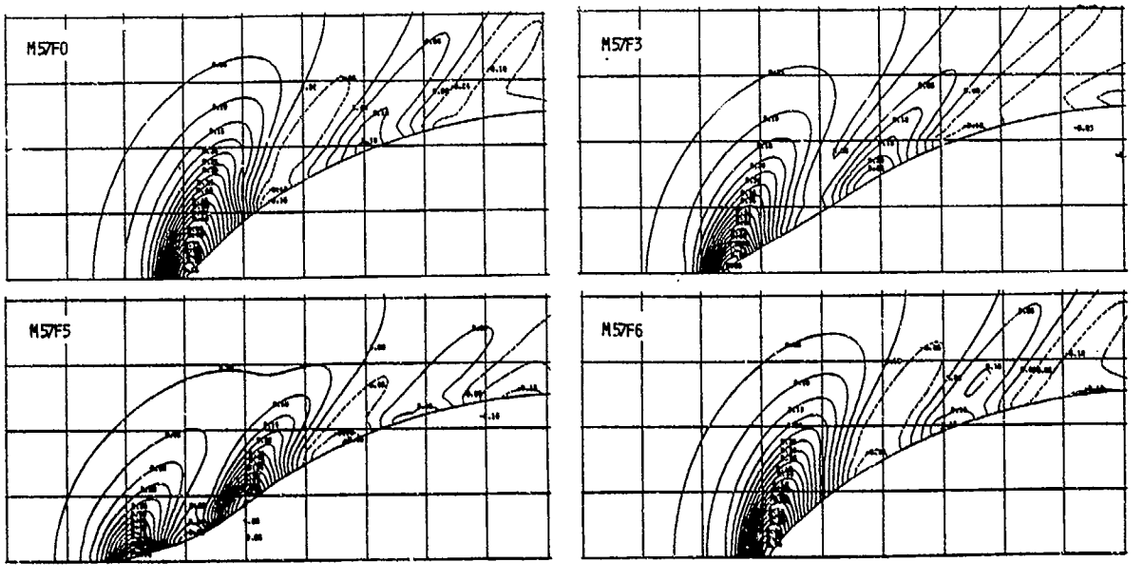

Fig.19 Comparison of computed wave contour maps of M57 series models in ballast condition.

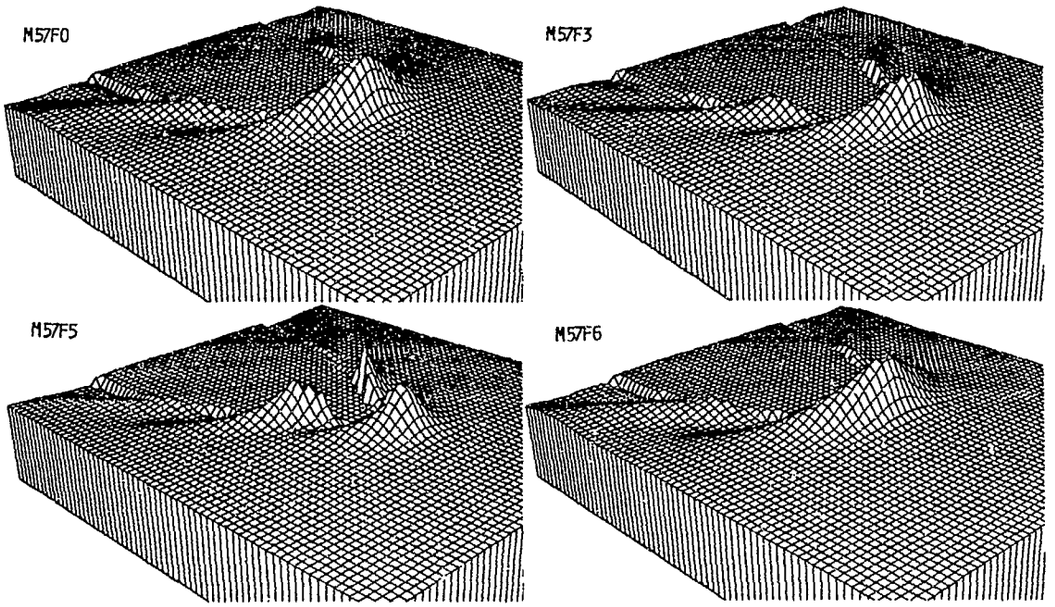

Fig.20 Comparison of computed perspective view of M57 series models in ballast condition.

is significant, a particular consideration or modification is needed in computations. However, the effect is not so important for low and middle speed ships as experimentally demonstrated in Fig.21. The difference in wave height is about 0.05H, that is, 1.5mm which is close to the order of error in measurement.

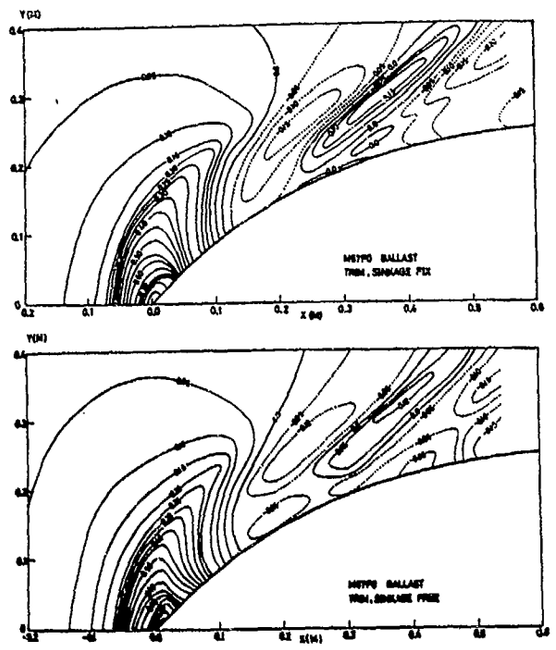

Fig.21 Measured contour maps of M57F0 in ballast condition showing the effect of sinkage and trim restriction.

The computed wave contour maps are compared in Figs.21 to 26. All the measurements except for the full-load condition were carried

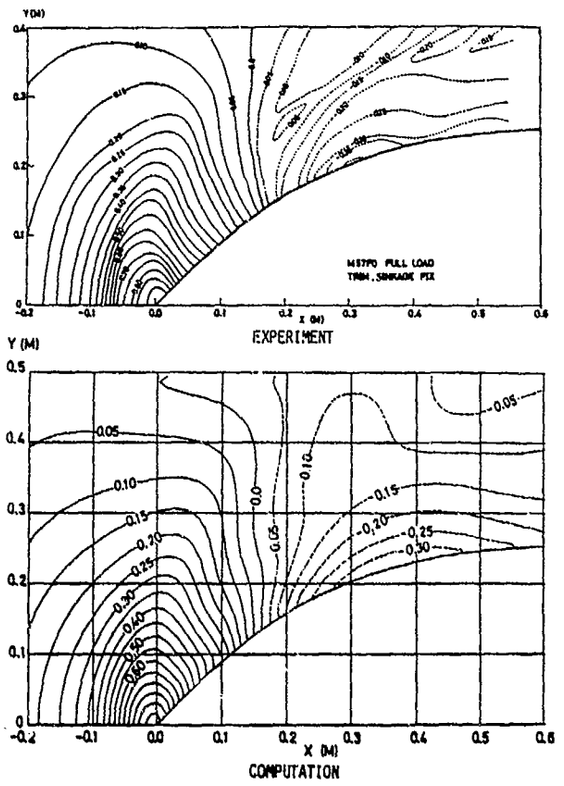

Fig.22 Comparison of contour maps of M57F0 in full-load condition.

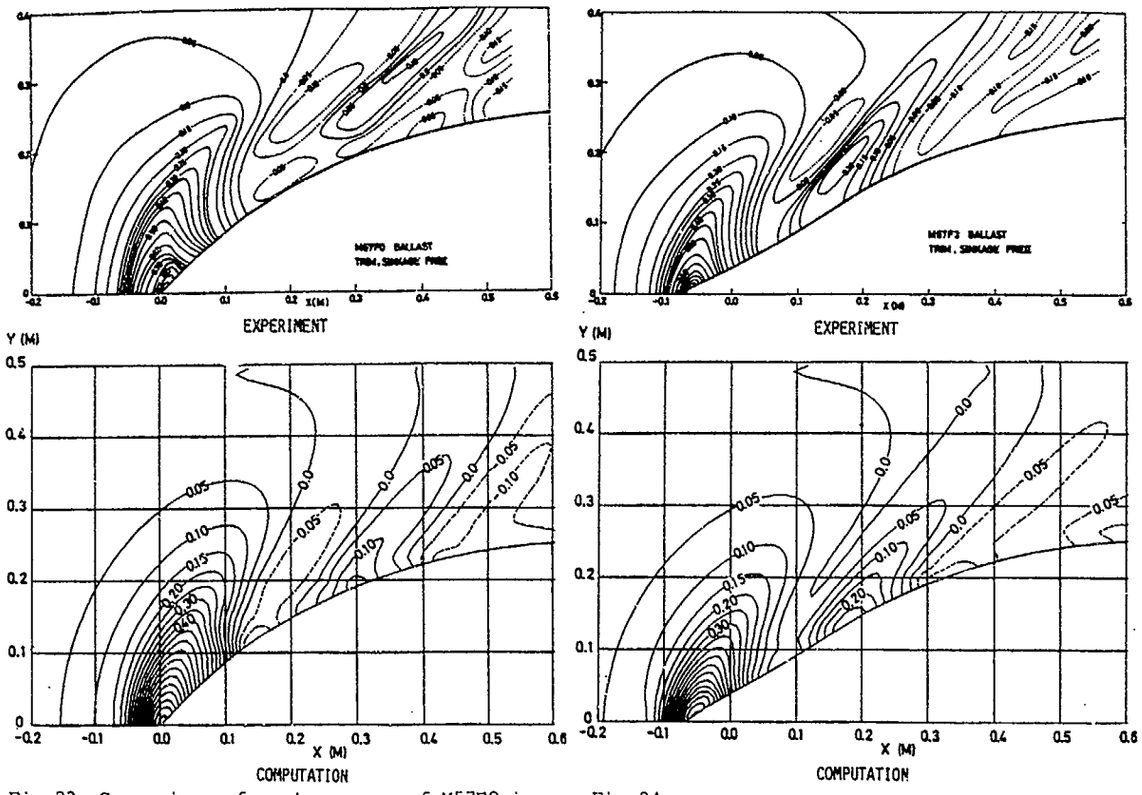

Fig.23 Comparison of contour maps of M57F0 in ballast condition.

Fig.24 same as Fig.23, M57F3.

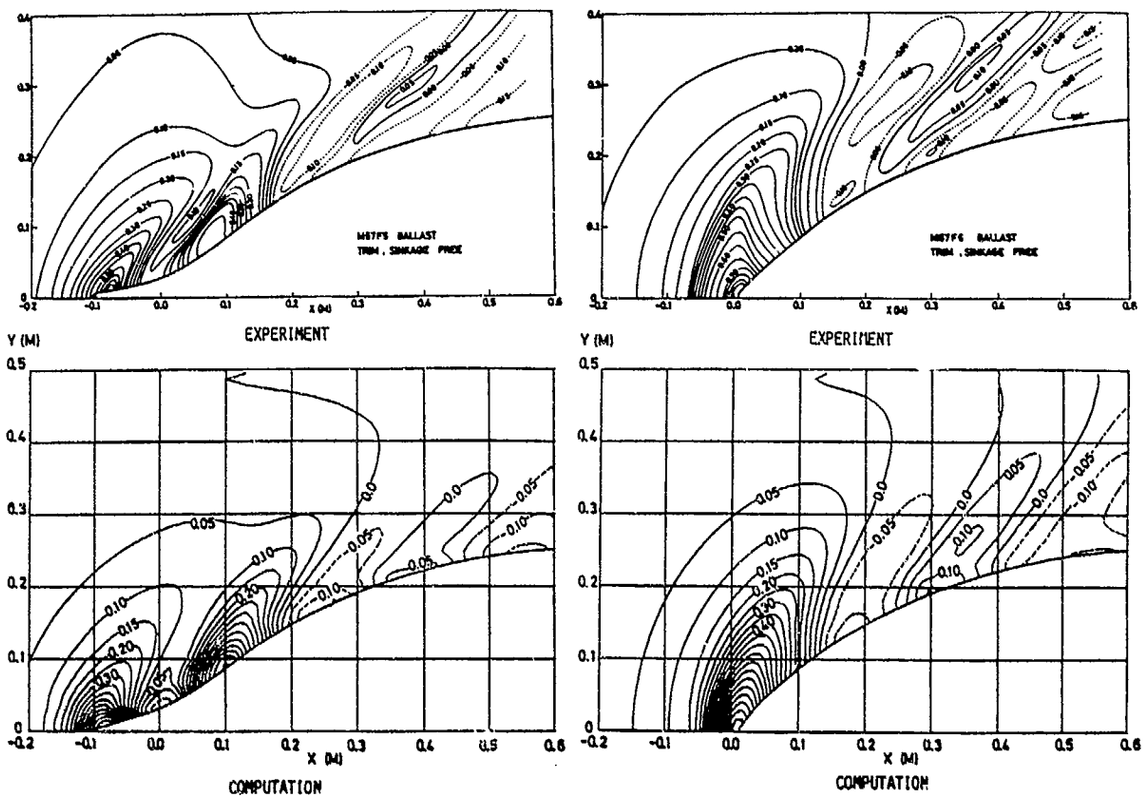

Fig.25 same as Fig.23, M57F5.

Fig.26 same as Fig.23, M57F6.

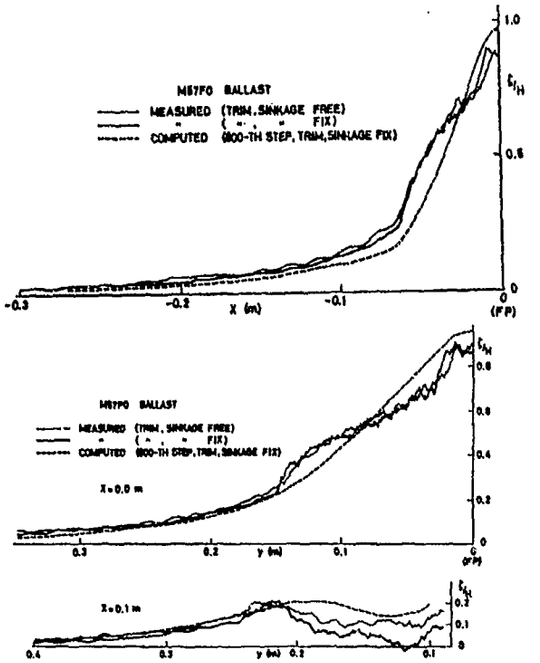

Fig.27 Comparison of measured and computed wave profiles on the centerline and two transverse lines of M57F0 in ballast condition.

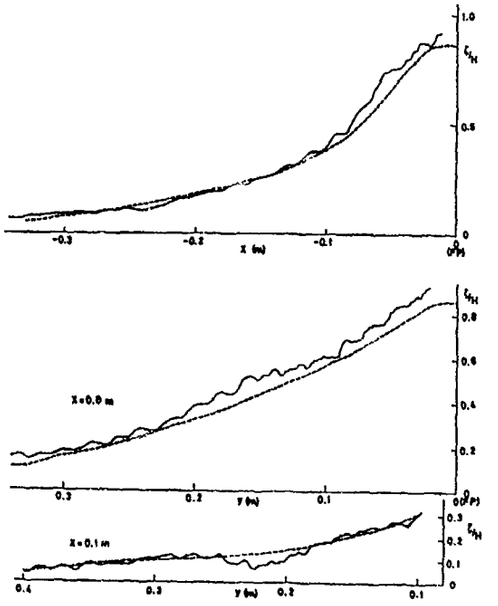

Fig.28 same as Fig.27, M57F0 in full-load condition.

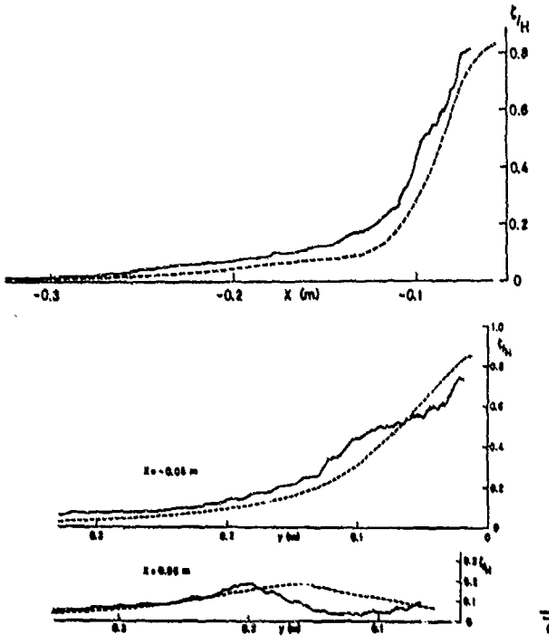

Fig.29 same as Fig.27, M57F3 in ballast condition.

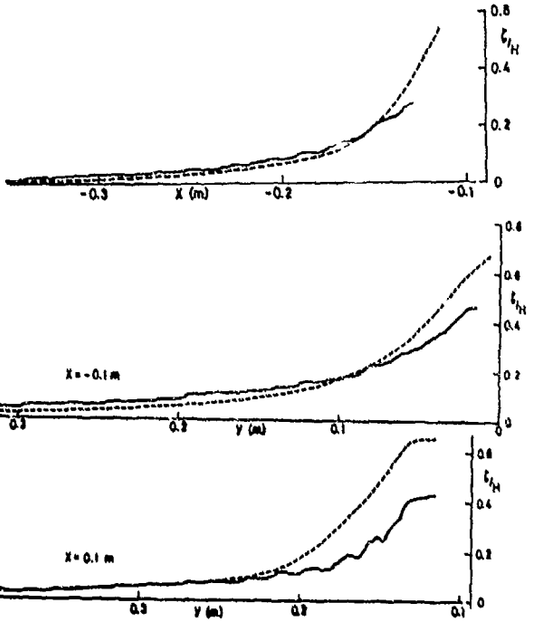

Fig.30 same as Fig.27, M57F5 in ballast condition.

out letting trim and sinkage free, despite the neglect of these movement in simulations. As is already noted in the previous cases of M55, the wave formation shows conspicuous differences between the two draft conditions. The configuration of the contours of the foremost wave is quite different and the second wave crest does not appear within the computational

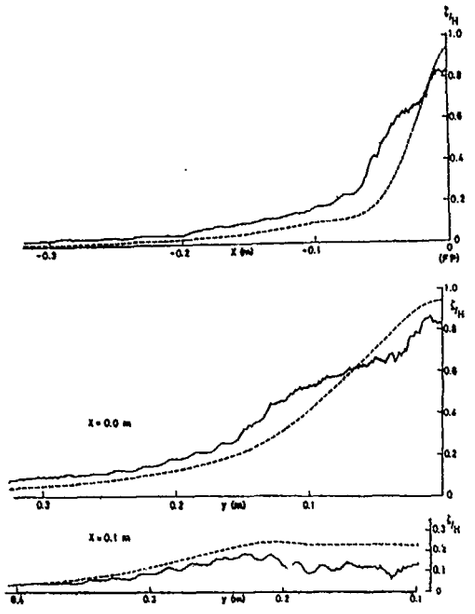

Fig.31 same as Fig.27, M57F6 in ballast condition.

domain in full-load condition while it is clearly generated in ballast condition. These significant change of waves due to the change of draft could not be explained by linear theories. Overall agreement is fairly good and it is especially so in the full-load condition. The most noticeable discrepancy appears on the second wave crest, to which complicated higher-order influences presumably due to the wave breaking and free surface turbulence will give effects.

In order to examine the details of agreement and disagreement some wave profiles are compared between simulation and experiment in Figs.27 to 31. Fig.27 shows that the effect of sinkage and trim is not significant. The measured profiles are reproduced from a recording paper of a pen-recorder and the recorded high-frequency fluctuation implies the occurrence of free surface turbulence. The agreement is most satisfactory in full-load condition, in which free surface turbulence is scarcely recorded. The measured wave profiles of M57F0,F3 and F6 in ballast condition show jump-like shape similar to a turbulent bore involving high-frequency fluctuation on and behind the jump. This implies that this jump-like shape is formed by wave breaking. The wave profile before wave breaking is supposed to show much better agreement with the simulated result. Therefore, the wave breaking motion seems to play a most significant role in the generation of the discrepancy. The remarkable discrepancy in the second wave crest, for instance at x=0.1m in Fig.30, is also attributable to the effect of wave breaking and subsequent turbulence generation. The degree of accuracy of the TUMMAC-IVvm1 method seems to be satisfactory unless significant wave breaking gives influences, and further improvement of the method will be attained when breaking motion is taken into account.

PART.2
BREAKING 2-D BOW WAVES

VI. Wave Breaking, Necklace Vortex

It is demonstrated in the previous section that the steepness of waves is imtimately related with wave breaking and that the agreement attained by the TUMMAC-IVvm1 method is inadequate when noticeable breaking occurs. The difference of the intensity of breaking motion is supposed to appear in the free surface turbulence, since wave breaking motion causes free surface turbulence.

Turbulence measurements were conducted with M55F0 and M55F3 [25]. The latter is a slight modification of M55F1. The measuring points are on the line parallel to the hull water-line and 10mm below the deformed free surface as seen in Fig.32. A split-type hot-film anemometer is used with the sampling time of 1 millisecond. The analysed turbulent kinematic energy and Reynolds shear stress are shown in Figs.33 to 36. It is noted that the difference of turbulence intensity is extremely large between the two. The difference of the nonlinear behavior of waves appears in a most exaggerated form in turbulence near the free surface. When this turbulence is of significant magnitude, its influence on the wave motion downstream may not be ignored. The understanding and theoretical explanation of the phenomena that start with wave breaking is of importance for the elucidation of the nonlinear wave mechanics and for the design of optimal hull form.

The nonlinear free surface flow around a bow of an advancing ship has been explained and discussed in terms of necklace vortex [26], wave breaking [10] and FSSW [11] [13] [14] since 1969. Recently similar experimental studies are made by other researchers [35] [36] [37] [38] [39]. However, no synthetic interpretation of the overall nonlinear phenomena is attained, although the authous explained the four developmental stages of FSSW through experimental analyses, namely, (a) formation of very steep nonlinear waves, (b) breaking or damping of wave crest and occurrence of energy deficit, (c) diffusion of energy deficit with free surface turbulence, and (d) formation of a momentum deficient wake far behind. The most nonlinear motions of wave

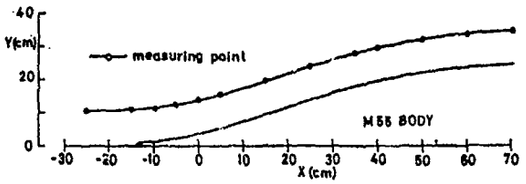

Fig.32 Points for turbulence measurement.

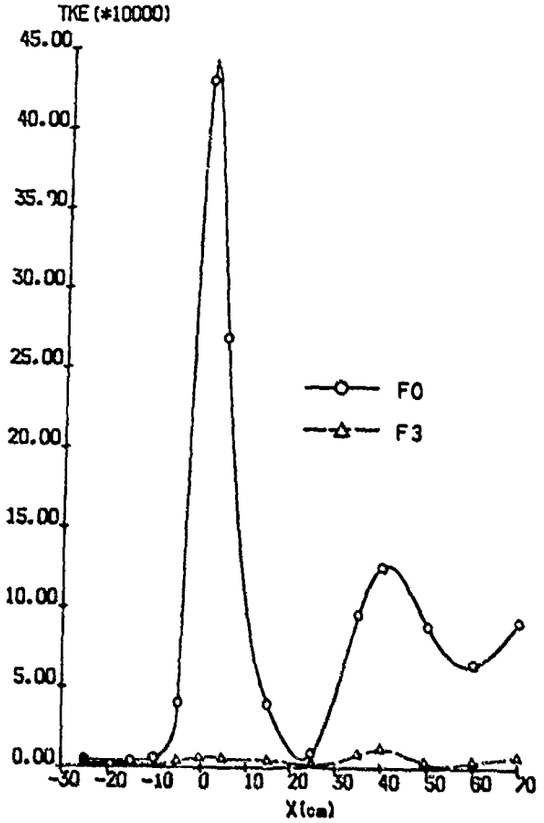

Fig.33 Longitudinal distribution of turbulent kinematic energy.

breaking and necklace vortex generation are associated with the stages (b) and (c). It seems to be easy to understand that steep waves maybreak and that overturning or spilling motion of breaking waves may produce vorticity. However, it is difficult to experimentally elucidate these developmental stages, since the fluid motion is usually very complicated involving remarkable turbulence.

The capability of a finite difference method for the simulation of wave breaking was demonstrated by Harlow et al.[27] through a numerical simulation of a breaking wave on a sloping beach. However, the subsequent numerical works seem to be tackled by a

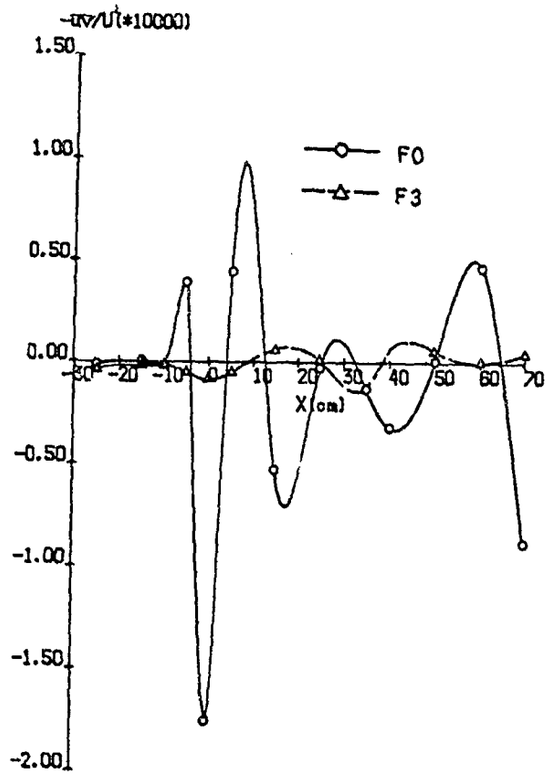

Fig.34 Longitudinal distribution of Reynolds shear stress.

boundary element method, for instance, by Longuet-Higgins et al.[28], Vinji et al.[29]. Despite the increasing number of research by a boundary element method the progress in the elucidation of wave breaking mechanics does not seem to be very remarkable. It seems to be clear that the boundary element method has substantial difficulties in the explanation of the wave motion after the stage of overturning. The overturning stage is only the beginning of the nonlinear behavior of breaking waves. Subsequent stages of the generation of wave impact load and vortices, which are full of nonlinear features, are of serious importance. Therefore, a finite difference method that has broader versatility is employed here for the simulation of 2-D breaking waves.

VII. The TUMMAC-Vot Method

The TUMMAC-V method was developed for the numerical study of nonlinear 2-D waves generated by an advancing floating body in deep water [30] [31] [32]. Since this method could not cope with the wave breaking motion, it is modified into TUMMAC-Vot version [33] [34].

The block diagram is shown in Fig.37. Since the fundamental solution algorithm and

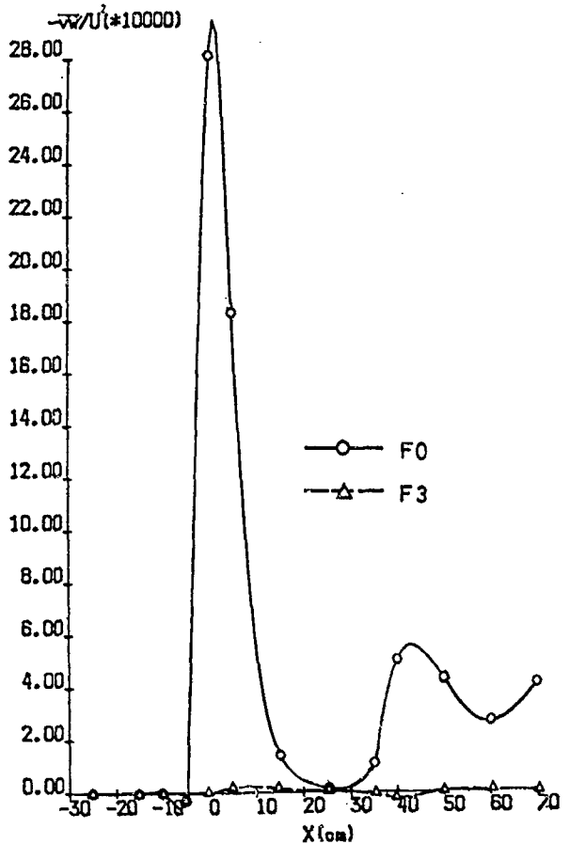

Fig.35 same as Fig.34.

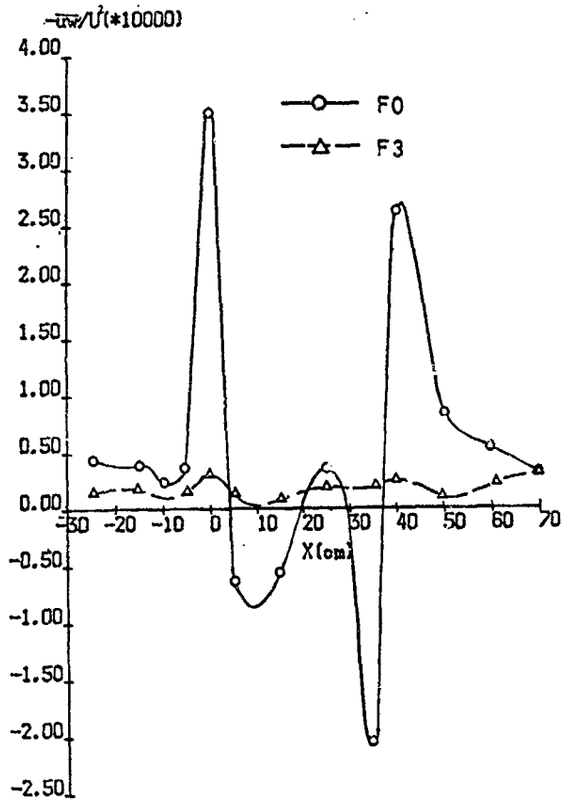

Fig.36 same as Fig.34.

the procedure are same with the TUMMAC-IVvm1 method, the equations and description of the computational procedure are not repeated here. The distinctive features of the TUMMAC-Vot method are the flagging, the determination of free surface and pressure computation, to which some explanations are given here.

All the cells are flagged. They are either a full-of-fluid cell (flagged F), an air cell (flagged A), a free surface cell (flagged S) or a body boundary cell (flagged B) as seen in Fig.38. The configuration of free surface is approximated by a succession of line segments of which end points are located on the underlying rectangular mesh system as seen in Fig. 39. An S-cell is defined as one that contains a segment of free surface. Flagging is also made for velocity and pressure depending on whether they are inside the segment or not. The use of segments instead of markers is advantageous for the expression of the free surface that is a multi-valued function of x-coordinate and for the flagging procedure. The computation of pressure is carried out at every inside pressure points. Outside velocities, which are necessary for the movement of segments and for the computation of convective terms, are not initially flagged and extrapolated from inside velocities with approximate zero-normal-gradient.

For the movement of segments a Lagrangian manner is used and the updated segments must have their end-points on the underlying mesh system as shown in Fig.39. In the solution of the Poisson equation for pressure by the SOR method the formula of "irregular star" is employed as seen in Fig.40. Four leg lengths for one pressure point are stored in memory.

Other particular consideration is necessary for the breaking motion just when the falling wave front touches the free surface below. The air region enclosed by the overturning wave is either filled with water when its area is approximately smaller than that of one cell or kept to be an air region to which free surface conditions are applied when it is sufficiently large.

VIII. Breaking Bow Waves in a Uniform Flow

A rectangular floating body of which length is 200mm and draft is 100mm is placed in a computational domain which is 2m long and 0.4m deep below the free-surface. The origin of the coordinate system being at the center of the body on the still free surface, the inflow boundary is located at x = -1.0m. The cell length DX is 10mm and the height DZ is 5mm, and then the number of cell in which pressure

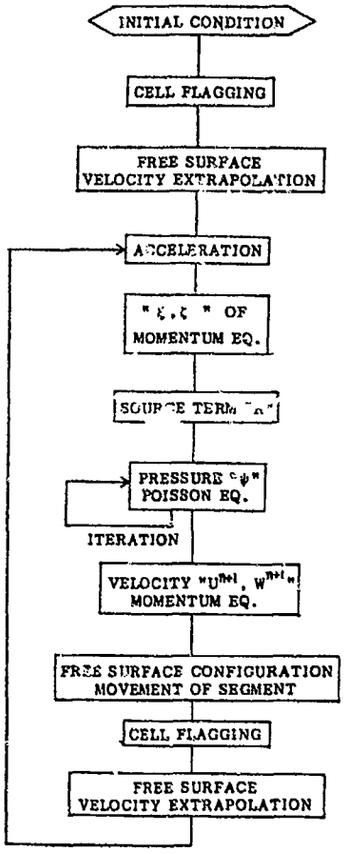

Fig.37 Block diagram of TUMMAC-Vot.

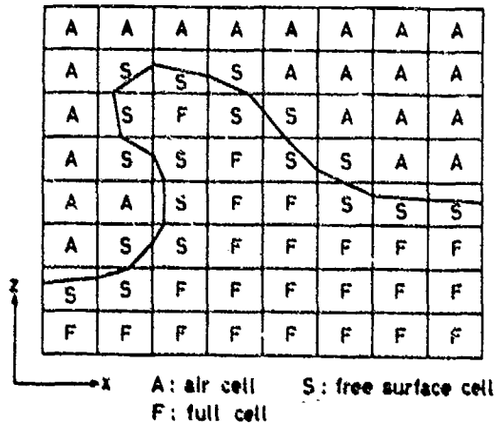

Fig.38 Cell flagging.

is computed is about 16000. The computations were undertaken at two Froude numbers based on draft Fd, i.e. 1.25 and 1.50. The uniform upstream is accelerated from rest to the above Froude numbers for 978 and 1404 time steps with the time increment of 0.00162 and 0.00135

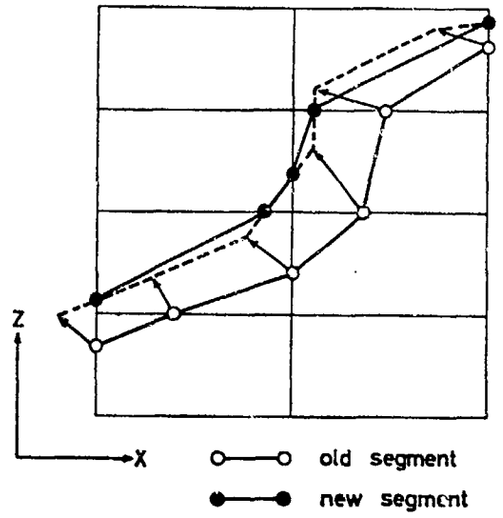

Fig.39 Movement of free surface segment.

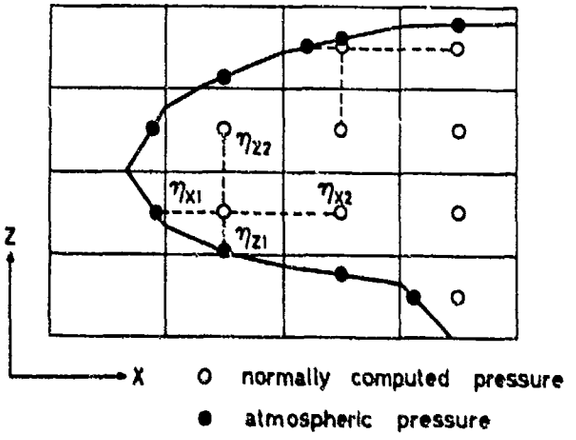

Fig.40 Pressure points and lags of "irregular stars".

sec, respectively. The actual kinematic viscosity 1.14×10^{6} m²/sec is used. The iteration number and time are denoted N and T, respectively.

Computed velocity vector fields after the accelerating stage are shown in Fig.41 for the case of Fd=1.25. Wave breaking motion similar to a spilling breaker occurs at the forward creeping wave front. The successive breaking motion produces vortical motion and the resultant vortical layer is gradually enlarged. The time development of vorticity is shown in contour maps in Fig.42. Significant vorticity is generated when the overturning wave front with forward velocity is connected with the forward face of the wave. The region with vorticity is extended both forward and back-

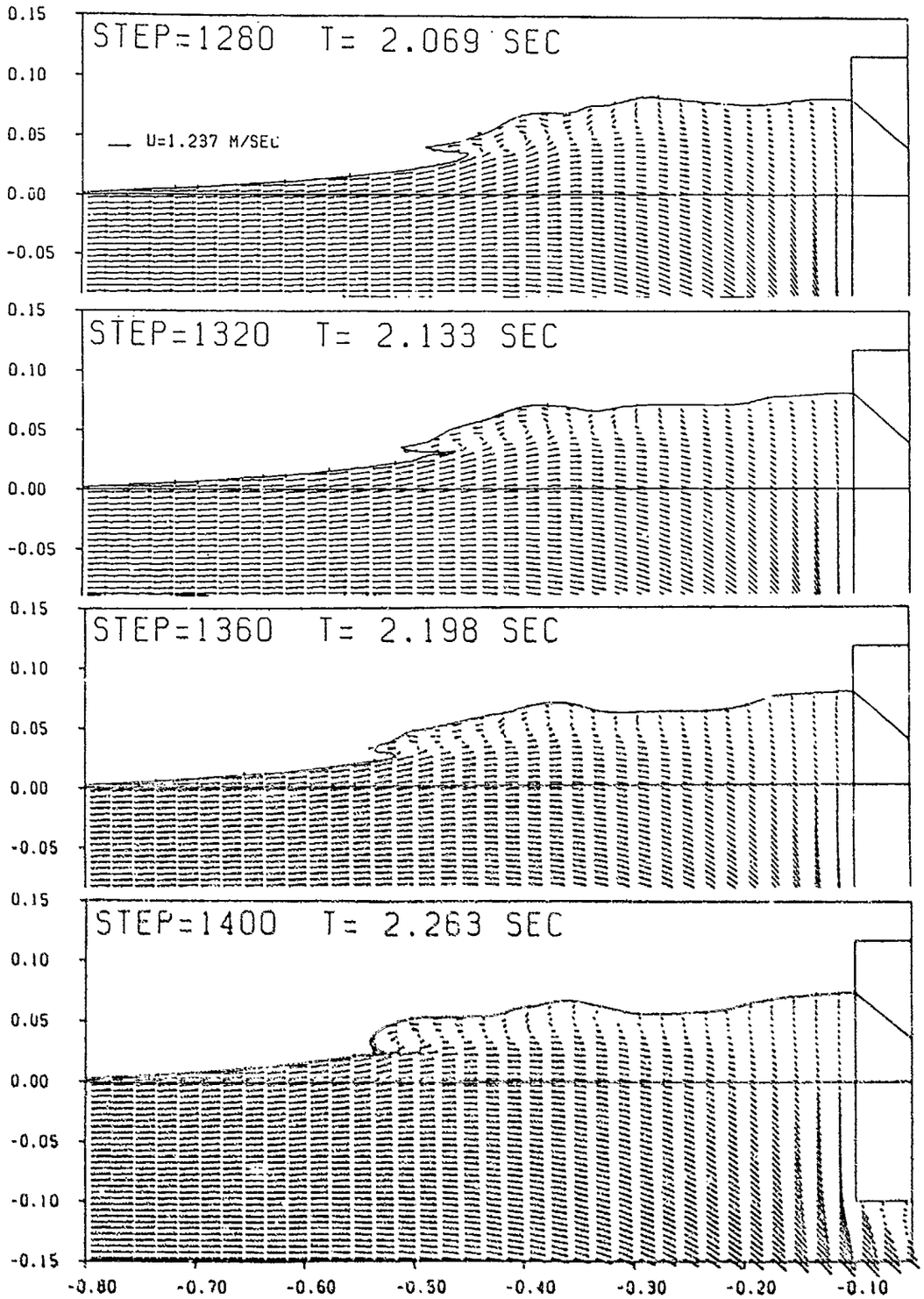

Fig.41 Velocity vector field of bow wave at Fd=1.25.

ward. The vorticity in the vicinity of the floating body is supposed to be associated with another vortex generation mechanism similar to that of horseshoe vortex.

The time sequence of wave profile at Fd=1.50 is shown in Fig.43. The breaking motion is much more evident. Plunging-type breakers are successively caused at the wave front that advances forward. The stern wave is also gradually developed without conspicuous dynamic motion and its almost steady profile

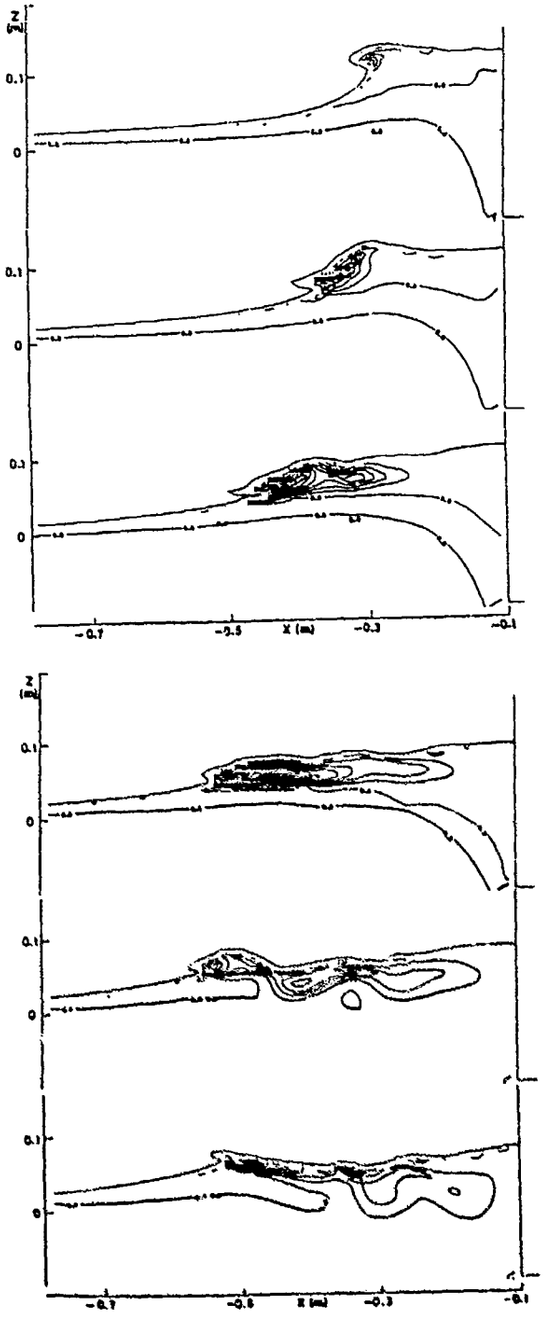

Fig.42 Time sequence of vorticity contour map at Fd=1.25, from T=1.745sec to 2.715sec at the interval of 0.194sec, the contour interval is $10m^2/sec$.

starts from the close proximity of the bottom of the floating body in this simulation. The details of the bow wave motion are shown in Fig.44. The overturning motion of large magnitude forms an enclosed air region and causes a vortical motion. The forward movement of the wave front ceases when it reaches x = -0.6m with the plunging motion being attenuated. It is worth noting that the increase of Froude number from 1.25 to 1.50 gives serious variation of the breaking motion, i.e. from spilling to plunging type. The difference between the two, therefore, is not supposed to be essential for the characteristics of breakers.

Pressure contours at four instances are shown in Fig.45 for the case of Fd=1.50. The high pressure region indicated by the circles is caused by the breaking motion. In particular, the high pressure is most obvious just when the falling wave front impinges the free surface below at the 1600th time step. The computed maximum pressure exceeds three times of the head of the uniform stream, the resolution of which is owing to the small time increment of the order of millisecond.

Although the computed results are not included in this paper, breaking motions do not occur in the simulation at Fd=1.00. A noticeable breaking motion which is resolved in the present computaion is not supposed to occur at Froude numbers below 1.00 in this 2-D case. The experimental study on ship bow waves in Section V also indicates that a breaking motion becomes conspicuous when the Froude number based on draft exceeds a certain value. A critical Froude number for the occurrence of bow wave breaking seems to exist.

The intense vorticity, high pressure and air-entrainment which are produced as consequences of breaking motions cause further complicated free surface motions as experimentally observed [31] [34]. The free surface is seriously turblulent with sound. The present simulation seems to be successful in the qualitative explanation of the generation of vorticity, high pressure and air-entrainment. However, quantitative agreement is not satisfactory. Further improvement is needed for the achivement of more realistic simulation, since at present the fluid motion is inevitably averaged in time and space and the turbulence model is not incorporated.

IX. Breaking Bow Waves in a Shear Flow

Shear flows are sometimes generated in circulating tanks and at sea with tidal currents, and they render influences on ship waves and consequently on wave resistance. Kayo and Takekuma [35] experimentally demonstrated the forward and backward movement of wave front due to the accelerated or decelerated free surface flow. In this section the influence of accelerated and decelerated shear flows on wave breaking is numerically simulated. The horizontal shear layers are produced by modifying the velocities at the inflow boundary. The uppermost velocity is accelerated or decelerated by 40% and other four velocities at the velocity points below are continuously modified with vertical distribution

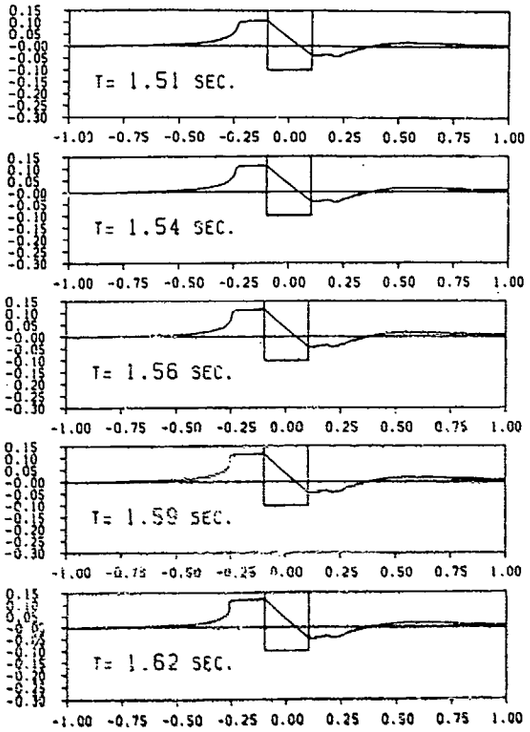

Fig.43(a) Time sequence of wave profile at Fd=1.50.

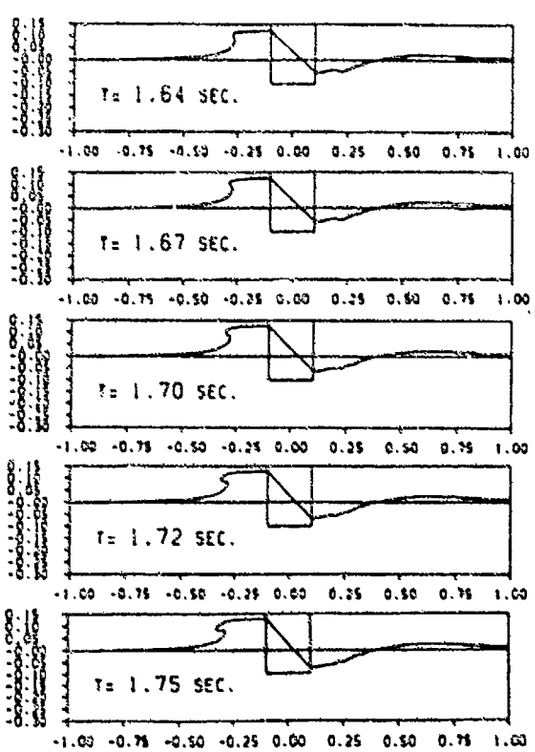

Fig.43(b) continued from Fig.43(a).

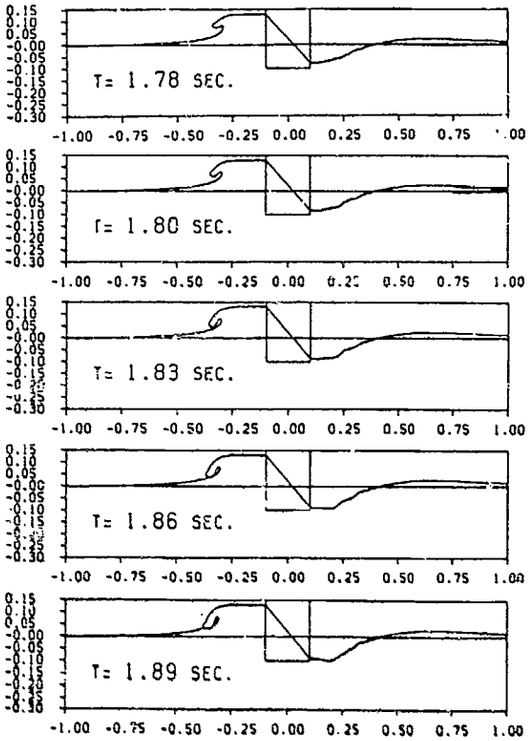

Fig.43(c) continued from Fig.43(b).

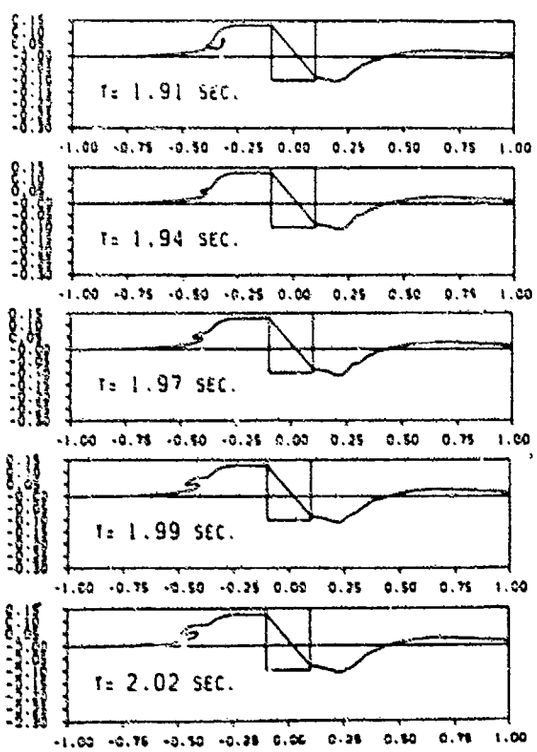

Fig.43(d) continued from Fig.43(c).

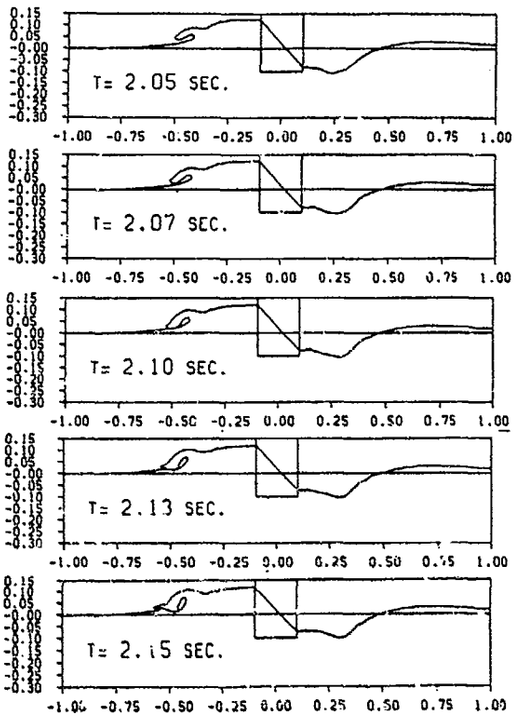

Fig.43(e) continued from Fig.43(d).

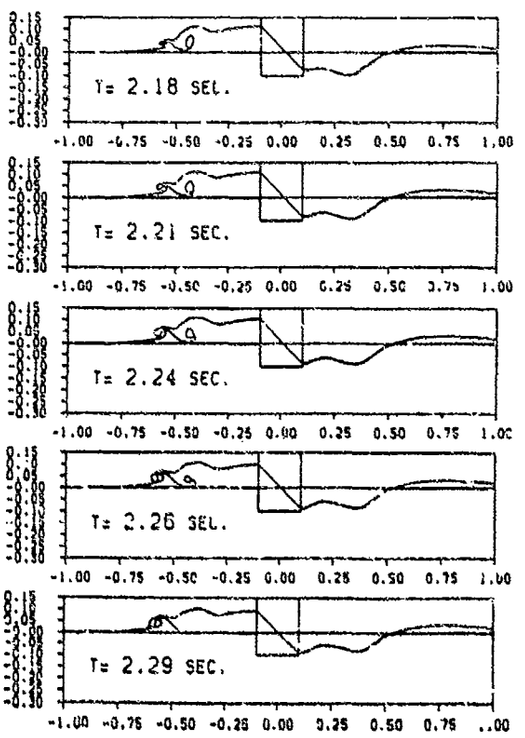

Fig.43(f) continued from Fig.43(e).

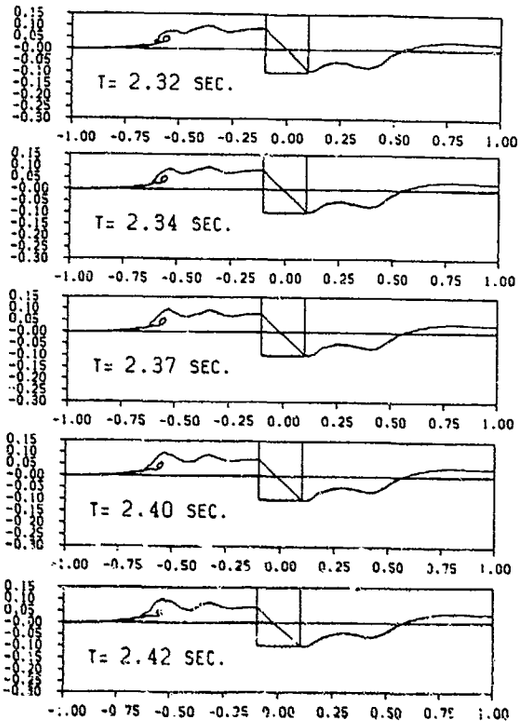

Fig.43(g) continued from Fig.43(f).

in parabolic curve. The simulation is conducted at Fd=1.25, while that at Fd=1.00 is described in Ref.[32] without breaking simulation.

The computed velocity vector fields of the accelerated and decelerated cases are shown in Figs.46 and 47, respectively, at the same time levels with Fig.41. The accelerated free surface flow magnifies the wave motion due to the large kinematic energy, while the decelerated free surface flow let the wave front advance forward and lower the wave level. In both cases a vortical flow with anticlockwise rotation is generated at the stagnant region just in front of the floating body, and it is more clearly observed in the decelerated case partly due to the accordance of the sign of rotation of the given shear flow.

Contour maps of velocities, vorticity γ and pressure are compared in Figs. 48 and 49. The breaking motion is more violent in the accelerated case as is observed. At this Froude number the increase of kinematic energy owing to the flow acceleration gives more significant effect on breaking motion than the vorticity of anticlockwise rotation caused by the free surface deceleration. However, the decelerated flow may play a little more important role about at the critical Froude number (Fd= 1.0) as seen in Ref.[32].

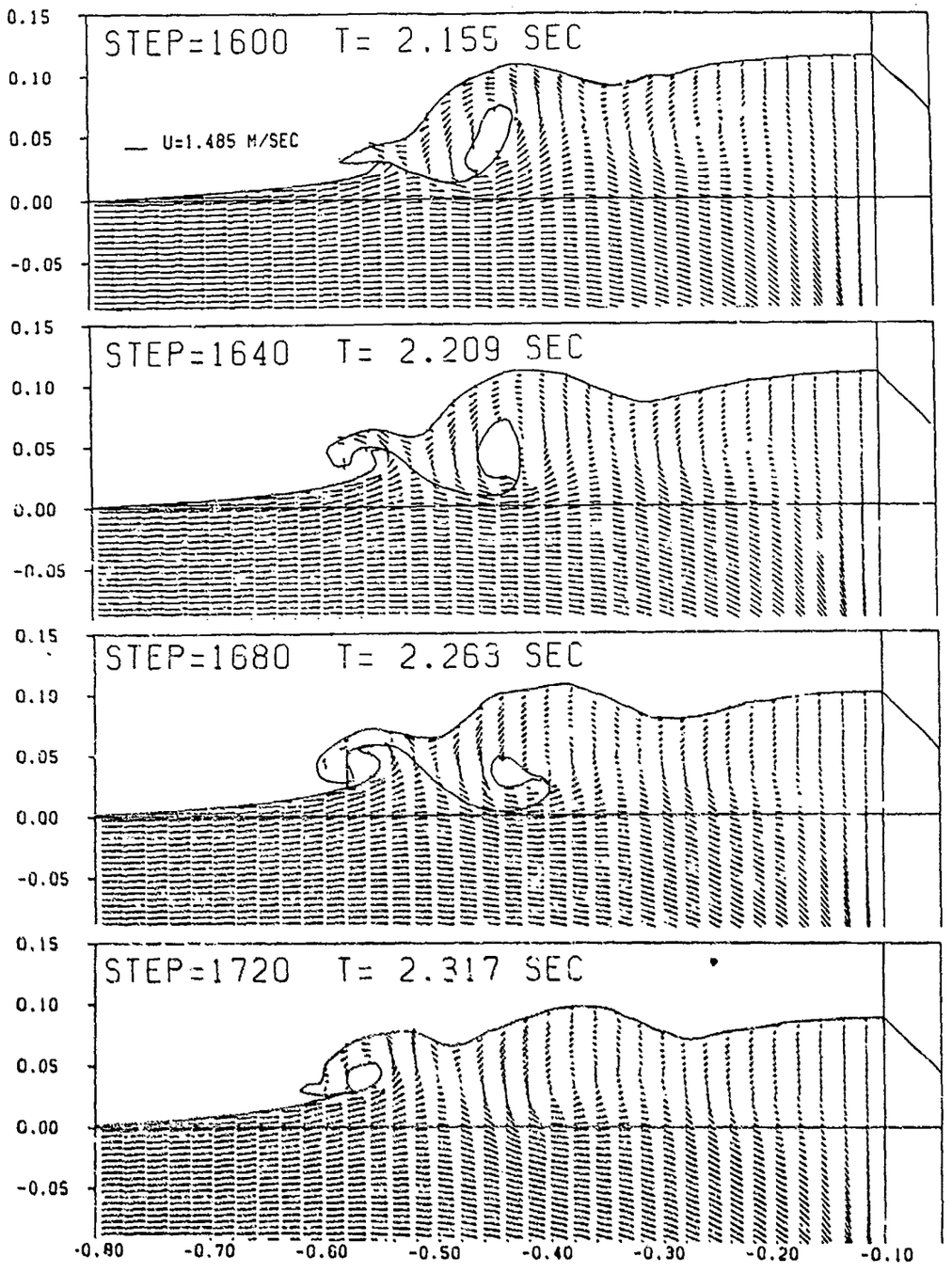

Fig.44 Velocity vector field of bow wave at Fd=1.50.

X. Evolution of Ship Wave

There are a number of argument for the complicated water flow around a bow. Kayo and Takekuma [35] claimed that a shear layer has an intimate relation with wave breaking and that the vortical motion in front of a bow is analogous to horseshoe vortex that occurs on a solid surface. The role of steep wave generation is not considered and the generation of a shear layer is not expained. Matsui et al. [36] pointed out a complicated vortical motion on the surface of a bow of a blunt ship. It is a little different phenomenon from the breaking motion at the wave front. Ogiwara et al. [37] elucidated the complicated flow field, but

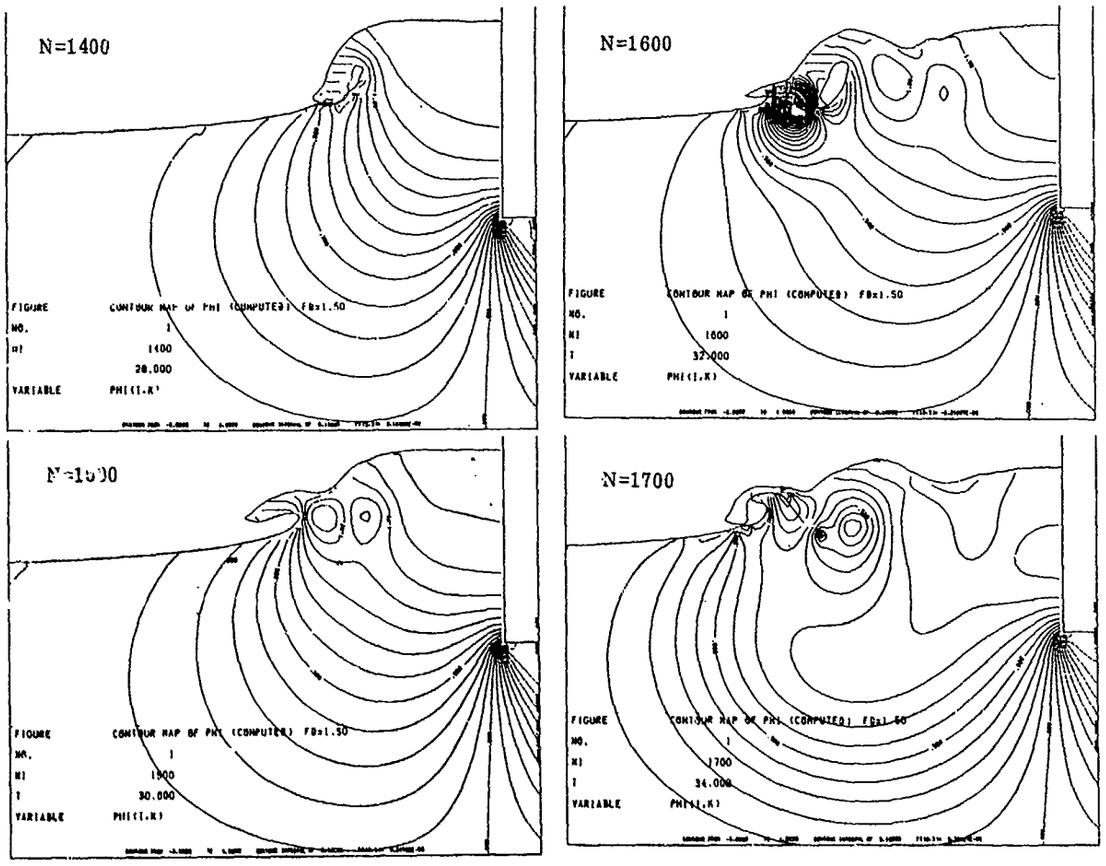

Fig.45 Contour maps of pressure ϕ at four instances of Fd=1.50, the contour interval is $0.1 m^2/sec^2$.

they do not put stress on the role of the Froude number based on draft. Takekuma and Eggers [38] showed the variation of wave front owing to the difference of bow geometry, which is one of the typical characteristics of free surface shock wave (FSSW) already elucidated by Miyata et al.[14]. Mori [39] claimed the role of viscous stress on the free surface in steepening of a wave. In general, they do not focus the attention on the generation of FSSW which is supposed to be the source of the succeeding nonlinear mechanics.

The simulations of bow waves of practical hull forms in PART 1 indicate that the numerical method that ignores viscous effects and wave breaking motions show fairly good agreement with the experimental results and that further improvement will be attained by taking into account the breaking motion. The simulations of 2-D breaking bow waves in PART 2 indicate that breaking waves cause further complicated motions, namely rotational flow, air-entrainment and free surface turbulence. It seems to be clear that among the many phenomena observed the most dominant is the generation of FSSW and the second is the breaking motion as far as bow waves at Froude numbers of ships are concerned. The viscous stress on the free surface should be negligibly weak.

The velocity profiles of a computed breaking 2-D wave (Fig.50) is compared with measured ones in the bow wave of a wedge model(Fig.51). The resemblance between the two is noticeable. The steep slope of velocity suddenly appears at the wave front and it is attenuated behind it. It is supposed to be generated by the steep wave slope and intensified by the breaking motion.

In terms of the bow flow two vortices are often discussed, they are necklace vortex and horseshoe vortex. The term of necklace vortex was used for vortices caused by wave breaking by Taneda and Amamoto [26]. The term of horseshoe vortex is currently used for the vortices generated as a result of the interaction of a boundary layer on a solid surface with a stagnant flow in front of a body, see Fig.52 for simplified 2-D illustration. Lugt [40] did not take notice of the difference between the two and called all the vortices of this kind necklace vortex, since the term of horseshoe vortex was reserved for the vortex system associated with 3-D wings with tip vortices. However, the present simulations and experimental results show that two kinds of vortex occur in a breaking bow wave.

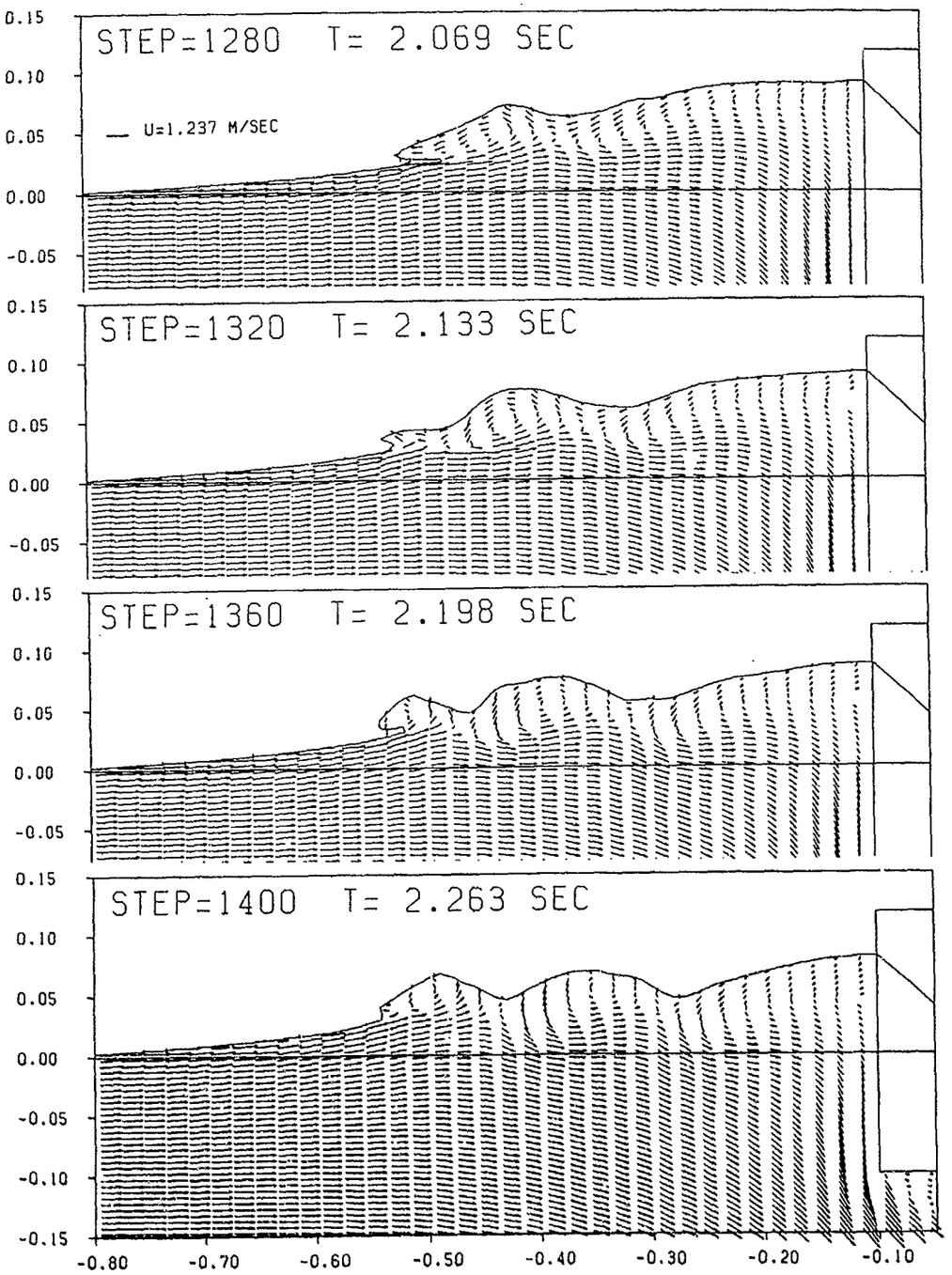

Fig.4b Velocity vector field at Fd=1.25 with an accelerated free surface flow.

The skematic stages of vortex generation are illustrated in Fig.53, which is drawn by simplifying the simulated 2-D velocity fields. The overturning of waves generates necklace vortex of which intensity depends on that of overturnig motion. The successive occurrence of breaking produces a vortical layer and this layer full of vorticity of anticlockwise rotation interacts with the flow at the stagnant region, and consequently a vortex similar to a horse-shoe vortex is generated in the proximity of the body. These stages are repeated. The generation of horseshoe vortex is quite different from that of necklace vortex caused by breakers. The role of boundary layer in case of a body with a solid surface is played by the

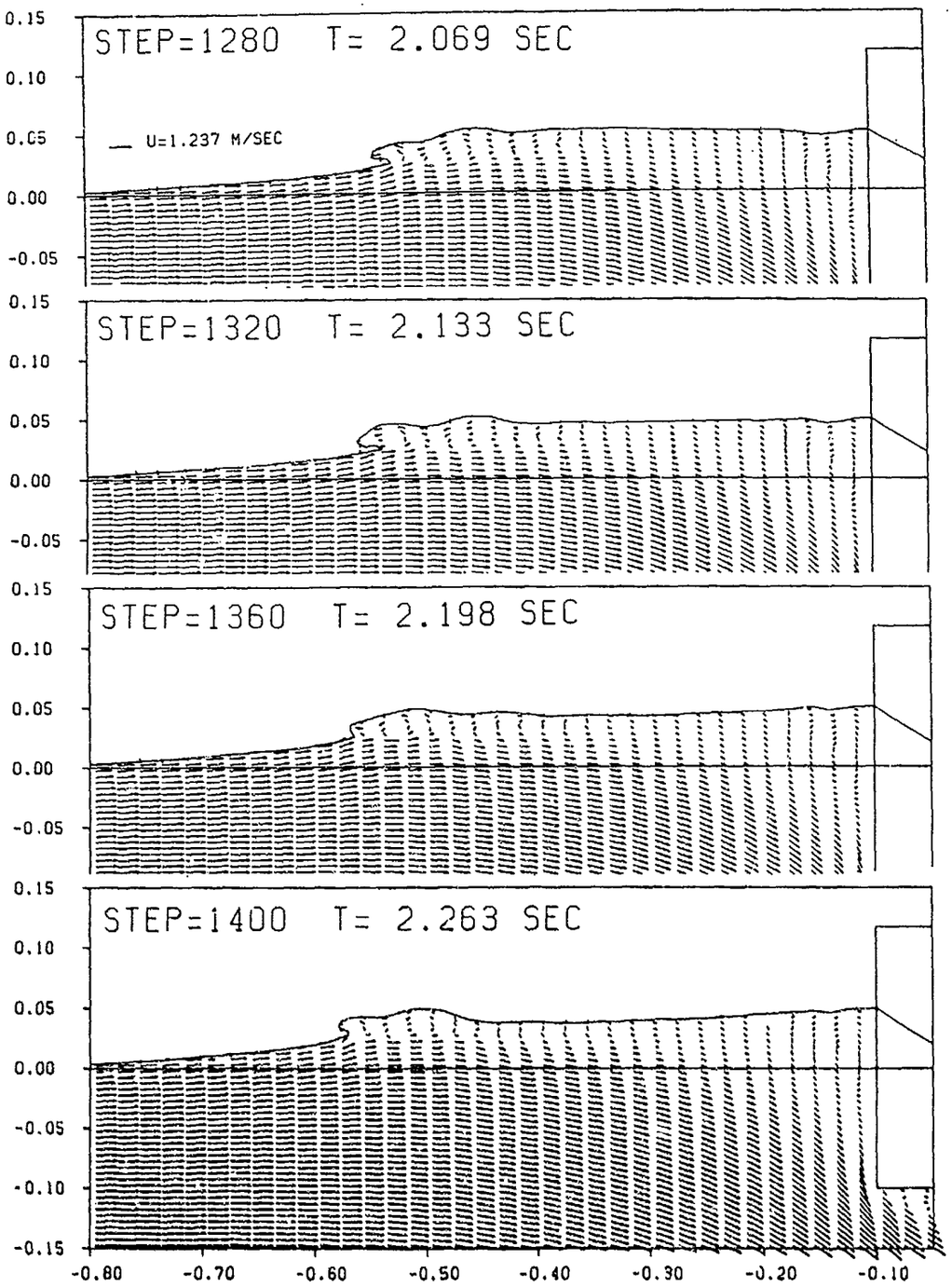

Fig.47 Velocity vector field at Fd=1.25 with a decelerated free surface flow.

vortical layer caused by breakers in the case of a body with a free surface. A steep vertical gradient of velocity that a steep non-breaking wave may produce also has the possibility to generate horseshoe vortex. However, the magnitude will be much smaller.

The above discussions are partly based on the 2-D simulations schematically illustrated in Fig.52, while both necklace and horseshoe vortices are three-dimensional in nature. However, the resemblance of Fig.50 with Fig. 51 seems to support the above intuitive discussions. In the flow field of bow waves both

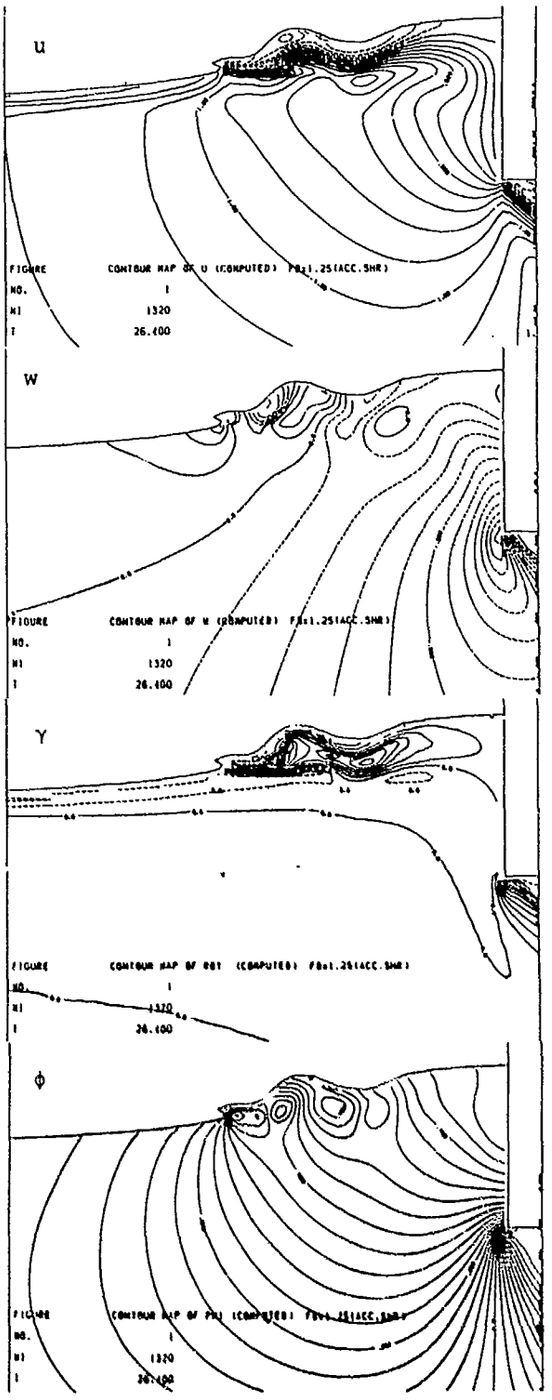

Fig.48 Contour maps of u, w, Y and ϕ at N=1320 in the case of accelerated free surface flow, the contour intervals are 0.1m/sec, 0.1m/sec, $10m^2/sec$ and $0.05m^2/sec^2$ respectively.

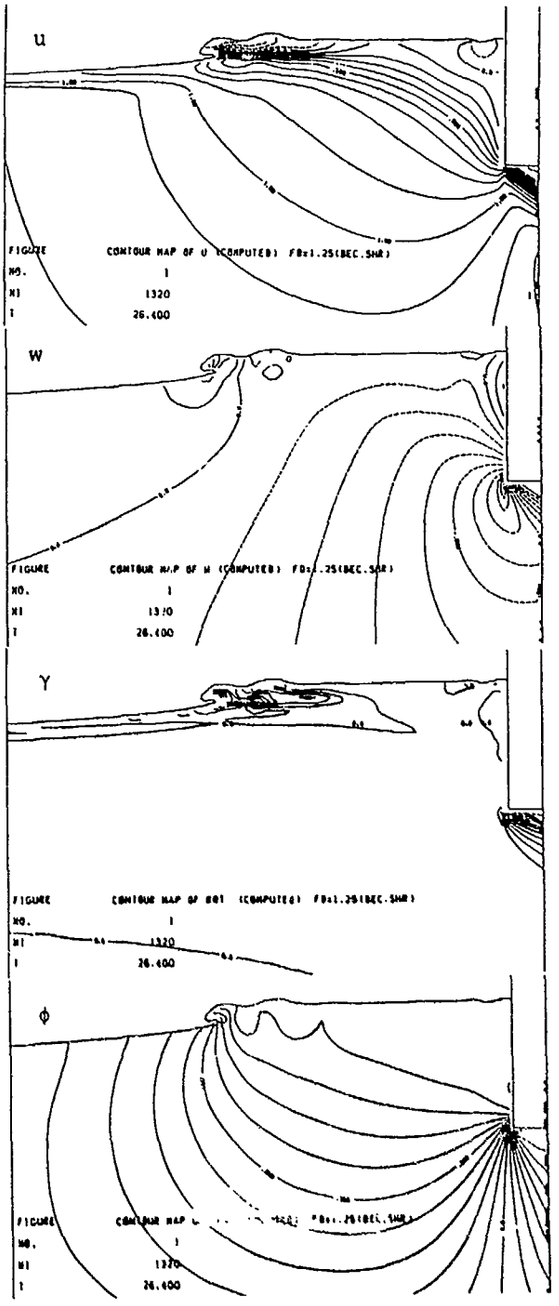

Fig.49 same as Fig.48, in the case of decelerated free surface flow.

necklace and horseshoe vortices occur. The role of the latter cannot be ignored. However, necklace vortices are usually more important, while horseshoe vortices almost disappear if the bow configuration is not so blunt as to generate a normal FSSW.

Wave breaking is the phenomenon of dissipating wave energy, and furthermore, the subsequent phenomena of vortex generation, air-entrainment and turbulence generation are related with viscous dissipation. On the other hand the role of dispersion in ship waves is

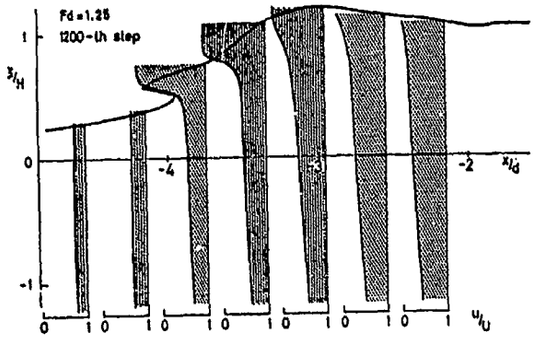

Fig.50 Computed velocity profiles at Fd=1.25.

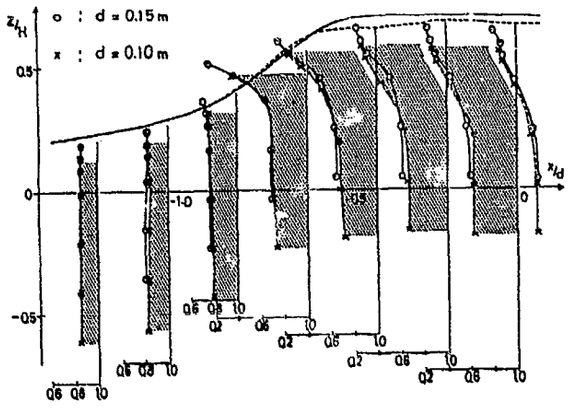

Fig.51 Measured velocity profile on a plane parallel to and a draft length away from the centerplane for a wedge model of $\alpha=45°$ at Fd=1.0.

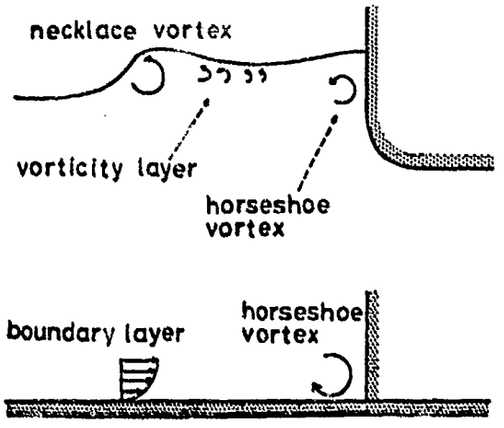

Fig.52 Necklace vortex and horseshoe vortex.

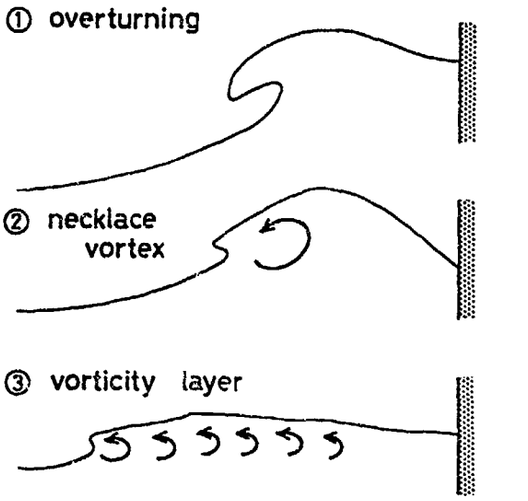

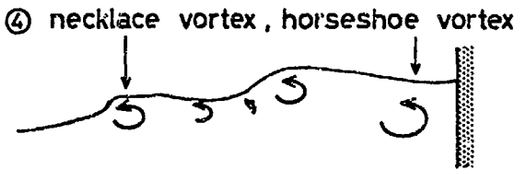

Fig.53 Vortex generation in bow waves.

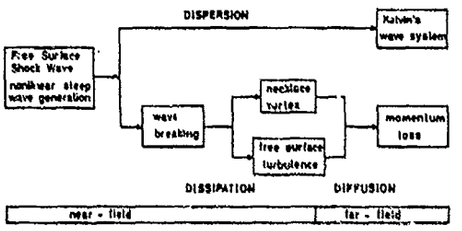

Fig.54 Evolution of ship wave.

well known with the Kelvin's wave system. Therefore, dissipation and dispersion are both important for ship waves. The nonlinear steep waves called FSSW are generated by a ship in the close vicinity and the wave energy concentrated in it is partly dissipated into momentum loss far behind through breaking and turbulence generation and partly spread to the far field by dispersion to form a Kelvin's wave system, as shown in Fig.54. The difference between the wave resistance derived from force measurement and that derived from wave analysis is attributed to the dissipation of wave energy. The importance of dispersion and dissipation in waves of forebodies depends on the hull geometry and the Froude number based on draft. A blunt bow generates waves of large height and steepness which are likely to break. Wave breaking does not occur unless the Froude number

based on draft exceeds a certain critical value. As already described, wave breaking is scarcely noted in the full-load condition of M57 while it is remarkable in the ballast condition. This is due to the difference of that Froude number, since the Froude number based on ship length is common to the two conditions.

XI. Concluding Remarks

Two versions of the TUMMAC method are described with a lot of computed results. The TUMMAC-IVvm1 method has succeeded in the simulation of FSSW generation and the TUMMAC-Vot method has been proved to be useful for the understanding of the mechanics of wave dissipation. The former method seems to be already available for the use of engineering purposes, since the generation of FSSW is the source of subsequent phenomena and wave generation itself gives resistance to a ship. By finding a better hull form among a series of hull the optimization procedure can be achived. However, for further advanced reliability of the numerical simulation used for engineering purposes the simulation of 3-D wave breaking and the modelling of free surface turbulence must be incorporated in the simulation method for ship waves in future.

The TUMMAC-IVvm1 method was developed for the simulation of nonlinear ship waves, characteristics of which were well clarified by experiments, and then its practical capability of discriminating a better hull form was aimed at by raising the degree of accuracy. On the other hand the TUMMAC-Vot method was developed to investigate into the very nonlinear phenomenon, to which experimental investigations find difficulties in whole elucidation because of the complixity and unsteadiness. These seems to be the two kinds of important usage of numerical experiment by a finite difference method.

The computations with the TUMMAC-IVvm1 code were executed by a super-computer HITAC S-810/20 and those with the TUMMAC-Vot code by a HITAC M-280 of the Computer Centre, the University of Tokyo. The maximum speed of S-810/20 is greater than 600 MFLOPS. Since 70% of the computations in TUMMAC-IVvm1 is vectorizedthe use of the super-computer is advantageous, while no part of TUMMAC-Vot is vectorized owing to the complexity of sorting and flagging. The CPU time required by the simulation of waves of forebodies is about one hour for respective case, and that required by the 2-D breaking simulation is about two hours when the computation is continued for 2000 time steps.

Acknowledgements

This research is supported by the Grant-in-Aid for Scientific Research of the Ministry of Education, Science and Culture and partly by the LINEC group of shipbuilders in Japan.

The authors wish to thank Mr.Y.Tsuchiya and graduate students for their supports, and also Ms K.Takahashi for her typewriting.

References

[1] T. Inui, From bulbous bow to free-surface shock wave--trends of 20 years' research on ship waves at the Tokyo University Tank. J. Ship Research, 25-3 (1981), 147-180.

[2] T. Inui and H. Miyata, On the optimization of overall performance of rudders (second report). J. Soc. Nav. Archit. Jpn. 145 (1979), 19-26, (in Japanese), also in Nav. Archit. Ocean Eng. 18, Soc. Nav. Archit. Jpn. (1980), 10-20, (in English).

[3] H. Miyata, Y. Tsuchiya, T. Inui and H. Adachi, Resistance reduction by stern-end-bulb (first report), J. Soc. Nav. Archit. Jpn. 148 (1980), 10-16.

[4] H. Miyata, Y. Tsuchiya and T. Inui, Resistance reduction by stern-end-bulb (second report). J. Soc. Nav. Archit. Jpn. 149 (1981), 1-10.

[5] H. Okamoto, A. Tanaka, T. Yamano, T. Inui and H. Miyata, Resistance reduction by stern-end -bulb(third report). J. Soc. Nav. Archit. Jpn. 152 (1982), 22-31.

[6] M. Nito, H. Kajitani, H. Miyata and T. Tsuchiya, Free surface shock waves and methods for hull form improvement (first report) J. Soc. Nav. Archit. Jpn. 150 (1981), 19-29.

[7] H. Miyata, H. Kajitani, M. Nito, K. Aoki, M. Nagahama and Y. Tsuchiya, Free surface shock waves and methods for hull form improvement (second report). J. Soc. Nav. Archit. Jpn. 152 (1982), 13-21.

[8] T. Inui, Wave-making resistance of ships. Soc. Nav. Archit. Mar. Eng. Trans. 70 (1962), 283-353.

[9] H. Miyata, H. Kajitani, S. Iwase, K. Ichiju, H. Tominaga and Y. Tsuchiya, Resistance reduction by a horizontal-bow-fin and a movable bulb. J. Kansai Soc. Nav. Archit. Jpn. 191 (1983), 17-30.

[10] E.Baba, A new component of viscous resistance of ships. J. Soc. Nav. Archit. Jpn. 125 (1969), 9-34.

[11] H. Miyata, T. Inui and H. Kajitani, Free surface shock waves around ships and their effects on ship resistance. J. Soc. Nav. Archit. Jpn 147 (1980), 1-9. also in Nav. Archit. Ocean Engng. 18 (1980), 1-9.

[12] M. Takahashi, H. Kajitani, H. Miyata and M. Kanai, Characteristics of free surface shock waves around wedge models. J. Soc. Nav. Archit. Jpn. 148 (1980), 1-9.

[13] H. Miyata, Characteristics of nonlinear waves in the near-field of ships and their effects on resistance. Proc. 13th Symposium Naval Hydrodynamics, Tokyo, Shipbuilding Research Association of Japan (1980), 335-351.

[14] H. Miyata and T. Inui, Nonlinear ship waves. Advances in Applied Mechanics, 24 (1984), 215-288.

[15] J. E. Welch, F. H. Harlow, J. P. Shannon and B. J. Daly, The MAC method. Los Alamos Scientific Lab. Report, LA-3425, Univ. California, Los Alamos, New Mexico (1966).
[16] H. Miyata, A. Suzuki and H. Kajitani, Numerical explanation of nonlinear nondispersive waves around bow. Proc. 3rd International Conference on Numerical Ship Hydrodynamics, Paris (1981), 37-52.
[17] A. Suzuki, H. Miyata, H. Kajitani and M. Kanai, Numerical analysis of free surface shock waves around bow by modified MAC-method (first report). J. Soc. Nav. Archit. Jpn. 150 (1981), 1-8.
[18] A. Masuko, H. Miyata and H. Kajitani, Numerical analysis of free surface shock waves around bow by modified MAC-method (second report). J. Soc. Nav. Archit. Jpn.152 (1982), 1-12.
[19] K. Aoki, H. Miyata, S. Nishimura and H. Kajitani, Numerical analysis of free surface shock waves around bow by modified MAC-method (third report). J. Soc. Nav. Archit. Jpn. 153 (1983), 13-20.
[20] K. Aoki, H. Miyata, A, Masuko and H. Kajitani, A numerical analysis of nonlinear waves generated by ships of arbitrary waterline (first report). J. Soc. Nav. Archit. Jpn. 154 (1983), 17-28.
[21] H. Miyata, K. Aoki and H. Kajitani, A numerical analysis of nonlinear waves generated by ships of arbitrary waterline (second report). J. Soc. Nav. Archit. Jpn. 155 (1984), 1-10.
[22] H. Miyata, S. Nishimura and A. Masuko, Finite difference simulation of nonlinear waves generated by ships of arbitrary three-dimensional configuration. J. Comput. Physics (to appear)
[23] H. Miyata and S. Nishimura, Finite-difference simulation of nonlinear ship waves. J. of Fluid Mech. 157 (1985), 327-357.
[24] C. W, Hirt, B. D. Nichols and N. C. Romero, SOLA- A numerical solution algorithm for transient fluid flows. Los Alamos Scientific Lab. Report LA-5852, Los Alamos, New Mexico (1975).
[25] T. Inoue and K. Hasebe, A method of hull form improvement using divided ship models. Graduation thesis of Univ. Tokyo, Dept. Nav. Archit. (1984).
[26] S. Taneda and H. Amamoto, Necklace vortex around bow. Bulletin No.31 Research Inst. Appl. Mech., Kyushu Univ., Jpn. (1969) 17-28.
[27] F. H. Harlow and A. A. Amsden, Fluid Dynamics. Los Alamos Scientific Lab. Report LA-4700, Los Alamos, New Mexico. (1971).
[28] M. S. Longuet-Higgins and E. D. Cokelet, The deformation of steep surface waves on water, I. A numerical method of computation. Proc. R. Soc. Lond. A350 (1976), 1-26.
[29] T. Vinji and P. Brevig, Numerical calculations of forces from breaking waves, Proc. Intern. Sympo. Hydrodynamics in Ocean Engineering, The Norwegian Institute of Technology, Trondheim(1981), 547-565.
[30] H. Miyata, H. Kajitani N. Suzuki and C. Matsukawa, Numerical and experimental analysis of nonlinear bow and stern waves of a two-dimensional body (first report). J. Soc. Nav. Archit. Jpn. 154 (1983), 48-55.
[31] H. Miyata, H. Kajitani, C. Matsukawa, N. Suzuki, M. Kanai and S. Kuzumi, Numerical and experimental analysis of nonlinear bow and stern waves of a two-dimensional body (second report). J. Soc. Nav. Archit. Jpn. 155 (1984), 11-17.
[32] H. Miyata, Nonlinear wave making of a two-dimensional advancing body. Theoretical and Applied Mech. Vol. 33, Univ. Tokyo Press (1985), 15-49.
[33] H. Miyata, N. Baba, H. Kajitani, T. Sato and M. Shirai, Numerical and experimental analysis of nonlinear bow and stern waves of a two-dimensional body (third report). ——Numerical simulation method for breaking waves—— J. Soc. Nav. Archit. Jpn. 156 (1984), 1-12.
[34] H. Miyata, H. Kajitani, M. Shirai, T. Sato, S. Kuzumi and M. Kanai, Numerical and experimental analysis of nonlinear bow and stern waves of a two-dimensinonal body (fourth report). ——Simulation of breaking waves and experimental analysis—— J. Soc. Nav. Archit. Jpn. 157(1985), 15-33.
[35] Y. Kayo and K. Takekuma, On the free surface shear flow related to bow wave-breaking of full ship models. J. Soc. Nav. Archit. Jpn. 149 (1981), 11-20.
[36] M. Matsui, T. Kitazawa and M. Nagahama, Observation of nonlinear waves around ship bow models. J. Kansai Soc. Nav. Archit. Jpn. 190 (1983), 63 -71.
[37] S. Ogiwara, A. Masuko, R. Sato and T. Tsutsumi, Experimental investigation on free surface flow related to bow wave breaking. J. Kansai Soc. Nav. Archit. Jpn. 194 (1984), 119-131.
[38] K. Takekuma and K. Eggers, Effect of bow shape on free-surface shear flow. Proc. 15th Sympo. Naval Hydrodynamics, Hamburg (1984).
[39] K. Mori, Necklace vortex and bow wave around blunt bodies. Proc. 15th Sympo. Naval Hydrodynamics, Hamburg (1984).
[40] H. J. Lugt, Numerical modelling of vortex flows in ship hydrodynamics. Proc. 3rd Intern. Conf. Numerical Ship Hydrodynamics. Paris (1981), 297-316.

DISCUSSION
of the paper
by H. Miyata

"FINITE-DIFFERENCE SIMULATION OF NON-BREAKING 3D BOW WAVES AN BREAKING 2D BOW WAVES"

DISCUSSION
by H.C. Raven

In general your calculations appear to give a fairly good prediction of the wave elevations. The velocity fields (Fig. 7 and 17), however, show some very strange features. It is useful to realize that in fact you are solving a nearly potential flow problem: the flow is considered to be laminar, for a Reynolds number of a few million, and free slip boundary conditions are imposed. Therefore there is no physical source of vorticity of any significance, except perhaps at the free surface

Still the resulting flow field is full of vorticity, you find separation from a smooth surface, and even at a large distance from the hull the flow does not resemble a potential flow; moreover, the "vortex sheet" found in the centerplane seems to follow a very strange path. Suppose that all this is due to numerical errors. Does not this make all other results (including the wave patterns) also unreliable?

Author's Reply

The vortices that appear in the simulations by TUMMAC-IV are supposed to be due to numerical error. However, the simulated bilge vortices seem to be similar to physically observed ones, although the effective Reynolds number in the simulations is smaller than the actual value due to the truncation error of the convective terms and the vortices are diffused. It is interesting to note that Rizzi and Eriksson (J. Fluid Mech. 153, 1985) successfully simulated vortices on a 3-D wing by a finite-difference method based on Euler's equations.

The interaction of bow waves with bilge vortices has not been considered to be of importance. The good agreement in wave geometry attained by our method seems to support this understanding.

DISCUSSION
by K. Eggers

I feel sorry to be unprepared for a deep discussion as this paper certainly deserves. Just one point: your computations for a 2-D rectangular cylinder showed a row of discrete vortices ahead of the cylinder, as displayed in Fig. 6. We have performed experiments in Hamburg in cooperation with Dr. Kayo from Mitsubishi with a semi-submerged circular cylinder and observed the flow by video camera after injecting tracers.

For all speeds considered we observed discrete vortices of alternating sign in the triangular dead water region behind the free-surface stagnation point ahead of the bow. I wonder if your program may be able to simulate even such phenomenon?

Author's Reply

I thank Prof. Eggers for his valuable discussion. The present method cannot simulate with satisfactory quantitative accuracy the viscous flow with turbulence and vortices which is generated by wave breaking and so on partly due to the lack of turbulence model and the insufficient degree of accuracy. However the strength of the horseshoe vortices is far weaker than that of the necklace vortices by wave breaking as seen in Fig. 42. It will be better to note that the flow visualization technique is not always useful for the understanding of the intensity of the fluid motions. Intense motions, often with turbulence, are difficult to be visualized by tracers and gentle motions are some times easily visualized. Most dominant phenomena seem to be satisfactorily simulated by the present method but the improvement of the method is necessary for the resolution of the more detailed phenomena that the discusser experimentally elucidated.

DISCUSSION by C.E. Hirt

Professor Miyata and his colleagues are to be commended for their excellent work in comparing experimental observation with detailed numerical computations. Their use of experimental evidence to guide improvements in numerical models, and conversely, the interpretation of wave tank data using detailed computer simulations is a landmark in the coupling of these two approaches for practical ship design problems.

Although the authors concentrated in comparisons of surface wave profiles, the occurrence in their simulations of large scale irrotational flow patterns under the vessel bulk is intriguing. Since these flow structures cannot be predicted by potential flow models, but are likely to be significant in design considerations, I would like to know if the authors have attempted to confirm these computed features below the surface with observations?

One final remark: the numerical techniques used for this work are not quite up to date. Use of variable mesh spacing in horizontal directions would most likely reduce computational times by at least a factor of 2 and possibly by an order of magnitude. Also,

there are better methods for defining the geometry, and more general three-dimensional, free surface tracking methods that would improve the resolution of the steep surface slopes observed on the leading bow waves. I'm sure many researchers are anxious to see further results from this group.

Author's Reply

I thank Dr. Hirt for his useful discussion and for his previous works which were useful to the development of the TUMMAC method.

The pressure distribution on the hull surface is compared with measurement and the overall agreement is good (see J. Soc. Nav. Arch. Japan, vol. 157, (1985)). By use of the computed pressure resistance derived from the integration of pressure distribution the hull form improvement will be made with better reliability. Notwithstanding the use of free-slip body condition the 3D vortex separation is simulated as observed in Figs. 7 and 17. Although comparison with observation is not made for the vortical flow, it seems to be clear that more advanced techniques will be necessary to have better agreement in viscous flows.

The use of variable mesh system in longitudinal and lateral directions does not always seem to me effective, since it may attenuate the waves that propagate to the far field by dispersion. The author's partial success is due to the balance of stability, accuracy, simplicity and economy of the developed computer codes. However, as the discusser pointed out, there are many points to which improvement can be made.

DISCUSSION
by Y. Hong

I would like to congratulate the authors for their extensive work. But I would like to ask the authors a question. Should the areas under the positive wave height and under the negative wave height be the same in each time step throughout Figures 43? If not, then the draft of the body should be different in each step.

Author's Reply

Thank you very much for your discussion. In all the computations in our paper, both in case of a ship model and in case of a 2-D box, the body is fixed to the coordinate system, which corresponds to the experimental condition in which the body is fixed to the towing carriage. If the movement of the body is allowed the draft changes and the trim movement will also take place. This corresponds to the free-to-trim-and-sinkage condition, to which our method cannot cope with at present. The volume of the fluid in the computational domain may be permitted to vary when proper open boundary conditions are imposed and fulfilled.

HORIZONTAL DISPLACEMENT OF HYDROFOILS BENEATH THE FREE SURFACE

by Jean-Pierre V. Cordonnier

Ecole Nationale Supérieure de Mécanique

NANTES FRANCE

Abstract.

The TUMMAC method is applied to the problem of simulating 2-D flows around hydrofoils moving at constant speed near the free surface. A finite-difference scheme is used to solve Navier-Stokes equations . The pressure is computed throughout the fluid by means of the simultaneous iterative method which is a modification of the successive over relaxation method. On the profile boundary, a no-slip condition is ensured by extrapolating velocities inside the hydrofoil. In order to let the waves free of breaking, a special treatment of the free surface condition is employed; small segments describe the free surface, every fluid cells are flagged. Computing tests are performed on the NACA4412 profile. The results show a fairly good qualitative agreement with experiments. A turbulence scheme is desirable in order to increase the computation accuracy.

I. Introduction.

The case of hydrofoils moving at constant speed beneath the free surface has often been studied theoretically as well as experimentally. Using potential theories, one can compute the flow around such hydrofoils but the results are very poor as soon as the depth of submergence becomes small [1]. The reason of this comes mostly from the great influence of the free surface which shows, as experimental tests demonstrated, two principal regimes of flow according as to whether the Froude number is high or low. In the first, which may be expected at high Froude numbers, the flow is smooth over the upper surface of the foil and no discontinuity occurs on the free surface. This was the starting point for nearly every theoretical treatment. However, if the foil approaches the free surface too closely, there will be some air ventilation and a flow separation on the upper surface [4, 5]. In the second major regime of flow, the free surface is disturbed by various types of gravity waves or hydraulic jumps. Such flows occur at low Froude numbers and they result in considerably different conditions as far as forces and pressures on the hydrofoil are concerned . So far, no exact dividing point between low and high Froude numbers may be asserted but it seems likely that it is closely related to the known effects of propagation velocity for two-dimensionnal channel waves.

The theory of hydrofoils running near the water surface is not new but all of the early investigations were concerned with computing the over-all forces on the foil, namely lift and drag, rather than the details of the local flow [2]. Furthermore, they were completely unable to solve the problem in most cases when the free surface is very non linear. In order to understand these non linear wave phenomena and to evaluate the forces caused by the non-linear behavior of waves on the body, a theoretical tool is elaborated which can cope with the non-linearity of waves as far as possible. A large demonstration of its ability in solving non-linear free surface flow problems has been performed. Many program codes are now available for 2D as well as 3D problems, stationnary or unstationnary, with finite or infinite depth [6 to 12]. The so-called TUMMAC (Tokyo University Modified Marker And Cell) method was developed at the University of Tokyo and resolves Navier-Stokes equations through a finite difference scheme. Year after year, many computationnal techniques were tested and a refined version is now available. The last improvement in the two-dimensionnal problem is the possibility of having a non-simply connected free surface elevation function with respect to the horizontal coordinate. Therefore, such a program code is just suitable for solving hydrofoil problems.

Without demonstrating again the general bases of the method, a short summary of the computational procedure is followed by an extensive statement of the boundary treatments. Some examples of computations are reported and their accuracy is estimated through comparisons with experiments.

II. The 2-D Hydrofoil problem.

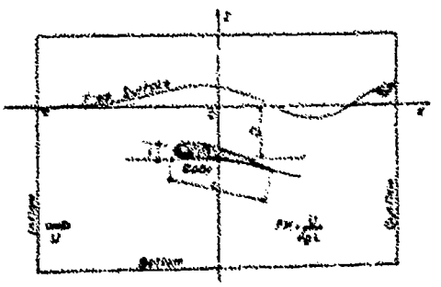

fig. 1 Computational domain.

The fluid domain is arbitrarily limited in space and divided into rectangular cells (fig. 1). The cell size is defined as DX, DZ respectively in the X and Z directions. Pressure is defined at the center of each cell and the velocities on the four sides (fig. 2).

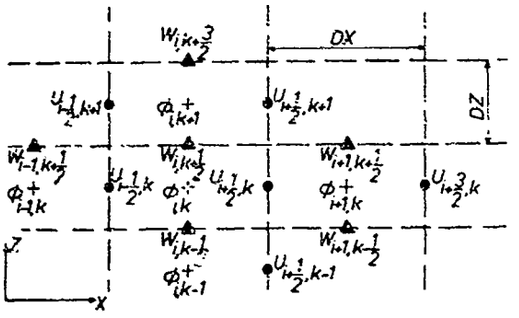

fig. 2 Finite difference scheme.

A finite difference form of the Navier Stokes equations is written using forward differencing in time. If (i, k) denotes the location of any cell center in the fluid, DT being the time increment, at the n+1 time step, velocities are obtained from the preceding time step through the following equations:

$$\left.\begin{aligned} U^{n+1}_{i+\frac{1}{2},k} &= \mathcal{U}^{n}_{i+\frac{1}{2},k} - DT.(\phi_{i+1,k} - \phi_{i,k})/DX \\ W^{n+1}_{i,k+\frac{1}{2}} &= \mathcal{W}^{n}_{i,k+\frac{1}{2}} - DT.(\phi_{i,k+1} - \phi_{i,k})/DZ \end{aligned}\right\} \quad (1)$$

where

$$\begin{aligned} \mathcal{U}^{n}_{i+\frac{1}{2},k} &= U^{n}_{i+\frac{1}{2},k} - DT.UC_{i+\frac{1}{2},k} \\ &+ \nu.DT[(U^{n}_{i-\frac{1}{2},k} + U^{n}_{i+\frac{3}{2},k} - 2.U^{n}_{i+\frac{1}{2},k})/DX^2 \\ &+ (U^{n}_{i+\frac{1}{2},k-1} + U^{n}_{i+\frac{1}{2},k+1} - 2.U^{n}_{i+\frac{1}{2},k})/DZ^2] \end{aligned}$$

$$\begin{aligned} \mathcal{W}^{n}_{i,k+\frac{1}{2}} &= W^{n}_{i,k+\frac{1}{2}} - DT.WC_{i,k+\frac{1}{2}} + g.DT \\ &+ \nu.DT[(W^{n}_{i-1,k+\frac{1}{2}} + W^{n}_{i+1,k+\frac{1}{2}} - 2.W^{n}_{i,k+\frac{1}{2}})/DX^2 \\ &+ (W^{n}_{i,k-\frac{1}{2}} + W^{n}_{i,k+\frac{3}{2}} - 2.W^{n}_{i,k+\frac{1}{2}})/DZ^2] \end{aligned}$$

The convective terms $UC_{i+1/2,k}$ and $WC_{i,k+1/2}$ are also obtained from the velocities at the n^{th} time step. In expressions (2), the space differencing technique is selected using parameter α: $\alpha = 0$ gives central differencing, $\alpha = 1$ corresponds to the donor-cell method and $0 < \alpha < 1$ is some hybrid method in-between.

$$\begin{aligned} UC_{i+\frac{1}{2},k} &= [(U^{n}_{i+\frac{1}{2},k} + U^{n}_{i+\frac{3}{2},k})^2 - (U^{n}_{i-\frac{1}{2},k} + U^{n}_{i+\frac{1}{2},k})^2]/(4.DX) \\ &+ \alpha.|(U^{n}_{i+\frac{1}{2},k} + U^{n}_{i+\frac{3}{2},k})|(U^{n}_{i-\frac{1}{2},k} - U^{n}_{i+\frac{3}{2},k}) - (U^{n}_{i-\frac{1}{2},k} + U^{n}_{i+\frac{1}{2},k})|(U^{n}_{i-\frac{1}{2},k} - U^{n}_{i+\frac{1}{2},k})|/(4.DX) \\ &+ [(W^{n}_{i,k+\frac{1}{2}} + W^{n}_{i+1,k+\frac{1}{2}})(U^{n}_{i+\frac{1}{2},k} - U^{n}_{i+\frac{1}{2},k+1}) - (W^{n}_{i,k-\frac{1}{2}} + W^{n}_{i+1,k-\frac{1}{2}})(U^{n}_{i+\frac{1}{2},k-1} - U^{n}_{i+\frac{1}{2},k})]/(4.DZ) \\ &+ \alpha.|(W^{n}_{i,k+\frac{1}{2}} + W^{n}_{i+1,k+\frac{1}{2}})(U^{n}_{i+\frac{1}{2},k} - U^{n}_{i+\frac{1}{2},k+1}) - (W^{n}_{i,k-\frac{1}{2}} + W^{n}_{i+1,k-\frac{1}{2}})(U^{n}_{i+\frac{1}{2},k-1} - U^{n}_{i+\frac{1}{2},k})|/(4.DZ) \end{aligned}$$

(2)

$$\begin{aligned} WC_{i,k+\frac{1}{2}} &= [(U^{n}_{i+\frac{1}{2},k} + U^{n}_{i+\frac{1}{2},k+1})(W^{n}_{i,k+\frac{1}{2}} + W^{n}_{i+1,k+\frac{1}{2}}) - (U^{n}_{i-\frac{1}{2},k} + U^{n}_{i-\frac{1}{2},k+1})(W^{n}_{i-1,k+\frac{1}{2}} + W^{n}_{i,k+\frac{1}{2}})]/(4.DX) \\ &+ \alpha.|(U^{n}_{i-\frac{1}{2},k} + U^{n}_{i-\frac{1}{2},k+1})(W^{n}_{i,k+\frac{1}{2}} - W^{n}_{i+1,k+\frac{1}{2}}) - (U^{n}_{i+\frac{1}{2},k} + U^{n}_{i+\frac{1}{2},k+1})(W^{n}_{i+1,k+\frac{1}{2}} - W^{n}_{i,k+\frac{1}{2}})|/(4.DX) \\ &+ [(W^{n}_{i,k+\frac{1}{2}} + W^{n}_{i,k+\frac{3}{2}})^2 - (W^{n}_{i,k-\frac{1}{2}} + W^{n}_{i,k+\frac{1}{2}})^2]/(4.DZ) \\ &+ \alpha.|(W^{n}_{i,k+\frac{1}{2}} - W^{n}_{i,k+\frac{3}{2}})|(W^{n}_{i,k+\frac{1}{2}} - W^{n}_{i,k+\frac{3}{2}}) - (W^{n}_{i,k+\frac{1}{2}} + W^{n}_{i,k+\frac{1}{2}})|(W^{n}_{i,k-\frac{1}{2}} - W^{n}_{i,k+\frac{1}{2}})|/(4.DZ) \end{aligned}$$

Using continuity equation, the pressure is computed by means of the Poisson equation of which finite difference expression is:

$$\phi_{i,k} = \left(\frac{\phi_{i+1,k} + \phi_{i-1,k}}{DX^2} + \frac{\phi_{i,k+1} + \phi_{i,k-1}}{DZ^2} - R_{i,k}\right)/\left[2.\left(\frac{1}{DX^2} + \frac{1}{DZ^2}\right)\right] \quad (3)$$

with

$$R_{i,k} = \left(\frac{\mathcal{U}_{i+\frac{1}{2},k} - \mathcal{U}_{i-\frac{1}{2},k}}{DX} + \frac{\mathcal{W}_{i,k+\frac{1}{2}} - \mathcal{W}_{i,k-\frac{1}{2}}}{DZ}\right)/DT$$

By means of a simultaneous iterative method, this equation is solved using:

$$\phi^{m+1}_{i,k} = \phi^{m}_{i,k} - \omega.D^{m}_{i,k}/\left[2\left(\frac{1}{DX^2} + \frac{1}{DZ^2}\right).DT\right] \quad (4)$$

where ω is a relaxation factor and $D^{m}_{i,k}$ the divergence of the cell:

$$D^{m}_{i,k} = \frac{U_{i+\frac{1}{2},k} - U_{i-\frac{1}{2},k}}{DX} + \frac{W_{i,k+\frac{1}{2}} - W_{i,k-\frac{1}{2}}}{DZ}$$

Iterations are stopped when the pressure difference between two consecutive approximations is less than a certain small quantity, chosen a priori.

During the time marching procedure, pressures are renewed throughout the fluid domain at every time step and the new pressure field gives a new velocity field from equations (1).

When a boundary cell is reached, depending on the boundary, some special conditions must be written. These conditions are approximately satisfied by imposing some extrapolated values to velocities outside the fluid domain. Five different boundaries have to be considered: the inflow and outflow boundaries, the bottom, the body and the free-surface.

III. Boundary treatments.

1. Inflow boundary:

This is the left-hand vertical side of the fluid

domain through which the fluid is supposed to flow with a uniform horizontal velocity. The flow starts at rest and is accelerated up to a predefined speed. Therefore, every $U_{1/2,k}$ have the same constant value depending on the time step and every $W_{-1,k+1/2}$ are equal to zero. These velocities are not renewed during the pressure computation.

2. Outflow boundary:

This is the right-hand vertical side of the fluid domain. Since the exact condition is impossible to write, the purpose of the condition on that boundary is to write something which should not generate upstream perturbations. The easiest solution is to keep velocities as constant in passing through that boundary. Since the result is not so bad. If N is the number of horizontal cells, the extrapolated velocities are :

$U_{N+3/2,k} = U_{N+1/2,k}$, $W_{N,k+1/2} = W_{N+1,k+1/2}$

3. Bottom boundary:

Two cases can be studied: rigid horizontal bottom at finite depth or infinite depth The case of a bottom at finite depth is treated in writing a no-slip boundary condition: $U_{I+1/2,1} = 0$, $W_{I,1/2} = 0$. In the infinite depth case, the bottom of the considered fluid domain is supposed to be connected to a domain where the flow is close to be potential. Therefore, extrapolated velocities are computed using potential theory:

$U_{I+1/2,1} = U_{pot}$, $W_{I,1/2} =$ p~

4. Body boundary:

The body is a completely submerged hydrofoil of any profile whose angle of incidence and depth of submergence are adjustable. The foil contour is replaced by a succession of line segments of which extremities are laying on the underlining rectangular mesh system. Each cell containing a segment is set as body boundary cell and is specially treated in the process of computing fluid characteristics (fig. 3)

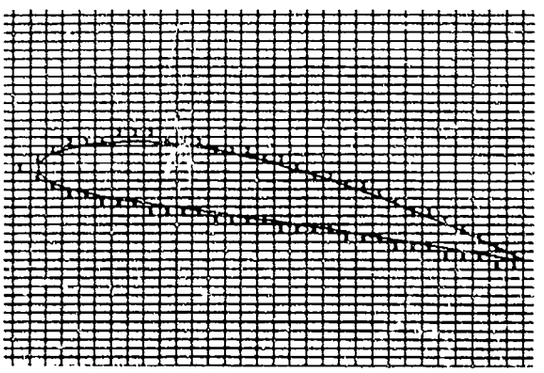

fig. 3 Body boundary cells.

Due to the body shape, there is not enough space inside the body to extrapolate velocities using the variables U(I,K) and W(I,K), (I,K) being any cell coordinates, as in the usual computing process. It is thus necessary to designate for each body boundary cell the places where velocities are unknown from standard computations and which from the computed values in the fluid are available for extrapolation. This is realized through "extrapolating factors".

Assuming a no-slip condition on that boundary and a velocity profile which is a square root function of the distance to the body surface, "extrapolating factors" are simply obtained:

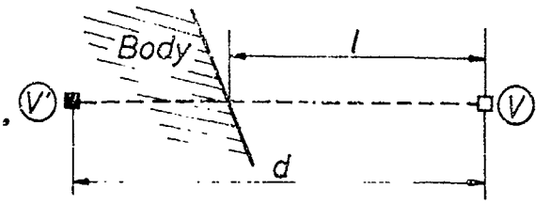

fig. 4 Extrapolating scheme.

$$V' = \boxed{EXF} \times V \quad with \quad \boxed{EXF} = -\sqrt{\frac{d-l}{l}}$$

d being either DX or DZ depending on the mesh line direction.

Eight different cell types can be distinguished and, for each, four "extrapolating factors" are defined as sketched in figure 5.

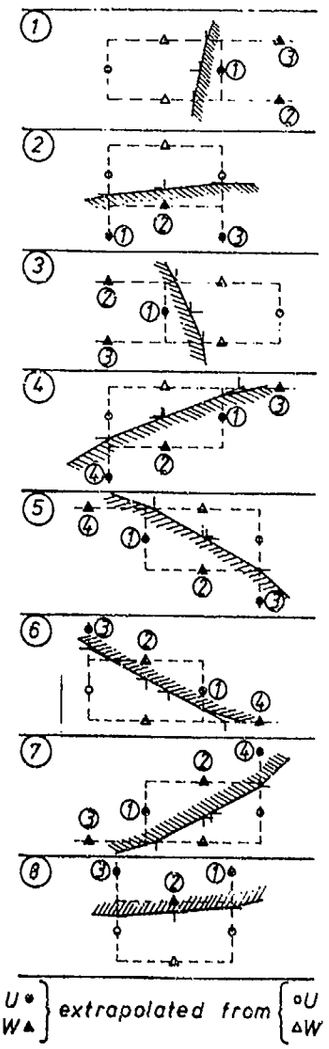

fig. 5 Cases of body boundary cells.

At the trailing edge of the foil, one more velocity is extrapolated as shown in figure 6.

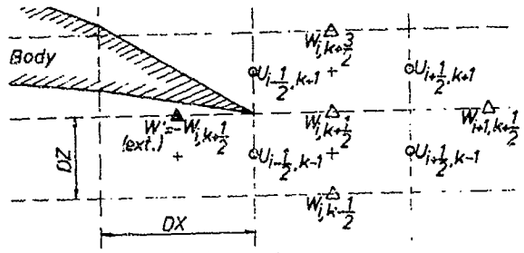

fig. 6 Trailing edge treatment.

5. Free surface boundary:

In order to leave the waves free of overturning and breaking, it is necessary to use a new technique.

At each time step, the free surface is approximated by a polygonal contour (fig. 7) and cells are flagged as -1: air cell, 0: surface cell or 1: full cell.

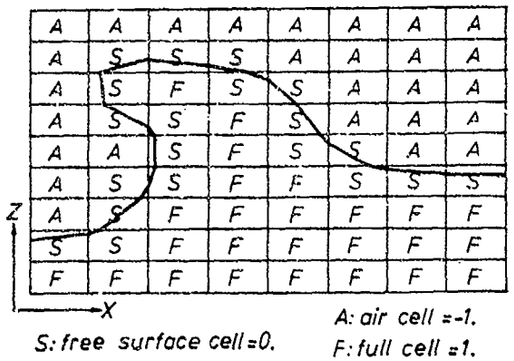

fig. 7 Free surface cell flagging.

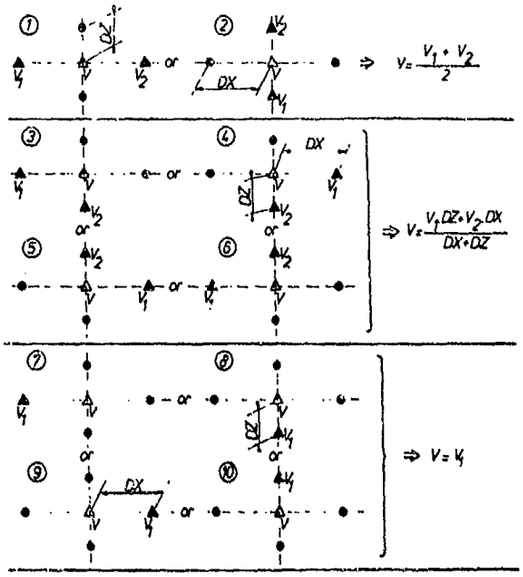

Δ to be extrapolated; ▲ flagged 1 or -1; ● flagged 0.

fig. 8 Free surface extrapolations.

Every velocities and preasures are also flagged: 1 if normally computed, 0 if not and -1 if extrapolated. Following the free surface contour, velocity extrapolations are performed in order to have approximately a zero normal gradient through the free surface. Depending on the flagging of the neighbouring velocities, various cases are studied (fig. 8). Uncomputed velocities are originally flagged 0. Once extrapolated they become -1. This procedure is repeated three times in order to avoid any lack in extrapolated velocities in computing convective terms and moving the free surface segments.

In free surface cells, pressure is computed using irregular star as shown in figure 9. Everywhere the pressure is not normally computed (flagged 0), it is set to the atmospheric pressure.

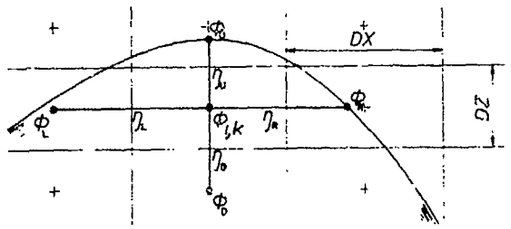

fig. 9 Free surface pressure scheme.

The Poisson equation for the pressure (3) is replaced by the following equation:

$$\Phi_{i,k} = \frac{\eta_L \eta_U \eta_R \eta_D}{\eta_U \eta_D + \eta_L \eta_R} \left[\frac{\eta_L \Phi_R + \eta_R \Phi_L}{\eta_L \eta_R (\eta_L + \eta_R)} + \frac{\eta_U \Phi_D + \eta_D \Phi_U}{\eta_U \eta_D (\eta_U + \eta_D)} - R_{i,k} \right] \quad (5)$$

A new free surface shape is obtained, at each time step, by moving free surface segments, following sketch of figure 10, in a Lagrangian manner.

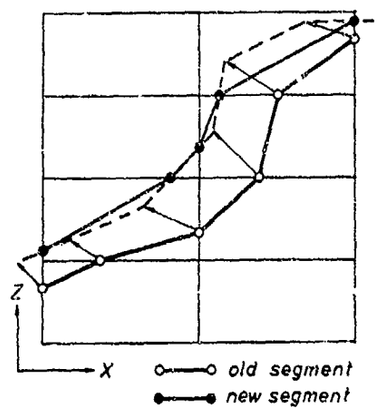

fig. 10 Free surface displacement.

Since the new contour is made of line segments, the end-points of which being not necessarily laying on the basic rectangular mesh system, a new polygonal contour is approximated as shown on figure 10. After the occurence of an overturning phenomenon, particular consideration is necessary when the falling wave touches the free surface below. The enclosed air region is filled with water if its area is small or kept to be an air region to

which free surface conditions are applied when it is sufficiently large. Furthermore, in the pressure computations, the presence of two boundaries in the same cell is treated as if there were no boundary. The two fluid regions, which are going to touch each other, are assumed to be connected.

IV. Application to NACA4412 profile.

The selected profile is NACA4412, a famous profile for its numerous experimental and theoretical studies. The mesh size is DX = 1 cm in the horizontal direction and DZ = 5 mm in the vertical one, so that a 30 cm cord length profile is devided into about 60 line segments. Two angles of incidence and three depths of submergence are considered: 10 and 20 degrees; 6, 12 and 30 centimeters. The fluid domain is 2,30 m long and 60 cm high so that about 30000 cells are describing the computing field (fig. 11). It extends from 1.5 m to -0.8 m in the X-direction and from -0.5 m to 0.1 m in the Z-direction.

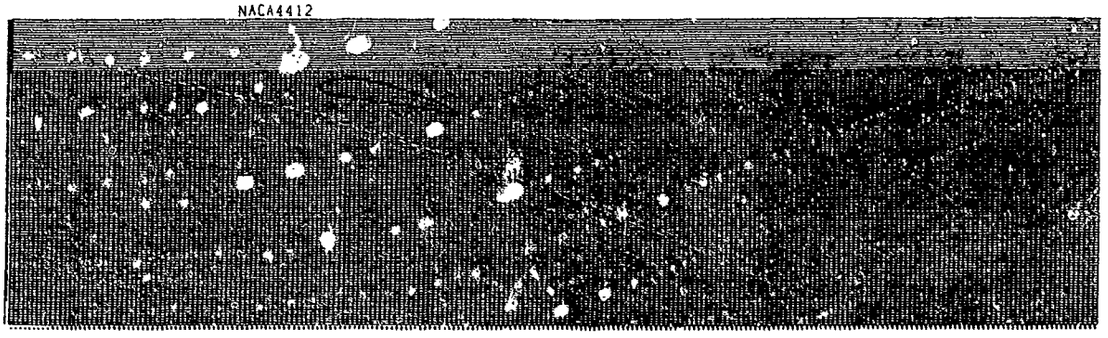

fig. 11

The uniform stream velocity is reached after a period of acceleration, the value of which is 6% of the gravitational one. The time increment is DT = 0.01 s and the kinematic viscosity of fresh water is: $\nu = 1.03 \times 10^{-6}$ m²/s.

After test computations, the relaxation factor ω is adjusted to 1.5 . Due to important pressure fluctuations when the foil angle of incidence is equal to 20 degrees, this parameter is reduced to 1 in computing pressures in the body boundary cells. Iterations in solving the Poisson equation for pressure are stopped if the number of iterations is greater than 50 (=divergence) or when the difference between two successive approximations of the pressure is less than: $0.0001 + 0.0004 * U^2$.

Three Froude numbers, based on the profile cord length, are considered: 0.43, 0.67 and 0.923.

V. Numerical results.

Computed velocity vector fields are shown on figures 12 through 15. For clarity, not all of the cell velocities are drawn: one over three in the X-direction, every one in the Z-direction.

Figure 12 presents a time sequence of eleven time steps during the occurrence of the wave over-turning and breaking. The foil angle of incidence is 10° and its depth of submergence 6 cm (measured at the mid-cord) below the undisturbed free surface. A quasi steady-state is reached after 1000 steps in which some confused fluid motion takes place behind the foil. The incident uniform flow velocity is 1.15 m/s which corresponds to a Froude number of 0.67.

Figure 13 is the case of a NACA4412 at 10° angle of attack, immersed at 12 cm, moving at three various Froude numbers: 0.43, 0.67 and 0.923. Here again, over-turning and breaking occurred except with the highest Froude number for which a real steady-state is reached.

The over-turning wave is again provoked for this high Froude number in increasing the foil angle of incidence (20°), even if the depth of submergence is equal to the profile cord length (30 cm) as shown on figures 14 and 15.

VI. Comparison with experiments.

From reference [3], lift and drag on the foil are evaluated from pressure measurements along the hydrofoil profile.

For comparison with these results, a roughly computed total force acting on the foil is computed at each time step from the pressures obtained inside the body boundary cells used in the TUMMAC simulation. Although the precision could be increased in extrapolating these pressures up to the body surface, this gives the order of magnitude of the estimated values. The results are as follows:

NACA4412, 30cm cord length			LIFT		DRAG	
Incidence	D (cm)	FN	Computed	Experiment	Computed	Experiment
10°	6	0.67	-0.15	-0.10	0.052	0.070
	12	0.43	0.502	0.460	0.160	0.135
		0.67	0.17	0.21	0.100	0.095
		0.923	0.23	0.40	0.072	0.082
20°			0.55	0.76	0.20	0.24
	30		1.00	1.42	0.330	0.295

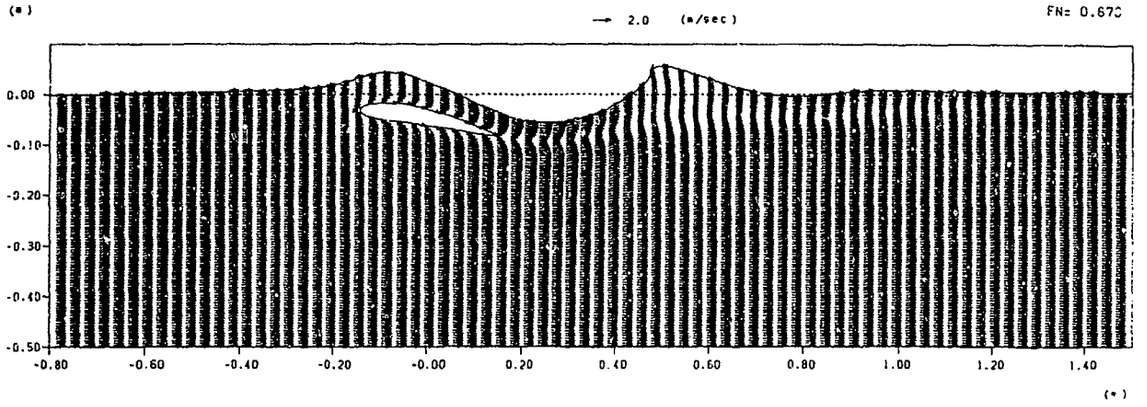

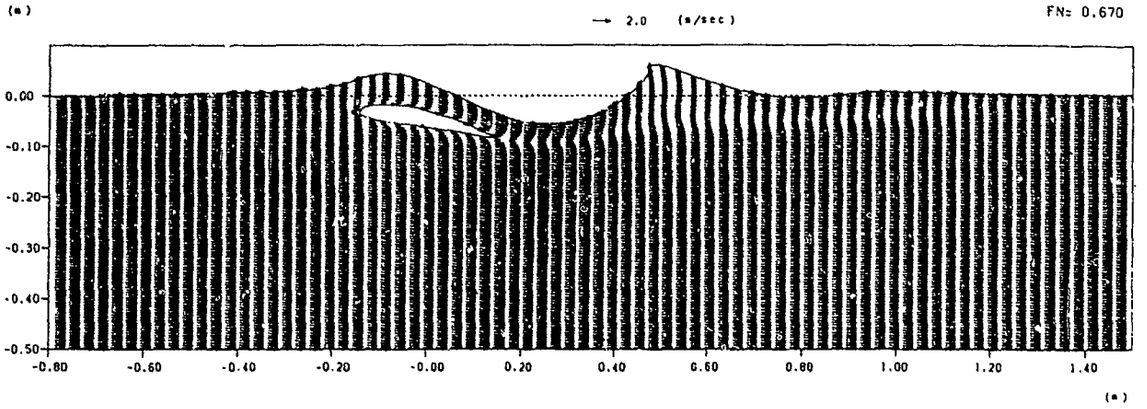

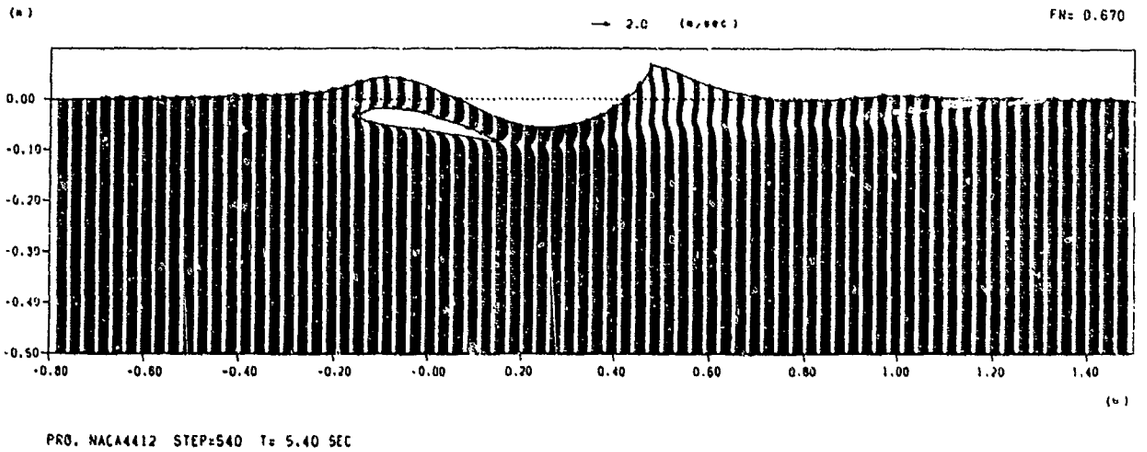

fig. 12(a). Computed velocity field. 10° angle of incidence. σ cm depth of submergence.

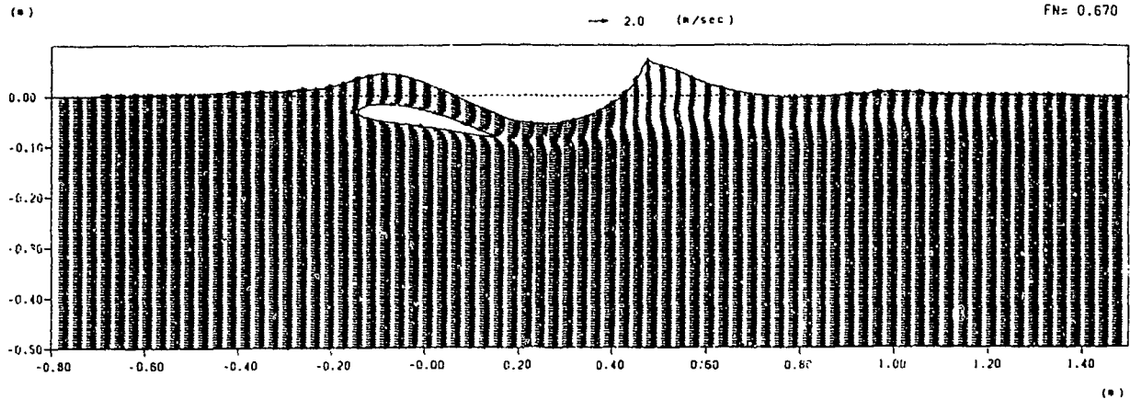

PRO. NACA4412 STEP=500 T= 5.60 SEC

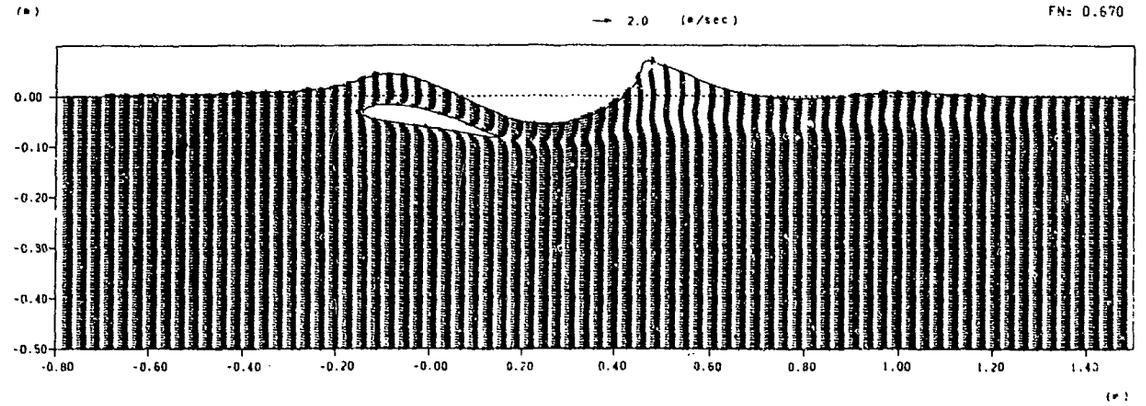

PRO. NACA4412 STEP=580 T= 5.80 SEC

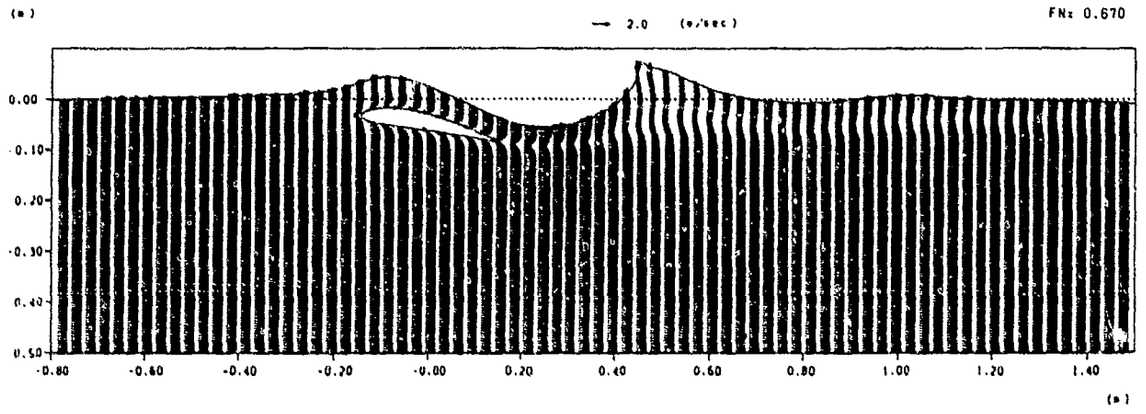

PRO. NACA4412 STEP=600 T= 6.00 SEC

fig 12(b). -idem-

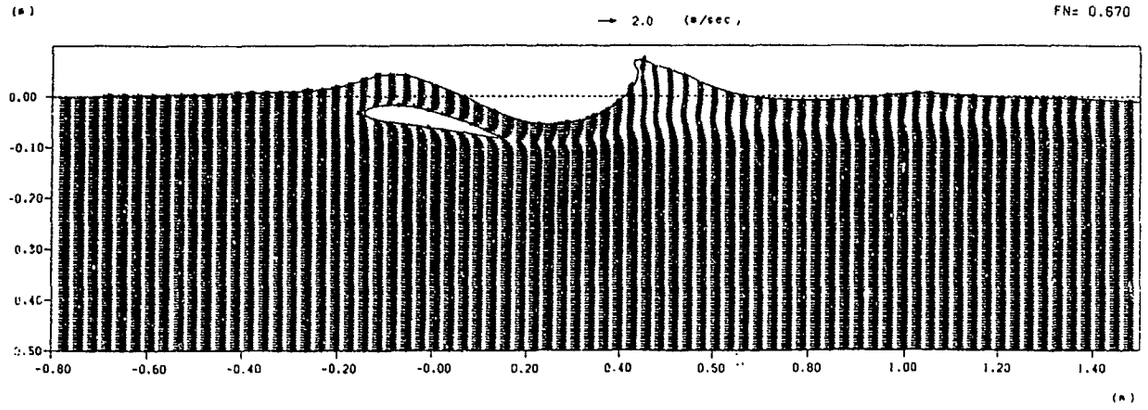

PRO. NACA4412 STEP=620 T= 6.20 SEC

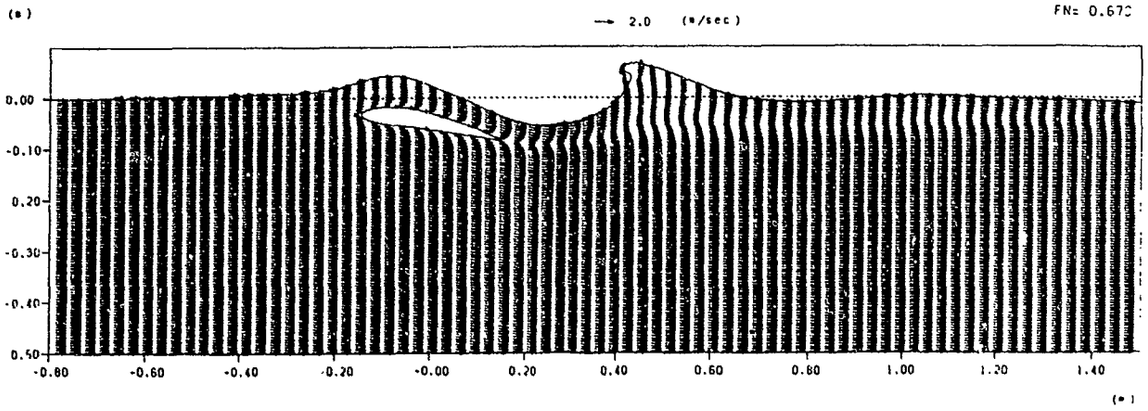

PRO. NACA4412 STEP=640 T= 6.40 SEC

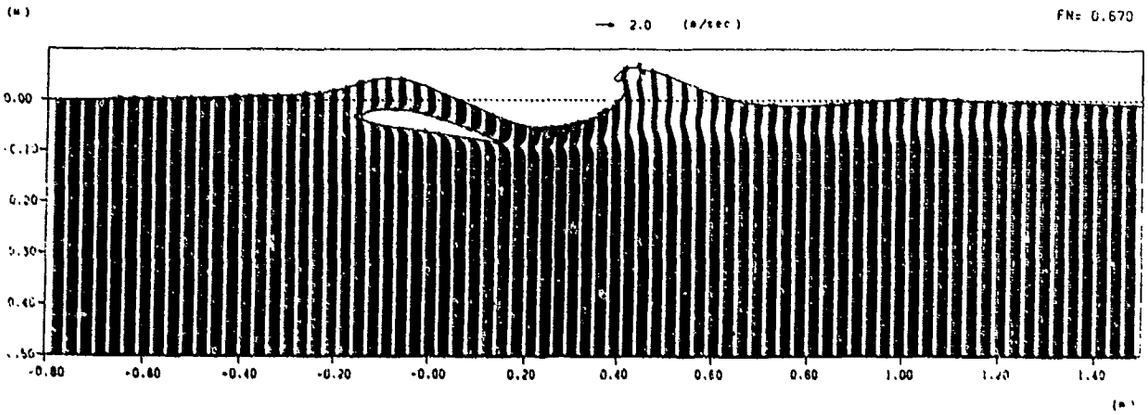

PRO. NACA4412 STEP=660 T= 6.60 SEC

fig. 12(a). -idem-

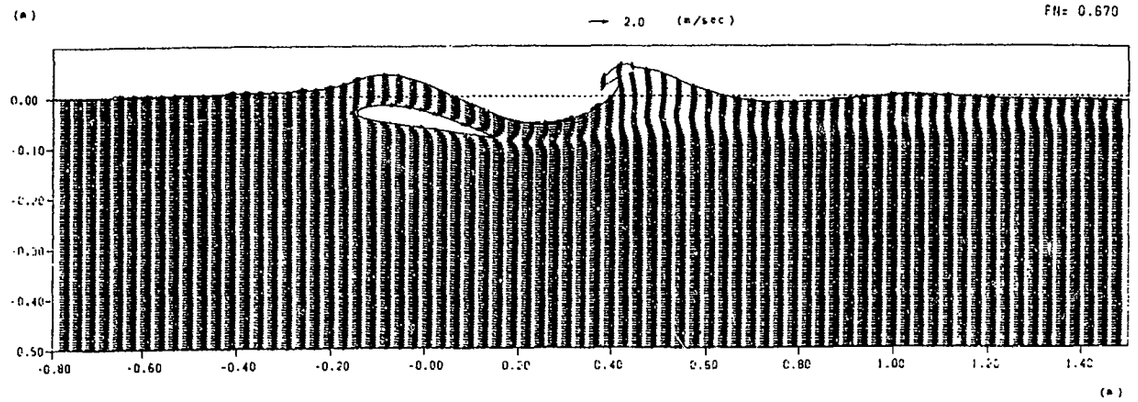

PRO. NACA4412 STEP=680 T= 6.80 SEC

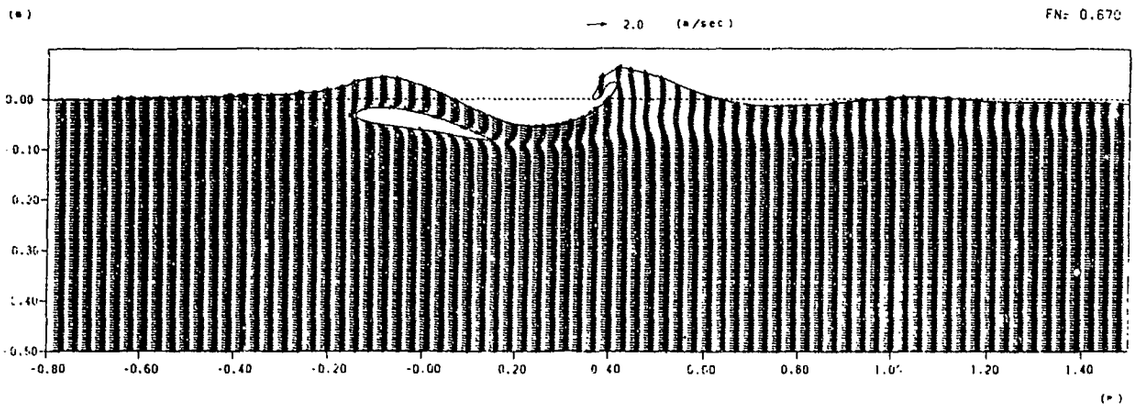

PRO. NACA4412 STEP=700 T= 7.00 SEC

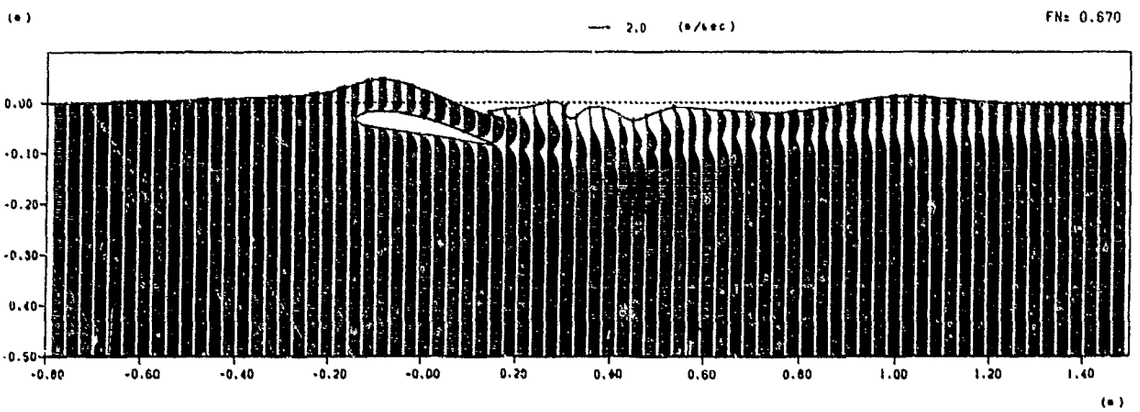

PRO. NACA4412 STEP=1000 T= 10.00 SEC

fig. 12(d). -idem-

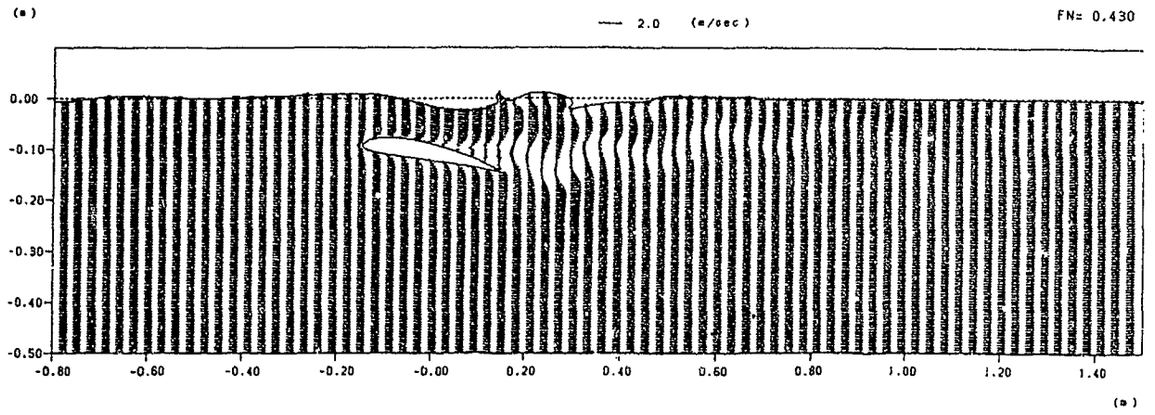

PRG. NACA4412 STEP=480 T= 4.80 SEC

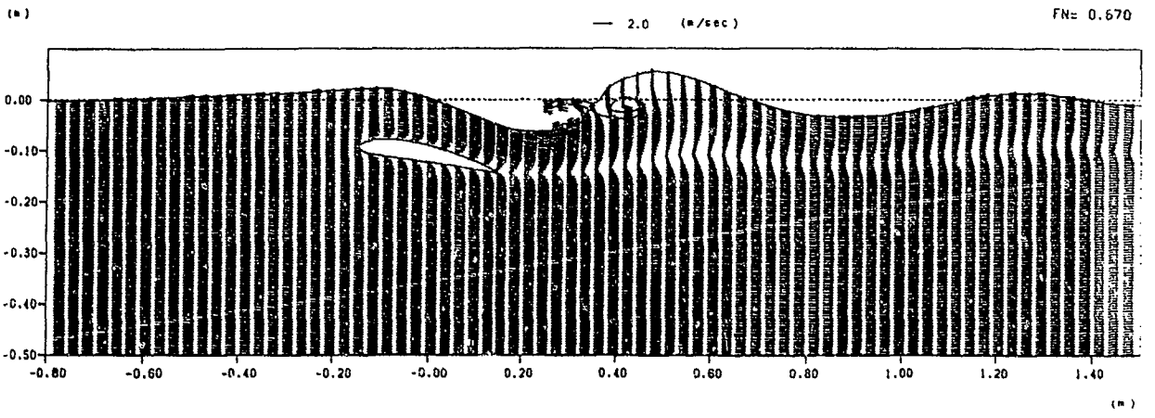

PRG. NACA4412 STEP=800 T= 8.80 SEC

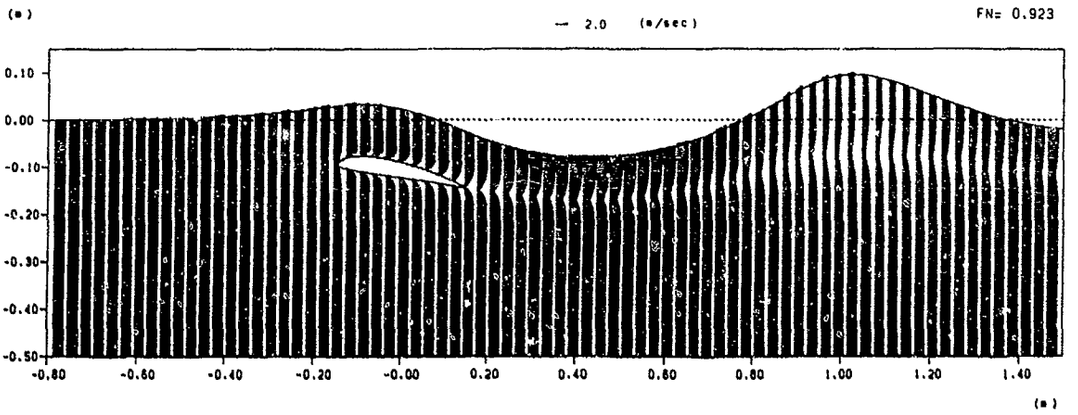

PRG. NACA4412 STEP=1000 T= 10.00 SEC

fig. 13. Computed velocity field. 10° angle of incidence. 12 cm depth of submergence.

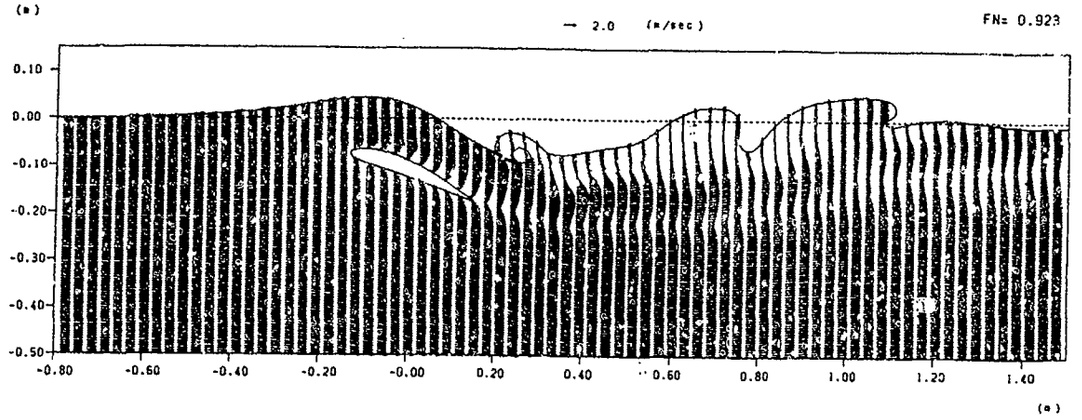

PRO. NACA4412 STEP=920 T= 9.20 SEC

fig. 14. Computed velocity field. 20° angle of incidence. 12 cm depth of submergence.

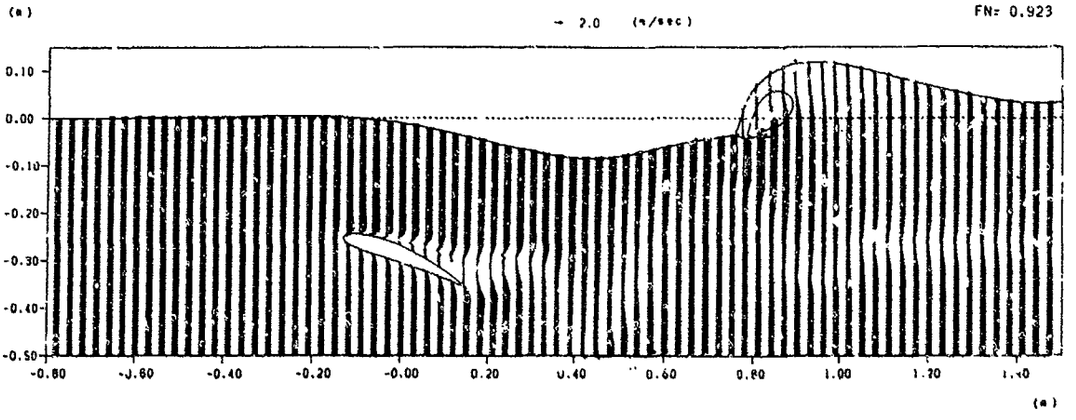

PRO. NACA4412 STEP=860 T= 8.60 SEC

fig. 15. Computed velocity field. 20° angle of incidence. 30 cm depth of submergence.

The comparison shows a fairly good agreement between numerical and experimental results. Considering that these are obtained in the process of creating a new numerical tool, a great deal of other numerical calculations is needed to improve the results.

VII. Concluding remarks.

All these numerical simulations are performed on the HITAC M-280 of the Computer Center, the University of Tokyo. One hour and half CPU time is generally needed for about thousand time steps. In order to reach quantitative accuracy, the cell size can be reduced but the computing cost will rapidly limit the number of cells.

Due to the intense vorticity which is developed inside the fluid by hydrofoils, very small eddies are present near the extrados side which cannot be simulated without appropriate turbulence scheme. This will be the next improvement of the TUMMAC method.

However, this new TUMMAC version is able to cope with very non-linear free surface effects. Overturning and breaking waves are very frequent phenomena in hydrodynamic problems and this program code will be very useful in solving such complicated fluid motions.

Acknowledgements.

This research has been made during a too short stay of the author at the University of Tokyo under a visiting program of the Japan Society for the Promotion of Sciences (JSPS) which is greatly acknowledged.

The author wish to thank Professor H. Miyata and his student team for their very efficient and friendful supports.

References.

[1] Y. T. Wu "A theory for hydrofoils of finite depth". J. of Math. Phys., vol. 33, 1954.

[2] B. R. Parkin, B. Perry and T. Yao-Tsu Wu "Pressure distribution on a hydrofoil running near the water surface". J. of Applied Physics, vol. 27, 1956.

[3] T. Nishiyama "Experimental investigation of the effect of submergence depth upon the hydrofoil section characteristics". J. Soc. Naval Arch. Japan, vol. 105, 1959.

[4] T. Nishiyama "Air-drawing and ventilating flow characteristics of a shallowly submerged hydrofoil section". A.S.N.E. Journal, 1961.

[5] T. Nishiyama "Similarity rule for characteristics of the shallowly submerged hydrofoil section". A.S.N.E. Journal, 1962.

[6,7,8] H. Miyata et al "Numerical analysis of free surface shock waves around bow by modified Mac-method" J. Soc. Naval Arch. Japan, vol. 150, 1981; vol. 152, 1982; vol. 153, 1983.

[9,10,11,12] H. Miyata et al "Numerical and experimental analysis of nonlinear bow and stern waves of a two-dimensional body". J. Soc. Naval Arch. Japan, vol. 154, 1983; vol. 155, 1984; vol. 156, 1984; vol. 157, 1985.

DISCUSSION
of the Paper
by Jean-Pierre V. Cordonnier

HORIZONTAL DISPLACEMENT OF HYDROFOILS BENEATH THE FREE SURFACE

DISCUSSION
by Kasuhiro Mori

In our experiments, which may correspond to the present computation, we experienced a different type of breaking from overturnings. It is a kind of free-surface turbulent flow where the main stream energy is transformed into turbulent energy. In your calculation this process seems to be skipped over.

Through my recent study based on the stability analysis, the pressure gradient in the vertical direction seems to play an important role for such a turbulent free-surface flow, we call it sub-breaking wave to distinguish from breakings with overturning. Are there any indications of change of its signs before the breaking in your calculations?

Have you not experienced any problems during the calculation at high speed as you increase the speed?

Author's Reply

As mentioned in the further improvements of the method, it is highly advisable to include a turbulence scheme in the process of simulating flows around hydrofoils, since the elementary cell size cannot be reduced without increasing computing costs. Since the so-called "sub-breaking" phenomenon appears as being originated from free surface turbulence, the present simulation has completely ignored it, due to a too-large elementary cell.

Since the initial acceleration is kept as a constant, the main difference between high and low speed computations is the time taken to reach the steady state flow. The computational domain must also be increased at high speed in order to include enough waves behind the foil.

DISCUSSION
by Ir. G. S. Rodenhuis

My comment concerns the accuracy of the difference schemes used in the TUNNAC method presented here and the numerical dispersion an inaccurate difference scheme may entail. At the free surface the computational star is irregular, at the solid boundaries extrapolation is used in order to define a no-slip condition on the boundary surface. It appears therefore to me, that it is very difficult to obtain properly balanced difference forms at the boundary cells and that numerical dispersion can hardly be avoided. Accordingly, it must be difficult with this method to predict flow behaviour adequately in a quantitative manner, in the case of rapidly varying, non-linear phenomena such as breaking surface waves. This brings me to suggest, that attention should be given to the problem of separating true physical effects and effects introduced by the numerical methods.

I would appreciate if the author could respond to this comment.

Author's Reply

The powerful ability of this kind of finite difference method will not be denied even if some numerical errors are included. The boundary integral method, for instance, can explain the over-turning motion which is only the beginning of the breaking wave motion. The numerical error can be diminished to a small allowable degree by employing higher-order differencing scheme, such as Adams-Bashforth method for time differencing, third-order upstream or fourth-order compact scheme for space differencing etc..., and/or finer mesh system.

DISCUSSION
By C.C. Haiung

I would like to comment on the flow instability over the hydrofoil. In one of my early experiments on models with a foil-like bulbous-bow, it was observed that the flow instability occurred above the bulbous-bow at a certain towing speed. Such phenomenon has not happened at either greater or less than that particular speed. It was then speculated that this could be due to the "hydraulic jump" occurring at the critical speed of $(gh)^{1/2}$, where h = mean depth of the bulb.

Author's Reply

During the various computing tests realised while completing the computer program, no hydraulic jump occurred above the foil. This is mainly due to the choice of incident velocities, away from the critical ons.

Nevertheless, the present simulation program is perfectly able to generate such physical phenomenon if it should appear.

DISCUSSION
By S.N. Yen

In the TUNNAC method, a higher order interpolation scheme is used to increase the accuracy of implementation of conditions at the free surface. This scheme has the smoothing effect which accumulates with time. I would like to suggest that the author studies this effect on the accuracy of the solu-

tion before any interpretation is made on the difference between the calculations and experiments.

Author's Reply

Some error is expected on the free surface in the TUMMAC method that uses an inflexible rectangular mesh system and a lot of efforts have been focussed here to improve accuracy and to minimize accumulation of error with time. Whether this error on the free surface is within an acceptable range or not can be judged by computations with various cell sizes, since the error is a function of the spacing. In the case of the TUMMAC-IV method for ship waves, this is studied and it is demonstrated that the error does not show unfavorable effect when DX is smaller than 1% of the ship length (see MIYATA and NISHIMURA, J. Fluid Mech. 157, 1985). The same kind of study will be made in the two-dimensional case with breaking, although the judgement is supposed to be a little more difficult since the flow is quite unsteady. The comparison with experimental results says only that the agreement is good considering pressures on the foil. The free surface elevation is still to be compared with the experimental one.

Session V

WAVEMAKING RESISTANCE AND FLOW

Session Chairman
H. Maruo
Yokohama National University
Yokohama, Japan

BOUNDARY INTEGRAL EQUATION METHOD FOR THE LINEAR WAVE RESISTANCE PROBLEM

Katsuo Suzuki

The National Defense Academy
Yokosuka, Japan

Abstract

A new boundary integral equation method to solve numerically three-dimensional steady-state wave- resistance problem with a linearized free-surface condition is developed in this paper with two aims to improve the reliability of Neumann-Kelvin solution and to make a first step toward non-linear wave-making problem. After checking the basic accuracy of the method using elementary waves a pilot study is performed for flows around a point doublet and Michell approximation for a Wigley hull. The discretized form of the present boundary equation is convinced to correspond exactly the linearized free-surface problem. Because the method is easy to be formulated, dealt with and checked, the reliable solution can be obtained and the wave resistance and the amplitude function can be easily calculated in high accuracy.

1. Introduction

A boundary integral equation (BIE) method for the three-dimensional steady-state wave-resistance problem with linearized free-surface condition is treated in this paper. The method is an expanded version to the three-dimensional problem of a part of the author's preliminary paper on the two-dimensional Neumann-Kelvin problem [1]. The present numerical technique is investigated with two aims. One of them is to develop a method to aim to solve Neumann-Kelvin problem at last by means of a new method unlike the usual one using wave-kernel functions. The other one is to make a first step toward the non-linear wave-making problem.

The problem of wave-making resistance of ships is observed recently to be treated as the fully non-linear problem by many authors. They make steady progress in this field [2,3,4,5,6]. Their success, however, does not always imply that the linear theory has an explicit limit and is of no use. We can not forget the role of the linear theory, Michell-Havelock theory, in the improvement of ship form [8]. While the wave resistance calculated by the linear theory is known to be occasionally far from the experimental ones, it is a fact, as indicated by Ogilvie [9], that the effect of diffraction (sheltering effect) of the ship-generated waves by the ship itself, one of the main causes of the difference, has not been fully investigated.

Neumann-Kelvin problem seems to be most suitable for examining the role of the linear theory since the solution contains the effect of the diffraction. The solution has been recognized as to improve the defects of the linear theory and has been thought as available. Numerical calculations for the Neumann-Kelvin problem were performed by various authors [10,11,12,13] and some of the natures of the Neumann-Kelvin solution were made clear by comparing with the Michell-Havelock theory. But the reported results seem not to be always identical with each other [12]. One of the reasons of the difference may result from the fact that the Neumann-Kelvin problem is fairy difficult to be solved numerically, especially the wave kernel function, Havelock source used in the almost all calculations, is a floorer.

Neumann-Kelvin solution has the other important side, the non-uniqueness problem. This was fixed positively in two-dimensional problem [1,14], that is, Neumann-Kelvin problem has infinitely many solutions. The solution refered as zero-vertical flux flow solution was proposed as the most reasonable one [1]. The eigen solution which has a weak singularity at the

corners between the free surface and the body surface was made clear to related to the change of the sinkage and trim [1,15]. These theoretical results were verified numerically in the two-dimensional problem [1] but not in the three-dimensional problem except one report [16], giving not so sufficient verification.

The dispersion of the calculated results, in spite of the important role of the Neumann-Kelvin problem, may not make ones feel so much reliability on the numerical results nor possibility on the Neumann-Kelvin problem itself, at least we can not examine the role of the solution correctly. The shortcut method to improve the reliability of Neumann-Kelvin solution is to compare with the results obtained by the other methods from the usual ones. This is one of the motivations to develop the BIE method presently for the linear wave-making problem.

The present method is developed also with the intention of applying to the non-linear wave-resistance problem. A lot of theories, methods and numerical calculations concerning the non-linear problem have been reported, in many of them the numerical results may agree well with the flow phenomenon. This agreement between the calculations and the phenomena is amenable to make us convinced that the theories or the formulae correctly represent the phenomena. Through the experience of numerical calculation we know that the above scheme is not always justified. The numerical computation technique (method), lying between the theories and the calculated results, may occasionally cause the unexpected results, different from what the theories denote. In fact, through computing steady wave phenomena by means of, say, boundary integral equation method or finite difference method, we know that somewhat little change of condition in computation may occasionally give the different numerical results. The above mentioned indicates that the numerical method, especially, for computing water waves, has to be checked carefully concerning the accuracy, the reliability and the suitability. For these purposes it is a shortcut way to compare the results obtained by the method on the assumption of the linear free-surface condition with the ones calculated by the well-known analytic method.

For the above described two aims, to prepare for calculating the Neumann-Kelvin solution by means of the other method from the usual one and to make a step toward the non-linear wave-resistance problem, a boundary integral equation method is adopted in this paper. The BIE method, using Rankin sources other from the wave kernel functions, has recently paid attention to [13]. The method has a benefit that the treatment, say, program coding, is easy and the computing time is relatively short. It is also considered that the method is easy to be expanded toward the non-linear problem. The method, however, has many points to be checked before applied to the actual problems, for it is not long after developed for the water wave problem and there are not a lot of accumulation of knowledge on the numerical techniques. The problems are following; which type of representation is suitable, Green's mixed form, Rankin source type or Dawson's form [4] ? ; how small size of meshes are adequate to subdivide the free-surface boundary ? ; how must the radiation condition (no waves at upstream) be treated ? ; what effect does the truncation of the infinite flow region give on the solution ?

The elemental parts of them were fixed in [1] for the two-dimensional Neumann-Kelvin problem. Green's type of representation seems superior in describing the solution in the BIE method, because the boundary conditions on the free surface and the body surface can be expressed in the representation itself by using partial integration and a usual technique applied in the potential theory. This is one of the benefits of the BIE method comparing with the other methods, say, finite difference method. It admits us to use larger size of meshes than the finite different methods.

Concerning the radiation condition an idea was shown to be successful [1], the condition of no-disturbance occuring in the upstream radiation region is given literally (the value of the perturbed potential vanishes there) and the usual linear free-surface condition is in same time satisfied there in the least- squares sense.

Various devices have been invented for treating the truncation region, upstream finite difference (open boundary) method [17], hibrid method of matching with the analytic solutions at the boundary [18], a method of representing the effect of truncated region by a integral over the truncation boundary [19]. Among them the upstream finite difference method is used succesfully. Butupstream, central and downstream finite difference techniques are considered as identical in mathematical

sense. Shortly speaking the author's opinion, the success of only upstream direction of the method shows that the technique does not rigorously equal to the mathematical equation and that the open boundary technique does not hold in mathematical sense. From the author's experience the numerical solution obtained by the open boundary technique depends on the position of truncation (wave node, loop or elsewhere), which can be shown also by a theoretical examination.

The truncation trouble was circumvented in [1] by putting the artificial singularities at a downstream position the strength of which was determined so as to make the wave motion vanish at downstream infinity. Accordingly the truncated downstream region can be neglected as same as the upstream region. This method has the other benefit that the forces and moments acting on the object can be easily obtained by calculating the ones acting on the wave-cancelling singularities while in the usual methods the pressure integration has to be done. The invention is applied in the present paper for three-dimensional problem in which the amplitude functions can be also calculated easily unlike the other direct methods.

In the following a pilot study is conducted by using the above mentioned method. At first a study on the mesh size is done by using so-called elementary waves (sinusoidal waves propagating in each direction).

Next, concerning a flow around a submerged dipole the basic performances of the method are checked by comparing with the analytic ones. At last Michell approximations are compared with the analytic results.

Neumann-Kelvin solution, one of the main purposes, is not calculated because of shortcoming of time and that of the computer capacity. The present paper must remain in a basic study while the some points and the knowhow for these numerical method will be made clear.

2. Formulation of Boundary Integral Equation

A source of disturbance (dipole, shiplike body) exits in a uniform flow with free-surface, the condition of which is assumed to be linearized, the bottom is infinitely deep. The frame of reference is fixed to the disturbance, x-axis in negative direction of uniform flow, z-axis upwards, (x,y)

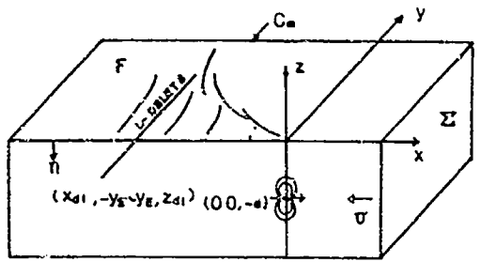

Fig.1 Coordinate Sytem

plane consisting in a unperturbed free-surface (see Fig.1). Let the velocity potential be

$$\Phi(x,y,z) = -Ux + \phi(x,y,z), \quad ...(1)$$

where U stands for velocity of the uniform flow and $\phi(x,y,z)$ perturbation velocity potential. The linearized free-surface condition is as follows;

$$\phi_{xx}(x,y,0) + \kappa_0 \phi_z(x,y,0) = 0,$$

$$\text{on } F \ (z = 0), \quad ...(2)$$

where $\kappa_0 = g/U^2$, the subscripts denotes the partial derivatives.

The solution, $\phi(x,y,z)$, of the free-surface flow problem is represented by Green's formula in the present paper. The integration region of Green's formula is generally expanded as including the infinite volume because the wave motion caused by the disturbance propagates to the infinite downstream region (almost inside two Kelvin angles). In order to apply Green's formula to the finite water surface region, a line (refered to as 'dl') on which artificial doublets are distributed is assumed to be put at an adequately downstream position, the axis being parallel to the y-axis. The strength of the artificial doublets are determined so as to make vanish the wave motion at far downstream. It will be proven later that the line doublets in two directions (x-, z-directions) can make any wave vanish. Then the integration region of Green's formula can be limited in finite region on the free-surface, of course, in sense of numerical calculation not in mathematics.

$$\phi(P) = \frac{1}{4\pi}\iint_{H+F+\Sigma+dl} [\phi_n(Q)G(P;Q) - \phi(Q)G_n(P;Q)]dS. \quad ...(3)$$

Here, n denotes normal derivative in inner direction to water region, P and Q mean fieldpoint(x,y,z) and the boundary point (x',y',z') respectively, G(P;Q) is Rankin source potential;

$$G(P,Q) = -1/r, \quad ...(4)$$

$$r^2 = (x-x')^2 + (y-y')^2 + (z-z')^2,$$

H means the surface of the disturbance object, F the free-surface (z=0) and dl the surface of cylinder of infinitesimal radius around the artificial doublets line located at $(x_{dl}, -y_{\Sigma} \sim y_{\Sigma}, z_{dl})$. Σ denotes the upstream, downstream and side boundary surfaces perpendicular to the free-surface limiting the flow field as including the object (see Fig.1) and in the numerical calculation the integral over Σ is neglected because the disturbance outside Σ has little effect on the solution. One of the reasons of adopting Green's formula (3) as the representation of the solution is stated in Introduction but there are other reasons, the treated quantities (velocity potential) in the representation has directly the physical meanings, the property of the obtained results can be easily inquired, the weak singularity, if it exits on the corner between the body surface and the free-surface, can be treated.

Write the representation (3) as the summation of the terms over H, F and dl;

$$\phi(P) = \phi_H(P) + \phi_F(P) + \phi_{dl}(P). \quad ...(5)$$

When the body is replaced by a point doublet located at $(0,0,z_D)$, the integration over H, $\phi_H(P)$ is written as follows;

$$\phi_H(P) = \phi_{DO}(P)$$
$$= -\frac{M}{4\pi} x/[\, x^2 + y^2 + (z-z_D)^2 \,]^{1/2}, \quad ...(6)$$

where M is strength of the doublet. For Michell approximation, $\phi_H(P)$ is written in the following.

$$\phi_H(P) = \phi_{HO}(P)$$
$$= \frac{1}{2\pi}\iint_H \frac{\partial f}{\partial x'}(x',z') \times 1/[(x-x')^2 + y^2 + (z-z')^2\,]^{1/2}\, dx'dz', \quad ...(7)$$

where $y = f(x,z)$ denotes the half breadth of the ship and H_0 is its center plane ($y = 0$). When the body is like a ship piercing the free-surface (this case is not calculated in the present paper), $\phi_H(P)$ includes the unknowns.

$$\phi_H(P) = \frac{1}{4\pi}\iint_H [\, \phi_n(Q)G(P;Q) - \phi(Q)G_n(P;Q) \,]dS. \quad ...(8)$$

To eliminate the ϕ_n term, consider the uniform flow inside the ship hull and we have,

$$0 = \frac{U}{4\pi}\iint_{H+F_0} [\, x'_n G(P;Q) - x' G_n(P;Q) \,]dS, \quad ...(9)$$

where F_0 stands for the free-surface inside the ship hull. Take the difference between (8) and (9) and use the boundary condition on H,

$$\phi_n(Q) - Ux'_n = 0, \text{ for } Q \in H. \quad ...(10)$$

Then we get the following form including only ϕ-term unknowns;

$$\phi_H(P) = -\frac{1}{4\pi}\iint_H \phi(Q)G_n(P;Q)dS + \frac{1}{4\pi}\iint_{H+F_0} x' G_n(P;Q)dS. \quad ...(11)$$

Here, it is noted that in numerical computation $G_n dS$ can be estimated by solid angle $-d\alpha$ [20]. If subdividing H into ΔH_i we have the following discretized formula;

$$4\pi\phi_{Hi} = \sum_{\Delta H_j} \alpha_{ij}(\phi_j - Ux'_j) - U\sum_{\Delta F_{0j}} \alpha_{ij} x', \quad ...(12)$$

where α_{ij} is solid angle for ΔH_j, ΔF_{0j} and $\alpha_{ij} = 2\pi$ when $Q \in H$. In order to calculate the solid angle, a formula of spherical excess in spherical trigonometry is available.

The second term of eq.(5) is written as follows;

$$\phi_F(P) = -\frac{1}{4\pi}\iint_F [\, \phi_{z'}(Q)G(P;Q) - \phi(Q)G_{z'}(P;Q) \,]dx'dy'. \quad ...(13)$$

Substitution of the free-surface condition (2) into the right hand side gives;

$$\phi_F(P) = \frac{1}{4\pi}\iint_F [\frac{1}{K_0}\phi_{x'x'}(Q)G(P;Q) - \phi(Q)G_{z'}(P;Q)\,]dx'dy'.$$

Integrate by part the first term of the integrand and we have;

$$4\pi\phi_F(P) = \iint_F \phi(Q)[\frac{1}{K_0}G_{x'x'}(P;Q) + G_{z'}(P;Q)\,]dx'dy' - \frac{1}{K_0}\oint_C [\, \phi_{x'}(Q)G(P;Q) - \phi(Q)G_{x'}(P;Q)\,]dy', \quad ...(14)$$

where C stands for the intersection between H and F the line integration over the boundary C_∞ between Σ and F is assumed to be neglected. The above representation makes us circumvent the explicit treatment of the free-surface condition. This is one of the bene-

fits of using Green's type of representation. The second term of the right hand side corresponds to the so-called line integral term in Neumann-Kelvin problem in the form, while the singular properties are different. The line integral term implies that the value of $\phi_x(Q)$ can be given arbitrarily on C, but this problem related to the non-uniqueness of Neumann-Kelvin solution will not be discussed here. In the case of the point doublet and Michell approximation, the line integral term in eq.(14) vanishes and discretization gives, when Q is on F,

$$4\pi\phi_{Fi} = 2\pi\phi_i + \frac{1}{\kappa_0}\sum_{\Delta F_j} Z_{ij}\,\phi_j \quad , \quad \ldots(15)$$

where

$$Z_{ij} = \oint_{\Delta F_j} G_{x'}(P_i,Q)dy'$$

$$= \frac{x_i - x_j}{(x_i-x_j)^2+(z_i-z_j)^2}\left[\frac{y_i-y}{r_{ij}}\right]_{y_j}^{y_{j+1}} \quad \ldots(16)$$

$$r_{ij}^2 = (x_i - x_j)^2 + (y_i - y_j)^2 + (z_i - z_j)^2.$$

When Q is not on F, $2\pi\phi_i$ is to be replaced by $\sum_{\Delta F_i} \alpha_{ij}\,\phi_j$.

The last term of the right hand side of eq.(5) can be written by the velocity potential of the line doublets in x- and y-directions as follows;

$$\phi_{dl}(P) = \frac{1}{4\pi}\int_{-y_E}^{y_E}\left[f(y')\frac{\partial}{\partial x'} + g(y')\frac{\partial}{\partial y'}\right] \times G(P;Q)dy', \quad \ldots(17)$$

where f(y) and g(y) denote the strength of the line doublets in x- and y-direction respectively. Discretization gives;

$$4\pi\phi_{dl_i} = \sum_{\Delta y_j}(Z_{ij}f_j + z_{ij}g_j), \quad \ldots(18)$$

where

$$Z_{ij} = \int_{\Delta y_j} G_{x'}(P;Q)dy',$$

$$= \frac{x_i - x_j}{(x_i-x_j)^2+(z_i-z_j)^2}\left[\frac{y_i-y}{r_{ij}}\right]_{y_j}^{y_{j+1}} \quad \ldots(19)$$

Substitution of eq.(11),(14) and (17) into eq.(5) and let the field point P be on F and H. Then we have the boundary integral equation with respect to the velocity potential and the line doublets;

$$2\pi\phi(P) + \iint_H \phi(Q)G_n(P;Q)dS$$

$$-\iint_F \phi(Q)\left[\frac{1}{\kappa_0}G_{x'x'}(P;Q) + G_{z'}(P;Q)\right]dx'dy'$$

$$-\frac{1}{\kappa_0}\oint_C \phi(Q)G_{x'}(P;Q)dy'$$

$$-\int_{-y_E}^{y_E}\left[f(y')\frac{\partial}{\partial x'} + g(y')\frac{\partial}{\partial z'}\right]G(P;Q)dy'$$

$$= U\iint_{H+F_0} x'G_n(P;Q)dS - \frac{1}{\kappa_0}\oint_C \phi_{z'}G(P;Q)dy',$$

for $P \in F$ and H. $\quad \ldots(20)$

This integral equation may be solved uniquely under some adequate radiation condition which will be shown in the later section. Discretize eq.(20) in the case of a point dipole or Michell approximation by using eq.(6),(7),(15) and (18) and let the point P be on F. Then we have the simulutaneous equation with respect to $\phi(P)$ on the free-surface as follows;

$$2\pi\phi_i - \frac{1}{\kappa_0}\sum_j Z_{ij}\,\phi_j - \sum_j (Z_{ij}\,f_j + z_{ij}\,g_j)$$

$$= \begin{cases} 4\pi\phi_{DOi}\,, & \text{for a point doublet,} \\ 4\pi\phi_{HOi}\,, & \text{for Michell approximation,} \end{cases}$$

for $P_i \in F$. $\quad \ldots(21)$

The field point P_i is assumed to be taken as the center point of the i-th mesh. The above formulation seems more simple and easier to be coded than the usual method, say, the finite difference method. Especially, eq.(21) does not need the numerical differenciation and the higher accuracy can be expected to be obtained. In fact, in the two-dimensional problem the size of mesh is satisfactory to be spaced by one tenth of a wave length while in the finite difference method one fourtieth is required in order to obtain the same accuracy [1].

An additional benefit of the wave cancelling line doublet is that the forces and moments acting on the object are evaluated by the ones acting on the line doublets. That is because in the region outside the control region no disturbances occur and any momentum flux does not flow out. This makes the calculation of the forces and moments easy, especially the wave resistance. The far downstream waves which is caused by the object without the wave-cancelling line doublets are equal to the inverse of waves caused by only the later. Accordingly the amplitude function in eq.(27) of the waves caused by the object can be written by the strength of the line-doublets as follows;

$$H(\theta) = -\frac{1}{4\pi}\int_{-\infty}^{\infty}\left[f(y')\frac{\partial}{\partial x'} + g(y')\frac{\partial}{\partial z'}\right]$$

$$\exp(\kappa_0\sec^2\theta\,(z' + ix'\cos\theta + iy'\sin\theta)dy'$$

$\quad \ldots(22)$

where (x',y') denotes the position of

the doublets line. The wave resistance can be calculated by the following formula;

$$Rw = 16\pi\rho\int_0^{\pi/2} |\kappa_0 H(\theta)|^2 \sec^3\theta\, d\theta. \quad ...(23)$$

The other forces and moments can be calculated by Lagally's formula. In the following only the results are shown. Let the velocity potential be divided by $\phi_{d\ell}(P)$ in eq.(5) and the other term;

$$\phi(P) = \phi_{d\ell}(P) + \phi_R(P).$$

The drag force is;

$$X = -\frac{1}{2}\rho\int_{d\ell}[\,\phi_{Rx'x'}(Q)f(y') + \phi_{Rx'z'}(Q)g(y')]dy', \quad ...(24)$$

where the integration region is the doublets line, the z-direction force;

$$Z = Z_F + Z_D, \quad ...(25)$$

$$Z_F = \rho\bar{U}\oint_{C_0}\phi(Q)dy',$$

$$Z = \frac{1}{2}\rho\int_{d\ell}[\,\phi_{Rz'x'}(Q)f(y') + \phi_{Rz'z'}(Q)g(y')]dy',$$

the trim moment;

$$M = M_F + M_D, \quad ...(26)$$

$$M_F = \rho\bar{U}\oint_C x'\phi(Q)dy' + \rho\bar{U}\iint_F \phi\,(Q)dx'dy',$$

$$M_D = \frac{1}{2}\rho\int_{d\ell}[\,\phi_{Rz'}(Q)f(y') - \phi_{Rx'}(Q)g(y')]dy'.$$

3.Error Estimation by Means of Elementary Waves

It is necessary to check the basic accuracy of the numerical solutions before solving the BIE for the actual problem. How large size of mesh is reasonable for the free-surface is the problem to be checked in this section. For the two-dimensional steady-state wave-resistance problem, when using the same method as the present paper, it is studied [1] that the mesh size is desirable to be spaced by one twentieth of a wave length and by one tenth if a little error is admittable. In order to obtain the reasonable size of mesh in three-dimensional problem the following estimation of errors is performed by using the elementary waves.

The free waves at far downstream of wave motions are generally expressed as the following form of velocity potential [21];

$$\phi(x,y,z) = \mathrm{Re}\ 4i\kappa_0\int_{-\pi/2}^{\pi/2} H(\theta)\exp[\kappa_0\sec^2\theta(z - ix\cos\theta - iy\sin\theta)\sec^2\theta\, d\theta,$$

where Re stands for real part of and $H(\theta)$ is complex and refered to as amplitude function. The form shows that the free waves consists of the elementary wave propagating in direction of θ ;

$$\phi_\theta(x,y,z) = \left\{\begin{matrix} C(\theta)\cos[\kappa_0\sec^2\theta(x\cos\theta + y\sin\theta)] \\ S(\theta)\sin[\kappa_0\sec^2\theta(x\cos\theta + y\sin\theta)] \end{matrix}\right\} \exp(\kappa_0 z\sec^2\theta) \quad ...(28)$$

Let the length of the free wave propagating in $\theta = 0$ be as $\lambda_0 = 2\pi/\kappa_0$ and we have the following relations of the length of free waves, λ_θ , propagating in θ-direction and, λ_x , of its projection to x-axis, λ_y, to y-axis.

$$\lambda_\theta/\lambda_0 = \cos^2\theta,$$

$$\lambda_x/\lambda_0 = \cos\theta, \text{ for } 0 \leq \theta \leq \pi/2 \quad ...(29)$$

$$\lambda_y/\lambda_0 = \cos^2\theta\,\mathrm{cosec}\theta.$$

The x-component of the wave length, λ_x, is one time λ_0 or less, but the y-component, λ_y, becomes infinitely large as θ approaches to $\pi/2$. From the view point of the two-dimensional criterion of mesh size, the free-surface may be subdivided by one twentieth of λ_0 in x-direction but must be infinitesimal in y-direction. This point makes the three-dimensional problem be difficult to be solved numerically. It may ,however, be possible to get a reasonable mesh size with a satisfactory accuracy from the actual point of view, for the amplitude of waves in large θ-direction is in fact small.

Now, it is necessary to estimate the error depending on the mesh size as a function of wave propagating direction, θ . The error can be assessedby calculating the following value obtained by substitution of the velocity potential, ϕ_θ , of the elementary wave (28) into the first two terms of the left hand side of eq.(21).

$$E_i = \phi_i - \frac{1}{2\pi\kappa_0}\sum_j \Xi_{ij}\phi_j \quad ...(30)$$

If the right hand side of eq.(30) has a high accuracy and $\phi(P)$ satisfies the linearized free-surface condition (2), then E_i must be zero approximately. Accordingly the value of eq.(30) turns

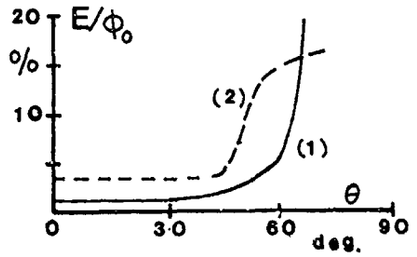

Fig.2 Error of Free-Surface Condition

out the index of how the free-surface condition holds true. The values are examined for the free-surface region, $|x| \leq \lambda_0$, $|y| < \lambda_0/2$, in two cases, (1) $N_x/\lambda_0 = 20$, $N_y/\lambda_0 = 11$, (2) $N_x/\lambda_0 = 10$, $N_y/\lambda_0 = 21$, where N_x, N_y mean the number of meshes per a wave length in x- and y-direction respectively. The values of E_i are checked near the center of the square free-surface region because the finite region effect can be neglected in the central region inside a distance of a quarter of wave length from the side boundary. The obtained results are plotted in Fig.2, ϕ_0 means amplitude of ϕ_θ.

The figure shows that the mesh size (1) is satisfactory for the waves propagating in $\theta < 60°$, i.e., $N_x/\lambda_0 = 20$, $N_y/\lambda_0 = 10$, but the mesh size of $N_y/\lambda_0 > 20$ has to be taken to express accurately the waves propagating in $\theta < 75°$. In any case it is shown to be difficult to express accurately high-frequency components ($\theta > 60°$) of the diverging waves. It is conjectured that the more severe condition has to be taken when using finite different method. At least the relation between the mesh size and the limit of expressible wave components must be taken into account when applying such a direct numerical method as the present one. The above mentioned nature of the present method is not always miserable and it does not seem a fatal defect because ,as stated before, the high-frequency components of the real waves caused by ship are usually weak. It is noted here that the larger the E_i value of eq.(30) is, the smaller amplitude the waves obtained by eq.(21) have.

4.Waves and Wave Resistance of a Point Doublet

In order to get the basic knowhow of the numerical method mentioned in the last section, waves caused by a

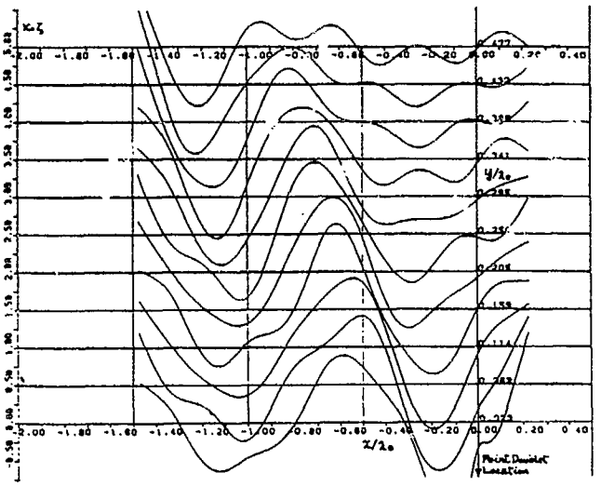

Fig.3 Wave Profiles for a Point Doublet without Radiation Condition ($\kappa_0 d = 0.5$)

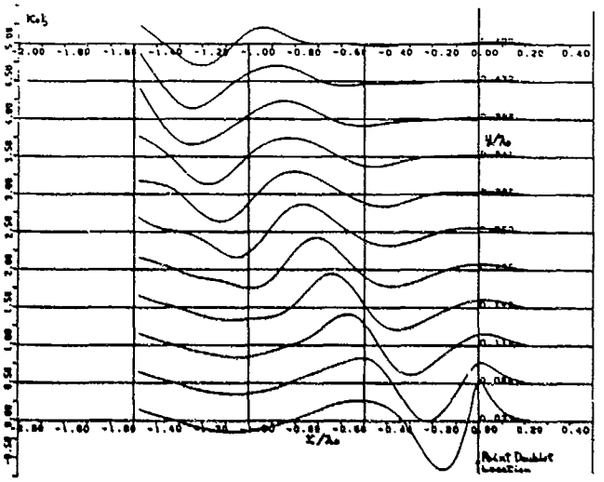

Fig.4 Wave Profiles for a Point Doublet ($\kappa_0 d = 0.5$)

submerged point doublet in a uniform flow are treated in this section. The location of the point doublet is $(0,0,z_0)$, $z_0 = -d$, the strength $m = M/Ud^3 = 8$. The control free-surface region is assumed as $-1.5 \leq x/\lambda_0 \leq 0.25$, $|y/\lambda_0| \leq 0.5$, the spacing of the meshes, $N_x/\lambda_0 = 20$, $N_y/\lambda_0 = 22$.

At first, the BIE (21) is tried to be solved without wave-cancelling line doublets and with no radiation conditions. The obtained wave profile at $\kappa_0 d = 0.5$ around the point doublet is shown in Fig.3. The waves are observed propagating upstream, too.

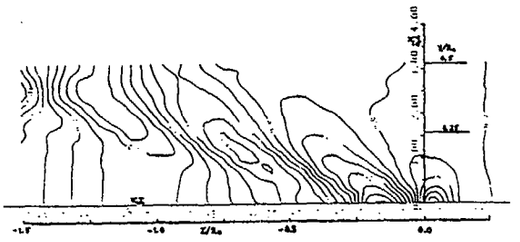

Fig.5 Wave Pattern for a Point Doublet (BIE, $\kappa_0 d=0.5$, $\Delta\kappa_0\zeta = 0.1$)

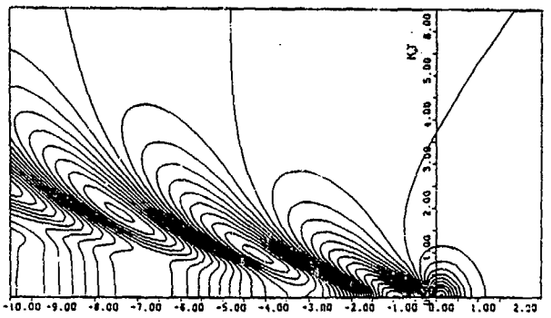

Fig.6 Wave Pattern for a Point Doublet (Analytic, $\kappa_0 d = 0.5$, $\Delta\kappa_0\zeta = 0.05$)

In fact the solution of the linearized steady-statethe wave-makingproblem is known to be analytically indefinite and some adequate physical condition, radiation condition, is needed to get a unique solution, for example, artificial viscous coefficient $\mu \to +0$. The obtained result must correspond to the analytic property of the indefinite solution. To analyze the indefinite solution of eq.(21), the well known SVD method, singular value decomposition [22], is applied to the coefficient matrix of the left hand side of eq.(21). The definite eigen solutions of eq.(21) which must be exist are not found in spite of the fact that in two-dimensional problem two eigen solutions, upstream and downstream propagating waves, were obtained [1]. The reason is due to, perhaps, somewhat numerical problem, the size of the coefficient matrix is too large for the SVD program.

Now, add the following radiation condition to the BIE (21) in the radiation region composed of the upstream first three columns of meshes;

$$\phi(x,y,0) = 0. \qquad \ldots(31)$$

This condition is imposed in the sense of least squares in the SVD method. Then, we have the waves propagating only downstream as shown in Fig.4, the wave heights are calculated by the derivatives of spline functions which are fitted to the obtained velocity potential. A trial to impose the radiation condition (31) only on the downstream radiation region instead of upstream makes the waves propagate upstream, completely symmetric to the before obtained waves. These results imply to correspond to the solution of the artificial viscouscoefficient μ being positive or negative in the analytic theory. Accordingly it is convinced that the BIE (21) is exactly the discretized form of the linear free-surface condition (2). Besides the same thing occurs when upstream or downstream finite difference is used. If central finite difference is used, the same results are obtained corresponding to which the radiation condition is imposed upstream or downstream. The wave pattern of Fig.4 is shown in Fig.5, which gives fairy good agreement with the analytically calculated contours in Fig.6.

The above good agreement is not always obtained. When moving the downstream truncation point, the numerical results differ from the analytical one as the case may be. It is due to neglecting the following effect of the truncation region;

$$\phi_\Sigma(P) = \frac{1}{4\pi}\iint_\Sigma [\,\phi_{n'}(Q)G(P;Q) - \phi(Q)G_{n'}(P;Q)]dy'dz'. \qquad \ldots(32)$$

In order to let the truncation effect be neglegible, introduce the artificial wave-cancelling line doublets. Consider the analytic condition of wave-free in far downstream before going into the numerical calculation. The velocity potential can be written as following form at infinitely far downstream;

$$\phi(P)/Ud = \mathrm{Re}\; 4\kappa_0 i\int_{-\pi/2}^{\pi/2} H(\theta) \exp[\kappa_0\sec^2\theta(z - ix\cos\theta - iy\sin\theta)] \sec^3\theta\, d\theta, \qquad \ldots(33)$$

where $H(\theta) = P(\theta) + iQ(\theta)$. The amplitude function, $H(\theta)$, for the line doublets in x- and y-directions are;

$$H_L(\theta)/d = \frac{1}{4\pi}\int_{-\infty}^{\infty}\left[\ell(y')\frac{\partial}{\partial x'} + g(y')\frac{\partial}{\partial y'}\right] \exp[\kappa_0\sec^2\theta(z + ix\cos\theta + iy\sin\theta)]dy'$$

$$= \frac{\kappa_0}{4\pi}\exp[\kappa_0\sec^2\theta(z_{d\ell} + ix_{d\ell}\cos\theta)] \quad x$$

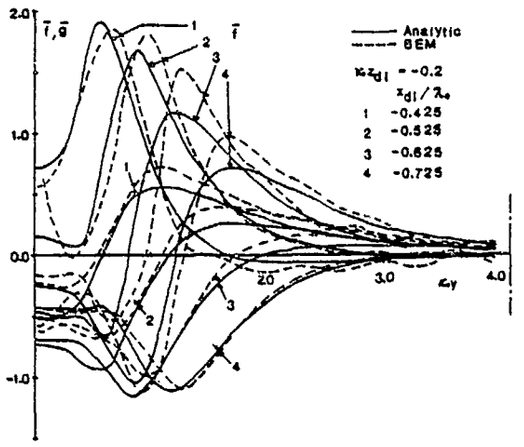

Fig.7 Comparison of Densities of Wave Cancelling Line Doublets ($\kappa_0 d$ = 0.5)

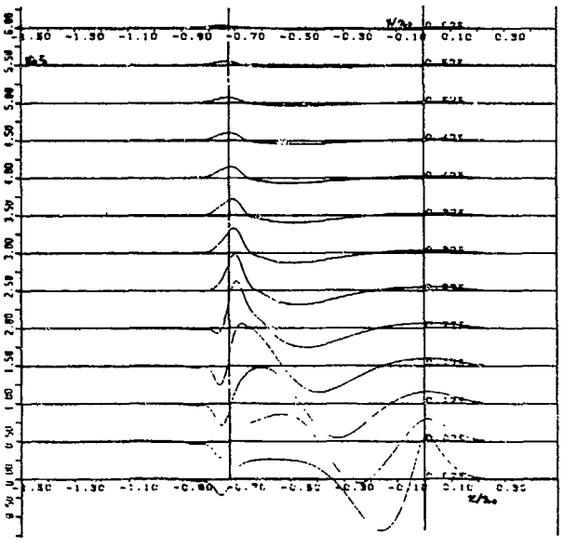

Fig.9 Wave Profile for a Point Doublet ($\kappa_0 d$ = 0.5)

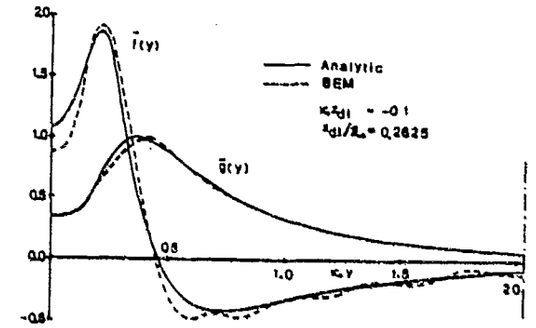

Fig.8 Comparison of Densities of Wave Cancelling Line Doublets ($\kappa_0 d$ = 0.25)

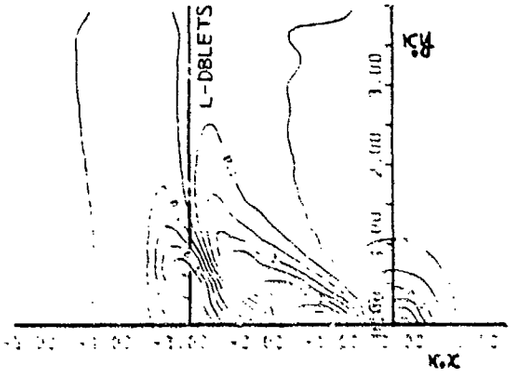

Fig.10 Wave Pattern for a Point Doublet ($\kappa_0 d$ = 0.5, x_{dl}/λ_0 = -0.425)

$$\times \quad [G(\theta) + i\cos\theta F(\theta)], \qquad \ldots(34)$$

where

$$\begin{Bmatrix} F(\theta) \\ G(\theta) \end{Bmatrix} \qquad \ldots(35)$$

$$= \int_{-\infty}^{\infty} \begin{Bmatrix} \bar{f}(y') \\ \bar{g}(y') \end{Bmatrix} \exp(i\kappa_0 y' \sec^2\theta \sin\theta)dy',$$

$\bar{f}(y) = f(y)/Ud^2$, $\bar{g}(y) = g(y)/Ud^2$ are non-dimensionalized strength of the line doublets. The wave free condition is given by;

$$H(\theta) + H_L(\theta) = 0,$$

$$\text{for any } |\theta| < \pi/2 \qquad \ldots(36)$$

$\bar{f}(y), \bar{g}(y)$ can be easily obtained by inverse Fourier transformation;

$$\bar{f}(y) + i\bar{g}(y) = 2i \int_{-\pi/2}^{\pi/2} (1 - i\cos\theta)$$

$$(1 + \sin^2\theta)\sec^2\theta H(\theta)/d$$

$$\exp(-\kappa_0 \sec^2\theta (z_{dl} + ix_{dl}\cos\theta +$$

$$iy \sin\theta))d\theta. \qquad \ldots(37)$$

As the amplitude function for the point doublet is;

$$H(\theta)/d = 1/4\pi \cdot m\kappa_0 d$$

$$\exp(-\kappa_0 d \sec^2\theta)\sec\theta, \qquad \ldots(38)$$

the strength of the wave-cancelling line doublets are obtained from eq.(37) as follows;

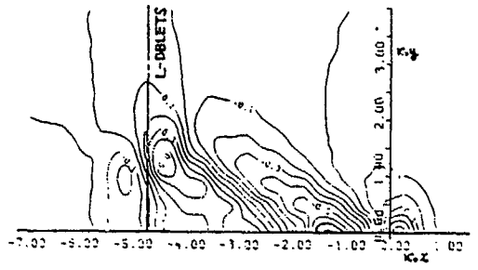

Fig.11 Wave Pattern for a Point Doublet ($\kappa_0 d = 0.5$, $x_{d\ell}/\lambda_0 = -0.725$)

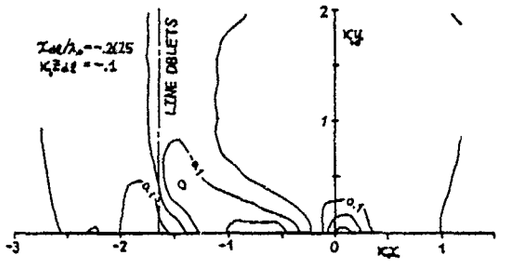

Fig.12 Wave Pattern for a Point Doublet ($\kappa_0 d = 0.25$, $x_{d\ell}/\lambda_0 = -0.2625$)

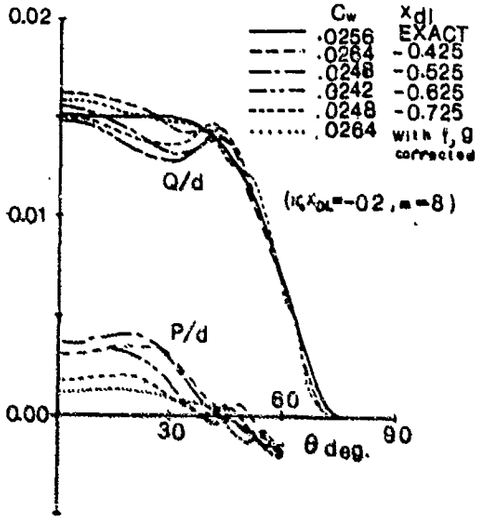

Fig.13 Comparison of Amplitude Functions ($\kappa_0 d = 0.5$)

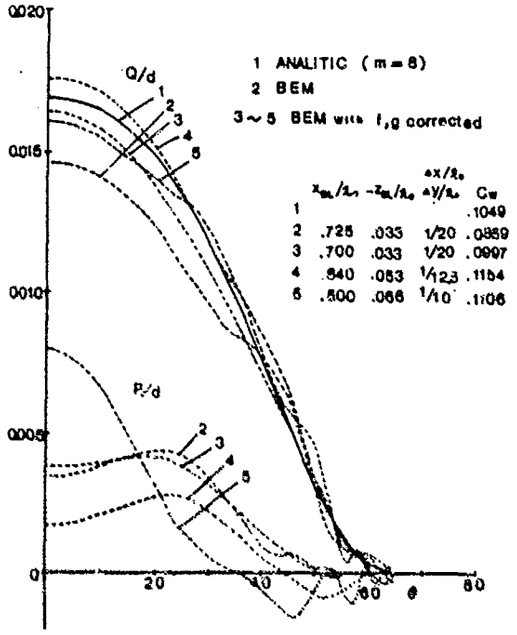

Fig.14 comparison of Amplitude Function ($\kappa_0 d = 1.5$)

$$\begin{Bmatrix} \bar{f}(y) \\ \bar{g}(y) \end{Bmatrix} = -m\kappa_0 d/\pi \int_0^{\pi/2} \exp[(-\kappa_0 \sec^2\theta\,(d + z_{d\ell}))] \cos(\kappa_0 y \sec^2\theta \sin\theta) \begin{Bmatrix} \sec\theta\cos(\kappa_0 x_{d\ell} \sec\theta) \\ \sin(\kappa_0 x_{d\ell} \sec\theta) \end{Bmatrix} d\theta \quad \ldots(39)$$

The densities, $\bar{f}(y)$, $\bar{g}(y)$, exist when $z_{d\ell} > -d$ and they decay exponentially as y tends to infinity.

In order to obtain the strength of the wave-cancelling line doublets in the numerical calculation, impose the radiation condition (31) in the downstream radiation region as same as the upstream. Then the densities, $\bar{f}(y)$, $\bar{g}(y)$, are expressed by the following Fourier series to circumvent the unnecessary oscillation;

$$\begin{Bmatrix} \bar{f}(y) \\ \bar{g}(y) \end{Bmatrix} = \sum_i \begin{Bmatrix} a_i \\ b_i \end{Bmatrix} \cos[(2i-1)\pi y/2y_\ell] \quad \ldots(40)$$

The calculated results of $\bar{f}(y)$, $\bar{g}(y)$ are plotted in Fig.7 and 8 comparing the analytic ones. They show fairy good agreement, especially at $\kappa_0 d = 0.25$. The wave profiles and

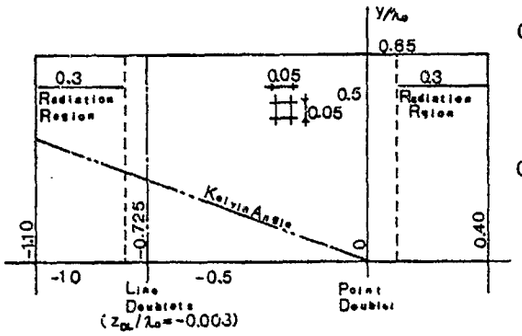

Fig.15 Standard Control Free-Surface Area

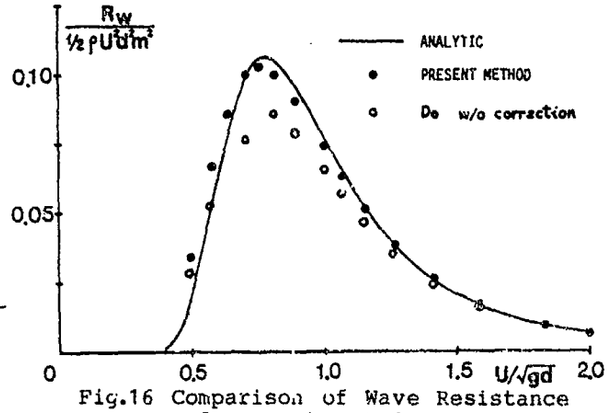

Fig.16 Comparison of Wave Resistance for a Point Doublet

wave patterns in these cases are shown in Fig.9 to 12. We can observe the wave motions disappear almost completely behind the wave-cancelling doublets line. Fig.13 and 14 show the amplitude functions obtained from eq.(34). Comparison with the analytic curves points out that the real part, $P(\theta)$, which is to be zero, has a little large values and the imaginary part, $Q(\theta)$, oscillates unnecessarily near $\theta = 40°$. One of the reasons may by due to truncating the control free-surface area in y-direction. Then the outerpolation of the densities of the line doublets is performed by assuming to have the following form in large y region;

$$\bar{f}(y),\ \bar{g}(y) \sim C \exp(-\lambda y), \quad \ldots(41)$$

where C and λ are constants to be determined. The corrected results are shown in Fig.13 and the amplitude functions seem to approach fairly to the analytic values. In the high-frequency angle region ($\theta > 60°$) the discrepancies are not improved correspondingly to the discussion in section 3 on the relation between the accuracy and the mesh size. Fig.13 shows also the calculations of varying the location of the cancelling doublets line. From the various cases of the locations it is concluded that the wave-cancelling doublets line can be moved near the point doublet to a quarter of wave length behind. Then the effect of the line doublets on the point doublet is small, additive Lagally force acting on the point doublet is at most 1 % of the wave resistance. Fig.14 shows the cases when the mesh sizes are larger, the maximum limit of mesh size is about one tenth of wave length. To obtain the stable solution the depth of the line doublets must be near two third of the x-direction size of mesh. When it locates too shallow or too deep, the densities of line doublets tend to oscillate near the ends.

From the previous discussion the control area of the free-surface, the mesh size, the radiation region and the location of the line doublets are decided as shown in Fig.15. Using this standard scheme, calculation is performed for various Froude numbers, $Fn = U/\sqrt{gd}$. The coefficients of wave resistance, $Rw/(1/2\rho U^2 d^2 m^2)$, obtained by eq.(23) are shown in Fig.16. The values with the densities of line doublets corrected agree well with the analytic ones.

5. Application to Michell approximation

The present BIE method is applied to Michell approximation for a first step toward actual problems on the basis of the knowhow previously obtained for a point doublet. Calculation is performed for a Wigley hull, the breadth length ratio, $B/L = 0.1$, the draft length ratio, $d/L = 0.0625$, the center plane is over $|x|/L < 0.5$, $y = 0$. The control area of free-surface is $-0.95 < x/L < 0.7$, $|y|/L < 0.75$. The mesh size is restricted by the computer capacity and it is set as $\Delta x/L = \Delta y/L = 0.05$. The subdivision number per a wave length are tabulated in Table 1 with respect to six wave numbers. The mesh size criterion obtained Section 3 implies that the subdivision number are not sufficient in low speeds, $\kappa_0 L > 12$. The location of

$\kappa_0 L$	N_x, N_y/λ_0
16	7.9
14	9.0
12	10.5
10	12.6
8	15.7
6	20.9

Table 1

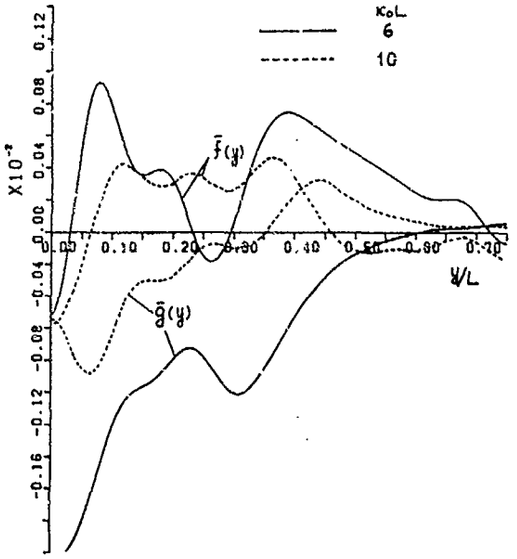

Fig.17 Densities of Line Doublets for Wigley Hull

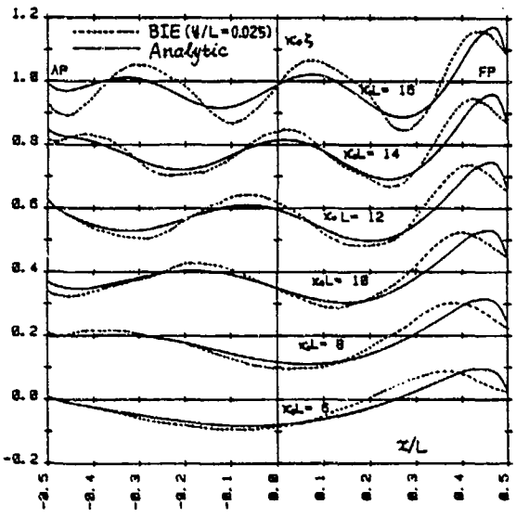

Fif.18 Comparison of Wave Profiles along Wigley Hull Surface

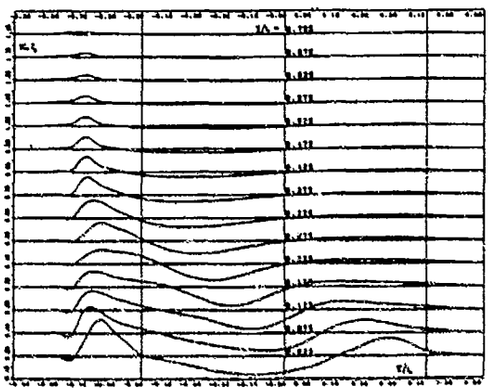

Fig.19 Wave Profile for Wigley Hull (K_0L = 6)

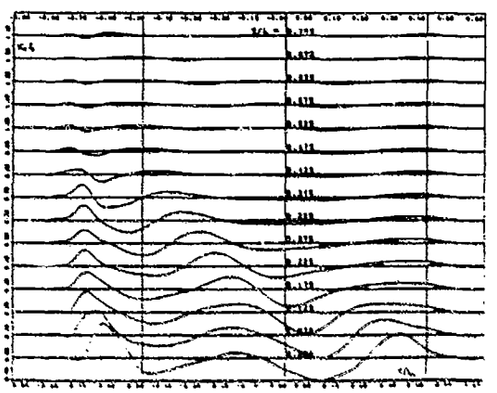

Fig.20 Wave Profiles for WigleyHull (K_0L = 10)

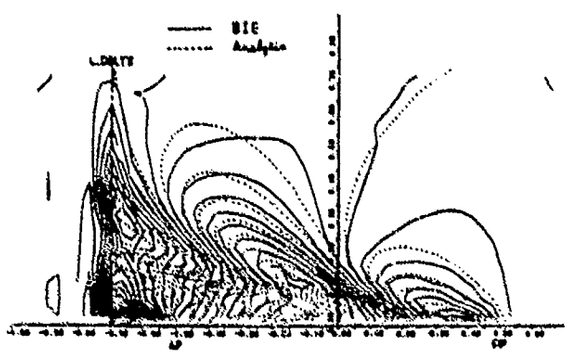

Fig.21 Comparison of Wave Pattern for Wigley Hull (K_0L = 6)

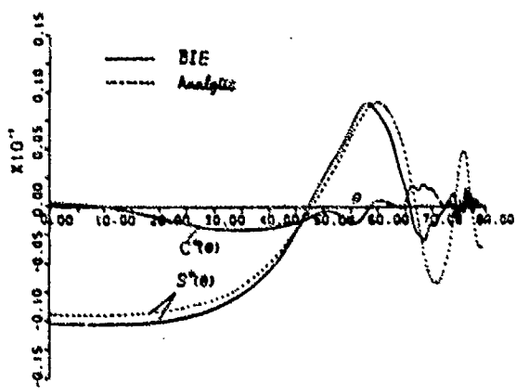

Fig.22 Comparison of Amplitude Function for Wigley Hull (K_0L = 6)

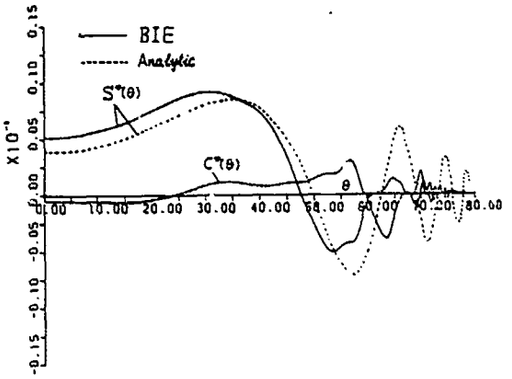

Fig.23 Comparison of Amplitude Function for Wigley Hull (K_0L = 6)

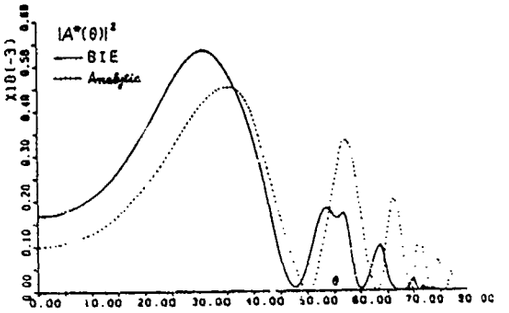

Fig.25 Comparisonof EnergySpectrum for Wigley Hull (K_0L = 10)

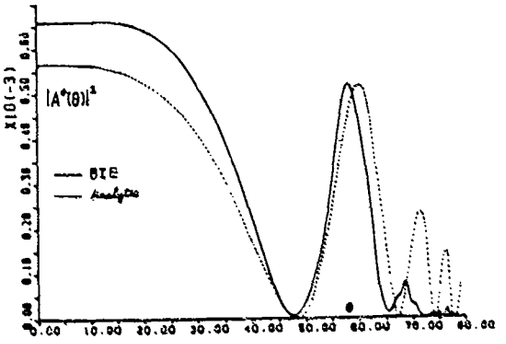

Fig.24 Comparison of EnergySpectrum for Wigley Hull (K_0L = 6)

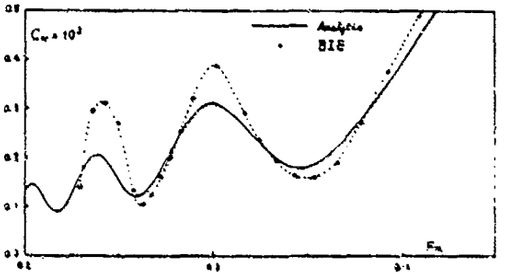

Fig.26 Comparison of Wave Resistance for Wigley Hull

the wave-cancelling doublets line is set at x_{dl}/L = -0.75, z_{dl}/L = -0.03. The upstream and downstream radiation regions consist of four end columns, respectively.

The calculated densities, $\tilde{f}(y) = f(y)/UL^2$, $\tilde{g}(y) = g(y)/UL^2$, of the wave cancelling line doublets are shown in Fig.17 for K_0L = 6, 10. They are not compared with the analytical ones but in low speeds they seem to oscillate unnecessarily.

In Fig.18 the wave profiles, $K_0\zeta$, obtained by the present BIE method are compared with the ones along the central plane calculated analytically by Michell theory. The plotted wave profile are calculated along a line of y/L = 0.025 (center of meshes). The wave profiles are shown in Fig.19, 20 (K_0L = 6, 10) and Fig.21 show the comparison of wave pattern with the analytic one. The wave-cancelling line doublets are observed to offset the waves caused by the ship almost completely The wave pattern seems to give fairy good agreement with the analytical one. Near the ship (its center plane) agreement is not satisfactory. This is why the present mesh size can not cover the severer change in y-direction of the waves near the ship than a point doublet. Accordingly the finer subdivision, especially in y-direction, is desirable for surface piercing bodies. Also near the side and upstream boundary good agreement may not be shown. Wider control area of free-surface is desirable but this is not so fatal problem.

The amplitude function is calculated from the densities of the wave-cancelling line doublets by using eq.(22) and (23). The weighted amplitude function defined as;

$$A^*(\theta) = C^*(\theta) + iS^*(\theta)$$

$$= 4K_0LH(\theta)/UL^2 \sec^{4k}\theta \quad , \ldots(42)$$

is plotted in Fig.22, 23 (K_0L = 6, 10)

with comparison to the analytic one. The amplitude spectra $|A^*(\theta)|^2$ is shown in Fig.24, 25. At high Froude number the calculated function gives good agreement with the analytic one in the low frequency angles ($\theta < 65°$) while its real part has non-zero small values. At low speed the agreement is limited to the low angle region ($\theta <$ 55°). This defects may be improved by increasing the subdivision number of meshes.

The wave resistance coefficient, defined as follows, is plotted in Fig.26;

$$C_w = R_w/(1/2\rho U^2 L^2). \quad ...(43)$$

In high speed region ($Fn = U/\sqrt{gL} >$ 0.32) the values calculated by the present method have good agreement with the analytic ones, their change seems a little larger than the analytic one. These may be improved by the larger number of meshes and the discrepancies in low speeds ($Fn < 0.25$) may be due to the mesh size.

On the basis of the previous results, it is suggested that the finer subdivision of the free-surface, especially in y-direction near the body, and the wider control area are needed for surface-piercing ships moving at lower usual speed. This direct improvement depends mainly on the capacity of the computer. Therefore the other invention, say, dividing the control area into two regions, near and far from the body, and use of iterationare desirable. Such a invention will be available when applying the present BIE method to the Neumann-Kelvin problem.

6.Concluding Remarks

On the basis of the previous calculations it is concluded that the present boundary integral equation method is available and effective to solve the linear wave resistance problem. In the following the features and knowhow of the present method are stated: The representation of the present BIE, which includes the free-surface condition in itself, demands no numerical differentiation and is very easy to dealt with. The unknowns, velocity potential, has physical meaning and the process after solving can be easily handled. No consideration of truncation effect is needed due to adopting the wave-cancelling line doublets, which is able to be laid to near the object by about a quarter free-wave length if the local waves are not so strong. Forces and moments acting on the body can be calculated by the strength of the line doublets and also the amplitude function can be easily obtained. The length of upstream and downstream radiation region needs about a quarter wave length. Concerning the size of free-surface mesh, one twentieth of wave length is desirable for a point doublet but for surface-piercing body the finer meshes are needed. If noting these points Neumann-Kelvin problem may be solved in high accuracy and by making use of these features the present method may be easily expanded to non-linear wave resistance problem.

References

[1] Suzuki, K., Numerical Studies of the Neumann-Kelvin Problem for a Two-Dimensional Semi-Submerged Body, 3rd International Conference on Ship Hydrodynamics, 1981.

[2] Baba, E., Wave Resistance of Ships in Low Speed, Mitsubishi Tech. Bulletin, No.109, 1976.

[3] Gadd, G. E., A Method of Computing the Flow and Surface Wave Pattern around Full Forms, Trans. Roy. Inst. Naval Architects, Vol.118, 1976.

[4] Dawson, C. W., A Practical Computer Method for Solving Ship-Wave Problems, 2nd International Conference on Ship Hydrodynamics, 1977.

[5] Miyata, H., Nishimura, S., Kajitani, H., Finite Difference Simulation of Non-Breaking 3-D Bow Waves and Breaking 2-D Bow Waves, to appear 4th International Conference on Numerical Ship Hydrodynamics, 1985.

[6] Eggers, K., Non-Kelvin Dispersive Waves around Non-Slender Ships, Schiffstechnik, Vol.28, 1981.

[7] Tulin, M. P., An Exact Theory of Gravity Wave Generation by Moving Bodies, Its Approximations, and its implications, 14th ONR Symp., 1982.

[8] Maruo, H., Bessho, M., Ships of Minimum Wave Resistance, J. Soc. Naval Archit. Japan, Vol.114, 1963.

[9] Ogilvie, T. F., Discussion to J.C.Dern et al, 2nd International Conference of Ship Hydrodynamics, 1977.

[10] Kusaka, Y., Inui, T., Kajitani, H., On the Hydrodynamical Source Singularities for Surface Ships with Special Reference to Line Integral, J. Soc.

Archit. Japan, Vol.138, 1975.

[11] Tsutsumi, T., On the Wave Resistance of Ships Represented by Source Distributed over the Hull Surface, Tran. West-Japan Soc. Naval Archit., No.51, 1976.

[12] Papers of the First and Second Workshop on Ship Wave-Resistance Computations, 1979, 1983.

[13] Papers of First to Third International Conference on Numerical Ship Hydrodynamics, 1975, 1977, 1981.

[14] Ursell, F., Mathematical Notes on the Two-Dimensional Kelvin-Neumann Problem of Ship Hydrodynamics, 13th ONR Symp., 1980.

[15] Suzuki, K., Continuity, Forces and Moments Acting on a Ship in Neumann-Kelvin Problem, Continued Workshop on Ship Wave-Resistance Computations, 1980.

[16] Suzuki, K., Calculation of Ship Wave Resistance with Special Reference to Sinkage, Workshop on Ship Wave-Resistance Computations, 1979.

[17] Orlanski, I., A Simple Boundary Condition for Unbounded Hyperbolic Flow, J. Comp. Physics, Vol.21, 1976.

[18] Yeung, R.,W., A Hybrid Integral-Equation Method for Time-Harmonic Free-Surface Flow, 1st International Conference on Numerical Ship Hydrodynamics, 1975.

[19] Seto, H., New Hybrid Element Approach to Wave Hydrodynamic Loading on Offshore Structures, 4th Int.Symp. on FEM in Flow Problem, 1982.

[20] Kellog, O. D., Foundations of Potential Theory, Dover Pub., 1953.

[21] Newmann, J. N., Marine Hydrodynamics, MIT press, 1977.

[22] Forsythe, G. E., Malcalm, M. A., Moler, C. B., Computer Methods for Mathematical Computations, Printice-Hall, 1977.

DISCUSSION
of the paper
by K. Suzuki

"Boundary Integral Equation Method for the Linear Wave Resistance Problem"

DISCUSSION
by R. Yeung

The present numerical formulation of the linear wave-resistance problem is essentially one that I have endeavored to advocate in the mid 70's (Yeung & Bouger, 1977, 1979). The focus of our method then was to use a "simple source formulation" and a rational treatment of the radiation condition. The computational benefits of such an approach are well described again here by Dr. Suzuki. The problem we solved was two-dimensional and the fundamental questions and solutions related to matching and radiation were carefully discussed in these works, which Dr. Suzuki was already aware of. Since my original work, time and (a shift of) interest had not permitted me to return to complete the three-dimensional problem. I am extremely glad that Dr. Suzuki has taken up the difficult challenge and is reporting success here.

There are considerable similarities as well as differences between Dr. Suzuki's treatment of truncation boundary and ours. Outside of the truncation region, our earlier works used eigen-functions in finite water depth, which include the complete effects of local disturbances as well as the wave-like kind. The wave-dipoles introduced here are the natural 3-D infinite-depth analog of the wave-like terms in our eigen series and is thus accurate only in the far field. The sine and cosine components of the free-wave terms canot be determined uniquely from the downstream end alone; an upstream condition was necessary--an important result that we had pointed out in our work. The uniqueness of the line dipole distribution used by Dr. Suzuki requires some justification. In fact, it is not entirely apparent that the Contributions from the truncation surface $\sum$ based on Green's Theorem and from the free-surface $\cap \sum$ line contour would yield the equivalence of longitudinal and tranverse dipoles as Dr. Suzuki assumed. Perhaps Dr. Suzuki will elaborate on this point briefly.

I would like to conclude my discussion by congratulating the author on presenting a very interesting paper.

Reference Cited

Yeung, R. W. and Bouger, Y.C., "A Hybrid Integral-Equation Method for Steady Two-dimensional Ship Waves", Int. J. Numer. Meth. in Engrg.#14, 317-336, 1979. (See also, Proc. 2nd Int. Conf. Numer Ship Hydrodyn. pp. 160-175, Sept. 19-21, 1977, Berkeley, Calif., (USA)

Author's Reply

I would like to say great thanks to Prof. Yeung for this essential and helpful comment. In the present paper we assumed two linearized systems of waves, wave system generated by a body and one by line doublets. Our method is based on the following two facts about the above two wave systems.
1) Any body-generated wave motion (free wave) can be canceled by the (free) waves which are generated by the line doublets and the distribution is uniquely determined by eq. (37).
2) It can be proved that when the total system has no propagating waves both upstream and downstream no (wavy) eigen solution exists in the system except each own wave-free solution.

Accordingly when the total system satisfies both the upstream and downstream radiation conditions it is concluded that the densities of the line doublets are uniquely determined except its own wave-free distributions. Then some errors due to the local wave terms remains on $\sum$ but they cause no essential results if $\sum$ is put far enough from the body and from the line doublets.

NUMERICAL EVALUATION OF THE NEAR- AND FAR-FIELD WAVE PATTERN AND WAVE RESISTANCE OF ARBITRARY SHIP FORMS

A. Barnell and F. Noblesse
David W. Taylor Naval Ship Research and Development Center
Bethesda, Maryland 20084

Abstract

The wave resistance and the far-field wave potential of a ship in steady forward motion in calm water are expressed as simple integrals involving the far-field wave-amplitude function in their integrands. The wave potential at the ship hull surface and in its vicinity likewise is expressed as a simple integral involving the near-field wave-amplitude function. These closely-related far- and near-field wave-amplitude functions are given by integrals over the mean wetted hull surface, the mean waterline and the mean free surface in the vicinity of the ship. A numerical method for accurately evaluating the wave-amplitude functions is presented. In this method, the integral over the upper portion of the hull is combined analytically with the integral around the waterline, prior to numerical integration. This analytical treatment of the contribution of the upper part of the hull shows that several terms in the hull and waterline integrals partially cancel out one another, and yields a modified waterline integral suited for accurate numerical evaluation. This is demonstrated by numerical calculations for five values of the Froude number varying between 0.5 and 0.1. The dependence of the numerical results upon the number of panels approximating the hull is investigated numerically.

1. Introduction

This study is concerned with the numerical calculation of the near- and far-field wave pattern and of the wave resistance of a ship advancing at constant speed in calm water. The numerical method is based on the nonlinear integro-differential equation obtained in [1] and given below for determining the disturbance velocity potential on the mean wetted-hull surface, and on the mean free surface in the vicinity of the ship where free-surface nonlinearities are important. In this equation and hereafter in this study, nondimensional coordinates and flow variables are used, with the length L and the speed U of the ship and the density ϱ of the water selected for reference. Also, the mean free surface is taken as the plane $z=0$ with the z axis pointing upwards, and the x axis is taken in the ship centerplane and pointing towards the bow.

The equation for determining the velocity potential $\phi = \Phi/UL$ takes the form

$$\phi(\vec{\xi}) = \psi(\vec{\xi}) + T(\vec{\xi};\phi). \tag{1}$$

This equation expresses the disturbance potential $\phi(\vec{\xi})$ at any point $\vec{\xi}$ on the mean wetted-hull surface or in the mean flow domain as the sum of the potential $\psi(\vec{\xi})$, which is defined explicitly in terms of the hull shape and the Froude number and thus is known a priori, and the potential $T(\vec{\xi};\phi)$, which is given by a nonlinear integro-differential transform of ϕ. Specifically, for a single-hull ship with port and starboard symmetry, the potentials $\psi(\vec{\xi})$ and $T(\vec{\xi};\phi)$ are defined by the expressions

$$\psi(\vec{\xi}) = F^2\int_c \bar{G}n_x^2 t_y dl + \int_h \bar{G}n_x da, \tag{2}$$

$$\begin{aligned} T(\vec{\xi};\phi) = {} & F^2\int_c [\bar{G}(t_x\partial\phi/\partial t - n_z t_y\partial\phi/\partial d) \\ & -(\phi-\phi_*)\partial\bar{G}/\partial x]t_y dl \\ & -\int_h(\phi-\phi_*)\partial\bar{G}/\partial n da + F^2\int_f \bar{G}\chi(\phi)dxdy, \end{aligned} \tag{3}$$

with

$$\begin{aligned} \chi(\phi) = {} & [\partial\phi/\partial x - (\nabla\phi)^2/2]\partial(\partial\phi/\partial z + F^2\partial^2\phi/\partial x^2)/\partial z \\ & -\partial(\nabla\phi)^2/\partial x + \nabla\phi\cdot\nabla(\nabla\phi)^2/2 + O(F^2\phi^3). \end{aligned} \tag{3a}$$

Equations (1)-(3) and (3a) may readily be obtained from equations (24), (24a-c) and (2) in [1]. In equations (2) and (3) c, h and f represent the positive halves of the mean waterline, of the mean wetted-hull surface and of the mean free surface, respectively, as is indicated in figure 1. Furthermore, $\vec{t}(t_x, t_y, 0)$ is the unit vector tangent to c and pointing towards the bow, $\vec{n}(n_x, n_y, n_z)$ is the unit vector normal to h and pointing into the water, dl is the differential element of arc length of c, and da is the differential element of area of h. In equations (1)-(3) and hereafter, $\vec{\xi}$ represents the "calculation point", that is the point where the potential is calculated, while the "integration point" in the integrals on c, h, f is denoted by $\vec{x}$. Furthermore, the notation

$$\phi \equiv \phi(\vec{x}) \text{ and } \phi_* \equiv \phi(\vec{\xi}) \tag{4a,b}$$

is used. In equation (3) $\partial\phi/\partial t$ represents the derivative of

ϕ in the direction of the tangent vector $\vec{t}$ to c, and $\partial\phi/\partial d$ is the derivative of ϕ in the direction of the vector $\vec{n}\times\vec{t}$, which is tangent to h and pointing downwards as is shown in figure 1.

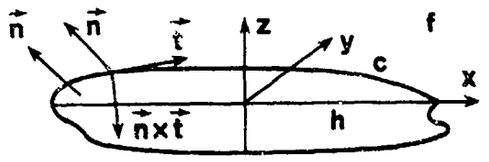

Figure 1. Definition Sketch for a Single-Hull Ship with Port and Starboard Symmetry

The nonlinear term $\chi(\phi)$ is associated with the nonlinearities in the free-surface boundary condition. If this term is neglected, equation (1) becomes a linear integro-differential equation for determining the potential on the mean wetted hull surface h+c. This linearized equation corresponds to the usual Neumann-Kelvin approximation. With the nonlinear free-surface term $\chi(\phi)$, equations (1)-(3) thus correspond to a generalized Neumann-Kelvin theory.

Finally, $\overline{G} \equiv \overline{G}(\vec{\xi};\vec{x})$ is the Green function for port and starboard symmetry defined as

$$\overline{G}(\vec{\xi};\vec{x}) = G(\vec{\xi};x,y,z) + G(\vec{\xi};x,-y,z), \qquad (5)$$

where $G(\vec{\xi};\vec{x})$ is the Green function associated with the linearized free-surface condition $\partial G/\partial\zeta+F^2\partial^2 G/\partial\xi^2 = 0$. The function $G(\vec{\xi};\vec{x})$ represents the velocity potential of the linearized flow created at point $\vec{\xi}(\xi,\eta,\zeta \leq 0)$ by a unit outflow at point $\vec{x}(x,y,z \leq 0)$, stemming from a submerged source if $z < 0$ or from a flux across the mean free surface if $z = 0$ as is shown in [2].

An iterative solution procedure, based on the recurrence relation $\phi^{(n+1)}(\vec{\xi}) = \psi(\vec{\xi})+T(\vec{\xi};\phi^{(n)})$ with $n \geq 0$ and $\phi^{(0)} \equiv 0$, may be used for solving equation (1). The first approximation in the sequence of iterative approximations $\phi^{(n)}$ is $\phi^{(1)} \equiv \psi$. The potential ψ, which is a generalization of the classical Michell thin-ship potential, was shown in [3, 4, 5, 6] to provide a qualitatively-acceptable approximation for slender ship forms. The foregoing recurrence relation thus corresponds to a slender-ship iterative solution procedure that takes advantage of the slenderness of ship forms.

The Green function may be expressed as the sum of a wavy term $W(\vec{\xi};\vec{x})$ representing the wave field behind the unit singularity at point $\vec{x}$ and a nonoscillatory near-field (local) term $N(\vec{\xi};\vec{x})$:

$$4\pi\, G(\vec{\xi};\vec{x}) = W(\vec{\xi};\vec{x}) + N(\vec{\xi};\vec{x}). \qquad (6)$$

By using this expression for the Green function in equations (2) and (3), we may express the potential $\phi(\vec{\xi})$ as the sum of a wave potential $\phi_W(\vec{\xi})$ and a nonoscillatory near-field potential $\phi_N(\vec{\xi})$:

$$\phi(\vec{\xi}) = \phi_W(\vec{\xi}) + \phi_N(\vec{\xi}). \qquad (7)$$

It is shown in [5] that the value of the wave resistance appears to be more sensitive to the wave potential than to the nonoscillatory near-field potential, for which it may be sufficient in practice to use a fairly simple algebraic approximation to the near-field term $N(\vec{\xi};\vec{x})$ in expression (6) for the Green function. The present study is concerned with the numerical evaluation of the wave potential and the related wave pattern, both in the vicinity of the ship and in its far field, and of the wave resistance. The numerical evaluation of the nonoscillatory near-field potential will be examined elsewhere.

2. The Wave Potential and the Wave Resistance

By using expression (6) for the Green function in equations (5), (2), (3), and (1), we may express the wave potential defined in equation (7) in the form

$$\phi_W(\vec{\xi}) = \psi_W(\vec{\xi}) + T_W(\vec{\xi};\phi), \qquad (8)$$

where the wave potentials ψ_W and T_W are defined as

$$4\pi\psi_W(\vec{\xi}) = F^2\int_c \overline{W} n_x^2 t_y dl + \int_h \overline{W} n_x da, \qquad (9a)$$

$$4\pi T_W(\vec{\xi};\phi) = F^2\int_c [\overline{W}(t_x\partial\phi/\partial t - n_z t_y \partial\phi/\partial d) - (\phi-\phi_*)\partial\overline{W}/\partial x]t_y dl \qquad (9b)$$

$$-\int_h (\phi-\phi_*)\partial\overline{W}/\partial n da + F^2\int_f \overline{W}\chi(\phi)dxdy.$$

In equations (9a,b), we have

$$\overline{W} \equiv \overline{W}(\vec{\xi};\vec{x}) = W(\vec{\xi};x,y,z) + W(\vec{\xi};x,-y,z). \qquad (10)$$

It may be seen from equations (7) and (7b) in [2] that the wave term $W(\vec{\xi};\vec{x})$ in equations (6) and (10) is given by the integral

$$W(\vec{\xi};\vec{x}) = 4\nu\, H(x-\xi)\int_{-\infty}^{\infty} \mathrm{Im}\, E(t;\vec{\xi})\, E^*(t;\vec{x})\, dt, \qquad (11)$$

where $H(x-\xi)$ is the usual Heaviside unit-step function, which is equal to 1 for $x > \xi$ and to 0 for $x < \xi$. ν is the inverse of the Froude number F, that is we have

$$\nu = 1/F \text{ with } F = U/(gL)^{1/2} \qquad (12a,b)$$

and $E(t;\vec{\xi})$ and $E^*(t;\vec{x})$ are the exponential functions

$$E(t;\vec{\xi}) = \exp[p^2\{\zeta+i(u\xi+v\eta)\}] \qquad (13a)$$

$$E^*(t;\vec{x}) = \exp[p^2\{z-i(ux+vy)\}]. \qquad (13b)$$

In equations (13a, b), and hereafter, the notation

$$p=(u^2+t^2)^{1/2},\ q=1/p,\ u=qv,\ v=qt \qquad (14a,b,c,d)$$

is used. It will be noted that we have

$$\nu \leqslant p \leqslant \infty \text{ and } F \geqslant q \geqslant 0 \text{ for } 0 \leqslant t \leqslant \infty, \text{ and} \tag{15a,b}$$

$$1 \geqslant u \geqslant 0 \text{ and } 0 \leqslant v \leqslant 1 \text{ with } u^2+v^2=1. \tag{16a,b,c}$$

By using equations (11) and (13a,b) in equation (10) we may then obtain

$$W(\vec{\xi};\vec{x}) = 4\nu H(x-\xi)\int_0^\infty \mathrm{Im}[E_+(t;\vec{\xi})+E_-(t;\vec{\xi})]\,[E_+^*(t;\vec{x})+E_-^*(t;\vec{x})]\,dt, \tag{17}$$

where $E_\pm(t;\vec{\xi})$ and $E_\pm^*(t;\vec{x})$ are defined as

$$E_\pm(t;\vec{\xi}) = \exp[p^2\{\zeta+i(u\xi\pm v\eta)\}] \tag{18a}$$

$$E_\pm^*(t;\vec{x}) = \exp[p^2\{z-i(ux\pm vy)\}] \tag{18b}$$

By using equation (17) in equations (9a,b) and interchanging the order of integration with respect to the integration variable t in the integral (17) and the integration point $\vec{x}$ in the line and surface integrals in equations (9a,b), we may express the potentials $\psi_W(\vec{\xi})$ and $T_W(\vec{\xi};\phi)$ in the form

$$\pi\nu\psi_W(\vec{\xi}) = \int_0^\infty \mathrm{Im}[E_+(t;\vec{\xi})+E_-(t;\vec{\xi})]\,[K_+^0(t;\xi)+K_-^0(t;\xi)]\,q\,dt, \tag{19a}$$

$$\pi\nu T_W(\vec{\xi};\phi) = \int_0^\infty \mathrm{Im}[E_+(t;\vec{\xi})+E_-(t;\vec{\xi})]\,[K_+^\phi(t;\vec{\xi})+K_-^\phi(t;\vec{\xi})]\,q\,dt, \tag{19b}$$

where the functions $K_\pm^0(t;\xi)$ and $K_\pm^\phi(t;\vec{\xi})$ are defined as

$$q\,K_\pm^0(t;\xi) = \int_{c_\xi} E_\pm^* n_x^2 t_y\,dl+\nu^2\int_{h_\xi} E_\pm^* n_x\,da, \tag{20}$$

$$q\,K_\pm^\phi(t;\vec{\xi}) = \int_{c_\xi}[E_\pm^*(t_x\partial\phi/\partial t-n_z t_y\partial\phi/\partial d) -(\phi-\phi_*)\partial E_\pm^*/\partial x]t_y\,dl -\nu^2\int_{h_\xi}(\phi-\phi_*)\partial E_\pm^*/\partial n\,da+\int_{f_\xi} E_\pm^*\chi(\phi)\,dx\,dy. \tag{21}$$

In equations (20) and (21), $E_\pm^* \equiv E_\pm^*(t;\vec{x})$ is given by equation (18b), and c_ξ, h_ξ, f_ξ represent the portions of c, h, f for which $x \geqslant \xi$, that is the portions of c, h, f that are upstream from the plane $x = \xi$. Equations (18b) and (14b,c) yield $\partial E_\pm^*/\partial x = -i\nu p E_\pm^*$ and $\partial E_\pm^*/\partial n \equiv \nabla E_\pm^*\cdot\vec{n} = -p^2 E_\pm^* n_\pm$ where $n_\pm$ is defined as

$$n_\pm = -n_z+i(un_x\pm vn_y). \tag{22}$$

Equation (21) may then be expressed in the form

$$q\,K_\pm^\phi(t;\vec{\xi}) = \int_{c_\xi} E_\pm^*[t_x\partial\phi/\partial t-n_z t_y\partial\phi/\partial d +i\nu p(\phi-\phi_*)]t_y\,dl +\nu^2 p^2\int_{h_\xi} E_\pm^* n_\pm(\phi-\phi_*)\,da+\int_{f_\xi} E_\pm^*\chi(\phi)\,dx\,dy. \tag{23}$$

Equations (8) and (19a,b) then show that the wave potential $\phi_W(\vec{\xi})$ in equation (7) is given by the integral

$$\pi\nu\phi_W(\vec{\xi}) = \int_0^\infty \mathrm{Im}[E_+(t;\vec{\xi})+E_-(t;\vec{\xi})]\,K(t;\vec{\xi})q\,dt \tag{24}$$

where $E_\pm(t;\vec{\xi})$ and q are given by equations (18a) and (14b), respectively, and the function $K(t;\vec{\xi})$ is defined as

$$K(t;\vec{\xi}) = K_+(t;\vec{\xi}) + K_-(t;\vec{\xi}), \text{ with} \tag{25}$$

$$K_\pm(t;\vec{\xi}) = K_\pm^0(t;\xi) + K_\pm^\phi(t;\vec{\xi}). \tag{26}$$

The function $K_\pm(t;\vec{\xi})$ thus is expressed as the sum of the function $K_\pm^0(t;\xi)$, which is defined explicitly in terms of the hull shape and the Froude number by equation (20), and the function $K_\pm^\phi(t;\vec{\xi})$ which involves the potential and is given by equation (23). We then have

$$q\,K_\pm(t;\vec{\xi}) = \int_{c_\xi} E_\pm^*[n_x^2+t_x\partial\phi/\partial t-n_z t_y\partial\phi/\partial d +i\nu p(\phi-\phi_*)]t_y\,dl +\nu^2\int_{h_\xi} E_\pm^*[n_x+p^2(\phi-\phi_*)n_\pm]\,da+\int_{f_\xi} E_\pm^*\chi(\phi)\,dx\,dy. \tag{27}$$

Far behind the ship, the nonoscillatory near-field potential $\phi_N(\vec{\xi})$ in equation (7) is negligible in comparison with the wave potential $\phi_W(\vec{\xi})$. Furthermore, the function $K(t;\vec{\xi})$ in expression (24) for the wave potential may be replaced by its far-field limit $K(t) \equiv K(t;\ \xi = -\infty)$; specifically, the function $K(t) = K_+(t)+K_-(t)$ is given by equation (27) where $K_\pm(t;\vec{\xi})$, c_ξ, h_ξ, f_ξ, and $\phi-\phi_*$ are replaced by $K_\pm(t)$, c, h, f, and ϕ, respectively. We then have

$$\pi\nu\phi(\vec{\xi}) \sim \int_0^\infty \mathrm{Im}[E_+(t;\vec{\xi})+E_-(t;\vec{\xi})]K(t)q\,dt \text{ as } \xi\to-\infty \tag{28}$$

The equation of the free surface far behind the ship is given by $\zeta(\xi,\eta) \sim F^2\partial\phi(\xi,\eta,\zeta=0)/\partial\xi$, so that we have

$$\pi\nu^2\zeta(\xi,\eta) \sim \int_0^\infty \mathrm{Re}[E_+(t;\xi,\eta)+E_-(t;\xi,\eta)]K(t)\,dt \quad \text{as } \xi\to-\infty \tag{29}$$

In this equation, we have $E_\pm(t;\xi,\eta) \equiv E_\pm(t;\xi,\eta,\zeta=0) = \exp[ip^2(u\xi\pm v\eta)]$. Equations (28) and (29) express the far-field wave pattern trailing behind the ship as a superposition of elementary plane progressive waves with amplitude given by $F^3p^2K(t)/\pi$ traveling at angle $\theta = \pm\tan^{-1}(Ft)$ with respect to the x axis. The function K(t) will then be referred to as the "far-field wave amplitude function", and the function $K(t;\vec{\xi})$ as the "near-field wave-amplitude function". The nondimensional wave resistance $r = R/\rho U^2L^2$ experienced by the ship can be determined from its far-field wave pattern by means of the Havelock integral [7], which here takes the form

$$\pi\nu^2 r = \int_0^\infty |K(t)|^2 q\,dt \tag{30}$$

Equations (30), (29), (28) and (24) thus express the wave resistance, the far-field wave-pattern and flow, and the wave potential on the hull surface and in its vicinity as simple integrals involving the far- or near-field wave-amplitude functions K(t) or $K(t;\vec{\xi})$ in their integrands. The near- and far-field wave potentials and the wave resistance can then be easily and accurately evaluated provided the wave-amplitude functions K(t) and $K(t;\vec{\xi})$ can be determined with sufficient accuracy. By the same token, no

realistic prediction of the near- and far-field wave potentials and of the wave resistance is possible if the wave-amplitude functions cannot be evaluated with sufficient accuracy. Accurate numerical evaluation of the near- and far-field wave-amplitude functions therefore is critical to the evaluation of the wave potential and the wave resistance, and thus is the focus of the present study.

It should be noted in particular that convergence of the improper integrals (24), (28), (29) and (30) is not obvious a priori. As a matter of fact, equation (27) indicates at first glance that $K_{\pm}(t;\vec{\xi}) \sim p \sim t$ as $t \to \infty$, stemming from the term $i\nu p(\phi-\phi_*)$ in the waterline integral at a point of stationary phase $udx \pm vdy = 0$. The improper integrals (30) and (29), and also the integrals (28) and (24) for $\zeta = 0$, would then appear to be divergent.

A large number of numerical calculations of the far-field wave-amplitude function K(t), often referred to as the Kochin wave spectrum function, have been reported in the literature on ship wave resistance. More precisely, the function K(t) is usually evaluated numerically and depicted as a function of $\theta = \tan^{-1}(Ft)$ for $0° \leq \theta \leq \theta_m < 90°$. The truncated limit of integration θ_m is usually taken as some value between 70° and 80°. However, it is not always clear that the function $K(\theta)$ is negligibly small for $\theta_m \leq \theta \leq 90°$, as is illustrated for instance in figures 11-15 and 26-31 in [8]. It is indeed plausible that the large discrepancies that can often be observed among calculations of ship wave resistance by various authors on the basis of theoretically-comparable numerical methods [3] may partly stem from variations in the selection of the value of θ_m, and more generally from the degree of accuracy with which the function $K(\theta)$ is evaluated numerically for values of θ close to 90°.

The main purpose of the present study is to present an accurate method for numerically evaluating the near- and far-field wave-amplitude functions. This method is based on a modified form of expression (27) for the function $q\,K(t;\vec{\xi})$ that is well suited for numerical evaluation for large values of t, and in particular establishes that it vanishes at $t \to \infty$.

3. The Near- and Far-Field Wave-amplitude Functions

It was shown in [1] and will be demonstrated again further on in this study that several terms in the integrals around the mean waterline and on the mean wetted-hull surface in equation (27) cancel out one another for crucial values of t, notably for $t = \mp udx/dy$ for which the phase $p^2(ux \pm vy)$ of the exponential term $E^*_{\pm}(t;\vec{x})$ is stationary. It therefore is highly desirable if not essential that the waterline integral and the hull integral in equation (27) be grouped together in some appropriate manner. In the method proposed in this study, the mean wetted-hull surface h is divided into two parts: the upper hull corresponding to $0 \geq z \geq -\delta$ and the lower hull for which $z \leq -\delta$, where δ is some fraction of the ship draft d, for instance $\delta = d/10$ or $d/20$. The upper hull is denoted by u and the lower hull by ℓ, so that we have $h = u+\ell$. The depthwise variation of the upper hull surface is approximated by a straight (but not necessarily vertical) segment. The depthwise variation of the potential inside u is also assumed to be linear. The depthwise integration in the integral on the upper hull surface in equation (27) can then be performed analytically, and the surface integral on u thus is reduced to a line integral around the mean waterline. The latter integral is combined with the waterline integral in equation (27), so that the contribution of the upper hull u+c is expressed as a modified line integral around the mean waterline c.

The near-field wave-amplitude function $K(t;\vec{\xi})$ may then be expressed as the sum of three components

$$K(t;\vec{\xi}) = K^u(t;\vec{\xi}) + K^{\ell}(t;\vec{\xi}) + K^f(t;\vec{\xi}) \tag{31}$$

representing the contributions of the upper hull u+c, of the lower hull ℓ, and of the portion of the free surface f where nonlinearities are important. It may readily be seen from equations (25) and (27) that the contributions of the lower hull and of the free surface are given by

$$q\,K^{\ell}(t;\vec{\xi}) = \nu^2 \int_{\ell_\xi} [n_x(E^*_+ + E^*_-) + p^2(\phi-\phi_*)(n_+ E^*_+ + n_- E^*_-)]da \tag{32}$$

$$q\,K^f(t;\vec{\xi}) = \int_{f_\xi} (E^*_+ + E^*_-)\chi(\phi)\,dxdy, \tag{33}$$

In equation (32), ℓ_ξ represents the portion of the lower hull for which $x \geq \xi$. Equations (25) and (27) also readily yield the following expression for the contribution of the upper hull u+c:

$$K^u(t;\vec{\xi}) = K^u_+(t;\vec{\xi}) + K^u_-(t;\vec{\xi}), \text{ with} \tag{34}$$

$$q\,K^u_{\pm}(t;\vec{\xi}) = \int_{c_\xi} E^*_{\pm}[n_x^2 + t_x \partial\phi/\partial t - n_x t_y \partial\phi/\partial d + i\nu p(\phi-\phi_*)]t_y dl + \nu^2 \int_{u_\xi} E^*_{\pm}[n_x + p^2(\phi-\phi_*)n_{\pm}]da, \tag{35}$$

where u_ξ is the portion of u upstream from the plane $x = \xi$. The far-field wave-amplitude function K(t) is also given by equations (31)-(35) with $K(t;\vec{\xi})$, $K^u(t;\vec{\xi})$, $K^{\ell}(t;\vec{\xi})$, $K^f(t;\vec{\xi})$, c_ξ, u_ξ, ℓ_ξ, f_ξ, $\phi-\phi_*$ replaced by $K(t)$, $K^u(t)$, $K^{\ell}(t)$, $K^f(t)$, c, u, ℓ, f, ϕ, respectively. An approximate form of expression (35) in terms of a line integral around the mean waterline is obtained below.

Let the mean waterline be defined by the parametric equations

$$x = a(\lambda) \text{ and } y = b(\lambda), \text{ with } \lambda_B \leq \lambda \leq \lambda_S, \tag{36}$$

where λ_B and λ_S correspond to the bow and the stern, respectively. The upper hull is approximated as follows:

$$\begin{aligned} x &= a(\lambda) + \alpha(\lambda)\,z \\ y &= b(\lambda) + \beta(\lambda)\,z \end{aligned} \quad \text{with} \quad \begin{matrix} \lambda_B \leq \lambda \leq \lambda_S \\ 0 \geq z \geq -\delta \end{matrix} \tag{37}$$

The notation

$$a' \equiv da(\lambda)/d\lambda, \text{ and similarly for } b', \alpha' \text{ and } \beta', \tag{38}$$

will be used. Also, let

$$\phi \equiv \phi(\lambda) \equiv \phi[a(\lambda), b(\lambda), 0] \tag{39}$$

represent the value of the potential at the point with coordinates $a(\lambda)$, $b(\lambda)$, 0 on c, and

$$\phi' \equiv d\phi(\lambda)/d\lambda. \tag{40}$$

The value of the potential at the point with coordinates $a(\lambda)-\alpha(\lambda)\delta$, $b(\lambda)-\beta(\lambda)\delta$, $-\delta$ on the lower curve bounding the upper hull is denoted by φ:

$$\varphi \equiv \varphi(\lambda) \equiv \phi[a(\lambda)-\alpha(\lambda)\delta, b(\lambda)-\beta(\lambda)\delta, -\delta]. \tag{41}$$

Equations (18b) and (37) show that the exponential $E^*_\pm \equiv E^*_\pm(t;\vec{x})$, with $\vec{x}$ on the upper hull, may be expressed in the form

$$E^*_\pm = E_\pm \exp[p^2(1-i\gamma_\pm)z], \tag{42}$$

where $E_\pm$ and $\gamma_\pm$ are defined as

$$E_\pm = \exp[-ip^2(ua \pm vb)] \text{ with } a = a(\lambda) \text{ and } b = b(\lambda) \tag{43}$$

$$\gamma_\pm = u\alpha \pm v\beta \text{ with } \alpha = \alpha(\lambda) \text{ and } \beta = \beta(\lambda). \tag{44}$$

The unit outward normal $\vec{n}$ to the upper hull surface is given by

$$\vec{n}\, da = \vec{m}\, d\lambda dz, \tag{45}$$

with $\vec{m} = (\partial\vec{x}/\partial\lambda)\times(\partial\vec{x}/\partial z)$. By using equations (37) we may then express the normal vector $\vec{m}$ in the form $\vec{m} = \vec{\nu} + \vec{\mu}z$, where the vectors $\vec{\nu}$ and $\vec{\mu}$ are defined as

$$\vec{\nu}(b', -a', \beta a' - \alpha b') \text{ and } \vec{\mu}(\beta', -\alpha', \beta\alpha' - \alpha\beta'). \tag{46a,b}$$

Equations (45) and (22) then yield

$$n_x da = (b' + \beta' z)\, d\lambda dz \text{ and } n_\pm da = (\nu_\pm + \mu_\pm z)\, d\lambda dz, \tag{47a,b}$$

where $\nu_\pm$ and $\mu_\pm$ are defined as

$$\nu_\pm = \alpha b' - \beta a' + i(ub' \mp va') \text{ and} \tag{48a}$$

$$\mu_\pm = \alpha\beta' - \beta\alpha' + i(u\beta' \mp v\alpha'). \tag{48b}$$

On the mean waterline we have $z = 0$, so that equations (47a), (45) and (46a) yield

$$n_x^2 = (b')^2/[(a')^2 + (b')^2](1+\varepsilon^2), \tag{49}$$

where ε is defined as

$$\varepsilon = (\alpha b' - \beta a')/[(a')^2 + (b')^2]^{1/2}. \tag{50}$$

Furthermore, we have $dl = [(a')^2 + (b')^2]^{1/2}\, d\lambda$, $t_x = -a'/[(a')^2+(b')^2]^{1/2}$, $t_y = -b'/[(a')^2+(b')^2]^{1/2}$ and $\partial\phi/\partial t = -\phi'/[(a')^2+(b')^2]^{1/2}$. We then have

$$t_y dl = -b' d\lambda \text{ and } t_x \partial\phi/\partial t = a'\phi'/[(a')^2+(b')^2]. \tag{51a,b}$$

Equations (45) and (46a) also yield

$$n_z t_y = b'(\alpha b' - \beta a')/[(a')^2+(b')^2](1+\varepsilon^2)^{1/2}. \tag{52}$$

Finally, the downward derivative $\partial\phi/\partial d$ is approximately given by $[\phi(a-\alpha\delta, b-\beta\delta, -\delta) - \phi(a,b,0)]/(\alpha^2\delta^2+\beta^2\delta^2+\delta^2)^{1/2}$. Equations (39) and (41) then yield

$$\partial\phi/\partial d \simeq (\varphi-\phi)/\delta(1+\alpha^2+\beta^2)^{1/2}. \tag{53}$$

Equations (49)-(52) then yield

$$[n_x^2 + t_x\partial\phi/\partial t - n_z t_y \partial\phi/\partial d + i\nu p(\phi-\phi_*)]t_y dl = -A d\lambda, \tag{54}$$

where A is defined by

$$A[(a')^2+(b')^2]/b' \simeq (b')^2/(1+\varepsilon^2) + a'\phi' + i\nu p(\phi-\phi_*)[(a')^2+(b')^2] + b'(\alpha b' - \beta a')(\phi-\varphi)/\delta(1+\alpha^2+\beta^2)^{1/2}(1+\varepsilon^2)^{1/2}. \tag{55}$$

By using equations (54), (42) and (47a,b), we may express equation (35) in the form

$$q\, K^u_\pm(t;\vec{\xi}) \simeq \nu^2 \int_{\lambda_B}^{\lambda_\xi} E_\pm (I_\pm - F^2 A)\, d\lambda, \tag{56}$$

where λ_ξ is the value of λ defined by the equation $a(\lambda_\xi) = \xi$, so that we have $x = \xi$ by equation (36). $E_\pm$ is the exponential defined by equation (43), and $I_\pm$ is the integral

$$I_\pm = \int_{-\delta}^{0} [b' + \beta' z + p^2(\phi-\phi_*)(\nu_\pm + \mu_\pm z)] \exp[p^2(1-i\gamma_\pm)z]\, dz. \tag{57}$$

For $\lambda = \lambda_\xi$, equation (37) shows that we have $x = \xi + \alpha(\lambda_\xi)z$. The variation $\alpha(\lambda_\xi)z$ in the value of x for $\lambda = \lambda_\xi$ and $0 \geq z \geq -\delta$ is small of order $\alpha\delta$. This small variation in the value of x has been neglected in equation (56). The potential $\phi \equiv \phi(\vec{x}) \equiv \phi(a+\alpha z, b+\beta z, z) \equiv \phi(z;\lambda)$ in equation (57) is approximated by the linear function $\phi(a,b,0) - [\phi(a-\alpha\delta, b-\beta\delta, -\delta) - \phi(a,b,0)]z/\delta \equiv \phi + (\phi-\varphi)z/\delta$ by equations (39) and (41). Equation (57) may then be expressed in the form

$$I_\pm = [b' + p^2(\phi-\phi_*)\nu_\pm]\, I_0^\pm + [\beta' + p^2(\phi-\phi_*)\mu_\pm + p^2(\phi-\varphi)\nu_\pm/\delta]\, I_1^\pm + [p^2(\phi-\varphi)\mu_\pm/\delta]\, I_2^\pm, \tag{58}$$

where $I_n^\pm$ are the integrals

$$I_n^\pm = \int_{-\delta}^{0} \{\exp[p^2(1-i\gamma_\pm)z]\}\, z^n\, dz.$$

These integrals can easily be evaluated analytically, and it may be verified that we have

$$I_0^{\pm} = \varepsilon_{\pm}(1-\Delta_{\pm}),\ I_1^{\pm} = -\varepsilon_{\pm}^2+\varepsilon_{\pm}(\varepsilon_{\pm}+\delta)\Delta_{\pm}, \tag{59a,b}$$

$$I_2^{\pm} = 2\varepsilon_{\pm}^3-2\varepsilon_{\pm}(\varepsilon_{\pm}^2+\delta\varepsilon_{\pm}+\delta^2/2)\Delta_{\pm}, \tag{59c}$$

where $\varepsilon_{\pm}$ and $\Delta_{\pm}$ are defined as

$$\varepsilon_{\pm} = q^2/(1-i\gamma_{\pm}) \tag{60}$$

$$\Delta_{\pm} = \exp[-p^2(1-i\gamma_{\pm})\delta] \tag{61}$$

Equations (43), (61) and (44) yield

$$E_{\pm}\Delta_{\pm} = e_{\pm}\exp(-p^2\delta), \tag{62}$$

where $e_{\pm}$ is defined as

$$e_{\pm} = \exp[-ip^2\{u(a-\alpha\delta)\pm v(b-\beta\delta)\}] \tag{63}$$

By using equations (58), (59a,b,c) and (62) in equation (56), we may then obtain

$$q\,K_{\pm}^{u}(t;\vec{\xi}) \simeq \nu^2\int_{\lambda_B}^{\lambda_\xi}[E_{\pm}F_{\pm}-\exp(-p^2\delta)e_{\pm}a_{\pm}]\,d\lambda, \tag{64}$$

where $F_{\pm}$ and $a_{\pm}$ are defined as

$$\begin{aligned}F_{\pm} &= \varepsilon_{\pm}[b'+p^2(\phi-\phi_*)\nu_{\pm}]\\ &\quad -\varepsilon_{\pm}^2[\beta'+p^2(\phi-\phi_*)\mu_{\pm}+p^2(\phi-\varphi)\nu_{\pm}/\delta]\\ &\quad +2\varepsilon_{\pm}^3p^2(\phi-\varphi)\mu_{\pm}/\delta-F^2A\end{aligned} \tag{65}$$

$$\begin{aligned}a_{\pm} &= \varepsilon_{\pm}[b'+p^2(\phi-\phi_*)\nu_{\pm}]\\ &\quad -\varepsilon_{\pm}(\varepsilon_{\pm}+\delta)[\beta'+p^2(\phi-\phi_*)\mu_{\pm}+p^2(\phi-\varphi)\nu_{\pm}/\delta]\\ &\quad +2\varepsilon_{\pm}(\varepsilon_{\pm}^2+\delta\varepsilon_{\pm}+\delta^2/2)\,p^2(\phi-\varphi)\mu_{\pm}/\delta\end{aligned}$$

The term $a_{\pm}$ may be expressed in the form

$$a_{\pm} = q^2[b_{\pm}+c_{\pm}(\varphi-\phi)/\delta]+d_{\pm}(\varphi-\phi_*), \tag{66}$$

where the coefficients $b_{\pm}$, $c_{\pm}$, $d_{\pm}$ are given by

$$b_{\pm} = (b'-\delta\beta'-\varepsilon_{\pm}\beta')/(1-i\gamma_{\pm}) \tag{66a}$$

$$c_{\pm} = (\nu_{\pm}-\delta\mu_{\pm}-2\varepsilon_{\pm}\mu_{\pm})/(1-i\gamma_{\pm})^2 \tag{66b}$$

$$d_{\pm} = (\nu_{\pm}-\delta\mu_{\pm}-\varepsilon_{\pm}\mu_{\pm})/(1-i\gamma_{\pm}) \tag{66c}$$

By using equations (55), (60) and (14b) we may express the term $F_{\pm}$ defined by equation (65) in the form

$$F_{\pm} = G_{\pm}-F^2[B_{\pm}+C_{\pm}(\phi-\varphi)/\delta] \tag{67}$$

where the terms $G_{\pm}$, $B_{\pm}$ and $C_{\pm}$ are defined as

$$\begin{aligned}G_{\pm} &= [p^2\varepsilon_{\pm}(\nu_{\pm}-\varepsilon_{\pm}\mu_{\pm})-iFpb'](\phi-\phi_*)\\ &\quad -F^2a'b'\phi'/[(a')^2+(b')^2]\end{aligned} \tag{68}$$

$$B_{\pm} = (b')^3/[(a')^2+(b')^2](1+\varepsilon^2)-u^2(b'-\varepsilon_{\pm}\beta')/(1-i\gamma_{\pm}) \tag{69}$$

$$\begin{aligned}C_{\pm} &= (b')^2(\alpha b'-\beta a')/[(a')^2+(b')^2](1+\alpha^2+\beta^2)^{1/2}(1+\varepsilon^2)^{1/2}\\ &\quad +u^2(\nu_{\pm}-2\varepsilon_{\pm}\mu_{\pm})/(1-i\gamma_{\pm})^2\end{aligned} \tag{70}$$

By using equations (60) and (14b,c) we may express the term $G_{\pm}$ defined by equation (68) in the form

$$\begin{aligned}G_{\pm} &= Fp[u\nu_{\pm}-ib'(1-i\gamma_{\pm})](\phi-\phi_*)/(1-i\gamma_{\pm})\\ &\quad -\varepsilon_{\pm}\mu_{\pm}(\phi-\phi_*)/(1-i\gamma_{\pm})-F^2a'b'\phi'/[(a')^2+(b')^2].\end{aligned}$$

Equations (48a), (44) and (16c) yield

$$u\nu_{\pm}-ib'(1-i\gamma_{\pm}) = \mp i(ua'\pm vb')(v\mp i\beta).$$

Furthermore, equation (43) readily yields

$$(E_{\pm})' \equiv dE_{\pm}/d\lambda = -ip^2(ua'\pm vb')E_{\pm}.$$

We may then obtain

$$\begin{aligned}E_{\pm}G_{\pm} &= \pm Fq(E_{\pm})'(\phi-\phi_*)(v\mp i\beta)/(1-i\gamma_{\pm})\\ &\quad -\varepsilon_{\pm}\mu_{\pm}E_{\pm}(\phi-\phi_*)/(1-i\gamma_{\pm})-F^2a'b'E_{\pm}\phi'/[(a')^2+(b')^2].\end{aligned}$$

An integration by parts yields

$$\begin{aligned}E_{\pm}G_{\pm} &= \pm Fq[E_{\pm}(\phi-\phi_*)(v\mp i\beta)/(1-i\gamma_{\pm})]'\\ &\quad \mp FqE_{\pm}[(\phi-\phi_*)(v\mp i\beta)/(1-i\gamma_{\pm})]'\\ &\quad -\varepsilon_{\pm}\mu_{\pm}E_{\pm}(\phi-\phi_*)/(1-i\gamma_{\pm})-F^2a'b'E_{\pm}\phi'/[(a')^2+(b')^2].\end{aligned}$$

We then have

$$\begin{aligned}E_{\pm}G_{\pm} &= \pm Fq\,[E_{\pm}(\phi-\phi_*)(v\mp i\beta)/(1-i\gamma_{\pm})]'\\ &\quad -F^2D_{\pm}E_{\pm}\phi'-R_{\pm}E_{\pm}(\phi-\phi_*)\end{aligned} \tag{71}$$

where the coefficients $D_{\pm}$ and $R_{\pm}$ are given by

$$D_{\pm} = a'b'/[(a')^2+(b')^2]-iu(\beta\pm iv)/(1-i\gamma_{\pm}), \tag{72}$$

$$R_{\pm} = \varepsilon_{\pm}\mu_{\pm}/(1-i\gamma_{\pm})\pm Fq[(v\mp i\beta)/(1-i\gamma_{\pm})]'. \tag{73}$$

By using equations (60), (48b), (44), (14c) and (16c) we may verify that we have

$$R_{\pm} \equiv 0. \tag{74}$$

Equations (67), (71) and (74) yield

$$E_{\pm}F_{\pm} = \pm Fq[E_{\pm}(\phi-\phi_*)(v\mp i\beta)/(1-i\gamma_{\pm})]'-F^2E_{\pm}A_{\pm} \tag{75}$$

where the term $A_{\pm}$ is defined as

$$A_{\pm} = B_{\pm}+C_{\pm}(\phi-\varphi)/\delta+D_{\pm}\phi', \tag{76}$$

with the coefficients $B_{\pm}$, $C_{\pm}$ and $D_{\pm}$ given by equations (69), (70) and (72). Equation (64) then becomes

$$q\,K_{\pm}^{u}(t;\vec{\xi}) \simeq \pm u[E_{\pm}(\phi-\phi_*)(v\mp i\beta)/(1-i\gamma_{\pm})]_{\lambda_B}^{\lambda_\xi}-I_{\pm}(t;\vec{\xi}), \tag{77}$$

where $I_{\pm}(t;\vec{\xi})$ is the integral

$$I_{\pm}(t;\vec{\xi}) = \int_{\lambda_B}^{\lambda_\xi}[A_{\pm}E_{\pm}+\nu^2\exp(-p^2\delta)\,a_{\pm}e_{\pm}]\,d\lambda. \tag{78}$$

The first term in equation (77) vanishes at the upper limit of integration λ_ξ since we have $\phi = \phi_*$ for $\lambda = \lambda_\xi$. The contribution of the lower limit of integration λ_B to the first term in equation (77) also yields a null contribution to the function $K^u(t;\vec{\xi})$ defined by equation (34). Indeed, equations (37) show that we have $b = 0$ and $\beta = 0$ at the bow (and also at the stern); equations (43) and (44) then yield $E_+ = \exp(-i\nu p a_B) = E_-$ and $\gamma_+ = u\alpha_B = \gamma_-$ for $\lambda = \lambda_B$.

Equations (34), (77) and (78) finally yield

$$q\,K^u(t;\vec{\xi}) \simeq -\int_{\lambda_B}^{\lambda_\xi} [A_+E_+ + A_-E_- + \nu^2\exp(-p^2\delta)(a_+e_+ + a_-e_-)]\,d\lambda, \tag{79}$$

where $E_\pm$ and $e_\pm$ are the exponential functions defined by equations (43) and (63), and $A_\pm$ and $a_\pm$ are the amplitude functions defined by equations (76) and (66). The coefficients $B_\pm$, $C_\pm$, $D_\pm$ and $b_\pm$, $c_\pm$, $d_\pm$ in expressions (76) and (66) for the amplitudes $A_\pm$ and $a_\pm$ are defined by equations (69), (70), (72) and (66a,b,c). In these equations, $\gamma_\pm$, $\varepsilon_\pm$, $\nu_\pm$ and $\mu_\pm$ are defined by equations (44), (60), (50) and (48a,b). Finally, a, b, α, β are the functions defining the shape of the upper hull, as is indicated by equations (37). The far-field wave-amplitude function $K^u(t)$ is also given by equation (79) where λ_ξ becomes λ_s and ϕ_* is ignored in expression (66) for the amplitude function $a_\pm$.

At a point where the phase of the exponential function $E_\pm$ is stationary we have $ua' \pm vb' = 0$, as may be seen from equation (43). Equations (16c), (14b,c) and (12a) then show that we have $(b')^2/[(a')^2+(b')^2] = u^2$ if $ua' \pm vb' = 0$, and equations (50) and (44) yield $\gamma_\pm = \pm\varepsilon$. Equations (69), (70) and (72) then become

$$B_\pm = \mp iu^2b'\varepsilon/(1+\varepsilon^2) + u^2q^2\beta'/(1\mp i\varepsilon)^2, \tag{80a}$$

$$C_\pm = u^2(\alpha b' - \beta a')/(1+\alpha^2+\beta^2)^{1/2}(1+\varepsilon^2)^{1/2} + u^2(\nu_\pm - 2\varepsilon_\pm\mu_\pm)/(1\mp i\varepsilon)^2, \tag{80b}$$

$$D_\pm = -iu^2(u\beta \mp v\alpha)/(1\mp i\varepsilon). \tag{80c}$$

The two terms in expression (72) for $D_\pm$ thus are combined into the single term shown in equation (80c) at a point of stationary phase of the exponential function $E_\pm$. The two terms on the right sides of equations (72) and (73) stem from the terms on the right side of equation (63). These terms correspond to the term $\nu^2p^2(\phi-\phi_*)n_\pm$ in the integral on the upper hull and the terms $i\nu p(\phi-\phi_*)t_y$ and $t_xt_y\partial\phi/\partial t$ in the integral on the waterline in equation (35). Equation (74) and equations (72) and (80c) then demonstrate that the aforementioned terms in the integrals around the mean waterline and on the mean wetted-hull surface in equation (27) partially cancel out one another and should be properly combined, as was already noted at the beginning of this section. In particular, it is interesting that the term $i\nu p(\phi-\phi_*)t_y$ in the integral around the mean waterline in equation (27) does not appear in the expression for the modified waterline integral defined by equations (79) and (76).

4. Numerical Evaluation of the Wave-Amplitude Functions

Equation (31) expresses the near-field wave-amplitude function as the sum of three terms corresponding to the contributions of the upper hull u+c, the lower hull ℓ and the free surface f, and defined by equations (79), (32) and (33), respectively. The far-field wave-amplitude function is defined by closely-related expressions. A simple approximate numerical method for evaluating the waterline integral in equation (79) and the surface integrals in equations (32) and (33) is presented in this section.

Numerical Evaluation of the Waterline Integral

Let $I_\pm(t;\vec{\xi})$ be the waterline integral

$$I_\pm(t;\vec{\xi}) = \int_{\lambda_B}^{\lambda_\xi} (A_\pm E_\pm + \nu^2 a_\pm e_\pm)\,d\lambda, \tag{81}$$

where $A_\pm$ and $a_\pm$ are the amplitude functions defined by equations (76) and (66), $E_\pm$ is the exponential function defined by equation (43), and $e_\pm$ is the exponential function defined by

$$e_\pm = \exp[p^2\{z_\delta - i(ux_\delta \pm vy_\delta)\}], \tag{82}$$

as may be seen from equations (79), (63) and (37). In equation (82) and hereafter we have $x_\delta \equiv a - \alpha\delta$, $y_\delta \equiv b - \beta\delta$ and $z_\delta \equiv -\delta$.

If the waterline is divided into a number of contiguous segments $\lambda_j \leqslant \lambda \leqslant \lambda_{j+1}$, we may express equation (81) in the form

$$I_\pm(t;\vec{\xi}) = \sum_{j=1}^{J} \int_{\lambda_j}^{\lambda_{j+1}} (A_\pm E_\pm + \nu^2 a_\pm e_\pm)\,d\lambda, \tag{83}$$

where $\lambda_1 = \lambda_B$ and $\lambda_{J+1} = \lambda_\xi$. The integrals over each segment $\lambda_j \leqslant \lambda \leqslant \lambda_{j+1}$ can easily be evaluated analytically if the arguments of the exponentials $E_\pm$ and $e_\pm$ are approximated by linear functions of λ and the amplitude functions $A_\pm$ and $a_\pm$ are represented by polynomials in λ.

By expressing λ in the form $\lambda = \lambda_j + (\lambda_{j+1} - \lambda_j)\mu$ with $0 \leqslant \mu \leqslant 1$ and replacing $a \equiv a(\lambda)$ by the linear approximation $a \simeq a_j + (a_{j+1} - a_j)\mu$, where $a_j \equiv a(\lambda_j)$ and $a_{j+1} \equiv a(\lambda_{j+1})$, and similarly for the functions $b(\lambda)$ and $x_\delta(\lambda)$, $y_\delta(\lambda)$, $z_\delta(\lambda)$ in equations (43) and (82), we may obtain

$$E_\pm \simeq E_j^\pm \exp[-i(\theta_{j+1}^\pm - \theta_j^\pm)\mu]. \tag{84a}$$

$$e_\pm \simeq e_j^\pm \exp[(w_{j+1}^\pm - w_j^\pm)\mu]. \tag{84b}$$

In these equations $\theta_j^\pm$, $\theta_{j+1}^\pm$ and $w_j^\pm$, $w_{j+1}^\pm$ represent the values of the functions $\theta_\pm$ and $w_\pm$ at the points λ_j and λ_{j+1}, where $\theta_\pm$ and $w_\pm$ are defined as

$$\theta_\pm = p^2(ua \pm vb) \text{ and } w_\pm = p^2[z_\delta - i(ux_\delta \pm vy_\delta)]; \tag{85a,b}$$

we thus have $\theta_j^\pm = p^2(ua_j \pm vb_j)$. Furthermore, $E_j^\pm$ and $e_j^\pm$ similarly represent the values of the exponential functions $E_\pm = \exp(-i\theta_\pm)$ and $e_\pm = \exp(w_\pm)$ at the point λ_j.

The coefficients $B_\pm$, $C_\pm$, $D_\pm$ and $b_\pm$, $c_\pm$, $d_\pm$ in expressions (76) and (66) for the amplitude functions $A_\pm$ and $a_\pm$ are taken as constant within each segment $\lambda_j \leqslant \lambda \leqslant \lambda_{j+1}$. The derivatives $\phi' \equiv d\phi(\lambda)/d\lambda$ and $(\phi-\varphi)/\delta$ of the potential are also taken as constant within each segment. Specifically, we have $\phi' \simeq (\phi_{j+1}-\phi_j)/(\lambda_{j+1}-\lambda_j)$ and $(\phi-\varphi)/\delta \simeq [(\phi_j-\varphi_j)/\delta_j + (\phi_{j+1}-\varphi_{j+1})/\delta_{j+1}]/2$ in the segment $[\lambda_j, \lambda_{j+1}]$. Equation (76) then shows that the amplitude function $A_\pm$ is taken as constant within each segment. However, the potential φ in the term $d_\pm(\varphi-\phi_*)$ in expression (66) for the amplitude $a_\pm$ is approximated by the linear function $\varphi \simeq \varphi_j+(\varphi_{j+1}-\varphi_j)\mu$ within the segment $[\lambda_j, \lambda_{j+1}]$. The amplitude $a_\pm$ is then approximated by the linear function

$$a_\pm \simeq a_0^\pm + a_1^\pm \mu, \tag{86}$$

where $a_0^\pm$ and $a_1^\pm$ are defined as

$$a_0^\pm = q^2[b_\pm + c_\pm(\varphi-\phi)/\delta] + d_\pm(\varphi_j-\phi_*), \tag{87a}$$

$$a_1^\pm = d_\pm(\varphi_{j+1}-\varphi_j). \tag{87b}$$

By using the foregoing approximations for the functions $E_\pm$, $e_\pm$, $A_\pm$ and $a_\pm$ and performing the change of variable $\lambda = \lambda_j+(\lambda_{j+1}-\lambda_j)\mu$ in equation (83), we may obtain

$$I_\pm(t;\vec{\xi}) \simeq \sum_{j=1}^{J} (\lambda_{j+1}-\lambda_j)[A_\pm P_\pm + \nu^2(a_0^\pm i_0^\pm + a_1^\pm i_1^\pm)], \tag{88}$$

where $P_\pm$ and $i_n^\pm$, with $n = 0$ and 1, are the integrals defined as

$$P_\pm = E_j^\pm \int_0^1 \exp[-i(\theta_{j+1}^\pm-\theta_j^\pm)\mu]\, d\mu,$$

$$i_n^\pm = e_j^\pm \int_0^1 \mu^n \exp[(w_{j+1}^\pm-w_j^\pm)\mu]\, d\mu.$$

These integrals can be evaluated analytically. We have

$$P_\pm = (E_j^\pm+E_{j+1}^\pm)/2 \text{ if } \theta_{j+1}^\pm=\theta_j^\pm \tag{89a}$$

$$P_\pm = i(E_{j+1}^\pm-E_j^\pm)/(\theta_{j+1}^\pm-\theta_j^\pm) \text{ if } \theta_{j+1}^\pm\neq\theta_j^\pm \tag{89b}$$

$$i_0^\pm = (e_j^\pm+e_{j+1}^\pm)/2 \text{ and } i_1^\pm = i_0^\pm/2 \text{ if } ||w_{j+1}^\pm-w_j^\pm||=0 \tag{90a,b}$$

$$i_0^\pm = (e_{j+1}^\pm-e_j^\pm)/(w_{j+1}^\pm-w_j^\pm) \text{ and} \tag{90c}$$

$$i_1^\pm = e_{j+1}^\pm/(w_{j+1}^\pm-w_j^\pm)-(e_{j+1}^\pm-e_j^\pm)/(w_{j+1}^\pm-w_j^\pm)^2 \tag{90d}$$
$$\text{if } ||w_{j+1}^\pm-w_j^\pm||\neq 0$$

By using equations (87a,b) we may obtain

$$a_0^\pm i_0^\pm + a_1^\pm i_1^\pm = q^2[b_\pm + c_\pm(\varphi-\phi)/\delta]p_\pm + d_\pm[(\varphi_j-\phi_*)p_j^\pm + (\varphi_{j+1}-\phi_*)p_{j+1}^\pm], \tag{91}$$

where $p_\pm = i_0^\pm$, $p_j^\pm = i_0^\pm - i_1^\pm$ and $p_{j+1}^\pm = i_1^\pm$. Equations (90a-d) then yield

$$p_\pm = (e_j^\pm+e_{j+1}^\pm)/2 \text{ and } p_j^\pm = p_\pm/2 = p_{j+1}^\pm \text{ if } ||w_{j+1}^\pm-w_j^\pm||=0, \tag{92}$$

$$p_\pm = (e_{j+1}^\pm-e_j^\pm)/(w_{j+1}^\pm-w_j^\pm) \tag{93a}$$

$$p_j^\pm = (e_j^\pm-p_\pm)/(w_j^\pm-w_{j+1}^\pm) \tag{93b}$$

$$p_{j+1}^\pm = (e_{j+1}^\pm-p_\pm)/(w_{j+1}^\pm-w_j^\pm) \tag{93c}$$
$$\text{if } ||w_{j+1}^\pm-w_j^\pm||\neq 0$$

Equations (79), (81), (82), (88), (76) and (91) finally yield the following expression for the contribution of the upper hull to the near-field wave-amplitude function

$$q\,K^u(t;\vec{\xi}) \simeq \sum_{j=1}^{J} (\lambda_j-\lambda_{j+1})\{(B+\nu^2q^2b) + D(\phi_j-\phi_{j+1})/(\lambda_j-\lambda_{j+1}) + (C-\nu^2q^2c)[(\phi_j-\varphi_j)/\delta_j+(\phi_{j+1}-\varphi_{j+1})/\delta_{j+1}]/2 + \nu^2[d_j(\varphi_j-\phi_*)+d_{j+1}(\varphi_{j+1}-\phi_*)]\} \tag{94}$$

where the coefficients B, b, C, c, D, d_j and d_{j+1} are defined as

$$B = B_+P_+ + B_-P_-,\ b = b_+p_+ + b_-p_-, \tag{95a,b}$$

$$C = C_+P_+ + C_-P_-,\ c = c_+p_+ + c_-p_-, \tag{95c,d}$$

$$D = D_+P_+ + D_-P_-, \tag{95e}$$

$$d_j = d_+p_j^+ + d_-p_j^-,\ d_{j+1} = d_+p_{j+1}^+ + d_-p_{j+1}^- \tag{95f,g}$$

In these equations, $P_\pm$ and $p_\pm$, $p_j^\pm$, $p_{j+1}^\pm$ are given by equations (89a,b) and (92), (93a,b,c) and $B_\pm$, $C_\pm$, $D_\pm$ and $b_\pm$, $c_\pm$, $d_\pm$ are given by equations (69), (70), (72), (80a,b,c) and (66a,b,c) together with equations (44), (48a,b), (50), (60) and (37). Furthermore, we have $\lambda_1 = \lambda_B$ and $\lambda_{J+1} = \lambda_\xi$ in equation (94). The contribution of the upper hull to the far-field wave-amplitude function is also given by equation (94) where the summation is extended over all the segments in the waterline and ϕ_* is replaced by 0.

Numerical Evaluation of the Hull-Surface Integral

Let us now consider the integral $K_\pm^{\mathcal{S}}(t;\vec{\xi})$ occurring in equation (32) and defined as

$$q\,K_\pm^{\mathcal{S}}(t;\vec{\xi}) = \nu^2 \int_{\mathcal{S}_\xi} E_\pm[n_x + p^2(\phi-\phi_*)n_\pm]\, da, \tag{96}$$

where $E_\pm \equiv E_\pm(t;\vec{x})$ is the exponential function given by

$$E_\pm = \exp[W_\pm(t;\vec{x})] \text{ with } W_\pm = p^2[z-i(ux\pm vy)]. \tag{97a,b}$$

The lower hull surface $\mathcal{S}$ is approximated by a set of contiguous plane triangles. On each of these elementary plane triangles n_x and $n_\pm \equiv -n_z+i(un_x\pm vn_y)$ are constant, so that equation (96) yields

$$q\,K_\pm^{\mathcal{S}}(t;\vec{\xi}) \simeq \nu^2 \sum (n_xI_\pm + p^2n_\pm J_\pm), \tag{98}$$

where the summation is carried over all the triangles that are upstream from the plane $x = \xi$, and $I_\pm$ and $J_\pm$ are

the integrals defined as

$$I_{\pm} = \int E_{\pm}\, da \text{ and } J_{\pm} = \int E_{\pm}(\phi-\phi_*)\, da. \qquad (99a,b)$$

The integration in equations (99a,b) is carried over the surface of any of the plane triangles in the lower hull.

Let $\vec{x}_j$ – with j = 1,2,3 – represent the position vectors of the three vertices of any plane triangle in the lower hull. The location of any point $\vec{x}$ inside that triangle can be defined by the parametric equation

$$\vec{x} = \vec{x}_1+\lambda\vec{x}_{12}+\mu\vec{x}_{13} \text{ with } 0\leqslant\lambda\leqslant 1 \text{ and } 0\leqslant\mu\leqslant 1-\lambda \qquad (100)$$

and $\vec{x}_{jk} \equiv \vec{x}_k-\vec{x}_j$ by definition. The vertices $\vec{x}_1$, $\vec{x}_2$, $\vec{x}_3$ are distributed counter clockwise for an observer located inside the hull. The unit outward normal $\vec{n}$ to the hull surface is then given by $\vec{n}\, da = (\partial\vec{x}/\partial\mu) \times (\partial\vec{x}/\partial\lambda)\, d\lambda d\mu = \vec{x}_{13} \times \vec{x}_{12}\, d\lambda d\mu$. We then have $\vec{n}\, da = \vec{m}\, d\lambda d\mu$ where $\vec{m}$ is the vector with components m_x, m_y, m_z given by

$$\begin{aligned} m_x &= y_{13}z_{12}-z_{13}y_{12}, \\ m_y &= z_{13}x_{12}-x_{13}z_{12}, \\ m_z &= x_{13}y_{12}-y_{13}x_{12}. \end{aligned} \qquad (101)$$

Equations (98) and (99a,b) then become

$$q\, K_{\pm}^{\ell}(t;\vec{\xi}) \simeq \nu^2 \sum (m_x o_0^{\pm} + p^2 m_{\pm} o_{\pm}), \qquad (102)$$

where $m_{\pm}$ is defined as

$$m_{\pm} = -m_z+i(um_x \pm vm_y), \qquad (103)$$

as may be seen from equation (22), and $o_0^{\pm}$ and $o_{\pm}$ are the following integrals

$$o_0^{\pm} = \int_0^1 d\lambda \int_0^{1-\lambda} d\mu\, E_* \text{ and} \qquad (104a)$$

$$o_{\pm} = \int_0^1 d\lambda \int_0^{1-\lambda} d\mu\, E_{\pm}(\phi-\phi_*). \qquad (104b)$$

By using equation (100) in equations (97a,b) we may obtain

$$E_{\pm} = E_1^{\pm} \exp(\lambda W_{12}^{\pm}) \exp(\mu W_{13}^{\pm}), \qquad (105)$$

where we have

$$E_j^{\pm} = \exp(W_j^{\pm}) \text{ with } W_j^{\pm} = p^2[z_j - i(ux_j \pm vy_j)] \qquad (106a,b)$$

and $W_{jk}^{\pm} \equiv W_k^{\pm} - W_j^{\pm}$. Equations (104a,b) and (105) then yield

$$o_0^{\pm} = E_1^{\pm} \int_0^1 d\lambda \exp(\lambda W_{12}^{\pm}) \int_0^{1-\lambda} d\mu \exp(\mu W_{13}^{\pm}) \qquad (107a)$$

$$o_{\pm} = E_1^{\pm} \int_0^1 d\lambda \exp(\lambda W_{12}^{\pm}) \int_0^{1-\lambda} d\mu \exp(\mu W_{13}^{\pm})(\phi-\phi_*). \qquad (107b)$$

Variation of the potential $\phi \equiv \phi(\lambda,\mu)$ within each plane triangle in the lower-hull surface is approximated by a linear function of λ and μ, as follows:

$$\phi \simeq \phi_1+\lambda\phi_{12}+\mu\phi_{13}, \qquad (108)$$

where we have

$$\phi_j \equiv \phi(\vec{x}_j) \qquad (109)$$

and $\phi_{jk} \equiv \phi_k-\phi_j$. By using equation (108) in equation (107b) we may then obtain

$$o_{\pm} \simeq o_1^{\pm}\phi_1+o_2^{\pm}\phi_2+o_3^{\pm}\phi_3-o_0^{\pm}\phi_*, \qquad (110)$$

where $o_1^{\pm}$, $o_2^{\pm}$, $o_3^{\pm}$ are defined as

$$o_1^{\pm} = o_0^{\pm}-o_2^{\pm}-o_3^{\pm} \qquad (111a)$$

$$o_2^{\pm} = E_1^{\pm} \int_0^1 d\lambda\, \lambda \exp(\lambda W_{12}^{\pm}) \int_0^{1-\lambda} d\mu \exp(\mu W_{13}^{\pm}) \qquad (111b)$$

$$o_3^{\pm} = E_1^{\pm} \int_0^1 d\lambda \exp(\lambda W_{12}^{\pm}) \int_0^{1-\lambda} d\mu\, \mu \exp(\mu W_{13}^{\pm}) \qquad (111c)$$

where equation (107a) was used.

Equations (32), (96), (102), (110) and (111a) finally yield the following expression for the contribution of the lower hull to the near-field wave-amplitude function:

$$\begin{aligned} q\, K^{\ell}(t;\vec{\xi}) \simeq \nu^2 \sum \{ & \gamma_0 \\ & + p^2\{\gamma_1(\phi_1-\phi_*)+\gamma_2(\phi_2-\phi_*)+\gamma_3(\phi_3-\phi_*)\}\}, \end{aligned} \qquad (112)$$

where the summation is carried over all the triangles upstream from the plane $x = \xi$, $\phi_j \equiv \phi(\vec{x}_j)$, and the coefficients γ_0 and γ_j are defined as

$$\gamma_0 = m_x(o_0^{+} + o_0^{-}) \text{ and} \qquad (113a)$$

$$\gamma_j = m_+ o_j^{+} + m_- o_j^{-} \text{ with } 1\leqslant j\leqslant 3. \qquad (113b)$$

The integrals (107a) and (111b,c) can be evaluated analytically. It may be verified that we have

$$o_0^{\pm} = (E_1^{\pm}+E_2^{\pm}+E_3^{\pm})/6 \text{ and } o_1^{\pm} = o_2^{\pm} = o_3^{\pm} = o_0^{\pm}/3 \text{ if } \|W_{12}^{\pm}\|+\|W_{23}^{\pm}\|+\|W_{31}^{\pm}\| = 0, \qquad (114)$$

where $W_{jk}^{\pm} \equiv W_k^{\pm} - W_j^{\pm}$, as was already defined, and $E_j^{\pm}$ and $W_j^{\pm}$ are defined by equations (106a,b). If $W_{kl}^{\pm} = 0$ but $U_j^{\pm} \neq 0$, with $U_j^{\pm}$ defined as

$$U_j^{\pm} = W_j^{\pm}-(W_k^{\pm}+W_l^{\pm})/2, \qquad (115)$$

the coefficients $o_0^{\pm}$, $o_j^{\pm}$, $o_k^{\pm}$ and $o_l^{\pm}$ are given by

$$o_0^{\pm} = C_j^{\pm}[E_j^{\pm}-(1+U_j^{\pm})F_j^{\pm}], \qquad (116a)$$

$$o_j^{\pm} = C_j^{\pm}(E_j^{\pm}+F_j^{\pm}+2R_j^{\pm}), \qquad (116b)$$

$$o_k^{\pm} = o_l^{\pm} = -C_j^{\pm}[(1+U_j^{\pm}/2)F_j^{\pm}+R_j^{\pm}]. \qquad (116c,d)$$

where $C_j^{\pm}$, $F_j^{\pm}$ and $R_j^{\pm}$ are defined as

$$C_j^{\pm} = V_j^{\pm}V_j^{\pm} \text{ with } V_j^{\pm} = 1/U_j^{\pm}. \qquad (117a,b)$$

$$F_j^{\pm} = (E_k^{\pm}+E_l^{\pm})/2 \text{ and } R_j^{\pm} = V_j^{\pm}(F_j^{\pm}-E_j^{\pm}). \qquad (117c,d)$$

Finally, in the general case when $W_{12}^{\pm} \neq 0$, $W_{23}^{\pm} \neq 0$ and $W_{31}^{\pm} \neq 0$ the coefficients $\sigma_0^{\pm}$ and $\sigma_j^{\pm}$ $(1 \leqslant j \leqslant 3)$ are given by

$$\sigma_0^{\pm} = -(F_1^{\pm}+F_2^{\pm}+F_3^{\pm}), \tag{118a}$$

$$\sigma_j^{\pm} = -[F_j^{\pm}+V_{kl}^{\mp}(F_{jk}^{\pm}+F_{lj}^{\pm})], \tag{118b}$$

where $V_{jk}^{\pm}$, $F_j^{\pm}$ and $F_{jk}^{\pm}$ are defined as

$$V_{jk}^{\pm} = 1/W_{jk}^{\pm}, \quad F_j^{\pm} = V_{jk}^{\mp}V_{lj}^{\mp}E_j^{\pm}, \tag{119a,b}$$

$$F_{jk}^{\pm} = V_{jk}^{\pm}V_{jk}^{\pm}(E_k^{\pm}-E_j^{\pm}). \tag{119c}$$

In equations (115)-(119), (j, k, l) represents any one of the three cyclic permutations (1,2,3), (2,3,1), (3,1,2).

Almost all of the plane triangular elements in the lower hull surface $\mathscr{S}$ can be combined in groups of two contiguous triangles forming a single quadrilateral element. The lower hull surface can then be approximated by a set of contiguous (non-plane) quadrilateral elements covering the whole or most of $\mathscr{S}$. If necessary, these quadrilateral elements may be supplemented by a small number of triangular elements. A quadrilateral element can be divided into two triangles in two different ways, as is shown in figure 2. The contribution of the quadrilateral element depicted in figure 2 to the surface integrals defining the wave-amplitude functions may then be taken equal to half the contributions of the four triangles with vertices identified by the integers (1,2,3), (2,3,4), (3,4,1), (4,1,2). Equation (112) then yields

$$\begin{aligned} q\,K^{\mathscr{S}}(1;\vec{\xi}) \simeq \nu^2 \sum [&\Gamma_0 + p^2\{\Gamma_1(\phi_1-\phi_*)+\Gamma_2(\phi_2-\phi_*) \\ &+\Gamma_3(\phi_3-\phi_*)+\Gamma_4(\phi_4-\phi_*)\}/2 \\ &+\{\gamma_0+p^2\{\gamma_1(\phi_1-\phi_*)+\gamma_2(\phi_2-\phi_*)+\gamma_3(\phi_3-\phi_*)\}] \end{aligned} \tag{120}$$

where the summation is carried over all the quadrilateral and triangular elements upstream from the plane $x = \xi$, and we have $\phi_j \equiv \phi(\vec{x}_j)$ and $\phi_* \equiv \phi(\vec{\xi})$ as was defined previously. The contribution of the lower hull to the far-field wave-amplitude function is also given by equation (120) if ϕ_* is ignored and the summation is extended to all the quadrilateral and triangular elements in the lower hull. The coefficients γ_0, γ_1, γ_2, γ_3 are associated with triangular elements and are defined by equations (113)-(119). The coefficients Γ_0, Γ_1, Γ_2, Γ_3, Γ_4 correspond to quadrilateral elements and are defined below.

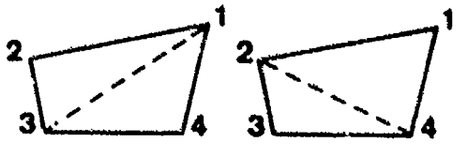

Figure 2. Approximation of a Quadrilateral Panel by Four Plane Triangular Panels

Let $\vec{x}_1$, $\vec{x}_2$, $\vec{x}_3$, $\vec{x}_4$ represent the position vectors of the vertices of a quadrilateral element, as in figure 2. Furthermore, let (i,j,k,l) represent any one of the four cyclic permutations (1,2,3,4), (2,3,4,1), (3,4,1,2), (4,1,2,3). The normal vector $\vec{m}(m_x, m_y, m_z)$ to the plane triangle with vertices $\vec{x}_j$, $\vec{x}_k$, $\vec{x}_l$ is denoted by $\vec{m}_i$. The x,y,z components of $\vec{m}_i$ may readily be obtained from equations (101):

$$\begin{aligned} m_i^x &= y_{jl}z_{jk}-z_{jl}y_{jk}, \\ m_i^y &= z_{jl}x_{jk}-x_{jl}z_{jk}, \\ m_i^z &= x_{jl}y_{jk}-y_{jl}x_{jk}. \end{aligned} \tag{121}$$

where $\vec{x}_{jk} \equiv \vec{x}_k - \vec{x}_j$ as was defined previously. Equation (103) takes the form

$$m_i^{\pm} = -m_i^z + \sqrt{-1}(um_i^x \pm vm_i^y). \tag{122}$$

Equations (113a,b) then yield

$$\Gamma_0 = \sum_{i=1}^{4} m_i^x(\varepsilon_i^+ + \varepsilon_i^-) \text{ and} \tag{123a}$$

$$\Gamma_j = \gamma_{jk} + \gamma_{jl} + \gamma_{ji} \text{ with } 1 \leqslant j \leqslant 4, \tag{123b}$$

where the coefficients γ_{ji} are defined as

$$\gamma_{ji} = m_i^+\varepsilon_{ji}^+ + m_i^-\varepsilon_{ji}^-. \tag{123c}$$

The coefficients $\varepsilon_i^{\pm}$ and $\varepsilon_{ji}^{\pm}$ are identical to the coefficients $\sigma_0^{\pm}$ and $\sigma_j^{\pm}$ in equations (113a,b) for the triangle corresponding to the integer i, that is the triangle with vertices $\vec{x}_j$, $\vec{x}_k$, $\vec{x}_l$.

Numerical Evaluation of the Free-Surface Integral

Comparison of equations (32) and (33) shows that the contribution of the free surface to the near-field wave-amplitude function may be evaluated numerically by using an expression similar to expression (120), although alternative, more efficient numerical methods can be devised by using the fact that the mean free surface f is flat. More precisely, the portion of the plane $z = 0$ outside the ship can be divided into a set of contiguous quadrilateral and triangular elements and linear variation may be assumed for the function $\chi(\phi)$ defined by equation (3a) within the triangular elements and within each of the four triangles that may be considered for any quadrilateral element. We may then obtain

$$\begin{aligned} q\,K^{f}(1;\vec{\xi}) \simeq \sum &(\Gamma_1\chi_1+\Gamma_2\chi_2+\Gamma_3\chi_3+\Gamma_4\chi_4)/2 \\ &+ (\gamma_1\chi_1+\gamma_2\chi_2+\gamma_3\chi_3) \end{aligned} \tag{124}$$

where the summation is carried over all the quadrilateral and triangular elements upstream from the line $x = \xi$, χ_j represents the value of the function $\chi(\phi)$ at the vertex $\vec{x}_j$, and the coefficients γ_j and Γ_j are associated with triangular and quadrilateral elements, respectively, and are defined as

$$\gamma_j = [x_{12}y_{13}-y_{12}x_{13}]\sigma_j^{+} + \sigma_j^{-}] \text{ with } 1 \leqslant j \leqslant 3, \tag{125}$$

and $\Gamma_j = \gamma_{jk} + \gamma_{jl} + \gamma_{ji}$ with $1 \leqslant j \leqslant 4$. (126)

The coefficients $\sigma_j^{\pm}$ are given by equations (116)-(119) and

the coefficients γ_{ji} are defined as

$$\gamma_{ji} = -m_i^z(\varepsilon_{ji}^+ + \varepsilon_{ji}^-), \tag{127}$$

where m_i^z is the z component of the normal vector $\vec{m}_i$ to the triangle i given by equation (121), and $\varepsilon_{ji}^{\pm}$ is identical to the coefficient $\sigma_j^{\pm}$ for the triangle i as was already noted below equation (123c). The contribution of the free surface to the far-field wave-amplitude function is also given by equation (124) where the summation must be extended to all the quadrilateral and triangular elements in the free-surface.

5. Numerical Study of the Far-Field Wave-Amplitude Function

Results of numerical calculations of the far-field wave-amplitude function K(t) based on expressions (31), (94) and (120) are presented and discussed below for a realistic hull form at five Froude numbers, namely at F = 0.5, 0.35, 0.25, 0.15, 0.1. The contribution of the free surface K^f, given by expression (124), was ignored in these calculations. In order to isolate the numerical errors that are directly associated with the calculation method of K(t) summarized by equations (31), (94) and (120), calculations were performed for a hull form defined mathematically, and approximate analytical expressions were used for the value of the velocity potential ϕ on the mean hull surface. In other words, the numerical errors associated with hull geometry approximations and velocity-potential calculations are eliminated from the calculations reported below.

The hull form for which numerical calculations have been performed has a sharp-ended bow region $0.25 \leqslant x \leqslant 0.5$, a cylindrical midship region $-0.25 \leqslant x \leqslant 0.25$, and a round-ended stern region $-0.5 \leqslant x \leqslant -0.25$. The top waterline (plane $z = 0$), the central buttock line (plane $y = 0$), and the framelines $x = \pm 0.475$, ± 0.45, ± 0.4, ± 0.35, ± 0.3 and ± 0.25 are depicted in figure 3. More precisely, the sharp-ended bow region is defined by the parametric equations

$$x = 1/2 - \lambda - (1 - \lambda/\lambda_1)[\alpha_0 + \alpha_1\mu]\mu\lambda_1$$

$$2y/b = (\lambda/\lambda_1)[1 - \mu][(2 - \lambda/\lambda_1)(1 + \mu) - \beta_0(1 - \lambda/\lambda_1)^2\mu]$$

$$-z/d = \mu[(1 - \lambda/\lambda_1)^2 + (\lambda/\lambda_1)^2(2 - \mu^2)^{1/2}][(1 - \lambda/\lambda_1)^2 + (\lambda/\lambda_1)^2]$$

where $0 \leqslant \lambda \leqslant \lambda_1$ and $0 \leqslant \mu \leqslant 1$. The midship region is taken as the elliptical cylinder defined by the parametric equations

$$x = 1/2 - \lambda$$

$$2y/b = \cos(\pi\mu/2)$$

$$-z/d = \sin(\pi\mu/2)$$

where $\lambda_1 \leqslant \lambda \leqslant 1 - \lambda_2$ and $0 \leqslant \mu \leqslant 1$. Finally, the round-ended stern region is defined by the parametric equations

$$x = -1/2 + \lambda_2 - \lambda_2(1 - \alpha_2\mu)\sin[\pi(\lambda - 1 + \lambda_2)/2\lambda_2]$$

$$2y/b = \cos[\pi(\lambda - 1 + \lambda_2)/2\lambda_2]\cos(\pi\mu/2)$$

$$-z/d = \sin(\pi\mu/2)$$

where $1 - \lambda_2 \leqslant \lambda \leqslant 1$ and $0 \leqslant \mu \leqslant 1$. The beam/length ratio b and the draft/length ratio d are taken equal to 0.15 and 0.06, respectively, and the constants λ_1, λ_2, α_0, α_1, α_2, β_0 are taken as $\lambda_1 = 0.25 = \lambda_2$, $\alpha_0 = 0.12 = \alpha_1$, $\alpha_2 = 0.21$, $\beta_0 = 0.2$.

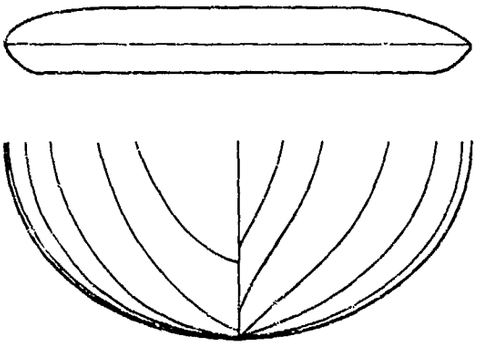

Figure 3. Waterline, Central Buttock Line, and Framelines of Hull Form Used for Numerical Calculations

The far-field wave-amplitude function K(t) associated with the above-defined hull form is depicted in figures 4a-d, 5a-d, 6a-d, 7a-d and 8a-d corresponding to F = 0.5, 0.35, 0.25, 0.15 and 0.1, respectively. Figures 4a, 5a, 6a, 7a and 8a depict the real and imaginary parts of the function qK_c^* corresponding to the contribution of the top waterline in equations (79) or (94). The function qK_c^* thus represents the modified waterline integral given by the expressions

$$qK_c^* \simeq -\int_{\lambda_B}^{\lambda_S} [A_+ E_+ + A_- E_-]\,d\lambda \tag{128a}$$

$$qK_c^* \simeq \sum_{j=1}^{N} (\lambda_j - \lambda_{j+1})[(B + D(\phi_j - \phi_{j+1})/(\lambda_j - \lambda_{j+1}) + C[(\phi_j - \omega_j)/\delta_j + (\phi_{j+1} - \omega_{j+1})/\delta_{j+1}]/2] \tag{128b}$$

Figures 4b, 5b, 6b, 7b and 8b depict the real and imaginary parts of the function qK_h^* corresponding to the sum of the contributions of the bottom waterline in equations (79) or (94) and of the lower hull defined by equations (32) or (120). The function qK_h^* thus represents the modified hull integral given by the expressions

$$F^2qK_h^* \simeq -\int_{\lambda_B}^{\lambda_S} [a_+ e_+ + a_- e_-]\exp(-p^2\delta)\,d\lambda + \int_0^{\lambda_B} [n_x(E_+^* + E_-^*) + p^2(n_+ E_+^* + n_- E_-^*)]\,d\lambda \tag{129a}$$

$$F^2qK_h^* \simeq q^* \sum_{j=1}^{N} (\lambda_j - \lambda_{j+1})[(b + p^2(d_j\omega_j + d_{j+1}\omega_{j+1}) - c[(\phi_j - \omega_j)/\delta_j + (\phi_{j+1} - \omega_{j+1})/\delta_{j+1}]/2] + \sum [\Gamma_0 + p^2(\Gamma_1\phi_1 + \Gamma_2\phi_2 + \Gamma_3\phi_3 + \Gamma_4\phi_4)]/2 \tag{129b}$$

The sum $qK'_c+qK'_h$ yields the far-field wave-amplitude function qK. The real and imaginary parts of the function qK(t) are depicted in figures 4c, 5c, 6c, 7c and 8c. The values of $\theta = \tan^{-1}(Ft)$ are also indicated in these figures. Finally, figures 4d, 5d, 6d, 7d and 8d depict the function $q||K(t)||^2$ whose integral yields the wave resistance, as is indicated by equation (30). A number of interesting features may be observed from figures 4a-d through 8a-d.

Comparisons of figures 4a to 4b through figures 8a to 8b indicate that the modified hull integral qK'_h vanishes faster than the modified waterline integral qK'_c as t increases. More precisely, figures 4b-8b show that the function qK'_h appears negligibly small, on the scale of these figures, for values of t greater than approximately 10.5, 14, 17.5, 24 and 30 for F = 0.5, 0.35, 0.25, 0.15 and 0.1, respectively. The shortest waves in the wave spectrum are then contained in the modified waterline integral. This finding has fortunate practical implications since the computing time required for evaluating the hull integral qK'_h, for a given hull form and for given values of F and t, is considerably larger than that required for evaluating the waterline integral qK'_c.

Figures 4a,b through 8a,b show that the magnitudes of the imaginary parts of the functions qK'_c and qK'_h are appreciably larger than the magnitudes of the corresponding real parts. Figures 6a and 6b also show that the magnitudes of the functions $qIm(K'_c)$ and $qIm(K'_h)$ are comparable for F = 0.25. For larger values of F, figures 4a,b and 5a,b show that the hull-integral function $qIm(K'_h)$ is slightly larger in magnitude than the waterline-integral function $qIm(K'_c)$. For smaller values of F on the other hand, figures 7a,b and 8a,b show that the magnitude of the function $qIm(K'_c)$ is significantly larger than that of the function $qIm(K'_h)$. More precisely, the ratio of the largest absolute values of the functions $qIm(K'_c)$ and $qIm(K'_h)$ is approximately equal to 0.8, 0.9, 1, 1.8 and 2.5 for F = 0.5, 0.35, 0.25, 0.15 and 0.1, respectively. The importance of the hull integral K'_h relative to the waterline integral K'_c therefore diminishes as the Froude number decreases.

Comparisons of the magnitudes of the first peaks of the functions $qIm(K'_c)$ and $qIm(K'_h)$ in figures 4a,b through 8a,b to the function $qIm(K) = qIm(K'_c)+qIm(K'_h)$ depicted in figures 4c through 8c indicate that the functions $qIm(K'_c)$ and $qIm(K'_h)$ partially cancel out one another for small values of t (for large values of t, the hull integral is much smaller than the waterline integral, as was noted previously). As a result of this partial cancellation of the component functions qK'_c and qK'_h, differences between the magnitudes of the real and imaginary parts of the sum qK are much less pronounced than for the functions qK'_c and qK'_h, especially for F = 0.5.

The values of $\theta = \tan^{-1}(Ft)$ corresponding to the values of t noted in figures 4a,b through 8a,b are indicated in figures 4c through 8c. It was noted previously that the hull-integral function qK'_h appears to be negligibly small for values of t greater than about 10.5, 14, 17.5, 24 and 30 for F = 0.5, 0.35, 0.25, 0.15 and 0.1, respectively. The values of θ corresponding to these values of F and t are 79.2°, 78.5°, 77.1°, 74.5° and 71.6°, respectively. Figures 4c through 8c show that the oscillations of the far-field wave-amplitude function with respect to the variable θ become extremely rapid as θ increases toward 90°.

Figures 4c,d through 8c,d show that the integrand $q||K(t)||^2$ of the Havelock wave-resistance integral (30) vanishes appreciably faster than the function K(t) as t increases. More precisely, figures 4d through 8d indicate that the function $q||K||^2$ becomes practically negligible for $t \simeq 11$, 13, 15, 24 and 15 for F = 0.5, 0.35, 0.25, 0.15 and 0.1, respectively.

Figures 4a,b,c through 8a,b,c show that the far-field wave-amplitude function K(t) is an oscillatory function of t. Knowledge of the approximate value of the pseudo period of these oscillations is very useful for accurate and efficient numerical evaluation of the integrals in expressions (28) and (30) defining the far-field wave potential and the wave resistance. The pseudo period Δt of the oscillations of the functions qRe(K) and qIm(K) depicted in figures 4c through 8c is represented in figure 9 versus $p \equiv (\nu^2+t^2)^{1/2}$, where $\nu = 1/F$, for F = 0.5, 0.35, 0.25, 0.15 and 0.1. The values of the pseudo period corresponding to the real and imaginary parts of the function qK(t) are identified by the symbols o and x, respectively, in figure 9. Two solid-line curves representing the functions 10/p and 20/p are also shown in this figure. The values of the pseudo period Δt depicted in figure 9 were determined from figures 4c through 8c by identifying the successive roots, t_i say, of the real and imaginary parts of the function qK(t). More precisely, the pseudo periods $\Delta t = t_{i+1}-t_i$ and $\Delta t = [(t_{i+1}-t_i)+(t_i-t_{i-1})]/2 = (t_{i+1}-t_{i-1})/2$ are computed from the roots t_i and assumed to hold at $(t_i+t_{i+1})/2$ and t_i, respectively. Figure 9 shows that the values of the pseudo period determined in this manner from figures 4c through 8c are fairly well bounded by the curves 10/p and 20/p, except for F = 0.5 and 0.25 for which a large number of the pseudo periods associated with the real and imaginary parts, respectively, of the function qK(t) are above the curve 20/p. The pseudo period of the oscillations of the function qK(t) may then be safely estimated by the simple approximation $C/(\nu^2+t^2)^{1/2}$, where C is a constant between 10 and 20.

Finally, it is interesting to compare the far-field wave-amplitude function qK(t) and the modified-hull-integral function $qK'_h(t)$ to the hull-integral function $qK_h(t)$ corresponding to the hull integral in equation (27) and given by equation (120), where the summation here is carried over all the quadrilateral panels in both the upper hull u and the lower hull ℓ. The real and imaginary parts of the whole-hull integral $qK_h(t)$ are depicted in figure 10 for F = 0.25, which should be compared to figures 6b and 6c representing the modified-hull integral $qK'_h(t)$ and the wave-amplitude function qK(t), respectively. Figure 10

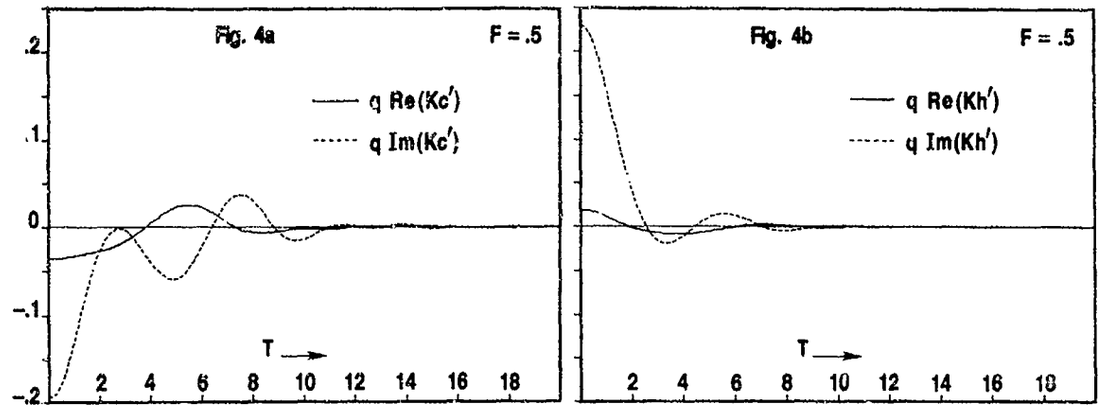
Fig. 4a
F = .5
q Re(Kc′)
q Im(Kc′)
.2
.1
0
-.1
-.2
T
2 4 6 8 10 12 14 16 18

Fig. 4b
F = .5
q Re(Kh′)
q Im(Kh′)
T
2 4 6 8 10 12 14 16 18

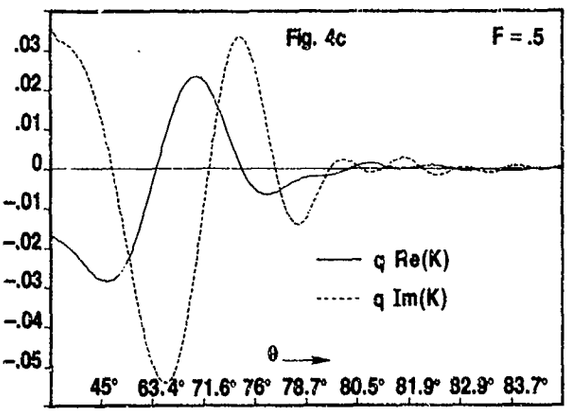
Fig. 4c
F = .5
q Re(K)
q Im(K)
.03
.02
.01
0
-.01
-.02
-.03
-.04
-.05
θ
45° 63.4° 71.6° 76° 78.7° 80.5° 81.9° 82.9° 83.7°

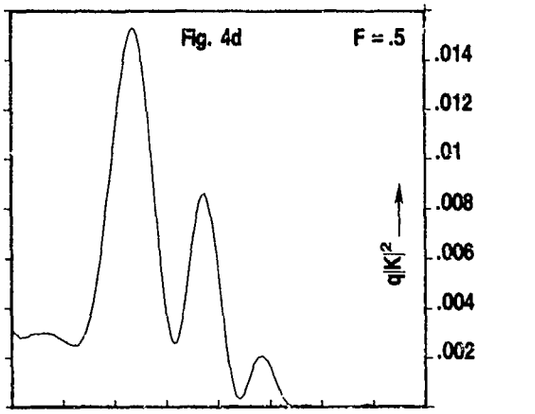
Fig. 4d
F = .5
q|K|²
.014
.012
.01
.008
.006
.004
.002

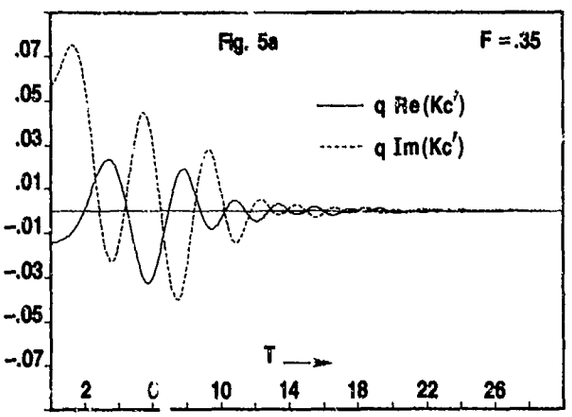
Fig. 5a
F = .35
q Re(Kc′)
q Im(Kc′)
.07
.05
.03
.01
-.01
-.03
-.05
-.07
T
2 6 10 14 18 22 26

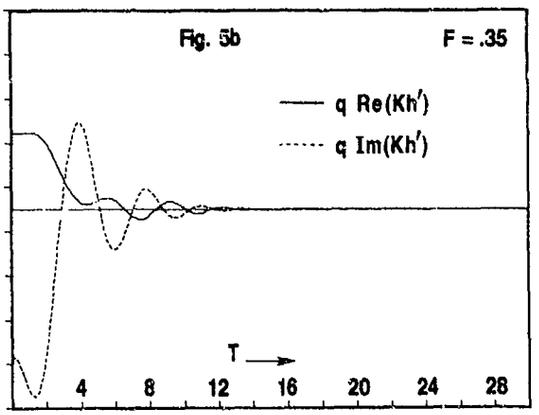
Fig. 5b
F = .35
q Re(Kh′)
q Im(Kh′)
T
4 8 12 16 20 24 28

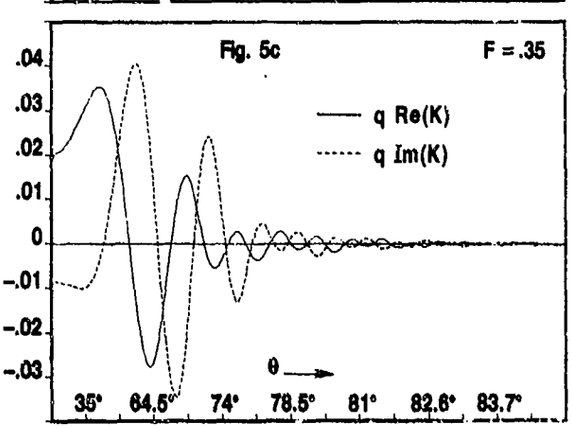
Fig. 5c
F = .35
q Re(K)
q Im(K)
.04
.03
.02
.01
0
-.01
-.02
-.03
θ
35° 64.5° 74° 78.5° 81° 82.6° 83.7°

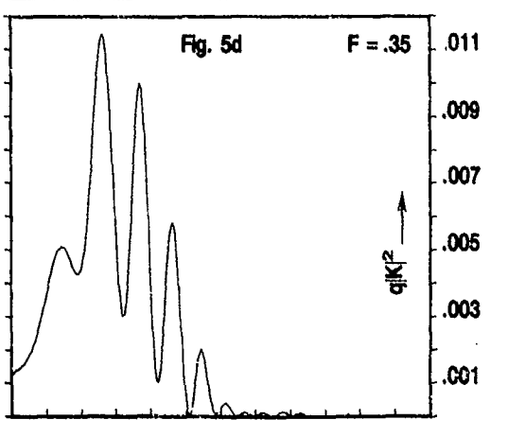
Fig. 5d
F = .35
q|K|²
.011
.009
.007
.005
.003
.001

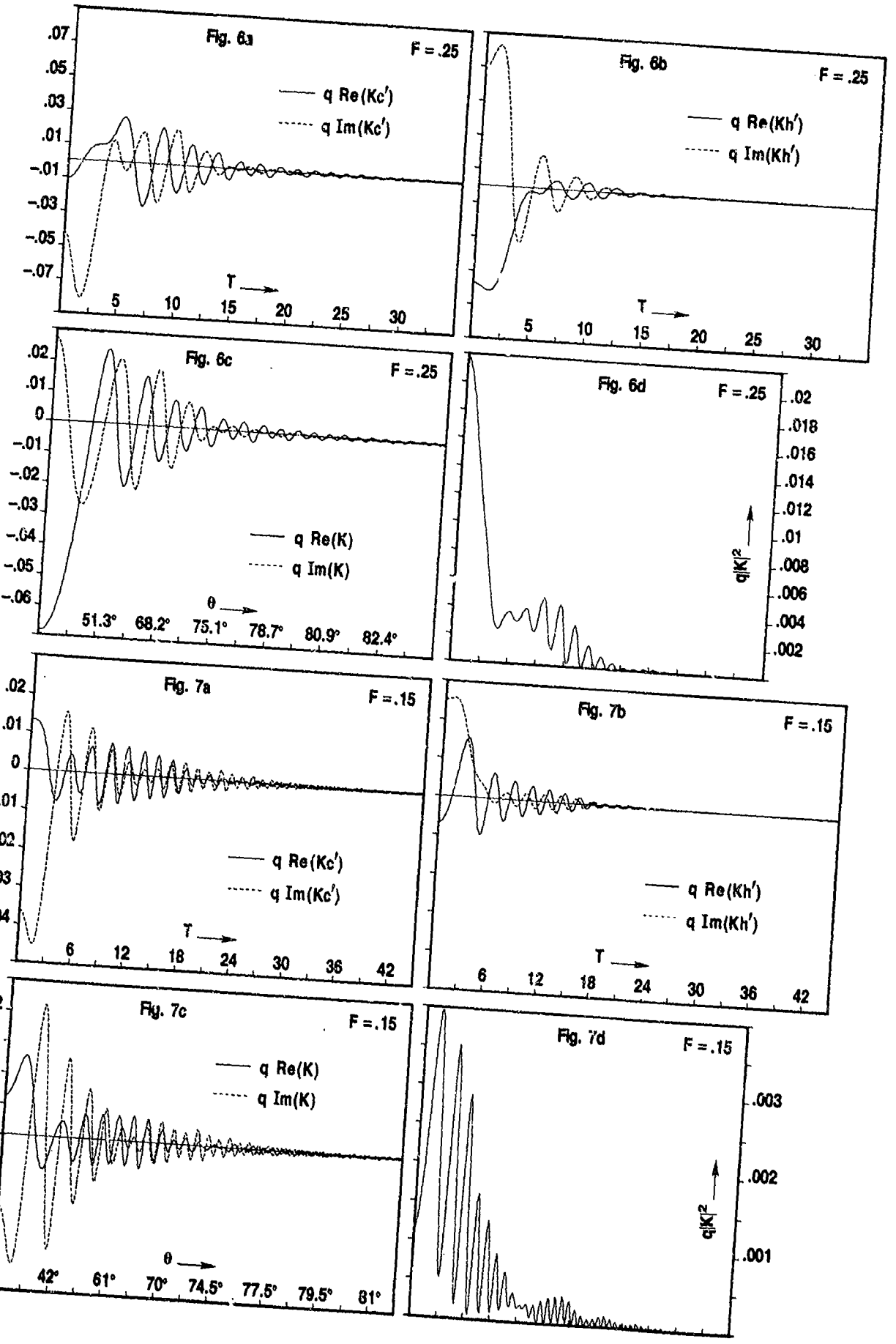
Fig. 6a
F = .25
q Re(Kc′)
q Im(Kc′)
.07
.05
.03
.01
-.01
-.03
-.05
-.07
T
5 10 15 20 25 30
Fig. 6b
F = .25
q Re(Kh′)
q Im(Kh′)
T
5 10 15 20 25 30
Fig. 6c
F = .25
q Re(K)
q Im(K)
.02
.01
0
-.01
-.02
-.03
-.04
-.05
-.06
θ
51.3° 68.2° 75.1° 78.7° 80.9° 82.4°
Fig. 6d
F = .25
q|K|²
.02
.018
.016
.014
.012
.01
.008
.006
.004
.002
Fig. 7a
F = .15
q Re(Kc′)
q Im(Kc′)
.02
.01
0
-.01
-.02
-.03
-.04
T
6 12 18 24 30 36 42
Fig. 7b
F = .15
q Re(Kh′)
q Im(Kh′)
T
6 12 18 24 30 36 42
Fig. 7c
F = .15
q Re(K)
q Im(K)
.02
.01
0
-.01
-.02
θ
42° 61° 70° 74.5° 77.5° 79.5° 81°
Fig. 7d
F = .15
q|K|²
.003
.002
.001

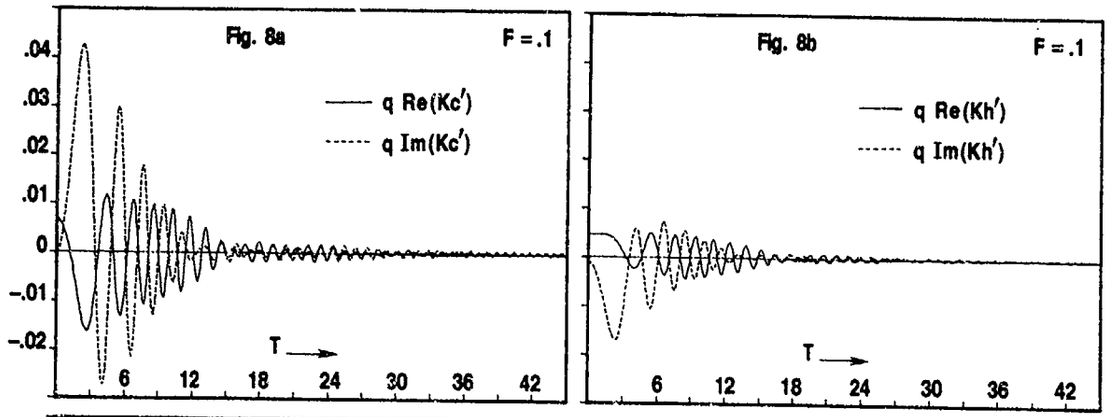
Fig. 8a
F = .1
q Re(Kc′)
q Im(Kc′)
.04
.03
.02
.01
0
-.01
-.02
T
6 12 18 24 30 36 42

Fig. 8b
F = .1
q Re(Kh′)
q Im(Kh′)
T
6 12 18 24 30 36 42

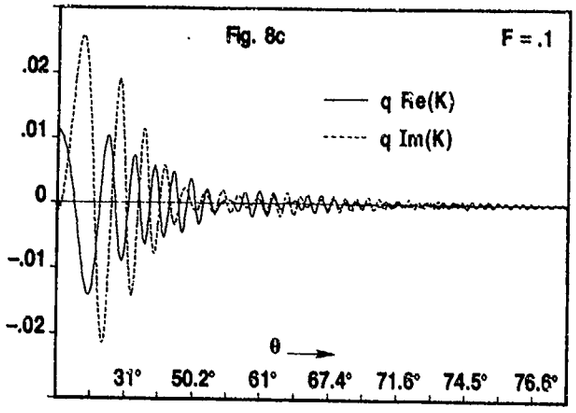
Fig. 8c
F = .1
q Re(K)
q Im(K)
.02
.01
0
-.01
-.02
θ
31° 50.2° 61° 67.4° 71.6° 74.5° 76.6°

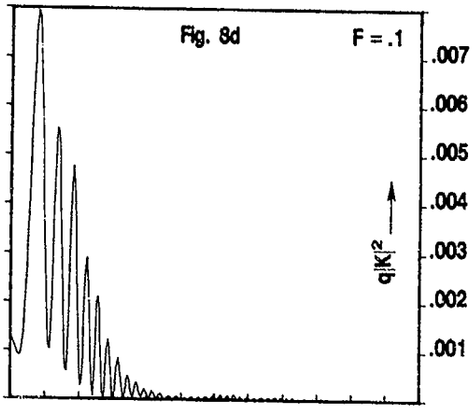
Fig. 8d
F = .1
q|K|²
.007
.006
.005
.004
.003
.002
.001

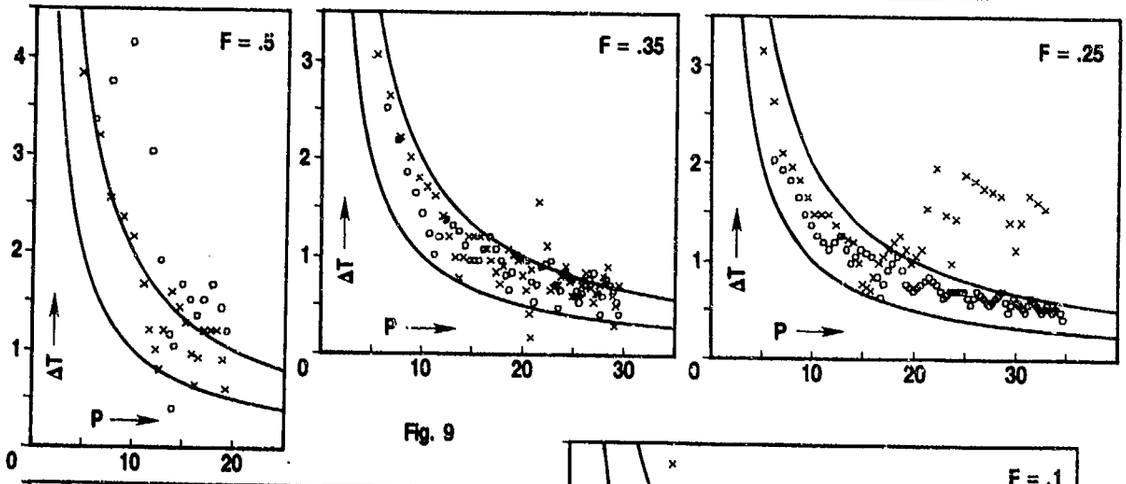
F = .5
F = .35
F = .25
ΔT
P
0 10 20 30

Fig. 9

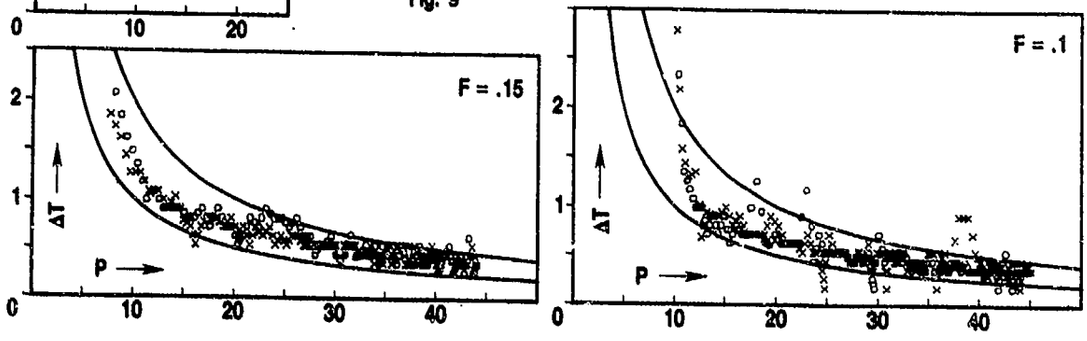
F = .15
F = .1
ΔT
P
0 10 20 30 40

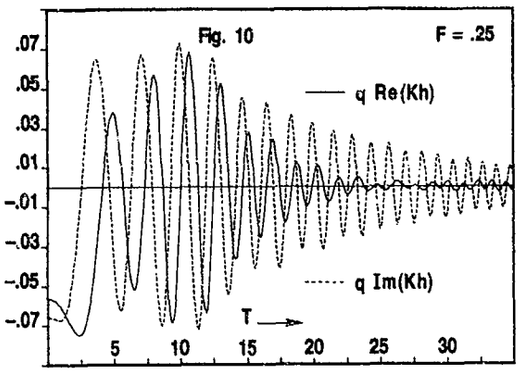

Figure 10. The Hull-surface Integral $qK_h(t)$

shows striking differences compared with both figures 6b and 6c. In particular, figures 6b,c show that the functions $qK_h'(t)$ and $qK(t)$ are negligibly small for t greater than about 17.5 and 35, respectively, whereas figure 10 indicates that the function $qK_h(t)$ decreases very slowly as t increases. As a matter of fact, numerical evaluation of the function $qK_h(t)$ for $35 \leqslant t \leqslant 60$ shows that it may not be regarded as negligibly small for t smaller than 60. The magnitude of the function qK_h is also appreciably larger than that of the function qK. The modified-hull integral qK_h' differs from the whole-hull integral qK_h in that the contribution of the upper portion of the hull to the hull integral qK_h is combined with the waterline integral in equation (27). The difference $qK - qK_h$ between the function qK and the hull integral qK_h depicted in figures 6c and 10, respectively, corresponds to the waterline integral in equation (27). Comparisons of figure 10 with figures 6b and 6c therefore illustrate the importance of the upper portion of the hull in the hull integral and of the waterline integral, respectively, in equation (27). Comparison of figures 10 and 6c also illustrates the advantage of the analytical treatment of the upper-hull-surface integral and of the waterline integral in equation (27), prior to numerical integration, performed in this study.

6. Influence of Size of Panels

The numerical results presented in figures 4a-d through 8a-d have been obtained by dividing the hull form defined previously in terms of separate parametric equations for the bow region $0 \leqslant \lambda \leqslant 0.25$, the midship region $0.25 \leqslant \lambda \leqslant 0.75$ and the stern region $0.75 \leqslant \lambda \leqslant 1$ into quadrilateral panels. These quadrilateral elements are defined by dividing the parametric space $0 \leqslant \lambda \leqslant 1$ and $0 \leqslant \mu \leqslant 1$ into constant-λ and constant-μ lines. More precisely, the segment $0 \leqslant \mu \leqslant 1$ is divided into Nyz equal subsegments, and each of the three segments $0 \leqslant \lambda \leqslant 0.25$, $0.25 \leqslant \lambda \leqslant 0.75$, $0.75 \leqslant \lambda \leqslant 1$ is divided into Nx/3 equal subsegments. The hull form is then divided into Nx·Nyz quadrilateral panels. The panel numbers Nx and Nyz were taken as Nx = 250 and Nyz = 40 for the calculations reported in figures 4a-d through 8a-d.

A numerical study of the influence of the panel numbers Nx and Nyz upon the precision of the numerical results is now presented. Figures 11a and 11b show the percentage relative error ε in the predicted values of the wave resistance, defined by the Havelock integral (30), corresponding to several values of Nx and Nyz. More precisely, figure 11a depicts the variation of ε as a function of Nyz for a fixed, large value of Nx taken equal to 250. Calculations have been performed for 7 values of Nyz equal to 8, 10, 12, 16, 24, 32 and 40. The relative error ε is computed on the basis of the wave-resistance value corresponding to Nyz = 40. Figure 11b, on the other hand, depicts the variation of ε as a function of Nx for a fixed, large value of Nyz taken equal to 40. Calculations have been performed for 9 values of Nx equal to 40, 60, 80, 100, 120, 150, 200, 250 and 300. The relative error ε is computed on the basis of the wave-resistance value corresponding to Nx = 300. Both figures 11a and 11b present results for F = 0.5, 0.35, 0.25, 0.15 and 0.1.

Figure 11a indicates that comparable relative errors ε are obtained for F = 0.35 and 0.5, on the one hand, and for F = 0.15 and 0.1, on the other hand, if a given value of Nyz is used. Furthermore, the relative error for F = 0.25 is smaller than that for F = 0.35 and 0.5, which is smaller than that for F = 0.15 and 0.1. For instance, figure 11a shows that we have $\varepsilon \simeq 0.4\%$ for F = 0.25, $\varepsilon \simeq 0.8\%$ for F = 0.35 and 0.5, and $\varepsilon \simeq 1.4\%$ for F = 0.15 and 0.1 if Nyz is taken equal to 24. Conversely, if a given relative error is desired, say $\varepsilon = 0.8\%$, figure 11a shows that Nyz must be taken equal to 18 for F = 0.25, 24 for F = 0.35 and 0.5, and 30 for F = 0.15 and 0.1. A smaller value of Nyz would probably be sufficient for F = 0.15 and 0.1 if a nonuniform subdivision of the segment $0 \leqslant \mu \leqslant 1$ is used, with smaller panels in the vicinity of the waterline since the lower part of the hull has a relatively small contribution to the wave-amplitude function at small Froude numbers. The reason for the fact that the relative error ε corresponding to a given value of Nyz is larger for F = 0.35 and 0.5 than for F = 0.25 may possibly be related to the previously-noted partial cancellation between the waterline integral and the hull integral, which is most pronounced at high Froude numbers. Figure 11a indicates that it should be sufficient to take Nyz equal to about 25, with a concentration of smaller panels close to the waterline.

Figure 11b indicates that the value of Nx which must be used if a given relative error is desired increases as the Froude number decreases. For instance, figure 11b shows that Nx must be taken approximately equal to 30 for F = 0.5, 48 for F = 0.35, 74 for F = 0.25, 85 for F = 0.15 and 170 for F = 0.1 if a relative error ε equal to 0.8% is desired. Figure 11b indicates that, for a given value of Nx, the relative error for F = 0.1 is appreciably larger than for F = 0.15, 0.25, 0.35 and 0.5. The relative error also appears to decrease less rapidly, as the value of Nx increases, for F = 0.5 than for the other values of F. The simple relation Nx = 17/F yields Nx = 34, 49, 68, 114 and 170 for F = 0.5, 0.35, 0.25, 0.15 and 0.1, respectively.

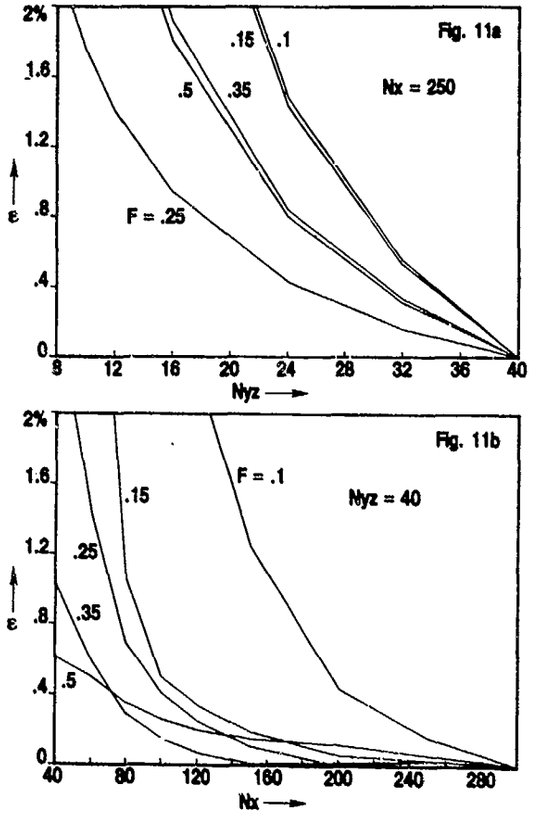

Figures 11a,b. Influence of Panel Numbers Nx and Nyz Upon Accuracy of Wave-resistance Calculation

Figure 11b indicates that this simple formula for Nx provides a reasonable guideline.

7. Conclusions

A method for numerically evaluating the near- and far-field wave potentials and the wave resistance of an arbitrary ship form advancing at constant speed in calm water has been presented. The method is based on the integral representations (24), (28) and (30), which express the near- and far-field wave potentials and the wave resistance, respectively, in terms of the near- and far-field wave-amplitude functions $K(t;\bar{\xi})$ and $K(t)$, respectively.

The closely-related near- and far-field wave-amplitude functions are defined by integrals over the mean wetted-hull surface, the mean waterline, and the mean free surface in the vicinity of the ship where free-surface nonlinearities may be important, as is indicated in equation (27). The hull-surface integral in this equation is split into two parts corresponding to the contributions of the upper and lower portions of the hull. The depthwise integration in the integral over the upper portion of the mean wetted hull is performed analytically by using linear approximations for the depthwise variations of the hull form and of the velocity potential. The upper-hull integral thus is reduced to an integral around the mean waterline, which is combined with the waterline integral in expression (27).

This combination of the contributions of the waterline and of the upper-hull surface shows that several terms in the hull and waterline integrals partially cancel out one another, and yields a modified waterline integral suited for accurate numerical evaluation. The analytical treatment of the contribution of the upper hull form presented in section 3 and the numerical results presented in section 5 demonstrate the paramount importance of the waterline integral in equation (27). In particular, the role of the waterline integral is well illustrated in figures 6b,c and 10. These figures also illustrate the advantage of the method for evaluating the wave-amplitude functions presented in this study.

The wave-amplitude functions thus are expressed as the sums of the modified waterline integrals K^u corresponding to the contribution of the upper portion of the hull, including the waterline, the lower-hull integrals K^ℓ corresponding to the contribution of the lower portion of the hull, and the free-surface integrals K^f accounting for free-surface nonlinearities, as is indicated in equation (31). A simple method for numerically evaluating the integrals (79) and (32) defining the functions K^u and K^ℓ, respectively, is presented in section 4. The numerical method is based upon approximating the hull form by an ensemble of quadrilateral panels composed of four plane triangles, together with linear approximation for the variation of the velocity potential within each component triangle. The expressions for the functions K^u and K^ℓ corresponding to these numerical approximations are given by equations (94) and (120), respectively.

Two main conclusions may be drawn from the numerical results presented in section 5. One conclusion is that it is useful to express the function qK^u+qK^ℓ in the form $qK'_c+qK'_h$, where qK'_c and qK'_h are the modified waterline and hull integrals defined by equations (128a,b) and (129a,b) for the far-field wave-amplitude function (and closely-related expressions for the near-field wave-amplitude function). The wave-amplitude functions thus are expressed as the sum of the modified waterline integrals K'_c, the modified hull integrals K'_h, and the free-surface integrals K^f. The major recommendation of this decomposition is that the modified hull integral qK'_h vanishes appreciably faster than the modified waterline integral qK'_c as t increases (the shortest waves in the wave spectrum are contained in the function qK'_c). A significant reduction in computing time may then be achieved since the computing time required for evaluating the hull integral qK'_h, for a given hull form and for given values of F and t, is considerably larger than that required for evaluating the waterline integral qK'_c.

Another conclusion which may be drawn from the numerical results presented in section 5 is that the pseudo period, Δt, of the oscillations of the wave-amplitude function $qK(t)$ may be safely estimated by the simple

approximation $C/(\nu^2+t^2)^{1/2}$, where $\nu = 1/F$ and C is a constant between 10 and 20. The wave-amplitude function qK(t) may then be evaluated numerically for the values, t_i say, of t defined by the recurrence relation $t_{i+1} = t_i + c/(\nu^2+t_i^2)^{1/2}$, with $i \geq 0$ and $t_0 = 0$. In this relation, c is the constant given by $c = C/N$ where N is the number of points per pseudo period at which it is desired to evaluate the function qK(t). In practice, N may be taken between 3 and 5, so that the constant c in the recurrence relation may be chosen between 2 and 7.

The influence of the size of the panels used for approximating the hull surface upon the precision of the numerical results was studied numerically in section 6. This numerical study shows that a fairly large number of panels must be used for very small Froude numbers. Furthermore, the numerical study presented in section 5 shows that the pseudo period of the oscillations of the wave-amplitude functions decreases with F, and that the largest value of t for which the amplitude functions must be evaluated (i.e. the smallest value of t for which these functions are negligibly small) increases as F decreases. All of these three factors result in an increase of computing time at small Froude numbers. The numerical method presented in section 4 for evaluating the waterline, hull-surface and free-surface integrals (79), (32) and (33) therefore becomes less practical at very small Froude numbers. A complementary analytical method, based on asymptotic evaluation of the foregoing integrals by using the methods of stationary phase and of steepest descent, for large values of $\nu = 1/F$, or more generally of $p^2 \equiv \nu^2+t^2$, would then be useful. This complementary analytical method will be presented elsewhere.

Acknowledgments

This study was supported by the Independent Research program and the General Hydrodynamics Research program at the David Taylor Naval Ship Research and Development Center.

References

1. F. Noblesse, "A Slender-ship Theory of Wave Resistance", J. Ship Research, Vol. 27 (1983) pp. 13-33.

2. F. Noblesse, "Alternative Integral Representations for the Green Function of the Theory of Ship Wave Resistance", J. Eng. Math., Vol. 15 (1981) pp. 241-265.

3. C.Y. Chen and F. Noblesse, "Comparison Between Theoretical Predictions of Wave Resistance and Experimental Data for the Wigley Hull", J. Ship Research, Vol. 27 (1983) pp. 215-226

4. C.Y. Chen and F. Noblesse, "Preliminary Numerical Study of a New Slender-ship Theory of Wave Resistance", J. Ship Research, Vol. 27 (1983) pp. 172-186.

5. F. Noblesse, "Numerical Study of a Slender-ship Theory of Wave Resistance", J. Ship Research, Vol. 29 (1985)

6. F. Noblesse, "Convergence of a Sequence of Slender-ship Low-Froude-Number Wave-Resistance Approximations", J. Ship Research, Vol. 28 (1984) pp. 155-162.

7. T.H. Havelock, "Wave Patterns and Wave Resistance", Trans. Inst. Naval Arch., Vol. 76 (1934) pp. 430-442.

8. W.T. Tsai, Y.J. Lin, and C.C. Liao, "Numerical Solution of the Neumann-Kelvin Problem and its Application to Ship Wave-Resistance Calculations", Proc. Second DTNSRDC Workshop on Ship Wave-Resistance Computations (1983) pp. 233-280.

DISCUSSION
of the paper
by F. Noblesse and A. Barnell

"NUMERICAL EVALUATION OF THE NEAR-AND-FAR-FIELD WAVE PATTERN AND WAVE RESISTANCE OF ARBITRARY SHIP FORMS"

DISCUSSION
by J. Baar

Dr. Noblesse and Mr. Barnell presented yet another in a long series of fine papers devoted to the steady ship wave problem. In particular, the careful step-by-step numerical analysis must be appreciated at its full value. Obtaining accurate solutions to the Neumann-Kelvin problem is one of of the most difficult tasks in numerical ship hydrodynamics (Reference 3 of the paper contains some revealing statistics in this respect).

Recently I obtained an encouraging confirmation of the "slender body" wave resistance theory of Noblesse (see Reference 1). Computations for the Wigley hull showed a very close agreement between Noblesse's "first order" wave resistance and predictions obtained by means of numerically "exact" source distributions. Small deviations occurred only at fairly high Froude numbers. Results of my investigation will soon be published.

Regarding the effect of the nonoscillatory nearfield disturbance, Noblesse has shown in Ref. 5 of his paper that a simple and crude approximation to this disturbance might surface. My experience seems to support this observation. The algebraic approximation proposed by Dr. Noblesse is based on a combination of the first terms in the ascending and asymptotic series expansions of the near-field disturbance. In an unpublished note* I derived the second term in the asymptotic series of the near-field disturbance. It can be expected that this result will yield a better approximation. Eventually such an approximation might remove all together what has been hitherto one of the major numerical difficulties occurring in the solution of the Neumann-Kelvin problem.

Author's Reply

We wish to thank Mr. Baar for his interesting and valuable discussion. Mr. Baar's discussion is especially appreciated because it addresses two important aspects of the numerical solution of the Neumann-Kelvin problem that are not examined in our paper, namely the convergence of the slender-ship iterative solution procedure and the calculaton of the nonoscillatroy nearfield potential ϕ_N.

The relatively-small differences between the wave-resistance values obtained by Mr. Baar for the Wigley hull form on the basis of the first-order slender-ship approximation ψ and of the numerically-exact potential ϕ in equation 1 are certainly encouraging.

The second term in the far-field asymptotic expansion of the nonoscillatory near-field term N in equation 6, which Mr. Baar has obtained, indeed ought to be useful, when combined with the known three terms in the near-field ascending series, for obtaining a fairly-simple composite approximation for N.

*"Mathematical analysis of the Kelvin Wave Source Potential", Brunel University, Uxbridge, 1985.

PROGRESS IN THE CALCULATION OF NON-LINEAR FREE-SURFACE POTENTIAL FLOWS IN THREE DIMENSIONS*

Lawrence K. Forbes,
Department of Mathematics,
University of Queensland,
St. Lucia, Queensland 4067,
AUSTRALIA.

Abstract

An efficient numerical method is presented for computing non-linear, three-dimensional potential flow about a pressure distribution moving over the free surface of a fluid. Some sample calculations are presented, and compared with the predictions of linearized theory. It is found that linearized and non-linear results are in reasonable agreement over the entire range of parameters for which solutions could be obtained. However, a maximum downstream wave height appears to exist in the non-linear case, presumably associated with the onset of wave breaking.

1. Introduction

This paper is concerned with the computation of fully non-linear, three-dimensional, potential flow due to a distribution of pressure moving with uniform velocity over the free surface of a fluid. In some approximation, the problem might represent flow due to a ship, although due to the absence of a contour of intersection between the free surface and a hull, the problem more properly corresponds to flow caused by an air-cushion vehicle. The problem has been chosen for its relative simplicity and to illustrate a numerical method which we believe will be of use in more complicated ship-hydrodynamical problems.

The linearized solution for flow due to an arbitrary distribution of pressure is well known, and may be found, for example in the article by Wehausen and Laitone [1]. Newman and Poole [2] considered the case of a distribution moving in a canal of finite width, and Tatinclaux [3] has catalogued linearized wave-resistance profiles for a variety of pressure distributions. Tatinclaux did not attempt the numerical evaluation of the free-surface profile, however, and in general this is a task comparable to the numerical solution of the full non-linear problem in difficulty and computer time requirements. For the rectangular Gaussian distribution considered in this study, a method is presented for the evaluation of the linearized surface elevation, and serves as a check on the non-linear results.

In recent years, several two-dimensional non-linear problems in free-surface hydrodynamics have yielded to numerical solution, and these studies are used to guide the investigation of the three-dimensional problem considered here. For example, von Kerczek and Salvesen [4] used a finite difference technique to solve for flow in a stream of finite depth due to a moving pressure distribution, and Schwartz [5] has considered the same problem in infinitely deep water. Both studies indicate that the two-dimensional wave resistance of the pressure distribution may become zero under certain circumstances, even when the assumptions of linear theory are no longer valid. Unlike von Kerczek and Salvesen [4], however, Schwartz [5] used a boundary integral method to solve his problem; such methods have the obvious advantage of reducing by one the number of dimensions involved in the formal statement of the problem, and of satisfying automatically the boundary condition at infinite depth within the fluid. In addition Schwartz used an inverse-plane formulation in which the velocity potential and streamfunction are taken as independent variables. Inverse-plane methods combined with boundary-integral techniques have also been used by Forbes and Schwartz [6] to solve for flow about a semi-circular obstacle placed on the bottom of a running stream, and by Vanden Broeck and Tuck [7] to investigate flow in the neighbourhood of the bow or stern of a two-dimensional, rectangular "ship". This latter paper indicates the complexity of flow caused by a body which is surface-piercing.

Inverse plane methods, first introduced by Stokes [8], afford a considerable simplification for problems involving a simply-connected fluid domain, since the unknown free-surface location is mapped simply to a straight line in the inverse plane, along which the streamfunction is constant. However, problems may also be formulated directly in the plane of the physical variables, with no loss of numerical efficiency when boundary-integral methods

* This research was initially supported by the ONR Special Focus Research Programme at the University of Iowa, number N00014-83-K-0136.

are used. Such an approach was adopted by Hess [9], although the solution to his integral equation was apparently sought by an iterative process which cannot converge, since the integral operator possesses a continuous spectrum, as has been shown by Forbes [10]. Successful iterative schemes for two-dimensional problems formulated in the physical plane may be found, for example, in articles by Forbes [11, 12].

For three-dimensional potential flows, Street [13] has shown that inverse methods preclude the use of boundary-integral techniques, so that of necessity, a physical-plane formulation is required. Such methods have, of course, been in existence for some time for problems not involving a free surface; of these, perhaps the best known is due to Hess and Smith [14, 15], although their method has, in fact, been improved somewhat by Landweber and Macagno [16].

Our aim in this paper is to demonstrate that numerical solutions of acceptable accuracy to the problem of three-dimensional non-linear flow caused by a moving pressure distribution may be generated by a new numerical method which is as efficient in three dimensions as Forbes' [11, 12] two-dimensional algorithms, and has the same potential for accuracy as the method of Landweber and Macagno [16]. Details of the problem formulation are given in section 2, and the numerical method itself appears in section 4. The linearized solution is described in section 3, and a presentation of the results of computation is given in section 5. Some possible extensions and improvements to the method are indicated in section 6.

2. Formulation

Consider a pressure distribution which is stationary with respect to a moving cartesian coordinate system in which the z-axis points vertically, as in Figure 1. The pressure distribution is assumed to be of the form $P_o P(x,y)$, where P_o is a constant which represents the maximum strength of the distribution and has the dimensions of pressure. The distribution is assumed to be symmetric about the plane $y=0$, so that $P(x,-y) = P(x,y)$, and to have some characteristic length $2L$ and width $2B$. Relative to the coordinate system, the fluid flows in the direction of the positive x-axis such that its speed infinitely far upstream is c . The downward acceleration of gravity, g , acts upon the fluid, which is assumed to be inviscid and incompressible, and to flow without rotation.

Dimensionless variables are defined forthwith, by choosing c as a reference velocity and L as a reference length. Since the flow is irrotational, it may be described by a velocity potential ϕ , which is made dimensionless by reference to the product cL . A particular flow is thus characterised by the length-based Froude number

$$F = \frac{c}{(gL)^{\frac{1}{2}}} ,$$

the dimensionless half-width

$$\beta = \frac{B}{L}$$

and dimensionless strength

$$\alpha = \frac{P_o}{\rho g L}$$

of the pressure distribution. Here, ρ denotes the fluid density. In these dimensionless coordinates, the pressure distribution now has characteristic length 2 and width 2β , as shown in Figure 1.

In the interior of the fluid, the velocity potential ϕ satisfies Laplace's equation

$$\nabla^2 \phi = 0 , \qquad (2.1)$$

since the fluid is assumed ideal. In addition,

$$\phi_x \to 1, \quad \phi_y \to 0, \quad \phi_z \to 0 \quad \text{as} \quad z \to -\infty . \qquad (2.2)$$

If the unknown free-surface elevation is described by the equation $z = \zeta(x,y)$, then the usual kinematic free-surface condition and Bernoulli equation may be written

$$\phi_x \zeta_x + \phi_y \zeta_y = \phi_z \quad \text{on} \quad z = \zeta \qquad (2.3)$$

and

$$\tfrac{1}{2}F^2(\phi_x^2+\phi_y^2+\phi_z^2) + \zeta + \alpha P = \tfrac{1}{2}F^2 \quad \text{on} \quad z = \zeta \qquad (2.4)$$

respectively. The radiation condition, that no waves be present upstream of the pressure distribution, leads at least to the requirement

$$\phi_x \to 1, \quad \phi_y \to 0, \quad \phi_z \to 0, \quad \zeta \to 0 \quad \text{as} \quad x \to -\infty, \qquad (2.5)$$

although these equations are not of themselves sufficient to prevent the appearance of upstream waves, and a stronger statement regarding the rates at which the above limiting values are approached might normally need to be made.

It remains to choose a suitable form for the pressure distribution function $P(x,y)$. An obvious choice is the piecewise constant function

$$P(x,y) = \begin{cases} 1, & \text{if } |x| \le 1 \text{ and } |y| \le \beta \\ 0, & \text{otherwise.} \end{cases}$$

This choice has been examined in detail by Tatinclaux [3], who showed that the wave resistance as a function of Froude number F exhibits wild oscillations as $F \to 0$. Our own numerical results confirm this behaviour, and also suggest that the expression for the linearized free-surface elevation does not give a bounded result everywhere. Accordingly, this case will not be considered further here.

For definiteness, we shall consider the

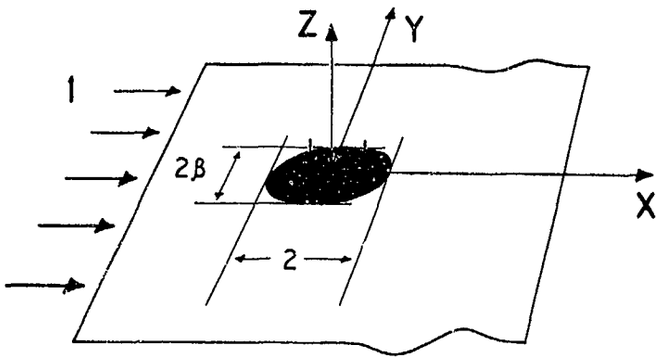

FIGURE 1: The non-dimensionalized flow configuration and coordinate system.

simple "rectangular Gaussian" pressure distribution

$$P(x,y) = e^{-x^2-y^2/\beta^2}, \qquad (2.6)$$

although the numerical technique developed here clearly has much wider applicability. The choice (2.6) leads to well-behaved expressions for the linearized solution, although the wave resistance plot lacks the customary maxima and minima at low Froude number, as will be seen presently.

An integrodifferential equation for the velocity potential at the free surface is derived by applying Green's third formula to the function $\phi-x$ in the volume V shown in Figure 2. By equations (2.1), (2.2) and (2.5), this function is harmonic and vanishes at infinity. Suppose $Q(x,y,z)$ is a fixed point on the free surface of the fluid and $P(\rho,\sigma,\tau)$ is a moveable point on any of the surfaces S_T, S_ε or S_∞ bounding volume V. The use of Green's third formula is equivalent to distributing simple (Rankine) sources over the entire free surface, since the Green function $1/R_{PQ}$ is assumed, and this is just the potential due to a point source located at P and observed from point Q. Here

$$R_{PQ} = [(\rho-x)^2+(\sigma-y)^2+(\tau-z)^2]^{\frac{1}{2}}$$

is the distance from P to Q, measured from point Q. Since the function $1/R_{PQ}$ is singular at Q, this point is excluded from the volume V by the small hemispherical surface S_ε placed about point Q. The surface S_T is the entire free surface $z=\zeta(x,y)$ punctured by a small circle of radius ε centred at Q, and S_∞ is a hemispherical surface of large radius centred at the origin. When $\varepsilon \to 0$ and surface S_∞ expands to infinity, there results Green's third formula

$$2\pi(\phi-x)_Q = \iint_{S_T}\left[(\phi-x)_P \frac{\partial}{\partial n_P}\left(\frac{1}{R_{PQ}}\right) - \frac{1}{R_{PQ}}\frac{\partial}{\partial n_P}(\phi-x)_P\right]dS_P , \qquad (2.7)$$

in which n_P denotes the normal to surface S_T at point P pointing into the fluid.

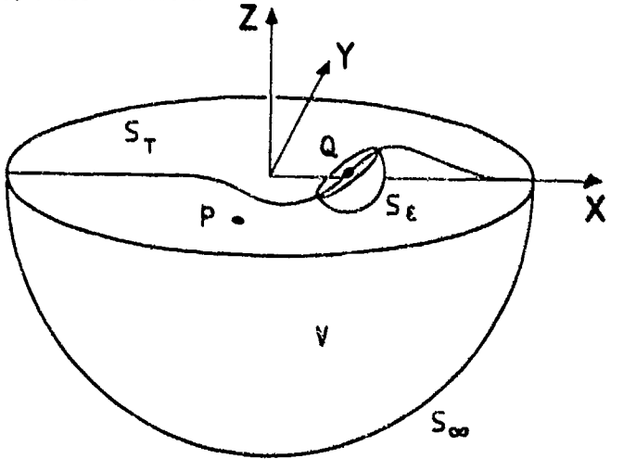

FIGURE 2: The domain of definition of the integrodifferential equation.

Surface S_T is now the entire free surface of the fluid with a circle of vanishingly small radius about Q excluded.

In anticipation of the forthcoming numerical work, the singularity is removed from the first term on the right hand side of equation (2.7), by writing the equation in the form

$$
\begin{aligned}
&2\pi(\phi-x)_Q \\
&= \iint_{S_T} \{(\phi-x)_P-(\phi-x)_Q\}\frac{\partial}{\partial n_P}\left(\frac{1}{R_{PQ}}\right) dS_P \\
&- \iint_{S_T} \frac{1}{R_{PQ}} \frac{\partial}{\partial n_P} (\phi-x)_P dS_P \\
&+ (\phi-x)_Q \iint_{S_T} \frac{\partial}{\partial n_P}\left(\frac{1}{R_{PQ}}\right) dS_P \quad . \qquad (2.8)
\end{aligned}
$$

A Taylor-series expansion of the first integrand when $P \to Q$, as described by Miloh and Landweber [17], confirms that it is indeed non-singular.

Following Landweber and Macagno [16], the last term in equation (2.8) may be evaluated in closed form, using the Gauss flux theorem

$$
\iint_S \frac{\partial}{\partial n_P}\left(\frac{1}{R_{PQ}}\right) dS_P = 0 \quad , \qquad (2.9)
$$

in which $S \equiv S_T + S_\varepsilon + S_\infty$ is the closed surface to volume V shown in Figure 2. The contribution from the surface S_ε in the limit $\varepsilon \to 0$ is easily seen to be -2π; similarly, because the free surface is asymptotically flat at infinity, the surface S_∞ is an exact hemisphere, and its contribution is thus 2π. These two contributions cancel, so that the remaining integral over the surface S_T is zero, by equation (2.9). The last term in equation (2.8) therefore vanishes exactly.

Because the first term on the right hand side of equation (2.8) is non-singular, the surface S_T may be replaced by the full free surface $z = \zeta(x,y)$. The second term has a weak, but integrable, singularity and the surface S_T may likewise be replaced by $z = \zeta$ in this term also. Using the definition

$$
n = \frac{\zeta_x i + \zeta_y j - k}{(1+\zeta_x^2+\zeta_y^2)^{\frac{1}{2}}} \qquad (2.10)
$$

of the inward-facing normal vector to the surface $z = \zeta(x,y)$, and the formula

$$
dS = \frac{dx\,dy}{|k.n|} \qquad (2.11)
$$

for the elemental area dS, equation (2.8) is written in the form

$$
\begin{aligned}
2\pi(\phi(Q)-x) &= \int_{-\infty}^{\infty}\int_{-\infty}^{\infty} \{\phi(P)-\phi(Q)-\rho+x\} \\
&\cdot \frac{\zeta(P)-\zeta(Q)-(\rho-x)\zeta_\rho(P)-(\sigma-y)\zeta_\sigma(P)}{[(\rho-x)^2+(\sigma-y)^2+(\zeta(P)-\zeta(Q))^2]^{3/2}} \, d\rho d\sigma \\
&+ \int_{-\infty}^{\infty}\int_{-\infty}^{\infty} \frac{\zeta_\rho(P)}{[(\rho-x)^2+(\sigma-y)^2+(\zeta(P)-\zeta(Q))^2]^{\frac{1}{2}}} \, d\rho d\sigma \qquad (2.12)
\end{aligned}
$$

The kinematic condition (2.3) has been used in the derivation of the last term in this expression. In view of the assumed symmetry of the pressure distribution function $P(x,y)$, the symmetry conditions

$$
\begin{aligned}
\zeta(x,-y) &= \zeta(x,y) \\
\zeta_x(x,-y) &= \zeta_x(x,y) \\
\zeta_y(x,-y) &= -\zeta_y(x,y) \\
\phi(x,-y,z) &= \phi(x,y,z)
\end{aligned} \qquad (2.13)
$$

apply, and are incorporated into equation (2.12). Consequently it is only necessary to consider the half-space $y \geq 0$.

The solution to this problem thus consists of determining the surface elevation $z = \zeta(x,y)$ and the velocity potential $\phi(x,y,\zeta(x,y))$ there, by solving the integro-differential equation (2.12) combined with the surface conditions (2.3) and (2.4), and subject to a radiation condition of the type (2.5). Values of ϕ at interior points of the fluid may then be generated using Green's third formula.

The vector force F on the pressure distribution may also be computed from the above solution according to the formula

$$
F = -\iint_S P(x,y) n \, dS \, ,
$$

which, in view of equations (2.10) and (2.11), yields the wave resistance

$$
D = -\int_{-\infty}^{\infty}\int_{-\infty}^{\infty} P(x,y)\,\zeta_x(x,y)\,dxdy \qquad (2.14)
$$

and the weight

$$
W = \int_{-\infty}^{\infty}\int_{-\infty}^{\infty} P(x,y)dxdy \qquad (2.15)
$$

of the distribution. For the pressure distribution function (2.6), equation (2.15) yields the weight

$$
W = w_{38} \, .
$$

3. The Linearized Solution

If the pressure distribution acting on the surface is weak, then α is small and linearization about uniform flow is possible. The result is well known, and the solution for arbitrary pressure distribution functions $P(x,y)$ is given by Wehausen and Laitone ([1], p.598). The linearized expressions for ϕ and ζ are

$$\phi(x,y,z) = x + \frac{\alpha}{4\pi^2}\iint_{-\infty}^{\infty} P(\xi,\eta)\,d\xi\,d\eta \cdot \int_0^{2\pi}\int_0^{\infty} \frac{ik\cos\theta \exp\{k[z+i(x-\xi)\cos\theta + i(y-\eta)\sin\theta]\}}{kF^2\cos^2\theta - 1}\,dk\,d\theta + O(\alpha^2) \tag{3.1}$$

and

$$\zeta(x,y) = \frac{\alpha}{4\pi^2}\iint_{-\infty}^{\infty} P(\xi,\eta)\,d\xi\,d\eta \cdot \int_0^{2\pi}\int_0^{\infty} \frac{k\,\exp\{ik[(x-\xi)\cos\theta + (y-\eta)\sin\theta]\}}{kF^2\cos^2\theta - 1}\,dk\,d\theta + O(\alpha^2)\,. \tag{3.2}$$

These expressions are formally divergent, due to the presence of a pole singularity in each integrand, and must therefore be interpreted in a manner which leads to a bounded solution free from upstream waves. This procedure is described by Havelock [18] and Wehausen and Laitone ([1], p. 475), and involves deforming the path of integration in the complex k-plane to avoid the pole singularity at $k_0 = (F^2\cos^2\theta)^{-1}$ in a semi-circle of vanishingly small radius centred at k_0.

When the pressure distribution function (2.6) is substituted into equations (3.1) and (3.2), the outer integrals may be evaluated at once. After the singular integrals have been interpreted appropriately, in the manner described above, the solution for ϕ and ζ finally becomes

$$\phi(x,y,z) = x - \frac{\alpha\beta}{\pi}\int_0^{\pi/2} b(\theta)\cos\theta \int_0^{\infty} \frac{e^{-a(\theta)k^2} f(k,\theta)}{k - b(\theta)}\,dk\,d\theta - \alpha\beta\int_0^{\pi/2} b^2(\theta)\cos\theta\, e^{zb(\theta)-a(\theta)b^2(\theta)} \cos(xb(\theta)\cos\theta)\cos(yb(\theta)\sin\theta)\,d\theta + O(\alpha^2) \tag{3.3}$$

and

$$\zeta(x,y) = \frac{\alpha\beta}{\pi}\int_0^{\pi/2} b(\theta)\int_0^{\infty} \frac{e^{-a(\theta)k^2} g(k,\theta)}{k - b(\theta)}\,dk\,d\theta - \alpha\beta\int_0^{\pi/2} b^2(\theta)e^{-a(\theta)b^2(\theta)} \sin(xb(\theta)\cos\theta)\cos(yb(\theta)\sin\theta)\,d\theta + O(\alpha^2)\,, \tag{3.4}$$

where the improper integrals are to be interpreted in the Cauchy principal-valued sense. Here,

$$\begin{aligned} a(\theta) &= \tfrac{1}{2}(\cos^2\theta + \beta^2\sin^2\theta) \\ b(\theta) &= \frac{1}{F^2\cos^2\theta} \\ f(k,\theta) &= ke^{kz}\sin(kx\cos\theta)\cos(ky\sin\theta) \\ g(k,\theta) &= k\cos(kx\cos\theta)\cos(ky\sin\theta)\,. \end{aligned} \tag{3.5}$$

The linearized wave drag is computed from equations (2.14) and (3.4). The final result is

$$D = \pi\alpha^2\beta^2\int_0^{\pi/2} b^3(\theta)\cos\theta\, e^{-2a(\theta)b^2(\theta)}\,d\theta + O(\alpha^3)\,, \tag{3.6}$$

where the functions $a(\theta)$ and $b(\theta)$ are defined in equations (3.5).

4. Numerical Methods

4a. Evaluation of the linearized solution.

This section reviews the numerical method used for the evaluation of the linearized solution given by equations (3.3) and (3.4). Both expressions require the evaluation of a singular integral of the form

$$\int_0^{\infty} \frac{f(k)e^{-ak^2}}{k - b}\,dk\,,$$

in which a is positive, and perhaps also small. This integral may be rendered non-singular by writing the identity

$$\int_0^\infty \frac{f(k)e^{-ak^2}}{k-b}\,dk = \int_0^\infty h(k)e^{-ak^2}\,dk + f(b)\int_0^\infty \frac{e^{-ak^2}}{k-b}\,dk\,, \qquad (4.1a)$$

where

$$h(k) = \frac{f(k) - f(b)}{k-b}\,. \qquad (4.1b)$$

The function $h(k)$ in equation (4.1b) is written as the sum of an even and an odd expression,

$$h(k) = \tfrac{1}{2}[h(k)+h(-k)] + \tfrac{1}{2}[h(k)-h(-k)]\,,$$

so that the first term on the right-hand side of equation (4.1a) becomes

$$\int_0^\infty h(k)e^{-ak^2}dk = \tfrac{1}{2}\int_{-\infty}^{\infty} h(k)e^{-ak^2}dk + \tfrac{1}{2}\int_0^\infty [h(k)-h(-k)]e^{-ak^2}dk\,.$$

A straightforward change of variable on the right-hand side of this equation leads to the result

$$\int_0^\infty h(k)e^{-ak^2}dk = \frac{1}{2\sqrt{a}}\int_{-\infty}^{\infty} e^{-t^2}h\left(\frac{t}{\sqrt{a}}\right)dt + \frac{1}{4\sqrt{a}}\int_0^\infty e^{-t}\left[h\left(\sqrt{\frac{t}{a}}\right) - h\left(-\sqrt{\frac{t}{a}}\right)\right]\frac{dt}{\sqrt{t}}\,. \qquad (4.2)$$

The first integral on the right-hand side of equation (4.2) is evaluated using a 20-point Hermite-polynomial quadrature rule. The integrand of the second term is finite at $t=0$, and consequently, this expression is evaluated by a 15-point Laguerre-polynomial quadrature rule (see Abramowitz and Stegun [19], p. 890).

It remains to evaluate the second integral in equation (4.1a). It is shown in the Appendix that this may be written in terms of non-singular integrals according to the relationship

$$\int_0^\infty \frac{e^{-ak^2}}{k-b}\,dk = (ab^2)^{\frac{1}{2}}\int_{-\infty}^{\infty} e^{-t^2}\frac{1-e^{t^2-ab^2}}{t^2-ab^2}\,dt + \frac{1}{2(ab^2)^{\frac{1}{2}}}\left[\sqrt{\pi} - \int_0^\infty \frac{e^{-t}}{\sqrt{t}+(ab^2)^{\frac{1}{2}}}\,dt\right]\,. \qquad (4.3)$$

The first integral is evaluated by a Hermite-polynomial quadrature rule, and the second by a Laguerre-polynomial rule, as above.

The singular integrals in equations (3.3) and (3.4) may thus be evaluated using equations (4.1) - (4.3). The integrations with respect to θ in equations (3.3), (3.4) and (3.6) are then performed using 96-th order Gaussian quadrature.

4b. Solution of the non-linear problem.

The full system (2.3) - (2.5) and (2.12) of non-linear equations is solved numerically by adapting the methods of Forbes and Schwartz [6] and Forbes [11] to three-dimensional geometries. The free surface $z = \zeta(x,y)$ in the half-space $y\geq 0$ is represented by discrete values $\zeta_{k\ell}$ on a rectangular lattice x_k, $k = 0,1,\ldots,N$, y_ℓ, $\ell = 0,1,\ldots,M$ distributed over some finite subset of the x-y half-plane. The points x_k are separated uniformly by an amount Δx, and the values y_ℓ are likewise uniformly spaced with interval Δy. The quantities x_0 and x_N are chosen to be large negative and large positive numbers, respectively; by the lateral symmetry of the problem $y_0 = 0$, and y_M is chosen to be appropriately large and positive.

The kinematic condition (2.3) and the Bernoulli equation (2.4) are combined to give

$$\tfrac{1}{2}F^2[\phi_x^2+\phi_y^2+(\phi_x\zeta_x+\phi_y\zeta_y)^2] + \zeta + \alpha P = \tfrac{1}{2}F^2 \quad \text{on } z = \zeta\,, \qquad (4.4)$$

where the symbols ϕ_x and ϕ_y denote the functions $\phi_x(x,y,\zeta(x,y))$ and $\phi_y(x,y,\zeta(x,y))$ respectively. By the chain rule of calculus, these functions may be eliminated in favour of derivatives of $\phi(x,y,\zeta(x,y))$ using the results

$$\frac{\partial}{\partial x}\phi(x,y,\zeta(x,y)) = \phi_x(x,y,\zeta(x,y)) + \phi_z(x,y,\zeta(x,y))\zeta_x$$
$$\frac{\partial}{\partial y}\phi(x,y,\zeta(x,y)) = \phi_y(x,y,\zeta(x,y)) + \phi_z(x,y,\zeta(x,y))\zeta_y\,. \qquad (4.5)$$

The functions ϕ_z in equations (4.5) are eliminated using the kinematic condition (2.3) to give

$$\phi_x(x,y,\zeta) = \frac{(1+\zeta_y^2)\frac{\partial}{\partial x}\phi(x,y,\zeta) - \zeta_x\zeta_y\frac{\partial}{\partial y}\phi(x,y,\zeta)}{1+\zeta_x^2+\zeta_y^2}$$

$$\phi_y(x,y,\zeta) = \frac{(1+\zeta_x^2)\frac{\partial}{\partial y}\phi(x,y,\zeta) - \zeta_x\zeta_y\frac{\partial}{\partial x}\phi(x,y,\zeta)}{1+\zeta_x^2+\zeta_y^2} \quad . \tag{4.6}$$

Equations (4.6) are substituted into equation (4.4), which eventually yields the relation

$$\frac{\partial\phi}{\partial x} = \frac{\zeta_x\zeta_y\frac{\partial\phi}{\partial y} + \left[(1+\zeta_x^2+\zeta_y^2)F(x,y)\right]^{\frac{1}{2}}}{1+\zeta_y^2} \tag{4.7}$$

in which

$$F(x,y) = (1+\zeta_y^2)\left[1 - \frac{2(\zeta+\alpha P)}{F^2}\right] - \left(\frac{\partial\phi}{\partial y}\right)^2$$

and $\partial\phi/\partial x$ and $\partial\phi/\partial y$ are the derivatives of the surface function $\phi(x,y,\zeta(x,y))$ on the left-hand side of equations (4.5).

The integrodifferential equation (2.12) is treated numerically by truncating its domain of integration to the rectangle $x_o \le x \le x_N$, $-y_M \le y \le y_M$. Following Forbes and Schwartz [6], equation (2.12) is evaluated at the midpoints $Q(x_{k-\frac{1}{2}}, y_\ell)$, $k = 1,\ldots,N$, $\ell = 0,1,\ldots,M$, since this allows freedom to specify conditions at the line of points (x_o, y_ℓ), $\ell = 0,1,\ldots,M$ in accordance with the radiation condition (2.5). In order to remove the singularity from the last term in equation (2.12), the Taylor-series expansion of the integrand about $P \to Q$ is identically subtracted and added to the integrand. This last term is thus re-written as

$$\int_{-y_M}^{y_M} d\sigma \int_{x_o}^{x_N} d\rho \left\{ \frac{\zeta_\rho(P)}{\left[(\rho-x)^2+(\sigma-y)^2+(\zeta(P)-\zeta(Q))^2\right]^{\frac{1}{2}}} - \frac{\zeta_x(Q)}{\left[(\rho-x)^2A(Q)+(\rho-x)(\sigma-y)B(Q)+(\sigma-y)^2C(Q)\right]^{\frac{1}{2}}} \right\}$$

$$+ J(A(Q),B(Q),C(Q),x,y,x_o,x_N,y_M)\zeta_x(Q) \quad ,$$

where

$$J(A,B,C,x,y,x_o,x_N,y_M) = \int_{x_o-x}^{x_N-x} ds \int_{-y_M-y}^{y_M-y} dt \frac{1}{(As^2+Bst+Ct^2)^{\frac{1}{2}}} \tag{4.8}$$

and

$$A(Q) = 1 + \zeta_x^2(Q)$$

$$B(Q) = 2\zeta_x(Q)\zeta_y(Q)$$

$$C(Q) = 1 + \zeta_y^2(Q) \quad .$$

The integral J in equation (4.8) may be evaluated in closed form, by making use of the indefinite integral

$$\int ds \int dt \frac{1}{\left[As^2+Bst+Ct^2\right]^{\frac{1}{2}}}$$

$$= \frac{t}{\sqrt{A}} \ln\{2As + Bt + 2\left[A(As^2+Bst+Ct^2)\right]^{\frac{1}{2}}\}$$

$$+ \frac{s}{\sqrt{C}} \ln\{2Ct + Bs + 2\left[C(As^2+Bst+Ct^2)\right]^{\frac{1}{2}}\}$$

$$+ h_1(s) + h_2(t) \quad ,$$

where h_1 and h_2 are arbitrary functions of integration.

After the symmetry relations (2.13) have been incorporated into the truncated integrodifferential equation (2.12), and the singularity in the last term removed in the manner described above, the equation takes the form

$$2\pi[\phi(x,y,\zeta(x,y))-x]$$

$$= \int_{x_o}^{x_N} d\rho \int_0^{y_M} d\sigma\{\phi(\rho,\sigma,\zeta(\rho,\sigma))-\phi(x,y,\zeta(x,y))-\rho+x\} \cdot K^{(1)}(\rho,\sigma,x,y)$$

$$+ \int_{x_o}^{x_N} d\rho \int_0^{y_M} d\sigma\{\zeta_\rho(\rho,\sigma)K^{(2)}(\rho,\sigma,x,y) - \zeta_x(x,y)S^{(2)}(\rho,\sigma,x,y)\}$$

$$+ \zeta_x(x,y)J(A,B,C,x,y,x_o,x_N,y_M) \quad . \tag{4.9}$$

in which $K^{(1)}$, $K^{(2)}$ and $S^{(2)}$ are functions

of the points P and Q, and also of ζ and its first derivatives. Equation (4.9) is evaluated at the half-intervals $x_{k-\frac{1}{2}}$, $k = 1,\ldots,N$, and the integrals are approximated by Simpson's rule. Values of the dependent variables at the half-intervals are interpolated onto whole-grid points by a three-point interpolation formula consistent with the parabolae fitted by the Simpson's rule integration.

Equations (4.7) and (4.9) are solved for the functions $\zeta(x,y)$ and $\phi(x,y,\zeta(x,y))$ by Newtonian iteration. Notice that, by expressing the surface conditions in the form (4.7), the need to solve for ζ and ϕ simultaneously by Newton's method is eliminated, resulting in an enormous reduction in computer storage and time requirements. Instead, $\zeta(x,y)$ is obtained at the surface mesh points by Newton's method, and the values of ϕ are then updated at each iteration of Newton's method, using the method of lines and a predictor-corrector approach to integrate equation (4.7).

To begin, an initial guess is made for the unknown vector of length $N(M+1)$ formed from the quantities $(\zeta_x)_{k\ell}$, $k = 1,\ldots,N$, $\ell = 0,1,\ldots,M$. These values are initially set to zero. The radiation condition (2.5) is imposed at $x=x_o$, so as to satisfy equation (4.7) exactly, by specifying

$$\zeta_{o\ell} = (\zeta_x)_{o\ell} = (\zeta_y)_{o\ell} = \left(\frac{\partial\phi}{\partial y}\right)_{o\ell} = 0 ,$$

$$\phi_{o\ell} = x_o ,$$

$$\left(\frac{\partial\phi}{\partial x}\right)_{o\ell} = [1-2\alpha F^{-2} P(x_o,y_\ell)]^{\frac{1}{2}} , \qquad (4.10)$$

$$\ell = 0,\ldots,M .$$

The free-surface elevation ζ is now obtained by trapezoidal rule integration, using equations (4.10) as initial conditions, according to the formula

$$\zeta_{k+1,\ell} = \zeta_{k\ell} + \tfrac{1}{2}\Delta x[(\zeta_x)_{k\ell} + (\zeta_x)_{k+1,\ell}] , \qquad (4.11)$$

$$k = 0,1,\ldots,N-1 , \quad \ell = 0,1,\ldots,M .$$

The values of ζ thus obtained from equation (4.11) are differentiated numerically, using five-point Lagrangian difference formulae, to obtain ζ_y at the surface mesh points.

A predictor-corrector method is next used to compute ϕ at the surface, from the values of ζ and its derivatives calculated above. Initial conditions are supplied by equations (4.10), so that, if ϕ^* denotes the predictor value, the two steps are as follows:

Predictor: $$\phi^*_{k+1,\ell} = \phi_{k\ell} + \Delta x\left(\frac{\partial\phi}{\partial x}\right)_{k\ell} \qquad (4.12)$$

compute $\left(\frac{\partial\phi^*}{\partial y}\right)_{k+1,\ell}$ by five-point differentiation

compute $\left(\frac{\partial\phi^*}{\partial x}\right)_{k+1,\ell}$ from equation (4.7)

Corrector: $$\phi_{k+1,\ell} = \phi_{k\ell} + \tfrac{1}{2}\Delta x\left[\left(\frac{\partial\phi}{\partial x}\right)_{k\ell} + \left(\frac{\partial\phi^*}{\partial x}\right)_{k+1,\ell}\right] \qquad (4.13)$$

compute $\left(\frac{\partial\phi}{\partial y}\right)_{k+1,\ell}$ and $\left(\frac{\partial\phi}{\partial x}\right)_{k+1,\ell}$ as above.

The integrodifferential equation (4.9), discretized and evaluated at the half-intervals $x_{k-\frac{1}{2}}$, $k = 1,\ldots,N$, yields a system of $N(M+1)$ algebraic equations for the unknowns $(\zeta_x)_{k\ell}$, $k = 1,\ldots,N$, $\ell = 0,1,\ldots,M$. This system is solved by Newton's method to obtain an improved estimate for the unknowns. The iteration (4.11)-(4.13) is then repeated until convergence is observed. The scheme converges quadratically, and about five iterations are required to satisfy equation (4.9) with a root-mean-squared residual error less than 10^{-8}.

The wave drag D is computed from equation (2.14) using straightforward Simpson's rule quadrature. As a check, equation (2.14) is also evaluated using double cubic-spline integration, in which the splines are integrated in closed form, and the results of the two methods are in good agreement.

5. Presentation of Results

In Figure 3, the linearized wave drag computed from equation (3.6) is shown as a function of Froude number F, for the dimensionless pressure strength $\alpha=0.01$. Results are displayed for the three different values $\beta=0.1$, 0.2 and 0.3 of the half-width of the pressure distribution. Perhaps surprisingly, the wave resistance fails to exhibit the local maxima and minima normally encountered at low Froude number, but instead approaches zero monotonically as $F\to 0$.

To attempt to reproduce the results of Figure 3 in the non-linear case would place an unreasonable demand on presently-available computing resources. Instead, a comparison of linear and non-linear results can be made more profitably by considering the fixed Froude number $F=0.7$. Results at other Froude numbers are expected to be qualitatively similar. Accordingly, we present in Figure 4 a comparison of the linearized and non-linear wave resistance as functions of pressure strength α, when $F=0.7$ and $\beta=0.2$.

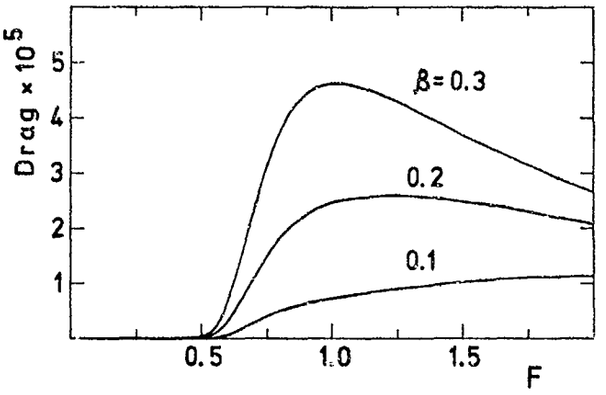

FIGURE 3: Linearized wave drag as a function of Froude number F , for three different values of β , and α=0.01 .

The linearized drag is shown with a solid line in Figure 4, and is a quadratic function of α , as indicated by equation (3.6). For small α , the linearized and non-linear results are in excellent agreement, as expected, but as α is increased, the non-linear values are seen to fall below the predictions of linearized theory. The difference, however, is not great, and for α=0.02 , the non-linear drag is still almost 90% of the linearized value.

The free-surface elevations at the centre-plane y=0 given by the linearized and non-linear solutions are contrasted in Figure 5, for the case F=0.7 , β=0.2 , α=0.02 . The linearized profile is sketched with a dashed line in the interval -5≤x≤5 . As mentioned in the introduction, the numerical evaluation of the linearized free-surface elevation is a difficult process, and in spite of the care taken here, it is nevertheless not possible to guarantee the accuracy of the result outside the interval shown. The non-linear result, shown with a solid line in Figure 5, is taken from a numerical solution with N=34 , M=6 , a total of 245 surface points, which took seven iterations and over three hours of computing time on an IBM 3083 E computer to achieve convergence. Both sets of results are in close agreement over much of the solution domain, although the non-linear wave heights are slightly less than those of the linearized waves, which is consistent with the results for wave resistance in Figure 4. The last half-wavelength or so downstream also appears to be in error for the non-linear solution;

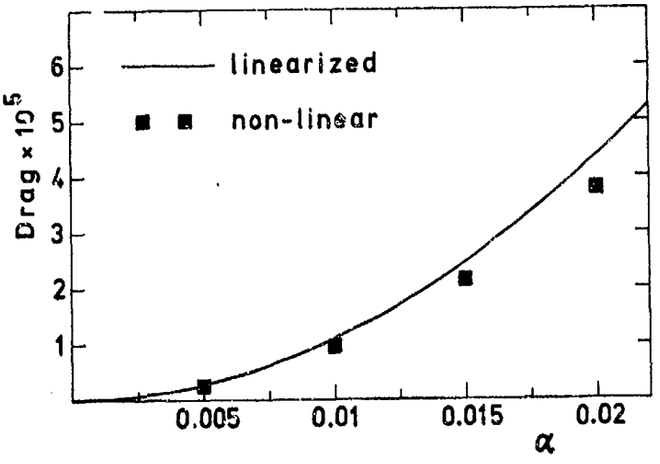

FIGURE 4: Linearized and non-linear wave drag as a function of α , when F=0.7 and β=0.2 .

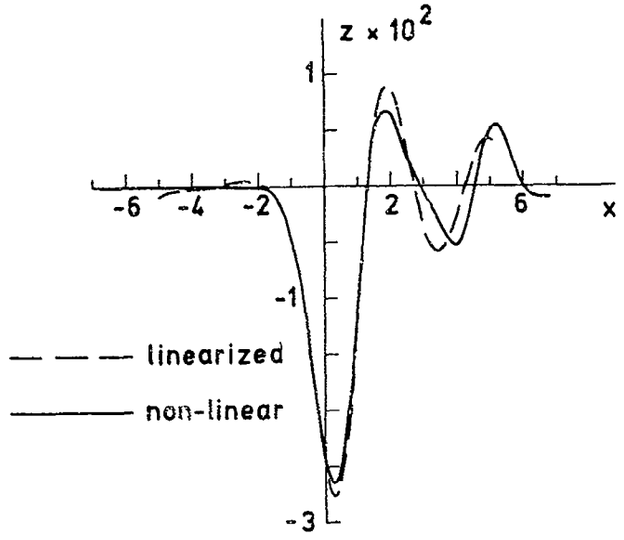

FIGURE 5: Linearized and non-linear surface elevation on the centre-plane $y=0$, for the case $F=0.7$, $\beta=0.2$, $\alpha=0.02$.

this is undoubtedly due to the downstream truncation of the domain of integration of the integrodifferential equation (2.12), and has been documented in detail elsewhere [6,11] for two-dimensional problems.

Figure 6 shows a perspective plot of the free surface for the non-linear solution obtained with $F=0.7$, $\beta=0.2$, $\alpha=0.01$. The surface has been extended by reflection about the plane $y=0$ in accordance with the symmetry conditions (2.13), and the values of y and ζ have been amplified by scale factors of 5 and 100 respectively. The surface exhibits an approximately elliptically -shaped depression in the vicinity of the origin, due to the presence of the pressure distribution, and the first downstream wave clearly forms a curved front, which opens towards the downstream side of the flow field.

In Figure 7, a perspective plot is shown for the free surface obtained from the non-linear solution for the case $F=0.7$, $\beta=0.2$, $\alpha=0.02$. A portion of this surface has already been sketched in Figure 5. This value $\alpha=0.02$ is the largest pressure strength for which Newton's method converged, and so it is possible that the non-linear waves in Figures 5 and 7 are approaching some maximum height at which wave-breaking would presumably take place. Of course the discretization of the

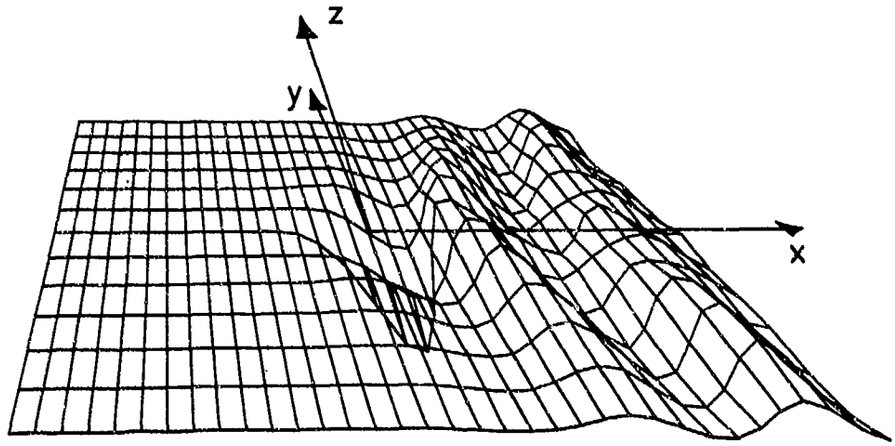

FIGURE 6: Perspective plot of the free-surface; $F=0.7$, $\beta=0.2$, $\alpha=0.01$ (non-linear case).

free surface in this study involved relatively few surface mesh points, and the use of larger numbers of grid points might enable higher waves to be obtained, although at greatly increased computational expense.

6. Discussion and Conclusions

A successful numerical method has been presented for the calculation of three-dimensional, steady potential flow involving a free surface, and represents a logical extension of earlier boundary-integral methods developed for two-dimensional flow problems [6,11,12]. Since it is not necessary to do so, no attempt has been made to "match" the numerical solution to a linearized downstream wave-field. However, it is possible that better accuracy might result from employing such a procedure, similar perhaps to that outlined by Lin, Newman and Yue [20]. Although the method is demanding on computer time, it is nevertheless very efficient, and the accurate numerical solution of many non-linear, three-dimensional free-surface problems reduces now merely to a question of expense. As is the case for two-dimensional problems, however, it is unclear how well the method can cope with the important class of surface-piercing flow problems.

Comparisons of linearized and non-linear wave drag indicate that the two are in close agreement over the entire interval in which solutions could be obtained. This is in contrast to the two-dimensional case, where linearized and non-linear wave drag may differ strongly, even for moderate values of wave height.

The free-surface elevations predicted by the linearized and non-linear solutions have also been compared and found to be in substantial agreement. This suggests that linearized theory is probably adequate to describe the free-surface elevation over most of the permissible values of F, β and α. In practice however, the expression for linearized wave elevation is generally of limited use, since it is difficult to evaluate accurately, particularly in the far field, and for arbitrary pressure distributions requires a computational effort comparable to the solution of the full non-linear problem. By contrast, the non-linear results do not suffer loss of accuracy in the far field, except that due to the downstream truncation of the integrodifferential equation, and the run-time of the method is essentially independent of the particular form chosen for the pressure distribution function.

It appears that some maximum value of the pressure strength α exists, at which incipient wave breaking occurs. The numerical results presented suggest that this value may be about $\alpha=0.02$, although more accurate computations would be needed to confirm this speculation.

References

[1] J.V. WEHAUSEN and E.V. LAITONE, "Surface waves", in: Handbuch der Physik, vol. 9 (1960), Springer-Verlag.

[2] J.N. NEWMAN and F.A.P. POOLE, "The wave resistance of a moving pressure distribution in a canal", Schiffstechnik, 9 (1962), 21-26.

[3] J.C. TATINCLAUX, "On the wave resistance of surface-effect ships", Trans. Soc. Naval Arch. and Marine Engineers, 83 (1975), 51-61.

[4] C. VON KERCZEK and N. SALVESEN, "Non-linear free-surface effects - the dependence on Froude number", in: Proc. 2nd. Int. Conf. on Numerical Ship Hydrodynamics, Berkeley (1977), 292-300.

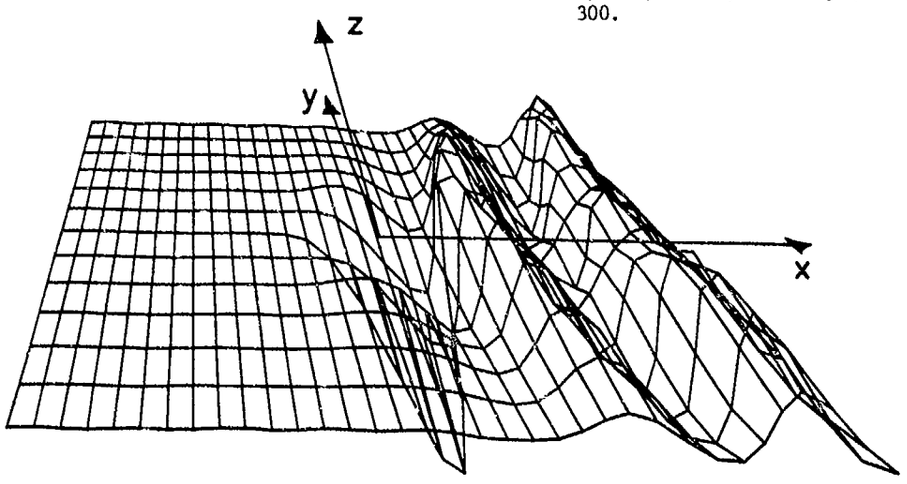

FIGURE 7: Perspective plot of the free-surface for $F=0.7$, $\beta=0.2$, $\alpha=0.02$ (non-linear case).

[5] L.W. SCHWARTZ, "Non-linear solution for an applied overpressure on a moving stream", J. Engineering Maths., 15 (1981), 147-156.

[6] L.K. FORBES and L.W. SCHWARTZ, "Free-surface flow over a semi-circular obstruction", J. Fluid Mech., 114 (1982), 299-314.

[7] J.-M. VANDEN BROECK and E.O. TUCK, "Computation of near-bow or stern flows, using series expansion in the Froude number", in: Proc. 2nd. Int. Conf. on Numerical Ship Hydrodynamics, Berkeley (1977), 371-381.

[8] G.G. STOKES, Mathematical and Physical Papers, vol. 1 (1880) Cambridge University Press.

[9] J.L. HESS, "Progress in the calculation of nonlinear free-surface problems by surface-singularity techniques", in: Proc. 2nd. Int. Conf. on Numerical Ship Hydrodynamics, Berkeley (1977), 278-284.

[10] L.K. FORBES, "Irregular frequencies and iterative methods in the solution of steady surface-wave problems in hydrodynamics", J. Engineering Maths., 18 (1984), 299-313.

[11] L.K. FORBES, "On the effects of non-linearity in free-surface flow about a submerged point vortex", J. Engineering Maths., to appear.

[12] L.K. FORBES, "A numerical method for non-linear flow about a submerged hydrofoil", J. Engineering Maths., to appear.

[13] R.L. STREET, "A review of numerical methods for solution of three dimensional cavity flow problems", in: Proc. 2nd. Int. Conf. on Numerical Ship Hydrodynamics, Berkeley (1977), 237-249.

[14] J.L. HESS and A.M.O. SMITH, "Calculation of non-lifting potential flow about arbitrary three-dimensional bodies", Douglas Aircraft Company Report no. ES 40622 (1962).

[15] J.L. HESS and A.M.O. SMITH, "Calculation of potential flow about arbitrary bodies", in: Progress in Aeronautical Sciences, vol. 8 (1967), Pergamon Press.

[16] L. LANDWEBER and M. MACAGNO, "Irrotational flow about ship forms", Iowa Institute of Hydraulic Research Report no. IIHR 123 (1969).

[17] T. MILOH and L. LANDWEBER, "Ship center-plane source distribution", J. Ship Research, 24 (1980), 8-23.

[18] T.H. HAVELOCK, "The wave pattern of a doublet in a stream", Proc. Roy. Soc. London, A 121 (1928), 515-523.

[19] M. ABRAMOWITZ and I.A. STEGUN (eds.), Handbook of Mathematical Functions, (1972), Dover.

[20] W.-M. LIN, J.N. NEWMAN and D.K. YUE, "Nonlinear forced motions of floating bodies", in: Proc. 15th Symp. on Naval Hydrodynamics, Hamburg (1984).

Appendix

Transformation of a singular integral.

To prove the identity (4.3), the change of variable $t = k-b$ is introduced into the left-hand side, giving

$$\int_0^\infty \frac{e^{-ak^2}}{k-b}\,dk = e^{-ab^2}\int_{-b}^\infty \frac{e^{-at^2}e^{-2abt}}{t}\,dt \qquad (A.1)$$

The quantity $\exp(-at^2+2abt)$ is identically subtracted and added to the numerator of the expression in the integrand of equation (A.1) to yield

$$\int_0^\infty \frac{e^{-ak^2}}{k-b}\,dk = e^{-ab^2}\left(\int_{-b}^{0} + \int_0^\infty\right) e^{-at^2}\,\frac{e^{-2abt}-e^{2abt}}{t}\,dt$$

$$+ e^{-ab^2}\left(\int_{-b}^{b} + \int_b^\infty\right) e^{-at^2}\,\frac{e^{2abt}}{t}\,dt\ . \qquad (A.2)$$

From the definition of a Cauchy principal-valued integral with a singularity at $t=0$, viz.

$$\int_{-b}^{b} f(t)dt = \lim_{\varepsilon\to 0}\left(\int_{-b}^{-\varepsilon} f(t)dt + \int_{\varepsilon}^{b} f(t)dt\right),$$

it is evident that the first and third integrals in equation (A.2) cancel, leaving

$$\int_0^\infty \frac{e^{-ak^2}}{k-b}\,dk = \tfrac{1}{2}\int_{-\infty}^{\infty} \frac{e^{-a(t+b)^2} - e^{-a(t-b)^2}}{t}\,dt$$

$$+ \int_b^\infty \frac{e^{-a(t-b)^2}}{t}\,dt\ . \qquad (A.3)$$

The first term on the right-hand side of equation (A.3) is now written

$$\tfrac{1}{2}\int_{-\infty}^{\infty} \frac{e^{-a(t+b)^2} - e^{-ab^2}}{t}\,dt$$

$$- \tfrac{1}{2}\int_{-\infty}^{\infty} \frac{e^{-a(t-b)^2} - e^{-ab^2}}{t}\,dt\ ,$$

and the changes of variable $u = t+b$ and $u = t-b$ in the first and second of these terms, respectively, gives

$$\int_0^\infty \frac{e^{-ak^2}}{k-b}\,dk = b\int_{-\infty}^{\infty} \frac{e^{-au^2} - e^{-ab^2}}{u^2 - b^2}\,du$$

$$+ \int_0^\infty \frac{e^{-au^2}}{u+b}\,du\ . \qquad (A.4)$$

Equation (4.3) may be obtained from (A.4) by first making the change of variable $t = u\sqrt{a}$ in the first term on the right-hand side. The second term is written

$$\frac{1}{b}\int_0^\infty e^{-au^2}du - \frac{1}{b}\int_0^\infty \frac{u\,e^{-au^2}}{u+b}\,du\ ,$$

and equation (4.3) follows, upon the change of variable $t = au^2$ in this term.

DISCUSSION
of the Paper
by Lawrence K. Forbes

PROGRESS IN THE CALCULATION OF NON-LINEAR FREE-SURFACE POTENTIAL FLOWS IN THREE DIMENSIONS

DISCUSSION
by V.J. Monacella

Section 4a. on the evaluation of the linearized solution seems to deserve comment. An analysis is provided whereby the Cauchy principal value integral is transformed to four infinite integrals two of which are evaluated by Hermite-polynomial quadratures and two by Laguerre-polynomial quadratures. There exist many methods for evaluating Cauchy principal value integrals but perhaps the most straightforward method** is one in which the singularity is ignored.

It was proved** that if the singularity is located at the midpoint of the range of integration then any quadrature for which the abscissae and weight functions are symmetrical about the singularity and which avoids the singularity itself can be used. The conditions on the quadrature impose no serious restrictions as they are properties of all even-order standard quadratures. Thus, using g(k) to represent the author's $f(k)\exp(-ak^2)$ the singular integral can be written

$$I=PV\int_0^\infty \frac{g(k)}{k-b}\,dk=PV\int_0^{2b}\frac{g(k)}{k-b}\,dk+\int_{2b}^\infty \frac{g(k)}{k-b}\,dk$$

The first integral on the right hand side can be approximated as just discussed. The second integral can be approximated by standard methods. It should be noted that the error term associated with the numerical integration of the first integral depends only on the quadrature chosen and the well behaved composite function $\frac{g(k)-g(b)}{k-b}$.

In particular, writing I in the standard form to apply Gauss integration formulas,

$$I = PV\int_{-1}^{1}\frac{g[b(k+1)]}{k}\,dk+\int_0^\infty \frac{g(k+2b)}{k+b}\,dk$$

the first integral can be evaluated by any even-order Gauss-Legandre quadrature, ignoring the singularity, and the latter integral by the Gauss-Laguerre quadrature. I would appreciate any insight that the author can offer regarding the efficiency of the two methods.

**Monacella, V.J., "On Ignoring the Singularity in the Numerical Evaluation of Cauchy Principal Value Integrals," David Taylor Model Basin Report 2356, Feb 1967

Author's Reply

I am indebted to Mr. V.J. Monacella for drawing my attention to his ingenious device for evaluating Cauchy principal-valued integrals numerically, simply by placing points symmetrically about the pole singularity and then ignoring it.

The discusser suggests that the integral in section 4a of the paper be written in the form

$$\int_0^\infty \frac{G(k)dk}{k-b} = I_1 + I_2,$$

in which $G(k) \equiv f(k)\exp(-ak^2)$, and

$$I_1 = \int_{-1}^{1}\frac{G[b(k+1)]dk}{k}$$

$$I_2 = \int_0^\infty \frac{G(k+2b)}{k+b}\,dk.$$

Certainly the integral I_1 can be evaluated to high accuracy using Mr. Monacella's device of ignoring the singularity, and this form now only involves two integrals, instead of the four which appear in my analysis.

My concern however is not with the evaluation of the integral I_1, which as pointed out by the discusser could be done efficiently in a variety of ways, but instead with the accuracy with which the integral I_2 may be evaluated, especially in the case when the constant a in the exponential term is very small, as may happen when the pressure distribution is narrow. As the discusser suggests, integral I_2 can be evaluated directly, effectively by multiplying and dividing the integrand by exp(-k), and applying the kGauss-Laguerre quadrature rule to the function G(k)exp(k). When a is small and a quadrature rule of moderate order is used however, this can involve substantial error. To get around this problem it would be necessary to exploit the fact that an exponential term $\exp(-ak^2)$ appears in the integrand, and attempt to rewrite integral I_2 in a form which enables the most effective use of Gauss-Hermite and Gauss-Laguerre quadratures. This would now involve at least three integrals, and a computational effort comparable with that required in section 4a of my paper.

Perhaps the most efficient method of evaluating the integral in section 4a might be to use the method given in that section when a is small, and to use Mr. Monacella's suggested form $I_1 + I_2$ when a is large.

DISCUSSION
by Katsuo Suzuki

My question is how the present numerical method deals with the case of Tatinclaux when the free-surface elevation is discontinuous along the line of $|y|=\beta$. $|x|<1$ as shown in the Figure S1, S2 obtained by the linearized theory.

Author's Reply

I thank Dr. Suzuki for his question concerning the behaviour of the numerical method when applied to Tatinclaux's piece-wise constant pressure distribution function, and for the diagrams he has supplied for the linearized surface elevation.

When the present numerical method is applied to a discontinuous surface pressure, results are obtained which are qualitatively similar to those presented in my paper. This, however, is a consequence of the fact that the finite differences cannot represent the discontinuity, and hence do not correspond to the behaviour of the exact non-linear solution. Indeed for two-dimensional problems, Van den Broeck and Tuck* show that a discontinuous pressure distribution leads to a linearized solution for which no non-linear solution exists. Three-dimensional problems are apparently even less tolerant of discontinuities in the pressure distribution function, since the linearized free-surface elevation becomes unbounded at the corner points of Tatinclaux's rectangular piecewise-constant pressure distribution. Certainly we must expect there to be no non-linear solution for such a pressure, and as the numerical mesh-sizes are refined in the present algorithm, then the behaviour of the present scheme must ultimately reflect this fact.

*Reference: J.-M. van den Broeck and E.O. Tuck, "Wave-less free-surface pressure distributions," Mathematical Research Center Technical Summary Report #2679, University of Wisconsin, Madison, Wisconsin (1984).

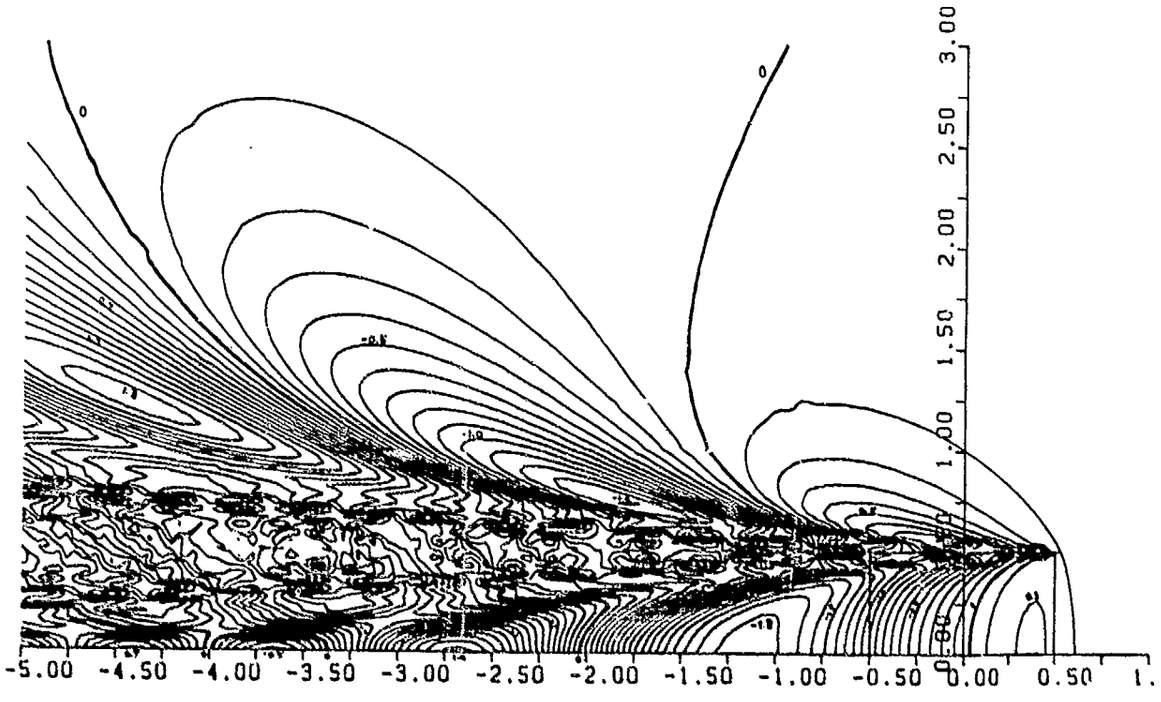

Figure S1 - Wave Pattern Generated by Pressure
$P(x,y)=1$, $|x|<0.5$, $|y|<0.5$, $k_0=1.0$, $\Delta k_0\zeta=0.1$

DISCUSSION
by K. Mori

According to my experience, the integration over the free-surface, eguation (2.14), depends strongly on the position of the computing domain. Significant surface gradients seem still to exist on your terminating surface X = 5.0.

Author's Reply

Dr. Mori expresses concern about the accuracy with which it is possible to evaluate the non-linear drag integral (2.14) numerically. As the discusser indicates, the downstream waves certainly have not decayed to insignificance at the terminating downstream surface, and so the surface gradients there are not necessarily small. This poses no difficulty in the present investigation, however, since the surface gradient function in the integrand of equation (2.14) is multiplied by the pressure distribution function (2.6), which decays exponentially rapidly away from the origin. For less well-behaved pressure distribution functions, Dr. Mori's observation could be of concern, however.

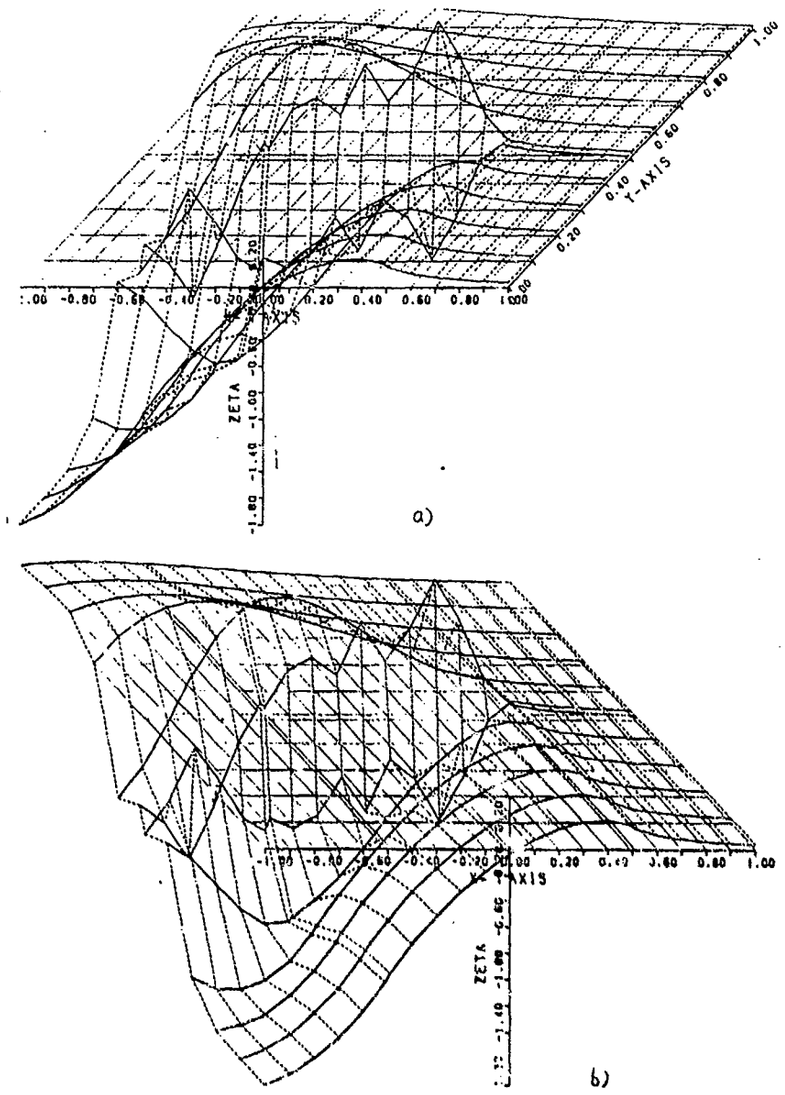

Figure S2 - Wave Heights Around Pressure $|x| < 0.5$, $|y| < 0.5$, $P(x,y)=1$, $k_o=1$

FORCES ON A SLENDER SHIP ADVANCING NEAR CRITICAL SPEED IN A SHALLOW CHANNEL

C.C. Mei
H.S. Choi

Massachussetts Institute of Technology
Cambridge, MA 02139

Abstract

In recent towing tank experiments by Huang et al. (1982) it has been established that a ship moving at a steady speed not far from the critical speed $\sqrt{gh}$, where h is the tank depth, radiates solitons upstream in an almost periodic manner. On the other hand, Wu and Wu (1982) have found similar results theoretically for two dimensional disturbances such as a pressure band moving along the free surface, by solving numerically the approximate equations of Boussinesq class for long waves in shallow water. In this paper, more recent work aimed at the prediction of two dimensional upstream solitons by a three-dimensional strut is reviewed and preliminary extensions for a slender ship are discussed.

1. Introduction

In several early experiments, it was observed that a steady state was difficult to achieve if the ship was towed at nearly the critical speed $\sqrt{gh}$ which is the propagation speed of infinitesimal long waves in shallow water. In addition to Thews and Landweber (1935, 1936) who were the first to discover such a phenomenon, Kinoshita (1946) also noticed similar behavior. In particular, he described the damming of water in front of the ship and the occurrence of backwater moving ahead of the ship and that "the stream around the ship remains no longer in a steady condition." Time-averages of the measured resistance, sinkage and trim were found to vary sharply with the speed in the vicinity of the critical speed. In similar experiments, Izubuchi and Nagasawa (1937) also found that the resistance curve shows a hump, and the trim of the ship changes abruptly, near the critical speed. These observations were further substantiated by the extensive experiments of Graff, Kracht and Weinblum (1964).

In earlier theories, the assumption of steadiness was understandably made. Michell (1898) and Joukowski (1903) independently derived the steady-state linearized theory. This approximation was further extended by Tuck (1966) for slender ships, by means of matched asymptotics. According to this kind of theory, the far field equation is elliptic for subcritical speeds, implying no steady waves, and hyperbolic for supercritical speeds, implying waves similar to those in supersonic aerodynamics. In the transcritical region, the linearized theory breaks down. Steady, one-dimensional hydraulic approximation was also advanced by Kreitner (1934) who found that the solution became singular near the critical speed.

Maruo (1948) was the first to suggest the use of a nonlinear theory similar to that of transonic aerodynamics. More calculations have been made subsequently by Lea and Feldman (1972) and by Maruo and Tachibana (1981) who however warn of the breakdown of the continuous solution at the critical speed. Unlike compressible aerodynamics, waves in shallow water are affected to some extent by dispersion, in addition to nonlinearity. Mei (1976) extended the Boussinesq approximation which contains dispersion and nonlinearity to leading order, to transcritical flow around a slender strut in horizontally unbounded water. His work is a generalization of Karpman (1967) who found that a slender strut in a high supercritical flow is governed by the KdV equation. All these theories are for steady state motions in a horizontally unbounded sea.

The experiments of Huang et al. (1982) and theory by Wu and Wu (1982) can be regarded as a turning point, for they have established decisively that either in a two dimensional flow or in a channel with a finite width, the response caused by a localized disturbance moving at a constant speed not far from $\sqrt{gh}$ is basically transient. Specifically, Huang et al. towed a model ship along the center line of a tank and noticed that, in addition to the expected ship waves in the wake, solitons which are uniform across the entire tank width are radiated ahead of the ship. If approached from below, the closer the Froude number $F = U/\sqrt{gh}$ is to unity, the greater are the frequency and amplitude of the solitons. By solving numerically a set of

C.C.Mei Dep't of Civil Engineering, Massachusetts Institute of Technology, Cambridge, Ma. 02139, USA
H.S.Choi Dep't of Naval Architecture, Seoul National University, Seoul 151, Korea

equations of the Boussinesq type, Wu and Wu investigated the waves due to a band of travelling pressure and found the same phenomenon; their response is necessarily two dimensional everywhere. Further theories and experiments for two dimensional disturbances travelling either above or beneath the water layer have confirmed and amplified these findings [Lee et al. (1984), Akylas (1984), Ertekin et al. (1984)].

The fact that a three-dimensional body such as a slender ship can give rise to two dimensional waves upstream is interesting. Firstly the tank width 2W is an obviously important parameter, along with the length 2L and beam 2B of the disturbance. Clearly if W is comparable to B and much less than L, the induced waves should be essentially uniform across the tank, both up and downstream; the two-dimensional theory already developed for B = W captures most of the physics. At the other extreme when W is much greater than L, the tank walls are effectively absent and two dimensional solitons need not arise and steady waves could exist and be describable by a nonlinear theory either with or without dispersion, depending on the slenderness of the disturbance [Maruo (1948, 1981) and Mei (1976)]. There are however intermediate cases which can be of interest. In the experiments by Huang et al. and by Ertekin et al. the ship length is roughly comparable to the channel width. Numerical computations by solving the full shallow water equations involving two horizontal space coordinates and time have been performed by Ertekin et al. (1985) for a rectangular pressure patch on the free surface. While there must be many canals which are so narrow relative to the dimensions of the ship, it is in the much wider ones that a ship is likely operated near the critical speed. By focussing attention to a small neighborhood of the critical speed, Mei (1985) has found that, for a certain class of width-to-length and slenderness ratios, the transcritical flow due to a thin strut is as simple as the two-dimensional case treated by Akylas (1984) in that the perturbed flow is essentially two dimensional and describable by a one-dimensional, inhomogenous KdV equation. In this paper we shall outline this theory and present some preliminary results of its extension to slender ships.

2. Approximate theory for a thin strut

Figure 1 depicts the geometry of a wall-sided strut along the axis of a channel. The length and the maximum beam of the strut are 2L and 2B respectively. The coordinate system is fixed on the ship with the origin located at the center of the mid-ship section. A uniform flow of velocity U begins at time t = 0 from left to right (bow to stern) of the ship.

For a potential flow, the exact governing equation and the boundary conditions are as follows. Let $\Phi(x,y,z,t)$ be the velocity potential of the flow, then,

$$\Phi_{xx} + \Phi_{yy} + \Phi_{zz} = 0, \quad -h < z < \zeta \tag{2.1}$$

in the fluid. On the free surface, the kinematic and dynamic conditions

$$\zeta_t + U\zeta_x + \Phi_x \zeta_x + \Phi_y \zeta_y = \Phi_z, \tag{2.2}$$

and

$$\Phi_t + g\zeta + U\Phi_x + \frac{1}{2}(\nabla\Phi)^2 = 0, \quad z = \zeta \tag{2.3}$$

must hold. On the horizontal channel bottom we must have

$$\Phi_z = 0, \quad z = -h \tag{2.4}$$

Let the hull of a wall-sided strut be $y = Y(x)$. On the hull, the flow must be tangential:

$$\Phi_y = (U + \Phi_x) Y_x, \quad y = Y(x) \tag{2.5}$$

On the channel bank, we require

$$\Phi_y = 0, \quad y = W \tag{2.6}$$

Before the flow starts, all is calm.

We now normalize these equations by introducing the following transformation

$$\zeta \to A\zeta, \quad \Phi \to \frac{gA}{U}\Phi, \quad (x,y) \to L(x,y)$$
$$z \to hz, \quad t \to \frac{L}{\sqrt{gh}}t, \quad Y \to BY \tag{2.7}$$

Unless otherwise stated, all variables are dimensionless from here on. The governing equations now become

$$\mu^2 \Delta\Phi + \Phi_{zz} = 0, \quad -1 < z < \epsilon\zeta \tag{2.8}$$

in the fluid, where

$$\Delta \equiv \frac{\partial^2}{\partial x^2} + \frac{\partial^2}{\partial y^2} \tag{2.9}$$

and

$$\Phi_z = \mu^2\left[F(\zeta_t + F\zeta_x) + \varepsilon(\Phi_x\zeta_x + \Phi_y\zeta_y)\right] \qquad z = \varepsilon\zeta \qquad (2.10)$$

$$F^2\mu^2\zeta + F\mu^2(\Phi_t + F\Phi_x) + \frac{1}{2}\varepsilon\left[\mu^2(\Phi_x^2 + \Phi_y^2) + \Phi_z^2\right] = 0 \qquad (2.11)$$

on the free surface,

$$\Phi_y = 0, \qquad y = W/L \qquad (2.12)$$

on the channel bank

$$\Phi_z = 0, \qquad z = -1 \qquad (2.13)$$

on the bottom, and

$$\Phi_y = \frac{1}{\varepsilon}\frac{B}{L}\left(F^2 + \varepsilon\Phi_x\right)Y_x \,, \quad y = \frac{B}{L}Y \qquad (2.14)$$

on the strut hull. The two dimensionless parameters

$$\mu = h/L \text{ and } \varepsilon = A/h \qquad (2.15)$$

are measures of dispersion and nonlinearity respectively.

We now assume that both ε and μ^2 are much less than unity. Following the usual procedure of shallow water approximation, we may introduce the Taylor expansion

$$\Phi = \Phi_0 - \frac{\mu^2}{2}(z+1)^2\Delta\Phi_0 + \frac{\mu^4}{4!}(z+1)^4\Delta\Delta\Phi_0 + \cdots \qquad (2.16)$$

After some straightforward manipulations and defining the depth average

$$\bar{\Phi} = \frac{1}{(1+\varepsilon\zeta)}\int_{-1}^{\varepsilon\zeta}\Phi\, dz \qquad (2.17)$$

one finds, when the effects of dispersion and nonlinearity are kept to the leading order only

$$\Delta\bar{\Phi} - D^2\bar{\Phi} - \frac{\varepsilon}{2F}D(\bar{\Phi}_x^2 + \bar{\Phi}_y^2) - \frac{\varepsilon}{F}\nabla\cdot[\bar{\Phi}\nabla\bar{\Phi}] + \frac{1}{3}\mu^2D^2\Delta\bar{\Phi} = O(\varepsilon^2, \varepsilon\mu^2, \mu^4), \qquad D = \partial/\partial t + F\partial/\partial x \qquad (2.18)$$

This equation is equivalent to the Boussinesq equation in a moving coordinate system. In view of the recent work of Ertekin et al. the direct numerical solution of (2.18) appears possible, but is still an arduous task. Let us examine the immediate neighborhood of the critical speed, in the manner of Mei (1976) for steady motion in an horizontally unbounded sea.

Clearly we want the slenderness of the strut to be

$$B/L = O(\varepsilon) \qquad (2.19)$$

Collecting all the twice-differentiated, linear terms on the left-hand side of (2.18) we get

$$(1-F^2)\bar{\Phi}_{xx} + \bar{\Phi}_{yy} - (\bar{\Phi}_{tt} + 2F\bar{\Phi}_{xt}) = O(\varepsilon, \mu^2) \qquad (2.20)$$

The right-hand side of (2.20) consists of nonlinear $O(\varepsilon)$ and dispersive $O(\mu^2)$ terms. Consider the case

$$\varepsilon = \mu^2 \ll 1 \qquad (2.21)$$

We now focus our attention to the immediate neighborhood of the critical speed and assume:

$$1 - F^2 = 2\alpha\mu^2 \qquad (2.22)$$

with $\alpha = O(1)$. Several situations may arise. Consider

$$W/L = O(1/\eta_0\,\mu^m) \qquad (2.23)$$

where η_0 is of order unity and the exponent m is still to be chosen. Let us rescale the y coordinate

$$y = \eta / \eta_0\mu^m \qquad (2.24)$$

so that the channel bank is at $\eta = 1$. Whether the term Φ_{yy} is comparable to the nonlinear and dispersive terms on the right of (2.20) depends on m. To consider the transient effect to leading order it is appropriate to renormalize time by

$$\tau = \mu^2 t \qquad (2.25)$$

We then obtain

$$\bar{\Phi}_{\eta\eta} = -(\mu^{2-2m}/\eta_0^2)\left[2\alpha\bar{\Phi}_{xx} - 2\bar{\Phi}_{\tau x} - 3\bar{\Phi}_x\bar{\Phi}_{xx} + \frac{1}{3}\bar{\Phi}_{xxxx}\right] + O(\mu^{4-4m}) \qquad (2.26)$$

The boundary condition on the hull becomes

$$\bar{\Phi}_\eta = \frac{1}{\varepsilon\mu^m\eta_0}\frac{B}{L}Y_x = \frac{BW}{h^2}Y_x \qquad (2.27)$$

If we choose

$$m = 1, \quad \text{i.e., } W/L = O(\mu^{-1}) \qquad (2.28)$$

and $\partial/\partial\tau \neq 0$, (2.28) is the so-called Kadomtsev-Petviashvilli (K-P) equation. For a compatible boundary condition on the hull, we take

$$B/L = O(\varepsilon\mu) = O(\mu^3) \tag{2.29}$$

The boundary condition on the channel bank is

$$\bar{\Phi}_\eta = 0 \ , \qquad \eta = 1 \tag{2.30}$$

With zero initial data this initial-boundary problem can be solved numerically. In the steady limit, Mei (1976) has pointed out that (2.26) reduces to the Tricomi equation in transonic aerodynamics if $\varepsilon \gg \mu^2$, i.e., if the strut is fairly thick.

If we choose

$$m = 1/2, \text{ i.e., } W/L = O(\mu^{-1/2}) \tag{2.31}$$

we should then renormalize y by

$$y = \frac{\eta}{\eta_0\sqrt{\mu}} \tag{2.32}$$

The boundary condition (2.27) can be rewritten as

$$\bar{\Phi}_\eta = \mu b Y_x \tag{2.33}$$

where

$$BW/h^2 = \mu b \ , \qquad b = O(1) \tag{2.34}$$

Now (2.26) and (2.33) imply that at the leading order, $\bar{\Phi}$ is independent of η. We now substitute the series

$$\bar{\Phi} = \Phi_0 + \mu\Phi_1 + \cdots \tag{2.35}$$

into (2.26) and (2.33), and easily obtain

$$-U_\tau + \alpha U_X - \frac{3}{2} U U_X + \frac{1}{6} U_{XXX} = \frac{1}{2} b \eta_0^2 Y_X \tag{2.36}$$

where $u = \Phi_{0X}$. Since

$$\zeta = -\Phi_{0X} + O(\mu) \tag{2.37}$$

according to (2.11), it follows that

$$\zeta_T - \alpha\zeta_X - \frac{3}{2}\zeta\zeta_X - \frac{1}{6}\zeta_{XXX} = \frac{\beta}{2} Y_X \tag{2.38}$$

where

$$\beta = b\eta_0^2 = \frac{B/W}{\mu^4} = O(1) \tag{2.39}$$

Equation (2.38) is an inhomogeneous KdV equation for the leading-order free surface height. It involves two parameters: α represents the departure from the critical speed, while β represents the blockage effect since B/W is the blockage coefficient. It can be solved numerically by several known algorithms, one of which will be described later.

3. Modification for a slender ship.

We again limit our attention to the case where $W/L = O(1/\sqrt{\mu})$ and consider a slender ship. Let the ship hull be described in cylindrical polar coordinates by $r - R(x,\theta)$. On the hull the kinematic condition is

$$\Phi_n = (U + \Phi_x) R_x \left[1 + (R_\theta/R)^2\right]^{-1/2} \tag{3.1}$$

Let R_0 be the characteristic radius of the cross section, i.e., R_0^2 is of the order of the maximum cross-sectional area. It is natural to expect that when

$$R_0^2 = O(Bh) = O(\mu^4 Wh) = O(\mu^{4.5} L^2) \tag{3.2}$$

the far field defined by

$$\frac{x}{L} = O(1), \quad \frac{y}{L} = O(\mu^{-1/2}), \quad \frac{z}{L} = O(\mu) \tag{3.3}$$

is still described by (2.38) if the blockage coefficient is of the same order as the thin strut with the slenderness given by (2.34), i.e.,

$$R_0/L = O(\mu^{2.25}) \tag{3.4}$$

Following Tuck (1966), we introduce the inner region

$$x = O(L), \ (y,z) = O(R_0) = O(\mu^{2.25} L) \tag{3.5}$$

As in the aerodynamics of a slender body, the velocity field in the inner region is approximately two dimensional in the cross-sectional planes. At the outer limit of the inner region, the effect of the body is to induce a radial flux of the strength q(x) proportional to the spatial rate of change of the cross-sectional area S(x), i.e.,

$$q(x) \sim S_x \tag{3.6}$$

The channel bottom is effectively at negative infinity. The potential in the inner region is approximately given by

$$\Phi = \hat{\Phi}_0(x,\tau) + \hat{\Phi}_p(x,\hat{y},\hat{z},\tau) \tag{3.7}$$

with

$$(\hat{y},\hat{z}) = (y,z)/R_0 \tag{3.8}$$

We point out that Tuck studied the case where the lateral dimension R_0 of the ship is of the same order as the water depth h; the outer limit of the inner solution can be matched to the inner limit of the outer solution directly. In concrast, here one must go through an intermediate region defined by

$$x = O(L),\ (y,z) = O(h) = O(\mu L) \tag{3.9}$$

It may be easily shown that to leading order the flow in the intermediate region is still two dimensional in the cross-sectional plane. Its outer limit consists of two sideward flows which are uniform in depth. The inner limit of the intermediate solution is represented by a distribution of sources along the centerline of the water plane. By matching with the inner solution, it is no surprise that the source strength of the intermediate solution must be directly related to the rate of change of the cross-sectional area, i.e.,

$$q = \frac{2}{\eta_0}\frac{\sqrt{\mu}\,L^2}{R_0^2} S_B S_x \tag{3.10}$$

where S_B is the blockage coefficient equal to the ratio of the maximum cross-section below the water line to the cross-section of the channel 2Wh. By comparing with the strut case, we may conclude that to the outer field observer, the ship can be replaced by an equivalent strut whose beam is given by

$$BY = WS_B S \tag{3.11}$$

Now the outer solution, i.e., the wave field, can be computed immediately from (2.38) with the right-hand side replaced by

$$\frac{1}{2}\frac{S_B}{\mu^4} S_x \tag{3.12}$$

The matching also determines the velocity potential around the ship,

$$\hat{\Phi}_0 = \Phi_0 \tag{3.13}$$

to leading order, which can be used to calculate the pressure field according to the Bernoulli equation. In terms of the inner region variables, the normalized pressure is

$$\hat{p} = p/\rho g h = -\left[\frac{\mu^4}{F^2}\Phi_t + \mu^2\Phi_x + \frac{\mu^4}{F^2}\left(\Phi_x^2 + \Phi_y^2 + \Phi_z^2\right)\right] \tag{3.14}$$

To leading order the pressure is given by

$$\hat{p} = -\mu^2\hat{\Phi}_x \tag{3.15}$$

which is uniform in the cross-sectional plane at any x. The total force on the ship is

$$\vec{e}_x R_w^* + \vec{e}_z L^* = \vec{e}_x\int_{-L}^{L} p\,S_x\,dx + 2\vec{e}_z\int_{-L}^{L} p\,Y\,dx \tag{3.16}$$

where the first term on the right stands for the wave drag and the second the lift. The moment can be defined in physical variables

$$M^* = \int_{-L}^{L} 2x\,p\,Y\,dx \tag{3.17}$$

Instead of the lift and moment one can alternatively use the sinkage and trim defined by

$$-L^* = 2\rho g\int_{-L}^{L}(s^* + x\theta_T)\,Y\,dx \tag{3.18}$$

$$M^* = 2\rho g\int_{-L}^{L} x(s^* + x\theta_T)\,Y\,dx \tag{3.19}$$

The dimensionless wave resistance and sinkage can be defined as:

$$R_w = R_w^*/\rho g \nabla \tag{3.20}$$

$$S = s^*/L \tag{3.21}$$

where ∇ is the displacement of the ship.

4. Numerical solution

The first task is to solve for ζ governed by (2.38). We adopt the explicit finite difference scheme of Johnson (1972)

$$\zeta_m^{n+1} = \zeta_m^{n-1} + \frac{\Delta\tau}{\Delta x}\left\{\alpha + \frac{1}{2}\left(\zeta_{m+1}^n + \zeta_m^n + \zeta_{m-1}^n\right)\right.$$
$$\left.\times\left(\zeta_{m+1}^n - \zeta_{m-1}^n\right) + \frac{1}{6}\frac{\Delta\tau}{(\Delta x)^3}\left(\zeta_{m+2}^n - 2\zeta_{m+1}^n + 2\zeta_{m-1}^n - \zeta_{m-2}^n\right) + \Delta\tau\beta S_x\right., \quad \zeta_m^n = \zeta(m\Delta x, n\Delta\tau) \tag{4.1}$$

For stability, the time and spatial discretization must satisfy the following inequality,

$$\frac{\Delta\tau}{\Delta x}\left(|\zeta| + \frac{4}{(\Delta x)^2}\right) < 1 \tag{4.2}$$

Thus the maximum value of the unknown also plays a role in the criterion. We find

$\Delta x = 0.1$, $\Delta\tau = 0.0005$ to be sufficient.

Figures 2 - 6 show the free surface profiles at several instances of time induced

by a parabolic ship with

$$S(x) = 1 - x^2 \quad , \quad |x| \leqslant 1 \qquad (4.3)$$

At a low subcritical speed, there is a soliton of low amplitude propagating ahead of the ship, with minor undulations in the wake. At a higher subcritical speed, more crests emerge ahead of the bow, the leading ones pull away the fastest, giving signs of forming separated solitons. At the critical speed, higher solitons of nearly uniform amplitudes are formed. This trend persists into the supercritical range. At high enough supercritical speed no more solitons are radiated; there is only some local disturbance. Although not designed for comparison with the narrow tank experiments, the calculated amplitudes of the leading solitons appear to agree with the measurements of Ertekin (1984) (see Mei,1985).

Graff et al. (1964) also reported measurements of the total resistance, sinkage and trim for a destroyer model of length 2L = 3 m in a tank of width 2W = 10.1 m. The ratio W/L is moderately large to be close to that assumed in the present theory. The ship model was only constrained laterally and longitudinally and is otherwise free to heave and pitch. It has a transom stern. Records for two depths are available. In Figure 7 we compare the calculated wave resistance with the measured residual resistance which is the total measured resistance minus the skin friction computed from the boundary layer theory for a flat plate. Near the critical speed the computed values oscillate in time; we have plotted as representative values the first maximum and the following minimum. The peaks in both theory and experiments occur at roughly the same speed. The quantitative agreement is understandably poor, since the residual resistance is the sum of wave and form drags.

In Figures 8 and 9 comparisons are made for the sinkage and the trim. Since the theoretical values are for a fixed ship and the experiments are for a motion-free ship, the comparison is not a strict one. Nevertheless the similarity between the two already suggests that the present simple theory is on the right course.

We are presently pursuing a higher order theory by the method of matched asymptotics, details of which will be presented in the future.

Acknowledgements

This study has been supported by the Fluid Mechanics Programs of the Office of Naval Research and the National Science Foundation. H.S.Choi also wishes to thank the Korean Science & Engineering Foundation for a fellowship which makes his visit at MIT possible.

References

Akylas,T.R. (1984). "On the Excitation of Long Nonlinear Water Waves by a Moving Pressure Distribution". J. Fluid Mech.,Vol. 141 pp.455-466.

Ertekin,R.C., Webster,W.C. and Wehausen,J.V. (1984). "Ship-Generated Solitons". Proc. 15th Symp. Naval Hydrodyn., Hamburg,pp.347-364.

Ertekin,R.C., Webster,W.C. and Wehausen,J.V. (1985). "Waves Caused by a Moving Disturbance in a Shallow Channel of Finite Width". (private communication).

Graff,W., Kracht,A. and Weinblum,G. (1964). "Some Extension of D.W.Taylor's Standard Series". Trans. SNAME, Vol. 72,pp.374-401.

Huang,D.B., Sibul,O.J. and Wehausen,J.V.(1982) "Ships in Very Shallow Water". Festkolloquium zur Emeritierung von Karl Wieghardt, Institut für Schiffbau der Universität Hamburg, Bericht Nr. 427(April 1983),pp.29-49.

Izubuchi,T. and Nagasawa,S. (1937). "Experimental Investigation on the Influence of Water Depth upon the Resistance of Ships". (in Japanese) JSNA, Vol.61,pp.165-206.

Johnson,R.S. (1972). "Some Numerical Solutions of a Variable Coefficient Korteweg-de Vries Equation". J. Fluid Mech.,Vol.54,pp.81-91.

Joukowski,N.E. (1903). "On the Wave of Translation". Complete Works 4 ONTI(1937).

Karpman,V.I. (1967). "The Structure of Two-dimensional Flow Around Bodies in Dispersive Media". Sov. Phys.,J. Exp. Theor. Phys. Vol.23, pp.1102-1111.

Kinoshita,M. (1946). "On the Restricted-Water Effect on Ship Resistance". JSNA, Vol.76(1954), pp.173-213.

Kreitner,J. (1934). "Uber den Schiffswiderstand auf beschränkten Wasser". W.R.H.

Lea,G.K. and Feldman,J.P. (1972). "Transcritical Flow Past Slender Ships". Proc. 8th Symp. Naval Hydrodyn., Paris,pp.1527-1541.

Lee,S.J., Yates,G.T. and Wu,T.Y. (1984). Discussion to the paper of Ertekin et al., Proc. 15th Symp. Naval Hydrodyn.,Hamburg.

Maruo,H. (1948). "On the Shallow Water Effect" (in Japanese) JSNA, Vol.84(1952),pp.1-15.

Maruo,H. and Tachibana,T. (1981). "An Investigation into the Sinkage of a Ship at the Transcritical Speed in Shallow Water". JSNA, Vol.150 pp.181-187.

Mei,C.C. (1976). "Flow Around a Thin Body Moving in Shallow Water". J. Fluid Mech.,Vol.77, pp.737-751.

Mei,C.C. (1985). "Radiation of Solitons by Slender Bodies Advancing in a Shallow Channel". J. Fluid Mech. (in press).

Michell,J.H. (1898). "The Wave Resistance of a Ship". Phil. Mag., Vol. 45.

Thews,J.G. and Landweber,L. (1935). "The Influence of Shallow Water on the Resistance of a Cruiser Model". US Exp. Model Basin,Navy Yard, Washington,D.C. Rep. No. 408.

Thews,J.G. and Landweber,L. (1936). "A Thirty-inch Model of the S.S. Clairton in Shallow Water". US Exp. Model Basin,Navy Yard,Washington, D.C.,Rep. No. 414.

Tuck,E.O. (1966). "Shallow-water Flows Past Slender Bodies". J. Fluid Mech.,Vol.26,pp.81-95.

Wu,D.M. and Wu,T.Y. (1982). "Three-dimensional Nonlinear Long Waves due to Moving Surface Pressure". Proc. 14th Symp. Naval Hydrodyn., Ann Arbor,pp.103-129.

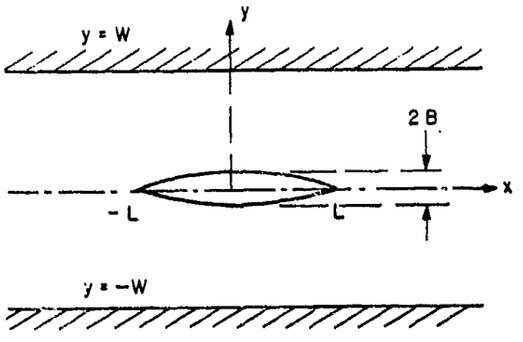

Figure 1 : Definition sketch of a strut moving in a channel.

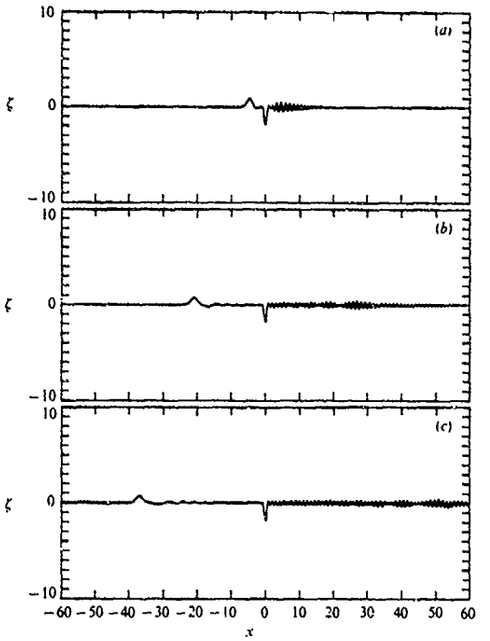

Figure 2 : Evolution of free surface due to a strut. From bow to stern $-1 < x < 1$, $\beta = 10.4$, $\alpha = 5$.
(a) $\tau = 1$,(b) 3,(c) 5.

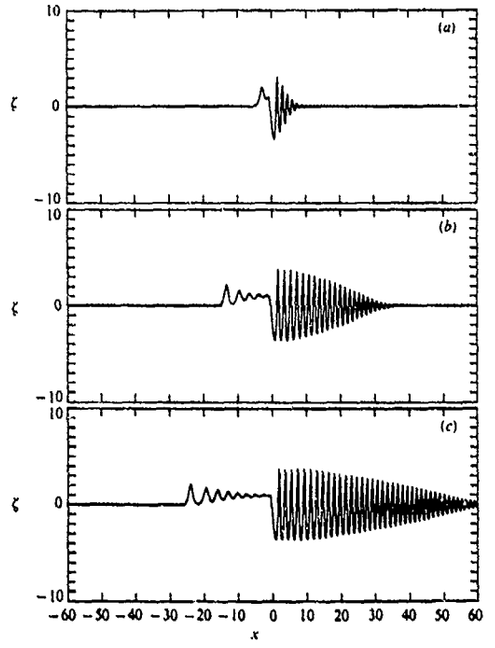

Figure 3 : Evolution of free surface due to a strut, $\beta = 10.4$, $\alpha = 2.5$.
(a) $\tau = 1$,(b) 3,(c) 5.

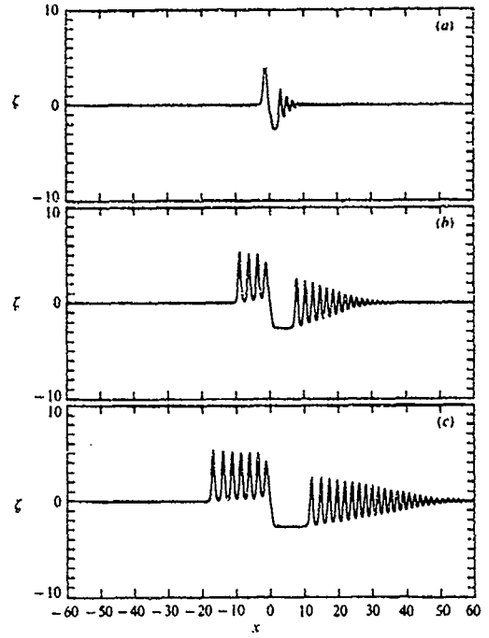

Figure 4 : Evolution of free surface due to a strut, $\beta = 10.4$, $\alpha = 0$(critical). (a) $\tau = 1$, (b) 3, (c) 5.

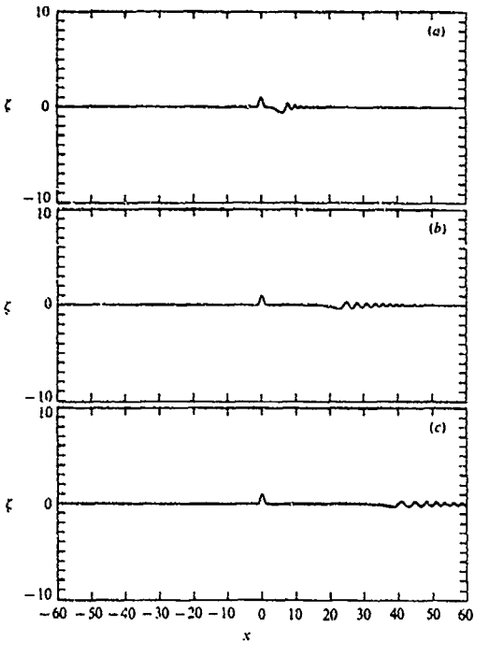

Figure 6 : Evolution of free surface due to a strut, $\beta = 10.4$, $\alpha = -5$. (a) $\tau = 1$, (b) 3, (c) 5.

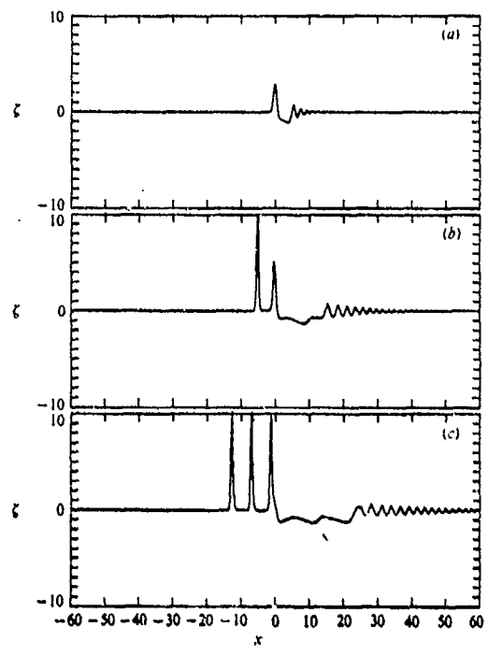

Figure 5 : Evolution of free surface due to a strut, $\beta = 10.4$, $\alpha = -2.5$. (a) $\tau = 1$, (b) 3, (c) 5.

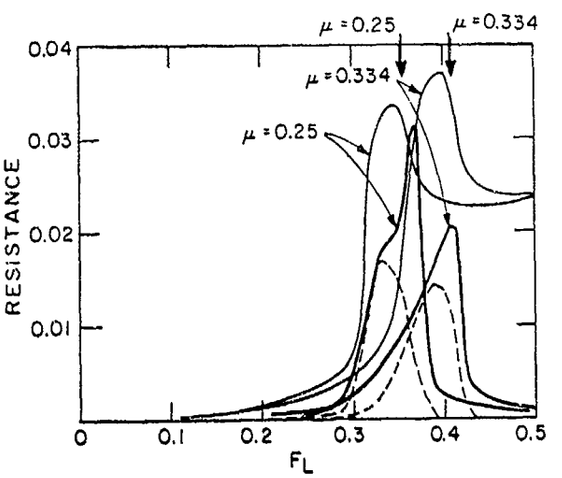

Figure 7 : Specific resistance. —— experiment ; ▬▬ theoretical first maximum ; - - - theoretical following minimum ; ↓ critical speeds.

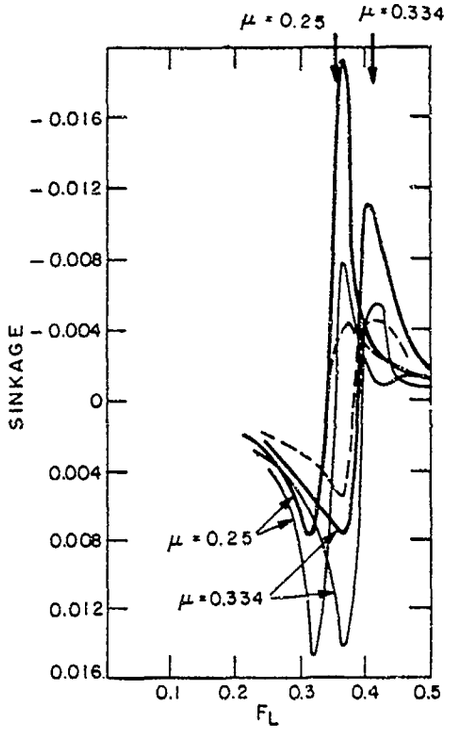

Figure 8 : Dimensionless sinkage positive downward. ——— experiment;
▬▬ theoretical first maximum ;
– – – theoretical following minimum;
↓ critical speeds.

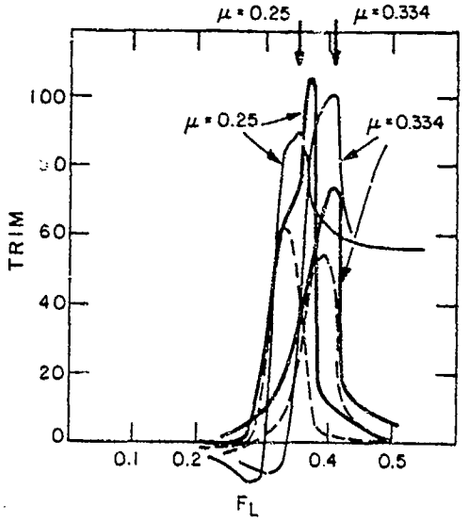

Figure 9 : Trim in minutes positive trim by stern. ——— experiment;
▬▬ theoretical first maximum ;
– – – theoretical following minimum;
↓ critical speeds.

CALCULATIONS OF VISCOUS EFFECTS ON SHIP WAVE RESISTANCE USING SIMPLIFIED BOUNDARY LAYER APPROACHES

Henry T. Wang
Naval Research Laboratory
Washington, D.C. 20375

Abstract

The paper investigates the effect of fluid viscosity on ship wave resistance for five ship hulls, three of which have extensive experimental data. The direct Michell thin ship and zeroth order slender ship theories are used to model the potential flow around the hull. The viscous flow is modeled by four relatively simple momentum integral boundary layer methods, which approximate the flow over the hull and in the wake by various axisymmetric and two-dimensional models. The calculated wave resistances are in generally good agreement with experimental data for two of the hulls, and in poor agreement for a third hull. The corrections due to the two-dimensional models change the wave resistance by lowering the magnitudes of the weighted amplitude function, without any appreciable changes in phase. The use of the axisymmetric model with equivalent volume changes both the magnitude and phase of the function.

1. Introduction

It is generally accepted that the paper by Michell [1], using thin ship theory laid the foundation for numerical calculations of ship wave resistance. In this theory, the ship is assumed to be sufficiently thin that the singularities may be placed directly on the hull centerplane, with their strengths simply given by the longitudinal derivative of the ship width. Efforts to improve the accuracy of the original Michell theory have been largely along three lines: better satisfaction of the hull boundary condition, more accurate approximation of the nonlinear free surface condition, and consideration of the effect of fluid viscosity on the wave resistance.

Perhaps the first notable improvement to the Michell hull boundary condition, in terms of a practical calculation procedure, is the "interpolation formula" proposed by Hogner [2], which reduces in its limiting cases to thin ship and flat ship theories. These limiting cases of the Hogner formula are discussed in great detail by Weinblum [3]. For conventional ship hulls, Hogner's approach differs from that of Michell in two principal aspects: the singularities are now placed on the actual hull surface instead of on the centerplane, and their strengths are obtained by a more accurate calculation of the longitudinal component of the normal to the hull. More recently, Koch and Noblesse [4] and Eggers [5], among others, have emphasized the importance of adding a line integral at the water surface to complete Hogner's original approach. The resultant modified Hogner approach, or zeroth order slender ship theory, as termed by Noblesse [6], remains a direct calculation procedure for the singularity strengths. Among indirect approaches, the simplest are those in which the free-surface terms in the Green's function are assumed to be negligible in computing the mutual influence of the hull singularities, such as the approach by Tsutsumi [7]. This results effectively in an infinite fluid problem for the singularity strengths. Finally, there are approaches, such as those by Chang [8] and Adachi and Takeshi [9], which solve the complete Neumann-Kelvin problem, in which all the free-surface effects are included. The principal difficulty in this approach is the need to calculate the influence of the troublesome near field terms in the Green's function.

Various approaches have been used to improve the free surface condition near the hull. One type of approach, used by Guilloton [10] and Hong [11], has been to employ transformation techniques to transform the physical coordinate system to a new coordinate system where the perturbed free surface is known. Gadd [12] and Dawson [13] use infinite fluid Rankine sources to model the hull and the shape of the free surface. A more recent approach has been that of Amromin et al. [14] who alter the strengths of the singularities based on the local free surface elevation. It may be noted that these approaches are usually at least as complex as the Neumann-Kelvin approaches since the near field free surface behavior must again be calculated.

The earliest efforts to account for the effect of viscosity by Wigley [15] and Havelock [16] consisted of finding simple empirical expressions or factors for the reduction in wave resistance or the stern singularity strengths. Later, they [17, 18] concentrated on finding the effect of different mathematical shapes simulating the displacement effect of the boundary layer flow in the stern-near wake region on the resultant wave resistance. These studies were obviously intended for ascertaining only overall trends of the viscous correction and are not tied to a particular ship geometry. The most recent studies have used high order flow theories to model the viscous flow in the stern and near wake, such as in [19-23]. In [19-21], the viscous flow is taken to give a displacement thickness which modifies the hull shape while in [22-23] the calculated viscous flow velocities are taken to interact with the potential flow velocities. Often, these complex viscous flow theories are used to modify a simple potential flow theory, such as thin ship theory.

The present paper investigates the effect of the displacement thickness due to four different momentum integral approximations for the hull boundary layer flow on the wave resistance calculated by using the previously mentioned direct thin ship and zeroth order slender ship theories. The four

approaches approximate the actual hull by an axisymmetric body of equivalent volume, an axisymmetric body of equivalent wetted area, a two-dimensional body of equivalent thickness, and the two-dimensional body extended into the wake. The use of the axisymmetric approximations was introduced by the author in a previous report [24] and do not appear to have been previously used in connection with wave resistance theories. The use of these low order boundary layer approximations is compatible, in terms of computer time requirements, with the simple potential flow theories. It is emphasized, however, that the boundary layer theories proceed entirely from first principles, without using any empirical or ad hoc correction factors. The calculations are performed for five ship hulls. Three of the hulls are the Wigley [25], Series 60 ($C_B = 0.60$) [25], and Sharma [26] strut, for which there are abundant experimental data. The fourth hull is a Series 60 hull with a straight stern contour, and the fifth hull is a Wigley hull with its width everywhere doubled.

The paper describes the potential flow wave resistance and boundary layer approaches which are used. The geometrical characteristics of the five hulls are described, including the shapes of the axisymmetric and two-dimensional shapes which are used to approximate the actual hull. The boundary layer thicknesses predicted by the various approaches are summarized. The effect of the viscous corrections on wave resistance are discussed in terms of overall coefficients as well as in terms of the amplitude functions, whose integral over wave direction leads to the wave resistance.

2. Potential Flow Wave Resistance Calculation Procedures

The problem is usually formulated in a coordinate system fixed to the ship. Figure 1 shows the coordinate system used in the present study, with origin at the forward perpendicular, x positive from stern to bow, y positive to port, and z positive upwards. The figure also shows the terminology used throughout the paper. In such a coordinate system, the potential ϕ for the modified Hogner or zeroth order slender ship theory is given by the sum of the following two integrals [6]

$$\phi = \int_{S_H} \sigma G ds + F_n^2 \int_C \sigma n_x \tau_y \sigma G dl \tag{1}$$

where σ is the source strength,

G is the Green's function for the Kelvin source which satisfies the dynamic and kinematic free surface condition,

ds is an elemental area on the hull surface,

$F_n^2 = \dfrac{U}{gL}$ is the Froude number squared,

U is the ship speed,

g is the gravity constant,

C is the waterline contour,

n_x is the longitudinal component of the normal to the hull,

τ_y is the y-component of the tangent to the waterline contour, and

dl is an element length along the waterline contour.

The value of σ is directly obtained from ship geometry, as follows

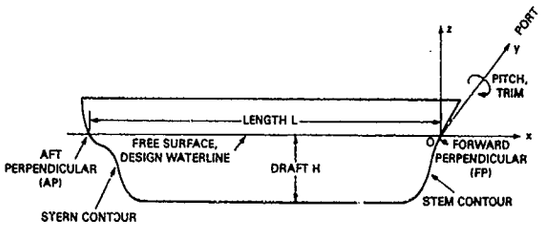

Figure 1. Ship Configuration and Coordinate System

$$\sigma(x, y, z) = \frac{-U}{4\pi} n_x \tag{2}$$

$$= \frac{-U}{4\pi} \left[\frac{\partial f/\partial x}{\sqrt{1 + (\partial f/\partial x)^2 + (\partial f/\partial z)^2}} \right]$$

where $f(x, z)$ is the local half-width of the ship.

Thin ship theory is obtained from the above theory if the ship beam B is assumed to be small enough such that the waterline integral is negligibly small, the integral over the hull surface S_H may be replaced by the centerplane S_0, and the terms $(\partial f/\partial x)^2$ and $(\partial f/\partial z)^2$ may be neglected. Equations (1) and (2) then respectively become

$$\phi = \int_{S_0} \sigma G ds \tag{3}$$

$$\sigma = \frac{-2U}{4\pi} \frac{\partial f}{\partial x} \tag{4}$$

where the factor of 2 in Eq. (4) indicates that the ship has port and starboard symmetry.

Various equivalent forms have been proposed for the Green's function G. A form which is particularly useful in the present study is that given by Wehausen and Laitone [27]

$$G = G_1 + G_2 + G_3 \tag{5}$$

$$G_1 = \frac{1}{r} - \frac{1}{r_1}, \tag{6}$$

$$G_2 = \frac{-4}{\pi} k_0 \int_0^{\pi/2} d\theta \sec^2\theta \int_0^{\infty} dk \frac{\exp k(z + z')}{k - k_0 \sec^2\theta} \cdot$$

$$\cos[k(x - x')\cos\theta] \cdot \cos[k(y - y')\sin\theta], \tag{7}$$

$$G_3 = -4k_0 \int_0^{\pi/2} d\theta \sec^2\theta \exp[k_0(z + z')\sec^2\theta] \cdot$$

$$\sin[k_0(x - x')\sec\theta] \cos[k_0(y - y')\sin\theta \sec^2\theta] \tag{8}$$

where x', y', z' denote respectively the x, y, z values of the source location,

$$r = \sqrt{(x - x')^2 + (y - y')^2 + (z - z')^2},$$

$$r_1 = \sqrt{(x - x')^2 + (y - y')^2 + (z + z')^2},$$

$k_0 = g/U^2$ is the fundamental wave number,

k is the wave number in the direction θ, and

θ is the direction of the wave component.

The terms G_1, G_2, and G_3 respectively represent infinite fluid, near field wave, and far field wave effects. The terms G_1 and G_2 are important in computing the near field flow, such as the wave profile near the hull or the mutual influence of the hull sources in the Neumann-Kelvin problem. In the present case, the source strengths are directly given by Eqs. (2) and (4), and it is only the far field wave disturbance G_3 which gives rise to the wave resistance. Thus, Eqs. (1) and (3) are integrated with

$$G = G_3 \tag{9}$$

The wave resistance is evaluated in terms of the dimensionless wave number in the y direction, k_y/k_0, following a procedure given in Eggers, Sharma, and Ward [28]. By applying Lagally's theorem to the source distribution, the wave resistance R_w is given by

$$R_w = -4\pi\rho \int_D \sigma \phi_x \, dD \tag{10}$$

where ρ is the fluid density,

$$\int_D = \int_{S_H} + \int_C \text{ for zeroth order slender ship} \tag{11a}$$

$$= \int_{S_0} \text{ for thin ship} \tag{11b}$$

By further noting that for the free waves which contribute to wave resistance, the following relationships between wave numbers k, k_x and k_y, and direction θ apply

$$w = \frac{k}{k_0} = \sec^2\theta,$$

$$u = \frac{k_y}{k_0} = \frac{k}{k_0} \sin\theta = \sec\theta \tan\theta,$$

$$s = \frac{k_x}{k_0} = \frac{k}{k_0} \cos\theta = \sec\theta, \tag{12}$$

the following expression for R_w in terms of u is derived [28]

$$R_w = \rho k_0^2 \frac{1}{4\pi} \int_{-\infty}^{\infty} \frac{1+\sqrt{1+4u^2}}{\sqrt{1+4u^2}} \cdot J[u, s(u)]\, \bar{J}[u, s(u)]\, du \tag{13}$$

where $J[u, s(u)]$ is the complex Kochin function defined by

$$J[u, s(u)] = 4\pi \int_D \sigma(x, y, z) \exp\left[k_0(isx + iuy + wz)\right], \tag{14}$$

$$s(u) = \left[1 + \frac{1}{2}\sqrt{1+4u^2}\right]^{1/2}, \tag{15a}$$

$$w(u) = \sqrt{u^2+s^2}, \text{ and} \tag{15b}$$

$\bar{J}$ is the complex conjugate of J

An alternate expression for R_w which is commonly used is given by

$$R_w = \frac{1}{2}\pi\rho U^2 \int_{-\pi/2}^{\pi/2} A^2(\theta) \cos^3(\theta)\, d\theta \tag{16}$$

Written in this form, the commonly plotted wave resistance weighted amplitude function $A^2(\theta)\cos^3\theta$ is explicitly shown. Equating Eqs. (13) and (16) and noting that

$$\frac{du}{d\theta} = \frac{d}{d\theta}(\sec\theta\tan\theta) = \frac{1+\sin^2\theta}{\cos^3\theta} \tag{17}$$

the dimensionless weighted amplitude function A^*/L^2 in terms of the integrand of Eq. (13) is given by

$$\frac{A^*}{L^2} = \frac{k_0^2}{2\pi^2 U^2 L^2} \frac{1+\sqrt{1+4u^2}}{\sqrt{1+4u^2}} \cdot J[u, s(u)]\, \bar{J}[u, s(u)] \frac{\cos^3\theta}{1+\sin^2\theta} \tag{18}$$

where $\frac{A^*}{L^2} = \frac{A^2(\theta)\cos^3\theta}{L^2}$.

3. Boundary Layer Calculation Procedures

Several reasons led to the use of low order boundary layer approaches to modify the potential flow theories. One reason is that an accurate boundary layer calculation procedure would involve using a three-dimensional potential flow theory to calculate the pressure distribution on the hull surface, tracing a series of streamlines, and using a high order boundary layer theory to calculate the boundary layer flow along each streamline. This would lead to a calculation procedure which is considerably more complex than the simple wave resistance theories outlined in the preceding section and thus negate the computational simplicity of these methods.

A second reason is that there are indications that a more accurate boundary layer calculation may not lead to better agreement of the calculated and measured wave resistances. In particular, Himeno [19] states that for the Series 60, $C_B = 0.70$ hull, boundary layer calculations including both cross flow and tangential flow effects give worse accuracy than calculations considering only tangential flow. Also, Kinoshita [21] finds for the case of a strut that there is relatively little difference in the wave resistance values for the case of a displacement thickness δ^* which is constant with depth and the more realistic case where δ^* varies with depth.

Finally, there is the assertion first stated by Guilloton [10] and restated by Gadd [12] that the displacement thickness makes a correction in the right direction for the wrong reason. Guilloton states that neglect of the nonlinear free surface condition generally leads to stern waves which are too large. The reduction of the singularity strengths in the stern region caused by adding the displacement thickness gives the desired reduction in the stern waves.

3.1 Equivalent Axisymmetric and Two-Dimensional Bodies

Thus, a simple momentum integral approach is used to model the tangential flow on three approximations of the actual hull. Two are equivalent axisymmetric bodies which are respectively equal in cross-sectional area and perimeter, at a given longitudinal section x, to that of a double model of the hull, defined as the underwater portion plus its reflection about the free surface. The radii R_V and R_W of the equal cross-sectional area and perimeter bodies are respectively given by

$$R_V(x) = \sqrt{\frac{2A(x)}{\pi}} \tag{19}$$

$$R_W(x) = \frac{2P(x)}{2\pi} \tag{20}$$

where $A(x)$ is the cross-sectional area of the underwater hull, and

$P(x)$ is the perimeter of the underwater hull.

It is easy to show that the R_V and R_W bodies respectively reproduce the volume and surface area of the double model of the hull.

The third approximation is a two-dimensional body which has half-width Y_2 at each section x given by the average of the half-width f over the draft H of the underwater hull at that section

$$Y_2(x) = \frac{\int_0^H f(x, z)\, dz}{H} \tag{21}$$

It is easy to show that the Y_2 body preserves the volume of the underwater hull.

For these bodies the tangential flow momentum integral boundary layer equation is calculated from the bow to the stern. The wake is then left open. To investigate the effect of a narrower wake, a fourth boundary layer approximation is added whereby the two-dimensional flow is extended into the wake until the wake flow variables reach asymptotic values.

3.2 Momentum Integral Equation

The boundary layer formulation is first given for the axisymmetric bodies and modifications for the two-dimensional and wake flow cases will be indicated later. The momentum integral equation for boundary layer flow along an axisymmetric body may be conveniently obtained from the tangential flow equation for a representative streamline on a hull, assuming all cross flow terms and derivatives normal to the streamline to be negligible [29]

$$\frac{d\theta}{ds} = \frac{C_f}{2} - (H+2)\frac{\theta}{U_e}\frac{dU_e}{ds} - \frac{\theta}{R}\frac{dR}{ds}. \qquad (22)$$

where

$\theta = \int_0^\delta \left(1 - \frac{u}{U_e}\right)\frac{u}{U_e}\,d\lambda$ is the momentum thickness, (23a)

δ is the boundary layer thickness where $\frac{u}{U_e} = 0.995$,

u is the velocity in the boundary layer,

U_e is the velocity at the edge of the boundary layer,

s is the arc length measured on the body, starting from the bow,

$C_f = \tau_w / \frac{1}{2}\rho U_e^2$ is the skin–friction coefficient, (23b)

τ_w is the shear stress on the body surface,

$H = \delta^*/\theta$ is the shape parameter, (23c)

$\delta^* = \int_0^\delta \left(1 - \frac{u}{U_e}\right) d\lambda$ is the displacement thickness, and (23d)

R is the radius of the body.

The coordinate system used in the boundary layer calculations has the longitudinal axis X positive from bow to stern, contrary to the sense for x for the ship hull shown in Fig. 1.

The three terms on the right hand side of Eq. (22) show that the boundary layer grows due to skin friction, adverse pressure gradient ($dU_e/ds < 0$), and streamline convergence ($dR/ds < 0$). Granville [30] suggests that the pressure distribution be calculated by using the R_ν equivalent body, and that the boundary layer growth be calculated by using the R_w equivalent body. This would tend to approximate the overall friction drag acting on the actual hull surface. However, it is not clear that the R_w body gives a better approximation to the streamline convergence term than the R_1 body. Equations (20) and (21) show that in the case of a ship with a vertical stern contour of zero width, the case for most of the ships considered in the present study, R_ν and R_w take on the following values at the stern end

$$R_\nu = 0 \qquad (24a)$$

and

$$R_w = \frac{4H}{\pi} \qquad (24b)$$

where H is the draft of the actual ship. Consideration of the last term in Eq. (22), and Eq. (24) shows that the R_ν body would tend to have a significantly larger streamline convergence effect than the R_w body. This will also be demonstrated by the figures showing the R_ν and R_w body representations of the various hulls. The importance of the streamline convergence term in boundary layer growth has been emphasized by Patel [31]. He basically shows that the boundary layer is thickest for certain streamlines lying intermediate between the free surface and keel, where the streamline convergence is the strongest. The boundary layer is thinnest in the keel area where there is streamline divergence, and of intermediate thickness near the free surface, where the streamlines tend to be straight. Thus, in order to emphasize the important streamline convergence effect, calculations were made using the R_ν as well as the R_w body.

Taking the distribution of U_e to be known (this calculation will be described below), two additional equations are required to solve for the 3 unknowns θ, C_f, and H in Eq. (22). The two additional equations were taken to be the well-known Ludwieg-Tillmann friction relation [32] and the entrainment equation of Head [33] and Standen [34]:

$$C_f = 0.246 \times 10^{-0.678H} R_\theta^{-0.268} \qquad (25)$$

and

$$\frac{d}{ds}(\theta G) + \theta G\left(\frac{1}{U_e}\frac{dU_e}{ds} + \frac{1}{R}\frac{dR}{ds}\right) = F(G), \qquad (26a)$$

$$G = 1.535\,(H - 0.7)^{-2.715} + 3.3, \qquad (26b)$$

and

$$F(G) = 0.0306\,(G - 3.0)^{-0.653} \qquad (26c)$$

where $R_\theta = U\theta/\nu$ is the Reynolds number based on momentum thickness and ν is the fluid kinematic viscosity. Equations (22) and (26) may be viewed as two equations for the two unknowns θ and H, with Eq. (25) furnishing an expression for C_f which appears in Eq. (22).

The specialization to the two-dimensional case is particularly simple. In this case, the streamlines are straight and the terms involving dR/ds in Eqs. (22) and (26a) are set equal to zero, resulting in the following simpler momentum and entrainment equations

$$\frac{d\theta}{ds} = \frac{C_f}{2} - (H+2)\frac{\theta}{U_e}\frac{dU_e}{ds} \qquad (27a)$$

$$\frac{d}{ds}(\theta G) + \theta G\frac{1}{U_e}\frac{dU_e}{ds} = F(G) \qquad (27b)$$

The case for the wake requires further changes to the above equations. The momentum equation takes a simpler form in that the friction coefficient $C_f = 0$, resulting in

$$\frac{d\theta}{ds} = \frac{d\theta}{dX} = -(H+2)\frac{\theta}{U_e}\frac{dU_e}{dX} \qquad (28a)$$

The equation for the shape factor H is taken to be the commonly used Squire-Young far wake relationship [35]

$$\frac{\ln(U/U_{e_t})}{H_t - 1} = \frac{\ln(U/U_{e_w})}{H_w - 1} \qquad (28b)$$

where the subscripts t and w respectively denote values at the tail of the body and in the wake. It is of interest to note that while Eq. (28b) was derived for the two-dimensional wake behind an airfoil, Hatano and Hotta [36] have found that it also approximates well the mean value of H in the three-dimensional wake flow behind a tanker.

Since Eq. (28b) does not hold in the near wake, Eqs. (28a) and (28b) were treated in the following manner, to ensure that the following far wake relations would hold. It is well known, from momentum considerations, that the two-dimensional far wake momentum thickness θ_∞ must be related to the drag D on the body, as follows

$$\theta_\infty = \frac{D}{\rho U^2} \qquad (29)$$

The drag on the body was approximated by the following formula [37], which gives the increase in drag over the flat plate friction as a function of body thickness ratio t/L

$$D = \rho U^2 \theta_{FPt} \, (1 + 2t/L) \tag{30}$$

where θ_{FPt} is the flat plate momentum thickness at the tail of the body. Substituting Eq. (30) in Eq. (29), and noting that $H = 1$ in the far wake, the following equation results for δ_E^* and θ_E

$$\delta_E^* = \theta_E = \theta_{FPt} \, (1 + 2t/L) \tag{31}$$

Thus, Eq. (28a) was essentially integrated backwards, starting with $\theta = \theta_E$. Typically, the continuous wake was approximated by 3 to 5 inclined segments, for each of which the change in δ^* was the same.

3.3 Choice of Initial Conditions

A number of procedures are available for choosing the initial point s and starting values for the dependent variables θ and H. These include the use of available experimental data or an analytic procedure, such as that outlined by García and Zazurca [38]. Here, the following, approximately uniform approach was used to make the parametric runs for the various ship cases. The location of transition is fixed at a value of s_0 corresponding to $X/L = 0.05$, a typical location for turbulence stimulators used in model tests. The initial value of the momentum thickness θ_0 is set equal to 0.7 of the corresponding value for a flat plate with the same length Reynolds number, while the initial value of the shape factor H_0 is set equal to the flat plate value, usually in the 1.4 to 1.5 range. This was largely based on the results of [29, 39, 40] which show that the boundary layer thicknesses θ and δ^* in the bow region are usually somewhat smaller than flat plate values, due to the favorable pressure gradient and streamline divergence in this region, while H is typically 1.4. Numerical experimentation showed that in the case of the displacement thickness δ^*, different choices of θ_0 and H_0 led to differences in the bow region which tended to propagate unchanged to the stern region. These differences were quite small and essentially negligible compared to values of δ^* in the stern region where most of the boundary layer growth takes place due to the adverse pressure gradient and streamline convergence.

3.4 Calculation of Pressure Distribution on Body Surface

In the present thin-boundary layer approach, where the pressure is assumed to be constant throughout its thickness, the edge velocity U_e appearing in Eqs. (22), (27a), and (28a) is simply related to the pressure p on the body by Bernoulli's equation.

$$U_e = U\sqrt{1 - C_p} \tag{32}$$

where $C_p = (p - p_0)/\left(\frac{1}{2}\rho U^2\right)$ is the pressure coefficient, and p_0 is the ambient pressure far from the body.

There are well-known numerical procedures, such as the Hess and Smith method [41], for calculating the potential distribution on arbitrary three-dimensional bodies to any desired degree of accuracy. While the method in [41] is straightforward, a number of numerical steps are involved, including matrix inversion. In the present study, the simple and direct slender-body and thin-airfoil theories, as outlined by Karamcheti [42], are used to calculate the pressure distribution. The accuracy of the method is improved by using two modifications which are described later. In addition to its obvious simplicity, the present choice of calculation methods was also based on consideration of the pressure accuracy requirements at both ends of the body (where slender-body and thin-airfoil theories are most inaccurate). The approach for obtaining initial conditions for the boundary layer calculations described above essentially makes it unnecessary to have an accurate description of the pressure at the bow end. At the stern end, it is well-known that the potential flow pressure distribution is substantially modified by the viscous flow.

In conventional slender-body and thin-airfoil theories, the longitudinal axis of the body is divided into a series of $N - 1$ line segments of length ΔX_i, over each of which is placed a source of uniform density q_i, where ΔX_i and q_i may vary from segment to segment. The potential of the source for the axisymmetric and two-dimensional cases, G_A and G_{2D}, are respectively given by

$$G_A = \frac{1}{r} = \frac{1}{\sqrt{(X - X')^2 + R^2}}, \text{ and} \tag{33a}$$

$$G_{2D} = \log \bar{R} = \log\sqrt{(X - X')^2 + Y^2} \tag{33b}$$

where (X, R) is the axisymmetric coordinate system, and (X, Y) is the two-dimensional coordinate system. The source strengths q_{Ai} and q_{2Di} are respectively given by

$$q_{Ai} = \frac{U}{4\pi}\left[\frac{dA}{dX}\right]_i = U2\pi R_{Vi}\left[\frac{dR_V}{dX}\right]_i \tag{34a}$$

$$q_{2Di} = \frac{U}{2\pi}\left[\frac{d2Y_2}{dX}\right]_i \tag{34b}$$

The resultant velocity at an arbitrary spatial point may be obtained by taking derivatives of G with respect to X and R (or X and Y), integrating over the ith source segment, and summing over the $N - 1$ segments. For the axisymmetric body, the consistent approximation for U_e/U is obtained by evaluating the velocities on the body surface (X, R), and neglecting higher powers of the velocity in the X-direction, but not in the R-direction. For the two-dimensional body, the consistent approximation is obtained by evaluating the velocities on the longitudinal axis $(X, 0)$ and neglecting higher powers of the velocities in both the X and Y directions. In the case of the wake flow, the values of U_e/U are simply obtained by evaluating the velocities for $X > L$.

To correct the well-known inaccuracies of the theory at the ends of the body, a singularity gap correction proposed by Moran [43] is applied at the bow and stern ends. In this approach, the singularity distribution does not extend all the way to the end, but there is a gap equal in length to one half of the nose radius of the body.

A second modification is made to account for the effect of viscous flow on the stern pressure distribution. It is well-known that U_e does not approach zero at the stern end, as predicted by potential flow theory. The modification consists of an iterative procedure. For the initial boundary layer calculation, the calculated values of U_e over the last 5% of the body are discarded and are replaced by a linear extrapolation of the calculated values for $X/L = 0.95$. The calculated displacement thickness δ^* is then added to the body, resulting in a somewhat larger body with a stern region which is significantly less blunt. For the second (and later) boundary layer calculations, the calculated U_e over the entire displacement body (up to the stern end, $X/L = 1.0$) is used. This is possible because of the much smoother variation of the shape of the stern region of the displacement body. The above procedure is repeated for a total of four iterations. In most cases, there is little difference in the calculated boundary layer characteristics between the third and fourth iterations.

4. HULL CHARACTERISTICS

4.1 Overall Geometric Characteristics

The ship hulls were chosen based on the availability of experimental data to validate the theoretical calculations, the existence of other thin and slender ship calculations to compare with the present approach, and the need to cover a range of geometrical characteristics to illustrate the boundary layer effect.

For three of the chosen hulls: Wigley [25], Series 60 ($C_B = 0.60$) [25], and Sharma strut [26] abundant experimental and calculated data are available for comparison purposes. The Series 60SC hull, which is the Series 60 hull with the curved stern contour replaced by a straight contour, was chosen largely to investigate the effect of stern contour shape on the differences between thin and slender ship theories. The Wig20 hull, which is the Wigley hull with twice the width, was chosen to investigate the boundary layer effect on a thicker hull.

Table 1 summarizes the principal geometric characteristics of the hulls: length L, beam-to-length ratio B/L, draft-to-length ratio H/L, beam-to-twice draft ratio $B/2H$, block coefficent C_B, and wetted area coefficient C_S, where

$$C_B = \frac{V_D}{LBH} \text{ is the block coefficient,} \tag{35a}$$

$$C_S = \frac{S_W}{L(2H + B)} \text{ is the wetted area coefficient,} \tag{35b}$$

V_D is the volume of the underwater hull, and

S_W is the wetted surface area.

The table shows that the length L used in the calculations for all the hulls, except the Sharma strut, is 6.1 m. This is representative of the length used in model tests of the Wigley and Series 60 hulls. The length used for the Sharma strut experiments was 2 m, as shown in the table.

Table 1 — Summary of Geometric Characteristics for the Five Ship Hulls

Ship Hull	L (m)	B/L	H/L	$B/2H$	C_B	C_S
Wigley	6.1	0.1	0.0625	0.80	0.44	0.66
Series 60	6.1	0.133	0.053	1.25	0.60	0.71
Sharma	2.0	0.05	0.150	0.17	0.66	0.95
Wig20	6.1	0.2	0.0625	1.60	0.44	0.61
Series 60SC	6.1	0.133	0.053	1.25	0.60	0.72

Table 2 gives the analytical formulas for the half-width f of the Wigley, Sharma, and Wig20 hulls. Figure 2 shows the stem and stern contours as well as the half-width section shapes for the Series 60 and Series 60SC hulls. Figure 2 shows that the Series 60 has a nonvertical stern contour and a slight deviation of the stem contour from the vertical, while the Series 60SC has a vertical stern contour. The other three hulls have vertical stem and stern contours.

4.2 Equivalent Body Representations

Figures 3, 4, 5, 6, and 7 respectively show the equivalent R_V, R_W, and Y_3 body representations of the Wigley, Series 60, Sharma, Series 60SC, and Wig20 hulls. Several points should be noted.

Table 2 — Formulas for the Half-Width f of Wigley, Sharma, and Wig20 Hulls

$x' = (x + L/2)/(L/2)$

$x' = -1$ is the aft perpendicular

$x' = +1$ is the forward perpendicular

1. Wigley hull

$$f_1 = \frac{B}{2}(1 - x'^2)[1 - (z/H)^2]$$

2. Sharma strut

$$f_2 = \frac{B}{2}(1 - x'^2)$$

3. Wig20 hull

$$f_3 = 2f_1$$

First, the figures show that the R_V body for all five hulls goes to zero with a large slope at both ends of the body. In particular, this would lead to large value of the streamline convergence term $(\theta/R)dR/ds$ in Eq. (22) and thus to a large value of θ at the stern. On the other hand, with the exception of the Series 60 hull, which has a nonvertical stern contour, the R_W body has only a small slope at both ends of the hull. This leads to a resultant small streamline convergence effect.

Secondly, the figures show that, with the exception of the Sharma strut, the R_V and R_W bodies agree fairly well with each other, except for the above mentioned discrepancies at the ends of the hull. This tends to indicate that a circle is a reasonable approximation for these hull cross sections. This is also verified by the fact that the ratios $B/2H$ for these hulls are not far from 1, the value for a double hull with a circular cross section. For the thin, deeply submerged Sharma strut, which is essentially a two-dimensional body, the value of $B/2H$ is much less than 1 and Fig. 4 shows that the R_V and R_W bodies differ widely. Figures 8, 9, and 10 show the equivalent bodies for the Sharma strut for larger values of B/L: 0.1, 0.2, and 0.3, respectively. The figures do show a better agreement of the R_V and R_W bodies as B approaches $2H$. However, even at $B/L = 0.3$, where $B/2H \cong 1$, the agreement between the R_V and R_W bodies is not as good as that of the other four hulls. This is largely due to the fact that the Sharma strut is wall-sided (half-width f does not vary with depth), while the other four hulls are non-wall-sided.

4.3 Computer Modeling of the Hulls

Table 3 summarizes the input geometrical data and Froude number range for the computer runs. The table gives:

- NX, the number of longitudinal X-stations at which the half-width f is input into the program
- NZ, the number of vertical z-stations at which f is input
- $Fn1$, the lowest Froude number Fn for which wave resistances are calculated
- $Fn2$, the highest Froude number for which wave resistances are calculated.

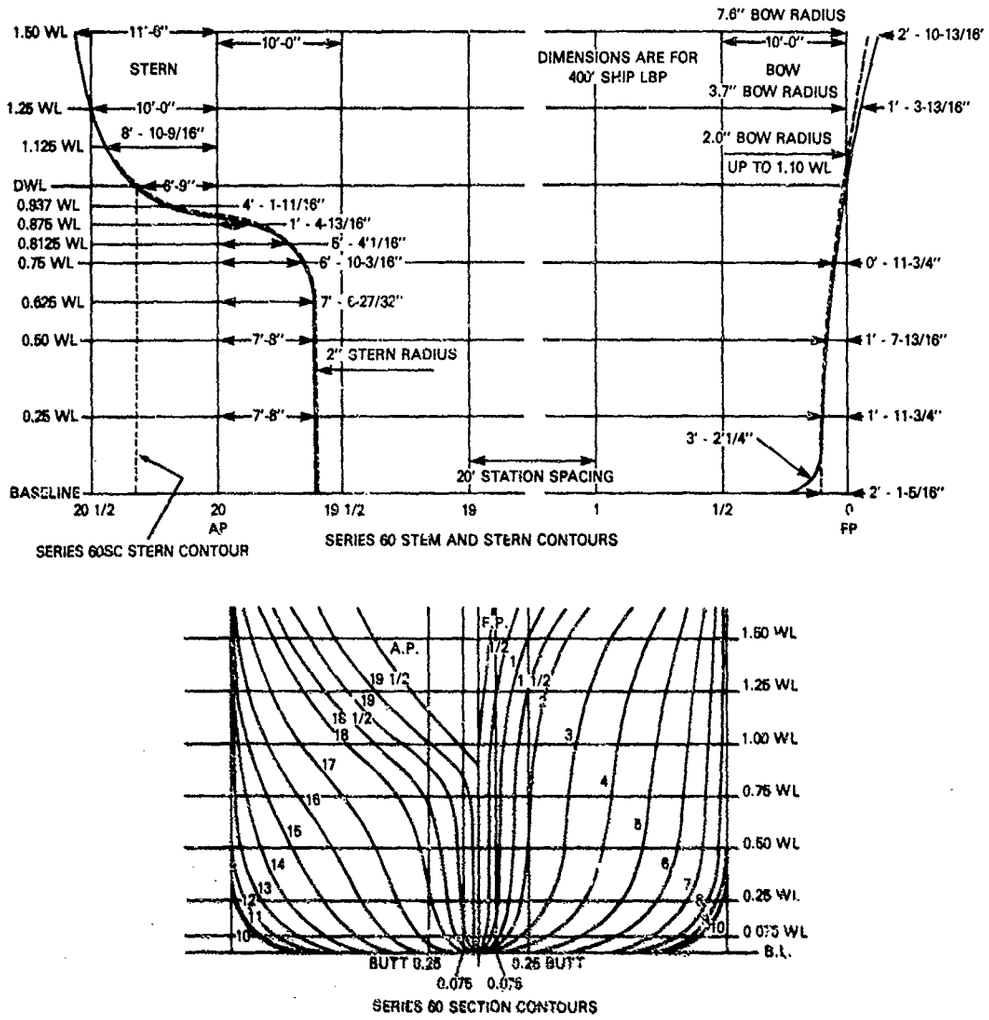

Figure 2. Geometric Description of Series 60 and Series 60SC Hulls, $C_B = 0.60$

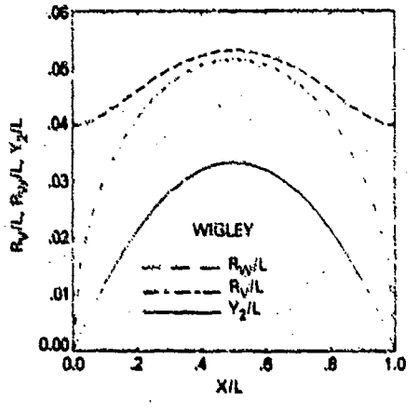

Figure 3. Equivalent Bodies for Wigley Hull

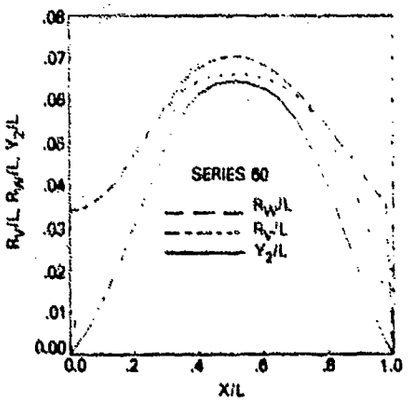

Figure 4. Equivalent Bodies for Series 60 Hull

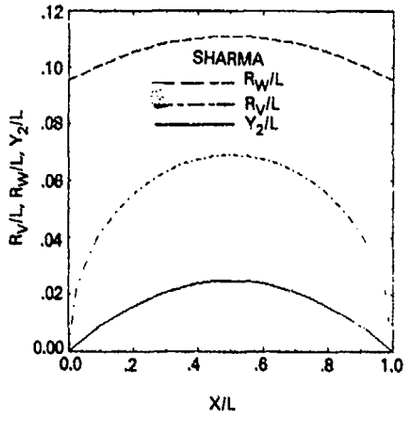

Figure 5. Equivalent Bodies for Sharma Strut

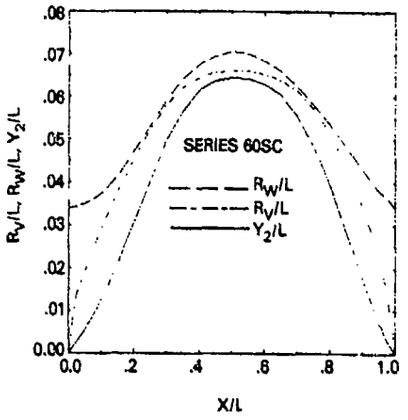

Figure 6. Equivalent Bodies for Series 60SC Hull

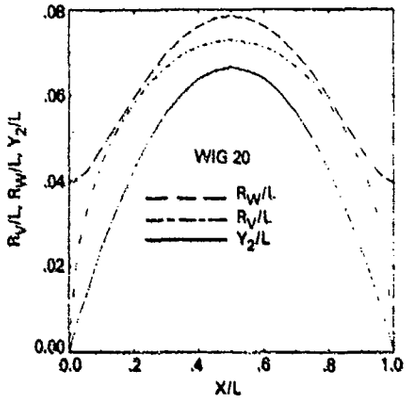

Figure 7. Equivalent Bodies for Wig20 Hull

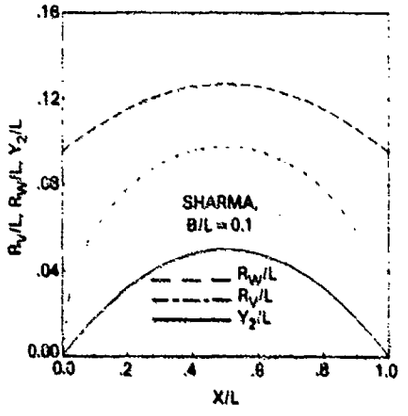

Figure 8. Equivalent Bodies for Sharma Strut, $B/L = 0.1$

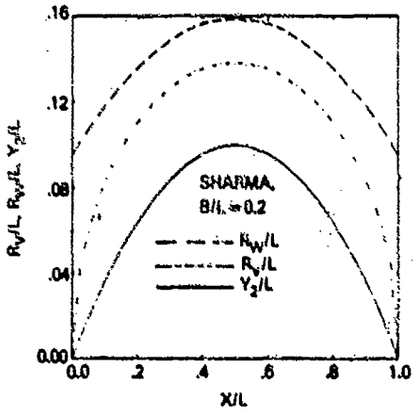

Figure 9. Equivalent Bodies for Sharma Strut, $B/L = 0.2$

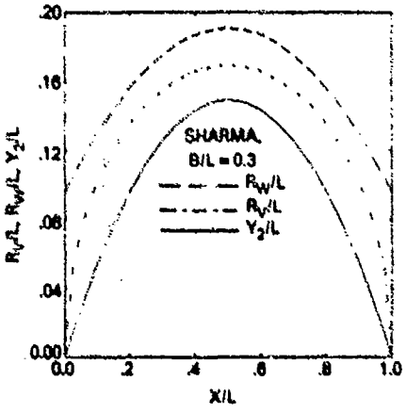

Figure 10. Equivalent Bodies for Sharma Strut, $B/L = 0.3$

Table 3 — Summary of Computer Runs for the Five Ship Hulls

Ship Hull	NX	NZ	$Fn1$	$Fn2$
Wigley	25	15	0.16	0.48
Series 60	25	7	0.14	0.36
Sharma	25	16	0.21	1.00
Wig20	25	15	0.16	0.48
Series 60SC	25	7	0.14	0.36

The value of NX for all the hulls is 25. For the three hulls which are analytically defined (Wigley, Sharma, and Wig20), NZ = 15 or 16. It is reduced to 7 for the Series 60 and Series 60SC hulls, which corresponds to the number of vertical stations at which f is tabulated in [25]. The Froude number range for the three hulls for which model test data are available (the Wigley, Series 60, and Sharma hulls) correspond to the experimental range. The Froude number ranges for the Series 60SC and Wig20 hulls respectively correspond to those for the parent Series 60 and Wigley hulls.

5. Boundary Layer and Wake Results

Before discussing the effect of the calculated boundary layer on the wave resistance and weighted amplitude spectral functions, it is of interest to note the behavior of the calculated boundary layer and wake flows. Table 4 shows δ_T^*/δ_{Fn}^*, the ratio of the calculated and flat plate displacement thickness at the tail for the three equivalent bodies for all five hulls. The table shows that, except for the Series 60 hull which has a curved stern contour, the R_W body gives the smallest value of δ_T^*, ranging from 1.1 to 1.9 times the flat plate value. This is due to a combination of the weaker pressure gradient on an axisymmetric body (compared to that on a two-dimensional body) and the previously noted small streamline convergence effect. The table shows that the strong streamline convergence for the R_P body gives the largest values of δ_T^*, ranging from 5.2 to 8.4 times the flat plate value. The Y_2 body gives values of δ_T^* which lie between those for the R_P and R_W bodies. This body has no streamline convergence but a stronger pressure gradient.

Table 4 — Ratio δ_T^*/δ_{Fn}^* at Stern End for R_W, R_P and Y_2 Bodies for the Five Ship Hulls

	Wigley	Series 60	Sharma	Wig20	Series 60SC
R_W	1.12-1.17	3.38-3.79	1.36-1.44	1.89-1.91	1.80-1.83
R_P	5.22-5.29	8.33-8.44	5.64-5.81	5.95-5.98	8.33-8.44
Y_2	1.75-1.75	2.96-2.97	1.49-1.50	3.36-3.43	2.96-2.97

Table 5 shows ranges for θ_E/θ_1 and δ_E^*/δ_T^*, which are respectively the ratios of the momentum and displacement thicknesses at the beginning and end of the two-dimensional wake, for the five hulls. The ratios are inversely related to B/L of the hull, and range from 0.4 to 0.8 for θ_E/θ_1 and 0.3 to 0.5 for δ_E^*/δ_T^*.

Table 5 — Ratio of Initial and Final Wake Momentum and Displacement Thicknesses, θ_E/θ_1, and δ_E^*/δ_T^*

Hull	θ_E/θ_1	δ_E^*/δ_T^*
Wigley	0.68-0.70	0.46
Series 60	0.53-0.56	0.31
Sharma	0.79-0.82	0.53-0.54
Series 60SC	0.53-0.56	0.31
Wig20	0.43-0.45	0.24-0.25

Most of the wake calculations were performed with the wake divided into 3 segments, each representing an equal change in δ^*. The end of the wake was chosen to be the X value at which the change in δ^* from δ_T^* had reached 0.99 of the required change ($\delta_T^* - \delta_E^*$). That is, at the selected end of the wake the error ϵ in the actual value of δ^*, δ_{Ea}^*, is 0.01, where ϵ is given by

$$\epsilon = \frac{\delta_{Ea}^* - \delta_E^*}{\delta_T^* - \delta_E^*} \tag{36}$$

where δ_E^* is given in Eq. (31). In order to give an indication of the wake lengths, Table 6 gives values of X_E/L for ϵ = 0.01 to 0.10 for the Wigley hull at Fn = 0.2. The table shows that X_E/L decreases from 3.0 at ϵ = 0.01 to 1.4 at ϵ = 0.1. Several computer runs for the Wigley hull show that the calculated wave resistance values show little change for ϵ between 0.01 and 0.05. Also, there is little change when the number of wake segments is increased from 3 to 5.

Table 6 — Variation of Wake End Point X_E/L with Error ϵ in End Value of δ^*, Wigley Hull, Fn = 0.2

ϵ	X_E/L
0.01	2.98
0.02	2.35
0.03	2.01
0.05	1.72
0.10	1.42

6. Wave Resistance Results

The wave resistance results are presented in terms of the wave resistance coefficient C_W given by

$$C_W = \frac{R_W}{\frac{1}{2}\rho U^2 S_W} \tag{37}$$

Figures 11, 12, 13, 14, and 15 respectively show the values of C_W for the Wigley, Series 60, Sharma, Series 60SC, and Wig20 hulls. Figure 11 shows the thin and slender ship values of C_W calculated by the present approach for no viscous correction, for the R_P body, for the Y_2 body, and for the Y_2 body + wake, the theoretical results for Lackenby as given in [25], the range of available experimental data corrected for sinkage and trim [44], and the recent measured data [45] specifically for a fixed model. Figure 12 again shows the thin and slender ship calculated values of C_W for no viscous correction, for the R_P body, for the Y_2 body, and for the Y_2 body + wake, the slender ship calculations of Scragg [46], and the range of experimental data given in [25], which are for a model free to sink and trim except for the four discrete points in the lower right hand corner of the figure. Figure 13 gives the thin ship calculated values for no viscous correction, for the R_P body, and for the Y_2 body, the calculated thin ship and measured values given in [26]. Figure 14 simply gives the ratios of the thin and slender ship values between the Series 60 and Series 60SC hulls, calculated with no viscous correction. Figure 15 shows the thin and slender ship calculated values for no viscous correction, and only the slender ship values for the R_P body, Y_2 body, and Y_2 body + wake.

The reasons for choosing the above particular sets of data (for example, consistently omitting the calculated results

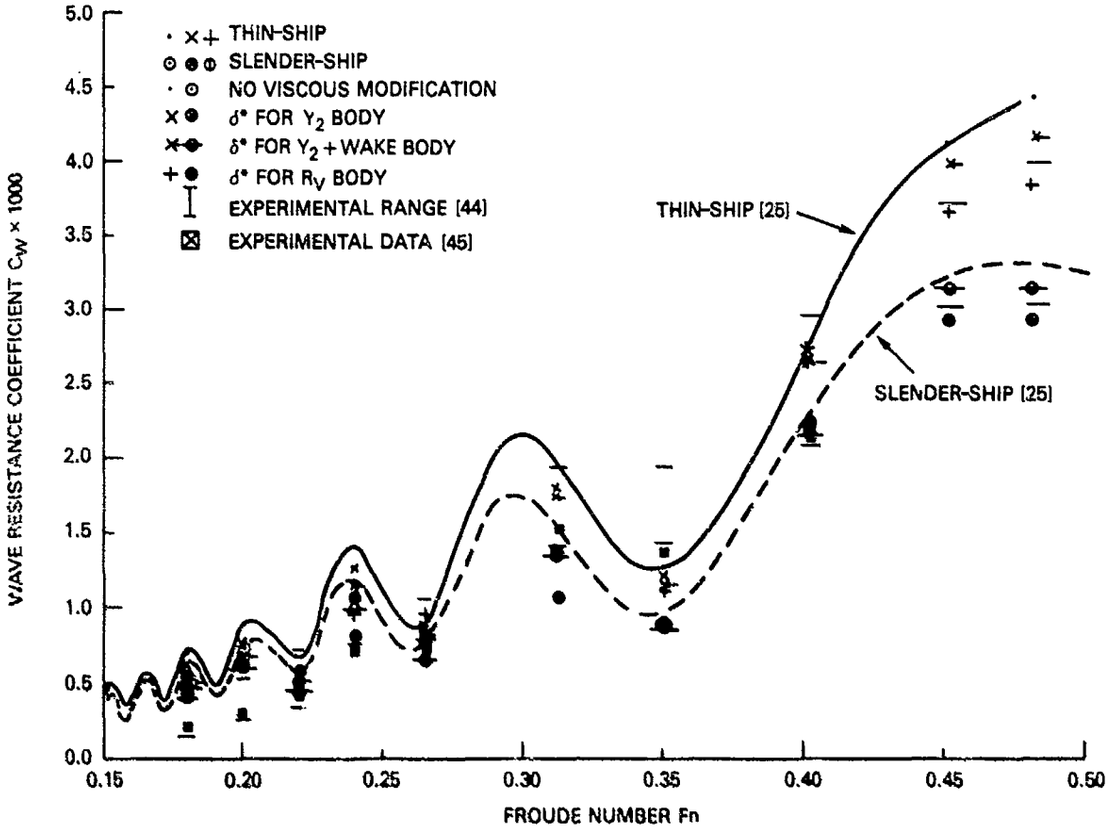

Figure 11. Wave Resistance Coefficients for Wigley Hull

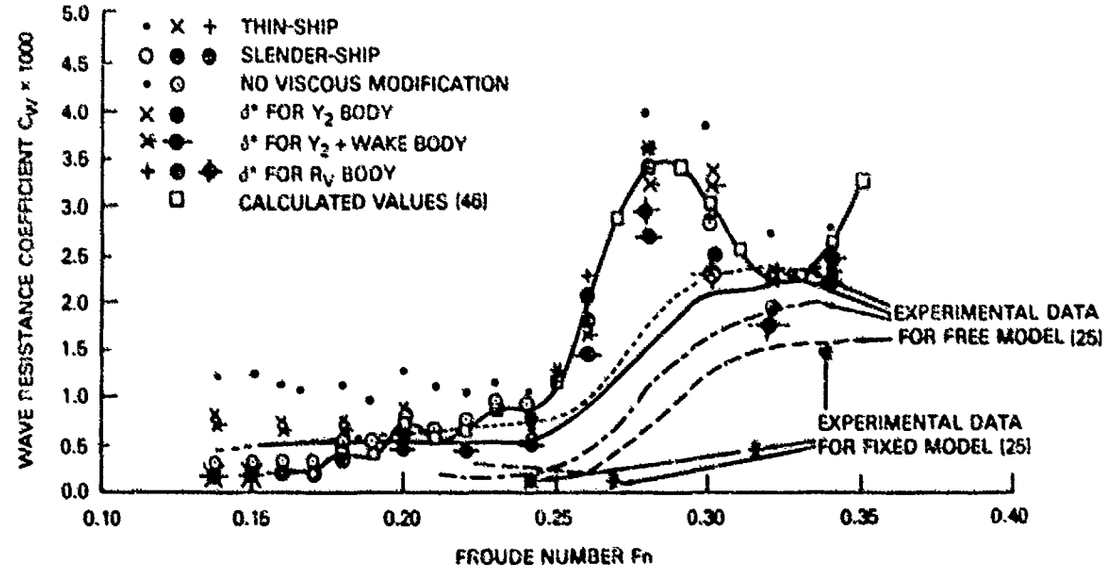

Figure 12. Wave Resistance Coefficients for Series 60 Hull

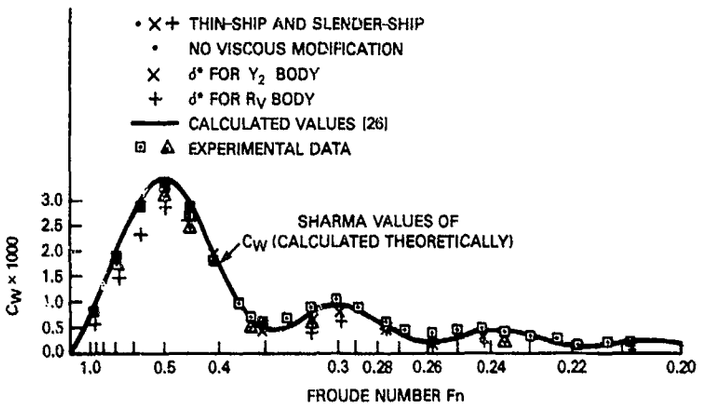

Figure 13. Wave Resistance Coefficients for Sharma Strut

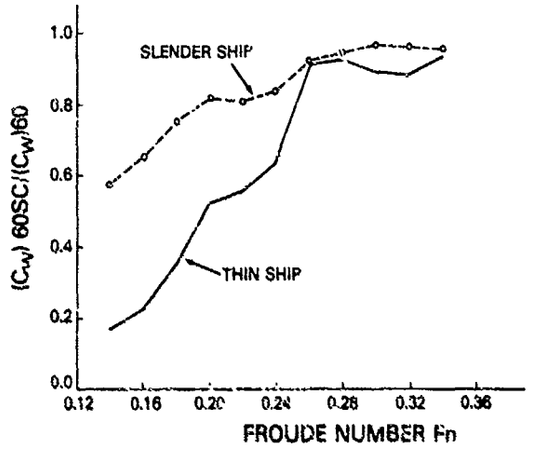

Figure 14. Wave Resistance Coefficients for Series 60SC Hull

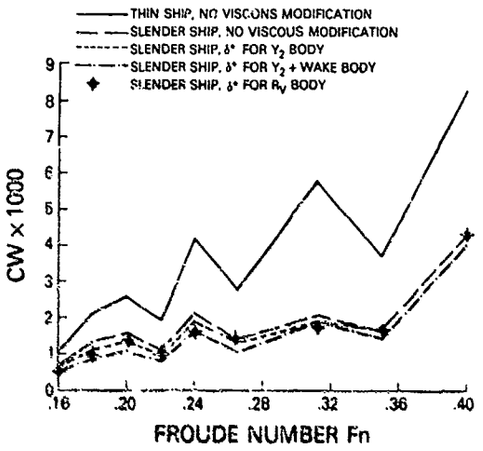

Figure 15. Wave Resistance Coefficients for Wig20 Hull

for the R_W body) will be given in the following discussion. The results are discussed in three ways:

(a) agreement of the potential flow results calculated by the present approach with other theoretical values using thin and slender ship theories,

(b) the differences between thin and slender ship theories for the different hulls, and

(c) the effect of the various boundary layer models on the calculated wave resistance.

6.1 Comparison with Other Calculations

In all cases, the agreement of the present calculated values with other theoretical values is quite good. In particular, the agreement of the present thin and slender ship calculated values is to within plotting accuracy with the corresponding results of Lackenby for the Wigley hull, as shown in Fig. 11. Similarly good agreement holds for the thin ship values calculated by the present approach and corresponding results by Sharma, as shown in Fig. 13. In the case of the Series 60 hull, Fig. 12 shows that there are small but noticeable differences between the slender ship results of the present approach and those of Scragg [46]. This is probably due to the use of triangular panels to model the hull surface in [46] while quadrilateral panels are used in the present approach.

6.2 Differences Between Thin and Slender Ship Theories

On the whole, differences are along expected lines. In the case of the thin Sharma strut, nearly all the thin and slender ship values, with or without viscous correction, agree to within plotting accuracy. For this reason, only the thin ship values are shown in Fig. 13. Also, in the case of the Wigley and Wig20 hulls, there is the expected trend that there are larger differences between the two theories for the thicker Wig20 hull. The differences between the theories is typically 30 percent for the Wigley hull, with $B/L = 0.1$, and rises to typically 100 percent for the Wig20 hull, which has $B/L = 0.2$.

Figure 12 shows that in the case of the Series 60, there is a large difference between the theories at low Froude numbers (the slender ship value is only 0.2 of the thin ship value at $Fn = 0.14$) between the theories at low Froude numbers. Figure 14 shows that this difference is substantially reduced when the stern contour is made vertical. Apparently the curved stern contour in the case of the Series 60 has the effect of placing most of the stern contour (which has zero width) very close to Station $19\frac{1}{2}$ (which has finite width) with resultant severe gradients of ship thickness. The modification to a straight stern contour has the effect of pushing back the stern contour from Station $19\frac{1}{2}$, leading to a more gentle gradient of ship thickness.

6.3 Effect of Boundary Layer Corrections

The reason for omitting all the results for the R_W body is as follows. For four of the five hulls, with the exception of the Series 60, the correction due to this body is extremely small and plotting these points would simply add to the clutter in the figures. This may have been inferred from the results of Table 4 which shows that for these hulls the R_W body gives the smallest boundary layer thickness. In the case of the Series 60 hull, the correction due to the R_W body is large, but is generally similar to that of the R_V body. Hence, the R_V results are again omitted.

In the case of the Series 60SC hull, the boundary layer corrections due to the R_V, Y_2, and Y_2 + wake bodies are similar to those of the Series 60 hull, and the correction due to the R_W body is small. Hence, Fig. 14 omits all boundary layer corrections results for this hull.

The results for the Wigley and Series 60 hulls show that the viscous corrections for a given equivalent body are similar for both thin and slender ship theories. Thus, viscous corrections are shown only for the Wig20 hull, for which there are no experimental data.

As in the case with previous studies in this area, the figures show that the addition of the displacement thickness usually, but not always, decreases C_W. The R_V body usually gives larger corrections to C_W for the thinner hulls, the Wigley and Sharma, while the Y_2 + wake body generally gives somewhat larger corrections for the thicker hulls, the Wig20 and Series 60. Apparently, for the thinner hulls, the streamline convergence effect (acting on the R_V body) which is strong but extends only over a short distance near the tail, dominates the adverse pressure gradient effect (of the Y_2 + wake body) which is less explosive but acts over a longer distance. The reverse is true for the thicker hulls. In the case of the Wigley hulls, the larger corrections due to the R_V body are generally somewhat more accurate than those due to the Y_2 + wake body in bringing the C_W values into better agreement with the data for a fixed model [45], which lie near the lower limit of the corrected range given in [44]. However, in the case of the Sharma hull, the corrections due to the R_V body substantially worsens the agreement with the experimental results. This is not surprising in view of the fact that the flow is essentially two-dimensional on this hull, with little streamline convergence. In the case of the Series 60 hull, the larger corrections due to the Y_2 + wake body bring the C_W values appreciably closer to the experimental points for a fixed model, although they still lie above these points.

Overall, the Y_2 + wake body makes corrections which are generally more consistent in bringing better agreement with experimental results than those due to the R_V body. In the case of hulls with vertical stern contours, the R_W body makes corrections which are entirely too small. The Y_2 body makes corrections which are somewhat smaller than those which include the wake.

7. Weighted Amplitude Function Results

Figures 16, 17, and 18 show the dimensionless weighted amplitude function A^*/L^2, defined in Eq. (18), for the following three cases, respectively, for which the wave resistance values exhibit various features of interest:

(a) Series 60, Series 60SC, Fn = 0.14
(b) Series 60, Fn = 0.32
(c) Wigley, Fn = 0.24

In Case (a), there is a large difference between the thin ship and slender ship values for C_W for the Series 60 hull, and a substantially smaller difference for the Series 60SC hull. In both Cases (b) and (c), the viscous corrections make rather large changes to the C_W values. Also, experimental data from Tsutsumi [47] are available for Case (b) and are included in Fig. 17. Case (c) corresponds to a Froude number for the Wigley hull at which the C_W values for both the R_V and Y_2 + wake wake bodies lie within the experimental range.

7.1 Series 60, Series 60SC, Fn = 0.14

Figure 16 shows that the high value of C_W for the thin ship case for the Series 60 hull is confirmed by the fact that this case, taken as the reference case, has the highest amplitudes. The thin ship case for the Series 60SC has substantially lower amplitudes than the reference case with essentially no change in shape. The slender ship case for the Series 60 hull has lower amplitudes, with some change in shape for $32° < \theta < 42°$, and $\theta > 75°$. The use of the Y_2 body lowers the amplitudes of the reference case with essentially no change in shape or shift in phase. On the other

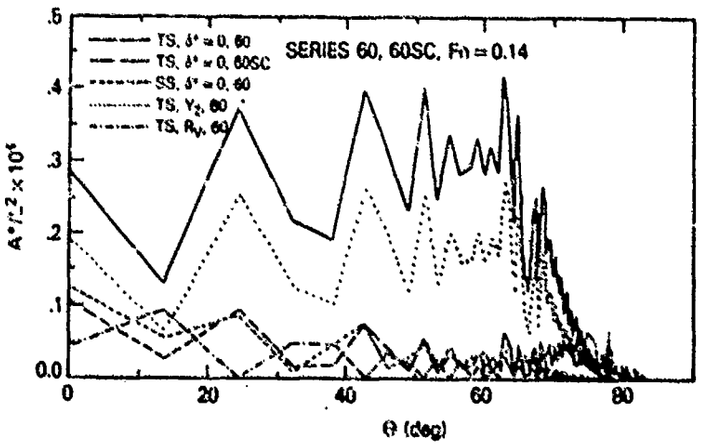

Figure 16. Weighted Amplitude Functions for Series 60, Series 60SC Hulls, $F_n = 0.14$

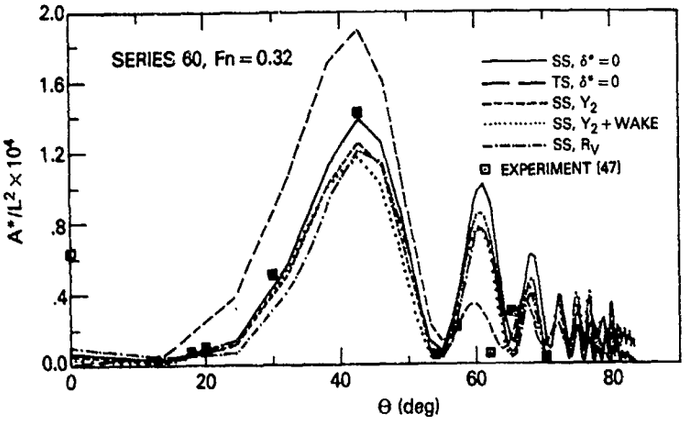

Figure 17. Weighted Amplitude Functions for Series 60 Hull, $F_n = 0.32$

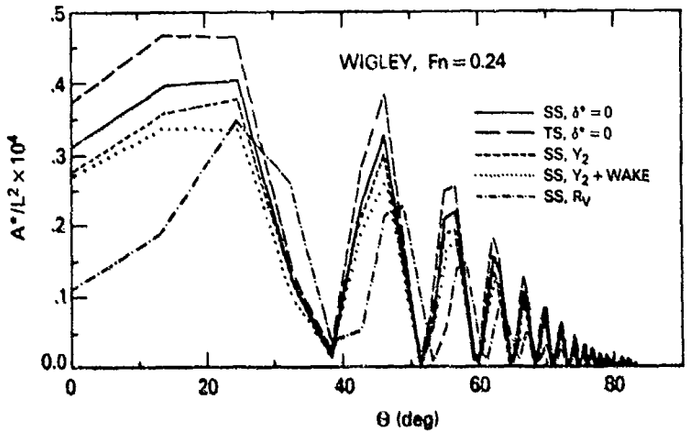

Figure 18. Weighted Amplitude Functions for Wigley Hull, $F_n = 0.24$

hand, the use of the R_V body not only lowers the amplitudes but results in a shape which is 180° out of phase with the reference case.

7.2 Series 60, Fn = 0.32

Here, the slender ship calculation with no viscous correction is taken as the reference case. The thin ship calculation has higher amplitudes in the dominant region $\theta < 50°$, which leads to the higher value of C_W shown in Fig. 12. However, the reference case has higher secondary peaks. The addition of the correction for the Y_2 body results in a noticeable general downward shift of the reference amplitudes for $\theta < 70°$, and the addition of the wake results in a further, smaller decrease of the amplitudes. Unlike the previous case, where the R_V body caused a phase shift of 180° relative to the potential flow case, here its amplitude shape agrees reasonably well with the amplitudes for the Y_2 and Y_2 + wake bodies.

For a free-running model, Tsutsumi [47] obtains a C_W value of approximately 2.1×10^{-3}, which agrees closely with the C_W value of the reference case. The figure shows that the equality is achieved through a redistribution of the amplitude function, with the experimental amplitudes higher for $\theta < 20°$ and the calculated amplitudes higher for $\theta > 60°$. It is encouraging to note that the agreement is good in the intermediate range $20° < \theta < 60°$.

7.3 Wigley, Fn = 0.24

The reference case will again taken to be the potential flow slender ship calculation. As noted in previous cases, the higher C_W value of the thin ship results from a raising of the amplitude values with no phase shift. Similarly, the reduction in C_W due to the Y_2 and Y_2 + wake bodies results from a reduction in the amplitudes with no appreciable phase shift. The use of the R_V body reduces the amplitudes and results in a phase shift of several degrees, which lies intermediate between the 180° phase shift observed for Case (a) and the lack of phase shift observed for Case (b).

7.4 Summary

The higher values of C_W for the thin ship theory relative to the slender ship theory arise from higher amplitudes for the thin ship case. There is no appreciable phase shift in the functions. Similarly, the reduction in C_W due to the Y_2 and Y_2 + wake bodies is due to a decrease in the amplitudes, with no perceptible phase shift. The use of the R_V body results in a reduction of the amplitudes and phase shifts ranging from 0 to 180°. For the Series 60 hull at Fn = 0.32, it is

shown that an equality in calculated and measured C_W results from a cancellation of differences in the amplitude function at low and high values of θ, with excellent agreement over an intermediate range of θ.

8. Conclusions

The effect of four boundary layer approaches on the wave resistances predicted by thin ship and zeroth order slender ship theories has been investigated. The four approaches consist of using axisymmetric bodies with equivalent wetted area (R_W body) and equivalent volume (R_V body), a two-dimensional body with equivalent thickness (Y_2 body) and this body with wake flow (Y_2 + wake body). The R_W body usually gives the smallest boundary layer thickness and, consequently, the smallest corrections to the wave resistances. This is due to a combination of the relatively weak pressure gradient on the axisymmetric body and a small streamline convergence effect. The R_V and Y_2 + wake bodies give corrections which are comparable in magnitude, with the R_V body giving the larger corrections for the thinner hulls and the reverse being true for the thicker hulls. For the thin Sharma strut, the R_V body gives corrections which are entirely too large. For the Wigley hull, the corrected predictions tend to bracket the data for a fixed model. For the Series 60 hull, the agreement is poor, with the calculated results lying above the fixed-model data.

The corrections for the Y_2 and Y_2 + wake bodies reduce the overall levels of the weighted amplitude function, without any appreciable shifts in phase. On the other hand, the use of the R_V body makes changes in phase as well as level of the function. In the case of the Series 60 hull, where the measured value of wave resistance coincides with a predicted value, the amplitude functions agree over the middle range of wave direction, with compensating differences at the lower and upper ranges.

Acknowledgment

This work was supported by the Naval Research Laboratory Computational Hydrodynamics Program.

References

1. Michell, J.H., "The Wave Resistance of a Ship," Philosophical Magazine, Vol. 45, No. 272, pp. 106-123, Jan. 1898.

2. Hogner, E., "Eine Interpolationsformel für den Wellenwiderstand von Schiffen," Jahrbuch der Schiffbautechnischen Gesellschaft, Vol. 33, pp. 452-456, 1932.

3. Weinblum, G., "Über die Berechnung des wellenbildenden Widerstandes von Schiffen, insbesondere die Hognersche Formel," Zeitschrift für angewandte Mathematik und Mechanik, Vol. 10, No. 5, pp. 453-466, Oct. 1930.

4. Koch, P. and Noblesse, F., "A Note on the Waterline Integral and the Thin-Ship Approximation," Workshop on Ship Wave-Resistance Computations, Vol. 2, pp. 515-522, Nov. 1979.

5. Eggers, K., "A Method for Assessing Numerical Solutions to a Neumann-Kelvin Problem," Workshop on Ship Wave-Resistance Computations, Vol. 2, pp. 526-537, Nov. 1979.

6. Noblesse, F., "A Slender-Ship Theory of Wave Resistance," Journal of Ship Research, Vol. 27, No. 1, pp. 13-33, March 1983.

7. Tsutsumi, T., "Calculation of the Wave Resistance of Ships by the Numerical Solution of Neumann-Kelvin Problem," Workshop on Ship Wave-Resistance Computations, Vol. 2, pp. 162-201, Nov. 1979.

8. Chang, M.S., "Wave Resistance Predictions by Using a Singularity Method," Workshop on Ship Wave-Resistance Computations, Vol. 2, pp. 202-214, Nov. 1979.

9. Adachi, H. and Takeshi, H., "Neumann-Kelvin Problem Solved by the Iterative Procedure Using Hess and Smith Solver Program," Second DTNSRDC Workshop on Ship Wave-Resistance Computations, pp. 281-320, Nov. 1983.

10. Guilloton, R., "L'Étude Théorique du Bateau en Fluide Parfait," Bulletin de l'Association Technique Maritime et Aéronautique, Vol. 1964, pp. 537-574, 1964.

11. Hong, Y.S., "Numerical Calculation of Second-Order Wave Resistance," Journal of Ship Research, Vol. 21, No. 2, pp. 94-106, June 1977.

12. Gadd, G.E., "Wave Theory Applied to Practical Hull Forms," International Seminar on Wave Resistance, pp. 149-158, Feb. 1976.

13. Dawson, C.W., "A Practical Computer Method for Solving Ship-Wave Problems," Second International Conference on Numerical Ship Hydrodynamics, pp. 124-135, Sep. 1977.

14. Amromin, E.L. et al., "On the Influence of Nonlinearity of Boundary Conditions at the Hull and Water Surface in the Problem of a Ship's Wave Resistance," Fifteenth ONR Symposium on Naval Hydrodynamics, pp. 419-426, Sep. 1984.

15. Wigley, W.C.S., "Comparison of Calculated and Measured Wave Resistances for a Series of Forms Not Symmetrical Fore and Aft," Transactions of the Institution of Naval Architects, Vol. 86, pp. 41-60, 1944.

16. Havelock, T.H., "Ship Waves: The Relative Efficiency of Bow and Stern," Proceedings of the Royal Society of London, Series A, Vol. 149, pp. 417-426, April 1935.

17. Wigley, C., "Effects of Viscosity on Wave Resistance," International Seminar on Theoretical Wave-Resistance, Vol. III, pp. 1293-1310, 1963.

18. Havelock, T.H., "Calculations Illustrating the Effect of Boundary Layer on Wave Resistance," Transactions of the Institution of Naval Architects, Vol. 90, No. 3, pp. 259-271, 1948.

19. Himeno, Y., "Displacement Effect of Three-Dimensional Turbulent Boundary Layer and Wake of Ship," International Seminar on Wave Resistance, pp. 299-303, Feb. 1976.

20. Larsson, L. and Chang, M.S., "Numerical Viscous and Wave Resistance Calculations Including Interaction," Thirteenth ONR Symposium on Naval Hydrodynamics, pp. 707-728, Oct. 1980.

21. Kinoshita, T., "Viscous Effect on Waves of Thin Ship," Thirteenth ONR Symposium on Naval Hydrodynamics, pp. 693-706, Oct. 1980.

22. Mori, K., "Calculation of Near Wake Flow and Resistance of Elliptic-Waterplane Ships," Thirteenth ONR Symposium on Naval Hydrodynamics, pp. 729-745, Oct. 1980.

23. Hatano, S. and Mori, K., "On the Effects of Wake Upon the Wave-Making Resistance," Journal of the West Japan Society of Naval Architects, Vol. 49, pp. 103-113, Nov. 1975 (in Japanese).

24. Wang, H.T., "Calculation of Viscous Effects on Ship Wave Resistance Using Axisymmetric Boundary Layer Approaches," Naval Research Laboratory Report 8881, May 1985.

25. Bai, K.J. and McCarthy, J.H. (ed.), Proceedings of the Workshop on Ship Wave-Resistance Computations, Vol. 1, Nov. 1979.

26. Sharma, S.D., "Some Results Concerning the Wavemaking of a Thin Ship," Journal of Ship Research, Vol. 13, No. 1, pp. 72-81, March 1976.

27. Wehausen, J.V. and Laitone, E.V., "Surface Waves," Encyclopedia of Physics, Vol. 9, pp. 446-778, Springer-Verlag, Berlin, 1960.

28. Eggers, K.W.H., Sharma, S.D., and Ward, L.W., "An Assessment of Some Experimental Methods for Determining the Wavemaking Characteristics of a Ship Form," Transactions of the Society of Naval Architects and Marine Engineers, Vol. 75, pp. 112-157, Nov. 1967.

29. von Kerczek, C., "Calculation of the Turbulent Boundary Layer on a Ship Hull at Zero Froude Number," Journal of Ship Research, Vol. 17, No. 2, pp. 106-120, June 1973.

30. Granville, P.S., "A Modified Froude Method for Determining Full-Scale Resistance of Surface Ships from Towed Models," Journal of Ship Research, Vol. 18, No. 4, pp. 215-223, Dec. 1974.

31. Patel, V.C., "Some Aspects of Thick Three-Dimensional Boundary Layers," Fourteenth ONR Symposium on Naval Hydrodynamics, pp. 999-1040, Aug. 1982.

32. Ludwieg, H. and Tillmann, W., "Untersuchungen über die Wandschubspannung in turbulenten Reibungsschichten," Ingenieur Archiv, Vol. 17, pp. 288-299, 1949. (English translation, NACA Technical Memorandum 1285, May 1950).

33. Head, M.R., "Entrainment in the Turbulent Boundary Layer," Aeronautical Research Committee Reports and Memoranda No. 3152, Sep. 1958.

34. Standen, N.M., "A Concept of Mass Entrainment Applied to Compressible Turbulent Boundary Layers in Adverse Pressure Gradients," American Institute of Aeronautics and Astronautics Paper No. 64-584, 1964.

35. Squire, H.B. and Young, A.D., "The Calculation of the Profile Drag of Aerofoils," Aeronautical Research Committee Reports and Memoranda No. 1838, Nov. 1937.

36. Hatano, S. and Hotta, T., "A Second Order Calculation of Three-Dimensional Turbulent Boundary Layer," Journal of the West Japan Society of Naval Architects, Vol. 53, pp. 33-40, March 1977 (in Japanese).

37. Hoerner, S.F., Fluid-Dynamic Drag, Hoerner Fluid Dynamics, Buck Town, New Jersey, p. 6-6, 1965.

38. García, J.M. and Zazurca, J.A.A., "Cálculo de la Resistencia Viscosa de un Buque a Partir de la de Cuerpos de Revolución Equivalentes," Ingeniería Naval, Vol. 44, No. 489, pp. 147-161, March 1976.

39. Joubert, P.N. and Matheson, N., "Wind Tunnel Tests of Two Lucy Ashton Reflex Geosims," Journal of Ship Research, Vol. 14, No. 4, pp. 241-276, Dec. 1970.

40. Matheson, N. and Joubert, P.N., "A Note on the Resistance of Bodies of Revolution and Ship Forms," Journal of Ship Research, Vol. 18, No. 3, pp. 153-168, Sep. 1976.

41. Hess, J.L. and Smith, A.M.O., "Calculation of Potential Flow About Arbitrary Bodies," Progress in Aeronautical Sciences, Vol. 8, Pergamon Press, New York, New York, pp. 1-138, 1967.

42. Karamcheti, K., Principles of Ideal-Fluid Aerodynamics, John Wiley and Sons, Inc., New York, New York, pp. 492-506, 568-584, 1966.

43. Moran, J.P., "Line Source Distributions and Slender-Body Theory," Journal of Fluid Mechanics, Vol. 17, pp. 285-304, Oct. 1963.

44. Chen, C.Y. and Noblesse, F., "Preliminary Numerical Study of a New Slender-Ship Theory of Wave Resistance," Journal of Ship Research, Vol. 27, No. 3, pp. 172-186, Sep. 1983.

45. Kajitani, H. et al., "The Summary of the Cooperative Experiment on Wigley Parabolic Model in Japan," Second DTNSRDC Workshop on Ship Wave-Resistance Computations, pp. 5-35, Nov. 1983.

46. Scragg, C.A., "A Numerical Investigation of the Slender-Ship Wave Resistance Approximation," Second DTNSRDC Workshop on Ship Wave-Resistance Computations, pp. 161-178, Nov. 1983.

47. Tsutsumi, T., "On the Wave Resistance of Ships Represented by Sources Distributed Over the Hull Surface," Journal of the West Japan Society of Naval Architects, Vol. 51, pp. 269-285, March 1976 (in Japanese).

INFLUENCE OF WAVES ON THE BOUNDARY LAYER OF A SURFACE-PIERCING BODY

Frederick Stern
Iowa Institute of Hydraulic Research
The University of Iowa
Iowa City, Iowa 52242, USA

Summary

The special features of the influence of waves on the boundary layer of a surface-piercing body are discussed and an overview of the complete boundary value problem formulation is provided. Results are then presented from three-dimensional boundary layer calculations for the Stokes-wave/flat-plate flow geometry. The results are for a single value of wave steepness but in considerable detail. Also, some preliminary experimental data are provided for a qualitative assessment of the calculations. Lastly, the complications and necessary extensions that are required for calculating ship boundary layers for nonzero Froude number are discussed and some preliminary results are presented for the Wigley hull.

I. Introduction

The boundary-layer development upon a body that intersects a free-surface can be greatly influenced by the presence of free-surface gravity waves. In particular, waves of sufficient steepness induce a region of flow separation near the free-surface, which is otherwise absent. The occurrence of separation significantly modifies both the viscous and the wave-resistance components, making this a problem of considerable engineering importance. In spite of this, very little detailed experimental or rigorous theoretical work has been done on this problem.

Most of the experimental data concerning the influence of free-surface waves on body boundary-layer development are for ship and offshore-structure resistance. Wu and Landweber (1963) and others have shown that, for ship models, the viscous resistance depends on the Froude number. Present methods for predicting forces on offshore structures (for example, Salvesen et al. 1982) require drag-coefficient data for surface-piercing circular cylinders oscillating in ambient wave fields. A compilation of such data (Sarpkaya and Isaacson 1981) shows large effects due to the presence of a wavy free-surface and wave-induced separation.

Surface shear-stress and pressure-distribution measurements have been made in towing tanks for various ship forms by Shearer and Cross (1965), Steele (1967), Steele and Pearce (1968), Tzou (1968), Huang and von Kerczek (1972) and Kajitani et al (1983). The results from these experiments show considerable influence of Froude number on the shear stress and pressure distributions along waterlines close to the free-surface. More recent towing-tank experiments (again for various ship forms) have included some mean-velocity-profile measurements within the boundary layer (Doi 1980, Nagamatsu 1981, Shahshahan 1985). Most of the data are limited to the stern and near-wake regions. Also, in all but the latter reference, the Froude-number range is limited. Again, the results indicate effects due to the presence of the free surface and a dependence on Froude number. Mean-velocity and turbulence measurements were made in the stern and near-wake region of a double-tanker model, in a circulating water channel, by Hotta and Hatano (1983). The data were obtained for one value of Froude number. The measurements indicate a local damping of the normal component of turbulence near the free-surface. This effect has also been observed in open-channel flows (Rodi 1980) and in recent measurements of free surface effects on the wake of a flat plate (Swean and Peltzer 1984).

Only one investigation has been concerned specifically with wave-induced separation (Chow 1967). Chow demonstrated wave-induced separation experimentally with two-dimensional struts mounted vertically and piercing the free surface in a hydraulic flume. The struts were designed for unseparated flow when no waves are present, that is, at large depths. For an airfoil-like strut, Chow observed regions of separated flow originating just beyond the wave trough and extending to the strut trailing edge (see figure 1). The depth of the separated-flow

region was on the order of the wave height. The length of the separated-flow region was shown to depend on Froude number. Chow also observed large secondary flow within the separated-flow region which he presumed was due to the curvature of the free-surface waves. He speculated that the flow separation was caused by the secondary flow.

Very few theoretical investigations of boundary-layer development on surface-piercing bodies have been performed. Furthermore, all of these investigations have been of an approximate nature and none have properly accounted for the free-surface kinematic and dynamic boundary conditions or the local damping of turbulence near the free surface. Most of the calculations that have been made utilize integral methods and assume small-cross-flow conditions (Lin and Hall 1966, Webster and Huang 1968, Gadd 1971, Adee 1972 and 1975, Sachdeva and Preston 1975, Doi 1980, Hinatsu and Takeshi 1985). Patel et al. (1983) calculated the boundary-layer along the body/wave intersection for Chow's model (see figure 1) and the Wigley hull using the small-cross-flow differential equations. These methods do indicate significant free-surface effects on boundary-layer development, including wave-induced separation at certain Froude numbers. Separation is judged to occur when the streamwise skin friction is zero or the cross-flow becomes large. In some cases, qualitative agreement with experimental data has been shown (Doi 1980 and Patel et al. 1983).

Very recently, Stern (1985) has performed an analytical and numerical study concerning the effects of waves on the boundary layer of a surface-piercing body. In this work, a more rigorous problem formulation is pursued in an effort towards putting the subject on a more solid foundation. Also, results are presented from three-dimensional laminar and turbulent boundary-layer calculations that demonstrate the influence of waves on boundary layer development, including the effects of the free-surface boundary conditions. The calculations are for the idealized geometry of a combination Stokes-wave/flat-plate. This geometry is considered optimum for the present investigation, since it is simple, yet the flow near the free surface is fully three-dimensional. Far from the free surface and for laminar flow, the solution is the well known Blasius one. Further details concerning this work will be discussed subsequently.

In the present paper, the special features of the influence of waves on the boundary layer of a surface-piercing body will be discussed. Next, the present approach (within the context of the earlier work) and the computational method used in making the calculations to be presented will be reviewed. Subsequently, results are presented from three-dimensional boundary layer calculations for the Stokes-wave/flat-plate geometry. The results are for a single value of wave steepness Ak but in considerable detail. Also, some preliminary experimental data are provided for the purpose of a qualitative assessement of the calculations. Lastly, the complications and necessary extensions that are required for calculating ship boundary layers for nonzero Froude number are discussed and some preliminary results are presented for the Wigley hull.

II. Physical Problem

Consider the development of the boundary-layer upon a ship-like body, moving steadily at velocity U_0 and intersecting the free-surface of an incompressible viscous fluid. This situation is depicted in figure 2. In distinction from the infinite fluid double-body problem, the present problem has special features due to the presence of the free surface and gravity waves (Patel et al. 1983):

* the external-flow pressure field is influenced by the body wave-making such that it is Froude-number dependent;

* at the free surface, which is itself unknown and to be determined as part of the solution, there are two nonlinear boundary conditions, a kinematic one and a dynamic one, that the solution must satisfy;

* the characteristics of the structure of turbulence are modified near a free surface; and

* waves of sufficient steepness induce a region of flow separation near the free surface, which is otherwise absent.

In order to elucidate the effects of these special features on the boundary-layer development it is necessary to examine the flow in the neighborhood of the body-boundary-layer/free-surface juncture in detail. As shown in figure 3, the flow field can be divided into five regions: I, potential-flow region in which viscous effects are negligible; II, free-surface boundary-layer region at a sufficient distance from the body that it is not influenced by the body boundary layer; III, body-boundary-layer region at a sufficient depth that it is not influenced by the free-surface boundary conditions; IV, body/free-surface boundary layer in the region very close to the free surface in which the free-surface boundary conditions have a significant influence; V, meniscus boundary-layer region. The nature of the

flow in regions I-III is well known and the flow field order-of-magnitude estimates are well established; however, this is not the case for regions IV and V.

In region I (potential flow), the flow is characterized by the nondimensional wave steepness parameter Ak (where A is the wave amplitude and k the wave number). For small-amplitude wave theory to be valid, $Ak \ll 1$.

Region II is the part of the free-surface boundary layer above region I and is due to the condition of zero stress on the free-surface in a viscous fluid (for example, Kinsman 1965 or Mei 1983). For laminar flow, the thickness of this boundary layer is

$$\delta_{fs} = \frac{\sqrt{2}}{k} R_w^{-1/2}$$

where $R_w = C/\nu k$ is the wave Reynolds number and $C = U_0$ is the wave celerity. δ_{fs} is of the same order of magnitude as the body boundary layer

$$\delta_b \sim R_b^{-1/2}$$

where $R_b = U_0 L/\nu$ is the body Reynolds number; since, for most circumstances, the wave length $\lambda \sim O(L)$. However, the free-surface boundary layer is very weak and has a negligible influence, $O(\delta_{fs}^2)$, on the potential flow kinematics and dynamics. Evidently, the zero-stress condition places a much less severe restriction on the flow field than the wall-boundary-layer no-slip condition, resulting in only minor adjustments to the potential-flow velocity field. The order-of-magnitude estimates for region II are the same as for region I.

Region III, is the body-boundary-layer region sufficiently deep below the free surface that it is not influenced by the free-surface boundary conditions. Based on region II considerations, it is expected that the [illegible] depth is of $O(\delta_b)$. At this depth the effects of the free surface are primarily transmitted through the external-flow pressure field. Over a large part of a ship-like body the thin-boundary-layer equations are applicable, and it is only in the stern region that it is necessary to solve the more complete partially-parabolic Reynolds equations (Patel 1982). In region III, the most important nondimensional parameter is $\varepsilon = \delta_b/L$ and, for thin-boundary-layer theory to be valid, $\varepsilon \ll 1$.

Region IV, is the body/free-surface overlap region where the effects of the free surface are due both to the influences of the external-flow pressure field and the kinematical and dynamical requirements of the free-surface boundary conditions. The kinematic boundary condition expresses the requirement that the free surface is a stream surface. The dynamic boundary condition expresses the requirement of continuity of the normal and tangential stresses across the free surface. The free-surface boundary conditions influence both the mean and the turbulent velocity components. The limited experimental data that are available indicate that, near a free surface, the normal component of turbulence is damped and the longitudinal and transverse components are increased. The turbulence structure near a solid wall shows similar characteristics, but there the situation is complicated by the influence of high strain rates due to the no-slip condition. It should be recognized that the complex effects just described cannot be simulated with an isotropic eddy-viscosity turbulence model. As will be discussed next, Stern (1985) has derived order-of-magnitude estimates for region IV for laminar flow and shown that the parameter Ak/ε is important in characterizing the flow. Different solution regimes can be identified depending on the magnitude of Ak/ε. For turbulent flow, due to the present uncertainties in turbulence modeling especially when a free surface is present, it is not possible to reach such definitive conclusions concerning the order-of-magnitude estimates and solution regimes for region IV. Note that region IV is kinematically similar to the flow in a streamwise corner for which it is known that two length scales are important and the thin-boundary-layer equations are not applicable.

The precise physics in Region V is a complex matter involving surface tension. It is known that the shape of the meniscus depends upon the nature of the body surface finish and that it can have a very sharp angle of contact. According to Mei (1983), this subject appears to be a poorly understood part of physical chemistry.

III. Approach

In the present investigation, which is for turbulent flow only, no attempt is made to resolve the details of the flow very near the free surface (regions IV & V), and as such, only an approximate symmetry boundary condition is applied on the mean free surface and a simple modification is made to a one equation turbulence model to account for the influence of the free surface. However, in order to appreciate the significance of such approximations, an overview of the more complete problem is now provided (see Stern (1985) for more details).

The boundary-value problem associated with the boundary layer development on a surface-piercing body differs from the infinite fluid double-body problem due to the presence of the free surface and gravity waves. In the latter problem, the free surface is flat and simply a plane of sym-

metry. In the former problem, on the free surface $z = \eta(x,y)$, there are two boundary conditions the solution must satisfy (see figure 4):

$$\text{kinematic boundary condition: } \hat{V} \cdot \hat{n} = 0 \qquad (1)$$

$$\text{dynamic boundary condition: } \tau_{ij} n_j = -\tilde{\tau}_{ij} n_j$$

where $\hat{V} = (U,V,W)$ is the fluid velocity vector, $n = (-\eta_x, -\eta_y, 1)$ is the outward normal vector to the free surface and τ_{ij} and $\tilde{\tau}_{ij}$ are the fluid and external stress tensors, respectively*. Within the boundary layer, the free surface is deformed and does not coincide with the potential-flow free surface; consequently, within the boundary layer, just as is the case in the outer flow, the free surface must be determined as part of the solution. The external stress is simply given by the difference between the ambient pressure p_0 and the surface tension pressure p_γ

$$\tilde{\tau}_{ij} = (p_0 - p_\gamma)\,\delta_{ij}$$

where δ_{ij} is the Kronecker-delta function. For turbulent flow, the fluid stress is given by

$$\tau_{ij} = -p\delta_{ij} + 2\mu\varepsilon_{ij} - \rho\,\overline{u_i u_j}$$

where μ is the fluid viscosity, ρ is the fluid density, p is the fluid pressure,

$$\varepsilon_{ij} = \frac{1}{2}(U_{i,j} + U_{j,i})$$

is the rate-of-strain tensor and $\overline{u_i u_j}$ are the Reynolds stresses. By means of the previous denfinitions, the free-surface boundary conditions (1) can be expressed by

$$-\eta_x U - \eta_y V + W = 0 \qquad (2)$$

$$p\eta_x - [2\mu U_x - \rho\overline{u^2}]\eta_x - [\mu(U_y + V_x) - \rho\overline{uv}]\eta_y + \mu(U_z + W_x) - \rho\overline{uw} = (p_0 - p_\gamma)\eta_x \qquad (3)$$

$$p\eta_y - [\mu(U_y + V_x) - \rho\overline{uv}]\eta_x - [2\mu V_y - \rho\overline{v^2}]\eta_y + \mu(V_z + W_y) - \rho\overline{vw} = (p_0 - p_\gamma)\eta_y \qquad (4)$$

$$-p - [\mu(U_z + W_x) - \rho\overline{uw}]\eta_x - [\mu(V_z + W_y) - \rho\overline{vw}]\eta_y + 2\mu W_z - \rho\overline{w^2} = -(p_0 - p_\gamma) \qquad (5)$$

Conditions (2)-(5) are to be applied on the unknown surface $z = \eta(x,y)$. Note that these conditions are linear in the free-surface slopes (η_x, η_y), and thus, in principle, two of the conditions can be used to eliminate (η_x,η_y) by expressing them in terms of the pressure difference $(p - p_0 + p_\gamma)$, the fluid velocity components, the rates-of-strain and the Reynolds stresses. The remaining two conditions, with (η_x,η_y) known, can then be used to provide boundary conditions in the solution of the mean-flow momentum equations. It should be pointed out, that additional free-surface boundary conditions may be required in the turbulence-model equations. No approximations have been made in deriving conditions (2)-(5) and, as such, the formulated boundary-value problem constitutes a fully nonlinear free-surface problem. Presumably, conditions (2)-(5) are sufficient, in conjunction with the remainder of the boundary-value problem, to render a unique solution, including the free-surface itself.

Consideration is now given to appropriate simplications of the free-surface boundary conditions that are consistent with small-amplitude waves. This is consistent with the usual approximation for calculating the outer wave potential in which linearized small-amplitude wave theory is used. To this end, it is necessary to know the order-of-magnitude estimates for region IV (see figure 3). In previous work, order-of-magnitude estimates have been derived for region IV for laminar flow by considering both the established order-of-magnitude estimates in the surrounding regions I-III and the requirements imposed by the free-surface boundary conditions. Referring to Table 1, it is seen that different solution regimes can be identified depending on the magnitude of Ak/ε. Only for small $Ak \sim O(\varepsilon^{1.5})$ or less are the free-surface boundary conditions of higher order. This is the small-cross-flow regime. For larger values of Ak, i.e., $O(\varepsilon^{1.5}) < Ak < O(\varepsilon)$, the role of the free-surface boundary conditions is significant; furthermore, a consistent formulation requires the solution of higher order boundary-layer equations. In fact, for $Ak \sim O(\varepsilon)$ the order of magnitude estimates in region IV become,

$$U \sim O(1); \qquad \frac{\partial}{\partial x} \sim O(1);$$

$$(V,W) \sim O(\varepsilon); \qquad \left(\frac{\partial}{\partial y}, \frac{\partial}{\partial z}\right) \sim O(\varepsilon^{-1})$$

which are identical to those used by Patel (1982) in deriving the partially-parabolic Reynolds equations. Thus, it is seen that region IV is analogous to the flow in a

* In the discussions to follow, the x coordinate is in the streamwise direction, the y coordinate is across the boundary layer and the z coordinate is in the vertical direction. Also, for ease of presentation, all equations are in Cartesian form.

streamwise corner as was indicated in Section II. For turbulent flow, it is not possible to reach such definitive conclusions concerning the order-of-magnitude estimates and solution regimes for region IV. This is due to the uncertainty of assigning orders of magnitude to the Reynolds stresses near a free surface. Tentatively, based on physical reasoning, the above conclusions are extended to turbulent flow also.

Table 1. Body/Free-Surface Boundary Layer Order-of-Magnitude Estimates

	order of magnitude		order of magnitude
U	1	η	Ak
V	ε	η_x	Ak
W	Ak	η_y	Ak/ε
$\partial/\partial x$	1		
$\partial/\partial y$	ε^{-1}	ν	ε^2
$\partial/\partial z$	Ak/ε^2		

The free-surface boundary conditions (2)-(5) are to be applied on the unknown surface $z = \eta(x,y)$. However, using the same technique as that used in the outer flow, conditions (2)-(5) can be expanded in a Taylor series about the known surface $z = 0$ and evaluated up to the desired order of approximation. To the lowest order of approximation conditions (2)-(5) are retained and simply evaluated on $z = 0$. Such a technique is restricted in the present application to $O(Ak/\varepsilon) > 1$ based on the previous order-of-magnitude analysis, since for $O(Ak/\varepsilon) < 1$ the Taylor series expansions are not convergent. Consequently, for $O(Ak/\varepsilon) < 1$ a small-amplitude-wave solution is not valid and the free-surface boundary conditions must be applied on the exact free surface $z = \eta$. For small-amplitude waves, and for laminar flow ($\overline{u_i u_j} = 0$), the free-surface boundary conditions (2)-(5) can be approximated by

$$-\eta_x U - \eta_y V + W = 0 \qquad (6)$$

$$-U_y\eta_y + U_z = 0 \qquad (7)$$

$$-V_y\eta_y + V_z + W_y = 0 \qquad \text{on } z = 0 \qquad (8)$$

$$-(p - p_0 + p_\gamma) + \mu[-U_z\eta_x - W_y\eta_y + 2W_z] = 0 \qquad (9)$$

The great advantage of this solution is that the boundary conditions can be applied on the surface (z=0).

In previous work (Stern 1985), the three-dimensional thin-boundary-layer equations were solved for the Stokes-wave/flat-plate flow geometry, using both an approximate and the small-amplitude-wave boundary conditions. The approximate boundary condition used was a symmetry (i.e., zero gradient) condition which corresponds to a small-cross-flow solution along the mean free surface and a fully three-dimensional solution below. Calculations were performed for both laminar and turbulent flow; however, the effects of the free-surface boundary conditions were investigated for laminar flow only. In this case the pressure difference $(p - p_0 + p_\gamma)$ in (9) was neglected. Conditions (6) and (8) were used to eliminate (η_x, η_y) in (7) and (9) which were solved for U_z and W_z respectively and used as boundary conditions for the solution of the momentum equations. The results are for small values of Ak only and are consistent with the order-of-magnitude analysis in showing that the influence of the free-surface boundary conditions is significant only in a region very close to the free-surface $z < Ak = \delta$. The results show interesting trends that are explained by reference to the free-surface boundary conditions. It is shown that, within the boundary layer, the potential-flow free surface is deformed in a manner that correlates closely with the cross-flow velocity (see figure 5). In fact, all the small-amplitude-wave free-surface properties are shown to correlate with $\pm W$. The results presented show trends that are very consistent with the behavior that would be expected based on physical reasoning. However, these results must be viewed with some caution due to the limitations of both the small-amplitude-wave solution and the use of thin-boundary-layer equations and numerics. The influence of large values of Ak was studied through the use of the symmetry boundary condition. In particular, it was shown how the boundary layer responds to the pressure-gradient changes along the plate length between favorable and adverse. Also, waves of sufficient steepness induce flow separation near the free surface in regions of large adverse pressure gradient p_x.

IV. Computational Method

The boundary-layer equations must be integrated numerically to obtain the velocity field for specified external flow pressure gradients and edge velocities. The fully implicit method of Nash and Scruggs (1976), originally developed for aircraft application, has been used. This method was improved by Patel et al. (1979, 1983 and 1985) and applied to bodies of revolution at incidence and to ship forms for zero Froude number. Below a brief review of the overall procedures is provided.

The three-dimensional thin-boundary-layer equations can be written in matrix vector form as

$$A_1 F + A_2 \frac{\partial F}{\partial x} + A_3 \frac{\partial F}{\partial z} + A_4 \frac{\partial F}{\partial y} + A_5 \frac{\partial^2 F}{\partial y^2} + A_6 = 0 \qquad (10)$$

where F = (U,W) and A_1 - A_6 are coefficient matrices. Consistent with thin-boundary-layer theory, the (x,y,z) curvilinear coordinate system is constructed such that the parametric curves x = constant and z = constant form an orthogonal grid upon the body surface and the y-coordinate is normal to the body surface. Such a coordinate system is only truly orthogonal on the body surface itself; however, the deviation from orthogonality off the body surface is presumed of higher order. By approximating each of the derivatives in (10) by finite differences, equation (10) can be expressed as

$$B_1F^{\ell}_{m+1,n} + B_2F^{\ell}_{m,n+1} + B_3F^{\ell}_{m,n} + B_4F^{\ell}_{m-1,n} + B_5F^{\ell}_{m,n-1} = B_6F^{\ell-1}_{m,n} - A_6 \qquad (11)$$

where (ℓ,m,n) are node-point indices in the (x,y,z) directions, respectively, and B_1 - B_6 are coefficient matrices composed of linear combinations of the A's divided by the appropriate spatial difference. In obtaining equation (11), the x-derivative in (10) is expressed as a backward difference, the first-order z- and y-derivatives are expressed using upwind differencing so as to preserve convective stability and lastly the second-order y-derivative is expressed using a central difference. Thus, the overall procedure is only first-order accurate. The finite-difference molecule associated with (11) is shown in figure 6. Note that both equations (10) and (11) are nonlinear since the coefficient matrices are functions of F. Equation (11) is solved by means of an alternating-direction-implicit (ADI) scheme.

The forward marching procedure advances in the positive x-direction from a cross-plane ℓ-1, where the solution is assumed to be known, to a cross-plane ℓ, at which a new solution is obtained from the solution of equation (11). The ADI scheme consists of scanning the cross-plane alternately in the n- and m-directions, converting equation (11) respectively into the successive forms

$$B_1F^{\ell}_{m+1,n} + B_3F^{\ell}_{m,n} + B_4F^{\ell}_{m-1,n} = C_1 \qquad (12)$$

$$B_2F^{\ell}_{m,n+1} + B_3F^{\ell}_{m,n} + B_5F^{\ell}_{m,n-1} = C_2 \qquad (13)$$

in which C_1 and C_2 contain the passive terms originating from the left-hand side of (11). The coefficients or equations (12) and (13) form a block-tridiagonal matrix which is solved by an extended Thomas algorithm. After each n- or m-scan, the continuity equation is integrated to obtain the V velocity component. The B and C matrices are updated in successive iterations until convergence is obtained with respect to the velocity components at each grid point within a specified tolerance.

The thickness of the integration domain is 1.26 δ(x,z), where δ is the boundary-layer thickness. Note that δ is determined as part of the solution. The number of grid points is kept constant in both the y- and z-directions. For laminar flow, a uniform distribution of grid points is used across the boundary layer. An expanding grid was used in the z-direction so as to allow for a higher concentration of grid points near the free-surface. A diverging geometric series was used for this purpose. The step size Δx is arbitrarily specified. The number of cross-plane grid points and the step size Δx are determined from accuracy and computer-cost considerations.

The boundary conditions imposed when solving equation (11) at each cross-plane are:

$$F = 0 \qquad \text{on } y = 0 \qquad (14)$$

$$\frac{\partial F}{\partial y} = 0 \qquad \text{on } y = 1.26\delta \qquad (15)$$

$$\frac{\partial F}{\partial z} = 0 \qquad \text{on } z = z_{max} \qquad (16)$$

$$\frac{\partial F}{\partial z} = C_3 \qquad \text{on } z = 0 \qquad (17)$$

Condition (14) is the no-slip condition: $F^{\ell}_{1,n} = 0$. Condition (15) imposes the condition that the viscous-flow solution merge smoothly with the outer potential flow and is implemented by

$$F^{\ell}_{MM-1,n} = F^{\ell}_{MM,n}$$

where MM is the maximum number of grid points across the boundary layer. The zero-gradient matching condition does not insure that the edge values $F^{\ell}_{MM,n}$ are identically (U_e, W_e) and small differences can occur; thus, after a converged solution is obtained at each cross-plane the velocity profiles are scaled with the known values of (U_e, W_e). Condition (16) is a symmetry condition and is implemented by

$$F^{\ell}_{m,NN-1} = F^{\ell}_{m,NN}$$

where NN is the maximum number of grid points in the z-direction. If W and p_z are zero on z_{max} then (16) becomes similar to a plane-of-symmetry condition. Lastly, condition (17) is the free-surface boundary condition. For the present circumstances, in which a symmetry boundary condition is used, $C_3 = 0$. Thus, condition (17) is simply implemented by

$$F^{\ell}_{m,0} = F^{\ell}_{m,1}$$

where n = 1 corresponds to the mean free surface.

If the turbulent motion is characterized by a single length scale, then it is expected that this scale must decrease towards a free surface due to geometrical restrictions. In the present investigation, a simple modification is made to a one-equation turbulence model to account for the influence of the free surface. This is consistent with the use of the symmetry-condition boundary condition. Specifically, the Bradshaw/Nash one-equation turbulence model, which was built into the original program, was used here also. In this procedure, an approximate form of the turbulent kinetic energy equation is solved in conjunction with the boundary-layer equations. The turbulent-kinetic-energy equation is put in the form

$$\frac{U}{h_1}\frac{\partial}{\partial x}(\overline{q^2}/2) + \frac{V}{h_2}\frac{\partial}{\partial y}(\overline{q^2}/2) + \frac{W}{h_3}\frac{\partial}{\partial y}(\overline{q^2}/2)$$

$$+ \frac{\overline{uv}}{2}\frac{1}{h_2}\frac{\partial U}{\partial y} + \frac{\overline{vw}}{2}\frac{1}{h_2}\frac{\partial W}{\partial y} + D - \varepsilon = 0 \qquad (18)$$

where

$$D = \frac{1}{h_2}\frac{\partial}{\partial y}\left(\frac{\overline{pv}}{\rho} + \frac{\overline{q^2 v}}{2}\right) \qquad (19)$$

$$\varepsilon = \nu[\overline{v^2 u} + \overline{w^2 v} + \overline{w^2 w}] \qquad (20)$$

The diffusion term (19) is represented by a bulk diffusion model

$$D = \frac{1}{h_2}\frac{\partial}{\partial y}\left[\frac{\overline{q^2}_{max}}{Q_e} a_2 \overline{q^2}\right] \qquad (21)$$

where

$\overline{q^2}_{max}$ = maximum value of $\overline{q^2}$ in the outer 3/4 of δ

$$Q_e = \sqrt{U_e^2 + W_e^2}$$

$$a_2 = 1.125\,(y/\delta)^4$$

The dissipation term (20) is represented by

$$\varepsilon = (\overline{q^2})^{3/2}/L_D \qquad (22)$$

where L_D is the dissipation length

$$L_D = 7.195\,\eta/(1 + 4\eta^2 + 5\eta^7) \qquad (23)$$

and η is the minimum distance of either y/δ or z/δ. Lastly, the Reynolds stresses are related to the turbulent kinetic energy by the empirical functions

$$\rho\,\overline{uv} = -.0225\sqrt{\overline{q^2}}\,L_D\frac{1}{h_2}\frac{\partial U}{\partial y}$$
$$\rho\,\overline{vw} = -.0255\sqrt{\overline{q^2}}\,L_D\frac{1}{h_2}\frac{\partial W}{\partial y} \qquad (24)$$

The turbulent-kinetic-energy equation (18) was solved in conjunction with the mean-flow momentum equations using the ADI procedure, as just described, with F = $(U, W, \overline{q^2})$. For turbulent flow, a nonuniform distribution of grid points is used across the boundary layer in which a higher concentration of grid points is placed near the wall.

V. Stokes-Wave/Flat-Plate Boundary Layer

Consider the flow field in the vicinity of a surface-piercing vertical flat plate moving in and at the same speed as a simple harmonic wave train. It is assumed that the plate is sufficiently thin that it generates no wave of its own. Such a flow can be simulated in a towing tank either by towing the plate at the same speed as a wave-maker generated harmonic wave train or by towing the plate and generating the wave train with a submerged horizontal foil afixed ahead of the plate leading edge. An experiment using the latter arrangement is presently under way at The University of Iowa's Institute of Hydraulic Research. Some preliminary results from this experiment are presented below for comparison with the computational results. Outside of the plate boundary layer, the flow is essentially inviscid (see figure 3) and can be represented mathematically as a second-order Stokes wave; that is, the fluid velocity field $\hat{V}_e$ for coordinates moving with the plate/wave system is simply given by:

$$\hat{V}_e = U_0\hat{e}_1 + \nabla\phi \qquad (25)$$

where ϕ is the velocity potential

$$\phi = -AU_0 e^{-kz}\sin kx \qquad (26)$$

with the dispersion relationship

$$U_0^2 = \frac{g}{k}(1 + (Ak)^2)$$

and (x,z) are Cartesian coordinates with x positive downstream and z positive downwards (see figure 7). The third coodinate y is normal to the plate and across the boundary layer. The origin is located at the plate-leading-edge/waterplane intersection. The potential-flow free-surface elevation $\eta(x)$ and piezometric pressure coefficient c_p are given by

$$\eta(x) = A\cos kx + \frac{1}{2}A^2 k\cos 2kx \qquad (27)$$

$$c_p(x,z) = 2Ak\,e^{-kz}\cos kx - (Ak)^2 e^{-2kz} \qquad (28)$$

With regard to calculating the boundary layer on the plate, the most important quantities are the edge velocities

$$U_e/U_0 = 1 - Ak\,e^{-kz}\cos kx \qquad (29)$$

$$W_e/U_0 = Ak\,e^{-kz}\sin kx \qquad (30)$$

and the pressure gradients

$$\frac{\partial}{\partial x}\left(\frac{p}{\rho U_0^2}\right) = -Ak^2 e^{-kz}\sin kx \qquad (31)$$

$$\frac{\partial}{\partial z}\left(\frac{p}{\rho U_0^2}\right) = -Ak^2 e^{-kz}\cos kx + k(Ak)^2 e^{-2kz} \quad (32)$$

The second order terms have been included since they have a significant influence for steep waves.

The wave elevation, edge velocities and pressure gradients are shown to first order in figure 7. Referring to figure 7, it is seen that four potential-flow regions can be distinguished. In region I, both p_z and p_x are favorable, $W_e > 0$ and accelerating, and $U_e < U_0$ and accelerating. In region II, p_x is favorable and p_z is adverse, $W_e > 0$ and decelerating, and $U_e > U_0$ and accelerating. In region III, both p_z and p_x are adverse, $W_e < 0$ and decelerating, and $U_e < U_0$ and decelerating. In region IV, p_z is favorable and p_x is adverse, $W_e < 0$ and accelerating, and $U_e < U_0$ and decelerating. Each of these regions has a distinct influence on the boundary-layer development.

Computational Results

Results are shown below for Reynolds number $R_0 = U_0 L/\nu = 1.65 \times 10^6$ and wave steepness $Ak = 0.24$. This corresponds to the experimental condition. In the discussions to follow, the (x,y,z) coordinates are non-dimensionalized based on the plate length L. Both L and the wave length $\lambda = 2\pi/k$ are given the value of one. Typically, 170 x-steps and 21 grid points across the boundary layer were used. An expanding grid was used in the z-direction with grid points z = (0.,.025,.062,.12,.2,.32,.5,.75). The results presented below were obtained by interpolation and are for z = (0.,.042,.084,.127, .253,.38,.75) which corresponds to the location of the exerimental data. Numerous checks were made to insure that the results were grid independent. Also, a strict convergence criteria was used, namely $\Delta F/Q_e < .00005$, and a minimum of three ADI sweeps were required at each cross-plane. The calculations were made on a Prime-750 computer and took about 1/2 hour of computing time. The calculations were begun as laminar flow at x = 0.001, with transition specified at x = .05 which corresponds to the location of the trip studs in the experiment. The Blasius solution based on local R_n was used for the initial conditions.

In the previous work, the edge conditions (U_e, W_e, p_x, p_z) were specified by equations (29)-(32) respectively. Alternatively, c_p (28) alone can be specified and the edge conditions obtained numerically; that is, (p_x, p_z) are obtained by numerical differentiation and (U_e, W_e) are obtained through the solution of the two-dimensional form of Euler's equations (the momentum equations without the viscous and Reynolds stress terms) at the boundary layer edge. These equations are solved implicitly using the same difference approximations as are employed for the full boundary layer equations. The present boundary layer calculations were made using the latter approach. Figure 8 shows both the exact and the edge velocity solution potential flow. Note that there are inaccuracies in the edge velocities which are an indication of the accuracy of the overall numerics. Also seen from figure 8, is the significant influence of the second order terms for this steep wave Ak = .24.

Figure 9 shows the streamwise displacement thickness δ^*. At large depths ($z<.5$), the solution asymptotically approaches the simple-two-dimensional turbulent flat plate boundary layer solution. At the greatest depth $z_{max} = .75$, this solution is recovered to within an error of only a few percent. Referring to figure 9, it is seen that, for $x < .1$, the displacement thickness is somewhat larger near the free surface than it is at greater depths. This is no doubt due to the initial conditions and the decrease in local R_n towards the free surface in this potential-flow region (see figure 7). Subsequently, for $x > .1$, the displacement thickness is reduced near the free surface as compared with greater depths. This reduction is due both to the favorable p_x in potential-flow regions I and II and to the favorable p_z in region I. A favorable p_x tends to accelerate the flow and thin the boundary layer in that region. A favorable p_z tends to drive the cross-flow away from the free surface and thin the boundary layer in that region. The minimum displacement thickness shows about 44 percent reduction and occurs near x = .45. For $x > .45$, the displacement thickness near the free surface increases such that for $x > .75$ it is greater near the free surface than it is at larger depths. This increase is initially due to adverse p_z in potential-flow region II which tends to drive the cross-flow towards the free surface and thickens the boundary layer in that region. This is compounded by continued adverse p_z in potential-flow region III and adverse p_x in regions III and IV. An adverse p_x tends to decelerate the flow and thicken the boundary layer in that region. The maximum displacement thickness shows about 75 percent increase and occurs near x = .99. Lastly, for $x > .99$, the dispalcement thickness near the free surface decreases until the end of the plate is reached at x = 1. This reduction is due to the favorable p_z in potential flow region IV. The other integral parameters (boundary-layer thickness, momentum thickness, shape parameter) all show similar and consistent trends to those described above for the displacement thickness.

The results for the wall-shear-stress magnitude τ_w and the angle β are shown in figures 10 and 11, respectively. Referring

to figure 10, it is seen that the wall-shear-stress behavior is consistent with the previously described displacement thickness, but in reverse trend. Note that the shear stress responds more quickly, and with greater intensity to changes in the potential flow than the displacement thickness. The maximum and minimum values show about a 85 percent and a 76 percent change from the deep solution respectively. Referring to figure 11, it is seen that the shear-stress angle

$$\beta = \tan^{-1} \lim_{y \to 0} \frac{W_y}{U_y}$$

can be directly correlated with p_z. In potential-flow region I, where p_z is favorable, β is positive. In regions II and III, where p_z is adverse, β is negative. Finally, in region IV, where p_z is again favorable, β is positive. Note that there is a lag in the β response to p_z such that β becomes negative at $x = .4$ and positive again at $x = .9$. It should be recognized that β indicates the direction of the cross-flow near $y = 0$ and it is in this low-inertia region that W first responds to changes in p_z. Thus, subsequent to a sign change in β, so-called S-type cross-flow profiles occur as will be shown next. The maximum and minimum values of β are 34° and -30° respectively.

The streamwise U and crossflow W velocity profiles and the turbulent kinetic energy q^2 profile at various cross-planes are shown in figures 12 to 15 for $z = (.042, .084, .127, .253)$ respectively. Referring to figures 12a to 15a, it can be seen that the U profiles show the influence of acceleration and deceleration phases of the potential flow. This becomes even clearer if the U profiles are normalized by U_e and are plotted vs. y/δ. Such a plot shows that for $x = .125$ the U profile is similar to the two-dimensional turbulent flat plate solution. Subsequently, during the acceleration phase, the U profile is fuller than the $x = .125$ profile, and finally, during the deceleration phase, as separation is approached, it becomes, less full. Referring to figures 12b to 15b, it can be seen that the W profiles clearly show the influence of the potential flow W_e and p_z. It is seen that initially, for $x = .125$ and .25, the crossflow is positive. Subsequently, beginning with the inner part of the profile first, the cross-flow becomes negative ($x = .375, .5, .625, .75$). Lastly, for $x = .875$ and 1., again beginning with the inner part of the profile first, the cross-flow becomes positive. Referring to figures 12c to 15c, it is seen that initially, during the acceleration phase, the maximum value of the turbulent kinetic energy occurs very close to the wall. Subsequently, during the deceleration phase, the maximum value moves outward towards the middle of the boundary layer. Finally, by comparing figures 12 to 15 the depthwise exponential decay of the wave influence is clearly seen.

Calculations were also made using the exact potential flow edge conditions (see figure 8). The results are very similar to those shown above. However, there are some differences: the maximum percent increase and minimum percent reduction for δ and τ_w as compared to the deep solution are (110, 34) and (89, 78) respectively; the maximum and minimum values of β are 42° and -31° respectively; and the minimum value of δ is not at the free-surface itself but at the next z-grid level.

Comparison with Preliminary Experimental Data

As previously mentioned, an experiment is presently underway using a model geometry designed specifically to simulate the Stokes-wave/flat-plate flow field. The objective of the experimental program is to obtain detailed measurements documenting the effects of waves on the boundary layer of a surface-piercing body, including the conditions leading up to wave-induced separation and the nature and extent of the separated flow. Presently, wave profile and mean-velocity profile measurements are being made. Also of interest are turbulence measurements.

Figure 16 shows a sketch of the experimental model installed in the towing tank. The horizontal foil fully spans the towing tank and is mounted to sidewall end plates which allow for the adjustment of the foils' submergence. Downstream of the foil is the vertically suspended flat plate. The plate is suspended such that both its lateral and longitudinal position can be adjusted. The model configuration was designed to generate waves that are as two-dimensional as possible and with as little disturbance by the plate as possible. Both the foil and plate are mounted to a trailer which is towed by the main carriage. This allows for easy access and optimum viewing. The foil geometry was designed based on the experiments of Salvesen (1966). Salvesen performed similar towing-tank experiments with a submerged horizontal foil (without the downstream plate) for the purpose of validating his higher-order wave theory for submerged two-dimensional bodies (Salvesen 1969). Of present interest is the ability to control both the wave steepness Ak and the wave length λ by adjustment of the foil submergence d and carriage speed U_0, respectively. Salvesen's results indicated that this would be possible with the present arrangement; however, the influence of the downstream plate was not known.

Some preliminary experiments have been performed to determine this influence and demonstrate the feasibility of the proposed model geometry. Figure 17 shows results from

these experiments. Shown in figure 17 are plots of Ak vs. Froude number based on the carriage speed U_0 and the foil chord length c ($F_n = U_0/\sqrt{gc}$) for various depths of foil submergence, d. The Ak values were determined from photographic records of the wave profiles on the plate. Also shown on figure 17 for comparison are results from Salvesen's experiments. Salvesen determined his wave profiles using a capacitance wire. The present experimental results indicate that the wave length λ can be predicted very accurately from the results of linear wave theory

$$\lambda = \frac{2\pi U_0^2}{g} \qquad (33)$$

This finding is consistent with Salvesen's results. Referring to figure 17, it is seen that for fixed U_0 the wave steepness Ak increases with decreasing foil submergence, as expected. Note that there are differences between the present results and Salvesen's; that is, for fixed U_0 and d the Ak values obtained with the present model are somewhat lower than Salvesen's. This is no doubt due to the damping influence of the downstream plate which was absent in Salvesen's experiments. The plate used in the preliminary experiments was constructed from an available aluminum sheet which required reinforcing L beams. In the future a new plexiglass plate will be used and it is expected that this will reduce the damping effect.

Some preliminary mean-velocity profile measurements have also been made using a three hole pitot tube and for U_0 = 4.5 fps and d = 1.21 ft. Figure 18 shows a photograph of the wave profile for this condition. Based on this photograph, it was determined that Ak ~ .24. Note the occurrence of wave-induced separation for this steep wave. The measurements are for four depths z = (.042,.084,.127,.253) and for up to seven axial locations x = (.25,.375,.5,.625,.75, .875, 1.) depending on the depth. Here, x and z have been normalized using the linear wave theory value for λ (33). The axial alignment of the plate for the velocity profile measurements was such that the leading edge of the plate was near the first wave crest.

Figure 19 shows a comparison of the measured edge velocities (U_e, W_e) with the Stokes' wave theoretical values. The agreement is good; however, the experimental data show a phase shift indicating that the wave trough was actually somewhat downstream of x = .5. This may be due to a misalignment of the axial position of the plate.

Figures 20 - 23 show the measured velocity profiles (U,W). Figure 24 shows the streamwise displacement thickness δ^* and the boundary layer thickness δ. Comparing figures 9 and 24 it is seen that similar trends in δ^* are exhibited in both the calculations and the experimental results. This is true for both the depthwise and streamwise variation. However, the magnitude of the experimental δ^* is significantly larger than the calculations and the depthwise variation of the experimental δ^* is not as large as that calculated. These differences are consistent with the fact that the surface of the aluminum plate used in the preliminary experiments is rough. Also, the influence and depthwise extent of the separation region exhibited in the experiment and not the calculation is unknown. Referring to figure 18, it is seen that experimentally for Ak ~ .24 the streamwise extent of separation is $.71 \leq x \leq 1$. In previous turbulent flow calculations for Rn = 5 x 10^6 and Ak = (.01, .2,.3,.35), separation only occurred for Ak = .35 and at x = .9.

The differences between the calculated and measured velocity profiles, as can be seen by comparing figures 12-15 and 20-23, are consistent with the previous discussion concerning the edge velocities and displacement thickness. Also, the measured W profiles show larger values then the calculated ones and the measured decay rate is such that initially (z = .042 and .084) the rate is small and subsequently (z = .127 and .253) the rate is large. The calculations show a more uniform exponential decay rate.

The agreement between the measurements and calculations is considered very satisfactory, especially considering the preliminary nature of the experiments and the approximations made in the calculations concerning the free-surface boundary conditions and turbulence modelling near a free surface. Note that the first measurement depth is greater than one boundary layer thickness below the free surface and thus such effects may not be discerneble at this depth as indicated in the previous work. The analogy between the present flow and the flow in a streamwise corner has already been pointed out. It should also be mentioned that for curved corner flow it is well known that the effects of lateral curvature are likely to be an order of magnitude larger than those due to Reynolds stress gradients (Johnston 1978). Thus for the present circumstances, especially for steep waves, pressure gradient effects may be predominant.

VI. Extensions for Ship Boundary Layers

Two complications arise in extending the previous work to practical ship forms. First, the body geometry is no longer flat; consequently, the equations of motion and computational grid are more complex. Second, and more importantly, determination of the external nonzero Froude number potential flow

for an arbitrary three-dimensional body is both a formidable task and a topic of current research. The present boundary-layer work in this area began only very recently and the progress to date is not complete or fully satisfactory. However, it is felt that the difficulties encountered are of interest and for this reason some preliminary results are presented below. The Wigley hull was selected for the initial calculations since the geometry is relatively simple and can be described analytically and some nonzero Froude number experimental data (pressure distributions and velocity profiles) is available (Kajatani et al. 1983 and Shahshahan 1985).

Preliminary Results for the Wigley Hull

The calculations were performed using a surface-related curvilinear coordinate system (s,t,n) where: s is the distance along waterlines; t is the distance around the girth; and n is the distance along the outward normal. The metric and curvature coefficients are expressed in terms of the surface equation

$$\hat{R} = x\hat{i} + f(x,z)\hat{j} + z\hat{k} \qquad (34)$$

where

$$f = .05[1-(2x-1)^2][1-(\frac{z}{.0625})^2]$$

by

$$h_1 = |\hat{R}_x|$$

$$h_3 = |\hat{R}_z|$$

$$K_{13} = \frac{1}{h_1 h_3}\frac{\partial h_1}{\partial z}$$

$$K_{31} = \frac{1}{h_1 h_3}\frac{\partial h_3}{\partial x}$$

The (x,y,z) coordinates are nondimensionalized based on the body length L and the origin is located at the bow/waterplane intersection. Note that the (s,t,n) system is not orthogonal; since, the angle between the s and t curves

$$\alpha = \cos^{-1}\frac{f_y f_z}{h_1 h_3}$$

is 90° only at ends and the midbody. The maximum deviation from orthogonality occurs near x = .2 and .8 where $|\alpha| = 3°$. The terms in the boundary layer equations associated with the nonorthogonality of the (s,t,n) coordinates have been neglected and are presumed small. In general, the coordinates have a significant influence. In particular, K_{31} attains large values $|K_{31}| \approx 2$ near x = .125 and .875.

The present state-of-the-art of calculation methods for nonzero Froude number potential flow for an arbitrary three-dimensional body is such that no exact method is yet available (Workshop on Ship Wave-Resistance Computations 1979, 1980, and 1983). One of the more promising methods to emerge from the Workshop is that of Dawson (1977). The method uses a simple Rankine source distribution over both the body surface and a local portion of the undisturbed free surface. The free surface boundary conditions are linearized in terms of the double-model velocity. Upstream waves are prevented by use of a one-sided, upstream, finite-difference operator for the free-surface condition. The above approximations are more accurate for low speeds. Results from an improved version of the XYZFS method of Dawson (Cheng et al 1983) have been used in performing the boundary layer calculations to be presented next. The hull was discretized using 192 panels (24 axial and 8 girthwise). The velocity and pressure field on the hull surface obtained from XYZFS was interpolated onto the boundary layer computational grid using piecewise Hermite splines.

The results shown are for $Rn = 6.33 \times 10^6$ which corresponds to the experimental condition of Shahshahan (1985). 86 x-steps and 21 grid points across the boundary layer were used. A uniform grid was used in the z-direction. The results were found to be sensitive to the number of grid points used in the z-direction with 8 grid points giving the best results. The calculations were begun as laminar flow at x = .0125, with transition specified at x=.05 which corresponds to the location of the trip studs in the experiment. The Blasius solution based on local Rn was used for the initial conditions. Calculations were made for Froude number F_n = (0.,.267,.316,.4); however, results are presented only for Fn = (0.,.267).

Figure 25 shows both the complete XYZFS and the edge velocity solution potential flow for Fn=0. It is seen that the inaccuracy in the edge velocity solution is increased as compared to previous results for the simple Stokes-wave pressure distribution. Boundary-layer calculations were made using both potential-flow solutions. Figure 26 shows the displacement thickess δ^* and figures 27 and 28 show the wall-shear-stress magnitude τ_w and angle β obtained using the edge velocity solution potential flow. The results are completely consistent with the imposed edge conditions; namely, initially on the forebody the flow is downward towards the keel and subsequently on the afterbody the flow is upward towards the waterplane. This results in the displacement thickness trends shown in figure 26. Note that the behavior of τ_w can be correlated with δ^*, p_x and U_e while that of β with p_z and W_e. The results

obtained using the complete XYZFS potental flow are similar to those shown above. The main differences are in the crossflow velocity component resulting in less exaggerated trends in the depthwise direction.

Figure 29 shows both the complete XYZFS and the edge velocity solution potential flow for Fn=.267. It is seen that the inaccuracy in the edge velocity solution is substantial, especially for W_e. In particular, the edge condition solution W_e indicates a convergence of the external flow streamlines towards z = .013 for x > .7 (see figure 29g) while this is not indicated by the XYZFS W_e (see figure 29e). It should be recognized that the c_p curve along z=0 is the nondimensional wave elevation within the context of linear wave theory and, as seen from figure 29, the wave steepness is large over much of the wave profile (x<.4 and x>.9). This is also indicated by the large pressure gradients p_x and p_z. Note that, for a Stokes wave of similar steepness, the second-order terms are important and have the influence of reducing p_z. Boundary layer calculations were made using both potential-flow solutions. Figure 30 shows the displacement thickness δ and figures 31 and 32 show the wall-shear-stress magnitude τ_w and angle β obtained using the edge velocity solution potential flow. It is seen that the solution is consistent with what might be expected based on the imposed edge conditions; however, for x>.7 the solution has become unstable and diverges. Actually, for x<.7, the solution for F_n=.267 is basically similar to the F_n=0 solution, with the differences consistent with the differences in the edge conditions; that is, the thickening of the boundary layer on the forebody near the keel is increased; on the midbody, for all depths, the boundary-layer thickness is increased and the shear stress (τ_w and β) shows oscillations. For x>.7, the rapid boundary-layer growth near the waterplane and its subsequent divergence are no doubt due to the combined effects of prolonged convergence of the external flow streamlines towards z=.013 and the large adverse p_x and p_z for x>.9. The results obtained using the complete XYZFS potential flow exhibit a similar solution divergence as that shown above for x>.7 only initiating near the start of the calculation. The results at the higher F_n=(.316,.4) are quite similar to those just described; however, as the F_n increases, the calculation difficulties begin for smaller values of x. This is contrary to expectation since the wave steepness appears to decrease with increasing F_n. However, it is consistent with the fact that the approximations used in the Dawson method are more accurate for lower F_n. To help put the results in perspective, the measured displacement thickness for this F_n by Shahshahan (1985) is shown in figure 33. The measurements are for the afterbody region .5<x<1 and show that initially (x=.5) the boundary layer is thickest near the keel and subsequently the trend is reversed such that, for x>.75, the boundary layer is thickest near the waterplane. By comparing figures 26,30, and 33, it is seen that the calculations for F_n=0 and for F_n=.267 and x<.7 are in qualatative agreement with the measurements.

Wherein lies the problem? In order to determine this, calculations were also made using measured and synthesized pressure distributions. The measured pressure distribution (see figure 34) was obtained from the wave profile and surface pressure measurements of Kajatani et al (1983). By comparing figure 34 and 29 it is seen that qualitatively the XYZFS and measured pressure distributions are in agreement. This was also found to be true for Fn = .316. The results obtained from the boundary layer calculations made using the measured pressure distribution showed similar tendencies as described above. However, in this case, there is also a large overgrowth of the boundary layer on the midbody near the keel. Finally, a pressure distribution was synthesized using the Stokes wave pressure distribution in order to simulate the Fn = .267 pressure distribution (see figure 35). As might be expected, the boundary layer calculation results obtained using the synthesized pressure distribution are well behaved and consistent with expectations.

Based on the above investigation it is believed that the primary source of the difficulty is in the specification of the external flow. The XYZFS and measured pressure distributions appear to provide too coarse a description for accurate boundary-layer calculations. Also higher-order effects may be important in the potential-flow solution. No doubt, a part of the difficulty is due to the limitations of the present boundary-layer computational method for large crossflows and crossflow pressure gradients. Future work will concentrate on clarification of these issues.

ACKNOWLEDGEMENT

I am pleased to acknowledge and thank Professor Landweber and Patel for their significant contributions to this work. Not only did they suggest the present topic to the author, but they also provided many helpful discussions. I would also like to acknowledge W.S. Hwang for his assistance in performing the experiments and B.H. Cheng of the Numerical Fluid Dynamics Branch of DTNSRDC for providing the XYZFS potential-flow calculations for the Wigley hull. This research was sponsored by the Office of Naval Research, Special Focus Research Program in Ship Hydrodynmics, under Contract N00014-83-

K-0136. The Graduate College of The University of Iowa provided a large share of the computer funds.

REFERENCES

Adee, B.H., 1972, "Boundary Layers on Ships", Ph.D. thesis, Univ. of Calif., Berkeley, CA, 56 pp.

Adee, B.H., 1975, "Fluid Flow Around a Ship's Hull", Proc. 1st Int. Conf. Numer. Ship Hydrodyn., Bethesda, MD, pp. 435-454.

Celik, I., Rodi, W. and Hossain, M.S., 1982, "Modelling of Free-Surface-Proximity Effects on Turbulence", Proc. Refined Modelling of Flows, Paris.

Chow, S.K., 1967, "Free-Surface Effects on Boundary-Layer Separation on Vertical Struts", Ph.D. Dissertation, The University of Iowa.

Doi, Y., 1980, "Observation of Stern Wave Generation", Proc. Continued Workshop on Ship Wave Resistance, Izu Shuzenji, Japan.

Gadd, G.E., 1971, "The Approximate Calculation of Turbulent Boundary Layer Development on Ship Hulls", Trans. R. Inst. Nav. Archit., 113:59-71.

Hinatsu, M. and Takeshi, H., 1985, "A Calculation Method for Resistance Prediction Including Viscid-Inviscid Interaction", Proc. 2nd Sym. Ship Viscous Resistance, Goteborg.

Hotta, T. and Hatano, S., 1983, "Turbulence Measurements in the Wake of a Tanker Model on and under the Free Surface", read at the Autumn Meeting of the Society of Naval Architects of Japan.

Huang, T.T. and von Kerczek, C., 1972, "Shear Stress and Pressure Distribution on a Surface Ship Model: Theory and Experiment", Ninth Symposium of Naval Hydrodynamics, Paris, France.

Johnston, J.P., 1978, "Internal Flow", Topics in Applied Physics, Vol. 12, Springer-Verloz, Berlin.

Kajitani, H. Mijata, H., Ikehata, M., Tanaka, H., Adachi, H., Namimatsu, M., and Ogiusia, S., (1983), "The Summary of the Cooperative Experiment on Wigley Parabolic Model in Japan", Proc. 2nd DTNSRDC Workshop on Ship Wave-Resistance Computations.

Kinsman, B. 1976, "Wind Waves", Prentice-Hall, Englewood Cliffs.

Lin, J.D. and Hall, R.S., 1966, "A Study of Flow Past a Ship-Like Body", Univ. Conn C.E. Dept. Rep. CE-66-7, 130 pp.

Mei, C.C. 1983, "The Applied Dynamics of Ocean Surface Waves", John Wiley & Sons, New York.

Nagamatsu, T. 1981, "Flow Measurements Near the Stern of a Model of a Full Form Ship", Proc. 30th Japan nat. Congress for Appl. Mech., Vol. 30, pp. 481-492.

Nash, J.F. and Patel, V.C., 1972, "Three Dimensional Turbulent Boundary Layers", SBC Tech books, Atlanta.

Patel, V.C. and Choi, D.H., 1979, "Calculation of Three-Dimensional Laminar and Turbulent Boundary Layers on Bodies of Revolution at Incidence", Proc. 2nd Sym. Turbulent shear Flow, London, pp. 179-217.

Patel, V.C. 1982, "Some Aspects of Thick Three-Dimensional Boundary Layers", Proc. 14th ONR Sym. Naval Hydrodynamics, Ann Arbor, MI, pp. 999-1040.

Patel, V.C., Sarda, O.P. and Shahshahan, A., 1983, "Calculation of Ship Boundary Layers", Proc. 4th Sym. Turbulent Shear Flow, Karlsruhe, p. 3.1.

Patel, V.C. and Baek, J.H., 1983, "Calculation of Boundary Layers and Separation on a Spheroid at Incidence", Proc. 2nd Sym. Numerical & Physical Aspects of Aerodynamic Flows, Long Beach, CA; Also, AIAA JOurnal, Vol. 23, pp. 55-63, 1985.

Rodi, W., 1980, "Turbulence Model and Their Application in Hydraulics" presented at the IAHR-Section on Fundmentals of Division II: Experimental and Mathematical Fluid Dynamics.

Sachdeva, R.C. and Preston, J.H., 1975, "Theoretical Calculation of Boundary Layers on Ship Hulls", Trans. N.E. Coast Inst. Eng. Shipbld. 92:17-22.

Salvesen, N., von Kerczek, C.H., Yue, D.K. and Stern, F., "Computations of Nonlinear Surge Motions of Tension Leg Platforms", OTC Paper #4394, 14th Annual Offshore Technology Conference, Houston, TX, May 1982, pp. 199-215.

Salvesen, J., 1966, "Second-Order Wave Theory for Submerged Two-Dimensional Bodies", ONR 6th Naval Hydrodynamics Symposium, Washington, D.C.

Salvesen, N., 1969, "On Higher-Order Wave Theory for Submerged Two-Dimensional Bodies", JFM, vol. 38.

Sarpkaya, T. and Isaacson, M., 1981, "Mechanics of Wave Forces on Offshore Structures", Van Nostrand Reinhold Company, New York.

Shahshahan, A. 1985, "Effects of Viscosity on Wavemaking Resistance of a Ship", Ph.D. thesis, The University of Iowa, Iowa City, Iowa.

Shearer, J.R. and Cross, J.J., (1965), "The Experimental Determination of the Components of Ship Resistance for a Mathematical Model", The Royal Inst. of Naval Arch.

Steele, B.N., 1967, "Measurements of Components of Resistance on a Tanker Model", National Physical Laboratory Ship Division Report No. 106.

Steele, B.N. and Pearce, G.B., 1968, "Experimental Determination of the Distribution of Skin Friction on a Model of a High Speed Liner", Transactions of Royal Institution of Naval Architects Vol. 110, p. 79.

Stern, F., 1985, "Effects of Waves on the Boundary Layer of Surface-Piercing Body", IIHR Report No. 288.

Swean, T.F. and Peltzer, R.D., 1984, "Free Surface Effects on the Wake of a Flat Plate", NRR Memo. Rep. 5426.

Tzou, K.T.S., 1968, "An Experimental Study of Shear Stress Variation on Series-60 Ship Model", Iowa Institute of Hydraulic Research Report No. 108.

Webster, W.C. and Huang, T.T., 1979, "Study of the Boundary Layer on Ship Forms", J. Ship Research, Vol. 14, pp. 153-167.

Wu, J. and Landweber, L. 1963, "Variation of Viscous Drag with Froude Number", Proc. 10th Int. Towing Tank Conf., 2:90-95.

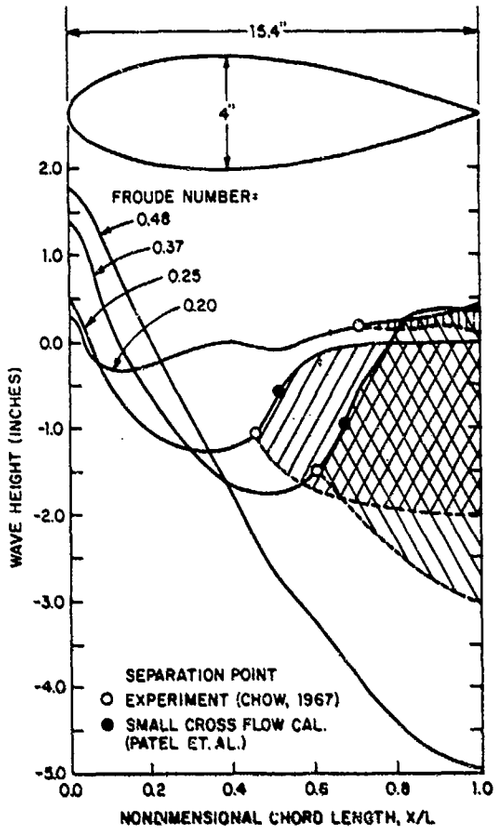

Figure 1. Experimental Wave-Induced Separation (Chow 1967)

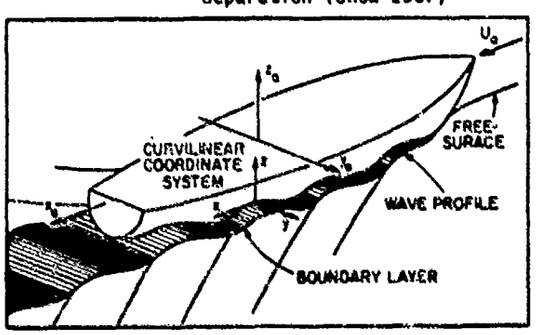

Figure 2. Definition Sketch

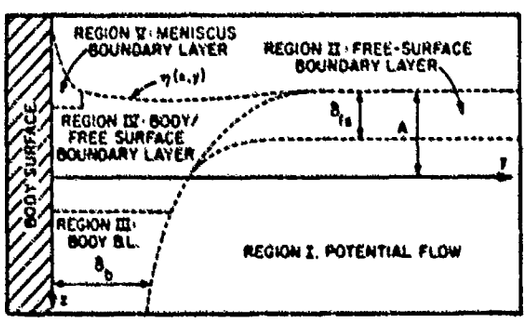

Figure 3. Flow Field Region Definition Sketch

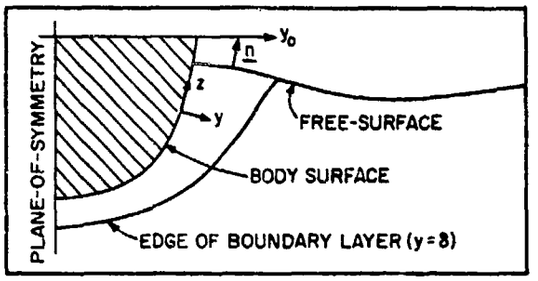

Figure 4. Body Cross-Section Plane

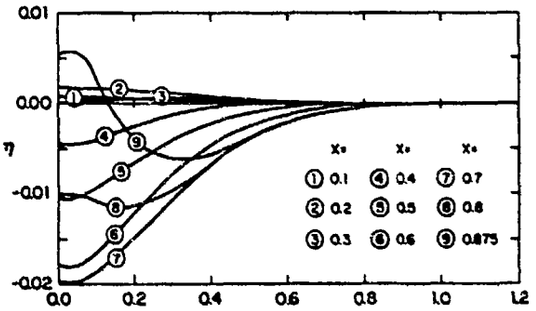

Figure 5. Free-Surface Elevation Within the Boundary Layer (Stern 1985)

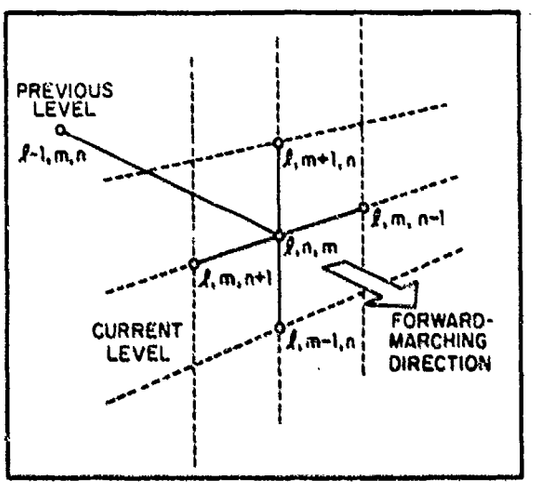

Figure 6. Finite-Difference Molecule

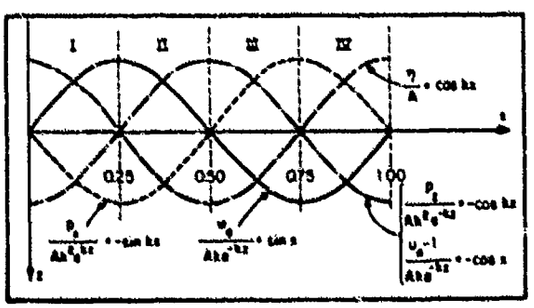

Figure 7. Potential-Flow Regions Definition Sketch

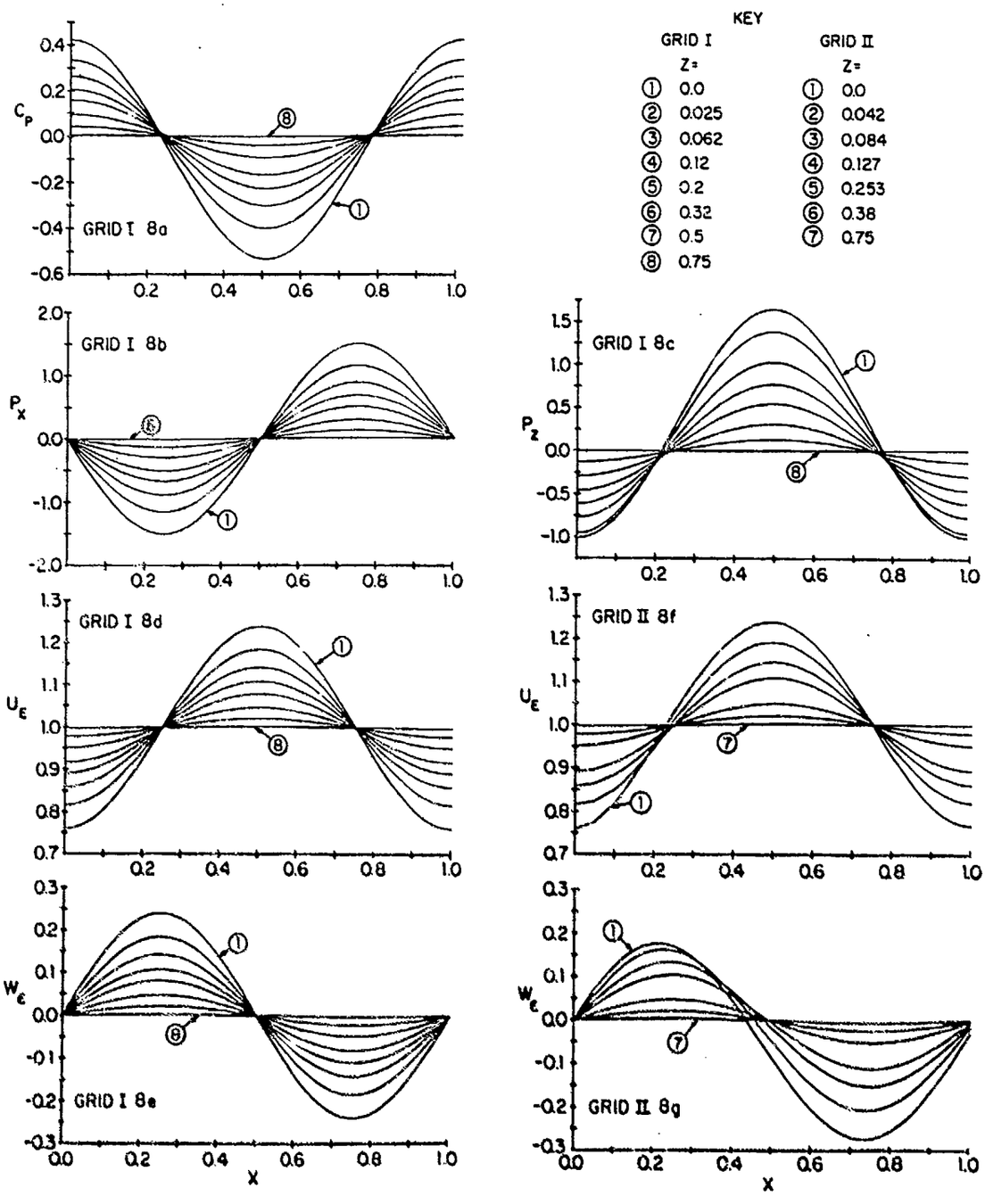

Figure 8. Exact and Edge Velocity Solution Potential Flow: (a) exact c_p; (b) exact p_x; (c) exact p_z; (d) exact U_e; (e) exact W_e; (f) edge velocity solution U_e; (g) edge velocity solution W_e

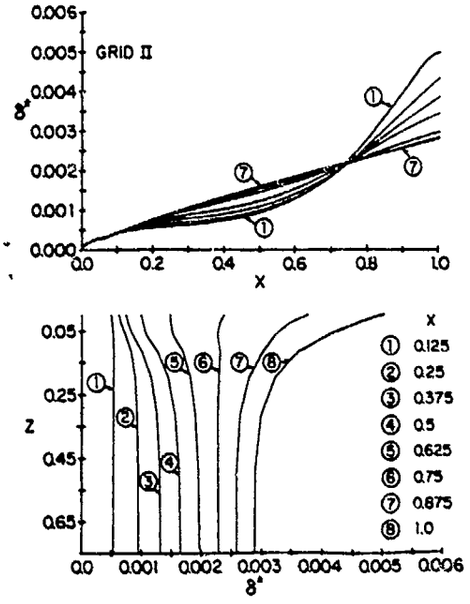

Figure 9. Displacement Thickness

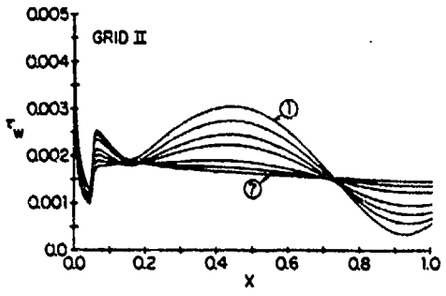

Figure 10. Wall-Shear-Stress Magnitude

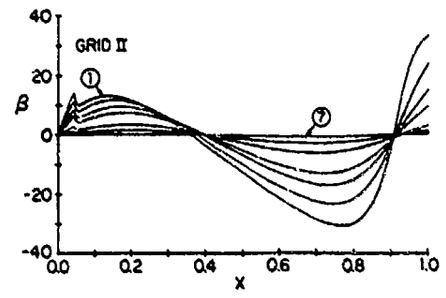

Figure 11. Wall-Shear-Stress Angle

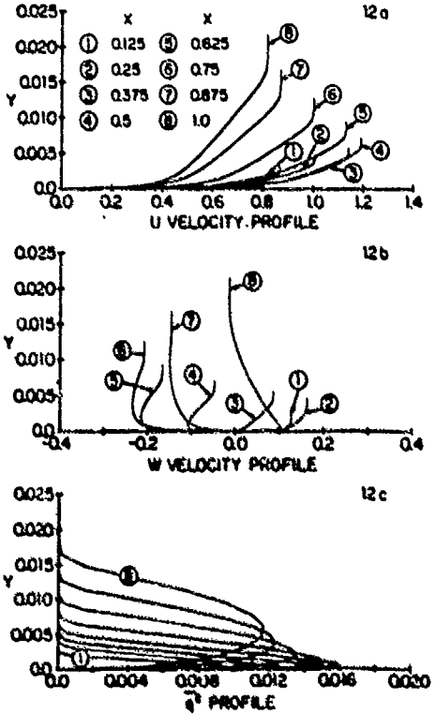

Figure 12. Velocity and Turbulent Kinetic Energy Profiles at z=.042

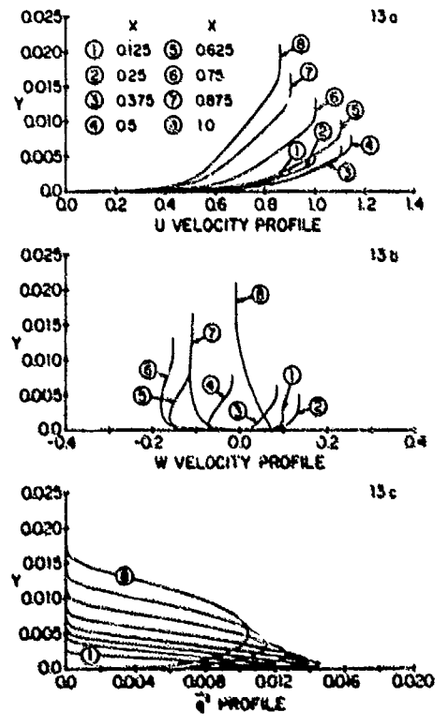

Figure 13. Velocity and Turbulent Kinetic Energy Profiles at z=.084

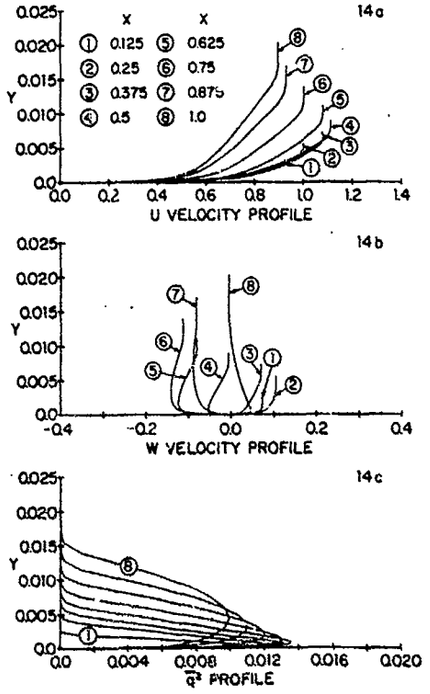

Figure 14. Velocity and Turbulent Kinetic Energy Profiles at z=.127

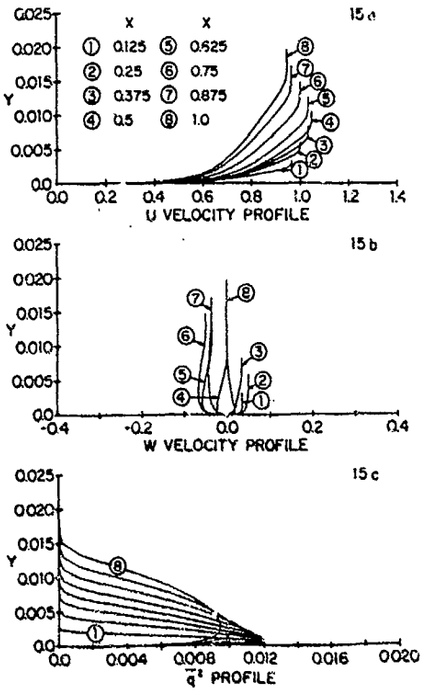

Figure 15. Velocity and Turbulent Kinetic Energy Profiles at z=.253

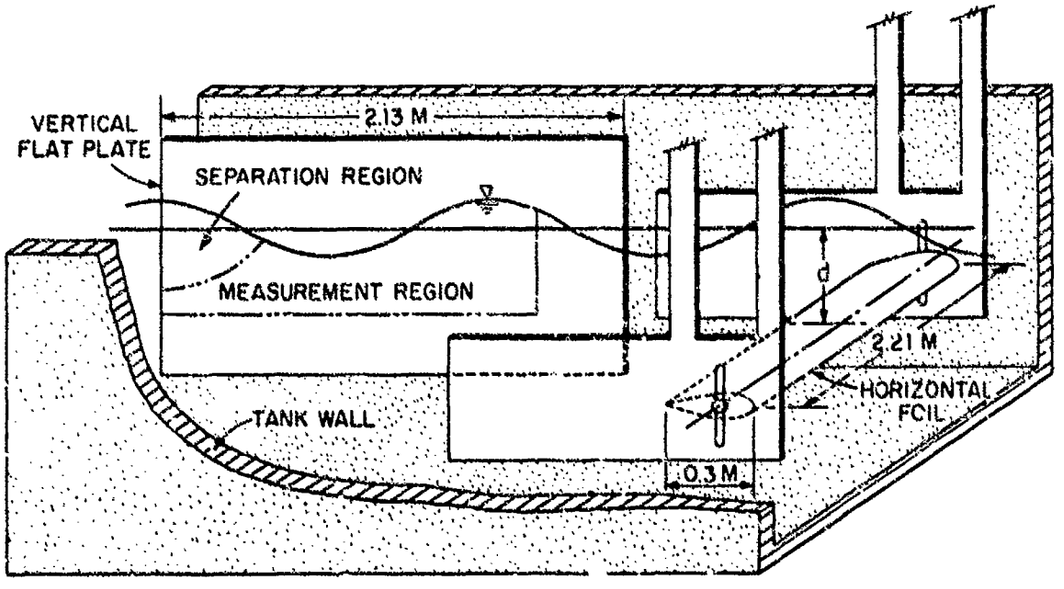

Figure 16. Experimental Model

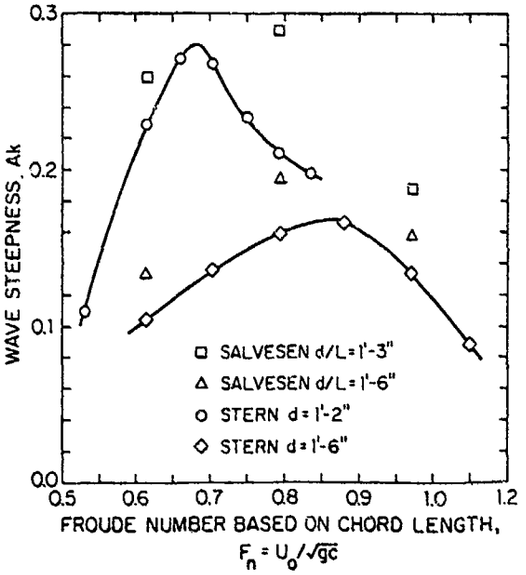

Figure 17. Wave Steepness

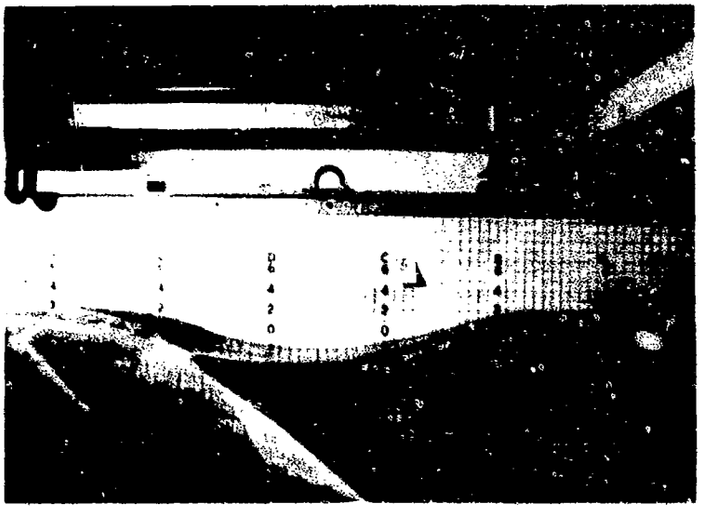

Figure 18. Wave Profile

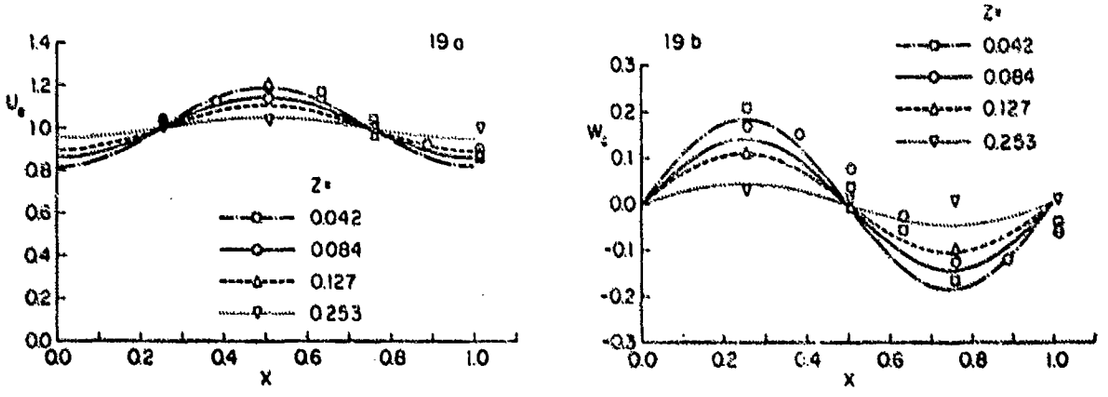

Figure 19. Measured Edge Velocities: (a) U_e; (b) W_e

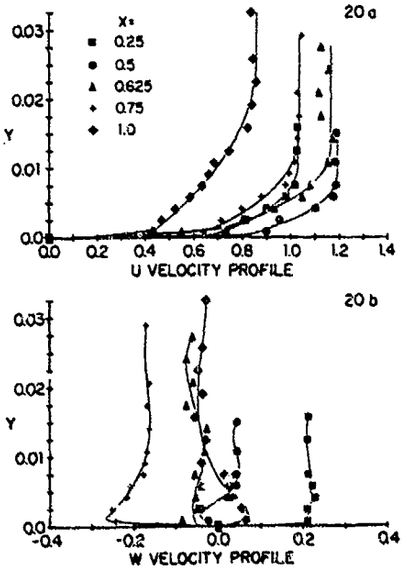

Figure 20. Measured Velocity Profiles at z = .042

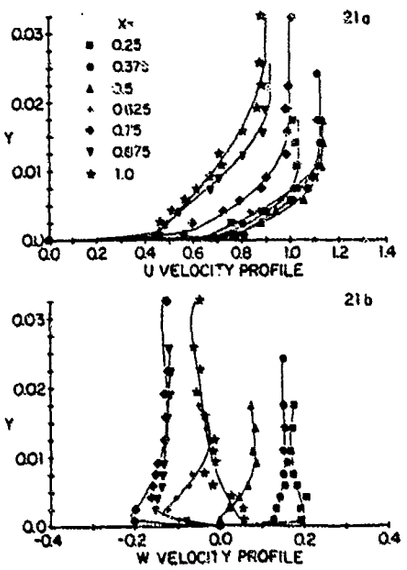

Figure 21. Measured Velocity Profiles at z=.084

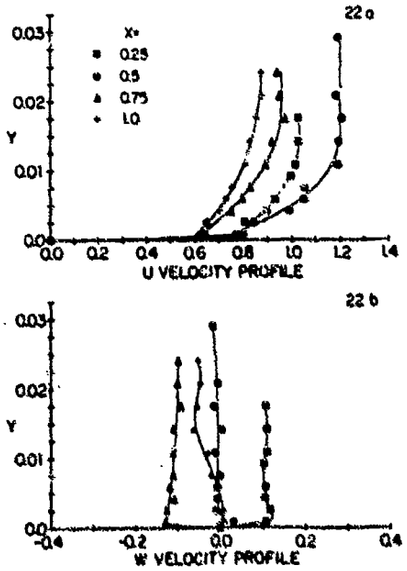

Figure 22. Measured Velocity Profiles at z=.127

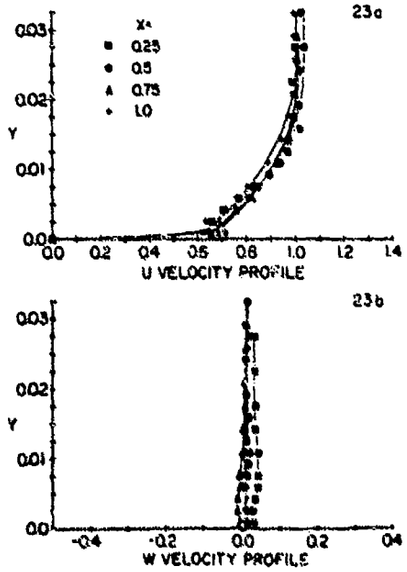

Figure 23. Measured Velocity Profiles at z=.253

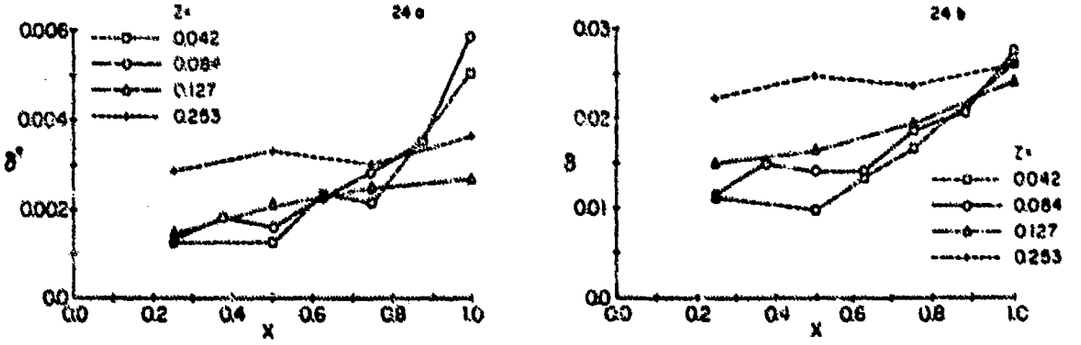

Figure 24. Measured Displacement and Boundary Layer Thickness: (a) δ^*; (b) δ

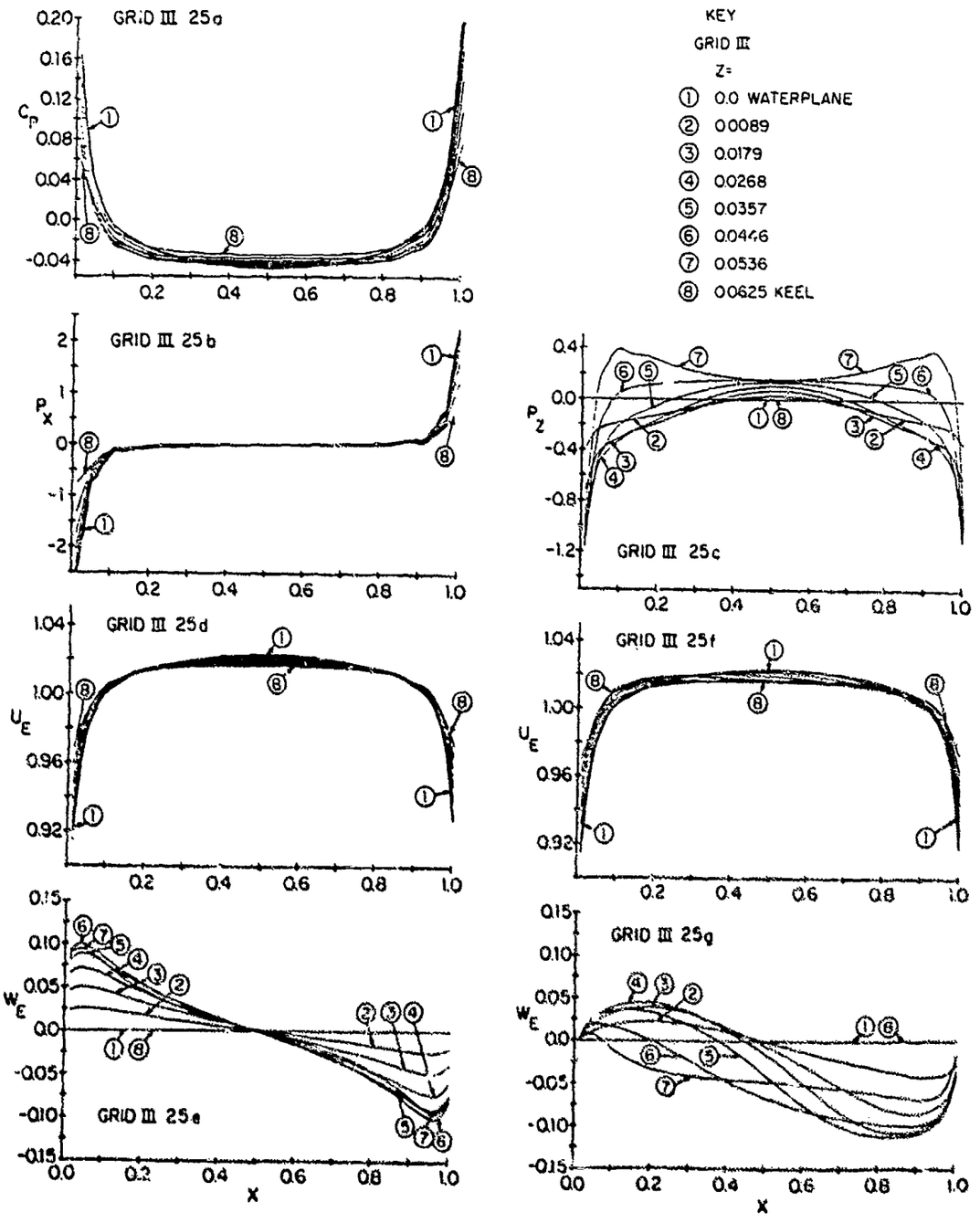

Figure 25. XYZFS and Edge Velocity Solution Potential Flow: (a) XYZFS C_p; (b) XYZFS P_x; (c) XYZFS P_z; (d) XYZFS U_e; (e) XYZFS W_e; (f) edge velocity solution U_e; (g) edge velocity solution W_e

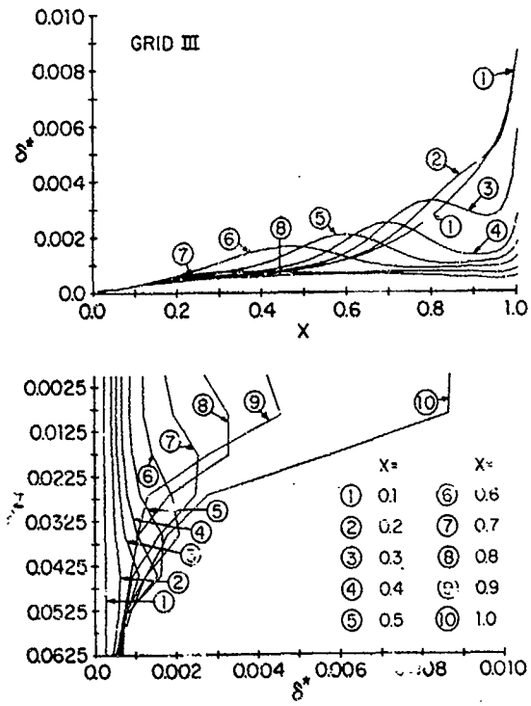

Figure 26. Displacement Thickness: $F_n = 0$

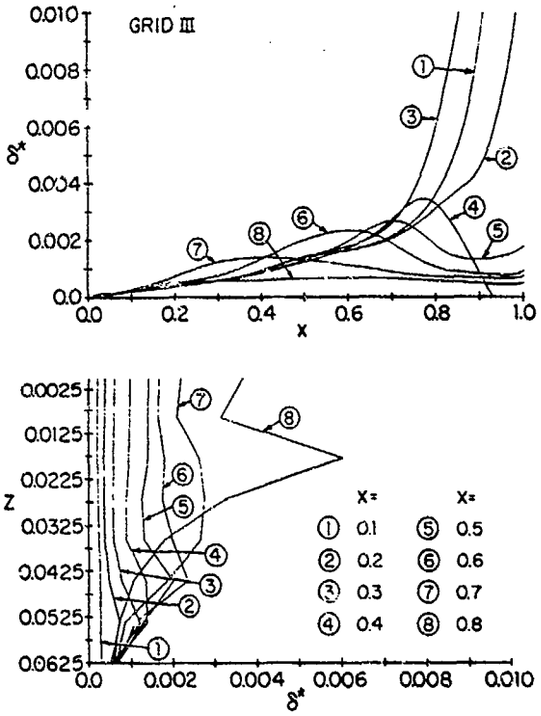

Figure 30. Displacement Thickness: $F_n = .267$

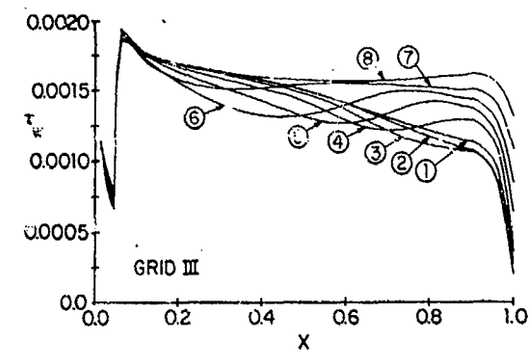

Figure 27. Wall-Shear-Stress Magnitude: $F_n=0$

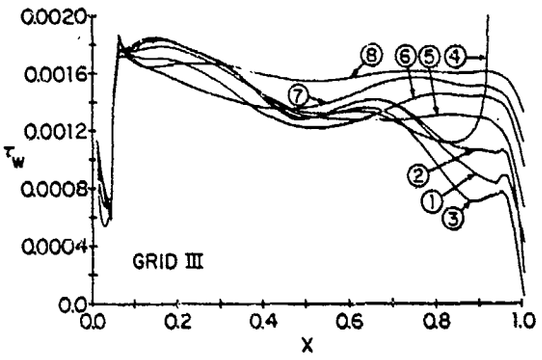

Figure 31. Wall-Shear-Stress Magnitude: $F_n = .267$

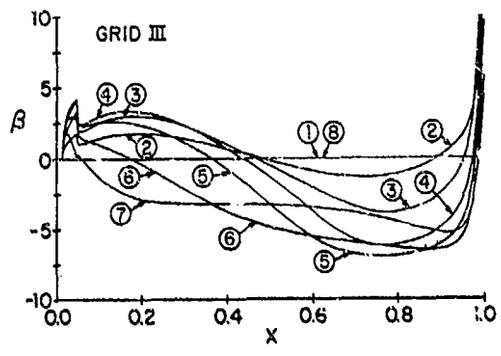

Figure 28. Wall-Shear-Stress Angle: $F_n = 0$

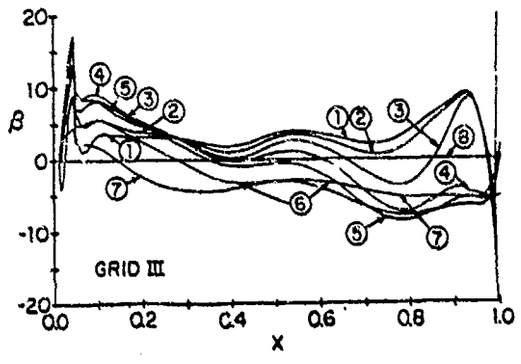

Figure 32. Wall-Shear-Stress Angle: $F_n = .267$

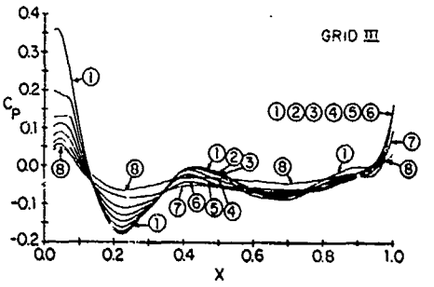

Figure 34. Measured Pressure Distribution (Kajatani et al. 1983): F_n = .267

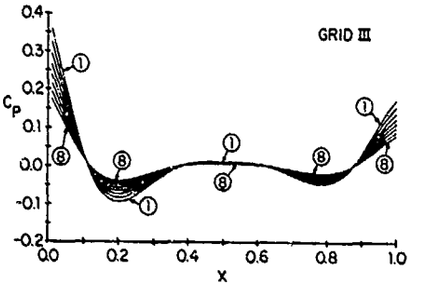

Figure 35. Synthesized Pressure Distribution: F_n = .265

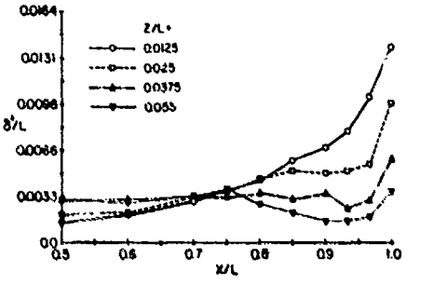

Figure 33. Measured Displacement Thickness (Shahshahan 1985): F_n = .267

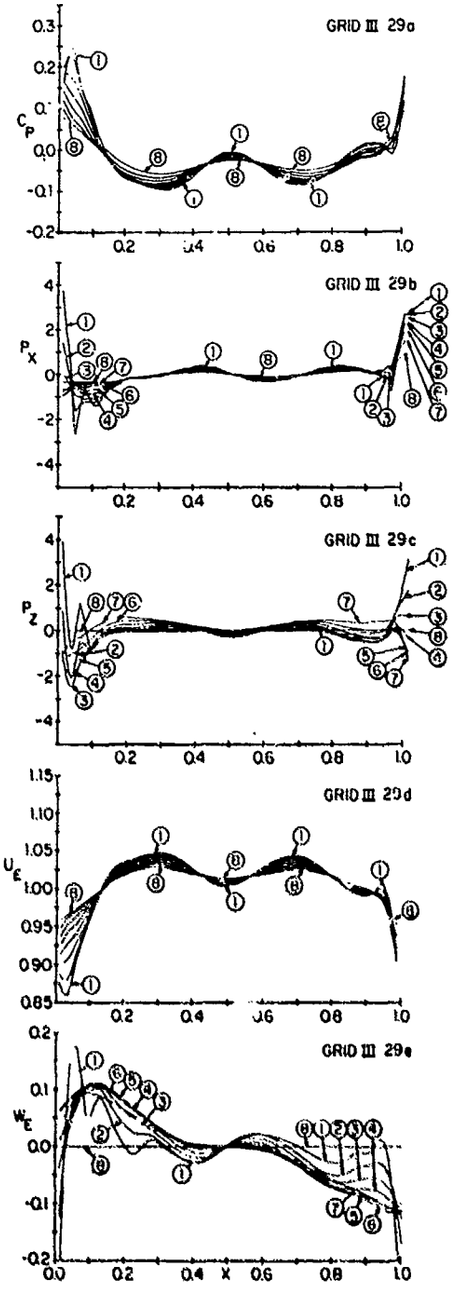

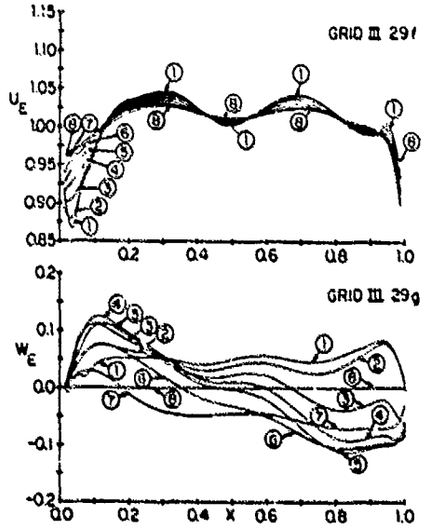

Figure 29. XYZFS and Edge Velocity Solution Potential Flow: (a) XYZFS C_p; (b) XYZFS P_x; (c) XYZFS P_z; (d) XYZFS U_e; (e) XYZFS W_e; (f) edge velocity solution U_e; (g) edge velocity solution W_e

DISCUSSION
of the paper
by F. Stern

"Influence of Waves on the Boundary Layer of a Surface-Piercing Body"

DISCUSSION
by H. Wang

I wish to commend you on your calculations, which bring out the differences in boundary layer characteristics between double-model and forward speed cases. I am specially interested in your displacement thickness results for the Wigley hull, shown in Figures 26 and 30. These basically show that for $x/L \leq 0.7$, the displacement thickness for Fn = 0.267 are somewhat larger than those for the double-model case, Fn = 0, with a larger difference at $x/L = 0.8$. It is, of course, unfortunate that you were not able to extend your calculations for Fn = 0.267 beyond $x/L = 0.8$, where the largest boundary layer growth takes place. Do you expect the differences between the Fn=0 and Fn=0.267 cases to monotonically increase with x/L? Do you expect these differences to increase or decrease for thicker ship hulls?

Author's Reply

In response to Dr. Wang I do not necessarily expect the largest differences between zero and nonzero Froude number boundary layer development to occur near the stern. It depends on the differences in the pressure distributions between zero and nonzero Froude numbers. Of course, the flow near the stern is dependent on the entire history of the upstream boundary layer development. For the particular case investigated (based on Figures 26 and 29) the largest differences may actually occur on the forebody. Since in general wavemaking increases with hull thickness I would expect larger differences between zero and nonzero Froude number boundary layer development to occur for thicker hull forms.

DISCUSSION
by Y. Lee

The author ought to be congratulated for the success in solving this difficult problem. However, I have two unclear points about the paper. First, from Equations (18) to (24) the one-equation turbulence modal is used. I am interested to know what is the specific modification made for the free surface. Second, the fluctuation of streamwise δ^* in the z-direction shown in Figures 26 and 30 along the water line indicates the instability of the thin boundary-layer solution in this region, as the Region II defined in Figure 3 of the paper. The validity of the thin boundary-layer solution, used by the author, in the region of the water line is questionable. The adopted plane-of-symmetry boundary condition, i.e. $C_3 = 0$ in Equation (17), at the water line is also nonrealistic. Would the author comment on this?

Author's Reply

In response to Dr. Lee, the modification of the turbulence model to account for the influence of the free surface is in the calculation of the dissipation length equation (23) where n is defined as the minimum of either y/δ or z/δ. As discussed in the paper, in the present investigation, which is for turbulent flow only, no attempt was made to resolve the details of the flow in the region very close to the free surface (region IV of figure 3), and as such, only an approximate symmetry boundary condition is applied on the mean free surface and the usual thin boundary layer equations have been used. The symmetry boundary condition corresponds to a small-cross-flow solution along the mean free surface and a fully three-dimensional solution below. Note that this is not equivalent to a plane-of-symmetry boundary condition. The laminar flow order-of magnitude estimates for region IV (see Table 1) indicate that the symmetry condition solution is valid only for extremely small wave steepness Ak. For larger values of Ak, the role of the free-surface boundary conditions is significant and a consistent formulation for region IV requires the solution of the partially-parabolic Navier-Stokes equations. For turbulent flow it is not possible to reach such definitive conclusions due to the uncertainty of assigning the orders of magnitude to the Reynolds stresses near a free surface. The good agreement between the present calculations and measurements both of which do not resolve the flow in region IV indicate that the Table 1 order-of-magnitude estimates may also be valid for turbulent flow. That is, the influence of the free-surface boundary conditions is confined to a region very close to the free surface.

Session VI

SUBMERGED BODIES AND GEOMETRY

Session Chairman
C.M. Lee
Office of Naval Research
Arlington, VA, U.S.A.

PREDICTION OF THE UNSTEADY HYDRODYNAMIC CHARACTERISTICS OF SUBMERSIBLE VEHICLES

Michael R. Mendenhall
Stanley C. Perkins, Jr.

Nielsen Engineering & Research, Inc.
510 Clyde Avenue
Mountain View, CA 94043

Abstract

A rational flow model to predict the nonlinear hydrodynamic forces and moments on a general submersible vehicle undergoing steady and unsteady maneuvers is described. The major physical flow phenomena over the submersible vehicle at high incidence angles are simulated, including the lee-side separation vorticity and the trailing vorticity from the lifting surfaces. The mutual interaction between the vehicle and the time-dependent flow field is considered in the prediction of the unsteady hydrodynamic characteristics at any specified instant in time. The hydrodynamic prediction method is coupled with a six-degree-of-freedom equation-of-motion solver to predict vehicle trajectories. Comparisons of measured and predicted results for static and steady flow conditions are presented to show verification of the method, and predicted results for an unsteady maneuver are presented to illustrate the use of the method.

Nomenclature

c_n	normal-force coefficient per unit length
C_A	axial-force coefficient
C_f	skin-friction coefficient
C_m	pitching-moment coefficient
C_n	yawing-moment coefficient
C_N	normal-force coefficient
C_p	pressure coefficient
C_Y	side-force coefficient
D	hull diameter
$\hat{i},\hat{j},\hat{k}$	unit vectors in x,y,z-system
I	moment of inertia
ℓ	hull length
m	mass
M'	pitching moment coefficient
N'	yawing-moment coefficient
p	rolling rate, and local static pressure
q	pitching rate
q_∞	free stream dynamic pressure, $\frac{1}{2}\rho V_\infty^2$
q'	nondimensional pitching rate, $q\ell/V_\infty$
r	yawing rate
r'	nondimensional yawing rate, $r\ell/V_\infty$
r_o	hull radius
R	radial distance
Re	Reynolds number
S_b	base area
S_r	reference area
t	time
V_∞	free stream velocity
$\forall$	hull volume
X'	axial-force coefficient
Y'	side-force coefficient
u,v,w	perturbation velocities
x,y,z	coordinate system, origin at CG
x_i,y_i,z_i	inertial coordinate system
$\bar{X},\bar{Y},\bar{Z}$	coordinate system, origin at nose
Z'	normal-force coefficient
α	angle of attack
α_c	angle between free stream velocity vector and body axis
β	angle of yaw
Γ	vortex strength
Δt	time increment
ΔX	axial length increment
θ	polar angle
ρ	free stream density
ϕ	roll angle and velocity potential
Φ	velocity potential
ψ	stream function
ω	rotation rate

Subscripts

$(\bar{\ })$	average
$(\dot{\ })$	derivative with time
$(\ )_{AM}$	apparent mass
$(\ )_B$	body
$(\ )_P$	point P on hull
$(\ )_s$	steady
$(\ )_u$	unsteady

Introduction

Operational requirements of modern submersible vehicles, whether free-

running or towed, can involve dynamic maneuvers which result in very high angles of incidence and large angular rates. Under these extreme flow conditions, the vehicle experiences nonlinear hydrodynamic forces and moments caused by flow separation and roll up of the hull lee-side vorticity (Fig. 1) and induced effects of trailing vorticity from lifting surfaces. In unsteady flow, the strength and position of these vortices and their induced effects are dependent on the history of the motion of the vehicle, and conversely, the motion of the vehicle in a maneuver is dependent on the vortex-induced hydrodynamic effects. Prediction of vehicle motion under such conditions requires a different approach from the traditional linear hydrodynamic prediction methods applicable to low angles of incidence and unseparated flow. Unsteady nonlinear techniques are required for predicting and understanding the complex flow phenomena associated with submersible vehicles in arbitrary maneuvers.

A rational flow model to simulate the major physical features of the complex flow near a submersible configuration undergoing steady or unsteady motions in incompressible flow is described in this paper. The prediction method, based on the rational flow modeling technique, is directed at the calculation of nonlinear hydrodynamic forces and moments without resort to empirical information; therefore, the method is applicable to general submersible configurations for which experimental data are not available. The genesis of the hydrodynamic method described herein is the discrete vortex cloud model of the lee-side vorticity shed from bodies alone at high angles of incidence (Ref. 1). The approach was extended to arbitrary configurations with control surfaces under steady turning conditions in Reference 2, and it was further extended to unsteady flow conditions in Reference 3. The latter effort also includes the capability to predict vehicle trajectories for specified initial conditions and control inputs.

The unsteady trajectory calculation uses a direct simulation approach in which the vehicle stability derivatives are not required a priori. Beginning with a steady flow condition, the equations of motion of the vehicle are integrated over a specified time interval. This results in a new vehicle position and attitude and modified flow conditions. Forces and moments on the vehicle, required in the equations of motion, are obtained at each instant in time by integration of the instantaneous pressure distribution on the vehicle. The shed vorticity in the wake of the vehicle is permitted to move in this interval under the influence of the external flow conditions, the vehicle, and the wake itself. The vortex wake represents the historical lag in the flow field which relates to the aft portion of the vehicle what happened at an earlier time on the nose. The early portions of the wake are eventually swept downstream past the base of the vehicle and their effect on the induced loads is lost forever.

In the remainder of this paper, a rational flow model developed to predict the nonlinear, unsteady hydrodynamic forces and moments acting on submersible vehicles undergoing large unsteady maneuvers is described. The motion of the vehicle is predicted as are the detailed loads acting on the vehicle components. The state of motion is described by the translational velocity components u, v, w and the angular velocity components p, q, r as a function of time. The following sections include a discussion of the approach to the problem and a description of the flow models and analysis required. The prediction method is evaluated through comparison of measured and predicted results for a variety of configurations under a range of flow conditions. Where data are not available, results are presented for general configurations and flow conditions to demonstrate the method.

General Approach

The objective of this paper is to describe a prediction method for submersible vehicles at high angles of incidence in a flow regime in which the hydrodynamic characteristics are dominated by nonlinear effects. The method represents the complex physical phenomena in the flow field adjacent to the vehicle, including both steady and unsteady hull separation vorticity and lifting surface trailing vorticity. Submersible vehicles can have a wide range of configurations and component arrangements, but for purposes of this discussion, the rational flow model is directed at axisymmetric hulls with fore and aft lifting surfaces (Fig. 2). Vehicle motion and trajectory are predicted with a direct calculation of the nonlinear hydrodynamic characteristics of the vehicle without resort to empirical information or prior knowledge of the vehicle stability derivatives.

The major nonlinear effect on a submersible vehicle at high incidence

angles in both steady and unsteady flow conditions is induced by the vortex wake which includes hull separation vorticity and lifting surface trailing vorticity. The hull separation vorticity is formed by boundary layer fluid leaving the body from separation points. This vorticity rolls up into a symmetric pair (Fig. 1) on hulls alone, but in the presence of lifting surfaces and its shed vorticity, the roll up is generally asymmetric. The associated induced effects become asymmetric in this case. The vortex-induced effects can dominate the nonlinear hydrodynamic forces and moments and thus have a major influence on the vehicle motion.

A successful approach to modeling the hull lee-side vorticity under steady flow conditions is the representation of the vortex wake by a cloud of discrete vortices. As described by this author (Refs. 1, 4 and 5) and other investigators (Refs. 6, 7, and 8), the vortex cloud model provides a reasonable means to predict effects of a complex flow phenomenon. The selected approach to the problem of maneuvering vehicles will start with the basic vortex cloud model and extend this model to the more complicated unsteady flows.

Calculation of the hydrodynamic characteristics of a submersible configuration under steady translation and rotation is carried out using an axial marching procedure in the same manner as the static approach (Ref. 1). This particular flow situation arises when a model is tested on a rotating arm experimental apparatus (Fig. 3) such that the rotation rate and onset angle of incidence are constant with time. The basic discrete vortex shedding and tracking model are unchanged; however, the surface pressure coefficient calculation and the vortex tracking procedures reflect the fact that the vehicle is in steady flow which is constant in time but changing along the body. The strength and position of the vortex wake on the body are a function of the motion of the body.

In unsteady flow conditions, the situation is more complex. The initial conditions, which must be steady, are computed as described above for specified velocities, angles, and rates. The predicted forces and moments on the vehicle are used to compute its motion over a small time interval, assuming the forces and moments and flow conditions are constant in the interval. The trajectory calculation produces new flow conditions and time rates of change of flow variables at the end of the time interval. The vortex wake moves downstream under the influence of the changing local flow during the interval Δt where it influences the pressure distribution on the body and subsequent separation. New vortices are added to the flow field, new forces and moments are computed, and the calculation procedure is repeated.

Analysis

Geometry Models

The rational flow model contained in the prediction method is comprised of three basic geometry models representing a hull, lifting surfaces, and a propulsion system. A sketch indicating the major components of a generic submersible configuration is shown in Figure 4. The flow models required to represent the configuration shown in this sketch are described in this section.

Hull. The hull is defined as a body of revolution without appendages. The hull volume effects are represented by a series of point sources and sinks distributed on the hull axis. A three-dimensional singularity distribution provides a potential flow model for calculating velocities at any point in the flow field outside the body surface and for calculating the surface pressure distribution on the hull surface. This type of three-dimensional representation is similar to that described in Reference 9 for missile shapes, but with modifications for modeling typical closed-body submersible shapes. These modifications include the source/sink spacing, a condition imposed on the solution that the sum of all source strengths be zero (to ensure that the surface described by the stream function is a closed surface), and conditions which enforce the existence of stagnation points at the body nose and the body tail.

The displacement thickness of the axial boundary layer can cause the effective volume of the hull to increase and affect the loadings. A correlation for determining a boundary layer displacement thickness as a function of axial position along the hull has been developed for use with the rational flow model. The correlations are based on the assumption of a 1/7th-power velocity profile relation and the inverse relationship between the displacement thickness and the hull radius (Ref. 10). The displacement thickness relation used to modify the actual hull shape to account for boundary layer effects aft of the maximum radius is given by

$$\delta^* = .04625\,(X-X_t)\,\frac{r_{max}}{r_o}\left(\frac{V_\infty}{\nu}\,(X-X_t)\right)^{-.2} \qquad (1)$$

Base separation effects are accounted for using the empirical 'equivalent base' approach described in Reference 11 in which the hull is assumed to be at constant pressure downstream of the axial position of separation. The equivalent base of the hull, for purposes of determining loading distributions, is the point at which the base area is

$$S_b = 0.117\,\forall^{2/3} \qquad (2)$$

Lifting Surfaces. The prediction method described herein permits two regions containing lifting surfaces, with each region containing up to 16 separate lifting surfaces or fins. Each fin is described with four points; that is, the method does not permit breaks in the leading edge and trailing edge. A fin may be attached to the body or to another fin as in an endplate.

Each surface is modeled using the vortex-lattice lifting surface method described in References 12 and 13. Horseshoe vortices are distributed on the lifting surface and are imaged inside the constant-radius hull section (Ref. 14). The strengths of the horseshoe vortices are obtained by satisfying the flow tangency condition at control points distributed over the lifting surface. This boundary condition includes induced effects from shed vorticity in the field, the presence of the hull, the impressed flow conditions (including angular rotation), and the image vortex system inside the hull. In addition, the boundary condition includes mutual interference from all lifting surfaces in the region under consideration.

The method has the option of representing each lifting surface as a fixed surface with dihedral and incidence or as a control surface with arbitrary deflection angle. In addition, the control surfaces may have the following three types of trailing-edge flap configurations: partial-span full-chord flap, partial-span partial-chord flap, and full-span partial-chord flap. The control surface deflection can be varied with time for unsteady flow conditions.

Propeller. The propulsion model included in the rational flow method is a single, stern mounted, unshrouded propeller for which open water performance data are available. The loads induced on a submersible configuration by the propeller consist of two parts: the direct loads on the propeller which are transmitted to the hull through the shaft and the loads induced by the propeller on the hull and stern appendages. Calculation of shaft loads is based on a combination of the McCarthy method for nonuniform axial flow (Ref. 15) and the Gutsche method for uniform inclined flow (Ref. 16). To calculate propeller-induced effects, the propeller is modeled as an actuator disk. The analytical representation is a semi-infinite vortex cylinder of constant diameter equal to the propeller diameter and of constant strength, γ, having the center of its upstream face located on the hull axis at the propeller axial station (Ref. 17). From the shaft loads analysis, the advance ratio, shaft forces, and the angle of the inflow relative to the shaft are known. They are used to determine the strength and the inclination of the axis of the vortex cylinder. The shaft loads analysis involves calculation of the velocity field at the propeller plane, which includes velocities due to vorticity in the field, the hull, impressed flow conditions (including angular rotation), and the hull wake. For any instant in time, the resulting actuator disk model is used to calculate propeller-induced velocities at any field point of interest.

Flow Phenomena

The nonlinear, hydrodynamic forces and moments acting on a submersible configuration undergoing maneuvers are associated with many different types of flow phenomena. These phenomena are both the result of and responsible for the nonlinear behavior of the vehicle. The individual components of the flow phenomena of importance are the hull nose and afterbody vorticity, the lifting surface trailing vorticity, and the propeller wake. A brief discussion of these phenomena is presented below.

First, consider the flow field of the hull alone in steady flow. At very low angles of attack, the flow is almost entirely attached to the hull with the possible exception of a small separated region near the stern. This particular separation region does not form a large wake near the hull, thus it does not have a large effect on the induced flow field near the submersible components with the exception of the propeller and possibly the aftmounted lifting surfaces. As the angle of attack increases, the axial-type separation region at the stern becomes a crossflow-type separation and moves forward on the hull. At angles of attack between 10 and 15 degrees, the

separation will reach the bow. Under these circumstances, a strong symmetric vortex field occurs on the lee-side of the hull as illustrated in Figure 1. This vortex field causes interference on the foremounted and aftmounted lifting surfaces, propeller, and the hull.

When the hull motion is unsteady, the vortex shedding described above will become unsteady and the vortex wake will change with time. It is necessary to maintain the history of the vortex wake by tracking the location of the vorticity as a function of time. The vorticity shed from the hull at any specified time is determined from the motion of the submersible and the influence of the wake.

Appendages on the submersible contribute to the flow phenomena in the vicinity of the vehicle. The lifting surfaces, when loaded through interference effects or direct motion of the vehicle, have a trailing vortex wake associated with their loading. This wake is made up of trailing vorticity representing the span load distribution, a trailing vortex associated with side-edge separation at the tip, a trailing vortex due to a leading-edge separation, and shed vorticity associated with the change in loading with time. These vortices must be included with the hull vortex field to properly model the complete wake. Interaction between the hull vortices and the vortices from the foremounted fins will change the entire wake configuration, and this will, in turn, have an effect on the wake-induced interference on the hull afterbody and modify its loading and subsequent shed vorticity.

The vortex field from the hull nose, foremounted fins, and hull afterbody moves aft with the flow to approach the aft fins. The relative position of the vortex field and these fins depends on the motion of the configuration during the time required for the vortices to reach these lifting surfaces. The unsteady loading on the aftmounted fins produces an associated trailing vortex wake similar to that described for the forward fins, including the shed vorticity due to the changing loading. This additional vorticity is included with the existing vortex field and tracked downstream to the propeller region and beyond.

The induced flow field of the propeller has an effect on the aft fins and on the aft portion of the hull. The propeller wake is also a function of the submarine motion and the wake-induced inflow into the propeller plane. The actuator disk model representing the propeller disk loading provides the required induced flow field.

Discrete Vortex Model. A major feature of the rational flow model is the discrete vortex wake on the lee-side of the hull. Using a procedure successful in similar flow model investigations (Refs. 1 and 18), the discrete vortex wake is developed at an instant in time in the following manner. The three-dimensional steady flow problem is reduced to a two-dimensional, unsteady, separated flow problem for solution. The two-dimensional solution is carried out in the crossflow plane where the flow about a hull in the presence of discrete vortices is obtained. At succeeding intervals of length on the body, the body cross section is changing, and a new vortex pair is shed into the flow field from the separation points. The discrete vortices forming the wake are allowed to move in the flow field under the influences of the free stream flow, the hull, and other vortices.

The calculation procedure starts at a crossflow plane near the hull nose where the potential pressure distribution on the hull is computed using the full Bernoulli equation. The boundary layer in the crossflow plane is examined for separation using the modified version of Stratford's laminar or turbulent separation criteria. At the predicted separation points, the strength of the separation vortex is determined by the vorticity flux contained in the boundary layer. The vorticity flux is summed into a single point vortex whose strength is a function of the vorticity, the axial integration interval, and the free-stream flow conditions. The shed vortices are placed in the outer field at such a position that the vortex and its image inside the hull exactly cancel the crossflow plane surface velocity at the separation point.

In unsteady flow, the discrete vortex method is virtually identical to that developed for steady flow conditions. The discrete vortex cloud at each axial station on the body is allowed to move with local flow conditions. Vortex tracking between time steps is carried out using average free-stream flow conditions, and subsequent vortex separation at a given axial station includes the effects of free-stream flow, the motion of the configuration, and the change in position and strength of the individual vortices in the field. Details of the calculation procedure for the unsteady

vortex model are given in a following section.

Trailing Vorticity. The lifting surfaces have a trailing vortex wake associated with their potential, attached-flow loading. This vortex system is obtained from the vortex-lattice method, which produces a trailing-vortex filament from each edge of the lattice network. Provisions are made in the rational flow method for the system of trailing vortices from each lifting surface to be distributed across the span or combined into a single trailing vortex located at the center of vorticity. Additional lift associated with flow separation along side edges and swept leading edges is accompanied by a separation vortex shed continually from these edges. The calculation procedure for obtaining the lateral position and strengths of separation vortices is described in References 19 and 20. All vortices (potential and separation) are modeled as free vortices aft of the associated lifting surfaces trailing edge, and they are allowed to interact with other vortices in the field.

In unsteady flow, changing loading on a lifting surface requires that a spanwise or longitudinal vortex be shed to represent the change in bound vortex strength between time steps. In the rational flow model, spanwise vortex filaments are included as part of the total trailing vortex field from each lifting surface. The axial filaments are free to move in crossflow planes under the interaction of the flow field, and the spanwise filaments always remain connected to the axial filaments.

Hydrodynamic Characteristics

The singularity models described in the previous sections provide a means to calculate induced velocities due to the flow field components at field points on and near the submersible configuration. These velocities, in conjunction with contributions from the free-stream and angular rotations of the body, are used to calculate pressure distributions on the hull surface and loads on the lifting surfaces. Determination of the component and overall loads on the submersible configuration is discussed in this section.

Pressure Distribution. The pressure coefficient at a point on a body undergoing unsteady motion is

$$C_{p_u} = C_{p_s} - \frac{2}{V_\infty^2}\frac{\partial \phi}{\partial t} \qquad (3)$$

where C_{p_s} is the instantaneous steady pressure coefficient. This result is obtained by a transformation of the Bernoulli equation from an inertial system to the body-fixed coordinate system (Fig. 5), where the last term in Equation (3) is the unsteady term in the inertial system caused by the motion of the vehicle and the associated changes in the flow field.

The instantaneous steady pressure coefficient is

$$C_{p_s} = \frac{V^2 - q_r^2}{V_\infty^2} - \frac{2\cos\alpha_c}{V_\infty}\frac{d\phi}{dX} \qquad (4)$$

where V is the speed in the inertial coordinate system of a point P fixed in the moving body system and q_r is the fluid velocity of the same point relative to the body-fixed system.

The components of the fluid velocity at P in the x,y,z system are:

due to body motion,

$$\hat{V}_\infty = -V_\infty\cos\alpha_c\hat{I} - V_\infty\sin\beta\hat{j} - V_\infty\sin\alpha\hat{k} \qquad (5a)$$

due to body rotation,

$$\hat{\omega} \times \hat{R}_p = (ry - qz)\hat{I} + (pz - rx)\hat{j} + (qx - py)\hat{k} \qquad (5b)$$

and due to perturbation velocities,

$$\hat{V}' = u\hat{I} + v\hat{j} + w\hat{k} \qquad (5c)$$

The angles of attack and yaw are

$$\sin\alpha = \sin\alpha_c\cos\phi \qquad (6)$$
$$\sin\beta = \sin\alpha_c\sin\phi$$

where α_c and ϕ are vehicle incidence and roll angles, respectively.

The perturbation velocities in Equation (5c) consist of induced velocity components due to body volume effects, shed vortices, and fins on the body if present. From Equation (5), the fluid velocity at P is

$$\hat{q}_r = \hat{V}' + \hat{V}_\infty + (\hat{\omega} \times \hat{R}_p) \qquad (7)$$

and the velocity of P with respect to the inertial reference frame is

$$\hat{V} = \hat{V}_{\infty_B} + (\hat{\omega}_B \times \hat{R}_p) \qquad (8)$$

The last term in Equation (4) represents the pressure due to a change in two-dimensional velocity potential from one crossflow plane to the next.

This term, in which ϕ is the two-dimensional velocity potential in crossflow planes, is required because of the use of two-dimensional singularities in the crossflow planes associated with the vortex wake shedding model. This term is 'unsteady' in the axial coordinate X, but steady in time. This concept is discussed in greater detail in Reference 1.

Reformulating Equation (3) using the components defined in Equations (7) and (8), the unsteady pressure coefficient on a body undergoing unsteady motion is

$$C_{p_u} = -\left(\left(\frac{u}{V_\infty}\right)^2 - \frac{2u}{V_\infty}\cos\alpha_c - \frac{2u}{V_\infty}\left(\frac{qz}{V_\infty} - \frac{ry}{V_\infty}\right) + \left(\frac{v}{V_\infty}\right)^2 - \frac{2v}{V_\infty}\sin\beta - \frac{2v}{V_\infty}\left(\frac{rx}{V_\infty} - \frac{pz}{V_\infty}\right) + \left(\frac{w}{V_\infty}\right)^2 - \frac{2w}{V_\infty}\sin\alpha - \frac{2w}{V_\infty}\left(\frac{py}{V_\infty} - \frac{qx}{V_\infty}\right)\right) - \left(\frac{2\cos\alpha_c}{V_\infty}\right)\frac{d\phi}{dX} - \frac{2}{V_\infty^2}\frac{\partial\phi}{\partial t} \qquad (9)$$

where ϕ is the full three-dimensional velocity potential.

The singularities making up the rational flow model consist of both two-dimensional and three-dimensional distributions. Each singularity is changing with time and contributes to the unsteady pressure term so long as the velocity potential satisfies the condition at infinity that it is equal to zero or a constant in the intertial reference frame.

The unsteady terms due to the three-dimensional source/sink distribution and due to the two-dimensional doublet term are obtained analytically; however, because of the discrete vortex formulation of the wake and the numerical integration procedure used in wake trajectory calculation, a simple differencing technique is applied to evaluate the unsteady terms representing the vortex wake.

Separation Line. The separation lines on the hull are required to specify the strength and position of the discrete wake vortices forming the feeding sheets. A turbulent boundary-layer separation criteria proposed by Stratford (Ref. 21) has been modified for three-dimensional effects in Reference 1. The modified turbulent criteria locates separation at the point where the relationship

$$C_p\left(\xi\frac{dC_p}{d\xi}\right)^{.5}(10^{-6}Re_\xi)^{-0.1} = 0.35\sin\alpha_c \qquad (10)$$

is satisfied. Note that C_p is the pressure coefficient referenced to ambient conditions at the minimum pressure point, and ξ is the boundary layer run length measured from a virtual origin.

A laminar separation criterion proposed by Stratford (Ref. 22) and modified for three-dimensional effects locates separation at the point where

$$C_p^{1/2}\left(\xi\frac{dC_p}{d\xi}\right) = 0.087\sin\alpha_c \qquad (11)$$

is satisfied. The constants on the right-hand sides of Equations (10) and (11) are nominal values selected from a range of values recommended in References 21 and 22.

Forces and Moments. At a given instant in time, the total forces and moments on a submersible are given by the sum of the forces and moments on its various components. These components include the hull, the lifting surfaces, and the propeller.

The instantaneous forces and moments on the hull are computed by integration of the pressure distribution around and along the body. At a specified station on the hull, the normal-force coefficient on an increment of length of the hull is

$$C_n = \frac{1}{D}\int_0^{2\pi} C_{p_u} r_o \cos\theta\, d\theta = \frac{\text{normal force per unit length}}{q_\infty D} \qquad (12)$$

and the total normal-force coefficient on the hull is

$$C_N = \frac{D}{S_r}\int_0^{\ell} c_n dX = \frac{\text{normal force}}{q_\infty S_r} \qquad (13)$$

The normal-force coefficient from Equation (13) is positive when the force on the hull is such that the hull would move vertically upward. In the standard nomenclature of Figure 6,

$$Z' = -C_N\frac{S_r}{\ell^2} \qquad (14)$$

The pitching-moment coefficient, positive when the bow is moved vertically upward, is

$$C_m = \frac{D}{S_r}\int_0^{\ell} c_n\left(\frac{X_m - X}{\ell_r}\right)dX \qquad (15)$$

In the standard nomenclature of Figure 6,

$$M' = C_m \frac{S_r \ell_r}{\ell^3} \tag{16}$$

The remaining force and moment coefficients in the X, Y, Z-coordinate system are:

side-force coefficient,

$$C_Y = -\frac{1}{S_r} \int_o^{\ell} \left(\int_o^{2\pi} C_{p_u} r_o \sin\theta d\theta \right) dX \tag{17}$$

yawing-moment coefficient,

$$C_n = -\frac{1}{S_r} \int_o^{\ell} \left(\int_o^{2\pi} C_{p_u} r_o \sin\theta d\theta \right) \left(\frac{X_m - X}{\ell_r} \right) dX \tag{18}$$

axial-force coefficient, excluding skin friction,

$$C_A = \frac{1}{S_r} \int_o^{\ell} \left(\int_o^{2\pi} C_{p_u} r_o \frac{dr_o}{dS} d\theta \right) dX \tag{19}$$

In the nomenclature of Figure 6,

$$Y' = C_Y \frac{S_r}{\ell^2} \tag{20}$$

$$N' = C_n \frac{S_r \ell_r}{\ell^3} \tag{21}$$

$$X' = -C_A \frac{S_r}{\ell^2} \tag{22}$$

The circular cross section hull does not contribute to the rolling moment.

The local skin friction on the hull in axial flow is based on the assumption of a 1/7th power law velocity profile in the boundary layer. The resulting skin-friction coefficient is

$$C_f = -.592 \left(\frac{V_\infty}{\nu} X \right)^{-.2} \tag{23}$$

where ν is the kinematic viscosity of the medium. The drag coefficient due to friction

$$C_{D_f} = \frac{2\pi}{S_r} \int_o^{\ell} r_o C_f dX \tag{24}$$

As the angle of incidence increases, the streamlines of the flow around the hull tend to be inclined to the body axis at the angle

$$\alpha_s = \tan^{-1}(2\tan\alpha_c) \tag{25}$$

The axial component of the friction drag is

$$C_{A_f} = C_{D_f} \cos\alpha_s \tag{26}$$

and in the nomenclature of Figure 6,

$$X'_f = -C_{A_f} \frac{S_r}{\ell^2} \tag{27}$$

As described in a previous section, horseshoe vortices are distributed on all lifting surfaces and imaged inside the hull. The loading acting on each lifting surface is calculated using the Kutta-Joukowski law for a force acting on a vortex filament. As described in Reference 23, the force per unit length, $\vec{F}$, acting on vortex vector, $\vec{\Gamma}$, is given by the vector product

$$\vec{F} = \vec{Q} \times \rho\vec{\Gamma} \tag{28}$$

where $\vec{Q}$ is the total flow velocity vector and ρ is the mass density of the fluid. The total velocity acting on a bound or trailing leg of a horseshoe vortex is made up of induced velocities due to the free stream, the hull, the vorticity in the field, and all of the other horseshoe vortices and their images.

Use of Equation (28) results in forces both normal to and within the plane of each lifting surface. The normal force on a given lifting surface represents the potential force for that surface. The inplane force coefficients are used in conjunction with a method to determine the additional nonlinear lift associated with flow separation along swept loading and side edges. This method, which is an extension of the Polhamus leading-edge suction analogy (Ref. 24), was developed from experimental data and is used to determine the fraction of leading-edge or side-edge suction converted to normal force. This correlation method is described in detail in Reference 19.

The vortex lattice lifting surface method described above is an attached flow model. Under certain flow conditions, individual surfaces can become very highly loaded due to large onset flows or large vortex-induced velocities and the predicted loading obtained using the attached flow model may exceed the loading that could physically be expected to occur on the surface. A means to include stall or separation effects on the lifting surface loadings, based in part on the method of Reference 25, is included in the prediction method.

A method for calculating axial force due to skin friction on the lifting surfaces is taken from Reference 26. The basis for this method is an empirical relationship for skin friction coefficient derived from data on flat plates (Ref. 27). The following expression, which includes adjustments for thickness and transition, is in-

cluded in the rational flow code to estimate the skin friction on the lifting surfaces.

$$C_{A_f} = \frac{2.656}{(Re_L)^{1/2}} \frac{A_{LS}}{S_r} [1 + 2 \frac{t}{c}] \qquad (29)$$

In this expression, A_{LS} is the lifting surface planform area and t/c is the maximum thickness-to-chord ratio.

Loads on the propeller are transmitted to the hull through the shaft and contribute to the overall configuration loads. Calculation of these loads in the rational flow model is carried out using a combination of two methods. The first, developed by McCarthy (Ref. 15), predicts the thrust and torque of an arbitrary propeller operating in a nonuniform but noninclined flow. The second, developed by Gutsche (Ref. 16) predicts the thrust, torque, inplane force, and thrust offset of a propeller in a uniform, inclined flow.

The propeller is assumed to exist in a quasi-steady-state condition by the instantaneous values of all flow velocities and the state of motion of the vehicle. The propeller inflow is assumed to consist of an axisymmetric contribution due to the hull and hull wake, an axisymmetric self-induced flow caused by the flow acceleration into the disk, and axial and tangential contributions due to the wakes of all upstream lifting surfaces and hull flow separation. The McCarthy analysis is first used to calculate thrust and torque for the noninclined part of the inflow. With the axisymmetric behavior known, the Gutsche method is used to calculate flow inclination effects. The final step consists of combining these results with open-water performance data for the particular propeller attached to the vehicle to obtain the components of shaft loads.

Maneuver Analysis. A common approach to the prediction of submersible trajectories involves the integration of the six-degree-of-freedom equations of motion of the submersible configuration over the time frame of interest. The standard equations of motion, such as those presented in References 28 and 29, are written in a form which requires the stability derivatives for the configuration for the range of flow conditions to be considered. Such a formulation creates difficulties when the stability derivatives are unknown. Such may be the case for a preliminary design configuration prior to testing, or when the flight regime involves nonlinear aspects which make it impossible or difficult to determine the derivatives experimentally.

The approach to the development of a trajectory prediction method based on the rational flow model involves a simplification of the standard stability derivative coefficient formulation using a direct force and moment coefficient formulation. In this approach, terms in the equations of motion associated with stability derivatives are replaced by the forces and moments obtained from the rational flow code at an instant in time. The modified equations of motion are shown below. These equations are for a configuration with its origin at the center of gravity, and the positive senses of forces, moments, velocities, and rotation rates are indicated in Figure 6. The angles ϕ, θ, and ψ are the Euler angles which relate to orientation of the body-fixed-coordinate system to the inertial system. The C_i coefficients and the subscript AM are added-mass terms. The added-mass forces and moments have been removed from the right-hand side of the equations of motion and the appropriate terms included on the left-hand side to remove numerical instability in the solution as discussed in Reference 30.

Axial Force:

$$(m-C_1)\dot{u} = m(uv-wq) + (X-X_{AM})-(W-B)\sin\theta \qquad (30)$$

Lateral Force:

$$(m-C_2)\dot{v} - C_3\dot{p} - C_4\dot{r} = m(wp-ur) + (Y-Y_{AM}) + (W-B)\cos\theta\sin\phi \qquad (31)$$

Normal Force:

$$(m-C_5)\dot{w} - C_6\dot{q} = m(uq-vp) + (Z-Z_{AM}) + (W-B)\cos\theta\cos\phi \qquad (32)$$

Rolling Moment:

$$(I_{xx}- C_7)\dot{p} - I_{xy}\dot{q} - (I_{zx}+ C_8)\dot{r} - C_9\dot{v} = (I_{yy}- I_{zz})qr + I_{zx}pq - I_{xy}pr + I_{yz}(q^2- r^2) + (K - K_{AM}) - y_B B\cos\theta\cos\phi + z_B B\cos\theta\sin\phi \qquad (33)$$

Pitching Moment:

$$(I_{yy} - C_{10})\dot{q} - I_{xy}\dot{p} - I_{yz}\dot{r} - C_{11}\dot{w} = (I_{zz} - I_{xx})rp + (N - N_{AM}) + z_B B\sin\theta + x_B B\cos\theta\cos\phi \qquad (34)$$

Yawing Moment:

$$(I_{zz} - C_{12})\dot{r} - (I_{zx} + C_{13})\dot{p} - I_{yz}\dot{q} - C_{14}\dot{v} = (I_{xx} - I_{yy})pq + I_{yz}rp - I_{zx}rq + I_{xy}(p^2 - q^2) + (N - N_{AM}) - x_B B \cos\theta\sin\phi - y_B B \sin\theta \qquad (35)$$

A trajectory calculation is carried out in the following manner. Starting with initial flow conditions, rotation rates, time rates of change of these quantities, and the initial position and orientation of the submersible configuration in the inertial coordinate system, a steady flow solution is obtained to provide a vortex wake and hydrodynamic forces and moments with which to begin the unsteady calculation. The unsteady calculation begins with the prediction of the missile motion from t=0 to t=Δt, where the time interval Δt must satisfy the relation

$$\Delta t < \frac{\Delta X}{(V_\infty \cos \alpha_c)_{t=0}} \qquad (36)$$

This interval was chosen to provide sufficient time for the changing vortex effects to influence the calculation before being swept past the base of the vehicle. For purposes of the trajectory calculation, it is assumed that the flow conditions and hydrodynamic forces and moments are constant over the Δt interval. Solution of the 6-DOF equations of motion results in new velocity components and coordinates of the configuration CG, angular rates, and orientation of the configuration at t_1.

The vortex wake is permitted to move in the time interval to its new position as summarized in a previous section (and further described in the following section). With the new wake position and the new flow conditions at t_1, the forces and moments on the submersible configuration are computed. This interactive process continues to the end of the specified trajectory calculation. The moving vortex wake forms the historical lag in the flow field which relates to the stern what happened at an earlier time at the bow. As the calculation progresses, the wake shed at an earlier time is swept downstream past the stern, and the effect on the vehicle is lost forever.

Calculation Procedure

The general steady and unsteady flow calculation procedure used in the rational flow method for a typical submersible configuration is outlined in this section. The calculation procedures for both steady and unsteady flow conditions are applicable to general configurations with arbitrary arrangements of lifting surfaces in an axisymmetric hull.

Steady Flow Conditions

The calculation of the hydrodynamic characteristics of a submersible configuration undergoing steady translational and rotational motions is carried out with a marching procedure starting at the nose of the vehicle. The basic method is the crossflow plane discrete vortex shedding analysis described in Reference 1. The calculation begins with the prediction of the shed vortex field and the loads between the nose and the leading edge of the first set of lifting surface, the foremounted fins in most cases. The separation vortex field at this axial station influences the loads on these fins, and the lifting surfaces in turn influence the loading on each other and on the hull adjacent to the surfaces. A trailing vortex system originating on the lifting surfaces is released into the flow field at the trailing edge, and these free vortices are included as part of the total shed vortex system for the remainder of the calculation.

The path of the entire vortex system is tracked along the length of the hull from the trailing edge of the forward fins to the leading edge of the aft fins. The vortices influence the pressure distribution on the hull, which has an effect on the separation points, the shed vorticity from the afterbody, and the hull loads. Separation vortices from the afterbody are added to the vortex field over the hull length between the forward and aft fins. In addition to the vortices, the propeller model influences the pressure distribution on the hull aft of the maximum radius position.

The vortex field from the nose, foremounted fins, and afterbody influences the loads on the aftmounted fins. There is also an upstream influence from the propeller. The loading on the individual fins produces a trailing vortex system analogous to that from the forward fins, and these vortices are included as part of the shed vortex system which is tracked from the trailing edge to the propeller. The flow field in the vicinity of the propeller (inflow) is calculated and the propeller loading is predicted.

The total forces and moments on the complete vehicle are the sum of the

forces and moments on the individual components. For a steady flow condition, the calculation is complete at this point.

Unsteady Flow Conditions

The calculation procedure for the prescribed initial flow conditions for an unsteady flow case is essentially the same as that for the steady flow case. Starting at t = 0 with prescribed initial flow conditions, angular rotation rates, accelerations, position of CG and orientation of the vehicle in the inertial coordinate system, propeller rotation rate, and control surface deflections, the loads and the shed vortex field on the configuration are calculated as described in the previous section. This is the starting condition for the unsteady calculation.

Separation vortex fields corresponding to the initial conditions at t = 0 are shown schematically in Figure 7(a) where only a hull is considered for this discussion. The discrete hull separation vortex positions are shown as dots at each X-station, and their paths are denoted by dashed lines. The individual vortices are identified as $\Gamma_{m,t}$ where the first subscript represents the X-station at which they are shed and the second subscript represents the appropriate time step.

An unsteady calculation begins with the calculation of the submarine motion from $t = t_o = 0$ to $t_1 = t_o + \Delta t$, where Δt is a specified value that must satisfy Equation (36). The vehicle trajectory is calculated by making the approximation that the flow conditions and loads at t = 0 are constant over the time interval Δt. The trajectory calculation produces new flow conditions and time rates of change of flow variables for $t_1 = t_o + \Delta t$. The existing vortex wake is allowed to move downstream a distance $\Delta X'$ under the influence of new local flow conditions during the interval Δt. The value of $\Delta X'$ is determined from the average conditions at $\Delta t/2$, such that

$$\Delta X' = \Delta t \, (\bar{V}_\infty \cos \bar{\alpha}_c) \qquad (37)$$

where $\bar{V}_\infty$ and $\bar{\alpha}_c$ are average values between time steps. For the wake trajectory calculation, the average flow conditions at $\Delta t/2$ are considered appropriate for the total interval. A new vortex field resulting from a calculation for which $\Delta X' = \Delta X$ is shown in Figure 7(b). Comparison of parts (a) and (b) of this figure illustrate how individual vortices are moved. In essence, the entire vortex field existing at t_o has been transported downstream a distance ΔX. Under the influence of the actual flow conditions at t_1 and the modified vortex field, the hull pressure distribution is predicted and a new separation calculation is carried out. The current situation at t_1 is shown in Figure 7(c) where the new vortices are shown as an addition to the previous field. This process continues to the end of the specified trajectory calculation or to the end of the prescribed maneuver.

Results

The ultimate evaluation of the rational flow model described in this paper must be made by comparisons of measured and predicted hydrodynamic characteristics on a variety of configurations under a wide range of flow conditions. In the absence of hydrodynamic data, comparisons with aerodynamic data on similar configurations will suffice. Comparisons of both steady and unsteady results are desirable to verify the methodology; however, other than static characteristics, only a small quantity of steady data exists and almost no unsteady data are available for these comparisons. In this section, static results at high angles of incidence are presented to further verify the discrete vortex cloud approach, steady turning results are used to examine effects of turn rate, and an arbitrary unsteady maneuver is described to illustrate the use of the method.

Static Characteristics

The prediction method was applied to a body of revolution, Model 4621, a configuration (Ref. 31) for which normal-force and pitching-moment coefficients are available for a range of angles of attack. Measured and predicted results are compared in Figure 8. The predicted results, including significant lee-side separation vortex effects, are in good agreement over the linear and nonlinear range of incidence angles.

In an effort to further evaluate the vortex-induced characteristics on a body of revolution at high angles of attack, it was necessary to consider aerodynamic data on a sharp nose body. A missile configuration consisting of a three-diameter ogive nose and a 7.7-diameter cylindrical afterbody is available in Reference 32 where pressure distributions, normal-force distributions, and total normal-force coefficients are presented for angles up to 24 degrees. The predicted cir-

cumferential pressure distribution 7.5 diameters from the nose at $\alpha = 15$ degrees is compared with experiment in Figure 9. The vortex cloud has a significant effect on the pressure distribution on the lee side, and the rational flow model successfully represents these effects. To illustrate the magnitude of the vortex-induced effects, the predicted potential results are shown as a dashed curve in this figure.

Measured and predicted axial distributions of normal force are compared in Figure 10. The predicted results for potential flow, which agree with slender body theory, are shown as a dashed curve. The agreement between experiment and theory is very good over most of the body length; however, near the base, some lack of agreement is apparent. This may be a base effect which is not adequately represented in the present predictions.

The total normal-force coefficient is shown in Figure 11. At lower angles of attack, the predicted results are in good agreement with the low Reynolds number experimental measurements, but at higher angles, the theory is in better agreement with the high Reynolds number results. This phenomenon is associated with the changing character of the separation on the body in a transition region; however, this effect is not considered in these predictions.

Results of further investigation of the effects of the shed vortex wake on the distribution of forces on an axisymmetric hull at angle of attack are shown in Figures 12 and 13. The measured normal-force distribution on the Akron airship hull (Ref. 33) is compared in Figure 12 with a potential distribution and a rational flow model result including vortex-induced effects. The presence of the vortex cloud improves agreement between experiment and theory; however, there is some disagreement on the aft portion of the hull. This may be caused by additional separation not included in the flow model, or it may be an indication of an effect of the hull boundary layer which is not considered in these calculations. The total normal-force and pitching-moment coefficients on the Akron hull alone are shown in Figure 13. A potential result and a rational flow model result are compared with experiment over the range of angles of attack. As seen previously, the vortex cloud has a significant influence on the predicted forces and moments, and it is essential in the prediction of nonlinear effects at high angles of attack.

An example of the predicted vortex cloud wake near the stern of the Akron airship hull is shown in Figure 14. Each symbol represents a discrete vortex forming a part of the wake, and the feeding sheet of vorticity from the separation point on either side of the hull is well defined as is the major rolled up portion of the wake.

Steady Turning Maneuver

A steady turning maneuver involves the vehicle at constant angles and constant angular rates. Such a maneuver is represented experimentally on a rotating-arm apparatus as illustrated in Figure 3. Measured pressure distributions on a 4:1 ellipsoid body of revolution in a steady pitching maneuver turn are available in Reference 34. Axial pressure distributions on the windward and leeward meridians are shown in Figure 15 for $q' = -.0717$ and angles of attack of 10 and 20 degrees. The flow is such that the body is at positive angle of attack and it is pitching nose downward so that the local angle of attack at the nose is greater than α and that at the stern is less. The effect of the separation vortex is illustrated in Figure 15 (b) where the potential result without separation is presented for comparison with the rational flow model result. The hull separation vorticity has a significant effect on the lee-side pressure distribution.

Similar steady turning data on a fully appended configuration are not available for comparison purposes in this paper; therefore, an arbitrary submersible vehicle was assembled to provide sample results to illustrate the capability of the rational flow model. As shown in Figure 4, a body of revolution is appended with two sets of four fins in a fore and aft configuration. Each lifting surface can be deflected as a control surface. This configuration is similar to that used in Reference 35 for illustration purposes for the rational flow model with the exception that an additional forward fin is considered herein.

Both static and steady-turning predicted results are shown in Figure 16 for the fully appended configuration. The predictions were made assuming a large-scale vehicle in a high-Reynolds number flow; therefore, the hull vortex separation characteristics are turbulent and have less effect on the hydrodynamic forces and moments. The solid curves in Figure 16 illustrate the static forces and moments on the vehicle at a range of yaw angles. The nonlinear effects at higher angles

are induced by the trailing vorticity from the forward fins and the small amount of hull shed vorticity.

Predicted results for the vehicle in a steady turning motion (r'=-.40) are also shown in Figure 16. The side force is similar in appearance to the static results, but the nonlinear effects are slightly more pronounced. The yawing moment is significantly different from the static results because of the shift in loading between the forward and aft fins as the sideslip angle changes. For example, the yawing moments at β = 20 and -20 degrees are nearly identical even though the side forces are quite different. Detailed examination of the loading on the individual components of the vehicle can identify the reasons for this unusual behavior. In Figure 17, the side force and yawing moment contribution of each major component of the vehicle are compared for β = 20 and -20 degrees. At β = 20 degrees, the side force is due to the nose and forward fin loadings. The aft fins are nearly unloaded because of the reduced local angle of incidence due to the turning effect and the induced flow field from the vorticity in the wake from the hull and the forward fins. The net effect is that the yawing moment is determined by the loading near the nose of the vehicle.

At β =-20 degrees, the loading on the nose is reversed because of the change in flow direction, as are the loadings on the fins. However, both forward and aft fins have nearly the same loading, and their contribution to the yawing moment have opposite sign. The cause for the similarity in loading of forward and aft fins in this flow condition is that the local flow angle at the aft fins is higher than before and the trailing vorticity from the forward fins is not in position to reduce the loading. The net effect is that the yawing moment at β =-20 degrees is dominated by the aft fins, but the sign and magnitude of the total moment is nearly the same for β = 20 degrees.

The previous case considers a high Reynolds number flow condition such that the separation from the hull is turbulent and the hull vortex effects are minimal. To illustrate the effect of strong hull vorticity, a low Reynolds number flow condition is considered such that the hull separation is laminar and the vortex wake is much stronger. Predicted results for static and steady turning conditions are shown in Figure 18. At low sideslip angles, the results are the same as those in Figure 16 as is expected because vortex-induced effects are small at low incidence angles. At higher angles, the shed vorticity from the hull is stronger than before, and the nonlinear effects are larger. The nonlinearities are much larger in the turning case because the local angles become large as do the vortex-induced forces. The yawing moment shown in Figure 18(b) also reflects the larger induced effects. The character of the moments changes because of the stronger vortex wake and the larger forces on individual components.

Unsteady Maneuver

Since experimental data are not available for comparison purposes, an example unsteady calculation is presented for the fully appended configuration used in the previous discussion. The initial condition of the vehicle is a straight ahead motion with all forces and moments balanced. A schedule of control surface deflections is shown in Figure 19(a). Note that the upper and lower aft rudders are offset slightly to counter the torque from the propulsion model. Over a short period of time, the aft rudders are deflected 20 degrees to initiate a port turn, and the rudders are held at a constant deflection angle for approximately 9 seconds. As the rudders are returned to a neutral position, the left and right forward fins are deflected to produce a counterclockwise rolling motion (looking forward). This condition is maintained to the end of the trajectory calculation. The objective of this maneuver is not to model a specific motion but to demonstrate the capability of the rational flow model and trajectory prediction.

The three coordinates of the position of the vehicle center of gravity are shown in Figure 19(b). Because of symmetry of the vehicle and the deflection schedule, the only apparent motion is in the y_i-direction as dictated by the turning maneuver. The vehicle is assumed neutrally bouyant; therefore, the depth does not change. The orientation of the vehicle is described by the three Euler angles ψ, θ, ϕ shown in Figure 19(c). Details of the forces and moments on the vehicle are available from the method at all points in the trajectory.

Conclusions

An engineering rational flow model to predict the hydrodynamic characteristics and motion of a generic submersible configuration in unsteady maneuvers has been described in this

paper. Comparisons of measured and predicted aerodynamic and hydrodynamic characteristics of a range of bodies of revolution for static flow conditions and steady turning maneuvers verify that the principal features of the flow phenomena are well represented for flow conditions beyond the linear range. A parametric series of calculations for generic large-scale and model-scale submersible configurations in static and steady flow conditions illustrate the capability of the method to predict the detailed hydrodynamic and flow field characteristics. Calculations for a powered generic submersible vehicle in which control surface deflections are varied as a function of time demonstrate the use of the method for predicting unsteady maneuvers.

The unsteady prediction method described in this paper has demonstrated the feasibility of an approach in which the nonlinear forces and moments are predicted for use in a direct calculation of the motion of a submersible vehicle. The method has application for the calculation of trajectories of submersible configurations under flow conditions for which stability derivatives are unknown.

References

1. Mendenhall, M. R., Spangler, S. B., and Perkins, S. C., Jr.: Vortex Shedding From Circular and Noncircular Bodies at High Angles of Attack. AIAA Paper 79-0026, Jan. 1979.

2. Perkins, S. C., Jr., Mendenhall, M. R., and Young, S. W.: Rational Flow Modeling of Submersible Vehicles. Vol. II - RATFLO Program Manual. Nielsen Engineering & Research, Inc. NEAR TR 265, Jan. 1982.

3. Perkins, S. C., Jr. and Mendenhall, M. R.: Hydrodynamic Analysis of Submersible Vehicles Undergoing Large Unsteady Maneuvers - Vol. II - SUBFLO Program Manual. Nielsen Engineering & Research, Inc. NEAR TR 341, Apr. 1985.

4. Mendenhall, M. R. and Perkins, S. C., Jr.: Prediction of Vortex Shedding from Circular and Noncircular Bodies in Supersonic Flow. NASA CR-3754, Jan. 1984.

5. Mendenhall, M. R., Perkins, S. C., Jr., and Lesieutre, D. J.: Prediction of the Nonlinear Aerodynamic Characteristics of Maneuvering Missiles. AIAA Paper 85-1776-CP, Aug. 1985.

6. Marshall, F. J. and Deffenbaugh, F. D.: Separated Flow Over Bodies of Revolution Using an Unsteady Discrete-Vorticity Cross Wake. Part 1 - Theory and Applications. NASA CR-2414, June 1974.

7. Wardlaw, A. B.: Multivortex Model of Asymmetric Shedding on Slender Bodies at High Angles of Attack, AIAA Paper 75-123, Jan. 1975.

8. Deffenbaugh, F. D. and Koerner, W. G.: Asymmetric Wake Development and Associated Side Force on Missiles at High Angles of Attack. Journal of Spacecraft and Rockets, Vol. 14, No. 3, pp. 155-162, Mar. 1977.

9. Goodwin, F. K., Nielsen, J. N., and Dillenius, M. F. E.: A Method for Predicting Three-Degreee-of-Freedom Store Separation Trajectories at Speeds up to the Critical Speed. AFFDL-TR-71-81, Nov. 1974.

10. Kuhn, G. D.: Computer Program for Calculation of Separated Turbulent Flows on Axisymmetric Bodies Including Exhaust Plume Effects. AEDC TR-79-4, Mar. 1979.

11. Smith, C. A. and Fidler, J. E.: Methods for Predicting Submersible Hydrodynamic Characteristics. NCSC TM 238-78, July 1977.

12. Dillenius, M. F. E., Perkins, S. C., Jr., and Mullen, J., Jr.: A General Method for Determining the Forces and Moments on Components of Finned Sections of Underwater Vehicles. NCSC-TM319-81, Dec. 1981.

13. Mendenhall, M. R., Spangler, S. B., Nielsen, J. N., and Goodwin, F. K.: Calculation of the Longitudinal Aerodynamic Characteristics of Wing-Flap Configurations with Externally Blown Flaps. NASA CR-2705, Sept. 1976.

14. Dillenius, M. F. E., Goodwin, F. K., and Nielsen, J. N.: Extension of the Method for Predicting Six-Degree-of-Freedom Store Separation Trajectories at Speeds up to the Critical Speed to Include a Fuselage with Noncircular Cross Section. Vol. I - Theoretical Methods and Comparisons with Experiment. AFFDL Report TR-74-130, Nov. 1974.

15. McCarthy, J. H.: On the Calculation of the Thrust and Torque Fluctuations of Propellers in Nonuniform Wake Flow. NSRDC Rept. 1533, Oct. 1961.

16. Gutsche, F.: The Study of Ships Propellers in Oblique Flow. Shiffbauforschung 3, 3/4 (1964), pp. 97-122, also Defense Research Information Center Translation No. 4306, Oct. 1975.

17. Kuchemann, D. and Weber, J.: Aerodynamics of Propulsion. McGraw-Hill Book Co., Inc., New York, 1953.

18. Spangler, S. B. and Mendenhall, M. R.: Further Studies of Aerodynamic Loads at Spin Entry. ONR Report No. CR212-225-3, June 1977.

19. Mendenhall, M. R. and Nielsen, J. N.: Effect of Symmetrical Vortex Shedding on the Longitudinal Aerodynamic Characteristics of Wing-Body-Tail Combinations. NASA-CR 2473, Jan. 1975.

20. Bollay, W. A.: Nonlinear Wing Theory and its Application to Rectangular Wings of Small Aspect Ratio. ZAMM, Vol. 19, 1939.

21. Stratford, B. S.: The Prediction of Separation of the Turbulent Boundary Layer. Jour. of Fluid Mech., Vol. 5, 1969, pp. 1-16.

22. Cebecci, T., Mosinskis, G. J., and Smith, A. M. O.: Calculation of Viscous Drag and Turbulent Boundary-Layer Separation on Two-Dimensional and Axisymmetric Bodies in Incompressible Flow. McDonnell Douglas Report No. MDC JO 973-01, Nov. 1970.

23. Milne-Thomson, L. M.: Theoretical Hydrodynamics, Fifth Edition. MacMillan Co., 1968.

24. Polhamus, E. C.: Prediction of Vortex-Lift Characteristics Based on a Leading-Edge Suction Analogy. AIAA Paper 69-1133, Oct. 1969. (Jour. of Aircraft, Vol. 8, No. 4, Apr. 1971, pp. 193-199).

25. McDonnell-Douglas Aircraft Co.: USAF Stability and Control DATCON. Revised Apr. 1978. Section 4.1.1.4.

26. Hoerner, S. F.: Fluid Dynamic Drag. Published by the Author, 1958.

27. Schultz-Grunow, F.: New Frictional Resistance Law for Smooth Plates. NASA TM-986, Sept. 1941. (Original article in Luftfahrtforschung, Vol. 17, No. 8, Aug. 1940, pp. 239-46).

28. Gertler, M. and Hagen, G. R.: Standard Equations of Motion for Submarine Simulation. Naval Ship Research and Development Center Report 2510, June 1967.

29. Feldman, J.: DTNSRDC Revised Standard Submarine Equations of Motion. DTNSRDC Rept. SPD-0393-09, June 1979.

30. Lloyd, A. R. J. M.: Progress Towards a Rational Method of Predicting Submarine Maneuvers. RINA International Symposium on Naval Submarines (Vol. II, Paper 21), London, May 1983.

31. Dempsey, E. M.: Static Stability Characteristics of a Systematic Series of Stern Control Surfaces on a Body of Revolution. DTNSRDC Rept. 77-0085, Aug. 1977.

32. Tinling, B. E. and Allen, C. Q.: An Investigation of the Normal-Force and Vortex-Wake Characteristics of an Ogive-Cylinder Body at Subsonic Speeds, NASA TN D-1297, Apr. 1962.

33. Freeman, H. B.: Pressure Distribution Measurements on the Hull and Fins of a 1/40th-Scale Model of the U.S. Airship "Akron." NACA Report 443, 1932.

34. Jones, R.: The Distribution of Normal Pressures on a Prolate Spheriod. ARC R&M 1061, Dec. 1925.

35. Summey, D. C. and Watson, K. P.: Rational Flow Modeling. Oceans '84 Conference, Washington, D. C., Sept. 1984.

Acknowledgement

The work reported herein was supported by the Naval Sea Systems Command.

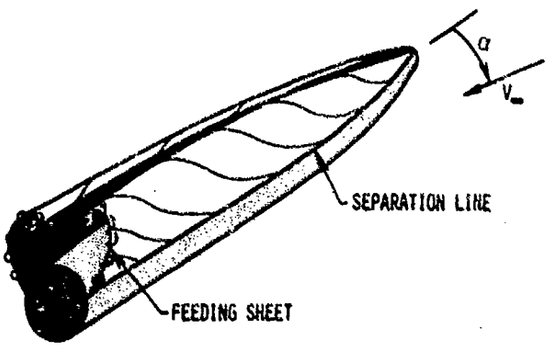

Fig. 1 Vortex formation on an inclined hull

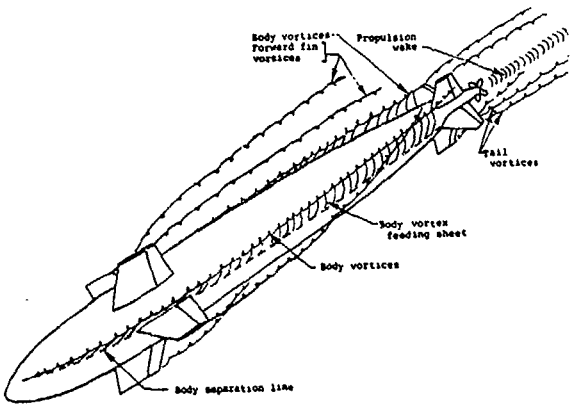

Fig. 2 Sketch of the flow field adjacent to a submersible vehicle in steady motion

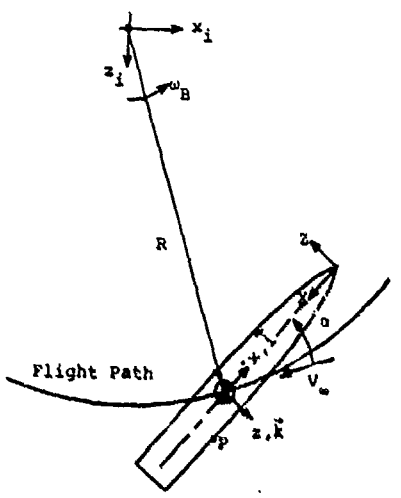

Fig. 3 Rotating arm apparatus for experimental modeling of steady flow conditions

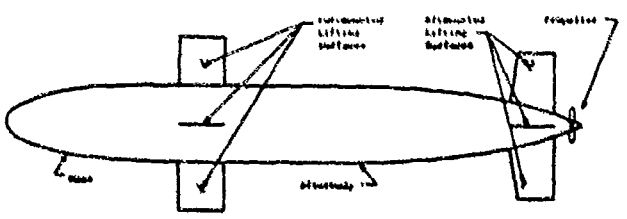

Fig. 4 Generic submersible configuration

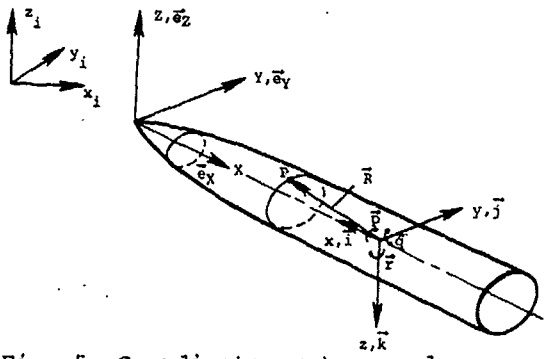

Fig. 5 Coordinate systems and nomenclature associated with pressure coefficient calculation

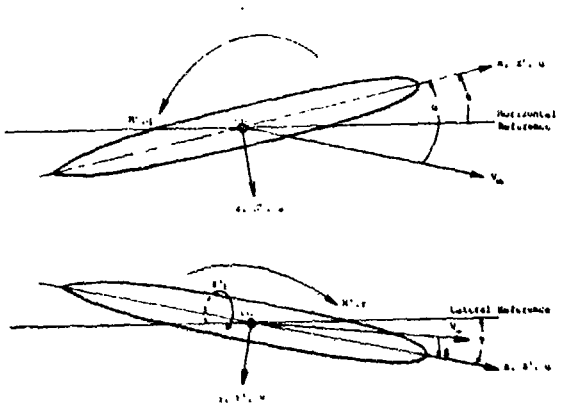

Fig. 6 Sketch showing positive directions of axes, angles, velocities, forces and moments for body-fixed x,y,z coordinate system

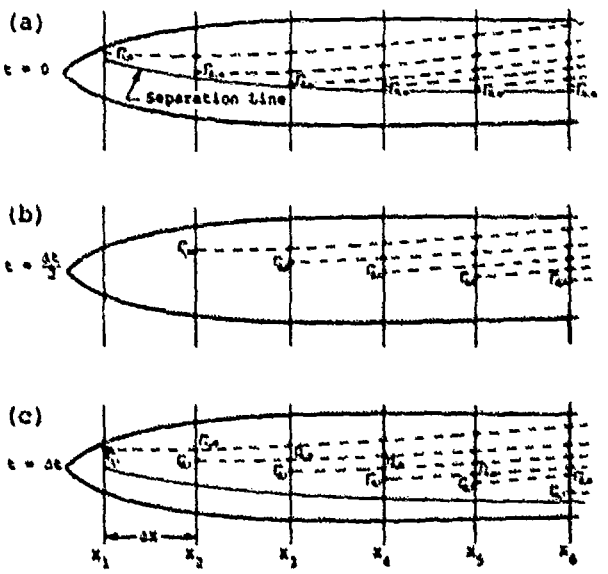

Fig. 7 Unsteady flow calculation procedure

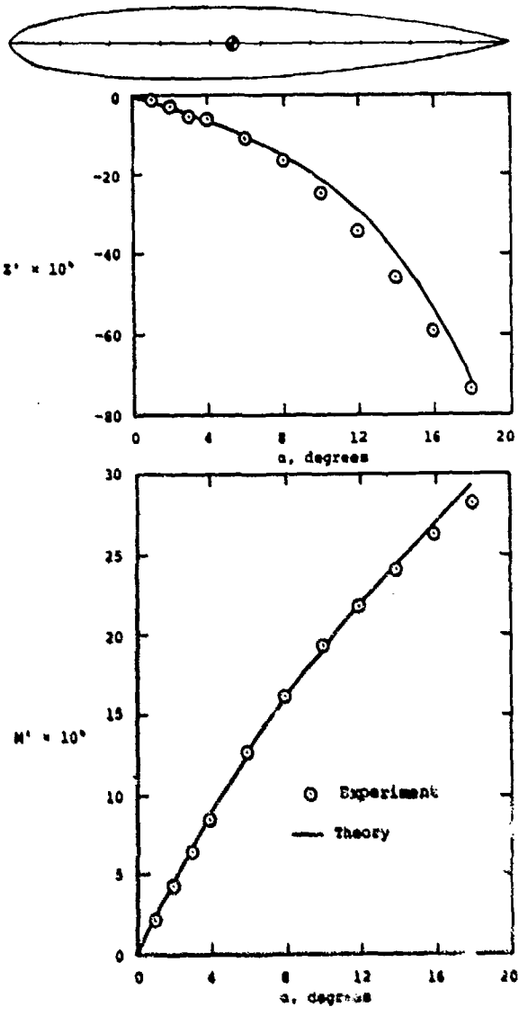

Fig. 8 Measured and predicted normal-force and pitching-moment coefficients on the NSRDC model 4621 hull

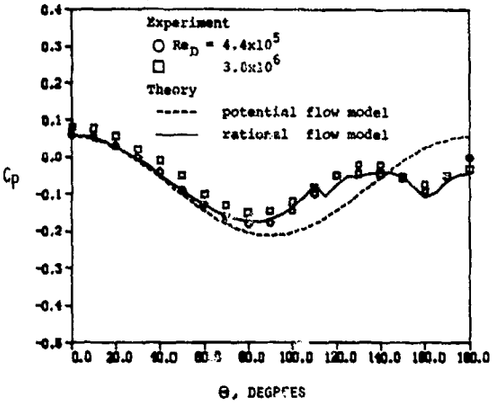

Fig. 9 Measured and predicted circumferential pressure distribution on an ogive-cylinder configuration; α = 15°; X/D = 7.5

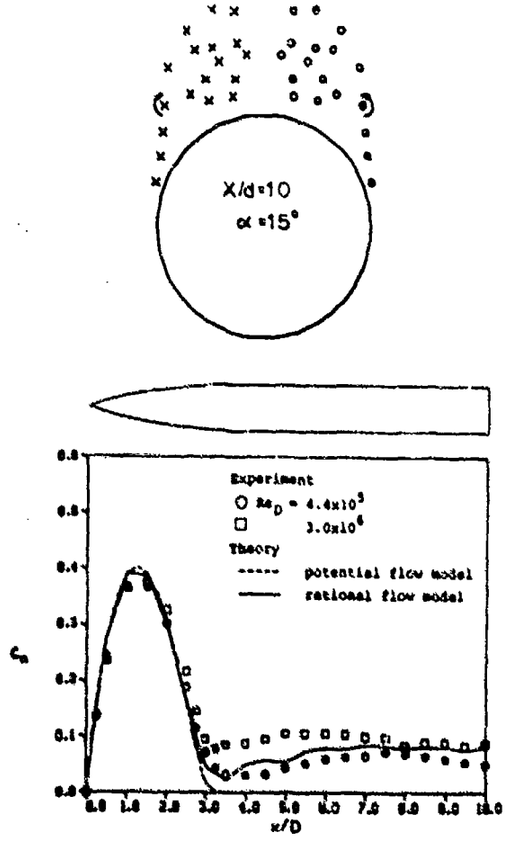

Fig. 10 Measured and predicted section normal-force coefficient on an ogive-cylinder configuration, α = 15

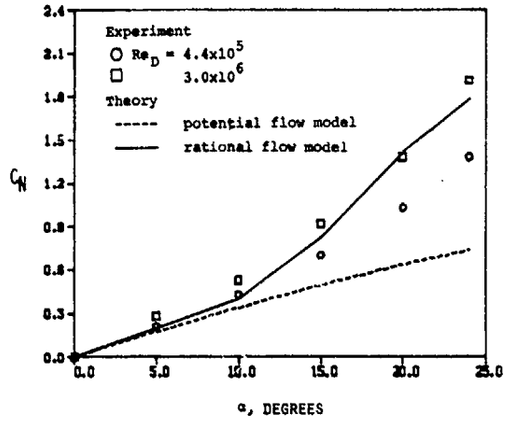

Fig. 11 Measured and predicted normal-force coefficient on an ogive-cylinder configuration

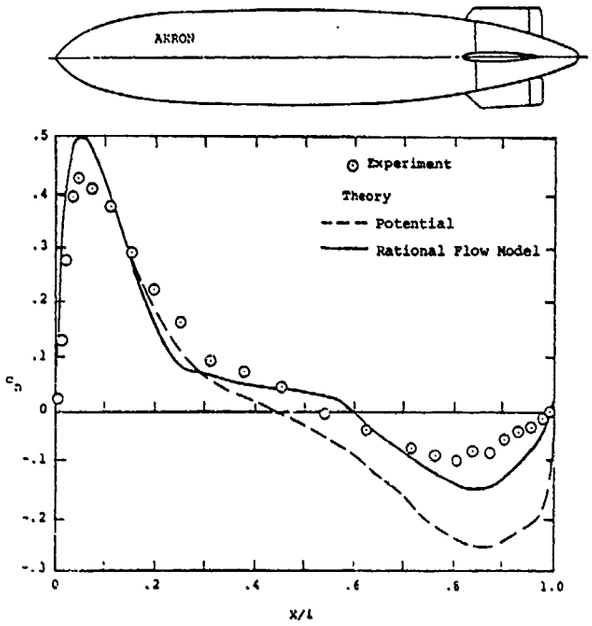

Fig. 12 Measured and predicted section normal-force coefficient on the Akron airship hull, α = 20°

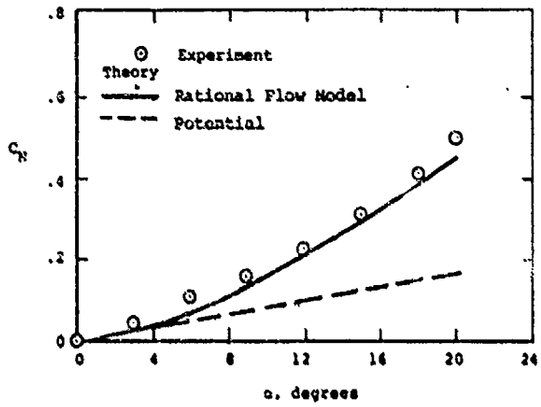

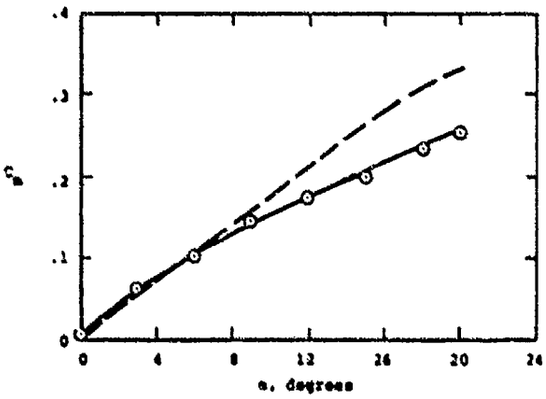

Fig. 13 Measured and predicted normal-force and pitching-moment coefficient on Akron airship hull

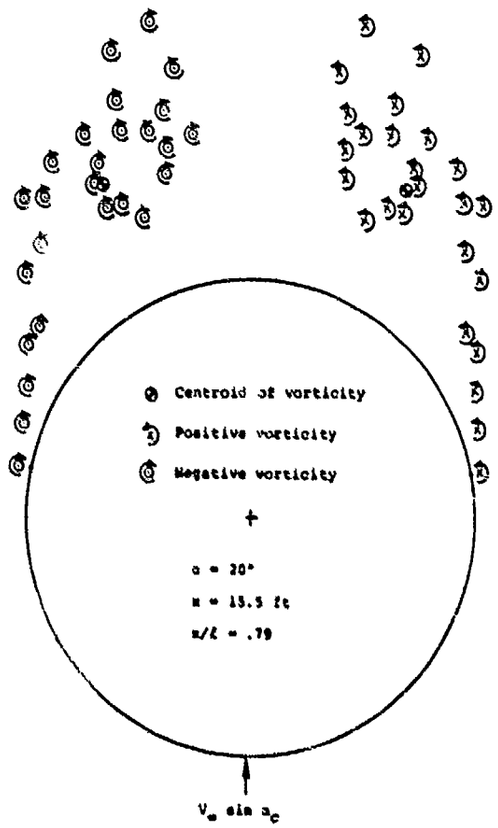

Fig. 14 Predicted discrete vortex wake on the lee side of the Akron airship hull, α = 20°

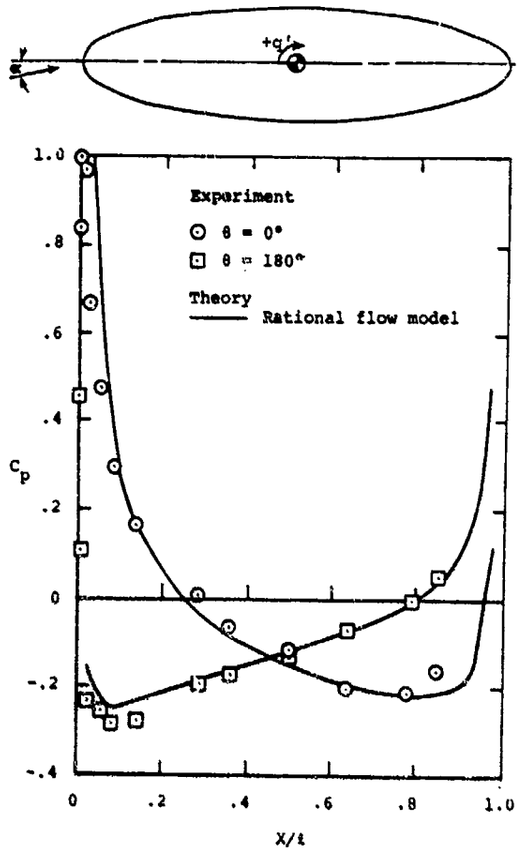

(a) $\alpha = 10°$, $q' = -.0717$

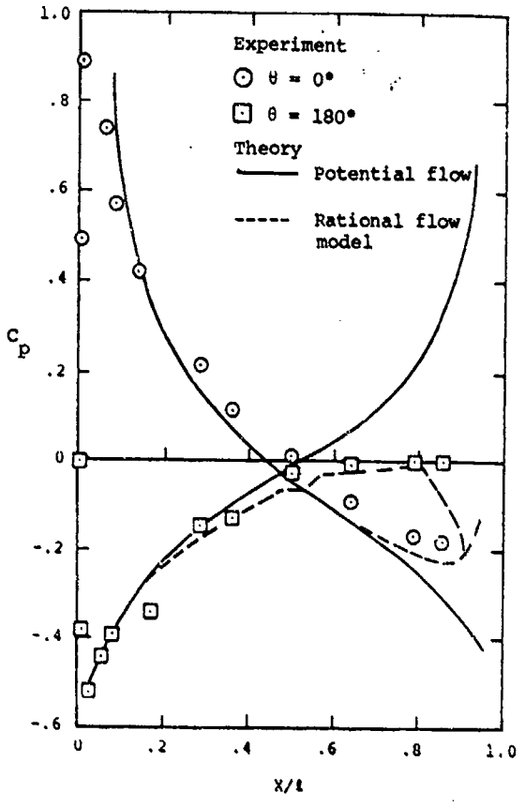

(b) $\alpha = 20°$, $q' = -.0717$

Fig. 15 Measured and predicted pressure distribution on a 4:1 ellipsoid body of revolution

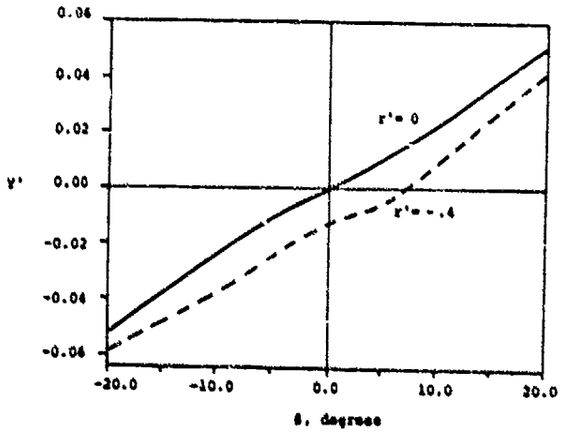

(a) Side-force coefficient

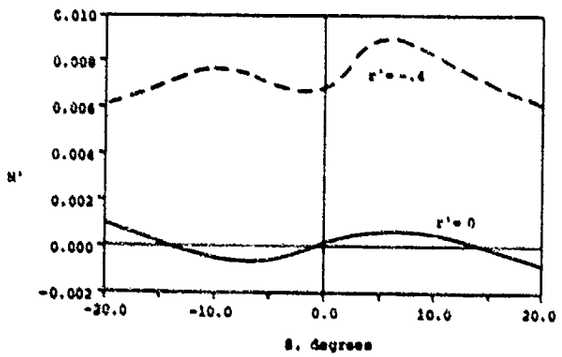

(b) Yawing-moment coefficient

Fig. 16 Predicted side-force and yawing-moment coefficients on a large-scale submersible vehicle

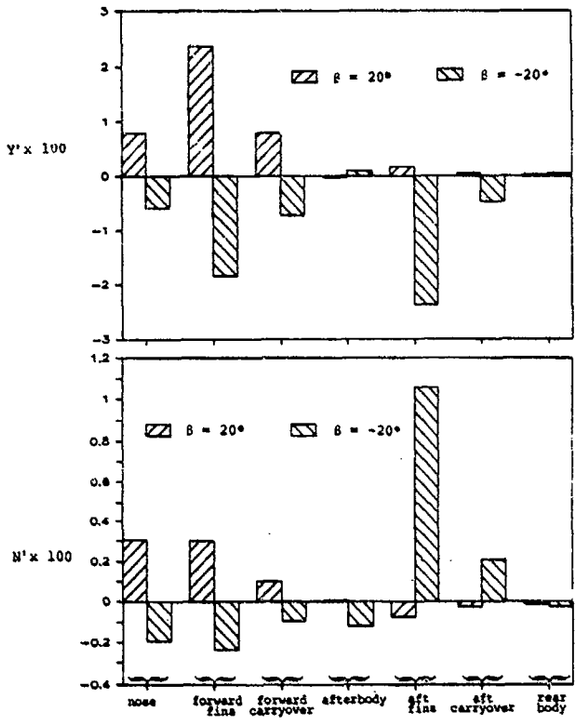

Fig. 17 Predicted component side-force and yawing-moment coefficients for a large-scale submersible vehicle, r'= -.40

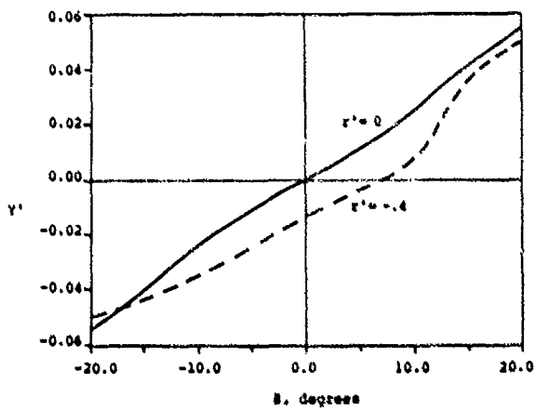

(a) Side-force coefficient

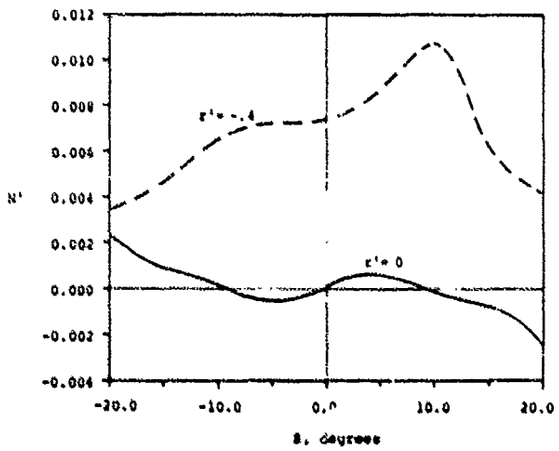

(b) Yawing-moment coefficient

Fig. 18 Predicted side-force and yawing moment coefficients on a small-scale submersible vehicle

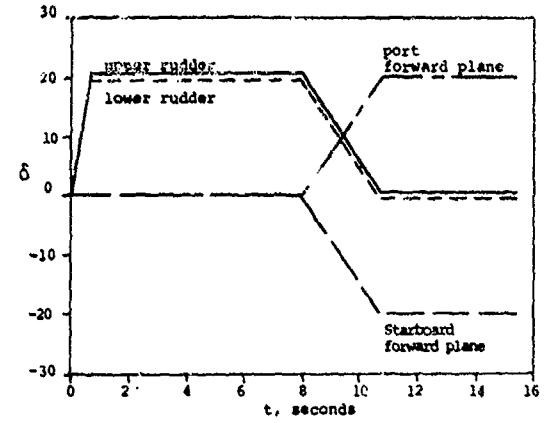

(a) Control surface deflection schedule

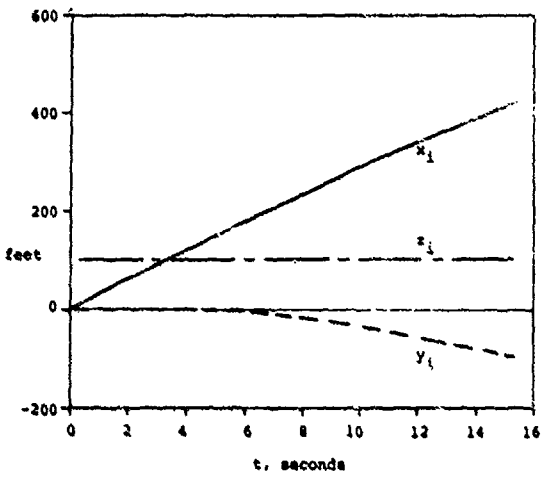

(b) Trajectory components

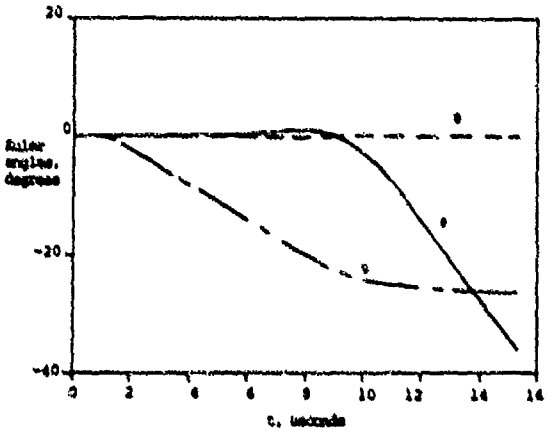

(c) Euler angles

Fig. 19 Predicted trajectory characteristics for a large-scale, fully-appended submersible vehicle

TRAJECTORY AND MOTION SIMULATION OF A BODY UNDER WAVES

A J Musker

Admiralty Research Establishment,
Haslar, Gosport, England

Abstract

A numerical model to calculate the motion history of a submerged body beneath waves is described. The model employs simple Rankine sources, distributed within the body, to generate the disturbance potential. A preliminary validation of the model is presented using both analytic and experiment data. The method has been used to investigate the effects of run times and the method of sea spectrum discretisation on the motion statistics in head seas.

The results support the hypothesis that once the wave system has sufficient components to ensure that its lowest beat frequency is smaller than the natural frequency (in pitch) of the body, the standard deviation of the depth signal will vary only slightly with an increase in the number of wave frequencies.

1. Introduction

This paper describes a numerical model to simulate the trajectory and motion of a submerged body beneath surface waves. The waves are assumed to be long-crested and irregular. Because the model operates in the time domain and is not strictly linearised, the possibility exists to simulate large changes in depth and speed in a deterministic sense.

The model employs Rankine-type singularities, distributed within the hull, whose strengths at any instant in time are assigned by the body kinematic condition that no fluid can pass through the hull's surface. This condition is treated 'exactly' in the sense that both the instantaneous translational and rotational velocity vectors of the hull are taken into account in order to calculate the normal velocity components at a large number of control points. The resulting disturbance potential is then combined with the incident wave potential to determine the flow field. This, together with the time derivative of the total velocity potential, is sufficient to compute the pressure around the body and hence the wave force and moment vectors. The disturbance on the surface caused by the presence of the body is considered to be negligibly small and is not included in the model. The actual trajectory and motion of the body are computed using the rigid body equations, together with certain hydrodynamic coefficients and derivatives (to model viscous effects) and computed wave force and moment terms appearing on the right hand sides. These coefficients are first measured experimentally using a planar motion mechanism (PMM) which imparts known motions to the body (or model) at deep submergence. These same motions are then simulated (as a separate exercise), using the above mentioned potential flow program, to predict the inviscid components for each of these coefficients. By regarding each measured coefficient as a linear superposition of a viscous and an inviscid term, the viscous effects can be readily estimated by a simple process of subtraction. In practice, this is performed by a separate computer program which is designed to create a master input file for a particular body geometry. This same program also inverts the matrix of influence coefficients (arising from the potential flow analysis) ready for use in the main program.

Numerical and towing-tank data are compared for the case of a body (with non-circular cross-section) which can be either completely restrained or lightly restrained using low-stiffness springs mounted on a carriage. The experimental arrangement is briefly described.

The numerical model has been used to assess the effect of run times on the ensuing motion statistics. Because the second order excitation manifests itself in the form of very low frequency components, long run times may be necessary in order to achieve statistically reliable results. This problem is compounded by the fact that these low frequencies can lie near the natural pitch period of the body so that the low frequency motion can be considerable. The effect of changing the number of discrete frequencies used to define the wave spectrum has also been studied in this context. The results are presented in a later section.

2. Methodology

2.1 Potential Flow Equations

Two sets of orthogonal 3-axis co-ordinate systems are used in the analysis (Figure 1). Earth-fixed axes, O'x'y'z', are chosen so that the O'x'y' plane lies on the mean free surface with O'x' in the direction of incident wave propagation (if there are no incident waves O'x' is arbitrary). The convention adopted for the O'z' axis is positive in the downward direction.

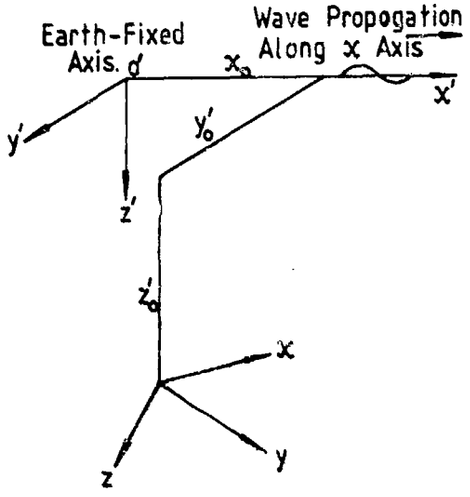

FIGURE 1. SYSTEM OF AXES.

Body axes, Oxyz, are used in the conventional sense. These may be regarded as having been rotated to assume an arbitrary orientation with respect to O'x'y'z' by the three Euler angles Ψ, θ and ϕ applied consecutively about the O'z', O'y' and O'x' axes respectively.

The origin of the body axes is chosen in accordance with the requirements of the singularity distribution used to model the flow; this will be dealt with in a later section. In the meantime, it should be stressed that although the origin may lie at the centre of mass for a restricted class of bodies this is by no means always the case.

The fluid is assumed to be inviscid, irrotational, incompressible and infinitely deep. A scalar velocity potential, Φ is defined such that

$$u'_f = -\frac{\partial \Phi}{\partial x'}$$
$$v'_f = -\frac{\partial \Phi}{\partial y'} \qquad (1)$$
$$w'_f = -\frac{\partial \Phi}{\partial z'}$$

where u'_f and v'_f are fluid velocity components in Earth axes.

The mass continuity equation is

$$\frac{\partial u'_f}{\partial x'} + \frac{\partial v'_f}{\partial y'} + \frac{\partial w'_f}{\partial z'} = 0 \qquad (2)$$

or, in terms of the velocity potential,

$$\frac{\partial^2 \Phi}{\partial x'^2} + \frac{\partial^2 \Phi}{\partial y'^2} + \frac{\partial^2 \Phi}{\partial z'^2} = 0 \qquad (3)$$

Body kinematics dictate that at any point on the body-fluid boundary there can be no flow of fluid across the normal to the boundary. Hence the fluid velocity component in the direction of the local normal vector, $\hat{n}$, must equal the corresponding velocity component, $\vec{V}$ associated with the point on the body defined by the intersection of the local normal vector and the body surface. Hence

$$-(\text{grad } \Phi).\hat{n} = \vec{V}' \cdot \hat{n} \qquad (4)$$

The convention adopted for $\hat{n}$ is that it should be in a direction pointing into the fluid and away from the body interior.

It is convenient at this point to define the velocity potential in terms of a known incident wave potential, Φ_I, and an unknown body disturbance potential, Φ_B. Hence

$$\Phi = \Phi_I + \Phi_B \qquad (5)$$

For a simple regular wave Φ_I takes the well-known form:

$$\Phi_I = \frac{gA}{\omega} \exp\left(\frac{2\pi z'}{\lambda} - \omega t\right) \exp\left(\frac{-2\pi x'}{\lambda}\right) \qquad (6)$$

which is correct to first order in (a/λ) where a is the wave amplitude, ω is the wave frequency in radians per second and λ is the wavelength.

For irregular waves, Φ_I becomes:

$$\Phi_I = \sum_{i=1}^{\infty} \left[\frac{g\zeta_i}{\omega_i} \exp\left(k_i z' - \omega_i t + \beta_i\right) \exp\left(-k_i x'\right)\right] \qquad (7)$$

where k_i is the ith wave-number $(= \omega_i^2/g)$ and β_i is the ith phase angle. The Bretschneider spectrum function [1] may be conveniently utilised to prescribe the wave amplitudes to be associated with the chosen frequencies.

As discussed in the previous section, the effect of the body on the free surface is ignored. Hence, for the purpose of calculating the body disturbance potential, ϕ_B, we consider only the perturbation required to ensure tangential flow at all the chosen control points on the body. This constraint on the solution implies that wave diffraction and radiation effects are negligible and so the proposed model is likely to be in error if the body is very close to the free surface. This is not a series drawback, however, for practical calculations.

2.2 Representation of Body Using Singularities

Before discussing the singularity distribution to be used to generate the body potential, the location and orientation of the body axes must first be decided. A degree of judgement is required here although for most practical cases the precise location used is by no means critical as long as certain guidelines are followed.

The Ox axis for the body should be chosen such that it passes near the centres of area of the body sections lying perpendicular to the axis. Ideally the points of intersection of the axis and the body should be near to the estimated forward and rear stagnation points, although this is of secondary importance. The stagnation points are here understood to correspond to pure longitudinal translation at deep submergence. Whilst it is unlikely that the longitudinal axis will pass through the centre of mass of the body, the resulting inconvenience is easily overcome. The origin of the body axes, o, is defined to be the mid-point of the body length, L, measured along the Ox axis.

The geometry of the body is best described initially using a cylindrical co-ordinate system (x, r_c, θ) which can then be converted into the orthogonal body axes already mentioned. The origin, O, is common to both these co-ordinate systems. The Ox axis is divided into 40 equal intervals for the purpose of defining the section geometry, $r_c = r_c(x, \theta)$. Two extra stations at $x = \pm (79L/160)$ are included in the neighbourhood of the above-mentioned stagnation points to improve the quality of the prediction.

A total of 330 singularities is used to represent the body, each of which is associated with its own unique 'body point'. A body point is a point on the body surface through which is constructed a line which is normal to the local tangent plane. The singularity associated with a particular body point is positioned inside the body along the local normal. The precise distance from the body point was chosen after some experimentation; a value of $0.6\, r_c$, were r_c is the radial co-ordinate of the body point, was finally selected as being suitable for most bodies of interest. Two singularities are positioned to correspond to the body points at $x = \pm (L/2)$, whilst the remaining singularities are distributed at the rate of 8 per station among the other 41 stations such that at any one station the body points are separated by 45 degree intervals in θ. It should be pointed out that any effects due to appendages are beyond the scope of the present work except in so far as they are already modelled in terms of the PMM derivatives for the case of deep submergence. The potential flow model relates only to the naked body.

2.3 Body Kinematics

The strengths of the singularities must be determined such that the total potential satisfies the kinematic condition expressed by equation (4). This applies to all body points, resulting in a set of equations equal in number to the number of unknown singularities. This leaves only equation (3) to be satisfied; it will be seen in the next section that this is done so automatically owing to the nature of the singularity employed.

Attention is focussed, therefore, on equation (4) which may be recast in scalar form, for the jth body point, as follows:

$$-l_j\left[\frac{\partial\phi}{\partial x}\right]_j - m_j\left[\frac{\partial\phi}{\partial y}\right]_j - n_j\left[\frac{\partial\phi}{\partial z}\right]_j = l_jU_j + m_jV_j + n_jW_j \qquad (8)$$

where l_j, m_j, n_j, are the direction cosines of the outward normal and U_j, V_j, W_j are the velocity components of the body point. All the parameters in equation (8) refer to Earth axes and therefore assume values which are dependent on the known instantaneous orientation and motion of the body axes and the fixed position of the body point with respect to the body axes.

Transformation to Earth axes involves a simple vector operation:

$$\begin{bmatrix} \bar{i}' \\ \bar{j}' \\ \bar{k}' \end{bmatrix} = \underline{T} \begin{bmatrix} \bar{i} \\ \bar{j} \\ \bar{k} \end{bmatrix} \qquad (9)$$

where $(\bar{i}', \bar{j}', \bar{k}')$ and $(\bar{i}, \bar{j}, \bar{k})$ are unit vectors associated with the Earth and body axes respectively and $\underline{T}$ is the transformation matrix.

Now the direction cosines (l, m, n), referred to body axes, are of course constant

for a particular body point. Referred to Earth axes, for use in equation (8), the direction cosines of the local outward normal are

$$\begin{bmatrix} l'_j \\ m'_j \\ n'_j \end{bmatrix} = T \begin{bmatrix} l_j \\ m_j \\ n_j \end{bmatrix} \qquad (10)$$

Similarly, the co-ordinates of a body point in Earth axes are

$$\begin{bmatrix} x'_j \\ y'_j \\ z'_j \end{bmatrix} = \begin{bmatrix} x'_o \\ y'_o \\ z'_o \end{bmatrix} + T \begin{bmatrix} x_j \\ y_j \\ z_j \end{bmatrix} \qquad (11)$$

where (x'_o, y'_o, z'_o) are the co-ordinates of the origin of the body axes.

Differentiation of equation (11) provides the required body point velocity components in Earth axes:

$$\begin{bmatrix} U'_j \\ V'_j \\ W'_j \end{bmatrix} = \frac{d}{dt} \begin{bmatrix} x'_j \\ y'_j \\ z'_j \end{bmatrix} = \frac{d}{dt} \begin{bmatrix} x'_o \\ y'_o \\ z'_o \end{bmatrix} + \frac{d}{dt}(T) \cdot \begin{bmatrix} x_j \\ y_j \\ z_j \end{bmatrix}$$

Hence, using equation (9):

$$\begin{bmatrix} U'_j \\ V'_j \\ W'_j \end{bmatrix} = T \begin{bmatrix} U_o \\ V_o \\ W_o \end{bmatrix} + \frac{d}{dt}(T) \cdot \begin{bmatrix} x_j \\ y_j \\ z_j \end{bmatrix} \qquad (12)$$

where U_o, V_o and W_o are the velocity components of the origin, O, in body axes.

The derivative term in the above equation gives rise to rates of change of ϕ, θ and ψ which must be related to the known angular rates p_b, q_b and r_b referred to body axes:

$$\begin{bmatrix} \dot{\phi} \\ \dot{\theta} \\ \dot{\psi} \end{bmatrix} = \begin{bmatrix} 1 & \sin\phi\tan\theta & \cos\phi\tan\theta \\ 0 & \cos\phi & -\sin\phi \\ 0 & \sin\phi\sec\theta & \cos\phi\sec\theta \end{bmatrix} \begin{bmatrix} p_b \\ q_b \\ r_b \end{bmatrix} \quad \left(\theta \neq \frac{\pi}{2}\right) \qquad (13)$$

Equation (8) can now be applied to any body point, in terms of parameters referred to body axes, by invoking equations (10), (12) and (13).

2.4 Calculation of Disturbance Potential

The velocity potential at a point associated with an isolated source of strength α is simply α/R_s, where R_s is the distance from the source (if α is negative the singularity becomes a sink). For the body in question, therefore, the disturbance potential, ϕ_B, at the jth body point is

$$\phi_B\left(x'_j, y'_j, z'_j, t\right) = \sum_{i=1}^{n} \frac{\alpha_i}{\sqrt{\left(x'_j - x'_{s_i}\right)^2 + \left(y'_j - y'_{s_i}\right)^2 + \left(z'_j - z'_{s_i}\right)^2}} \qquad (14)$$

where $\left(x'_{s_i}, y'_{s_i}, z'_{s_i}\right)$ are the co-ordinates, in Earth-fixed axes, of the singularity, α_i, associated with the ith body point and n is the number of body points. Hence equation (8) becomes:

$$\sum_{i=1}^{n} \left[\alpha_i \left(\frac{l_j\left(x_j - x_{s_i}\right) + m_j\left(y_j - y_{s_i}\right) + n_j\left(z_j - z_{s_i}\right)}{\left[\left(x_j - x_{s_i}\right)^2 + \left(y_j - y_{s_i}\right)^2 + \left(z_j - z_{s_i}\right)^2\right]^{3/2}} \right) \right]$$

$$= l'_j U'_j + m'_j V'_j + n'_j W'_j$$

$$+ \sum_{i=1}^{n_w} \frac{a_i k_i g}{\omega_i} \exp\left(-k_i z'_j\right) \left[l'_j \cos\left(k_i x'_j - \omega_i t + \beta_i\right) - n'_j \sin\left(k_i x'_j - \omega_i t + \beta_i\right) \right] \qquad (15)$$

This represents a system of n simultaneous linear equations in the n unknowns, α_i. For a particular body geometry, the matrix of influence coefficients remains constant and hence a single matrix inversion is required. The solution vector is then found by matrix multiplication at each time step in the simulation. Differentiation of equation (15) provides the time derivative of the strength of the ith singularity:

$$\sum_{i=1}^{n}\left[\frac{d\alpha_i}{dt}\left(\frac{l_j\left(x_j - x_{s_i}\right) + m_j\left(y_j - y_{s_i}\right) + n_j\left(z_j - z_{s_i}\right)}{\left[\left(x_j - x_{s_i}\right)^2 + \left(y_j - y_{s_i}\right)^2 + \left(z_j - z_{s_i}\right)^2\right]^{3/2}}\right)\right]$$

$$= l_j\left(\dot{U}_o - y_j\dot{r}_b + z_j\dot{q}_b\right)$$

$$+ m_j\left(\dot{V}_o - z_j\dot{p}_b + x_j\dot{r}_b\right)$$

$$+ n_j\left(\dot{W}_o - x_j\dot{q}_b + y_j\dot{p}_b\right)$$

$$+ \frac{dl'_j}{dt}\sum_{i=1}^{n_w}\frac{a_i k_i g}{\omega_i}\exp\left(-k_i z'_j\right)\cos\left(k_i x'_j - \omega_i t + \beta_i\right)$$

$$- \frac{dn'_j}{dt}\sum_{i=1}^{n_w}\frac{a_i k_i g}{\omega_i}\exp\left(-k_i z'_j\right)\sin\left(kx'_j - \omega_i t + \beta_i\right)$$

$$- l'_j\sum_{i=1}^{n_w}\frac{a_i k_i^2 g}{\omega_i}\exp\left(-k_i z'_j\right)\left[W'_j\cos\left(k_i x'_j - \omega_i t + \beta_i\right)\right.$$

$$\left. + \left(U'_j - \frac{\omega_i}{k_i}\right)\sin\left(k_i x'_j - \omega_i t + \beta_i\right)\right]$$

$$+ n'_j\sum_{i=1}^{n_w}\frac{a_i k_i^2 g}{\omega_i}\exp\left(-k_i z'_j\right)\left[W'_j\sin\left(k_i x'_j - \omega_i t + \beta_i\right)\right.$$

$$\left. - \left(U'_j - \frac{\omega_i}{k_i}\right)\cos\left(k_i x'_j - \omega_i t + \beta_i\right)\right] \qquad (16)$$

where $\frac{dl'_j}{dt}$ and $\frac{dn'_j}{dt}$ are found by differentiating equation (10). This represents a further n simultaneous equations which are solved in the same manner as α_i.

The partial time derivative of the disturbance potential, associated with the movement of the singularities through the fluid, can now be calculated:

$$\left(\frac{\partial\phi_s}{\partial t}\right)_j = \sum_{i=1}^{n}\frac{\frac{d\alpha_i}{dt}}{\sqrt{\left(x_j - x_{s_i}\right)^2 + \left(y_j - y_{s_i}\right)^2 + \left(z_j - z_{s_i}\right)^2}}$$

$$+ \sum_{i=1}^{n}\alpha_i\frac{U'_i\left(x'_j - x'_{s_i}\right) + V'_i\left(y'_j - y'_{s_i}\right) + W'_i\left(z'_j - z'_{s_i}\right)}{\left[\left(x_j - x_{s_i}\right)^2 + \left(y_j - y_{s_i}\right)^2 + \left(z_j - z_{s_i}\right)^2\right]^{3/2}} \qquad (17)$$

In this equation U'_i, V'_i and W'_i represent the instantaneous velocity components in Earth axes of the ith singularity. The pressure at the jth body point then follows from the unsteady form of Bernoulli's theorem:

$$p_j = \rho\left(\frac{\partial\phi}{\partial t} - \frac{1}{2}\left|\text{grad }\phi\right|^2\right)_j \qquad (18)$$

2.5 Calculation of Force and Moment Vectors

In order to quantify the force and moment vectors, the body is represented by a large number of surface panels defined by the body points (336 panels are defined by the 330 body points used in the present analysis). Each panel is divided into six triangular sub-panels such that their vertices are formed at intervals in θ of 15 degrees at all the longitudinal stations (See Figure 2). The panel geometry is so arranged as to be symmetrical about the x-z plane since this is a plane of symmetry for typical body shapes.

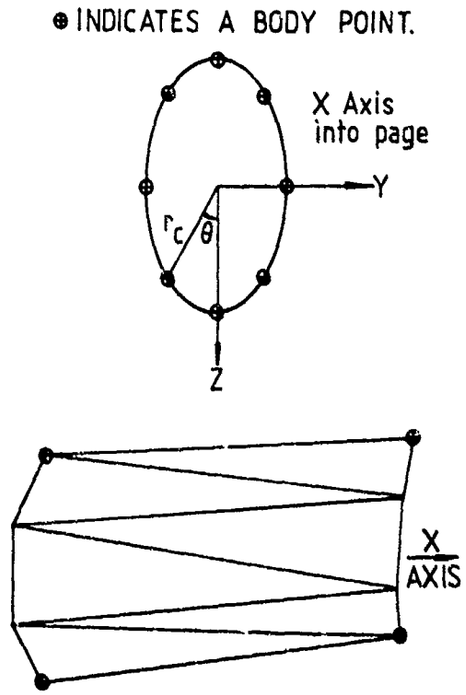

FIGURE 2. PANEL LAYOUT.

The pressure at the centroid of each sub panel is interpolated from the known pressures at the neighbouring body points and the contributory force and moment vectors are calculated. The total force and moment vectors are then found by summation over the whole body. A sextic surface interpolation procedure based on Everett's formula [2] is used to find the pressure at the six centroids contained within each panel. The procedure relies on a knowledge of the pressures at 24 surrounding body points. The interpolated pressures have been found to be in excellent agreement with values computed directly from the velocity potential at the centroids. This latter method is impractical to use routinely since it is very expensive in computer time.

The instantaneous force vector, $\vec{F}$, can now be expressed in terms of the unit vectors, $\hat{i}$, $\hat{j}$ and $\hat{k}$ as follows:

$$\vec{F} = \sum_{j_1=1}^{336} \sum_{i_1=1}^{6} \left[\left(P_{i_1} A_{i_1} l_{i_1} \right)_{j_1} \hat{i} + \left(P_{i_1} A_{i_1} m_{i_1} \right)_{j_1} \hat{j} + \left(P_{i_1} A_{i_1} n_{i_1} \right)_{j_1} \hat{k} \right] \quad (19)$$

where, for the j_1th panel, P_{i_1} refers to the interpolated pressure at the centroid of the i_1th sub-panel, A_{i_1} refers to the area of the i_1th sub-panel and $(l_{i_1}, m_{i_1}, n_{i_1})$ are the direction cosines of the inward normal at the i_1th centroid. Similarly, the instantaneous moment vector, $\vec{M}$, about the centre of mass is:

$$\vec{M} = \sum_{j_1=1}^{336} \sum_{i_1=1}^{6} \left[\left[P_{i_1} A_{i_1} \left[n_{i_1} \left(y_{i_1} - y_o \right) - m_{i_1} \left(z_{i_1} - z_o \right) \right] \right] \hat{i} + \left[P_{i_1} A_{i_1} \left[l_{i_1} \left(z_{i_1} - z_o \right) - n_{i_1} \left(x_{i_1} - x_o \right) \right] \right] \hat{j} + \left[P_{i_1} A_{i_1} \left[m_{i_1} \left(x_{i_1} - x_o \right) - l_{i_1} \left(y_{i_1} - y_o \right) \right] \right] \hat{k} \right] \quad (20)$$

where (x_o, y_o, z_o) are the body co-ordinates of the centre of mass.

It should be pointed out that the above expressions relate only to inviscid effects associated with the incident waves and the motion of the body. Viscous effects are modelled by incorporating empirical data from planar motion mechanism (PMM) tests on a deeply submerged model. These data take the form of various hydrodynamic dervatives and coefficients (see, for example, Abkowitz[3]). Such data, of course, have both inviscid and viscous effects embedded in them. Since the strategy thus far has been to include all inviscid effects (within the context of the physical assumptions made), such contributions to the measured derivative data may be quantified by running the computer program for a series of fixed manoeuvres chosen to simulate the PMM tests. In this way, the calculated contributions can be subtracted from the measured data to provide estimates of the non-dimensional forces and moments which are of purely viscous origin. These additional forces and moments are then added to the expressions given in equations (19) and (20) before being applied to the dynamic model for the rigid body.

2.6 Motion Calculation

To compute the motion of the body, a new set of body axes is chosen such that the origin is at the centre of mass. The usual equations of motion for a rigid body are then invoked, with appropriate terms on the right hand sides to model the hydrodynamic and external forces and moments.

$$m\left(\left[\dot{U}_o - V_o r_b + W_o q_b \right] \hat{i} + \left[\dot{V}_o - W_o p_b + U r_b \right] \hat{j} + \left[\dot{W}_o - U_o q_b + V_o p_b \right] \hat{k} \right)$$

$$= \vec{F} + (\text{viscous, propulsion, control, weight, buoyancy}) \text{terms} \quad (21)$$

and

$$\left[I_x \dot{p}_b + \left(I_z - I_y \right) q_b r_b \right] \hat{i} + \left[I_y \dot{q}_b + \left(I_x - I_z \right) r_b p_b \right] \hat{j} + \left[I_z \dot{r}_b + \left(I_y - I_x \right) q_b p_b \right] \hat{k}$$

$$= \vec{M} + (\text{viscous, propulsion, control, weight, buoyancy}) \text{terms} \quad (22)$$

where $\vec{F}$ and $\vec{M}$ are given by equations (19) and (20). This pair of vector equations represents a set of six first order, ordinary differential equations in U_o, V_o, W_o, P_b, q_b, and r_b. It has been found that the following difference procedure (in this case for U_o) provides a sufficiently accurate integration of the equations:

$$\left(U_o \right)_t = \left(U_o \right)_{t-\Delta t} + \tfrac{1}{2} \Delta t \left[3 \left(\dot{U}_o \right)_{t-\Delta t} - \left(\dot{U}_o \right)_{t-2\Delta t} \right] \quad (23)$$

where Δt is the chosen step length. The latter is not critical provided it is not significantly larger than 10% of the shortest time period used to represent the seaway.

2.7 Computer Simulation

The computer program has been implemented on a PRIME 750 machine acting as a host to a Floating Point Systems AP120B vector processor equipped with a dedicated disk sub-system. The AP120B machine is a high speed peripheral floating-point arithmetic vector processor. The pipe-lined architecture enables array indexing, loop counting, data fetching from memory and arithmetic operations in the separate adder and multiplier to be performed simultaneously and at high speed (clock cycle 167 ns).

Data which are constant for a whole simulation run (such as the inverse of the matrix of influence coefficients) are stored on the disk sub system for rapid retrieval by the AP120B at each time step in the calculation and post-processing operations. The program is coded using a combination of FORTRAN IV, APFORTRAN and APAL (Array Processor Assembly Language) to achieve maximum speed consistent with ease of use. The execution time is currently approximately three times slower than real time, although real time could easily be achieved with the addition of a solid state bulk memory in place of the disk sub-system.

3. Validation

3.1 Overview

The numerical model described in this paper has been used to predict a large number of flows for which analytical or experimental results are available. For the purpose of the present paper, attention is focussed on three typical validation exercises, the results of which are broadly representative of the overall performance of the model.

3.2 Comparions with Analytical Solutions

Predictions for a 2:1 prolate spheroid for both pure translation (along its major axis) and rotation (about its minor axis) are compared with analytical solutions due to Lamb [4] in Figures 3 and 4. They appear to be in excellent agreement.

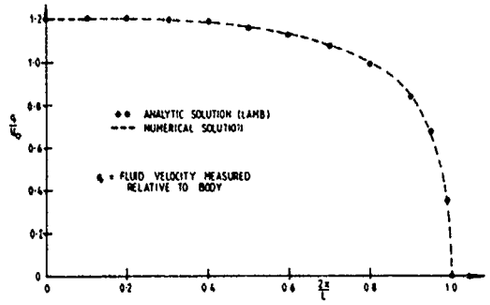

Fig 3. Fluid velocity distribution for 2 : 1 prolate spheroid in axial flow.

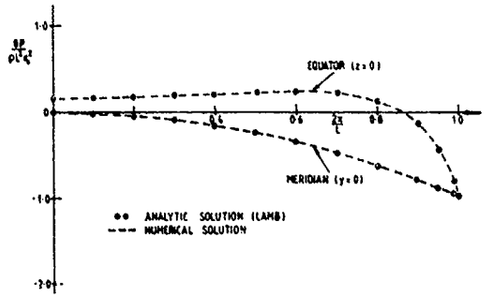

Fig 4. Pressure distribution for spinning 2 : 1 prolate spheroid.

The case of a restrained, infinite circular cylinder has recently been investigated analytically by Wilmott [5] using the method of matched asymptotic expansions. His results are nearly identical to those of Ogilvie [6]. Figures 5 and 6 show the results for the first and second order heave force amplitude compared with the present numerical model. It should be pointed out that for the purpose of this validation exercise the first and second order components for the numerical model were computed using a simple statistical analysis of the time history for the total hydrodynamic force. In an actual simulation application there would of course be no requirement to distinguish between first and second order components.

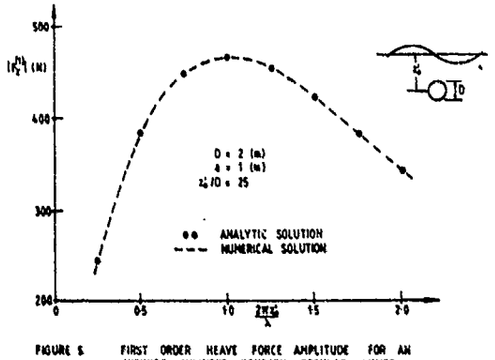

FIGURE 5 FIRST ORDER HEAVE FORCE AMPLITUDE FOR AN INFINITE CYLINDER BENEATH REGULAR WAVES

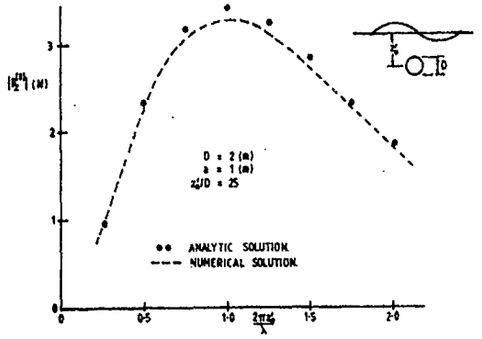

FIGURE 6. SECOND ORDER HEAVE FORCE AMPLITUDE FOR AN INFINITE CYLINDER BENEATH REGULAR WAVES

3.3 Restrained Body Beneath Regular Waves

Towing tank experiments were conducted with the aim of measuring both heave force and pitch moment for a restrained, non-axisymmetric body undergoing self-propulsion beneath regular waves.

Routine procedures were adopted to conduct these tests, the results of which were analysed digitally using standard time series analysis software. The body had a length to beam ratio of 8.7 and was submerged at a depth (to axis) to length ratio of 0.16. Results for a typical run in head seas, with forward speed, are shown in Figures 7 to 10. These figures also show the numerical predictions (depicted by the solid curve) for the purpose of comparison.

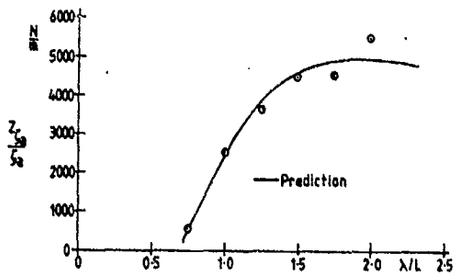

FIGURE 7 AMPLITUDE OF 1st ORDER HEAVE FORCE.

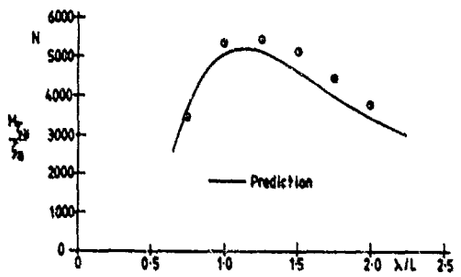

FIGURE 8 AMPLITUDE OF 1st ORDER PITCH MOMENT.

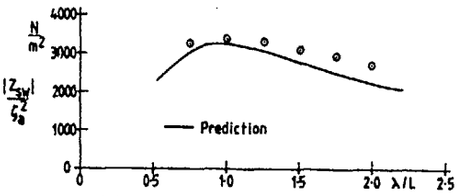

FIGURE 9 MEAN HEAVE FORCE.

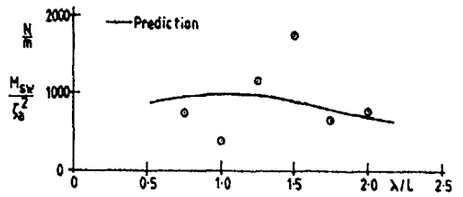

FIGURE 10 MEAN PITCH MOMENT

The considerable scatter in the data for the second order pitch moment is attributable to the extreme difficulty in reliably extracting a small non-zero mean from a finite-length record. Nevertheless, the overall agreement appears to be good.

3.4 Lightly Restrained Body Beneath Regular Waves

Modifications to the above experiment were made to allow the body to respond to the regular wave excitation. This was done using linear bearings on the towing struts. The mean vertical force due to the waves was checked by two low-stiffness (1000 $N.m^{-1}$) springs and the associated heave displacement was measured using sliding potentiometers (See Figure 11). A standard wave probe was positioned level with the forward end of the model and midway between the model and the tank wall. A simple elasticity analysis was included in the equations of motion to allow for flexure of the swords - this was considered significant in some cases.

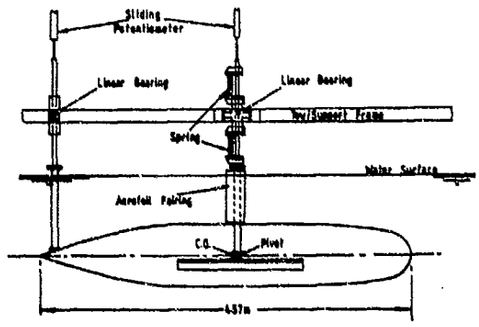

FIGURE 11 EXPERIMENT ARRANGEMENT

Figure 12 shows the preliminary results from this experiment for the amplitude of the oscillatory heave displacement (non-dimensionalised by the wave amplitude).

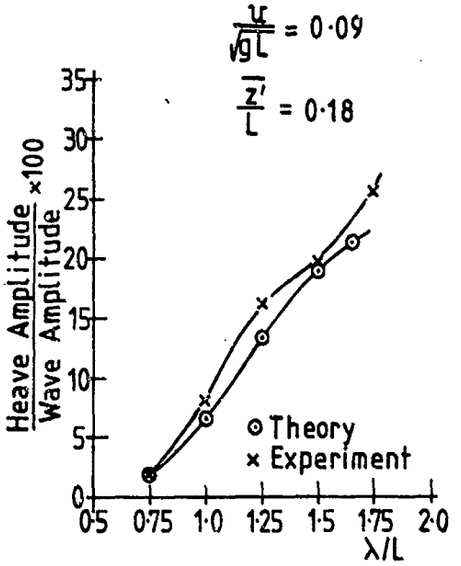

FIGURE 12 HEAVE RESPONSE FOR LIGHTLY RESTRAINED BODY

It should be pointed out that the dimensionless mean depth quoted in the Figure is a nominal one in so far as the wave amplitudes used were different for each wave-length. This was necessary to ensure a sufficiently large heave response consistent with waves of acceptable quality. However, because the wave amplitudes were different, the suction forces gave rise to different mean spring deflections and hence mean depths. Nevertheless, the data have been presented on the one graph for convenience. Despite some disparity at $\lambda/L = 1.25$, the agreement appears to be satisfactory, bearing in mind the difficulty in performing such an experiment and the associated paucity of the data. It is planned to perform a similar but more comprehensive experiment in the near future.

4. Preliminary Evaluation Using Irregular Waves

4.1 Introduction

The numerical model has been evaluated for use with a Bretschneider sea spectrum [1]; two parameters are of importance in this context since their values may significantly affect the ensuing predictions. The parameters are the run time, or length of simulation, and the number of discrete frequency components used to represent the spectrum (n_w in Equation (7)).

The accuracy of the predicted results will be questionable if the run time with irregular waves is too short, even if the body motion has reached a quasi steady state and initial transients have decayed, since the number of low frequency depth excursions observed in the trajectory depends on the length of run. It was thought that the statistics for a short run might therefore bear little resemblance to the corresponding statistics for a long run.

Similarly, the motion statistics will be sensitive to the number of wave frequencies used to represent the spectrum. In the program, these frequencies are equally spaced between zero and a user-selectable maximum. The program also employs a user-selectable seed for a random number generator to set the phases of the individual wave components. The use of too few frequencies may be insufficient to resolve the motions actually incurred by a submerged body in the ocean environment. This is because the lowest beat frequency of the wave system may be higher than the natural frequency (in pitch) of the body, whilst the converse applies if n_w is large. This difference may have a severe effect on the low frequency motion of the body and in consequence the results for small n_w may be unrelated to those for large n_w.

For the purpose of the present paper, attention is focussed on the standard deviation of the depth signal referred to the centre of mass of the body. A body geometry broadly representative of the one used in the previous experiment was chosen for this investigation, except that in this case a form of depth control, which was identical for all the runs, was incorporated within the program. The following parameters were used:

$$\frac{z'}{L} = 0.2;\ \frac{U}{\sqrt{gL}} = 0.12;\ \frac{\lambda_m}{L} = 2;\ \text{sea-state} = 5$$

where λ_m is the modal wavelength. Two different run lengths were used for the investigation. The long runs comprised 280 modal periods whilst the short runs comprised 42 modal periods.

4.2 Effect of run-length

Four short runs were conducted, each with a different seed but all with $n_w = 150$. These were then repeated using the larger run length. The results are summarised in Table 1.

Seed	Depth Standard Deviation / Mean Depth	
	Short Run	Long Run
0.5	0.0269	0.0296
0.6	0.0402	0.0350
0.7	0.0307	0.0389
0.8	0.0400	0.0312
Mean Value	0.0345	0.0338

It can be seen that for this particular series of runs the mean values of the normalised standard deviation are nearly identical.

4.3 Effect of n_w

Four long runs were conducted for various numbers of wave frequencies. The results are shown in Figure 13. The mean values measured for 25 or fewer wave frequencies increase rapidly with an increase in the number of wave frequencies. For 32 or more waves, however, the mean value changes only slightly with an increase in the number of wave frequencies. It is speculated that once the wave system has sufficient components to ensure that its lowest beat frequency is smaller than the natural frequency (in pitch) of the body, the mean depth standard deviation will vary only slightly with an increase in the number of wave frequencies.

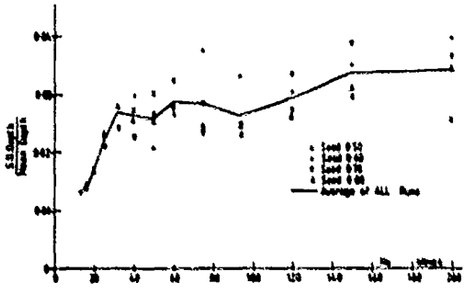

FIGURE 13 DEPTH STANDARD DEVIATION FOR VARIOUS n_w (LONG RUNS)

This is supported in Figures 14 and 15 where the depth auto spectral densities are shown for n_w 16 and 150 respectively. In the case of 150 wave frequencies there is a substantial amount of low frequency motion which is absent when $n_w = 16$.

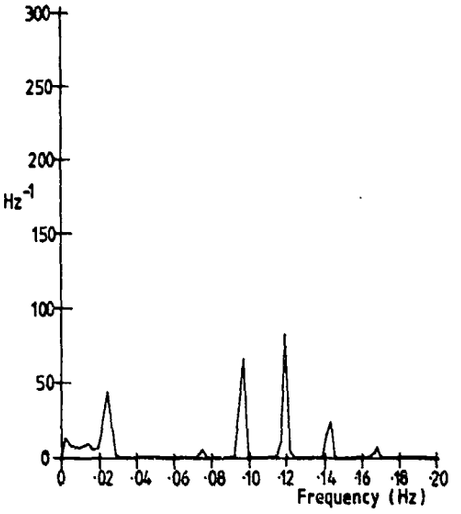

FIGURE 14 DEPTH ASD FOR LONG RUN WITH 16 WAVES.

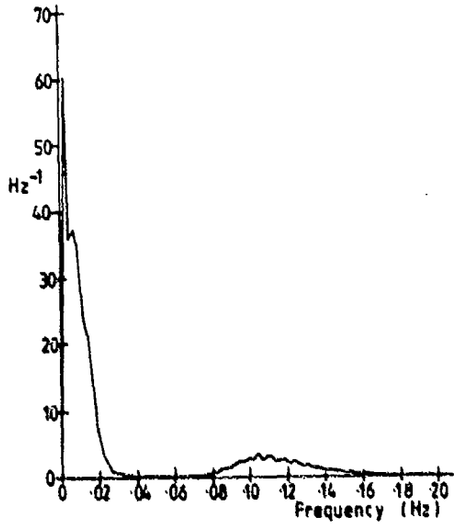

FIGURE 15 DEPTH ASD FOR LONG RUN WITH 150 WAVES

5. Conclusions

A simple method of computing the trajectory and motion of a submerged body under waves has been presented. The method has been tested against both analytic and experiment data and the agreement has been found to be satisfactory for regular waves. Further validation is required for the case of irregular waves. A numerical study has shown that the method of synthesis of the sea spectrum in terms of its discrete frequencies is apparently more critical than the length of each computer simulation.

References

1. Bretschneider, C L. Wave Variability and Wave Spectra for Wind Generated Gravity Waves. Beach Erosion Board, Corps of Engineers, TM118, 1959.

2. Buckingham, R A. Numerical Methods, Pitman Press, London, 1957.

3. Abkowitz, M A. Lectures on Ship Hydrodynamics - Steering and Manoeuvrability. Hydro- and Aerodynamics Laboratory, Lyngby, Denmark. Report No. Hy-5, May 1964.

4. Lamb, Sir Horace. Hydrodynamics, Cambridge University Press, London, 1932.

5. Wilmott, P. The Asymptotic Solution of Models in Theoretical Mechanics. D Phil Thesis, Oxford University, 1985.

6. Ogilvie, T F. First and Second Order Forces on a Cylinder submerged under a Free Surface. J Fluid Mechanics, 16, p 451, 1963.

DISCUSSION
of the paper
by A.J. Musker

"TRAJECTORY AND MOTION OF A BODY UNDER WAVES"

DISCUSSION
by H. Wang

You use an interesting approach whereby the viscous terms are obtained from experimental results for a deeply submerged model and wave diffraction and radiation effects are neglected in the potential flow problem. I would appreciate your clarification of the following points. 1. Does the approach contain a check, such as a calculation of the vertical velocities at the free surface, $z' = 0$, to estimate the error in neglecting the effect of the body on the free surface? 2. Why did you choose to place the singularities inside the body, and what were the considerations leading to your final choice of $0.6\ r_c$? Do you find that this approach breaks down and/or becomes less accurate (than, for example a method which places the sources on the body surface) as the body becomes blunter? 3. Figure 13 shows the expected trend that the scatter of the results increases with number of wave frequencies n_w. As a result, the average of all runs stays relatively constant at around 0.028 for $30 < n_w < 95$, and then increases monotonically to 0.035 at $n_w = 200$. Did you consider averaging over more than 4 runs at the higher values of n_w in order to get more accurate average values?

Author's Reply

In an earlier version of the numerical model an image system was included to generate a rigid plane at $z' = 0$; this added sophistication led to changes in the pertinent forces and moments of less than three percent typically. Accordingly, the image system was excluded in the version described in the present paper.

The desire to reduce computing times to a minimum was the motivation in utilizing point sources rather than panels with constant source density. Physically the point sources must be positioned inside the body in order for them to generate the boundary surface at all correctly. The choice of $0.6r_c$ for the location along the inward normal was arrived at on a trial and error basis and represents a compromise between accuracy and numerical stability for those geometries of most interest. Surprisingly, the method becomes slightly more accurate as the body becomes blunter and in all cases behaves better near the stagnation points than the source density method.

Unfortunately, the computational effort associated with generating Fig. 13 was such as to preclude using more than four points per value of n_w.

A COMBINATION CONFORMAL-TRANSFINITE MAPPING METHOD FOR GRIDS ABOUT FIN-AFTERBODY COMBINATIONS*

Gilbert H. Hoffman

Applied Research Laboratory
The Pennsylvania State University
State College, PA - U.S.A.

Abstract

An algebraic procedure is presented for the generation of a smooth computational grid about an afterbody-fin configuration. The method makes use of a sequence of conformal transformations to upwrap the geometry and remove the corner singularities at the fin trailing edge and tail of the afterbody. A 3-D grid is generated by stacking a sequence of 2-D grids of the C-type on predetermined, smooth tubular surfaces. Clustering is accomplished by a sequence of one-dimensional stretching functions in physical space. Examples are presented to show the character of the resulting grid.

I. Introduction

The problem treated in this paper is the generation of a surface fitted grid in the stern region of an undersea vehicle, specifically an axisymmetric pointed afterbody with four identical, symmetric, constant chord fins. In many respects this problem is similar to the airplane wing-fuselage problem. The desired grid is to be used for either inviscid or viscid incompressible flow calculations and hence must have proper clustering ability to resolve regions of high flow gradients. An algebraic approach is used which is an outgrowth of earlier 3-D grid generation work on a fin-cylinder configuration [1].

Algebraic grid generation methods for three-dimensional (3-D) flow problems have the advantage over their differential equation counterparts in speed and ability to handle high aspect ratio cells without difficulty. Where the algebraic methods are sometimes at a disadvantage is in treating a wide variety of boundary shapes with a single code.

Since 1979 grids about wing-body configurations have been successfully generated by several algebraic approaches. Eriksson [2] has generated a single-block nonorthogonal 3-D grid using transfinite interpolation where geometric data is specified only on the boundaries. Since no internal surfaces are specified, grid quality is controlled, especially near a surface, by incorporating out-of-surface parametric derivatives. Smith [3] uses the patched grid approach where the domain is divided into regions with boundaries of a simplier character than the overall region. On the interior of each six-sided sub-region transfinite interpolation is used to generate the grid. His treatment extends only to the wing tips which limits its usefulness. A third and quite different approach has been taken by Caughey and Jameson [4]. Their technique generates a boundary-conforming coordinate system by a sequence of conformal and shearing transformations to yield a nearly orthogonal computational domain. The grid is then generated by simple linear interpolation. Shmilovich and Caughey [5] have recently extended this technique to include a tail surface. The Caughey-Jameson procedure was developed for use with the 3-D transonic FLO codes.

One of the major difficulties in algebraic grid generation is preventing corner singularities on the boundaries from propagating into the grid. Any interpolation method will propagate such singularities into the interior. Differential equation grid generation schemes suffer no such problem because of the diffusive action of the elliptic operator. Corner singularities are always present in 3-D configurations at wing/fin trailing edges and tail points on pointed bodies. A method for removing these singularities in algebraic grid generation has been developed by Vinokur and Lombard [6] for 2-D geometries. Their method consists of patching a conformal hinge point transformation in a small region near the corner to a grid in the remainder of the domain generated by transfinite interpolation. They successfully applied this method in generating a patched grid in a domain consisting of a backward facing

*This research was sponsored jointly by the Office of Naval Research and Naval Sea Systems Command.

step at the end of a nozzle exhausting into a cylindrical diffuser.

The algebraic method adopted here was originally inspired by the work of Caughey and Jameson in unwrapping a geometry as much as possible to produce a parallelpiped with nearly straight boundaries. This procedure is of the stacking type where a 3-D grid is produced by a sequence of 2-D grid generation operations. In the present method stacked tubular surfaces of circular cross-section are first determined and then a C-type grid generated on each surface. In the process of generating these surfaces as well as in unwrapping the airfoil, corner singularities are removed by application of a hinge point transformation to the entire boundary. The present approach thus differs from that of Vinokur and Lombard in being global rather than local in the use of the hinge point transformation. The result is a smooth boundary with a slowly varying tangent. A grid which is orthogonal at all boundaries is then generated on the interior by transfinite interpolation. By using a sequence of one-dimensional stretching functions in physical space, precise control is maintained over the clustering at all boundaries.

II. Analysis

Geometry of Computational Domain

We start by defining the geometry for which a surface-fitted grid is to be generated.

(1) The afterbody is of circular cross-section and has a smooth but otherwise arbitrary meridian profile that closes at the tail point.
(2) Four identical fins of constant unit chord and infinite span, consisting of symmetric airfoil sections, are mounted 90 degrees apart with their chord planes passing through the afterbody centerline. The trailing edges of the fins are located upstream of the tail point a distance d_{TL}.
(3) The computational domain consists of the region interior to an outer cylinder of radius r_{TIP} and exterior to the afterbody, bounded upstream and downstream by planes normal to the afterbody centerline (the initial value and outflow planes).

A schematic of the geometry and computational domain is shown in Fig. 1 and a head-on view showing the coordinate system in the crossflow plane appears in Fig. 2. Since the fins are identical and equally spaced there are four planes of symmetry at $\theta = 0$, $\pi/4$, $\pi/2$ and $3\pi/4$. Thus, only the section $-\pi/4 \leq \theta \leq 0$ is considered in generating a grid and in the flowfield calculation.

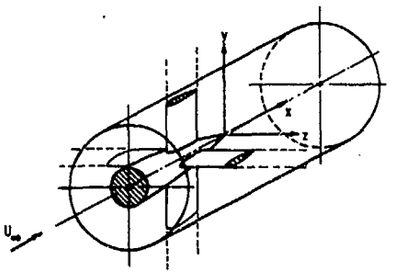

Figure 1. Schematic of Geometry and Computational Domain.

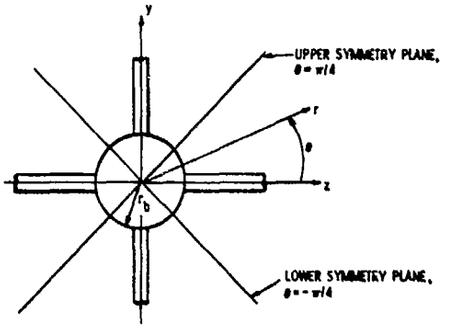

Figure 2. Planes of Symmetry.

Grid Stacking Procedure

The simplest grid stacking scheme, such as that in Ref. [4], makes use of a shearing transformation to distribute a sequence of two-dimensionally produced grids in the third spatial direction. Unfortunately the shearing transformation causes surface corner discontinuities to propagate into the grid. In the present case of a pointed tail body, Fig. 3 illustrates the situation that would exist in the meridian plane if a shearing transformation were used. Along the vertical line through the tail point, $x = x_T$, lines of constant η have discontinuous slopes.

What is needed is a transformation to produce η = constant lines that does not propagate corner discontinuities. The hinge point (power law) conformal transformation has this desired property. At the tail point (corner discontinuity) we write

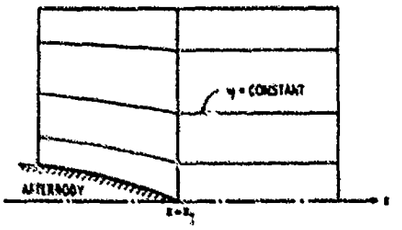

Figure 3. Grid in Meridian Plane using Shearing Transformation.

$$w = z^n \quad , \tag{1}$$

where the real axis is aligned with the axis of symmetry, and

$$z = x + iy \quad , \tag{2}$$

$$w = u + iv \quad , \tag{3}$$

$$n = \frac{\pi}{\pi - \hat{\theta}_T} \quad . \tag{4}$$

The tail angle $\hat{\theta}_T$ is defined in the meridian plane schematic given in Fig. 4. Equation

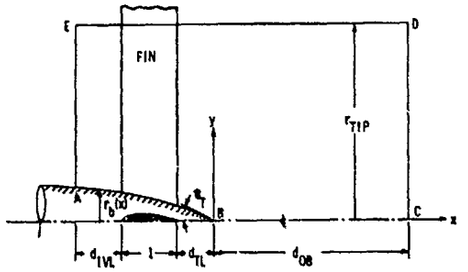

Figure 4. Meridian Plane View of Geometry and Computational Domain.

(1) maps the sector $0 \leq \hat{\theta} \leq \pi - \hat{\theta}_T$ above the real axis onto the upper half plane. If Eq. (1) is applied to the entire bounding curve in the meridian plane, A-B-C-D-E-A, the corner at the tail point B is eliminated in the w (hinge) plane. Then interpolating a grid in the hinge plane, upon transformation, will produce a smooth grid (except at B) in the physical plane which can be used for stacking.

The only difficulty in determining w (given z), or vice-versa, arises from the exponent n not being an integer so that one must be careful to select the proper Riemann sheet. In Ref. [7] a simple test is given on the real part of z (or w) to determine the correct Riemann sheet.

The image of boundary A-B-C-D-E-A in the hinge plane is shown schematically in Fig. 5 and has the appearance of a water spout. Segment BC remains straight because the real axis in the z plane is coincident with BC. For convenience,

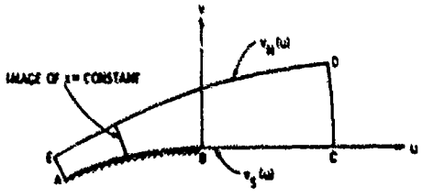

Figure 5. Meridian Boundary Image in Hinge Plane.

the transformed boundary segments will be denoted by point-of-compass notation. Thus A-B-C is $v_S(u)$ and E-D is $v_N(u)$.

To accommodate the inflow and outflow boundaries (lines A-E and C-D in Fig. 5) as well as the leading and trailing edges of the fin, vertical lines must remain vertical in the physical plane. This requirement acts as a constraint on the transformation from the hinge to the physical plane.

The simplest scheme for producing a grid in the hinge plane is a shearing transformation on the image of x = constant lines. Thus the normalized variable $\bar{r}$ is defined as

$$\bar{r} = \left(\frac{v - v_S}{v_N - v_S}\right)_{x=\text{const.}} \quad . \tag{5}$$

At this point the distribution of $\bar{r}_j$ is assumed known. Thus in the interior v is given by

$$v_{i,j} = v_{S_i} + \bar{r}_j \left(v_N - v_S\right)_i \quad , \tag{6}$$

where the index i is constant on x = constant lines. Thus at point (i,j) the values of x_i and $v_{i,j}$ are known. Then $(y,u)_{i,j}$ are determined by iteratively solving Eq. (1).

Using the above procedure, a smooth curve $y_S(x)$ is determined in the meridian plane for each value of $\bar{r}$ = constant. By revolving $y_S(x)$ about the x-axis a tubular coordinate surface is obtained which is smooth and non-developable (except when it is a cylinder). On each of these surfaces a surface fitted grid is determined as though the surface were developable, then projected back onto the surface. This means that given (x,θ), r is determined by interpolation of the tubular meridian-plane curve $r_S(x) = y_S(x)$. For the projection method to work properly, the foil subtended angle $\theta_F(x)$ must be computed to account for the variable $r_S(x)$ from

$$\theta_F = \sin^{-1}\left(\frac{y_F}{r_S}\right) \quad , \tag{7}$$

where $y_F(x)$ is the airfoil semi-thickness distribution. Lagrange cubic interpolation is used to determine r, given x, from the previously determined values of r_S.

Clustering of $\bar{r}$ = constant lines near the body surface is needed to resolve the viscous layer whereas further away, where flow gradients diminish, these lines can be further apart. A one-sided stretching function is therefore appropriate to determine the grid line spacing in the meridian plane.

Vinokur [8] has determined approximate criteria for the development of one- and

two-sided stretching functions of one variable which give a uniform truncation error independent of the governing differential equation or difference algorithm. He investigates several analytic functions but finds that only tan z, where z is real or pure imaginary, satisfies all of his criteria. These stretching functions were used in the predecessor grid generation scheme [1] and are also used here.

Since $\bar{r}$ is already a normalized variable, its distribution is given by

$$\bar{r} = 1 + \frac{\tanh\left[\frac{1}{2}\Delta\phi(\xi - 1)\right]}{\tanh\frac{\Delta\phi}{2}} \quad , \qquad (8)$$

where ξ is the normalized generating variable given by

$$\xi = \frac{j - 1}{N_{\bar{r}}} \quad ,$$

and $\Delta\phi$ is the solution of

$$S_0 = \frac{\sinh\Delta\phi}{\Delta\phi} \quad , \qquad (9)$$

and

$$S_0 = \frac{d\xi}{d\bar{r}}(0) \quad ,$$

$N_{\bar{r}}$ = number of intervals in $\bar{r}$ = KMAX - 1 .

Grid Generation on a Tubular Surface

Grid generation in the $\bar{x} - \bar{\theta}$ plane is accomplished in three stages. The first stage involves a sequence of conformal transformations to unwrap the airfoil, symmetry lines and initial and outflow lines into a quadrilateral with a slowly varying height. The unwrapping transformations are the basis for producing a C-grid about the airfoil. The second stage involves translation and rotation of coordinates about the image of the airfoil trailing edge, followed by a hinge point transformation to eliminate the corner at the trailing edge. The third stage makes use of transfinite interpolation to determine the grid in the hinge plane that is orthogonal at all boundaries. Since the boundaries in the hinge plane are smooth and have a slowly varying tangent, transfinite interpolation will produce a smooth grid in which non-orthogonality in the interior is held to a minimum. The grid in the physical plane is obtained by taking the inverse of the sequence of transformations. Since the intermediate transformations are conformal, the orthogonality at boundaries and grid smoothness will be preserved in the physical plane. Spacing of grid lines is determined on appropriate boundaries in the physical plane by use of stretching functions.

Once the coordinates of the fin airfoil (x_F, θ_F) are specified on an $\bar{r}$ = constant tubular surface, the first step, in preparation for the unwrapping transformation, is to scale the (x, θ) coordinates according to

$$\left.\begin{aligned} \bar{x} &= 4(x - d_S) + \ell n\, 2 \\ \bar{\theta} &= 4\theta \end{aligned}\right\} \qquad (10)$$

where d_S is the location of the singular point in the unwrapping transformation and is just inside the leading edge of the airfoil. The stretching factor 4 is required by the unwrapping transformation so that the upper limit on $\bar{\theta}$ will be $\pm\pi$ (the upper and lower symmetry planes are at $\theta \pm \pi/4$).

In Refs. 1 and 4, $\bar{x}$ is translated but not magnified whereas $\bar{\theta}$ is magnified as above. Unequal scaling is of course not conformal so that orthogonality of the grid cannot be maintained at the boundaries. The resulting grid in the $\bar{x} - \bar{\theta}$ plane will be highly flattened and thus highly non-orthogonal.

On an $\bar{r}$ = constant surface the boundaries and coordinate system in the $\bar{x} - \bar{\theta}$ plane are sketched in Fig. 6. Because of symmetry, only the region $-\pi \le \bar{\theta} \le 0$ needs to be considered. The airfoil can be unwrapped by applying the conformal transformation,

$$\bar{x} + i\bar{\theta} = \ell n\left[1 - \cosh(\xi + i\eta)\right] \quad . \qquad (11)$$

Equation (11) maps the region below the $\bar{x}$-axis to positive ξ in the band $0 \le \eta \le \pi$. Figure 7 presents a schematic of the boundaries in the $\xi - \eta$ plane. The initial value line (IVL) A-B-C is seen to map into a near semi-circle.

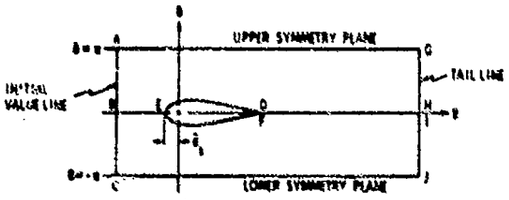

Figure 6. Computational Domain, $\bar{r}$ = Constant Surface.

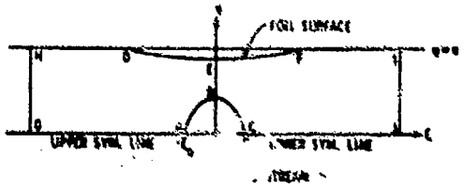

Figure 7. Boundaries in $\xi - \eta$ Plane.

Following Ref. 1, the corners at points A and C can be eliminated by applying the conformal transformation,

$$\bar{\xi} + i\bar{\eta} = \xi + i\eta + \frac{\xi_0^2}{\xi + i\eta} \quad , \qquad (12)$$

where ξ_0 is defined in Fig. 7. Equation (12) has the effect of nearly straightening out the IVL. The geometry of the boundaries in the $\bar{\xi} - \bar{\eta}$ plane is shown in Fig. 8.

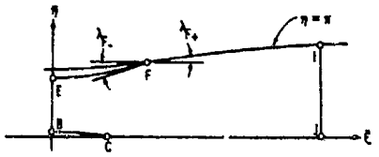

Figure 8. Boundaries in Positive $\bar{\xi} - \bar{\eta}$ Plane.

In Ref. 1 a shearing transformation is used to generate a grid in the $\bar{\xi} - \bar{\eta}$ plane. For airfoils with non-zero trailing edge angles this procedure produces discontinuous metric coefficients across the line $\bar{\xi} = \bar{\xi}_F$. To eliminate the effect of the corner at the trailing edge (point F) a procedure similar to the generation of the smooth curves in the meridian plane is used. The $\bar{\xi} - \bar{\eta}$ coordinates are first translated and rotated about point F according to

$$\left.\begin{aligned} \hat{x} &= (\bar{\xi}_F - \bar{\xi})\cos\lambda_{F_-} + (\bar{\eta}_F - \bar{\eta})\sin\lambda_{F_-} \\ \hat{y} &= -(\bar{\xi}_F - \bar{\xi})\sin\lambda_{F_-} + (\bar{\eta}_F - \bar{\eta})\cos\lambda_{F_-} \end{aligned}\right\} , \qquad (13)$$

where the positive $\hat{x}$ axis points toward point E, the airfoil leading edge, and λ_{F_-} is the trailing edge angle in the $\bar{\xi} - \bar{\eta}$ plane. The translated and rotated $\bar{\xi} - \bar{\eta}$ boundaries are sketched in Fig. 9.

The final step in producing a smooth boundary is to apply a hinge point transformation to $(\hat{x},\hat{y})$ to eliminate the corner at point F. Equation (1) applies provided $z = \hat{x} + i\hat{y}$ and

$$n = \frac{\pi}{\pi - \Delta\lambda} \quad , \qquad (14)$$

where

$$\Delta\lambda = \lambda_{F_-} - \lambda_{F_+} \quad . \qquad (15)$$

The resulting boundary in the hinge plane is sketched in Fig. 10. Once a grid in the hinge plane is produced by transfinite interpolation, the transformation sequence is reversed to obtain the grid in the $x - \theta$ plane.

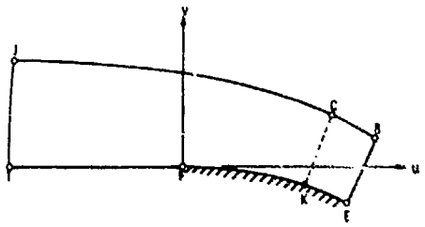

Figure 10. Boundaries in Hinge Plane.

Part of the present grid generation strategy is to force one of the coordinate lines normal to the airfoil to pass through point C, the corner point. This point on the airfoil is denoted by letter K — see Fig. 10. Such a line provides a natural division between those lines intersecting the airfoil from the IVL, B-C, and the lower symmetry line, C-J.

An effective method of locating point K that prevents reflexes on the connecting segment C-K is to construct a circular arc between C and K which is normal to both boundaries. Under this assumption the relation between the coordinates at C and K is found to be

$$\frac{u_C - u_K}{v_K - v_C} = \tan\left[\tfrac{1}{2}\left(\phi_C + \phi_K\right)\right] \quad . \qquad (16)$$

where

$$\tan\phi = \frac{du}{dv} \quad . \qquad (17)$$

Supplementing Eq. (16) by the equation for the airfoil image, $v_S(u)$, gives two equations for the two unknowns u_K and v_K.

Equation (16), together with the airfoil image equation, can be solved iteratively by the following formula, derivable from Newton's method:

$$u_K^{(n+1)} = u_K^{(n)} + \Delta u_K^{(n)} \qquad (18)$$

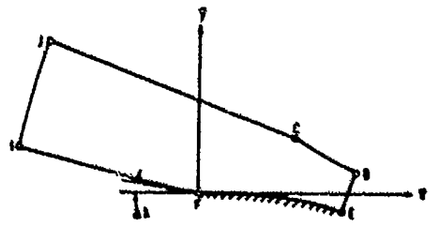

Figure 9. Translated and Rotated Boundaries in $\hat{x} - \hat{y}$ Plane.

where

$$\Delta u_K^{(n)} = \left\{ \frac{u_C - u_K + (v_C - v_K)\tan\left[\frac{1}{2}(\phi_C + \phi_K)\right]}{1 + \tan\phi_K \tan\left[\frac{1}{2}(\phi_C + \phi_K)\right]} \right\}^{(n)} . \tag{19}$$

The right-hand-side of Eq. (19) is evaluated from values at point K at the n^{th} iteration level. In the determination of $v_K^{(n)}$ and $\tan\phi_K^{(n)}$, Lagrange cubic interpolation is used. Convergence of u_K is quite rapid, requiring usually about four or five iterations to reach $|\Delta u_K| < 10^{-6}$. Once $(u,v)_K$ are known, $(\bar{x},\theta)_K$ are found by the inverse transformation of the mapping sequence.

In the x - θ plane, the two-sided stretching function of Vinokur is used to generate the grid point distributions on the stagnation streamline B-E and the airfoil-wake centerline E-K-F-I. For segment B-E a single stretching function is used whereas for segment E-K-F-I, a sequence of three stretching functions is required.

The two-sided stretching function for the normalized variable t is given by

$$t = \frac{\tanh(\xi\Delta\phi)}{A\sinh\Delta\phi + (1 - A\cosh\Delta\phi)\tanh(\xi\Delta\phi)} , \tag{20}$$

where ξ is the normalized generating variable of constant step size, Δφ is the solution of the transcendental equation

$$B = \frac{\sinh\Delta\phi}{\Delta\phi} \tag{21}$$

and

$$A = (S_0/S_1)^{1/2} \tag{22}$$

$$B = (S_0 S_1)^{1/2} \tag{23}$$

and S_0 and S_1 are dimensionless slopes defined as

$$S_0 = \frac{d\xi}{dt}(0) ,$$

$$S_1 = \frac{d\xi}{dt}(1) ,$$

which control the clustering at t = 0 and t = 1.

The reason for using two-sided stretching functions on segments E-K, K-F and F-I is to provide clustering at all segment end points. It is needed at point E because of the rapid drop in pressure downstream of the stagnation point, at point K to provide a more nearly uniform grid distribution on the inflow line and at points F and I to resolve the flow at the airfoil trailing edge and tail of the body respectively. Since the arc length step size at points K and F should be continuous, not all of the parameters (S_0,S_1) are independent. If (S_0,S_1) are specified on E-K and S_1 is specified on K-F and F-I, then S_0 on these latter segments must be calculated to satisfy continuity of step size at the segment junctions. The relation is

$$(S_0)_{KF} = (S_1)_{EK} \cdot \frac{s_{KF}}{s_{EK}} \cdot \frac{N_{EK}}{N_{KF}} , \tag{24}$$

where s denotes arc length of the segment and N the number of intervals on the segment. A similar expression holds on segment F-I.

Normalized pseudo-computational variables $\hat{\xi}$ and $\hat{\eta}$ are defined such that the interior of the quadrilateral in Fig. 10 in the u - v plane transforms to the interior of the unit square in the $\hat{\xi}$ - $\hat{\eta}$ plane. The transformation from the computational domain to the hinge-plane domain is given in terms of the position vector $\vec{r}$:

$$\vec{r}(\xi,\eta) = \begin{bmatrix} u(\hat{\xi},\hat{\eta}) \\ v(\hat{\xi},\hat{\eta}) \end{bmatrix} , \tag{25}$$

where $0 \le \hat{\xi} \le 1$, $0 \le \hat{\eta} \le 1$.

Specifying the distribution of the position vector $\vec{r}$ and its normal derivatives on the four boundaries in the $\hat{\xi}$ - $\hat{\eta}$ plane is equivalent to defining the grid on the boundaries in the hinge plane and ultimately, the x - θ plane.

The transfinite interpolation method used here is the extension of Eriksson [2] as specialized by Vinokur and Lombard [6]. The relation for $\vec{r}$, using point-of-compass notation for the boundaries, is

$$\begin{aligned}
\vec{r}(\hat{\xi},\hat{\eta}) = {} & \vec{r}_S(\hat{\xi})E(\hat{\eta}) + \vec{r}_N(\hat{\xi})F(\hat{\eta}) + \vec{r}_{\eta_S}(\hat{\xi})G(\hat{\eta}) \\
& + \vec{r}_{\eta_N}(\hat{\xi})H(\hat{\eta}) + E(\hat{\xi})[\vec{r}_W(\hat{\eta}) - \vec{r}_{SW}E(\hat{\eta}) \\
& - \vec{r}_{NW}F(\hat{\eta}) - \vec{r}_{\eta_{SW}}G(\hat{\eta}) - \vec{r}_{\eta_{NW}}H(\hat{\eta})] \\
& + F(\hat{\xi})[\vec{r}_E(\hat{\eta}) - \vec{r}_{SE}E(\hat{\eta}) - \vec{r}_{NE}F(\hat{\eta}) \\
& - \vec{r}_{\eta_{SE}}G(\hat{\eta}) - \vec{r}_{\eta_{NE}}H(\hat{\eta})] \\
& + G(\hat{\xi})[\vec{r}_{\xi_W}(\hat{\eta}) - \vec{r}_{\xi_{SW}}E(\hat{\eta}) - \vec{r}_{\xi_{NW}}F(\hat{\eta})
\end{aligned}$$

$$- \vec{r}_{\xi\eta_{SW}} G(\hat{\eta}) - \vec{r}_{\xi\eta_{NW}} H(\hat{\eta})]$$

$$+ H(\hat{\xi})[\vec{r}_{\xi_E}(\hat{\eta}) - \vec{r}_{\xi_{SE}} E(\hat{\eta}) - \vec{r}_{\xi_{NE}} F(\hat{\eta})$$

$$- \vec{r}_{\xi\eta_{SE}} G(\hat{\eta}) - \vec{r}_{\xi\eta_{NE}} H(\hat{\eta})] \qquad (26)$$

where E, F, G and H are cubic blending functions given by

$$\left.\begin{aligned} F(u) &= u^2(3 - 2u) \\ G(u) &= u(1 - u)^2 \\ H(u) &= u^2(u - 1) \\ E(u) &= 1 - F(u) \end{aligned}\right\} . \qquad (27)$$

Equation (26) thus provides a smooth blending on the interior of the given distribution of grid points and normal derivatives on the boundaries. A typical grid in the hinge plane obtained by transfinite interpolation is shown in Fig. 11.

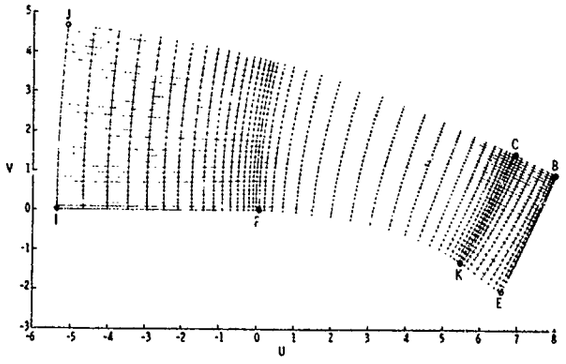

Figure 11. Typical Grid in Hinge Plane using Transfinite Interpolation.

The evaluation of the various derivatives on the boundaries in Eq. (26) follows the prescription given by Vinokur and Lombard and is presented in detail in Appendix II of Ref. 7.

The procedure described above produces a C-grid in the x - θ plane in the region upstream of the tail line I-J. Because $\hat{\xi}$ = constant lines in the upstream grid are normal to I-J (and I-J is straight as well as normal to the wake centerline), a downstream grid can easily be created which has continuity through first derivatives across I-J. The addon grid which has these characteristics is a Cartesian grid with the same θ distribution at I-J as the upstream grid. Distributing grid points on the x-direction downstream of I-J is accomplished by a one-sided Vinokur stretching function with the parameter S_0 determined by requiring continuity of Δx on either side of I-J.

Computational Grid

If indices i, j and k denote the coordinates $\hat{\xi}$, $\hat{\eta}$ and $\bar{r}$, then the computational coordinates x, y and z may be conveniently defined as

$$\left.\begin{aligned} X &= i - 1 \quad , \quad 1 \leq i \leq i_{max} \\ Y &= j - 1 \quad , \quad 1 \leq j \leq j_{max} \\ Z &= k - 1 \quad , \quad 1 \leq k \leq k_{max} \end{aligned}\right\} . \qquad (28)$$

The advantage of this system is that the computational step size in the three directions is unity which simplifies the metric coefficient calculations.

III. Results and Discussion

The afterbody-fin grid generation code is called TAILGRID and consists of about 1600 FORTRAN statements. It is written in double precision arithmetric and computes in terms of real variables only. To date all grid generation has been done on a VAX 11/782 computer with CPU per grid point found to be about 7×10^{-3} sec. Thus computing a surface containing 1500 points requires approximately 10 sec.

The airfoil family chosen for testing the grid generation procedure was the NACA symmetric four digit series. The equation for this profile is

$$y_F = -5\tau(0.2969\sqrt{x} - 0.1281x - 0.3516x^2$$

$$+ 0.2843x^3 - 0.1015x^4) \quad , \qquad (29)$$

where τ is the maximum thickness expressed as a fraction of the chord. In the original equation for y_F, see Eq. (6.2) of Ref. 9, the coefficient of x is given as 0.12600 which causes the airfoil to have a finite trailing edge thickness ($y_{TE} = 0.0021$). Since the grid generation procedure requires zero trailing edge thickness, the coefficient of x was modified as shown in Eq. (29). Interpolation is used liberally on the airfoil in the grid generation process; thus an accurate definition of y_F versus x is a necessity. Usually 100 points on the airfoil are computed for this purpose with clustering at the leading edge.

Figure 12 illustrates a typical 2-D grid produced by this method before projection onto a tubular surface. In this example, clustering is used at the foil leading and trailing edges as well as at point K. The foil section is an NACA 0012. Further 2-D examples which illustrate the effects of various input parameters may be found in Ref. 7.

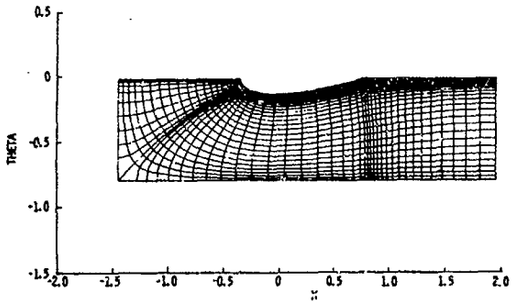

Figure 12. Typical 2-D Grid Produced by Present Method.

For a 3-D test problem the afterbody meridian profile was represented by the following analytic function:

$$r_b(\mu) = r_{b_1} F(\mu) - d_{bod} \tan \hat{\theta}_T G(\mu) \quad , \qquad (30)$$

where

$$\mu = -\frac{x}{d_{bod}} \quad ,$$

d_{bod} = afterbody length ,

r_{b_1} = initial afterbody radius ,

and F and G are the cubic blending functions defined by Eq. (27). The particular values chosen for the afterbody parameters are

$$r_{b_1} = 0.75 \quad , \quad d_{bod} = 2.5 \quad , \quad \tan \hat{\theta}_T = 0.50 \quad ,$$

which produce a fairly full profile with a tail half angle of 26.6 degrees.

The meridian plane view of the test problem geometry, computational domain and intermediate surface is shown in Fig. 13. Two views of each $\bar{r}$ = constant surface are presented, the first from below and in front and the second from the side. These views are shown in Figs. 14 through 19. A composite side view showing the position of each surface relative to the other is presented in Fig. 20. In this example, the same type of clustering is used as in Fig. 12.

In a grid stacking procedure each grid on a surface is generated somewhat independently of the other. The dependence is indirect through the geometry and not direct as in the case of partial differential equation grid generation schemes or fully 3-D algebraic schemes. Thus for 3-D grids generated by stacking one of the primary concerns is with smoothness in the stacking direction. In the present method, the only reason that the grid changes in the

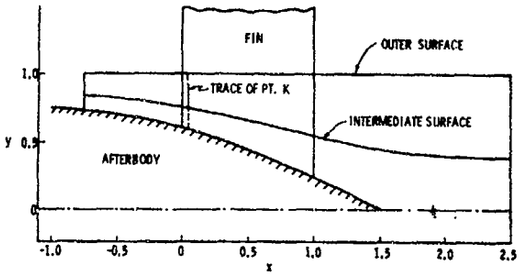

Figure 13. Meridian Plane View of Test Problem Geometry.

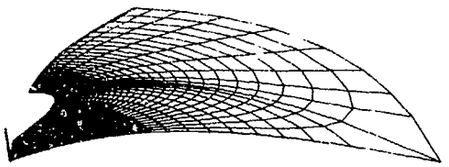

Figure 14. Front View of Afterbody Grid.

Figure 15. Side View of Afterbody Grid.

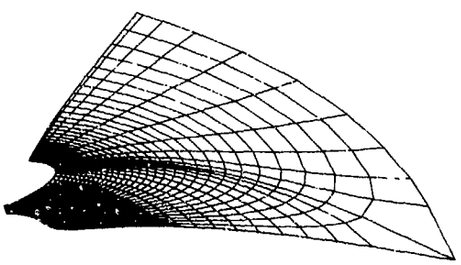

Figure 16. Front View of Intermediate Surface Grid.

Figure 17. Side View of Intermediate Surface Grid.

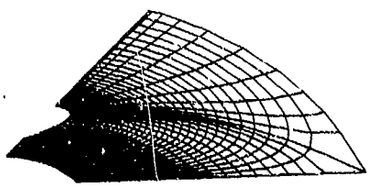

Figure 18. Front View of Outer Surface Grid.

Figure 19. Side View of Outer Surface Grid.

Figure 20. Composite View of Afterbody, Intermediate and Outer Surface Grids.

$x - \theta$ plane from surface to surface is that the airfoil image is changing. As $\bar{r}$ increases, the airfoil image, according to Eq. (7), is shrinking in terms of maximum thickness approximately as $1/r_g$. Although the total arc length of the airfoil image is also shrinking slightly as $\bar{r}$ increases, the clustering parameters are fixed and hence the airfoil point distribution on each surface is always in the same proportion. As the airfoil image grows thinner, point K slowly moves toward the leading edge. The trace of point K in the meridian plane is shown in Fig. 13. On the other hand, the distribution of points on the stagnation line remains the same independent of $\bar{r}$. Of course close to the surface of the afterbody in the vicinity of the tail the grid shrinks rapidly to reflect the pointed nature of the tail and the axis singularity. This feature would exist whether or not stacking were used. Thus because the airfoil image is varying slowing as $\bar{r}$ increases and the points on the image remain in the same proportion of arc length, the present method can be expected to produce a grid of high quality in the stacking direction.

One aspect of the current strategy of point placement on boundaries is not entirely satisfactory. Although the circular arc method of point placement in the hinge plane works well on the lower symmetry line, it leaves something to be desired on the IVL. Coupled with the singularity at the corner (point C) and the orthogonality requirement at boundaries, clustering at point K was found to be necessary to achieve a reasonable point spacing near point C on the IVL. This clustering would probably not be necessary if a different strategy were used to locate the points on the IVL. One possibility would be to space them in the $x - \theta$ plane in the same proportion of arc length as along the airfoil between the leading edge and point K. Downstream of point K the strategy would remain as before.

References

(1) Hoffman, G. H., "Grid Generation about a Fin-Cylinder Combination," ARL/PSU TM 83-45, Applied Research Laboratory, The Pennsylvania State University (30 March 1983).

(2) Eriksson, L. E., "Generation of Boundary-Conforming Grids Around Wing-Body Configurations using Transfinite Interpolation," AIAA Jour., 20, 1313-1320 (1982).

(3) Smith, R. E., Jr. and R. A. Kudlinski, "Algebraic Grid Generation for Wing-Fuselage Bodies," AIAA Paper 84-0002, presented at AIAA 22nd Aerospace Sciences Meeting, Reno, NV (9-12 January 1984).

(4) Caughey, D. A. and A. Jameson, "Numerical Calculation of Transonic Potential Flow about Wing-Body Combinations," AIAA Jour., 17, 175-181 (1979).

(5) Shmilovich, A. and D. A. Caughey, "Grid Generation for Wing-Tail-Fuselage Configurations," in Advances in Grid Generation, ASME FED - Vol. 5, 189-197, presented at Applied Mechanics, Bioengineering and Fluids Engineering Conference, Houston, TX (20-22 June 1983).

(6) Vinokur, M. and C. K. Lombard, "Algebraic Grid Generation with Corner Singularities," in Advances in Grid Generation, ASME FED - Vol. 5, 99-106, presented at Applied Mechanics, Bioengineering and Fluids Engineering Conference, Houston, TX (20-22 June 1983).

(7) Hoffman, G. H., "Algebraic Grid Generation about a Fin-Afterbody Configuration," ARL/PSU TM 85-57, Applied Research Laboratory, The Pennsylvania State University (12 April 1985).

(8) Vinokur, M., "On One-Dimensional Stretching Functions for Finite-Difference Calculations," NASA CR-3313 (October 1980).

(9) Abbott, Ira H. and A. E. Von Doenhoff, Theory of Wing Sections, Dover Publishers (1959).

A POROSITY TECHNIQUE FOR THE DEFINITION OF OBSTACLES IN RECTANGULAR CELL MESHES

C. W. Hirt and J. M. Sicilian

Flow Science, Inc.
Los Alamos, New Mexico
August 1985

Abstract

Boundary fitted coordinates or adaptive mesh schemes have obvious advantages for the numerical solution of ship hydrodynamics problems. They also introduce a variety of numerical difficulties. For example, special generators must be devised to construct suitable meshes that fit the desired boundaries while maintaining convex cells with reasonable aspect ratios. Sometimes numerical stability requirements impose unacceptable time-step limits because of a few mesh cells with exceptionally small sizes. Numerical algorithms based on these methods also tend to be more complicated because of the added complexity associated with the changing shapes and orientations of the mesh cells.

In this paper we describe an alternative technique for computing flows bounded by complicated geometric shapes. Grid distortion problems are eliminated by using a grid composed of rectangular cells. Geometric boundaries are defined within this grid using a porosity technique in which the porosity has a zero value within obstacles and a unit value elsewhere.

Certain consistency requirements are presented that guide the porosity formulation into a numerical solution algorithm that has good stability properties. The resulting formulation can be used with the full Navier-Stokes equations or for potential flow applications. In either case, free surfaces of arbitrary deformation may be included using the Volume-of-Fluid (VOF) technique.

I. Introduction

A problem frequently confronting numerical analysts is how to represent complex geometric boundaries. For instance, in many fluid flow problems the flow region is bounded by curved walls, or variously-shaped obstacles may be embedded within the flow. In such cases the modeler is often driven to complicated finite-element methods or to simplified approximations, such as replacing curves by stair-step surfaces.

Although finite-element methods have achieved considerable success in many applications, their geometric flexibility is achieved at the expense of more complicated numerical algorithms. Furthermore, these methods may be subject to numerical accuracy and stability problems when the shapes and sizes of the elements vary rapidly from one element to the next.

Low order finite-element and finite-difference methods based on meshes of rectangular cells are logically simpler, easier to program, and easier to analyze for their stability and accuracy properties.

It is natural, therefore, to seek ways to model curved boundaries in these schemes.

A number of noteworthy attempts have been made to model curved boundaries in codes designed for incompressible fluid flow analysis. Viecelli [1] used a marker particle technique to represent arbitrary boundaries in a Marker-and-Cell type code. His scheme, which involved a pressure adjustment to prevent flow crossing a boundary, was quite successful for a variety of free surface flow calculations [2]. Hirt, et al [3] and McMaster and Gong [4] have used a somewhat simpler scheme in which selected velocities are adjusted in cells to satisfy a zero normal velocity boundary condition. When free surfaces are present, however, this method can lead to an over specification of the boundary conditions. This method also introduces some difficulties with regard to fictitious fluxes of mass and momentum across boundaries unless precautions are taken to specify values for flow variables outside the boundary.

Another possibility for modeling curved boundaries in rectangular grids is through the use of a variable porosity formulation. This concept is the subject of the present paper. True porous media flow models have existed for a long time. Usually a porous flow is dominated by viscous stresses arising from numerous tiny flow paths with a large surface-to-volume ratio. More recently the concept of a variable porosity has been used as a means of representing flow regions containing distributed obstructions that are too small to be resolved by the cells in a discrete grid. For example, codes used to model coolant flow in nuclear reactor cores [5,6,7] have employed this concept as a means of representing the fractional flow volumes and areas surrounding bundles of fuel rods and other structures.

The idea we wish to explore here is the use of a porosity that changes abruptly from unity to zero across a rigid boundary. The usual fluid dynamic equations are to hold in the region where the porosity is unity. Regions with zero porosity, that is, with zero flow volume are obstacle regions. Although this is a simple idea, it does not appear to have been previously explored as a general procedure.

In the next section we describe the porosity concept in more detail and derive the modifications needed in the fluid dynamic equations to include variable porosity effects. For simplicity, this discussion will be limited to two-dimensional, inviscid and incompressible flow, but the basic ideas can easily be extended to compressible, viscous and three-dimensional situations. In fact, some three-dimensional examples will be used as illustrations. The primary contribution of this paper is contained in Section III, which describes the special considerations needed to numerically approximate equations containing a discontinuous porosity. The numerical representation of a variable porosity is most conveniently defined in terms of fractional areas and volumes open to flow. Thus, the method described in this paper is referred to as the Fractional Area/Volume Obstacle Representation (FAVOR) Method. Section IV contains a discussion of such matters as numerical stability, accuracy and the relationship of the FAVOR method with other methods for representing obstacle boundaries. The question of accuracy will require a digression into the accuracy of nonuniform rectangular grids in general. This is done in Section IV.A, where it will be shown that approximations of conservation laws must lose some formal accuracy in variable grids. Examples illustrating the use of this new technique are presented in Section V.

II. Formulation of Equations

Equations describing fluid flow in a region containing multiple obstacles can be conveniently derived using the mathematical concept of generalized functions. This will be outlined in the next section. Then a brief discussion will be given of the methods used to reduce these equations to approximations on discrete grids. As might be expected, there are several steps in this reduction where, depending on the assumptions made, different approximating equations may be produced. Some attention will be given to the most important of these steps and justifications will be presented for the selections made.

A. Porous-Media Equations

To derive the equations for porous media we make use of the theory of generalized functions [8]. With this approach, boundary conditions at fluid-obstacle interfaces are automatically isolated in a convenient way. Let us consider by way of illustration the density equation,

$$\partial\rho/\partial t + \nabla\cdot\rho\underline{u} = 0 \qquad (1)$$

where ρ is the density and $\underline{u}$ is the fluid velocity. The density equation holds at all points occupied by fluid. A generalized (Heaviside) function of the spatial coordinate vector $\underline{x}$ and denoted by $H(\underline{x})$ is defined such that

$$H(\underline{x}) = \begin{cases} 1.0, & \text{if } \underline{x} \text{ is in the fluid} \\ 0.0, & \text{if } \underline{x} \text{ is in an obstacle.} \end{cases} \qquad (2)$$

If we now multiply the density equation by the step function H, the resulting equation can be considered as defined at all points in space. It agrees with the original equation, Eq. (1), in the fluid and is identically zero at points located in obstacles. The density function can be analytically continued into the obstacles in any manner for, as we shall see, its value in these regions will not be important.

The next step is to move the H function inside the time and spatial derivatives. To carry out the transposition, we shall need to evaluate derivatives of the step function H. Fortunately, it is known that the gradient of a step function is another generalized function - the delta function,

$$\nabla H(\underline{x}) = -2H\underline{n}\delta(\underline{x}-\underline{x}_s) \qquad (3)$$

where $\underline{x}_s$ is any point on the interface (surface) between the fluid and an obstacle. The vector $\underline{n}$ is a unit normal to the interface at location $\underline{x}_s$ and is directed out of the fluid. A formal derivation of Eq. (3) can be made using the techniques in Ref. [8], but we can see that it is intuitively correct from the following argument. Derivatives of H away from an interface are zero because H is then a constant function. For the same reason, a derivative of H parallel to an interface must also be zero. Gradients normal to an interface are infinite when evaluated at the interface because there H undergoes a step change. On the other hand, integration of a normal derivative of H across an interface gives a result of unity according to its definition. These properties are just those of a delta function, and this suggests the form of Eq. (3). The factor of 2H on the right side of the equation is introduced for convenience, but since H is discontinuous where the delta function is nonzero, a prescription is needed for evaluating the integral of such a product. The rule is

$$\int_{-1}^{+1} Q(z)\delta(z)dz = (Q_+ + Q_-)/2 \qquad (4)$$

where subscripts refer to values of Q on either side of z=0. Using this rule it is easy to see that the factor of 2H in Eq. (3) is consistent because an integration of that equation across $\underline{x}_s$ does produce an identity.

If the fluid-obstacle interfaces are time dependent, then we will also need the time derivative of H. This time dependency can only arise from a shifting of the boundary points with time. The time rate of change of boundary point $\underline{x}_s$ is just the velocity of the boundary $\underline{v}_s$, i.e.,

$$(d\underline{x}_s/dt) = \underline{v}_s \qquad (5)$$

Therefore, using the chain rule for differentiation the necessary time derivative is,

$$\partial H/\partial t = -(d\underline{x}_s/dt)\nabla\cdot H$$

$$= 2H\underline{v}_s\cdot\underline{n}\delta(\underline{x}-\underline{x}_s) \qquad (6)$$

Now, using Eq. (2) and Eq. (6) the density equation multiplied by H can be rewritten as

$$(\partial\rho H/\partial t) + \nabla\cdot(\rho H\underline{u})$$

$$+ 2\rho H(\underline{u}-\underline{v}_s)\,\underline{n}\delta(\underline{x}-\underline{x}_s) = 0 \qquad (7)$$

The last term involving the delta function is identically zero. To see this, first note that it is zero everywhere except at a fluid-obstacle boundary. At such a boundary it only has meaning when it is integrated across the boundary, but the integral is proportional to $(\underline{u}-\underline{v}_s)\cdot\underline{n}$ which is zero because the fluid velocity normal to an obstacle boundary must equal the normal velocity of the boundary.

A similar derivation can be used to derive the corresponding inviscid momentum equations in a porous medium, so that the final equations have the form

$$(\partial\rho H/\partial t) + \nabla\cdot(\rho H\underline{u}) = 0 \qquad (8a)$$

$$(\partial\rho H\underline{u}/\partial t) + \nabla\cdot(\rho H\underline{u}\underline{u}) = -H\nabla p + H\underline{g} \qquad (8b)$$

where p is the fluid pressure and $\underline{g}$ is a body acceleration (e.g., gravity).

This is a special form of the porous-media equations in which the porosity is a discontinuous function. That is, the porosity is either 0.0 or 1.0. To apply this result to a material like sand where the positions of individual sand grains are unknown, it is first necessary to perform an ensemble average on Eqs. (8). Only H varies in the ensemble average because it depends implicitly on the arrangement of the obstacles (i.e., the sand grains). Therefore, after averaging we replace H in Eqs. (8) with its ensemble average, say f. The quantity $f(\underline{x})$ is the average porosity (or it may be equivalently interpreted as the probability that an obstacle does not exist at location $\underline{x}$). For our purposes we wish to keep Eqs. (8) as they are so that we may use H to describe well-defined arrays of obstacles.

B. Coarse-Scale Approximations

Let us integrate the density equation over a small volume in space, R, with boundary surface S. Within R there will, in general, be subregions containing fluid and subregions containing obstacles. The interfaces between these regions within R will be denoted by I. The average of the density equation over region R is

$$\frac{1}{R}\int_R \left(\frac{\partial\rho H}{\partial t} + \nabla\cdot\rho H\underline{u}\right)dR = 0 \qquad (9)$$

where R is here used for both the volume of the region and as an indicator for the limits of

integration. Since R is independent of time, the leading term in Eq. (9) is

$$\frac{1}{R}\int_R \frac{\partial}{\partial t}(\rho H)dR = \frac{\partial}{\partial t}(\frac{1}{R}\int_R \rho H dR) \quad (10)$$

In making finite-volume approximations for numerical solution algorithms, the region R would be one element or cell of a grid that divides the flow region into a set of control volumes. For a useful approximation, the grid cells must be chosen small enough so that within a cell the dependent variables describing the flow can be treated as constants (or possibly as having some simple spatial variation). Neglecting flow variations over scales covered by region R compared to variations over the entire region of interest is called the coarse-scale approximation. When this assumption is satisfied, the density in the volume integration in Eq. (10) can be replaced by its mean value so that

$$\frac{1}{R}\int_R \rho H dR = \rho V \quad (11)$$

where

$$V = \frac{1}{R}\int_R H dR \quad (12)$$

The quantity V is defined, for arbitrary R, as the fractional volume open to flow.

A similar result can be obtained for the divergence term in Eq. (9). First, Gauss' divergence theorem is used to reduce the volume integration to a surface integral.

$$\frac{1}{R}\int_R \nabla\cdot\rho H\underline{u} dR = \frac{1}{R}\int_S \rho\underline{u}\cdot\underline{n} H dS \quad (13)$$

The integral is the flux of fluid out of region R through the open portion of its boundary S. Usually the boundary is subdivided into a set of segments S such that the coarse-scale approximation can be applied to each segment. For example, for segment i,

$$\frac{1}{S_i}\int_{S_i} \rho\underline{u}\cdot\underline{n} H dS_i = \rho\underline{u}\cdot\underline{n}_i A \quad (14)$$

where

$$A = \frac{1}{S_i}\int_{S_i} H dS_i \quad (15)$$

The quantity A is defined, for arbitrary S_i, as the fractional area open for flow across surface S_i.

If the functions V and A are continuous and differentiable, it can be shown that they must be equal to the same function. However, our goal is the derivation of finite-volume equations in which these quantities may be discontinuous functions. Thus, we see that several fractional volumes and areas must be associated with each control volume.

C. Pressure Gradient Averages

Consider the volume averaging process applied to the pressure gradient term appearing in Eq. (8b),

$$\frac{1}{R}\int_R H\nabla p dR . \quad (16)$$

An alternative form is

$$\frac{1}{R}\int_R \{\nabla(pH) - p\nabla H\}dR$$

$$= \frac{1}{R}\int_R \{\nabla(pH) + 2Hp\underline{n}\delta(\underline{x}-\underline{x}_s)\}dR \quad (17)$$

$$= \frac{1}{R}\int_S pH\underline{n} dS + \frac{1}{R}\int_I p\underline{n} dI$$

where the last integral has been reduced using Eq. (4) and I indicates

integration over all fluid-obstacle interfaces located within R. This alternative form is easy to interpret: the first integral is the pressure force acting on the fluid along the open portion of the surface S that surrounds R, the second integral is the pressure force acting on the fluid at all interior fluid-obstacle interfaces.

The question is, which of these forms, Eq. (16) or Eq. (17), is best suited for finite-volume approximations? When the pressure is nearly constant within R, both expressions are approximately zero and neither one is preferable over the other. However, when there is a hydrostatic equilibrium, the pressure gradient is constant and the expression in Eq. (16) reduces immediately to $V\nabla p$.

When there is a hydrostatic equilibrium, the second term on the right side of Eq. (17) is equal to the net buoyant force experienced by the obstacles within R and cannot be ignored. In any case, neither term on the right side of Eq. (17) can be easily approximated in this limit. Some authors have used the coarse-scale approximation $\nabla(pV)$ for the first term, but since the second term cannot be ignored, this is not a useful or convenient approximation. Thus, for a coarse-scale approximation it is best to assume the pressure gradient rather than the pressure is nearly constant.

In dynamic situations, when the pressure differs from hydrostatic, the approximation, $V\nabla p$, is not exact for it neglects non-viscous drag effects imposed on the fluid by the obstacles. If these drag forces are significant, it is necessary to add them separately to the approximation. When doing this, however, it must be remembered that buoyant forces on obstacles are not to be included in the addition.

III. Finite-Volume Equations

A mesh of nonuniform rectangular cells will be used as the basis for our finite-volume equations. Using a nonuniform mesh helps us identify some points regarding accuracy and also allows a comparison of the FAVOR method with more standard techniques. Some simplifications are in order, however, to keep the presentation manageable. Thus, the following development will be limited to the case of two-dimensional, incompressible fluid flow with constant density. The density equation, Eq. (8a), with the density divided out is referred to as the continuity equation. After dividing the momentum equations by ρ the ratio of pressure to constant density will again be denoted by p. Extensions to three-dimensional flows or to flows with variable density is straightforward.

Dependent variables are to be placed at staggered grid locations as illustrated in Fig. 1A. The staggered grid dates back to the Marker-and-Cell (MAC) method [9] and is particularly well suited for approximations based on the primitive variables, pressure and velocity.

A simplified subscript notation, Fig. 1B, will be used to indicate mesh locations relative to a generic cell center at (i,j). Location (i,j) will be denoted by the subscript C. In general, upper case letters N, S, E, and W denote shifts in the principal compass directions by one integer. For instance, E refers to location (i+1,j), while N refers to location (i,j+1). Similarly, the lower case letters n, s, e, and w will denote corresponding shifts of half integer values. Multiple integer shifts are represented by repeated letters. The order of the letters is unimportant. Some examples should make it clear how this convenient notation works.

$$u_{i,j} = u_C$$

$$u_{i+1/2,j} = u_e$$

$$u_{i+1/2,j+1/2} = u_{ne}$$

$$u_{i-3/2,j+2} = u_{NNWw}$$

$$\delta x_i = \delta x_C$$

Using finite-volume and time averages, the density and momentum equations can be reduced to discrete (difference) equations. This formal reduction, however, involves a variety of integrated quantities at different mesh locations. These quantities must be treated as independent unless limit properties or consistency arguments can be found to eliminate them as unknowns. For instance, we will find that consistency requires certain quantities at one mesh location to be simple combinations of similar quantities at neighboring locations.

We begin by averaging the continuity equation over a generic mesh cell (i,j) and over the time interval from t to t+δt,

$$(V^{n+1}-V^n)/\delta t + (\langle Hu\rangle_e-\langle Hu\rangle_w)/\delta x_C + (\langle Hv\rangle_n-\langle Hv\rangle_s)/\delta y_C = 0 \qquad (18)$$

where V is the volume integral defined in Eq. (12) and angled brackets indicate the time and surface averages defined as

$$\langle Q\rangle = \frac{1}{\delta t}\int dt \frac{1}{S}\int_S Q\,dS \ . \qquad (19)$$

Strictly speaking, there are two different angled-bracket averages appearing in Eq. (18): those containing a u-velocity are integrated with respect to the y-direction, while those containing v-velocities are integrated with respect to the x-direction. This will not cause confusion since we are considering each quantity with a different argument or at a different location as an independent quantity.

The momentum equation for the u-velocity located at mesh position e is to be averaged in space over a rectangle that extends from location C to location E, see Fig. 2. Integrating over this region and over time interval δt we have

$$(\overline{Hu}^{n+1} - \overline{Hu}^n)/\delta t + (\langle Huu\rangle_E - \langle Huu\rangle_C)/\delta x_e + (\langle Hvu\rangle_{ne} - \langle Hvu\rangle_{se})/\delta y_C = -V_e(p_E-p_C)/\delta x_e + V_e g_x \qquad (20)$$

where Guass' theorem has been used to reduce the divergence term to surface integrals, and where $\delta x_e = (\delta x_C + \delta x_E)/2$. The overbar indicates a volume average similar to that in Eq. (12). For the pressure terms, we have used the coarse-scale approximation described earlier, in which the pressure gradients are roughly constant in time.

The averaged equations, Eqs. (18) and (20), involve many undefined quantities. To proceed further we must either introduce ad hoc approximations or seek some additional equations that will reduce the number of unknowns. One possibility is to look for consistency relationships. For instance, in the original differential equations, Eqs. (8), the density equation can be subtracted from the momentum equation to give an equation for just the velocity, i.e.,

$$(\partial \underline{u}/\partial t) + \underline{u}\cdot\nabla\underline{u} = -\nabla p + \underline{g} \qquad (21)$$

This type of equation manipulation is essential for deriving shock wave jump conditions in compressible flow, Bernoulli's equation and many other

useful relationships. It is reasonable, therefore, to require our discretized equations to have the same property. The goal is to separate the discretized continuity equation, Eq. (18), from Eq. (20) so that the resulting equation will be a discrete approximation to Eq. (21). It is immediately obvious that this cannot be done unless the bar-average of the product Hu appearing in the time-derivative term in Eq. (20) is separable into a product of bar-averages. Similarly, the angled-bracket averages, which involve a product of two velocities, must be separable into a product of averages in which one factor is of the form appearing in Eq. (18). Thus, for consistency with the equation separation process, we must first require relations of the form

$$\begin{aligned} \overline{Hu}_e &= V_e u_e \\ \langle Huu\rangle_C &= \langle Hu\rangle_C u^*_C \\ \langle Hvu\rangle_{ne} &= \langle Hv\rangle_{ne} u^*_{ne} \end{aligned} \qquad (22)$$

The u_e in the first relation is centered at the cell edge where we started the averaging process so no special notation is used to mark this quantity. The u* velocities appearing in the second two relations are located at cell positions other than the primary, staggered mesh positions so these quantities have the superscript *. We shall interpret these relations as definitions for these new quantities. That is, relations (22) are needed for their form, but no approximations have been made if we consider them as definitions.

Using these definitions, the time derivative term in Eq. (20) can be rewritten in the form

$$[(V_e^{n+1}-V_e^n)u_e^n+V_e^{n+1}(u_e^{n+1}-u_e^n)]/\delta t \qquad (23)$$

Again using the definitions, Eq. (22), and adding and subtracting inside the parentheses, terms equal to the u_e times each of the angled bracket terms, we can rearrange Eq. (20) to

$$\begin{aligned} &V_e^{n+1}(u_e^{n+1}-u_e^n)/\delta t \\ &+[\langle Hu\rangle_E(u^*_E-u_e)+\langle Hu\rangle_C(u_e-u^*_C)]/\delta x_e \\ &+[\langle Hv\rangle_{ne}(u^*_{ne}-u_e)+\langle Hv\rangle_{se}(u_e-u^*_{se})]/\delta y_C \\ &= -V_e(p_E-p_C)/\delta x_e+V_e g_x - D_e u_e^n \end{aligned} \qquad (24)$$

where D_e is given by the expression,

$$\begin{aligned} D_e = (V_e^{n+1}-V_e^n)/\delta t+(\langle Hu\rangle_E-\langle Hu\rangle_C)/\delta x_e \\ + (\langle Hv\rangle_{ne}-\langle Hv\rangle_{se})/\delta y_C \end{aligned} \qquad (25)$$

Equation (24) is almost the discretized version of Eq. (21), except that it has the extra term containing D_e. However, D_e looks like the left side of the discrete continuity equation, Eq. (18), evaluated at the cell edge location e and not at a cell center as is Eq. (18). To complete the equation separation we note that D_e could be rewritten as

$$D_e = (\delta x_E D_E+\delta x_C D_C)/(\delta x_E+\delta x_C) \ , \qquad (26)$$

where the D's on the right side are now cell-centered expressions, if we make the following correspondences

$$\begin{aligned} \langle Hu\rangle_C &= (\langle Hu\rangle_e+\langle Hu\rangle_w)/2 \\ \langle Hv\rangle_{ne} &= (\delta x_C\langle Hv\rangle_n \\ &\quad +\delta x_E\langle Hv\rangle_{nE})/(\delta x_C+\delta x_E) \\ V_e &= (\delta x_C V_C+\delta x_E V_E)/(\delta x_C+\delta x_E) \end{aligned} \qquad (27)$$

These relations express the way

quantities at intermediate mesh locations are related to similar quantities at their primary locations. Using them, the D_e term appearing in Eq. (24) is identically zero when Eq. (18) is satisfied and we have completed the desired equation separation.

If we do a similar reduction on the v-momentum equation, then combine all assumptions and consistency requirements, the momentum equations can now be written as,

$$(u_e^{n+1}-u_e^n)/\delta t + (f_{xE}Q_E+f_{xC}Q_C+f_{xn}Q_n+f_{xs}Q_s)/V_e^{n+1} = -(p_E-p_C)/\delta x_e+g_x \qquad (28a)$$

$$(v_n^{n+1}-v_n^n)/\delta t + (f_{ye}R_e+f_{yw}R_w+f_{yN}R_N+f_{yC}R_C)/V_n^{n+1} = -(p_N-p_C)/\delta y_n+g_y \qquad (28b)$$

where

$$Q_E = 2\langle Hu\rangle_E(u_E^*-u_e^n)/\delta x_E\ , \qquad f_{xE} = \delta x_E/(\delta x_C+\delta x_E)$$

$$Q_C = 2\langle Hu\rangle_C(u_e^n-u_C^*)/\delta x_C\ , \qquad f_{xC} = \delta x_C/(\delta x_C+\delta x_E)$$

$$Q_n = 2\langle Hv\rangle_{ne}(u_{ne}^*-u_e^n)/\delta y_C\ , \qquad f_{xn} = 1/2$$

$$Q_s = 2\langle Hv\rangle_{se}(u_e^n-u_{se}^*)/\delta y_C\ , \qquad f_{xs} = 1/2 \qquad (29)$$

$$R_e = 2\langle Hu\rangle_{ne}(v_{ne}^*-v_n^n)/\delta x_C\ , \qquad f_{ye} = 1/2$$

$$R_w = 2\langle Hu\rangle_{nw}(v_n^*-v_{nw}^n)/\delta x_C\ , \qquad f_{yw} = 1/2$$

$$R_N = 2\langle Hv\rangle_N(v_N^*-v_n^n)/\delta y_N\ , \qquad f_{yN} = \delta y_N/(\delta y_C+\delta y_N)$$

$$R_C = 2\langle Hv\rangle_C(v_n^n-v_C^*)/\delta y_C\ , \qquad f_{yC} = \delta y_C/(\delta y_C+\delta y_N)$$

On the right side of Eq. (28a) we have dropped the factor V_e/V_e^{n+1} because we could just as well have used V_e^{n+1} on the right side of Eq. (24). A similar factor has been dropped from Eq. (28b). Equation (28a) has the desired form of Eq. (21) because the Q_E and Q_C terms defined in Eq. (29) are approximations for $Hu(\partial u/\partial x)$ while Q_n and Q_s are approximations of $Hv(\partial u/\partial y)$. The f factors are weighting factors dependent on the cell sizes. In a uniform grid the f's are all equal to one half.

To summarize, relations (27), which were used to give the discretized equations the same separation property as the differential equations, have reduced the number of unknowns in the discretized equations. Unfortunately, there are still more unknowns than equations. The remaining unknowns are,

$$u_e\ ,\ v_n\ ,\ p_C$$
$$u_C^*\ ,\ u_{ne}^*\ ,\ \langle Hu\rangle_e \qquad (30)$$
$$v_C^*\ ,\ v_{ne}^*\ ,\ \langle Hv\rangle_n$$

Quantities u_e, v_n, and p_C are the primary variables at the staggered mesh locations we designated at the outset. All remaining quantities are secondary unknowns that must still be specified.

A coarse-scale approximation could be used to separate out the H-function from the two unknowns in which it appears.

$$\langle Hu\rangle_e = A_e u_e^* \qquad \langle Hv\rangle_n = A_n v_n^* \tag{31}$$

where A_e and A_n are the fractional areas open to flow at the sides of a mesh cell and two new velocity averages have been introduced. Now all the secondary unknowns (indicated by a superscript *) have a similar form: i.e., they are all related to surface-time averages of velocities.

Up to this point the equations derived are essentially "exact" in that we have only made substitutions in terms of new unknowns, but to proceed further we must now introduce approximations that relate these unknowns to the primary dependent variables. First, it should be noted that no time levels have been assigned to the various fluxing velocities. If time level n+1 values are used, the resulting equations are implicit and would require a complicated procedure for their simultaneous solution. Using only time level n values results in explicit equations that are easy to solve, but it is well known that these equations may be numerically unstable unless the approximations are carefully chosen [10]. Before deciding on suitable approximations, it will be worthwhile to first look into questions of accuracy and stability.

IV. Other Matters

A. Accuracy in a Nonuniform Mesh

The horizontal advection of momentum in Eq. (28a) is contained in the sum $f_{xE}Q_E + f_{xC}Q_C$. Accuracy refers to how rapidly this finite-volume expression approaches the limiting differential for $Hu(\partial u/\partial x)$ at location e as δt and the volume of the cell are reduced to infinitesimal values. If the difference between the finite-volume and limiting forms is proportional to the N-th power of δt and M-th power of the cell size, the accuracy is said to be N-th order in time and M-th order in space.

A typical approximation is to identify the $\underline{u}^*$ velocity in Eq. (31) with the $\underline{u}$ velocity defined in Eq. (22). In other words, equate surface and volume averaged quantities at the same location. If in Q_E we then set u_E^* equal to an average of the neighboring boundary centered velocities,

$$u_E^* = (u_e^n + u_{eE}^n)/2 \tag{32}$$

this corresponds to a centered difference approximation. Q_E is then a second order (in space) approximation to $Hu(\partial u/\partial x)$ at location E. A similar centered approximation in Q_C makes it a second order approximation at location C. Unfortunately, the combination of the two Q's is only first order accurate at location e because in a nonuniform mesh the f-weighting factors do not have the correct values. A correct second order approximation at e requires the interpolated expression $f_{xC}Q_E + f_{xE}Q_C$, while the expression $f_{xC}Q_C + f_{xE}Q_E$ is second order only at the midpoint between locations C and E. Since this point does not correspond to location e (unless the mesh is uniform), Eq. (28a) cannot be more than first order accurate at position e.

If a donor cell or upstream approximation is used for the u_E^* velocity, then the situation is worse. For instance, if the velocity is positive, then Q_E is zero and $f_{xC}Q_C$ becomes a second order approximation at location C, but at e the approximation is zeroth order accurate because the first term in a Taylor series expansion about e will have the extra coefficient $\tfrac{1}{2}f_{xC}$. In a mesh

with slowly varying cell sizes $2f_{xC}$ can be significantly different from unity. For example, a 20% change in neighboring cell sizes produces a 10% error in the coefficient.

Now consider the vertical advection terms in Eq. (28a). Regardless of whether a centered or donor cell assumption is used for the u^* velocities, the Q_n and Q_s terms are zeroth order accurate approximations for $Hv(\partial u/\partial y)$, because only y_C appears in these expressions. That is, first or higher order derivative approximations require the appearance of y_N and y_S values if the mesh is nonuniform. A special choice for the Q's does exist, however, that will produce a first order approximation for these terms.

We conclude, therefore, that consistent finite-volume equations based on a staggered mesh are formally first-order accurate in a nonuniform mesh. A first-order approximation can be achieved using the donor cell approximation only if we give up the rigorous conservation form of the equations, for example, by modifying the f-weighting factors. A simple choice for these factors that produces a first order approximation is,

$$f_{xE}=f_{xC}=1/2$$

$$f_{xn}=\delta y_C/(\delta y_C+\delta y_N)\ ,\ f_{xs}=\delta y_C/(\delta y_C+\delta y_S)$$

$$f_{ye}=\delta x_C/(\delta x_C+\delta x_E)\ ,\ f_{yw}=\delta x_C/(\delta x_C+\delta x_W)$$

$$f_{yN}=f_{yC}=1/2 \qquad (33)$$

If we do not permit approximations that use values separated by more than one δx or one δy, the approximations can never be more than first order accurate.

B. Stability Considerations

It is important to consider what numerical stability requirements must be imposed on the FAVOR method. This is particularly necessary if the fractional volume of a cell is allowed to approach zero, which may occasionally happen when a curved boundary is embedded in a mesh.

A rigorous analytical treatment of stability is not possible because the coefficients of the advection terms are not constant. However, we can make a heuristic assessment based on effective advection speeds. In the case of a uniform mesh with unit area/volume fractions the usual stability conditions for an explicit approximation are that fluid must not move across more than one cell in one time step. In two dimensions this condition is usually replaced by the restriction that fluid not move more than one fourth of the cell width so that the maximum possible volume fluxed out of the four sides of the cell will not exceed the volume of the cell.

Referring to Eqs. (28), (29), and (31) we note that in the FAVOR method the advection velocities are multiplied by the ratio of a fractional side area to a fractional volume. These modified velocities must still conform with the requirement that the maximum volume fluxed out of a cell not exceed the cell volume. Therefore, to see how stability is influenced by FAVOR we must investigate the values of area to volume ratios appearing in the finite-volume equations. Only two limiting cases need to be considered. For a typical u velocity, say u_e, suppose cell C to its left is almost closed off (i.e., V_C is almost zero). This closure may be due to an obstacle surface oriented either vertically or horizontally, see Fig. 3A. In the vertical case A_e and V_E will be unity, and A_n and V_N will be equal to V_C. Because the fractional volume V_e appearing in the u-velocity equation is a weighted average of V_C and V_E, Eq. (27), it can be shown that the maximum area to volume ratio appearing Eq. (28a) is $A_e/V_e = (\delta x_C + \delta x_E)/\delta x_E$, which is equal to 2.0 in a

uniform mesh. A factor of two increase in the effective advection velocities causes no serious problems for stability.

The second case to consider is a horizontal surface that is tending to close off cell C and cell E, see Fig. 3B. In this instance V_e is tending to zero (with both V_C and V_E) and the worst case is associated with vertical advection through the fully open top cell faces. It appears that the vertical flux $A_n v_n/V_e$ is tending to infinity as V_e tends to zero. However, v_n is simultaneously tending to zero in this case because the continuity equation requires $A_n v_n \delta x_C$ to be proportional to $A_e u_e \delta y_C$, and the vertical flux is then proportional to $u_e \delta y_C / \delta x_C$. Therefore, the vertical advective flux is actually bounded and stability of the momentum equations is again easily maintained.

These simple considerations show that the FAVOR method, as formulated in this paper, should have no serious stability problems, even when mesh cells are closed off to a tiny fraction of their original size. This expectation has been verified in numerous calculations and will be demonstrated in Section V.

C. Relationship between FAVOR and Other Obstacle Methods

When the area and volume fractions are all set to unity, The FAVOR scheme reduces to a standard type of nonuniform mesh approximation. Using this observation, we can see how FAVOR is related to other obstacle representations. Suppose we wish to model the presence of a rigid, vertical wall in a grid of equal-sized cells, but the wall does not coincide with a grid line. The standard procedure would be to introduce one cell of smaller size at the wall (i.e., a nonuniform mesh) so that the wall would then lie at a grid line, as shown in the top sketch of Fig. 4. Here the small cell has width h and the wall lies at its left boundary. In the FAVOR scheme we keep a uniform mesh, but define the wall's presence by assigning fractional areas and volumes to the cell containing the wall. This is indicated in the bottom sketch of Fig. 4, where the shaded area represents the region of zero porosity. Now, to evaluate the two approaches let us compare the difference equations that would be used in each case for the u_e velocity. In making this comparison it must be noted that $V_C \delta x$ is equal to h. The reader can easily carry out the details so we simply state that the two equations are identical except for the pressure gradient terms. In the FAVOR method the gradient is evaluated as a pressure difference over a distance δx, while in the nonuniform mesh it is evaluated as a difference over a distance $(\delta x+h)/2$. Also, the spatial locations of P_C and v_n are different in the two cases.

A similar comparison can be made for the v_n velocity. In this instance the two evaluations result in identical difference equations, including the pressure gradients. Furthermore, the continuity equation is the same in both cases.

Now we note that the difference in variable locations in the two approaches is less than one cell width, so these approximations differ by a term that is first order in space. The pressure gradient difference noted above is also of first order. Thus, FAVOR agrees to first order with a nonuniform mesh approximation, but since the latter can only be first order accurate we conclude that the FAVOR method does not reduce the accuracy of the approximations.

Other techniques for embedding curved or diagonal boundaries in a rectangular mesh [1,2,3,4] rely on first order spatial interpolation or extrapolation approximations. Therefore, FAVOR is also comparable in accuracy to these methods.

D. Boundary Conditions

The formulation of the FAVOR method would make it appear that no special considerations are needed at obstacle boundaries. Unfortunately, this is true only in the differential formulation, but not in the finite-volume approximations. A simple example will illustrate the problem. Figure 5A shows a two-dimensional duct with parallel walls oriented at an angle to the grid lines of a uniform mesh. Fractional cell areas and volumes are used to define the duct walls. Since the walls are not aligned with the cell diagonals, there is a wide range of fractional cell sizes. A uniform flow of incompressible fluid, directed from left to right, was initially defined in the duct as shown in Fig. 5B. This velocity was held constant at the left side of the mesh, while at the right side a constant pressure condition was maintained. Under these conditions the flow should remain constant and uniform. In Fig. 5C we see this is not the case. A parabolic-like profile has developed after the flow has moved approximately one duct length. The dashed and vertical lines were added to emphasize this velocity profile.

These poor results are caused by advective flux approximations that require a velocity component located inside an obstacle. In Fig. 5C we used zero values for these velocities and as a consequence an unrealistically low flux was computed that eventually produced the artificial boundary layer. To correct this defect a simple device is required; the difference expressions for all fluxes are formulated in terms of velocity derivatives. Then, all the derivatives at interfaces are set to zero. In this way all boundaries become free-slip boundaries. (When viscous shear stresses are wanted they can be added as separate force contributions.) A repeat calculation of the duct problem using this boundary treatment is shown in Fig. 5D. Here we see the flow now remains nicely uniform, even though the calculation was further complicated with a non-uniform mesh spacing in the horizontal direction.

The maximum velocity component computed in Fig. 5D is actually 1.5% larger than the initial horizontal velocity. This small discrepancy arises because there are a few cells where the fractional volume open for fluid is less than 1%. In the code we somewhat arbitrarily set any cell face area or cell volume that is less than 1% open to be a zero area or zero volume. Consequently, at these locations small perturbations modify the otherwise uniform flow. The 1% cutoff on fractional areas and volumes has been found to be a useful practical limit. This example is a good illustration of the stability of the FAVOR scheme when used with a wide range of fractional volumes.

V. Examples

All the examples described in this section were obtained using the HYDR-3D program [11]. This program is a general purpose analysis tool for compressible or incompressible flow that uses the FAVOR method to provide a general geometric modeling capability. For incompressible flows, the program uses the Volume of Fluid (VOF) technique to track free surfaces and two-fluid interfaces.

A. Potential Flow around a Cylinder

As a first demonstration of the usefulness of the Fractional Area/Volume Obstacle Representation method, we have computed the potential flow about an impulsively accelerated cylinder. More specifically, the Euler equations were solved for the impulsive acceleration of flow from rest to a uniform speed about a fixed cylinder. Since the velocity field generated in one time step is proportional to the gradient of a scalar (the pressure) and satisfies the continuity equation, the resulting

flow is potential flow. If the fluid starts from rest, the theoretical (inertial) drag coefficient [12] should be 2.0 which arises from the combined effect of an acceleration needed to set the fluid into motion and an acceleration needed to establish flow about the cylinder.

For this calculation the mesh used is illustrated in Fig. 6. The large mesh region minimizes influences from the boundaries, but the cylinder is only resolved by about 4 to 5 cells across its radius. A generator program, which was used to automatically set the fractional areas and volumes, produced a volume for the cylinder that was 0.5% smaller than the exact volume.

Figure 6B shows a portion of the computed potential velocity field in the immediate vicinity of the cylinder. The computed inertial drag coefficient based on the acceleration that set the flow into motion in one time step was 2.05, or 2.5% larger than the theoretical value. This is remarkably good considering that pressure forces on the coarsely defined cylinder were simply computed using cell-centered pressures times the adjacent cell face areas occupied by the obstacle.

B. Cylindrical Tank Slosh

To show the effectiveness of the FAVOR method for problems having free surfaces we have investigated the problem of fluid slosh in a right circular cylinder. For low amplitude sloshing there is an analytic theory with which to make comparisons. This is an ideal test case because the geometry can be modeled exactly using cylindrical coordinates or approximated with the fractional areas/volumes of the FAVOR technique in a Cartesian coordinate system. A third possibility is to use a Cartesian mesh with cells either fully open or fully blocked to produce a stepped-boundary that approximately defines the cylinder. These three cases are illustrated in Fig. 7. In the middle plot, the curved boundary actually used in the FAVOR calculation is not shown by the method used to plot the surface perspective.

The slosh problem consists of shaking the tank sinusoidally in a horizontal direction and measuring the fluid height at the side wall. Because of symmetry only one half of the tank needs to be modeled. Figure 8 shows a comparison of the first two methods in terms of the time histories of the computed fluid heights. There is no significant difference in the results obtained with the cylindrical mesh and with the Cartesian mesh using the FAVOR scheme. However, the cylindrical mesh calculation required about 10 times more computational time because the small cells near the central axis required a smaller time step to maintain stability. Thus, the FAVOR method is seen to work extremely well and, for this example, required an order of magnitude less CPU time.

The relatively poor performance of the third method, which used a stepped boundary approximation, is shown in Fig. 9. Finally, Fig. 10 shows that either of the first two results are in close agreement with linear theory [13]. (The time shift between the two curves in this plot is only about one computational time step.)

Total computational time on a CDC 7600 computer for 588 mesh cells and 172 time cycles was 2.87 min using the Cartesian mesh. (In the cylindrical mesh 798 cells were used and the time required for 677 time cycles was 31 min.).

C. Spherical Tank Slosh

A problem closely related to the above is slosh in a spherical tank when it is shaken horizontally. For the 50% filled case there is also a linear theory with which to make comparison [14]. Using FAVOR to define the spherical tank in a

rectangular, Cartesian grid, we produced the results shown in Fig. 11. Here the computed and theoretical fluid heights at the side wall are almost indistinguishable, which again confirms the effectiveness of the FAVOR method.

D. Wigley Model 1805A

To illustrate the use of the FAVOR method for ship-wave resistance problems, we calculated the flow about an impulsively started Wigley Model 1805A ship. This problem has previously been solved numerically by various researchers. Dawson [15] used this model as a test of his panel method, while Ohring and Telste [16] solved the transient problem using a finite-difference solution of the linearized potential flow equations.

Following Dawson, we define the body surface by

$$y = 0.75(1-z^2)(1-x^2/64)(1-0.6x^2/64), \tag{34}$$

and have used his recommended flow region (3/8L wide, 1/4L upstream and downstream of the body, and 3/16L deep, where L is the body length). Figure 12 shows a cross section of the mesh with the midship section drawn in (only one half of the problem is modeled because of symmetry). The mesh was chosen to roughly correspond to Dawson's resolution of 64 panels on the body and 224 panels on the free surface. In our case the mesh consisted of 24x12x10 = 2880 cells in the flow region. At time zero the flow was impulsively accelerated to a value corresponding to a Froude number of $u/\sqrt{gL} = 0.503$.

Figure 13 shows the computed flow resistance, $C_R = R/(\rho u^2 Ld)$, in comparison with the results of Ohring and Telste, where R is the computed force and d the draft. Except for a peculiar fluctuation observed around 0.75 body traversal times, the computed wave resistance goes almost monotonically to a steady value that is slightly below the experimentally observed value of 0.0044 (lower dashed line in Fig. 13). The fluctuation is probably a numerical artifact, but its exact origin has not been determined. A second calculation at a Froude number of 0.45, Fig. 13, did not exhibit this problem. In this case the computed wave resistance lies between the thin ship prediction and the experimentally observed value.

It is interesting that we do not see the oscillatory transients observed by Ohring and Telste. This may be due to the non-linear treatment and more exact body boundary conditions that we have used. It is known, for example, that nonlinear advection effects can have a smoothing influence on wave interactions. The wave profile computed along the body in the 0.503 Froude number case is shown in Fig. 14. Here the agreement along the stern half of the body is good, but along the bow half the wave heights are not as good as one would desire. In particular, the height of the bow wave is under predicted. This could have been a consequence of using the Wigley hull shape above the still water level (SWL). If the model tests used a straight-sided model above the SWL, one would expect to see a larger bow wave. Unfortunately, no information was available to us regarding the actual model geometry in this region.

References

1. Viecelli, J.A., "A Method for Including Arbitrary External Boundaries in the MAC Incompressible Fluid Computing Technique," J. Comp. Phys., 4, 543 (1969).

2. Viecelli, J.A., "A Computing Method for Incompressible Flows Bounded by Moving Walls," J. Comp. Phys. 8, 119 (1971).

3. Hirt, C.W., Nichols, B.D., and Romero, N.C., "SOLA-A Numerical Solution Algorithm for Transient Fluid Flows," Los Alamos Scientific Laboratory report LA-5852 and "Addendum," LA-5852, Add. (1975).

4. McMaster, W.H. and Gong, E. Y., "PELE-IC User's Manual," Lawrence Livermore Laboratory report UCRL-52609 (1979).

5. Stewart, C.W., et al, "COBRA-IV: The Model and the Method," Battelle Pacific Northwest Laboratories report BNWL-2214 (1977).

6. Domanus, H.M., et al, "COMMIX-1A: A Three-Dimensional Transient Single-Phase Computer Program for Thermal-Hydraulic Analysis of Single and Multicomponent Systems, Vol.I: User's Manual," NUREG/CR-2896 (1983).

7. "TRAC-PD2: An Advanced Best-Estimate Computer Program for Pressurized Water Reactor Loss-of-Coolant Accident Analysis," Los Alamos National Laboratory report LA-8709-MS and NUREG/CR-2054 (1981).

8. Lighthill, M.J., Introduction to Fourier Analysis and Generalized Functions, Cambridge Univ. Press (1958).

9. Harlow, F.H. and Welch, J.E., "Numerical Calculations of Time-Dependent, Viscous, Incompressible Flow," Phys. of Fluids, 8, 2182 (1965).

10. Hirt, C.W., "Heuristic Stability Theory for Finite-Difference Equations," J. Comp. Phys. 2, 339 (1968).

11. Sicilian, J.M. and Hirt, C.W., "HYDR-3D: A Solution Algorithm for Transient 3D Flow," Flow Science, Inc. report FSI-84-00-3 (1984).

12. Sarpkaya, T., "Separated Flow about Lifting Bodies and Impulsive Flow about Cylinders," AIAA Jour. 4, 414 (1966).

13. Hunt, B. and Priestley, N., "Seismic Water Waves in a Storage Tank," Bull. Seismological Soc. Am. 68, 487 (1978).

14. Budiansky, B. "Sloshing of Liquids in Circular Canals and Spherical Tanks," J. Aero/Space Sci., 27, No. 3 (1960).

15. Dawson, C.W., "A Practical Computer Method for Solving Ship-Wave Problems," Proc. Second International Conf. Num. Ship Hydro., UCB (1977).

16. Ohring, S. and Telste, J., "Numerical Solutions of Transient Three-Dimensional Ship-Wave Problems," Proc. Second International Conf. Num. Ship Hydro., UCB (1977).

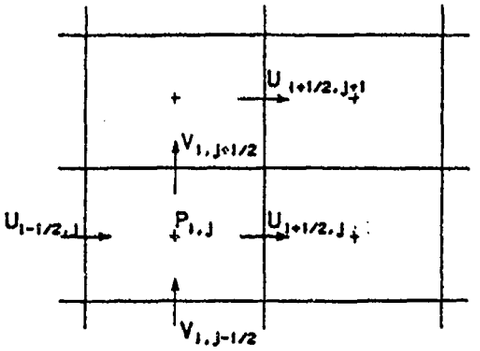

A

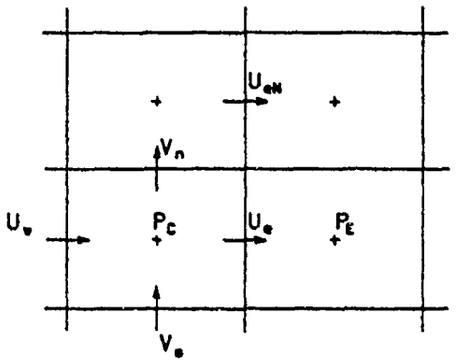

B

Fig. 1. Location of primary variables in mesh cell (A). Simplified notation used in text (B).

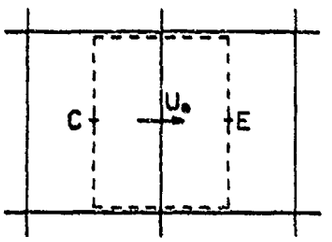

Fig. 2. Control volume (dashed line) for horizontal momentum equation.

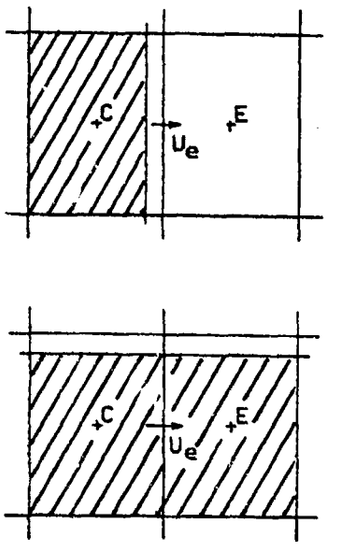

Fig. 3. Small cell volumes considered for worst-case stability estimates. Vertical interface (top) and horizontal interface (bottom).

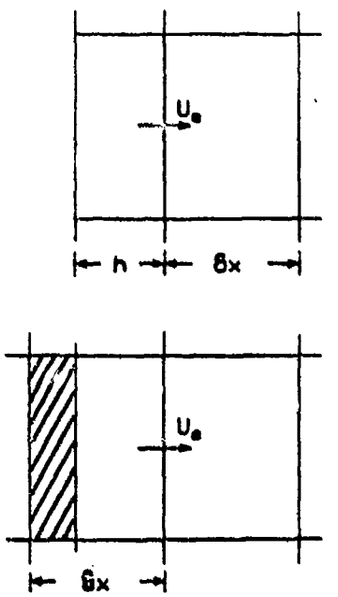

Fig. 4. Non-uniform mesh (top) compared with FAVOR method in uniform mesh (bottom).

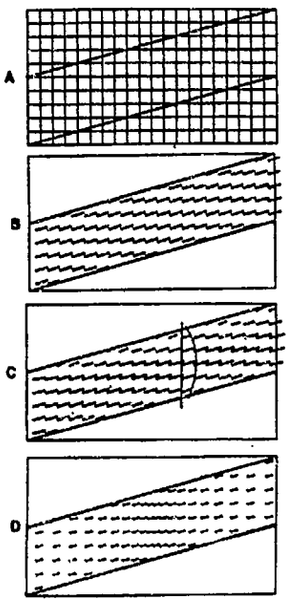

Fig. 5. Diagonal duct problem. (A) Duct orientation in mesh. (B) Initial uniform flow. (C) Calculated flow showing wall effect. (D) Calculated flow with wall boundary condition corrections.

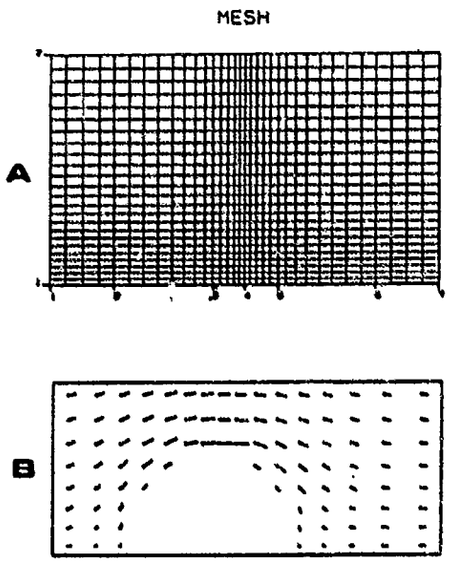

Fig. 6. Mesh used for flow about cylinder (A). Calculated potential flow in region near cylinder (B).

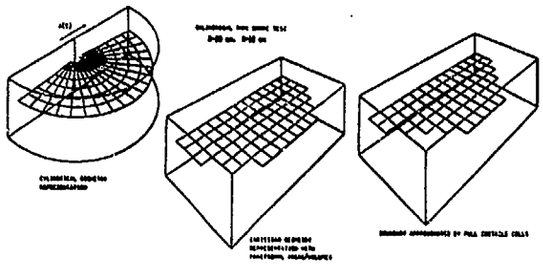

Fig. 7. Three models for cylindrical tank slosh. (A) Cylindrical coordinates. (B) FAVOR method in Cartesian coordinates. (C) Stepped boundary in Cartesian coordinates.

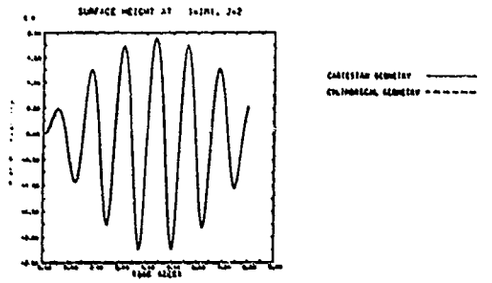

Fig. 8. Comparison of FAVOR method with cylindrical coordinate results for surface height versus time.

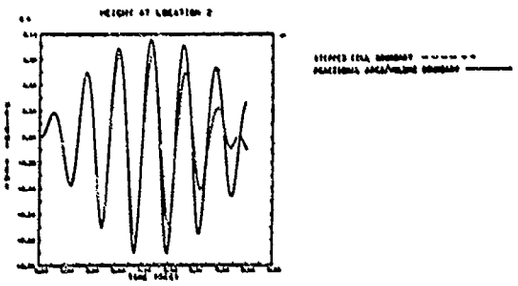

Fig. 9. Comparison of FAVOR method with stepped boundary results (dashed).

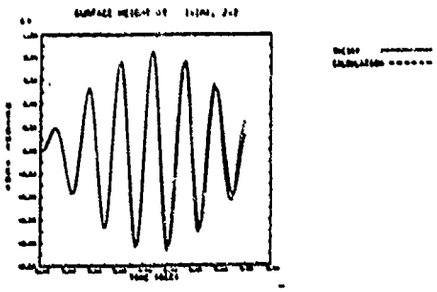

Fig. 10. Comparison of FAVOR method (dashed) with theory.

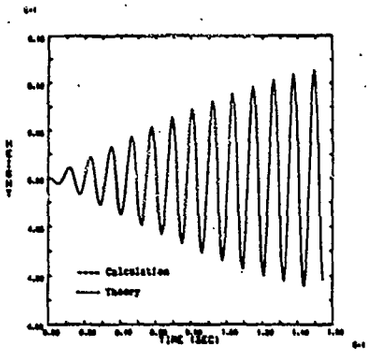

Fig. 11. Comparison of FAVOR calculations with theory for spherical tank slosh.

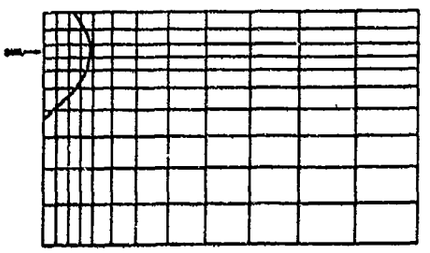

Fig. 12. Transverse mesh used for Wigley model calculation showing midship section.

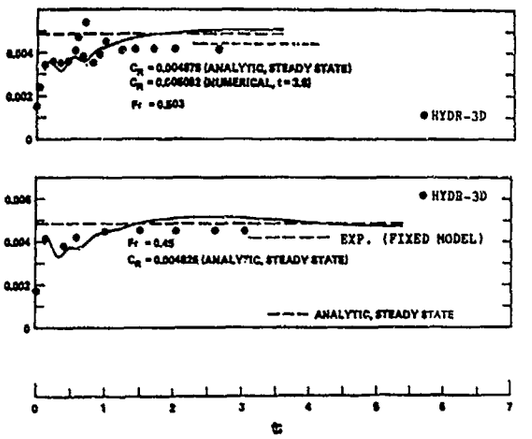

Fig. 13. Wave resistance versus time (in body lengths traversed) from Ref. 16. Froude number 0.503 top, 0.45 bottom.

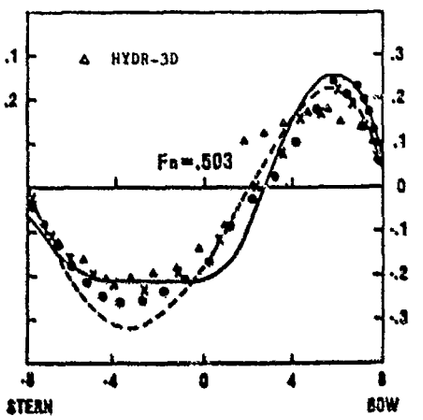

Fig. 14. Comparisons of computed wave profile with data from Ref. 15.

Session VII

VISCOUS FLOWS

Session Chairman
L. Landweber
University of Iowa
Iowa City, IA, U.S.A.

SHIP BOUNDARY LAYER AND WAKE CALCULATION WITH A PARABOLISED NAVIER-STOKES SOLUTION SYSTEM

M. Hoekstra and H.C. Raven
Maritime Research Institute Netherlands
The Netherlands

Abstract

A numerical method for the calculation of the viscous flow past a ship's stern under neglection of free surface effects is presented. The method is based on a solution of the Parabolised Navier-Stokes equations in a boundary-fitted coordinate system. The two main aspects of the solution procedure are

a) the global iteration process, needed to allow for upstream pressure influences. The convergence properties of this process are improved by adding to the equations a non-physical source term, vanishing upon convergence, as well as by applying successive step size reduction.
b) the local solution of the discretised equations at each step of a downstream marching process by a "strongly implicit" or "approximate factorisation" technique, maintaining a strong coupling between the equations.

The improvements as compared with an earlier version of the method are discussed. Results of application to the Wigley parabolic hull show that 10 global iteration cycles suffice to obtain a converged solution.

Nomenclature

C_p	pressure coefficient; $C_p = (p-p_\infty)/\frac{1}{2}\rho U_\infty^2$
i,j,k	grid node counters, associated with the ξ, η, ζ coordinate directions respectively
L	reference length (= ship length)
m	local iteration number
n	sweep number
p	pressure
Rn	Reynolds number based on U_∞ and L
u	contravariant velocity component in ξ-direction
U_∞	reference velocity (= ship speed)
v, w	physical velocity components in η, ζ direction respectively
x, y, z	Cartesian coordinates (cf. Fig. 1)
α	relaxation factor of local iteration
α_s	partial canceling parameter
ξ, η, ζ	boundary-fitted coordinates (cf. Fig. 1)
Φ_{jk}	vector of dependent variables $\begin{pmatrix} u_{jk} \\ w_{jk} \\ p_{jk} \end{pmatrix}$

Derivatives are written in suffix notation; e.g. $p_\xi \equiv \frac{\partial p}{\partial \xi}$

I. Introduction

Since the time of William Froude, naval architects have been accustomed to separate the still-water resistance of a ship into two main components, the viscous resistance and the wave resistance. Over the years this decomposition has proved to be very useful, because the interdependency of the two parts is weak under the conditions of high Reynolds number and low Froude number. Indeed, the analysis of model tests is usually based on a complete independency.

Numerical ship hydrodynamics has the prospect of once being able to deal with the integral problem where waves and viscous flow interact. However, at present, the decomposition is common practice here too. On the one hand there is a class of computational methods for the wave pattern generated by the ship; they are based on inviscid flow theory. On the other hand efforts are made to compute the viscous flow under neglection of (or with prescribed) free surface disturbances.

In this paper we shall be concerned with a method belonging to the latter category. We consider a double model of the submerged part of a ship's hull in an unbounded uniform flow - directed from bow to stern - and try to compute the steady part of the flow disturbance. At the high Reynolds numbers of practical interest, viscous effects in the flow are confined to a fairly narrow region surrounding the hull and extending into the wake (BLW region). This suggests a domain-decomposition approach in which each subdomain has its own mathematical description of the flow. In the effectively inviscid and irrotational flow outside the BLW region the velocity field can be derived from a velocity potential satisfying a Laplace equation. For the flow in the forebody part of the BLW region thin-boundary-layer theory is a satisfactory description. But further aft a more sophisticated viscous flow theory, something between boundary-layer theory and the full Navier-Stokes equations, must be used.

For the computation of the flow in this rear part of the BLW region, a PARabolised NAvier-Stokes SOlution System (PARNASSOS) has been developed at the Maritime Research Institute Netherlands. It is a special purpose program in that its application has deliberately been restricted to incompressible external flows. It is therefore markedly different from methods based on general purpose flow solvers.

The main features and first applications of PARNASSOS were reported in /1/, early 1985. Since then, several improvements have been realised. This paper gives again an outline of the system with emphasis on the numerics. Section II explains the grid generation process. The mathematical formulation is presented in Section III, followed by a detailed discussion of the numerical solution procedure in Section IV. Results of the recalculation of the flow past the Wigley parabolic ship form are presented and discussed in Section V. The paper concludes with a summary of the main achievements.

II. Grid generation

In accordance with the problem specification given in the introduction, the computation domain encloses the rear

part of the BLW region. Somewhere along the hull we choose an inlet plane; an outlet plane will be located at some distance behind the hull where the pressure can be supposed to have resumed a practically undisturbed level.
Taking advantage of the symmetry of the flow with respect to the longitudinal centreplane of the hull and the plane corresponding with the undisturbed free surface, we arrive at a domain as sketched in Fig. 1.

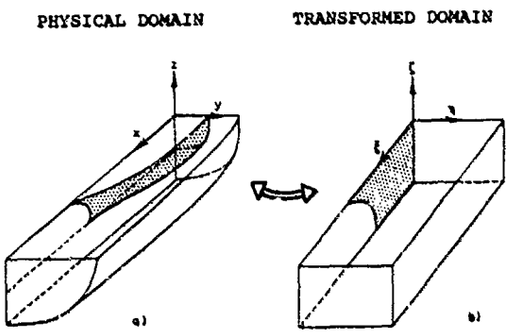

Fig. 1 Computation domain

Of course, the lateral extension of the BLW region (thickness of the boundary layer) is not known a priori. By taking the width of the domain about twice an estimated boundary layer thickness we are sure to include BLW.

A suitable coordinate system has now to be chosen for the purpose of discretisation of the flow equations. For a proper resolution of the steep velocity gradients near the hull surface a body-fitted grid is indispensable. Besides a Cartesian x,y,z system, we therefore introduce the coordinates ξ,η,ζ (Fig. 1)

To keep the relation between the two systems simple, we postulate $\xi = x$, i.e. all transverse sections of the physical domain are coordinate surfaces ξ = constant. The problem of generating a 3D mesh is then reduced to establishing a suitable grid in all transverse planes; by connecting points with equal η,ζ values in successive planes we obtain the ξ-lines (which will be smooth provided the boundaries of the domain are smooth).

Non-orthogonality of the ξ,η,ζ system is implied by the choice $\xi = x$. But the η and ζ lines in transverse sections are defined by an orthogonal mapping of a rectangle onto the section shape. The resulting partial orthogonality of the grid allows several simplifications in the general formulation of the governing equations and reduces the number of geometric data to be stored. At the same time we must accept the appearance of isolated boundary singularities in the transformation, for it is possible that a section of the physical domain does not have four 90° corners. This can happen in sections along the hull, but it certainly will be the case in wake sections, which are topologically triangular so that a virtual fourth corner has to be introduced (Fig. 2). We position that fourth corner on the straight extension of the keel line or - if the ship has a Hogner type stern - of the propeller axis. But wherever positioned, an awkward singularity is unavoidable.

The orthogonal mapping is accomplished by the combination of a conformal mapping according to a generalised Schwarz-Christoffel method /2/ and a linear transformation on the η-coordinate normal to the hull (to give all transformed sections the same height). We shall not go into the details of the

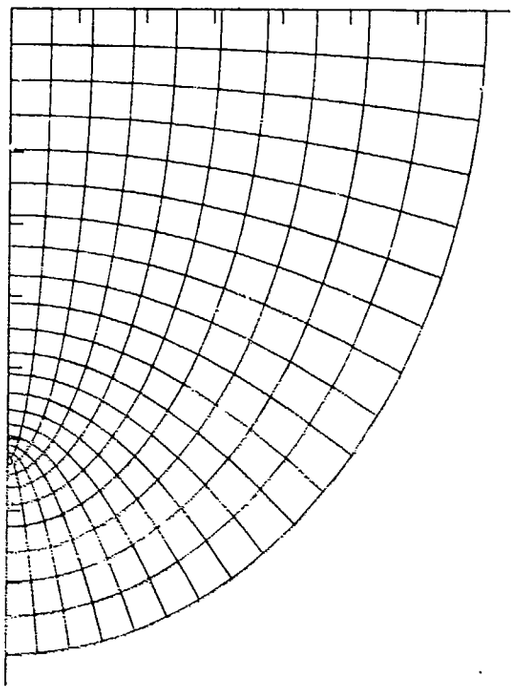

Fig. 2 Example of grid in a transverse plane in the wake (without stretching)

procedure here. More information can be found in /1/ and /2/. Grid stretching (in η-direction) is not included in the transformation, but is applied in the transformed plane.

The analytical transformation formula gives us directly the values of the transformation coefficients y_η, y_ζ, z_η and z_ζ for any point η, ζ. The choice $\xi = x$ further implies $x_\xi = 1$, $x_\eta = x_\zeta = 0$. To complete the matrix of transformation coefficients we determine y_ξ and z_ξ numerically (2nd order central differencing). Derivatives of the transformation coefficients, needed for the evaluation of Christoffel symbols, are also calculated by numerical differentiation.

The transformation coefficients, their derivatives and the physical coordinates x, y, z (y and z being determined by numerical integration of the transformation formula) for all grid points are stored on a disk file. The geometrical coefficients appearing in the flow equations are determined each time they are needed. The question whether it is more efficient to determine these data once and for all (a matter of CP versus IO time) is still under investigation.

III. Mathematical formulation

Parabolised Navier-Stokes equations

As a mathematical model for the flow we need something between the full Navier-Stokes equations and the boundary-layer equations, for the latter are inadequate while the solution of the first is not feasible in an application like ours.

First of all time-averaging of the turbulent velocity fluctuations and momentum fluxes is needed, which leads us to the Reynolds equations, to be supplemented with a turbulence model. But even their solution is troublesome, mainly because of the elliptic nature. This means that a disturbance at some point in the flow may influence the solution in any other point (and not just downstream points) via convection, diffusion and/or pressure propagation. Therefore, the Reynolds equations are not suited for a solution as an initial/boundary value problem; normally, a simultaneous solution of the set of four equations in - for our applications - typically 50.000 nodes is required.

For flows with a predominant flow

direction (as here the ξ-direction) it is generally accepted that propagation of disturbances in the direction opposite to the main flow via convection or diffusion must be insignificant if present at all. Thus we further simplify our mathematical model by neglecting diffusion along ξ-lines. Moreover, the terms associated with convective momentum transport in ξ-direction are omitted wherever such transport is directed upstream. (N.B.: flow separation leading to relatively weak recirculation is not excluded!). This brings us to what we call the Parabolised Navier-Stokes (PNS) equations.

Because the term "parabolised" can easily be misunderstood some furtner explanations are added. In contrast to what its name suggests, the set of PNS-equations is elliptic (at least in subsonic flow; /3/). Although the transfer of influences upstream via convection and diffusion has been removed, the possibility of propagation of pressure influences in negative ξ-direction is still there. In order to reproduce this effect in the numerical solution, a downstream grid node must be involved in the discretisation of the p_ξ term. Now, by supposing the pressure at this downstream node to be "known", an effective parabolisation is achieved. The ξ-coordinate becomes time-like and we are allowed to obtain the solution in a downstream marching process, exactly as when solving the parabolic boundary-layer equations /4/. However, this downstream marching process has to be repeated several times (global iteration) to actually allow the pressure to convey its influence upstream. Thus in each marching sweep we solve a parabolic set of equations but the final solution is that of an elliptic system.

Like the boundary-layer equations, the PNS-equations are a reduced form of the Navier-Stokes equations. But as a mathematical model, they go far beyond the reach of boundary-layer theory. There is no singular behaviour near separation and an important feature like the viscous pressure resistance becomes calculable. This is because the pressure is retained as an extra dependent variable. The set of equations consists therefore of three (instead of two) momentum equations plus the continuity equation.

Others have used the momentum equations in combination with a Poisson equation for the pressure, solving the continuity equation only indirectly /5, 6/. The introduction of the Poisson equation may be justifiable in 3D internal flow applications, but there is no need to use it in velocity/pressure formulations for external flows. On the contrary, when the PNS-equations are regarded as an extension of boundary-layer theory, it is natural to consider the extra equation (η-momentum equation) as the primary equation for the extra variable (the pressure). The usual boundary-layer solution procedure is then so to speak a particular case of the PNS-solver.

Equations in curvilinear coordinates

Tensor formalisms are helpful in writing the equations in terms of the ξ,η,ζ coordinates, but not without some important decisions on our part. Which three components of the momentum equation (a vector equation) are selected and what are the dependent variables?

The equations in PARNASSOS express

momentum conservation along the ξ,η,ζ lines (contravariant formulation) but other plausible choices are the directions of the reciprocal base (covariant formulation) or the Cartesian x,y,z directions. In the contravariant form, however, it is easiest to exploit the fairly-thin-shear-layer character of the flow by different treatment of the normal, girthwise and longitudinal momentum equations. A price to be paid is that the attractive strong-conservation form of the Cartesian formulation is not applicable.

As to the dependent variables there is a similar freedom of choice. Using the primitive variables velocity and pressure one has still to decide on the decomposition of the velocity vector. In /1/ the contravariant velocity components were used but, being non-physical, they exhibit excessive gradients near a grid singularity. Therefore, we now use the contravariant component u in ξ-direction (which in our coordinate system happens to be equal to the Cartesian velocity in x-direction) but the physical velocity components in η-direction (v) and ζ-direction (w).

The final equations are lengthy and complicated, because of the stress terms in particular. The nature of the flow allows us to drop the latter in the normal momentum equation. Thus the equations contain first but no second η-derivatives of v and p. This is reflected in the boundary conditions, summarised below.

Boundary conditions

$\zeta=\zeta_{min}$	(inlet plane)	u,v and w given
$\zeta=\zeta_{max}$	(outlet plane)	$p_\zeta=0$
$\eta=\eta_{min}$	(hull surface)	u=v=w=0
	(central symmetry plane)	$u_\eta=w_\eta=0$; v=0
$\eta=\eta_{max}$	(external boundary)	u,w and p given
$\zeta=\zeta_{min}$	(central symmetry plane)	$u_\zeta=v_\zeta=p_\zeta=0$; w=0
$\zeta=\zeta_{max}$	(undisturbed free surface)	$u_\zeta=v_\zeta=p_\zeta=0$; w=0

The conditions to be prescribed at the external boundary are obtained from a potential flow calculation. Since the external potential flow in its turn depends to some extent on the flow in the viscous flow region, there is an interaction effect to be considered, but having chosen the outer boundary of our calculation domain well away from the boundary layer edge, the interaction will be weak. If necessary, viscous-inviscid interaction effects can then be taken into account by incorporating an adjustment of the boundary conditions in the global iteration process.

Turbulence model

Let us finally turn to the turbulence modeling, which is far from a trivial matter in stern flow fields. For instance, it is one thing to know that streamline curvature has a strong effect on the turbulence, but quite another to develop a practical turbulence model in which these effects are elegantly incorporated. Even two-equation models, let alone the zero and one-equation models, are defective in this respect.

In the development of PARNASSOS the selection of a suitable turbulence model has not yet been given due consideration, because priority was given to the settling of the numerical matters.

Provisionally we use an isotropic eddy-viscosity model based on algebraic relations for velocity and length scales /7/ with adaptations for application in a wake /8/.

IV. Solution method

Pressure field iteration

As explained in Section III the parabolisation is accomplished by using a "known" value for the downstream pressure $p_{i+1,j,k}$ in the equations for grid point (i,j,k). (Here, i, j, k are grid node counters in ξ, η, ζ directions). This value is explicitly updated after each sweep. However, $p_{i,j,k}$ is modelled implicitly in all momentum equations to allow an immediate adjustment of the pressure field; otherwise singular behaviour at a separation point is to be expected.

A central difference approximation for p_ξ would uncouple $(p_\xi)_i$ from p_i, probably resulting in similar problems. Therefore we apply a two-point forward scheme

$$(p_\xi)_i^{(n)} = (p_{i+1}^{(n-1)} - p_i^{(n)})/\Delta\xi. \qquad (1)$$

This defines an iterative pressure field determination: in each sweep we calculate a new pressure $p^{(n)}$ which is stored on a disk file for use in the next sweep. Through the $p_{i+1}^{(n-1)}$ contribution in p_ξ, the influence of the previous sweep is allowed to propagate one step upstream. Thus subsequent sweeps are related through the pressure field only; previous-sweep velocities do not occur in the iteration scheme. If everywhere $|p_i^{(n)} - p_i^{(n-1)}|$ is less than a given tolerance the converged solution for pressure and velocity field has been obtained.

Source term

Experience has shown that the global iteration procedure described above is only marginally stable for wavelike pressure disturbances that often originate from regions of negative normal velocity, e.g. reattachment regions /1/. These pressure waves travel upstream during the global iteration without noticeable damping and inhibit the convergence.

Indeed, with the p_ξ-scheme (1), a pressure disturbance that is shifted upstream one step per sweep without change in magnitude has no influence on p_ξ. Damping can only be effected together with the normal momentum and continuity equations and their boundary conditions, but this effect may be quite weak.

Following Israeli and Lin /9/ we now modify the ξ-momentum equation by introducing a (non-physical) source term that vanishes upon convergence:

$$SX_{i,j,k} = SX_{i-1,j,k} + p_{i,j,k}^{(n)} - p_{i,j,k}^{(n-1)}, \qquad (2)$$

with $SX_{1,j,k} = 0$.
The ξ-momentum equation (here given in Cartesian form) then becomes:

$$\frac{Du}{Dt} + \frac{1}{\rho\Delta x}\left(p_{i+1,j,k}^{(n-1)} - 2p_{i,j,k}^{(n)} - SP_{i,j,k}\right) + \text{viscous terms} = 0, \qquad (3)$$

where

$$SP_{i,j,k} = SP_{i-1,j,k} + p_{i-1,j,k}^{(n)} - p_{i,j,k}^{(n-1)}. \qquad (4)$$

This modified equation is easily seen to be sensitive to such undamped pressure waves; the doubling of the coefficient of $p^{(n)}_{i,j,k}$ suggests an amplitude reduction by one half in every sweep.

To gain a better insight into the meaning of this source term and its effect on the stability we consider the Poisson-like equation for the pressure implied in the momentum equations. From the momentum equations that contain $p_{i,j}$, in a 2D-case for simplicity, one can derive:

$$\sigma p^{(n)}_{i,j-1} + \sigma p^{(n)}_{i,j+1} - (2\sigma+1)p^{(n)}_{i,j} + $$

$$- p^{(n-1)}_{i,j} + p^{(n)}_{i-1,j} + p^{(n-1)}_{i+1,j} =$$

$$-\rho\Delta x^2\Big[\frac{(\frac{Du}{Dt}+\text{visc.})_{i,j}-(\frac{Du}{Dt}+\text{visc.})_{i-1,j}}{\Delta y} +$$

$$+\frac{(\frac{Dv}{Dt})_{i,j+\frac{1}{2}} - (\frac{Dv}{Dt})_{i,j-\frac{1}{2}}}{\Delta y}\Big], \qquad (5)$$

where $\sigma = (\Delta x)^2/(\Delta y)^2$

The terms at the right are evaluated in sweep number (n), simultaneously with $p^{(n)}_{i,j}$, and give some feedback through a change of the velocity field as has just been mentioned. To simplify the analysis we neglect this weak effect and consider the right hand side as fixed.

We then observe that the discretised Poisson equation is solved by an iterative scheme that is rather unusual because of the appearance of the $p^{(n-1)}_{i,j}$ term. The source term SX modifies this scheme to the conventional Successive Line Relaxation:

$$\sigma p^{(n)}_{i,j-1} + \sigma p^{(n)}_{i,j+1} - (2\sigma+2)p^{(n)}_{i,j} +$$

$$+ p^{(n)}_{i-1,j} + p^{(n-1)}_{i+1,j} = \text{R.H.S.}, \qquad (6)$$

the right hand side being identical with the one written out above.

A stability analysis for both methods can be made by assuming a pressure perturbation $\Delta p^{(n)} = c^{(n)}e^{i(k_x x+k_y y)}$. For the original scheme without source term we find an amplification factor

$$\lambda_1 = \frac{c^{(n)}}{c^{(n-1)}} = \frac{1-e^{ik_x\Delta x}}{2\sigma(\cos k_y\Delta y-1)-1+e^{-ik_x\Delta x}}; \qquad (7)$$

but with the source term included

$$\lambda_2 = \frac{-e^{ik_x\Delta x}}{2\sigma(\cos k_y\Delta y-1)-2+e^{-ik_x\Delta x}}. \qquad (8)$$

Taking into account the fact that according to our experience the most persisting perturbations are smooth in normal direction with $k_y\Delta y \ll 1$, we can approximate

$$|\lambda_1| = \sqrt{\frac{1-\cos k_x\Delta x}{1-\cos k_x\Delta x+k_y{}^2\Delta x^2}}, \qquad (9)$$

$$|\lambda_2| = \sqrt{\frac{1}{5-4\cos k_x\Delta x+k_y{}^2\Delta x^2}}. \qquad (10)$$

Both amplification factors are always less than unity, but λ_2 is usually much smaller. In particular, for $k_y\to 0$ and $k_x\Delta x$ finite, $\lambda_1\to 1$ and

$$\lambda_2 \to \sqrt{\frac{1}{5-4\cos k_x\Delta x}} < 1.$$

Therefore, for large $\frac{y_{max}}{\Delta x}$, pressure waves can be present for which the unchanged iteration scheme is marginally

stable unless the coupling with the velocity field provides an adequate damping. This sensitivity to $\frac{y_{max}}{\Delta x}$ partly corresponds with experience by others /9, 10/. The source term stabilises the procedure in such cases.

In fact, in all our calculations the use of the source term was very satisfactory and led to a perfectly stable pressure iteration. In the present version of our program it is, therefore, always used. A possible drawback is the introduction of a non-physical term in the equations as long as the pressure field has not converged. This may sometimes result in somewhat unusual velocity fields (e.g. velocity overshoot in a wake) in the first sweeps.

Successive stepsize reduction

Another modification that greatly improves the pressure field convergence is a one-dimensional multigrid-like solution sequence /10/. The pressure influence progresses only one step $\Delta\xi$ per sweep; moreover, if $\Delta\xi$ is small, $|p_i^{(n)} - p_i^{(n-1)}|$ cannot be large without unduly affecting p_ξ and, as a result, the velocity field. Therefore it is useful first to make a few sweeps with a large $\Delta\xi$ in order to allow a rapid approach of the correct pressure level, and then to reduce $\Delta\xi$ in a few stages as much as needed for accuracy. Of course the velocities, too, are solved with the same step sizes.

For consistency, the ξ-derivatives of geometric data must also be adapted to these various step sizes. If they have been determined beforehand by central differencing on the finest grid it may occur that the coarse-grid sweeps do not encounter local coordinate line curvatures. Inconsistencies may then arise, e.g. between the various y_η-values and their derivatives $y_{\eta\xi}$. So it is desirable to use the same step size in the geometry differencing as in the solution sweep. Each $\Delta\xi$-reduction then requires the preparation of a new geometry file with modified ξ-derivatives.

Linearisation and differencing

Having dealt with the treatment of p_ξ in the ξ-momentum equation we now have obtained an elliptic system of equations for u_i, v_i, w_i and p_i at each station $\xi = \xi_i$. This will be solved by means of an iterative procedure, denoted by "local iteration" here (as opposed to the global iteration described before). In order to improve its stability and convergence we aim at the strongest coupling and implicitness as is practical. In this context, implicitness is to be understood as the use of current-iteration values instead of previous iterates.

Therefore we apply Newton linearisation to the convective terms in the momentum equations, which preserves their coupling. Only some unimportant viscous and convective terms resulting from the coordinate transformation are modelled explicitly to simplify the algorithm; this has been found to have no effect on the convergence rate.

To facilitate the coupled solution we use a nonstaggered grid; all variables are defined at nodal points (i,j,k). ξ-derivatives of the velocities are approximated by a three-point second-order backward scheme; all normal derivatives and second order ζ-derivatives by central differences.

First-order ζ-derivatives, however, are approximated by a 4-point quadratic scheme. For velocity derivatives this is the QUICK scheme /11/ but for p_ζ the orientation is changed to downstream (referring to the transverse velocity component w). The use of this scheme instead of the conventional central differencing turned out to be essential to avoid oscillations in some conditions.

The quadratic schemes used are:

$$f_\zeta = (2f_{k+1} + 3f_k - 6f_{k-1} + f_{k-2})/6\Delta\zeta$$

$$p_\zeta = (-p_{k+2} + 6p_{k+1} - 3p_k - 2p_{k-1})/6\Delta\zeta$$

for $w > 0$ and

$$f_\zeta = (-f_{k+2} + 6f_{k+1} - 3f_k - 2f_{k-1})/6\Delta\zeta$$

$$p_\zeta = (2p_{k+1} + 3p_k - 6p_{k-1} + p_{k-2})/6\Delta\zeta$$

for $w < 0$, where f is any of the velocity components u, v, w.

These schemes involve points outside the "5-point star" (consisting of the points (i,j,k), (i,j-1,k), (i,j+1,k), (i,j,k-1) (i,j,k+1)). This is impractical unless they are split into an implicit part and an explicit correction. Previously the splitting was defined as:

$$f_\zeta = (2f_{k+1} + 2f_k - 4f_{k-1})/6\Delta\zeta + \\ + \overline{(f_k - 2f_{k-1} + f_{k-2})/6\Delta\zeta}$$

and similarly for the other derivatives. The overbar denotes a previous iterate. However, this introduced an instability into the scheme, giving rise to the occurrence of alternating solutions in the iteration process. Similar problems are mentioned in /12/. At present the implicit part is a simple two-point upwind scheme (but downwind for p), which satisfies the requirements of diagonal dominance and consistency with the derivatives being modelled. This modification considerably improved the convergence and stability of the iterative solution method.

These difference approximations are substituted in the momentum and continuity equations. The ξ- and ζ-momentum equations are centered at nodal points (i,j,k). However, both the continuity and the η-momentum equation are first order differential equations in η, the latter owing to the neglection of viscous terms. Therefore we center these equations at intermediate points: $(i,j-\frac{1}{2},k)$ for the continuity equation, $(i,j+\frac{1}{2},k)$ for the η-momentum equation. Accordingly we find the wall pressure from the η-momentum equation at the first half-point from the wall without the need of prescribing a wall boundary condition for it.

Thus we arrive at a coupled set of linear equations in 5-point star form, but with an additional v-contribution:

$$PP_{jk}\Phi_{j-1,k} + Q_{jk}\Phi_{j,k} + R_{jk}\Phi_{j+1,k} + S_{jk}\Phi_{j,k-1} + \\ + T_{jk}\Phi_{j,k+1} + XX_{jk}v_{j,k} + ZZ_{jk} = 0 \qquad (13)$$

where the unknown vector $\Phi_{jk} \equiv \begin{pmatrix} w_{jk} \\ p_{jk} \end{pmatrix}$.

Due to the coupling, PP, Q, R, S and T are full 3x3 blocks. The continuity equation is written in the form

$$v_{j,k} = FF_{jk}v_{j-1,k} + AA_{jk}(u_{j,k}+u_{j-1,k}) +$$

$$+BB_{jk}(w_{j,k}+w_{j-1,k}) + CC_{jk}(w_{j,k+1}+w_{j-1,k+1})$$

$$+DD_{jk}(w_{j,k-1}+w_{j-1,k-1}) + EE_{jk} \quad . \qquad (14)$$

Approximate factorisation

From the variety of iterative methods applicable to such systems of equations we have chosen one that has the desired coupling and implicitness properties, the Strongly Implicit Procedure (SIP) /13, 14/, which is an approximate factorisation technique.

Apart from the term $XX_{jk}v_{j,k}$ the system (13) can be represented by

$$M\Phi = q \qquad (15)$$

Each line of M contains the coefficient blocks PP_{jk}, ... T_{jk} of the equations for one grid point. Therefore M is a pentadiagonal matrix. The principle of approximate factorisation is to replace M by an approximation M+N that is easily decomposed in sparse lower and upper triangular matrices:

$$M+N=LU$$

The solution of (15) can then be found by an iterative process

$$LU\Phi^{m+1} = N\Phi^{m} + q, \qquad (16)$$

where m is the iteration number.

Different choices of L, U and N define different factorisation methods /15/. For the SIP the factors L and U each have only three nonzero diagonals, which makes the solution of (16) particularly simple.

First

$$LD = M\Phi^{m} + q \qquad (17)$$

is solved for a vector D.
The right hand side is computed from previous iterates, while the left hand side involves $D_{j,k}$, $D_{j+1,k}$ and $D_{j,k-1}$. The latter two are known if we start at the outer edge j = NY and work towards the wall for increasing k.

Next, the solution follows from

$$U\Phi^{m+1} = D \qquad (18)$$

which involves Φ^{m+1}_{jk}, $\Phi^{m+1}_{j-1,k}$ and $\Phi^{m+1}_{j,k+1}$ and is, therefore, solved for decreasing k, starting at the wall and working towards the outer edge. Thus the transverse plane is swept twice in each iteration, first from left to right and downward to find D, then from right to left and upward to find the solution Φ.

For the SIP variant that we use at present, the only nonzero diagonals of the error matrix N are those corresponding to the points (j+1,k+1) and (j-1,k-1); all other elements of LU and M are equal. Thus the system solved in each iteration differs from the original equation (13) by explicit terms in $\Phi^{(m)}_{j+1,k+1}$ and $\Phi^{(m)}_{j-1,k-1}$. Since these relate to rather distant points this contribution is in general fairly small, and a rapid convergence of the iteration may be expected. Moreover, no explicit values are used for variables in the 5-point star nodes; thus each iteration contains implicit derivatives in all directions, as opposed to e.g. ADI methods.

A slight modification /14/ is needed to account for the normal velocity contribution $XX_{jk}v_{j,k}$ in (13), which for clarity was left out in the description above. The solution algorithm is changed to

$$U\Phi^{m+1} = D + C\, v^{m+1} \qquad (19)$$

where C has only one nonzero diagonal relating to point (j-1,k). The elements of C, and of a similar contribution in (17), are derived by making use of the continuity equation, which is also solved together with (19). This distinct treatment of v and the continuity equation makes the algorithm a good deal simpler than what would be required for the 4 x 4 system obtained otherwise. In difficult cases some underrelaxation of (19) has turned out to be helpful. Furthermore, before starting the iteration at a new ξ-station the velocities found in the previous marching sweep are read in from a disk file to be used as initial values. This considerably improves the convergence in later sweeps.

Partial canceling of explicit terms

A further [illegible] of $N\Phi^{-1}$ is aimed at by the method of Stone /13/. This consists in approximating the explicit variables by

$$\Phi_{j+1,k+1} \approx \Phi_{j,k+1} + \Phi_{j+1,k} - \Phi_{jk}$$
$$\Phi_{j-1,k-1} \approx \Phi_{j,k-1} + \Phi_{j-1,k} - \Phi_{jk} \qquad (20)$$

which is correct to $O(\Delta\eta\Delta\zeta)$ and has a suitable form to be included in the LU decomposition. Now only the error in this approximation appears in $N\Phi^m$; in the iterative method this amounts to using

$$\Phi_{j+1,k+1} = \alpha_s(\Phi_{j+1,k} + \Phi_{j,k+1} - \Phi_{jk}) +$$
$$+ \overline{\Phi_{j+1,k+1}} - \alpha_s\overline{(\Phi_{j+1,k} + \Phi_{j,k+1} - \Phi_{j,k})} \qquad (21)$$

Here α_s is an iteration parameter that for smoothly varying Φ would be expected to be unity but must in practice be varied between 0 and 1 /13/. Therefore this method is called "partial canceling of explicit terms".

For $\alpha_s = 0$ we obtain the method described before. Otherwise N contains more non-zero diagonals, so each iteration requires more work, particularly if α_s is varied as recommended. A few numerical tests showed that in fact the partial canceling somewhat accelerates the convergence; values of $\alpha_s > 0.7$ were needed to give a noticeable effect. The improvement in convergence rate does not really seem to be worth the extra work and complexity, at least in the convection-dominated flows dealt with. Therefore this modification has not been included in our program.

Linear and nonlinear iterations

The local iteration procedure described is needed because of the presence of a factorisation error N. But in addition the coefficients L, U and q in (16) contain a number of explicit terms that also require iteration; these relate to the nonlinear convective terms, a few minor viscous and convective terms resulting from the coordinate transformation, and the 4-point ζ-difference scheme corrections.

In previous calculations /1/ all these explicit terms were updated in every iteration, so the nonlinearity was solved for in the course of the SIP iteration. This has turned out to be

inefficient. In general, far more iterations are needed for the SIP than for correctly finding the other explicit terms; and it takes much computation time to evaluate the coefficients in the 5-point star equations each time anew, since these are quite complicated in the coordinate system used.

In the present version of the program each "nonlinear" iteration (with new determination of coefficients) is followed by a number (up to 10) of iterations with fixed L and U matrices, in which only the right hand side $N\Phi^m$ is updated.

Some more storage is needed to save the matrices L, U and N, but these iterations for a linear system are more than 6 times as fast as full nonlinear iterations. This modification led to a reduction of the total computation time of about 50%, depending on the degree of nonlinearity.

Summary of improvements

Let us close this section by summarising the improvements that have been made with respect to the earlier version of PARNASSOS presented in /1/.

- the physical velocity components v and w are being used instead of their contravariant counterparts to obtain a better behaviour of the solution near a geometrical singularity;
- the stability of the local iteration has been improved by a modified implicit/explicit splitting of the difference scheme for ζ-derivatives;
- better convergence can be obtained within a given computation time by making extra SIP iterations without recalculating the matrix of coefficients;
- ξ-derivatives of geometrical quantities have been made consistent with the actual step size in the current sweep.

V. Application

The method has been applied to the flow past the stern of the Wigley hull. Although results for the same case were already reported in /1/, the improvements in the solution procedure made us decide to recalculate them.

The Wigley parabolic hull is a mathematical ship form defined by the offset function

$$y = \frac{B}{2}\left[1-\left(\frac{2x}{L}\right)^2\right]\left[1-\left(\frac{z}{H}\right)^2\right]$$

$$\left(-\frac{L}{2} \le x \le \frac{L}{2}\ ;\ -H \le z \le 0\right)$$

with $B = 0.1\ L$ and $H = 0.0625\ L$. For the present calculations the inlet plane of the computation domain was chosen at $2x/L = 0.04$ and the outlet plane at $2x/L = 2.00$. Externally, the domain was bounded by the relevant part of the elliptic cylinder

$$\left(\frac{y}{a}\right)^2 + \left(\frac{z}{b}\right)^2 = 1;\ x \text{ arbitrary}$$

with $a = 0.07\ L$ and $b = 0.09\ L$. The values for a and b are greater than those used in /1/ because the desirability of a wider computational domain had emerged from an analysis of the results.

The step size in x-direction was constant and equal to $\Delta x = \Delta\xi = 0.02L$ on the finest grid. But the first sweeps were made with either a fourfold or a double step size. By the intentional location of the inlet plane one step aft of the midship section we made sure that all sweeps included station $2x/L = 1.0$, where a pressure peak is expected. This eliminated the shift of this peak with each grid refinement that may have retarded the convergence of the results in /1/.

In all 50 transverse planes a 40x21 grid was generated, giving a total number of 42000 grid nodes. In ξ,η,ζ space the mesh was uniform in ζ-direction but stretched in η-direction. Beyond $2x/L = 1.0$ (in the wake) the shape of the domain cross section did not change, hence the mesh properties became ξ-invariant there.

The calculations were carried out at a Reynolds number based on ship length equal to $Rn = 7.4 * 10^6$. The boundary conditions at the inlet plane were to some extent based on experimental data for the same Rn /16/. Coles' velocity profiles were generated corresponding to measured momentum thicknesses and skin friction coefficients. But the initial value of w was set to zero (no crossflow). The boundary conditions for u, w and p at the outer boundary were obtained from a calculation of the potential flow around the hull. The Hess & Smith method was applied with 1600 source panels on the complete double model. These conditions were not adjusted in later sweeps because the viscous-inviscid interaction was supposed to be negligible. The initial pressure field was derived by assigning the pressure at a grid node on the outer boundary to all grid nodes on the same η-line, i.e. the pressure was made uniform across the boundary layer.

Convergence of the SIP

The convergence of the local iteration process can be judged by inspection of the residues of the four equations and/or the maximum changes in the dependent variables between two successive iteration cycles. We shall use the latter approach to illustrate the behaviour of our solution.

The convergence rate of the SIP turned out to depend significantly on the x-position and was evidently related to the severity of the geometrical singularity at the keel and its extension. In the forward part of the calculation domain, where an underrelaxation factor $\alpha = 0.5$ was applied, the convergence rate amounted to about one order of magnitude reduction of the changes in the variables per 12 iteration cycles in the first sweep. It improved gradually in later sweeps when the iteration process started with a good first guess obtained from the preceding sweep. Typical results are shown for $2x/L = 0.52$ in the first and seventh sweep (Figs. 3 and 4). Of the non-linear iterations (Nos. 0, 1, 7, 12, 17, 21 and 24) those preceded by a linear one usually gave rise to a small jump in the changes of the variables. Presumably the convergence could still have been improved by choosing a greater value for α.

Further downstream the convergence rate worsened and a tendency to instability

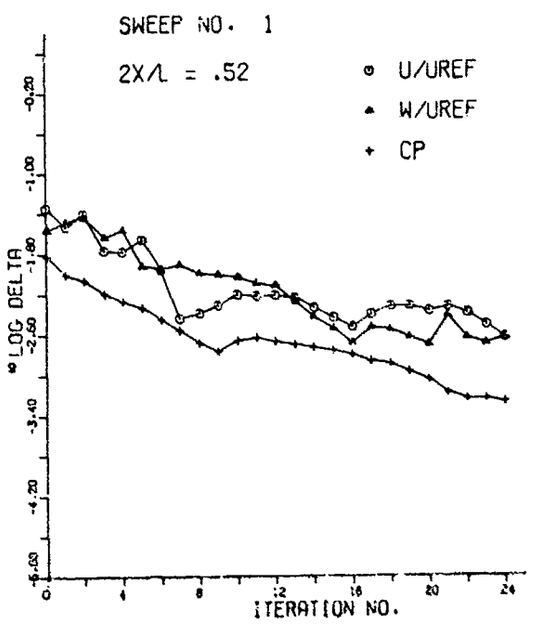

Fig. 3 Convergence history of local iteration process

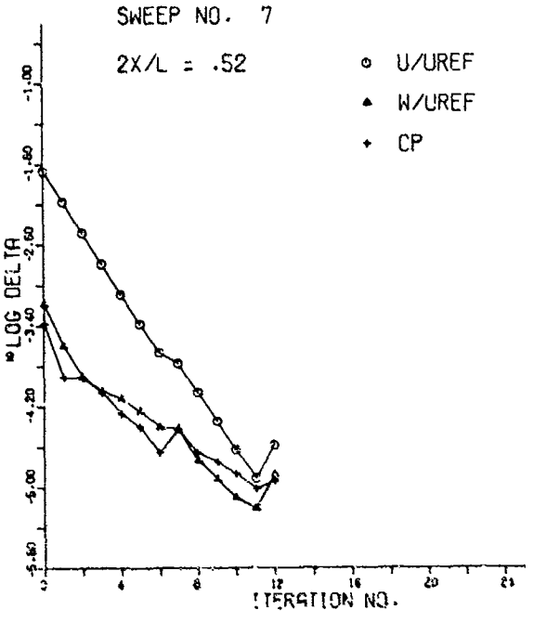

Fig. 4 Convergence history of local iteration process

was observed when the value 0.5 was retained for the relaxation factor. The results in Fig. 5 for 2x/L = 1.0 were obtained with α reduced to 0.2. Thus the solution could be made to converge slowly.

We do not think that the SIP itself can be blamed for this unfavourable behaviour. The key to further improvements should be found in a detailed study of the solution near the grid singularity.

However this may be, the final solution of the 10th sweep converged even near the stern to within a tolerance of 10^{-3} for the nondimensional velocity components and $2.*10^{-4}$ for C_p.

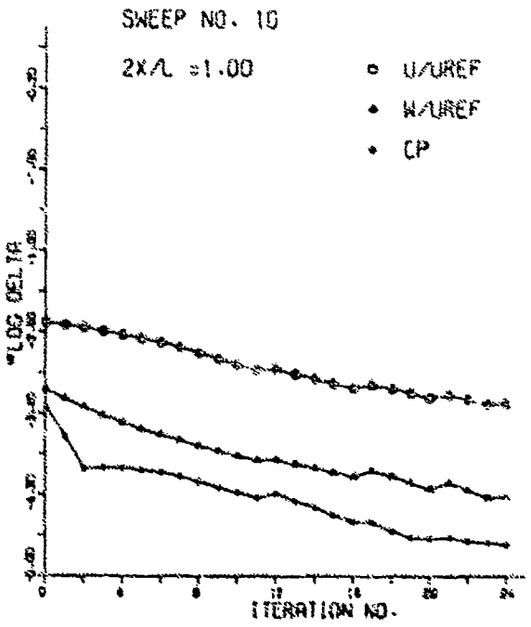

Fig. 5 Convergence history of local iteration process

Convergence of global iteration process

The global iteration process started with two sweeps on a mesh with a fourfould step size in x-direction ($\Delta x = 0.08L$), followed by three sweeps with $\Delta x = 0.04L$. Subsequently, five sweeps were made on the finest mesh ($\Delta x = 0.02L$). The last sweeps were restricted to the region near the stern ($0.6 < 2x/L < 1.4$) because elsewhere the pressure field had already converged to 10^{-4} (C_p value).

The convergence is illustrated in Figs. 6 and 7, where the wall pressure along a line ζ = constant has been plotted versus x for several sweeps. The changes in the pressure between the 8th and the 10th sweep are hardly noticeable on the scale of the figures. After the 10th sweep, everywhere the C_p-convergence was better than 10^{-3}. The robustness of the process may even better be appreciated by examining Fig. 8, in which the change of the wall pressure between successive sweeps on the finest grid has been plotted. There is a monotonous reduction of the change by approximately a factor 2 per sweep. Notice also the upstream shift of the peaks by one step per sweep.

We conclude that the performance of the global iteration process is quite satisfactory.

Miscellaneous results

Lines of equal velocity in x-direction are shown for some stations in Fig. 9. A sequence of vector plots, showing the transverse velocity components in the wake, is presented in Fig. 10. A vortical motion can be observed,

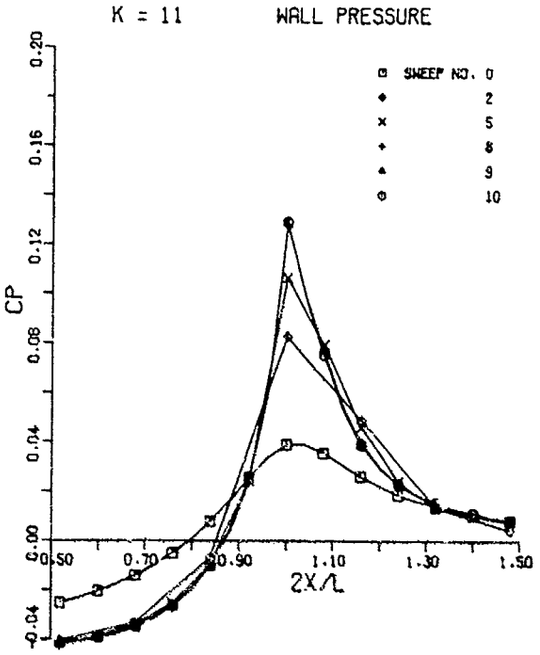

Fig. 6 Convergence of global iteration process

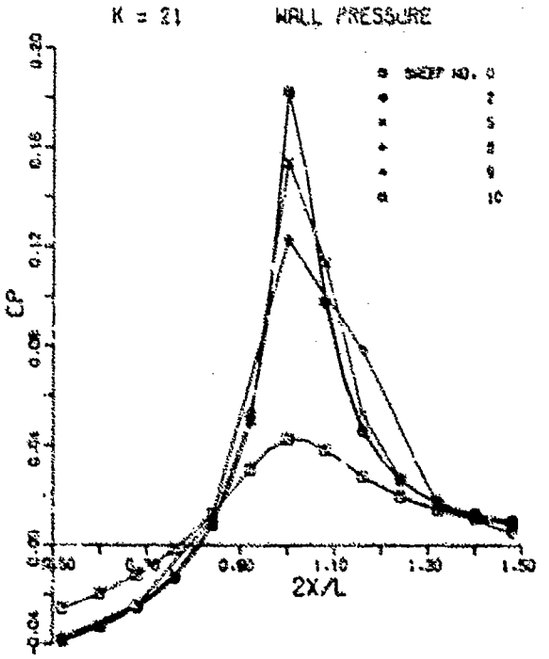

Fig. 7 Convergence of global iteration process

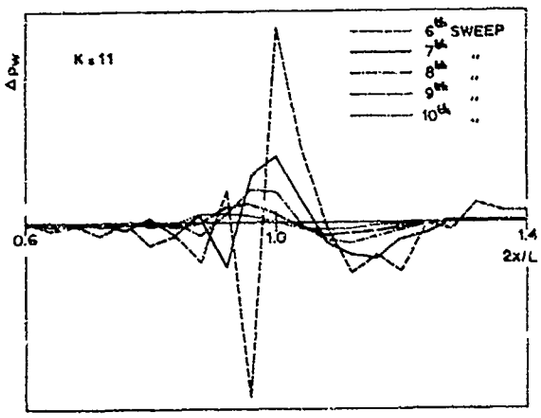

Fig. 8 Change of wall pressure in subsequent sweeps

spreading gradually with increasing x. Notice, however, that the transverse velocities are only a few per cent of the ship speed. The flow pattern looks a lot better than similar results in /1/, which displayed false longitudinal vorticity near the outer boundary. The difference must be attributed primarily to the greater width of the calculation domain. In other words, viscous-inviscid interaction ought not to have been neglected in /1/.

A comparison of the wall pressure in viscous flow (as computed by PARNASSOS) and in potential flow (Hess & Smith solution) is given in Fig. 11. Obviously, viscosity tends to equalise the pressure. Significant viscous effects are present only very close to the stern as may be expected for a slender ship like the Wigley hull. The wall pressure at 2x/L = 1.0 is compared with experimental data at a somewhat lower Rn /17/ in Fig. 12. Taking into account the difference in Rn (the pressure at the stern increases with increasing Rn) the correspondence is quite good.

The total computation time for this case, including the running time of the grid generation and potential flow programs, amounted to ca. 4000 CPU seconds on a Cyber 175 computer.

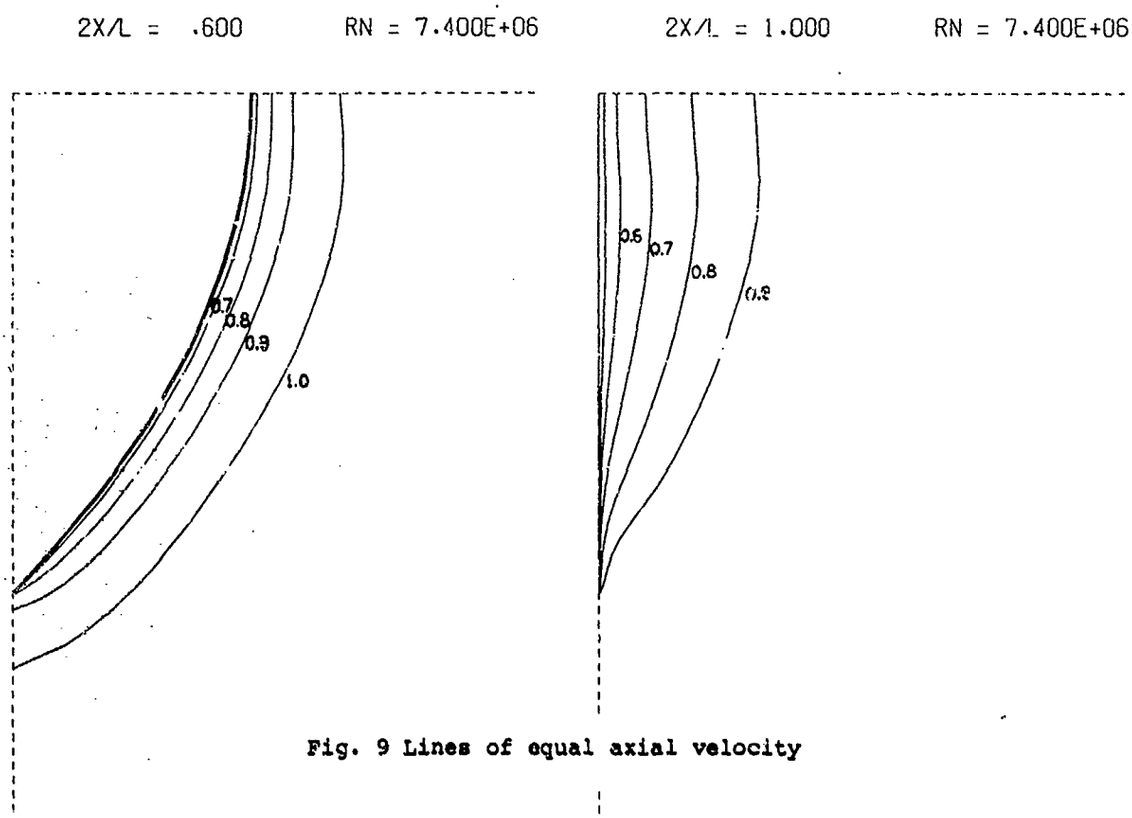

Fig. 9 Lines of equal axial velocity

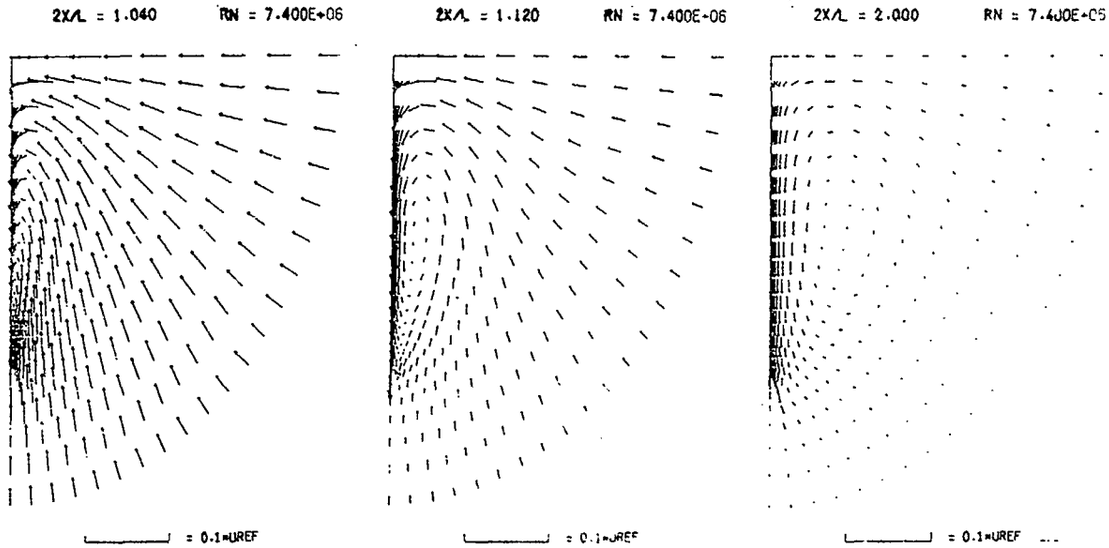

Fig. 10 Transverse velocity components in the wake

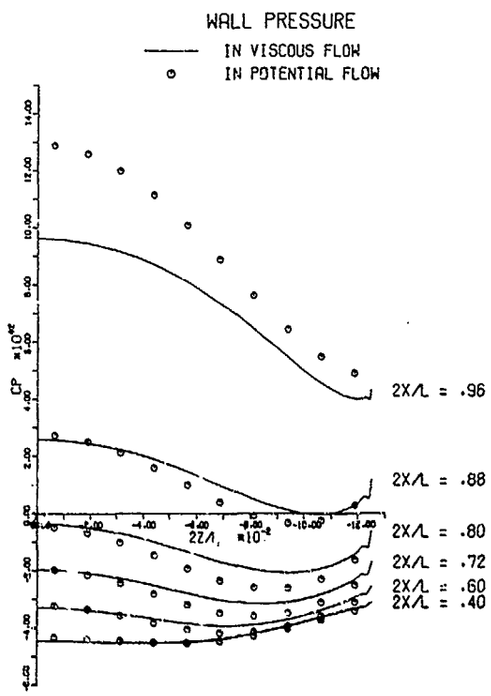

Fig. 11 Comparison of wall pressure in potential and viscous flow

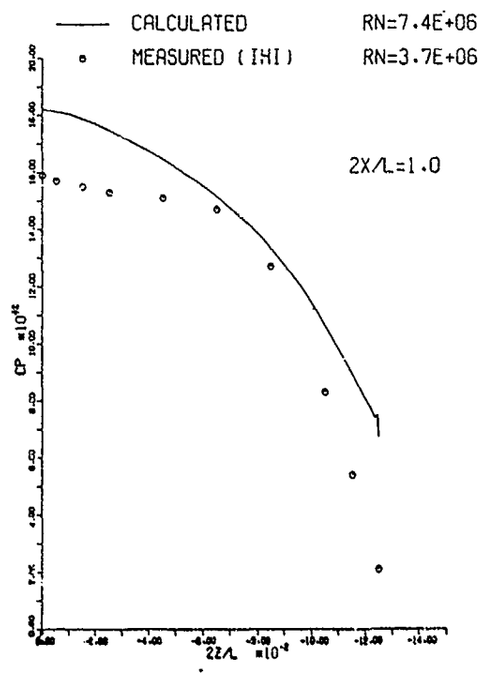

Fig. 12 Comparison of wall pressure at $\frac{2x}{L} = 1.0$ with experimental data

VI. Conclusions

In the foregoing a method has been presented for the solution of the Parabolised Navier-Stokes equations in external flow applications. The use of a general boundary-fitted coordinate system warrants the applicability of the method to a wide range of ship forms. Three momentum equations plus the continuity equation are solved in contravariant formulation, the pressure and the velocity components in the direction of the coordinate axes of the body-fitted system being the dependent variables. The solution is obtained in a multiple sweep marching procedure which involves two iteration processes, viz. a global iteration process (multiple sweeps) to recapture the elliptic nature of the equations and a local iteration process at each step of the downstream marching procedure.

From the application of the method to the flow past the stern of a slender mathematical ship form (Wigley hull) the following conclusions may be drawn:

1. By the introduction of a source term and by adopting a step-size reduction scheme, a safe and efficient global iteration process has been achieved. In 10 sweeps the pressure field converged to within 0.1% of the stagnation pressure.
2. The convergence characteristics of the local iteration process are unfavourably influenced by the presence of a grid singularity. Although the associated problems have been alleviated by using physical instead of contravariant velocity components and by modifying the explicit/implicit splitting of the QUICK scheme, the rate of convergence is still not as good as one would wish. This does not alter the fact that the final solution satisfies convergence criteria that are amply sufficient for practical purposes.
3. The efficiency of the solution procedure has been greatly improved by updating the coefficients in only a part of the cycles of the local iteration process.
4. Improvements due to Stone's partial canceling scheme were found to be too small to justify its application.
5. Further work is needed on turbulence modeling, the solution near a grid singularity and the overall efficiency. Additional applications, including viscous-inviscid interaction, to more complicated ship forms are to be made.

References

1. Raven, H.C. and Hoekstra, M.: "A Parabolised Navier-Stokes Solution Method for Ship Stern Flow Calculations", 2nd Int. Symp. on Ship Viscous Resistance, Göteborg, March 1985.
2. Hoekstra, M.: "A Generalised Schwarz-Christoffel Transformation for Coordinate Generation in Symmetrical Interior, Exterior and Annular Domains", NSMB Report No. 50304-3-SR, October 1983.
3. Briley, W.R. and McDonald, H.: "Three-dimensional Viscous Flows with Large Secondary Velocity", Jnl. Fl. Mech., Vol. 144, pp. 47-77, 1984.

4. Rubin, S.G. and Lin, A.: "Marching with the Parabolized Navier-Stokes Equations", Israel Jnl. Technology, Vol. 18, 1980, pp. 21-31.
5. Patankar, S.V. and Spalding, D.B.: "A Calculation Procedure for Heat, Mass and Momentum Transfer in Three-Dimensional Parabolic Flows", Int. Jnl. Heat and Mass Transfer, Vol. 15, 1972, pp. 1787-1805.
6. Harlow, F.H. and Welch, J.E.: "Numerical Calculation of Time-Dependent Viscous Incompressible Flow of Fluid with Free Surface", Physics of Fluids, Vol. 8, pp. 2182-2189, 1965.
7. Cebeci, T. and Smith, A.M.O.: "Analysis of Turbulent Boundary Layers", Academic Press, Novembe 1974.
8. Cebeci, T. and Meier, H.U.: "Modelling Requirements for the Calculation of the Turbulent Flow around Airfoils, Wings and Bodies of Revolution", AGARD Conf. on Turbulent Boundary Layers - Experiments, Theory and Modelling, The Hague, Sept. 1979.
9. Israeli, M. and Lin, A.: "Numerical Solution and Boundary Conditions for Boundary Layer Like Flows", 8th Int. Conf. on Num. Methods in Fluid Dyn., Aachen, June 1982.
10. Rubin, S.G. and Reddy, D.R.: "Analysis of Global Pressure Relaxation for Flows with Strong Interaction and Separation", Computers and Fluids, Vol. 11, pp. 281-306, 1983.
11. Leonard, B.P.: "A Stable and Accurate Convective Modelling Procedure Based on Quadratic Upstream Interpolation", Comp. Meth. Appl. Mech. and Eng., Vol. 19, June 1979, pp. 59-98.
12. Han, T., Humphrey, J.A.C. and Launder, B.E.: "A Comparison of Hybrid and Quadratic-Upstream Differencing in High Reynolds Number Elliptic Flows", Comp. Meth. Appl. Mech. and Eng., Vol. 29, Oct. 1981, pp. 81-95.
13. Stone, H.L.: "Iterative Solution of Implicit Approximations of Multidimensional Partial Differential Equations", SIAM Jnl. Num. Anal., Vol. 5, Sept. 1968, pp. 530-558.
14. Rubin, S.G.: "Incompressible Navier-Stokes and Parabolized Navier-Stokes Solution Procedures and Computational Techniques", Comp. Fluid Dyn. Lecture Series, Von Karman Inst., March 1982.
15. Meijerink, J.A. and Van der Vorst, H.A.: "Guidelines for the Usage of Incomplete Decompositions in Solving Sets of Linear Equations as They Occur in Practical Problems", Jnl. Comp. Phys., Vol. 44, pp. 134-155, 1981.
16. Hogben, N.: "Record of a Boundary-Layer Exploration on a Mathematical Ship Model", NPL Ship Report 52, July 1964.
17. Kajitani, H.: "An Evaluation and Visualization of Viscous Flow around Wigley Model", 2nd Int. Symp. on Ship Viscous Resistance, Göteborg, March 1985.

DISCUSSION
of the paper
by M. Hoekstra, H.C. Raven

SHIP BOUNDARY LAYER AND WAKE CALCULATION WITH A PARABOLISED NAVIER-STOKES SOLUTION SYSTEM

DISCUSSION
by V.C. Patel

1. In the paper, it is noted that the influence of pressure propagates upstream one step per sweep. The convergence of the complete solution in 10 global sweeps is quite surprising in view of this and the fact that the number of streamwise steps appears be to greater than 10 even in a coarse mesh.

2. The generation of the coordinates by conformal mapping of different sections may present numerical difficulties in connecting the sections in the axial direction and in the evaluation of the geometric terms associated with the variations in that direction when the method is applied to ship hulls with rapid changes in the stern geometry.

3. The outer boundary of the solution domain is placed at two boundary-layer thicknesses from the hull and potential-flow conditions are prescribed there. There are two disadvantages to this. One is that the boundary layer thickness is not known a priori and therefore a rather generous allowance must be made for it and the wake. The second is that the solutions must be repeated several times, updating the outer potential flow each time, to account for the viscous-inviscid interaction.

4. Although I fully appreciate your position on the use of the normal momentum equation to update the pressure, this approach would make future vectorization of your program rather difficult, if not impossible.

5. Our experience with the Wigley hull indicates that this is a weak interaction problem. New difficulties arise when such methods are applied to the strong interactions present on practical hull forms.

Author's Reply

We thank Professor Patel for his comments. Our replies are as follows:
1. Obviously convergence always means that further changes are less than a specified tolerance. Although the upstream influence of the pressure is strictly speaking of infinite extent, there is only a bounded domain where it exceeds that tolerance. In the present case this bounded region can be covered in 10 sweeps. Furthermore it may be noticed that the number of steps the pressure may have travelled is 19 instead of 10: we made two sweeps with a fourfold step size, three with a double stepsize and 5 with a single stepsize.

2. The conformal mapping at each transverse plane is determined by the shape of the frameline and the outer boundary. Therefore a longitudinal connection of corresponding points results in a grid that is at least as smooth as the hull itself. Rapid changes in stern geometry will require a small longitudinal step size, regrdless of the grid generation procedure.

3. The great advantage of using separate solution methods for viscous and inviscid flows is the efficiency. A panel method is far more efficient in solving the inviscid flow than a finite-difference method, and it allows us to put the grid points where they are really needed: in the viscous domain. The need to make a generous guess of the thickness of the viscous domain does not basically change this. Although we have neglected the viscous-inviscid interaction up to now we plan to incorporate it in the global iteration by updating the inviscid flow between sweeps. This will only moderately increase the calculation time.

4. It is not quite clear to us why our treatment of the normal momentum equation would inhibit vectorization, since it has the same 5-point star form as the other momentum equations. A greater obstacle might be the recurrent formulation of matrix solvers (the SIP in our method, the tridiagonal matrix algorithm in yours).

We have already successfully applied our method to a number of more critical cases (separation bubbles, vortex separation, trailing edge flows), see our Ref. 1. Application to practical hull forms will presently be undertaken.

DISCUSSION
by H. Wang

First, I would like to express my appreciation of your outlining the computational details of your approach. Calculation accuracy and computer time requirements can vary greatly among two nominally similar approaches, in this case the parabolised Navier-Stokes solution system. For example, you point out that your approach of fixing the L and U matrices in Eq. (16) for a number of iterations reduces computer time by one-half.

I would like to know if you tried other variations at your downstream outlet plane, for which you set $p_\xi = 0$ at $x/L = 1.0$, i.e., the wake extends 0.5L aft of the ship stern. While it seems reasonable that $p_\xi \approx 0$ at this point, viscous flow variables such as velocities and thicknesses may still be noticeably different from asymptotic values. Did you check the values of these variables at the outlet plane? Also, the choice of wake length should depend on the stern shape as well as ship length, i.e., a blunt stern would require a longer wake length.

Author's Reply

We did not test other downstream pressure conditions in the present case. Less restrictive conditions would be e.g. $P_{XX} = 0$ or $P_X = (P_E)_X$. But, because in the rear part of our domain, C_p <0.004 and P_X is about 0.3.% of the maximum pressure gradient this is not supposed to have any influence on the results. We could not check the calculated velocities against asymptotic values since the latter are not known for general 3D flows. It may be noticed that the PNS equations do not require the specification of a downstream boundary condition for the velocities. The choice of the location of the down-stream boundary is not much of a problem. In the first sweeps a long domain can be chosen, which for later sweeps can be truncated based on an assessment of the intermediate results.

NUMERICAL SOLUTIONS OF THE FLOW OVER THE STERN AND IN THE WAKE OF SHIP HULLS

by

H.C. Chen and V.C. Patel

Iowa Institute of Hydraulic Research
The University of Iowa
Iowa City, Iowa 52242 USA

ABSTRACT

The numerical method for the solution of the partially-parabolic Reynolds equations, being developed by the authors [5,6,7], has been extended and applied to calculate the flow over the stern and in the wake of double models of ship hulls. The results are compared with the available water-channel and wind-tunnel data to illustrate the capabilities of the method and, at the same time, point out the major difficulties not only in the development of comprehensive numerical methods but also in assessing their performance. Although quite encouraging results have been obtained for both cases, this study indicates the need for improvements in grid-generation techniques and handling of the wall boundary conditions in turbulence models in numerical methods.

I. INTRODUCTION

As evidenced by the papers presented at the two recent meetings on ship viscous resistance [1,2], and those in the viscous-flow sessions at the last three ONR Symposia on Naval Hydrodynamics, considerable research effort has been devoted in recent years to the development of numerical calculation procedures for the complex turbulent flow over ship sterns and in ship wakes. An overview of the different types of approaches can be found in the Report of the Resistance Committee of the 17th ITTC [3]. Following a review of the then available experimental data, Patel [4] made several observations concerning the most desirable characteristics of calculation methods for such flows. On that basis, the authors have developed a new method. This was first presented in [5], along with typical results for two-dimensional, axisymmetric and simple three-dimensional flows. Since then, the method has undergone some revisions, particularly with respect to the calculation of the pressure field, and it has been subjected to numerous additional tests. The basic elements of the method are described in some detail in [6], and a comprehensive set of calculations for the relatively simple and experimentally well-documented case of axisymmetric flow are presented in [7].

The present paper is concerned with the application of the method to the three-dimensional flow on arbitrary ship hulls. The important features of the method are first summarized and some of the major changes made since the publication of [6] are described. Two particular hulls are then selected to demonstrate the potential of the method. These are the Wigley hull and the SSPA Cargo Liner, for which extensive data are available. These forms demonstrate the practical difficulties of generating numerical grids which satisfy all of the conflicting requirements for accurate calculations of the flow over ship hulls. Since such difficulties are expected to arise in all numerical techniques, this aspect of the problem is discussed in some detail. Finally, the results of the calculations are compared with experiments.

II. OUTLINE OF THE CALCULATION METHOD

It is assumed that the flow over the stern and in the wake of a ship hull can be adequately described by the so-called partially-parabolic (or semi-elliptic, or parabolized) Reynolds-averaged Navier-Stokes equations. Thus, viscous and turbulent diffusion terms in a preselected, predominant flow direction are neglected. Although this assumption is usually invoked so that marching numerical techniques can be used, here it is not very critical since the solution to a steady problem is sought by a time-marching scheme and, as demonstrated in [7], the algorithms of the present method can be readily generalized to a fully-elliptic (i.e., to the full Reynolds equations) capability.

The independent space variables in the complete equations are first transformed into a general, nonorthogonal coordinate system. This is a partial transformation since the dependent variables, namely the velocity components, are left in a convenient ship-

based orthogonal system, say $x^i (i = 1,2,3)$. The second derivatives with respect to the transformed longitudinal coordinate are then neglected, making the equations parabolic in that direction. For turbulent flow, closure of the equations is effected by the well known k-ε model, the two differential equations of which are approximated in the same manner. Thus, the problem is reduced to the solution of five convective-transport equations of the form

$$g^{22}\phi_{\eta\eta} + g^{33}\phi_{\zeta\zeta} = 2A_\phi\phi_\zeta + 2B_\phi\phi_\eta + D_\phi\phi_\xi + E_\phi\phi_t + S_\phi \qquad (1)$$

with $\phi = (U,V,W,k,\varepsilon)$, and the equation of continuity

$$(b_1^1U + b_2^1V + b_3^1W)_\xi + (b_1^2U + b_2^2V + b_3^2W)_\eta + (b_1^3U + b_2^3V + b_3^3W)_\zeta = 0 \qquad (2)$$

in the six unknowns: ϕ and p, where p is the pressure which is contained in the source terms S_ϕ, (U,V,W) are the components of the mean-velocity vector in the orthogonal coordinates x^i, k is turbulent kinetic energy, ε is its rate of dissipation, and the coefficients involve terms arising from the transformation of the orthogonal coordinates to the numerical coordinates (ξ,η,ζ).

As explained in [6], the first step in the calculation procedure is to select a solution domain in the physical plane, determine the appropriate boundary conditions, and then construct a computational grid. Here we use a solution domain that is large enough to capture the entire zone of viscous-inviscid interaction and therefore avoid the need to perform separate viscous- and inviscid-flow solutions, and iterative matching between them. Thus, in both transverse directions the solution domain extends from the ship surface and the wake centerline to distances of the order of one ship length, where the appropriate boundary conditions are simply zero pressure and constant axial velocity. In place of the no-slip condition on the hull surface, we use a modified "wall-function" approach which requires that the law-of-the-wall (suitably extended to three-dimensional flows and including stress-gradient corrections) and turbulence equilibrium conditions are satisfied at two grid points adjacent to the surface. This establishes a relationship between the wall-shear velocity U_τ and the boundary conditions required at the first grid node for the numerical solution. In the longitudinal direction, the solution domain extends from about midships, where thin boundary-layer conditions are prescribed, to several ship-lengths downstream of the stern, where parabolic conditions, appropriate for a far wake, are enforced.

The coordinates in the solution domain are generated numerically from a solution of three Poisson equations relating the numerical coordinates (ξ,η,ζ) to the physical orthogonal coordinates (x^i) with metrics h_i:

$$g^{11}x^i_{\xi\xi} + g^{22}x^i_{\eta\eta} + g^{33}x^i_{\zeta\zeta} + 2g^{12}x^i_{\xi\eta} + 2g^{13}x^i_{\xi\zeta} + 2g^{23}x^i_{\eta\zeta} + f^1x^i_\xi + f^2x^i_\eta + f^3x^i_\zeta = \frac{1}{h_1h_2h_3}\frac{\partial}{\partial x^i}\left(\frac{h_1h_2h_3}{h_ih_i}\right);\ i = 1,2,3 \qquad (3)$$

These equations involve the specification of the three grid-control functions f^i, which are chosen to obtain the desired concentration of the grid in the neighborhood of solid surfaces and in regions of large changes in the flow properties. In order to facilitate the application of wall boundary conditions, it is necessary to impose two further requirements on the grid. First, it is desirable to adopt a grid that is orthogonal at the boundaries, and second, for the two-point wall function approach used here it is necessary to ensure that the first two grid points near the surface lie in the law-of-the-wall region. The three grid-control functions are obviously insufficient to ensure a grid that satisfies all of these requirements. In practical applications, therefore, certain trade-offs have to be made. These will be discussed later with reference to specific hull forms.

Once the numerical grid has been generated, the geometric coefficients in equations (1) and (2) are known. These equations are solved in successive iterations. The transport equations (1) are solved first using the so-called finite-analytic method by assuming that the pressure gradients, which occur in the source terms, are known (e.g., zero pressure throughout the solution domain at the outset). In the finite-analytic method, the equations are first linearized in each local rectangular numerical element ($\Delta\xi=\Delta\eta=\Delta\zeta=1$) and solved analytically using a combination of linear and exponential functions for boundary conditions. The solution provides a discretization formula which relates the value of ϕ at the center of the element to the (still unknown) values at the corner points of the element. An assembly of these results in a system of algebraic equations for the nodal values, which is then solved by standard techniques. The partially-parabolic approximations enable such a solution to be marched from upstream to downstream.

The pressure field assumed in the solution of the transport equations is next updated by the use of a two-step pressure-correction procedure similar to the well known SIMPLER algorithm. In almost all previous applications of such procedures, the solutions have been marched from upstream to downstream, in order to minimize computer storage. However, this approach leads to rather slow convergence of the iterations between the velocity and pressure fields. Since the pressure field is elliptic, it is indeed possible to solve the pressure equations by marching upstream from the downstream boundary. Although this approach involves some increase in storage, the rate of convergence of the overall solution is greatly accelerated. Indeed, the pressure information propagates throughout the domain within the first iteration.

The complete solution procedure thus involves downstream-marching calculations of the transport quantities, followed by a solution of the pressure field. For a given velocity and turbulence field, i.e. after each solution of the transport equations, the pressure-correction equations are solved to convergence by several internal iterations, yielding a global pressure correction scheme. In almost all cases that have been calculated thus far, convergence has been achieved in less than 25 global sweeps, i.e., velocity and pressure updates. Further details of the equations and numerical solution procedures are contained in [6].

III. SHIP HULLS CONSIDERED

Among the ships for which calculations have been carried out with the present method are the Wigley parabolic ship and the SSPA Cargo Liner. The former, which is among the four hull forms selected for the ITTC Cooperative Experimental Program [3], has been used as a test case in many analytical and numerical studies of wave resistance and for comparisons of results obtained with the different approaches to this problem. Quite extensive data exist for this hull not only on the resistance components and wavemaking [3], but also on the viscous flow on double models. Measurements of the mean-velocity field and Reynolds stresses on double models have been reported by Hatano and Hotta [8] and Sarda and Patel [9,10], the latter being particularly detailed, while other experiments are still in progress. Calculations for this case are of special interest since the geometry is simple but the flow exhibits all of the basic features observed on practical forms. For example, usual boundary-layer approximations are not valid all along the sharp keel, there is a large girthwise variation in the thickness of the viscous flow at the stern, and the wake develops from a sharp vertical stern of finite depth. As we shall see, the latter feature poses rather severe problems in grid generation. The second hull is more representative of practical forms. It has been used extensively as a test case for boundary-layer calculation methods [11], all of which break down some distance ahead of the stern. Mean-flow data on a double model of this hull were obtained by Larsson [12], and corresponding measurements of the Reynolds stresses were reported by Lofdahl and Larsson [13,14]. It should be noted, however, that the data for this case are restricted to the flow over the hull and do not extend into the wake. Calculations for both cases will be compared with the available data to illustrate the performance of the method and the difficulties involved.

The framelines and longitudinal sections of the two hulls are shown in Figure 1. The Wigley hull is specified by the equation

$$|Y| = [B/2]\{1-(2X/L - 1)^2\}\{1 - (Z/H)^2\} \qquad (4)$$

where (X,Y,Z) are Cartesian coordinates, as shown, with the origin on the waterline at the bow, L is total length, B = 0.100L is the beam, and H = 0.0625L is the draft. The Cartesian coordinates of the SSPA liner are available only in a tabular form [12].

IV. SOLUTION DOMAINS AND NUMERICAL GRID

For both the hulls considered here, the solution domain in the longitudinal direction extends from midship, X = 0.5L, to far downstream in the wake, X = 2.302L. In the cross-sectional planes, the domain extends from the hull surface and wake centerline to a cylindrical boundary one ship-length, $R = (Y^2 + Z^2)^{1/2} = L$, away from the ship axis. As we shall see later, this is considered adequately far for the application of uniform-flow boundary conditions, i.e., $U = U_o$ and $p = 0$.

In order to generate the numerical coordinates in the solution domain, equations (3) are solved using an exponential scheme [6] after prescribing appropriate grid-control functions f^i. The selection of the grid-control functions is by no means a straightforward procedure. However, since they are independent of the x^i-coordinate system used to describe the physical domain, it is convenient to generate the numerical body-fitted coordinates in terms of the Cartesian coordinates (X,Y,Z) specifying the hull geometry and later transform them to the cylindrical polar coordinate system (X,R,θ) which is used to specify the velocity components in the equations of motion.

For ship-flow calculations it is convenient to choose $\xi = \xi(X)$, i.e., the con-

stant-ξ stations are the transverse sections. With this choice, equations (3) reduce to

$$g^{11}x_{\xi\xi} + f^1 x_\xi = 0 \tag{5a}$$

$$g^{11}r_{\xi\xi} + g^{22}r_{\eta\eta} + g^{33}r_{\zeta\zeta} + 2g^{12}r_{\xi\eta} + 2g^{13}r_{\xi\zeta} + 2g^{23}r_{\eta\zeta} + f^1 r_\xi + f^2 r_\eta + f^3 r_\zeta = \frac{1}{r} \tag{5b}$$

$$g^{11}\theta_{\xi\xi} + g^{22}\theta_{\eta\eta} + g^{33}\theta_{\zeta\zeta} + 2g^{12}\theta_{\xi\eta} + 2g^{13}\theta_{\xi\zeta} + 2g^{23}\theta_{\eta\zeta} + f^1\theta_\xi + f^2\theta_\eta + f^3\theta_\zeta = 0 \tag{5c}$$

relating the numerical coordinates (ξ,η,ζ) to the cylindrical coordinates (x,r,θ) made dimensionless by L. Equivalently, equations (5) can also be written in nondimensional Cartesian coordinates (x,y,z) as

$$g^{11}y_{\xi\xi} + g^{22}y_{\eta\eta} + g^{33}y_{\zeta\zeta} + 2g^{12}y_{\xi\eta} + 2g^{13}y_{\xi\zeta} + 2g^{23}y_{\eta\zeta} + f^1 y_\xi + f^2 y_\eta + f^3 y_\zeta = 0 \tag{6a}$$

$$g^{11}z_{\xi\xi} + g^{22}z_{\eta\eta} + g^{33}z_{\zeta\zeta} + 2g^{12}z_{\xi\eta} + 2g^{13}z_{\xi\zeta} + 2g^{23}z_{\eta\zeta} + f^1 z_\xi + f^2 z_\eta + f^3 z_\zeta = 0 \tag{6b}$$

where $y = r\sin\theta$, $z = r\cos\theta$, and θ is the circumferential or girthwise angle measured from the keel to the waterline. As noted above, the control functions f^i are the same in both coordinate systems and, in principle, equations (5) and (6) yield the same numerical coordinates if the same control functions are employed. Numerically, however, the coordinates used to specify the hull geometry influence the accuracy of the calculated numerical coordinates. Since the variation of the surface coordinates (y,z) is much smoother than that of (r,θ) for the two hulls considered here, it is desirable to use equations (6) instead of (5) for the generation of the numerical coordinates. For the numerical solutions, it is convenient to rewrite equations (6) in the form

$$g^{11}(y_{\xi\xi}-2ay_\xi) + g^{22}(y_{\eta\eta}-2by_\eta) + g^{33}(y_{\zeta\zeta}-2cy_\zeta) + 2g^{12}y_{\xi\eta} + 2g^{13}y_{\xi\zeta} + 2g^{23}y_{\eta\zeta} = 0 \tag{7a}$$

$$g^{11}(z_{\xi\xi}-2az_\xi) + g^{22}(z_{\eta\eta}-2bz_\eta) + g^{33}(z_{\zeta\zeta}-2cz_\zeta) + 2g^{12}z_{\xi\eta} + 2g^{13}z_{\xi\zeta} + 2g^{23}z_{\eta\zeta} = 0 \tag{7b}$$

where a, b, and c are modified control functions defined by

$$2a = -\frac{f^1}{g^{11}}$$
$$2b = -\frac{f^2}{g^{22}} \tag{8}$$
$$2c = -\frac{f^3}{g^{33}}$$

In order to solve equations (7), it is necessary to prescribe the boundary conditions and the control functions. The boundary conditions are determinend by the desired number of grid points in the axial (ξ), radial (η) and circumferencial (ζ) directions. The first station ξ = 1, is located at X = 0.5L, and the last station, ξ = LL, is placed at X = 2.302L. Thus, there are, LL stations in the axial direction. In the radial direction, there are MM points; η = 1 corresponding to the hull and wake centerplane, and η = MM being the exterior boundary, R = L. In the circumferential, or girthwise direction, NN stations are used, with ζ = 2 and NN - 1 corresponding to the keel ($\theta = 0^0$) and the waterline ($\theta = 90°$), respectively; and ζ = 1 and NN used to enforce the plane-of-symmetry conditions. In the calculations presented here, we have used (LL,MM,NN) = (30,19,10) for the Wigley hull and (30,19,14) for the SSPA liner.

There are no general rules for the determination of the most suitable grid-control functions. Thus far, we have utilized rather simple functions, based largely on previous experience with more simple geometries. Since the choice of the distribution of points in the axial direction is relatively easy, we choose

$$2a = \frac{x_{\xi\xi}}{x_\xi} = \text{fn}\ (\xi\ \text{only}) \tag{9}$$

Thus, the function a is related to the preselected distribution of the axial stations, which is chosen to concentrate points near the stern and in the near wake.

In a similar manner, the function c is related to the grid distribution in the circumferential or girthwise direction, $\theta = \tan^{-1}(y/z) = \theta(\zeta)$, on the outer boundary at the upstream station, i.e.

$$2c = \frac{\theta_{\zeta\zeta}}{\theta_\zeta} = \text{fn}\ (\zeta\ \text{only}) \tag{10}$$

This function also remains fixed during the iterative solutions of the grid-generation equations.

The specification of the function b, which controls the grid distribution in the η-direction, requires much greater care

for several reasons. First, in the present treatment of the wall boundary conditions, it is necessary to require at least the first two near-wall grid points to lie in the law-of-the-wall region ($50 < y^+ < 1000$, say). Second, it is desirable, but not necessary, to have an orthogonal grid in the wall region to facilitate the application of these boundary conditions. Third, the grid concentration must be such that there is a sufficient number of points across the viscous region whose thickness varies greatly in the axial as well as in the girthwise directions. Fourth, and perhaps the most difficult, is the problem of obtaining sufficiently accurate solutions in the neighborhood of geometrical singularities (i.e., curvature discontinuities) in the hull, namely along the keel of the Wigley model and at the waterline in the stern region of the double-model of the SSPA liner. It is obvious that not all of these requirements can be met by a single grid-control function. Many different approaches were attempted during the course of the present study, but most led to unacceptable grid behavior either at the keel or along the waterline. For example, requiring b to satisfy the orthogonality condition on the hull and in the planes of symmetry resulted in a cross-over of grid lines at the keel of the Wigley hull and in a very coarse grid distribution through the boundary layer along the waterline of the SSPA liner. A compromise solution, which appears to be satisfactory in both cases, was arrived at by prescribing the grid distribution $z = z(\eta)$ on the keel plane, $\zeta = 2$ ($\theta = y = 0$), and relating the function b to that distribution through

$$2b = \frac{1}{r_\eta}\left(r_{\eta\eta} + \frac{g^{33}}{g^{22}} r_{\zeta\zeta} - \frac{1}{r}\right)\Big|_{\zeta=2}$$

$$= \frac{1}{z_\eta}\left(z_{\eta\eta} + \frac{g^{33}}{g^{22}} z_{\zeta\zeta}\right)\Big|_{\zeta=2} = fn\,(\xi,\eta) \qquad (11)$$

Thus, b is invariant in the circumferential direction. Since b depends upon the transverse curvature of the grid lines in the keel plane (through $z_{\xi\xi}$), which is not known initially, unlike the functions a and c, it has to be updated during the iterative solution of the grid-generation equations until a fully-converged control function and grid is obtained.

With the Neumann boundary conditions specified on all boundaries of the solution domain, equations (7) were solved by a tridiagonal matrix algorithm with an under-relaxation factor of 0.7. For both hulls, the solutions converged within 60 iterations and required approximately 180 seconds on the Prime 9950 computer.

Figures 2 and 3 show several partial views of the numerical coordinates generated for the two hulls. It is seen that the coordinates are nearly orthogonal at each cross section. The adequacy and shortcomings of these coordinates will be discussed following the presentation of the solutions of the partially-parabolic equations obtained with these coordinates.

V. CALCULATIONS AND RESULTS

The numerical grids discussed in the previous section were utilized to solve the partially-parabolic equations (1,2) with the method outlined in Section II. For both hulls, the initial conditions at midship ($X = 0.5L$) were determined from the boundary-layer thickness calculated for the appropriate Reynolds number by the method of Patel et al. [15]. For simplicity, the longitudinal component of velocity, U, within the boundary layer was determined from a 1/7-power law, the transverse component, W, was assumed to be zero (i.e. no crossflow) and, consistent with the boundary-layer approximations, the longitudinal derivative of the normal component, V, was set equal to zero. Outside the boundary layer, the distribution of U was assumed to follow an inverse-square law with distance from the potential-flow velocity at the edge of the boundary layer to the uniform-stream velocity, U_o, at the outer boundary of the solution domain. The distributions of the two turbulence parameters, namely k and ε, were specified from standard flat-plate correlations within the boundary layer and set to zero outside.

The geometric coefficients associated with the numerical grid and the aforementioned initial conditions are the only inputs required in the flow-calculation computer program. The sweeps or global iterations in the solution procedure are started with zero pressure assumed throughout the solution domain. As in the previous calculations [6,7], the solutions converge in about 20 sweeps. For example, Figure 4 shows the pressure distribution along the waterline of the SSPA hull predicted after different iterations. It is seen that quite satisfactory convergence is achieved in 20 sweeps.

Before presenting the results and comparisons with experimental data it is useful to briefly mention some of the experimental details which should be borne in mind in the interpretation of the comparisons and evaluation of the solutions. Data on double models of the Wigley hull have been obtained by Hatano and Hotta [8] in a water channel and by Sarda and Patel [9,10] in a wind tunnel. The former were carried out at a rather low Reynolds number, $Re = U_o L/\nu = 8.0 \times 10^5$, while the latter were made at $Re = 4.5 \times 10^6$. Both include measurements of velocity

profiles and Reynolds stresses at several longitudinal stations, along four potential-flow streamlines in the former, and four waterlines in the latter. Also, the measurements of [8] were made in boundary-layer coordinates, i.e., along local surface normals, while those of [9,10] were carried out in ship-based Cartesian coordinates (X,Y,Z). The mean-flow measurements of Larsson [12] on the double model of the SSPA hull, and the corresponding turbulence data of Lofdahl [13], are also restricted to boundary-layer traverses along a few potential-flow streamlines. Since the calculations are performed in a nonorthogonal body-fitted coordinate system, the transverse sections being one set of coordinate surfaces, direct comparisons of all quantities of interest, e.g. the velocity components and the Reynolds stresses, at all measurement stations is not possible, especially since the data stations are too coarsely spaced to accurately carry out the extensive interpolations that are involved. For example, in the thick boundary layer over the stern, the near-wall measurements correspond to a transverse section which may be considerably upstream of that which corresponds to the data at larger normal distances. It is rather surprising that these difficulties have not received much careful consideration in previous work on this subject.

In view of the aforementioned difficulties, it is possible to make only limited comparisons between the calculations and experiments. As shown earlier, the surface pressure distribution provides an excellent test of the convergence of the solutions. Previous experience with a variety of iterative methods has shown that this is also the most difficult quantity to calculate accurately. At the same time, it is perhaps the easiest quantity that can be measured, although the data are subject to wind-tunnel blockage effects. If the latter can be quantified, comparisons between measured and calculated pressures provide a meaningful test of calculation procedures.

The most direct and quantitative comparisons between experiment and calculations involving the least amount of uncertainty are the velocity profiles across the boundary layer along the two planes of symmetry, namely the keel and the waterline, since on both hulls these lines are straight and no interpolation in the data is required. Unfortunately, there are no data in the waterline plane on the SSPA hull.

As noted above, the differences in the experimental and computational coordinates become particularly important in making comparisons between calculated and measured velocity components at points off the planes of symmetry. Qualitative comparisons can be made of the contours of the longitudinal velocity component (the so-called isowake lines) in a transverse section to provide a picture of the three dimensionality of the stern viscous flow since the magnitude of the longitudinal component is not greatly affected by the choice of coordinates. Nevertheless, such comparisons have to be judged with some caution since the measured contours are determined from data taken along the normals to the hull at a few discrete girthwise stations.

All quantities in the results presented and discussed below have been made dimensionless using the fluid density, ship length L and freestream velocity U_0, as appropriate. Also, with 20 sweeps required to achieve convergence, the solutions for the Wigley and the SSPA hulls took approximately 50 and 75 minutes, respectively, on the Prime 9950 computer.

(a) The Wigley Hull

Figure 5 shows the calculated pressure distributions along the waterline and the keel at $Re = 4.5 \times 10^6$. Also shown are the results of the potential-flow solutions obtained at the DTNSRDC using the XYZ program. The data are due to Sarda and Patel [9,10] and are restricted to the waterline since no pressure taps can be placed along the sharp keel. The data indicate some scatter. Unfortunately, pressure distributions were not measured in the experiments of Hatano and Hotta and therefore it is not possible to ascertain the reasons for the scatter. Nevertheless, it is clear from Figure 5 that the present results are in agreement with the potential-flow solutions in the upstream thin boundary-layer region but are higher than the measurements in the stern region. The level of disagreement between the data and both calculations over the midbody is consistent with the expected tunnel-blockage effect in this experiment but the reason for the disagreement at the stern is not clear.

The development of the boundary layer in the planes of symmetry is shown in Figures 6(a) and 6(b), corresponding to the two Reynolds numbers in the experiments of [8] and [9,10]. Perhaps the most important observation to be made here is that the rapid increase in the boundary-layer thickness along the waterline, and the corresponding decrease along the keel, is captured by the calculations. The development of the girthwise three dimensionality of the viscous domain over the stern, which started with a nearly uniform thickness at midship, is clearly evident. It is also important to note that the keel data of [8] shown in Figure 6(a) are those taken in the vertical centerplane and not along the local surface normal. The flow

in the triangular region between the two is not accessible to thin boundary-layer theory due to the curvature discontinuity. Conventional boundary-layer calculations, which impose plane-of-symmetry conditions along the local surface normal simply ignore this region and therefore predict a much thicker boundary layer at the keel. Although the calculated velocity profiles are in reasonable agreement with both sets of data, some systematic differences are evident, particularly in the near wake. These are associated with the rather coarse grid (see Figure 2) which results from the abrupt termination of the hull at the vertical stern. Further refinement of the grid is obviously needed to explore this region in greater detail.

The calculated contours of constant U-component of mean velocity, and projections of the velocity vector in the transverse planes, are shown in Figures 7 and 8, respectively, at a few representative sections for the higher Reynolds number of [9,10]. The corresponding results at the lower Reynolds number are qualitatively similar. These again indicate the evolution of the three dimensional shear flow over the stern. In particular, Figure 8 shows that, in the transverse sections, the crossflow is directed from the keel towards the waterline. This is the principal reason for the thickening of the boundary layer along the waterline. Even though the data of [9,10] were obtained in transverse sections, the use of Cartesian coordinates in the experiments, and nonorthogonal coordinates in the calculations, imply that a considerable amount of interpolation is required to make meaningful quantitative comparisons. These, and other more detailed evaluations, are still in progress.

(b) The SSPA Hull

The pressure distribution along the waterline and the wake centerline for this hull was presented in Figure 4 to show the rate of convergence of the iterative solutions, but the lack of data along this line precluded any comparison with experiments. The corresponding results along the keel are shown in Figure 9, along with the measurements. Figure 10 shows the girthwise pressure distributions at several transverse sections. As pointed out by Larsson [12] in his original report, the data are subject to wind-tunnel blockage effects. In fact, Larsson carried out potential-flow calculations with and without tunnel constraints to estimate this effect. These estimates have been used here to correct the data. The corrected values are also shown in Figures 9 and 10. It is clear from these that the calculations faithfully reproduce all of the trends observed in the experiments. Figure 10 indicates that the calculations are in better quantitative agreement with the corrected data.

The calculated variation of pressure in the flow field cannot be compared with experiment since such data are usually not available. Nevertheless, this is of interest in the study of viscous-inviscid interaction. Figure 11 shows the calculated pressure field in the vertical centerplane (i.e. the keel plane) at several longitudinal stations in the stern region. From the near uniformity of pressure beyond distances of the order of 0.45L from the hull, it is concluded that the placement of the exterior boundary of the computation domain at a distance of one shiplength is adequate to capture the interaction. The large variation of pressure in the vertical plane is quite surprising in view of the fact that the boundary layer along the keel remains thin. This suggests that the pressure interaction is global. Similar variations of pressure are of course present at all girthwise stations.

The development of the viscous flow in the longitudinal direction is shown in Figure 12 in the form of profiles of the longitudinal velocity component, U. The calculations and measurements along the keel can be compared without ambiguity or uncertainty. However, due to the absence of data in the waterline plane, comparisons have been made here between calculations and experiments at somewhat different stations. At each section, we have chosen the solution along a numerical grid line, ζ = constant, which is closest to a streamline station in the measurements. However, since no interpolations have been made, the difference between the calculations along a grid line in the transverse section and the data in boundary-layer coordinates along the local surface normal must be borne in mind in evaluating these. The differences are estimated to be of the order of 3% of the longitudinal velocity. Even with these uncertainties, it is clear from Figure 12 that the calculations accurately reproduce the high level of three-dimensionality of the flow that develops over the stern from a thin boundary layer of nearly constant thickness at midship. The rapid thinning of the boundary layer along the keel and the equally dramatic growth closer to the waterline is also clearly evident.

The contours of constant U are shown at several transverse stations in Figure 13, along with those determined by Larsson [11] from his measurements [12]. It is seen that the calculations reproduce the growth of the viscous domain in practically all important respects. In particular, the region of the thin boundary layer near the keel and the thickening around midgirth are predicted with reasonable accuracy. The somewhat greater spread of the contours in the outer regions in the experiments is undoubtedly due to the fact that they do not correspond precisely to the transverse sections, as has been noted above.

The projections of the calculated velocity vectors in the transverse sections, shown in Figure 14, provide a picture of the crossflow and normal velocities. We note that, at the upstream sections, the crossflow is directed from the keel to the waterline, as in the case of the Wigley hull. However, closer to the stern, there appears to be a reversal in the direction of the crossflow around midgirth, although the magnitudes are rather small. This reversal is responsible for the local thickening of the boundary layer shown in Figure 13. Thus, the overall flow features are in agreement with the experimental observations. While the present calculations show the development of a weak vortical flow, there is no evidence for the formation of a clearly identifiable longitudinal vortex imbedded in the stern flow.

(c) Some General Observations

In addition to the specific comments already made concerning the results for the two hulls, it is of interest to point out certain other features of the solutions which are common to both hulls. These are as follows:

1) A closer examination of the numerical grids used here (Figures 2 and 3) reveals that they are rather coarse at the extreme stern and in the very near wake. This problem is associated with the abrupt changes in the hull geometries and needs further attention in the grid-generation technique. It appears that grid-control functions other than the simple ones used here may be necessary to resolve the flow in this region without greatly increasing the number of grid points.

2) From Figures 6 and 12 it is evident that the first numerical grid point in the thick boundary layer along the waterline lies at a rather large distance from the hull, leaving the flow in the near-wall region unresolved. This is the result of the requirement that the first grid point be in the region of the logarithmic law-of-the-wall, $y^+ > 50$, say, and is an example of the trade offs that have to be made in the determination of an appropriate numerical grid. At the low Reynolds numbers of the experiments, and with the reduction in the wall shear-stress associated with the locally thick boundary layer, this condition is met at somewhat large distances from the surface. While this is an unexpected limitation of the wall-function approach in three-dimensional flows, it should be remarked that the resulting solutions are still quite accurate outside the wall layer. If the resolution of the wall layer is required, it may become necessary to abandon the wall functions in favor of more elaborate (and computationally more expensive) treatment of the near-wall turbulence.

3) We note that all of the comparisons with experimental data made thus far have been restricted to the flow over the hull in spite of the fact that the solutions extend well downstream into the wake (X = 2.3L). While there is no data in the wake of the SSPA hull, the recent measurements of Sarda and Patel [9,10] on the Wigley hull extend upto X = 1.8L and offer an opportunity to investigate the development of the wake flow. These comparisons will be made after improving the grid resolutions in the stern region. Calculations are also under way for other hull forms for which similar data are available.

4) Comparisons between the calculations and turbulence data which are available for the Wigley and the SSPA hulls need to be examined to ascertain the performance of the turbulence model. This would require more careful consideration of the differences in the coordinates, as already mentioned.

5) Although calculations performed with a coarser grid for the SSPA hull during the course of the present study, and many previous solutions for simpler geometries, indicate that the finite-analytic numerical scheme is remarkably insensitive to grid spacing, systematic studies are necessary to investigate the grid-dependence of the solutions, particularly with regard to the accuracy with which the numerical coordinates describe the rapid changes in hull geometry near the stern.

VI. CONCLUSIONS

The progress made in the development of a very general numerical method for the calculation of the complex, three-dimensional, turbulent flow over the stern and in the wake of arbitrary ship forms has been described. The solutions obtained thus far appear to be quite satisfactory. This study also points out two major difficulties in dealing with complex three-dimensional flows: one is the accurate numerical resolution of such flows in regions of rapid changes in geometry, and the other is the assessment of the results by comparisons with what must be regarded as quite comprehensive experiments. The resolution of the former lies in more detailed numerical investigations, while that of the latter should be addressed jointly in future numerical as well as physical experiments.

ACKNOWLEDGEMENTS

The research reported here was supported jointly by the Office of Naval Research under the Special Focus Research Program in Ship Hydrodynamics, Contract N00014-83-K-0136, and the General Hydromechanics Research Program of the Naval Sea Systems Command, technically administered by the David W. Taylor Naval Ship Research and Development Center, under Contract N00014-81-K-0200.

REFERENCES

[1] Second Int. Sym. on Ship Viscous Resistance, SSPA, Goteborg, Sweden, 18-20 Mar. 1985.

[2] Osaka Int. Colloquium on Ship Viscous Flow, Osaka Univ., Osaka, Japan, 23-25 Oct. 1985.

[3] Report of the Resistance Committee, Proc. 17th ITTC, Goteborg, Sweden, Sept. 1964, Vol. 1, pp. 75-138.

[4] Patel, V.C., "Some Aspects of Thick Three-Dimensional Boundary Layers", Proc. 14th ONR Sym. Naval Hydrodynamics, Ann Arbor, MI, Aug. 1982, pp. 999-1040.

[5] Chen, H.C. and Patel, V.C., "Calculation of Stern Flows by a Time-Marching Solution of the Partially-Parabolic Equations", Proc. 15th ONR Sym. Naval Hydrodynamics, Hamburg, FRG, Aug. 1984, pp. 505-523.

[6] Chen, H.C. and Patel, V.C., "Calculation of Trailing-Edge, Stern and Wake Flows by a Time-Marching Solution of the Partially-Parabolic Equations", Iowa Inst. of Hydraulic Res., IIHR Rept. 28[illegible] Apr. 1985.

[7] Patel, V.C. and Chen, H.C., "The Flow Over the Tail and in the Wake of Axisymmetric Bodies: A Review of the State-of-the-Art", Proc. Osaka Int. Colloquium on Ship Viscous Flow, Osaka, Japan, 23-25 Oct. 1985.

[8] Hatano, S. and Hotta, T., "Turbulence Measurements in the Flow Around a Body in a Circulating Water Channel", Trans. West-Japan Soc. Nav. Arch., Vol. 64, 1[illegible].

[9] Sarda, O.P., Ph.D. Dissertation, The University of Iowa. Under preparation, 1985.

[10] Sarda, O.P. and Patel, V.C., "An Experimental Study of Turbulent Flow Past a Ship Hull", Proc. 5th Sym. Turb. Shear Flows, Cornell Univ., NY, 7-9 Aug. 1985.

[11] Larsson, L. (Ed), "SSPA-ITTC Workshop on Ship Boundary Layers 1980", Proc., SSPA, Goteborg, Sweden, Publ. Nr. 90, 1981.

[12] Larsson, L., "Boundary Layers of Ships. Part III: An Experimental Investigation of the Turbulent Boundary Layer on a Ship Model", SSPA, Goteborg, Sweden, Rept. 86, 1974.

[13] Lofdahl, L., "Measurements of the Reynolds Stress Tensor in the Thick Three-Dimensional Boundary Layer Near the Stern of a Ship Model", Doctoral Dissertation, Chalmers Univ., Goteborg, Sweden, 1982.

[14] Lofdahl, L. and Larsson, L., "Turbulence Measurements Near the Stern of a Ship Model", J. Ship Res., Vol. 28, pp. 186-201, 1984.

[15] Patel, V.C., Sarda, O.P., and Shahshahan, A., "Calculation of Ship Boundary Layers", Proc. 4th Sym. Turbulent Shear Flows, Karlsruhe, FRG, p. 3.1, 1983.

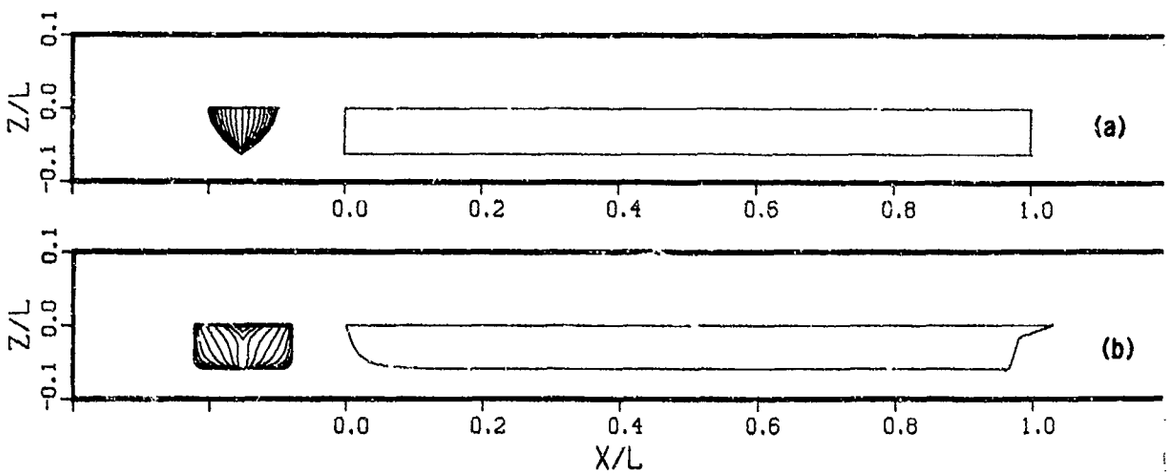

Figure 1. Framelines and Longitudinal Sections of the (a) Wigley, and (b) SSPA, Hulls

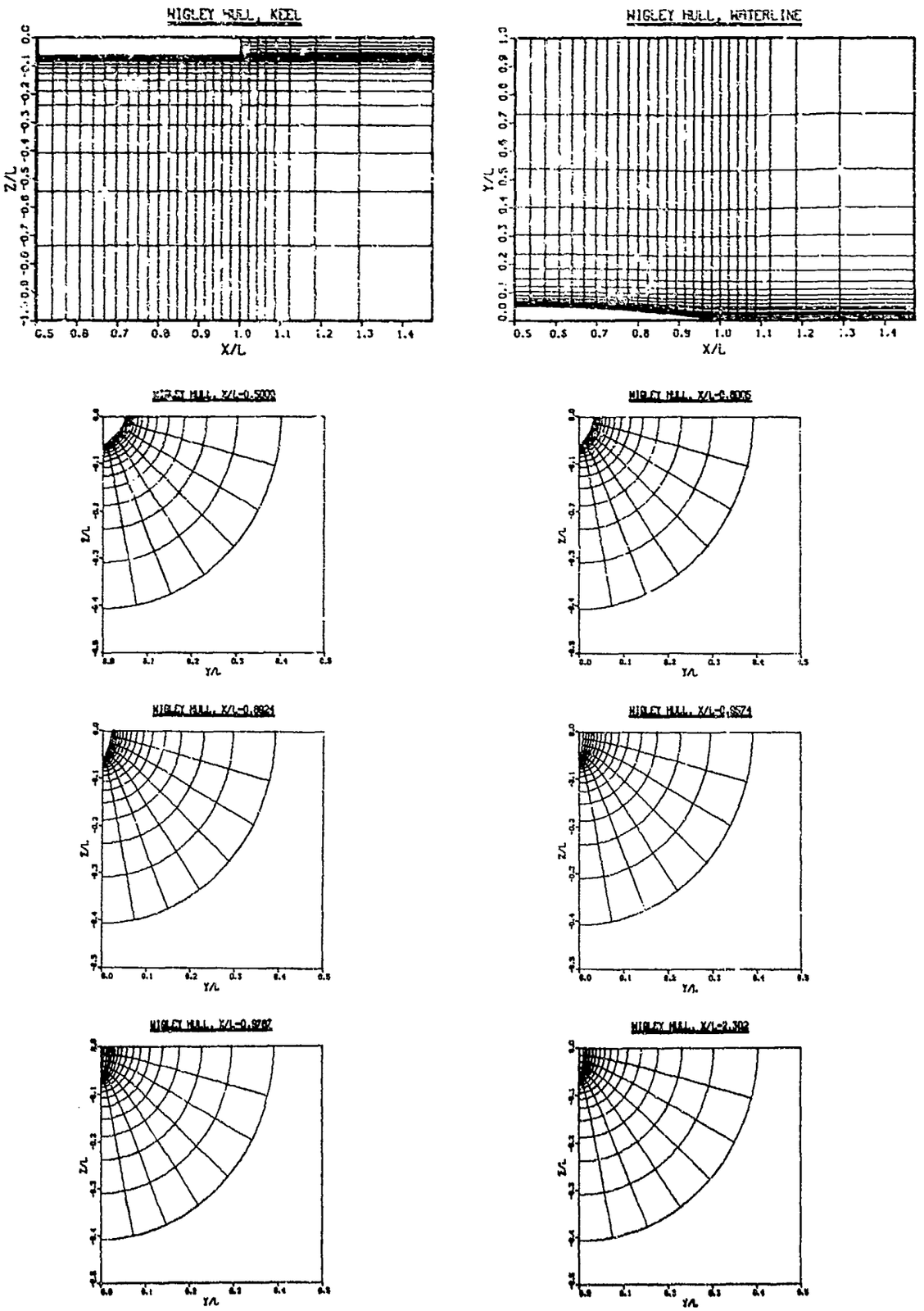

Figure 2. Numerical Coordinates: Wigley Hull (partial views)

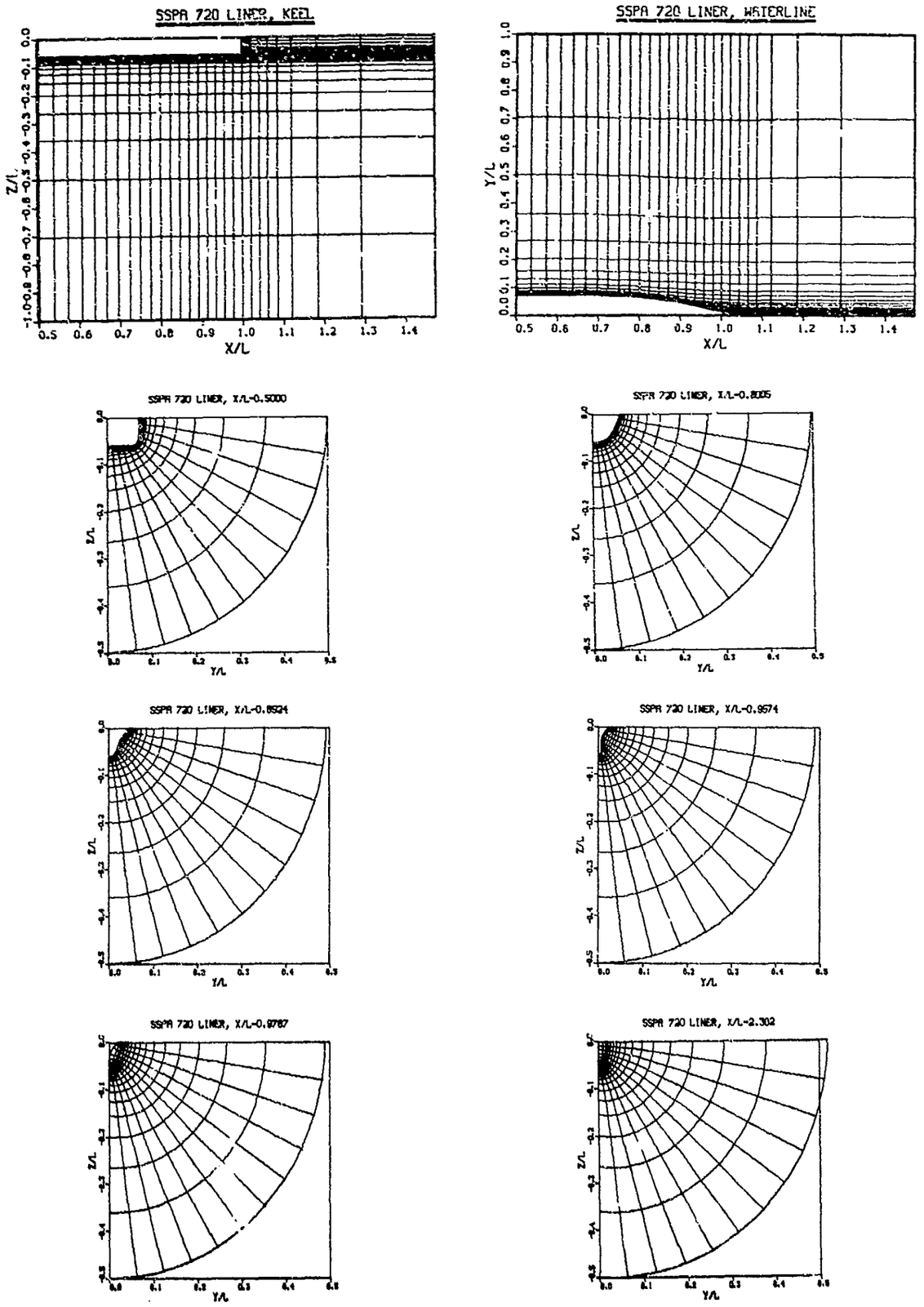

Figure 3. Numerical Coordinates: SSPA Hull (partial views)

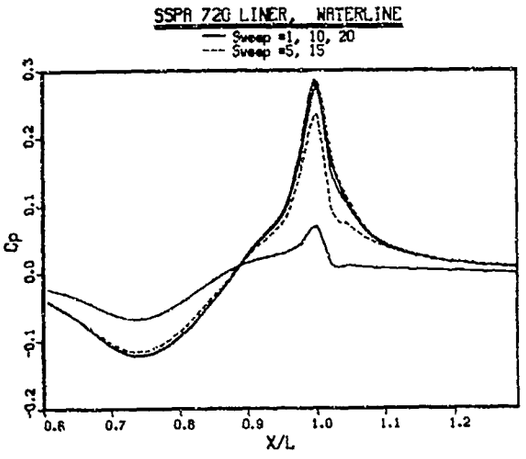

Figure 4. Convergence of Pressure Distribution along the Waterline of the SSPA Hull

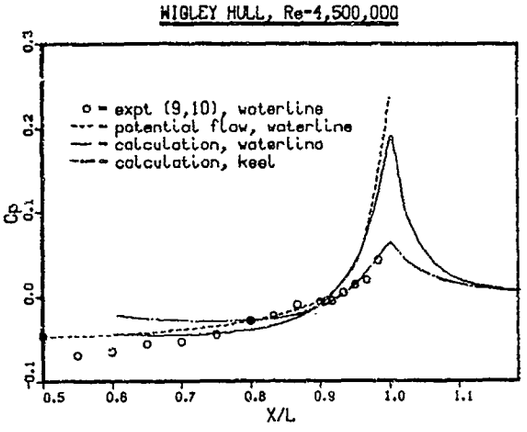

Figure 5. Pressure Distribution along the Waterline and Keel: Wigley Hull

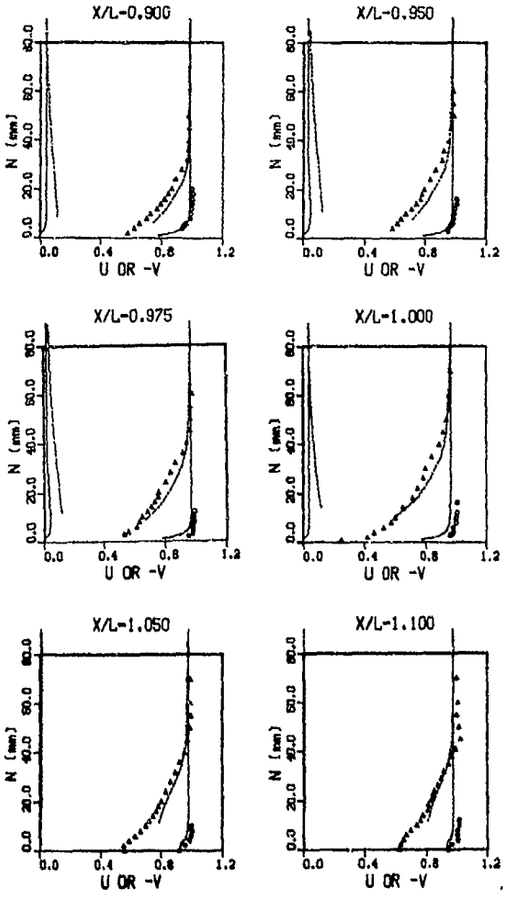

Figure 6(a). Velocity Profiles along the Waterline and Keel: Wigley Hull Experiments of [8]

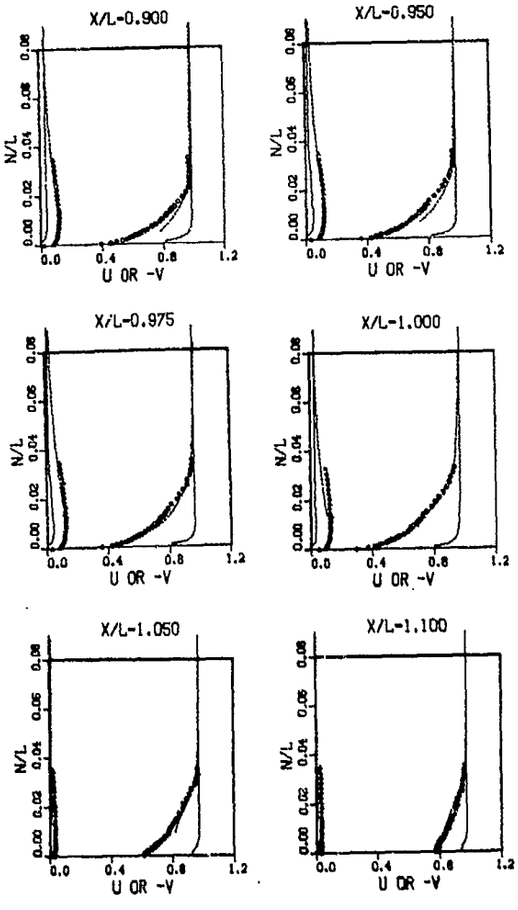

Figure 6(b). Velocity Profiles along the Waterline and Keel: Wigley Hull Experiments of [9,10]

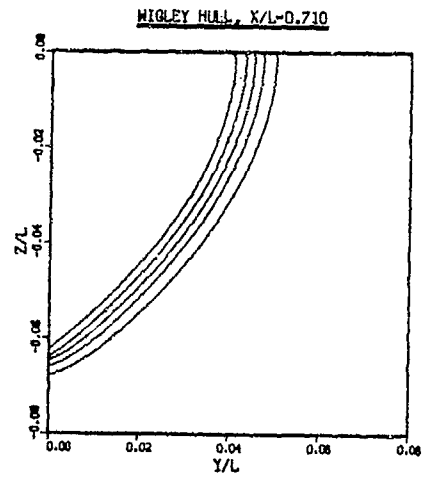

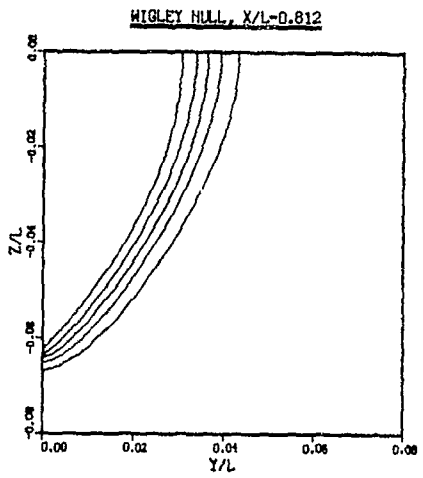

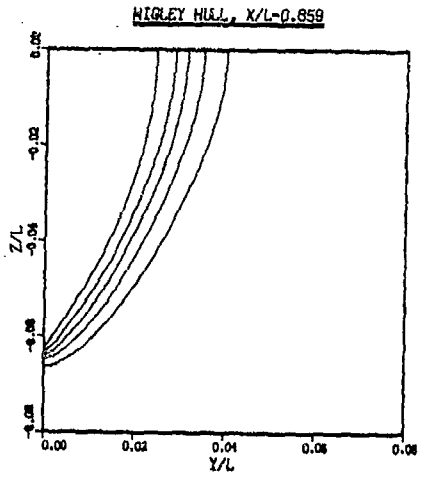

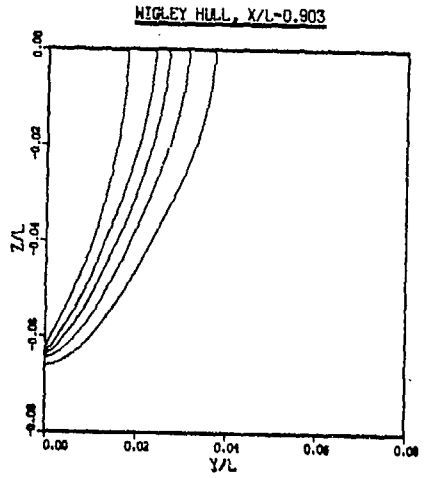

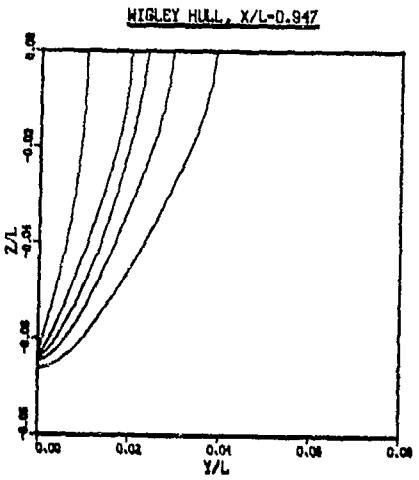

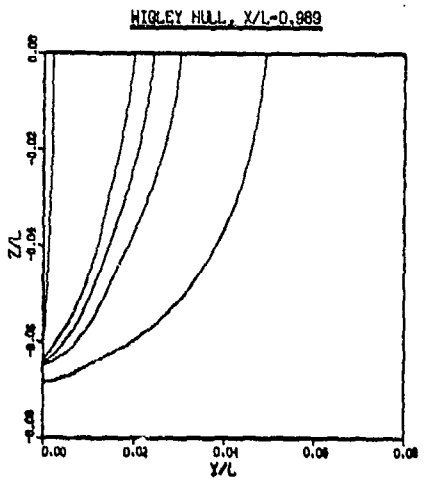

Figure 7. Contours of Constant Axial Velocity (U); Wigley Hull
U/U_0 = 0.8; 0.85; 0.9; 0.95

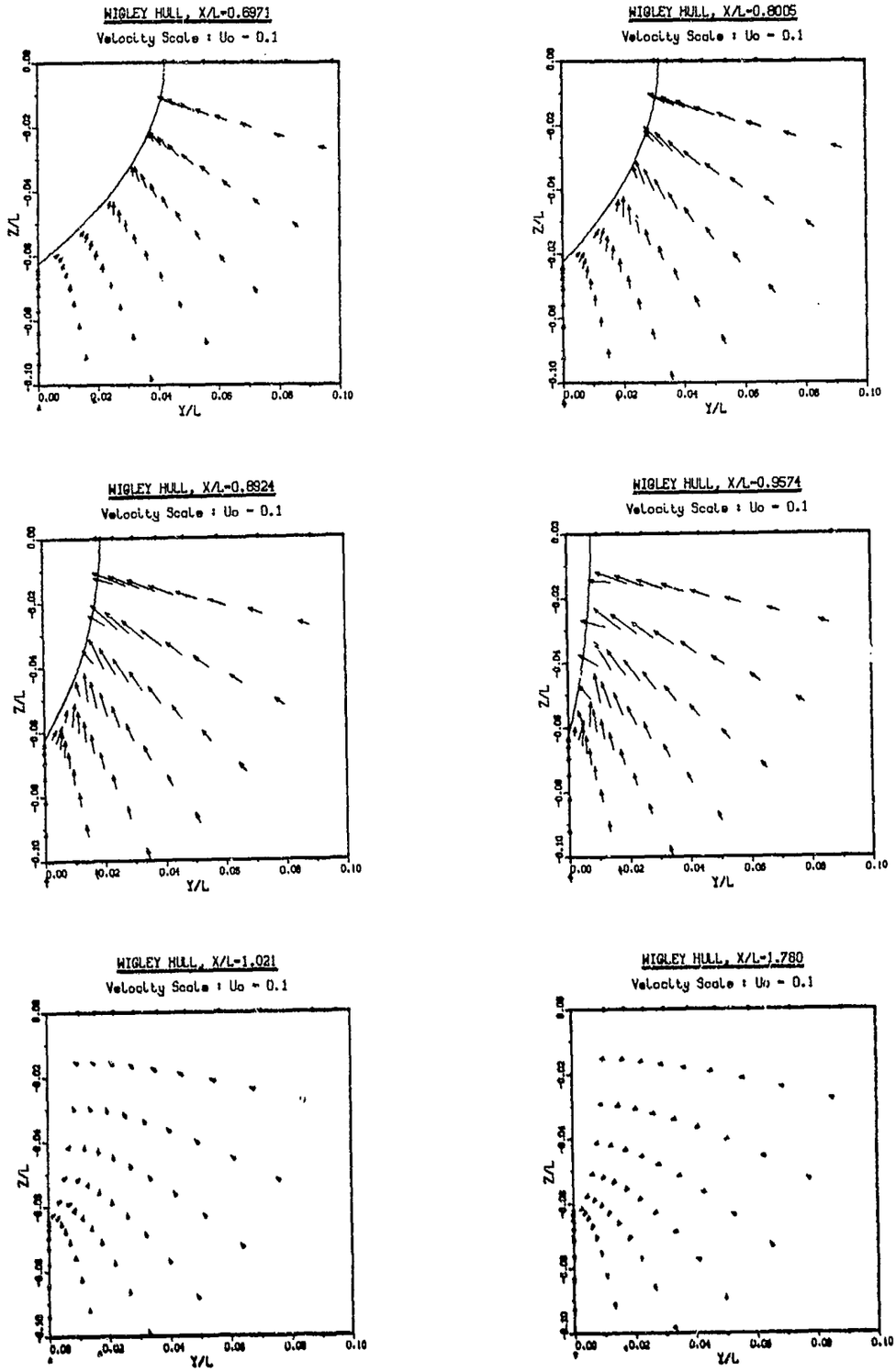

Figure 8. Projections of the Velocity Vector in Transverse Sections; Wigley Hull

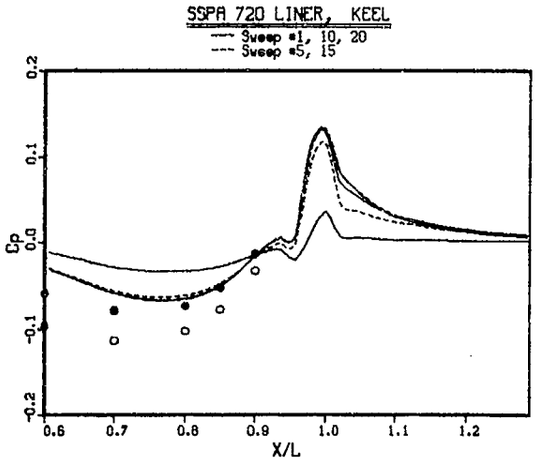

Figure 9. Pressure Distribution Along the Keel of the SSPA Hull o, Experiments [12]; e, Corrected; —— Calculations

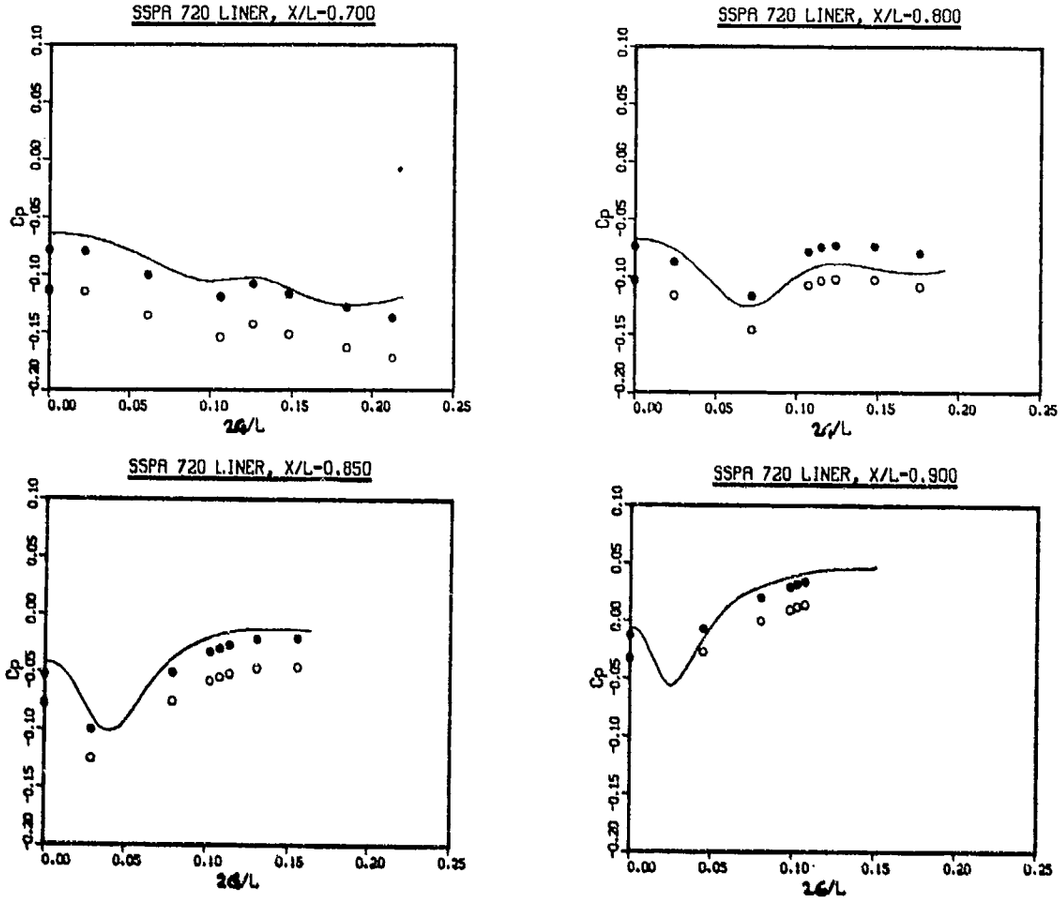

Figure 10. Girthwise Pressure Distributions on the SSPA Hull o, Experiments [12]; e, Corrected; —— Calculations

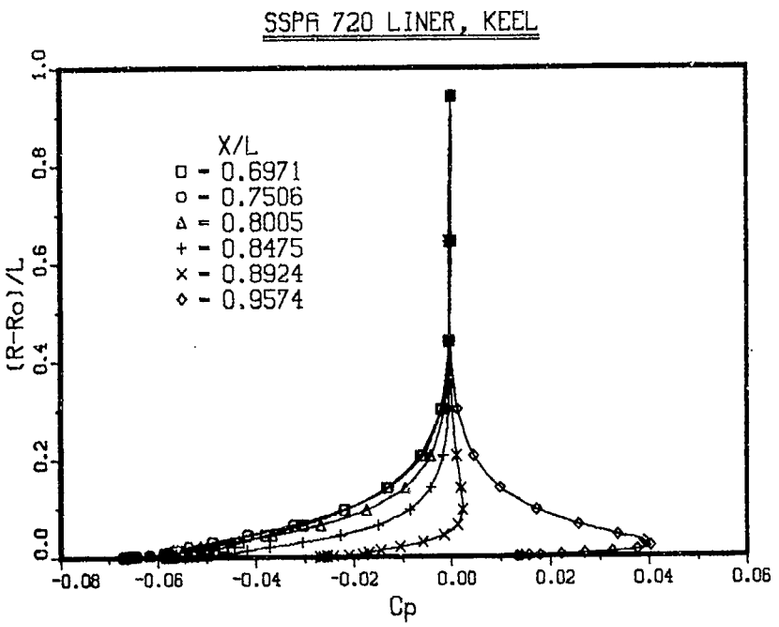

Figure 11. Calculated Variation of Pressure in the Vertical (Keel)Plane: SSPA Hull

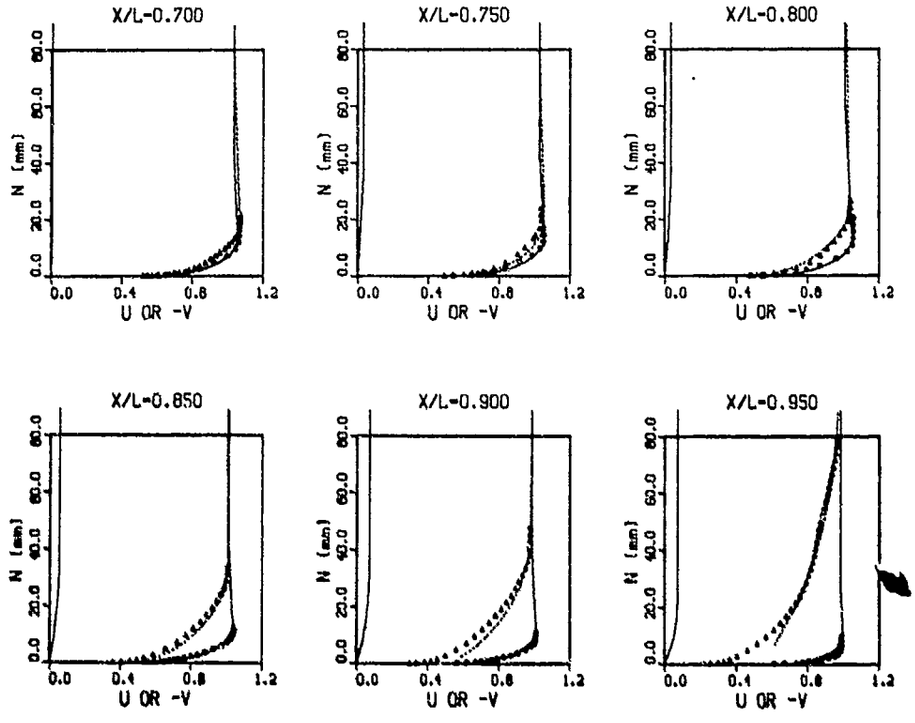

Figure 12. Axial-Velocity Profiles along the Keel and below the Waterline on the SSPA Hull
o,△Experiments; ——— Calculations

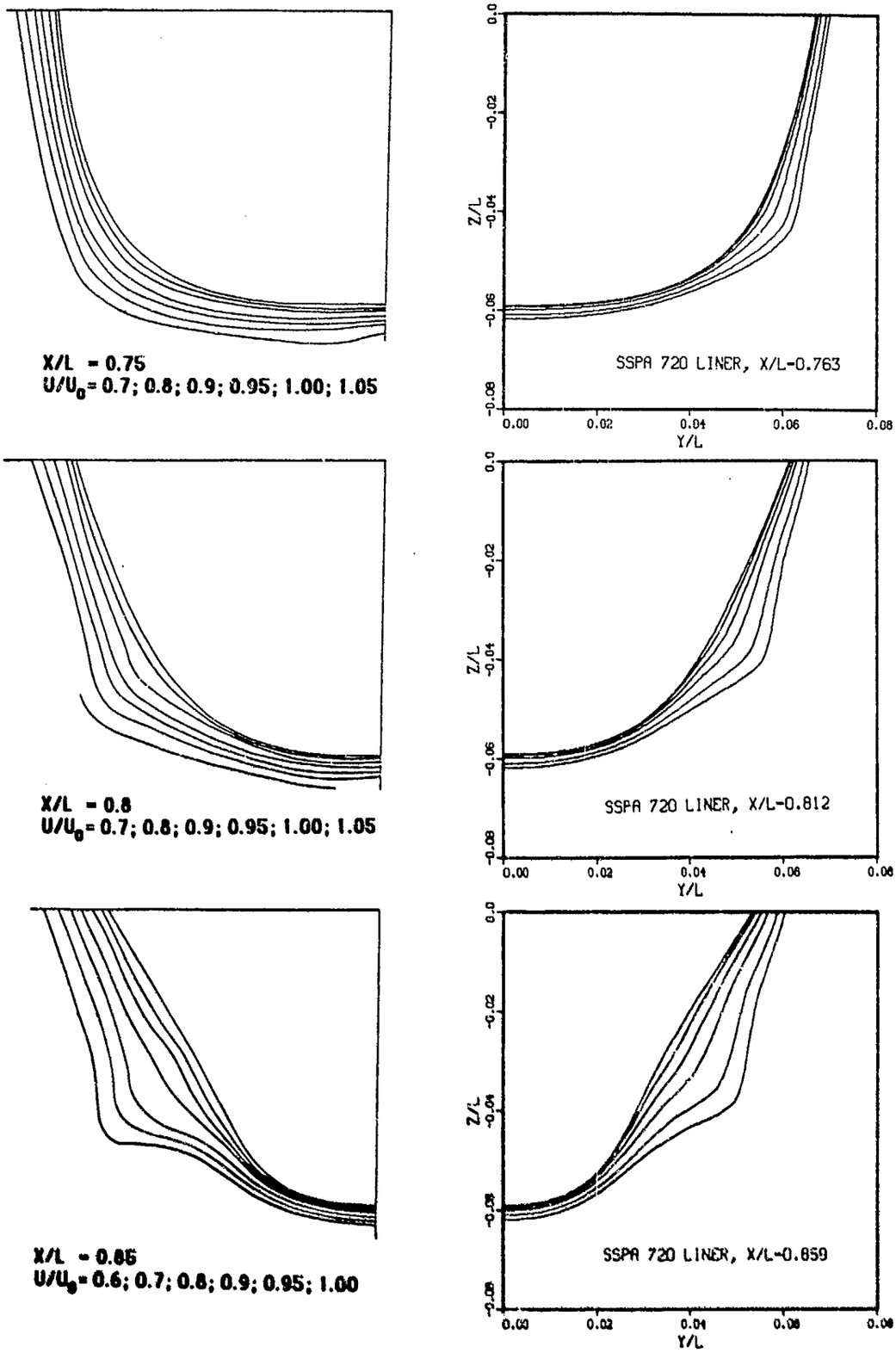

Figure 13. Contours of Constant Axial Velocity: SSPA Hull

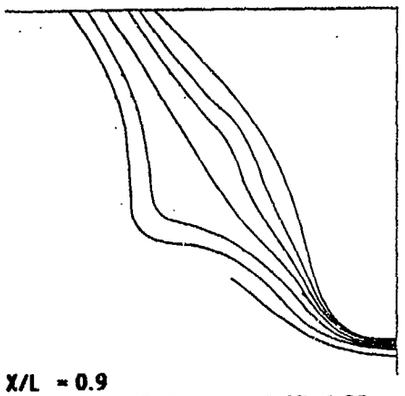

X/L = 0.9
U/U_0 = 0.6; 0.7; 0.8; 0.9; 0.95; 1.00

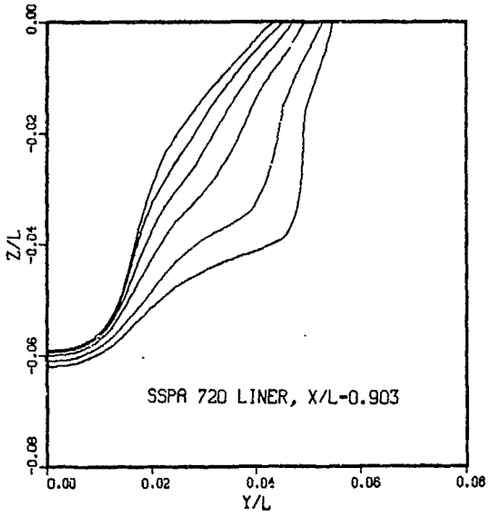

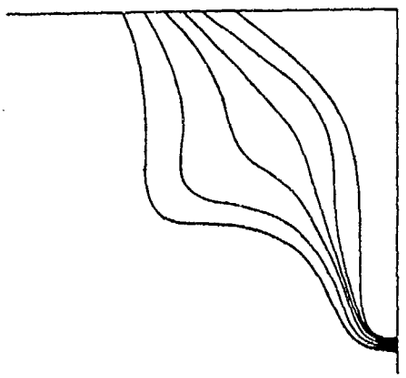

X/L = 0.95
U/U_0 = 0.6; 0.7; 0.8; 0.9; 0.95

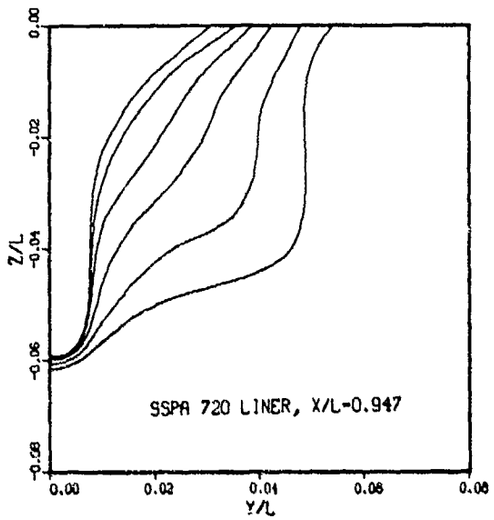

From Experiments

Calculated: U/U_0 = 0.6; 0.7; 0.8; 0.9; 0.95

Figure 13. Continued

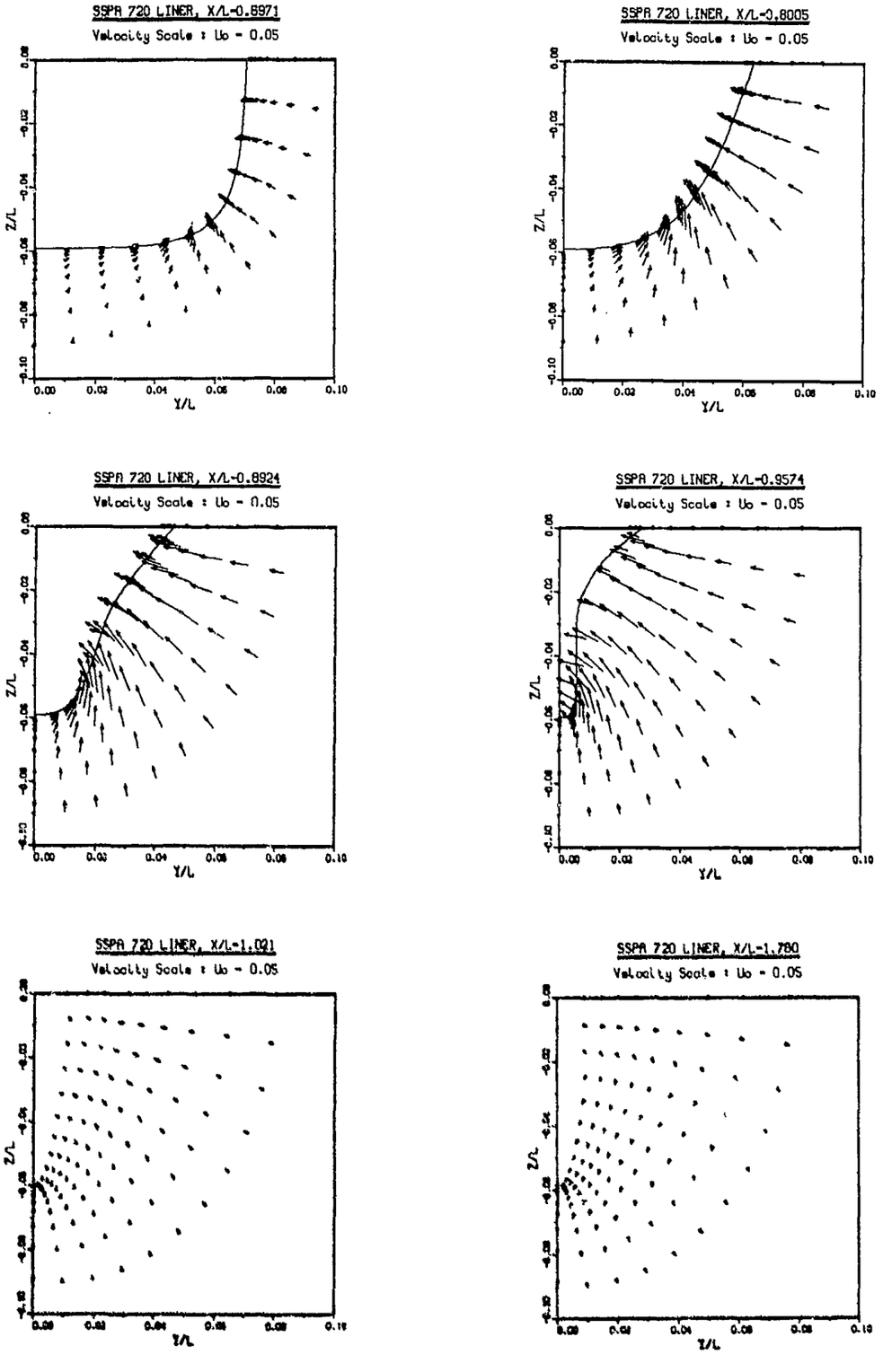

Figure 14. Projections of the Velocity Vector in Transverse Sections: SSPA Hull

DISCUSSION
of the Paper
by H.C. Chen and V.C. Patel

NUMERICAL SOLUTIONS OF THE FLOW OVER THE STERN AND IN THE WAKE OF SHIP HULLS

DISCUSSION
by H.C. Raven

This paper and the previous one allow an interesting comparison of two methods that solve basically the same equations but with completely different numerical treatment. Chen and Patel determine the velocity components from the associated momentum equations and use a Poisson-like pressure correction to satisfy continuity, while we derive the normal velocity from continuity and the pressure from the normal momentum equation. Furthermore, they use untransformed velocity components, a staggered mesh, uncoupling of all equations and solution by the scalar tridiagonal matrix algorithm; instead we use contravariant or physical velocity components, a regular mesh, and a fully coupled solution by the Strongly Implicit Procedure at each downstream step. Less essential differences are present in the difference approximations, the turbulence model, and, in the examples shown, the grid spacings and the extent of the physical domain. The method of Chen and Patel thus largely follows the methodology of general purpose flow solvers as TEACH or PHOENICS, for which the application to both internal and external flows necessitates the use of a pressure correction method and the wish to add other transport equations easily (e.g. for heat transfer) prohibits the use of a coupled algorithm. In our opinion these features are a definite drawback in difficult applications, e.g. a vortex separation calculated on a sufficiently fine mesh, and can make the convergence of the iterative procedures uncertain.

Still the method presented by the authors works very well in the applications shown. The convergence rate of our method may be slightly better (10 sweeps instead of 20); on the other hand, Chen and Patel have an advance in the implementation of a turbulence model. It will be interesting to make further comparisons between these methods and their performance.

Author's Reply

We are well aware of the differences and similarities between our two methods, and also among other methods of this type. However, it is perhaps premature to judge the relative merits of these methods since they have not all been applied to a wide range of hull forms. We believe it will be useful to hold a specialty workshop in the near future to evaluate the status of stern- and wake-flow calculation methods.

DISCUSSION
By Yu-Tai Lee

The predicted pressure distributions for the Wigley and SSPA hulls, shown in Figures 5, 9, and 10, deviate from the original measured data with the wind-tunnel blockage. Because of the flexibility of the numerical grid generation in the present approach, it may be worth calculating one internal flow with wind tunnel wall effect as a benchwork calculation.

Author's Reply

Yes, the present method can be used to directly assess the influence of wind-tunnel blockage by placing the outer boundary of the solution domain to coincide with the tunnel walls and applying the appropriate boundary conditions there. We plan to conduct such an investigation to clarify blockage effects.

NEAR-WAKE COMPUTATIONS BY SOLVING THE VORTICITY TRANSPORT EQUATION ON A BODY-FITTED COORDINATE SYSTEM

Kazu-hiro Mori* and Nobuki Ito**
* Hiroshima University, Saijo Higashi-Hiroshima 724 JAPAN
** Sumitomo Heavy Industry, Hiratuka 254 JAPAN

Abstract

A new method to predict near wake flows is proposed where the time dependent fully elliptic vorticity transport equation is used as governing equation together with the boundary layer equation. The flow field is supposed to be simulated by a sudden move of a body to which a vorticity layer is attached to a certain position. The attached vorticity layer is equivalent to the steady boundary layer flow. The equation is solved by the time marching method on a body-fitted coordinate system. The two-equation model is invoked for the turbulent closure. The wakes of 2-dimensional elliptic cylinder and a SSPA-720 hull form are calculated. The separated flow with a recirculation is well predicted in case of the elliptic cylinder. The ship wake is also predicted within a moderate computing time.

1. Introduction

It is one of the important problems in ship hydrodynamics to estimate the near wake flow of ships theoretically. So far it is carried out either by the boundary layer approximation or the partially parabolic approximation. In some cases, however, separations with recirculating flows make those approximations invalid any more. Recently calculations based on the full Navier-Stokes equation are carried out [1],[2],[3]. Some of them have been applied to ship wake predictions with prospective successes.

The present study is an extention and generalization of the previous works on ship-wake calculations [4],[5],[6]. A common feature of this series is to use more than a single equation as governing equations depending on the flow characteristics; the boundary layer approximation is positively appreciated up to the position where flows are perfectly free from separation and it is switched into the full vorticity transport equation.

Such a combined use of governing equations makes the computing time and memory storage less. At the same time the well-developed potential flow and boundary layer flow calculations are highly appreciated as far as they work.

The use of the vorticity transport equation together with Biot-Savart's law was first applied by J. C. Wu and et al.[7] to predict wake flows. It has several advantages over other methods where the velocity field is directly solved or the stream function is used. First of all, the pressure term has disappeared from the basic equation; this makes it easy to take account of viscosity-inviscid interaction. They are easily realized by a simple addition of the vorticity-induced velocity to the potential velocity component. Secondly the outer boundary conditions for the vorticity equation are definitely clear; the vorticity is zero. And the computing domain is limited only in the non-zero vorticity region which is usually much narrower than the viscous flow region. The boundary layer flow is smoothly matched with the wake flow through vorticities. Thirdly, because Biot-Savart's law is applicable to the 3-dimensional flow also, the present method can calculate the 3-dimensional field by the same manner as the 2-dimensional.

In the present paper the vorticity transport equation is solved together with the k-ε model for the turbulent closure system by the time-marching method. The potential flow calculation is carried out by the well-developed panel method while the boundary layer by the integral method.

A body fitted coordinate system, proposed by Thompson[8], is adopted

here for the boundary conditions to be predicted more accurately. The accurate description of boundary geometries is still more important in the present scheme where the boundary values for vorticities are required.

In the present paper the near wake flows of a 2-dimensional elliptic cylinder and SSPA-720 hull form are calculated. Comparisons are made between the results by the body fitted coordinates system and by the Cartesian coordinate system, and with the measured.

2. Basic Equation and Computational Method

2.1 Basic Equation

In a right handed Cartesian coordinate (x_1,x_2,x_3) the time dependent vorticity transport equation is written in a following form:

$$\frac{\partial \omega_i}{\partial t}=\omega_n\frac{\partial u_i}{\partial x_n}-u_n\frac{\partial \omega_i}{\partial x_n}+\frac{\partial}{\partial x_n}\left(\nu_e\frac{\partial \omega_i}{\partial x_n}\right)$$

$$+\frac{\partial \nu_e}{\partial x_j}\frac{\partial^2 u_k}{\partial x_n^2}-\frac{\partial \nu_e}{\partial x_k}\frac{\partial^2 u_j}{\partial x_n^2}$$

$$+\frac{\partial^2 \nu_e}{\partial x_j \partial x_n}\left(\frac{\partial u_n}{\partial x_k}+\frac{\partial u_k}{\partial x_n}\right)-\frac{\partial^2 \nu_e}{\partial x_k \partial x_n}\left(\frac{\partial u_j}{\partial x_n}+\frac{\partial u_n}{\partial x_j}\right) \quad (1)$$

where the summation convention is used and i,j,k are in the order of 1,2,3,1,2; t is the time, u_i and ω_i are the mean velocity components and the vorticity components in the x_i-direction respectively. The vorticity is defined by,

$$\omega_i=\frac{\partial u_k}{\partial x_j}-\frac{\partial u_j}{\partial x_k} \quad (2)$$

ν_e is the effective kinematic viscosity coefficient which is related to the Reynolds stress by,

$$\nu_e=\nu+\nu_t \quad (3)$$

$$-\overline{u_i'u_j'}=\nu_t\left(\frac{\partial u_j}{\partial x_i}+\frac{\partial u_i}{\partial x_j}\right) \quad (4)$$

where ν is the kinematic viscosity coefficient, $-\overline{u_i'u_j'}$ is the Reynolds stress. The eddy kinematic viscosity ν_t is calculated from the k-ε model;

$$\frac{\partial \phi}{\partial t}+u_n\frac{\partial \phi}{\partial x_n}=\frac{\partial}{\partial x_n}\left(\frac{\nu_e}{P_{r\phi}}\frac{\partial \phi}{\partial x_n}\right)+C_{1\phi}G_e\frac{\phi}{k}-C_{2\phi}\frac{\phi\varepsilon}{k} \quad (5)$$

$$k;\phi=k,\ P_{rk}=1.00,\ C_{1k}=1.00,\ C_{2k}=1.00$$

$$\varepsilon;\phi=\varepsilon,\ P_{r\varepsilon}=1.23,\ C_{1\varepsilon}=1.44,\ C_{2\varepsilon}=1.92 \quad (6)$$

$$G_e=\nu_t\left(\frac{\partial u_j}{\partial x_n}+\frac{\partial u_n}{\partial x_j}\right)\frac{\partial u_j}{\partial x_n} \quad (7)$$

$$\nu_t=C_d\frac{k^2}{\varepsilon},\quad C_d=0.09 \quad (8)$$

The velocity assumed to be consisting with the two components; one is the potential component and the other is the component due to the vorticity;

$$u_i=\frac{\partial \phi}{\partial x_j}-\frac{1}{4\pi}\iiint_V\left\{\frac{\omega_j}{r^3}(x_k-x_{k0})-\frac{\omega_k}{r^3}(x_j-x_{j0})\right\}dV_0 \quad (9)$$

where ϕ is the total velocity potential including the uniform flow. The second term is the induced component by the vorticity and the integration is carried out over the non-zero vorticity region V (see Fig.1). equation(9) means that once the vorticity distribution is determined which is definitely limited the velocity field beyond V is calculated by adding the induced velocity to the potential component. It can be smoothly matched to the inviscid flow field. This is one of the great advantages of the present method; the computing domain is limited and the interaction between the inviscid and the viscid is easily taken into account.

2.2 Body-fitted coordinate system

The vorticity transport equation is solved on a body-fitted coordinate system to minimize numerical errors due to the complicated hull geometry. Here we follow the method originally proposed by Thompson[8].

The body-fitted coordinate system (ξ,η,ζ) can be generated by solving a partial differential equation given by,

$$A_{11}x_{i\xi\xi}+A_{22}x_{i\eta\eta}+A_{33}x_{i\zeta\zeta}$$

$$+2(A_{12}x_{i\xi\eta}+A_{23}x_{i\eta\zeta}+A_{31}x_{i\zeta\xi})$$

$$+J^2(x_{i\xi}P_1+x_{i\eta}P_2+x_{i\zeta}P_3)=0 \quad (10)$$

where

$$A_{ij}/J^2=\xi_{i_x}\xi_{j_x}+\xi_{i_y}\xi_{j_y}+\xi_{i_z}\xi_{j_z}$$

$$\xi_1=\xi,\ \xi_2=\eta,\ \xi_3=\zeta \quad (11)$$

$$J=\begin{vmatrix} x_\xi & y_\xi & z_\xi \\ x_\eta & y_\eta & z_\eta \\ x_\zeta & y_\zeta & z_\zeta \end{vmatrix}$$

By equation (10) (x,y,z) can be determined which is corresponding to the given (ξ,η,ζ).

P_i can be arbitrarily chosen depending on the geometry. Either,

$$P_i=p_iA_{ii}/J^2 \quad , \quad p_i=-x_{j\xi_i\xi_i}/x_{j\xi_i} \tag{12}$$

or,

$$P_i=-a\,\mathrm{sgn}(\xi_i-\xi_i^0)\exp(-b|\xi_i-\xi_i^0|)$$
$$-c\,\mathrm{sgn}(\xi_i-\xi_i^0)\exp[-d\{(\xi_i-\xi_i^0)^2+(\xi_j-\xi_j^0)^2+(\xi_k-\xi_k^0)^2\}^{\frac{1}{2}}]$$
$$i\neq j\ ,\ j\neq k\ ,\ k\neq i \tag{13}$$

or their linear combination is commonly used, where $i,j,k=1,2,3$ and $i=j, j=k, k=i$, a,b,c,d are constants.

Equation (12) is convenient to generate grids according to the prescribed intervals. The first term of equation (13) makes the plane $\xi_i=$constant concentrate to a given plane of $\xi_i=\xi_i^0$, while the second to a point of $(\xi_i^0,\xi_j^0,\xi_k^0)$. Greater values of the constants a and c make the intervals of coordinates more concentrated. By trial and error in equations (12) and (13), desired grids are generated.

The differentiations of a function $f(x_1,x_2,x_3,t)$ with respect to x_i can be transformed into,

$$f_{x_i}=\sum_{n=1}^{3} f_{\xi_n}\xi_{n_{x_i}}$$

$$f_{x_ix_j}=\sum_{n=1}^{3}\sum_{m=1}^{3} f_{\xi_n\xi_m}\xi_{n_{x_i}}\xi_{m_{x_j}}+\sum_{n=1}^{3} f_{\xi_n}\xi_{n_{x_ix_j}} \tag{14}$$

$$\nabla^2 f=\Big(\sum_{n=1}^{3}\sum_{m=1}^{3} A_{nm}f_{\xi_n\xi_m}+\sum_{n=1}^{3} f_{\xi_n}P_n\Big)/J^2$$

$$(f_t)_{x,y,z}=(f_t)_{\xi,\eta,\zeta}-\sum_{n=1}^{3} f_{x_n}(x_{n_t})_{\xi,\eta,\zeta}$$

on the body-fitted coordinate system, where

$$x_1=x\ ;\ x_2=y\ ;\ x_3=z$$
$$\xi_1=\xi\ ;\ \xi_2=\eta\ ;\ \xi_3=\zeta \tag{15}$$

By making use of equation (14), the basic equations (1) to (9) can be rewritten on the body fitted coordinate (ξ,η,ζ).

2.3 Computational methods

In the present computing scheme, a flow model is assumed as follows; a body which is at rest with a vorticity layer around it suddenly moves with a constant speed. The vorticity layer on the body corresponds to the steady boundary layer at that speed. Then a wake develops in a downstream by the convection and diffusion of vorticity. This flow model can be realized by the following computational procedure.

In the beginning the potential flow calculation is carried out done all over the flow region. Then the boundary layer calculation for the steady flow is executed up to a point where no significant upstream effects of separation are supposed to exist. The integral method[9] is used for the boundary layer calculation from which the vorticities are given by,

$$\omega_{s1}=0$$

$$\omega_t=-\frac{U_\delta}{\delta}\frac{H-1}{2}\left(\frac{y'}{\delta}\right)^{(H-3)/2}$$

$$\omega_n=-U_\delta\left(\frac{y'}{\delta}\right)^{(H-1)/2}\{K_{12}+\frac{1}{2}[\frac{\partial H}{h_2\partial\eta}(\log\frac{y'}{\delta}-\frac{H^2-2H-1}{H(H+1)})-\frac{\partial\theta}{h_2\partial\eta}\frac{(H-1)}{\theta}]\} \tag{16}$$

where y; the normal distance, ω_{s1}; the streamwise vorticity, ω_t; the crosswise vorticity, ω_n; the normal vorticity, h_2; the metric coefficient, K_{12}; the geodesic curvature, δ; the boundary layer thickness, U_δ; the velocity of boundary layer edge, θ; the momentum thickness and H; the shape facter.

For the wake calculations equations (1) and (5) are expressed in the explicit time-marching finite difference forms. A modified upwind differencing method is used for the convection terms and the centered differencing method for the diffusion terms.

Calculations are carried out through the following iterations. First k and ε are determined at $t=t+\Delta t$ which provide ν_e; and then $\omega_1,\omega_2,\omega_3$ are obtained. The velocity field at $t=t+\Delta t$ is determined from equation (9) by making use of the obtained vorticity

distribution. The calculations to solve equations (1) to (5) are limited within the domain V, while the velocity field can be determined beyond it. This sequence, shown in Fig.2, is iterated until a steady or quasi-steady solution is obtained.

The time step Δt is important in the explicit method. It is determined by von Neumann's stability analysis [10],

$$\Delta t \leq \mathrm{Min}\{2/[4(D_{11}+D_{22}+D_{33})-2(C_1+C_2+C_3) + (D_{12}+D_{23}+D_{31})]\} \quad (17)$$

where $D_{12}+D_{23}+D_{31}>0$ is assumed and C_i, D_{ij} are defined as follow,

$$C_i = -\sum_{n=1}^{3} u_n \xi_{i_n} + \nu_e P_i$$

$$D_{ij} = \frac{\nu_e}{j^2} A_{ij} \quad (18)$$

Min( ) in equation (17) means to use the minimum Δt on the mesh point at that time.

Because the problem is an initial-boundary value problem, initial and boundary values must be assigned. They are tabulated in Table 1 and 2. $B_{bl}, B_h, B_{out}, B_x, B_{wl}$ are the boundaries of the computing region V, as shown in Fig.1; B_{bl} is the terminating surface of the boundary layer calculation, B_h is the hull surface, B_{out} is the outer boundary and B_x is the terminating

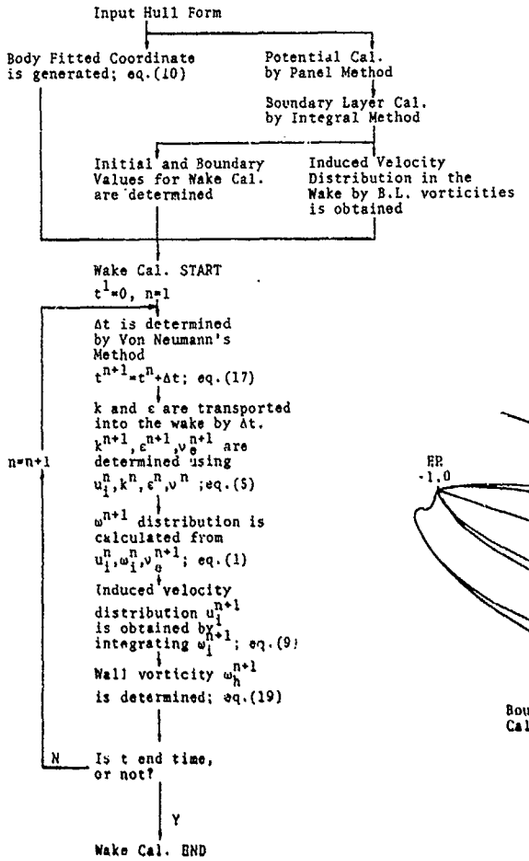

Fig.2 Computational sequence

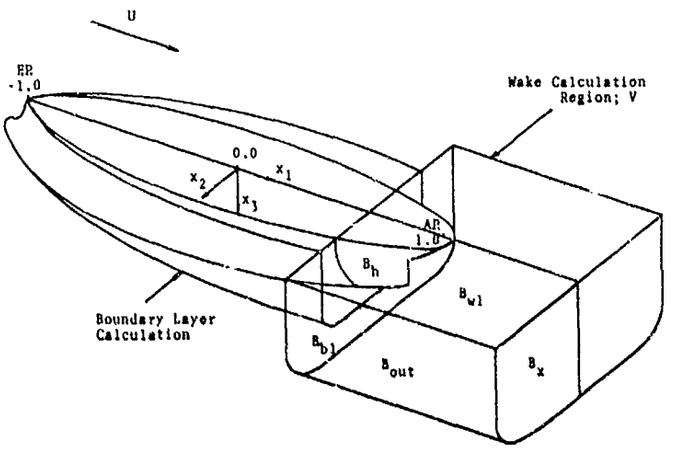

Fig.1 Coodinate system and definitions

	V	B_{bl}	B_h
k	$\begin{cases} k_{bl} & x_1 \leq 1.2 \\ 0 & x_1 > 1.2 \end{cases}$	k_{bl}	0
ϵ	$\begin{cases} \epsilon_{bl} & x_1 \leq 1.2 \\ 0 & x_1 > 1.2 \end{cases}$	ϵ_{bl}	0
ω_i	0	$\omega_{i_{bl}}$	ω_{i_h}
u_i	$\partial\theta/\partial x_i$	$u_{i_{bl}}$	0

Table 1 Initial conditions

	B_{bl}	B_h	B_{out}	B_x	B_{wl}	B_{cl}
k	k_{bl}	0	0	$\partial^2 k/\partial x_1^2=0$	$\partial k/\partial x_3=0$	$\partial k/\partial x_2=0$
ϵ	ϵ_{bl}	0	0	$\partial^2 \epsilon/\partial x_1^2=0$	$\partial \epsilon/\partial x_3=0$	$\partial \epsilon/\partial x_2=0$
ω_1	$\omega_{i_{bl}}$	ω_{i_h}	0	$\partial^2 \omega_1/\partial x_1^2=0$	0	0
ω_2			0		0	$\partial \omega_2/\partial x_2=0$
ω_3			0		$\partial \omega_3/\partial x_3=0$	0

Table 2 Boundary conditions

surface in the x_1 direction (the downstream boundary). The subscript bl refers values on B_{bl} which are obtained by the preceding boundary layer calculation.

The boundary values of vorticity on B_h, ω_{i_h} at $t=t+\Delta t$ is assumed to be provided in terms of the velocity at $t=t$,

$$\omega_{i_h} = u_{k_\eta} \eta_{x_j} - u_{j_\eta} \eta_{x_k} \tag{19}$$

The computing domain is extended at each time step so that the vorticities on B_x and B_{out} are definitely zero. After B_x reaches a certain position, however, beyond which the computing domain is not extended anymore, the second derivative of the vorticity with respect to x is imposed to be zero on B_x instead.

Initial values for k, ε, ν_e are provided by the Cebeci-Smith model on B_{bl}. For the sake of prompting the diffusion of the vorticity, the same distributions as those on B_{bl} are extended up to x=1.2 instead of zero.

3. Computed results and discussions

3.1 2-Dimensional Elliptic Cylinder

Near wake flow of an elliptic cylinder is chosen for the 2-dimensional calculation. It has a blunt trailing edge and significant separated flows are likely to take place which are hardly possible to be predicted by methods based upon the boundary layer assumption.

The ratio of the minor and major axes of the elliptic cylinder model is 0.125. It is designated EM-125 here. The flow is parallel to the major axis (in the direction of x-axis) of the elliptic cylinder. The referred Reynolds number is 1.68×10^6, corresponding to the conditions of the velocity measurement. All the results are shown in non-dimensionalized forms by the uniform flow velocity and the half length of models, unless otherwise stated, but the same nomenclatures are used. The origin is at the midship.

As shown in Fig.3, the boundaries B_x, B_{out}, B_h and B_{bl} are mapped into $\xi=50$, $\eta=+20$, $\eta=0$ and $\xi=1$ respectively to form a rectangle computing domain. The trailing edge (A.P.) is mapped to the point of $\xi=16$ and $\eta=0$.

For the present transformation P_1, P_2 are chosen as follows;

$$\begin{aligned} P_1 &= -1.5\times10^3 \,\mathrm{sgn}(\xi-16)\, \exp(-0.1|\xi-16|) \\ &\quad -5.0\times10^4 \,\mathrm{sgn}(\xi-16)\, \exp[-0.8\{(\xi-16)^2 \\ &\quad +(\eta-0)^2\}^{\frac{1}{2}}] \\ P_2 &= -\frac{A_{22}}{J^2}\left(\frac{y_{nn}}{y_\eta}\right)_{\xi=1} \\ &\quad -5.0\times10^3 \,\mathrm{sgn}(\eta-0)\, \exp[-0.8\{(\xi-17)^2 \\ &\quad +(\eta-0)^2\}^{\frac{1}{2}}] \end{aligned} \tag{20}$$

P_1 makes the ξ-axes to concentrate around a point $(\xi,\eta)=(16,0)$, while the first term of P_2 gives the basic η-grid size at $\xi=1$ and the second term modifies it.

The grid for the actual computations is shown in Fig.4 where the curves correspond to the ξ and η=constant lines.

The potential flow is described by,

$$\frac{\partial\phi}{\partial x} = \frac{1}{2(1-b)} \frac{\cosh 2\xi - \cos 2\eta - b\sinh 2\xi}{\cosh^2\xi - \cos^2\eta} U$$

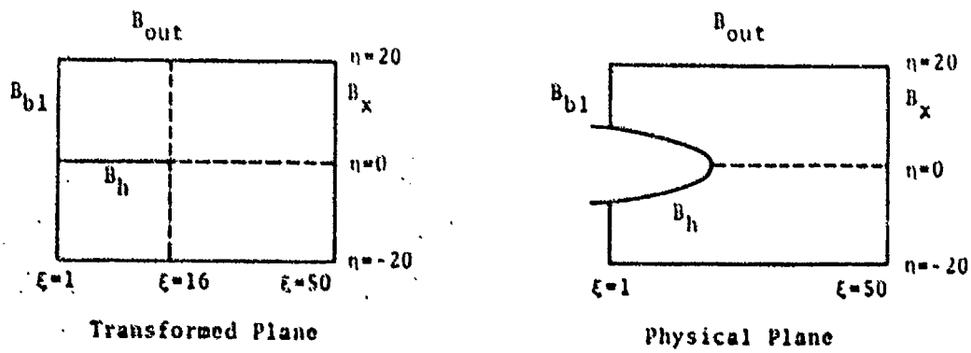

Fig.3 2-dimensional grid generation

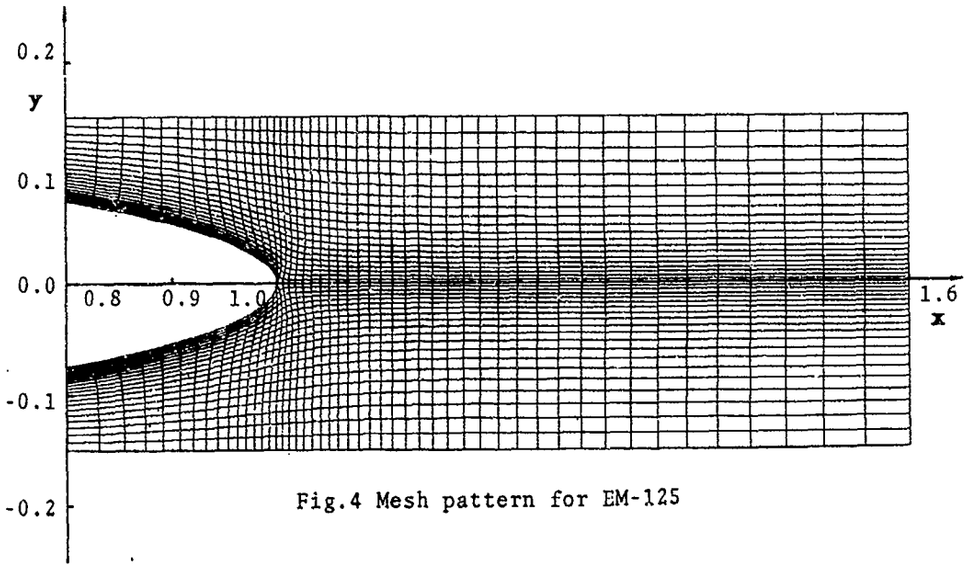

Fig.4 Mesh pattern for EM-125

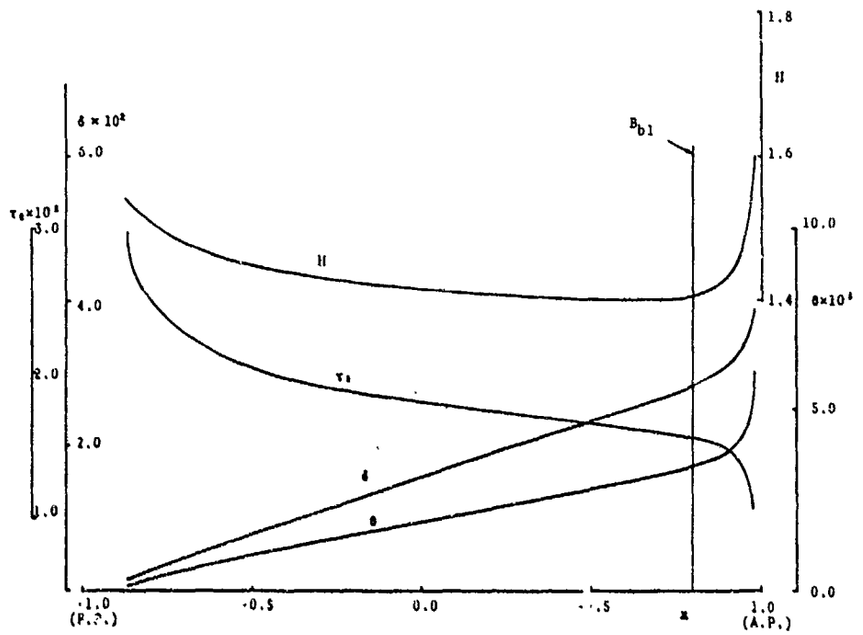

Fig.5 Results of boundary layer calculation for EM-125

$$\frac{\partial \phi}{\partial y} = -\frac{b}{2(1-b)} \frac{\sin 2\eta}{\cosh^2 \xi - \cos^2 \eta} U \qquad (21)$$

$$x+iy = \sqrt{1-b^2}\cosh(\xi+i\eta),\ i=\sqrt{-1} \qquad (22)$$

The results of the boundary layer calculation are shown in Fig.5. τ_0 is non-dimensionalized by ρU_0^2. The calculations are quite stable up to around x=0.8 beyond which H starts to increase steeply. B_{b1} is assumed at x=0.8 where reliable results can be assured. An additional v-component velocity,

$$v_{add} = 0.1U \sin(2\pi t/0.74) \qquad (23)$$

is added to the uniform flow for t<0.37. This disturbance makes the flow asymmetric, if any, within a reasonable computing time. The constant 0.74 is the fluctuating period of wake flow and 0.1 is the amplitude; they are apriori chosen here. It is examined that neither the period nor the amplitude affect the final solution. Fig.6 shows the computed results of vorticity distribution at several time steps. t is

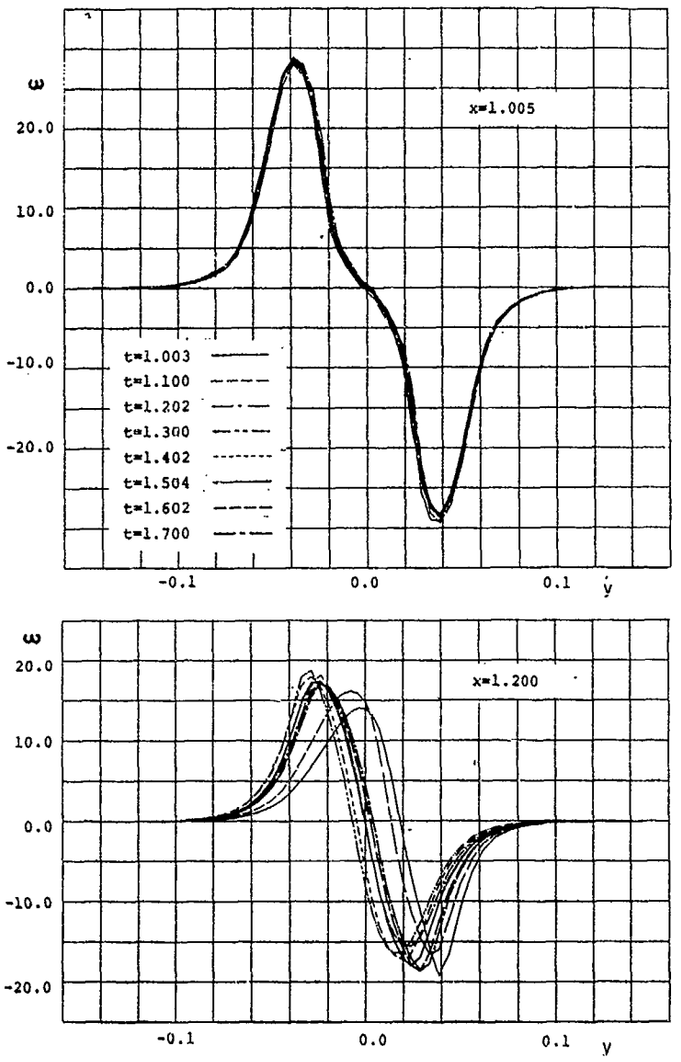

Fig.6 Vorticity distribution for EM-125

the non-dimensionalized time by L/2U. The results show almost converged at t=1.7. In Fig.7 the calculated velocity distributions at x=1.0(A.P.) and x=1.2(in wake) are compared with the experimental data. The results obtained on the Cartesian coordinate system[6] are also shown there. u and v are the velocity components in the x- and y-directions respectively. The differences between the two calculations are rather little and they are in good accordance with the measured.

In Fig.8 the flow patterns at t=1.6 are shown which are obtained on the body-fitted and the Cartesian coordinate systems. Differences are observed in the vicinity of hull and in the recirculating region behind the body; the flow seems to direct into the hull in the Cartesian coordinate case. This means that the employment of the body-fitted coordinate makes the hull surface conditions to be satisfied more strictly not only for the velocity but for the vorticity.

It is disclosed that the solution for k, ε has not converged locally in the recirculating region. There may be some limitations for the use of the k-ε model with the standard constants for such a recirculating region. Fig.9 may support this guess. It shows the comparison of computed ν_e with the measured for EM-200 whose ratio of axes is 0.200. The results at x=1.005 show

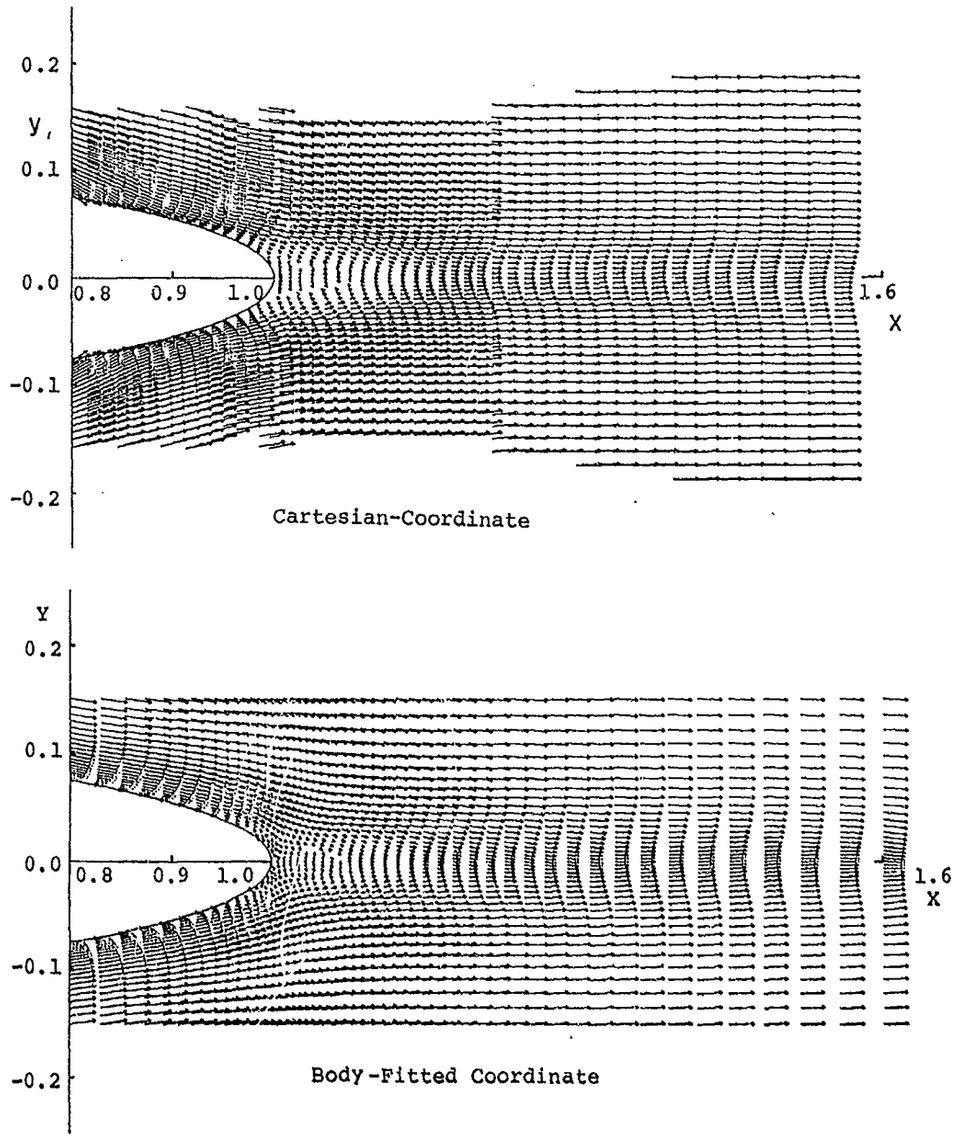

Fig.8 Flow patterns of EM-125 at t=1.6

poorer agreements with the measured than those at x=1.100 although fluctuations are still more intensive.

The viscous drag coefficient of a body is placed in a uniform flow is given by the momentum theorem.

$$R=\int_{-\infty}^{\infty}(H_{\infty}-H)\,dy-\frac{1}{2}\rho\int_{-\infty}^{\infty}\{(U-u)^2-v^2\}dy \qquad (24)$$

where R is the viscous drag and H is the total pressure. The suffix ∞ means the values at the upstream. The integration is carried out at a certain section in the wake. From the 2-dimensional Reynolds equation, the y-direction gradient of the total pressure is expressed as follows.

$$\frac{1}{\rho}\frac{\partial H}{\partial y}=-\omega_3 u+\frac{\partial}{\partial x}\{\nu_e(\frac{\partial v}{\partial x}+\frac{\partial u}{\partial y})\}+\frac{\partial}{\partial y}(2\nu_e\frac{\partial v}{\partial y}) \qquad (25)$$

Substituting equation (25) into equation (24), the viscous drag is rewritten, in terms of ω, ν_e and u,v;

$$R=\rho\int_{-\infty}^{\infty}\int_{-\infty}^{y'}\omega_3 u-\frac{\partial\nu_e\omega_3}{\partial x}-2(\frac{\partial\nu_e}{\partial x}\frac{\partial u}{\partial y}-\frac{\partial\nu_e}{\partial y}\frac{\partial u}{\partial x})\}dy'dy$$

$$-\frac{1}{2}\rho\int_{-\infty}^{\infty}\{(U-u)^2-v^2\}dy \qquad (26)$$

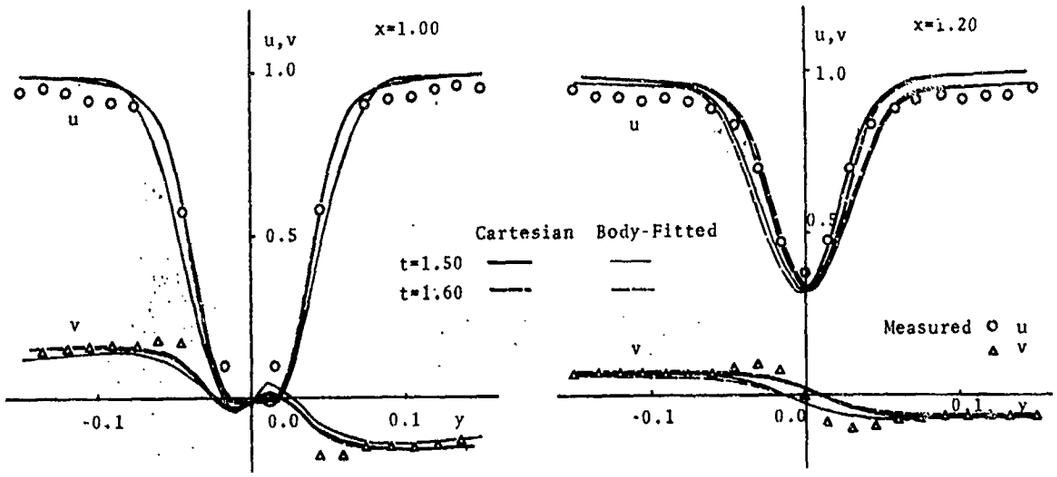

Fig.7 Comparisons of velocity distributions obtained by Cartesian and Body Fitted Coordinates (EM-125)

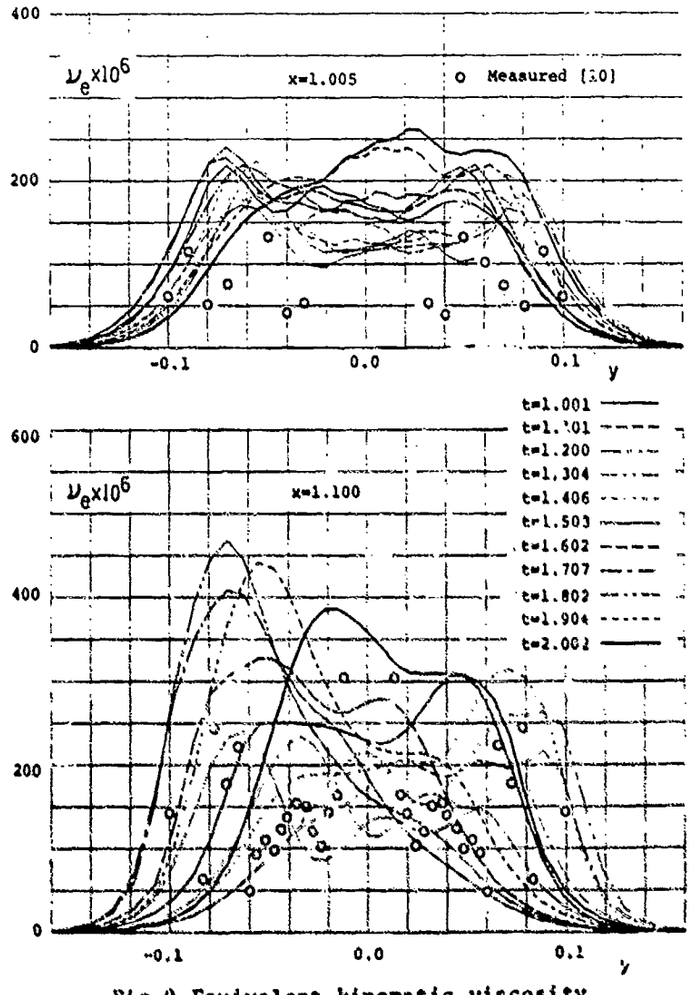

Fig.9 Equivalent kinematic viscosity coefficient distribution (EM-200)

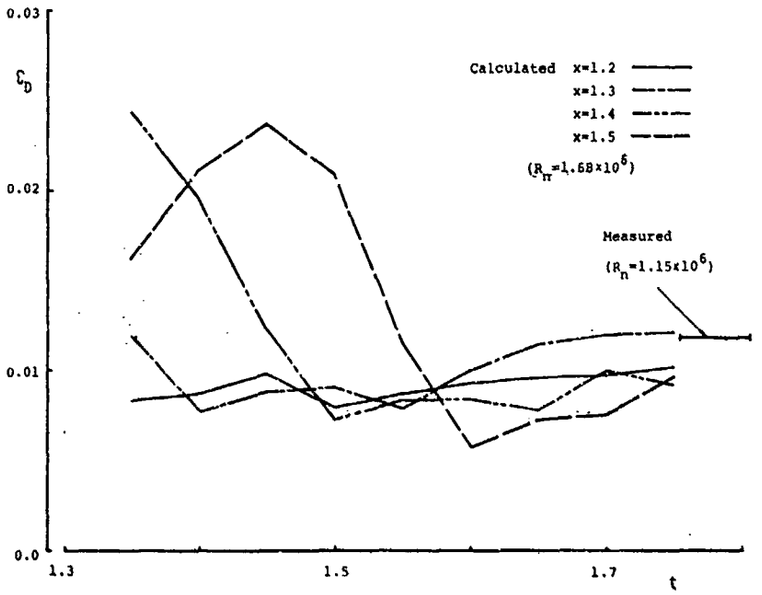

Fig.10 Viscous drag coefficient distribution for EM-125

In case of blunt bodies the use of equation (26) is expected to be much more accurate than the pressure integration over hull.

The viscous drag coefficient of EM-125 is calculated by equation (26). The infinite integration appearing in equation (26) is carried out only in the domain where the velocity is smaller than the potential velocity component.

The calculations are carried out at several control sections whose results are presented in Fig.10 in a non-dimensional form by $1/2\rho U^2 L$. The measured result is obtained by the wake survey method at R_n=1.9. The Reynolds number is 1.15×10^6 which dose not match with that of computation.

It is found that, though the flow pattern seems almost steady t=1.7, the viscous drag still fluctuates with time and depends on the position of control section. The calculated drag coefficients, however, seem to converge and to come close to the measured.

Through the present calculations we can conclude that the present scheme works well to yield satisfactory predictions of near wake flows and the use of the body-fitted coordinate system improve the accuracy of the hull-surface condition.

3.2. 3-Dimensional Ship Wake

SSPA-720(C_b=0.675) model is used for the present computation. The Reynolds number is 6.6×10^6. All the experimental data here shown are referred from [9].

The grid generation is carried out 2-dimensionally at each x=constant plane to save computing time. As shown in Fig.11 the computing domain is transformed into the rectangular solid; the surrounding surfaces such as the downstream boundary B_x, the outer boundary B_{out}, the upstream boundary B_{bl}, the hull surface B_h, the free surface boundary B_{wl} and the center plane B_{cl} are mapped to ξ=30, η=18, ξ=1, η=1, ζ=1 and ζ=18 respectively. In this calculation ξ is the function only of x.

The generated grids at x=0.8 and 1.0 are shown in Fig.12. There were not any special difficulties to generate them for this case. About 1 minute computing time by HITAC-M200H is additionally required for their generation.

The procedure for the wake-calculation is the same as the 2-dimensional case. Two simplifications are made to save computing time and memory storages. One is to skip the induced-velocity calculations once for every 5 step except the vicinity of the hull. The other is to satisfy the hull sur-

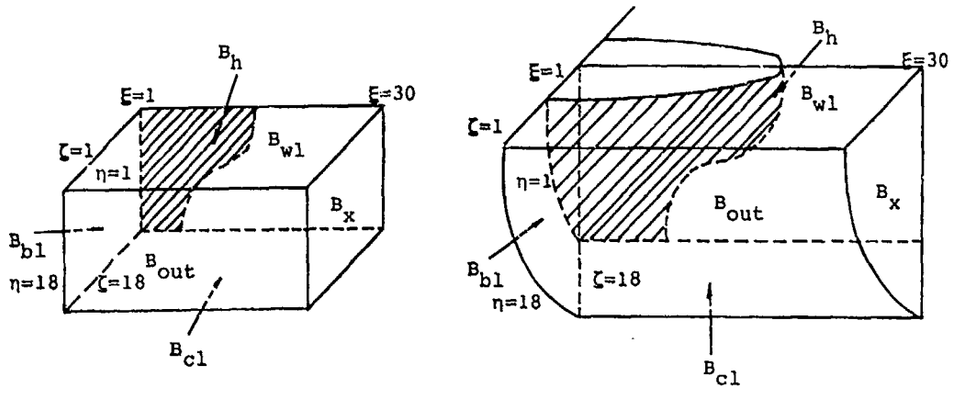

Transformed Plane Physical Plane

Fig.11 3-dimensional grid generation

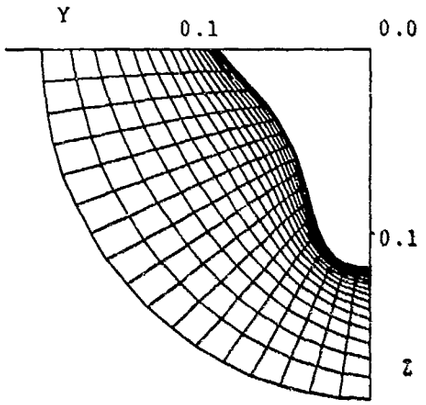

X=0.8

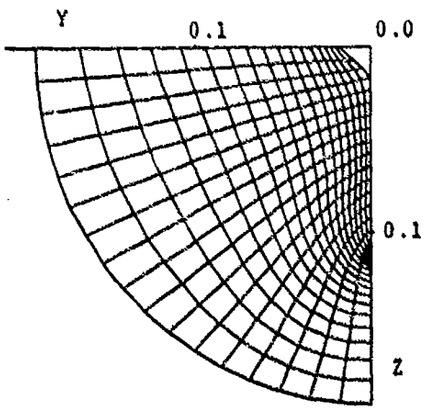

X=1.0

Fig.12 Grid generations for SSPA-720 model

face condition for the induced-velocity only for the normal component and the tangential component is set free.

The potential flow is calculated by the panel method. The boundary layer calculation is carried out up to $x=0.8(B_{bl})$ by the integral method where the Mager model is invoked for the velocity profiles. The results are shown in Fig.13.

Fig.13 shows the results of the boundary layer calculations at x=0.7 and 0.8. The measured results at x=0.7 are referred for comparisons. The calculation is carried out by the integral method where the Mager Velocity-profile model is used [9]. At x=0.7 the calculated boundary layer parameters are in good accordance with the experimental ones, but H and θ have a little smaller values at the hollow part of the body plan. The reason is that the boundary layer approximation is gradually breaking down around such a part. After some consideration about the CPU time and the accuracy, B_{bl} is determined at x=0.8. The results at x=0.8 are used as the upstream boundary values for the wake calculation.

In Fig.14 the streamwise and cross flow velocity profiles at the positions B and C in the x=0.9 section are shown; positions are shown in Fig.15. Velocities and coordinates are nondimensionalized by the boundary layer edge velocity and the measured boundary layer thickness respectively. The calculated velocity distribution at B is in good accordance with the measured except in the vicinity of the wall, while a poor agreement is at C. This is because the point C is in the wake of the bilge vortex and the computed results cannot simulate it. Details on this disagree-

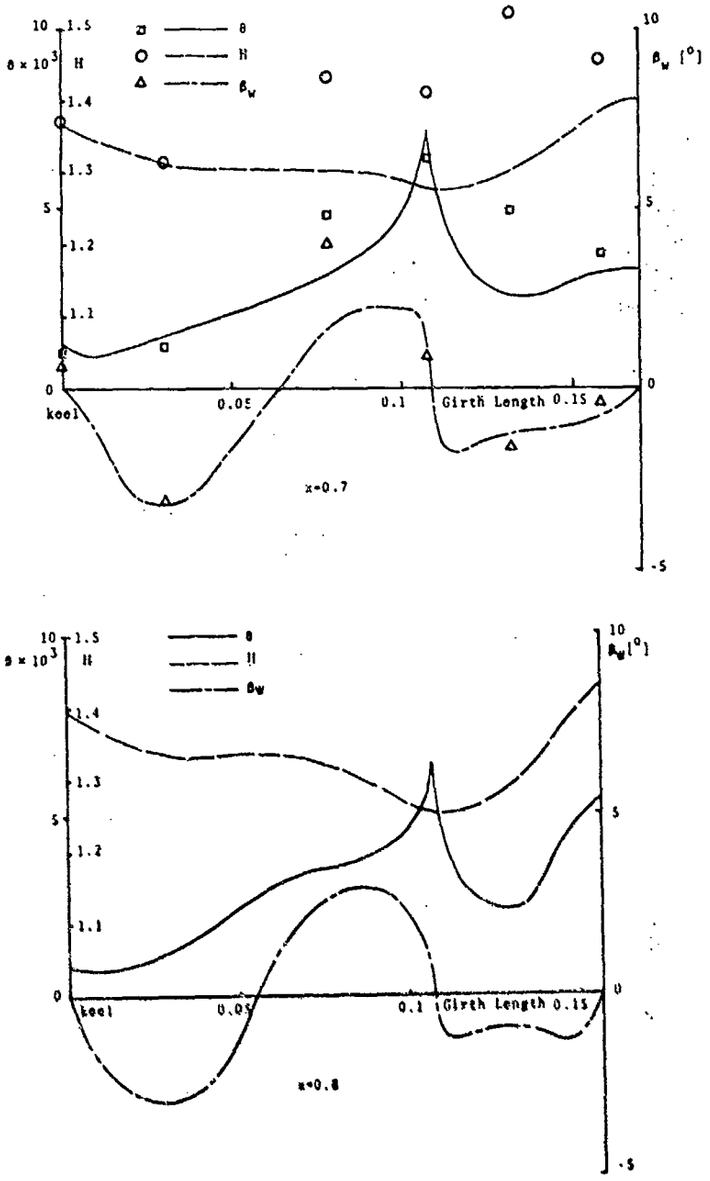

Fig.13 Boundary layer calculation results for SSPA-720 at x=0.7 and x=0.8

ment will be discussed later.

Flow vectors at x=0.9, 1.0 and 1.1 are shown in Fig.15. An intensive downward flow in the vicinity of the hull is observed. Although it is not so intensive, such a downward flow often observed in experiments as a reverse cross flow. Contrarily to our expectation, the body surface condition seems to be of little accuracy; appreciable normal components to the hull are still observed. This may be due to the grid sizes in the tangential directions which are not small enough compared with those of the normal direction. Another possible reason may be the assumption that the source distribution on the hull is constant over a panel. A finer grid scheme may contribute more or less to improve.

Fig.16 shows the equi-wake contours at x=0.9, 1.0 and 1.1. The mea-

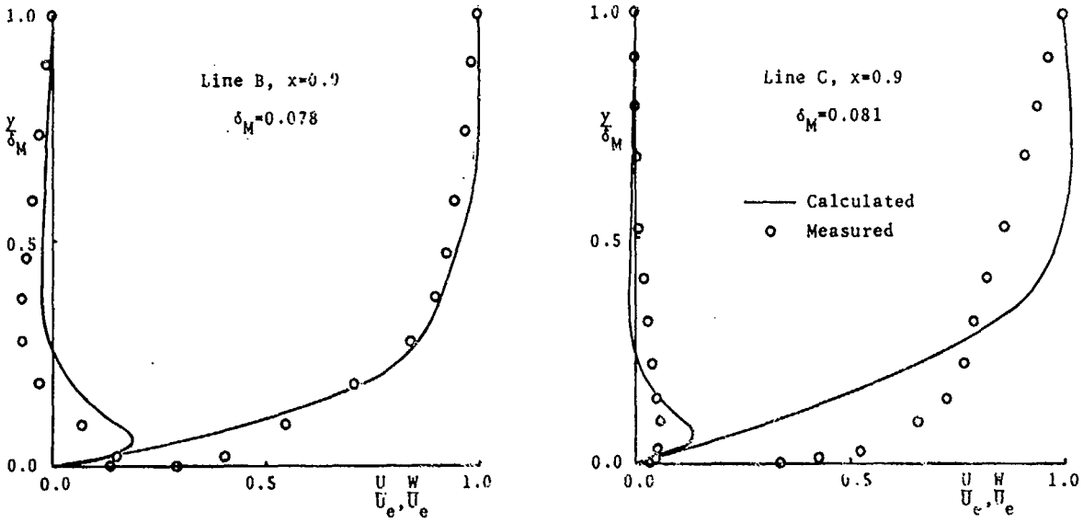

Fig.14 Velocity distributions at x=0.9

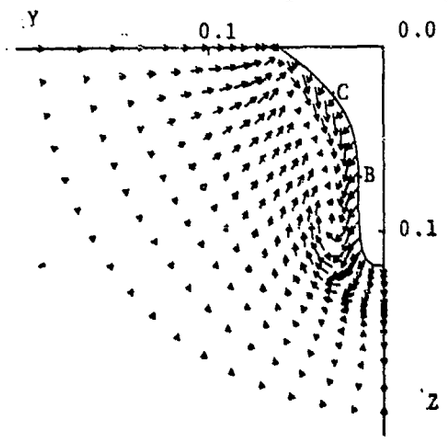

T=0.4, X=0.9

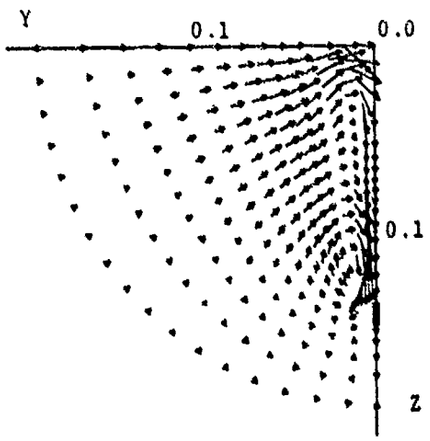

T=0.4, X=1.0

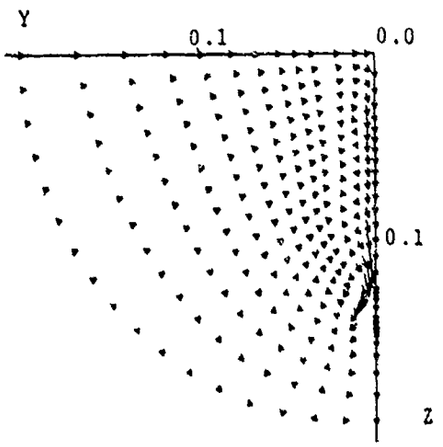

T=0.4, X=1.1

Fig.15 Flow patterns for SSPA-720

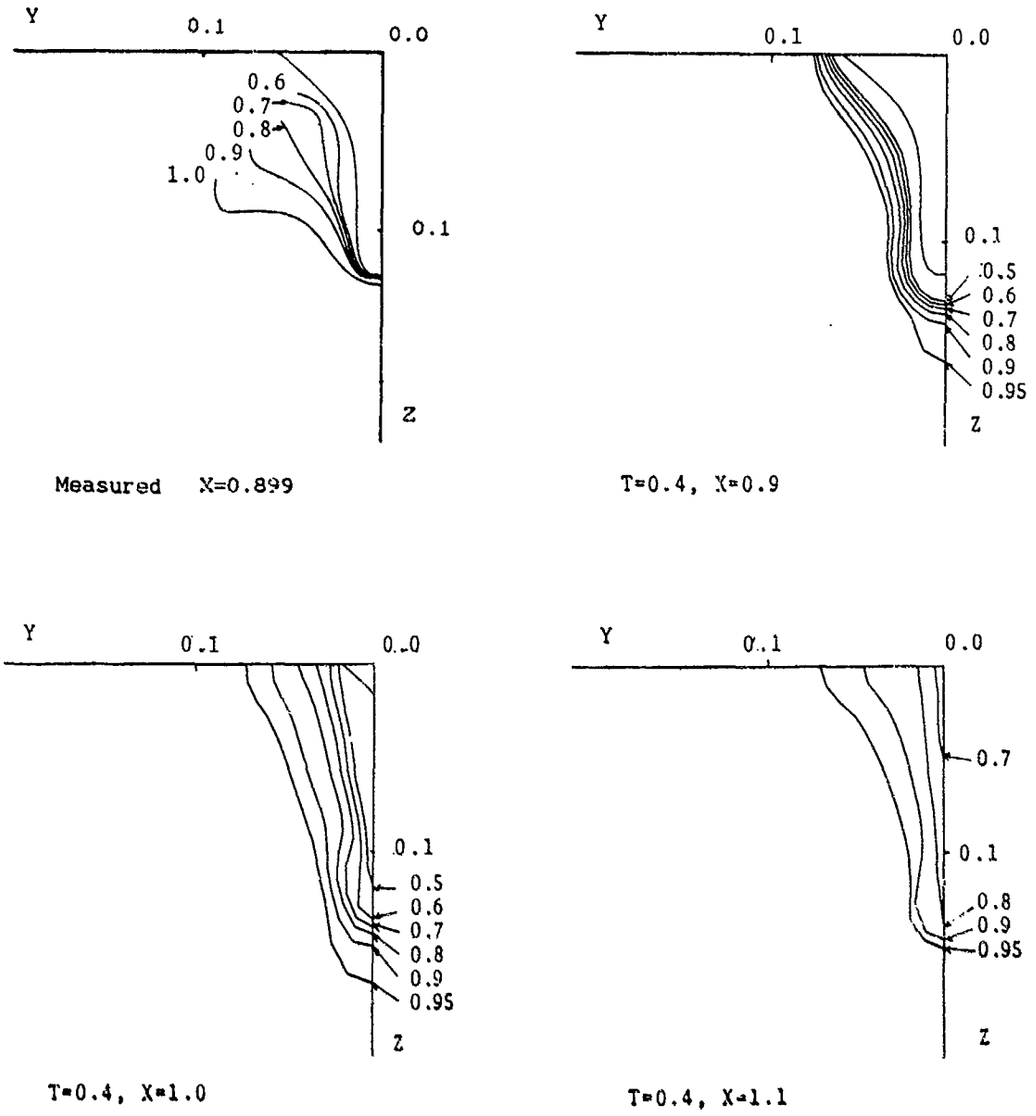

Fig.16 Wake contours for SSPA-720

sured contour at x=0.899 is also shown for comparison.

The calculated results simulate the equi-lines of 0.6 or 0.7 rather well but not so well those of 0.8 and 0.9. The bulges of the equi-lines of 0.9 or 1.0, observed in the experimental data, are supposed to be due to the bilge vortex. As stated previously, in the present computation, the flow field up to x=0.8 is calculated by the boundary layer approximation with the Mager velocity-profile model and the results at x=0.8 are used as the upstream boundary values for the wake calculation. Although the computing time is much saved, the use of the boundary layer approximation up to x=0.8 seems the reason for the poor simulation of the bulge-like equi-wake contours, for the Mager model can not afford any bilge vortices. It may be suggested, therefore, that the bilge vortex can not be simulated even by a full equation unless the upstream boundary condition is carrying it. Of course if the machine can afford, the choice of a wider computing region for the vorticity transport equation may improve further.

Although there are several rooms for improvements, the present numerical

scheme can be extended to practical uses with a certain accuracy. The vorticity distribution, which is obtained in the course of the present calculation, may provide another important information for stern flow problems. The computational time for the SSPA-720 case is about 2 hours for 100 time-steps by HITAC-M200H of Information Processing Center at Hiroshima University.

4. Concluding remarks

A new wake calculation method which is based on a combined set of governing equations of the vorticity transport equation and the boundary layer equation have been proposed. Near wake flows of a 2-dimensional elliptic cylinder and SSPA-720 model are calculated. In the case of the 2-dimensional calculation, good results are obtained, while the results of the 3-dimensional calculation have still room for improvements.

The utilization of the boundary layer approximation contributed significantly to save computer memories and CPU time.

For the turbulent closure the k-ε model was invoked which simulated quite well except the far wake and the recirculating flow region. For the model to be applied for such flow regions, a more suitable set of empirical constants may be needed.

The use of the body fitted coordinate system can make the boundary conditions predicted more precisely. It does not make significant differences in computing time from the Cartesian coordinate system.

Reference

[1] Shirose, Y., Muraoka, K. and Tsutsumi, T.: Numerical Simulation of Separated Flow around Two-dimensional and Axisymmetric Bodies at Various Reynolds Numbers, 2nd International Symposium on Ship Viscous Resistance, Goteborg (1985).

[2] Tzabiras, G. D.: On The Calculation of The 3-D Reynolds Stress Tensor by Two Algorithms, 2nd International Symposium on Ship Viscous Resistance, Goteborg (1985).

[3] Malin, M. R., Rosten, H. I., Spalding, D. B. and Tatchell, D. G.: Application of PHOENICS to Flow Around Ship's Hulls, 2nd International Symposium on Ship Viscous Resistance, Goteborg (1985).

[4] Hatano, S., Mori, K., Fukushima, N. and Yamazaki, R.: Calculation of Velocity Distributions in Ship Wake, J. Soc. Naval Arch. Japan, Vol.139(1975).

[5] Mori, K. and Doi, Y.: Approximate Prediction of Flow Field around Ship Stern by Asymptotic Expansion Method, J. Soc. Naval Arch. Japan, Vol.144(1978).

[6] Mori, K. and Ito, N. : Wake Calculations around 2-Dimensional Elliptic Cylinders by Time-Dependent Vorticity Transport Equation, J. Soc. Naval Arch. Japan, Vol.154 (1983).

[7] Wu, J. C. and Thompson, J. F.: Numerical Solutions of Time-Dependent Incompressible Navier-Stokes Equations Using An Integro-Differential Formulation, Computer & Fluids Vol.1(1973).

[8] Thompson, J. F.: Numerical solution of flow problems using body-fitted coordinate systems, Computational Fluid Dynamics, Hemisphere Publishing Corporation (1980).

[9] SSPA-ITTC Workshop on Ship Boundary Layer 1980, Edited L. Larrson, Publications of SSPA, No.90(1980).

[10] Roche, P. J.: Computational Fluid Dynamics, Hermos Publishers(1976).

DISCUSSION
of the paper
by K. Mori and N. Ito

"NEAR-WAKE COMPUTATIONS BY SOLVING THE VORTICITY TRANSPORT EQUATION ON A BODY-FITTED COORDINATE SYSTEM"

DISCUSSION
by V.C. Patel

The advantage of using the vorticity-transport equation lies in the fact that the numerical solution is confined only to the rotational flow. However, quite extensive experience with this approach in laminar, and principally two-dimensional, flows indicates that the solutions are highly sensitive to the treatment of the vorticity boundary condition at solid walls. This suggests that for TURBULENT FLOW one must very carefully model the flow very close to the wall, i.e. resolve the velocity gradients in the sublayer, the blending zone and the logarithmic layer. The k-ε model that you use certainly does not do this (see the recent review of near-wall turbulence models by Patel, Rodi and Scheuerer, AIAA Journal, Vol. 23, p. 1308, Sept 1985). From the results presented in your Figure 16, it is evident that insufficient vorticity is being generated at the hull and that it is not diffusing in the manner observed in the experiment. This is underscored by the results shown in Figure 14, where we see that the calculated velocity profiles are like those in a laminar flow, and the vorticity (velocity gradient) in the wall region is grossly in error.

Author's Reply

Thank you for your kind comments and useful suggestions. Careful treatments of the turbulent flow in the very vicinity of the wall should be reminded in any computations. In this sense we admit that our numerical scheme has also a room for improvements. We think, however, that the insufficient results for the 3-D computations which you pointed out are mainly coming from the numerical treatments of the image system of the vorticity. Additional source and circulation distributions on the hull are required to cancel the induced velocity there. In the 3-D computations, we neglected the latter distribution and used rather coarse panels for the source distribution simply to save the computing time. We did accurately for the 2-D case.

It is true that the boundary value of vorticity on the solid surface is not definite. Fortunately, in our scheme, the region where it is required is limited to the small part close to the trailing edge and the vorticity, which is proportional to the skin friction, has not so large values. We do not think, therefore, that it is a fatal difficulty. It is an important merit that the computing domain is much smaller that that where the velocity-pressure scheme is solved, as you pointed out. Another important merit, which may be still more important is that the governing equation is not carrying the pressure terms. This means the pressure field is relaxed. We need not care about matching the equations from the boundary layer approximation to the full equation even where the pressure may not be constant across the (thick) boundary layer.

We think the vorticity can be the important physical quantity which may help sound understandings of the complicated stern flow.

DISCUSSION by H.C. Raven

It is not very clear to me how the boundary conditions on the hull surface are satisfied. The induced velocity field is needed to cancel these. But according to Fig. 2 this potential velocity is not updated during the time stepping; so only at t=0 the normal boundary condition would be satisfied. The no-slip condition is imposed by specifying a boundary value w_h $(t + \Delta t)$ expressed in the velocity field at time t.

Solving the vorticity equations and deriving the velocity field from the Biot-Savart law one should arrive at exactly the same wall vorticity again. In other words, the vorticity at the wall is not allowed to vary in time except by numerical inaccuracies.

Since I can hardly imagine that these suppositions are correct, could the authors explain their implementation of the boundary conditions?

Other comments concern the numerical accuracy. If the longitudinal momentum is accurately conserved, the momentum deficit at different x-positions in the wake must approach the same steady-state limit. Fig. 10 is not very convincing in this respect. Finally, using 18 or 20 points through the boundary layer in a high Reynolds number turbulent flow without employing wall functions might be insufficient.

Author's Reply

Thank you for your discussion (!) As you pointed out, an additional potential velocity field is necessary to satisfy the hull surface condition. As mentioned in the fourth paragraph of section 3.2, we did so by distributing an additive source on the hull (we have to apologize for not mentioning definitely in Fig. 2). We think, however, the accuracy for the

additive source distribution was not enough, for we used the same panel scheme as those used for the potential component; for the induced velocity field to be canceled, more finite mesh or higher approximation for the source strength on a panel may be necessary.

(2) We cannot understand your comment that one should have the same wall vorticity at any time. The velocity field changes at each time step and eventually the corresponding vorticity may change. This can be easily confirmed from the definition of the vorticity.

(3) As in Fig. 7, the flow field is still unsteady. The momentum theorem cannot be applied to the steady flow exactly speaking. Another reason is that the integration in the lateral direction is, as mentioned in the text, carried out only in the domain where the velocity is smaller than the potential component.

STUDY OF 3-D SHIP BOUNDARY LAYERS BY MEANS OF AN INVERSE METHOD

J. Piquet and M. Visonneau

Computational Fluid Dynamics Group
LHN - ENSM - 1 rue de la Noë
44072 Nantes Cedex - FRANCE

Abstract

This work is concerned with the development of an inverse mode solution of the three dimensional boundary layer equations. Reasons for investigating this problem are first discussed and rest on the possibility of marching in the unaccessible zones by means of a Flare-type approximation without encountering any type of singularity. The method developped is a generalisation of Carter method [1978] and uses either the standard or the zigzag box scheme.

Threedimensional results are reported including the prolate spheroid at incidence [19] and the SSPA 720 ship model [20], [21] for which it is shown that given displacement thicknesses resulting from the direct mode allow successful recovery of the external velocity and boundary-flow given and computed with the help of the direct mode.

1.-Introduction

The development of prediction techniques for flow field containing separated regions is of fundamental importance since separation influences the performance of engineering devices such as wings, compressors, inlets... ; it concerns also heat transfer applications as the location of separation greatly influences the values of heat transfer coefficients. Prediction techniques for separated flows can also lead to a better understanding of trailing edge flow phenomena and their influence on the configuration of flow past wings. Endly, they can be also a valuable tool of investigation of ship stern flows which must be accurately computed if hull-propeller interactions are considered.

In the absence of separation, inviscid and boundary-layer flow theories can usually be applied in a weakly coupled procedure to yield sufficiently accurate solution : an initial computation of the inviscid velocity field gives the far field condition for the boundary layer calculation which in turn provides an estimation of the displacement thickness. The effect of the boundary layer on the inviscid flow can be accounted for by adding the displacement thickness to the original surface geometry and repeating the inviscid flow calculation. Usually the iteration is terminated at this point not only because the result appears often to be sufficient but also because the iterative method converges very slowly. Methods of the above type where the external flow is prescribed for the boundary-layer equations are called direct methods. It is well known that they lead in the two-dimensional case to a singularity at the point of vanishing skin-friction coefficient. Catherall & Mangler[1966] were the first to use an inverse method in which they relaxed the pressure by prescribing the displacement thickness. The pressure was a result of the computation and the method allowed the integration past the separation point into the reversed flow leading to solutions in agreement with solutions of the full Navier-Stokes equations, as demonstrated for instance by Briley & Mc Donald-[1975]. This ability to march downstream of separation is the main reason for which inverse methods can be used profitably for a large variety of flow situations including test of calculation models, design and optimization of boundary layer characteristics.

In the three-dimensional case, things appear less clear as separation is not clearly defined. Lighthill[1963] considered the convergence of skin-friction lines onto a particular skin-friction line originating from a saddle point as a necessary condition for flow separation. From experiments, it is now widely accepted that two different types of separation can be distinguished: (I) an "open separation" characterized by a longitudinal vortex along a regular separation line resulting from a thickening viscous layer, (II) a "closed" separation for which vorticity is shed away by a sudden breakaway from the surface along a singular separation line. More recently, Tobak & Peake [1982] used the notions of topological structure, structural stability and bifurcation to introduce a distinction between local and global properties of the flow: (I) when the skin-friction line, towards which wall streamlines converge, is issued from a saddle point, the separation is global and the topological flow structure is altered, (II) the limiting streamline can also be local and leads to a local separation without modification of the topological flow structure as on the spheroid at low incidence. Unfortunately, the parameters that control the occurence of separation are not known.

From a numerical point of view, direct boundary layer calculation methods fail to describe separation. Numerical solutions indicate that a numerical "breakdown" occurs close to an area where the

streamlines focus together onto an enveloppe. By analyzing a system of integral boundary layer equations, Cousteix & Houdeville[1981] have demonstrated that it is possible to avoid singularities by using an inverse formulation. For all these reasons, some work has been done concerning inverse boundary layer solutions for threedimensional flows [13], [14], [30], [44].

In this study, the development of an inverse method is examined for turbulent three dimensional flows by means of a finite difference method. The selected method is an extension of the method of Carter[1978] along lines somewhat different from the extension of Formery & Delery[1981]. This finite difference method uses the general boundary layer formulation of Cebeci-Chang-Kaups[1979] and their source code provides the basis of the inverse procedure.

The paper is outlined as following: section 1 is concerned with basic equations which are of course the same both for direct and inverse modes. Section 2 discusses the shortcomings of the numerical method and describes its application to the threedimensional Zigzag Box Scheme. For the sake of conciseness, Standard Box Scheme which has also been coded is not considered here. Section 3 discusses numerical results for the SSPA 720 and the prolate spheroid at incidence. In section 4, advantages and disadvantages of interactive formulations are examined and an attempt of generalization of the Veldman's quasi-instantaneous formulation is sketched.

1.-Basic equations

The governing boundary layer equations for three dimensional incompressible laminar and turbulent flows in a curvilinear non orthogonal coordinate system (Fig. 1) are given by:

$$\left(\bar{U}h_2\sin\theta\right)_x + \left(\bar{W}h_1\sin\theta\right)_z + \left(\bar{V}h_1h_2\sin\theta\right)_y = 0. \quad (1a)$$

$$\frac{\bar{U}}{h_1}\bar{U}_x + \frac{\bar{W}}{h_2}\bar{U}_z + \bar{V}\bar{U}_y - K_1\bar{U}^2\cot\theta + K_2\bar{W}^2\csc\theta + K_{12}\bar{U}\bar{W} = -\frac{\csc^2\theta}{h_1}\rho^{-1}\bar{P}_x + \frac{\cot\theta\csc\theta}{h_2}\rho^{-1}\bar{P}_z + \left(\nu\bar{U}_y - \overline{u'v'}\right)_y \quad (1b)$$

$$\frac{\bar{U}}{h_1}\bar{W}_x + \frac{\bar{W}}{h_2}\bar{W}_z + \bar{V}\bar{W}_y - K_2\bar{W}^2\cot\theta + K_1\bar{U}^2\csc\theta + K_{21}\bar{U}\bar{W} = -\frac{\cot\theta\csc\theta}{h_1}\rho^{-1}\bar{P}_x - \frac{\csc^2\theta}{h_2}\rho^{-1}\bar{P}_z + \left(\nu\bar{W}_y - \overline{v'w'}\right)_y \quad (1c)$$

Here, h_1 and h_2 are the metric coefficients: they generally depend on x and z: θ is the angle between x and z coordinates; K_1 and K_2 are the geodesic curvatures of the curves z=const. and x=const. respectively and:

$$K_1 = \frac{1}{h_1h_2\sin\theta}\left[\left(h_2\cos\theta\right)_x - h_{1z}\right]; \quad K_2 = \frac{1}{h_1h_2\sin\theta}\left[\left(h_1\cos\theta\right)_z - h_{2x}\right]$$

$$K_{12} = \frac{1}{\sin\theta}\left[-\left(K_1 + \frac{1}{h_1}\theta_x\right) + \cos\theta\left(K_2 + \frac{1}{h_2}\theta_z\right)\right]$$

$$K_{21} = \frac{1}{\sin\theta}\left[-\left(K_2 + \frac{1}{h_2}\theta_z\right) + \cos\theta\left(K_1 + \frac{1}{h_1}\theta_x\right)\right]$$

At the edge of the boundary layer (1b,c) are satisfied by $U=U_e(x,z)$; $W=W_e(x,z)$; while, for y=0:

$$\bar{U} = \bar{V} = \bar{W} = 0 \quad ; \quad \overline{u'v'} = \overline{v'w'} = 0 \quad (2)$$

The solution of (1) subject to boundary conditions (2) requires initial conditions on two planes intersecting the body along coordinate lines. The construction of these initial conditions for a ship-like hull is difficult due to the variety of bow shapes. An ad-hoc starting procedure is given in C^{2}K code and it has been supplemented by a Blottner & Ellis[1975] type procedure for the prolate spheroid.

In the case of rectilinear motion of the body, $W=P_z=0$ on the plane of symmetry of the hull, causing (1c) to be trivial. However, differentiation with respect to z removes singularities and leads to the so-called longitudinal attachment line equations which can be written:

$$\left(\bar{U}h_2\sin\theta\right)_x + h_1\sin\theta\,\bar{W}_z + \left(\bar{V}h_1h_2\sin\theta\right)_y = 0. \quad (3a)$$

$$\frac{\bar{U}}{h_1}\bar{U}_x + \bar{V}\bar{U}_y - \cot\theta\,K_1\bar{U}^2 = \frac{U_e}{h_1}U_{ex} - K_1U_e^2\cot\theta + \left(\nu\bar{U}_y - \overline{u'v'}\right)_y \quad (3b)$$

$$\frac{\bar{U}}{h_1}\bar{W}_{zx} + \bar{V}\bar{W}_{zy} + \frac{\bar{W}_z^2}{h_2} + K_{21}\bar{U}\bar{W}_z = \frac{U_e}{h_1}W_{zex} + \frac{W_{ze}^2}{h_2} + K_{21}U_eW_{ze} + \left[\nu\bar{W}_{zy} - \left(\overline{v'w'}\right)_z\right]_y \quad (3c)$$

with boundary conditions:

$$y=0 : \bar{U} = \bar{V} = \bar{W}_z = 0 \; ; \; y=\delta : \bar{U} = U_e \; , \; \bar{W}_z = W_{ze} \quad (4)$$

For turbulent flows, closure assumptions are necessary for Reynolds stresses $-\overline{u'v'}$ and $-\overline{v'w'}$ which are modelled with a newtonian closure of Boussinesq type. The turbulent viscosity ν_T is specified by the two-layer algebraic model of Cebeci & Smith[1974].

The mapping of the ship hull given by a succession of unit circles is performed by a James method as developped by Halsey[1979]. The coordinate system is completed by spline fits in the planes z=const. for y=y(x) and z=z(x) which yield derivatives allowing the computation of K_1, K_2, K_{12} and K_{21}.

The boundary layer equations are solved in a transformed coordinate system using Lees-Levy-Mangler variables:

$$x = x \quad ; \quad z = z \; ; \; d\eta = \sqrt{\frac{U_e}{\nu s}}\,dy \quad ; \quad s = \int_0^x h_1\,dx \quad (5)$$

while a two component vector potential is introduced:

$$\bar{U}h_2\sin\theta = -\psi_y \; ; \; \bar{W}h_1\sin\theta = \phi_y \; ; \; \bar{V}h_1h_2\sin\theta = -\psi_x - \phi_z \quad (6)$$

then, f and g are defined as:

$$\psi = \sqrt{\nu s U_e}\,h_2\sin\theta\,f(x,z,\eta) \; ; \; \phi = \sqrt{\nu s U_e}\frac{U_e}{U_e}h_1\sin\theta\,g(x,z,\eta) \quad (7)$$

so that $U=U_ef'$; $W=U_{re}fg'$ where the dot abbreviates for the η derivative. To transform the longitudinal attachment line equations, the ϕ component is defined by $W_zh_1\sin\theta = \phi_y$ so that $Vh_1h_2\sin\theta = -\psi_x - \phi$ where ψ and ϕ are still specified by (9) so that now $W_z = U_{re}fg''$.

Even if the need of such a transformed coordinate system loses of its evidence for coupling problems, it is felt to allow, as in the direct mode, a

more optimal distribution of mesh points in the boundary layer. Moreover, it permits more easily the switching from one mode to another.

Substitution of (5) (6a) (7) in (1) gives:

$$(bf'')'+\overline{m}_1 ff''+m_7 f''g+m_2(1-f'^2)+m_5\left(\frac{W_e}{U_{ref}}-f'g'\right)$$
$$+m_8\left(\frac{W_e^2}{U_{ref}^2}-g'^2\right)=\frac{s}{h_1}\left(f'f'_x-f''f_x\right)+m_6\left(g'f'_z-f''g_z\right) \qquad (8a)$$

$$(bg'')'+\overline{m}_1 fg''+m_7 g''g+m_3(1-f'^2)+m_5\left(\frac{W_e}{U_{ref}}-f'g'\right)$$
$$+m_3\left(\frac{W_e^2}{U_{ref}^2}-g'^2\right)=\frac{s}{h_1}\left[f'\left(g'-\frac{W_e}{U_{ref}}\right)_x-g''f_x\right]+m_6\left[\left(\frac{g'^2}{2}-\frac{W_e^2}{2U_{ref}^2}\right)_z-g''g_z\right] \qquad (8b)$$

where:

$$\overline{m}_1=\frac{1}{2}\left[1+\frac{s}{h_1 U_e}U_{ex}\right]+\frac{s}{h_1 h_2 \sin\theta}(h_2\sin\theta)_x$$

$$m_3=-sK_2\frac{U_{ref}}{U_e}\cot\theta\ ;\ m_5=\frac{s}{h_2}\frac{U_{ref}}{U_e^2}U_{e_z}+sK_{12}\frac{U_{ref}}{U_e}\ ;\ m_6=\frac{s}{h_2}\frac{U_{ref}}{U_e}$$

$$m_7=\frac{s}{h_1 h_2\sin\theta}\cdot\frac{1}{\sqrt{U_e s}}\left(\sqrt{U_e s}\,h_1\frac{U_{ref}}{U_e}\sin\theta\right)_z\ ;$$

$$m_8=sK_2\frac{U_{ref}^2}{U_e^2}\cot\theta\ ;\ m_2=\frac{s}{h_1 U_e}U_{ex}-sK_1\cot\theta$$

while substitution of (5), (6b), (7) in (3) yields:

$$(bf'')'+m_1 ff''+m_6 f''g+m_2(1-f'^2)=\frac{s}{h_1}\left(f'f'_x-f_x f''\right) \qquad (9a)$$

$$(bg'')'+m_1 fg''+m_6 g''g+m_3\left(\frac{W_{ze}^2}{U_{ref}^2}-g'^2\right)+sK_{21}f'\left(\frac{W_{ze}}{U_{ref}}-g'\right)=$$
$$=\frac{s}{h_1}\left[f'\left(g'-\frac{W_{ze}}{U_{ref}}\right)_x-f_x g''\right] \qquad (9b)$$

where:

$$m_1=\frac{1}{2}\left[1+\frac{s}{h_1 h_2\sin\theta}(h_2\sin\theta)_x\right]+\frac{s}{2h_1 U_e}U_{ex}$$

2. - The numerical method

In the direct mode, the foregoing equations (8) (9) are solved by using the Cebeci-Chang-Kaups method [1979]. In the inverse mode, their formulation and their source code have been used as a starting point for the construction of the inverse code. Various inverse methods can be invented according to the choice of the prescribed functions. Smith[1982] advocates the specification of a transpiration velocity and adds an equation for the component of vorticity of the external flow normal to the surface, so that only one input is needed. Unfortunately, the system of integral equations have been reported to be ill conditionned (Wigton & Yoshihara[1982]). Because the most often known characteristics of the boundary layer are the displacement thicknesses, these are selected as the prescribed functions.

This choice has been shown to behave properly by Cousteix & Houdeville[1981] who performed successful computations by using an integral method for an infinite swept wing, and it has also been used by Formery & Delery[1979] and Radwan & Lekoudis [1984].

The streamfunctions f and g will not be used as they go to infinity, rather streamfunction perturbations are introduced which go to zero at the edge of the boundary layer and thus allow displacement effects to be more accurately introduced. Several choices are possible and (10) has been selected:

$$\hat{f}=f-\left\{f'(\eta-\Delta_1^*\cos\alpha)-g'\frac{U_{ref}}{U_e}\Delta_1^*\cos(\theta-\alpha)\right\} \qquad (10a,b)$$
$$\hat{g}=g-\left\{g'[\eta-\Delta_2^*\cos(\theta-\alpha)]+f'\frac{U_e}{U_{ref}}\Delta_2^*\cos\alpha\right\}$$

where:

$$\Delta_1^*=\frac{1}{q_e}\sqrt{\frac{U_e}{\nu s}}\int_0^\infty(U_e-\overline{U})\,dy\ ;\ \Delta_2^*=\frac{1}{q_e}\sqrt{\frac{U_e}{\nu s}}\int_0^\infty(W_e-\overline{W})\,dy\ ;\ q_e=|\vec{V}_e| \qquad (11a,b)$$

Auxiliary variables u, v, w, t are introduced:

$f'=u$; $g'=w$; $u'=v$; $w'=t$

so that (10a,b) gives:

$$\hat{f}'=v\left(\Delta_1^*\cos\alpha-\eta\right)+t\frac{U_{ref}}{U_e}\Delta_1^*\cos(\theta-\alpha) \qquad (12a)$$

$$\hat{g}'=v\frac{U_e}{U_{ref}}\Delta_2^*\cos\alpha+t\left[\Delta_2^*\cos(\theta-\alpha)-\eta\right] \qquad (12b)$$

The numerical solution can then be obtained by a zigzag second-order box scheme with Newton iterations on the non linear term. Unknowns are f_j, g_j, u_j, v_j, w_j, t_j at each node (x_n, z_k, η_j) for $j=1,\ldots,N-1$ and $U_e(x_n,z_k)$; $W_e(x_n,z_k)$.

While numerical boundary conditions at j=N are:

$$\hat{f}_N=\hat{g}_N=0\ ;\ u_N=1;(v_N=0);\ w_N=\frac{W_e(x_n,z_k)}{U_{ref}};(t_N=0)$$

so that the linearized difference equations for the system can be written under the following form:

$$\delta u_j-\delta u_{j-1}-\frac{h_j}{2}(\delta v_j+\delta v_{j-1})=(r_1)_j \qquad \text{for } u'=v$$

$$\delta w_j-\delta w_{j-1}-\frac{h_j}{2}(\delta t_j+\delta t_{j-1})=(r_2)_j \qquad \text{for } w'=t$$

$$\delta\hat{f}_j-\delta\hat{f}_{j-1}+(\gamma_1)_j\delta v_j+(\gamma_2)_j\delta v_{j-1}+$$
$$+(\gamma_3)_j\delta t_j+(\gamma_4)_j\delta t_{j-1}+(\gamma_{11})_j\delta U_e=(r_3)_j \qquad \text{for (12a)}$$

$$\delta\hat{g}_j-\delta\hat{g}_{j-1}+(\lambda_1)_j\delta v_j+(\lambda_2)_j\delta v_{j-1}+(\lambda_3)_j\delta t_j+$$
$$+(\lambda_4)_j\delta t_{j-1}+(\lambda_{11})_j\delta U_e+(\lambda_{12})_j\delta W_e=(r_4)_j \qquad \text{for (12b)}$$

$$(\zeta_1)_j\delta u_j+(\zeta_2)_j\delta u_{j-1}+(\zeta_3)_j\delta v_j+(\zeta_4)_j\delta v_{j-1}+(\zeta_5)_j\delta w_j$$
$$+(\zeta_6)_j\delta w_{j-1}+(\zeta_7)_j\delta\hat{f}_j+(\zeta_8)_j\delta\hat{f}_{j-1}+(\zeta_9)_j\delta\hat{g}_j$$
$$+(\zeta_{10})_j\delta\hat{g}_{j-1}+(\zeta_{11})_j\delta U_e+(\zeta_{12})_j\delta W_e=(r_5)_j \qquad \text{for (8a)}$$

$$(\beta_1)_j\delta u_j+(\beta_2)_j\delta u_{j-1}+(\beta_3)_j\delta w_j+(\beta_4)_j\delta w_{j-1}+(\beta_5)_j\delta t_j$$
$$+(\beta_6)_j\delta t_{j-1}+(\beta_7)_j\delta\hat{f}_j+(\beta_8)_j\delta\hat{f}_{j-1}+(\beta_9)_j\delta\hat{g}_j$$
$$+(\beta_{10})_j\delta\hat{g}_{j-1}+(\beta_{11})_j\delta U_e+(\beta_{12})_j\delta W_e=(r_6)_j \qquad \text{for (8b)}$$

Values of $(\zeta_\alpha)_j$, $(\beta_\alpha)_j$, $(\gamma_\alpha)_j$, $(\lambda_\alpha)_j$, $(r_\alpha)_j$ are omitted for the sake of conciseness. They differ for longitudinal attachment lines where they are somewhat simpler (for instance $(\gamma_3)_j=(\gamma_4)_j=(\gamma_{11})_j=0$, $(\lambda_{11})_j=(\zeta_{12})_j=0$ and W_e is replaced by W_{ze}). In the three-dimensional case, they depend on whether a standard or zigzag box scheme is used.

No slip conditions are (j=0):

$$\delta u_o = \delta w_e = \delta\hat{f}_0 = \delta\hat{g}_o = 0$$

while outer flow conditions are written on j=N:

$$\delta u_N = \delta\hat{f}_N = \delta\hat{g}_N = \delta W_e - U_{ej}\,\delta W_N = 0$$

The linear system to be solved is thus of the following form:

$$B_j\delta_{j-1} + A_j\delta_j + C_j\delta_{j+1} + D_j\delta_E = R_j \quad j=1,\ldots,N-1$$

$$B_N\delta_{N-1} + A_N\delta_N + D_N\delta_E = R_N$$

$$B_E\delta_N + D_E\delta_E = R_E$$

where

$$\delta_E = [\delta U_e, \delta W_e]^T ; \quad \delta_j = [\delta u_j, \delta w_j, \delta\hat{f}_j, \delta\hat{g}_j, \delta v_j, \delta t_j]^T$$

$$\begin{Vmatrix} A_o & C_o & & & & D_o \\ B_1 & A_1 & C_1 & & 0 & D_1 \\ & & & & & \\ & B_j & A_j & C_j & & D_j \\ & & & & & \\ 0 & & & B_N & A_N & D_N \\ & & & & B_E & D_E \end{Vmatrix} \cdot \begin{Vmatrix} \delta_o \\ \delta_1 \\ \\ \delta_j \\ \\ \delta_N \\ \delta_E \end{Vmatrix} = \begin{Vmatrix} R_o \\ R_1 \\ \\ R_2 \\ \\ R_N \\ R_E \end{Vmatrix}$$

This 6x6 block tridiagonal system with one column is solved with an ad-hoc LU factorization which is realized by the subroutine SOLV6C.

The method has been coded both for the attachment line equations and for the three dimensional problem with a standard box scheme and with a zigzag box scheme. The zigzag scheme is necessary for the ship geometries for which three dimensional computations are started from the vertical plane of symmetry where $W_e < 0$.

3. -Results

(i) Prolate spheroid

Numerical computations of separation round bluff bodies have been especially performed on the prolate spheroid at incidence. Such a simple geometry for which an inviscid solution is analytically known isolates conveniently specific difficulties of boundary layer computations.

Let us first consider the plane of symmetry problem which is a specific while interesting particular case in that it differs from the two-dimensional problem in the presence of lateral flow convergence or divergence and from the twodimensional problem in the absence of a crossflow. Moreover, it can be computed and checked independently.

Wang[1974][1975] in the laminar case, Lecointe[1979] in the transitional and turbulent case have computed this type of flow. Most recent results were provided by Cebeci et Al[1980] who showed that for an angle of attack less than 42°, the laminar separation occured downstream of the leeside of the spheroid (aspect ratio 1:4) while for plane layers round airfoils, the separation was close to the leading edge. Moreover a circumferential reversal occurs so that a lateral wall divergence is present downstream the pressure minimum implying a rapid thickening of the boundary layer which absorbs inviscid fluid. For an incidence greater than 42°, the separation is close to the nose.

Once the situation is known in the plane of symmetry, the computation can be performed outside of it. At low incidence, a line of pressure minimum starting close to the windside near the nose moves towards the leeside downstream; before finding this pressure minimum the circumferential flow meets an adverse pressure gradient and is thus deflected downwards leading to an accumulation of the flow on an "open" separation line l_s which is responsible of the emission of longitudinal vortices and terminates to a nodal point downstream (Han & Patel[1979]). At 10° of incidence, experiments indicate that the difference between potential flow and experiments is quite small on the upper third part of the spheroid. Patel & Baek[1981] computations with a ADI method show for $Re=1.6\ 10^6$ a circumferential flow reversal on C_{fe} some degrees before a lateral reversal line l_s (called XFR) defined apparently by $\vec{\tau}_w \cdot \vec{v}_e = 0$. The skin friction direction changes very abruptly, its modulus becomes very small while the boundary layer thickness thickens very quickly. Similar results have been found by Ragab[1982][1985].

For $Re=7.2\ 10^6$, similar phenomena are found but more downstream and less abruptly. Serious numerical difficulties appear in these regions which lead to a divergence of the computation for $x/L \geq .44$ for $Re = 1.6\ 10^6$ and $x/L \geq .88$ at $Re = 7.2\ 10^6$. Similar computations due to Cebeci [1984] with his characteristic scheme at 30° exclude the possibility of marching downstream from the leeside plane of symmetry while the marching from the windside is limited about $\theta = 110°$. Strong evidence of a A-zone accessible to the computations is therefore present in every work. The boundary ∂A which limits the "OK" of accessibility can be identified on the windside with l_s which appears to be a limiting streamline in the sense that it is tangent to the skin friction at every point.

Interactions are not accounted for and the solution behaves as if a singularity of Brown[1965] type was present. This gives some credit to several models of interaction analogue to those proposed by Smith[1982] for slender wing bodies and by Riley[1979] for slender conical flows at incidence. When marching from the leeside, things appear less clear: while at 6° of attack, l_a seems partly to coincide with l_s, the progression of the computation which was not possible from the leeside at 30° is limited at lower incidences by the direction of the inviscid streamline so that it is not possible to march further than the streamline subcharacteristic corresponding to the top of the arrow.

Even if such computations do not answer the question of the threedimensional separation and particularly of the birth of l_s, strong evidence of a Brown singularity appears in every computation so that an inverse method should be useful while the need of a lateral flare approximation does not seem evident "a priori".

The lateral reversal line seems to behave in such a way that $\vec{\tau}_w \cdot \vec{v}_e = 0$. If $\vec{\tau}_w \cdot \vec{v}_e$ becomes negative in the unaccessible zone, for the independence rule to be satisfied, the standard box scheme is unadequate as it is unstable for negative aspect ratios and therefore a zigzag box scheme

must be considered.

Comparisons between direct and inverse mode computations around a prolate spheroid (excentricity 4:1; incidence 6°) are now presented. In order to rule out the problem of high incidence flows, a special starting procedure has been implemented which uses the orthogonal coordinate system of Blottner & Ellis[1973]. Direct mode computations start in the immediate vicinity of the stagnation point where Blasius & Howarth developments provide the initial laminar conditions on the first parallel coordinate adjacent to the pole located at the stagnation point. The solution is then marched "away" using the Cebeci-Chang-Kaups method ($0 \leq \bar{x}/L \leq 0.05$). Because of the divergence of coordinate lines downstream and also because the boundary layer does not thicken in the same way over and under the nose, a rezoning of the computation back to the "natural body system" downstream is performed. Fig. 2 shows superpositions of the two meshes which are used: one of them starts from the stagnation point and the other one from the pole of the spheroid.

(a) Comparisons are first carried out in the *forepart* of the prolate spheroid ($0.04 \leq \bar{x}/L \leq 0.20$). Solutions used in the plane of symmetry result only from a direct mode method and all calculations are done by marching from the windward plane of symmetry. Although not necessary when the flow is attached, double precision is used as it should be useful for the investigation of the separated zones. 30 points girthwise and about 90 points through the thickness are used in the results presented here. Δ^*_1 and Δ^*_2 displacement thickness distributions resulting from the direct mode computations are used as inputs of the inverse mode. Two types of variables are considered: the wall variables $v_{wall} = \partial u/\partial\eta(\eta=0)$, $t_{wall} = \partial w/\partial\eta(\eta=0)$ and the edge components of the velocity U_e and W_e. Whereas direct computations are performed without any problem, slight girthwise oscillations appear in the inverse mode results which grow monotonically as one proceeds downstream, leading to a divergence of the inverse mode. Various smoothing procedures have been tested to suppress these oscillations without any success. The inverse formulation seems to require smaller longitudinal and transversal steps to converge than the direct mode, especially in the nose region because of high curvatures and longitudinal variations of the pressure gradient.

(b) Comparisons are now carried out in the *middle part* of the body ($0.40 \leq \bar{x}/L \leq 1.28$) where curvatures and longitudinal variations of the pressure are smaller. Direct mode computations proceed downstream without difficulty, leading to regular girthwise distributions of v_{wall}, t_{wall} (fig. 4c-d). From $\bar{x}/L = 1.00$, the flow is characterized by a rapid thickening of the boundary layer, the maxima of Δ^*_1 and Δ^*_2 occuring near the windward plane ($\theta \simeq 130°$) (Fig. 4a-b). In the thick region, v_{wall} decreases rapidly as a circumferential flow reversal is observed near the wall. Direct computations stop at $\bar{x}/L = 1.32$ where the first non-converged point is reached. No attempt was done to reduce the accessible zone by starting the computations from the leeward plane. The displacement thicknesses obtained from direct mode calculations were used as inputs for the inverse mode calculations. Fig. 4c-f show the evolution of the wall and edge variables v_{wall}, t_{wall}, U_e, W_e at different x-stations using both the direct and inverse formulations. An excellent agreement is observed on the components of the edge velocity U_e, W_e, like on the wall variables v_{wall}, t_{wall} (while some slight oscillations surprisingly appear after $\bar{x}/L = 1.00$ in a region where the crossflow component is maximum and positive). Until now, no attempt has been done to extrapolate the displacement thicknesses and continue the inverse calculations beyond the direct mode unaccessible zone. Such results should be available in a near future.

(ii) SSPA 720 ship model

Computations relative to the SSPA 720 ship model[20],[21] (Fig. 3) usually start at $\bar{x}/L=-0.6$. Initial values are generated from experiments giving β_w, u_τ/q_e and $\delta^+=\delta u_\tau/\nu$ by the method of Coles and Thompson. Direct mode computations are performed from $\bar{x}/L = -0.6$ to $\bar{x}/L = 0.05$ and comparisons between the direct and inverse results are carried out from $\bar{x}/L = 0.05$ to $\bar{x}/L = 0.50$ in order to validate the inverse approach.

As for the prolate spheroid, solutions used in the plane of symmetry result from a direct mode method. The boundary layer grid on the surface is taken of equal spacing in the z direction and of variable spacing in the x direction in agreement with the CFL condition. 21 points girthwise and about 50 points through the thickness are used in the results presented here. Fig. 5a-b show the evolution of the displacement thicknesses Δ^*_1 and Δ^*_2 for several x-stations. Boundary layer remains thin in the vicinity of the keel ($z = 0.$) while it grows rapidly as one goes along the hull ($z = 0.50$) because of the convergence of potential streamlines. The aftpart of the hull is characterized by a large growth of Δ^*_1, the existence of a second maximum which doesn't seem to be corroborated by the experiments, and by a rapid change in the Δ^*_2 distribution from positive to large negative values. Fig. 5c-f show comparisons for U_e, W_e, $\partial u/\partial\eta(\eta=0.)$, $\partial w/\partial\eta(\eta=0.)$ between the direct and inverse modes. From $\bar{x}/L = 0.05$ to $\bar{x}/L = 0.3$, the agreement is quite satisfactory; the present slight discrepancies are due to the irregularity of the Δ^*_1 and Δ^*_2 distributions. From $\bar{x}/L = 0.4$ to $\bar{x}/L = 0.5$, the agreement is good near the keel and the waterline, where the boundary layer is thin, while large discrepancies are present for $0.3 \leq z \leq 0.8$. In this region, because of the rapid growth of the boundary layer, good predictions from the direct computations can hardly be expected since they rest on a thin boundary layer theory. Consequently, Δ^*_1 and Δ^*_2 distributions are ill predicted, this leads to incorrect results for the inverse mode computations.

4.-Towards the computation of strong interaction

Up to now, two formulations can be used:
(i) Global formulations for which the same equations are used in the whole field (parabolized, partially-parabolic or Navier-Stokes equations). With respect to triple-deck theory, equations used are valid through the complete triple-deck structure so that the interaction is included in the model to the price of the consideration of a-priori negligeable terms in some parts of the field. The main advantages are the following: the normal pressure variation is correctly accounted for, the formulation should be correctly vectorizable, no singularity occurs when separation

is passed through, the computation can be carried out downstream into the wake in a very easy way. These have to be paid by the fact that the solutions can be obtained only on quite coarse grids (with respect to storage capabilities of available computers) and, therefore, that few points can be located in the viscous zone, inducing a fair description of forces. To this category belong, for instance, the works of Abdelmeguid et Al [1979], Markatos et Al[1980], Muraoka[1980][1982], Tzabiras[1985], Chen & Patel [1984], Raven & Hoekstra[1985] which are mainly devoted to the study of ship stern flows. (ii) Interactive formulations for which the computational zone is splitted into two domains. With respect to the triple-deck theory, one of the domains corresponds to the lower deck alone, the other domain includes both the main deck and the upper deck. Equations differ in each domain and they are solved interactively by a coupling technique simulating the connection between the upper and the lower deck through the relationship between the pressure field in the boundary layer and the displacement effect. The advantages lie in the fact that the system of equations which are solved are well adapted to each domain; less storage being consumed, a better description of the viscous zone results from the possibility of locating more grid points there. But the degree of validity of the interactive methods depend on the degree of generality of the viscous model. At present, only thin boundary layer equations are considered (see nevertheless Whittfield[1985]. Moreover, such methods should be less vectorizable because of the interaction law. Endly, the computations downstream into the wake are more difficult to handle, especially if thin boundary layer theory is retained for the viscous domain, not only because of geometrical reasons but also because the computation of the wake may influence the convergence of the interaction law.

The choice of the best method remains an opened question and probably, as long as storage memories of computers will not be considerably increased, no universal answer to this question will be given. The future of interactive methods is probably conditioned by the answer to the following questions:

1- While the singularity problem seems to condition the two-dimensional case, what is the dominant effect in the three-dimensional case? Separation does not appear then to be a prerequisite for a significant thickening of the boundary layer as is well known from the study of the aftpart of an axisymmetric body or of the ship stern flow. The thickening of the viscous zone and the increase of the normal velocity component appear progressively because of the convergence of streamlines in planes parallel to the wall. The absence of catastrophic behaviour is a common feature of these flows together with the generation of a longitudinal vorticity component and an associated vortex motion similar (but less intense) to that observed on slender bodies at high incidence. Therefore, thin direct boundary layer computations can be carried out almost to the trailing lines but numerical results are known to disagree with experiments because the thin boundary layer assumptions are not fulfilled. In other cases, like the prolate spheroid at incidence, thin direct boundary layer equations cannot be used downstream of a singular line (the so-called OK of accessibility of Cebeci et Al[1981]). Nevertheless, the experience of threedimensional integral methods suggests that, to a certain extent, thin boundary layer equations may still be used, inverse mode techniques allowing singularities to be suppressed; but how far the computations can be carried out remains unclear.

2-Is the inverse mode solution of boundary layer equations the best suited to rule out the problem of threedimensional singularities? What can be obtained from an interactive procedure, the viscous kernel of which rests on the thin boundary layer approximation? Or stated equivalently: to what extent such an interactive procedure is able to give correct results if a separation is present? The first threedimensional computations of separated flows on wings and prolate spheroids with integral formulations show that the validity domain of inverse methods is larger than that for direct methods but it is not yet possible to compute a complete separated flow. Cebeci et Al[1981] using a twodimensional coupling assumption have obtained interesting strong interaction results on threedimensional wings. Therefore $p_y = 0$ does not seem a serious penalty in this case. More encouraging are the computations due to Huang & Chang[1985] on the aftpart of slender NSRDC bodies for which $p_y \neq 0$. A pressure correction together with a weak coupling technique are sufficient to improve the solution to a point such that both the interactive solutions and "parabolized Navier-Stokes" solutions agree correctly with experimental data. But, in these last cases, separation is not significant.

3-How is it possible to generalize the coupling techniques used in two dimensions and what will be the convergence rate of threedimensional interaction laws? It is only possible to give a partial answer which will now be sketched. Let us suppose that for $y > \delta(x,z)$ the flow is inviscid; while, for $y < \delta(x,z)$ boundary layer equations are used to describe the viscous zone. Two patching conditions are necessary at $y=\delta(x,z)$. One is relative to the inviscid velocity components parallel to the wall which, as a first approximation, should be equal to the edge-boundary layer velocity component parallel to the wall. The other is relative to the normal velocity component. It is obtained by defining the inviscid velocity components in the boundary layer domain by means of a Taylor serie near $y=\delta$:

$$V_e(x,z,y) \simeq V_e(x,z,\delta) + (y-\delta)\left.\frac{\partial V_e}{\partial y}\right|_{y=\delta}$$

where index e refers to the inviscid flow. Eliminating $\partial V_e/\partial y|_{y=\delta}$ by means of the continuity equation and integrating through the boundary layer from 0 to δ, one is left with the so-called entrainment equation:

$$V(x,z,\delta) = -\frac{1}{h_1 h_3 \sin\theta}\left\{\frac{\partial}{\partial x}\left[h_3 \sin\theta\,(q_e\Delta_1 - U_e\delta)\right] + \right.$$
$$\left. + \frac{\partial}{\partial z}\left[h_1 \sin\theta\,(q_e\Delta_2 - W_e\delta)\right] + \frac{1}{h_1 h_3}\left[h_3 U_e\frac{\partial \delta}{\partial x} + h_1 W_e\frac{\partial \delta}{\partial z}\right]\right. \quad (13)$$

where:

$$\Delta_1 = \int_0^\delta \frac{U_e - \bar{U}}{q_e}\,dy \;;\; \Delta_2 = \int_0^\delta \frac{W_e - \bar{W}}{q_e}\,dy \;;\; q_e = |\vec{V}_e|$$

The patching condition for the condition $V(x,z,\delta) = V_e(x,z,\delta)$ needs now to be specified. A first possibility is given by a "displacement effect patching" at $y=\delta^*$ where the Lighthill surface $y=\delta^*(x,z)$ is defined by the fact that the inviscid flow slips on it:

$$V_e(x,z,\delta^*) = \frac{U_e}{h_1}\frac{\partial \delta^*}{\partial x} + \frac{W_e}{h_3}\frac{\partial \delta^*}{\partial z}$$

(13) implies that:

$$\frac{\partial}{\partial x}\left[h_3 \sin\theta \left(q_e \Delta_1 - U_e \delta^*\right)\right] + \frac{\partial}{\partial z}\left[h_1 \sin\theta \left(q_e \Delta_2 - W_e \delta^*\right)\right] = 0$$

A most interesting choice consists in a "wall patching": what is now specified is:

$$V_e(x,z,0) = \frac{1}{h_1 h_3 \sin\theta}\left\{\frac{\partial}{\partial x}(h_3 \sin\theta\, q_e \Delta_1) + \frac{\partial}{\partial z}(h_1 \sin\theta\, q_e \Delta_2)\right\}$$

In this case the transpiration velocity is defined at the wall so that the inviscid flow is computed on the same domain as that corresponding to the non interactive case and it can be therefore obtained with the same code.

Having specified the *form* of the coupling, let us examine what iterative methods can be used. The output of the boundary layer computation is a functional relationship $\vec{v}_e = B(\delta^*)$: $\vec{rot}\ \vec{v}_e = 0$ where B is a local operator corresponding to Prandtl equations with their boundary conditions. The domain of B^{-1} is limited as separation is excluded. The output of the inviscid computation is a second functional relationship $\vec{v}_e = P(\delta^*)$; $\vec{rot}\ \vec{v}_e = 0$ where P is a non local operator at y=0. P gives an accurate description of the influence of the boundary layer on the inviscid flow. Le Balleur[1980] discusses direct

$\vec{v}_e^{(m)} = P(\delta^{*(m-1)})$, $\delta^{*(m)} = B^{-1}(\vec{v}_e^{(m)})$

and inverse

$\delta^{*(m)} = P^{-1}(\vec{v}_e^{(m-1)})$, $\vec{v}_e^{(m)} = B(\delta^{*(m)})$

iterative methods for the coupling and shows that if one wants to avoid the difficult switch from the direct to the inverse mode, a semi-inverse iterative method should be used. In this case (Le Balleur[1980], Carter[1979]), two pressure fields and two velocity fields are simultaneously used: one $(\vec{v}_e^{(m)}, p_e^{(m)})_e$ obtained from an direct solution of Euler equations; the other $(\vec{v}_e^{(m)}, p_e^{(m)})_v$ obtained from an inverse solution of boundary layer equations. The resulting edge velocities are then used to adjust the displacement thickness of the aforecomputed cycle; this is done the most often by the following underrelaxation (Carter[1979]):

$$\delta^{*(m+1)} = \delta^{*(m)} + \omega\, \delta^{*(m)}\left(1 - \frac{U_{eV}^{(m)}}{U_{eP}^{(m)}}\right)$$

Veldman[1981] advocates the use of a simultaneous approach in which the P operator is approximated under the form $\vec{v}_e = I(\delta^*)$ of an interaction law. In this case, $\vec{v}_e = I(\delta^*)$ and $\vec{v}_e = I(\delta^*)$ are regarded as two equations with two unknowns which have to be solved without iteration.

The interaction law should be chosen as simple as possible to allow the quasisimultaneous numerical treatment but it should also give a sufficiently accurate description of the interaction. The rapid convergence of the method being well established in two dimensional cases, we shall now discuss its practical implementation in the three dimensional case. Let us consider that a straightforward solution U_e of the inviscid problem has been obtained on the body and let us note $\vec{v}_e = U_e + \delta\vec{v}_e$ the solution of the coupled viscous-inviscid problem at the edge of the boundary layer. As seen from the inviscid fluid, the boundary layer acts like a transpiration velocity and $\delta\vec{v}_e = \vec{grad}\ \delta\phi$ so that the perturbed potential $\delta\phi$ satisfies: $\Delta(\delta\phi) = 0$; $\delta\phi = 0$ at infinity; $\partial\delta\phi/\partial n_{body} = V_e(x,z,0)$ known for the wall-patching case.

In the threedimensional case, the potential solution at any point $\underline{x}$ of the inviscid domain is given by

$$\delta\phi(\underline{x}) = -\frac{1}{4\pi}\iint_{\partial B} \sigma(\underline{x}')\frac{1}{|\underline{x}-\underline{x}'|}\, da(\underline{x}') \qquad (14)$$

where the body surface ∂B supports the unknown source distribution σ from which the normal velocity component at $\underline{x}$ on the surface results:

$$\vec{V}.\vec{n}\,|_{\partial B} = \iint_{\partial B} \sigma(\underline{x})\, K(\underline{x},\underline{x}')\, da(\underline{x}')$$

where

$$K(\underline{x},\underline{x}') = \frac{\vec{n}(\underline{x})}{4\pi}.\frac{\underline{x}-\underline{x}'}{|\underline{x}-\underline{x}'|^3}$$

σ can be computed from a Fredholm integral equation of second type:

$$\frac{1}{2}\sigma(\underline{x}) + \iint_{\partial B} \sigma(\underline{x}')\, K(\underline{x},\underline{x}')\, da(\underline{x}') = V_e(x,z,0)$$

which traduces the non local character of P. The approximation of Veldman consists in the omission of the surface integral over ∂B. Therefore, $\sigma(\underline{x}) = 2\, V_e(x,z,0)$ is used in (14) and:

$$\delta\phi(\underline{x}) = -\frac{1}{2\pi}\iint_{\partial B} \frac{V_e(\xi,\eta,0)\, d\xi\, d\eta}{\sqrt{(x-\xi)^2+(z-\eta)^2}} \qquad (15)$$

In the twodimensional case, because the Green function is a logarithm, one is left with Veldman equation:

$$\delta U_e(x) = \frac{1}{\pi}\oint_{x_i}^{x_f} \frac{d(U_e\delta^*)/d\xi}{x-\xi}\, d\xi$$

If the interaction law is not accurate enough, an iterative procedure

$\vec{v}_e^{(m)} - I\,\delta^{*(m)} = P(\delta^{*(m-1)}) - I\,\delta^{*(m-1)}$;

$\vec{v}_e^{(m)} - B(\delta^{*(m)}) = 0$ can be used, but the surface integral has to be computed at each iteration. Endly, the equations for δU_e and δW_e obtained from (15) have to be solved simultaneously with the boundary layer equations. Once the discretization of the interaction law has been carried out, the inverse boundary layer code appears to be well suited for a numerical coupling with the discretized equations for $\delta U_e(x_n, z_k)$ and $\delta W_e(x_n, z_k)$. Such a coupling procedure usually avoids completely the need of underrelaxation.

5.-Conclusion

The foregoing computations on the prolate spheroid and on the SSPA ship model demonstrate the feasability of an inverse mode solution of boundary layer equations round a complex geometry, although the sensitivity to the lack of smoothness of thickness distributions appears quite high. The interactive coupling with the potential flow, which is the final goal, remains to be performed.

-Acknowledgments

Authors are indebted to Pr. T. Cebeci for providing us with a source listing of C^2K method. Partial financial support of DRET through contract 83-218 is also gratefully acknowledged.

-Bibliography

[1] Abdelmeguid, A. M. ; Markatos, N. C. ; Muraoka, K. & Spalding, D. B. [1979]. A comparison between Parabolic and Partially-parabolic Solution Procedures for Three-Dimensional Turbulent Flow Around Ship's Hulls; Appl. Math. Modelling, Vol. 3, p. 249.

[2] Blottner, F. G. & Ellis, M. A. [1973]. Finite Difference Solution of the incompressible Three-dimensional Boundary Layer Equations for a Blunt Body: Comp. & Fluids, Vol. 1, pp. 133-158.

[3] Briley, W. R. & Mc Donald, H. [1975]. Numerical prediction of incompressible Separation Bubbles: J. Fluid Mech., Vol. 69, Pt. 4, pp. 631-656.

[4] Brown, S. N. [1965]. Singularities Associated with Separating Boundary Layers; Phil. Trans. Roy. Soc. A, Vol. 257, pp. 409-444.

[5] Carter, J. E. [1978]. Inverse Boundary Layer Theory and Comparison with experiments. NASA TP 1208 .

[6] Catherall, D & Mangler, K. W. [1966]. The Investigation of the Two Dimensional Laminar Boundary Layer Equations past the Point of Vanishing Skin Friction: J. Fluid Mech., Vol. 26, Pt. 1, pp. 163-182.

[7] Cebeci, T. [1984]. Problems and Opportunities with Three Dimensional Boundary Layers. AGARD to appear.

[8] Cebeci, T. ; Chang, K. C. & Kaups, K. [1978]. A Three Dimensional General Method for calculating Three Dimensional Laminar and Turbulent Boundary Layers on Ship Hulls; Proc. 12th. Symp. Naval Hydrodynamics (Washington).

[9] Cebeci, T. ; Chen, L. T. ; Chang, K. C. & Peavey, C. C. [1985]. An Interactive Scheme for Three Dimensional Transonic Flows; Proc. 3rd. Symp. Num. Phys. Aspects of Aerodynamic Flows. Ed. - Cebeci, T. Cal. Univ., Long Beach pp. 11-39/49.

[10] Cebeci, T. ; Khattab, A. D. & Stewartson, K. [1981]. Three-Dimensional Laminar Boundary Layers and the OK of accessibility; J. Fluid Mech., Vol. 107, pp. 57-87.

[11] Cebeci, T. & Smith, A. M. O. [1974]. Analysis of Turbulent Boundary Layers. Ed. Academic Press.

[12] Chen, H. C. & Patel, V. C. [1984]. Calculation of Stern Flows by a time Marching Solution of Partially Parabolic Equations; Proc. 15th. ONR Symp. on Naval Hydrodynamics, Hamburg, FRG.

[13] Coustelx, J. & Houdeville, R. [1981]. Singularities in Three-Dimensional Turbulent Boundary Layer Calculations and Separation Phenomena. AIAA Journ., Vol. 19, N°8, pp. 976-985.

[14] Formery, M. & Delery, J. [1981]. Méthode aux Différences finies en mode inverse de la couche limite turbulente tridimensionnelle; La Rech. Aérosp., N°5, pp. 301-313.

[15] Halsey, N. D. [1979]. Potential Flow Analysis of Multielement Airfoils using Conformal Mapping; AIAA Journ., Vol. 17, N°12, pp. 1281-1298.

[16] Han, T. Y. & Patel, V. C. [1979]. Flow Separation on a Spheroid at Incidence; J. Fluid Mech., Vol. 92, pp. 643-657.

[17] Hoekstra, M. & Raven, H. C. [1980]. Calculation of Viscous-Inviscid Interaction in the Flow past a Ship Afterbody. ; Proc. 13th. Symp. on Naval Hydrodynamics (Tokyo), Shipbuilding Res. Assoc. Japan, pp. 585-600.

[18] Huang, T. T. & Chang, M. S. [1985]. Computation of Velocity and Pressure Variation across Thick Turbulent Stern Flows; Proc. 3rd. Symp. Num. - Phys. Aspects of Aerodynamic Flows. Ed. Cebeci, - T., Cal. Univ., Long Beach, pp. 10-1/20.

[19] Kreplin, H. P. ; Vollmers, H. & Meier, H. U. [1982]. Measurements of the Wall Shear Stress on an Inclined Prolate Spheroid; Z. Flugwissen. Weltraumforsch., Vol. 6, pp. 248-252.

[20] Larsson, L. [1974]. Boundary Layers on Ships. Part III: an Experimental Investigation of the Turbulent Boundary Layer on a Ship Model; SSPA Rept. N°46.

[21] Larsson, L. [1981]. SSPA-ITTC Workshop on Ship Boundary Layers- Proceedings; SSPA Rept. N°90.

[22] Le Balleur, J. C. [1980]. Calcul des Ecoulements a Forte Interaction Visqueuse au moyen de Méthodes de Couplage; AGARD-CP 291 Computation of Viscous Inviscid Interactions, Paper 1.

[23] Lecointe, Y. [1979]. Contribution à l'Etude des Couches Limites Laminaires, Transitionnelles et Turbulentes sur un Ellipsoide de Révolution en Incidence; Thèse Doct. Ing. Univ. Nantes.

[24] Lighthill, M. J. [1963]. Laminar Boundary Layers; Rosenhead, L. Ed. Oxford Clarendon Press.

[25] Markatos, N. C. ; Malin, M. R. & Tatchell, D. G. [1980]. Computer Analysis of Three Dimensional Turbulent Flows around Ship's Hulls; Proc. Inst. Mech. Engr. London, Vol. 194, pp. 239-248.

[26] Muraoka, K. [1980]. Calculation of a Thick Boundary Layer and Wake of Ships by a Partially Parabolic Method; Proc. 13th. Symp. on Naval Hydrodynamics, (Tokyo), Shipbuilding Res. assoc. Japan, pp. 601-616.

[27] Muraoka, K. [1982]. Calculation of Viscous Flow around Ships with Parabolic and Partially Parabolic Flow Solution Procedure; Trans. West Japan Soc. Naval Arch., Vol. 63, pp. 13-29.

[28] Patel, V. C. [1982]. Some Aspects of Thick Three Dimensional Boundary Layers; Proc. 14th. - ONR Symp. on Naval Hydrodynamics (Ann Arbor), pp. 999-1040.

[29] Patel, V. C. & Baek, J. H. [1983]. Calculation of Boundary Layers and Separation on a Spheroid at

Incidence; Proc. 2nd. Symp. Num. & Phys. Aspects of Aerodynamic Flows, Ed. Cebeci, T., Cal. Univ. Long Beach.

[30] Radwan, S. F. & Lekoudis, S. G. [1984]. Boundary Layer Computations in the Inverse Mode for Incompressible Flows over Infinite Swept Wings; AIAA Journ., Vol. 22, N°6, pp. 737-743.

[31] Radwan, S. F. & Lekoudis, S. G. [1985]. Calculations of the Incompressible Turbulent Boundary Layer on an Ellipsoid in the Inverse Mode; AIAA Paper 85-1654; AIAA 18th. Fluid Dyn., Plasma Dyn. & Laser Conf. (Cincinatti).

[32] Ragab, S. A. [1982]. A Method for the Calculation of Three-Dimensional Boundary Layers with Circumferential Reversed Flow on Bodies; AIAA Paper 82-1023, AIAA/ASME 3rd. Jt. Therm., Fluids, Plasma & Heat Transf. Conf. (St Louis).

[33] Ragab, S. A. [1985]. Steady and Unsteady Boundary Layers on Prolate Spheroids at High Incidence; AIAA Paper 85-1708, AIAA 18th. Fluid Dyn., Plasma Dyn. & Plasma Conf. (Cincinatti).

[34] Raven, H. C. & Hoekstra, M. [1985]. A Parabolized Navier Stokes Solution Method for Ship Stern Flow Calculations; Proc. 2nd. Int. Symp. Ship Viscous Resistance, SSPA Ed. Larsson, L. pp.-14: 1/27.

[35] Riley, N. [1979]. Separation from a Smooth Surface on a Slender Conical Flow; J. Eng. Maths., Vol. 13, N°1, pp. 75-91.

[36] Smith, F. T. [1978]. Three-Dimensional Viscous and Inviscid Separation of a Vortex Sheet from a Smooth non Slender Body; RAE-TR-78095.

[37] Smith, P. D. [1982]. The Numerical Computation of Three Dimensional Boundary Layers; IUTAM Symp. Turbulent Boundary Layers, Ed. Fernholz & Krause, Springer Verlag, pp. 265-285.

[38] Tobak, M. & Peake, D. J. [1982]. Topology of Three Dimensional Separated Flows; Ann. Rev. Fluid Mech., Vol. 14, pp. 61-85.

[39] Tsabiras, G. D. [1985]. On the Calculation of the 3-D Reynolds Stress Tensor by two Algorithms; Proc. 2nd. Int. Symp. on Ship Viscous Resistance, SSPA, Larsson, L. Ed., pp. 15: 1/19.

[40] Veldman, A. E. P. [1980]. The Calculation of Incompressible Boundary Layers with Strong Viscous-Inviscid Interaction; AGARD CP-291 Computation of Strong Viscous-Inviscid Interaction, Paper 12.

[41] Wang, K. C. [1974]. Boundary Layer over a Blunt Body at High Incidence with an open-type of Separation; Proc. R. Soc. London A, Vol. 340, pp. 33-55.

[42] Wang, K. C. [1975]. Boundary Layer over a Blunt Body at Low Incidence with Circumferential Reversed Flow; J. Fluid Mech., Vol. 72, pp. 49-65.

[43] Whittfield, D. L. [1985]. Viscous-Inviscid Interaction Computations using a Pseudo Navier-Stokes Approach; Proc. 3rd. Symp. Num. Phys. Aspects of Aerodynamic Flows, Ed. Cebeci, T., Cal. Univ. Long Beach, pp. 4-1/16.

[44] Wigton, L. B. & Yoshihara, H. [1983]. Viscous-Inviscid Interactions with a Three-Dimensional Boundary Layer Code; Proc. 2nd. Symp. Num. Phys. Aspects of Aerodynamic Flows, Ed. Cebeci, -T., Cal. Univ. Long Beach.

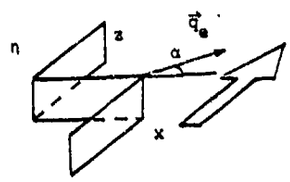

Fig. 1- 3-D Zig-zag Box Scheme

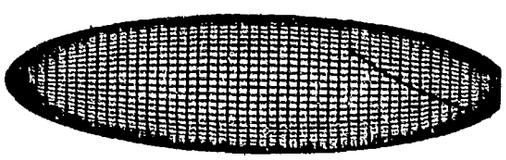

Fig. 2- 1:4 Prolate Spheroid ($0 \leq \bar{x}/L \leq 2.$) Superposition of Blottner & Ellis and natural meshes; zone of accessibility

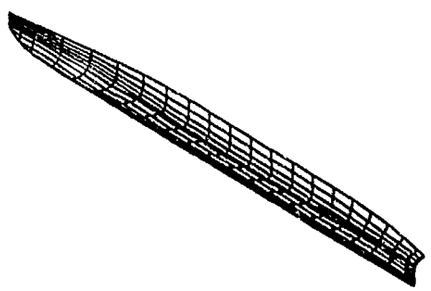

Fig. 3- SSPA 720 ship model ($-1 \leq \bar{x}/L \leq 1.$)

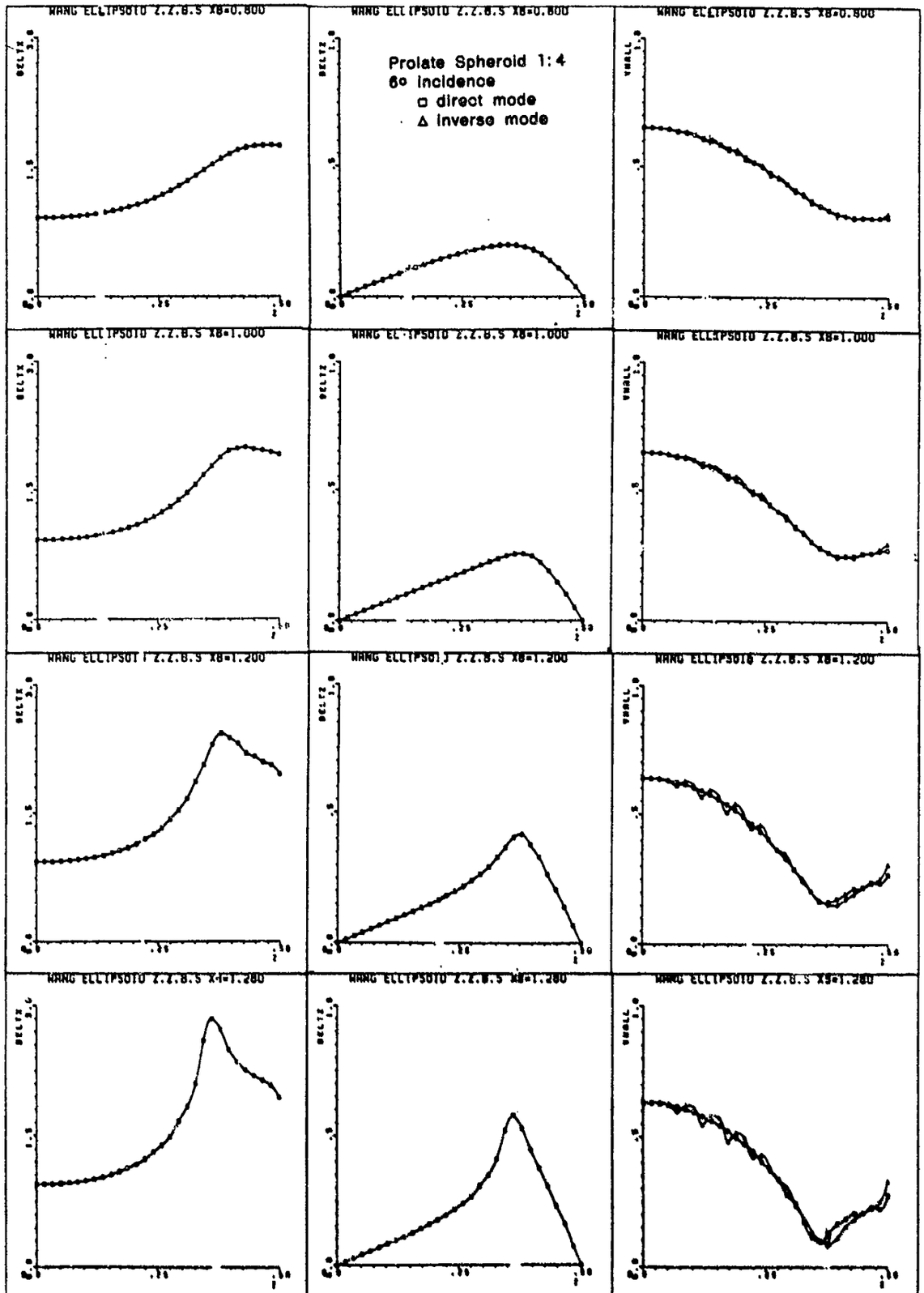

Fig. 4a– Δ_1^n displacement thickness X/L = 0.8; 1.0; 1.2; 1.28;

Fig. 4b– Δ_2^n displacement thickness same legend as fig. 4a

Fig. 4c– v_{wall} distribution same legend as fig. 4a

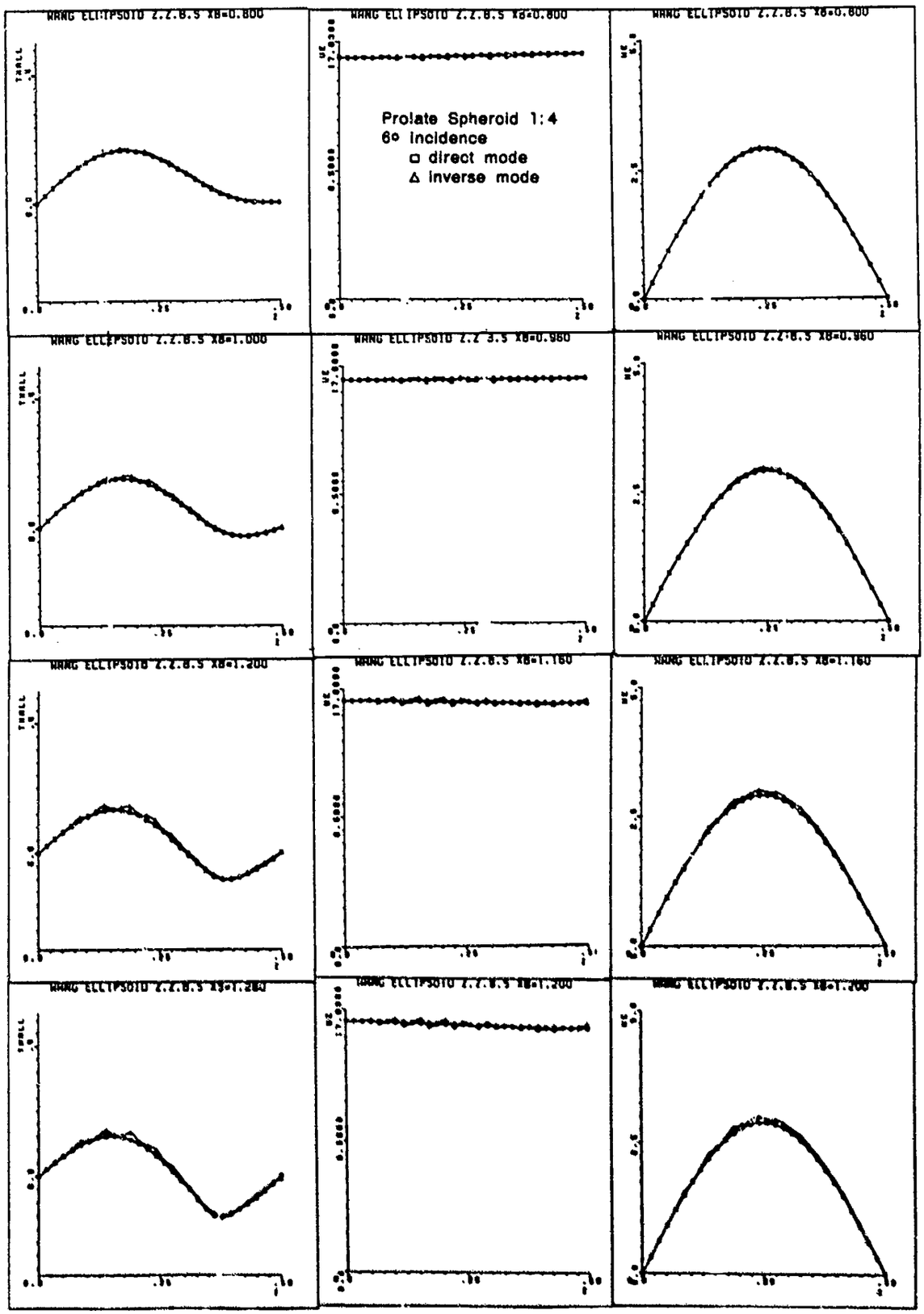

Fig. 4d- t_{wall} distribution
same legend as fig. 4a

Fig. 4e- U_e distribution
$\bar{z}/L$ = 0.8; 0.98; 1.16; 1.2;

Fig. 4f- W_e distribution
same legend as fig. 4e

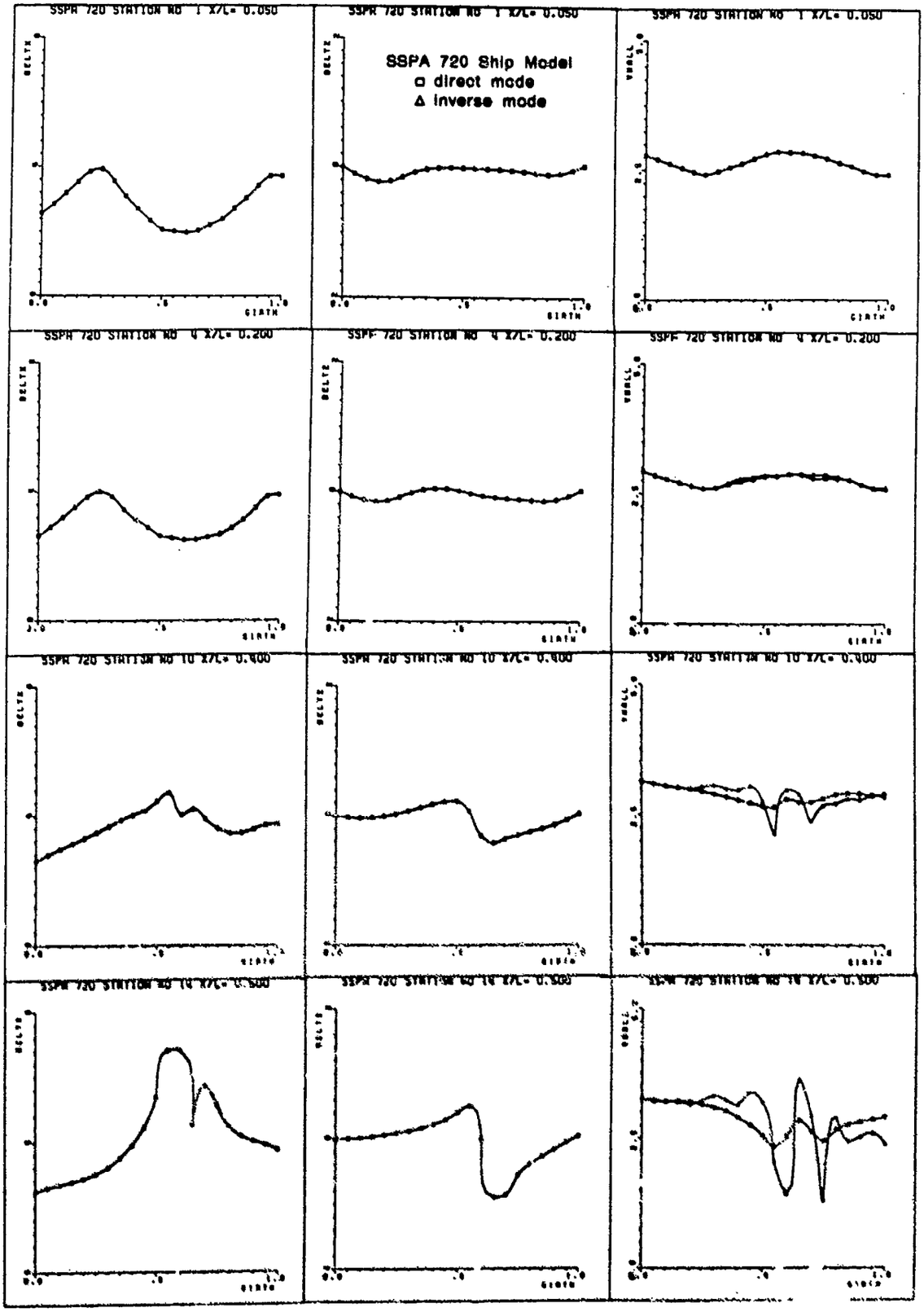

Fig. 5a- Δ_i^* displacement thickness Fig. 5b- Δ_j^* displacement thickness Fig. 5c- V_{wall} distribution
x/L = 0.05;0.2;0.4;0.5; same legend as fig. 5a same legend as fig. 5a

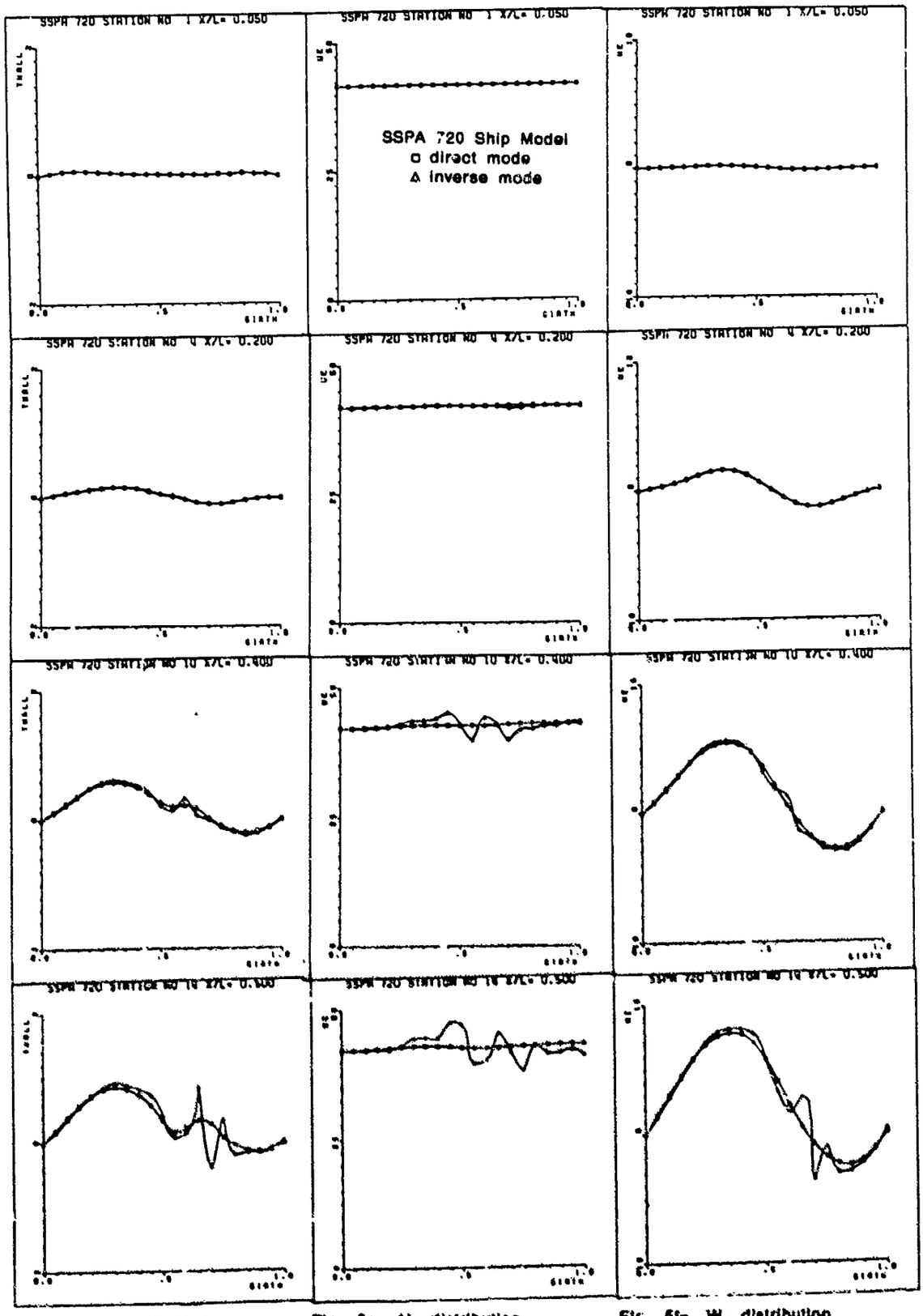

Fig. 5d- t_{wall} distribution same legend as fig. 5a

Fig. 5e- U_e distribution same legend as fig. 5a

Fig. 5f- W_e distribution same legend as fig. 5a

DISCUSSION
of the paper
by J. Piquet and M. Visonneau

"Study of 3D Ship Boundary Layers by Means of an Inverse Method"

DISCUSSION
by V.C. Patel

I appreciated your slides comparing global and local interaction methods, and particularly your summary of the difficulties associated with each approach in three-dimensional flows.

The oscillations observed in the freestream velocity components in your inverse solutions (in Figures 5e and 5f, and to a lesser degree in figures 4e and 4f) may turn out to be rather critical in determining the eventual success of the inverse method since the 3D boundary layer responds to the gradients of these components. If these originate from a lack of smoothness of the calculated inputs, what hope is there of damping them out in a complete interactive calculation?

Author's Reply

Some inverse computations have been done [14] on wings without wiggles because computed displacement thicknesses deteriorate only close to the separation and because of the absence of transverse curvature terms. When transverse curvature terms are present, a more refined grid along z should be tested in order to be sure that numerical oscillations are due to the lack of smoothness of the calculated inputs (compare Fig. 4f with [31]). It is not known whether such problems appear if experimental thicknesses are used to provide the inputs for the inverse calculation (these are not easy to obtain).

The flows considered in Fig. 4 and 5, are very different. Fig. 4 refers to the prolate spheroid at incidence for which direct boundary layer computations terminate at the OK of accessibility; the failure of the computations occurs very abruptly because the displacement thicknesses remain satisfactory close to the OK. For this reason, the agreement between the direct and the inverse mode is quite reasonable.

Fig. 5 refers to the SSPA 720 for which displacement effects appear progressively. Although the direct boundary layer computations converge (even very close to the stern), the displacement thicknesses are known to be incorrect because of normal pressure gradients (see Fig. 5a, 5b). The found oscillations could result from the inputs as they appear especially in regions of strong crosswise or longitudinal variations of the displacement thicknesses.

It is true that the wall transpiration could be oscillating. There is some hope that (15) could indeed give a more regular potential perturbation as the integral over ∂B is a convolution product.

It is felt that, for lifting problems, a viscous-inviscid interactive calculation could be more hopeful than a global interaction method. For a "dragging" problem where the thickening of the boundary layer is progressive and due to a longitudinal vorticity component and to the occurrence of a normal pressure gradient, a local interaction method could be less appropriate.

COMPUTATION OF THE TIP VORTEX GENERATION PROCESS FOR SHIP PROPELLER BLADES

T.R. Govindan, R. Levy and S.J. Shamroth
Scientific Research Associates, Inc.
Glastonbury, CT USA

ABSTRACT

The tip vortex flow field has a significant influence on the performance of a ship propeller. The ability to compute the tip vortex flow field would be a valuable aid in the design of ship propellers, and in the analysis of their performance. The present paper examines and demonstrates the feasibility of computing the tip vortex generation process with a forward-marching computation procedure. For the purpose of this study simple geometry test cases were considered in laminar flow. The effects of blade rotation and blade twist on the tip vortex generation process were included and studied in the analysis. While the results of the computations are qualitative in nature, they demonstrate the capability of the forward-marching procedure to compute the flow processes in tip vortex generation. The flow field is computed from a set of three-dimensional viscous flow equations with no empiricism introduced for the vorticity generated and shed at the propeller tip.

1. INTRODUCTION

The tip vortex flow field plays a significant role in the performance of a ship propeller. The low pressure region found at the center of a tip vortex may lead to cavitation. The presence of cavitation in the flow field has serious consequences in terms of structural, acoustic, and performance considerations. A better understanding of the tip vortex generation process and a method of analysing the tip vortex flow field would provide valuable help in the design of ship propellers.

The flow field in the tip region is complex, three-dimensional, and viscous with large secondary velocities. The large secondary velocities preclude the possibility of using conventional boundary layer solution techniques to compute the tip vortex flow field. On the other hand, a solution of the full Navier-Stokes equations that adequately resolves the tip vortex flow field would require formidable computational resources. Therefore, an approximate set of three-dimensional viscous flow equations which is applicable to the tip vortex flow field but which does not require the resources needed for the solution of the full Navier-Stokes equations is sought. The parabolized Navier-Stokes equations represent such a set. These equations contain in them all the physical processes of tip vortex generation and can be solved economically by forward marching procedures.

The attractive possibility of using a forward-marching procedure to compute the tip vortex generation process is examined in this paper. With the focus being on the computation of the vortex generation process, simplified blade geometry was used in the test cases. Thus, geometry consisted of a slab-type blade of constant thickness with a rounded tip. Effects of blade leading and trailing edges were neglected. Test cases were computed to study the effects of blade rotation and blade twist on the vortex generation process. A brief outline of the forward-marching procedure and a discussion of the results of the computation of the vortex generation process are presented in this paper.

2. THE FORWARD MARCHING COMPUTATION PROCEDURE FOR SHIP PROPELLER TIP FLOW FIELDS

The forward marching computation procedure used for the solution of the parabolic Navier-Stokes equations provides an economical and accurate method for computing many three-dimensional viscous flow fields. This procedure, initially developed for internal flow fields (Refs. 1-3), has been extended to the computation of the ship propeller tip flow field. The governing equations and the computational scheme are presented in this section. This procedure is capable of considering both fixed and rotating coordinate systems.

Governing equations are derived through approximations made relative to a curvilinear coordinate system fitted to and aligned with the flow geometry under consideration. The coordinate system is chosen such that the streamwise or marching coordinate either coincides with or is at least approximately aligned with a known inviscid primary flow direction as determined, for example, by a potential flow for the given geometry. Transverse coordinate surfaces must be approximately perpendicular to solid walls or bounding surfaces, since diffusion is permitted only in these transverse coordinate surfaces.

Equations governing primary flow velocity U_p, and a secondary vorticity, Ω_n, normal to transverse coordinate surfaces are derived utilizing approximations which permit solution of the governing equations as an initial-value problem, provided reversal of the composite streamwise velocity does not occur. Terms representing diffusion normal to transverse coordinate surfaces (in the streamwise direction) are neglected. Secondary flow velocities are determined from scalar and vector surface potential calculations in transverse coordinate surfaces, once the primary velocity and secondary vorticity are known. With the computed velocity field, the pressure field associated with the velocity field can be determined.

2.1 Primary-Secondary Velocity Decomposition

In what follows, vectors are denoted by an overbar, and unit vectors by a caret. The analysis is based on decomposition of the overall velocity vector field $\bar{U}$ into a primary flow velocity $\bar{U}_p$ and a secondary flow velocity $\bar{U}_s$. The overall or composite velocity is determined from the superposition

$$\bar{U} = \bar{U}_p + \bar{U}_s \tag{1}$$

The primary flow velocity is represented as

$$\bar{U}_p = U_p \hat{i}_p \tag{2}$$

where $\hat{i}_p$ is a known inviscid primary flow direction determined, for example, from an *a priori* potential flow solution for the geometry under consideration. A streamwise coordinate direction from a body fitted coordinate system could be used as an approximation to this potential flow direction. The primary velocity $\bar{U}_p$ is determined from solution of a primary flow momentum equation. The secondary flow velocity U_s is derived from scalar and vector surface potential denoted ϕ and ψ, respectively.

If $\hat{i}_n$ denotes the unit vector normal to transverse coordinate surfaces, if ρ is density, and if ρ_o is an arbitrary constant reference density, then $\bar{U}_s$ is defined by

$$\bar{U}_s \equiv \nabla_s \phi + (\rho_o/\rho)\nabla x \hat{i}_n \psi \tag{3}$$

where ∇_s is the surface gradient operator defined by

$$\nabla_s \equiv \nabla - \hat{i}_n(\hat{i}_n \cdot \nabla) \tag{4}$$

It follows that since $\hat{i}_n \cdot \bar{U}_s = 0$, then U_s lies entirely within transverse coordinate surfaces. Equation (3) is a general form permitting both rotational and irrotational secondary flows and will lead to governing equations which may be solved as an initial-boundary value problem. The overall velocity decomposition (1) can be written

$$\bar{U} = U_p \hat{i}_p + \nabla_s \phi + (\rho_o/\rho)\nabla x \hat{i}_n \psi \tag{5}$$

2.2 Surface Potential Equations

Equations relating ϕ and ψ with U_p, ρ, and the secondary vorticity component Ω_n can be derived using Eq. (5) as follows: From continuity,

$$\nabla \cdot \rho \bar{U} = 0 = \nabla \cdot \rho U_p \hat{i}_p + \nabla \cdot \rho \nabla_s \phi + \rho_o \nabla \cdot \nabla x \hat{i}_n \psi \tag{6}$$

and from the definition of the vorticity based on the secondary flow within the transverse surfaces, Ω_n

$$\hat{i}_n \cdot \nabla x \bar{U} \equiv \Omega_n = \hat{i}_n \cdot \nabla x\, U_p \hat{i}_p + \hat{i}_n \cdot \nabla x (\rho_o/\rho)\, \nabla x\, \hat{i}_n \psi + \hat{i}_n \cdot \nabla \times \nabla_s \phi \tag{7}$$

Since the last term in each of Eqs. (6 and 7) is zero by vector identity, Eqs. (6 and 7) can be written as

$$\nabla \cdot \rho \nabla_s \phi = -\nabla \cdot \rho U_p \hat{i}_p \tag{8}$$

$$\hat{i}_n \cdot \nabla x\, (\rho_o/\rho)\, \nabla x \hat{i}_n \psi = \Omega_n - \hat{i}_n \cdot \nabla \times U_p \hat{i}_p \tag{9}$$

Note that the last term in Eq. (9) is identically zero in a coordinate system for which $\hat{i}_n$ and $\hat{i}_p$ have the same direction, and would be small if $\hat{i}_n$ and $\hat{i}_p$ are approximately aligned. In any event, given a knowledge of U_p, Ω_n and ρ, the surface potentials ϕ and ψ can be determined by a

two-dimensional elliptic calculation in transverse coordinate surfaces at each streamwise location. In turn, $\bar{U}_s$ can be computed from Eq. (3), and the composite velocity $\bar{U}$ will satisfy continuity. Equations for U_p and Ω_n are obtained from the equations governing momentum and vorticity, respectively.

The streamwise momentum equation is given by

$$\hat{i}_p \cdot [\,(\bar{U}\cdot\nabla)\bar{U} + (\nabla P)/\rho] = \hat{i}_p \cdot \bar{F} + \hat{i}_p \cdot \bar{R} \tag{10}$$

where P is pressure and ρF is force due to viscous stress and terms in F representing streamwise diffusion are neglected. $\rho\bar{R}$ is the additional force due to a rotating coordinate system; where $\bar{R} = -2\bar{\omega} \times \bar{U} - \bar{\omega}\times(\bar{\omega} \times \bar{r})$, ω is the angular velocity of the coordinate system and $\bar{r}$ is the radius vector from the rotation axis. The pressure term in the streamwise momentum equation (10) can be taken from a simpler analysis such as a potential flow analysis. While this results in a set of equations which can be solved by forward marching, the surface pressures which are due to the pressure field imposed upon the flow are the potential flow pressures. Since the actual surface pressures are often of primary interest, a new estimate of the actual surface pressure which includes viscous and secondary flow effects can be computed from the resulting velocity field in the following manner.

The momentum equations in the transverse surfaces are:

$$\begin{aligned} \hat{i}_1 \cdot [(\rho\bar{U}\cdot\nabla)\,\bar{U} + \nabla P - \rho\bar{F} - \rho\bar{R}] &= 0 \\ \hat{i}_2 \cdot [(\rho\bar{U}\cdot\nabla)\,\bar{U} + \nabla P - \rho\bar{F} - \rho\bar{R}] &= 0 \end{aligned} \tag{11}$$

Equation (11) represents components of the momentum vector in the transverse surfaces:

$$\hat{i}_1\,(\hat{i}_1\cdot[(\rho\bar{U}\cdot\nabla)\,\bar{U} + \nabla P - \rho\bar{F} - \rho\bar{R}]) + \hat{i}_2\,(\hat{i}_2\cdot[(\rho\bar{U}\cdot\nabla)\,\bar{U} + \nabla P - \rho\bar{F} - \rho\bar{R}]) \tag{12}$$

The divergence of this vector can be written as a Poisson equation for the pressure P at each transverse surface:

$$\nabla_s^2 P = \nabla_s^2 (P_I + P_c) = -\frac{\partial}{\partial x_1}(\hat{i}_1 \cdot [(\rho\bar{U}\cdot\nabla)\,\bar{U} - \rho\bar{F} - \rho\bar{R}]) - \frac{\partial}{\partial x_2}(\hat{i}_2 \cdot [(\rho\bar{U}\cdot\nabla)\,\bar{U} - \rho\bar{F} - \rho\bar{R}]) \tag{13}$$

where P_I is the imposed pressure, P_c is a viscous correction to the pressure field and x_1 and x_2 are coordinates in the $\hat{i}_1$ and $\hat{i}_2$ directions, respectively. Equation (13) can be solved for the pressure correction, P_c, at each computational station using Neuman boundary conditions derived from Eq. (12). The use of Neuman boundary conditions requires an additional parameter which is only a function of the normal direction, $P_v(x_3)$, in order to set the level of the pressure field. For external flows $P_v(x_3)$ is set to match the imposed pressure at an appropriate far field location.

2.3 Secondary Vorticity

The equation governing Ω_n is obtained by cross differentiating each of the transverse momentum equations (11). Eliminating the pressure in the two equations results in a single equation for the transport of the vorticity normal to the transverse surface. This equation has the form

$$\bar{U}\cdot\nabla\Omega_n - \bar{\Omega}\cdot\nabla U_n = G_n + C + i_n\cdot(\nabla\times\bar{R}) \tag{14}$$

where G_n is the normal component of

$$\bar{G} = \nabla \times \bar{F} \tag{15}$$

and C is a collection of curvature terms arising from changes in orientation of the transverse surfaces as a function of streamwise coordinate.

2.4 Governing System of Equations

A complete system of five coupled equations governing U_p, Ω_n, ϕ, ψ, and P is given by Eqs. (8), (9), (10), (14) and (13). Ancillary relations (5) is given for the composite velocity. In reference 2, these equations are given in general orthogonal coordinates and in reference 3 in nonorthogonal coordinates.

2.5 Numerical Method

Since techniques for obtaining the basic potential flow solution are well known and numerous, they need not be enumerated or discussed here. Instead, the present development concentrates on describing the numerical method used to solve the system of governing equations. Streamwise derivative terms in the governing equations have a form such as $u_1\partial(\ )/\partial x_1$, and because the streamwise velocity u_1 is very small in the viscous dominated region near no-slip walls, it is essential to use implicit algorithms which are not subject to stringent stability restrictions unrelated to accuracy requirements. Although it is possible to devise algorithms for solution of the governing

equations as a fully coupled implicit system, such algorithms would require considerable iteration for the system of equations treated here, and this would detract from the overall efficiency. The present method is semi-implicit and seeks to reduce the amount of iteration required and yet avoid the more severe stability restrictions of explicit algorithms. The method partitions the system of governing equations into subsystems which govern the primary flow, the secondary flow, and the turbulence model. The primary-flow subset of equations contains the streamwise momentum equation. The secondary-flow subset of equations contains the secondary vorticity equation and the scalar and vector potential equations. These subsystems are decoupled using an ad hoc linearization in which secondary velocity components and turbulent viscosity are lagged, and are solved sequentially during each axial step.

2.6 Summary of Algorithm

The governing equations are replaced by finite-difference approximations. Three-point central difference formulas are used for all transverse spatial derivatives. Analytical coordinate transformations are employed as a means of introducing a nonuniform grid in each transverse coordinate direction, as appropriate to concentrate grid points in the wall boundary layer regions. Second-order accuracy for the transverse directions is rigorously maintained. Two-point backward difference approximations are used for streamwise derivatives, although this is not essential.

To solve the primary flow subsystem of viscous equations a scalar ADI scheme is used for the momentum equation.

Given the solution for the primary flow, the secondary flow subsystem can be solved. First, the scalar potential equation (continuity) is solved using a scalar iterative ADI scheme. Next, the secondary vorticity and vector potential equations are written as a fully implicit coupled system and solved using an iterative linearized block implicit (LBI) scheme (cf. Briley and McDonald (4)). In selecting boundary conditions for the secondary flow subsystem, care must be taken to ensure that the final secondary velocity satisfies the no-slip condition accurately. Zero normal derivatives of ϕ are specified in the scalar potential equation, and this boundary condition corresponds to zero normal velocity. It is not possible to simultaneously specify the tangential velocity, however, and thus the ϕ-contribution to the secondary velocity will have a nonzero tangential (slip) component, denoted v_t, at solid boundaries. In the coupled vorticity and vector-potential equations, both normal and tangential velocity components can be specified as boundary conditions, since these equations are solved as a coupled system. By choosing (a) zero normal velocity, and (b) $-v_t$ as the ψ-contribution to the tangential velocity, the slip velocity v_t arising from the ϕ calculation is cancelled, and the composite secondary flow velocity including both ϕ and ψ contributions will satisfy the no-slip condition exactly.

A summary of the overall algorithm used to advance the solution a single axial step follows. It is assumed that the solution is known at the n-level x^n and is desired at x^{n+1}.

(1) The imposed streamwise pressure gradient distribution is determined from an a priori inviscid potential flow.

(2) The momentum equation is solved to determine u^{n+1}.

(3) Using values now available for u^{n+1}, the scalar potential equation (8) is solved using an iterative scalar ADI scheme, to obtain ϕ^{n+1}. This ensures that the continuity equation is satisfied.

(4) The equations for vorticity (15) and vector potential (9) form a coupled system for Ω^{n+1} and ψ^{n+1} which is solved as a coupled system using an iterative LBI scheme.

(5) Values for the transverse velocities v_s and w_s are computed from Eq. (3).

(6) Using the computed velocity field, the transverse pressure field is computed from Eq. (13) by an iterative scalar ADI scheme.

2.7 Boundary Conditions for the Tip Vortex Flow Computations

Figure 1 shows a perspective view of a constant thickness blade with a rounded tip. This simplified model of a propeller blade neglects the effects of the leading and trailing edges. The model, however, was not expected to change the basic flow mechanisms of tip vortex generation; the object of the computations in this paper. Figure 2 shows a cross-section of the propeller tip and the computational grid at a typical streamwise station. A computational grid that wraps around the tip was chosen to provide adequate resolution of the tip region and a smooth grid distribution.

The cross-sectional computation coordinate system, shown in Figure 2, has four boundaries where boundary conditions for the governing equations must be specified. Inboard are boundaries (1) and (2), the blade surface is boundary (3), and the far field is boundary (4) Boundary conditions must be specified for the streamwise velocity in the streamwise momentum equation, for the scalar potential in the scalar potential equation, and for the vector

and streamwise vorticity in the coupled vector potential-streamwise vorticity equations. The conditions that were specified for the tip vortex flow computations are considered in this section.

The flow at the inboard boundaries (1) and (2) was assumed to be two-dimensional (no spanwise variation) with no flow penetration of the secondary velocity through the boundaries. The normal gradient of the scalar potential was set to zero and the vector potential was set to a constant (normal velocity set to zero). The streamwise vorticity was set to zero as the compatible condition with the vector potential and the streamwise velocity was extrapolated from the interior flow field. The boundary conditions specified on the inboard boundaries are only approximate but were found not to affect the qualitative computed behavior of the tip vortex generation process. In Reference [5], boundary conditions based on the induced velocity field by the blade have been developed. These conditions will be incorporated in future work on the ship propeller tip flow field.

The boundary condition along boundary (3), the blade, was the no-slip condition on a solid surface. To satisfy this condition the normal gradient of the scalar potential (the normal velocity) was set to zero. In the coupled vector potential and vorticity equations the normal component of the rotational velocity was set to zero and the tangential component was set equal and opposite to the tangential component of the velocity generated by the scalar potential. These conditions allowed an implicit specification of the vector potential and the vorticity on the no-slip boundary (as discussed in Section 2.6). The resultant secondary velocity field satisfies the no-slip conditions on the boundary. The streamwise velocity was also set to zero at the solid boundary.

Far field conditions were specified on boundary (4). The streamwise velocity was extrapolated from the interior flow field. The scalar potential was set to a constant so that the tangential component of the irrotational velocity was zero. This condition allowed outflow through the boundary due to the displacement effect of the boundary layers on the blade. The angle of incidence of the flow specified a component of the transverse velocity on the boundary. The vector potential was obtained by integrating this component of the transverse velocity along the boundary. The streamwise vorticity was set to zero.

3. RESULTS

Three test cases were chosen to demonstrate the capability of the forward-marching procedure to compute the tip vortex generation process. The test cases were:

(1) Tip vortex flow for a straight blade with rounded tip,
(2) Tip vortex flow for a rotating straight blade with rounded tip, and
(3) Tip vortex flow for a rotating twisted blade with rounded tip.

These test cases were chosen to demonstrate the computation of the basic flow processes in tip vortex generation, and the effects of blade rotation and blade twist on the tip flow field. Laminar flow was assumed in all the cases since the qualitative nature of the tip vortex generation process remains the same in laminar and turbulent flow. Further, the streamwise pressure gradient which is input to the forward-marching procedure was assumed to be zero for all the cases presented here.

3.1 Computation of the Tip Vortex Flow for a Straight Blade with Rounded Tip

A constant thickness blade with a rounded tip was the first test case considered for the tip vortex flow computation. Figure 1 shows a perspective view of the geometry of the blade near the tip. Figure 2 shows the cross-section of the blade tip and the computational grid at a typical streamwise station. The important geometric and flow parameters used in the computation were the following:

Blade thickness (t)	=	1.0
Blade chord	=	20.0t
Reynolds number (based on t)	=	1000.0
Initial boundary layer thickness	=	0.20t
Incidence angle	=	6°

A computational grid of 60 streamwise stations and a 47 x 30 cross-section grid was used. Grid points were clustered in regions of high flow gradients such as near the propeller surface and in the tip region. The computation was started on the blade ($x/t = 0.0$) with the assumed initial boundary layer thickness.

Figure 3 shows the development of the tip vortex computed by the code. The upper half of the figure shows the development of the tip vortex in term of contours of the streamwise velocity while the lower half shows the same development in terms of contours of streamwise vorticity. Computations from five streamwise stations ($x/t = 2.0, 4.0, 7.0, 11.0, 20.0$) were chosen to display the development of the tip vortex. An initial overall view of Figure 3 shows a large scale flow process at the tip of the blade in terms of both the streamwise velocity and streamwise vorticity.

At $x/t = 2.0$ (Figure 3), the streamwise velocity contours show the initial development of the flow. The boundary layer on the suction side of the blade has thickened while the boundary layer on the pressure side remains thin. The thickening of the boundary layer on the suction side is due to the transport of low momentum fluid from the pressure side boundary layer around the tip to the suction

side. The same flow process is seen in the streamwise vorticity contours as a transport of vorticity around the tip.

At x/t = 4.0, the tip flow field begins to show the accumulation of low momentum fluid on the suction side of the tip region. This accumulation is characterized by the "bulge" in the streamwise velocity contours representing the region of the low streamwise velocity fluid. The streamwise vorticity contours at this station show the convection of vorticity into this region. Further, the vorticity contours also start to "peel" off the suction surface indicating the initial stages of the roll-up of the low momentum fluid. At x/t = 7.0 and x/t = 11.0, the streamwise velocity contours show the further rapid accumulation of the low momentum fluid in the tip region. The streamwise vorticity contours at these stations show the roll up of the tip flow into the tip vortex. The vorticity contours emanating from the suction surface, visible clearly at x/t = 11.0, are indicative of the outward (toward the tip) transverse velocities in the region due to roll-up of the tip vortex. The results at x/t = 20.0 show the completion of the tip vortex formation. The vortex has separated from the suction surface as it is convected downstream by the streamwise velocity. The vortex is sustained by the continued transport of vorticity from the pressure surface into the vortex core. Also evident from Figure 3 is the inward track of the center of the vortex along the suction side. That, indeed, the flow in the tip region has rolled up into the tip vortex is clearly visualized by a vector plot of the transverse velocity field. Figure 4 shows a vector plot of the transverse velocity field at x/t = 7.0 and x/t = 20.0. The transverse velocity field at x/t = 7.0 clearly shows the initial roll-up of the flow in the tip region into a vortex. The large transverse velocities (about 30% of the free stream velocity) around the tip that convect the low momentum fluid from the pressure side to the suction side are also seen. The transverse velocity field at x/t = 20.0 shows the strong tip vortex on the suction side. The inward track of the center of vortex along the suction side is also seen in the two vector plots.

Figures 3 and 4 clearly show the development of the tip vortex generation process. It should be noted that this process has been calculated from a set of three-dimensional, viscous flow equations which have a no-slip condition at the propeller blade surface. The vortex generation and roll-up is a result of the secondary flow separation, and the computed results obtained are in excellent qualitative agreement with experimentally observed physical processes (Refs. 6 and 7). The calculations clearly show that the tip vortex problem can be analyzed from a consideration of the basic physical phenomena without resorting to empirical models.

3.2 Computation of the Tip Vortex Flow for a Rotating Straight Blade with Rounded Tip

As the second test case in the computation of the tip vortex generation process, the straight blade described in the previous section (section 3.1) was rotated so as to provide an advance ratio of 1.0. The remaining flow and geometric parameters were retained from the previous test case.

Blade Thickness	(t)	= 1.0
Blade Chord		= 20.0t
Reynolds Number (based on t)		= 1000.0
Initial Boundary Layer Thickness		= 0.20t
Incidence Angle		= 6°
Advance Ratio		= 1.0

A computational grid of 60 streamwise stations and a 47 x40 cross-section grid was used in the computations. As before, grid points were clustered in regions where high flow gradients were anticipated.

Figure 5 shows the development of the tip vortex computed by the PEPSIG code for the rotating blade. The figure is formatted in the same manner as Figure 3 for the stationary blade. The upper half of the figure shows the development of the tip vortex in terms of contours of the streamwise velocity while the lower half shows the same development in terms of contours of streamwise vorticity. A comparison of Figure 5 with Figure 3 for the stationary case shows the same basic flow mechanisms that result in the generation of the tip vortex. These mechanisms are the transport of low momentum fluid from the pressure side boundary layer to the suction side by the transverse velocity, the accumulation of this low momentum fluid on the suction side of the tip region, and the roll-up of this accumulated fluid into the tip vortex. The differences between the rotating and non-rotating cases are in a matter of the details of the flow structure. These differences will be discussed in this section. A vector plot of the transverse velocity field at two streamwise stations are shown in Figure 6. As in the stationary case, the vector plot shows a clear visualization of the tip vortex. The vector plot at x/t = 7.0 shows the early development of the tip vortex while the plot at x/t = 20.0 shows the developed tip vortex on the suction side of the tip region.

The differences in the tip vortex flow field between the stationary and rotating blade test cases can be seen by comparing Figures 3 and 5. From an overall point of view, the location of the tip vortex for the rotating blade is higher than the stationary blade. This difference is due to the fact that low streamwise velocity regions in the vortex are regions of higher absolute tangential velocity in the rotating blade. The corresponding increase in the centrifugal force keeps the

vortex at a higher location for the rotating blade. In a similar manner, the increase in the absolute tangential velocity in the boundary layers on the suction and pressure surfaces and the corresponding increase in the centrifugal forces that is not balanced by the pressure forces imposed from the outer flow results in outward flow in the boundary layers. This outward flow changes the streamwise vorticity distribution in the vicinity of the blade surfaces. The outward flow in the boundary layers is clearly seen in the vector plot of the transverse velocities near the blade surfaces (Figure 6, x/t = 20.0).

3.3 Computation of the Tip Vortex Flow for a Rotating Twisted Blade with Rounded Tip

As a final test case to demonstrate the capability of the forward marching procedure to compute the tip vortex generation process in ship propellers, a computation was carried out of the tip flow field for a rotating twisted blade. The twisted blade geometry was chosen to demonstrate the capability of the forward marching procedure and the geometry package to handle the complex blade shapes typical of a ship propeller. For the purposes of the demonstration computation, the blade twist was specified such that all radial sections of the blade maintained a constant angle of incidence with respect to the incoming flow. The remaining flow and geometry parameters were retained from the previous two test cases.

Blade thickness (t)	=	1.0
Blade chord	=	20.0t
Reynolds number (based on t)	=	1000.0
Initial boundary layer thickness	=	0.20t
Incidence angle	=	6°
Advance ratio	=	1.0

Geometric twist specified to maintain constant angle of incidence at all radial blade sections

Perspective views of the twisted blade are shown in Figure 7. A computational grid of 60 streamwise stations and a 47 x 40 cross-section grid was used in the computations. Figure 8 shows the computational grid at two streamwise stations (x/t = 1.0, 20.0). The change in the lean of the blade along the chord due to blade twist can be seen from this figure. The geometry package adjusts the grid distribution automatically at each cross-section to compensate for the blade twist. This capability in the geometry package can be seen in the computation grid generated at x/t = 1.0 and x/t = 20.0 in Figure 8.

Figures 9, 10 and 11 show the generation of the tip vortex computed for the rotating twisted blade. Figure 9 shows the initial development of the flow field. The computation shows the initial transport of low momentum fluid from the pressure side to the suction side as in the previous test case. The transverse velocity field is a potential flow like field around the tip. As in the previous test cases, Figures 10 and 11 show the accumulation of low momentum fluid on the suction side of the tip region, and the roll-up of the fluid into the tip vortex. The outward flow in the boundary layers due to rotation can also be seen in the vector plot of the transverse velocity field in Figure 11. The change in the lean of the blade along the blade chord due to blade twist can be seen from the Figures 9, 10 and 11.

With the solution of the velocity field at each streamwise station, it is possible to compute the transverse pressure field associated with the generated transverse velocity field. Figure 12 shows a contour plot of the computed transverse pressure field at x/t = 2.0 and x/t = 4.0. At x/t = 2.0, the pressure contours show a drop in the pressure as the flow accelerates over the rounded tip onto the suction side. The minimum pressure was computed in the region of the rounded tip. At x/t = 4.0, these minimum pressure contours move toward the suction side as the tip vortex begins to form. Figure 13 shows the computed pressure field at two downstream stations, x/t = 11.0 and x/t = 20.0. At x/t = 11.0, the low pressure region has moved to the suction side and a minimum pressure region has formed over the center of the tip vortex. At x/t = 20.0, the pressure contours show the further development of the pressure field with the tip vortex. The minimum pressure region continues to be associated with the center of the tip vortex. These computations clearly demonstrate the ability of the PEPSIG code to compute the pressure field associated with the tip vortex and compute the low pressure region at the center of the vortex. This low pressure field would determine the cavitation characteristics of the propeller tip flow field. Figure 14 shows a streamwise contour plot of the computed pressure field on the suction side of the blade. Superimposed on this figure is the track of the vortex obtained from the computations. After an initial transient in the pressure field, the formation of the low pressure region along the vortex track is evident. The resulting track is qualitatively as expected.

Typical computer run times for the tip vortex flow field computations were about 120 seconds for the straight blade cases using 84600 grid points and about 160 seconds for the twisted blade case using 112,800 grid points. These computations were carried out on a CRAY-1 computer system with a partially vectorized code.

4. CONCLUSIONS

The present analysis has clearly demonstrated the feasibility of utilizing a three-dimensional forward marching analysis for the tip vortex generation problem. Although the calculations made to date represent an initial study and have not yet attempted to assess quantitative results, the following observations are evident.

1. The capability of the forward-marching procedure to compute the tip vortex generation process has been demonstrated. The computations are economical compared to computing solutions of the full Navier-Stokes equations for tip vortex flow fields.

2. The computations show the qualitative features of the tip vortex flow field observed in experimental data. The results show capability of the procedure to compute the low pressure region in the flow associated with the tip vortex and help in identifying regions of the flow field that may be susceptible to cavitation.

3. The effects of blade rotation on the tip vortex flow field are computed with the procedure. These are readily seen in the radial outward flow deep within the boundary layer on the blade surface of the rotating blades.

Future efforts will aim at a quantitative assessment.

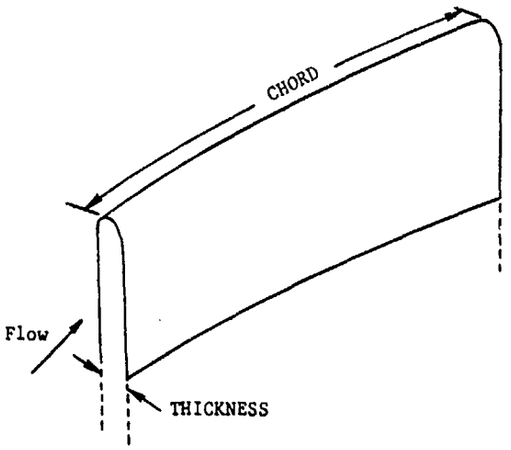

Fig. 1 - Perspective view of the straight blade.

ACKNOWLEDGEMENT

This work was sponsored by the Office of Naval Research under Contract N00014-83-C-0768.

REFERENCES

1. Briley, W.R. and McDonald, H.: Analysis and Computation of Viscous Subsonic Primary and Secondary Flows. AIAA Paper 79-1453, 1979.

2. Kreskovsky, J.P., Briley, W.R. and McDonald, H.: Prediction of Laminar and Turbulent Primary and Secondary Flows in Strongly Curved Ducts, NASA CR-3388, February 1981.

3. Levy, R., Briley, W.R. and McDonald, H.: "Viscous Primary/Secondary Flow Analysis for Use with Nonorthogonal Coordinate Systems". AIAA Paper 83-0556, 1983.

4. Briley, W.R. and McDonald, H.: "On the Structure and Use of Linearized Block Implicit Schemes", Journal of Computational Physics, Vol. 34, 1980.

5. Lin, S.-J., Levy, R., Shamroth, S.J. and Govindan, T.R.: A Three-Dimensional Viscous Flow Analysis for the Helicopter Tip Vortex Generation Problem, NASA Contractor Report 3906, 1985.

6. Francis, M.S. and Kennedy, D.A.: "Formation of a Trailing Vortex", J. Aircraft, Vol. 16, No. 3, 1979.

7. Chigier, N.A. and Corsiglia, V.R.: "Tip Vortices - Velocity Distributions", 27th Annual National V/STOL Forum, American Helicopter Society, Washington, DC, 1971.

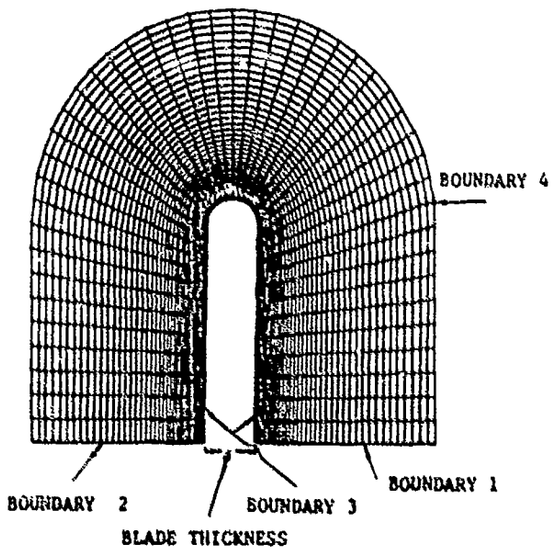

Fig. 2 - Transverse computation grid at a typical streamwise station.

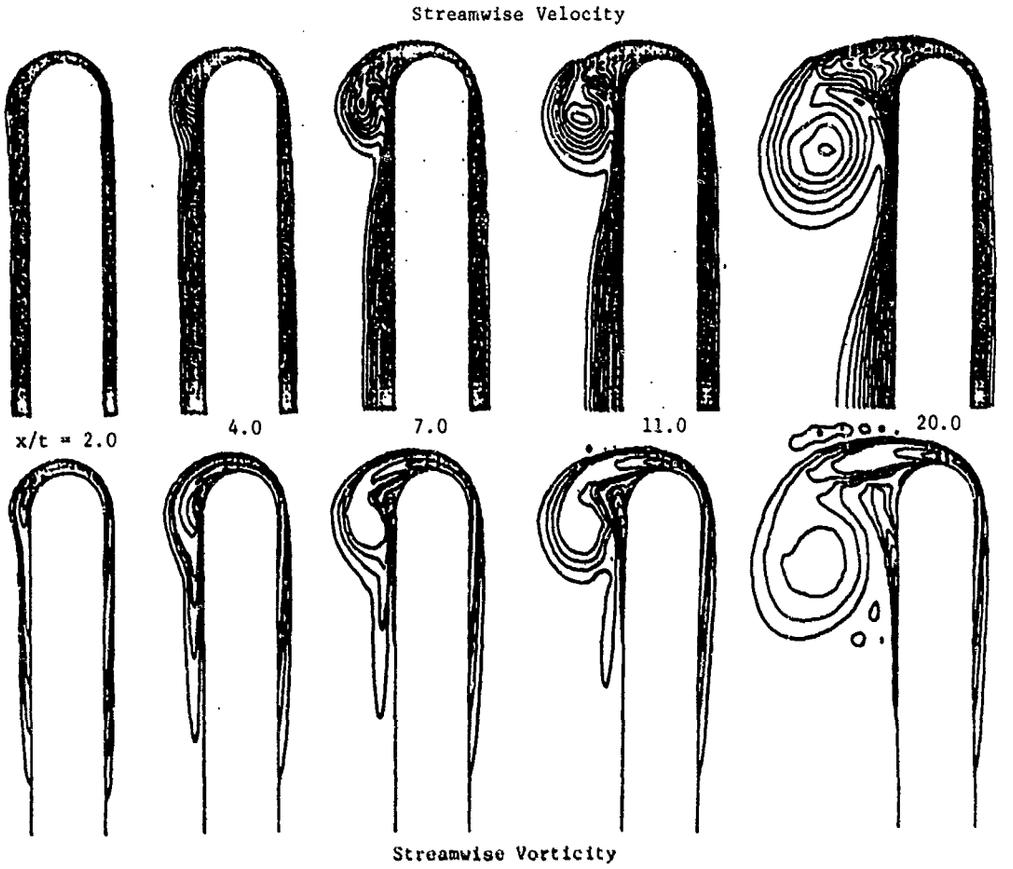

Fig. 3 - Tip vortex generation for a straight blade.

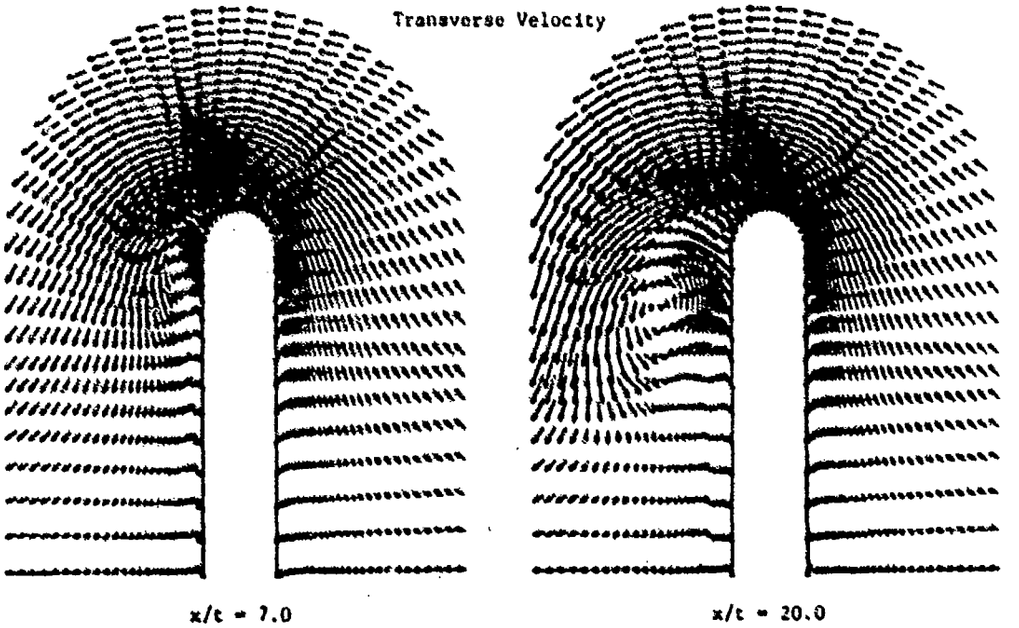

Fig. 4 - Vector plot for a straight blade.

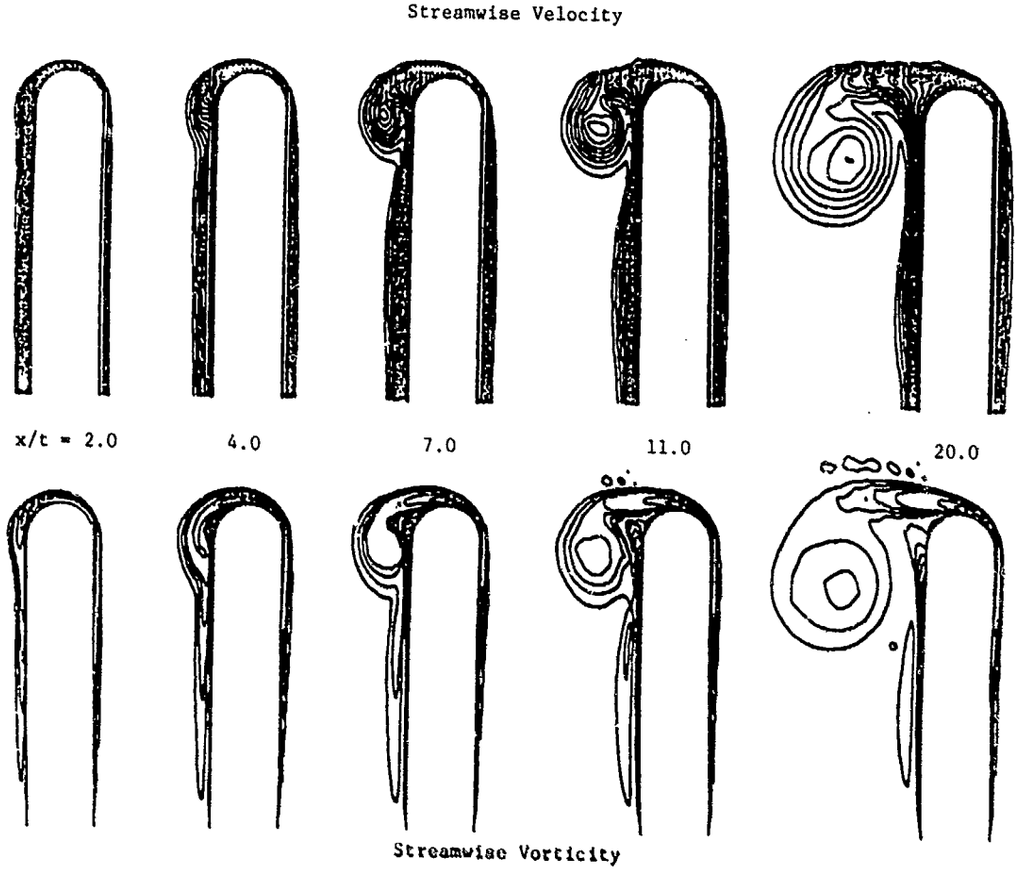

Fig. 5 - Tip vortex generation for a rotating straight blade.

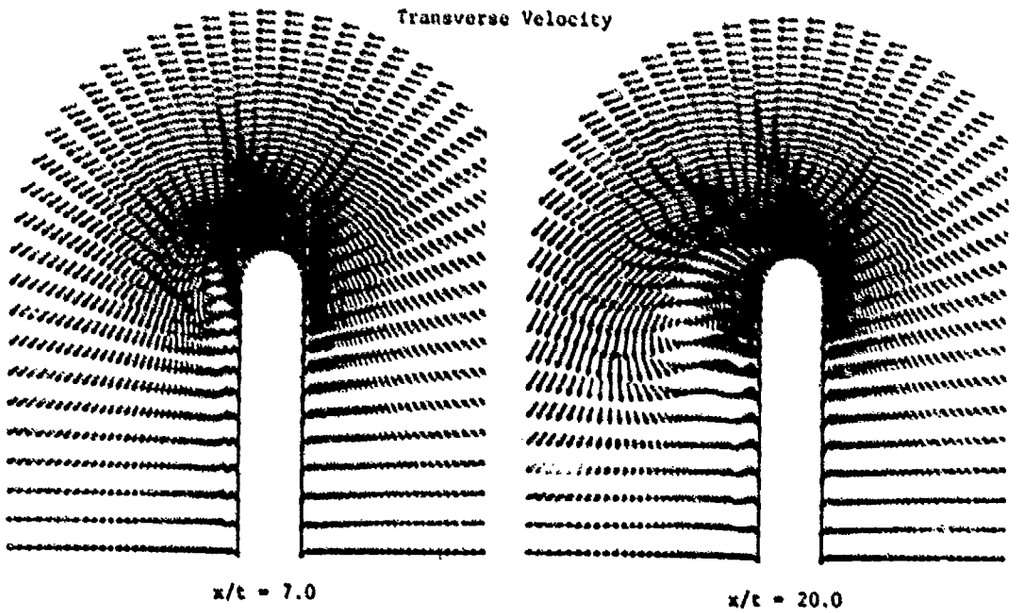

Fig. 6 - Vector plot for a rotating straight blade.

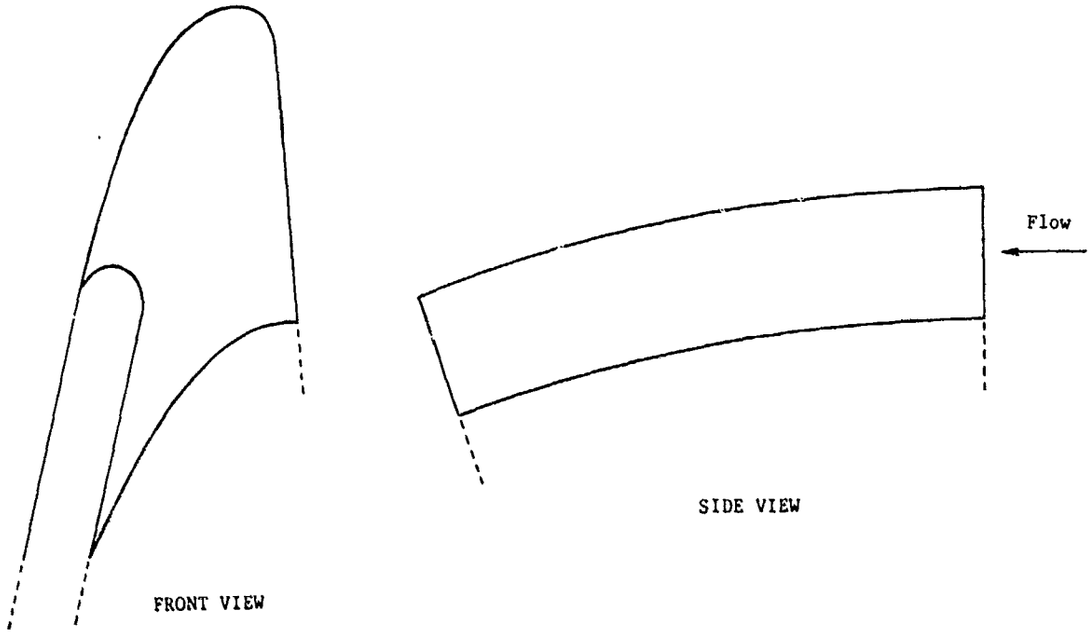

Fig. 7 - Perspective views of the twisted blade.

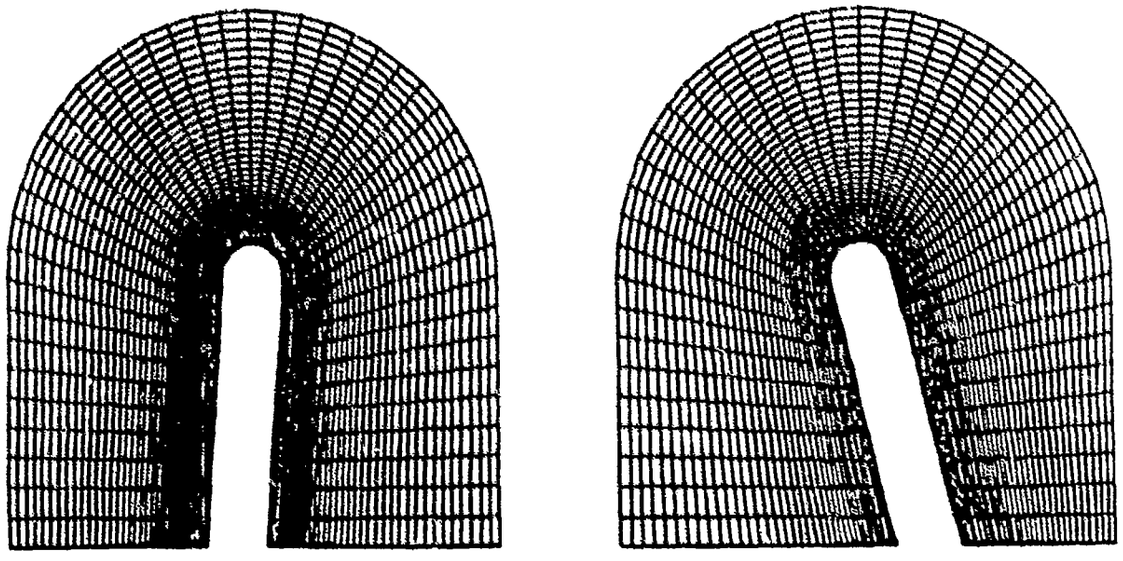

x/t = 1.0

x/t = 20.0

Fig. 8 - Computation grid for the twisted blade (front view).

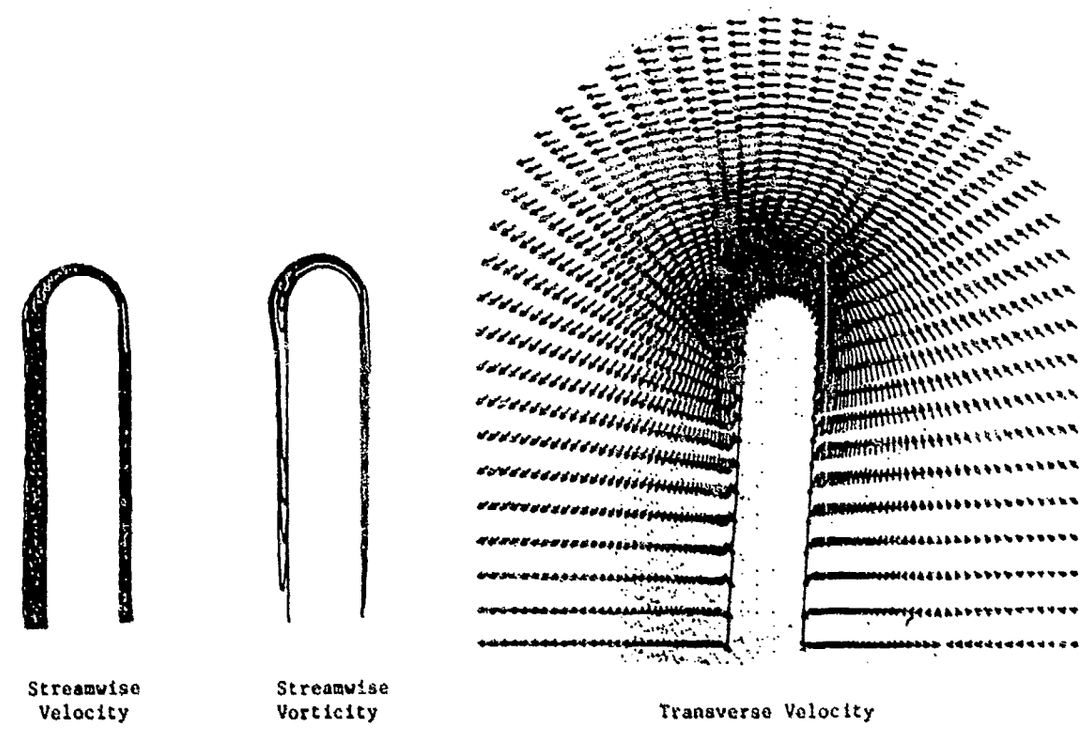

Fig. 9 - Tip vortex generation for twisted rotating blade (x/t = 2.0).

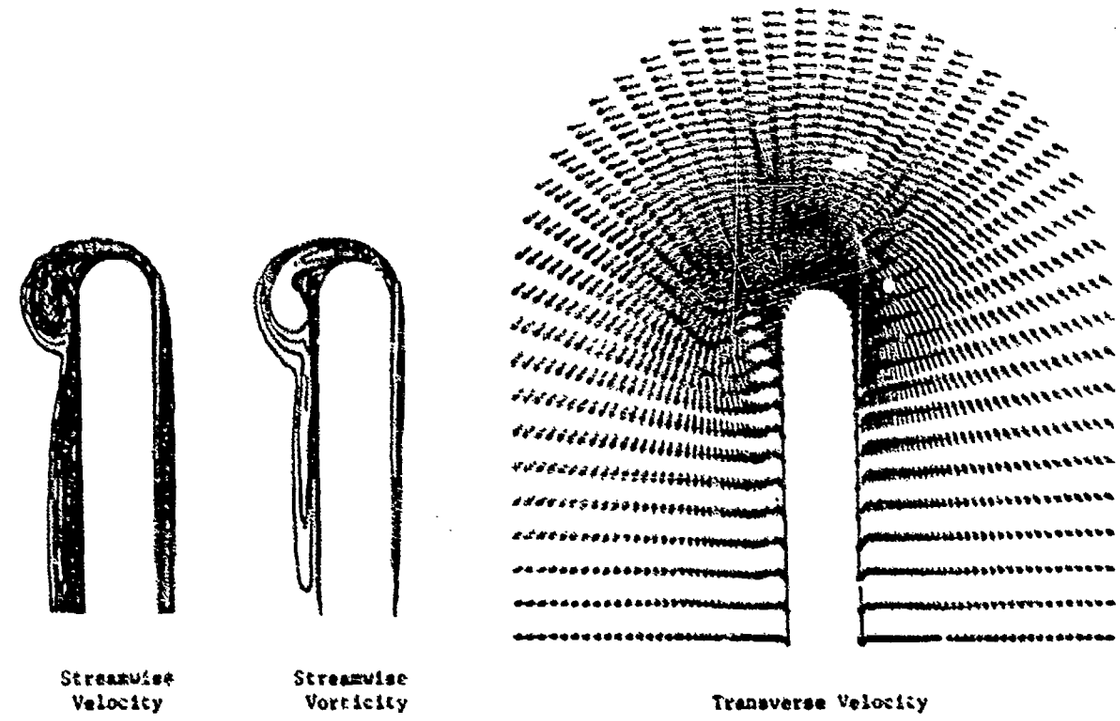

Fig. 10 - Tip vortex generation for twisted rotating blade (x/t = 7.0).

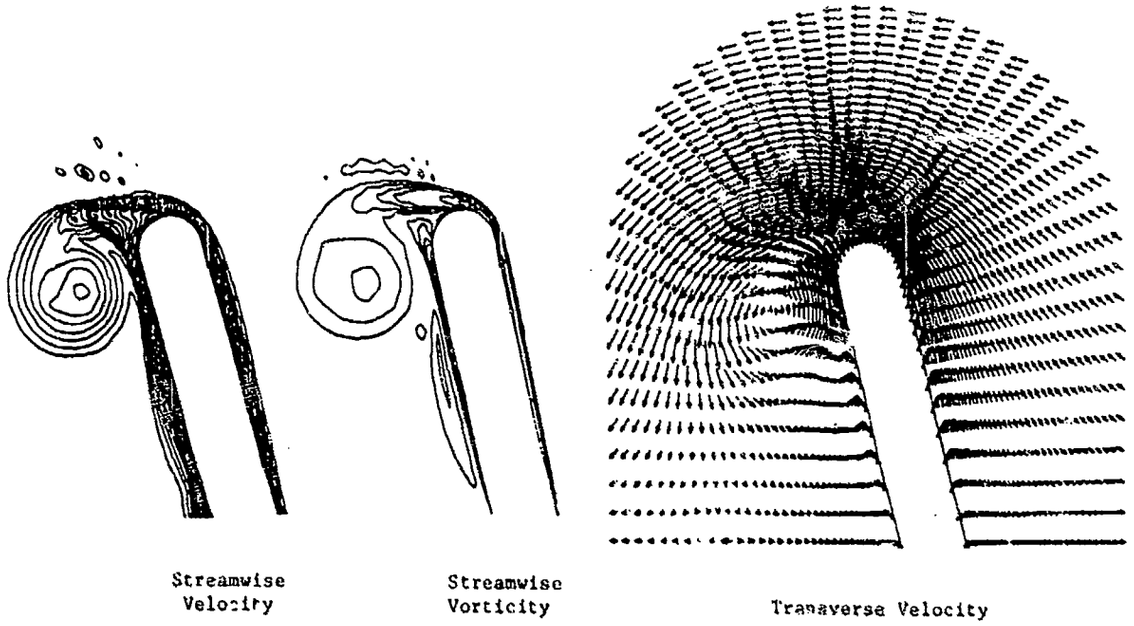

Fig. 11 - Tip vortex generation for twisted rotating blade (x/t = 20.0).

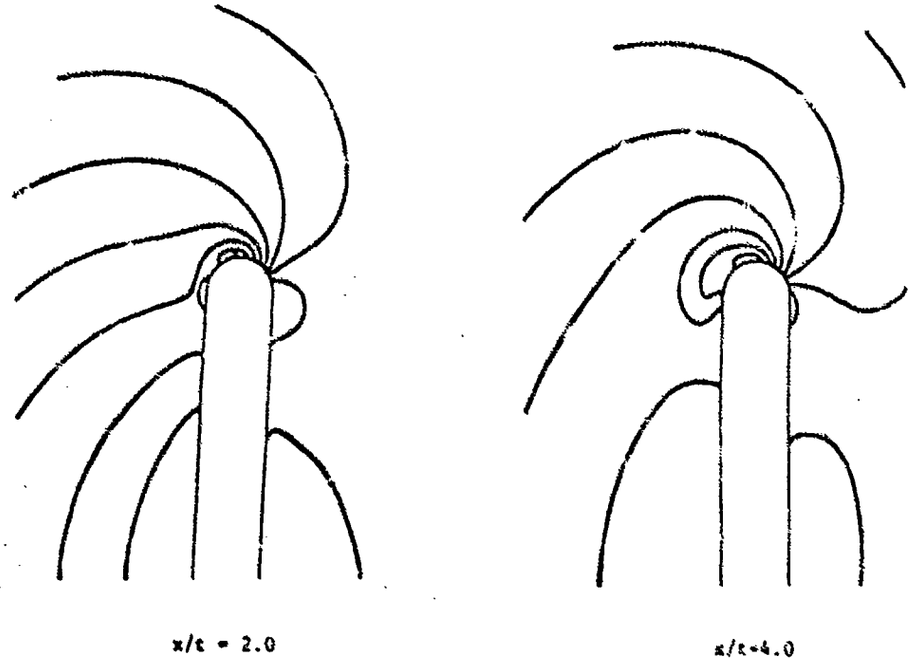

Fig. 12 - Transverse pressure field for rotating twisted blade.

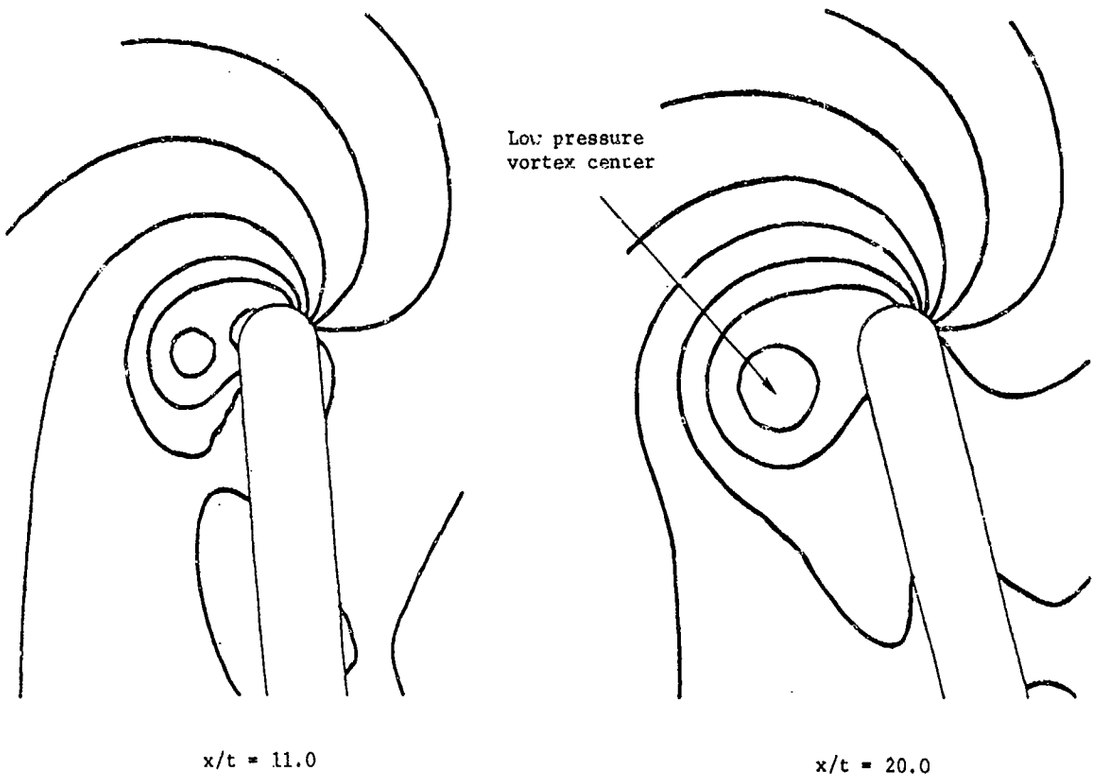

Fig. 13 - Transverse pressure field for rotating twisted blade.

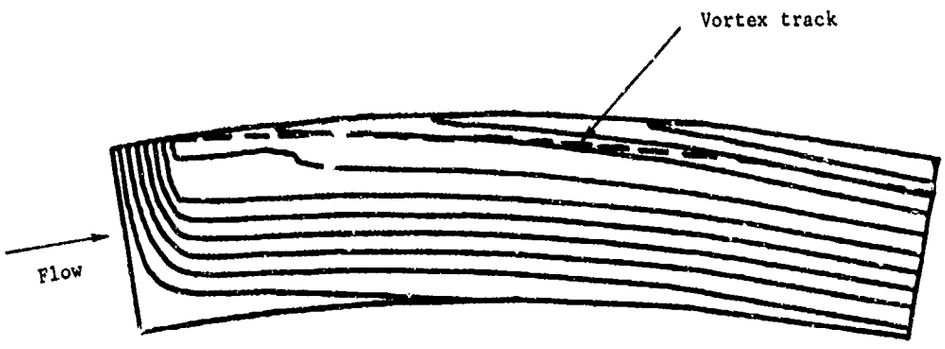

Fig. 14 - Streamwise contours of the pressure field (suction side).

DISCUSSION
of the paper
by T.R. Govindan, R. Levy and S.J. Shamroth

"COMPUTATION OF TIP VORTEX GENERATION PROCESS FOR SHIP PROPELLER BLADES"

DISCUSSION
by T.T. Huang

It would be much more beneficial to the readers if the authors could provide the numerical results in all the figures presented. We believe this requested revision will improve the quality of your paper, which is a significant contribution in the Conference.

Authors Reply

Figure 13 has been revised below to include computed values of the pressure coefficient (Cp) at the low pressure vortex center. These numerical values were computed for the particular geometry and flow conditions and may be typical of values that would be computed for other blade geometries and flow conditions.

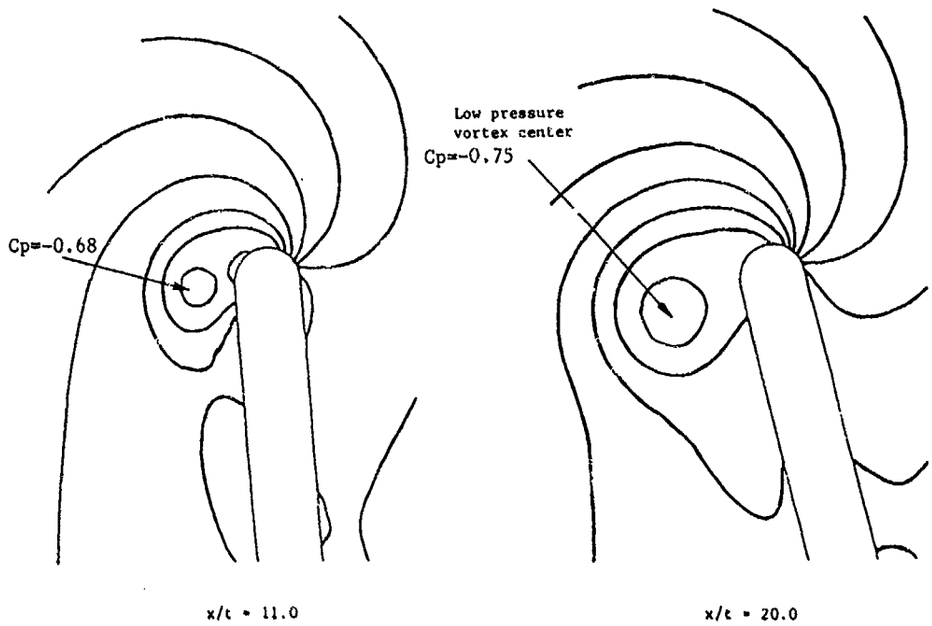

Figure 13 - Transverse pressure field for rotating twisted blade.

DISCUSSION
by V.C. Patel

1. The secondary flow and the tip vortex you have calculated is obviously driven by the imposed external flow. How was this selected, and is it representative of that existing on a propeller blade?

2. Since the streamwise pressure gradient is assumed to be known (equal to zero in all the present calculations), and the transverse pressure field is calculated (as shown in Figures 12 and 13) by marching once in the downstream direction, is it not necessary to make additional sweeps of the solution domain to update the longitudinal pressure gradients?

Author's Reply

1. The secondary flow and tip vortex generation that has been computed is "driven" by the imposed free-stream boundary conditions, primarily the free-stream angle of attack (6 degrees) which was chosen to be representative of that existing on a propeller blade. As described in the paper, a streamwise pressure gradient field (obtained, for example, from solution of elliptic governing equations subject to downstream boundary conditions) can be imposed in the forward-marching procedure to include in the computation effects of downstream boundary conditions. Such an imposed streamwise pressure gradient field was not included in the present computations and was not necessary for the demonstration computations of the tip vortex generation process.

2. The treatment of the stremwise pressure gradient as known, in the streamwise momentum equation, is viewed as a physical approximation rather than a trial guess to be removed by interation. The present approximating euations determine a new 3D pressure field, consistent with the transverse momentum equations (Figure 12 and 13). Multiple streamwise sweeps of the flow domain are not needed to solve the set of approximate flow equations, since this set is a well posed initial-value problem, and consequently, these appoximations lead to considerable economy in the solution procedure.

The set of approximate equations solved by the forward-marching procedure contain in them the flow features of tip vortex generation. These are the generation and roll-up of the tip vortex, the large secondary velocities associated with the tip vortex, and the distortion of the primary velocity field and pressure field by the tip vortex; all of which are present in the flow predictions given in the paper.

Not included in the present approximating equations is the effect of the perturbed streamwise pressure gradient or streamwise momentum balance due to the computed pressure field. This effect could be included by solving the Navier-Stokes equations and would be included if a convergent "guess and correct" multiple-sweep iteration procedure were devised such that the (corrected) pressure field computed from the transverse momentum equations converged to that assumed for the streamwise momentum equation. In either case, the approximating equations being solved are elliptic and subject to downstream boundary conditions. In general, elliptic equations are far more costly to solve than well-posed initial value problems.

LIST OF PARTICIPANTS

ALAEZ, Jose A., Canal De Experiencias Hidrodinamicas De El Pardo, Madrid,SPAIN
ANGELL, Thomas S., University of Delaware, Newark, DE, USA
ANKUDINOV, V., Tracor Hydronautics Inc, Laurel, MD, USA
ANTHONY, Douglas G., David Taylor Naval Ship R&D Center, Bethesda, MD, USA
BAAR, Job J.H., Brunel University, Uxbridge, Middlesex,UK
BAITIS, Eric A., David Taylor Naval Ship R&D Center, Bethesda, MD, USA
BARNELL, Alexander, David Taylor Naval Ship R&D Center, Bethesda, MD, USA
BAUBEAU, Robert, Bassin D'Essais Des Carenes, Paris, FRANCE
BECK, Robert F., University of Michigan, Ann Arbor, Michigan, USA
BENTSON, James, Polytechnic Institute of New York, Farmingdale, NY, USA
BORDA, Gary, David Taylor Naval Ship R&D Center, Bethesda, MD, USA
BOURIANOFF, G., Austin Research Assoc., Austin, TX, USA
BRABANSKI, M.L., David Taylor Naval Ship R&D Center, Bethesda, MD, USA
BREIT, Stephen R., Massachussetts Institute of Technology, Cambridge, MA, USA
BRESLIN, John, Davidson Laboratory, Stevens Institute, Hoboken, NJ, USA
CALDEIRA-SARAIVA, F., British Maritime Technology Ltd., Wallsend, UK
CALISAL, Sander, University of British Columbia, Vancouver, BC, CANADA
CARRIER, George, Harvard University, Cambridge, MA, USA
CHAMBERLAIN, Robert R., University of Alabama, University, AL, USA
CHANG, Ming, David Taylor Naval Ship R&D Center, Bethesda, MD, USA
CHEN, Benjamin Y., David Taylor Naval Ship R&D Center, Bethesda, MD, USA
CHEN, Hamn-Ching, The University of Iowa, Iowa City, IA, USA
CHENG, Bill, David Taylor Naval Ship R&D Center, Bethesda, MD, USA
CHOI, Hang S., Massachussetts Institute of Technology, Cambridge, MA, USA
CIESLOWSKI, Daniel S., David Taylor Naval Ship R&D Center, Bethesda, MD, USA
CLEMENT, A., Laboratoire d'Hydrodynamique Navale, ENSM, Nantes, FRANCE
CLEMENT,Marie, Bassin d'Essais des Carenes, Paris, FRANCE
CODER, David W., David Taylor Naval Ship R&D Center, Bethesda, MD, USA
COLEMAN, R.M., David Taylor Naval Ship R&D Center, Bethesda, MD, USA
CORDONNIER, Jean-Pierre, Laboratoire d' Hydrodynamique Navale, ENSM, Nantes, FRANCE
COX, Bruce D., Hydrodynamics Research Associates, Rockville, MD, USA
COX, Geoffrey G., David Taylor Naval Ship R&D Center, Bethesda, MD, USA
DAI, Charles M., David Taylor Naval Ship R&D Center, Bethesda, MD, USA
DAY, William G., David Taylor Naval Ship R&D Center, Bethesda, MD, USA
DEAN, Janet, David Taylor Naval Ship R&D Center, Bethesda, MD, USA
DE RUITER, Johan C.C., Delft Hydraulics Laboratory, Delft, THE NETHERLANDS
DERN, Jean Claude, Bassin D'Essais Des Carenes, Paris, FRANCE
DOBAY, Gabor F., David Taylor Naval Ship R&D Center, Bethesda, MD, USA
EGGERS, Klaus, Institut fur Schiffbau der Universitat Hamburg, Hamburg, FRG
ETTER, Robert, David Taylor Naval Ship R&D Center, Bethesda, MD, USA
FERRANT, Pierre, Laboratoire d'Hydrodynamique Navale, ENSM, Nantes, FRANCE
FISHER, Stephen, David Taylor Naval Ship R&D Center, Bethesda, MD, USA
FUJINO, Masataka, University of Tokyo, Tokyo, JAPAN
GALLAGHER, P., University of Glasgow, Hydrodynamics Lab., Glasgow, UK
GARCIA-GOMEZ, Amadeo, Canal De Experiencias Hidrodinamicas De El Pardo, Madrid, SPAIN
GOVINDAN, T.R., Scientific Research Associates, Glastonbury, CT, USA
GRAHAM, Ross W., Defence Research Est. Atlantic, Dartmouth, NS, CANADA
GRANVILLE, Paul, David Taylor Naval Ship R&D Center, Bethesda, MD, USA
GREELEY, David S., Atlantic Applied Research Corp., Burlington, MA, USA

GREENHOW, Martin, University of Manchester, Manchester, UK
GROVES, Nancy C., David Taylor Naval Ship R&D Center, Bethesda, MD, USA
GU, Mao-Xiang, China Ship Scientific Research Center, Wuxi, Tiangsu, CHINA
HAUSSLING, Henry J., David Taylor Naval Ship R&D Center, Bethesda, MD, USA
HAWKINS, Seth, David Taylor Naval Ship R&D Center, Bethesda, MD, USA
HENRY, Charles J., Electric Boat Div., General Dynamics Corp., Groton, CT, USA
HERMANS, Aad J., Delft University of Technology, Delft, THE NETHERLANDS
HIRT, Cyril W., Flow Science, Inc., Los Alamos, NM, USA
HOCQUET, Philippe, Bassin D'Essais Des Carenes, Paris, FRANCE
HOFFMAN, Gilbert H., ARL, Penn State University, State College, PA, USA
HONG, Young, David Taylor Naval Ship R&D Center, Bethesda, MD, USA
HSIAO, George C., University of Delaware, Newark, DE, USA
HSIUNG, Prof. C.C., Technical University of Nova Scotia, Halifax, NS, CANADA
HSU, Chun Che, David Taylor Naval Ship R&D Center, Bethesda, MD, USA
HUANG, Thomas T., David Taylor Naval Ship R&D Center, Bethesda, MD, USA
HUIJSMANS, R.H.M., Netherlands Ship Model Basin (MARIN), Wageningen, THE NETHERLANDS
HUNT, Lee M., Naval Studies Board, National Research Council, Washington, DC, USA
HURWITZ, Rae, David Taylor Naval Ship R&D Center, Bethesda, MD, USA
ITO, Nobuki, Hiroshima University, Hiroshima, JAPAN
JAMI, A., Groupe Hydrodynamique Navale, ENSTA, Palaiseau, FRANCE
JAYNE, John, David Taylor Naval Ship R&D Center, Bethesda, MD, USA
JENSEN, Peter S., Danish Maritime Institute, Lyngby, DENMARK
JOHNSTON, John W., David Taylor Naval Ship R&D Center, Bethesda, MD, USA
KARAFIATH, Gabor, David Taylor Naval Ship R&D Center, Bethesda, MD, USA
KIM, Yoon-Ho, David Taylor Naval Ship R&D Center, Bethesda, MD, USA
KLEINMAN, Ralph, University of Delaware, Newark, DE, USA
KNUTSON, Richard, David Taylor Naval Ship R&D Center, Bethesda, MD, USA
KOPP, Paul J., David Taylor Naval Ship R&D Center, Bethesda, MD, USA
KOSTILAINEN, Valter, Helsinki University of Technology, Espoo, FINLAND
KUX, Jurgen, Institut fur Schiffau der Universitat Hamburg, Hamburg, FRG
LAI, Ron J., David Taylor Naval Ship R&D Center, Bethesda, MD, USA
LANDWEBER, Louis, The University of Iowa, Iowa City, IA, USA
LEA, George K., National Science Foundation, Washington, DC, USA
LEE, Choung-Mook, Office of Naval Research, Arlington, VA, USA
LEE, Wah T., David Taylor Naval Ship R&D Center, Bethesda, MD, USA
LEE, Yu-Tai, David Taylor Naval Ship R&D Center, Bethesda, MD, USA
LENOIR, M., Groupe Hydrodynamique Navale, ENSTA, Palaiseau, FRANCE
LEVY, Ralph, Scientific Research Associates, Glastonbury, CT, USA
LIAPIS, S., University of Nichigan, Ann Arbor, MI, USA
LIN, Wan-Chin, David Taylor Naval Ship R&D Center, Bethesda, MD, USA
LIN, Woei-Min, ORI, Rockville, MD, USA
LIU, Han lieh, David Taylor Naval Ship R&D Center, Bethesda, MD, USA
LOVAAS, John H., A.S Veritec, Hovik, NORWAY
LUCAS, Thomas, David Taylor Naval Ship R&D Center, Bethesda, MD, USA
LUGT, Hans J., David Taylor Naval Ship R&D Center, Bethesda, MD, USA
MAIXNER, Michael R., Naval Postgraduate School Monterey, CA, USA
MARUO, Hajime, Yokohama National University, Yokohama, JAPAN
MC CARTHY, Justin H., David Taylor Naval Ship R&D Center, Bethesda, MD, USA
MC CREIGHT, William R., David Taylor Naval R&D Center, Bethesda, MD, USA
MC GREGOR, R.C., University of Glasgow, Hydrodynamics Lab, Glasgow, UK
MC KEE, Glenn, Davidson Laboratory, Stevens Institute, Hoboken, NJ, USA
MEI, Chiang C., Massachusetts Institute of Technology, Cambridge, MA, USA
MELLISH, Robert W., David Taylor Naval Ship R&D Center, Bethesda, MD, USA
MENDENHALL, Michael, Nielsen Engineering & Research Inc., Mountain View, CA, USA
MESSALLE, Richard, David Taylor Naval Ship R&D Center, Bethesda, MD, USA
MEYERS, William G., David Taylor Naval Ship R&D Center. Bethesda, MD, USA
MILLER, Ronald, David Taylor Naval Ship R&D Center, Bethesda, MD, USA
MIYATA, H., University of Tokyo, Tokyo, JAPAN
MOLIN, Bernard, I.F.P., Rueil - Malmaison, FRANCE
MONACELLA, Vincent J., David Taylor Naval Ship R&D Center, Bethesda, MD, USA
MORGAN, William B., David Taylor Naval Ship R&D Center, Bethesda, MD, USA
MORI, Kazu-hiro, Hiroshima University, Hiroshima, JAPAN
MOUSSOUROS, Minos, Naval Surface Weapons Center, White Oak, MD, USA
MUSKER, Anthony, J., Admiralty Research Est., Haslar, Gosport, Hampshire, UK
NAGLE, Toby, David Taylor Naval Ship R&D Center, Bethesda, MD, USA
NEU, Wayne, L., Virginia Polytechnic Institute, Blacksburg, VA, USA

NEWMAN, J. NICHOLAS, Massachusetts Institute of Technology, Cambridge, MA, USA
NOBLESSE, Francis, David Taylor Naval Ship R&D Center, Bethesda, MD, USA
O'DEA, John F., David Taylor Naval Ship R&D Center, Bethesda, MD, USA
OGIWARA, Seikoo, Ishikawajima-Harima Heavy Industries, Ltd., Yokohama, JAPAN
OKAN, M. Barbaros, British Maritime Technology Ltd. , Wallsend, UK
OVERTON, Margery F., North Carolina State University, Raleigh, NC, USA
PATEL, V.C., The University of Iowa, Iowa City, IA, USA
PETTERSEN, Bjornar, Massachussetts Instutute of Technology, Cambridge, MA, USA
PIQUET, J., Laboratoire d' Hydroynamique Navale, ENSM, Nantes, FRANCE
POT, G., Groupe Hydrodynamique Navale, ENSTA, Palaiseau, FRANCE
POWELL, Alan, David Taylor Naval Ship R&D Center, Bethesda, MD, USA
PUKHNACHOV, V.V., Lavrentyev Institute of Hydrodynamics, Novosibirsk, USSR
RAVEN, H., Netherlands Ship Model Basin (MARIN), Wageningen, THE NETHERLANDS
REED, Arthur M., David Taylor Naval Ship R&D Center, Bethesda, MD, USA
RICHER, Jean-Philipe, Institut de Recherche de la Construction Navale, Paris, FRANCE
RISPIN, Paul, David Taylor Naval Ship R&D Center, Bethesda, MD, USA
ROACHE, Patrick J., Ecodynamics Research Associates, Albuquerque, NM, USA
RODENHUIS, G. S., Danish Maritime Institute, Lyngby, DENMARK
ROMATE, Johan, Neth. Org. for Advancement of Pure Research (ZWO), The NETHERLANDS
ROTHBLUM, Richard, David Taylor Naval Ship R&D Center, Bethesda, MD, USA
RUBIN, Michael B., David Taylor Naval Ship R&D Center, Bethesda, MD, USA
SAEIDI, Sohrab, Electric Boat Div., General Dynamics Corp., Fitchville, CT, USA
SALVESEN, Nils, Science Applications Inc., Annapolis, MD, USA
SAVITSKY, Daniel, Davidson Laboratory, Stevens Institute, Hoboken, NJ, USA
SCHOT, Joanna, David Taylor Naval Ship R&D Center, Bethesda, MD, USA
SCHWARZENBERG, David A., David Taylor Naval Ship R&D Center, Bethesda, MD, USA
SCLAVOUNOS, Paul D., Massachussetts Institute of Technology, Cambridge, MA, USA
SEIDL, Ludwig, University of Hawaii, Honolulu, HI, USA
SHAMROTH, Stephen, Scientific Research Associates, Glastonbury, CT, USA
SHIDLOVSKY, Vsevolod P., Computing Center, USSR Academy of Sciences, Moscow, USSR
SILVER, Andrew L., David Taylor Naval Ship R&D Center, Bethesda, MD, USA
SPALDING Malcom L., University of Rhode Island, Kingston, R.I., USA
STERN, Fred, University of Iowa, Iowa City, IA, USA
STEWART, William I., David Taylor Naval Ship R&D Center, Bethesda, MD, USA
STORI, Massimo, INSEAN, Rome, ITALY
SUN, Beqi, China Ship Scientific Research Center, Wuxi, Tiangsu, CHINA
SUZUKI, Katsuo, The Defense Academy, Yokosuka JAPAN
TELSTE, John, David Taylor Naval Ship R&D Center, Bethesda, MD, USA
TZOU, K., Westinghouse Inc., Annapolis, MD, USA
URAM, Earl M., Naval Underwater Systems Center, New London, CT, USA
VAN ESELTINE, R., David Taylor Naval Ship R&D Center, Bethesda, MD, USA
VISONNEAU, M., Laboratoire d'Hydrodynamique Navale, ENSM, Nantes, FRANCE
WALDEN, David, David Taylor Naval Ship R&D Center, Bethesda, MD, USA
WALITT, Leonard, California Research and Technology Inc, Whatsworth, CA, USA
WANG, Henry T., Naval Research Laboratory, Washington, DC USA
WEHAUSEN, John V., University of California, Berkeley, CA USA
WILSON, Michael B., David Taylor Naval Ship R&D Center, Bethesda, MD, USA
YAMASAKI, Keiichi, University of Tokyo, Tokyo, JAPAN
YANG, Cheng I., David Taylor Naval Ship R&D Center, Bethesda, MD, USA
YEN, S. M., University of Illinois, Urbana, Illinois, USA
YEUNG, Ronald W., University of California, Berkeley, CA, USA
YIM BOHYUN, David Taylor Naval Ship R&D Center, Bethesda, MD, USA

Naval Studies Board

Robert J. Hermann, Chairman
United Technologies Corporation

Bernard F. Burke
Massachusetts Institute of Technology

George F. Carrier
Harvard University

Seymour J. Deitchman
Institute for Defense Analyses

Philip M. Diamond
The Aerospace Corporation

Ivan A. Getting
Los Angeles, CA

Willis M. Hawkins
Lockheed Corporation

John C. Hopkins
Los Alamos National Laboratory

Benjamin Huberman
Consultants International Group, Inc.

David W. Hyde
Science Applications International Corporation

Ray L. Leadabrand
Science Applications International Corporation

Reuven Leopold
NKF Engineering, Inc.

Chester M. McKinney, Jr.
Applied Research Laboratory

Vincent V. McRae
Rockville, MD

William J. Moran
Los Altos, CA

Robert M. Powell
Lockheed Missiles & Space Co., Inc.

Allan R. Robinson
Harvard University

John W. Rouse, Jr.
University of Texas at Arlington

Robert C. Spindel
Woods Hole Oceanographic Institution

Peter Swerling
Swerling, Manasse & Smith, Inc.

Raymond T. Tate
Raymond Tate Associates, Inc.

Staff

Lee M. Hunt
Staff Director